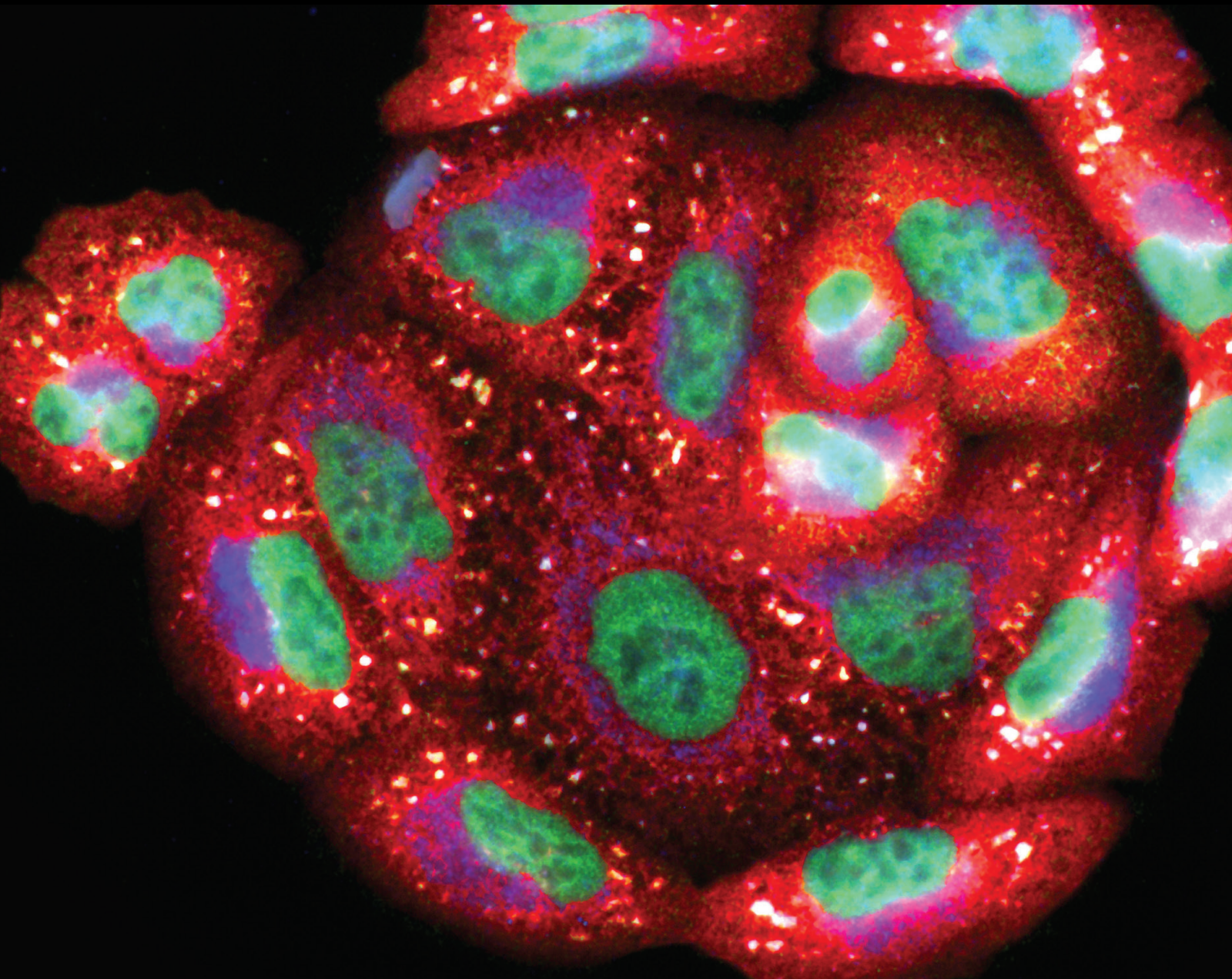


# Role of RNA Modifications in Oxidative Stress: From Mechanisms to Therapeutic Approaches

Lead Guest Editor: Tian Li

Guest Editors: Cornelia M. Wilson and Yazhou He





---

# **Role of RNA Modifications in Oxidative Stress: From Mechanisms to Therapeutic Approaches**

Oxidative Medicine and Cellular Longevity

---

**Role of RNA Modifications in  
Oxidative Stress: From Mechanisms to  
Therapeutic Approaches**

Lead Guest Editor: Tian Li

Guest Editors: Cornelia M. Wilson and Yazhou He



---

Copyright © 2024 Hindawi Limited. All rights reserved.

This is a special issue published in "Oxidative Medicine and Cellular Longevity" All articles are open access articles distributed under the Creative Commons Attribution License, which permits unrestricted use, distribution, and reproduction in any medium, provided the original work is properly cited.

# Chief Editor

Jeannette Vasquez-Vivar, USA

## Associate Editors

Amjad Islam Aqib, Pakistan  
Angel Catalá , Argentina  
Cinzia Domenicotti , Italy  
Janusz Gebicki , Australia  
Aldrin V. Gomes , USA  
Vladimir Jakovljevic , Serbia  
Thomas Kietzmann , Finland  
Juan C. Mayo , Spain  
Ryuichi Morishita , Japan  
Claudia Penna , Italy  
Sachchida Nand Rai , India  
Paola Rizzo , Italy  
Mithun Sinha , USA  
Daniele Vergara , Italy  
Victor M. Victor , Spain

## Academic Editors

Ammar AL-Farga , Saudi Arabia  
Mohd Adnan , Saudi Arabia  
Ivanov Alexander , Russia  
Fabio Altieri , Italy  
Daniel Dias Rufino Arcanjo , Brazil  
Peter Backx, Canada  
Amira Badr , Egypt  
Damian Bailey, United Kingdom  
Rengasamy Balakrishnan , Republic of Korea  
Jiaolin Bao, China  
Ji C. Bihl , USA  
Hareram Birla, India  
Abdelhakim Bouyahya, Morocco  
Ralf Braun , Austria  
Laura Bravo , Spain  
Matt Brody , USA  
Amadou Camara , USA  
Marcio Carochio , Portugal  
Peter Celec , Slovakia  
Giselle Cerchiaro , Brazil  
Arpita Chatterjee , USA  
Shao-Yu Chen , USA  
Yujie Chen, China  
Deepak Chhangani , USA  
Ferdinando Chiaradonna , Italy

Zhao Zhong Chong, USA  
Fabio Ciccarone, Italy  
Alin Ciobica , Romania  
Ana Cipak Gasparovic , Croatia  
Giuseppe Cirillo , Italy  
Maria R. Ciriolo , Italy  
Massimo Collino , Italy  
Manuela Corte-Real , Portugal  
Manuela Curcio, Italy  
Domenico D'Arca , Italy  
Francesca Danesi , Italy  
Claudio De Lucia , USA  
Damião De Sousa , Brazil  
Enrico Desideri, Italy  
Francesca Diomede , Italy  
Raul Dominguez-Perles, Spain  
Joël R. Drevet , France  
Grégory Durand , France  
Alessandra Durazzo , Italy  
Javier Egea , Spain  
Pablo A. Evelson , Argentina  
Mohd Farhan, USA  
Ioannis G. Fatouros , Greece  
Gianna Ferretti , Italy  
Swaran J. S. Flora , India  
Maurizio Forte , Italy  
Teresa I. Fortoul, Mexico  
Anna Fracassi , USA  
Rodrigo Franco , USA  
Juan Gambini , Spain  
Gerardo García-Rivas , Mexico  
Husam Ghanim, USA  
Jayeeta Ghose , USA  
Rajeshwary Ghosh , USA  
Lucia Gimeno-Mallench, Spain  
Anna M. Giudetti , Italy  
Daniela Giustarini , Italy  
José Rodrigo Godoy, USA  
Saeid Golbidi , Canada  
Guohua Gong , China  
Tilman Grune, Germany  
Solomon Habtemariam , United Kingdom  
Eva-Maria Hanschmann , Germany  
Md Saquib Hasnain , India  
Md Hassan , India

Tim Hofer , Norway  
John D. Horowitz, Australia  
Silvana Hrelia , Italy  
Dragan Hrnčić, Serbia  
Zebo Huang , China  
Zhao Huang , China  
Tariq Hussain , Pakistan  
Stephan Immenschuh , Germany  
Norsharina Ismail, Malaysia  
Franco J. L. , Brazil  
Sedat Kacar , USA  
Andleeb Khan , Saudi Arabia  
Kum Kum Khanna, Australia  
Neelam Khaper , Canada  
Ramoji Kosuru , USA  
Demetrios Kouretas , Greece  
Andrey V. Kozlov , Austria  
Chan-Yen Kuo, Taiwan  
Gaocai Li , China  
Guoping Li , USA  
Jin-Long Li , China  
Qiangqiang Li , China  
Xin-Feng Li , China  
Jialiang Liang , China  
Adam Lightfoot, United Kingdom  
Christopher Horst Lillig , Germany  
Paloma B. Liton , USA  
Ana Lloret , Spain  
Lorenzo Loffredo , Italy  
Camilo López-Alarcón , Chile  
Daniel Lopez-Malo , Spain  
Massimo Lucarini , Italy  
Hai-Chun Ma, China  
Nageswara Madamanchi , USA  
Kenneth Maiese , USA  
Marco Malaguti , Italy  
Steven McAnulty, USA  
Antonio Desmond McCarthy , Argentina  
Sonia Medina-Escudero , Spain  
Pedro Mena , Italy  
V́ctor M. Mendoza-Núñez , Mexico  
Lidija Milkovic , Croatia  
Alexandra Miller, USA  
Sara Missaglia , Italy

Premysl Mladenka , Czech Republic  
Sandra Moreno , Italy  
Trevor A. Mori , Australia  
Fabiana Morroni , Italy  
Ange Mouithys-Mickalad, Belgium  
Iordanis Mourouzis , Greece  
Ryoji Nagai , Japan  
Amit Kumar Nayak , India  
Abderrahim Nemmar , United Arab Emirates  
Xing Niu , China  
Cristina Nocella, Italy  
Susana Novella , Spain  
Hassan Obied , Australia  
Pál Pacher, USA  
Pasquale Pagliaro , Italy  
Dilipkumar Pal , India  
Valentina Pallottini , Italy  
Swapnil Pandey , USA  
Mayur Parmar , USA  
Vassilis Paschalis , Greece  
Keshav Raj Paudel, Australia  
Ilaria Peluso , Italy  
Tiziana Persichini , Italy  
Shazib Pervaiz , Singapore  
Abdul Rehman Phull, Republic of Korea  
Vincent Pialoux , France  
Alessandro Poggi , Italy  
Zsolt Radak , Hungary  
Dario C. Ramirez , Argentina  
Erika Ramos-Tovar , Mexico  
Sid D. Ray , USA  
Muneeb Rehman , Saudi Arabia  
Hamid Reza Rezvani , France  
Alessandra Ricelli, Italy  
Francisco J. Romero , Spain  
Joan Roselló-Catafau, Spain  
Subhadeep Roy , India  
Josep V. Rubert , The Netherlands  
Sumbal Saba , Brazil  
Kunihiro Sakuma, Japan  
Gabriele Saretzki , United Kingdom  
Luciano Saso , Italy  
Nadja Schroder , Brazil

Anwen Shao , China  
Iman Sherif, Egypt  
Salah A Sheweita, Saudi Arabia  
Xiaolei Shi, China  
Manjari Singh, India  
Giulia Sita , Italy  
Ramachandran Srinivasan , India  
Adrian Sturza , Romania  
Kuo-hui Su , United Kingdom  
Eisa Tahmasbpour Marzouni , Iran  
Hailiang Tang, China  
Carla Tatone , Italy  
Shane Thomas , Australia  
Carlo Gabriele Tocchetti , Italy  
Angela Trovato Salinaro, Italy  
Rosa Tundis , Italy  
Kai Wang , China  
Min-qi Wang , China  
Natalie Ward , Australia  
Grzegorz Wegrzyn, Poland  
Philip Wenzel , Germany  
Guangzhen Wu , China  
Jianbo Xiao , Spain  
Qiongming Xu , China  
Liang-Jun Yan , USA  
Guillermo Zalba , Spain  
Jia Zhang , China  
Junmin Zhang , China  
Junli Zhao , USA  
Chen-he Zhou , China  
Yong Zhou , China  
Mario Zoratti , Italy

# Contents

---

**Retracted: The Risk Model Based on the Three Oxidative Stress-Related Genes Evaluates the Prognosis of LAC Patients**

Oxidative Medicine and Cellular Longevity

Retraction (1 page), Article ID 9803802, Volume 2024 (2024)

**Retracted: LINC00092 Modulates Oxidative Stress and Glycolysis of Breast Cancer Cells via Pyruvate Carboxylase-Mediated AKT/mTOR Pathway**

Oxidative Medicine and Cellular Longevity

Retraction (1 page), Article ID 9864513, Volume 2023 (2023)

**Retracted: Targeted Diagnosis, Therapeutic Monitoring, and Assessment of Atherosclerosis Based on Mesoporous Silica Nanoparticles Coated with cRGD-Platelets**

Oxidative Medicine and Cellular Longevity

Retraction (1 page), Article ID 9850592, Volume 2023 (2023)

**Retracted: Identification of MMP9 as a Novel Biomarker to Mitochondrial Metabolism Disorder and Oxidative Stress in Calcific Aortic Valve Stenosis**

Oxidative Medicine and Cellular Longevity

Retraction (1 page), Article ID 9831674, Volume 2023 (2023)

**Retracted: Allicin Inhibits Osteosarcoma Growth by Promoting Oxidative Stress and Autophagy via the Inactivation of the lncRNA MALAT1-miR-376a-Wnt/ $\beta$ -Catenin Signaling Pathway**

Oxidative Medicine and Cellular Longevity

Retraction (1 page), Article ID 9817464, Volume 2023 (2023)

**Retracted: Identification of Nine M6A-Related Long Noncoding RNAs as Prognostic Signatures Associated with Oxidative Stress in Oral Cancer Based on Data from The Cancer Genome Atlas**

Oxidative Medicine and Cellular Longevity

Retraction (1 page), Article ID 9796081, Volume 2023 (2023)

**Retracted: Inflammation and Oxidative Stress Role of S100A12 as a Potential Diagnostic and Therapeutic Biomarker in Acute Myocardial Infarction**

Oxidative Medicine and Cellular Longevity

Retraction (1 page), Article ID 9789872, Volume 2023 (2023)

**Retracted: ZNF354C Mediated by DNMT1 Ameliorates Lung Ischemia-Reperfusion Oxidative Stress Injury by Reducing TFPI Promoter Methylation to Upregulate TFPI**

Oxidative Medicine and Cellular Longevity

Retraction (1 page), Article ID 9785630, Volume 2023 (2023)

**Retracted: Homeobox A1 Facilitates Immune Escape and Alleviates Oxidative Stress in Lung Adenocarcinoma**

Oxidative Medicine and Cellular Longevity

Retraction (1 page), Article ID 9758648, Volume 2023 (2023)



**Retracted: Exosomal miR-27b-3p Derived from Hypoxic Cardiac Microvascular Endothelial Cells Alleviates Rat Myocardial Ischemia/Reperfusion Injury through Inhibiting Oxidative Stress-Induced Pyroptosis via Foxo1/GSDMD Signaling**

Oxidative Medicine and Cellular Longevity

Retraction (1 page), Article ID 9754765, Volume 2023 (2023)

**Retracted: Exploring the Temporal Correlation of Sarcopenia with Bone Mineral Density and the Effects of Osteoblast-Derived Exosomes on Myoblasts through an Oxidative Stress-Related Gene**

Oxidative Medicine and Cellular Longevity

Retraction (1 page), Article ID 9832387, Volume 2023 (2023)

**Retracted: Oxidative-Damaged Mitochondria Activate GABARAPL1-Induced NLRP3 Inflammasomes in an Autophagic-Exosome Manner after Acute Myocardial Ischemia**

Oxidative Medicine and Cellular Longevity

Retraction (1 page), Article ID 9824094, Volume 2023 (2023)

**Retracted: Chrysophanol Ameliorates Hemin-Induced Oxidative Stress and Endoplasmic Reticulum Stress by Regulating MicroRNA-320-5p/Wnt3a Pathway in HT22 Cells**

Oxidative Medicine and Cellular Longevity

Retraction (1 page), Article ID 9813195, Volume 2023 (2023)

**Retracted: PTBP1 as a Promising Predictor of Poor Prognosis by Regulating Cell Proliferation, Immunosuppression, and Drug Sensitivity in SARC**

Oxidative Medicine and Cellular Longevity

Retraction (1 page), Article ID 9821803, Volume 2023 (2023)

**Retracted: Knockdown of miR-372-3p Inhibits the Development of Diabetic Cardiomyopathy by Accelerating Angiogenesis via Activating the PI3K/AKT/mTOR/HIF-1 $\alpha$  Signaling Pathway and Suppressing Oxidative Stress**

Oxidative Medicine and Cellular Longevity

Retraction (1 page), Article ID 9819824, Volume 2023 (2023)

**Retracted: Leukemia Inhibitory Factor Facilitates Self-Renewal and Differentiation and Attenuates Oxidative Stress of BMSCs by Activating PI3K/AKT Signaling**

Oxidative Medicine and Cellular Longevity

Retraction (1 page), Article ID 9819142, Volume 2023 (2023)

**Retracted: Identification of ATG7 as a Regulator of Proferroptosis and Oxidative Stress in Osteosarcoma**

Oxidative Medicine and Cellular Longevity

Retraction (1 page), Article ID 9819050, Volume 2023 (2023)

**Retracted: LINC00958 Inhibits Autophagy of Bladder Cancer Cells via Sponge Adsorption of miR-625-5p to Promote Tumor Angiogenesis and Oxidative Stress**

Oxidative Medicine and Cellular Longevity

Retraction (1 page), Article ID 9812826, Volume 2023 (2023)

## Contents

**Retracted: Circular RNA hsa\_circ\_0002360 Promotes Proliferation and Invasion and Inhibits Oxidative Stress in Gastric Cancer by Sponging miR-629-3p and Regulating the PDLIM4 Expression**  
Oxidative Medicine and Cellular Longevity  
Retraction (1 page), Article ID 9793618, Volume 2023 (2023)

**Retracted: Siglec-15 Regulates the Inflammatory Response and Polarization of Tumor-Associated Macrophages in Pancreatic Cancer by Inhibiting the cGAS-STING Signaling Pathway**  
Oxidative Medicine and Cellular Longevity  
Retraction (1 page), Article ID 9793031, Volume 2023 (2023)

**Retracted: Decreased Polymorphonuclear Myeloid-Derived Suppressor Cells and ROS Production Correlated Closely with Bronchopulmonary Dysplasia in Preterm Infants**  
Oxidative Medicine and Cellular Longevity  
Retraction (1 page), Article ID 9769486, Volume 2023 (2023)

**Retracted: miR-124-3p Delivered Using Exosomes Attenuates the Keratinocyte Response to IL-17A Stimulation in Psoriasis**  
Oxidative Medicine and Cellular Longevity  
Retraction (1 page), Article ID 9876751, Volume 2023 (2023)

**Retracted: ZFP36 Inhibits Tumor Progression of Human Prostate Cancer by Targeting CDK6 and Oxidative Stress**  
Oxidative Medicine and Cellular Longevity  
Retraction (1 page), Article ID 9865647, Volume 2023 (2023)

**Retracted: Novel Therapeutic Mechanism of Adipose-Derived Mesenchymal Stem Cells in Osteoarthritis via Upregulation of BTG2**  
Oxidative Medicine and Cellular Longevity  
Retraction (1 page), Article ID 9860569, Volume 2023 (2023)

**Retracted: Breast Cancer Exosome-Derived miR-425-5p Induces Cancer-Associated Fibroblast-Like Properties in Human Mammary Fibroblasts by TGF $\beta$ 1/ROS Signaling Pathway**  
Oxidative Medicine and Cellular Longevity  
Retraction (1 page), Article ID 9857678, Volume 2023 (2023)

**Retracted: Delicaflavone Represses Lung Cancer Growth by Activating Antitumor Immune Response through N6-Methyladenosine Transferases and Oxidative Stress**  
Oxidative Medicine and Cellular Longevity  
Retraction (1 page), Article ID 9856261, Volume 2023 (2023)



**Retracted: Macrophage-Derived Exosomes in TLR9 $^{-/-}$  Mice Ameliorate Sepsis-Induced Mitochondrial Oxidative Stress and Apoptosis in Cardiomyocytes**  
Oxidative Medicine and Cellular Longevity  
Retraction (1 page), Article ID 9846950, Volume 2023 (2023)

**Retracted: miR-494-3p Promotes Erastin-Induced Ferroptosis by Targeting REST to Activate the Interplay between SP1 and ACSL4 in Parkinson's Disease**

Oxidative Medicine and Cellular Longevity




Retraction (1 page), Article ID 9846028, Volume 2023 (2023)

**[Retracted] Breast Cancer Exosome-Derived miR-425-5p Induces Cancer-Associated Fibroblast-Like Properties in Human Mammary Fibroblasts by TGF $\beta$ 1/ROS Signaling Pathway**

Yue Zhu , He Dou, Yuqi Liu, Pingyang Yu, Fucheng Li, Youyu Wang, and Min Xiao 

Research Article (28 pages), Article ID 5266627, Volume 2022 (2022)

**[Retracted] Novel Therapeutic Mechanism of Adipose-Derived Mesenchymal Stem Cells in Osteoarthritis via Upregulation of BTG2**

Qinyan Yang , Li Jin, Qian Ding, Wei Hu, HaiBo Zou, Mingming Xiao, Keyuan Chen, Yue Yu, Jin Shang, Xiaolun Huang , and Yizhun Zhu 




Research Article (15 pages), Article ID 9252319, Volume 2022 (2022)

**[Retracted] miR-124-3p Delivered Using Exosomes Attenuates the Keratinocyte Response to IL-17A Stimulation in Psoriasis**

Simin Liu  and Jian Gong














Research Article (11 pages), Article ID 6264474, Volume 2022 (2022)

**[Retracted] LINC00958 Inhibits Autophagy of Bladder Cancer Cells via Sponge Adsorption of miR-625-5p to Promote Tumor Angiogenesis and Oxidative Stress**

Ying Xiao, Tao Wang, Xiao Cheng, Fangwen Liu, You Wu , Limin Ma , and Wenguang Li 



Research Article (14 pages), Article ID 2435114, Volume 2022 (2022)

**[Retracted] Identification of ATG7 as a Regulator of Proferroptosis and Oxidative Stress in Osteosarcoma**

Runyi Jiang , Shaohui He , Haiyi Gong , Yao Wang , Wei Wei , Jun Chen , Jinbo Hu , Chen Ye , Shuchen LiuHuang , Saiying Jin , Haifeng Wei , Wei Xu , and Jianru Xiao 




Research Article (19 pages), Article ID 8441676, Volume 2022 (2022)

**[Retracted] Macrophage-Derived Exosomes in TLR9<sup>-/-</sup> Mice Ameliorate Sepsis-Induced Mitochondrial Oxidative Stress and Apoptosis in Cardiomyocytes**

Xiang Li , Junyu Luo, Yanmei Li, Lu Jia, Yuejin Li, Shili Ye, Lanlan Liu, Yanxuan Yu, Yonggang Lu, and Yunpeng Luan 

Research Article (13 pages), Article ID 5719974, Volume 2022 (2022)






**[Retracted] Oxidative-Damaged Mitochondria Activate GABARAPL1-Induced NLRP3 Inflammasomes in an Autophagic-Exosome Manner after Acute Myocardial Ischemia**

Tiechun Zhang, Dongyao Hou, Jianrong He, Xue Zeng, Ruixue Liu, Liangming Liu, Tao Li, Yingbin Xiao, Ruiyan Ma , He Huang , and Chenyang Duan 

Research Article (19 pages), Article ID 7958542, Volume 2022 (2022)





## Contents

**[Retracted] Targeted Diagnosis, Therapeutic Monitoring, and Assessment of Atherosclerosis Based on Mesoporous Silica Nanoparticles Coated with cRGD-Platelets**

Wei Zhang , Zheng Lv, Yupeng Zhang, Subash C. B. Gopinath , Yi Yuan , Deyou Huang , and Liu Miao 





Research Article (19 pages), Article ID 6006601, Volume 2022 (2022)

**[Retracted] Identification of MMP9 as a Novel Biomarker to Mitochondrial Metabolism Disorder and Oxidative Stress in Calcific Aortic Valve Stenosis**

Cong Liu, Ruixue Liu, Zhezhe Cao, Qiao Guo, He Huang , Liangming Liu, Yingbin Xiao , Chenyang Duan , and Ruiyan Ma 


Research Article (14 pages), Article ID 3858871, Volume 2022 (2022)

**[Retracted] Decreased Polymorphonuclear Myeloid-Derived Suppressor Cells and ROS Production Correlated Closely with Bronchopulmonary Dysplasia in Preterm Infants**

Wangkai Liu , Sitao Li, Yushan Li, Wei Shen, Haitian Chen, Xiaoyu Li, Linnuan Cai, Fan Wu, Yumei Liu , Qiong Meng , and Xiaoyun Jiang 












Research Article (8 pages), Article ID 9010354, Volume 2022 (2022)

**[Retracted] Knockdown of miR-372-3p Inhibits the Development of Diabetic Cardiomyopathy by Accelerating Angiogenesis via Activating the PI3K/AKT/mTOR/HIF-1 $\alpha$  Signaling Pathway and Suppressing Oxidative Stress**

Zhimin Han, Danyang Zhao, Mengfan Han, Rongjin Zhang, and Yongmei Hao 




Research Article (11 pages), Article ID 4342755, Volume 2022 (2022)

**[Retracted] Exploring the Temporal Correlation of Sarcopenia with Bone Mineral Density and the Effects of Osteoblast-Derived Exosomes on Myoblasts through an Oxidative Stress-Related Gene**

Jingsong Chen , Jie Shen , Xili Yang , Huiting Tan , Ronghua Yang , Cuiying Mo , Ying Wang , Xiaojun Luan , Wenhua Huang , Guoqiang Chen , and Xuejuan Xu 


Research Article (18 pages), Article ID 9774570, Volume 2022 (2022)

**[Retracted] ZFP36 Inhibits Tumor Progression of Human Prostate Cancer by Targeting CDK6 and Oxidative Stress**

Dongbo Yuan, Yinyi Fang, Weiming Chen, Kehua Jiang, Guohua Zhu, Wei Wang, Wei Zhang, Ganhua You , Zhenyu Jia , and Jianguo Zhu 




Research Article (24 pages), Article ID 3611540, Volume 2022 (2022)

**[Retracted] Siglec-15 Regulates the Inflammatory Response and Polarization of Tumor-Associated Macrophages in Pancreatic Cancer by Inhibiting the cGAS-STING Signaling Pathway**

HuaGen Li, RongXuan Zhu, XiaoLong Liu, Kai Zhao, and DeFei Hong 








Research Article (14 pages), Article ID 3341038, Volume 2022 (2022)

**[Retracted] Leukemia Inhibitory Factor Facilitates Self-Renewal and Differentiation and Attenuates Oxidative Stress of BMSCs by Activating PI3K/AKT Signaling**

Youde Liang , Ruiping Zhou, Xin Liu , Lin You, Chang Chen, Xiaoling Ye, Wei Wei, Jie Liu, Jiawei Dai, Kaixiong Li, and Xiangxiang Zhao 



Research Article (28 pages), Article ID 5772509, Volume 2022 (2022)

**[Retracted] Inflammation and Oxidative Stress Role of S100A12 as a Potential Diagnostic and Therapeutic Biomarker in Acute Myocardial Infarction**

Jian Xie , Changjun Luo , Binhai Mo , Yunhua Lin , Guoqing Liu , Xiantao Wang , and Lang Li 




Research Article (19 pages), Article ID 2633123, Volume 2022 (2022)

**[Retracted] Circular RNA hsa\_circ\_0002360 Promotes Proliferation and Invasion and Inhibits Oxidative Stress in Gastric Cancer by Sponging miR-629-3p and Regulating the PDLIM4 Expression**

Zhengyuan Yu, Jing Lan, Wei Li, Li Jin, Feng Qi, Chen Yu , and Hao Zhu 


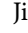
Research Article (20 pages), Article ID 2775433, Volume 2022 (2022)

**[Retracted] Delicaflavone Represses Lung Cancer Growth by Activating Antitumor Immune Response through N6-Methyladenosine Transferases and Oxidative Stress**

Xuewen Wang, Dafen Xu, Bing Chen, Dandan Huang, Zhijun Li, Yuxia Sui, Fei Lin, Hong Yao , Huang Yuan Li , and Xinhua Lin 

Research Article (16 pages), Article ID 8619275, Volume 2022 (2022)

**[Retracted] miR-494-3p Promotes Erastin-Induced Ferroptosis by Targeting REST to Activate the Interplay between SPI1 and ACSL4 in Parkinson's Disease**

Jianjun Ma , Xiaohuan Li, Yongyan Fan, Dawei Yang, Qi Gu, Dongsheng Li, Siyuan Chen, Shaopu Wu, Jinhua Zheng , Hongqi Yang, and Xue Li





Research Article (17 pages), Article ID 7671324, Volume 2022 (2022)

**[Retracted] Chrysophanol Ameliorates Hemin-Induced Oxidative Stress and Endoplasmic Reticulum Stress by Regulating MicroRNA-320-5p/Wnt3a Pathway in HT22 Cells**

Xu Zhao, Dongge Qiao, Dongsheng Guan, Kun Wang, and Yinglin Cui 



Research Article (19 pages), Article ID 9399658, Volume 2022 (2022)

**[Retracted] Identification of Nine M6A-Related Long Noncoding RNAs as Prognostic Signatures Associated with Oxidative Stress in Oral Cancer Based on Data from The Cancer Genome Atlas**

Li Shan , Ye Lu , Yihua Song, Xiaoli Zhu , Cheng-Cheng Xiang, Er-Dong Zuo, and Xu Cheng 


Research Article (18 pages), Article ID 9529814, Volume 2022 (2022)

**[Retracted] ZNF354C Mediated by DNMT1 Ameliorates Lung Ischemia-Reperfusion Oxidative Stress Injury by Reducing TFPI Promoter Methylation to Upregulate TFPI**

Qi Shi, Nana Feng, Qingyun Ma, Shaohua Wang, Huijun Zhang, Dayu Huang, Jiayuan Sun , and Meng Shi 

Research Article (18 pages), Article ID 7288729, Volume 2022 (2022)



**[Retracted] Exosomal miR-27b-3p Derived from Hypoxic Cardiac Microvascular Endothelial Cells Alleviates Rat Myocardial Ischemia/Reperfusion Injury through Inhibiting Oxidative Stress-Induced Pyroptosis via Foxo1/GSDMD Signaling**

Baojian Zhang, Chao Sun, Yaozhong Liu, Fan Bai, Tao Tu, and Qiming Liu 


Research Article (19 pages), Article ID 8215842, Volume 2022 (2022)

## Contents




**[Retracted] LINC00092 Modulates Oxidative Stress and Glycolysis of Breast Cancer Cells via Pyruvate Carboxylase-Mediated AKT/mTOR Pathway**

Wei Chen, Yushan Liu, Shaohong Kang, Xinying Lv, Wenfen Fu, Jie Zhang , and Chuangui Song   
Research Article (21 pages), Article ID 5215748, Volume 2022 (2022)





**[Retracted] Allicin Inhibits Osteosarcoma Growth by Promoting Oxidative Stress and Autophagy via the Inactivation of the lncRNA MALAT1-miR-376a-Wnt/ $\beta$ -Catenin Signaling Pathway**

Wenpeng Xie, Wenjie Chang, Xiaole Wang, Fei Liu, Xu Wang, Daotong Yuan, and Yongkui Zhang   
Research Article (14 pages), Article ID 4857814, Volume 2022 (2022)


**[Retracted] The Risk Model Based on the Three Oxidative Stress-Related Genes Evaluates the Prognosis of LAC Patients**

Qiang Guo , Xiao-Li Liu, Hua-Song Liu, Xiang-Yu Luo, Ye Yuan, Yan-Mei Ji, Tao Liu, Jia-Long Guo , and Jun Zhang   
Research Article (19 pages), Article ID 4022896, Volume 2022 (2022)

**[Retracted] PTBP1 as a Promising Predictor of Poor Prognosis by Regulating Cell Proliferation, Immunosuppression, and Drug Sensitivity in SARC**

Haiyi Gong , Aimin Jiang, Runyi Jiang, Yao Wang, Dan Zhang , Zhipeng Wu , and Jianru Xiao   
Research Article (26 pages), Article ID 5687238, Volume 2022 (2022)

**[Retracted] Homeobox A1 Facilitates Immune Escape and Alleviates Oxidative Stress in Lung Adenocarcinoma**

Fen Zhao, Hui Tian, Xinchao Liu, Yuanxiazhi Guan, Ying Zhu, Peng Ren, Jianbo Zhang, Yinjun Dong, and Lei Fu   
Research Article (34 pages), Article ID 4102666, Volume 2022 (2022)

## Retraction

# Retracted: The Risk Model Based on the Three Oxidative Stress-Related Genes Evaluates the Prognosis of LAC Patients

### Oxidative Medicine and Cellular Longevity

Received 8 January 2024; Accepted 8 January 2024; Published 9 January 2024

Copyright © 2024 Oxidative Medicine and Cellular Longevity. This is an open access article distributed under the Creative Commons Attribution License, which permits unrestricted use, distribution, and reproduction in any medium, provided the original work is properly cited.

This article has been retracted by Hindawi following an investigation undertaken by the publisher [1]. This investigation has uncovered evidence of one or more of the following indicators of systematic manipulation of the publication process:

- (1) Discrepancies in scope
- (2) Discrepancies in the description of the research reported
- (3) Discrepancies between the availability of data and the research described
- (4) Inappropriate citations
- (5) Incoherent, meaningless and/or irrelevant content included in the article
- (6) Manipulated or compromised peer review

The presence of these indicators undermines our confidence in the integrity of the article's content and we cannot, therefore, vouch for its reliability. Please note that this notice is intended solely to alert readers that the content of this article is unreliable. We have not investigated whether authors were aware of or involved in the systematic manipulation of the publication process.

Wiley and Hindawi regrets that the usual quality checks did not identify these issues before publication and have since put additional measures in place to safeguard research integrity.

We wish to credit our own Research Integrity and Research Publishing teams and anonymous and named external researchers and research integrity experts for contributing to this investigation.

The corresponding author, as the representative of all authors, has been given the opportunity to register their agreement or disagreement to this retraction. We have kept a record of any response received.

### References

- [1] Q. Guo, X. Liu, H. Liu et al., "The Risk Model Based on the Three Oxidative Stress-Related Genes Evaluates the Prognosis of LAC Patients," *Oxidative Medicine and Cellular Longevity*, vol. 2022, Article ID 4022896, 19 pages, 2022.

## *Retraction*

# **Retracted: LINC00092 Modulates Oxidative Stress and Glycolysis of Breast Cancer Cells via Pyruvate Carboxylase-Mediated AKT/mTOR Pathway**

### **Oxidative Medicine and Cellular Longevity**

Received 26 December 2023; Accepted 26 December 2023; Published 29 December 2023

Copyright © 2023 Oxidative Medicine and Cellular Longevity. This is an open access article distributed under the Creative Commons Attribution License, which permits unrestricted use, distribution, and reproduction in any medium, provided the original work is properly cited.

This article has been retracted by Hindawi, as publisher, following an investigation undertaken by the publisher [1]. This investigation has uncovered evidence of systematic manipulation of the publication and peer-review process. We cannot, therefore, vouch for the reliability or integrity of this article.

Please note that this notice is intended solely to alert readers that the peer-review process of this article has been compromised.

Wiley and Hindawi regret that the usual quality checks did not identify these issues before publication and have since put additional measures in place to safeguard research integrity.

We wish to credit our Research Integrity and Research Publishing teams and anonymous and named external researchers and research integrity experts for contributing to this investigation.

The corresponding author, as the representative of all authors, has been given the opportunity to register their agreement or disagreement to this retraction. We have kept a record of any response received.

### **References**

- [1] W. Chen, Y. Liu, S. Kang et al., “LINC00092 Modulates Oxidative Stress and Glycolysis of Breast Cancer Cells via Pyruvate Carboxylase-Mediated AKT/mTOR Pathway,” *Oxidative Medicine and Cellular Longevity*, vol. 2022, Article ID 5215748, 21 pages, 2022.



## *Retraction*

# **Retracted: Targeted Diagnosis, Therapeutic Monitoring, and Assessment of Atherosclerosis Based on Mesoporous Silica Nanoparticles Coated with cRGD-Platelets**

### **Oxidative Medicine and Cellular Longevity**

Received 26 December 2023; Accepted 26 December 2023; Published 29 December 2023

Copyright © 2023 Oxidative Medicine and Cellular Longevity. This is an open access article distributed under the Creative Commons Attribution License, which permits unrestricted use, distribution, and reproduction in any medium, provided the original work is properly cited.

This article has been retracted by Hindawi, as publisher, following an investigation undertaken by the publisher [1]. This investigation has uncovered evidence of systematic manipulation of the publication and peer-review process. We cannot, therefore, vouch for the reliability or integrity of this article.

Please note that this notice is intended solely to alert readers that the peer-review process of this article has been compromised.

Wiley and Hindawi regret that the usual quality checks did not identify these issues before publication and have since put additional measures in place to safeguard research integrity.

We wish to credit our Research Integrity and Research Publishing teams and anonymous and named external researchers and research integrity experts for contributing to this investigation.

The corresponding author, as the representative of all authors, has been given the opportunity to register their agreement or disagreement to this retraction. We have kept a record of any response received.

### **References**

- [1] W. Zhang, Z. Lv, Y. Zhang et al., “Targeted Diagnosis, Therapeutic Monitoring, and Assessment of Atherosclerosis Based on Mesoporous Silica Nanoparticles Coated with cRGD-Platelets,” *Oxidative Medicine and Cellular Longevity*, vol. 2022, Article ID 6006601, 19 pages, 2022.

## *Retraction*

# **Retracted: Identification of *MMP9* as a Novel Biomarker to Mitochondrial Metabolism Disorder and Oxidative Stress in Calcific Aortic Valve Stenosis**

### **Oxidative Medicine and Cellular Longevity**

Received 26 December 2023; Accepted 26 December 2023; Published 29 December 2023

Copyright © 2023 Oxidative Medicine and Cellular Longevity. This is an open access article distributed under the Creative Commons Attribution License, which permits unrestricted use, distribution, and reproduction in any medium, provided the original work is properly cited.

This article has been retracted by Hindawi, as publisher, following an investigation undertaken by the publisher [1]. This investigation has uncovered evidence of systematic manipulation of the publication and peer-review process. We cannot, therefore, vouch for the reliability or integrity of this article.

Please note that this notice is intended solely to alert readers that the peer-review process of this article has been compromised.

Wiley and Hindawi regret that the usual quality checks did not identify these issues before publication and have since put additional measures in place to safeguard research integrity.

We wish to credit our Research Integrity and Research Publishing teams and anonymous and named external researchers and research integrity experts for contributing to this investigation.

The corresponding author, as the representative of all authors, has been given the opportunity to register their agreement or disagreement to this retraction. We have kept a record of any response received.

### **References**

- [1] C. Liu, R. Liu, Z. Cao et al., "Identification of *MMP9* as a Novel Biomarker to Mitochondrial Metabolism Disorder and Oxidative Stress in Calcific Aortic Valve Stenosis," *Oxidative Medicine and Cellular Longevity*, vol. 2022, Article ID 3858871, 14 pages, 2022.

## *Retraction*

# **Retracted: Allicin Inhibits Osteosarcoma Growth by Promoting Oxidative Stress and Autophagy via the Inactivation of the lncRNA MALAT1-miR-376a-Wnt/ $\beta$ -Catenin Signaling Pathway**

### **Oxidative Medicine and Cellular Longevity**

Received 26 December 2023; Accepted 26 December 2023; Published 29 December 2023

Copyright © 2023 Oxidative Medicine and Cellular Longevity. This is an open access article distributed under the Creative Commons Attribution License, which permits unrestricted use, distribution, and reproduction in any medium, provided the original work is properly cited.

This article has been retracted by Hindawi, as publisher, following an investigation undertaken by the publisher [1]. This investigation has uncovered evidence of systematic manipulation of the publication and peer-review process. We cannot, therefore, vouch for the reliability or integrity of this article.

Please note that this notice is intended solely to alert readers that the peer-review process of this article has been compromised.

Wiley and Hindawi regret that the usual quality checks did not identify these issues before publication and have since put additional measures in place to safeguard research integrity.

We wish to credit our Research Integrity and Research Publishing teams and anonymous and named external researchers and research integrity experts for contributing to this investigation.

The corresponding author, as the representative of all authors, has been given the opportunity to register their agreement or disagreement to this retraction. We have kept a record of any response received.

### **References**

- [1] W. Xie, W. Chang, X. Wang et al., "Allicin Inhibits Osteosarcoma Growth by Promoting Oxidative Stress and Autophagy via the Inactivation of the lncRNA MALAT1-miR-376a-Wnt/ $\beta$ -Catenin Signaling Pathway," *Oxidative Medicine and Cellular Longevity*, vol. 2022, Article ID 4857814, 14 pages, 2022.

## *Retraction*

# **Retracted: Identification of Nine M6A-Related Long Noncoding RNAs as Prognostic Signatures Associated with Oxidative Stress in Oral Cancer Based on Data from The Cancer Genome Atlas**

### **Oxidative Medicine and Cellular Longevity**

Received 26 December 2023; Accepted 26 December 2023; Published 29 December 2023

Copyright © 2023 Oxidative Medicine and Cellular Longevity. This is an open access article distributed under the Creative Commons Attribution License, which permits unrestricted use, distribution, and reproduction in any medium, provided the original work is properly cited.

This article has been retracted by Hindawi, as publisher, following an investigation undertaken by the publisher [1]. This investigation has uncovered evidence of systematic manipulation of the publication and peer-review process. We cannot, therefore, vouch for the reliability or integrity of this article.

Please note that this notice is intended solely to alert readers that the peer-review process of this article has been compromised.

Wiley and Hindawi regret that the usual quality checks did not identify these issues before publication and have since put additional measures in place to safeguard research integrity.

We wish to credit our Research Integrity and Research Publishing teams and anonymous and named external researchers and research integrity experts for contributing to this investigation.

The corresponding author, as the representative of all authors, has been given the opportunity to register their agreement or disagreement to this retraction. We have kept a record of any response received.

## **References**

- [1] L. Shan, Y. Lu, Y. Song et al., "Identification of Nine M6A-Related Long Noncoding RNAs as Prognostic Signatures Associated with Oxidative Stress in Oral Cancer Based on Data from The Cancer Genome Atlas," *Oxidative Medicine and Cellular Longevity*, vol. 2022, Article ID 9529814, 18 pages, 2022.

## *Retraction*

# **Retracted: Inflammation and Oxidative Stress Role of S100A12 as a Potential Diagnostic and Therapeutic Biomarker in Acute Myocardial Infarction**

### **Oxidative Medicine and Cellular Longevity**

Received 26 December 2023; Accepted 26 December 2023; Published 29 December 2023

Copyright © 2023 Oxidative Medicine and Cellular Longevity. This is an open access article distributed under the Creative Commons Attribution License, which permits unrestricted use, distribution, and reproduction in any medium, provided the original work is properly cited.

This article has been retracted by Hindawi, as publisher, following an investigation undertaken by the publisher [1]. This investigation has uncovered evidence of systematic manipulation of the publication and peer-review process. We cannot, therefore, vouch for the reliability or integrity of this article.

Please note that this notice is intended solely to alert readers that the peer-review process of this article has been compromised.

Wiley and Hindawi regret that the usual quality checks did not identify these issues before publication and have since put additional measures in place to safeguard research integrity.

We wish to credit our Research Integrity and Research Publishing teams and anonymous and named external researchers and research integrity experts for contributing to this investigation.

The corresponding author, as the representative of all authors, has been given the opportunity to register their agreement or disagreement to this retraction. We have kept a record of any response received.

### **References**

- [1] J. Xie, C. Luo, B. Mo et al., "Inflammation and Oxidative Stress Role of S100A12 as a Potential Diagnostic and Therapeutic Biomarker in Acute Myocardial Infarction," *Oxidative Medicine and Cellular Longevity*, vol. 2022, Article ID 2633123, 19 pages, 2022.

## *Retraction*

# **Retracted: ZNF354C Mediated by DNMT1 Ameliorates Lung Ischemia-Reperfusion Oxidative Stress Injury by Reducing TFPI Promoter Methylation to Upregulate TFPI**

### **Oxidative Medicine and Cellular Longevity**

Received 26 December 2023; Accepted 26 December 2023; Published 29 December 2023

Copyright © 2023 Oxidative Medicine and Cellular Longevity. This is an open access article distributed under the Creative Commons Attribution License, which permits unrestricted use, distribution, and reproduction in any medium, provided the original work is properly cited.

This article has been retracted by Hindawi, as publisher, following an investigation undertaken by the publisher [1]. This investigation has uncovered evidence of systematic manipulation of the publication and peer-review process. We cannot, therefore, vouch for the reliability or integrity of this article.

Please note that this notice is intended solely to alert readers that the peer-review process of this article has been compromised.

Wiley and Hindawi regret that the usual quality checks did not identify these issues before publication and have since put additional measures in place to safeguard research integrity.

We wish to credit our Research Integrity and Research Publishing teams and anonymous and named external researchers and research integrity experts for contributing to this investigation.

The corresponding author, as the representative of all authors, has been given the opportunity to register their agreement or disagreement to this retraction. We have kept a record of any response received.

### **References**

- [1] Q. Shi, N. Feng, Q. Ma et al., “ZNF354C Mediated by DNMT1 Ameliorates Lung Ischemia-Reperfusion Oxidative Stress Injury by Reducing TFPI Promoter Methylation to Upregulate TFPI,” *Oxidative Medicine and Cellular Longevity*, vol. 2022, Article ID 7288729, 18 pages, 2022.

## *Retraction*

# **Retracted: Homeobox A1 Facilitates Immune Escape and Alleviates Oxidative Stress in Lung Adenocarcinoma**

### **Oxidative Medicine and Cellular Longevity**

Received 26 December 2023; Accepted 26 December 2023; Published 29 December 2023

Copyright © 2023 Oxidative Medicine and Cellular Longevity. This is an open access article distributed under the Creative Commons Attribution License, which permits unrestricted use, distribution, and reproduction in any medium, provided the original work is properly cited.

This article has been retracted by Hindawi, as publisher, following an investigation undertaken by the publisher [1]. This investigation has uncovered evidence of systematic manipulation of the publication and peer-review process. We cannot, therefore, vouch for the reliability or integrity of this article.

Please note that this notice is intended solely to alert readers that the peer-review process of this article has been compromised.

Wiley and Hindawi regret that the usual quality checks did not identify these issues before publication and have since put additional measures in place to safeguard research integrity.

We wish to credit our Research Integrity and Research Publishing teams and anonymous and named external researchers and research integrity experts for contributing to this investigation.

The corresponding author, as the representative of all authors, has been given the opportunity to register their agreement or disagreement to this retraction. We have kept a record of any response received.

### **References**

- [1] F. Zhao, H. Tian, X. Liu et al., “Homeobox A1 Facilitates Immune Escape and Alleviates Oxidative Stress in Lung Adenocarcinoma,” *Oxidative Medicine and Cellular Longevity*, vol. 2022, Article ID 4102666, 34 pages, 2022.

## Retraction

# Retracted: Exosomal miR-27b-3p Derived from Hypoxic Cardiac Microvascular Endothelial Cells Alleviates Rat Myocardial Ischemia/Reperfusion Injury through Inhibiting Oxidative Stress-Induced Pyroptosis via Foxo1/GSDMD Signaling

### Oxidative Medicine and Cellular Longevity

Received 26 December 2023; Accepted 26 December 2023; Published 29 December 2023

Copyright © 2023 Oxidative Medicine and Cellular Longevity. This is an open access article distributed under the Creative Commons Attribution License, which permits unrestricted use, distribution, and reproduction in any medium, provided the original work is properly cited.

This article has been retracted by Hindawi, as publisher, following an investigation undertaken by the publisher [1]. This investigation has uncovered evidence of systematic manipulation of the publication and peer-review process. We cannot, therefore, vouch for the reliability or integrity of this article.

Please note that this notice is intended solely to alert readers that the peer-review process of this article has been compromised.

Wiley and Hindawi regret that the usual quality checks did not identify these issues before publication and have since put additional measures in place to safeguard research integrity.

We wish to credit our Research Integrity and Research Publishing teams and anonymous and named external researchers and research integrity experts for contributing to this investigation.

The corresponding author, as the representative of all authors, has been given the opportunity to register their agreement or disagreement to this retraction. We have kept a record of any response received.

## References

- [1] B. Zhang, C. Sun, Y. Liu, F. Bai, T. Tu, and Q. Liu, "Exosomal miR-27b-3p Derived from Hypoxic Cardiac Microvascular Endothelial Cells Alleviates Rat Myocardial Ischemia/Reperfusion Injury through Inhibiting Oxidative Stress-Induced Pyroptosis via Foxo1/GSDMD Signaling," *Oxidative Medicine and Cellular Longevity*, vol. 2022, Article ID 8215842, 19 pages, 2022.



## Retraction

# Retracted: Exploring the Temporal Correlation of Sarcopenia with Bone Mineral Density and the Effects of Osteoblast-Derived Exosomes on Myoblasts through an Oxidative Stress–Related Gene

### Oxidative Medicine and Cellular Longevity

Received 1 August 2023; Accepted 1 August 2023; Published 2 August 2023

Copyright © 2023 Oxidative Medicine and Cellular Longevity. This is an open access article distributed under the Creative Commons Attribution License, which permits unrestricted use, distribution, and reproduction in any medium, provided the original work is properly cited.

This article has been retracted by Hindawi following an investigation undertaken by the publisher [1]. This investigation has uncovered evidence of one or more of the following indicators of systematic manipulation of the publication process:

- (1) Discrepancies in scope
- (2) Discrepancies in the description of the research reported
- (3) Discrepancies between the availability of data and the research described
- (4) Inappropriate citations
- (5) Incoherent, meaningless and/or irrelevant content included in the article
- (6) Peer-review manipulation

The presence of these indicators undermines our confidence in the integrity of the article's content and we cannot, therefore, vouch for its reliability. Please note that this notice is intended solely to alert readers that the content of this article is unreliable. We have not investigated whether authors were aware of or involved in the systematic manipulation of the publication process.

Wiley and Hindawi regrets that the usual quality checks did not identify these issues before publication and have since put additional measures in place to safeguard research integrity.

We wish to credit our own Research Integrity and Research Publishing teams and anonymous and named external researchers and research integrity experts for contributing to this investigation.

The corresponding author, as the representative of all authors, has been given the opportunity to register their

agreement or disagreement to this retraction. We have kept a record of any response received.

### References

- [1] J. Chen, J. Shen, X. Yang et al., "Exploring the Temporal Correlation of Sarcopenia with Bone Mineral Density and the Effects of Osteoblast-Derived Exosomes on Myoblasts through an Oxidative Stress–Related Gene," *Oxidative Medicine and Cellular Longevity*, vol. 2022, Article ID 9774570, 18 pages, 2022.

## Retraction

# Retracted: Oxidative-Damaged Mitochondria Activate GABARAPL1-Induced NLRP3 Inflammasomes in an Autophagic-Exosome Manner after Acute Myocardial Ischemia

### Oxidative Medicine and Cellular Longevity

Received 1 August 2023; Accepted 1 August 2023; Published 2 August 2023

Copyright © 2023 Oxidative Medicine and Cellular Longevity. This is an open access article distributed under the Creative Commons Attribution License, which permits unrestricted use, distribution, and reproduction in any medium, provided the original work is properly cited.

This article has been retracted by Hindawi following an investigation undertaken by the publisher [1]. This investigation has uncovered evidence of one or more of the following indicators of systematic manipulation of the publication process:

- (1) Discrepancies in scope
- (2) Discrepancies in the description of the research reported
- (3) Discrepancies between the availability of data and the research described
- (4) Inappropriate citations
- (5) Incoherent, meaningless and/or irrelevant content included in the article
- (6) Peer-review manipulation

The presence of these indicators undermines our confidence in the integrity of the article's content and we cannot, therefore, vouch for its reliability. Please note that this notice is intended solely to alert readers that the content of this article is unreliable. We have not investigated whether authors were aware of or involved in the systematic manipulation of the publication process.

In addition, our investigation has also shown that one or more of the following human-subject reporting requirements has not been met in this article: ethical approval by an Institutional Review Board (IRB) committee or equivalent, patient/participant consent to participate, and/or agreement to publish patient/participant details (where relevant).

Wiley and Hindawi regrets that the usual quality checks did not identify these issues before publication and have since put additional measures in place to safeguard research integrity.

We wish to credit our own Research Integrity and Research Publishing teams and anonymous and named external researchers and research integrity experts for contributing to this investigation.

The corresponding author, as the representative of all authors, has been given the opportunity to register their agreement or disagreement to this retraction. We have kept a record of any response received.

### References

- [1] T. Zhang, D. Hou, J. He et al., "Oxidative-Damaged Mitochondria Activate GABARAPL1-Induced NLRP3 Inflammasomes in an Autophagic-Exosome Manner after Acute Myocardial Ischemia," *Oxidative Medicine and Cellular Longevity*, vol. 2022, Article ID 7958542, 19 pages, 2022.

## Retraction

# Retracted: Chrysophanol Ameliorates Hemin-Induced Oxidative Stress and Endoplasmic Reticulum Stress by Regulating MicroRNA-320-5p/Wnt3a Pathway in HT22 Cells

### Oxidative Medicine and Cellular Longevity

Received 1 August 2023; Accepted 1 August 2023; Published 2 August 2023

Copyright © 2023 Oxidative Medicine and Cellular Longevity. This is an open access article distributed under the Creative Commons Attribution License, which permits unrestricted use, distribution, and reproduction in any medium, provided the original work is properly cited.

This article has been retracted by Hindawi following an investigation undertaken by the publisher [1]. This investigation has uncovered evidence of one or more of the following indicators of systematic manipulation of the publication process:

- (1) Discrepancies in scope
- (2) Discrepancies in the description of the research reported
- (3) Discrepancies between the availability of data and the research described
- (4) Inappropriate citations
- (5) Incoherent, meaningless and/or irrelevant content included in the article
- (6) Peer-review manipulation

The presence of these indicators undermines our confidence in the integrity of the article's content and we cannot, therefore, vouch for its reliability. Please note that this notice is intended solely to alert readers that the content of this article is unreliable. We have not investigated whether authors were aware of or involved in the systematic manipulation of the publication process.

Wiley and Hindawi regrets that the usual quality checks did not identify these issues before publication and have since put additional measures in place to safeguard research integrity.

We wish to credit our own Research Integrity and Research Publishing teams and anonymous and named external researchers and research integrity experts for contributing to this investigation.

The corresponding author, as the representative of all authors, has been given the opportunity to register their

agreement or disagreement to this retraction. We have kept a record of any response received.

### References

- [1] X. Zhao, D. Qiao, D. Guan, K. Wang, and Y. Cui, "Chrysophanol Ameliorates Hemin-Induced Oxidative Stress and Endoplasmic Reticulum Stress by Regulating MicroRNA-320-5p/Wnt3a Pathway in HT22 Cells," *Oxidative Medicine and Cellular Longevity*, vol. 2022, Article ID 9399658, 19 pages, 2022.

## Retraction

# Retracted: PTBP1 as a Promising Predictor of Poor Prognosis by Regulating Cell Proliferation, Immunosuppression, and Drug Sensitivity in SARC

### Oxidative Medicine and Cellular Longevity

Received 20 June 2023; Accepted 20 June 2023; Published 21 June 2023

Copyright © 2023 Oxidative Medicine and Cellular Longevity. This is an open access article distributed under the Creative Commons Attribution License, which permits unrestricted use, distribution, and reproduction in any medium, provided the original work is properly cited.

This article has been retracted by Hindawi following an investigation undertaken by the publisher [1]. This investigation has uncovered evidence of one or more of the following indicators of systematic manipulation of the publication process:

- (1) Discrepancies in scope
- (2) Discrepancies in the description of the research reported
- (3) Discrepancies between the availability of data and the research described
- (4) Inappropriate citations
- (5) Incoherent, meaningless and/or irrelevant content included in the article
- (6) Peer-review manipulation

The presence of these indicators undermines our confidence in the integrity of the article's content and we cannot, therefore, vouch for its reliability. Please note that this notice is intended solely to alert readers that the content of this article is unreliable. We have not investigated whether authors were aware of or involved in the systematic manipulation of the publication process.

Wiley and Hindawi regrets that the usual quality checks did not identify these issues before publication and have since put additional measures in place to safeguard research integrity.

We wish to credit our own Research Integrity and Research Publishing teams and anonymous and named external researchers and research integrity experts for contributing to this investigation.

The corresponding author, as the representative of all authors, has been given the opportunity to register their agreement or disagreement to this retraction. We have kept a record of any response received.

### References

- [1] H. Gong, A. Jiang, R. Jiang et al., "PTBP1 as a Promising Predictor of Poor Prognosis by Regulating Cell Proliferation, Immunosuppression, and Drug Sensitivity in SARC," *Oxidative Medicine and Cellular Longevity*, vol. 2022, Article ID 5687238, 26 pages, 2022.

## Retraction

# Retracted: Knockdown of miR-372-3p Inhibits the Development of Diabetic Cardiomyopathy by Accelerating Angiogenesis via Activating the PI3K/AKT/mTOR/HIF-1 $\alpha$ Signaling Pathway and Suppressing Oxidative Stress

### Oxidative Medicine and Cellular Longevity

Received 20 June 2023; Accepted 20 June 2023; Published 21 June 2023

Copyright © 2023 Oxidative Medicine and Cellular Longevity. This is an open access article distributed under the Creative Commons Attribution License, which permits unrestricted use, distribution, and reproduction in any medium, provided the original work is properly cited.

This article has been retracted by Hindawi following an investigation undertaken by the publisher [1]. This investigation has uncovered evidence of one or more of the following indicators of systematic manipulation of the publication process:

- (1) Discrepancies in scope
- (2) Discrepancies in the description of the research reported
- (3) Discrepancies between the availability of data and the research described
- (4) Inappropriate citations
- (5) Incoherent, meaningless and/or irrelevant content included in the article
- (6) Peer-review manipulation

The presence of these indicators undermines our confidence in the integrity of the article's content and we cannot, therefore, vouch for its reliability. Please note that this notice is intended solely to alert readers that the content of this article is unreliable. We have not investigated whether authors were aware of or involved in the systematic manipulation of the publication process.

Wiley and Hindawi regrets that the usual quality checks did not identify these issues before publication and have since put additional measures in place to safeguard research integrity.

We wish to credit our own Research Integrity and Research Publishing teams and anonymous and named external researchers and research integrity experts for contributing to this investigation.

The corresponding author, as the representative of all authors, has been given the opportunity to register their agreement or disagreement to this retraction. We have kept a record of any response received.

### References

- [1] Z. Han, D. Zhao, M. Han, R. Zhang, and Y. Hao, "Knockdown of miR-372-3p Inhibits the Development of Diabetic Cardiomyopathy by Accelerating Angiogenesis via Activating the PI3K/AKT/mTOR/HIF-1 $\alpha$  Signaling Pathway and Suppressing Oxidative Stress," *Oxidative Medicine and Cellular Longevity*, vol. 2022, Article ID 4342755, 11 pages, 2022.

## Retraction

# Retracted: Leukemia Inhibitory Factor Facilitates Self-Renewal and Differentiation and Attenuates Oxidative Stress of BMSCs by Activating PI3K/AKT Signaling

### Oxidative Medicine and Cellular Longevity

Received 20 June 2023; Accepted 20 June 2023; Published 21 June 2023

Copyright © 2023 Oxidative Medicine and Cellular Longevity. This is an open access article distributed under the Creative Commons Attribution License, which permits unrestricted use, distribution, and reproduction in any medium, provided the original work is properly cited.

This article has been retracted by Hindawi following an investigation undertaken by the publisher [1]. This investigation has uncovered evidence of one or more of the following indicators of systematic manipulation of the publication process:

- (1) Discrepancies in scope
- (2) Discrepancies in the description of the research reported
- (3) Discrepancies between the availability of data and the research described
- (4) Inappropriate citations
- (5) Incoherent, meaningless and/or irrelevant content included in the article
- (6) Peer-review manipulation

The presence of these indicators undermines our confidence in the integrity of the article's content and we cannot, therefore, vouch for its reliability. Please note that this notice is intended solely to alert readers that the content of this article is unreliable. We have not investigated whether authors were aware of or involved in the systematic manipulation of the publication process.

Wiley and Hindawi regrets that the usual quality checks did not identify these issues before publication and have since put additional measures in place to safeguard research integrity.

We wish to credit our own Research Integrity and Research Publishing teams and anonymous and named

external researchers and research integrity experts for contributing to this investigation.

The corresponding author, as the representative of all authors, has been given the opportunity to register their agreement or disagreement to this retraction. We have kept a record of any response received.

### References

- [1] Y. Liang, R. Zhou, X. Liu et al., "Leukemia Inhibitory Factor Facilitates Self-Renewal and Differentiation and Attenuates Oxidative Stress of BMSCs by Activating PI3K/AKT Signaling," *Oxidative Medicine and Cellular Longevity*, vol. 2022, Article ID 5772509, 28 pages, 2022.

## Retraction

# Retracted: Identification of ATG7 as a Regulator of Proferroptosis and Oxidative Stress in Osteosarcoma

### Oxidative Medicine and Cellular Longevity

Received 20 June 2023; Accepted 20 June 2023; Published 21 June 2023

Copyright © 2023 Oxidative Medicine and Cellular Longevity. This is an open access article distributed under the Creative Commons Attribution License, which permits unrestricted use, distribution, and reproduction in any medium, provided the original work is properly cited.

This article has been retracted by Hindawi following an investigation undertaken by the publisher [1]. This investigation has uncovered evidence of one or more of the following indicators of systematic manipulation of the publication process:

- (1) Discrepancies in scope
- (2) Discrepancies in the description of the research reported
- (3) Discrepancies between the availability of data and the research described
- (4) Inappropriate citations
- (5) Incoherent, meaningless and/or irrelevant content included in the article
- (6) Peer-review manipulation

The presence of these indicators undermines our confidence in the integrity of the article's content and we cannot, therefore, vouch for its reliability. Please note that this notice is intended solely to alert readers that the content of this article is unreliable. We have not investigated whether authors were aware of or involved in the systematic manipulation of the publication process.

Wiley and Hindawi regrets that the usual quality checks did not identify these issues before publication and have since put additional measures in place to safeguard research integrity.

We wish to credit our own Research Integrity and Research Publishing teams and anonymous and named external researchers and research integrity experts for contributing to this investigation.

The corresponding author, as the representative of all authors, has been given the opportunity to register their agreement or disagreement to this retraction. We have kept a record of any response received.

### References

- [1] R. Jiang, S. He, H. Gong et al., "Identification of ATG7 as a Regulator of Proferroptosis and Oxidative Stress in Osteosarcoma," *Oxidative Medicine and Cellular Longevity*, vol. 2022, Article ID 8441676, 19 pages, 2022.

## Retraction

# Retracted: LINC00958 Inhibits Autophagy of Bladder Cancer Cells via Sponge Adsorption of miR-625-5p to Promote Tumor Angiogenesis and Oxidative Stress

### Oxidative Medicine and Cellular Longevity

Received 20 June 2023; Accepted 20 June 2023; Published 21 June 2023

Copyright © 2023 Oxidative Medicine and Cellular Longevity. This is an open access article distributed under the Creative Commons Attribution License, which permits unrestricted use, distribution, and reproduction in any medium, provided the original work is properly cited.

This article has been retracted by Hindawi following an investigation undertaken by the publisher [1]. This investigation has uncovered evidence of one or more of the following indicators of systematic manipulation of the publication process:

- (1) Discrepancies in scope
- (2) Discrepancies in the description of the research reported
- (3) Discrepancies between the availability of data and the research described
- (4) Inappropriate citations
- (5) Incoherent, meaningless and/or irrelevant content included in the article
- (6) Peer-review manipulation

The presence of these indicators undermines our confidence in the integrity of the article's content and we cannot, therefore, vouch for its reliability. Please note that this notice is intended solely to alert readers that the content of this article is unreliable. We have not investigated whether authors were aware of or involved in the systematic manipulation of the publication process.

In addition, our investigation has also shown that one or more of the following human-subject reporting requirements has not been met in this article: ethical approval by an Institutional Review Board (IRB) committee or equivalent, patient/participant consent to participate, and/or agreement to publish patient/participant details (where relevant).

Wiley and Hindawi regrets that the usual quality checks did not identify these issues before publication and have since put additional measures in place to safeguard research integrity.

We wish to credit our own Research Integrity and Research Publishing teams and anonymous and named external researchers and research integrity experts for contributing to this investigation.

The corresponding author, as the representative of all authors, has been given the opportunity to register their agreement or disagreement to this retraction. We have kept a record of any response received.

### References

- [1] Y. Xiao, T. Wang, X. Cheng et al., "LINC00958 Inhibits Autophagy of Bladder Cancer Cells via Sponge Adsorption of miR-625-5p to Promote Tumor Angiogenesis and Oxidative Stress," *Oxidative Medicine and Cellular Longevity*, vol. 2022, Article ID 2435114, 14 pages, 2022.



## Retraction

# Retracted: Circular RNA hsa\_circ\_0002360 Promotes Proliferation and Invasion and Inhibits Oxidative Stress in Gastric Cancer by Sponging miR-629-3p and Regulating the PDLIM4 Expression

### Oxidative Medicine and Cellular Longevity

Received 20 June 2023; Accepted 20 June 2023; Published 21 June 2023

Copyright © 2023 Oxidative Medicine and Cellular Longevity. This is an open access article distributed under the Creative Commons Attribution License, which permits unrestricted use, distribution, and reproduction in any medium, provided the original work is properly cited.

This article has been retracted by Hindawi following an investigation undertaken by the publisher [1]. This investigation has uncovered evidence of one or more of the following indicators of systematic manipulation of the publication process:

- (1) Discrepancies in scope
- (2) Discrepancies in the description of the research reported
- (3) Discrepancies between the availability of data and the research described
- (4) Inappropriate citations
- (5) Incoherent, meaningless and/or irrelevant content included in the article
- (6) Peer-review manipulation

The presence of these indicators undermines our confidence in the integrity of the article's content and we cannot, therefore, vouch for its reliability. Please note that this notice is intended solely to alert readers that the content of this article is unreliable. We have not investigated whether authors were aware of or involved in the systematic manipulation of the publication process.

In addition, our investigation has also shown that one or more of the following human-subject reporting requirements has not been met in this article: ethical approval by an Institutional Review Board (IRB) committee or equiva-

lent, patient/participant consent to participate, and/or agreement to publish patient/participant details (where relevant).

Wiley and Hindawi regrets that the usual quality checks did not identify these issues before publication and have since put additional measures in place to safeguard research integrity.

We wish to credit our own Research Integrity and Research Publishing teams and anonymous and named external researchers and research integrity experts for contributing to this investigation.

The corresponding author, as the representative of all authors, has been given the opportunity to register their agreement or disagreement to this retraction. We have kept a record of any response received.

### References

- [1] Z. Yu, J. Lan, W. Li et al., "Circular RNA hsa\_circ\_0002360 Promotes Proliferation and Invasion and Inhibits Oxidative Stress in Gastric Cancer by Sponging miR-629-3p and Regulating the PDLIM4 Expression," *Oxidative Medicine and Cellular Longevity*, vol. 2022, Article ID 2775433, 20 pages, 2022.

## Retraction

# Retracted: Siglec-15 Regulates the Inflammatory Response and Polarization of Tumor-Associated Macrophages in Pancreatic Cancer by Inhibiting the cGAS-STING Signaling Pathway

### Oxidative Medicine and Cellular Longevity

Received 20 June 2023; Accepted 20 June 2023; Published 21 June 2023

Copyright © 2023 Oxidative Medicine and Cellular Longevity. This is an open access article distributed under the Creative Commons Attribution License, which permits unrestricted use, distribution, and reproduction in any medium, provided the original work is properly cited.

This article has been retracted by Hindawi following an investigation undertaken by the publisher [1]. This investigation has uncovered evidence of one or more of the following indicators of systematic manipulation of the publication process:

- (1) Discrepancies in scope
- (2) Discrepancies in the description of the research reported
- (3) Discrepancies between the availability of data and the research described
- (4) Inappropriate citations
- (5) Incoherent, meaningless and/or irrelevant content included in the article
- (6) Peer-review manipulation

The presence of these indicators undermines our confidence in the integrity of the article's content and we cannot, therefore, vouch for its reliability. Please note that this notice is intended solely to alert readers that the content of this article is unreliable. We have not investigated whether authors were aware of or involved in the systematic manipulation of the publication process.

Wiley and Hindawi regrets that the usual quality checks did not identify these issues before publication and have since put additional measures in place to safeguard research integrity.

We wish to credit our own Research Integrity and Research Publishing teams and anonymous and named external researchers and research integrity experts for contributing to this investigation.

The corresponding author, as the representative of all authors, has been given the opportunity to register their agreement or disagreement to this retraction. We have kept a record of any response received.

### References

- [1] H. Li, R. Zhu, X. Liu, K. Zhao, and D. Hong, "Siglec-15 Regulates the Inflammatory Response and Polarization of Tumor-Associated Macrophages in Pancreatic Cancer by Inhibiting the cGAS-STING Signaling Pathway," *Oxidative Medicine and Cellular Longevity*, vol. 2022, Article ID 3341038, 14 pages, 2022.

## Retraction

# Retracted: Decreased Polymorphonuclear Myeloid-Derived Suppressor Cells and ROS Production Correlated Closely with Bronchopulmonary Dysplasia in Preterm Infants

### Oxidative Medicine and Cellular Longevity

Received 20 June 2023; Accepted 20 June 2023; Published 21 June 2023

Copyright © 2023 Oxidative Medicine and Cellular Longevity. This is an open access article distributed under the Creative Commons Attribution License, which permits unrestricted use, distribution, and reproduction in any medium, provided the original work is properly cited.

This article has been retracted by Hindawi following an investigation undertaken by the publisher [1]. This investigation has uncovered evidence of one or more of the following indicators of systematic manipulation of the publication process:

- (1) Discrepancies in scope
- (2) Discrepancies in the description of the research reported
- (3) Discrepancies between the availability of data and the research described
- (4) Inappropriate citations
- (5) Incoherent, meaningless and/or irrelevant content included in the article
- (6) Peer-review manipulation

The presence of these indicators undermines our confidence in the integrity of the article's content and we cannot, therefore, vouch for its reliability. Please note that this notice is intended solely to alert readers that the content of this article is unreliable. We have not investigated whether authors were aware of or involved in the systematic manipulation of the publication process.

In addition, our investigation has also shown that one or more of the following human-subject reporting requirements has not been met in this article: ethical approval by an Institutional Review Board (IRB) committee or equivalent, patient/participant consent to participate, and/or agreement to publish patient/participant details (where relevant).

Wiley and Hindawi regrets that the usual quality checks did not identify these issues before publication and have since put additional measures in place to safeguard research integrity.

We wish to credit our own Research Integrity and Research Publishing teams and anonymous and named external researchers and research integrity experts for contributing to this investigation.

The corresponding author, as the representative of all authors, has been given the opportunity to register their agreement or disagreement to this retraction. We have kept a record of any response received.

### References

- [1] W. Liu, S. Li, Y. Li et al., "Decreased Polymorphonuclear Myeloid-Derived Suppressor Cells and ROS Production Correlated Closely with Bronchopulmonary Dysplasia in Preterm Infants," *Oxidative Medicine and Cellular Longevity*, vol. 2022, Article ID 9010354, 8 pages, 2022.

## Retraction

# Retracted: miR-124-3p Delivered Using Exosomes Attenuates the Keratinocyte Response to IL-17A Stimulation in Psoriasis

### Oxidative Medicine and Cellular Longevity

Received 20 June 2023; Accepted 20 June 2023; Published 21 June 2023

Copyright © 2023 Oxidative Medicine and Cellular Longevity. This is an open access article distributed under the Creative Commons Attribution License, which permits unrestricted use, distribution, and reproduction in any medium, provided the original work is properly cited.

This article has been retracted by Hindawi following an investigation undertaken by the publisher [1]. This investigation has uncovered evidence of one or more of the following indicators of systematic manipulation of the publication process:

- (1) Discrepancies in scope
- (2) Discrepancies in the description of the research reported
- (3) Discrepancies between the availability of data and the research described
- (4) Inappropriate citations
- (5) Incoherent, meaningless and/or irrelevant content included in the article
- (6) Peer-review manipulation

The presence of these indicators undermines our confidence in the integrity of the article's content and we cannot, therefore, vouch for its reliability. Please note that this notice is intended solely to alert readers that the content of this article is unreliable. We have not investigated whether authors were aware of or involved in the systematic manipulation of the publication process.

Wiley and Hindawi regrets that the usual quality checks did not identify these issues before publication and have since put additional measures in place to safeguard research integrity.

We wish to credit our own Research Integrity and Research Publishing teams and anonymous and named external researchers and research integrity experts for contributing to this investigation.

The corresponding author, as the representative of all authors, has been given the opportunity to register their agreement or disagreement to this retraction. We have kept a record of any response received.

### References

- [1] S. Liu and J. Gong, "miR-124-3p Delivered Using Exosomes Attenuates the Keratinocyte Response to IL-17A Stimulation in Psoriasis," *Oxidative Medicine and Cellular Longevity*, vol. 2022, Article ID 6264474, 11 pages, 2022.

## Retraction

# Retracted: ZFP36 Inhibits Tumor Progression of Human Prostate Cancer by Targeting CDK6 and Oxidative Stress

### Oxidative Medicine and Cellular Longevity

Received 20 June 2023; Accepted 20 June 2023; Published 21 June 2023

Copyright © 2023 Oxidative Medicine and Cellular Longevity. This is an open access article distributed under the Creative Commons Attribution License, which permits unrestricted use, distribution, and reproduction in any medium, provided the original work is properly cited.

This article has been retracted by Hindawi following an investigation undertaken by the publisher [1]. This investigation has uncovered evidence of one or more of the following indicators of systematic manipulation of the publication process:

- (1) Discrepancies in scope
- (2) Discrepancies in the description of the research reported
- (3) Discrepancies between the availability of data and the research described
- (4) Inappropriate citations
- (5) Incoherent, meaningless and/or irrelevant content included in the article
- (6) Peer-review manipulation

The presence of these indicators undermines our confidence in the integrity of the article's content and we cannot, therefore, vouch for its reliability. Please note that this notice is intended solely to alert readers that the content of this article is unreliable. We have not investigated whether authors were aware of or involved in the systematic manipulation of the publication process.

Wiley and Hindawi regrets that the usual quality checks did not identify these issues before publication and have since put additional measures in place to safeguard research integrity.

We wish to credit our own Research Integrity and Research Publishing teams and anonymous and named external researchers and research integrity experts for contributing to this investigation.

The corresponding author, as the representative of all authors, has been given the opportunity to register their agreement or disagreement to this retraction. We have kept a record of any response received.

### References

- [1] D. Yuan, Y. Fang, W. Chen et al., "ZFP36 Inhibits Tumor Progression of Human Prostate Cancer by Targeting CDK6 and Oxidative Stress," *Oxidative Medicine and Cellular Longevity*, vol. 2022, Article ID 3611540, 24 pages, 2022.

## Retraction

# Retracted: Novel Therapeutic Mechanism of Adipose-Derived Mesenchymal Stem Cells in Osteoarthritis via Upregulation of BTG2

### Oxidative Medicine and Cellular Longevity

Received 20 June 2023; Accepted 20 June 2023; Published 21 June 2023

Copyright © 2023 Oxidative Medicine and Cellular Longevity. This is an open access article distributed under the Creative Commons Attribution License, which permits unrestricted use, distribution, and reproduction in any medium, provided the original work is properly cited.

This article has been retracted by Hindawi following an investigation undertaken by the publisher [1]. This investigation has uncovered evidence of one or more of the following indicators of systematic manipulation of the publication process:

- (1) Discrepancies in scope
- (2) Discrepancies in the description of the research reported
- (3) Discrepancies between the availability of data and the research described
- (4) Inappropriate citations
- (5) Incoherent, meaningless and/or irrelevant content included in the article
- (6) Peer-review manipulation

The presence of these indicators undermines our confidence in the integrity of the article's content and we cannot, therefore, vouch for its reliability. Please note that this notice is intended solely to alert readers that the content of this article is unreliable. We have not investigated whether authors were aware of or involved in the systematic manipulation of the publication process.

Wiley and Hindawi regrets that the usual quality checks did not identify these issues before publication and have since put additional measures in place to safeguard research integrity.

We wish to credit our own Research Integrity and Research Publishing teams and anonymous and named external researchers and research integrity experts for contributing to this investigation.

The corresponding author, as the representative of all authors, has been given the opportunity to register their agreement or disagreement to this retraction. We have kept a record of any response received.

### References

- [1] Q. Yang, L. Jin, Q. Ding et al., "Novel Therapeutic Mechanism of Adipose-Derived Mesenchymal Stem Cells in Osteoarthritis via Upregulation of BTG2," *Oxidative Medicine and Cellular Longevity*, vol. 2022, Article ID 9252319, 15 pages, 2022.

## Retraction

# Retracted: Breast Cancer Exosome-Derived miR-425-5p Induces Cancer-Associated Fibroblast-Like Properties in Human Mammary Fibroblasts by TGF $\beta$ 1/ROS Signaling Pathway

### Oxidative Medicine and Cellular Longevity

Received 20 June 2023; Accepted 20 June 2023; Published 21 June 2023

Copyright © 2023 Oxidative Medicine and Cellular Longevity. This is an open access article distributed under the Creative Commons Attribution License, which permits unrestricted use, distribution, and reproduction in any medium, provided the original work is properly cited.

This article has been retracted by Hindawi following an investigation undertaken by the publisher [1]. This investigation has uncovered evidence of one or more of the following indicators of systematic manipulation of the publication process:

- (1) Discrepancies in scope
- (2) Discrepancies in the description of the research reported
- (3) Discrepancies between the availability of data and the research described
- (4) Inappropriate citations
- (5) Incoherent, meaningless and/or irrelevant content included in the article
- (6) Peer-review manipulation

The presence of these indicators undermines our confidence in the integrity of the article's content and we cannot, therefore, vouch for its reliability. Please note that this notice is intended solely to alert readers that the content of this article is unreliable. We have not investigated whether authors were aware of or involved in the systematic manipulation of the publication process.

Wiley and Hindawi regrets that the usual quality checks did not identify these issues before publication and have since put additional measures in place to safeguard research integrity.

We wish to credit our own Research Integrity and Research Publishing teams and anonymous and named external researchers and research integrity experts for contributing to this investigation.

The corresponding author, as the representative of all authors, has been given the opportunity to register their agreement or disagreement to this retraction. We have kept a record of any response received.

### References

- [1] Y. Zhu, H. Dou, Y. Liu et al., "Breast Cancer Exosome-Derived miR-425-5p Induces Cancer-Associated Fibroblast-Like Properties in Human Mammary Fibroblasts by TGF $\beta$ 1/ROS Signaling Pathway," *Oxidative Medicine and Cellular Longevity*, vol. 2022, Article ID 5266627, 28 pages, 2022.

## Retraction

# Retracted: Delicaflavone Represses Lung Cancer Growth by Activating Antitumor Immune Response through N6-Methyladenosine Transferases and Oxidative Stress

### Oxidative Medicine and Cellular Longevity

Received 20 June 2023; Accepted 20 June 2023; Published 21 June 2023

Copyright © 2023 Oxidative Medicine and Cellular Longevity. This is an open access article distributed under the Creative Commons Attribution License, which permits unrestricted use, distribution, and reproduction in any medium, provided the original work is properly cited.

This article has been retracted by Hindawi following an investigation undertaken by the publisher [1]. This investigation has uncovered evidence of one or more of the following indicators of systematic manipulation of the publication process:

- (1) Discrepancies in scope
- (2) Discrepancies in the description of the research reported
- (3) Discrepancies between the availability of data and the research described
- (4) Inappropriate citations
- (5) Incoherent, meaningless and/or irrelevant content included in the article
- (6) Peer-review manipulation

The presence of these indicators undermines our confidence in the integrity of the article's content and we cannot, therefore, vouch for its reliability. Please note that this notice is intended solely to alert readers that the content of this article is unreliable. We have not investigated whether authors were aware of or involved in the systematic manipulation of the publication process.

Wiley and Hindawi regrets that the usual quality checks did not identify these issues before publication and have since put additional measures in place to safeguard research integrity.

We wish to credit our own Research Integrity and Research Publishing teams and anonymous and named external researchers and research integrity experts for contributing to this investigation.

The corresponding author, as the representative of all authors, has been given the opportunity to register their agreement or disagreement to this retraction. We have kept a record of any response received.

### References

- [1] X. Wang, D. Xu, B. Chen et al., "Delicaflavone Represses Lung Cancer Growth by Activating Antitumor Immune Response through N6-Methyladenosine Transferases and Oxidative Stress," *Oxidative Medicine and Cellular Longevity*, vol. 2022, Article ID 8619275, 16 pages, 2022.



## Retraction

# Retracted: Macrophage-Derived Exosomes in TLR9-/- Mice Ameliorate Sepsis-Induced Mitochondrial Oxidative Stress and Apoptosis in Cardiomyocytes

### Oxidative Medicine and Cellular Longevity

Received 20 June 2023; Accepted 20 June 2023; Published 21 June 2023

Copyright © 2023 Oxidative Medicine and Cellular Longevity. This is an open access article distributed under the Creative Commons Attribution License, which permits unrestricted use, distribution, and reproduction in any medium, provided the original work is properly cited.

This article has been retracted by Hindawi following an investigation undertaken by the publisher [1]. This investigation has uncovered evidence of one or more of the following indicators of systematic manipulation of the publication process:

- (1) Discrepancies in scope
- (2) Discrepancies in the description of the research reported
- (3) Discrepancies between the availability of data and the research described
- (4) Inappropriate citations
- (5) Incoherent, meaningless and/or irrelevant content included in the article
- (6) Peer-review manipulation

The presence of these indicators undermines our confidence in the integrity of the article's content and we cannot, therefore, vouch for its reliability. Please note that this notice is intended solely to alert readers that the content of this article is unreliable. We have not investigated whether authors were aware of or involved in the systematic manipulation of the publication process.

Wiley and Hindawi regrets that the usual quality checks did not identify these issues before publication and have since put additional measures in place to safeguard research integrity.

We wish to credit our own Research Integrity and Research Publishing teams and anonymous and named external researchers and research integrity experts for contributing to this investigation.

The corresponding author, as the representative of all authors, has been given the opportunity to register their agreement or disagreement to this retraction. We have kept a record of any response received.

### References

- [1] X. Li, J. Luo, Y. Li et al., "Macrophage-Derived Exosomes in TLR9-/- Mice Ameliorate Sepsis-Induced Mitochondrial Oxidative Stress and Apoptosis in Cardiomyocytes," *Oxidative Medicine and Cellular Longevity*, vol. 2022, Article ID 5719974, 13 pages, 2022.

## Retraction

# Retracted: miR-494-3p Promotes Erastin-Induced Ferroptosis by Targeting REST to Activate the Interplay between SP1 and ACSL4 in Parkinson's Disease

### Oxidative Medicine and Cellular Longevity

Received 20 June 2023; Accepted 20 June 2023; Published 21 June 2023

Copyright © 2023 Oxidative Medicine and Cellular Longevity. This is an open access article distributed under the Creative Commons Attribution License, which permits unrestricted use, distribution, and reproduction in any medium, provided the original work is properly cited.

This article has been retracted by Hindawi following an investigation undertaken by the publisher [1]. This investigation has uncovered evidence of one or more of the following indicators of systematic manipulation of the publication process:

- (1) Discrepancies in scope
- (2) Discrepancies in the description of the research reported
- (3) Discrepancies between the availability of data and the research described
- (4) Inappropriate citations
- (5) Incoherent, meaningless and/or irrelevant content included in the article
- (6) Peer-review manipulation

The presence of these indicators undermines our confidence in the integrity of the article's content and we cannot, therefore, vouch for its reliability. Please note that this notice is intended solely to alert readers that the content of this article is unreliable. We have not investigated whether authors were aware of or involved in the systematic manipulation of the publication process.

Wiley and Hindawi regrets that the usual quality checks did not identify these issues before publication and have since put additional measures in place to safeguard research integrity.

We wish to credit our own Research Integrity and Research Publishing teams and anonymous and named external researchers and research integrity experts for contributing to this investigation.

The corresponding author, as the representative of all authors, has been given the opportunity to register their agreement or disagreement to this retraction. We have kept a record of any response received.

### References

- [1] J. Ma, X. Li, Y. Fan et al., "miR-494-3p Promotes Erastin-Induced Ferroptosis by Targeting REST to Activate the Interplay between SP1 and ACSL4 in Parkinson's Disease," *Oxidative Medicine and Cellular Longevity*, vol. 2022, Article ID 7671324, 17 pages, 2022.

## Retraction

# Retracted: Breast Cancer Exosome-Derived miR-425-5p Induces Cancer-Associated Fibroblast-Like Properties in Human Mammary Fibroblasts by TGF $\beta$ 1/ROS Signaling Pathway

### Oxidative Medicine and Cellular Longevity

Received 20 June 2023; Accepted 20 June 2023; Published 21 June 2023

Copyright © 2023 Oxidative Medicine and Cellular Longevity. This is an open access article distributed under the Creative Commons Attribution License, which permits unrestricted use, distribution, and reproduction in any medium, provided the original work is properly cited.

This article has been retracted by Hindawi following an investigation undertaken by the publisher [1]. This investigation has uncovered evidence of one or more of the following indicators of systematic manipulation of the publication process:

- (1) Discrepancies in scope
- (2) Discrepancies in the description of the research reported
- (3) Discrepancies between the availability of data and the research described
- (4) Inappropriate citations
- (5) Incoherent, meaningless and/or irrelevant content included in the article
- (6) Peer-review manipulation

The presence of these indicators undermines our confidence in the integrity of the article's content and we cannot, therefore, vouch for its reliability. Please note that this notice is intended solely to alert readers that the content of this article is unreliable. We have not investigated whether authors were aware of or involved in the systematic manipulation of the publication process.

Wiley and Hindawi regrets that the usual quality checks did not identify these issues before publication and have since put additional measures in place to safeguard research integrity.

We wish to credit our own Research Integrity and Research Publishing teams and anonymous and named external researchers and research integrity experts for contributing to this investigation.



The corresponding author, as the representative of all authors, has been given the opportunity to register their agreement or disagreement to this retraction. We have kept a record of any response received.

### References

- [1] Y. Zhu, H. Dou, Y. Liu et al., "Breast Cancer Exosome-Derived miR-425-5p Induces Cancer-Associated Fibroblast-Like Properties in Human Mammary Fibroblasts by TGF $\beta$ 1/ROS Signaling Pathway," *Oxidative Medicine and Cellular Longevity*, vol. 2022, Article ID 5266627, 28 pages, 2022.

## Research Article

# Breast Cancer Exosome-Derived miR-425-5p Induces Cancer-Associated Fibroblast-Like Properties in Human Mammary Fibroblasts by TGF $\beta$ 1/ROS Signaling Pathway

Yue Zhu , He Dou, Yuqi Liu, Pingyang Yu, Fucheng Li, Youyu Wang, and Min Xiao 

Department of Breast Surgery, Harbin Medical University Cancer Hospital, Harbin, 150081 Heilongjiang, China

Correspondence should be addressed to Min Xiao; [xiaomin@hrbmu.edu.cn](mailto:xiaomin@hrbmu.edu.cn)

Received 24 May 2022; Revised 14 September 2022; Accepted 27 September 2022; Published 30 November 2022

Academic Editor: Tian Li

Copyright © 2022 Yue Zhu et al. This is an open access article distributed under the Creative Commons Attribution License, which permits unrestricted use, distribution, and reproduction in any medium, provided the original work is properly cited.

The connection between the cellular microenvironment and tumor cells is crucial for tumor progression. However, the process by which normal fibroblasts (NFs) become cancer-associated fibroblasts (CAFs) is unknown, and mounting evidence suggests that some microRNAs (miRNAs) have an important role in converting NFs into CAFs. Breast cancer (BC) has been proven to have enhanced miR-425-5p expression in order to support progression. We discovered that human mammary fibroblasts (HMFs) could uptake BC cell line-derived exosomes to change their properties, promoting the switch to the CAF phenotype and increasing cell motility, as evidenced by an increase in CAF activation-related marker protein expression and cell proliferation, invasion, and migration. Transfection of exosomes is obtained from BC cells, and miR-425-5p inhibitors suppressed the aforementioned effects as well as lowered chemokine levels and gene expression related with proliferation and metastasis. By suppressing the expression of its target gene TGF $\beta$ RII (TGF $\beta$ 1 receptor), miR-425-5p enhanced the transition of HMFs to the CAF phenotype. MDA-MB-231 cells and CAFs stimulated by HMF absorption of MDA-MB-23-derived exosomes showed similar proliferation, invasion, migration, and expression of -SMA, FAP, CXCL1, IL-6, TGF $\beta$ 1, P21, P27, Ki67, vimentin, E-cadherin, N-cadherin,  $\alpha$ -catenin, fibronectin, and MMP-2. TGF $\beta$ 1 overexpression enhanced ROS production. Finally, we found that HMFs transiently transfected with miR-425-5p can promote tumor growth in vivo. Finally, these findings provide fresh insight on miR-425-5p as an important mediator of the interaction between BC cells and stroma.

## 1. Introduction

Worldwide, breast cancer (BC) is the most often diagnosed malignancy among females. Incidence of breast cancer is rising annually in China, reflecting a recent trend [1]. In recent years, BC mortality has decreased as a result of continuous advancements in early detection, surgical technology, radiotherapy, and chemotherapy, as well as the individualization of endocrine therapy and molecular targeted therapy [2]. However, BC remains the largest cause of cancer-related deaths among women globally. Therefore, it is essential to investigate the pathophysiology of BC.

As a result of a sequentially complex process involving tumor cells, the host, and the tumor microenvironment, tumor recurrence and metastasis have long been important

obstacles in cancer therapy and a major focus of cancer research [3]. The tumor microenvironment is a distinguishing feature of the tumor; it is a local homeostatic environment formed of tumor-infiltrated immune cells, stromal cells, and active mediators released by these cells, all of which play an important role in tumor progression [4]. All fibroblasts found inside and around tumor tissues are referred to as cancer-associated fibroblasts (CAFs), and they are the primary components of the tumor microenvironment, promoting tumor invasion and metastasis via direct or indirect interaction with tumor cells [5]. CAFs can generate a pretransfer microenvironment in a prospective metastatic organ prior to tumor metastasis. It encourages the establishment of metastatic lesions by providing a favorable growing environment for tumor cells that reach specific

TABLE 1: The sequences of the primers.

Gene	Forward (5'-3')	Reverse (5'-3')
miR-425-5p	AGGATAGTCCATGTTAGGAA	AGCCCTGCAAAGACTGGTAGCG
TGF $\beta$ 1	ATGCTGTAGTAGTAGGTGT	CTGTGTCTCAATACGTCT
TGF $\beta$ RII	TGTGTCACTGTACCTGTAA	ACTGTGTGTAAGTGTA
Vimentin	GCAACTGTGTCCACAA	CGAGCTGTGTTGTATGCATGT
E-cadherin	GTGTAAGTGAATGCTAGCTAA	CCCATGTACCATGTAACA
N-cadherin	TTGCAGCTGCAATCGTAGTG	ACTCTGTGATCTGACTGAA
$\alpha$ -Catenin	CCGCTAGTGTAAGCCAAATGCC	CGTGACAATGTACCTGAAAC
Fibronectin	GCAACGCATGTCTGTGTAACA	AATGACATGGTAGAACAA
MMP2	CCATGACGATATGTAGTAG	ACGTGACATGTCTGCTGAA
CXCL1	TTAACCTCCGTGTAATGCG	ATGTGACGTGCATGACTG
IL-6	GTAATGTGACGCGTGTA	CCGACGTGGCTCCATAAACA
P27	AACGTGTAGTGTAGGATA	CGTAGCTACCTAGATCCGTG
Ki67	TAACGCGCTTGTGTAGTGA	GTAGGTAAGGTTCCAGTA
P21	AACAAATGGACGTGCAAA	TAAGAGCTGGCTGTGTCCT
U6	TTCGGTTAAATTGCCCCAGAC	CGCACCTAAGGCGAGTA
GAPDH	CCCGCAGTTAGCCAACCTCTCG	CGTCTTACACACAGGTAACGAA

organs. CAFs play a role in the occurrence and progression of BC. However, their activation and molecular mechanism of action are unknown [6].

Exosomes are membranous nanoscale vesicles found in the extracellular matrix that have a diameter of approximately 30-100 nm. Exosomes' functions in the tumor microenvironment have drawn more attention lately [7]. By transporting miRNAs, long noncoding RNAs (lncRNAs), and messenger RNAs, exosomes can facilitate information exchange between tumor cells and the tumor microenvironment. It suggests that exosomes have potential utility in tumor diagnosis and treatment [8, 9]. miRNAs are a family of noncoding single-stranded RNA molecules between 19 and 22 nucleotides in length that are encoded by endogenous genes. It has been demonstrated that exosomes enhance the transport and transmission of microRNAs between cells and protect them from RNase degradation. When exosomes containing specific miRNAs are picked up by receptor cells, they are able to not only influence gene expression but also directly interact with specific proteins, thereby compromising their biological function [10]. Further research is needed to determine if miRNA transported by tumor cell-derived exosomes enters the tumor microenvironment to regulate CAF activation, thereby driving BC's recurrence and metastasis.

## 2. Materials and Methods

**2.1. Human Breast Cancer Cell Lines.** These human breast cancer cell lines, MDA-MB-231 and BT-549, were obtained from the Shanghai Cell Bank of the Chinese Academy of Sciences for the purpose of this inquiry. They were grown in Dulbecco's Modified Eagle's Medium (DMEM; Hangzhou Sijiqing Bioengineering Materials Co., Ltd., Hangzhou, Zhejiang, China) at a temperature of 37 degrees Celsius and a

carbon dioxide concentration of 5%. The medium also contained 10% fetal bovine serum (FBS), 100 units of penicillin per milliliter, and streptomycin (100 micrograms per milliliter). When the confluence reached between 70 and 80 percent, it was necessary to initiate subculture.

**2.2. Human Mammary Fibroblasts (HMFs).** HMFs that were cultured in DMEM supplemented with 10% FBS, penicillin 100 U/ml, and streptomycin 100 U/ml were provided by ATCC (USA).

**2.3. Exosome Extraction from Cancer Cells and Serum of BC Patients.** After 10 minutes at 3000 rpm, the breast cancer cell culture supernatant was called conditioned medium. MDA-MB-231 and BT-549 exosomes were precipitated using this solution (System Biosciences, Mountain View, CA, USA). ExoQuick-TC exosome pellet was introduced overnight to breast cancer conditioned medium and centrifuged for 30 minutes at 1500 rpm and 5 minutes at 3000 rpm. Exosome pellets were resuspended in 250-500 microliters of cell culture medium and cultured for 72 hours with recipient cells. Exosome-removed medium was recovered after 90 minutes at 25,000 rpm. Serum samples from 67 women with breast cancer and 67 healthy donors were kept at -80°C at the Harbin Medical University Cancer Hospital. There were no significant differences in general characteristics between two groups. The study protocol was approved by the ethics committee of the Harbin Medical University Cancer Hospital. All patients signed the informed consent forms. For 30 minutes at 4°C, the supernatant was centrifuged at 2000 rpm with BC cancer patients' sera and healthy donors' sera. Next, the exosomes were isolated by utilizing the whole exosome isolation reagent (Invitrogen, Carlsbad, CA, USA). An exosome suspension was added to the copper EM grids, and subsequently, the phosphotungstic acid was added. After

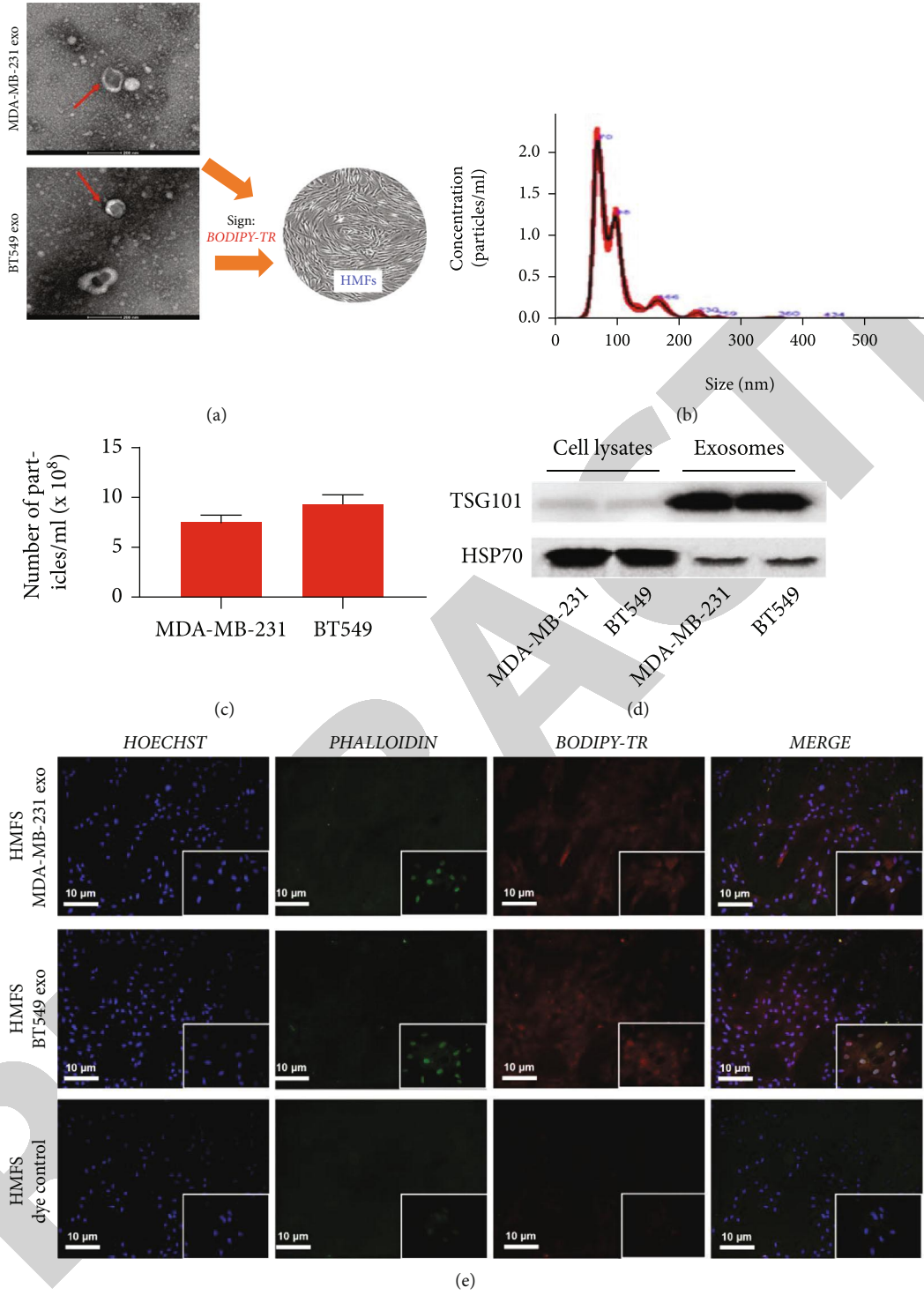


FIGURE 1: Continued.

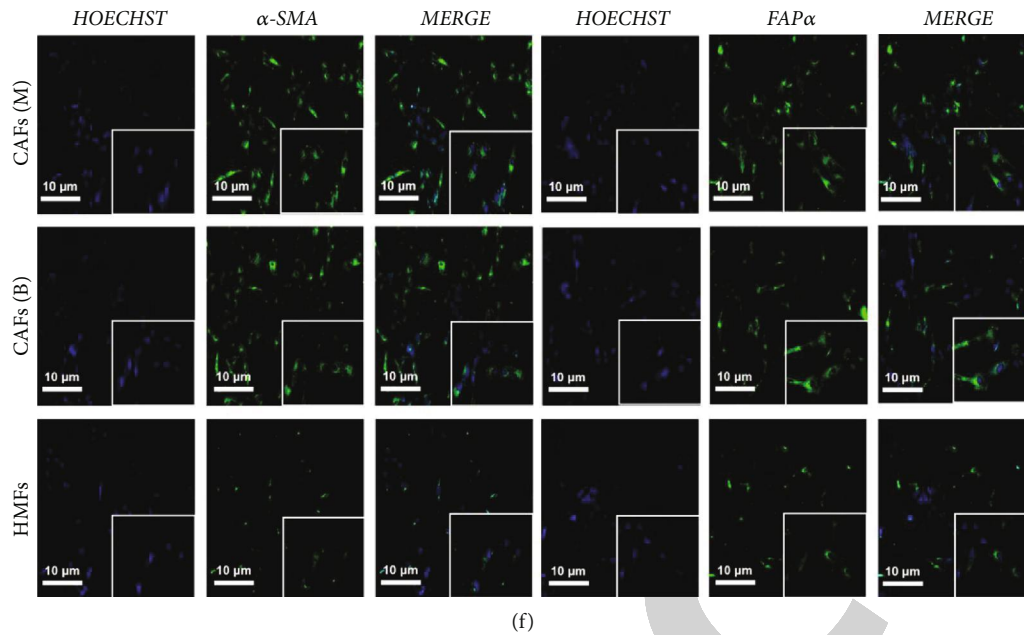


FIGURE 1: Exosomes derived from MDA-MB-231 and BT549 cells promoted the transition of HMFs to the CAF phenotype. (a) Exosome identification by TEM. (b) Size distribution of MDA-MB-231- and BT549-derived exosome diameters. (c) Detection of TSG101 and HSP70 protein expression by western blot. (d) Human mammary fibroblasts. (e) Exosome uptake assay observed HMFs taking in MDA-MB-231- and BT549-derived exosomes. (f) Immunofluorescence staining observed the expression of  $\alpha$ -SMA and FAP $\alpha$  in HMFs uptaking MDA-MB-231 and BT549 cell-derived exosomes.

drying, TEM was utilized to evaluate the shape and size of the exosomes. NanoSight NS300 Nanoparticle Tracking Analyzer (NS300) was used to assess the concentration of exosomes, their size distribution, and their zeta potential (Malvern, UK). Exosome markers TSG101 and HSP70 were used in western blot analysis.

**2.4. Exosome Uptake Assay.** Before beginning the test in 6-well Transwell plates with  $0.4 \mu\text{m}$  pore size filters, an initial step was taken to culture 200,000 MDA-MB-231 and BT49 cells in complete DMEM for 24 hours. This was done before the test ever began (Corning, Sigma-Aldrich). After that, the cells were subjected to some tests. BODIPY TR ceramide was mixed with exosomes from MDA-MB-231 and BT49 cells, which resulted in the incorporation of a dye into the exosomes (Invitrogen). For a full five minutes, the liquid was vigorously stirred in all directions before being drained. The excess dye from the labeled exosomes was removed using an ultracentrifuge that ran at  $100,000g$  for an hour at a temperature of  $4^\circ\text{C}$ . The exosome pellet was cleaned with PBS three times after it was removed from the ultracentrifuge and placed back into the centrifuge. The pellet was brought back to life with the assistance of PBS. Six hours after the experiment was initiated in PBS and 4% paraformaldehyde, HMF cells were labeled with exosomes that were tagged with BODIPY TR ceramide. Following that, the cells were washed in PBS for a second time (PFA).

**2.5. Immunofluorescence Staining.** For 15 minutes, a 10% formalin (Sigma 47036) solution was added to a 0.5% saponin (Sigma 4771) solution. This fixed the cell cultures. The

cells were then washed three times with PBS that did not have any calcium or magnesium in it. The cells were then made more permeable with a 1% Triton X-100 solution, and then, they were washed three times with PBS. The cells were then stained with a blocking buffer made of 1% bovine serum albumin (Sigma) and 1% goat IgG (research on immunology at Jackson). Fluorescence microscopy was done with 50 ng/ml of DAPI from Life Science Technology and monoclonal rabbit or mouse anti-human primary antibodies ( $\alpha$ -SMA and FAP) (respectively). Between 100 and 110, glycerol was used to seal the slides, and a fluorescence microscope was used to look at them (Olympus).

**2.6. Fluorescence In Situ Hybridization (FISH).** The 6-FAM-tagged miR-425-5p FISH probe was donated by the Gema Company. Paraformaldehyde was used to fix HMFs, and PBS was used to rinse them. Afterward, the cells were washed with PBS and digested with proteinase K (Sangon, Shanghai) for 5 minutes at  $37^\circ\text{C}$ . First, cells were fixed in 1% paraformaldehyde and then denatured with 70%, 85%, and 100% alcohol as specified in the table to dehydrate them. After denatured hybridization solution probes were placed on cell slides and denatured for 3 minutes, the probes were hybridized overnight at  $42^\circ\text{C}$  light at  $73^\circ\text{C}$  for denatured hybridization solution probes. At  $37^\circ\text{C}$ , the slides were pretreated with 0.1 percent NP-40/2SSC and 50 percent formamide/2SSC before being washed at room temperature with DAPI staining solution. This study made use of laser confocal microscopy (LCM) images (Leica, Mannheim, Germany).

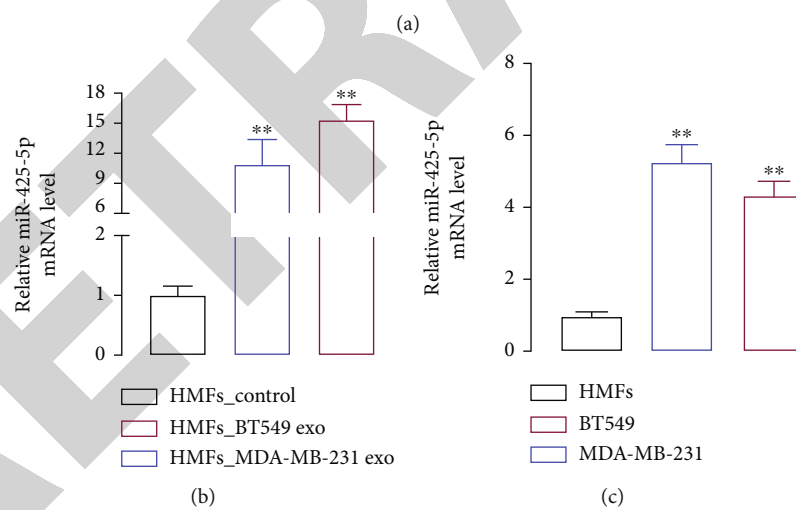
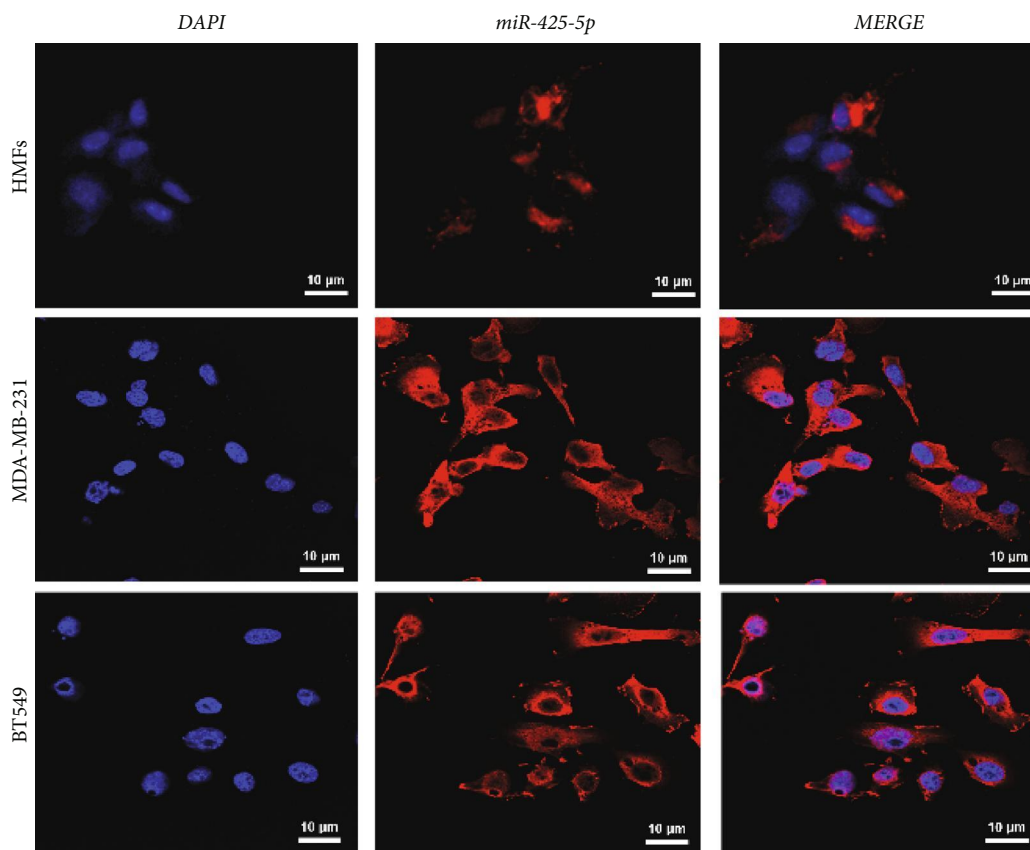


FIGURE 2: Continued.



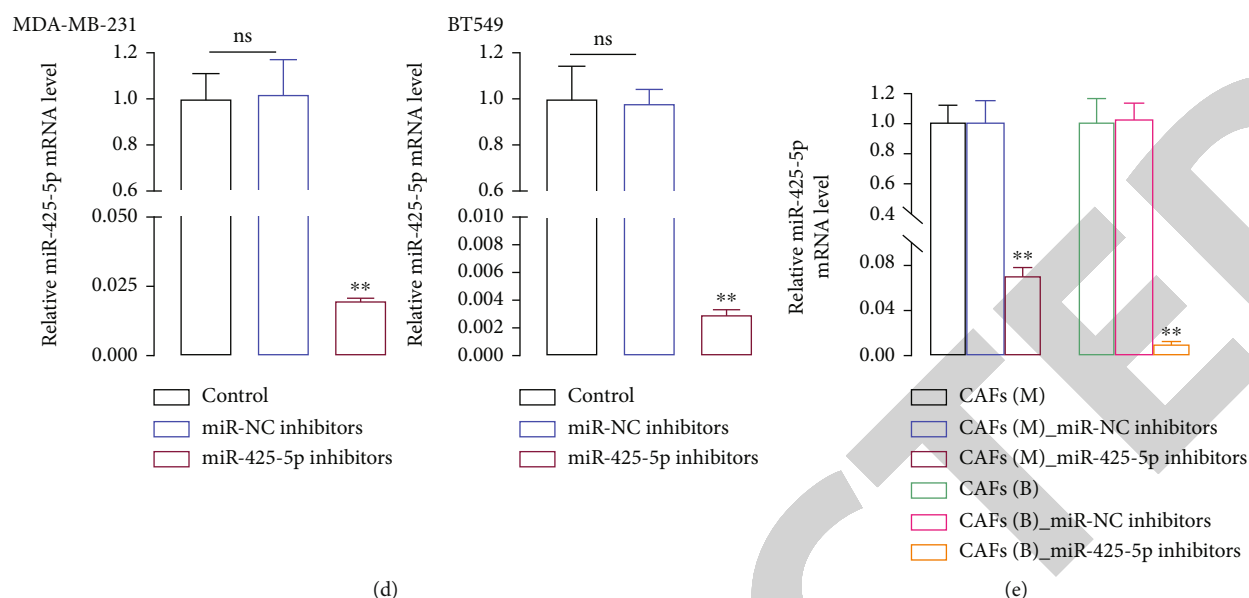


FIGURE 2: miR-425-5p was highly expressed in exosomes derived from MDA-MB-231 and BT549 cells. (a) The location of miR-425-5p in HMFs, MDA-MB-231, and BT549 cells by FISH. (b) The level of miR-425-5p in HMFs, MDA-MB-231, and BT549 cells by RT-PCR. (c) The level of miR-425-5p in HMFs, MDA-MB-231, and BT549 cell-derived exosomes by RT-PCR. (d) miR-425-5p inhibitors were transfected into MDA-MB-231 and BT549 cells to detect the level of miR-425-5p by RT-PCR. (e) The level of miR-425-5p in HMFs uptaking exosomes from miR-425-5p transfected MDA-MB-231 and BT549 cells by RT-PCR. Experimental data presented as means  $\pm$  standard deviation. Experiment was repeated 3 times. \*\* $P < 0.01$  compared with the HMFs, HMFs\_exo, control, and CAFs(M/B) groups.

**2.7. Intracellular ROS Levels.** The DCFH-DA approach was used in order to get an idea of how the ROS levels have changed relatively. Following transfection, the cells were subjected to a treatment with 10 mmol/L OD DCFH-DA for a period of 30 minutes. Following three washes, the cells were positioned on a fluorescence analyzer (BioTek, USA), and the excitation/emission wavelength was adjusted to 488/525 nm. After then, an assessment of the results was made. The values are shown as a percentage of the relative fluorescence that the control group possessed in comparison to the fluorescence of the experimental group.

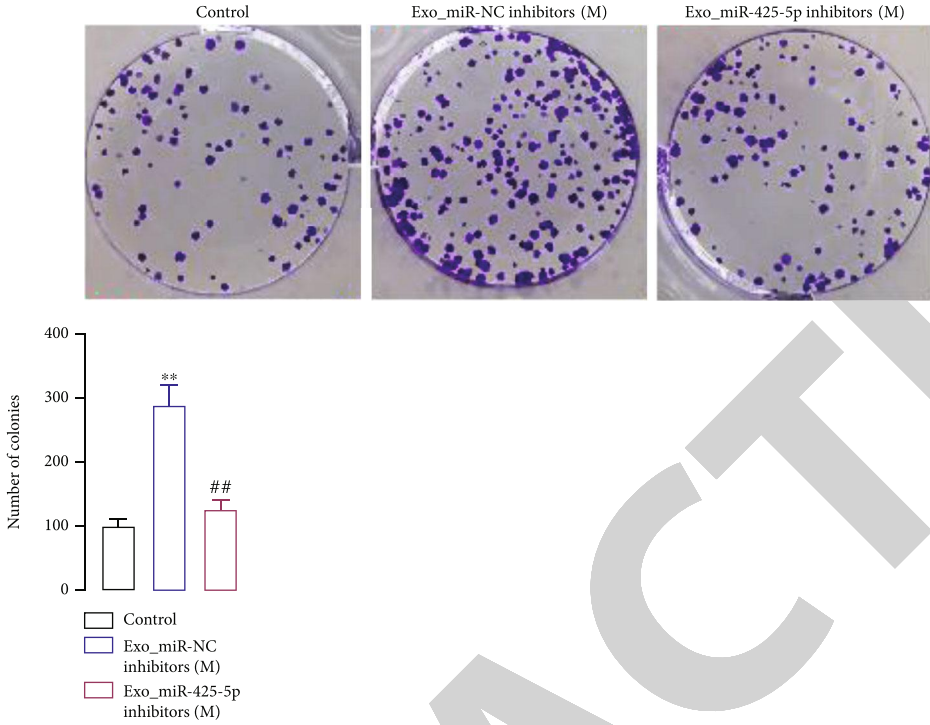
**2.8. Western Blot.** In order to separate proteins from exosomes, the Exosomal RNA and Protein Extraction Kit (101Bio) was utilized in a manner that was compliant with the guidelines provided by the manufacturer. The total protein was extracted using RIPA lysis buffer (Beyotime, Shanghai, China), and the protein concentration was determined using a Pierce BCA protein detection kit. This experiment was carried out in Shanghai, China (Thermo Fisher Scientific, Waltham, MA, USA). After loading 25 g of proteins onto a 10% SDS-PAGE gel and separating them using that gel, the proteins were concentrated on a 5% SDS-PAGE gel and then transferred to a polyvinylidene fluoride membrane (Merck Millipore, Billerica, MA, USA). After blocking with 5% bovine serum albumin for 2 hours, anti-TGF1, anti-SMA, anti-FAP, anti-CXCL1, anti-IL-6, anti-TGFRB1II, anti-P21, anti-P27, anti-Ki67, anti-vimentin, and anti-E-cadherin antibodies were injected. Anti-TGF1, anti-SMA, and anti-FAP secondary antibodies were found to be present in the sample after a blocking treatment of 5% bovine serum albumin for two hours. Anti-N-cadherin, anti-catenin, anti-fibronectin, anti-MMP-2, anti-GAPDH,

anti-TSG101, and anti-HSP70 antibodies were utilized in this work. All of the antibodies were diluted as directed by the manufacturer, and then, they were incubated at 4 degrees Celsius for one whole night. After that, the primary antibodies were treated with goat anti-rabbit or goat anti-mouse IRDye<sup>TM</sup> 800CW secondary antibodies at room temperature for one hour. The Odyssey imaging system was utilized to perform the functions of scanning and processing on the images (LI-COR, Lincoln, NE, USA).

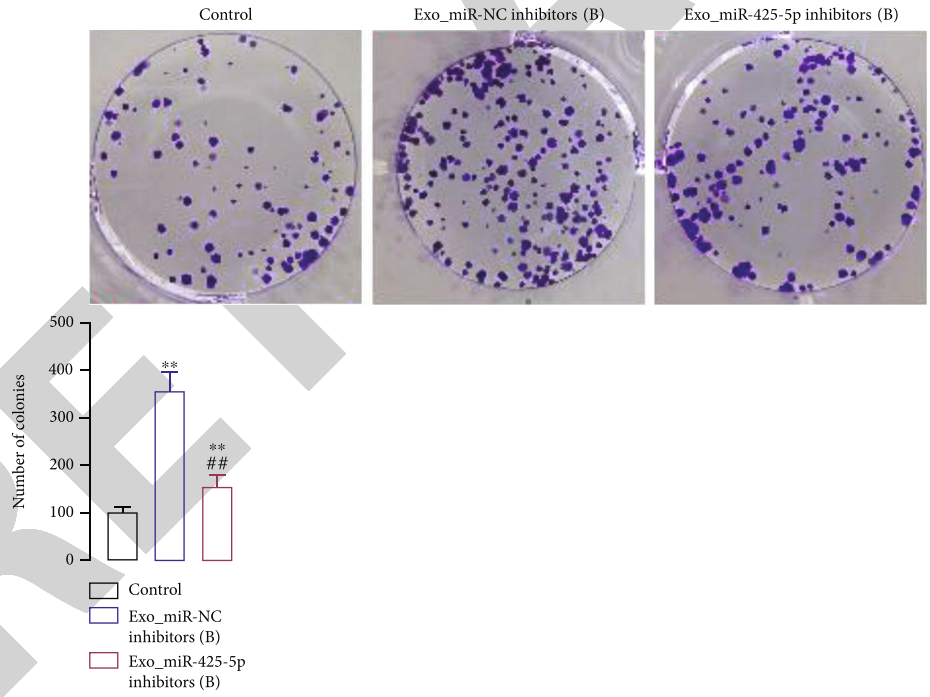
**2.9. Real-Time PCR (RT-PCR) Analysis.** TaqMan miRNA detection technique was utilized in order to provide an accurate reading on the concentrations of miR-425-5p and U6 (Life Technologies, Shanghai, China). Following the completion of reverse transcription, complementary DNA was synthesized with the help of the RT-Master Mix (manufactured by TaKaRa Bio in Shiga, Japan), and RT-PCR with StepOne-Plus RT-PCR equipment was used to determine the levels of mRNA expression (Applied Biosystems, Foster City, CA, USA). The primers that were utilized in this research are outlined in Table 1.

**2.10. Dual-Luciferase Reporter Assay.** miR-425-5p was discovered to have the potential to be targets for TargetScan (<http://www.targetscan.org/>). After transfection, a period of 24 hours was spent using the Dual Luciferase Reporter Assay 22 System to check for the presence of luciferase activity (Promega, Madison, WI, USA).

**2.11. miR-425, TGF $\beta$ 1, and TGF $\beta$ R2 Transfection In Vitro.** From Biomics Biotechnology Co., Ltd., we purchased the miR-425-5p inhibitors and negative control (miR-NC

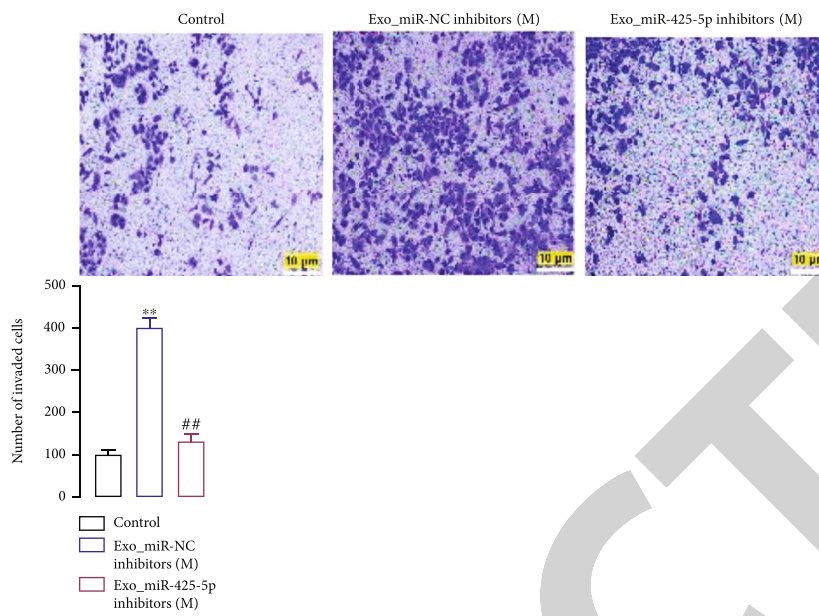


(a)

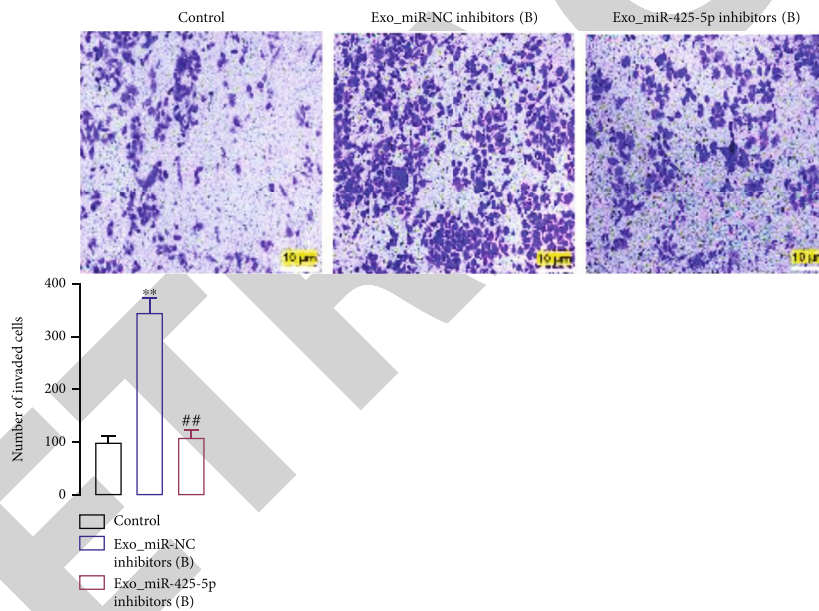


(b)

FIGURE 3: Continued.



(c)



(d)

FIGURE 3: Continued.

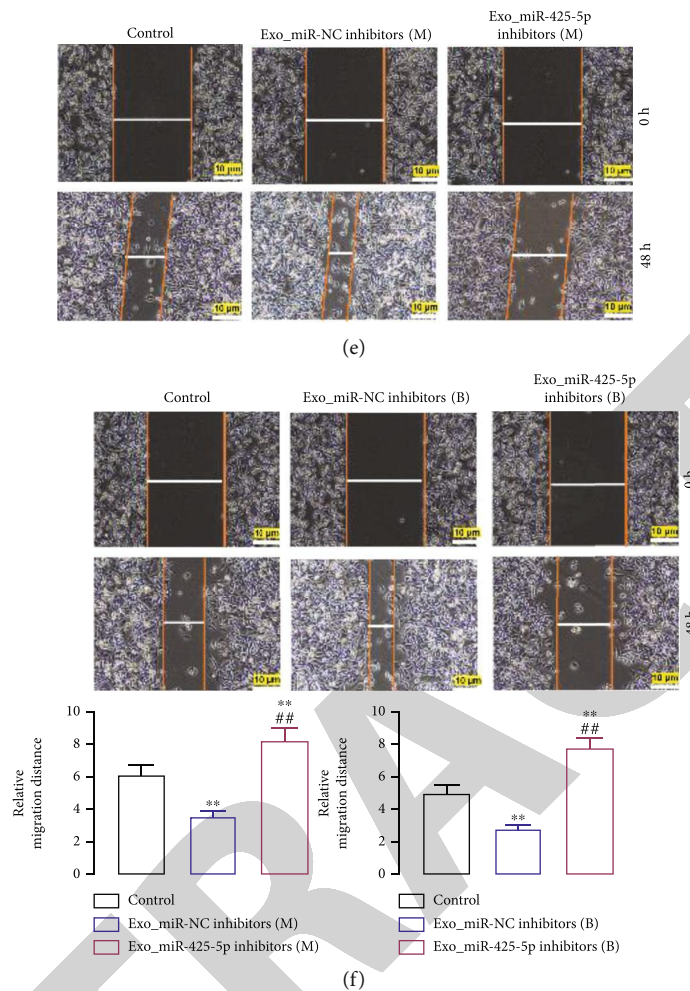


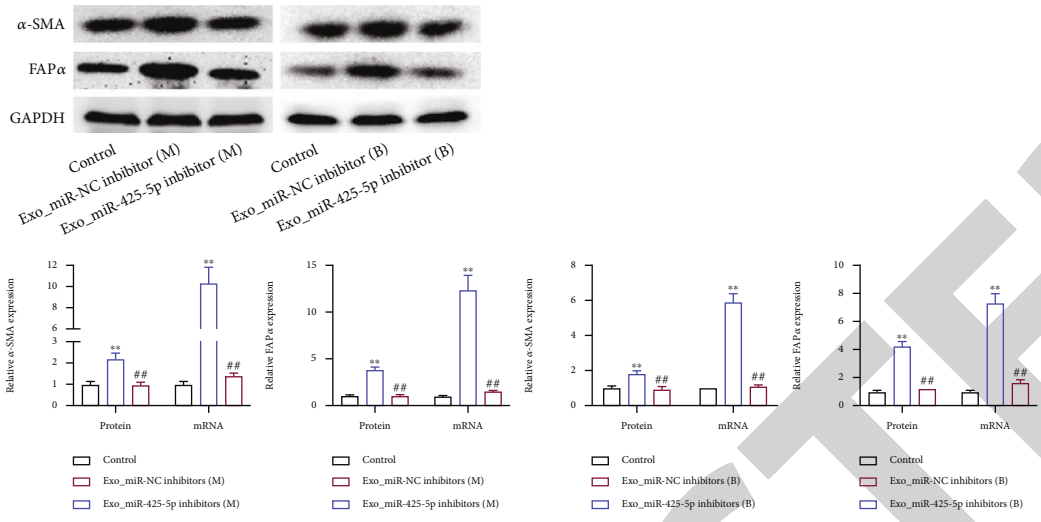
FIGURE 3: BC cell-derived exosomes induced proliferation, invasion, and migration of HMFs and expedited HMF switch to CAF phenotype. In HMFs uptaking exosomes from miR-425-5p inhibitors transfected MDA-MB-231 and BT549 cells, the cell proliferation (a, b), invasion (c, d), and migration (e, f) were detected by clone formation, Transwell, and scratch-wound assays. Experimental data presented as means  $\pm$  standard deviation. Experiment was repeated 3 times. \*\* $P < 0.01$  compared with the control group. ## $P < 0.01$  compared with the exo\_miR-NC inhibitor group.

inhibitors), as well as the miR-425-5p mimics and negative control (miR-NC mimics), as well as the TGF1 siRNA (TGF1 knockdown (TGF1-KD)), TGFRII siRNA (TGFRII-KD), and negative control (NC-KD) (Nantong, Jiangsu, China). Both the pcDNA 3.1 vector expressing TGF1 (also known as TGF1 overexpression (TGF1-OE)) and the pcDNA 3.1 vector that did not express TGF1 (NC-OE) were provided by UNIBIO Biotechnology Co., Ltd. (Chongqing, China). They were converted into HMFs by utilizing Lipofectamine 2000 as the transfection agent (Invitrogen, Carlsbad, CA, USA).

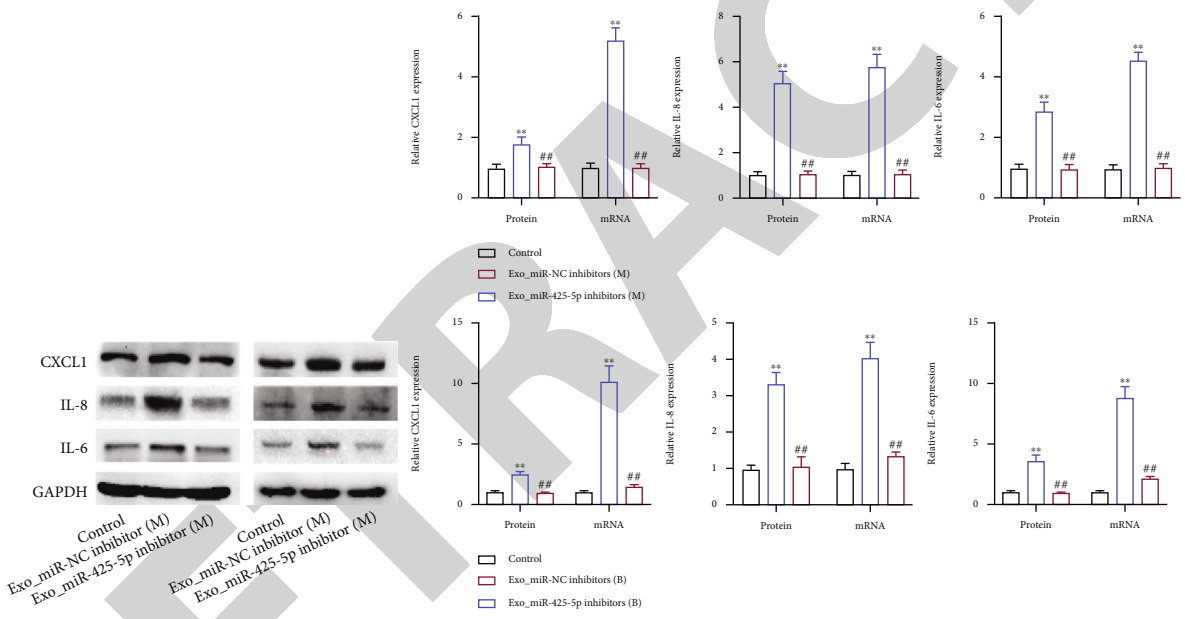
**2.12. Wound Healing Assay.** At a temperature of 37 degrees Celsius, cells were grown in 6-well plates in a solution that included 1% fetal bovine serum. The plates were kept at a constant temperature (five times the normal cell population). Once the cells had reached 100% confluence, we were able to successfully streak the monolayer using a pipette tip. After being washed twice in PBS, the cells were grown in culture for forty-eight hours at a temperature of 37 degrees Cel-

sius and 5% carbon dioxide. Under a microscope, pictures were obtained of cells that had been collected at 0 hours and 48 hours after the injury, respectively (TS100-F, Nikon, Tokyo, Japan).

**2.13. Transwell Invasion Assay.** Research on invasion was carried out inside of a chamber that had been coated in Matrigel (BD BioCoat, Corning). While the lower chamber of the Transwell device contained medium containing 10% FBS, the upper chamber was seeded with  $1 \times 10^4$  cells that were suspended in medium that did not include any serum. In the trials involving invasion, the cells were grown on Matrigel Transwell inserts that had previously been coated in Matrigel. Following an incubation period of 24 hours, the cells that had remained on the upper side of the membrane were eliminated. On the other hand, the cells that had migrated to the bottom surface of the membrane were fixed and stained with 0.1% crystal violet to determine where



(a)



(b)

FIGURE 4: Continued.

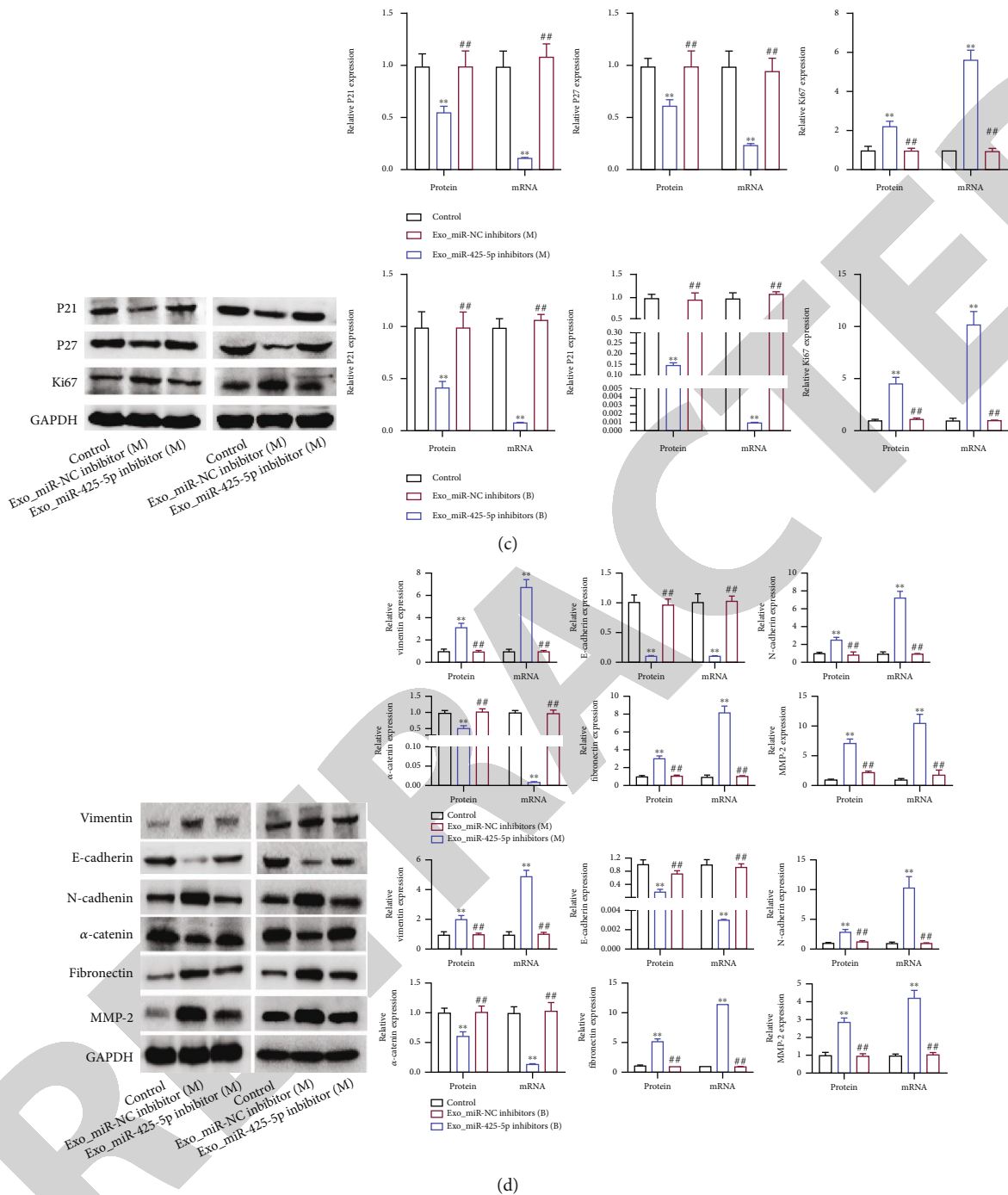
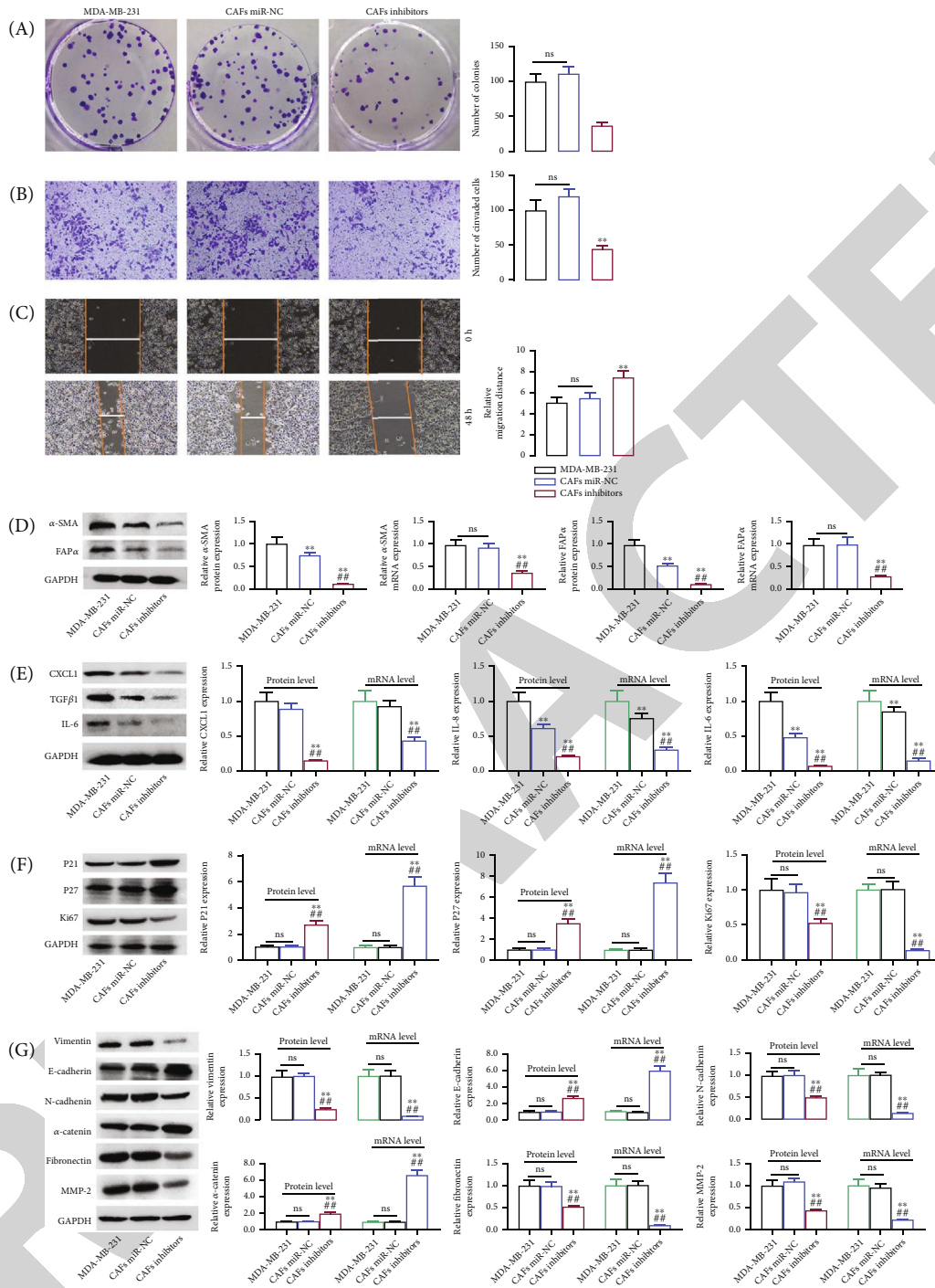


FIGURE 4: BC cell-derived exosomes induced protein expression to expedite HMF switch to CAF phenotype. In HMFs uptaking exosomes from miR-425-5p inhibitors transfected MDA-MB-231 and BT549 cells, the expression of  $\alpha$ -SMA and FAP $\alpha$  (a), CXCL1, TGF $\beta$ 1, and IL6 (b), P21, P27, and Ki67 (c), and vimentin, E-cadherin, N-cadherin,  $\alpha$ -catenin, fibronectin, and MMP2 (d) were detected by RT-PCR and western blot assays. Experimental data presented as means  $\pm$  standard deviation. Experiment was repeated 3 times. \*\* $P < 0.01$  compared with the control group. ## $P < 0.01$  compared with the exo\_miR-NC inhibitor group.

they were located. Images of the labeled cells were obtained using the microscope (Nikon).

**2.14. Colony Formation Assay.** Before being planted directly into 6-well plates at a density of  $5 \times 10^2$  cells per well, the cells were digested, and the growth conditions were set at 37 degrees Celsius with 5% carbon dioxide.

The cells were grown in culture at a temperature of 37 degrees Celsius with 5% carbon dioxide. After being incubated for two weeks, it was washed with phosphate buffered saline (PBS) three times before being examined (PBS). After being fixed in 100% ethanol for 30 minutes, the cells were then stained with hematoxylin for 20 minutes so that their structure could be seen. This process



**FIGURE 5: Exosomal miR-425-5p stimulated HMF switch to CAF phenotype.** In miR-425-5p transfected CAFs (HMFs uptaking exosomes from MDA-MB-231 cells), cell proliferation (a), invasion (b), migration (c), the expression of  $\alpha$ -SMA and FAP $\alpha$  (d), CXCL1, TGF $\beta$ 1, and IL6 (e), P21, P27, and Ki67 (f), and vimentin, E-cadherin, N-cadherin,  $\alpha$ -catenin, fibronectin, and MMP2 (g) were detected by RT-PCR and western blot assays. Experimental data presented as means  $\pm$  standard deviation. Experiment was repeated 3 times. \*\* $P < 0.01$  compared with the MDA-MB-231 group. ## $P < 0.01$  compared with the CAF miR-NC group.

took place so that the structure of the cells could be seen. In order to obtain an impression of the highest possible quality, the slab was first blasted dry and then dried with a hair drier. A colony is regarded to be a real colony whenever it has more than 50 cells in it.

**2.15. Animal Experiment.** The Institutional Animal Care and Use Committee of Heilongjiang Province, China, gave its approval to every animal study being conducted there. The mice were kept in a sterile environment and fed a special diet that was pathogen-free (SPF) for a period of three to four

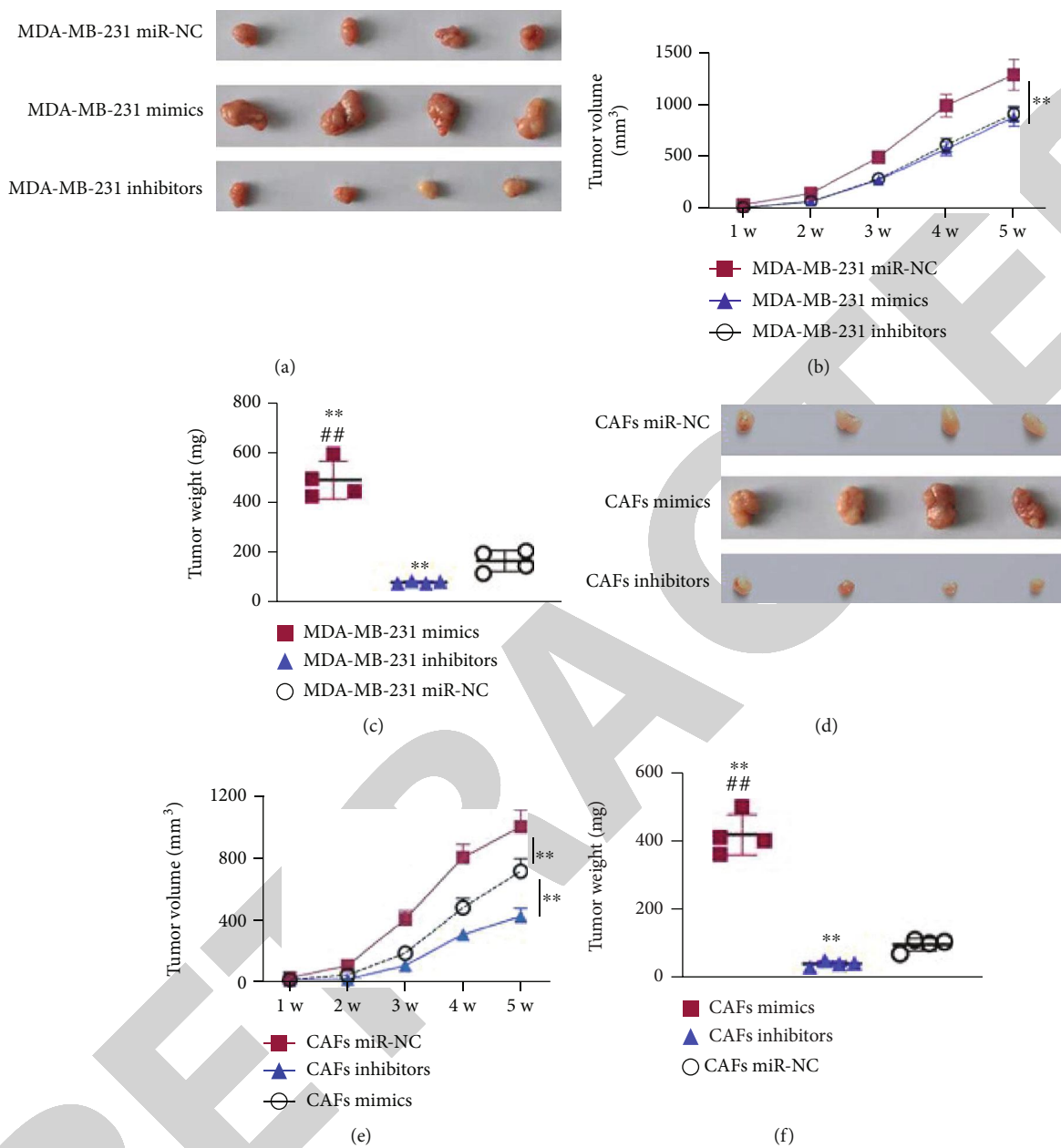
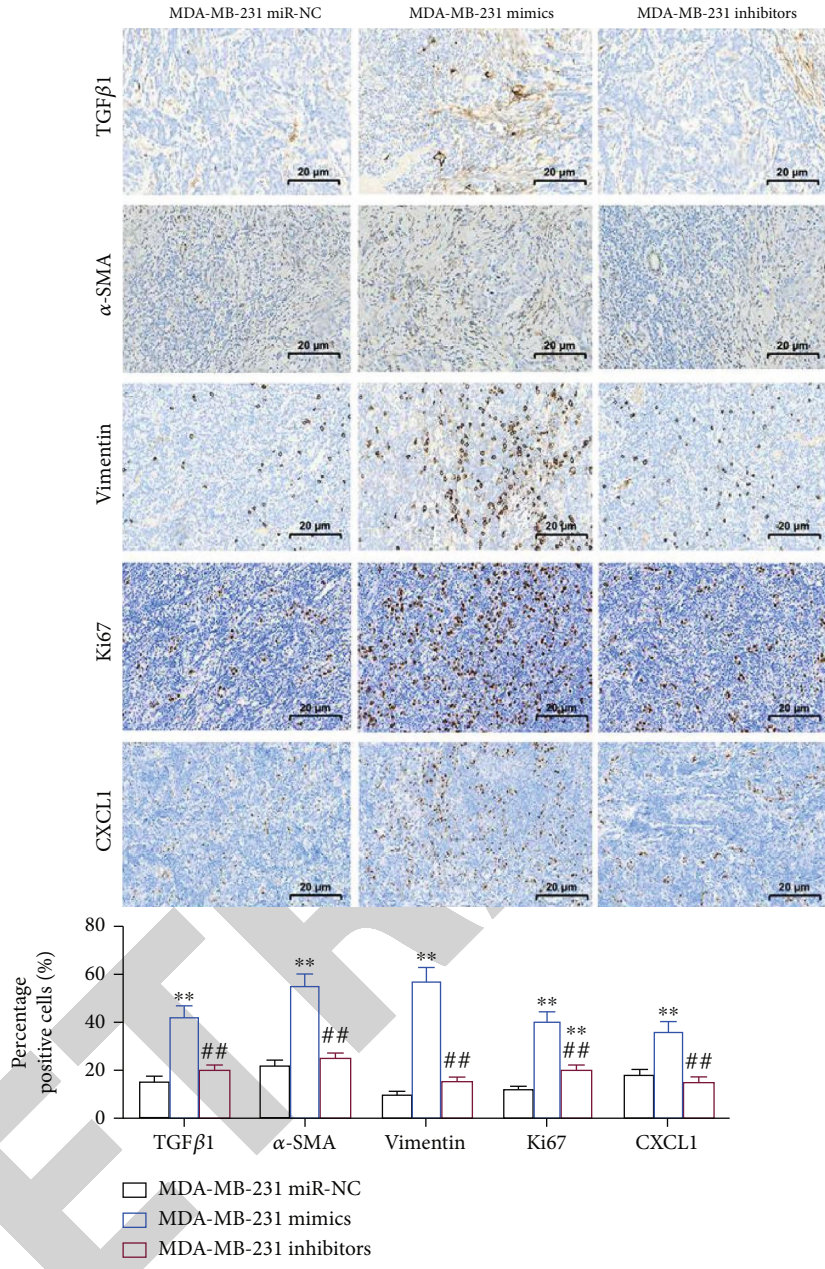


FIGURE 6: Continued.





(g)

FIGURE 6: Continued.

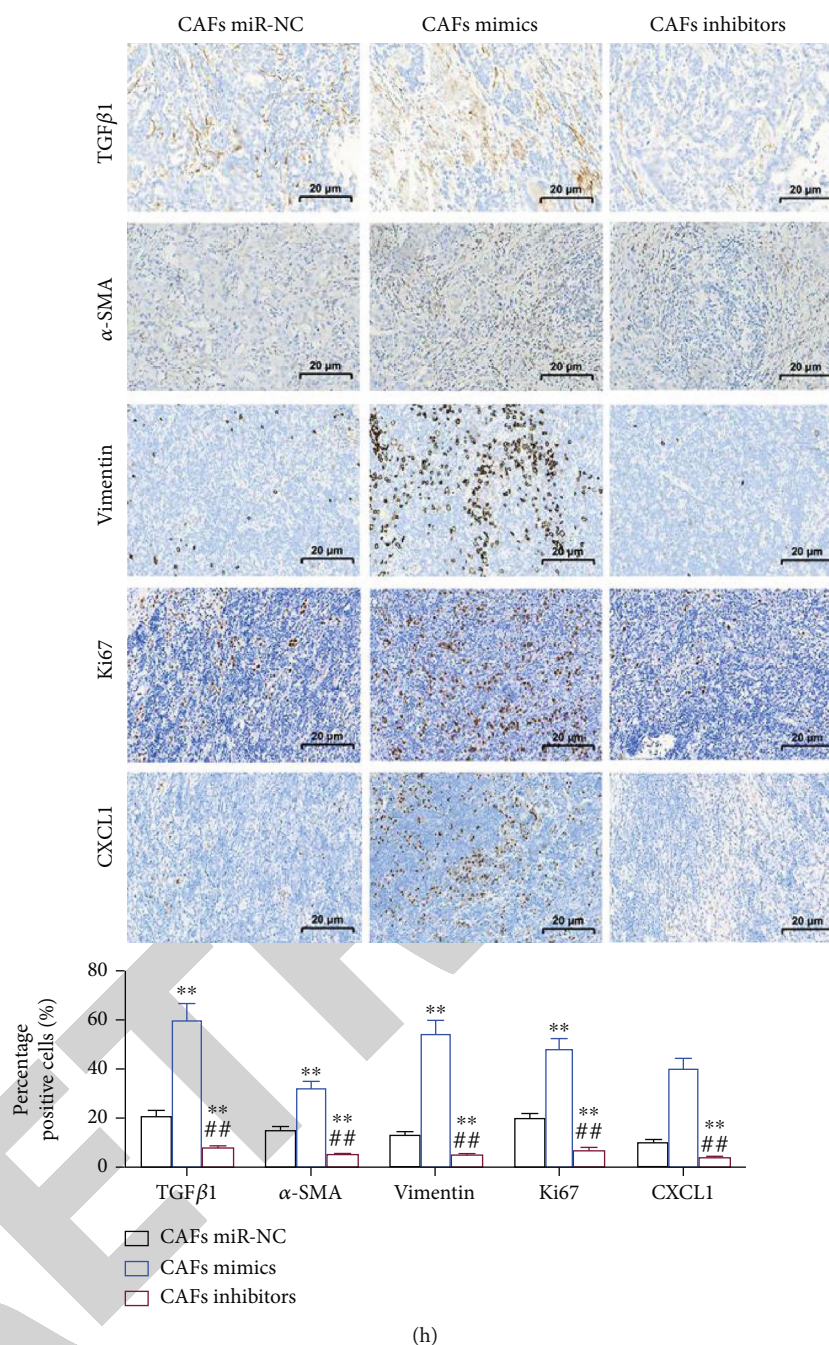


FIGURE 6: Exosomal miR-425-5p stimulated tumor growth *in vivo*. (a) Tumors in mice transplanted with miR-NC transfected MDA-MB-231 cells and miR-425-5p mimics/or inhibitors transfected MDA-MB-231 cells. (b) Growth curve of tumors in different groups. (c) Tumor weight in different groups. (d) Tumors in mice transplanted with miR-NC transfected CAFs and miR-425-5p mimics/or inhibitors transfected CAFs. (e) Growth curve of tumors in different groups. (f) Tumor weight in different groups. (g, h) IHC staining showed the expression of TGFβ1, α-SMA, vimentin, Ki67, and CXCL1 in different groups. Experimental data presented as means ± standard deviation. Experiment was repeated 3 times. \*\* $P < 0.01$  compared with the MDA-MB-231 miR-NC/CAF miR-NC group. ## $P < 0.01$  compared with the MDA-MB-231 mimics/CAF mimics group.

weeks (Better Biotechnology Co., Ltd., Nanjing, China). The mice's weight ranged from 14 to 28 grams at the beginning of the study (Better Biotechnology Co., Ltd., Nanjing, China). Following the completion of the therapy, the cells were trypsinized and then dissolved in a buffer solution. Each group received an equal amount of cells, which were

all adjusted to the same concentration per milliliter of growing medium. The quantity of cells was also kept exactly the same. Cell suspensions were surgically inserted into the thighs of hairless mice (0.5 ml). After that, each of the nudized rats was given food to determine whether or not any tumors had developed. Every week, we measured the

Position 197-203 of TGFBR2 3' UTR mut 5' ...CUAUGCCUUUGACAUUGUCAUAG...  
Position 197-203 of TGFBR2 3' UTR wt 5' ...CUAUGCCUUUGACAUUGUCAUAG...  
has-miR-425-5p 3' AGUUGCCCUCACUAGCACAGUAA

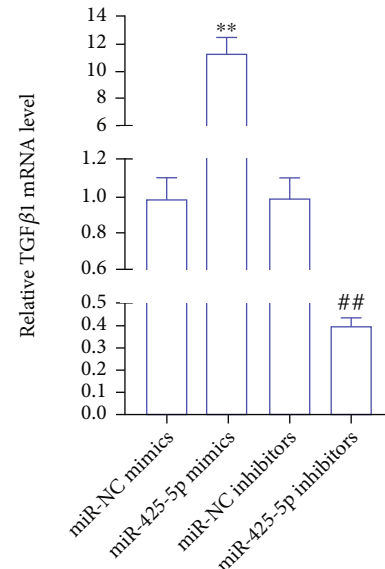
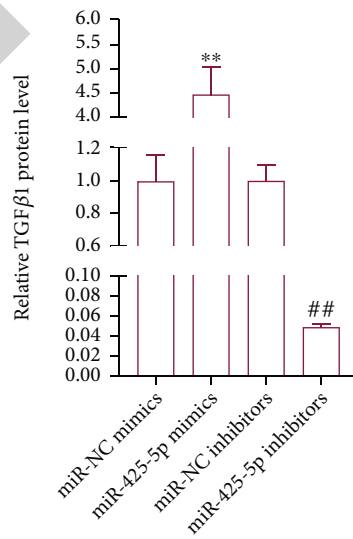
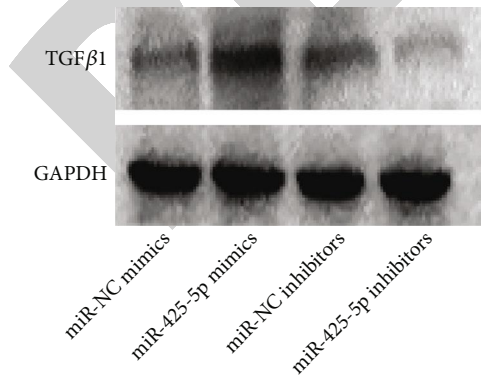
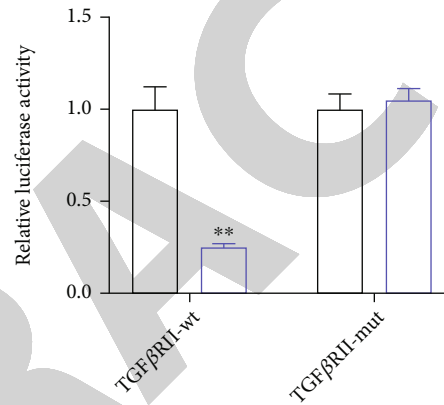
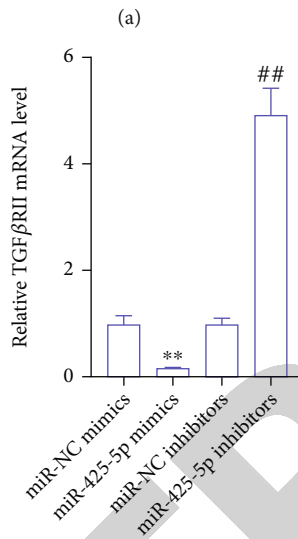
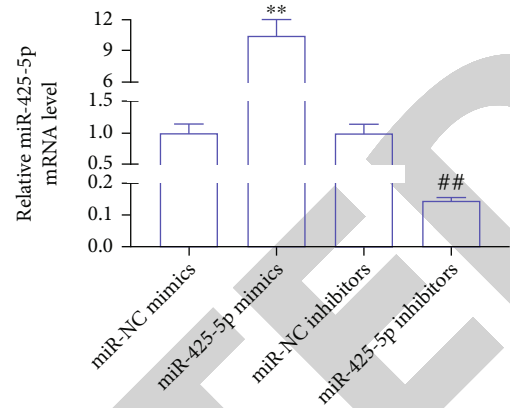
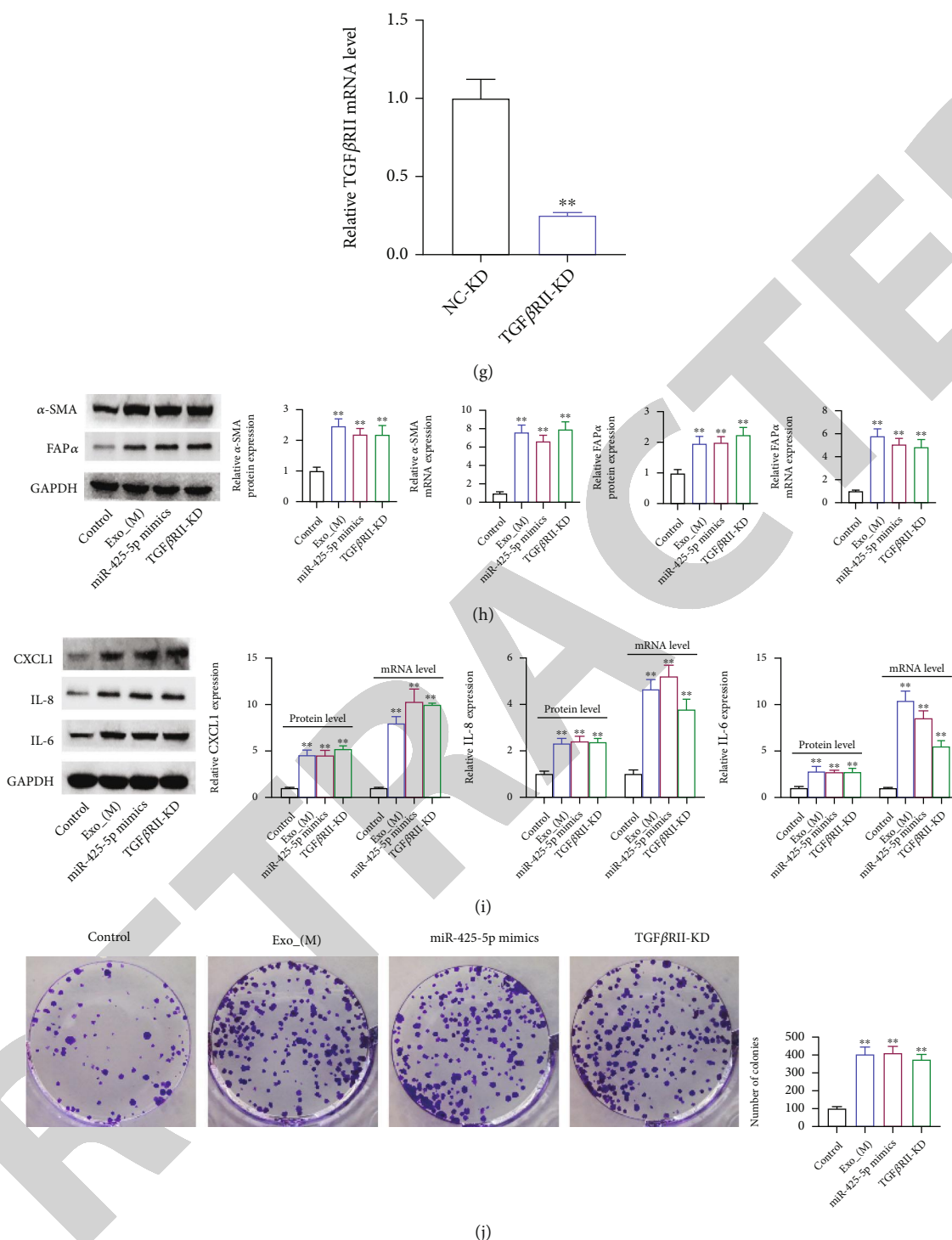


FIGURE 7: Continued.



**FIGURE 7:** miR-425-5p upregulated TGFβ1 expression via targeting TGFβRII-inhibition to promote HMF switch to CAF phenotype. (a) TargetScan database showing a target gene of miR-425-5p was TGFβRII. The expression level of miR-425-5p (b) and TGFβRII (c) in miR-425-5p mimics/inhibitors transfected HMFs by RT-PCR. (d) Dual-luciferase reporter assay detected the luciferase activity in cells cotransfected with TGFβRII-wt/or mut and miR-425-5p mimics. (e, f) TGFβ1 expression in miR-425-5p mimics/or inhibitors transfected HMFs was detected by RT-PCR and western blot assays. (g) The expression of TGFβRII in si-TGFβRII transfected HMFs was detected by RT-PCR. The expression of α-SMA and FAPα (h), CXCL1, IL8, and IL6 (i), and cell proliferation (j) were detected by RT-PCR and western blot, clone formation assays in HMFs uptaking MDA-MB-231-derived exosomes. Experimental data presented as means ± standard deviation. Experiment was repeated 3 times. \*\**P* < 0.01 compared with the miR-NC mimics, miR-425-5p mimics, NC-KD, and control group. ##*P* < 0.01 compared with the miR-NC inhibitors and NC-OE groups.

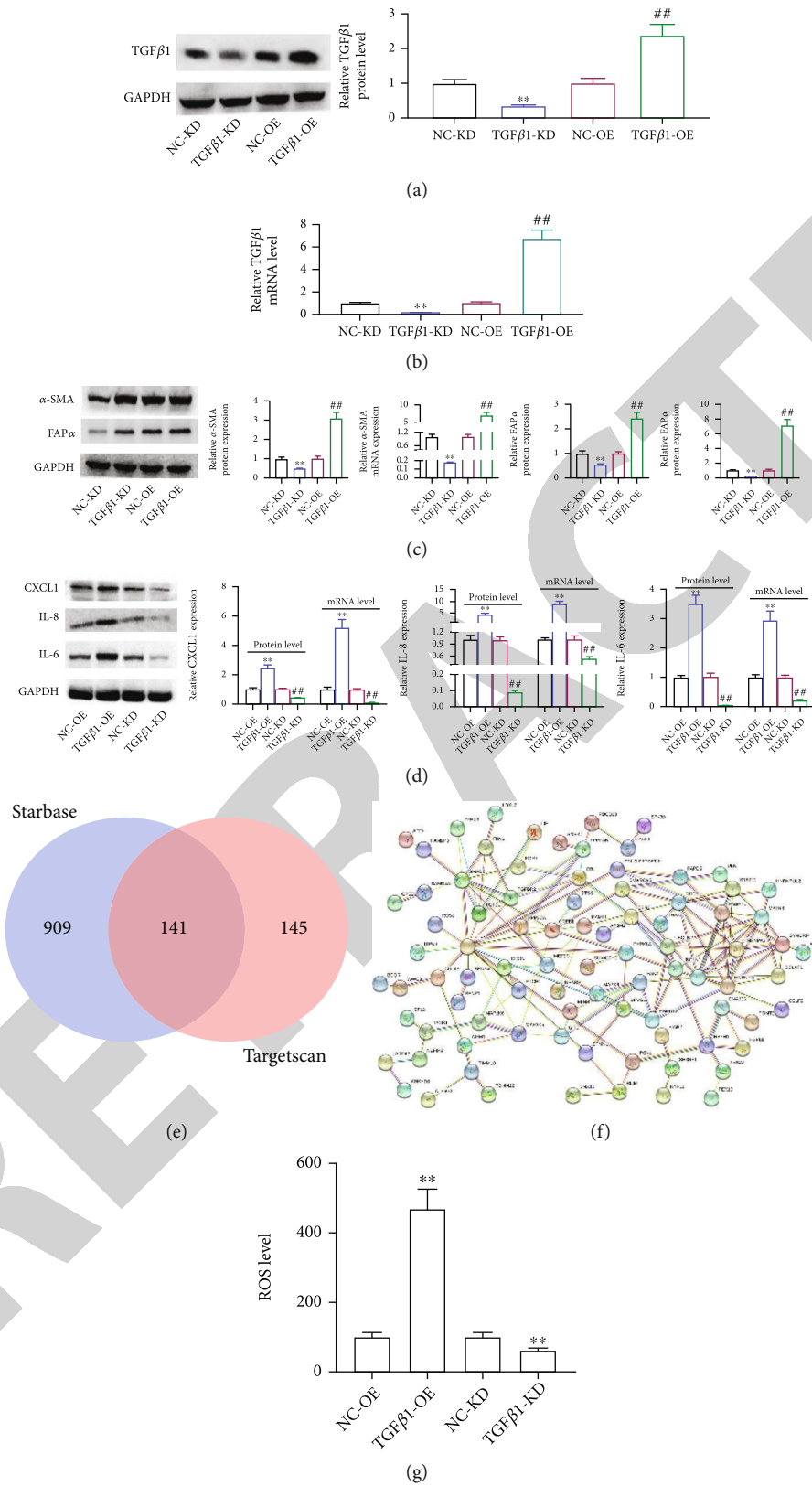


FIGURE 8: TGFβ1 promoted ROS production to promote HMF switch to CAF phenotype. siRNA-TGFβ1 and overexpression-TGFβ1 were transfected into HMFs; the expression TGFβ1 (a, b), α-SMA and FAPα (c), and CXCL1, IL-8, and IL-6 (d) were detected by RT-PCR and western blot assays. (e) Venn analysis of overlapping genes. (f) A PPI network based on STRING website. (g) ROS level. Experimental data presented as means ± standard deviation. Experiment was repeated 3 times. \*\* $P < 0.01$  compared with the NC-KD group. ## $P < 0.01$  compared with the NC-OE group.

volume of the tumor with a caliper to get an accurate reading. In the study of mice that were sacrificed five weeks following the start of the experiment, tumor development curves and tumor weights were produced and compared.

**2.16. Immunohistochemistry.** Following a roasting period of thirty minutes at a temperature of 65 degrees Celsius, tissue slices were removed from the oven, deparaffinized using xylene and alcohol, and then sliced to a thickness of four meters. After the xylene deparaffinization process was complete, the slices were treated with hydrogen peroxide at a concentration of 3 percent in order to suppress the activity of endogenous peroxidase. After antigen retrieval, the sections were treated with bovine serum albumin (BSA) at a concentration of 1 percent in order to reduce nonspecific binding. Using IgG and IgG2a in conjunction with the appropriate secondary antibodies, we were able to detect TGF-1 (1:800), B-SMA (1:500), vimentin (1:400), Ki67 (1600), and CXCL1 (1:800). To detect TGF-1 (1:800), B-SMA (1:500), and vimentin (1:400), as well as Ki67 (1600), we used the appropriate secondary antibodies (1600) (1:3000). After being stained with DAB and hematoxylin for a considerable amount of time, the slices were evaluated and assessed by two separate observers. The existence of tumor cells as well as the degree of staining was taken into consideration when determining the final grades.

**2.17. Construction and Verification of Risk Prediction Model.** R (v3.6.1) features LASSO regression and multivariate Cox regression analysis. “glmnet” avoided model overfitting with LASSO regression. “Survival’s” multivariate analysis determined the model’s final variables using LASSO regression. Each patient’s risk score was calculated using regression coefficients and gene expression levels. BC patients have prognostic risk scores. We categorized BC patients using the median risk score. Long-term survival rates were compared using Kaplan-Meier curves and the log-rank test. This study used ROC and AUC to evaluate risk models. Gene transcription heatmaps and risk score maps were used to evaluate the model.

**2.18. Statistical Analysis.** During the course of this inquiry, each experiment was carried out using at least three biological replicates. The mean and standard deviation are both shown in the table that is located above. GraphPad Prism8 and SPSS 22.0 were the software packages that were applied in order to carry out statistical analysis (IBM, Armonk, NY, USA). When comparing two groups, the *t*-test for independent samples was utilized; however when comparing several groups, the one-way analysis of variance was utilized. In order to determine whether or not there were any changes that were statistically significant, the Kaplan-Meier curves and the log-rank test were applied to the overall survival analysis. The Pearson correlation test was applied to the data gathered for the investigation of correlation (Pearson correlation coefficient). The two-sided *P* value of 0.05 indicated that there was a difference that may be considered statistically significant ( $n = 3$ ).

### 3. Results

**3.1. Exosomes Derived from MDA-MB-231 and BT549 Cells Promoted the Transition of HMFs to the CAF Phenotype.** Exosomes from MDA-MB-231 and BT549 cells were examined and characterized, indicating that they exhibit a typical membrane structure and diameter of less than 100 nm under TEM (Figures 1(a) and 1(b)). The exosome marker protein TSG101 was significantly increased, and HSP70 was remarkably decreased by western blot (Figure 1(c)). Following that, exosomes from MDA-MB-231 and BT549 cells were cultured with HMFs in an attempt to induce HMFs to acquire the CAF phenotype (Figure 1(d)). The findings demonstrated that HMFs could uptake exosomes from MDA-MB-231 and BT549 cells (Figure 1(e)), and that these HMFs had high levels of  $\alpha$ -SMA and FAP $\alpha$  expression (Figure 1(f)). Therefore, these cells were given the names CAFs(M) and CAFs(B).

**3.2. miR-425-5p Was Highly Expressed in Exosomes Derived from MDA-MB-231 and BT549 Cells.** FISH assay revealed that miR-425-5p (red) was expressed in HMFs, MDA-MB-231, and BT549 cells (Figure 2(a)), but its expression level and number were significantly higher in MDA-MB-231 and BT549 cells than in HMFs (Figure 2(b)). Meanwhile, miR-425-5p expression was noticeably higher in exosomes isolated from MDA-MB-231 and BT549 cells when compared to HMFs (Figure 2(c)). Subsequently, miR-425-5p inhibitors were transfected into MDA-MB-231 and BT549 cells to reduce miR-425-5p expression (Figure 2(d)). After that, to inhibit miR-425-5p expression in CAFs, exosomes were extracted from MDA-MB-231 and BT549 cells that had been transfected with miR-425-5p inhibitors (Figure 2(e)).

**3.3. miR-425-5p Inhibitors Inhibited the Proliferation, Invasion, and Migration of HMFs Induced by Exosomes.** To determine whether exosomes can induce HMFs the switch to CAFs phenotype, we examined the motility of HMFs that had ingested exosomes using the clone formation, Transwell, and cell scratch tests. The results indicated that MDA-MB-231 and BT549 cell exosome-containing HMFs significantly increased proliferation (Figure 3(a)), invasion (Figure 3(c)), and migration (Figure 3(e)). However, HMFs that incorporated exosomes from miR-425-5p inhibitor-transfected MDA-MB-231 and BT549 cells had significantly lower proliferation (Figure 3(b)), invasion (Figure 3(d)), and migration (Figure 3(f)) capacities than HMFs that did not.

**3.4. Exosomes Derived from BC Cells Accelerated the Transition of HMFs to the CAF Phenotype.** We used exosomes derived from miR-425-5p inhibitors transfected MDA-MB-231 and BT549 cells to coinubate with HMFs and detect related gene expression in order to further elucidate the role of miR-425-5p on exosomes secreted by BC cells in the conversion of HMFs to CAF phenotype. The changes in the expression of these genes were compared to those in HMFs treated with nontransfected BC cell exosomes. Western blot and RT-PCR analysis revealed that exosomes from MDA-MB-231 and BT549 cells significantly

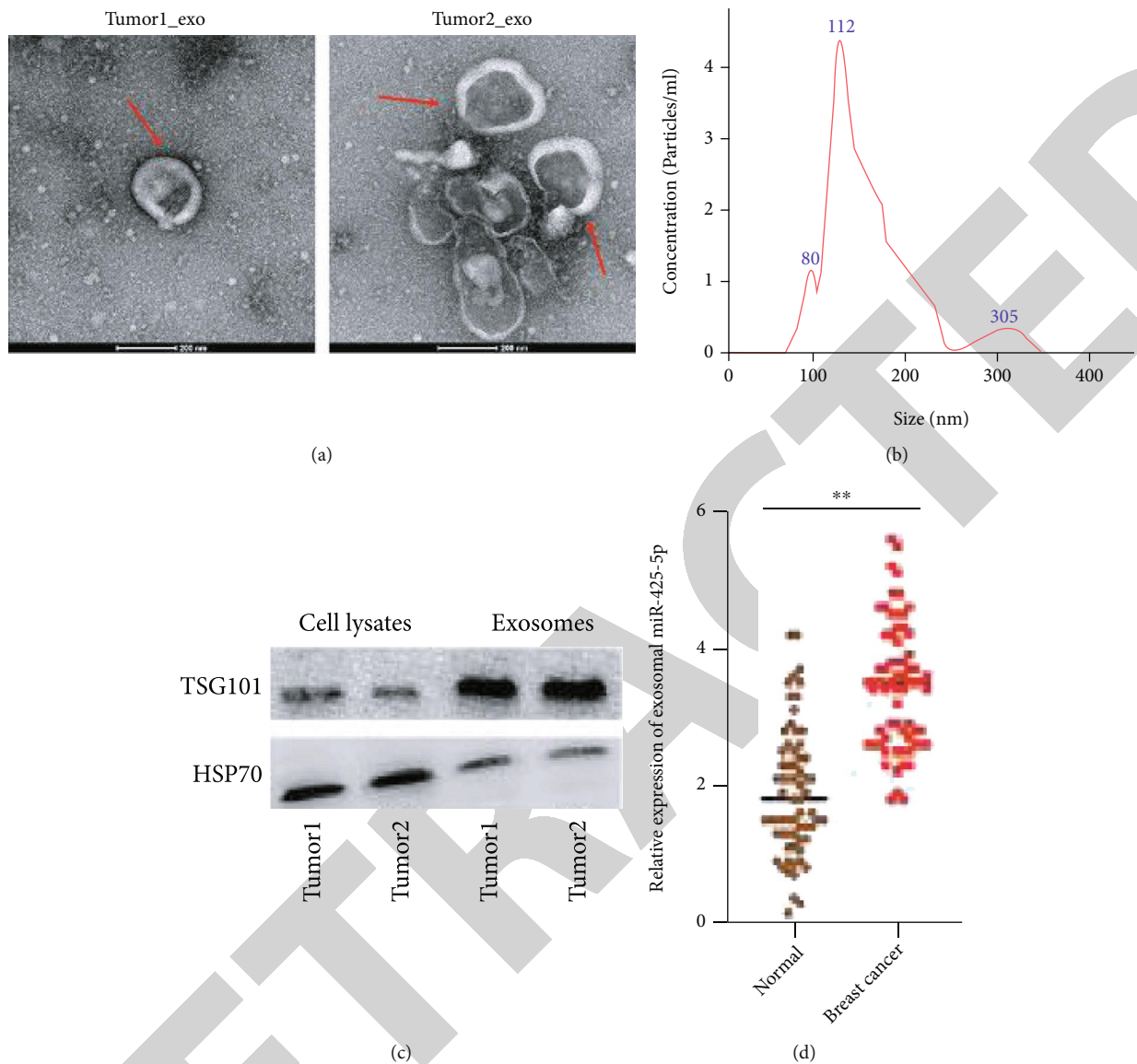


FIGURE 9: Continued.

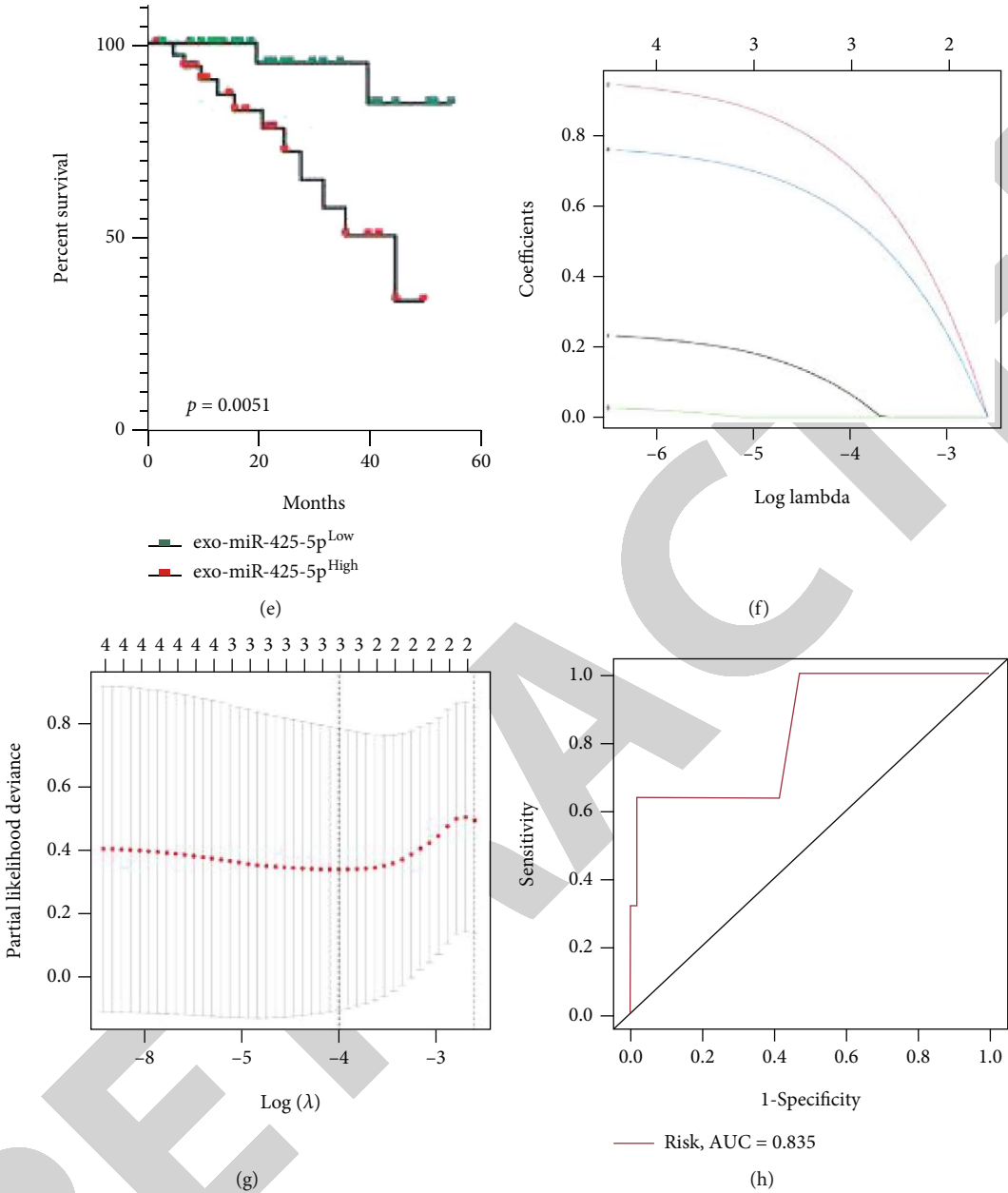


FIGURE 9: Continued.



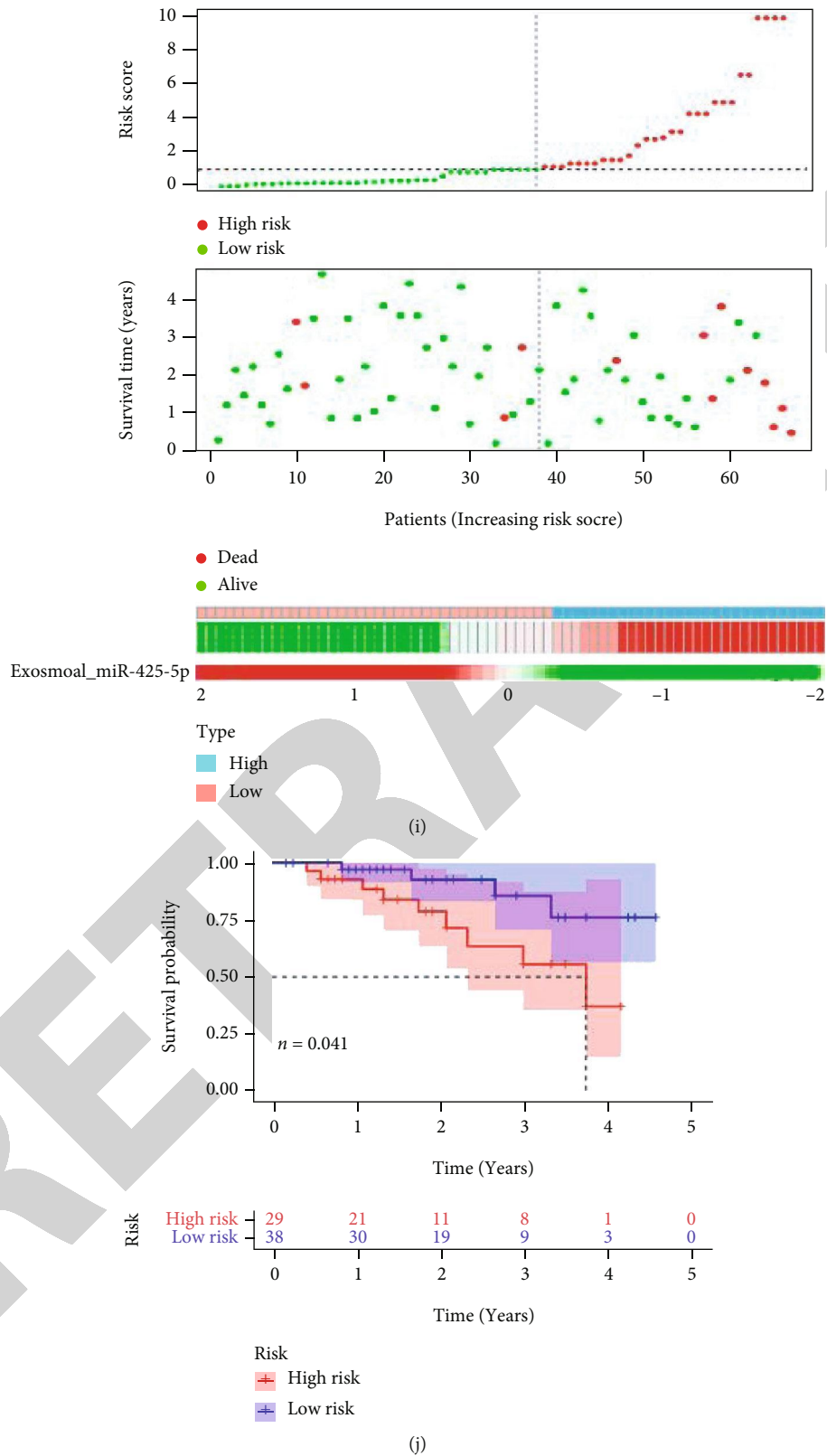
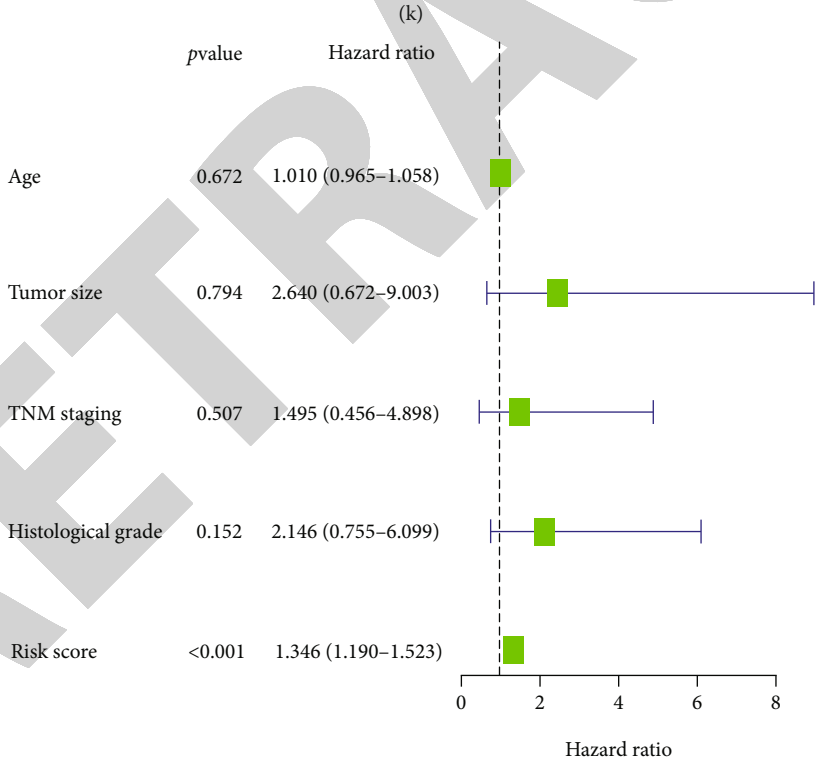
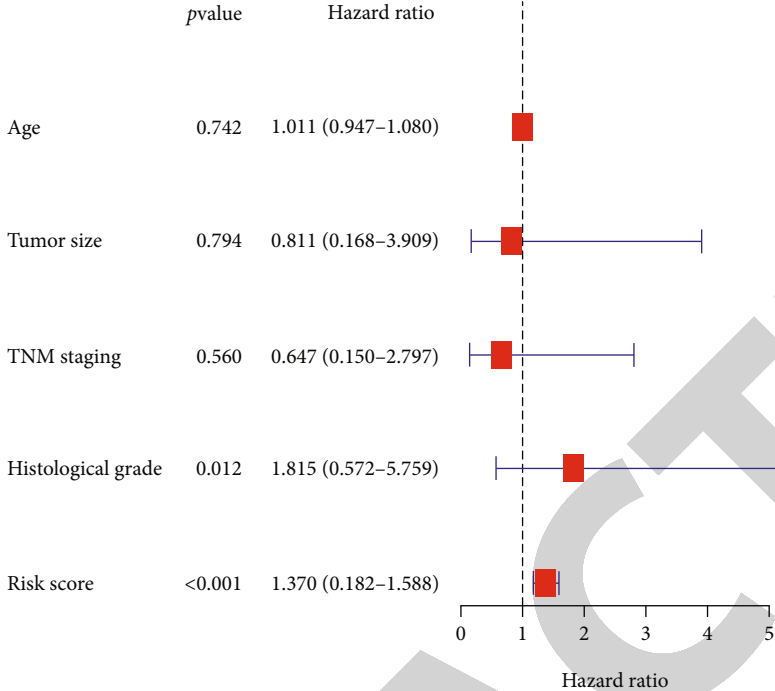


FIGURE 9: Continued.



(l)  
FIGURE 9: Continued.

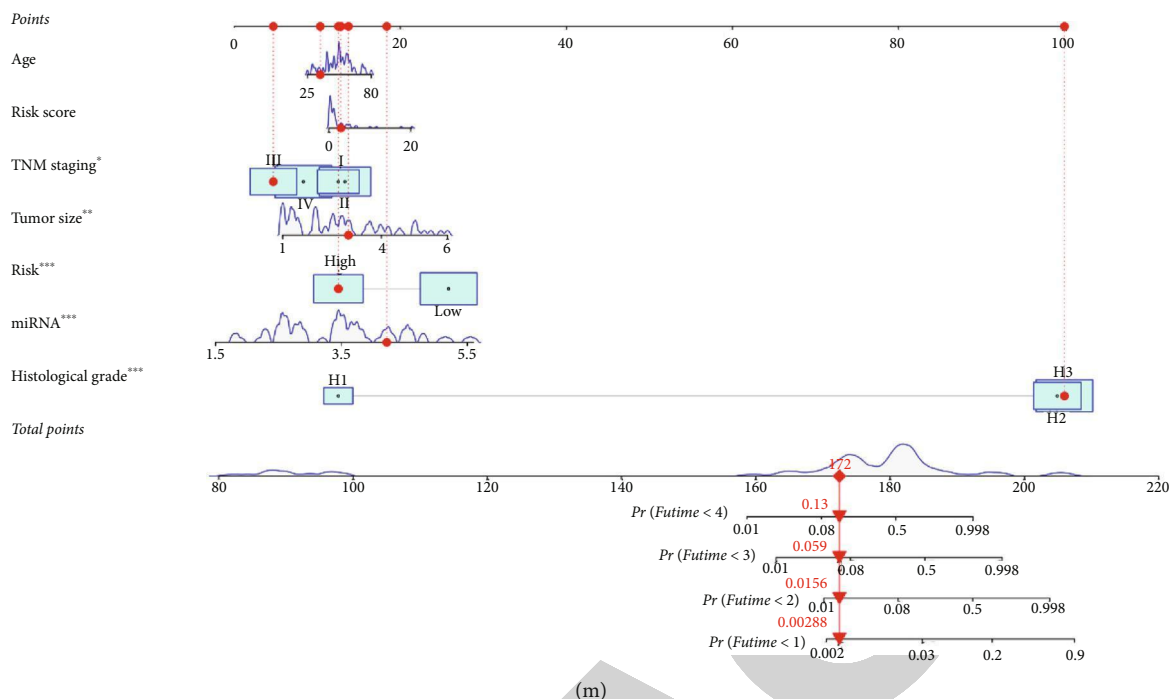


FIGURE 9: Construction of prognostic model for exosomal miR-425-5p in BC patients. (a) Exosome from blood of BC patient identification by TEM. (b) Size distribution of MDA-MB-231- and BT549-derived exosome diameters. (c) Detection of TSG101 and HSP70 protein expression by western blot. (d) The mRNA level of miR-425-5p was detected in exosomes from blood between healthy donors and BC patients. (e) Kaplan-Meier survival analysis for miR-425-5p expression in exosomes from blood of BC patients. (f, g) LASSO Cox analysis identified 4 factors correlated with the overall survival. (h) The ROC curve showed that the AUC of the 4-factors prognostic model was 0.835. (i) Risk score distribution, survival overview, and the heatmap showing the expression profiles of miR-425-5p from exosomes in the high- and low-risk groups. (j) The patients in the high-risk group exhibited a worse overall survival than those in the low-risk group. (k) Independent prognostic analysis showed that the 4-factor risk signature was significantly correlated with the OS of BC patients by a univariate Cox regression analysis. (l) Independent prognostic analysis showed that the 4-factor risk signature was significantly correlated with the OS of BC patients by a multivariate Cox regression analysis. (m) The nomogram of risk score and clinical characteristics. LASSO: least absolute shrinkage and selection operator; ROC: receiver operating characteristic; AUC: area under curve; OS: overall survival. Experimental data presented as means  $\pm$  standard deviation. Experiment was repeated 3 times. \*\* $P < 0.01$  compared with the normal group.

increased the expression of  $\alpha$ -SMA and FAP $\alpha$  and promoted the levels of CXCL1, TGF $\beta$ 1, and IL-6 in HMFs (Figures 4(a) and 4(b)). However, exosomes from miR-425-5p inhibitor-transfected BC cells decreased the expression of the above genes in HMFs and reversed the effects of exosomes from BC cells on P21, P27, and Ki67 (Figure 4(c)). Four genes, including vimentin, N-cadherin, fibronectin, and MMP2, are expressed more frequently by exosomes from BC cells than two other genes, including  $\alpha$ -catenin and E-cadherin, in HMFs. These effects were abolished when exosomes from BC cells were transfected with miR-425-5p inhibitors (Figure 4(d)).

**3.5. Exosomal miR-425-5p Stimulated HMF Switch to the CAF Phenotype.** Following that, we would transfected miR-425-5p inhibitors into CAFs that were HMFs ingesting exosomes from MDA-MB-231 cells in order to determine whether exosomal miR-425-5p is the primary factor promoting the HMFs to adopt the CAFs phenotype. The proliferation, invasion, and migration abilities of MDA-MB-231 cells and CAFs were consistent, implying that HMFs ingested exosomes from MDA-MB-231 cells that exhibited

distinct CAF phenotype characteristics (Figures 5(a)–5(c)). However, miR-425-5p inhibitors could significantly restrain the proliferation, invasion, and migration of CAFs. The expressions of  $\alpha$ -SMA, FAP $\alpha$ , CXCL1, IL-6, TGF $\beta$ 1, P21, P27, Ki67, vimentin, N-cadherin,  $\alpha$ -catenin, fibronectin, MMP2, and E-cadherin were not significantly different between the CAFs miR-NC and the MDA-MB-231 groups (Figures 5(d)–5(g)). On the contrary, transfection of CAFs with miR-425-5p inhibitors results in a decrease in  $\alpha$ -SMA, FAP $\alpha$ , CXCL1, IL-6, TGF $\beta$ 1, Ki67, vimentin, N-cadherin, fibronectin, and MMP2 and an increase in P21, P27, E-cadherin, and  $\alpha$ -catenin (Figures 5(d)–5(g)).

**3.6. Exosomal miR-425-5p Stimulated Tumor Growth In Vivo.** Tumor formation experiments in naked mice revealed that MDA-MB-231 cells transfected with miR-425-5p mimics were significantly more tumorigenic than MDA-MB-231 cells or MDA-MB-231 cells transfected with miR-425-5p inhibitors. However, there was no difference between MDA-MB-231 cells transfected with miR-NC and MDA-MB-231 cells transfected with miR-425-5p inhibitors in terms of their capacity to cause tumors (Figures 6(a)–6(c)).

TABLE 2: Clinicopathological variables and exosomal miR-425-5p expression in 67 breast cancer patients.

Variables	Cases ( <i>n</i> = 67)	Exosomal miR-425-5p		$\chi^2$	P value
		Low	High		
Ages (years)				1.697	0.193
≤ 50	28	16	12		
> 50	39	16	23		
Tumor size (cm)				27.771	0.000*
≤ 2	28	24	4		
>2	39	8	31		
TNM staging				5.280	0.022*
I-II	30	19	11		
III-IV	37	13	24		
Histological grade				17.541	0.000*
Well differentiated	9	8	1		
Moderately differentiated	24	16	8		
Poorly differentiated	34	8	26		

After that, HMFs fed exosomes derived from MDA-MB-231 cells demonstrated oncogenicity *in vitro* (Figure 6(d)). Transfection of CAFs with miR-425-5p mimics increased the oncogenicity *in vitro*, whereas transfection with miR-425-5p inhibitors decreased the oncogenicity *in vitro* (Figures 6(e) and 6(f)). IHC staining revealed that miR-425-5p inhibitors suppressed the intensity of TGF $\beta$ 1,  $\alpha$ -SMA, vimentin, Ki67, and CXCL1 expressions in tumor tissues of mice injected with MDA-MB-231 cells (Figure 6(g)). Similarly, miR-425-5p mimics further strengthened the expression intensity of TGF $\beta$ 1,  $\alpha$ -SMA, vimentin, Ki67, and CXCL1 in tumor tissues of mice injected with CAFs derived from MDA-MB-231 cells, while miR-425-5p inhibitors suppressed the expression intensity of TGF $\beta$ 1,  $\alpha$ -SMA, vimentin, Ki67, and CXCL1 to the greatest extent possible in tumor tissues (Figure 6(h)).

**3.7. miR-425-5p Upregulated TGF $\beta$ 1 Expression via Inhibiting TGF $\beta$ R2 to Promote HMFs Switch to the CAF Phenotype and Increasing ROS Level.** According to the TargetScan database, miR-425-5p was targeting TGF $\beta$ R2, also known as the TGF $\beta$ 1 receptor (Figure 7(a)). miR-425-5p mimics increased miR-425-5p expression while decreasing TGF $\beta$ R2 expression when transfected into HMFs, whereas miR-425-5p inhibitors decreased miR-425-5p expression while increasing TGF $\beta$ R2 expression (Figures 7(b) and 7(c)). The dual-luciferase reporter assay revealed that cells cotransfected with TGF $\beta$ R2-wt and miR-425-5p mimics had significantly decreased luciferase activity, while cells cotransfected with TGF $\beta$ R2-mut and miR-425-5p mimics remained substantially unchanged (Figure 7(d)). Next, miR-425-5p mimics transfection increased TGF $\beta$ 1 expression while transfection of its inhibitors suppressed TGF $\beta$ 1 expression (Figures 7(e) and 7(f)). In order to detect changes in the expression of genes related to CAF phenotype transition, chemotaxis, and inflammation, siRNA-TGF $\beta$ R2 was transfected into HMFs to inhibit its expression (Figure 7(g)). Our findings showed that miR-425-5p mimics, or siRNA-TGF $\beta$ R2 treated HMFs, BC cells, and exosomes secreted by

these cells were highly expressed in  $\alpha$ -SMA and FAP $\alpha$  (Figure 7(h)). In addition, miR-425-5p mimics treatment HMFs and siRNA-TGF $\beta$ R2 transfection in HMFs could elevate the expression of CXCL1, IL-6, and TGF $\beta$ 1 similar to what occurs in exosomes from BC cells (Figure 7(i)). Then, we found that exosomes from BC cells, miR-425-5p mimics, and TGF $\beta$ R2 knockout all have the same ability to promote proliferation and invasion of HMFs (Figure 7(j)). After inhibiting TGF $\beta$ 1 expression in HMFs (Figures 8(a) and 8(b)), the expression of  $\alpha$ -SMA, FAP $\alpha$ , CXCL1, IL-6, and TGF $\beta$ 1 was significantly decreased (Figures 8(c) and 8(d)). On the other hand, TGF $\beta$ 1 promoted the expression of  $\alpha$ -SMA, FAP $\alpha$ , CXCL1, and IL-6 (Figures 8(c) and 8(d)). We obtained 141 intersected target genes from two database (TargetScan and starBase) (Figure 8(e) and Sup Table 1 and Table 2). Based on the STRING website (<https://cn.string-db.org/>), STRING analysis showed that a protein-protein interaction (PPI) network included TGF $\beta$ 1, TGF $\beta$ R2, and ROS (Figure 8(f)). Our results showed that TGF $\beta$ 1 increased ROS levels (Figure 8(g)).

**3.8. Construction of Prognostic Model for Exosomal miR-425-5p in BC Patients.** We discovered that functional miR-425-5p was substantially expressed in exosomes from BC cells. As a result, we studied the differential expression of miR-425-5p in human serum exosomes. Serum samples from 67 cancer patients and healthy donors were used to isolate and identify exosomes. The shape of exosomes from BC patients is illustrated in Figure 9(a). The exosomes' size range was within 200 nm, with a median of 112 nm (Figure 9(b)). Exosome marker protein TSG101 significantly increased, while exosome marker protein HSP70 significantly decreased, according to a western blot analysis (Figure 9(c)). miR-425-5p was substantially expressed in exosomes from serum of BC patients as compared to healthy donors, as shown by RT-PCR (Figure 9(d)). "miR-425-5p high" patients with BC were those whose exosomal miR-425-5p expression levels were at or above the exosomal miR-425-5p median value (3.5). We observed a favorable correlation between exosomal miR-

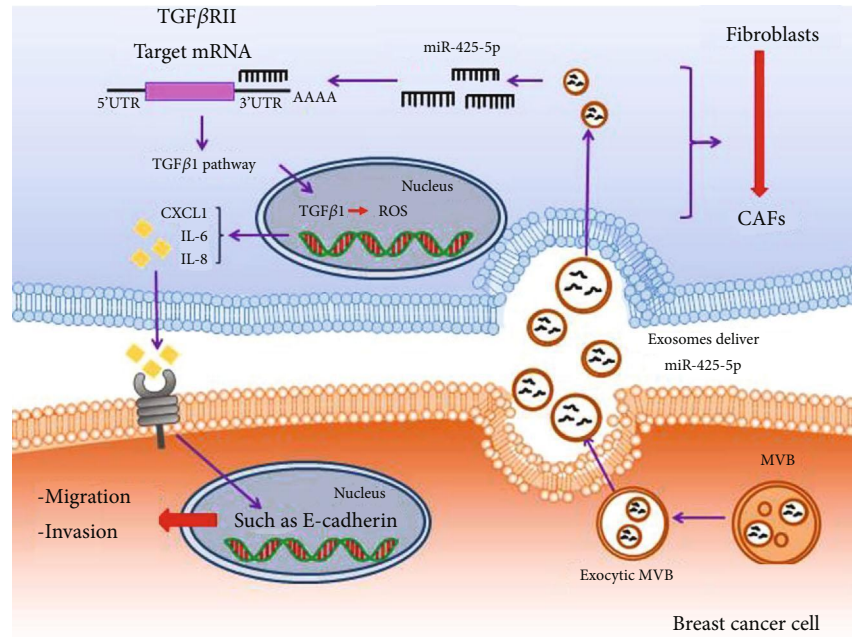


FIGURE 10: The schematic diagram depicts the regulatory mechanism of exosomes deliver miR-425-5p in HMF switch to CAF phenotype. Exosomal miR-425-5p promoted HMF switch to CAF phenotype via inhibiting TGFβRII expression to activate TGFβ1 signaling pathway, thereby playing tumor-promoting abilities in normal fibroblasts.

425-5p expression and tumor size, TNM staging, and histological grade, but not with age (Table 2). BC patients with exosomal miR-425-5p<sup>high</sup> had a poor prognosis (Figure 9(e)). The LASSO regression analysis was performed, and the above four variables, including age, tumor size, TNM staging, and histological grade, were selected for the multivariate Cox regression analysis (Figures 9(f) and 9(g)). According to the findings, the ROC curve's AUC for these four parameters was 0.835 (Figure 9(h)). Based on the median value of exosomal miR-425-5p, the risk score of each patient was calculated, and the patients were divided into high- and low-risk groups, suggesting that the highly expressed miR-425-5p group has a higher risk score (Figure 9(i)). Kaplan-Meier curve demonstrated that the prediction model was more effective, and BC patients in the high-risk category had a lower OS rate (Figure 9(j)). Independent prognostic analysis revealed a significant correlation between the 4-factor risk signature and the OS of BC patients by the univariate Cox regression ( $P < 0.001$ , HR = 1.370, 95% CI = 1.182-1.586) and the multivariate Cox regression analyses ( $P < 0.001$ , HR = 1.346, 95% CI = 1.190-1.523) (Figures 9(k) and 9(l)). A nomogram was built that integrated clinicopathological features with risk score, risk-group, and exosomal\_miR-425-5p expression to predict the survival features of BC patients, as shown in Figure 9(m).

#### 4. Discussion

Tumor cells and stromal cells both contribute to the formation of the tumor microenvironment by the secretion of extracellular matrix components such as fibronectin, collagen, proteoglycans, glycoproteins, growth factors, and matrix metalloproteinases [7, 11]. The interaction of epi-

thelial and mesenchymal cells is required for the conversion of NFs to CAFs [12]. CAFs as extracellular matrix are one of the most abundant nonlymphocyte components of tumor microenvironment. CAFs can regulate tumor cell metabolism, migration, stem cell phenotype, and extracellular matrix restructuring, which in turn promotes tumor angiogenesis, proliferation, invasion, and metastasis of tumor cells [5]. To determine whether breast cancer-derived exosomes may successfully promote the conversion of HMFs to CAFs, it is crucial to examine whether the HMFs that take up exosomes generated by breast cancer cells exhibit the phenotypic and motor features of CAFs. Our findings indicate that HMFs consuming tumor-secreted exosomes have enhanced cell proliferation, motility, and invasion capacities as well as high levels of  $\alpha$ -SMA and FAP $\alpha$ , which are classical biomarkers for CAFs. High expression of  $\alpha$ -SMA and FAP $\alpha$  is closely associated with poor prognosis in tumor patients. This suggests that exosomes secreted by breast cancer cells can promote the transformation of fibroblasts into CAFs.

In recent years, studies have found that miRNAs loaded with breast cancer cell-derived exosomes may influence the tumor microenvironment and consequently affect the invasion and metastasis of breast cancer [13]. It was reported that exosomal miR-21 promoted cisplatin resistance in esophageal squamous cell carcinoma [14]. For example, miRNA dysregulation in melanoma has been shown to promote CAF activation via induction of epithelial-mesenchymal transition (EMT), which in turn alters the secretory phenotype of CAFs in the stroma [15]. miR-425-5p may act on oncogene in breast cancer given that it has been demonstrated to promote tumor progression and that it is significantly upregulated in breast cancer [16],

gastric cancer [17], lung cancer [18], and other tumors. In addition, an interesting study confirmed that the highly expressed miR-425-5p in pancreatic cancer was significantly positively correlated with the expression of inflammatory factor (IL-23) [19]. In summary, these studies point to miR-425-5p as a comprehensive factor that can regulate the pathophysiology of cancer. In this study, we found that miR-425-5p was not only expressed in breast cancer cells but also expressed in HMFs. What distinguishes HMFs from breast cancer cells is that miR-425-5p expression is significantly lower, suggesting that miR-425-5p may be a “bridge” molecule between HMFs and CAFs. After that, miR-425-5p inhibitors were transfected into breast cancer cells; the exosomes of the above cells were then retaken by HMFs, demonstrating a significant increase in cell proliferation, invasion, and migration. However, we found that miR-425-5p inhibitor uptake significantly reduced the increased proliferation, migration, and invasion induced by exosomes derived from breast cancer cells. This reversely demonstrated that miR-425-5p could be transmitted to HMFs through exosomes to increase cell motility. In light of the diverse phenotypic characteristics of CAFs, the epithelial-mesenchymal transition-associated proteins vimentin, E-cadherin, and N-cadherin; migration invasion-related proteins  $\alpha$ -catenin, fibronectin, and MMP2 [20]; chemokine CXCL1, inflammatory factor IL-6, and TGF $\beta$ 1 [21]; and proliferation-associated proteins P21, P27, and Ki67 were selected as judge indicators for the conversion of HMFs to CAFs [22]. The results indicated that uptake of exosomes derived from breast cancer cells increased expression of CXCL1, IL-6, TGF $\beta$ 1, Ki67, vimentin, N-cadherin, fibronectin, and MMP2 in HMFs and inhibited the expression of P21, P27,  $\alpha$ -catenin, and E-cadherin expressions. Based on the above experimental results, we determined that breast cancer cell sourced-exosomes can promote the phenotype transformation of HMFs to CAFs. However, miR-425-5p inhibitors greatly decreased the ability of breast cancer cell-derived exosomes to induce the transformation of HMFs into CAF phenotypes. We transfected miR-425-5p inhibitors into HMFs uptaking BC cell-derived exosomes and found that the cell motility and phenotypic characteristics were consistent with those of HMFs uptaking BC cell-derived exosomes transfected with miR-425-5p inhibitors. These provide additional evidence that BC cell-derived exosomes can promote the conversion of HMFs to CAFs by delivering miR-425-5p.

It is a classic mechanism for miRNA to act on the occurrence and development of tumors by inhibiting its downstream target genes [23]. Here, we found that TGF $\beta$ R2 is a target gene of miR-425-5p and can be significantly inhibited by it. TGF $\beta$ R2 is one of the receptors for TGF $\beta$ 1, and it is the only one that can independently accept TGF $\beta$ 1 in the absence of another ligand, thus affecting the activation of TGF $\beta$  signaling pathway, which is involved in cell growth, apoptosis, differentiation, proliferation, migration, and epithelial-mesenchymal transformation, among other functions [24]. It reported that TGF $\beta$ 1 induced oxidative stress to generate ROS production and that TGF $\beta$ 1 was the most effective cytokine for inducing the transformation of NFs to CAFs [25, 26]. It is reported that TGF $\beta$ 1 induces ROS production to promote

EMT development and cancer progression [27–29]. Interestingly, many studies have been reported on the role of TGF $\beta$ R2 in inhibiting and promoting cancer [30, 31]. This study focuses for the first time on the relationship between exosome-derived miRNAs and the TGF $\beta$ 1/ROS pathway during the phenotypic transformation of CAFs. In this study, we found that TGF $\beta$ R2 knockout can promote the phenotypic transformation of HMFs to CAFs, which is analogous to the function of TGF $\beta$ 1 expression in this process. Our understanding of this is as follows: TGF $\beta$ 1 binds TGF $\beta$ R2 in large quantities, which leads to decreased expression of TGF $\beta$ R2 in cells, but activates TGF $\beta$  signal to increase TGF $\beta$ 1 release; TGF $\beta$ 1 overexpression generated ROS, thus promoting the transformation of HMFs to CAF phenotype. Our results also showed that miR-425-5p mimics upregulated TGF $\beta$ 1 expression and promoted the phenotype transformation from HMFs to CAFs.

Finally, we established a prognostic risk model by identifying miR-425-5p expression in plasma exosomes of BC patients and found that patients with high miR-425-5p expression in exosomes had a significantly better prognostic. In addition, miR-425-5p is associated with poor prognosis in BC patients. It showed that exosome-derived miR-425-5p offers fresh insights into the occurrence and development of BC and provides a potential novel target for molecular therapy for patients with BC.

However, in this study, the mechanism and action of exosome-derived miR-425-3p in BC is only described at the molecular level, and the transcriptional level (e.g., transcriptome sequencing) of patient blood samples was not explored. We will keep increasing the sample size in subsequent studies and look into its function in immune activity in the tumor microenvironment.

In conclusion, the involvement of miR-425-5p in reprogramming the microenvironment via inhibition of TGF $\beta$ R2 expression and production of ROS to activate TGF $\beta$ 1/ROS signaling pathway, thereby promoting tumor growth in normal fibroblasts via EMT, migration, and invasion, in addition to its tumor-growth role (Figure 10), endows this miRNA with a significant therapeutic potential in breast cancer.

## Data Availability

The data will be available upon reasonable requests from the corresponding author.

## Conflicts of Interest

All authors declared that they have no conflict of interest.

## Authors' Contributions

Yue Zhu and He Dou contributed equally to this article.

## Acknowledgments

This study was supported by the National Natural Science Foundation of China (81872145) and Heilongjiang Province Postdoctoral Research Foundation (LBH-Q18078).

## Retraction

# Retracted: Novel Therapeutic Mechanism of Adipose-Derived Mesenchymal Stem Cells in Osteoarthritis via Upregulation of BTG2

### Oxidative Medicine and Cellular Longevity

Received 20 June 2023; Accepted 20 June 2023; Published 21 June 2023

Copyright © 2023 Oxidative Medicine and Cellular Longevity. This is an open access article distributed under the Creative Commons Attribution License, which permits unrestricted use, distribution, and reproduction in any medium, provided the original work is properly cited.

This article has been retracted by Hindawi following an investigation undertaken by the publisher [1]. This investigation has uncovered evidence of one or more of the following indicators of systematic manipulation of the publication process:

- (1) Discrepancies in scope
- (2) Discrepancies in the description of the research reported
- (3) Discrepancies between the availability of data and the research described
- (4) Inappropriate citations
- (5) Incoherent, meaningless and/or irrelevant content included in the article
- (6) Peer-review manipulation

The presence of these indicators undermines our confidence in the integrity of the article's content and we cannot, therefore, vouch for its reliability. Please note that this notice is intended solely to alert readers that the content of this article is unreliable. We have not investigated whether authors were aware of or involved in the systematic manipulation of the publication process.

Wiley and Hindawi regrets that the usual quality checks did not identify these issues before publication and have since put additional measures in place to safeguard research integrity.

We wish to credit our own Research Integrity and Research Publishing teams and anonymous and named external researchers and research integrity experts for contributing to this investigation.

The corresponding author, as the representative of all authors, has been given the opportunity to register their agreement or disagreement to this retraction. We have kept a record of any response received.

### References

- [1] Q. Yang, L. Jin, Q. Ding et al., "Novel Therapeutic Mechanism of Adipose-Derived Mesenchymal Stem Cells in Osteoarthritis via Upregulation of BTG2," *Oxidative Medicine and Cellular Longevity*, vol. 2022, Article ID 9252319, 15 pages, 2022.

## Research Article

# Novel Therapeutic Mechanism of Adipose-Derived Mesenchymal Stem Cells in Osteoarthritis via Upregulation of BTG2

Qinyan Yang <sup>1,2,3,4</sup> Li Jin,<sup>1</sup> Qian Ding,<sup>1</sup> Wei Hu,<sup>1</sup> HaiBo Zou,<sup>1,2,3,4</sup> Mingming Xiao,<sup>1</sup> Keyuan Chen,<sup>1</sup> Yue Yu,<sup>1</sup> Jin Shang,<sup>2,3,4</sup> Xiaolun Huang <sup>1,2,3,4</sup> and Yizhun Zhu <sup>1</sup>

<sup>1</sup>State Key Laboratory of Quality Research in Chinese Medicine & School of Pharmacy, Macau University of Science and Technology, Taipa, China

<sup>2</sup>Department of Hepatobiliary and Pancreatic Surgery Center, Cell Transplantation Center, Sichuan Provincial People's Hospital, University of Electronic Science and Technology of China, Chengdu, China

<sup>3</sup>Chinese Academy of Sciences Sichuan Translational Medicine Research Hospital, Chengdu 610072, China

<sup>4</sup>Clinical Immunology Translational Medicine Key Laboratory of Sichuan Province, Sichuan Provincial People's Hospital, University of Electronic Science and Technology of China, China

Correspondence should be addressed to Xiaolun Huang; [huangxiaolun@med.uestc.edu.cn](mailto:huangxiaolun@med.uestc.edu.cn) and Yizhun Zhu; [yzzhu@must.edu.mo](mailto:yzzhu@must.edu.mo)

Received 11 June 2022; Revised 27 August 2022; Accepted 5 September 2022; Published 15 October 2022

Academic Editor: Tian Li

Copyright © 2022 Qinyan Yang et al. This is an open access article distributed under the Creative Commons Attribution License, which permits unrestricted use, distribution, and reproduction in any medium, provided the original work is properly cited.

**Background.** Osteoarthritis (OA) is a debilitating and degenerative joint disease, which is characterized by progressive destruction of articular cartilage. Mesenchymal stem cells (MSCs) have been implicated in the treatment of OA. However, the function of adipose-derived MSCs (AD-MSCs) in OA and its underlying mechanism remain obscure. **Aim.** We aimed to explore the function of AD-MSCs in OA and investigate its potential regulatory mechanism. **Methods.** A guinea pig model of OA was constructed. AD-MSCs injected into the articular cavity of OA guinea pigs were viewed by *in vivo* bioluminescence imaging. The effect of AD-MSCs on the gonarthrosis of OA guinea pigs was evaluated through both macroscopic and microscopic detections. The detailed molecular mechanism was predicted by GEO databases and bioinformatics tools and then verified via mechanism experiments, including ChIP assay, DNA pulldown assay, and luciferase reporter assay. **Results.** AD-MSCs had a significant positive therapeutic effect on the gonarthrosis of the OA model, and the overall effects of it was better than that of sodium hyaluronate (SH). B-cell translocation gene 2 (BTG2) was significantly downregulated in the articular cartilage of the OA guinea pigs. Furthermore, BTG2 was positively regulated by Krüppel-like factor 4 (KLF4) in AD-MSCs at the transcriptional level. AD-MSCs performed an effect on KLF4 expression at the transcriptional levels. **Conclusion.** AD-MSCs suppresses OA progression through KLF4-induced transcriptional activation of BTG2. Our findings revealed an AD-MSC-dominated therapeutic method for OA.

## 1. Introduction

Osteoarthritis (OA) is the most prevalent musculoskeletal disease and a significant healthcare burden on the public since it attacks about 10% of men and 18% of women more than 60 years old [1]. Articular cartilage degradation, subchondral bone sclerosis, inflammation, and osteophyte formation are key characteristics of OA [2]. Oxidative stress, a major cause of chronic inflammation, is increased in OA cartilage. It occurs based on an imbalance between the production of reactive oxygen species (ROS) and their removal

by the antioxidant defense system [3]. Due to inadequate blood supply of articular cartilage and high differentiation of chondrocytes [4], the therapeutic efficacy of OA is always limited.

Mesenchymal stem cells (MSCs) are multipotent adult cells that can be isolated from various adult or neonatal tissues, which has been used in the clinical management of OA [5]. For example, the intra-articular injection of bone marrow-derived MSCs (BM-MSCs) contributes to the regeneration in knee osteoarthritis [6]; Human synovial fluid-derived MSCs (SF-MSCs) have the potential to affect



TABLE 1: Macroscopic evaluation of cartilage repair.

Criteria	Appearance	Points
Degree of defect repair	In level with surrounding cartilage	4
	75% repair of defect depth	3
	50% repair of defect depth	2
	25% repair of defect depth	1
	0% repair of defect depth	0
Integration to border zone	Complete integration with surrounding cartilage	4
	Demarcating border <1 mm	3
	3/4 of graft integration, 1/4 with a notable border >1 mm	2
	1/2 of graft integration with surrounding cartilage, 1/2 with a notable border >1 mm	1
	From no contact to 1/4 of graft integration with surrounding Cartilage	0
Macroscopic appearance	Intact smooth surface	4
	Fibrillated surface	3
	Small, scattered fissures or cracks	2
	Several, small or few but large fissures	1
	Total degeneration of grafted area	0
Overall repair assessment	Grade I: normal	12
	Grade II: nearly normal	11-8
	Grade III: abnormal	7-4
	Grade IV: severely abnormal	3-0

cartilage repair in OA [7]. Nowadays, the mechanisms of BM-MSCs and SF-MSCs in OA have been widely reported [8–11]. In addition to BM-MSCs and SF-MSCs, many studies have also discussed the function of adipose-derived MSCs (AD-MSCs) in OA [12, 13]. As reported previously, small molecules like miRNAs in extracellular vesicles from AD-MSCs may be associated with OA pathogenesis [14]. Besides, AD-MSCs could regulate the expression of inflammatory cytokines and bone morphogenetic proteins to ameliorate OA [15]. However, the detailed mechanism of AD-MSCs in attenuating OA progression remains unknown.

To probe into the potential mechanism by which AD-MSCs regulated OA, we established a guinea pig model of OA. From the GEO database, we analyzed OA-related genes and selected BTG2 as the further research object. Subsequently, we conducted mechanism investigation to verify the involvement of KLF4-induced BTG2 in AD-MDCs-mediated OA. RNA-induced oxidative stress is closely related with disease progression [16, 17]. In this study, we also detected the effect of BTG2 on oxidative stress. In a word, our current study unveiled a novel potential molecular mechanism of AD-MSCs functioning in the treatment of OA.

## 2. Materials and Methods

**2.1. Animal Model of OA.** Fifty-six guinea pigs weighing 350–400 g were randomly divided into four groups after one week of adaptive feeding. The eight guinea pigs from the first

group were sham-operated (control group without any other treatment subsequently), and the other three groups of 48 guinea pigs were received medial meniscus transection (MMT): the skin was cut on the medial side of the knee joint, the medial ligament was cut for exposing the medial meniscus, and then the meniscus was cut from the incision and sutured. After two weeks of regular feeding, three groups of guinea pigs that underwent MMT were renamed according to indicated treatments: MSC group (experimental group), sodium hyaluronate (SH) group (Bausch & Lomb, China; positive control group), and normal saline (NS) group (Double Crane, China; negative control group). For the MSC group, 100  $\mu$ L CFDA-labeled AD-MSC suspension ( $1 \times 10^7$  cells/mL) of P5 generation was injected into the joint cavity; for the SH group, 100  $\mu$ L SH (0.5 mL/5 mg) was injected into the joint cavity; for NS group, 100  $\mu$ L NS was injected into the joint cavity. There were 8 guinea pigs in the control group and 16 in each of the rest three groups. Then, half of the animals from each group were sacrificed three weeks after indicated injections, and the other half were sacrificed after eight weeks of injection. Afterwards, the joints were collected, and the articular cartilages were observed and photographed. Three individuals scored the cartilage defects independently to evaluate the articular cartilage damage, with the joint score scale shown in Table 1. And then, the cartilages were subjected to HE staining, safranin O-fast green staining, toluidine blue staining, Sirius red staining, and immunocytochemistry for type II collagen (Col2) as described [18, 19]. All procedures were carried out in accordance with the guidelines by the

Division of Animal Control and Inspection of the Department of Food and Animal Inspection and Control of Macau and were approved by the Animal Care and Use Committee (ACUC) of the Macau University of Science and Technology (SCXK-2018-0010).

**2.2. Magnetic Resonance Imaging (MRI) of Knee Joints of OA Guinea Pigs.** At the 3<sup>rd</sup> and 8<sup>th</sup> week after the construction of the guinea pig model of OA, BioSpec70/20USR MRI (Bruker, Germany) was performed on a 7.0 T MRI system using a 40-mm mouse body coil. Parameters for the T2 imaging sequence were set as TR = 2100 ms, TE = 40 ms, FOV = 20 mm × 20 mm, layer stick = 0.5 mm, and MTX = 200 × 200. T2 relaxation time was calculated from the sagittal plane through the center of the cartilage repair site using the Bruker Para Vision 6.0 system. MRI images showed the filling of cartilage injury, and the T2\_mapping sequence was used to measure the regeneration of cartilage defect at the 3<sup>rd</sup> and the 8<sup>th</sup> week after injection. Guinea pig joint samples were imaged for the control, NS, and SH groups, and samples were observed for the MSC group.

**2.3. Bipedal Balance Pain Testing.** To analyze the weight distribution of both feet, guinea pigs were put in an angled plexiglass chamber and assessed via a bipedal balance tester (Stoelting Co; Wood Dale, IL, USA). In detail, each hind paw of guinea pigs was put on a separate force plate, with force exerted by each hind limb (in grams) determined within 5 seconds. Each guinea pig was subjected to three independent tests, and the data were calculated as the average value. The sensitivity of the injured side is uniformly expressed as the injured/non-injured weight percentage. The tests were carried out 3 or 8 weeks after indicated injections before the animals were sacrificed.

**2.4. Cell Culture.** AD-MSCs were isolated and extracted by collagenase method. Wash the adipose tissue, and add 0.75 mg/mL type I collagenase solution for 30 minutes at 37°C. Gently discard the supernatant without disturbing the precipitated cells, resuspended with an appropriate amount of normal saline and mixed well. Centrifuge at room temperature 300g for 10 minutes. Carefully suck off the supernatant. Suction pipette head should be placed on the upper liquid level of the centrifuge tube to thoroughly remove grease. Add normal saline to the precipitate and resuspended the mixed cells. Filter the cell suspension with a 100- $\mu$ m cell filter, followed by the criteria [20], in Mesenchymal Stem Cell Basal Medium (MSCBM) (Dakewe, Chengdu, China) with 5% Knockout Serum Replacement (KSDR) (EliteGro, TX, USA). Primary cells were defined as passage 0, and cells passaged to the fifth generation were used for *in vitro* experiments (Chengdu Baimeisen Biological Technology Co. Ltd. provided the AD-MSCs and culture methods). The identification of AD-MSCs was described in Figure S1. The human embryonic kidney cell (HEK293T) cell line obtained from American Type Culture Collection (ATCC, Manassas, VA, USA) was cultivated in RPMI-164 medium with 10% FBS. The above cells were grown in a humid incubator which was set with 5% CO<sub>2</sub> and 37°C.

**2.5. Quantitative Real-Time Polymerase Chain Reaction (qRT-PCR).** The qRT-PCR analysis was performed as previously described [21]. Total RNA was extracted from tissues and cells with TRIzol reagent. A PrimeScript-RT Kit was applied to reverse transcribe the total RNA to synthesize cDNA. qRT-PCR was performed with SYBR Green PCR Kit. RNA expression was calculated by 2<sup>- $\Delta\Delta$ Ct</sup> method and normalized to GAPDH.

**2.6. Measurement of ROS Production and Superoxide Dismutase (SOD) Production.** Cellular ROS Assay Kit (ab113851, Abcam, Cambridge, MA, USA) was utilized to detect intracellular ROS levels as per the manufacturer's instructions. SOD activity was measured using SOD Determination Kit (19160, Sigma-Aldrich, St. Louis, MO, USA) according to the manufacturer's instructions [16]. The level of SOD (U/mg protein) was examined using Synergy-2 microplate reader (BioTek, Winooski, VT, USA).

**2.7. Flow Cytometry Analysis.** Flow cytometry was conducted as previously described [22]. AD-MSCs at the fifth passage reached 80% confluence and were trypsinized, washed, centrifuged, and resuspended in PBS. Subsequently, AD-MSCs were incubated with antibodies against CD90, CD105, and CD73 and the negative control Neg CKTL, which were then subjected to flow cytometry analysis.

**2.8. Chromatin Immunoprecipitation (ChIP) Assay.** ChIP assay was performed to validate the interaction between KLF4 and BTG2 promoter by using the ChIP assay kit as previously described [23]. AD-MSCs were first cross-linked in 4% paraformaldehyde and then sonicated into chromatin fragments of 200-1000 bp, which were incubated with anti-KLF4 or negative control anti-IgG. Subsequently, the chromatin was incubated with magnetic beads. Finally, the precipitated DNAs were purified and analyzed by qRT-PCR.

**2.9. Western Blot Assay.** Total proteins were tissues or cells using RIPA lysis buffer (Beyotime Institute of Biotechnology, China). Protein concentration was determined by using BCA Protein Assay Kit (Abcam, China) according to the manufacturer's instructions. After separation by PAGE, total proteins were transferred onto PVDF (Millipore, USA) membranes and blocked by 5% BSA for 1 h at room temperature. Then, PVDF membranes were incubated with primary antibodies at 4°C overnight. The primary antibodies were as follows: BTG2 (1 : 1000), KLF4 (1 : 1000), and actin (1 : 2000) (Abcam, USA). Next, the membranes were washed with TBST three times and incubated with secondary antibody HRP-labeled goat antirabbit IgG for 1 h at room temperature. Protein expressions were determined using Uvitec Alliance software (Eppendorf, Germany).

**2.10. Luciferase Reporter Assay.** To verify the bond of KLF4 to BTG2 promoter, the BTG2 promoter contained KLF4 binding sites, or mutant binding sites was separately subcloned into pGL3 luciferase reporter vector to build the constructs. The constructs were cotransfected with si-KLF4 or si-KLF4 into HEK293T cells. The luciferase activities were

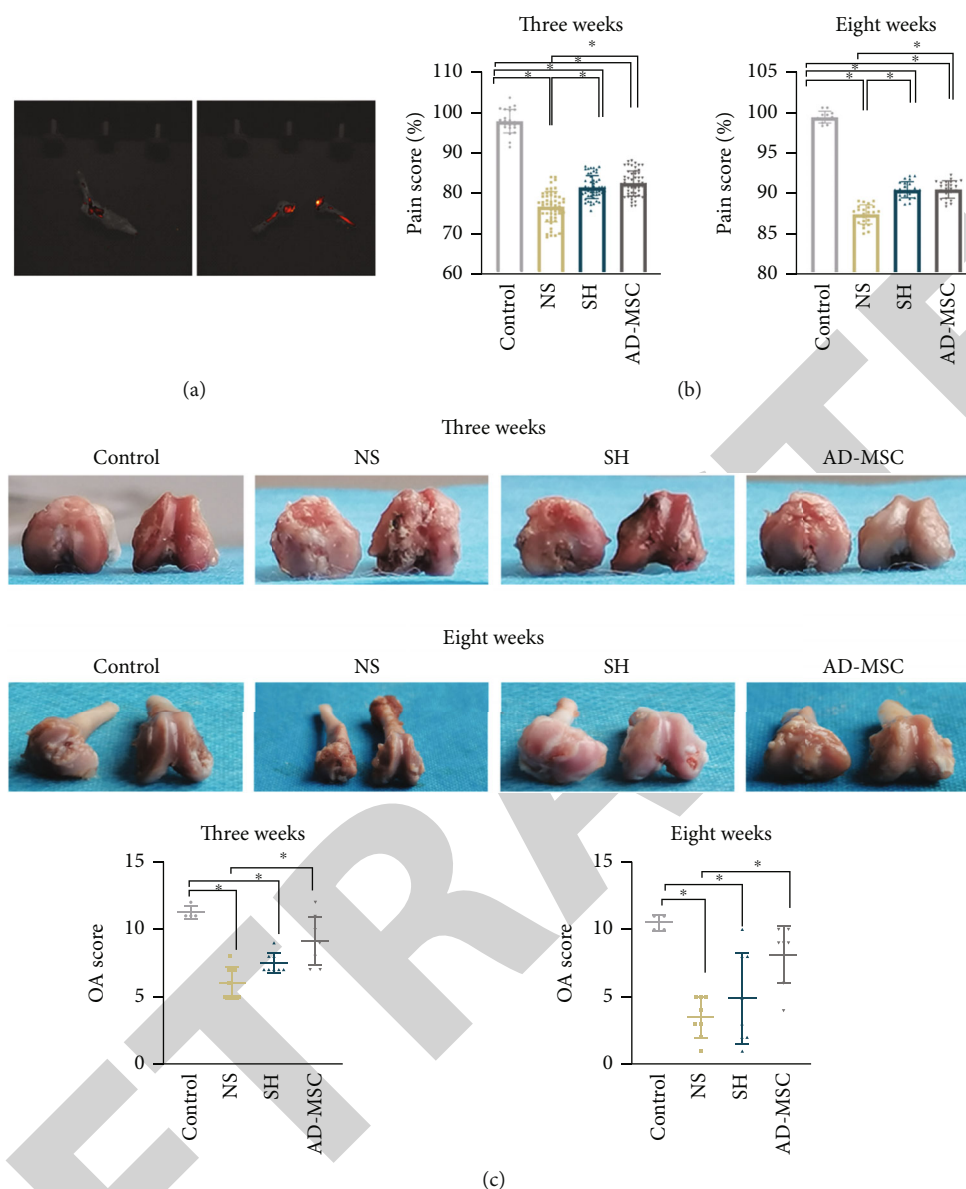


FIGURE 1: AD-MSCs are effective in treating guinea pig model of OA. (a) AD-MSCs marked with CFDA were observed through *in vivo* bioluminescence imaging. (b) Four different groups of OA guinea pigs treated at the 3<sup>rd</sup> and the 8<sup>th</sup> week were subjected to bipedal balance pain testing, with the pain scores of animals in four groups calculated. The sample number for control group at three weeks and eight weeks is separately 24 and 12; the sample number for other three groups at three weeks and eight weeks is separately 54 and 24. (c) The articular cartilages of guinea pigs from indicated groups were photographed, and the damages were scored.  $N = 4$  in control group;  $N = 8$  in other three groups.  $*P < 0.05$ .

analyzed utilizing the Dual-Luciferase Reporter Assay System [24] and normalized to Renilla luciferase activity.

**2.11. DNA Pulldown Assay.** As previously described [25], DNA pulldown assay was conducted to prove the affinity of KLF4 to BTG2 promoter. Cell lysates and BTG2 promoter-specific biotinylated probes were incubated for 2 h at room temperature with streptavidin-agarose beads to form DNA-protein-beads complexes. The complexes were then separated on a magnetic rack. The pulled-down complex was washed six times with 1 mL ice-cold tris-buffered saline and eluted in 80  $\mu$ L protein elution buffer at

95°C for 5 min. Proteins were separated by gel electrophoresis and measured by western blot.

**2.12. Statistical Analysis.** For animal experiments,  $N = 4$  in the control group and  $N = 8$  in other three groups. For cell experiments,  $N = 3$  in each group. Each independent experiment was operated at least three times to ensure the accuracy of the results, and experimental data of three or more replicates were illustrated as the means  $\pm$  SD. The statistical analysis was made by using SPSS 19.0 software with the method of Student's *t*-test or one-way ANOVA. The data were regarded as statistically significant when  $P < 0.05$ .

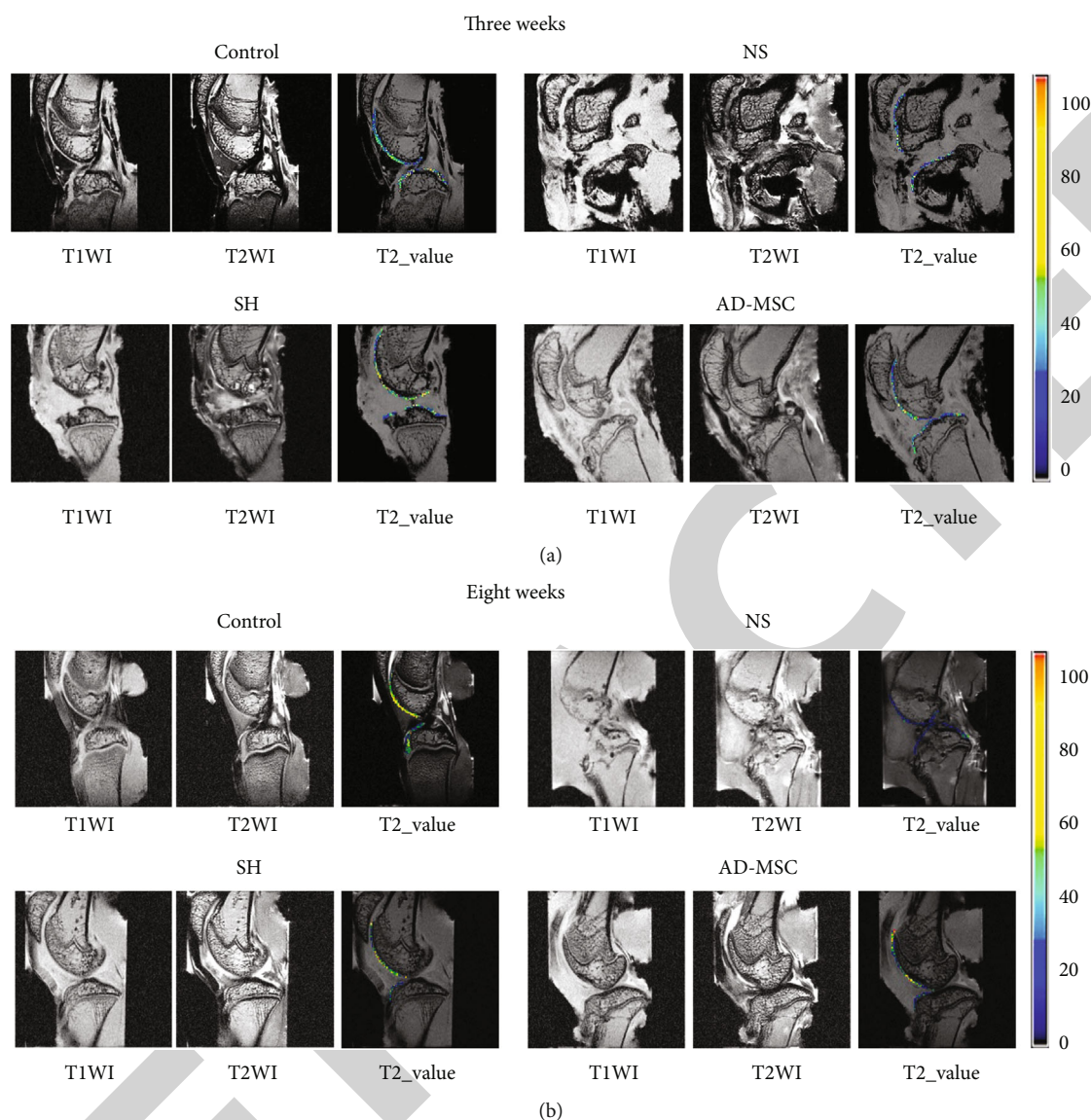


FIGURE 2: The MRI results of knee joints from OA guinea pigs. (a and b) At the 3<sup>rd</sup> and the 8<sup>th</sup> week after indicated injections, MRI was applied to observe the knee-joint of guinea pigs from indicated groups.  $N = 4$  in the control group;  $N = 8$  in other three groups.

### 3. Results

**3.1. AD-MSCs Exhibit Therapeutic Effect on Guinea Pig Model of OA.** To investigate the impact of AD-MSCs on OA, we established an OA model in guinea pigs. As shown in Figure 1(a), AD-MSCs marked with CFDA were observed in the joint area, and cells were concentrated on the articular cartilage surface. After injections, all of the guinea pigs were observed for 3 weeks. It was found that the action competence of guinea pigs treated with MMT gradually weakened. Next, we discovered from the bipedal balance pain testing data that the pain sensitivity of guinea pigs was evidently strengthened in NS groups than other groups after 3 weeks, and such eigenvalue was then partly recovered after 8 weeks. The MSC group looked a little better than the SH group after 3 weeks (although not significant). However, the results

seemed to be similar after 8 weeks between the guinea pigs injected with AD-MSCs and those injected with SH (Table 1) (Figure 1(b)).

Additionally, MMT-induced articular cartilage damage in OA guinea pigs was relieved by treatment with AD-MSCs or SH after 3 weeks and even after 8 weeks. Compared with the control group, the knee cartilage of guinea pigs in the NS group was damaged after 3 weeks, with an uneven surface and terrible inflammatory exudation beneath. Additionally, the SH group and the AD-MSCs group had partial cartilage defects. The cartilage surface was more intact in the AD-MSCs group than in the SH group after 3 weeks. After 8 weeks, the knee cartilage in the NS group was severely damaged, even with bone corrosion. In comparison, the cartilage in the SH group appeared to be partially defective and imperfection. The AD-MSCs group showed remarkable

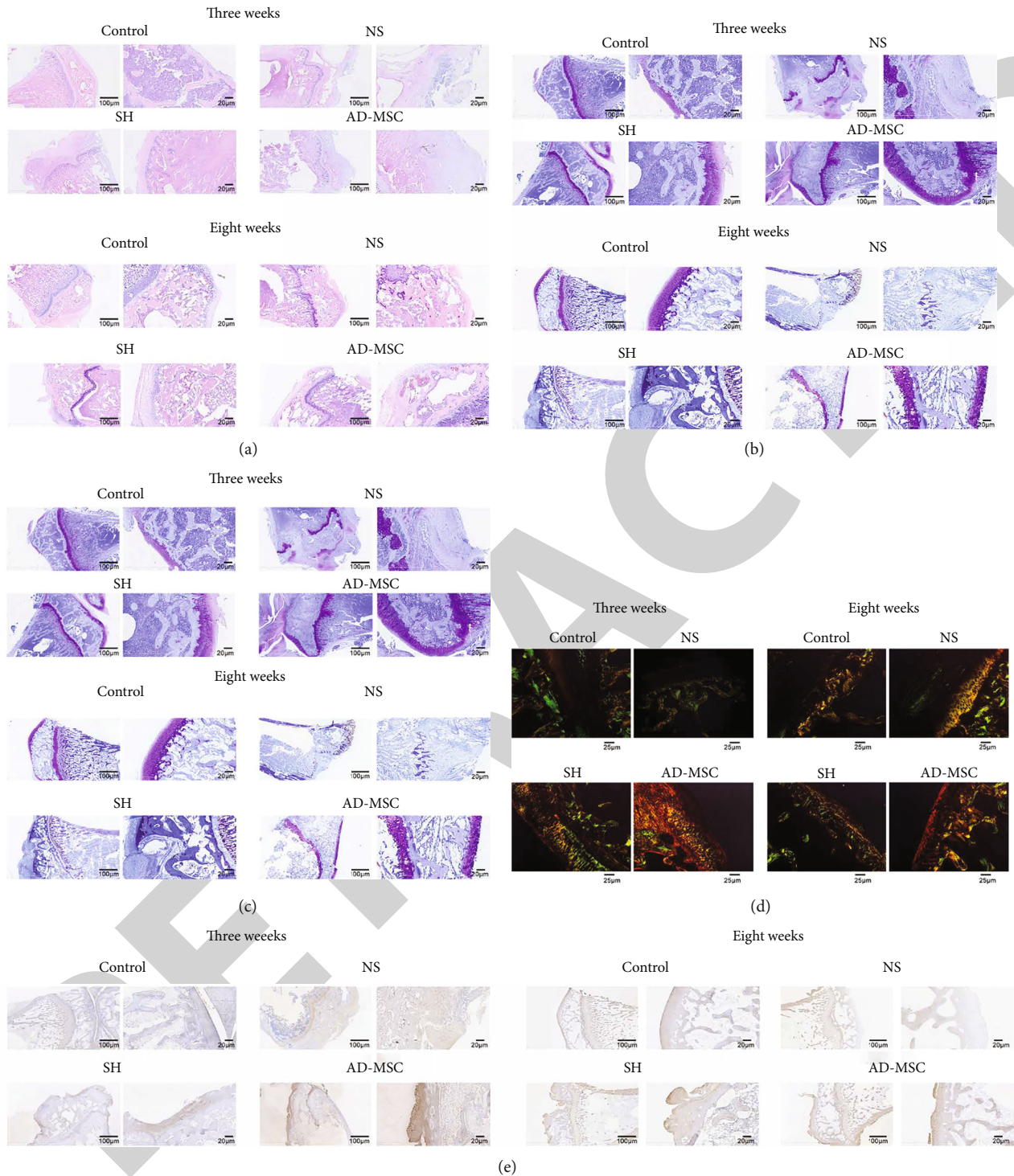


FIGURE 3: AD-MSCs have therapeutic effects on the gonarthrosis of OA guinea pigs. (a) HE staining was utilized to measure the articular cartilage tissues from guinea pigs in four groups (NS, SH, AD-MSC, and control) at the 3<sup>rd</sup> week and the 8<sup>th</sup> week after indicated treatments.  $N = 4$  in the control group;  $N = 8$  in other three groups. All left images: scale bar = 100  $\mu\text{m}$ . All right images: scale bar = 20  $\mu\text{m}$ . (b–d) Safranin O-fast green staining (All left images: scale bar = 100  $\mu\text{m}$ . All right images: scale bar = 20  $\mu\text{m}$ ), toluidine blue staining (All left images: scale bar = 100  $\mu\text{m}$ . All right images: scale bar = 20  $\mu\text{m}$ ), and sirius red staining (scale bar = 25  $\mu\text{m}$ ) of the articular cartilage tissues from guinea pigs in the four groups at the 3<sup>rd</sup> and 8<sup>th</sup> weeks after indicated treatments.  $N = 4$  in the control group;  $N = 8$  in the other three groups. (e) Immunocytochemistry was conducted to examine the expression of Col2 in indicated articular cartilage tissues.  $N = 4$  in the control group;  $N = 8$  in other three groups. All left images: scale bar = 100  $\mu\text{m}$ . All right images: scale bar = 20  $\mu\text{m}$ .

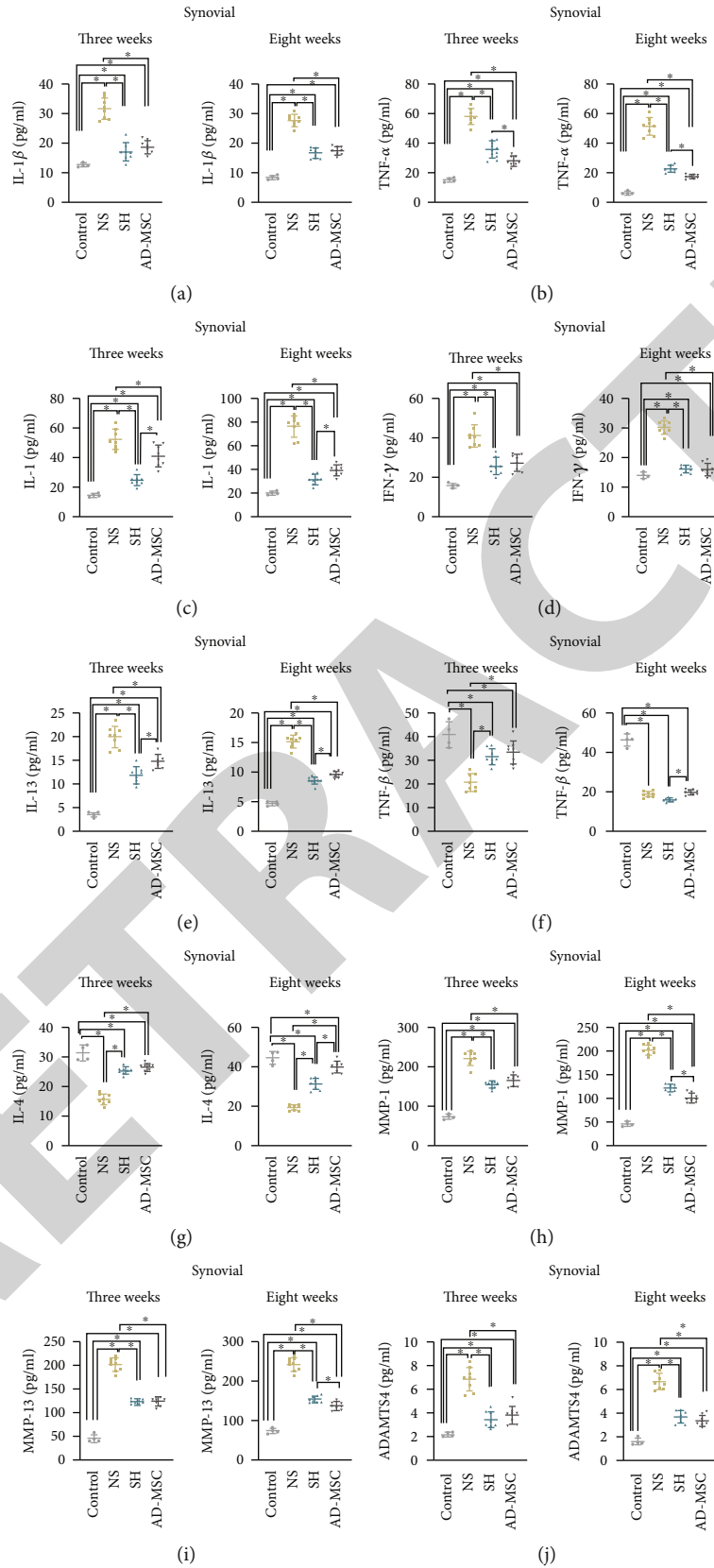


FIGURE 4: Continued.

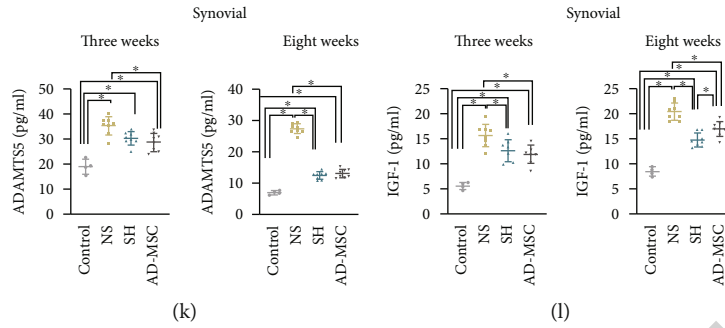


FIGURE 4: The effects of AD-MSCs on the changes of inflammatory-associated cytokines. (a–l) ELISA examined the content of inflammation- and OA-related factors, including IL-1 $\beta$ , TNF- $\alpha$ , IL-1, IFN- $\gamma$ , IL-13, TGF- $\beta$ , IL-4, IGF1, ADAMTS4, ADAMTS5, MMP-1, and MMP-13 in the synovial fluid of articular cavity obtained from guinea pigs in four groups (NS, SH, AD-MSC, and control) after 3 or 8 weeks of injections. Number of replicates.  $N = 4$  in the control group;  $N = 8$  in other three groups.  $*P < 0.05$ .

changes. With most of the articular cartilage covered and only left a tiny loss of ostiole, the damage seemed to be repaired after 8 weeks (Figure 1(c)).

To compare the joint damage in different groups, the OA gross joint score system was used to evaluate the injured joint. It turned out that the joint damage in AD-MSCs group was remarkably repaired. Both the AD-MSCs group and the SH group exhibited higher OA scores compared with the NS group after 3 weeks. After 8 weeks, OA score in the AD-MSCs group and the SH group was also higher than the NS group (Figure 1(c)). In sum, AD-MSCs exhibit therapeutic effect on guinea pig model of OA.

**3.2. AD-MSCs Repair the Cartilage of the Guinea Pig OA Model.** The above results indicated that the therapeutic effect of AD-MSCs on OA was better than SH treatment. However, the specific difference between AD-MSCs and SH treatments was unclear, especially the results after 8 weeks. According to the MRI images, we observed that the cartilages of knee joints were indeed injured after MMT treatment at both 3 and 8 weeks, and AD-MSCs or SH injection could lead to the regeneration of cartilage defects.

Normal articular cartilage surface is clear and smooth. Its morphology on MRI is intact, and its thickness is uniform. MRI image of the AD-MSCs group showed that its articular cartilage was similar to that of the control group after 3 weeks. The cartilage of the SH group was a little thin, while the integrity was fair. Nonetheless, there was still some inflammation in the joint cavity of SH group. Furthermore, MRI image of NS group showed a largest cartilage wear, a serious joint cavity deformation with osteolysis, and a severe inflammatory reaction after 3 weeks (Figure 2(a)).

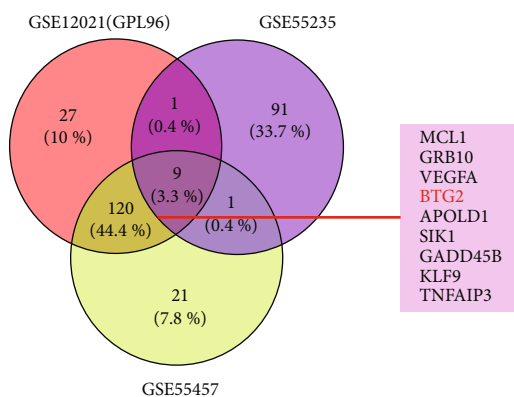
The results in the SH group after weeks were similar to those after 3 weeks, with thinner cartilage, fair integrity, and some inflammation in the joint cavity. The cartilage of the AD-MSCs group was similar to the SH group, and the cartilage was repaired and intact. The NS group had apparent cartilage damage and severe joint cavity deformation. The articular surface was severely worn, and the medial tibial plateau and femoral joints were incomplete. Even the subchondral bone was lost with osteolysis (Figure 2(b)).

Altogether, AD-MSCs treatment for OA is more effective than SH treatment.

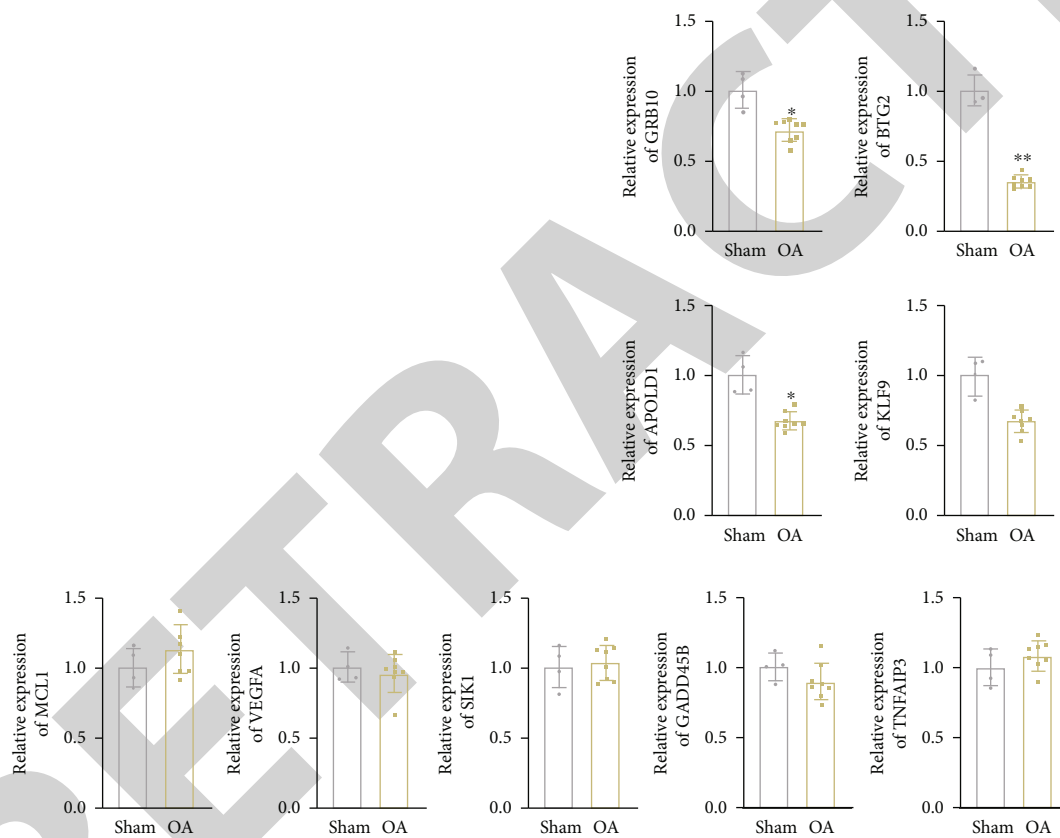
**3.3. AD-MSCs Have Therapeutic Effects on the Gonarthritic Cartilage Tissues in OA Guinea Pig.** We further evaluated the microscopic changes induced by AD-MSCs on the gonarthritic in OA guinea pigs through the macroscopic observation. As shown in HE staining, the articular cartilage tissues were evidently damaged in guinea pigs treated with MMT followed by NS treatment, while SH and AD-MSCs treatments repaired MMT-induced damages after 3 weeks and 8 weeks. Articular cartilage defects were similar in the SH and AD-MSCs groups, and both groups were superior to the NS groups. Furthermore, the loss of cartilage matrix in the NS group was severe, accompanied by the infiltration of some inflammatory cells after 3 weeks (Figure 3(a)). Compared with the control group, there were articular cartilage defects in all other three groups after 8 weeks. The articular cartilage defects in the SH group and the AD-MSCs group were partially repaired with little loose structure and morphological changes. Although the inflammatory state subsided after 8 weeks, there was no significant repair of articular cartilage defect in the NS group (Figure 3(a)).

Similar results were also observed through safranin O-fast green staining. After 3 weeks, the staining of the SH group was deeper than that of the AD-MSCs group, despite the results in the AD-MSCs group being significantly better than the NS group. The NS group had little staining because of the partial loss of cartilage (Figure 3(b)). However, the cartilage defects in the AD-MSCs group were repaired better than that in the SH group after 8 weeks. In the NS group, cartilage damage and loss were obvious, and no repair traces were found (Figure 3(b)).

Furthermore, toluidine blue staining was performed to detect the content of glycosaminoglycan (GAG), an important component of the cartilage extracellular matrix (ECM). Staining of the articular cartilage of the knee joint in the AD-MSCs group was stratified. The staining of the SH group was inferior to that of the AD-MSCs group. Besides, the NS group took less color after 3 weeks, even no blue-colored part was observed after 8 weeks (Figure 3(c)).



(a)



(b)

FIGURE 5: Continued.



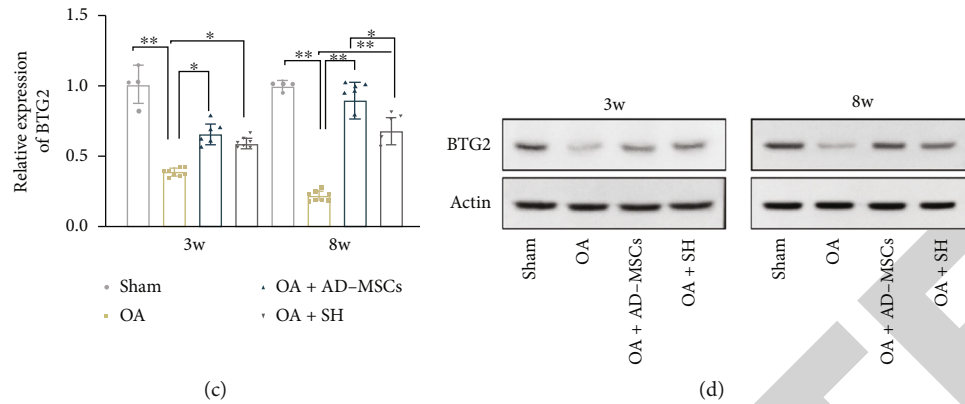


FIGURE 5: BTG2 is significantly downregulated in the articular cartilage of OA guinea pig. (a) GEO database was applied to predict OA-related genes through common selection of GES12021, GSE55235, and GES55457 with  $\log_{2}FC < -1.0$  and  $P < 0.05$ . (b) qRT-PCR was used to examine the expression of the nine selected genes (GRB10, BTG2, APOLD1, KLF9, MCL1, VEGFA, SIK1, GADD45B, and TNFAIP3) in the OA group ( $n = 8$ ) compared with the Sham group ( $n = 4$ ). (c) BTG2 expression in the articular cartilage obtained from guinea pigs in four groups (NS, SH, MSC, and control) after 3 or 8 weeks of injections.  $N = 4$  in the control group;  $N = 8$  in other three groups.  $*P < 0.05$ .  $**P < 0.01$ . (d) Western blot assay was conducted to verify the protein level of BTG2 among the different animal groups in different time point.  $N = 3$  in each group.

Sirius red staining was further used to visualize significant collagen matrix deposition in the regenerated tissues of each group. Under the polarized light microscope, there was mainly yellowish green in the control group after 3 weeks and 8 weeks. However, the AD-MSCs group appeared richly bright in red, yellow, and green due to active tissue repair, especially lasted after 8 weeks. The SH group showed yellow and green, with loose tissue arrangement and partial reticular structure after 3 weeks and 8 weeks. Tissue repair degree weakened obviously after 8 weeks. The NS group showed dull green color and weak refraction after 3 weeks and 8 weeks. In terms of the degree of the collagen matrix deposition of gonarthrosis in guinea pigs after 3 weeks and 8 weeks, the tendency of four groups was MSC>SH>NS>control (Figure 3(d)).

Immunocytochemistry staining of Col2, which was explicitly expressed in newborn tissues and articular cartilage tissues, was performed in four groups. Col2 was widely localized in the intercellular space and extracellular matrix in the SH group, especially in the AD-MSCs group after 3 weeks and 8 weeks. In contrast, the staining of the NS group was slight, and the cartilage tissue of NS group damaged severely after 3 weeks and 8 weeks compared with the control group (Figures 3(e)). These data indicated that AD-MSCs have better therapeutic effects on the gonarthrosis cartilage tissues of OA guinea pigs than SH treatment.

**3.4. The Effects of AD-MSCs on the Changes of Inflammatory-Associated Cytokines.** The infiltration of inflammatory cells was observed in the pathological section and staining. To identify the inflammation conditions, we tested the levels of inflammation-associated cytokines in four groups. As a result, we found that the contents of proinflammatory cytokines including IL-1 $\beta$ , TNF- $\alpha$ , IL-1, IFN- $\gamma$ , and IL-13 in the serum and synovial fluid were enhanced in the NS group, whereas such enhancement was offset by AD-MSCs or SH treatment for both 3 and 8 weeks

(Figures 4(a)–4(e) and Figure S2A–S2E). Meanwhile, the decreased levels of anti-inflammatory factors (TGF- $\beta$  and IL-4) induced by NS treatment was enhanced by AD-MSCs or SH treatment for both 3 and 8 weeks (Figures 4(f) and 4(g) and Figure S2F–S2G). Likewise, the levels of MMP-1 and MMP-13 were changed along with proinflammatory cytokines in the serum and synovial fluid (Figures 4(h) and 4(i) and Figure S2H–S2I). As two OA-related factors, ADAMTS4 and ADAMTS5 were enhanced in the NS group compared to the control group and were reduced by AD-MSCs and SH injection for either 3 or 8 weeks (Figures 4(j) and 4(k) and Figure S2J–S2K). Similarly, the articular cartilage repair factor IGF-1 was also highly expressed in the NS group, but this tendency was partly counteracted in the AD-MSCs group and the SH group (Figure 4(l) and Figure S2L). All the data showed that AD-MSCs alleviates the gonarthrosis in OA guinea pigs.

**3.5. BTG2 Is Significantly Downregulated in the Articular Cartilage of OA Guinea Pig.** Subsequently, we explored the detailed regulatory mechanism of AD-MSCs in treating OA. Searching from the GEO database (<https://www.ncbi.nlm.nih.gov/geo/>), we selected 9 differential expressed genes ( $\log_{2}FC < -1.0$ ) related to OA progression from the datasets GES12021, GSE55235, and GES55457, including MCL1, GRB10, VEGFA, BTG2, APOLD1, SIK1, GADD45B, KLF9, and TNFAIP3 (Figure 5(a)). Through qRT-PCR analysis, we found that BTG2 exhibited the most significant declined expression in the OA group in comparison with the Sham group (Figure 5(b)). Therefore, we chose BTG2 for further studies. At the same time, BTG2 expression was markedly increased in the AD-MSCs group and the SH group, especially in the AD-MSCs group (Figures 5(c) and 5(d)). Since oxidative stress is closely related with OA progression, we also detected the oxidative stress in the chondrocytes of the OA model with BTG2 overexpression. It was uncovered that ROS accumulation was decreased after overexpression of

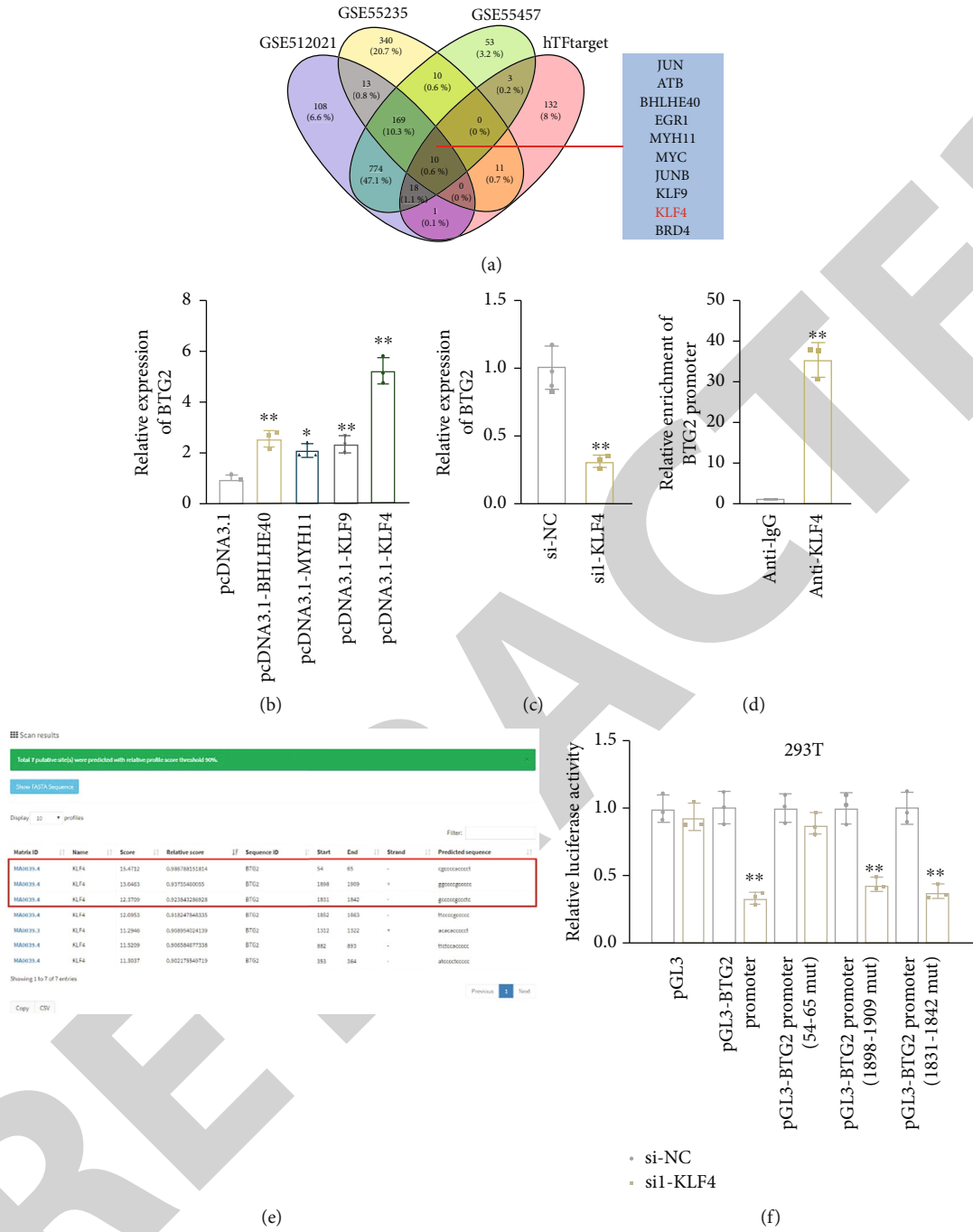


FIGURE 6: Continued.

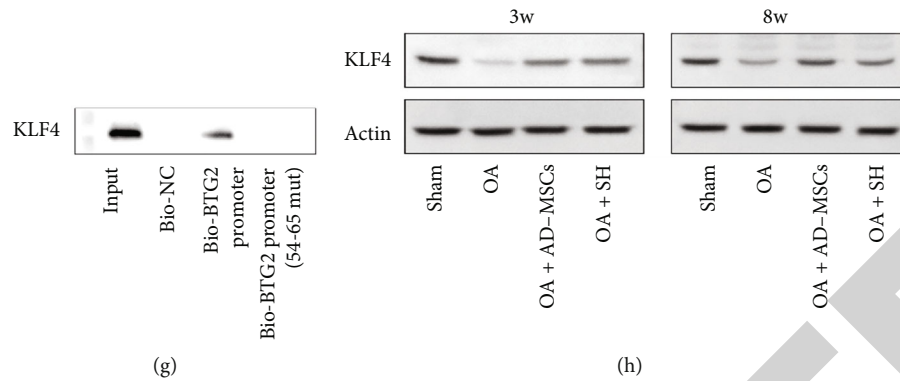


FIGURE 6: KLF4 activates BTG2 expression in AD-MSCs. (a) Potential TFs for BTG2 were selected out through intersecting hTFtarget prediction subset with GEO datasets GES12021, GSE55235, and GES55457 ( $P < 0.05$ ,  $\log_{2}FC < 0$ ). (b) BTG2 expression was examined by qRT-PCR in chondrocyte separately transfected with overexpression vector of four indicated TFs.  $N = 3$  in each group. (c) qRT-PCR examined the expression of BTG2 after KLF4 silencing.  $N = 3$  in each group. (d) ChIP assay was conducted to examine the binding of KLF4 to BTG2 promoter. IgG served as a negative control.  $N = 3$  in each group. (e) The binding sites of KLF4 in the BTG2 promoter were predicted through the JASPAR tool. (f) Luciferase reporter assay was conducted to prove the binding fragment that was responsible for the interaction between KLF4 and BTG2 promoter.  $N = 3$  in each group. (g) DNA pull-down assay was conducted to verify the affinity of KLF4 to BTG2 promoter.  $N = 3$  in each group.  $*P < 0.05$ .  $**P < 0.01$ . (h) Western blot assay was conducted to verify the protein level of KLF4 among the different animal groups in different time point.  $N = 3$  in each group.

BTG2 (Figure S3A). Meanwhile, the SOD activity was enhanced in BTG2-overexpressed group (Figure S3B). In sum, BTG2 is downregulated in the articular cartilage of OA and may suppress oxidative stress.

### 3.6. KLF4 Transcriptionally Induces BTG2 in Chondrocytes.

Furthermore, we explored the upstream molecular mechanism of BTG2 in chondrocytes of the OA model. Transcription factors (TFs) are crucial regulators of their target genes. Hence, we firstly applied hTF target (<http://bioinfo.life.hust.edu.cn/hTFtarget#!/>) to predict BTG2-associated TFs and then intersected this subset with GES12021, GSE55235, and GES55457 ( $P < 0.05$ ,  $\log_{2}FC < 0$ ) to select potential TFs functioned in OA. As a result, 10 candidates, including JUN, ATF3, BHLHE40, EGR1, MYH11, MYC, JUNB, KLF9, KLF4, and BRD4, were screened out (Figure 6(a)). Among these candidates, BHLHE40, MYH11, and KLF9 have not been reported in OA yet, and KLF4 has been recognized as a suppressor of OA [26, 27]. Next, we overexpressed these four candidate TFs and found that KLF4 exhibited the most significant effect on BTG2 expression (Figure 6(b)). In addition, BTG2 expression was notably decreased after KLF4 interference (Figure 6(c)). Next, ChIP data manifested the strong enrichment of BTG2 promoter in the anti-KLF4 group compared with the control anti-IgG group (Figure 6(d)). The binding sites between KLF4 and BTG2 promoters predicted using the JASPAR tool (<http://jaspar.genereg.net/>) are exhibited in Figure 6(e). Luciferase reporter assay indicated that after KLF4 downregulation, the luciferase activity of pGL3 vector with full-length BTG2 promoter, 1898-1909-mutated BTG2 promoter, or 1831-1842-mutated BTG2 promoter was declined, while that of pGL3 vector containing BTG2 promoter with mutated 54-65 fragment was almost unchanged (Figure 6(f)). It was also verified by DNA pull-down assay that KLF4 could be pulled down by the probe biotinylated with full-length

BTG2 promoter rather than that with the BTG2 promoter contained mutated 54-65 fragments (Figure 6(g)). Furthermore, the protein level of KLF4 among the different animal groups has been examined by western blotting. The results showed that KLF4 expression was markedly increased in the AD-MSCs group and SH group after 3 weeks and 8 weeks, especially in the AD-MSCs group after 8 weeks (Figure 6(h)). The above findings indicated that KLF4 is a transcriptional activator of BTG2.

## 4. Discussion

OA represents the most prevalent chronic joint disease characterized by the degradation of articular cartilage and remodeling of the underlying bone [28]. MSCs have been reported as an important treatment option for OA [29]. Besides, the mechanism of AD-MSCs in OA has been explored from the perspective of clinical application [13, 30, 31].

In our study, we tried to verify the regulatory role of AD-MSCs in the OA model of guinea pigs. During the research, we observed that AD-MSCs were effective in mitigating the gonarthrosis of OA guinea pigs, and the overall effect was better than that of SH, a kind of well-accepted therapy for OA [32]. The observation was consistent with current literature that AD-MSCs are a useful method to treat OA [13], especially knee OA [33].

Currently, it is well-recognized that inflammation plays a central role in OA pathogenesis [34]. Here, we discovered the elevation of proinflammatory factors and the decrease of anti-inflammatory factors in the serum and synovial fluid of OA guinea pigs, while the injection of AD-MSCs or SH counteracted the changes. The findings were consistent with the previous discovery that AD-MSCs elicits anti-inflammatory roles in OA [35]. Besides, OA-related factors, including MMP-1, MMP-13 [36], IGF1 [37], ADAMTS4, and ADAMTS5 [38], were all enhanced in the serum and

synovial fluid of OA guinea pigs, and AD-MSCs and SH could offset their elevation. However, TGF- $\beta$  expression was higher in both serum and synovial fluid after 3 weeks and higher in the AD-MSCs group and the SH group than that in the NS group. This is possible because active regenerative tissue of the knee joint was often associated with higher levels. The interaction of various cytokines might induce the decline in overall expression in the serum and synovial fluid after 8 weeks.

To unveil the acting therapeutic mechanism of AD-MSCs in OA, we selected OA-related genes from GEO database. Through further qRT-PCR analysis, we focused on BTG2, a significantly downregulated gene in the articular cartilage from OA guinea pigs. BTG2 has been reported as a tumor suppressor to regulate many biological processes in cancers [39]. Moreover, BTG2 has been identified as an inflammation-related gene [40]. Notably, a former report also suggested that BTG2 is one of the candidate genes related to methotrexate resistance in patients with rheumatoid arthritis [41].

BTG2 has been demonstrated to protect human mammary epithelial cells from oxidative stress [42]. Furthermore, Imran and Lim have revealed that oxidative stress could elevate BTG2 expression and finally regulating various biological cell phenotypes [43]. RNA-induced oxidative stress is closely related with disease progression [16, 17]. In this study, we evaluated the ROS level and SOD concentration in the chondrocytes of the OA model with BTG2 overexpression. We uncovered that BTG2 overexpression reduced the ROS level but enhanced the SOD activity suggesting that BTG2 might suppress oxidative stress in OA.

The current study is the first one to detect the role of BTG2 in OA. BTG2 plays as a molecular switch for the transformation from cell proliferation to differentiation by controlling the exit of a cell cycle as well as the subsequent terminal differentiation [44]. It has a vital role in the maturation of stem cells [45]. Another research showed that the increased stem cells differentiation percentage into neural lineage cells was accompanied by an increasing BTG2 expression level [46]. In our current study, we revealed that activation of the BTG2 molecular switch caused more stem cells to transform from proliferation to differentiation, ultimately resulting in an improved differentiation percentage into cartilage cells. According to the expression level of BTG2, it also increased in AD-MSCs.

Transcription factors (TFs) are one of the main regulators for the critical genes. KLF4 is an evolutionarily conserved zinc finger-containing transcription factor that modulates diverse cellular processes such as cell growth, proliferation, and differentiation [47]. Moreover, KLF4 has already been proven to work as a suppressor of OA progression [26, 27]. KLF4 enhanced expression of major cartilage extracellular matrix (ECM) genes and SRY-box transcription factor-9 and suppressed mediators of inflammation and ECM-degrading enzymes [48]. Another study viewed that KLF4 was negatively modulated by miR-7 and KLF4 was downregulated in human OA tissues and OA chondrocyte [27]. Similar research found that lncRNA MEG3 can promote chondrocyte proliferation and inhibit inflammation

by sponging miR-9-5p to induce KLF4 expression [49]. Here, we predicted KLF4 as a potential upstream regulator for BTG2 in OA. We demonstrated the transcriptional activation of KLF4 on BTG2. Our findings about the relationship between KLF4 and BTG2 in OA suggested a potential novel regulatory pathway in OA progression.

In conclusion, our study revealed that AD-MSCs exert effective therapeutic effects on the gonarthrosis depending on the upregulation of KLF4-regulated BTG2. Based on plenty of research work, bone marrow or adipose tissue-isolated MSCs have shown great potential for cartilage repair in clinical trials. The findings of current study can help provide some theoretical guidance for the treatment of AD-MSCs on OA.

However, limitations in the current study remain ineligible. First, the mechanism of AD-MSCs-mediated transcriptional activity of KLF4 remains to be investigated. Second, the intercellular molecular transmission which affected the OA progression need to be further explored. Importantly, lack of investigation on clinical samples is also a major limitation of our current study. Therefore, we will further explore these mechanisms in our future study and validate relevant molecular mechanism in clinical samples.

## Data Availability

All data was within the manuscript.

## Conflicts of Interest

The authors declare that they have no conflicts of interest.

## Authors' Contributions

Qinyan Yang, Li Jin, and Xiaolun Huang contributed equally to this work and should be considered as co-first authors.

## Acknowledgments

This research was supported by the Macau Science and Technology Development Fund (FDCT (0007/2019/AKP, 0021/2020/AGJ, and 0011/2020/A1)), the National Natural Science Foundation of China (No. 81973320), and the Key Technology R&D Program of Science and Technology Commission Foundation of Tianjin (20YFZCSY00460).

## Supplementary Materials

*Supplementary 1.* Figure S1: (A) The surface antigens of AD-MSCs (Neg CKTL, CD90, CD105, and CD73) were measured by flow cytometry.  $N = 3$  in each group. (B) Differentiation to osteoblasts was demonstrated with phase contrast and by Alizarin Red staining, Oil Red staining, and Alcian blue staining.  $N = 3$  in each group.

*Supplementary 2.* Figure S2: AD-MSCs attenuate inflammation in OA guinea pigs. (A-L) ELISA examined the content of inflammation- and OA-related factors, including IL-1 $\beta$ , TNF- $\alpha$ , IL-1, IFN- $\gamma$ , IL-13, TGF- $\beta$ , IL-4, IGF1, ADAMTS4, ADAMTS5, MMP-1, and MMP-13 in the serum of articular

cavity obtained from guinea pigs in four groups (NS, SH, AD-MSC, and control) after 3 or 8 weeks of injections.  $N = 4$  in the control group;  $N = 8$  in other three groups.  $*P < 0.05$ .

**Supplementary 3.** Figure S3: BTG2 suppresses oxidative stress. (A) ROS production was detected in chondrocytes of the OA model transfected with pcDNA3.1 empty vector or BTG2 expression vector by flow cytometry. (B) SOD production was measured in chondrocytes with BTG2 overexpression.  $N = 3$  in each group.  $**P < 0.01$ .

**Supplementary 4.** Figure S4: graphical abstract. A graphical abstract was plotted to illustrate the functions and mechanism of AD-MSCs in OA.

## References

- [1] S. Glyn-Jones, A. J. R. Palmer, R. Agricola et al., "Osteoarthritis," *Lancet*, vol. 386, no. 9991, pp. 376–387, 2015.
- [2] S. C. Vlad, T. Neogi, P. Aliabadi, J. D. T. Fontes, and D. T. Felson, "No association between markers of inflammation and osteoarthritis of the hands and knees," *The Journal of Rheumatology*, vol. 38, no. 8, pp. 1665–1670, 2011.
- [3] M. Y. Ansari, N. Ahmad, and T. M. Haqqi, "Oxidative stress and inflammation in osteoarthritis pathogenesis: role of polyphenols," *Biomedicine & Pharmacotherapy*, vol. 129, article 110452, 2020.
- [4] A. F. Steinert, S. C. Ghivizzani, A. Rethwilm, R. S. Tuan, C. H. Evans, and U. Nöth, "Major biological obstacles for persistent cell-based regeneration of articular cartilage," *Arthritis Research & Therapy*, vol. 9, no. 3, pp. 213–213, 2007.
- [5] Y. H. Chang, H. W. Liu, K. C. Wu, and D. C. Ding, "Mesenchymal stem cells and their clinical applications in osteoarthritis," *Cell Transplantation*, vol. 25, no. 5, pp. 937–950, 2016.
- [6] E. C. Doyle, N. M. Wragg, and S. L. Wilson, "Intraarticular injection of bone marrow-derived mesenchymal stem cells enhances regeneration in knee osteoarthritis," *Knee Surgery, Sports Traumatology, Arthroscopy*, vol. 28, no. 12, pp. 3827–3842, 2020.
- [7] P. Neybecker, C. Henrionnet, E. Pape et al., "In vitro and in vivo potentialities for cartilage repair from human advanced knee osteoarthritis synovial fluid-derived mesenchymal stem cells," *Stem Cell Research & Therapy*, vol. 9, no. 1, p. 329, 2018.
- [8] Y. Tao, J. Zhou, Z. Wang et al., "Human bone mesenchymal stem cells-derived exosomal miRNA-361-5p alleviates osteoarthritis by downregulating DDX20 and inactivating the NF- $\kappa$ B signaling pathway," *Bioorganic Chemistry*, vol. 113, article 104978, 2021.
- [9] Z. Jin, J. Ren, and S. Qi, "Human bone mesenchymal stem cells-derived exosomes overexpressing microRNA-26a-5p alleviate osteoarthritis via down-regulation of PTGS2," *International Immunopharmacology*, vol. 78, article 105946, 2020.
- [10] X. Xu, Y. Liang, X. Li et al., "Exosome-mediated delivery of kartogenin for chondrogenesis of synovial fluid-derived mesenchymal stem cells and cartilage regeneration," *Biomaterials*, vol. 269, article 120539, 2021.
- [11] M. Qiu, D. Liu, and Q. Fu, "MiR-129-5p shuttled by human synovial mesenchymal stem cell-derived exosomes relieves IL-1 $\beta$  induced osteoarthritis via targeting HMGB1," *Life Sciences*, vol. 269, article 118987, 2021.
- [12] E. Damia, D. Chicharro, S. Lopez et al., "Adipose-derived mesenchymal stem cells: are they a good therapeutic strategy for osteoarthritis?," *International Journal of Molecular Sciences*, vol. 19, no. 7, p. 1926, 2018.
- [13] Y. Song, H. du, C. Dai et al., "Human adipose-derived mesenchymal stem cells for osteoarthritis: a pilot study with long-term follow-up and repeated injections," *Regenerative Medicine*, vol. 13, no. 3, pp. 295–307, 2018.
- [14] E. Ragni, C. Perucca Orfei, P. de Luca et al., "miR-22-5p and miR-29a-5p are reliable reference genes for analyzing extracellular vesicle-associated miRNAs in adipose-derived mesenchymal stem cells and are stable under inflammatory priming mimicking osteoarthritis condition," *Stem Cell Reviews and Reports*, vol. 15, no. 5, pp. 743–754, 2019.
- [15] J. H. Cheng, C. C. Hsu, S. L. Hsu et al., "Adipose-derived mesenchymal stem cells-conditioned medium modulates the expression of inflammation induced bone morphogenetic protein-2, -5 and -6 as well as compared with shockwave therapy on rat knee osteoarthritis," *Biomedicine*, vol. 9, no. 10, p. 1399, 2021.
- [16] H. Liu, L. Wang, X. Weng et al., "Inhibition of Brd4 alleviates renal ischemia/reperfusion injury-induced apoptosis and endoplasmic reticulum stress by blocking FoxO4-mediated oxidative stress," *Redox Biology*, vol. 24, article 101195, 2019.
- [17] M. W. Park, H. W. Cha, J. Kim et al., "NOX4 promotes ferroptosis of astrocytes by oxidative stress-induced lipid peroxidation via the impairment of mitochondrial metabolism in Alzheimer's diseases," *Redox Biology*, vol. 41, article 101947, 2021.
- [18] S. Hu, C. Zhang, L. Ni et al., "Stabilization of HIF-1 $\alpha$  alleviates osteoarthritis via enhancing mitophagy," *Cell Death & Disease*, vol. 11, no. 6, pp. 481–481, 2020.
- [19] H. Fang, L. Huang, I. Welch et al., "Early changes of articular cartilage and subchondral bone in the DMM mouse model of osteoarthritis," *Scientific Reports*, vol. 8, no. 1, pp. 2855–2855, 2018.
- [20] M. Dominici, K. le Blanc, I. Mueller et al., "Minimal criteria for defining multipotent mesenchymal stromal cells. The International Society for Cellular Therapy position statement," *Cytotherapy*, vol. 8, no. 4, pp. 315–317, 2006.
- [21] Y. Wang, D. Yu, Z. Liu et al., "Exosomes from embryonic mesenchymal stem cells alleviate osteoarthritis through balancing synthesis and degradation of cartilage extracellular matrix," *Stem Cell Research & Therapy*, vol. 8, no. 1, p. 189, 2017.
- [22] Q. Chen, Y. Liu, X. Ding et al., "Bone marrow mesenchymal stem cell-secreted exosomes carrying microRNA-125b protect against myocardial ischemia reperfusion injury via targeting SIRT7," *Molecular and Cellular Biochemistry*, vol. 465, no. 1-2, pp. 103–114, 2020.
- [23] Y. Jiang, W. Cao, K. Wu et al., "LncRNA LINC00460 promotes EMT in head and neck squamous cell carcinoma by facilitating peroxiredoxin-1 into the nucleus," *Journal of Experimental & Clinical Cancer Research*, vol. 38, no. 1, p. 365, 2019.
- [24] G. Li and Q. Kong, "LncRNA LINC00460 promotes the papillary thyroid cancer progression by regulating the LINC00460/miR-485-5p/Raf1 axis," *Biological Research*, vol. 52, no. 1, p. 61, 2019.
- [25] G. Xu, Y. Yi, H. Lyu et al., "DNA methylation suppresses chitin degradation and promotes the wing development by inhibiting Bmara-mediated chitinase expression in the silkworm, *Bombyx mori*," *Epigenetics & Chromatin*, vol. 13, no. 1, p. 34, 2020.

## Retraction

# Retracted: miR-124-3p Delivered Using Exosomes Attenuates the Keratinocyte Response to IL-17A Stimulation in Psoriasis

### Oxidative Medicine and Cellular Longevity

Received 20 June 2023; Accepted 20 June 2023; Published 21 June 2023

Copyright © 2023 Oxidative Medicine and Cellular Longevity. This is an open access article distributed under the Creative Commons Attribution License, which permits unrestricted use, distribution, and reproduction in any medium, provided the original work is properly cited.

This article has been retracted by Hindawi following an investigation undertaken by the publisher [1]. This investigation has uncovered evidence of one or more of the following indicators of systematic manipulation of the publication process:

- (1) Discrepancies in scope
- (2) Discrepancies in the description of the research reported
- (3) Discrepancies between the availability of data and the research described
- (4) Inappropriate citations
- (5) Incoherent, meaningless and/or irrelevant content included in the article
- (6) Peer-review manipulation

The presence of these indicators undermines our confidence in the integrity of the article's content and we cannot, therefore, vouch for its reliability. Please note that this notice is intended solely to alert readers that the content of this article is unreliable. We have not investigated whether authors were aware of or involved in the systematic manipulation of the publication process.

Wiley and Hindawi regrets that the usual quality checks did not identify these issues before publication and have since put additional measures in place to safeguard research integrity.

We wish to credit our own Research Integrity and Research Publishing teams and anonymous and named external researchers and research integrity experts for contributing to this investigation.

The corresponding author, as the representative of all authors, has been given the opportunity to register their agreement or disagreement to this retraction. We have kept a record of any response received.

### References

- [1] S. Liu and J. Gong, "miR-124-3p Delivered Using Exosomes Attenuates the Keratinocyte Response to IL-17A Stimulation in Psoriasis," *Oxidative Medicine and Cellular Longevity*, vol. 2022, Article ID 6264474, 11 pages, 2022.

## Research Article

# miR-124-3p Delivered Using Exosomes Attenuates the Keratinocyte Response to IL-17A Stimulation in Psoriasis

Simin Liu <sup>1</sup> and Jian Gong<sup>2,3</sup>

<sup>1</sup>School of Clinical Medicine, Jiangxi University of Chinese Medicine, Nanchang, Jiangxi 330004, China

<sup>2</sup>Department of Integrated Traditional Chinese and Western Medicine, Dermatology Hospital of Jiangxi, Nanchang, Jiangxi 330001, China

<sup>3</sup>Jiangxi Provincial Clinical Research Center for Skin Diseases, Nanchang, Jiangxi 330001, China

Correspondence should be addressed to Simin Liu; liusimin@jxutcm.edu.cn

Received 27 July 2022; Revised 5 September 2022; Accepted 19 September 2022; Published 12 October 2022

Academic Editor: Tian Li

Copyright © 2022 Simin Liu and Jian Gong. This is an open access article distributed under the Creative Commons Attribution License, which permits unrestricted use, distribution, and reproduction in any medium, provided the original work is properly cited.

**Background and Objective.** To explore the effect of miR-124-3p delivered by exosomes on psoriatic keratinocytes stimulated by IL-17A. **Methods.** NHEKs, HaCaT cells, and HEK 293T cells were treated with IL-17A. CCK-8 assays were performed to detect cell activity, and immunofluorescence staining and Western blotting were performed to detect the protein expression of STAT3. After isolation of exosomes via ultracentrifugation, the contents of miR-124-3p and oxidative stress markers such as superoxide dismutase (SOD), malondialdehyde (MDA), and glutathione peroxidase (GSH-Px) in keratinocytes were measured. Subsequently, transcriptomic analysis was performed using RNA-seq. Data were analysed by using the “edgeR” package within R. After verifying the abnormally expressed genes stimulated by IL-17A, a dual luciferase reporter assay was used to determine the interaction between miR-124-3p and STAT3. Finally, BALB/c mice were used to establish a psoriasis model for analysis. The effect of elevated miR-124-3p on the psoriasis mouse model was determined by exosomal delivery of miR-124-3p. **Results.** IL-17 intervention enhanced the cell activity of keratinocytes ( $P < 0.05$ ). miR-124-3p was identified by RNA-seq as one of the differentially expressed miRNAs stimulated by IL-17A. miR-124-3p overexpression induced decreased STAT3 and MDA levels, increased SOD and GSH-Px levels in keratinocytes, and alleviated emergency responses of sclerosis damage ( $P < 0.05$ ). The dual luciferase reporter assay results confirmed that STAT3 was regulated by miR-124-3p in a targeted manner ( $P < 0.05$ ). Finally, miR-124-3p delivered by exosomes effectively alleviated the pathological manifestations and oxidative stress responses of psoriatic mice. **Conclusions.** miR-124-3p regulates keratinocyte activity via STAT3 in response to IL-17A stimulation. The ectopic expression of miR-124-3p in psoriatic skin reduces IL-17A-induced inflammation and inhibits the STAT3 pathway, thus alleviating the symptoms of psoriasis. The findings of this study suggest that exosomes can be used to therapeutically deliver miR-124-3p to keratinocytes and psoriatic lesions, which may provide novel insight for psoriasis treatment.

## 1. Introduction

Psoriasis is a common chronic papulosquamous skin disease characterized by sharply demarcated, erythematous, pruritic plaques with silvery scales. Plaques are commonly located in the trunk, limb extensor surfaces, and scalp [1]. Psoriasis occurs worldwide and presents in all ages, affecting 2–3% of people globally [2, 3]. There are multiple types of psoriasis, including plaque psoriasis, which accounts for approximately 85% of cases, and pustular, guttate, palmoplantar, erythrodermic, and inverse psoriasis [4]. The infil-

trating leukocytes in psoriasis patients release growth factors, cytokines, and chemokines such as VEGF, TNF- $\alpha$ , IL-17, IL-22, CXCL8, and CXCL2, affecting the proliferation and differentiation of epidermal keratinocytes, thus leading to the onset of disease. Recent studies have revealed that psoriasis is comorbid with multiple diseases, such as stroke, cardiometabolic disorder, and chronic kidney disease, resulting in overall reduced life expectancy and quality of life in patients [5]. Therefore, it is imperative to explore novel therapeutic strategies to improve the treatment of psoriasis.

Exosomes are nanosized vesicles (50-150 nm in diameter) released by various cells and play critical roles in intercellular communication in diverse biological and pathological processes [6]. There are proteins, mRNAs, and miRNA species within the exosomes. MicroRNAs (miRNAs) are small single-stranded noncoding RNAs of approximately 22 nucleotides that regulate gene expression posttranscriptionally by binding to target mRNAs [7]. miRNAs usually interact with the mRNA 3'UTR and, in some circumstances, with the CDS or 5'UTR to induce mRNA degradation and translational repression [8]. Previous studies have revealed that miRNAs regulate many biological functions, including inflammatory signalling pathways and DNA repair. Dysregulation of miRNAs is associated with multiple diseases, such as cancers, immune diseases, and psoriasis [9–12]. In recent studies, several miRNAs, such as miR-155, miR-378a, and miR-125, have been identified as dysregulated in psoriasis. miRNAs can be used as molecular therapeutics in the treatment of various diseases, and exosomes are currently an ideal vehicle for the delivery of miRNAs to diseased cells and tissues [13]. The significant effects of exosome-delivered miRNAs in recipient cells provide insight into psoriasis treatment [14].

Signal transducer and activator of transcription 3 (STAT3) is a transcription factor encoded by the STAT3 gene. STAT3 is involved in skin lesions of psoriasis. Previous studies have demonstrated that in skin lesions of psoriatic patients, STAT3 phosphorylation levels were higher than those in normal skin [15]. *In vivo* studies with transgenic mice demonstrated that constitutive activation of STAT3 in keratinocytes leads to skin lesions such as human psoriatic plaques [16]. STAT3 is essential for the differentiation of TH17 helper T cells, which contributes to many autoimmune diseases [17]. STAT3 also regulates the expression of genes that control cell survival, cell proliferation, and angiogenesis along with transcription factors such as NK-kB [18]. IL-6 and IL-20 family members, as well as some other cytokines and growth factors, can stimulate cells through activation of STAT3 [17]. In psoriasis, it has been shown that the IL-17, IL-22, and IL-23 signalling pathways are associated with STAT3. STAT3 has been validated as a promising therapeutic target in treating psoriasis [19, 20].

In this study, we aimed to investigate miRNAs that are associated with the pathogenesis of psoriasis. We conducted RNA sequencing to reveal dysregulated miRNAs within keratinocytes stimulated with IL-17 and successfully identified a panel of miRNAs differentially expressed in IL-17A-stimulated keratinocytes compared with nonstimulated controls. One of those miRNAs overexpressed in IL-17A-treated keratinocytes was miR-124-3p. We aimed to explore the function of miR-124-3p *in vitro* by overexpressing it in keratinocytes as well as *in vivo* by exosome delivery. We hypothesized that exosome-delivered miR-124-3p would alleviate psoriasis progression by targeting STAT3. Overall, our work validated the regulatory roles of miR-124-3p in response to cytokines in the context of psoriasis both *in vitro* and *in vivo*. The findings of our study may provide evidence for the application of exosome-delivered miRNAs in the treatment of autoimmune skin diseases.

## 2. Materials and Methods

**2.1. Cell Culture and Cell Transfection.** Normal human epidermal keratinocyte NHEKs (Cat. No. PCS-200-011) and human embryonic kidney cell lines HEK 293T cells (Cat. No. CRL-11268) were provided by the American Type Culture Collection (ATCC, Manassas, Virginia, USA). The human epidermal keratinocyte cell line HaCaT (Cat. No. GDC0106) was purchased from the China Center for Type Culture Collection (Wuhan, China). The cells were cultured in Dulbecco's modified Eagle's medium (DMEM) (Keygentec) in 5% CO<sub>2</sub> at 37°C with 10% foetal bovine serum (Wisent) and 100 U/ml penicillin and streptomycin (Keygentec). For IL-17A treatment, HEK 293T cells or HaCaT cells were first seeded in 96-well plates at 1 × 10<sup>4</sup> cells/well and then starved overnight. The next day, IL-17A (R&D) was added to a final concentration of 100 ng/ml for the indicated times [21].

For cell transfection, miRNA mimics and a scrambled RNA fragment (negative control) were provided by RIBO-BIO (Guangzhou, China). The cells were cultured in 6-well plates for 12 hr to reach 75% confluence. Then, 100 nmol/l miRNA mimics were transfected into cells using Lipofectamine according to the manufacturer's instructions (Thermo Fisher Scientific). Forty-eight hours after transfection, the cells were harvested and collected for subsequent assays.

**2.2. CCK-8 Assay.** After the indicated treatments, HaCaT cells were plated into 96-well plates at 1 × 10<sup>4</sup> cells per well. Twenty-four hours after transfection, the medium was replaced, and the cells were incubated with IL-17A (100 ng/ml) for up to 72 hrs. Next, 10 μl of CCK-8 (Vazyme, Nanjing, China) reagent was added to each well at the indicated time points (0, 24, 48, and 72 h) and cultured for another 2 hr according to the manufacturer's instructions. The absorbance value was measured at 460 nm using a microplate reader (Bio-Rad, Hercules, CA, USA) [22].

**2.3. Immunofluorescent Staining.** HaCaT cells (1 × 10<sup>4</sup>) were first plated on sterile cover slips in a 12-well plate. The next day, the cells were stimulated with the respective reagents (IL-17A, PeproTech, 100 ng/ml). After treatment, the cells were washed with PBS, fixed with 4% paraformaldehyde for 10 minutes, and then permeabilized with 0.1% Triton X-100 (Thermo Fisher Scientific) for 10 minutes. Following permeabilization, the cells were blocked with 2% bovine serum albumin for 1 hr and then incubated with primary antibodies overnight at 4°C (phospho-STAT3 Ab, AF3293, Affinity Biosciences; STAT3 Ab, AF6294, Affinity Biosciences). Next, the cells were incubated with dye-labelled secondary antibody for 1 hr at 37°C. Then, the cells were washed with PBS and incubated with FITC-labelled phalloidin (Thermo Fisher Scientific) for 30 minutes at room temperature. Images were captured by a confocal laser scanning microscope (FV3000, Olympus, Japan) and analysed using ImageJ software [23].

**2.4. RT-qPCR.** First, samples were isolated with TRIzol reagent (Invitrogen), and total RNA was extracted following chloroform extraction and isopropanol precipitation. cDNA synthesis was performed with a HiScript II One Step RT-PCR Kit (Vazyme). Real-time PCR was performed with



ChamQ Universal SYBR qPCR Master Mix (Vazyme). The expression level of genes was normalized to GAPDH and analysed by the  $2^{-\Delta\Delta Ct}$  method. For miRNA quantification, total RNA was first reverse transcribed with a miRNA reverse transcription kit (Thermo Fisher Scientific), including primers for miR-124-3p (Thermo Fisher Scientific). The relative level of miR-124-3p was normalized to U6 using the  $2^{-\Delta\Delta Ct}$  method [24].

**2.5. Exosome Isolation and Quantification.** Exosomes were isolated with the ultracentrifugation method following a publicly available protocol [25]. Briefly, first, the cell supernatant containing exosomes was centrifuged at approximately  $300 \times g$  for 5 minutes to remove cells and then centrifuged at  $12,000 \times g$  for 45 minutes to remove debris. Next, the supernatant was collected and filtered through  $0.22 \mu m$  filters (Merck Millipore) to remove microvesicles, cell debris, and other large particles. Finally, the filtered supernatant was centrifuged in a Beckman Coulter Ultracentrifuge at  $100,000 \times g$  at  $4^\circ C$  for 90 minutes to obtain pellet exosomes. After washing with PBS and centrifuging at  $120,000 \times g$  for 90 minutes, the purified exosomes were quantified with a Human Exosome ELISA Kit (Novus) according to the manufacturer's instructions.

**2.6. Exosome Characterization with Nanoparticle Tracking Analysis.** Purified exosomes ( $100 \mu l$ ) were analysed with a NanoSight LM10-HSB instrument (A&P Instrument Co.) for nanoparticle tracking analysis (NTA) at room temperature. The mean size of exosomes and size distribution data were analysed with NTA 2.2 software [25].

**2.7. Loading miR-124-3p into Exosomes with Electroporation.** To load miR-124-3p into the exosomes,  $50 \mu g$  miR-124-3p mimic was gently mixed with  $100 \mu g$  purified exosomes in  $200 \mu l$  electroporation buffer at  $4^\circ C$  [25]. After electroporation at 400 V and  $50 \mu F$  for three cycles with a 30 ms pulse/2 s pause, the mixture was incubated at  $37^\circ C$  for 30 min and centrifuged at  $100,000 \times g$  for 70 min to remove unbound miR-124-3p. Exosomes were then isolated as described above and washed once with cold PBS. RNA was extracted from pellets using TRIzol reagent (Invitrogen), and the loading efficiency of miR-124-3p into exosomes was measured with RT-qPCR.

**2.8. Western Blot.** To prepare whole-cell lysates, samples were first lysed with RIPA buffer (Beyotime, Shanghai, China) on ice and then centrifuged at  $13,000 \times g$  for 10 minutes at  $4^\circ C$ . The protein concentration was measured using a bicinchoninic acid (BCA) protein assay kit (CWBI). An equal amount of protein was separated by 12% SDS-PAGE. Following separation through electrophoresis, the proteins were transferred to PVDF membranes. After blocking with 5% nonfat milk or 2% BSA, the membrane was incubated with primary antibodies at  $4^\circ C$  overnight (phospho-STAT3 Ab, AF3293, Affinity Biosciences; STAT3 Ab AF6294, Affinity Biosciences) with actin as a loading control and then incubated at room temperature with HRP-conjugated secondary antibodies for 1 hr in the dark. The signal was developed with ECL Reagent (Beyotime) according to the manufacturer's directions and imaged with a chemiluminescent imaging system ChemiDoc (Bio-Rad) [26].

**2.9. Transcriptomic Analysis and Enrichment Analysis.** Transcriptomic analysis was performed using RNA-seq. Data were analysed by using the "edgeR" package within R [27]. Enrichment analysis was performed with the "clusterProfiler" package within R [28].

### 2.10. Dual-Luciferase Reporter Assay

**2.10.1. Plasmid Construction.** The target sequences of miR-124-3p in STAT3 were predicted by the StarmirDB database (<https://fold.wadsworth.org/starmirDB.php>). Wild-type STAT3 3'UTR sequences containing the miR-124-3p binding sites were amplified by PCR, and mutant sequences were constructed by site-directed mutagenesis by substituting the seed regions with miR-124-3p. The wild-type or mutant STAT3 plasmids were synthesized and constructed by GenScript (Nanjing, China) and inserted into the pmirGLO plasmid (GenePharma). HEK 293T cells were seeded in 24-well plates at  $1 \times 10^4$  cells/well and cultured to 80% confluence before transfection. Subsequently, luciferase constructs were cotransfected with miR-124-3p mimic or scramble miRNAs into HEK 293T cells using Lipofectamine 3000 following the manufacturer's manual. The Dual-Luciferase Reporter Assay System (Promega) was used to measure the luciferase activity after incubation for 48 hr.

**2.10.2. Mouse Model.** Wild-type male BALB/c mice (8 weeks, 20-25 g) were purchased from Beijing Vital River Laboratory Animal Technology. To overexpress miR-124-3p,  $3 \mu g$  human miR-124-3p mimic or scramble miRNA mimics were packaged in InvivoFectamine 3.0 Reagent or  $50 \mu g$  exosomes containing miR-124-3p were injected into the shaved back skin of BALB/c mice at Days 0, 1, and 3 intradermally [29]. To establish psoriasis mouse models, the backs of the mice were shaved with a  $2 \times 3$  cm area, and  $50$  mg 5% imiquimod (IMQ, Med-ChemExpress) was applied topically to this area [30]. Vernier callipers (Deli) were used to measure the back skin thickness every 2 days at three different sites within IMQ-treated regions. Scales 0 to 4 (0, healthy; 1, mild; 2, moderate; 3, severe; and 4, very severe) were assigned by three independent researchers for erythema, scaling, and thickness of the IMQ-treated region. The Ethics Committee for Animal Research of School of Clinical Medicine, Jiangxi University of Chinese Medicine, reviewed and approved the experimental protocols.

**2.10.3. Histopathology and Immunohistochemistry Staining.** The mouse skin tissues were excised, washed with PBS, fixed in formalin, embedded in paraffin, and sliced into  $5 \mu m$  sections. Then, the tissue sections were stained with haematoxylin for 10 minutes and eosin (Sigma-Aldrich) for 3 minutes at room temperature and observed under a light microscope (Olympus) for histological evaluation. For immunohistochemistry staining, the slides were first deparaffinized. Antigen retrieval was performed at  $100^\circ C$  for 20 minutes in a steamer in 0.01 M sodium citrate buffer with pH 6.0. After blocking with 1% BSA for 30 min at room temperature, the cells were incubated with primary antibody (Ki67 Ab, AF0198, Affinity Biosciences; phospho-STAT3 Ab, AF3293, Affinity Biosciences; STAT3 Ab, AF6294, Affinity Biosciences) for 45 min and HRP-conjugated secondary antibody for 30 min at room

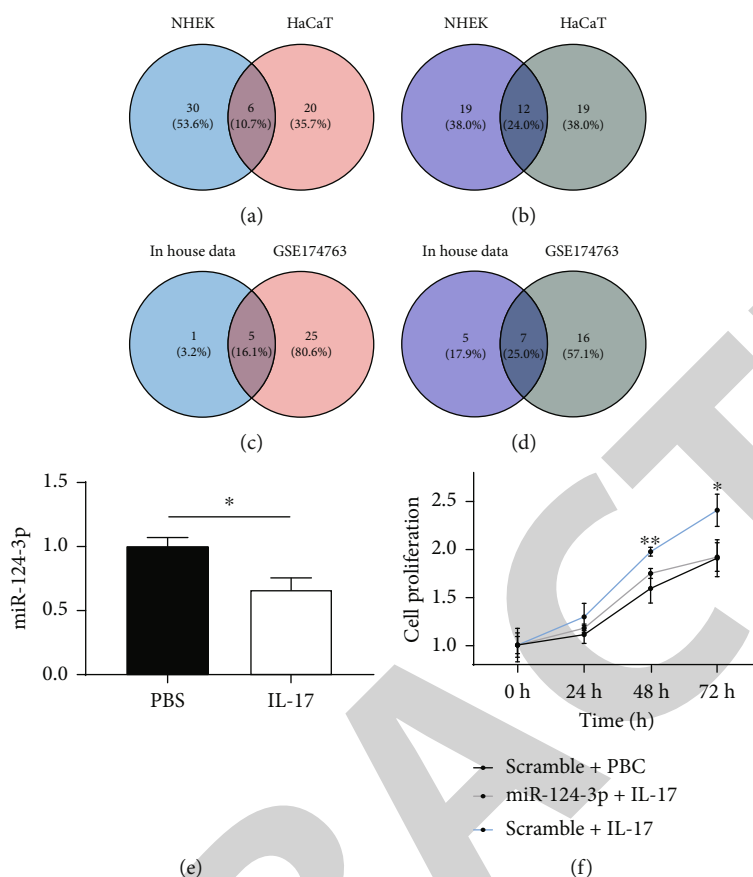


FIGURE 1: miR-124-3p inhibits IL-17A-mediated keratinocyte proliferation. RNA extracted from NHEKs treated with IL-17 ( $n = 3$ ), HaCaT cells treated with IL-17A ( $n = 3$ ), and PBS-treated control cells ( $n = 3$ ) was used for small RNA-seq. (a) Venn diagrams showing 6 upregulated microRNAs in both NHEKs and HaCaT cells treated with IL-17A. (b) Venn diagrams showed 12 downregulated microRNAs in both NHEKs and HaCaT cells treated with IL-17A. (c) Venn diagrams showed that 5 upregulated microRNAs were also upregulated in lesioned skin samples in the GSE174763 dataset. (d) Venn diagrams showed that 7 downregulated microRNAs were also downregulated in lesioned skin samples in the GSE174763 dataset. (e) qPCR analysis of miR-124-3p in HaCaT cells treated with IL-17A ( $n = 6$ ) and PBS ( $n = 6$ ). The expression level was normalized to U6. (f) CCK-8 assay of cells treated with IL-17A and miR-124-3p at 0, 24, 48, and 72 hrs. \* $p < 0.05$ , \*\* $p < 0.01$ , and \*\*\* $p < 0.001$ .

temperature. A DAB Horseradish Peroxidase Colour Development Kit (Beyotime) was applied, and the sections were incubated for approximately 3 minutes. The images were observed and photographed using a light microscope [30].

**2.10.4. Statistical Analysis.** Statistical analysis was performed with R. Data are presented as the mean  $\pm$  standard deviation (SD). Differences between groups were evaluated by a  $t$ -test or one-way analysis of variance (ANOVA). A  $p$  value less than 0.05 was regarded as statistically significant.

### 3. Results

In this study, we explored the function and regulatory mechanism of miR-124-3p in psoriasis progression *in vitro* and *in vivo*. miR-124-3p was downregulated in IL-17A-treated keratinocytes as well as in skin samples from psoriasis patients. STAT3 was directly targeted by miR-124-3p, and miR-124-3p overexpression reversed the IL-17A-induced increase in STAT3 expression in keratinocytes. miR-124-3p overexpression inhibited IL-17-enhanced proliferation,

reduced oxidative stress in keratinocytes *in vitro*, and attenuated inflammation and skin thickness in psoriasis mouse models. The findings of our study may provide potential therapeutic targets for psoriasis treatment.

**3.1. miR-124-3p Inhibits IL-17A-Mediated Keratinocyte Proliferation.** We identified 67 miRNAs differentially expressed at least 2-fold in NHEKs stimulated with IL-17 and 57 miRNAs differentially expressed at least 2-fold in HaCaT cells stimulated with IL-17 (Figures 1(a) and 1(b)). Among them, 5 miRNAs were upregulated in both cell lines (Figure 1(c)), and 7 miRNAs were downregulated in both cell lines (Figure 1(c)), and they were further confirmed in patient samples in the public dataset GSE174763. miR-124-3p was significantly downregulated in IL-17A-stimulated keratinocytes, as well as in keratinocytes from psoriatic skin lesions (Figure 1(d)). The results of RT-qPCR analysis confirmed the decreased levels of miR-124-3p in keratinocytes treated with IL-17A (Figure 1(e)). We next tested whether miR-124-3p had functional roles in keratinocytes. We stimulated cells with IL-17A and found that IL-17A increased

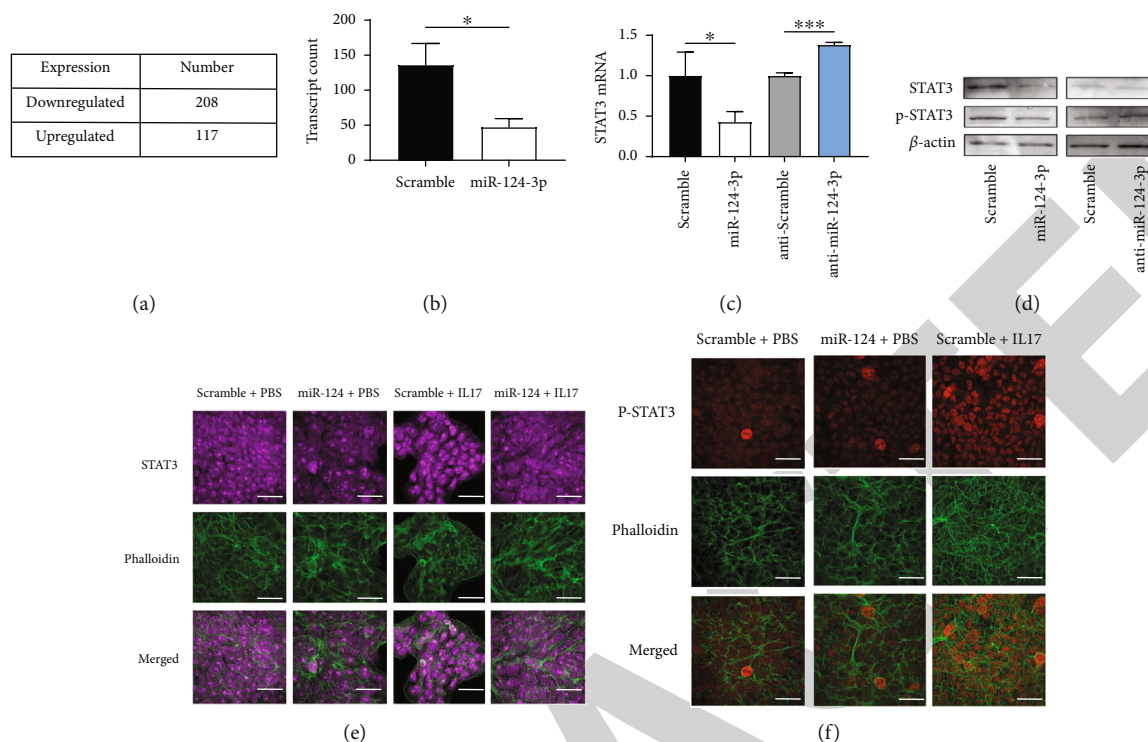


FIGURE 2: miR-124-3p inhibits STAT3 in keratinocytes. RNA extracted from HaCaT cells transfected with miR-124-3p ( $n = 3$ ) and scramble miRNA ( $n = 3$ ) was used for RNA-seq. (a) A total of 208 genes were downregulated, and 117 genes were upregulated in HaCaT cells transfected with miR-124-3p. (b) Transcript count of STAT3 in sequencing samples from cells transfected with scramble miRNAs or miR-124-3p mimic. (c) qPCR analysis of STAT3 expression in HaCaT cells transfected with miR-124-3p mimic or miR-124-3p inhibitor. Data were normalized to GAPDH. (d) Western blot analysis of STAT3 and p-STAT3 protein expression in HaCaT cells transfected with miR-124-3p mimic or miR-124-3p inhibitor. Actin was used as a loading control. (e) Immunostaining of STAT3 in HaCaT cells treated with IL-17A and miR-124-3p. (f) Immunostaining of p-STAT3 in HaCaT cells treated with IL-17A and miR-124-3p. \* $p < 0.05$ , \*\* $p < 0.01$ , and\*\*\* $p < 0.001$ .

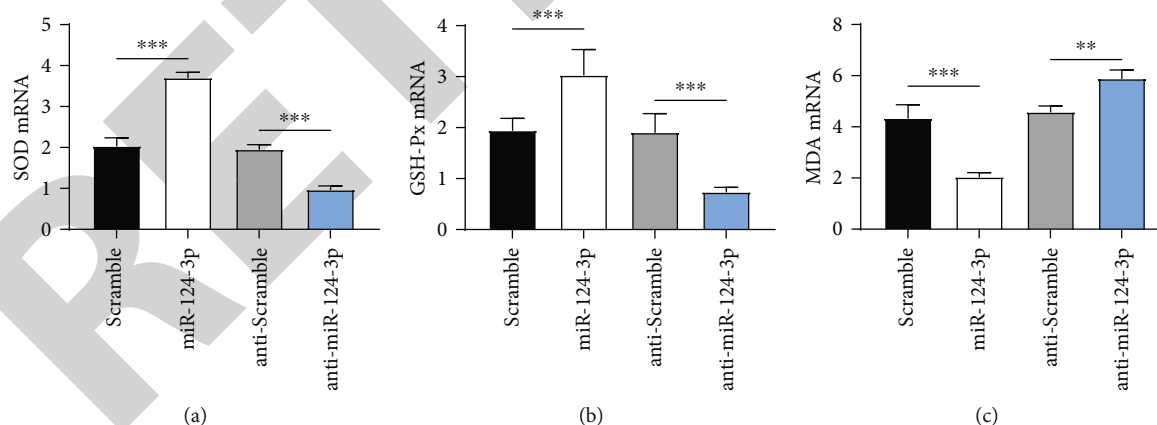


FIGURE 3: miR-124-3p affects oxidative stress responses in keratinocytes. (a) The mRNA levels of SOD in keratinocytes after the indicated treatments. (b) GSH-Px mRNA levels in keratinocytes after the indicated transfections. (c) MDA mRNA levels in keratinocytes after the indicated transfections. \* $p < 0.05$ , \*\* $p < 0.01$ , and\*\*\* $p < 0.001$ .

cell proliferation, while overexpression of miR-124-3p in HaCaT cells reduced the proliferation rate induced by IL-17A (Figure 1(f)).

**3.2. miR-124-3p Inhibits STAT3 in Keratinocytes.** As dysregulation of miRNAs in psoriatic keratinocytes may affect the

pathogenesis of psoriasis, we explored the potential role of miR-124-3p. We overexpressed miR-124-3p in keratinocytes and performed RNA-seq. As shown in Figure 2(a), 117 genes were upregulated at least 2-fold, and 208 genes were downregulated at least 2-fold. By intersecting the genes with miR-124-3p predicted targets, we found that STAT3 was a

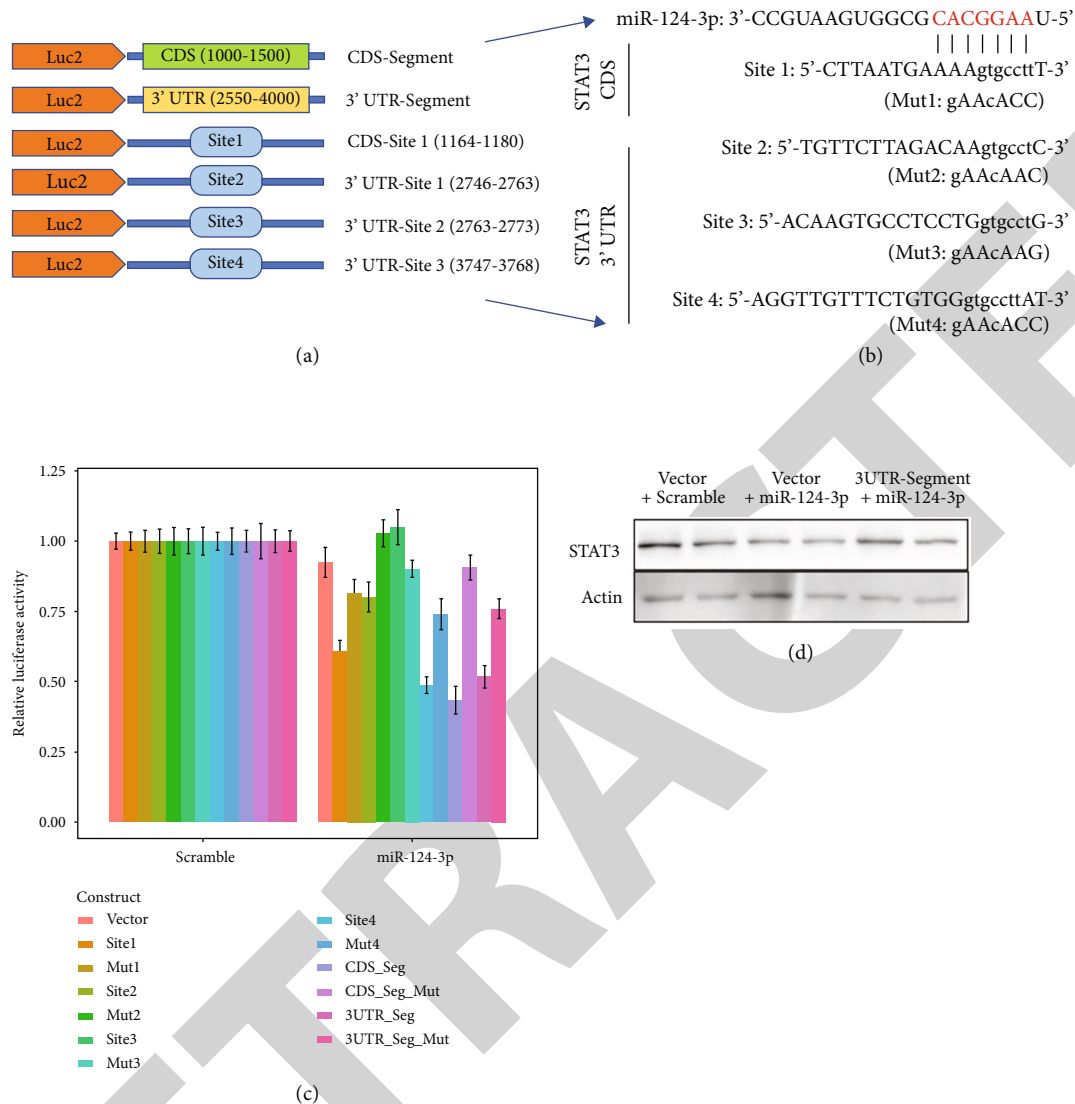


FIGURE 4: miR-124-3p directly targeted STAT3 in keratinocytes. (a) Graph showing the luciferase constructs used to confirm the direct targeting of STAT3 mRNA by miR-124-3p. (b) Graph showing the predicted binding sites of miR-124-3p in STAT3 mRNA and designed mutant sequences used in the luciferase assay. (c) Luciferase activity in HEK 293T cells cotransfected with the respective constructs and miR-124-3p mimic or scramble miRNAs. (d) Western blot analysis showed that cotransfection of the STAT3 3'UTR segment and miR-124-3p could rescue the miR-124-3p downregulating effect on STAT3 in HaCaT cells. \* $p < 0.05$ , \*\* $p < 0.01$ , and \*\*\* $p < 0.001$ ; # $p < 0.05$ , ## $p < 0.01$ , and ### $p < 0.001$ . \*wild-type sequence vs. vector; #mutant sequence vs. wild-type sequence.

potential gene directly targeted by miR-124-3p (Figure 2(b)). When we overexpressed miR-124-3p in keratinocytes in vitro, we found that STAT3 mRNA levels decreased (Figure 2(c)) as well as the protein level (Figure 2(d)). We then stimulated HaCaT cells with IL-17 and found that STAT3 expression levels increased. Overexpression of miR-124-3p reduced the STAT3 level as well as p-STAT3 level even in the presence of IL-17 stimulation (Figures 2(e) and 2(f)).

**3.3. miR-124-3p Affects Oxidative Stress Responses in Keratinocytes.** To confirm the influence of miR-124-3p on oxidative stress in keratinocytes, we measured the oxidative stress markers SOD, MDA, and GSH-Px in cells. The results also showed increased SOD and GSH-Px and decreased

MDA at the mRNA level when miR-124-3p was overexpressed in keratinocytes in vitro, which was completely contrary to the results after IL-17 stimulation (decreased SOD and GSH-Px mRNA and elevated MDA mRNA after IL-17 stimulation) (Figures 3(a)–3(c)).

**3.4. miR-124-3p Directly Targeted STAT3 in Keratinocytes.** To test whether miR-124-3p directly targets STAT3, we performed luciferase reporter assays. As shown in Figure 4(a), the StarmirDB database (<https://sfold.wadsworth.org/starmirDB.php>) predicted multiple miR-124-3p binding sites in the STAT3 mRNA 3'UTR. We cloned miR-124-3p binding sites as well as mutant sequences in luciferase constructs (Figure 4(b)). As shown in Figure 4(c), overexpression of miR-124-3p reduced luciferase activity compared to

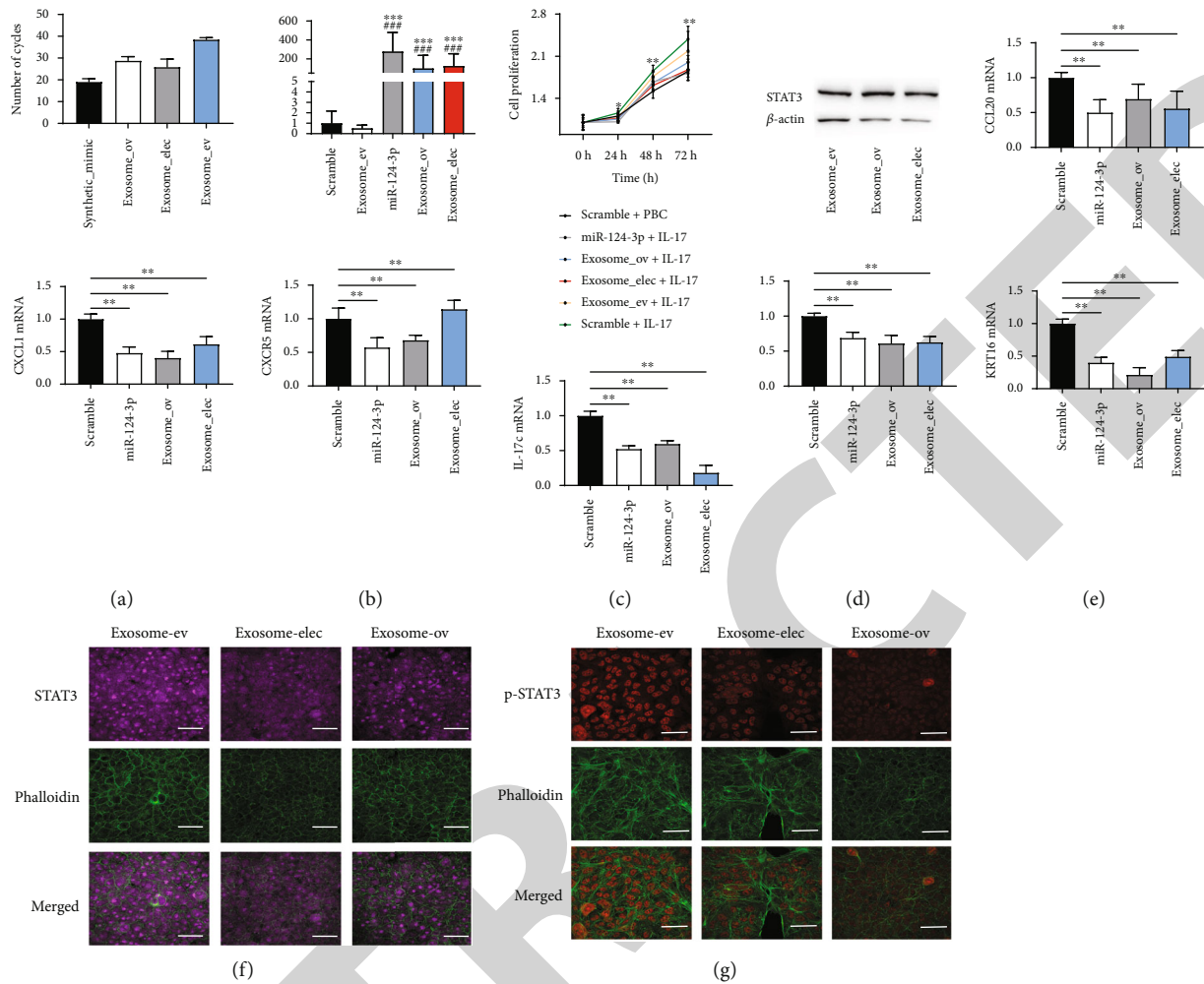


FIGURE 5: *In vitro* delivery of miR-124-3p in HaCaT cells with exosomes as delivery cargo. (a) qPCR analysis of miR-124-3p levels in exosomes from the miR-124-3p overexpression stable cell line (Exosome\_ov), electroporation-treated exosomes (Exosome\_elec), and exosomes from the scramble miRNA overexpression stable cell line (Exosome\_ev). The miR-124-3p mimic (Synthetic\_mimic) was used as a positive control. (b) qPCR analysis of miR-124-3p levels in cells coincubated with Exosome\_ev, Exosome\_ov, and Exosome\_elec. Cells transfected with scramble by RNAiMax were used as a negative control, and cells transfected with miR-124-3p mimic were used as a positive control. (c) Western blot showing STAT3 protein expression in HaCaT cells coincubated with Exosome\_ov or Exosome\_elec. (d) CCK-8 assay of cells treated with IL-17A and Exosome\_ov, Exosome\_elec, Exosome\_ev, or miR-124-3p at 0, 24, 48, and 72 hrs. (e) qPCR analysis of CXCR5, IL22, KRT16, IL17C, CXCL1, and CCL20 expression in HaCaT cells treated with IL-17A and Exosome\_ov, Exosome\_elec, Exosome\_ev, or miR-124-3p. (f) Immunostaining of STAT3 in HaCaT cells coincubated with Exosome\_ov or Exosome\_elec and IL-17A. (g) Immunostaining of p-STAT3 in HaCaT cells coincubated with Exosome\_ov or Exosome\_elec and IL-17A. \* $p < 0.05$ , \*\* $p < 0.01$ , and \*\*\* $p < 0.001$ .

scramble miRNAs in site 1, site 2, site 4, CDS segment, and 3' UTR segment constructs, while the luciferase activity was partially recovered in seed region mutant constructs. When we cotransfected miR-124-3p and the 3' UTR segment in HaCaT cells, we found that the STAT3 expression level was higher than that in cells transfected with only miR-124-3p (Figure 4(d)). These results indicated that miR-124-3p directly targets the STAT3 3' UTR, thus regulating protein expression.

**3.5. In Vitro Delivery of miR-124-3p in HaCaT Cells with Exosomes as Delivery Cargo.** Previous studies have shown that exosomes can be used as cargo to deliver miRNAs or siRNAs; thus, we tested whether miR-124-3p can be delivered via engineered exosomes. We used 2 different methods

to generate exosomes containing miR-124-3p as described in previous studies [25, 31]. In the first method, we stably expressed miR-124-3p in HEK 293T cells and purified exosomes after 48 hr of incubation. In the second method, we first purified exosomes from regular HEK 293T cells and loaded miR-124-3p mimics using electroporation. As shown in Figure 5(a), both methods resulted in exosomes loaded with miR-124-3p, with electroporation demonstrating higher yield but larger variation. When we incubated the exosomes with HaCaT cells, we found that exosomes generated by both methods had similar efficiency in fusion with HaCaT cells and delivered miR-124-3p into cells, as shown in Figure 5(b). When HaCaT cells were stimulated with IL-17A, we found that incubation with exosomes containing

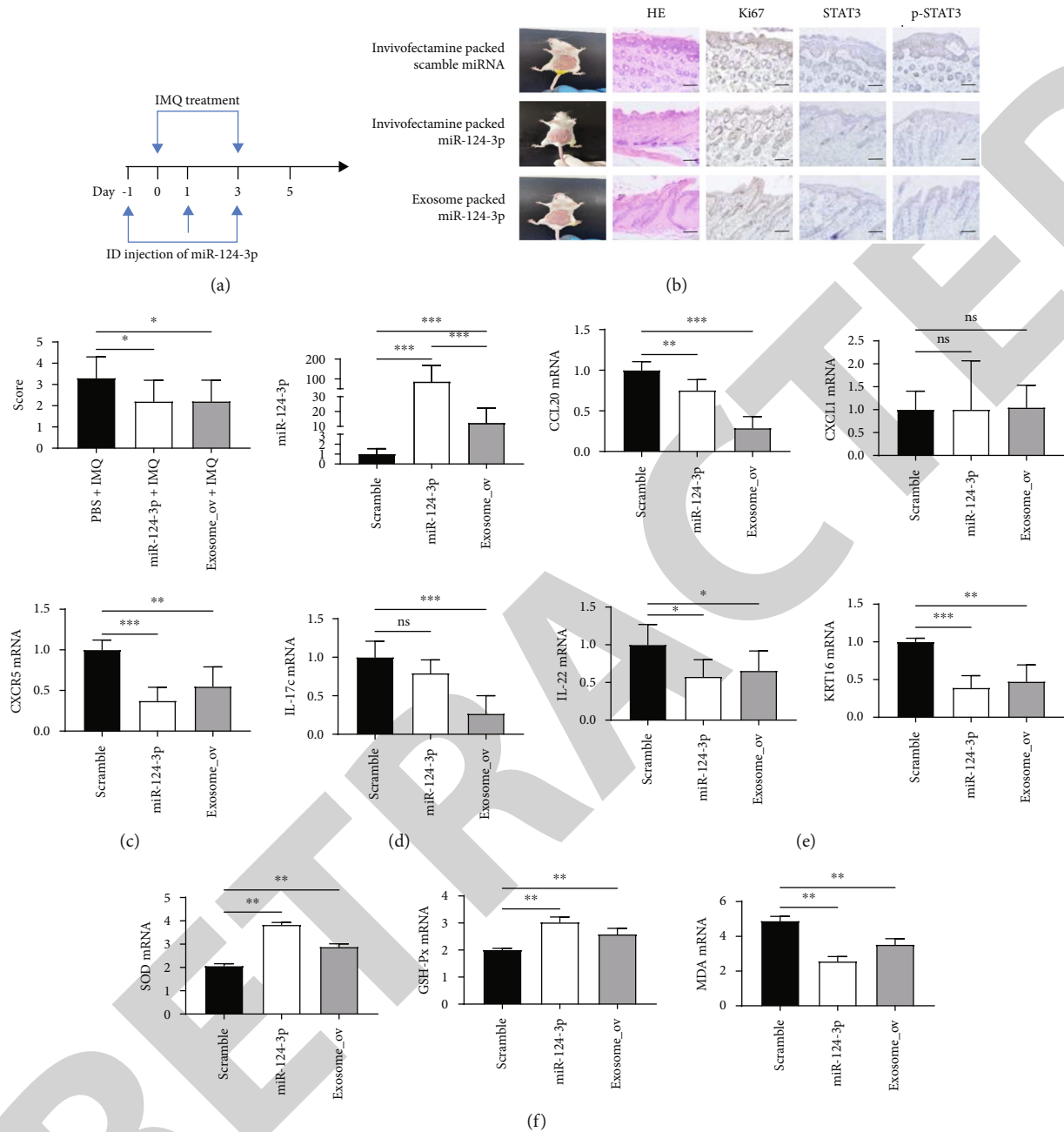


FIGURE 6: *In vivo* delivery of miR-124-3p with exosomes reduced IMQ-induced psoriasis. (a) Graph showing the experimental design. (b) Graph showing the back skin of mice, H&E staining of back skin samples, and IHC staining for Ki67, STAT3, and p-STAT3 protein in back skin samples from mice injected with Exosome\_ov, miR-124-3p or scramble miRNAs in combination with IMQ. (c) Clinical scores of mouse back skins in each group ( $n = 10$ ). (d) qPCR analysis of miR-124-3p levels in the back skin samples of the corresponding mouse model ( $n = 5$ ). (e) qPCR analysis of Cxcr5, Il22, Krt16, Il17c, Cxcl1 and Ccl20 expression in the back skin samples of the corresponding mouse model ( $n = 5$ ). (f) The results of oxidative stress damage. \* $p < 0.05$ , \*\* $p < 0.01$ , and \*\*\* $p < 0.001$ .

miR-124-3p reduced STAT3 expression in the presence of IL-17A stimulation (Figures 5(c), 5(f), and 5(g)) and reduced the cell proliferation rate induced by IL-17A (Figure 5(d)). qPCR analysis of psoriasis-related genes showed that CXCR5, IL22, KRT16, IL17C, CXCL1, and CCL20 expression was also reduced in cells incubated with exosomes containing miR-124-3p, which was similar to the effect of transfection with miR-124-3p mimic by RNAiMAX (Figure 5(e)).

**3.6. *In Vivo* Delivery of miR-124-3p with Exosomes Reduced IMQ-Induced Psoriasis.** Then, we tried to determine whether *in vivo* delivery of miR-124-3p could relieve IMQ-induced psoriasis in BALB/c mice. Synthetic miR-124-3p mimics or exosomes containing miR-124-3p were injected into the back skin of mice treated with IMQ (Figure 6(a)). As expected, IMQ treatment caused erythema and induced cell proliferation (Figure 6(b)). The skin thickness also increased

after IMQ treatment. Intradermal delivery of miR-124-3p by exosomes increased miR-124-3p levels in mouse skin (Figure 6(d)). Clinical scores showed that miR-124-3p overexpression relieved skin inflammation and reduced skin thickness (Figure 6(c)). Delivery of miR-124-3p with InvivoFectamine also relieved the symptoms caused by IMQ. In histological analysis, we found that the epidermal thickness significantly decreased in the miR-124-3p-treated groups. Ki67 staining within skin samples showed that the number of proliferating cells decreased in mice injected with miR-124-3p (Figure 6(b)). In addition, qPCR showed that some psoriasis-related genes, such as Ccl20, Cxcr5, Krt16, and Il17c, significantly decreased when miR-124-3p was overexpressed *in vivo*. (Figure 6(e)). Finally, analysis of oxidative stress markers also revealed that when miR-124-3p was overexpressed in mice, SOD and GSH-Px increased, while MDA decreased, suggesting effectively controlled oxidative stress responses (Figure 6(f)). Taken together, our results showed that increased miR-124-3p expression could reduce psoriasis-like skin inflammation, and delivery of miR-124-3p could be a potential therapy to treat psoriasis *in vivo*.

#### 4. Discussion

In this study, we found that miR-124-3p attenuated the inflammatory responses caused by IL-17A in keratinocytes. The expression of miR-124-3p was decreased in IL-17A-treated keratinocytes. miR-124-3p overexpression reversed the increase in STAT3 expression and keratinocyte proliferation rate induced by IL-17A treatment. The oxidative stress and expression of psoriasis-related genes were inhibited by the delivery of exosomes carrying miR-124-3p *in vivo*. Our findings suggest miR-124-3p as a potential therapeutic target for psoriasis treatment.

Recent studies have shown that keratinocytes play important roles in modulating skin inflammation instead of acting as passive targets within the skin immunity environment [32]. Knockout of IL-17RA in keratinocytes in mice attenuated skin inflammation caused by IMQ, while IL-17RA knockout in other cell types did not show attenuation, indicating that keratinocytes are key targeting cells for IL-17A-induced psoriasis [33]. In our study, we found that IL-17A treatment significantly enhanced the proliferation potential of keratinocytes, which was consistent with previous findings. miR-124-3p directly targeted STAT3 in keratinocytes. STAT3 plays critical roles in regulating inflammatory responses and is important for epidermal homeostasis within skin. STAT3 is activated in keratinocytes of psoriatic lesions and promotes the proliferation of keratinocytes. Previous studies have shown that the topical application of a STAT3 inhibitor could inhibit psoriasis onset in a mouse model [19] and in clinical trials [20]. In this study, we found that the expression of STAT3 was negatively regulated by miR-124-3p in psoriasis, and STAT3 expression showed a significant increase after stimulation with IL-17A, which was consistent with previous studies. In addition, the oxidative stress reaction is an important pathological process in the development of psoriasis. Keratinocytes stimulated by inflammatory reactions can cause serious inflammatory

changes and destroy the original functions of cells. A study also indicated that oxidative stress caused by reactive oxygen species also promotes psoriasis by activating STAT3 [34]. We have found in previous studies that the peripheral blood of psoriasis patients is clearly hyperoxidized [35], which is consistent with our research (after IL-17 stimulation, SOD and GSH-Px in cells decreased, but MDA increased), further supporting the relationship between psoriasis and oxidative stress injury. Moreover, significant alleviation of oxidative stress responses was observed in keratinocytes and psoriatic mice after miR-124-3p was elevated, while miR-124-3p inhibition exhibited the opposite effects on oxidative stress in keratinocytes. The results of *in vivo* assays demonstrated that STAT3 was highly expressed in the skin lesions of psoriatic rats, and miR-124-3p, which directly targets STAT3 at the 3'UTR, reduced the severity of psoriatic lesions induced by IMQ in mice, which was consistent with previous findings. These results indicate that STAT3 could be an effective therapeutic target in psoriasis treatment.

Although liposomes such as InvivoFectamine used in this study could effectively deliver miRNAs *in vivo*, this reagent is not suitable for use in clinical practice due to stability, safety, and off-target effects [36, 37]. A previous study showed that exosomes purified from cells transfected with let-7a miRNA could inhibit cancer cell growth in mice [38]. These results indicate that exosomes are a promising cargo in clinical practice for DNA or RNA delivery with multiple advantages over liposomes. In our study, we revealed that HEK 293T cells stably transfected with miR-124-3p could generate exosomes containing abundant miR-124-3p. Compared to electroporation, this method is more convenient and avoids the problem of aggregation seen in electroporation. The different cells and miRNA mimics used compared with previous studies may cause the difference in miRNA introduction efficiency. Furthermore, we compared the effect of the exosome delivery system *in vitro* and found that exosomes containing miR-124-3p stably overexpressing miR-124-3p constructs in HEK 293 T cells were more efficient than electroporation. Moreover, compared to delivering miR-124-3p with InvivoFectamine *in vivo*, exosomes were safer and exhibited fewer side effects in mice injected with exosomes. Our findings may provide novel insight into antipsoriasis therapy.

However, there are still some limitations in this study. First, the mechanism of exosome-mediated communication between HEK 293T and HaCaT cells was not explored. Second, whether STAT3 overexpression could rescue the effects of miR-124-3p delivered by exosomes remains to be further investigated. Third, the clinical application of engineered exosomes is challenged by the comprehensive molecular and functional characterization before each treatment, which requires the improvement of automatic preparation of disease-targeted exosomes in the future.

#### 5. Conclusion

miR-124-3p modulates keratinocyte activity via STAT3 upon stimulation by IL-17A. Ectopic expression of miR-124-3p in psoriatic skin alleviates IL-17A-induced

inflammation and inhibits the STAT3 pathway, thus relieving psoriatic symptoms.

### Data Availability

The datasets used and/or analysed during the current study are available from the corresponding author on reasonable request.

### Ethical Approval

All procedures were conducted in accordance with the Institutional Animal Care Guidelines of Jiangxi University of Chinese Medicine and were approved by the Experimental Animal Ethics Committee of Jiangxi Province, China (approval No. JZLLSC20220590).

### Conflicts of Interest

No potential conflict of interest was reported by the authors.

### Authors' Contributions

SML designed the study and wrote the manuscript. SML and JG conducted the experiments. JG performed data analysis and prepared tables and figures. All authors have reviewed and approved the article.

### Acknowledgments

This study was supported by the General Projects of Science and Technology Plan of Jiangxi Province Administration of Traditional Chinese Medicine (No. 2021B108).

### References

- [1] C. E. M. Griffiths, A. W. Armstrong, J. E. Gudjonsson, and J. N. W. N. Barker, "Psoriasis," *Lancet*, vol. 397, no. 10281, pp. 1301–1315, 2021.
- [2] A. W. Armstrong, "Psoriasis," *JAMA Dermatology*, vol. 153, no. 9, p. 956, 2017.
- [3] S. Mehrmal, P. Uppal, N. Nedley, R. L. Giesey, and G. R. Delost, "The global, regional, and national burden of psoriasis in 195 countries and territories, 1990 to 2017: a systematic analysis from the global burden of disease study 2017," *Journal of the American Academy of Dermatology*, vol. 84, no. 1, pp. 46–52, 2021.
- [4] W. H. Boehncke and M. P. Schön, "Psoriasis," *The Lancet*, vol. 386, no. 9997, pp. 983–994, 2015.
- [5] C. A. Elmetts, C. L. Leonardi, D. M. R. Davis et al., "Joint AAD-NPF guidelines of care for the management and treatment of psoriasis with awareness and attention to comorbidities," *Journal of the American Academy of Dermatology*, vol. 80, no. 4, pp. 1073–1113, 2019.
- [6] J. Zhang, S. Li, L. Li et al., "Exosome and exosomal microRNA: trafficking, sorting, and function," *Genomics, Proteomics & Bioinformatics*, vol. 13, no. 1, pp. 17–24, 2015.
- [7] J. O'Brien, H. Hayder, Y. Zayed, and C. Peng, "Overview of microRNA biogenesis, mechanisms of actions, and circulation," *Frontiers in Endocrinology*, vol. 9, pp. 1–12, 2018.
- [8] H. Zhou and I. Rigoutsos, "MiR-103a-3p targets the 5' UTR of GPRC5A in pancreatic cells," *RNA*, vol. 20, no. 9, pp. 1431–1439, 2014.
- [9] T.-S. Wong, X.-B. Liu, B. Yee-Hang Wong, R. Wai-Man Ng, A. Po-Wing Yuen, and W. W. Ignace, "Mature miR-184 as potential oncogenic microRNA of squamous cell carcinoma of tongue," *Clinical Cancer Research*, vol. 14, no. 9, pp. 2588–2592, 2008.
- [10] Å. Ø. Solvin, K. Chawla, L. C. Olsen et al., "MicroRNA profiling of psoriatic skin identifies 11 miRNAs associated with disease severity," *Experimental Dermatology*, vol. 31, no. 4, pp. 535–547, 2022.
- [11] S. Corbetta, V. Vaira, V. Guarnieri et al., "Differential expression of microRNAs in human parathyroid carcinomas compared with normal parathyroid tissue," *Endocrine-Related Cancer*, vol. 17, no. 1, pp. 135–146, 2010.
- [12] A. M. Ardekani and M. M. Naeini, "The role of microRNAs in human diseases," *Avicenna Journal of Medical Biotechnology*, vol. 2, no. 4, pp. 161–179, 2010.
- [13] G. Liang, S. Kan, Y. Zhu, S. Feng, W. Feng, and S. Gao, "Engineered exosome-mediated delivery of functionally active miR-26a and its enhanced suppression effect in HepG2 cells," *International Journal of Nanomedicine*, vol. 13, pp. 585–599, 2018.
- [14] L. Pasquali, A. Svedbom, A. Srivastava et al., "Circulating microRNAs in extracellular vesicles as potential biomarkers for psoriatic arthritis in patients with psoriasis," *Journal of the European Academy of Dermatology and Venereology*, vol. 34, no. 6, pp. 1248–1256, 2020.
- [15] E. Calautti, L. Avalle, and V. Poli, "Psoriasis: a STAT3-centric view," *International Journal of Molecular Sciences*, vol. 19, no. 1, p. 171, 2018.
- [16] S. Sano, K. S. Chan, S. Carbajal et al., "Stat3 links activated keratinocytes and immunocytes required for development of psoriasis in a novel transgenic mouse model," *Nature Medicine*, vol. 11, no. 1, pp. 43–49, 2005.
- [17] U. Kaufmann, S. Kahlfuss, J. Yang, E. Ivanova, S. B. Koralov, and S. Feske, "Calcium signaling controls pathogenic Th17 cell-mediated inflammation by regulating mitochondrial function," *Cell Metabolism*, vol. 29, no. 5, pp. 1104–1118.e6, 2019.
- [18] R. M. Andrés, M. C. Montesinos, P. Navalón, M. Payá, and C. M. Terencio, "NF- $\kappa$ B and STAT3 inhibition as a therapeutic strategy in psoriasis: *in vitro* and *in vivo* effects of BTH," *Journal of Investigative Dermatology*, vol. 133, no. 10, pp. 2362–2371, 2013.
- [19] H. Qiong, L. Han, N. Zhang et al., "Glycyrrhizin improves the pathogenesis of psoriasis partially through IL-17A and the SIRT1-STAT3 axis," *BMC Immunology*, vol. 22, no. 1, pp. 1–11, 2021.
- [20] K. Miyoshi, M. Takaishi, K. Nakajima et al., "Stat3 as a therapeutic target for the treatment of psoriasis: a clinical feasibility study with STA-21, a Stat3 inhibitor," *Journal of Investigative Dermatology*, vol. 131, no. 1, pp. 108–117, 2011.
- [21] B. Chen, C. Li, G. Chang, and H. Wang, "Dihydroartemisinin targets fibroblast growth factor receptor 1 (FGFR1) to inhibit interleukin 17A (IL-17A)-induced hyperproliferation and inflammation of keratinocytes," *Bioengineered*, vol. 13, no. 1, pp. 1530–1540, 2022.
- [22] D. Xu and J. Wang, "Downregulation of cathepsin B reduces proliferation and inflammatory response and facilitates differentiation in human HaCaT keratinocytes, ameliorating IL-17A



## Retraction

# Retracted: LINC00958 Inhibits Autophagy of Bladder Cancer Cells via Sponge Adsorption of miR-625-5p to Promote Tumor Angiogenesis and Oxidative Stress

### Oxidative Medicine and Cellular Longevity

Received 20 June 2023; Accepted 20 June 2023; Published 21 June 2023

Copyright © 2023 Oxidative Medicine and Cellular Longevity. This is an open access article distributed under the Creative Commons Attribution License, which permits unrestricted use, distribution, and reproduction in any medium, provided the original work is properly cited.

This article has been retracted by Hindawi following an investigation undertaken by the publisher [1]. This investigation has uncovered evidence of one or more of the following indicators of systematic manipulation of the publication process:

- (1) Discrepancies in scope
- (2) Discrepancies in the description of the research reported
- (3) Discrepancies between the availability of data and the research described
- (4) Inappropriate citations
- (5) Incoherent, meaningless and/or irrelevant content included in the article
- (6) Peer-review manipulation

The presence of these indicators undermines our confidence in the integrity of the article's content and we cannot, therefore, vouch for its reliability. Please note that this notice is intended solely to alert readers that the content of this article is unreliable. We have not investigated whether authors were aware of or involved in the systematic manipulation of the publication process.

In addition, our investigation has also shown that one or more of the following human-subject reporting requirements has not been met in this article: ethical approval by an Institutional Review Board (IRB) committee or equivalent, patient/participant consent to participate, and/or agreement to publish patient/participant details (where relevant).

Wiley and Hindawi regrets that the usual quality checks did not identify these issues before publication and have since put additional measures in place to safeguard research integrity.

We wish to credit our own Research Integrity and Research Publishing teams and anonymous and named external researchers and research integrity experts for contributing to this investigation.




The corresponding author, as the representative of all authors, has been given the opportunity to register their agreement or disagreement to this retraction. We have kept a record of any response received.

### References

- [1] Y. Xiao, T. Wang, X. Cheng et al., "LINC00958 Inhibits Autophagy of Bladder Cancer Cells via Sponge Adsorption of miR-625-5p to Promote Tumor Angiogenesis and Oxidative Stress," *Oxidative Medicine and Cellular Longevity*, vol. 2022, Article ID 2435114, 14 pages, 2022.

## Research Article

# LINC00958 Inhibits Autophagy of Bladder Cancer Cells via Sponge Adsorption of miR-625-5p to Promote Tumor Angiogenesis and Oxidative Stress

Ying Xiao,<sup>1,2,3</sup> Tao Wang,<sup>2,4</sup> Xiao Cheng,<sup>2,3</sup> Fangwen Liu,<sup>1,2</sup> You Wu <sup>1</sup>, Limin Ma <sup>1,2</sup> and Wenguang Li <sup>1,2</sup>

<sup>1</sup>Department of Urological Surgery, Affiliated Hospital of Nantong University, Nantong, Jiangsu 226001, China

<sup>2</sup>School of Medicine, Nantong University, Nantong, Jiangsu 226001, China

<sup>3</sup>Key Laboratory for Neuroregeneration of Jiangsu Province and Ministry of Education, Co-Innovation Center of Neuroregeneration, Nantong University, Nantong, Jiangsu 226001, China

<sup>4</sup>Department of Pathology, Affiliated Hospital of Nantong University, Nantong, Jiangsu 226001, China

Correspondence should be addressed to You Wu; [tdfywuyou@163.com](mailto:tdfywuyou@163.com), Limin Ma; [tdfymlm@163.com](mailto:tdfymlm@163.com), and Wenguang Li; [ntlwg@ntu.edu.cn](mailto:ntlwg@ntu.edu.cn)

Received 4 July 2022; Revised 26 August 2022; Accepted 8 September 2022; Published 10 October 2022

Academic Editor: Tian Li

Copyright © 2022 Ying Xiao et al. This is an open access article distributed under the Creative Commons Attribution License, which permits unrestricted use, distribution, and reproduction in any medium, provided the original work is properly cited.

**Objective.** This study further explored LINC00958's role in promoting tumor angiogenesis (AG) and oxidative stress (OS) development by inhibiting BC cell autophagy through sponge adsorption of miR-625-5p. **Methods.** BC patients and healthy controls who visited our hospital between June 2017 and February 2019 were selected as the research group (RG) and the control group (CG), respectively, with a total of 133 study subjects. Peripheral blood LINC00958 and miR-625-5p in both cohorts of participants were detected. Additionally, human bladder transitional cell carcinoma cells (T24 and J82) and human normal urothelial cells (SV-HUC-1) were purchased. Alterations in cell biological behavior were observed after transfecting miR-625-5p-mimics, miR-625-5p-inhibition, and miR-625-5p-NC sequences into these cells, respectively. Besides, ELISA was performed to quantify inflammatory factors (IFs), AG indicators, and OS indexes in cells. Subsequently, a double luciferase reporter (DLR) assay was performed to verify the targeting relationship between LINC00958 and miR-625-5p. Finally, BALB/c-nu nude mice were purchased, and T24 cells transfected with silenced LINC00958 and miR-625-5p expression sequences were used to establish subcutaneous tumors to observe tumor growth and pathological changes. **Results.** RG exhibited higher LINC00958 and lower miR-625-5p than CG. LINC00958 and miR-625-5p were strongly linked to myometrial invasion (MI), lymph node metastasis (LNM), distant metastasis (DM), and histology in BC patients, and the increase of LINC00958 and the decrease of miR-625-5p predicted an increased risk of prognostic death in such patients. After miR-625-5p inhibition, the capacity of BC cells to proliferate, invade, and migrate enhanced and the AG, inflammatory response, and OS injury increased, while the apoptosis rate and autophagy ability decreased. The DLR assay revealed inhibited LINC00958WT fluorescence activity by miR-625-5p-mimics, while the biological behavior of BC cells cotransfected with sh-LINC00958 and miR-625-5p-inhibition had no difference with the functions of sh-control and miR-625-5p-NC cotransfected cells. Finally, the nude mouse tumorigenesis experiment showed that the tumor mass, volume, and histopathological features of the sh-LINC00958 group were decreased compared with the sh-control group, while those of the miR-625-5p-inhibition group were increased versus miR-625-5p-NC. **Conclusions.** In BC, LINC00958 is highly expressed while miR-625-5p is underexpressed. LINC00958 can inhibit cell autophagy to enhance cell activity; promote OS, inflammation, and AG; and regulate tumor immunity by targeting miR-625-5p, thus participating in the development of BC.

## 1. Introduction

Bladder cancer (BC), as a clinical high-incidence malignancy, is called “two major killers of male urogenital system” together with prostate cancer [1]. BC has a predilection for men aged 50-70 but may occur in all age groups, including children [2]. Bladder urothelial carcinoma, accounting for more than 90% of all BC cases, is the most common type of BC. It is precisely because of the strong migration ability of bladder epithelial cells that BC often has strong metastasis ability [3]. In the face of the great threat posed by BC, a condition with high incidence, strong metastasis, and poor prognosis, exploring and finding an effective and safe means of diagnosis and treatment have become a clinical focus and difficulty.

In the pathogenic research of modern tumor diseases, long-chain noncoding RNAs (lncRNAs) are one of the focuses of attention [4]. In our previous studies, LINC00958 has been found to promote BC cell growth and epithelial-mesenchymal transition via inhibiting the SAPK/JNK axis [5], but the downstream target genes involved in changes in BC cell behavior regulated by LINC00958 remain unclear. Therefore, this study intends to carry out a comprehensive analysis to address this limitation. Through Starbase, an online target gene prediction website, we preliminarily screened the downstream potential target genes of LINC00958, among which miR-625-5p attracted our attention. Located on human chromosome 14q23.3, this gene was first found to have an aberrant expression in the whole genome of cervical cancer and was subsequently confirmed to be of important potential significance in urogenital tumors such as prostate cancer and endometrial cancer [6–8]. Although the direct relationship between miR-625-5p and BC has not been verified yet, some studies have found that miR-625-5p can form a feedback channel with Runx1t1/TCF4 and promote BC progression under the action of RBM24 [9], which also preliminarily reveals the possible close relationship between miR-625-5p and the occurrence and development of BC. Furthermore, Wang et al. and Yang et al. directly pointed out that LINC00958 is able to promote cervical cancer and lung adenocarcinoma cell metastasis by mediating miR-625-5p [10, 11]. Therefore, we speculate that LINC00958 may also participate in the occurrence and development of BC through miR-625-5p. However, no study has yet analyzed the effect of LINC00958 on BC via miR-625-5p. In addition, miR-625-5p was also found to be a gene closely related to placental oxidation [12]. As we all know, in BC, it is confirmed that the occurrence and development of BC are promoted because of severe oxidative stress in urothelial cells [13]. This further illustrates the potential relationship between LINC00958, miR-625-5p, and BC.

Consequently, this study analyzes the role played by LINC00958 and miR-625-5p in BC through experiments to fill in the gap of previous studies, aimed at providing references for a deeper clinical understanding of the pathogenic mechanism of LINC00958 in BC.

## 2. Materials and Methods

**2.1. Patient Data.** BC patients admitted between June 2017 and February 2019 were selected as the research group

(RG) for retrospective analysis, with a total of 133 study subjects. According to the inclusion criteria (BC diagnosis by pathological biopsy in our hospital, age range: 18-70 years, and complete medical records), 74 patients with BC were selected. After further screening based on the exclusion criteria (multiple tumors, cardiovascular diseases, autoimmune defects, mental disorders, liver and kidney dysfunction or abnormalities, hospital referrals, and loss to follow-ups), 52 BC patients were finally enrolled. In addition, healthy subjects during the same period were selected as the control group (CG). According to the eligibility criteria (routine physical examination subjects in our hospital, with complete medical records, age range of 18-70 years, normal physical examination results, no major medical history, and willingness to participate in this study), 81 healthy controls were finally included. All the research participants signed the informed consent form by themselves. In order to ensure the reliability of the experimental results, we first compared the clinical baseline data between the two cohorts of subjects included. The results showed no statistical difference in age, sex, and other data between RG and CG ( $P > 0.05$ , Table 1), suggesting comparability.

**2.2. qRT-PCR Detection.** The blood samples of both cohorts that were routinely examined at admission were used for qRT-PCR detection. We used TRIzol to isolate total RNA from the sample to be tested and then reverse transcribed it into cDNA for PCR reaction under the following conditions that were run for 35 cycles: 95°C/30 s, 95°C/5 s, 65°C/30 s, and 72°C/30 s. Using GAPDH and U6 as internal reference (with primer sequences constructed by American Invitrogen, Table 2), LINC00958 and miR-625-5p expression was calculated by  $2^{-\Delta\Delta CT}$  [14].

**2.3. Follow-Up for Prognosis.** A 36-month follow-up was performed on BC patients. The termination event was death, and the 3-year survival of BC patients was recorded.

**2.4. Cell Data.** Human bladder transitional cell carcinoma T24 and J82 cells and human normal urothelial SV-HUC-1 cells, all supplied by ATCC, were cultured in a 10% fetal bovine serum- (FBS-) supplemented medium under the conditions of 37°C and 5CO<sub>2</sub>. The sh-LINC00958 of targeted silencing LINC00958 and the corresponding negative control sh-control, as well as miR-625-5p mimic sequence (miR-625-5p-mimics), inhibitor sequence (miR-625-5p-inhibition), and negative control group (miR-625-5p-NC), were all constructed by GenePharma and were transfected into T24 and J82 by referring to Lipofectamine 2000 instructions. PCR detected miR-625-5p expression to verify the transfection success rate.

**2.5. Cell Proliferation Ability Assay.** Cells were seeded into 6-well plates with 4 multiple wells set in each group. At 24 h, 48 h, 72 h, and 96 h of culture, CCK-8 solution (10 μL) was added to one well. A microplate reader read the absorbance at 450 nm wavelength, and the growth curve was drawn. Additionally, cells were inoculated into 6-well plates at 200 cells/mL, and 500 μL FBS was added to each well on the 5th day after plate laying. The supernatant was discarded

TABLE 1: Comparison of clinical baseline data.

	Research group ( $n = 52$ )	Control group ( $n = 81$ )	$t$ or $\chi^2/P$
Age	61.33 $\pm$ 5.96	62.36 $\pm$ 5.40	1.031/0.305
Sex			
Male	47 (90.38)	72 (88.89)	0.075/0.784
Female	5 (9.62)	9 (11.11)	
Smoking			
Yes	37 (71.15)	65 (80.25)	1.465/0.226
No	15 (28.85)	16 (19.75)	
Myometrial invasion			
Yes	15 (28.85)	—	
No	37 (71.15)	—	
Lymph node metastasis			
Yes	13 (25.00)	—	
No	39 (75.00)	—	
Distant metastasis			
Yes	11 (21.15)	—	
No	41 (78.85)	—	
Histological grading			
High	11 (21.15)	—	
Middle	9 (17.31)	—	
Low	32 (61.54)	—	

TABLE 2: Primer sequences.

	F (5'-3')	R (5'-3')
LINC00958	CAGCGAAAGGCAGCTGATTC	ATAAAGTGGTCTGGGCCTGC
GAPDH	GAAGGTGAAGGTCGGAGTC	GAAGATGGTGATGGGATTTC
miR-625-5p	GGGGAGGGGGAAAGTTCTA	GTGCGTGTCTGGAGTCCG
U6	GCTTCGGCAGCACATATACTAAAT	CGCTTCACGAATTTGCGTGCAT

after colony formation was visible to the naked eye. Then, the cells were fixed with 4% paraformaldehyde and stained with 0.1% crystal violet for counting [15].

**2.6. Cell Invasiveness Ability Assay.** Cells ( $5 \times 10^4$  cells/mL) were inoculated in the upper chamber where 300 mL serum-free medium was added, and Matrigel gel was added between the Transwell chambers. The cell culture solution containing 10% FBS was added into the lower chamber. After 24 h of culture, the surface suspended cells were wiped with Q-tips, immobilized, and stained, and the transmembrane cells were counted in 5 randomly selected target fields [16].

**2.7. Wound-Healing Assay.** The cell concentration was adjusted to  $4 \times 10^5$ /mL, and the cells were seeded into 6-well plates. When the growth density reaches 80-90%, a  $10 \mu\text{L}$  pipette tip was used to draw a vertical line in the culture plate. The scratch area was observed 24 h later, and the cell migration rate was calculated as  $(0 \text{ h scratch distance} - 24 \text{ h scratch distance})/0 \text{ h scratch distance} \times 100\%$  [17].

**2.8. Protein Relative Expression Detection.** RIPA lysed the cells to extract the total protein. After BCA quantification, the protein was transferred to a PVDF membrane by SDS electrophoresis, followed by 10 min of blocking with 5% defatted milk, as well as overnight incubation ( $4^\circ\text{C}$ ) with monoclonal primary antibodies Bax (1:1000), cleaved-caspase3 (1:1000), cleaved-caspase9 (1:1000), LC3-II (1:1000), Beclin1 (1:1000), p62 (1:1000), and GAPDH (1:1000). The next day, the membrane was washed and added with the horseradish peroxidase-labeled secondary antibody goat anti-rabbit IgG (1:5000). Protein antibodies were purchased from Invitrogen, USA. ECL was used for color development 4 h later. Then, protein bands were scanned for the analysis of relative expression of proteins by TotalLab Quant with  $\beta$ -actin as the internal reference. The relative expression level of the target protein was represented by the ratio of the gray value of the target protein to the gray value of the internal reference protein [18]. All antibodies were purchased from Abcam, China.

**2.9. ELISA.** After trypsin lysis, the cells were centrifuged and resuspended. Inflammatory factors (IFs) including interleukin-

(IL-) 1 $\beta$ , IL-6, and IL-8; angiogenesis- (AG-) related indices vascular endothelial growth factor (VEGF), VEGF receptor 2 (VEGFR2), and epidermal growth factor (EGF); and oxidative stress (OS) markers superoxide dismutase (SOD), malondialdehyde (MDA), and reactive oxygen species (ROS) were detected following ELISA kit instructions.

**2.10. Double Luciferase Reporter (DLR) Assay.** LINC00958's potential downstream target genes were analyzed by Starbase (URL: <https://starbase.sysu.edu.cn/>). The potential binding site of miR-625-5p was used to construct the LINC00958 3'UTR vector (mutation mode: A/T and G/C exchanged). LINC00958 3'UTR wild-type (WT) and mutant (MUT) plasmids were constructed and cloned into pGL3 luciferase reporter vector, which was subsequently transfected into miR-625-5p-mimics, miR-625-5p-inhibition, and miR-625-5p-NC, respectively. The DLR analysis system calculated the fluorescence expression 24 h later [19].

**2.11. Animal Information.** Twenty BALB/c-nu nude mice supplied by Beijing Vital River Laboratory Animal Technology (Animal License No. SCXK [Beijing] 2021-0006) were raised in cages (three mice per cage) where they were allowed to eat and drink freely.

**2.12. Establishment of BC Subcutaneous Tumor-Bearing Mice.** Mice were randomized into 4 groups, and  $4 \times 10^6$  T24 cells transfected with sh-control, sh-LINC00958, miR-625-5p-NC, and miR-625-5p-inhibition were injected into the mouse left armpit subcutaneous tissue, respectively. One mouse was selected from each group every 3 days and sacrificed under anesthesia. The whole subcutaneous tumor-bearing tissue was removed for weighing and volume measurement. Nine days later, all the mice were killed, and the tumor-bearing tissues were taken out and fixed with formaldehyde for HE staining [20].

**2.13. Statistics and Methods.** In this study, all experiments were repeated three times. The statistical analysis was carried out by SPSS22.0 software. Count data, denoted by ( $n(\%)$ ), was compared by the Chi-squared test between groups. The statistical methods for measurement data denoted by  $\chi \pm s$  included independent samples  $t$ -test, one-way ANOVA, and Bonferroni post hoc testing. Correlation analysis was performed by the Pearson correlation coefficient. For patient survival, it was calculated by the Kaplan-Meier method and compared by the Log-rank test.  $P < 0.05$  indicated the presence of statistical significance.

### 3. Results

**3.1. LINC00958 and miR-625-5p Levels in BC.** The test showed that the peripheral blood LINC00958 in RG was  $3.21 \pm 0.41$ , which was significantly higher than that in CG ( $P < 0.05$ , Figure 1(a)), while the peripheral blood miR-625-5p in RG ( $2.05 \pm 0.54$ ) was notably lower versus CG ( $P < 0.05$ , Figure 1(b)). According to Pearson correlation coefficient analysis, peripheral blood LINC00958 and miR-625-5p in RG were significantly and negatively correlated ( $P < 0.05$ , Figure 1(c)).

**3.2. Relationship between LINC00958, miR-625-5p, and BC Patients' Clinicopathologic Feature.** The comparison identified no statistical differences in LINC00958 and miR-625-5p levels among patients of different ages, genders, and smoking status ( $P > 0.05$ ), indicating no significant correlation between the two genes with the above clinical features. However, in patients with myometrial invasion (MI), lymph node metastasis (LNM), distant metastasis (DM), and high histological grade, LINC00958 was significantly upregulated ( $P < 0.05$ ) while miR-625-5p was underexpressed ( $P < 0.05$ , Table 3), suggesting a close connection between the two genes and these clinical features.

**3.3. Prognostic Implications of LINC00958 and miR-625-5p in BC.** Ten BC patients died during the 3-year follow-up, with an overall mortality of 20%. The peripheral blood LINC00958 in the dead patients was  $3.66 \pm 0.33$ , which was notably upregulated compared with the surviving patients ( $P < 0.05$ , Figure 2(a)), while miR-625-5p was  $1.55 \pm 0.38$ , lower than that in the surviving patients ( $P < 0.05$ , Figure 2(b)). Taking the median expression levels of the two as the boundary, patients were subdivided into the corresponding high (LINC00958  $\geq 3.21$ ,  $n = 24$ ; miR-625-5p  $\geq 2.05$ ,  $n = 29$ ) and lower (LINC00958  $< 3.21$ ,  $n = 28$ ; miR-625-5p  $< 2.05$ ,  $n = 23$ ) groups of LINC00958 and miR-625-5p. Further, the prognosis survival curve was plotted, which showed that the 3-year total mortality was evidently higher in the high LINC00958 group than in the low LINC00958 group ( $P < 0.05$ , Figure 2(c)) and higher in the low LINC00958 group versus the high miR-625-5p group ( $P < 0.05$ , Figure 2(d)).

**3.4. Impacts of miR-625-5p on BC Cell Biological Behavior.** Similarly, it can be seen that miR-625-5p expression in T24 and J82 was  $0.99 \pm 0.13$  and  $1.19 \pm 0.13$ , respectively, which was lower compared with SV-HUC-1 ( $P < 0.05$ , Figure 3(a)). miR-625-5p expression was found to be the highest in the miR-625-5p-mimics group among the three groups, while that in the miR-625-5p-inhibition group was lower compared with the miR-625-5p-NC group ( $P < 0.05$ , Figure 3(b)), confirming the successful transfection. Subsequently, in the CCK-8 experiment, the miR-625-5p-mimics group exhibited notably lower cell absorbance than the miR-625-5p-inhibition and miR-625-5p-NC groups at 72 h, while the miR-625-5p-inhibition group showed higher absorbance than the miR-625-5p-NC group ( $P < 0.05$ , Figures 3(c) and 3(d)). Consistent results were found in the cell cloning experiment, namely, the cell cloning rate of the miR-625-5p-mimics group was the lowest among the three groups, while that of the miR-625-5p-inhibition group was higher as compared to the miR-625-5p-NC group ( $P < 0.05$ , Figure 3(e)). Finally, in the Transwell experiment, we can see that the number of membrane-penetrating cells in the miR-625-5p-mimics group was  $32.67 \pm 4.16$ ,  $29.33 \pm 5.86$ , significantly lower than that in the other two groups, while the number of membrane-penetrating cells in the miR-625-5p-inhibition group was  $163.00 \pm 9.54$ ,  $172.67 \pm 11.50$ , higher compared with the miR-625-5p-NC group ( $P < 0.05$ , Figure 3(f)). The cell scratch-wound test results showed a

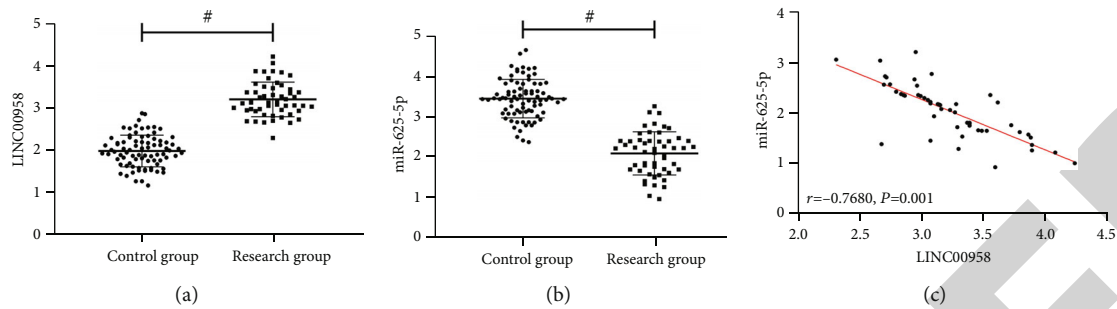


FIGURE 1: LINC00958 and miR-625-5p levels in BC: (a) comparison of peripheral blood LINC00958 between the research group ( $n = 52$ ) and the control group ( $n = 81$ ); (b) comparison of peripheral blood miR-625-5p between the research group ( $n = 52$ ) and the control group ( $n = 81$ ); (c) correlation between peripheral blood LINC00958 and miR-625-5p in the research group ( $n = 52$ ).  $^{\#}P < 0.05$ .

TABLE 3: Relationship between LINC00958, miR-625-5p, and BC patients' clinicopathologic feature.

	$n$	LINC00958	$t$ or $F/P$	miR-625-5p	$t$ or $F/P$
Age	<61 years old	$3.18 \pm 0.35$	0.512/0.611	$2.09 \pm 0.41$	0.390/0.698
	$\geq 61$ years old	$3.24 \pm 0.46$		$2.03 \pm 0.63$	
Sex	Male	$3.20 \pm 0.42$	0.724/0.355	$2.05 \pm 0.57$	0.230/0.819
	Female	$3.27 \pm 0.41$		$2.11 \pm 0.33$	
Smoking	Yes	$3.23 \pm 0.44$	0.497/0.621	$2.04 \pm 0.60$	0.372/0.711
	No	$3.17 \pm 0.35$		$2.08 \pm 0.40$	
Myometrial invasion	Yes	$3.57 \pm 0.36$	4.765/<0.001	$1.65 \pm 0.48$	3.880/<0.001
	No	$3.07 \pm 0.34$		$2.22 \pm 0.48$	
Lymph node metastasis	Yes	$3.60 \pm 0.35$	4.639/<0.001	$1.54 \pm 0.39$	4.684/<0.001
	No	$3.08 \pm 0.35$		$2.23 \pm 0.48$	
Distant metastasis	Yes	$3.73 \pm 0.29$	6.186/<0.001	$1.54 \pm 0.41$	4.029/<0.001
	No	$3.07 \pm 0.32$		$2.19 \pm 0.49$	
Histological grading	High	$3.70 \pm 0.32$	15.060/<0.001	$1.49 \pm 0.34$	12.630/<0.001
	Middle	$3.43 \pm 0.33$		$1.98 \pm 0.43$	
	Low	$2.98 \pm 0.26$		$2.27 \pm 0.48$	

lower cell migration rate in the miR-625-5p-mimics group compared with the other two groups and a higher migration rate in the miR-625-5p-inhibition group versus the miR-625-5p-NC group ( $P < 0.05$ , Figure 3(g)). Moreover, apoptosis rates were found to be the highest in the miR-625-5p-mimics group among the three groups, while those in the miR-625-5p-inhibition group were lower compared with the miR-625-5p-NC group ( $P < 0.05$ , Figure 3(h)).

**3.5. Impacts of miR-625-5p on Immunity and Autophagy of BC Cells.** ELISA results showed lower MDA, ROS, IL-1 $\beta$ , IL-6, IL-8, VEGF, VEGFR2, and EGF levels while higher SOD levels in the miR-625-5p-mimics group compared with the other two groups ( $P < 0.05$ ); when compared to the miR-625-5p-NC group, MDA, ROS, IL-1 $\beta$ , IL-6, IL-8, VEGF, VEGFR2, and EGF were higher in the miR-625-5p-inhibition group, and SOD was lower ( $P < 0.05$ , Figures 4(a)–4(c)). Further, the detection of autophagy proteins revealed that LC3-II, Beclin1, and p62 in the miR-625-5p-mimics group were  $0.87 \pm 0.08$ ,  $1.01 \pm 0.07$ , and  $0.92 \pm 0.06$ , respec-

tively, which were the highest among the three groups, while the data in the miR-625-5p-inhibition group were  $0.12 \pm 0.03$ ,  $0.08 \pm 0.06$ , and  $0.10 \pm 0.02$ , respectively, which were the lowest ( $P < 0.05$ , Figures 4(d) and 4(e)).

**3.6. Verification of Targeting Relationship between LINC00958 and miR-625-5p.** We found through Starbase the binding complementary loci between LINC00958 and miR-625-5p (Figure 5(a)), so we further used the DLR assay to validate the relationship between the two genes. The results determined that the LINC00958-WT fluorescence activity after miR-625-5p-mimics transfection was  $0.35 \pm 0.07$ , which was obviously lower compared with that after miR-625-5p-NC transfection ( $P < 0.05$ ), while after miR-625-5p-inhibition transfection, the fluorescence activity of LINC00958-MUT increased obviously ( $P < 0.05$ , Figure 5(b)), indicating a targeted regulatory relationship between the two. After transfection of SH-LINC00958 into T24 and J82, miR-625-5p levels in these cells were markedly upregulated compared with sh-control transfected cells ( $P < 0.05$ , Figure 5(c)).

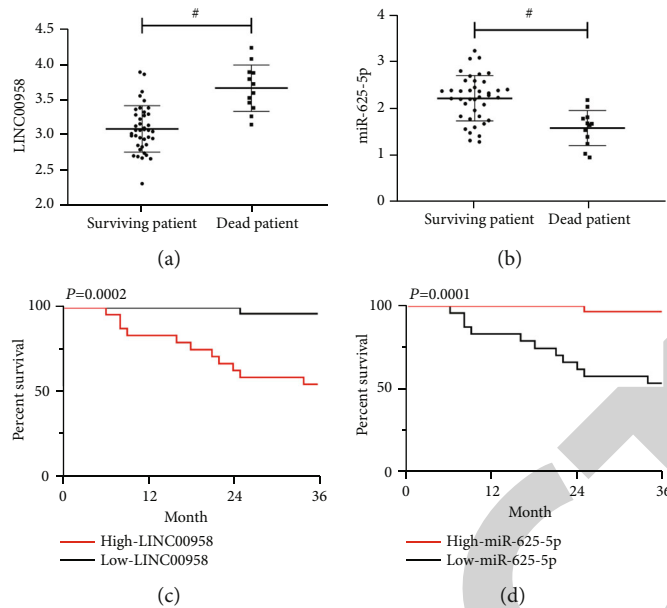


FIGURE 2: Prognostic implications of LINC00958 and miR-625-5p in BC: (a) comparison of LINC00958 between dead patients ( $n = 10$ ) and surviving patients ( $n = 42$ ); (b) comparison of miR-625-5p between dead patients ( $n = 1$ ) and surviving patients ( $n = 42$ ); (c) the 3-year survival curve of the high ( $n = 24$ ) and low ( $n = 28$ ) LINC00958 groups; (d) the 3-year survival curve of the high ( $n = 29$ ) and low ( $n = 23$ ) miR-625-5p groups.  $^{\#}P < 0.05$ .

**3.7. LINC00958 Affects BC Cell Biological Behavior via Sponge Adsorption of miR-625-5p.** Cells with different transfections were grouped as follows: group A: sh-control+miR-625-5p-NC, group B: sh-control+miR-625-5p-inhibition, group C: sh-LINC00958+miR-625-5p-NC, group D: sh-LINC00958+miR-625-5p-inhibition, and group E: sh-LINC00958. Then, the biological behaviors of the above groups of cells were examined. First of all, CCK-8 and cell cloning experiments showed that the cell optical density and cloning rate of group B were the highest among the five groups; no evident differences were found between groups A and D and between groups C and E ( $P > 0.05$ ), among which groups C and E had lower cell optical density and cloning rate than groups A and D ( $P < 0.05$ , Figures 6(a)–6(c)). Groups A and D also showed a similar number of membrane-penetrating cells and cell mobility ( $P < 0.05$ ), lower than those in group B ( $P < 0.05$ ). Nor were there any notable differences between groups C and E in the number of membrane-penetrating cells and cell mobility ( $P > 0.05$ ), which were lower compared with groups A and D ( $P < 0.05$ , Figures 6(d) and 6(e)). Finally, the detection results of the apoptotic rate were the lowest in group B and highest in groups C and E, while their levels in groups A and D were higher compared with group B and lower compared with groups C and E ( $P < 0.05$ , Figure 6(f)).

**3.8. LINC00958 Affects Immunity and Autophagy in BC Cells via Sponge Adsorption of miR-625-5p.** In subsequent tests, it was found that the conditions of the five groups of cells were basically consistent with the abovementioned biological behaviors; that is, there was no difference in all test results between groups A and D and between groups C and E

( $P > 0.05$ ). Among them, MDA, ROS, IL-1 $\beta$ , IL-6, IL-8, VEGF, VEGFR2, and EGF in groups A and D were lower versus group B and higher versus groups C and E ( $P < 0.05$ ); on the contrary, SOD in groups A and D was higher compared with group B and lower versus groups C and E ( $P < 0.05$ , Figures 7(a)–7(c)). Similarly, autophagy proteins LC3-II, Beclin1, and p62 in groups A and D were lower compared with groups C and E, but higher than those in group B ( $P < 0.05$ , Figures 7(d) and 7(e)).

**3.9. Impacts of LINC00958 and miR-625-5p on Tumorigenesis.** First, comparing the tumor-bearing growth of mice in each group (Figure 8(a)), it was found that the tumor mass and volume in the sh-LINC00958 group were markedly lower compared with the sh-control group ( $P < 0.05$ , Figures 8(b) and 8(c)), while those in the miR-625-5p-inhibition group were higher versus the miR-625-5p-NC group ( $P < 0.05$ , Figures 8(d) and 8(e)). HE staining exhibited that the sh-control and miR-625-5p-NC groups had relatively few cells with small nuclei and few cytokinesis and mitosis but showed relatively more necrotic cells and neutrophil and lymphocyte infiltration. Compared with the sh-control and miR-625-5p-NC groups, the tumor tissue of the sh-LINC00958 group was significantly improved, with more dense cells and rich cytoplasm, increased mitosis, and decreased inflammatory cell infiltration. The tumor tissue damage in the miR-625-5p-inhibition group was the most serious, with a large number of cells showing pyknosis and necrosis, and the infiltration of neutrophils/lymphocytes was extremely serious (Figure 8(f)). Therefore, lowering LINC00958 can inhibit BC growth, while reducing miR-625-5p can promote BC growth.

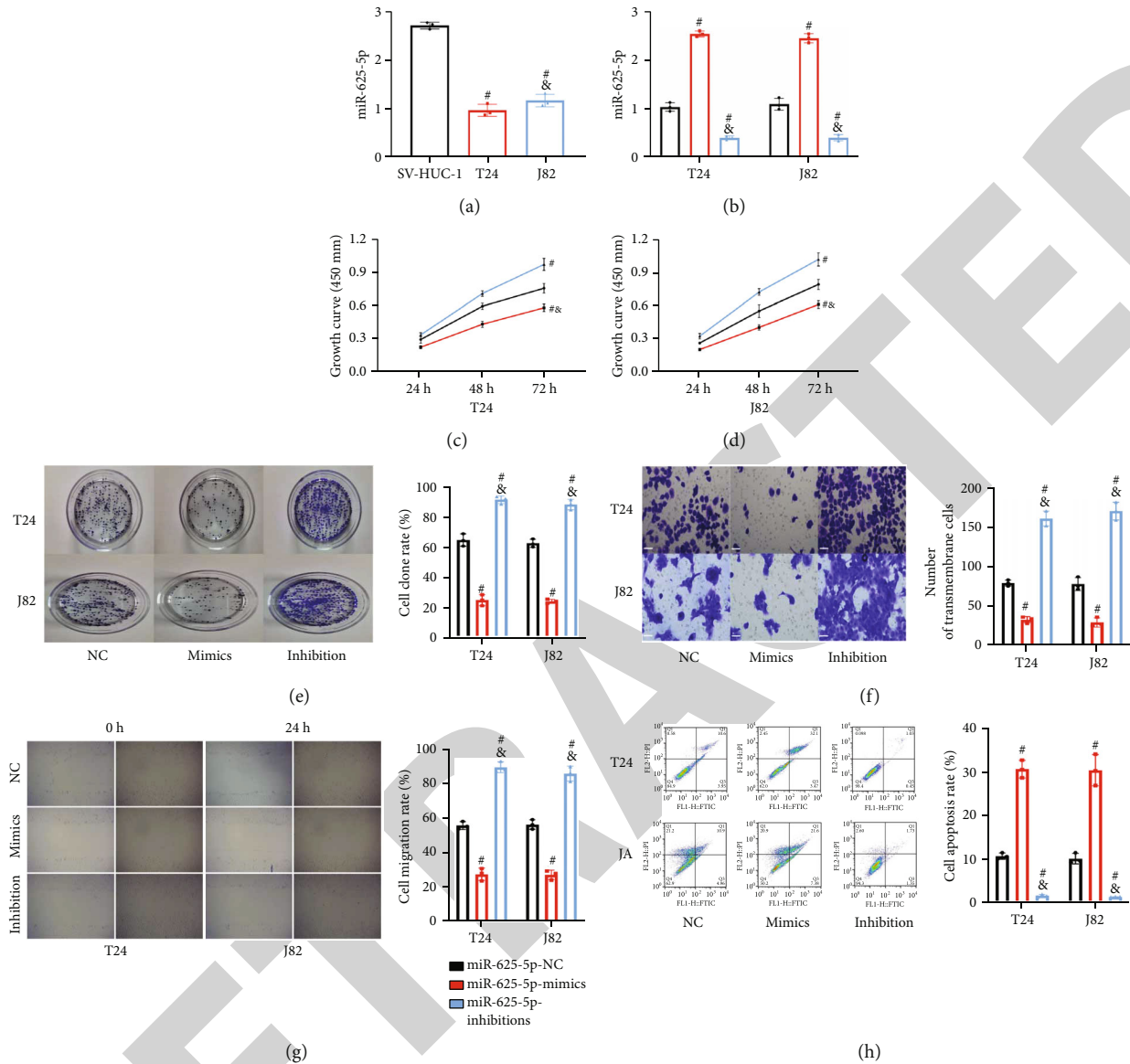


FIGURE 3: Impacts of miR-625-5p on BC cell biological behavior ( $n = 3$ ): (a) comparison of miR-625-5p expression among T24, J82, and SV-HUC-1; (b) PCR verification of transfection success rate of miR-625-5p-mimics, miR-625-5p-NC, and miR-625-5p-inhibition; (c, d) CCK-8 assay was used to detect the effect of miR-625-5p on the growth of T24 and J82 cells; (e) clonal formation experiment was used to detect the effect of miR-625-5p on the proliferation of T24 and J82 cells; (f) Transwell assay was used to detect the influence of miR-625-5p on the invasiveness ability of T24 and J82 cells (200x); (g) cell scratch assay was used to detect the influence of miR-625-5p on the migration ability of T24 and J82 cells; (h) flow cytometry assay was used to detect the influence of miR-625-5p on the apoptotic ability of T24 and J82 cells. Compared with miR-625-5p-NC group ( $^*P < 0.05$ ); compared with miR-625-5p-mimics group ( $^{\&}P < 0.05$ ).

#### 4. Discussion

In modern clinical research, it is agreed that the breakthrough in the diagnosis and treatment of neoplastic diseases lies in miRNAs due to their following advantages: (1) they can be conveniently detected in human blood, body fluids, tissues, cells, and other samples; (2) the quantitative analysis results are more objective and accurate, allowing them to be excellent and potential tumor markers [21]; and (3) due to the regulation and influence of miRNAs on the cell life cycle, they can be molecular therapeutic targets for tumors in the future to achieve the purpose of killing tumor cells, thus

overcoming the problem that tumors are difficult to completely cure at present [22]. In the previous research, we have clarified the mechanism of LINC00958 in BC [5], but there are still two unsolved problems. First, no clinical tests have been carried out, resulting in the inability to determine the clinical expression of LINC00958 in BC. Second, the downstream target genes involved in LINC00958 regulation of BC cell activity remain to be explored. In view of the above two problems, this study launched a more comprehensive and complete analysis to address its limitations.

First of all, we screened the potential downstream target genes of LINC00958 and initially focused on miR-625-5p



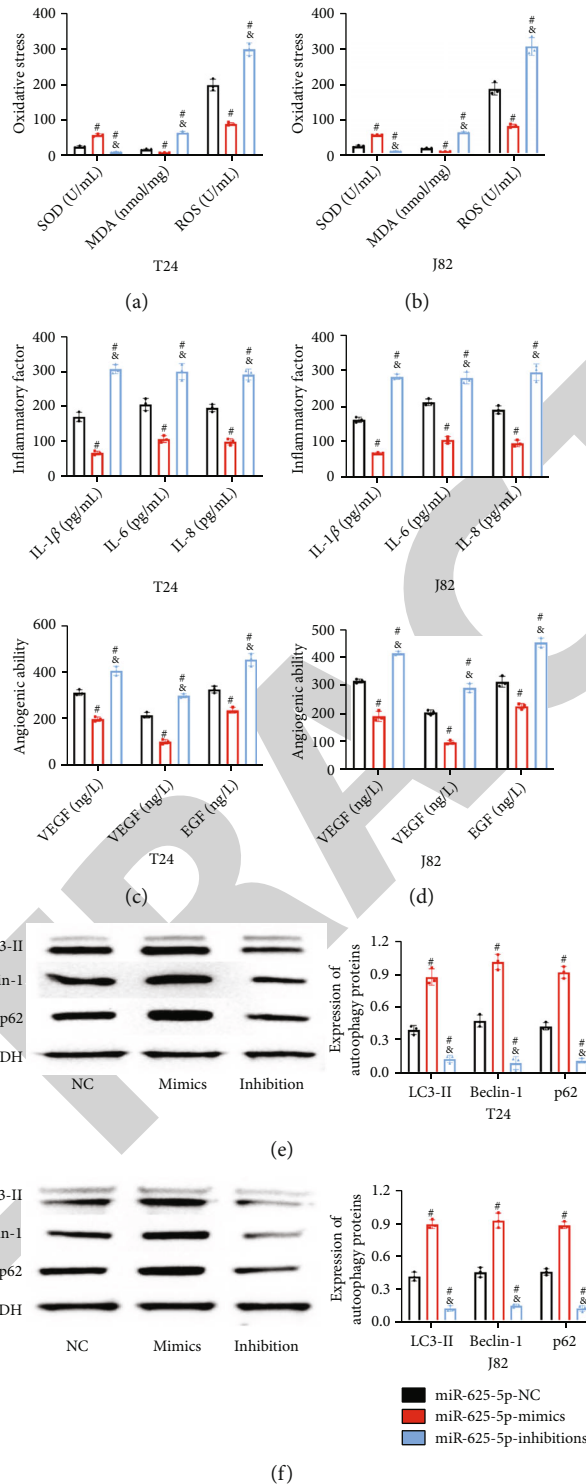


FIGURE 4: Impacts of miR-625-5p on immunity and autophagy of BC cells ( $n = 3$ ): (a) impact of miR-625-5p on BC oxidative stress; (b) impact of miR-625-5p on inflammatory responses of BC; (c) impact of miR-625-5p on BC angiogenesis; (d) impact of miR-625-5p on T24 autophagy; (e) impact of miR-625-5p on J82 autophagy. Compared with miR-625-5p-NC group ( $^{\#}P < 0.05$ ); compared with miR-625-5p-mimics group ( $^{\&}P < 0.05$ ).

based on the results of previous studies. Our clinical examination results showed upregulated LINC00958 and underexpressed miR-625-5p in BC patients, indicating an inverse connection between the two genes in BC. This is consistent with the results of our previous research and related studies

[23, 24], confirming that LINC00958 is involved in the occurrence and development of BC and that its mechanism of action may be bound up with miR-625-5p. In the subsequent analysis of the relationship between them and clinical pathology of BC patients, the two genes were found to have a

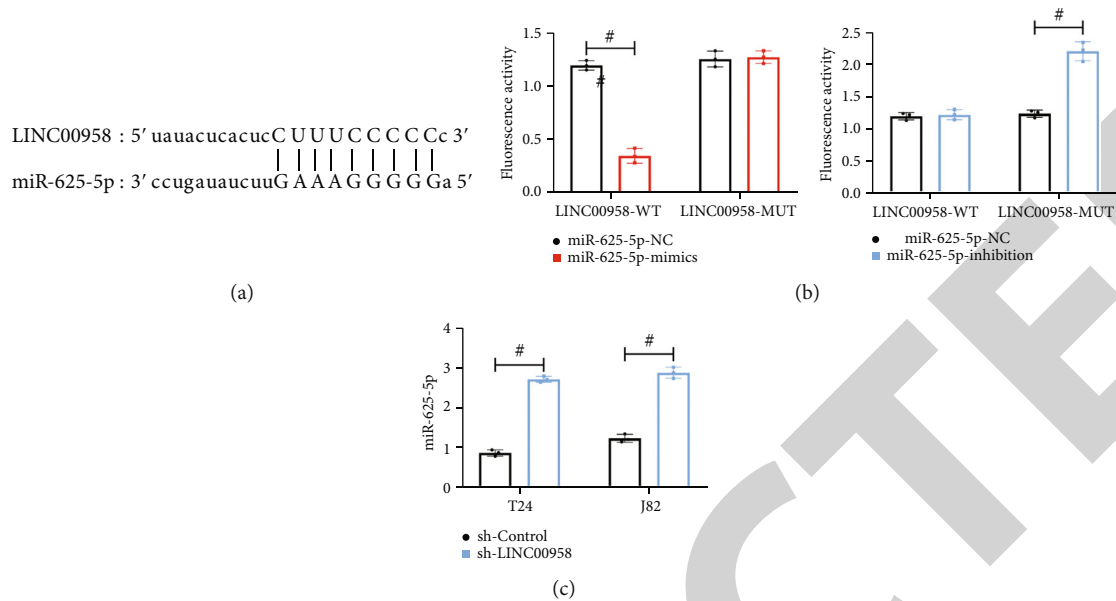


FIGURE 5: Verification of targeting relationship between LINC00958 and miR-625-5p ( $n = 3$ ): (a) binding complementary loci of LINC00958 and miR-625-5p; (b) DLR assay; (c) impact of LINC00958 on miR-625-5p expression.  $^{\#}P < 0.05$ .

close connection with MI, LNM, DM, and histological grade of BC, which once again verifies our view. This is in consistency with our expectation, as we have confirmed through previous studies that overexpressed LINC00958 in BC can promote the ability of tumor cells to proliferate and invade [5]. While the relationship between miR-625-5p and BC clinicopathological features can further confirm the involvement of miR-625-5p in BC. In the prognostic follow-up, higher LINC00958 and lower miR-625-5p were determined in the surviving patients than in the dead. Further, the prognosis survival curve showed that both the increase of LINC00958 and the decrease of miR-625-5p predicted an increased risk of death in BC patients. It also suggests the potential of the two genes to become the prognostic markers of BC in the future, which can assist clinicians to understand the prognosis of BC patients more quickly, so as to carry out the targeted intervention in a more timely manner to provide more reliable security for patients. The expression in tissues is reported to be more accurate [25], while the clinical analysis in this study was conducted based mainly on blood samples due to the convenience of obtaining blood samples. Hence, LINC00958 and miR-625-5p in BC tissues and adjacent tissues should be detected for validation in the follow-up experiments.

*In vitro*, we also found decreased miR-625-5p in BC cells. After suppressing miR-625-5p, the ability of BC cells to proliferate, invade, and migrate was found to be enhanced, and the apoptosis ability was decreased, but the reverse was true after the expression of miR-625-5p was increased. Thus, miR-625-5p with low expression in BC can also promote BC cell activity and accelerate the malignant progression of BC. Referring to past literature, we also found that the low expression of miR-625-5p can promote glioma invasion and the pathological process of gastric cancer [26, 27], which can also verify the accuracy of the results

of this experiment. Besides, OS, inflammation, AG, and tumor immunity are all important pathological changes in the immune studies of BC progression [28–30]. In a study on tumor microcirculation, inhibiting the above reaction processes is also regarded as one of the reliable ways to curb tumor development [31]. Therefore, we also explored alterations in OS, inflammatory responses, AG, and tumor immunity of BC cells under the influence of miR-625-5p. Consistently, miR-625-5p inhibition was accompanied by promoted OS injury, inflammation, AG, and tumor immunity changes of cells, while increasing miR-625-5p inhibited these changes. It also demonstrates the potential of miR-625-5p as a therapeutic target for BC, with great significance in future clinical applications. Autophagy is an evolutionarily conserved and important process for the turnover of intracellular substances in eukaryotes; in tumor cells, autophagy can be activated to induce cell death, which is hailed as the key to future molecular targeted therapy [32, 33]. Existing evidence shows that the autophagy ability of cells is obviously inhibited in BC and can be reactivated via increasing miR-625-5p [34, 35], which validates our view. From this, we can definitely know that miR-625-5p, which is underexpressed in BC, can participate in the development of BC by inhibiting autophagy, enhancing cell activity, regulating tumor immunity, and promoting OS responses, inflammation, and AG.

Finally, we used the DLR assay to verify the relationship between the two genes. The results identified that LINC00958-WT and MUT fluorescence activities were affected by miR-625-5p, and miR-625-5p expression in BC cells was increased after LINC00958 was inhibited, which was consistent with the above clinical examination results, confirming that LINC00958 negatively and targeted modulated miR-625 in BC. Through the rescue experiment, we also found reduced cell OS reaction, inflammatory

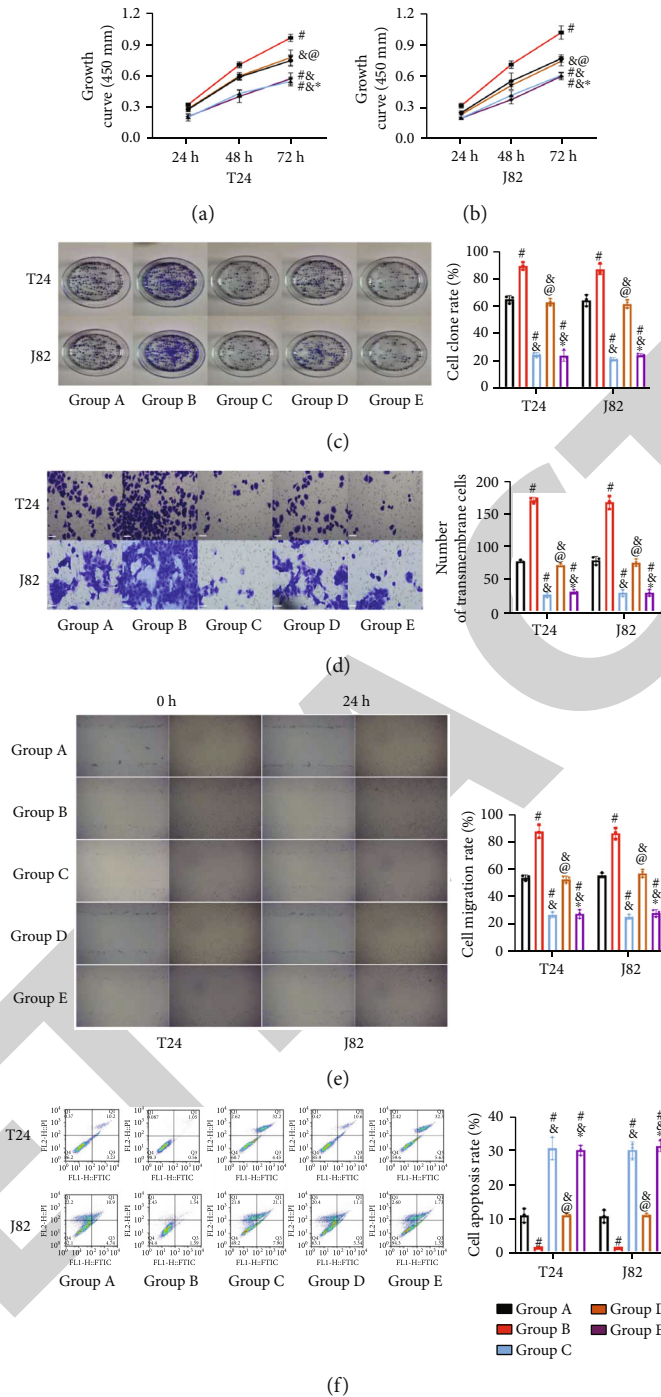


FIGURE 6: LINC00958 affects BC cell biological behavior via sponge adsorption of miR-625-5p ( $n = 3$ ): (a, b) CCK-8 experiment detects the growth ability of T24 and J82 cells; (c) the clone formation test detects the proliferation ability of T24 and J82 cells; (d) Transwell assay detects the T24 and J82 cell invasion ability (200x); (e) cell scratch assay detects the T24 and J82 cell migration ability; (f) flow cytometry detects the T24 and J82 cell apoptosis rate. Compared with group A ( $^{\#}P < 0.05$ ); compared with group B ( $^{\&}P < 0.05$ ); compared with group C ( $^{\textcircled{a}}P < 0.05$ ); compared with group D ( $^*P < 0.05$ ).

responses, and AG and activated autophagy after inhibiting LINC00958, further demonstrating the important influence of LINC00958 on BC. Furthermore, cotransfection of LINC00958+miR-625-5p into cells resulted in similar cell biological behavior and pathological changes to those with sh-control+miR-625-5p-NC cotransfection, indicating that

miR-625-5p completely reversed the effect of inhibiting LINC00958 on BC cells. Moreover, the cells cotransfected with sh-LINC00958 and miR-625-5p-NC were basically the same as those transfected with sh-LINC00958 alone, confirming that LINC00958 participates in various functional changes of BC cells by targeting miR-625-5p. In the nude

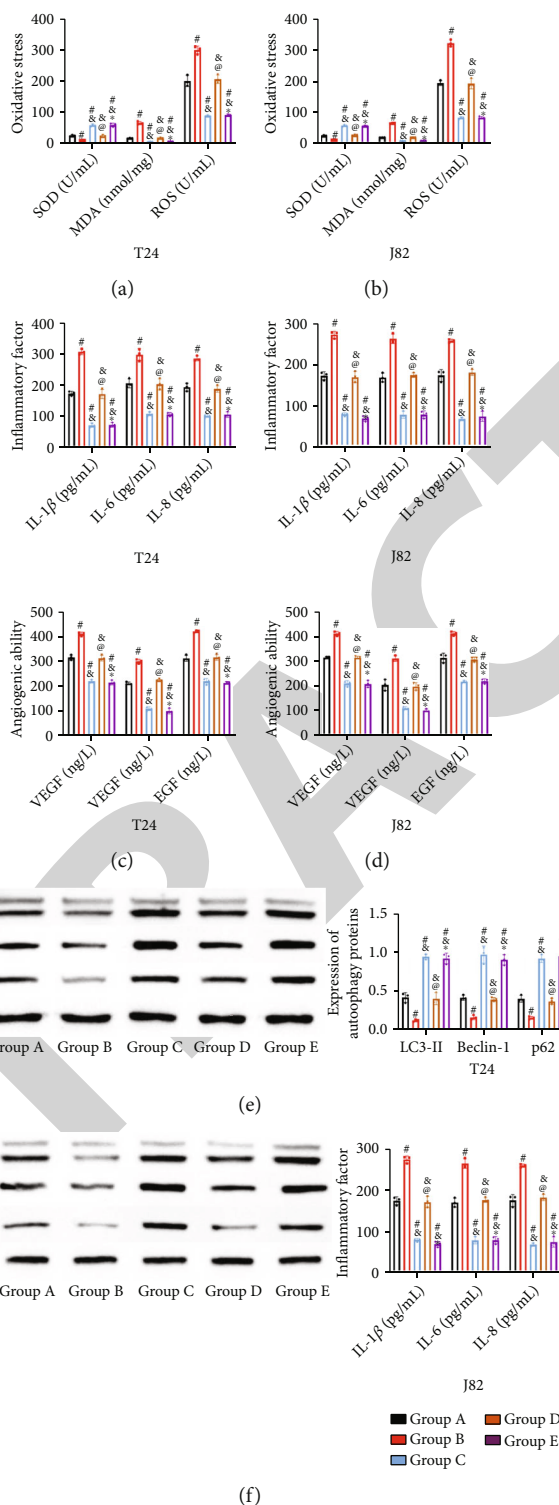


FIGURE 7: LINC00958 affects immunity and autophagy in BC cells via sponge adsorption of miR-625-5p: (a) oxidative stress response in BC cells; (b) inflammatory response in BC cells; (c) angiogenic capacity of BC cells; (d) autophagy capacity in T24; (e) autophagy capacity in J82. Compared with group A ( $^*P < 0.05$ ); compared with group B ( $^{\&}P < 0.05$ ); compared with group C ( $^@P < 0.05$ ); compared with group D ( $^*P < 0.05$ ).

mouse tumorigenesis experiment, we also found obviously inhibited tumor growth and improved pathological changes after silencing LINC00958, while completely opposite results

were observed following miR-625-5p silencing. These results not only verified the influence of LINC00958 and miR-625-5p on living BC tumors but also preliminarily revealed the

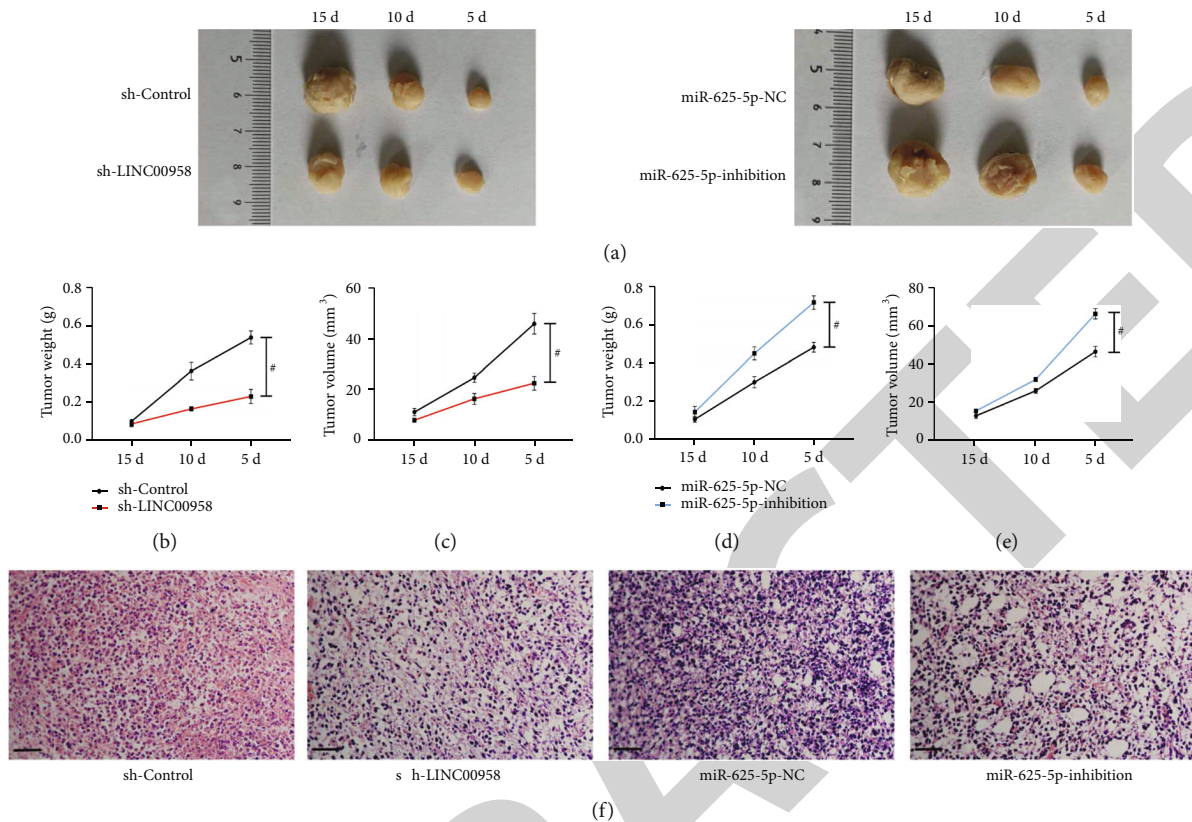


FIGURE 8: Impacts of LINC00958 and miR-625-5p on tumorigenesis: (a) the results of the tumorigenesis test in nude mice; (b, c) impacts of LINC00958 on tumorigenesis; (d, e) impacts of miR-625-5p on tumorigenesis; (f) HE staining of tumor tissue sections (100x). # $P < 0.05$ .

significance of LINC00958 and miR-625-5p, which may be therapeutic targets that contribute to a breakthrough for future diagnosis and treatment of BC.

**4.1. Limitations.** Due to the short study period, the small number of cases included in this study, and the relatively short follow-up time, we have been unable to assess the long-term prognosis of patients. Second, we should also verify the effect of LINC00958 and miR-625-5p on the prognosis of BC patients by COX analysis. Finally, we should collect cancerous and paracancerous tissues from BC patients as test samples to confirm the expression of LINC00958 and miR-625-5p, as tissue samples are more accurate than blood samples for PCR experiments. These are the limitations of this study, which will be addressed through future supplementary research.

## 5. Conclusion

LINC00958 was highly expressed in BC, and miR-625-5p was underexpressed. LINC00958 is involved in BC by targeting miR-625-5p to inhibit cell autophagy, enhance cell activity, regulate tumor immunity, and promote OS, inflammation, and AG. Both genes are of great significance to the diagnosis and treatment of BC and are expected to be a breakthrough in the clinical treatment of BC.

## Data Availability

The datasets used and/or analyzed during the current study are available from the corresponding authors on reasonable request.

## Ethical Approval

All procedures were conducted in accordance with the Institutional Animal Care guidelines of Nantong University and were approved by the Experimental Animal Ethics Committee of Jiangsu Province, China (approval No. 20190303-18).

## Conflicts of Interest

The authors have no conflicts of interest to declare.

## Authors' Contributions

W.G.L. and L.M.M. performed the study concept and designed this work; Y.X. and T.W. performed experiments and drafted the manuscript; Y.W. and X.C. collected and analyzed data; F.W.L. carried out manuscript supervision and revision. All authors read and approved the final paper. Ying Xiao and Tao Wang contributed equally to this work.

## Acknowledgments

This work was supported by the National Natural Science Foundation of China (No. 81802580, No. 81771571, and No. 31971276) and Science and Technology Project of Nantong City (No. JC2018102).

## References

- [1] K. C. DeGeorge, H. R. Holt, and S. C. Hodges, "Bladder cancer: diagnosis and treatment," *American Family Physician*, vol. 96, no. 8, pp. 507–514, 2017.
- [2] V. G. Patel, W. K. Oh, and M. D. Galsky, "Treatment of muscle-invasive and advanced bladder cancer in 2020," *CA: a Cancer Journal for Clinicians*, vol. 70, no. 5, pp. 404–423, 2020.
- [3] R. H. Martinez Rodriguez, O. Buisan Rueda, and L. Ibarz, "Bladder cancer: present and future," *Medicina Clinica*, vol. 149, no. 10, pp. 449–455, 2017.
- [4] M. C. Bridges, A. C. Daulagala, and A. Kourtidis, "LNCcation: lncRNA localization and function," *Journal of Cell Biology*, vol. 220, no. 2, 2021.
- [5] Y. Xiao, L. He, Y. Dong, Y. Huang, L. Ma, and W. Li, "Highly Expressed LINC00958 Modulates the growth and epithelial-mesenchymal transition of bladder cancer cells Through SAPK/JNK Signaling pathway," *Cancer Biotherapy & Radiopharmaceuticals*, vol. 2022, 2022.
- [6] C. Sanchez-Jimenez, I. Carrascoso, J. Barrero, and J. M. Izquierdo, "Identification of a set of miRNAs differentially expressed in transiently TIA-depleted HeLa cells by genome-wide profiling," *BMC Molecular Biology*, vol. 14, no. 1, 2013.
- [7] C. Aktan, C. Cal, B. Kaymaz et al., "Functional roles of miR-625-5p and miR-874-3p in the progression of castration resistant prostate cancer," *Life Sciences*, vol. 301, article 120603, 2022.
- [8] Y. Wang, L. Yin, and X. Sun, "CircRNA hsa\_circ\_0002577 accelerates endometrial cancer progression through activating IGF1R/PI3K/Akt pathway," *Journal of Experimental & Clinical Cancer Research*, vol. 39, no. 1, pp. 1–16, 2020.
- [9] Y. W. Yin, K. L. Liu, B. S. Lu et al., "RBM24 exacerbates bladder cancer progression by forming a Runx1t1/TCF4/miR-625-5p feedback loop," *Experimental & Molecular Medicine*, vol. 53, no. 5, pp. 933–946, 2021.
- [10] L. Wang, Y. Zhong, B. Yang et al., "LINC00958 facilitates cervical cancer cell proliferation and metastasis by sponging miR-625-5p to upregulate LRR8E expression," *Journal of Cellular Biochemistry*, vol. 121, no. 3, pp. 2500–2509, 2020.
- [11] L. Yang, L. Li, Z. Zhou et al., "SP1 induced long non-coding RNA LINC00958 overexpression facilitate cell proliferation, migration and invasion in lung adenocarcinoma via mediating miR-625-5p/CPSF7 axis," *Cancer Cell International*, vol. 20, no. 1, p. 24, 2020.
- [12] L. Deng, Y. Lu, D. Yang et al., "Placental transcriptome sequencing combined with bioinformatics predicts potential genes and circular RNAs associated with hemoglobin Bart's hydrops fetalis syndrome," *The Journal of Obstetrics and Gynaecology Research*, vol. 48, no. 2, pp. 313–327, 2022.
- [13] Cancer Genome Atlas Research Network, "Comprehensive molecular characterization of urothelial bladder carcinoma," *Nature*, vol. 507, no. 7492, pp. 315–322, 2014.
- [14] S. Fleige and M. W. Pfaffl, "RNA integrity and the effect on the real-time qRT-PCR performance," *Molecular Aspects of Medicine*, vol. 27, no. 2-3, pp. 126–139, 2006.
- [15] K. Hanlon, A. Thompson, L. Pantano et al., "Single-cell cloning of human T-cell lines reveals clonal variation in cell death responses to chemotherapeutics," *Cancer Genetics*, vol. 237, pp. 69–77, 2019.
- [16] J. Marshall, "Transwell® invasion assays," *Methods in Molecular Biology*, vol. 769, pp. 97–110, 2011.
- [17] S. Martinotti and E. Ranzato, "Scratch wound healing assay," *Methods in Molecular Biology*, vol. 2109, pp. 225–229, 2020.
- [18] L. Pillai-Kastoori, A. R. Schutz-Geschwender, and J. A. Harford, "A systematic approach to quantitative Western blot analysis," *Analytical Biochemistry*, vol. 593, article 113608, 2020.
- [19] T. Clement, V. Salone, and M. Rederstorff, "Dual luciferase gene reporter assays to study miRNA function," *Methods in Molecular Biology*, vol. 1296, pp. 187–198, 2015.
- [20] L. Zhang, X. Yang, and M. Wen, "Optimal scanning concentration of MR imaging for tumor-bearing nude mice with SPIO-shRNA molecular probe," *Scientific Reports*, vol. 10, no. 1, article 18655, 2020.
- [21] A. M. Yu, Y. H. Choi, and M. J. Tu, "RNA drugs and RNA targets for small molecules: principles, progress, and challenges," *Pharmacological Reviews*, vol. 72, no. 4, pp. 862–898, 2020.
- [22] N. F. Rizvi, J. P. Santa Maria, A. Nahvi et al., "Targeting RNA with small molecules: identification of selective, RNA-binding small molecules occupying drug-like chemical space," *SLAS DISCOVERY: Advancing the Science of Drug Discovery*, vol. 25, no. 4, pp. 384–396, 2020.
- [23] H. Zhen, P. Du, Q. Yi, X. Tang, and T. Wang, "LINC00958 promotes bladder cancer carcinogenesis by targeting miR-490-3p and AURKA," *BMC Cancer*, vol. 21, no. 1, p. 1145, 2021.
- [24] H. Zhang, C. Feng, M. Zhang et al., "miR-625-5p/PKM2 negatively regulates melanoma glycolysis state," *Journal of Cellular Biochemistry*, vol. 120, no. 3, pp. 2964–2972, 2019.
- [25] R. B. Maerkedahl, H. Frokiaer, L. Lauritzen, and S. B. Metzdorff, "Evaluation of a low-cost procedure for sampling, long-term storage, and extraction of RNA from blood for qPCR analyses," *Clinical Chemistry and Laboratory Medicine*, vol. 53, no. 8, pp. 1181–1188, 2015.
- [26] H. Su, D. Zou, Y. Sun, and Y. Dai, "Hypoxia-associated circDENND2A promotes glioma aggressiveness by sponging miR-625-5p," *Cellular & Molecular Biology Letters*, vol. 24, no. 1, p. 24, 2019.
- [27] Z. Chen, H. Wu, Z. Zhang, G. Li, and B. Liu, "LINC00511 accelerated the process of gastric cancer by targeting miR-625-5p/NFIX axis," *Cancer Cell International*, vol. 19, no. 1, p. 351, 2019.
- [28] M. D. Jelic, A. D. Mandic, S. M. Maricic, and B. U. Srdjenovic, "Oxidative stress and its role in cancer," *Journal of Cancer Research and Therapeutics*, vol. 17, no. 1, pp. 22–28, 2021.
- [29] C. P. Liao, R. C. Booker, J. P. Brosseau et al., "Contributions of inflammation and tumor microenvironment to neurofibroma tumorigenesis," *The Journal of Clinical Investigation*, vol. 128, no. 7, pp. 2848–2861, 2018.
- [30] T. Li, G. Kang, T. Wang, and H. Huang, "Tumor angiogenesis and anti-angiogenic gene therapy for cancer," *Oncology Letters*, vol. 16, no. 1, pp. 687–702, 2018.
- [31] S. Reuter, S. C. Gupta, M. M. Chaturvedi, and B. B. Aggarwal, "Oxidative stress, inflammation, and cancer: how are they

## Retraction

# Retracted: Identification of ATG7 as a Regulator of Proferroptosis and Oxidative Stress in Osteosarcoma

### Oxidative Medicine and Cellular Longevity

Received 20 June 2023; Accepted 20 June 2023; Published 21 June 2023

Copyright © 2023 Oxidative Medicine and Cellular Longevity. This is an open access article distributed under the Creative Commons Attribution License, which permits unrestricted use, distribution, and reproduction in any medium, provided the original work is properly cited.

This article has been retracted by Hindawi following an investigation undertaken by the publisher [1]. This investigation has uncovered evidence of one or more of the following indicators of systematic manipulation of the publication process:

- (1) Discrepancies in scope
- (2) Discrepancies in the description of the research reported
- (3) Discrepancies between the availability of data and the research described
- (4) Inappropriate citations
- (5) Incoherent, meaningless and/or irrelevant content included in the article
- (6) Peer-review manipulation

The presence of these indicators undermines our confidence in the integrity of the article's content and we cannot, therefore, vouch for its reliability. Please note that this notice is intended solely to alert readers that the content of this article is unreliable. We have not investigated whether authors were aware of or involved in the systematic manipulation of the publication process.

Wiley and Hindawi regrets that the usual quality checks did not identify these issues before publication and have since put additional measures in place to safeguard research integrity.

We wish to credit our own Research Integrity and Research Publishing teams and anonymous and named external researchers and research integrity experts for contributing to this investigation.

The corresponding author, as the representative of all authors, has been given the opportunity to register their agreement or disagreement to this retraction. We have kept a record of any response received.

### References

- [1] R. Jiang, S. He, H. Gong et al., "Identification of ATG7 as a Regulator of Proferroptosis and Oxidative Stress in Osteosarcoma," *Oxidative Medicine and Cellular Longevity*, vol. 2022, Article ID 8441676, 19 pages, 2022.

## Research Article

# Identification of ATG7 as a Regulator of Proferroptosis and Oxidative Stress in Osteosarcoma

Runyi Jiang <sup>1</sup>, Shaohui He <sup>1,2</sup>, Haiyi Gong <sup>1</sup>, Yao Wang <sup>1</sup>, Wei Wei <sup>1</sup>, Jun Chen <sup>3</sup>,  
Jinbo Hu <sup>1,2</sup>, Chen Ye <sup>1,4</sup>, Shuchen LiuHuang <sup>5</sup>, Saiying Jin <sup>5</sup>, Haifeng Wei <sup>1,2</sup>,  
Wei Xu <sup>1</sup>, and Jianru Xiao <sup>1</sup>

<sup>1</sup>Spinal Tumor Center, Department of Orthopaedic Oncology, Changzheng Hospital, Second Military Medical University, Shanghai 200003, China

<sup>2</sup>Department of Orthopaedic Surgery, No. 905 Hospital of PLA Navy, Second Military Medical University, Shanghai 200050, China

<sup>3</sup>Department of Pathology, Changzheng Hospital, Second Military Medical University, Shanghai 200003, China

<sup>4</sup>School of Medical Instrument and Food Engineering, University of Shanghai for Science and Technology, Shanghai 200093, China

<sup>5</sup>School of Design and Innovation, China Academy of Art, Hangzhou, China

Correspondence should be addressed to Shaohui He; heshaoahui1025@163.com, Haifeng Wei; weihfspine@163.com, Wei Xu; xuweichangzheng@hotmail.com, and Jianru Xiao; czxiaojianru@163.com

Received 4 May 2022; Revised 8 September 2022; Accepted 13 September 2022; Published 8 October 2022

Academic Editor: Tian Li

Copyright © 2022 Runyi Jiang et al. This is an open access article distributed under the Creative Commons Attribution License, which permits unrestricted use, distribution, and reproduction in any medium, provided the original work is properly cited.

**Background.** Ferroptosis has gained significant attention from oncologists as a vital outcome of oxidative stress. The aim of this study was to develop a prognostic signature that was based on the ferroptosis-related genes (FRGs) for osteosarcoma patients and explore their specific role in osteosarcoma. **Methods.** The training cohort dataset was extracted from the Therapeutically Applicable Research to Generate Effective Treatments (TARGET) database. Different techniques like the univariate Cox regression, least absolute shrinkage and selection operator (LASSO) regression, multivariate Cox regression analyses, and the Kaplan-Meier (KM) survival analyses were utilized to develop a prognostic signature. Then, the intrinsic relationship between the developed gene signature and the infiltration levels of the immune cells was further investigated. An external validation dataset from the Gene Expression Omnibus (GEO) database was employed to assess the predictive ability of the developed gene signature. Subsequently, the specific function of potential FRG in affecting the oxidative stress reaction and ferroptosis of osteosarcoma cells was identified. **Results.** A prognostic signature based on 5 FRGs (CBS, MUC1, ATG7, SOCS1, and PEBP1) was developed, and the patients were classified into the low- and high-risk groups (categories). High-risk patients displayed poor overall survival outcomes. The risk level was seen to be an independent risk factor for determining the prognosis of osteosarcoma patients ( $p < 0.001$ , hazard ratio: 7.457, 95% CI: 3.302-16.837). Additionally, the risk level was associated with immune function, which might affect the survival status of osteosarcoma patients. Moreover, the findings of the study indicated that the expression of ATG7 was related to the regulation of oxidative stress in osteosarcoma. Silencing the ATG7 gene promoted the proliferation and migration in osteosarcoma cells, suppressing the oxidative stress and ferroptosis process. **Conclusions.** A novel FRG signature was developed in this study to predict the prognosis of osteosarcoma patients. The results indicated that ATG7 might regulate the process of oxidative stress and ferroptosis in osteosarcoma cells and could be used as a potential target to develop therapeutic strategies for treating osteosarcoma.

## 1. Introduction

Osteosarcoma (OS) is reported to be a very prevalent type of malignant bone tumor affecting children and teenagers, and

it has an annual incidence rate of 4.4 per million people [1]. With the advent of chemotherapy, the prognosis of patients with localized OS has substantially improved, with the long-term overall survival rate increasing from <20% to 65-70%



[2, 3]. However, survival outcomes for patients with metastases and those who poorly responded to initial treatment are still low, with an estimated 5-year survival rate of ~25% for patients aged between 2 and 68 years [4]. The role of common regulated cell death (RCD) processes, such as autophagy and apoptosis, in treating OS patients is still controversial [5, 6]. Therefore, it is crucial to seek other novel and efficient approaches to OS treatments.

One of the key distinguishing features of tumor cells is their high energy metabolism [7]. Reactive oxygen species (ROS) are commonly generated accompanied by increased metabolism, which causes oxidative stress in tumor cells [8]. Generally, the balance of ROS is crucial for normal cell growth and survival [9]. High ROS produces DNA damage which further leads to more mutations and initiation of cancers [10, 11]. In addition, high ROS also causes lipid, protein, and DNA damage to normal cells, often leading to apoptosis [12, 13]. However, the apoptotic machinery is damaged in cancer cells as well, which results in more tumor cell proliferation in turn [9]. The studies on ROS are vast and controversial. Since ROS plays a vital role in the onset and progression of tumors, regulating the antioxidative stress in tumor cells might open a new direction for treating tumors.

Ferroptosis, which is a Fe-dependent form of RCD that is activated by excessive lipid peroxidation due to the lethal accumulation of ROS, attracted the attention of many oncologists [14]. In comparison to the noncancerous cells, the tumor cells display an increased Fe demand to enable growth [15], and ROS is an important product of metabolism in cancer cells [7]. Studies have shown that ferroptosis could be induced in OS cells by experimental reagents (such as erastin and RSL3) through extrinsic or intrinsic pathways [16–18]. In addition, sorafenib, a drug reported to induce ferroptosis, suppresses tumor growth, angiogenesis, and metastatic potential in OS cells [19]. These findings provided the theoretical foundation for OS treatments by inducing ferroptosis by altering the oxidative stress balance in OS cells. Thus, therapy targeting ferroptosis-related genes (FRGs) might be a novel way to treat OS, especially metastatic and insensitive to initial treatment patients. Although ferroptosis is observed to play a vital role in different malignant or benign tumors [20, 21], their specific function and prognostic values in OS remain largely unknown.

In this report, the RNA sequencing results and the corresponding clinical data of the OS patients were downloaded from the Therapeutically Applicable Research to Generate Effective Treatments (TARGET) database. Then, the expression of the FRGs was analyzed in OS patients, and a novel prognostic multigene signature was generated that was based on the FRGs derived from the TARGET cohort. Then, its prognostic significance was verified using a Gene Expression Omnibus (GEO) cohort. Moreover, the potential role of candidate FRG in oxidative stress and tumor development in OS cells was validated by experiments. The results of this study have yielded an FRG that could potentially be used as a therapeutic target for developing effective strategies to treat OS.

## 2. Materials and Methods

**2.1. Data Collection.** RNA sequencing data and the related clinical information of 101 OS patients were obtained from the TARGET cohort (<https://ocg.cancer.gov/programs/target>, Figure S1). The following inclusion criteria were used for further screening: (1) OS patients with confirmed survival status and active follow-up, (2) survival time > 0 months, and (3) complete information of metastatic status in the clinical records. The exclusion criteria were as follows: (1) patients with missed follow-ups, (2) unknown or 0 survival months, and (3) duplicate samples. Among those, 93 OS patients were finally included in the training cohort for further study, and the RNA sequencing data of these patients were normalized to transcripts per million (TPM) values before analyses. In addition, the GSE21257 sequence (Platform GPL10295) was retrieved from the Gene Expression Omnibus (GEO) cohort (<https://www.ncbi.nlm.nih.gov/geo/query/acc.cgi?acc=GSE21257>) as the validation dataset. This dataset comprised 53 OS patients, including 34 (64.1%) samples with metastasis and 19 (35.9%) samples without metastasis. 200 FRGs were analyzed in this study (Table S1).

**2.2. Identification of Osteosarcoma Subclusters.** The nonnegative matrix factorization (NMF) was performed after a filtering procedure using the R package “NMF” to cluster the obtained FRGs. Candidate genes with mean expression < 0.05 were discarded. The selected FRGs were then subjected to a univariate Cox regression analysis to assess the correlation between the selected candidate genes and the survival rate using the “survival” R package. Genes with  $p < 0.05$  were chosen for sample clustering.

**2.3. Designing and Validating the Prognostic Model Based on FRGs.** The Kaplan-Meier (KM) curves were used to decipher the significant prognostic FRGs using the results of the univariate Cox regression analysis ( $p < 0.05$ ), and genes with  $p \leq 0.01$  were subjected to the least absolute shrinkage and selection operator (LASSO) regression analysis. R packages like “survminer” and “glmnet” were used for these analytical techniques, respectively. LASSO regression is excellent for narrowing down the candidate genes and minimizing the risk of overfitting [22]. Ultimately, the results of LASSO regression were included in the multivariate Cox regression analysis, and the  $\beta$  value (the regression coefficient of each gene integrated within this model) was evaluated for each FRG. This was used for developing the formula for estimating the risk score for patients.

$$\text{Risk score} = \sum_i^n (\text{Coefficient}_{\text{mRNA}_i} * \text{Expression}_{\text{mRNA}_i}). \quad (1)$$

Individuals were classified into the low- and high-risk subgroups (categories) based on their median risk scores, and the likelihood of survival was compared between both groups. The “survivalROC” R package was used to create the receiver operating characteristic (ROC) curves, which were then used to calculate the performance score of the

developed FRG signature models based on the area under the ROC curves (AUC-ROC). Finally, the predictive power of the developed model was evaluated using Harrell's concordance index (C-index). Following a reordering of the subjects according to their risk scores, the risk curves, the survival status-based scatterplot, and heatmap of the expression of FRGs were plotted. For additional validation, the GSE21257 cohort was obtained from the GEO database. Briefly, the "scale" function was used for the purpose of normalizing the expression level of every FRG expression in the external cohort, and the same procedure was used to determine risk scores for the validation cohort. Using the ideal cutoff value, patients included in the GSE21257 dataset were also divided into the low- or high-risk subgroups to confirm the accuracy of the developed model.

**2.4. Independent Prognostic Analysis by Incorporating the "Risk Score."** The "risk score," a binary variable (low-/high-risk group) as a new potential factor, were combined with other clinical features to build a new dataset for further prognostic analysis. The univariate and multivariate Cox regression analyses were used to determine the significant prognostic clinical factors. Factors having a  $p$  value  $< 0.05$  of both the Cox regression analyses were included to develop a nomogram, with the help of the R-package "rms" to anticipate the survival likelihood of the OS patients. Factors like AUC, C-index, and calibration curves were used to assess the accuracy of the generated nomogram, and ROC curves of each clinical factor and decision curve analysis (DCA) were employed to determine if the risk level could be utilized as an independent prognostic factor.

**2.5. Gene Ontology (GO) Analyses and Immune Signature of the Subgroups.** The differentially expressed genes (DEGs) existing in the high- and low-risk subgroups in the training dataset were extracted using the "limma" package. Genes with adjusted  $p$  value  $< 0.05$  and  $|\log_2FC| \geq 1$  were considered DEGs and subjected to GO enrichment analyses by applying the "ClusterProfiler" package.

Furthermore, the immune cell types in two subgroups were evaluated by TIMER2.0 (<http://timer.cistrome.org>), and the activity of the 13 immune-linked functions was determined with single-sample gene set enrichment analysis (ssGSEA) using the "GSVA" R package. Furthermore, immune checkpoint gene analysis was also carried out to ascertain ferroptosis-linked potential immune checkpoint genes. Functional analyses were also carried out using the validation dataset.

**2.6. Exploration of the Relationship between ATG7 and Oxidative Stress in OS.** Patients were categorized into 2 subgroups based on the optimal cut-off value of the ATG7 expression. DEGs between both groups could be identified using the above criteria. GO enrichment analyses were then performed to examine the differences between both groups. Additionally, ssGSEA was utilized to assess the differences (variations) in the oxidative stress pathways that were differentially expressed in the ATG7 groups.

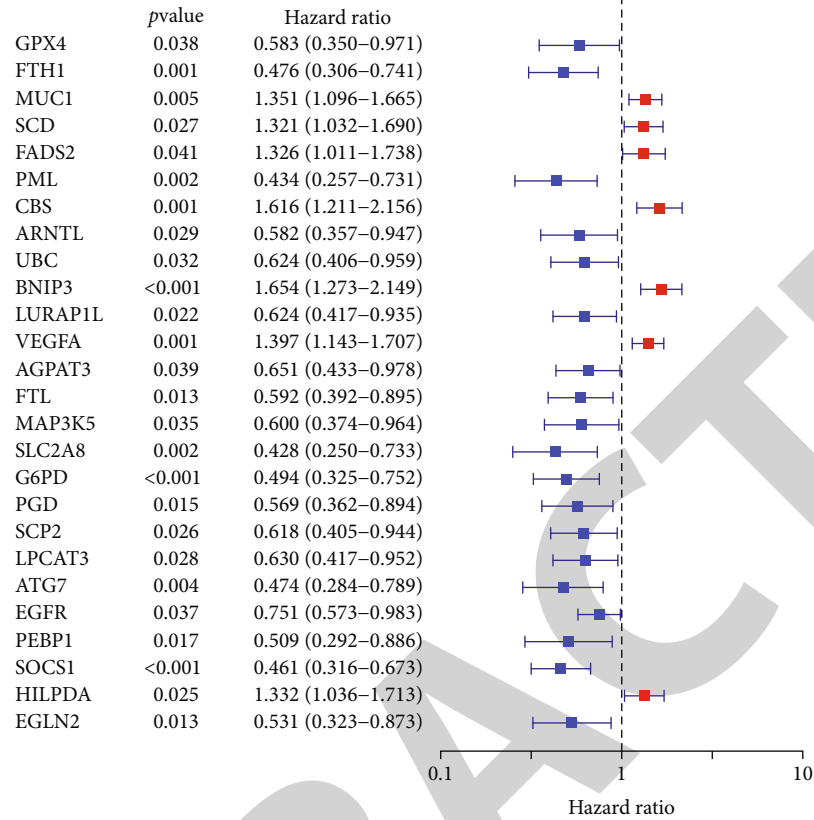
**2.7. Cell Culture.** OS cell lines (MG63, HOS) and the human bone marrow mesenchymal stem cells (hBMSC) were procured from the National Collection of Authenticated Cell Cultures (Shanghai, China). The MG63 and HOS cell lines were cultured using DMEM, while the hBMSC lines were cultured in  $\alpha$ -MEM. All the media were supplemented with fetal bovine serum (10%  $v/v$ ) (FBS, Gibco) and the penicillin/streptomycin solution (P/S, 100 U/ml, Gibco). All cell lines were cultured in the humidified carbon dioxide incubator (5%  $CO_2$ , 37°C temperature).

**2.8. ATG7 RNA Interference.** The OS cell line, MG63, was cultured in 6-well culture plates until they achieved a 60% confluency before the cells were transfected with ATG7-RNAi (3  $\mu$ l, 40 pmol) in a serum-free medium, in the presence of lipofectamine 3000 (2  $\mu$ l, Thermo, USA), based on the manufacturer's instructions. After incubating the transfection mixture for 6 h, MG63 cells were maintained in a fresh medium. After 48 h, the Western blotting (WB) technique was used to test the effects of ATG7 gene silencing. siRNAs for ATG7 (siATG7-1: GCCTGCTGAGGAGCTC TCCAT; siATG7-2: CCTAAAGAAGTACCACTTCTA) and the negative siRNA control (siNC) were synthesized by the Genepharma Technologies (Shanghai, China).

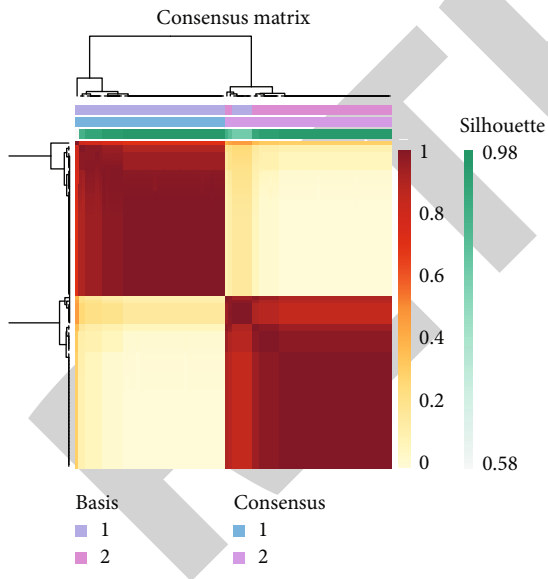
**2.9. Cell Viability and Migration.** The siATG7-transfected MG63 cells were seeded into the 96-well culture plates. Cell viability was assessed using the Cell Counting Kit-8 (CCK8) reagent (Vazyme, A311-02-AA) based on the kit instructions. All the cells were incubated with the CCK8 reagent for 60 min at a temperature of 37°C, and the absorbance values (450 nm) were noted at differing time points (days 1, 2, 3, and 4). Moreover, the CellTiter-Glo luminescent Cell Viability Assay (G7572, Promega, USA) was used to test the viability of the MG63 cells that were treated using the RSL3 (10  $\mu$ M), a ferroptosis inducer (Selleck, S8155), after silencing the ATG7 gene. These cells recorded the luminescence at various time points (0, 12, 24, and 48 h) [23].

Cells, in the logarithmic growth phase, were cultured into the 6-well culture plates for a minimum of 7 days and stained using 0.1% ( $v/v$ ) crystal violet for conducting the colony formation assay. Using the Transwell chambers (pore size: 8 mm, Corning), the cells were resuspended in the serum-free medium (200  $\mu$ l) and placed in the upper chamber for performing the migration tests. The lower chambers were then filled with the DMEM (500  $\mu$ l), supplemented with FBS (10%  $v/v$ ), and incubated for 24 h. The cells were then stained using 0.1% ( $v/v$ ) crystal violet after being fixed with 4% ( $v/v$ ) paraformaldehyde. The Image-Pro Plus 6.0 software was used for counting the migrating cells, and the bright-field images were captured using an Olympus inverted microscope (Media Cybernetics, USA).

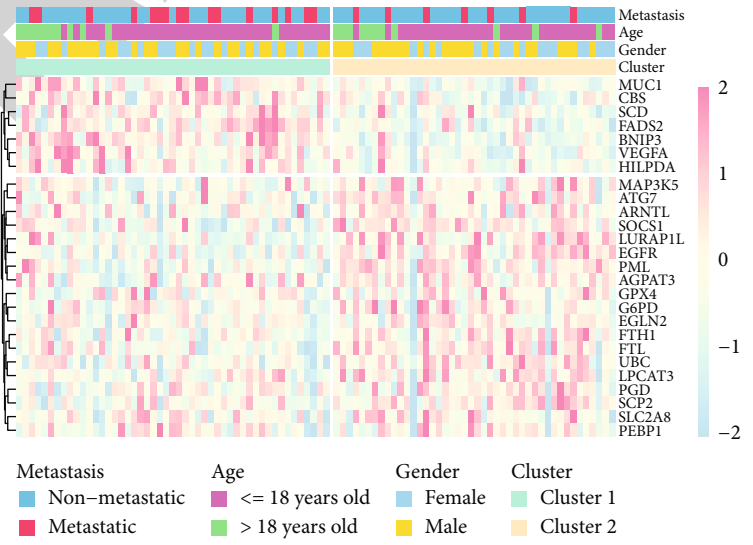
**2.10. Determining the Malondialdehyde (MDA), Superoxide Dismutase (SOD), and Lipid ROS Concentrations.** MDA concentration was measured following kit instructions (Beyotime, S0131S). In addition, the cells were stained using C11-BODIPY (D3861, Thermo Fisher Scientific, USA), followed by flow cytometry to measure the lipid ROS



(a)



(b)



(c)

FIGURE 1: Continued.

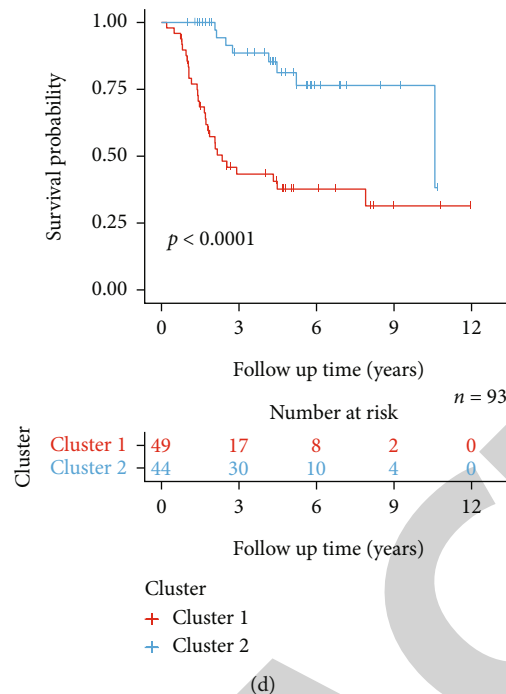


FIGURE 1: Tumor classification depending on the 26 ferroptosis-related genes. (a) Univariate Cox regression analysis of 26 FRGs. (b) NMF clustering for 93 osteosarcoma patients based on 26 FRGs. (c) Heatmap depicting the expression of the 26 FRGs in both clusters. (d) The KM curves of both clusters (Log-rank test:  $*p < 0.05$ ,  $**p < 0.01$ , and  $***p < 0.001$ ).

production [24]. SOD activity was measured using the WB technique. It is noteworthy that the ATG7-silenced MG63 cells should undergo RSL3-induced ferroptosis for about 12h before all measurements.

**2.11. Iron Accumulation.** The level of iron in the MG63 cells was measured in two ways. One tested the free ferrous iron ( $\text{Fe}^{2+}$ ) using a commercial Fe assay kit (ab83366, Abcam) based on the kit instructions, and in another technique, the expression of FTH1 was tested following the WB technique. RSL3-induced ferroptosis (12h) was also implemented in MG63 cells transfected with siATG7 before measuring.

**2.12. Quantitative Real-Time Polymerase Chain Reaction (qPCR) and Western Blotting Techniques.** Total RNA was extracted with the help of the TRIzol reagent (Thermo Fisher Scientific, Waltham, MA, USA). Reverse transcription and qPCR techniques were performed utilizing the PrimeScript™ RT Master Mix and SYBR Premix ExTaq (Takara, Kyoto, Japan), based on the kit instructions. The data were assessed using the  $2^{-\Delta\Delta C_t}$  technique.

Total proteins were extracted using the RIPA buffer, then loaded uniformly onto the SDS-PAGE (sodium dodecyl sulfate, 10%) gel, and transferred to the nitrocellulose membranes. The membranes were then blocked with bovine serum albumin (BSA, 5%) and incubated with the primary antibodies such as anti-FTH1 (ABclonal, A19544), anti-SOD (Cell Signaling Technology, 71G8), anti-ATG7 (Abcam, ab52472), and anti-GAPDH (Sigma-Aldrich, USA). Thereafter, the membranes were washed and incubated with horseradish peroxidase- (HRP-) conjugated sec-

ondary antibodies. Finally, the membranes were washed and imaged using the ChemiDoc XRS+ System (Bio-Rad Laboratories, USA).

**2.13. Statistical Analysis.** All the data were statistically analyzed using R software (ver. 4.0.1) and GraphPad Prism 8.0. All the quantitative data were expressed as mean standard deviation (SD), whereas the categorical variables were presented using counts and percentage values. Wilcox test was employed to detect the DEGs and evaluate the GO enrichment and immune-linked functions, whereas the log-rank test was employed to analyze the overall survival rate of OS patients. The  $t$ -test was used to examine the findings of the experiments. Each experiment was carried out at least 3 times, with representative findings. Differences with a two-tailed  $p < 0.05$  were considered statistically significant ( $*p < 0.05$ ,  $**p < 0.01$ , and  $***p < 0.001$ ).

### 3. Results

**3.1. Identification of OS Subclusters Based on FRGs.** A total of 200 candidate FRGs were initially obtained from the RNA-seq dataset training cohort. The univariate Cox regression results revealed that 26 FRGs (including 7 risk and 19 protective genes) fulfilled the inclusion criteria and were depicted in the forest plot (Figure 1(a)). NMF was performed to determine potential characteristics in the gene expression profiles by decomposing the initial matrix into 2 nonnegative matrices [25]. The 26 FRGs were then subjected to the NMF analysis. The 93 OS were categorized into two clusters depending on the optimum  $k$  value, based on

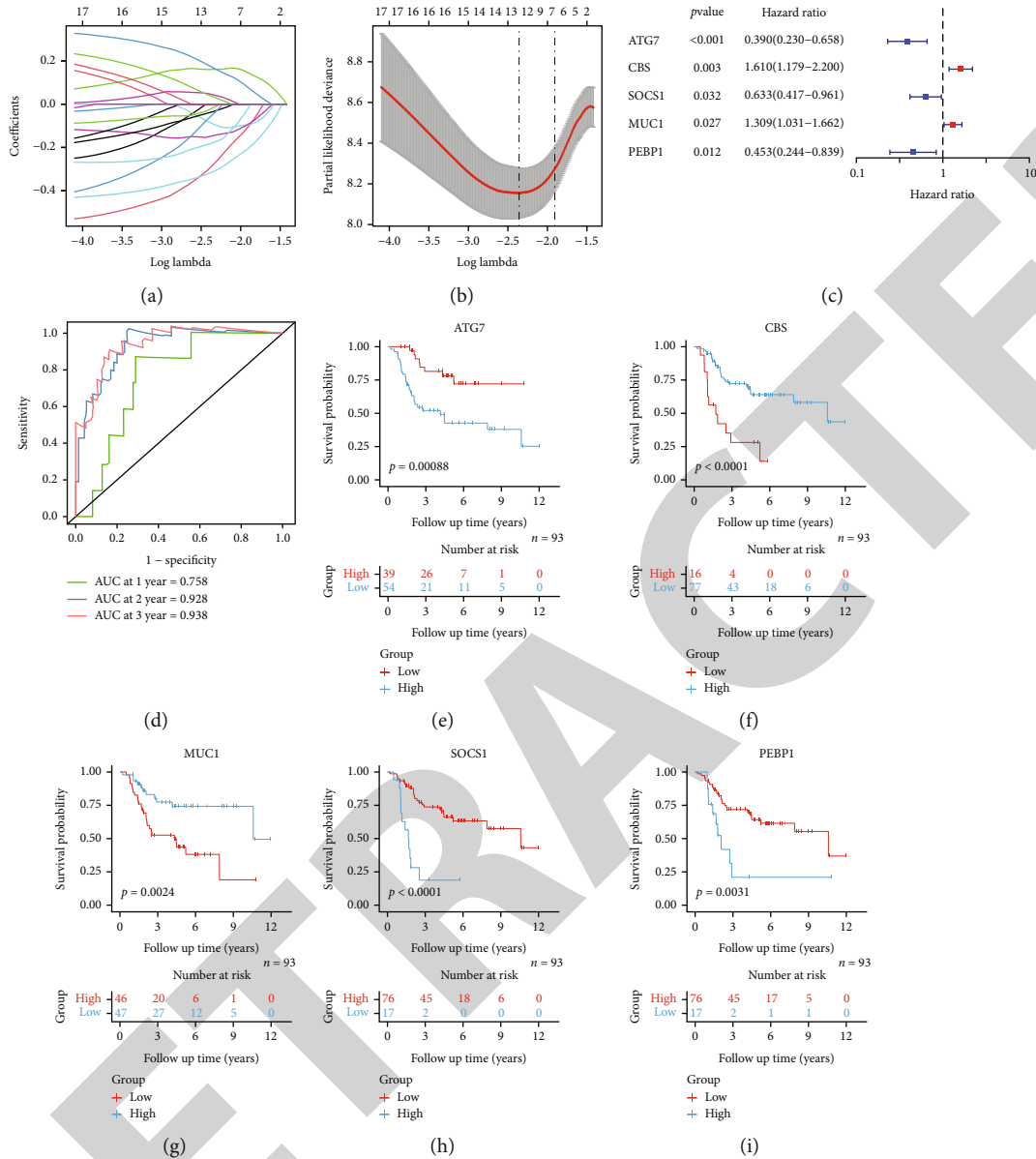


FIGURE 2: Development of a 5 FRGs-based prognostic signature using the training dataset. (a) LASSO regression analysis of 19 identified FRGs. (b) Cross-validation analysis to tune the parameter selection process in a LASSO regression model. (c) Multivariate Cox regression analysis of 5 FRGs to develop a prognostic signature. (d) ROC curves indicate the prognostic model using 5 FRGs. (e–i) The KM curves of the 5 identified FRGs (Log-rank test: \* $p < 0.05$ , \*\* $p < 0.01$ , and \*\*\* $p < 0.001$ ).

their correlation coefficient values (Figures 1(b), S2A). The consensus matrix heatmap exhibited a sharp and clear boundary, illustrating that the samples had robust and stable clusters with  $k = 2$ . Consensus matrix heatmaps of other  $k$  values ( $k = 3-6$ ) are shown in Figure S2B. The differential expression of the 26 FRGs between the two subclusters is shown in the heatmap pattern (Figure 1(c)). The KM curves indicated a significant difference in overall survival for patients between the identified clusters ( $p < 0.0001$ , Figure 1(d)).

**3.2. Development of Prognostic Gene Signature Using the Training Cohort.** Out of the 26 FRGs identified in the univariate analysis, the KM analysis demonstrated that 19 FRGs sat-

isfied the set criteria of  $p \leq 0.01$  and hence were selected for additional analysis. Using the LASSO regression analysis, multivariate Cox regression was applied to 12 FRGs based on their optimal  $\lambda$  values (Figures 2(a) and 2(b)). Finally, 5 FRGs were identified to construct a prognostic FRG signature (Figure 2(c)), containing 2 risk FRGs (CBS, MUC1) and 3 protective FRGs (ATG7, SOCS1, and PEBP1). The risk scores were estimated following formula as follows: Risk score =  $(-0.9427 * \text{ATG7 exp.}) + (0.4763 * \text{CBS exp.}) + (0.2692 * \text{MUC1 exp.}) + (-0.4567 * \text{SOCS1 exp.}) + (-0.7295 * \text{PEBP1 exp.})$ . The C-index (0.82) and AUC values for 1-, 2-, and 3-year survival rates of OS patients were 0.758, 0.928, and 0.938, respectively (Figure 2(d)), which indicated the favorable predictive value of this prognostic model. The association of

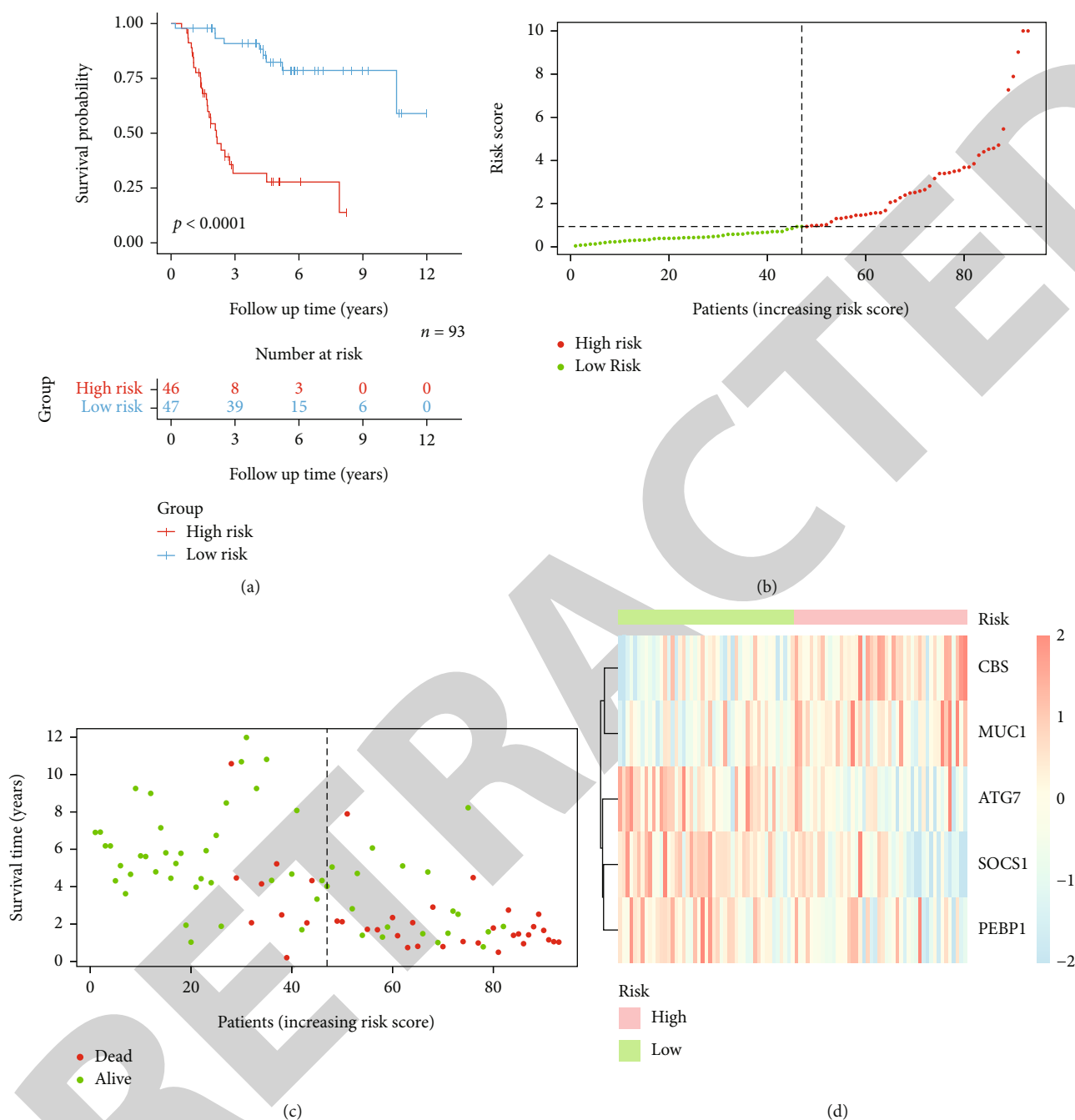


FIGURE 3: The difference in prognosis and gene expression levels between both the risk groups included in the training dataset. (a) KM curves of patients in the two risk groups. (b) Distribution of individual patients based on the risk scores. (c) Distribution of the survival duration for each patient in the two risk groups (left: low-risk population; right: high-risk population). (d) Heatmap highlighting the FRG expressions in the two risk groups (Log-rank test: \* $p < 0.05$ , \*\* $p < 0.01$ , and \*\*\* $p < 0.001$ ).

the overall survival rate with the 5 identified FRGs has been shown in Figures 2(e)–2(i). KM curves of the FRGs excluded in the prognostic signature are shown in Figure S3.

Depending on the median risk scores, 93 OS patients were categorized into the low- and high-risk subgroups. The findings revealed a significant difference in the disease prognosis between the 2 categories ( $p < 0.001$ , Figure 3(a)). Risk curves and scatterplots were generated to demonstrate the risk scores and survival status of every patient (Figures 3(b) and 3(c)), illustrating that the high-risk group

patients showed a worse prognosis compared to the low-risk patients. The heatmaps also showed a differential expression of 5 FRGs in the two groups (Figure 3(d)).

**3.3. Independent Prognostic Value of the FRG Signature.** Univariate and multivariate Cox regression analyses were used for assessing if the risk level, as the binary variable derived from the risk score, could be used as an independent prognostic factor (Figures 4(a) and 4(b)). The results indicated that metastasis status ( $p < 0.001$ , HR: 3.656, 95% CI: 1.875–

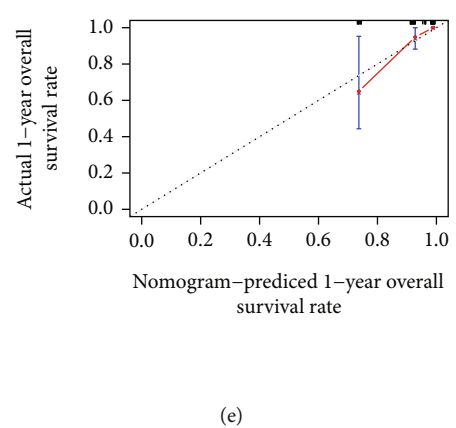
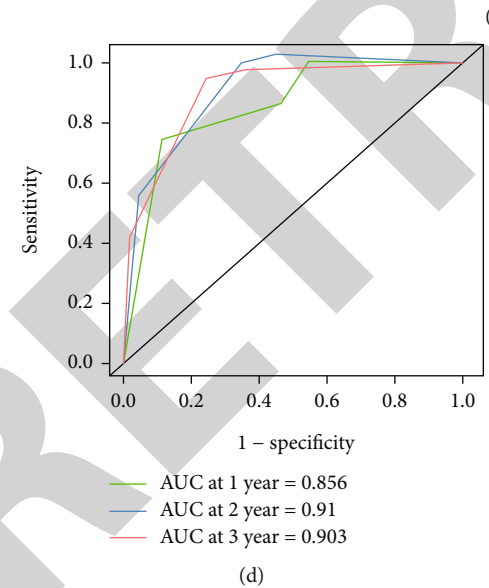
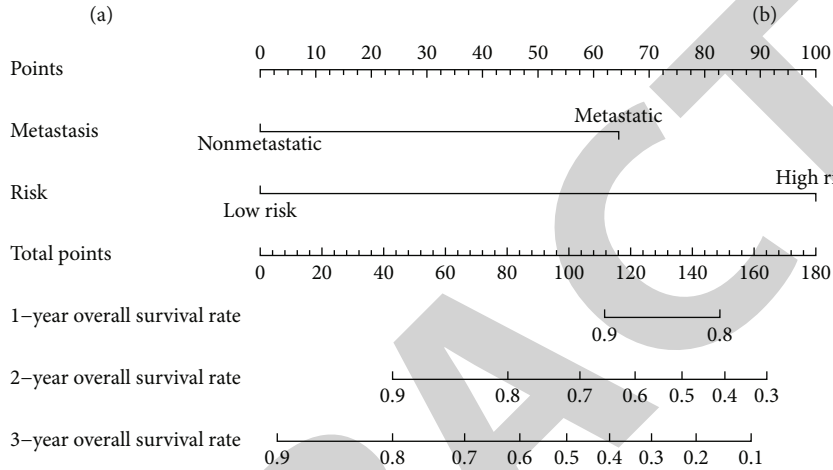
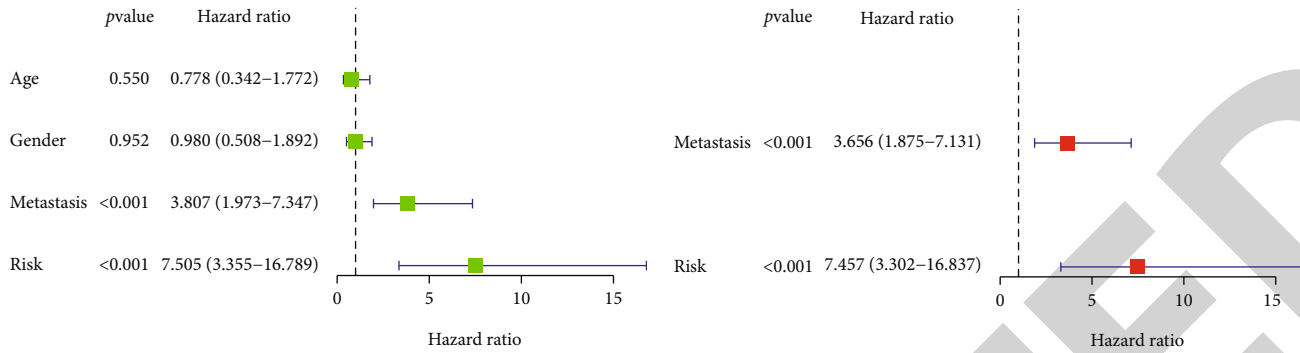


FIGURE 4: Continued.

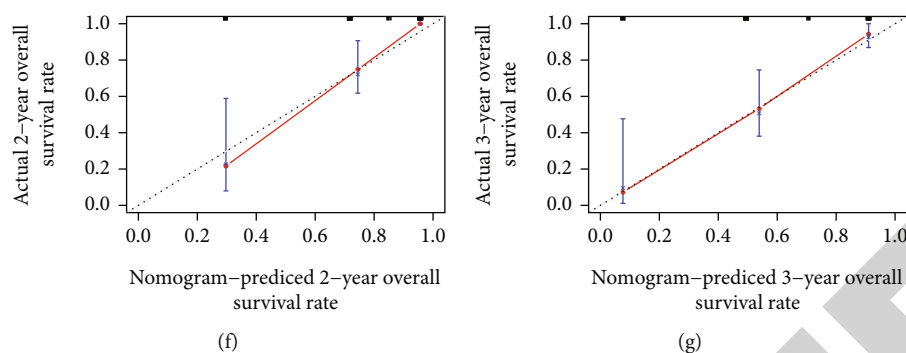


FIGURE 4: Identifying the risk level as the independent risk factor in a training dataset. (a) Results of univariate Cox regression analysis of OS patients' clinical information, including risk level. (b) Results of multivariate Cox regression analysis of clinical information including risk level. (c) A nomogram that can predict the 1-, 2-, and 3-year survival rates of OS patients. (d) ROC curves examine the predictive ability of the newly established nomogram. (e–g) The agreement between the predicted probabilities and observed outcomes in the nomogram over 1, 2, and 3 years, respectively.

7.131) and risk levels were independent prognostic factors that influenced the overall survival rate of OS patients ( $p < 0.001$ , HR: 7.457, 95% CI: 3.302–16.837). Additionally, ROC curves and DCA of each clinical factor manifested that risk level was a more robust factor in predicting overall survival rates than any other clinical factor (Figure S4A–B). Depending on the results generated by the multivariate Cox regression analysis, a nomogram was developed to visually evaluate the prognosis of OS patients (Figure 4(c)). Moreover, the C-index (0.799), AUC at 1-, 2-, and 3-year survival predictions (Figure 4(d)), and the calibration plots (Figures 4(e)–4(g)) depicted the effectiveness of this nomogram in anticipating the survival status of OS patients.

**3.4. Functional Analyses of the FRG Risk Model in the Training Cohort.** A total of 58 DEGs (adjusted  $p$  value  $< 0.05$ ;  $|\text{absolutelog}_2\text{FC}| \geq 1$ ) were detected in the high- and low-risk groups, out of which 44 DEGs were downregulated, whereas 14 were upregulated. The results of the GO enrichment analysis demonstrated that the immune response and antigen processing and presentation were the primary biological processes (BPs). At the same time, the MHC protein-related complex was the most abundant cellular component (CCs), while the molecule functions (MFs) were primarily related to the MHC protein complex binding or activity (Figure 5(a)). Moreover, the relationship between immune-related functions and risk scores was investigated. The high- and low-risk groups showed a statistically significant difference in the composition of the immune cells. The low-risk group contained a higher number of immune cells like macrophages, CD4<sup>+</sup> T cells, CD8<sup>+</sup> T cells, and natural killer (NK) cells (Figure 5(b)). Similarly, the results showed that the activities of the checkpoint molecules and the immune-related functions were significantly lower in the high-risk OS patients compared to the low-risk OS patients ( $*p < 0.05$ ,  $**p < 0.01$ , and  $***p < 0.001$ , Figures 5(c) and 5(d)).

**3.5. External Validation of the FRG Signature.** The GSE21257 dataset containing gene and clinical information of 53 OS patients was utilized as an external validation

cohort. OS patients were categorized into 2 different risk groups based on their optimized cutoff values. The two risk groups in the validation dataset showed a significant difference in their disease prognosis ( $p < 0.01$ , Figure 6(a)). Consistently, the risk curve and scatterplots suggested better outcomes for the low-risk group OS patients compared to OS patients in the high-risk groups in the validation dataset (Figures 6(b) and 6(c)). Additionally, in agreement with the training cohort, the risk (CBS, MUC1) and protective genes (ATG7, SOCS1, and PEBP1) from the GSE21257 dataset were primarily expressed in the high- and low-risk categories, respectively (Figure 6(d)). The AUC values of the ROC curves were 0.755, 0.725, and 0.679 for the 1-, 2-, and 3-year overall survival prediction, respectively (Figure 6(e)), which revealed satisfactory feasibility and stability of the constructed FRG signature model. Moreover, a similar distribution pattern was found during the GO enrichment analysis (Figure 7(a)) and immune-related characteristics for the validation cohort (Figures 7(b)–7(d)).

**3.6. Influence of the Differentially Expressed ATG7 on Oxidative Stress in OS.** A total of 48 DEGs (18 downregulated and 30 upregulated genes) were found in the low and high expressed ATG7 groups (Figure 8(a)). The DEGs were partly enriched in oxidative stress-related BPs like regulation of hydrogen peroxide-mediated programmed cell death and multiple oxidative stress-related MFs such as oxygen oxidoreductase (deaminating) activity for several compounds. Meanwhile, the expression of ATG7 may affect the activity of the ferritin receptor (Figure 8(b)). In addition, the results showed that the oxidative stress-related pathways like the regulation of oxidative stress response, regulation of the oxidative stress-induced cell death, and the regulation of transcription from the RNA polymerase II promoter in response to the oxidative stress differ significantly between both groups ( $*p < 0.05$ ,  $**p < 0.01$ ; Figure 8(c)).

**3.7. The Different Expressions of Five FRGs in OS Cells and hBMSC.** Consistent with the above findings, qPCR showed that the 2 risk FRGs (CBS and MUC1) were highly



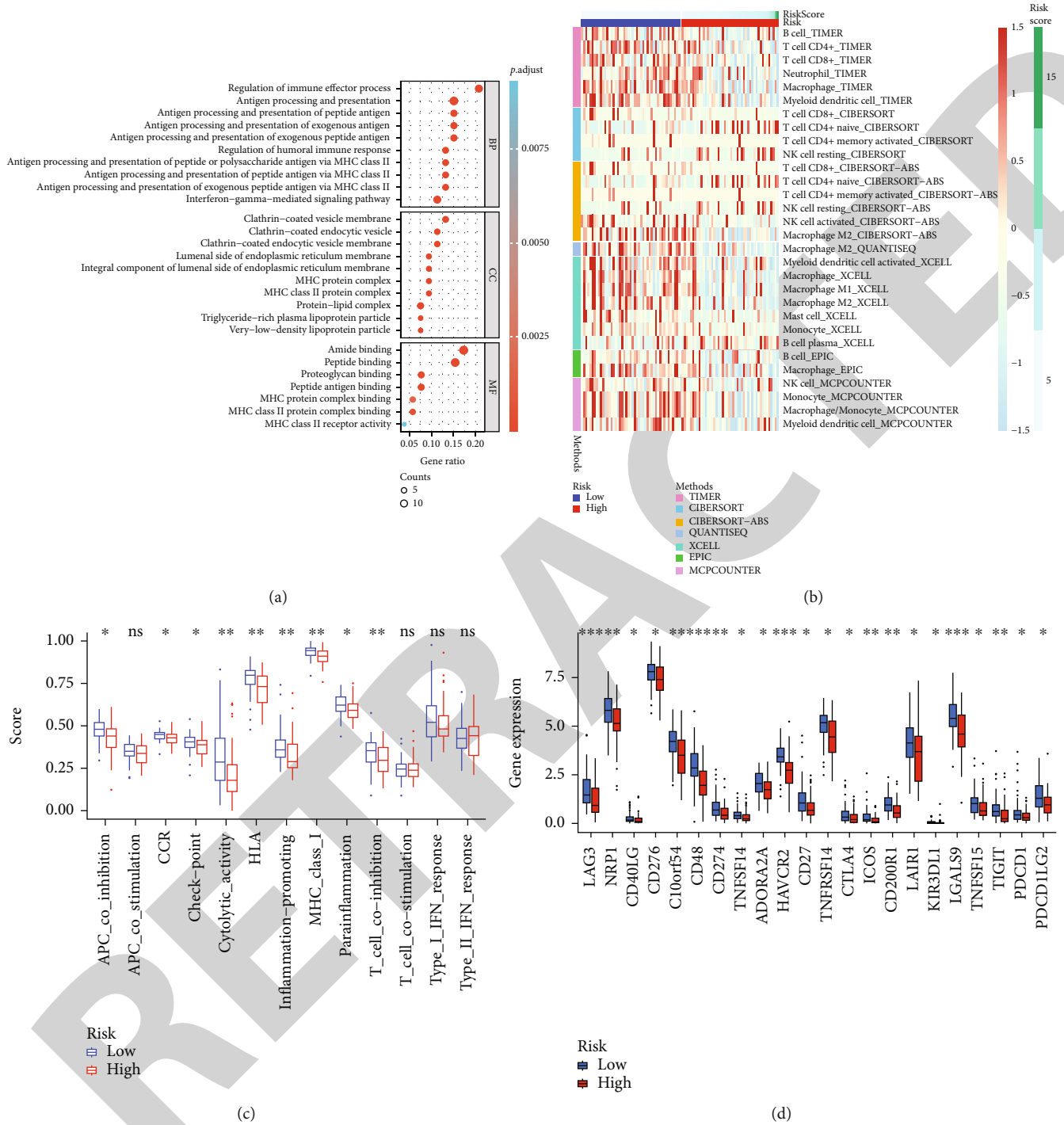


FIGURE 5: Functional analysis of the low- and high-risk groups in the training cohort. (a) GO enrichment analysis based on DEGs between the 2 risk groups. (b) Distinct composition of the immune cells in both risk groups. (c) The scores of 13 immune-related functions to evaluate the immune activities in the two risk groups. (d) Differentially expressed immune checkpoints in the two risk groups (Wilcox: \*  $p < 0.05$ , \*\*  $p < 0.01$ , and \*\*\*  $p < 0.001$ ).

expressed in both OS cell lines (MG63, HOS), and the expression of the 3 protective FRGs (SOCS1, PEBP1, and ATG7) was higher in hBMSC (Figure 9(a)). As autophagy played a crucial role in drug resistance in OS and ATG7 was an essential gene in the autophagy family, the ATG7 gene was selected for further experiments. The results of qPCR and WB further showed that ATG7 expression

was downregulated in the MG63 cells rather than hBMSC (Figure 9(b)). This evidence was consistent with all the findings noted in the study.

**3.8. ATG7 Suppressed OS Progression via Mediating Oxidative Stress and Ferroptosis.** The CCK8 and colony formation assays demonstrated that silencing the ATG7 gene

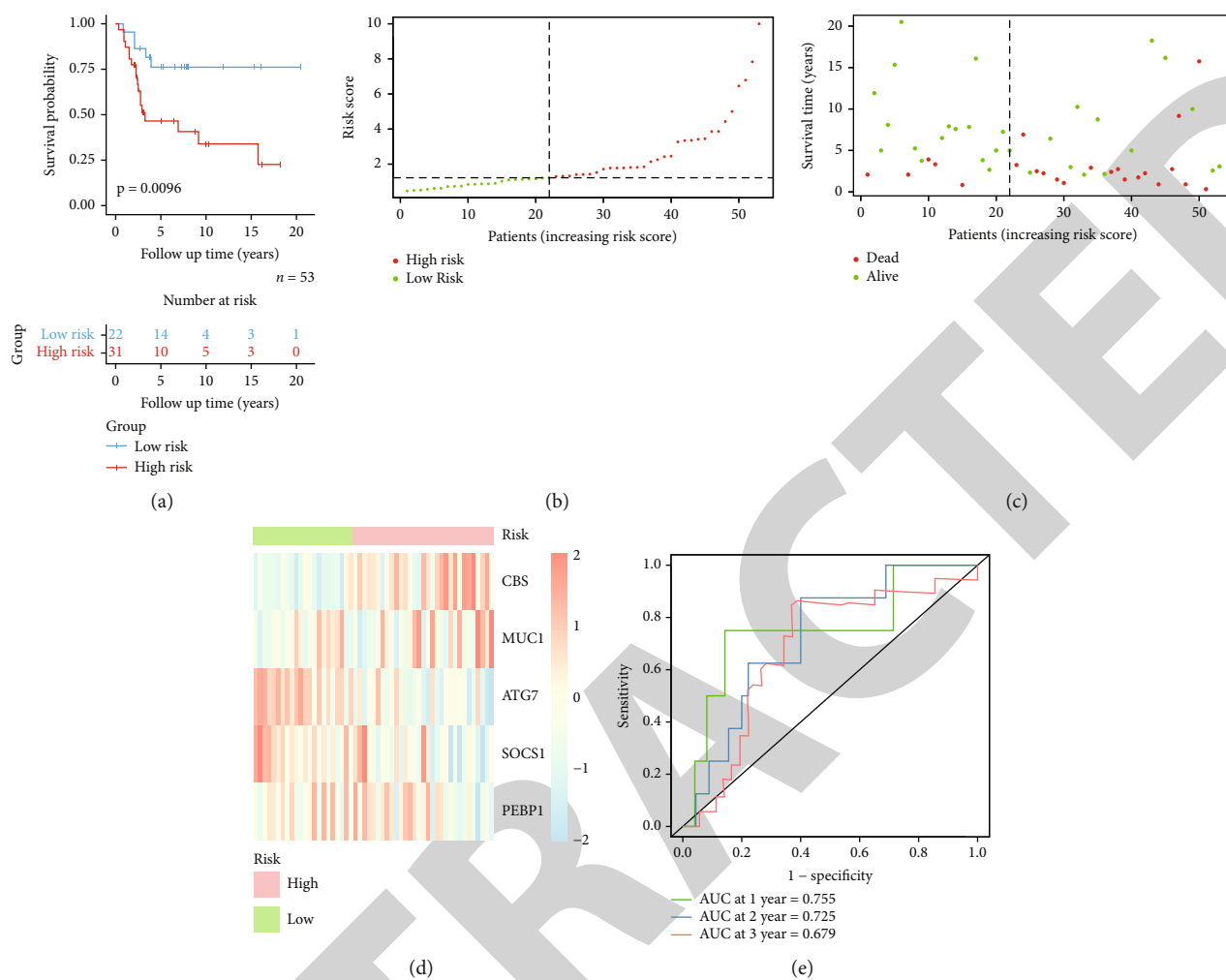


FIGURE 6: The difference in prognosis and gene expression levels between both risk groups in the validation dataset. (a) The KM curves demonstrate the distinct overall survival rates in patients from both risk groups. (b) Distribution of patients depending on their risk scores. (c) Distribution of survival duration for every patient (left: low-risk group; right: high-risk group). (d) Heatmap showing the expression levels of 5 FRGs in both risk categories. (e) ROC curves assessed the predictive ability of the 5 FRGs' signature (Log-rank test: \* $p < 0.05$ , \*\* $p < 0.01$ , and \*\*\* $p < 0.001$ ).

significantly promoted OS cell proliferation capability (\*\* $p < 0.01$ , \*\*\* $p < 0.001$ ; Figures 9(c) and 9(d)). At the same time, enhanced migration ability was found in ATG7-knockdown OS cells (\*\*\* $p < 0.001$ , Figure 9(e)). These findings indicated that the ATG7 gene might inhibit the proliferation and migration capabilities of the malignant OS cells.

Subsequently, it was noted that the ATG7 gene silencing suppressed the increase in MDA activity, especially when the OS cells encountered oxidative stress (\*\*\* $p < 0.001$ , Figure 10(a)). Similarly, lipid ROS was also reduced when ATG7 was silenced in OS cells (\*\*\* $p < 0.001$ , Figure 10(b)). In consistency with the above findings, a decrease in the proportion of cell death (\*\*\* $p < 0.001$ , Figure 10(c)) with a reduction in the  $Fe^{2+}$  levels (\*\*\* $p < 0.001$ , Figure 10(d)) was found in the siATG7 groups. On the other hand, SOD and FTH1 expression levels were significantly elevated in the ATG7-deficient OS cells (Figure 10(e)). These results indicated that silencing ATG7 might suppress oxidative stress and ferroptosis in OS cells.

## 4. Discussion

Increased oxidative stress is closely related to RCD [26]. As a novel RCD process, ferroptosis is seen to play a crucial role in cancer biology and this process was characterized by its unique gene expression, morphology, and molecular pathways [27, 28]. Ferroptosis could be initiated via regulating different intrinsic or extrinsic pathways. The intrinsic pathway was driven by blocking the intracellular antioxidant enzymes (like glutathione peroxidase, GPX4) [14]. However, the extrinsic pathway involved the inhibition of the cell membrane transporters like the cystine/glutamate transporter (also called the system  $Xc^-$ ) or by the activation of the iron transporters like lactoferrin and serotransferrin [29]. Furthermore, a few earlier studies also reported that many clinical drugs could initiate ferroptosis by inhibiting system  $Xc^-$  or GPX4 [30–32], providing a new way of treating cancer for oncologists. The canonical chemotherapy for OS combines high-dose methotrexate, doxorubicin, and

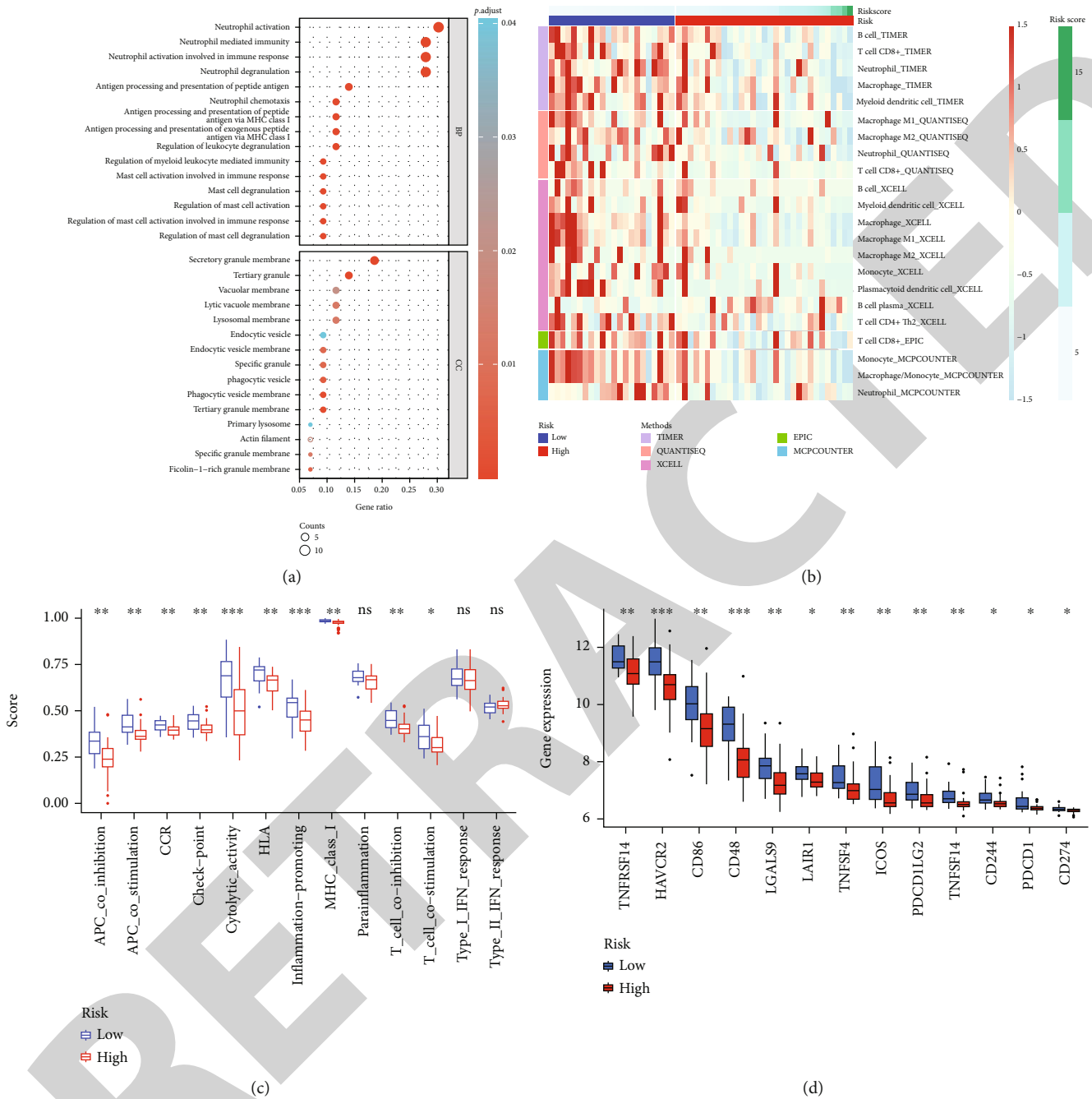


FIGURE 7: Functional analysis of both the risk groups in the validation dataset. (a) GO enrichment analysis based on the DEGs in both risk groups. (b) Comparing the immune cell components in both the risk groups. (c) The scores of 13 immune-related functions to evaluate the immune activities in two risk groups. (d) Differentially expressed immune checkpoints between the high- and low-risk groups (Wilcox: \*  $p < 0.05$ , \*\*  $p < 0.01$ , and \*\*\*  $p < 0.001$ ).

cisplatin (MAP) [2, 33]. However, this strategy poses little effect on drug-resistant, recurrent, or metastatic OS patients [4]. Studies on ferroptosis in bone tumors, especially in OS, are still lacking. Therefore, this study is aimed at exploring the potential effects of the ferroptosis process on OS patients.

In this study, a novel multigene prognostic signature was constructed for OS patients. Gene signature models have been used in the past to predict the prognosis of patients

with different types of cancers [34–36]. This study systematically explored the expression of 200 FRGs in OS tumor tissue samples and their associations with patients' overall survival. Similarly, the results of this study indicated that this five-FRG-based signature could be used for classifying OS patients into 2 clusters with different prognoses and molecular characteristics. Interestingly, patients with high expression of protective FRGs seemed to have better prognoses. Therefore, it was hypothesized in this study that ferroptosis

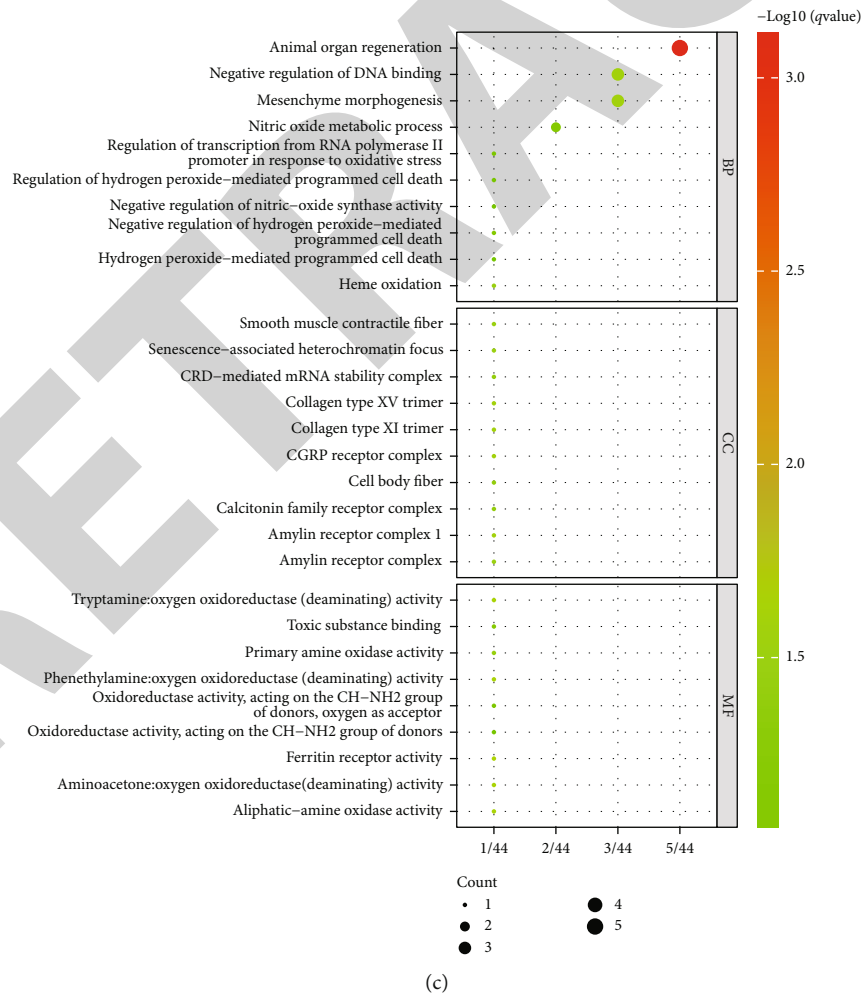
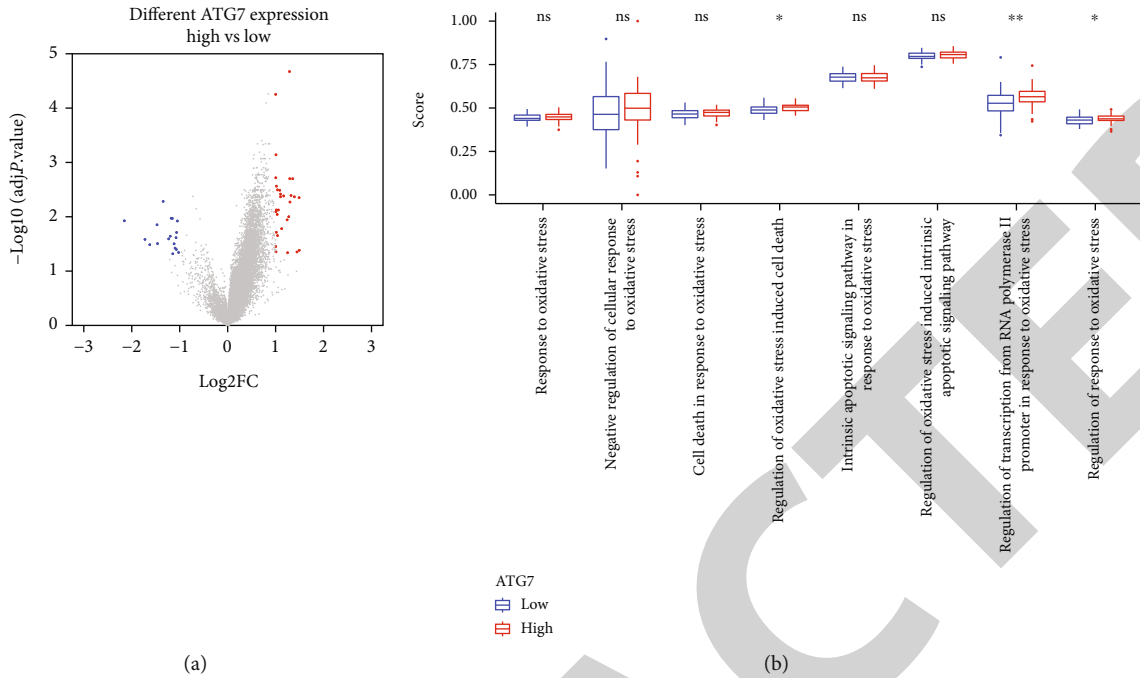


FIGURE 8: Analyses of the different groups regarding ATG7 expression. (a) DEGs identified between the low- and high-ATG7 expression groups (blue: downregulated genes; red: upregulated genes). (b) GO enrichment analysis in the differentially expressed ATG7 groups. (c) The different oxidative stress pathways in the two groups.

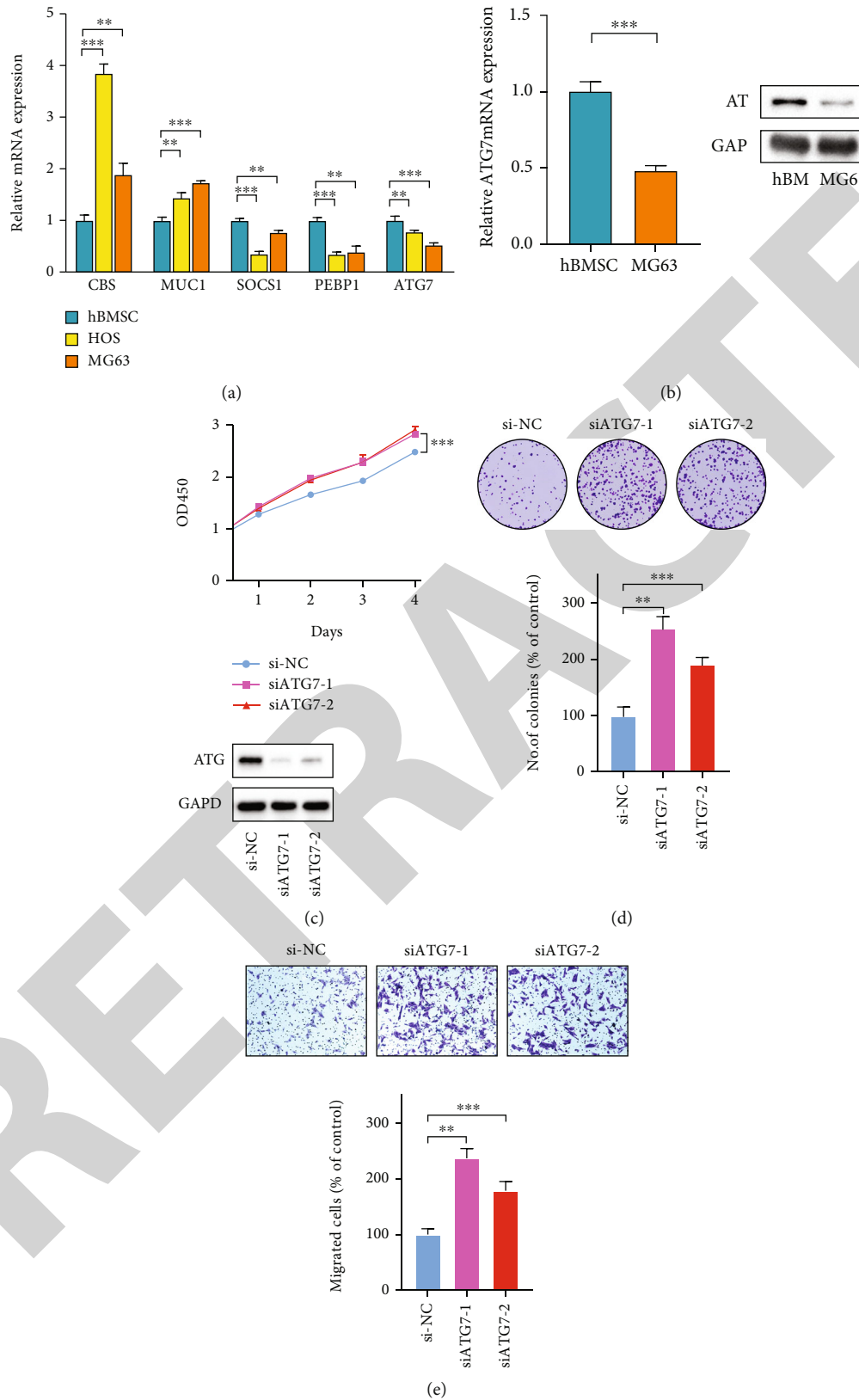


FIGURE 9: Validation of ATG7 expression and function in OS cells. (a) Relative mRNA expression of 5 candidate FRGs in OS cells and hBMSC. (b) mRNA and protein expressions of ATG7 in hBMSC and MG63 cell lines. (c) The CCK8 assay examines the OS cell proliferation ability after ATG7 silencing and examines ATG7 silencing efficiency. (d) Identifying the influence of ATG7 silencing on OS cell proliferation by colony information assay. (e) Transwell assays examine OS cell migration capability after silencing ATG7 ( $n = 3$ ;  $t$ -test:  $*p < 0.05$ ,  $**p < 0.01$ , and  $***p < 0.001$ ).

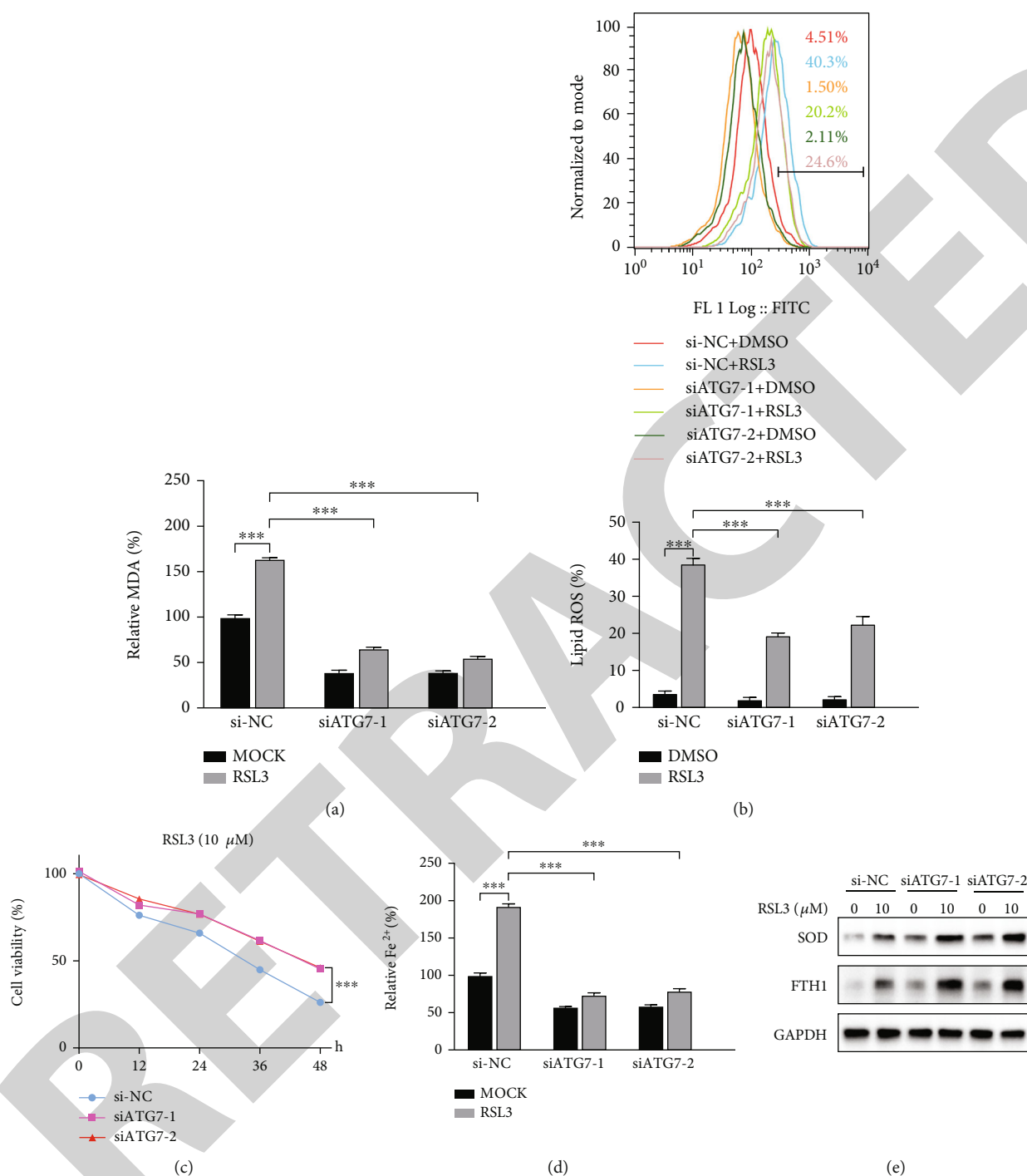


FIGURE 10: The effect of ATG7 silencing in oxidative stress and ferroptosis in MG63 cells. (a) Cell viability test of ferroptosis-induced MG63 cells after silencing ATG7. (b) Histograms showing the effect of ATG7 silencing in the production of lipid ROS in MG63 cells. (c) Examination of the MDA levels in ferroptosis-induced MG63 cells after ATG7 silencing. (d) Examination of the Fe<sup>2+</sup> levels in ferroptosis-induced MG63 cells after silencing ATG7. (e) The expression of SOD and FTH1 after silencing ATG7 (*n* = 3; RSL3: 10 μM; time: 12 h; *t*-test: \**p* < 0.05, \*\**p* < 0.01, and \*\*\**p* < 0.001).

might affect OS patients' prognosis, and constructing a prognostic model based on the FRGs for OS patients could be helpful.

Although the application of ferroptosis in tumors has been extensively studied in the past, the probable relationship between ferroptosis and tumor immunity needs further

investigation. Previous studies have reported that the interferon-gamma (IFNγ) molecules secreted from the CD8<sup>+</sup> T cells promoted the ferroptosis and lipid peroxidation processes in the malignant cells [37]. Furthermore, ferroptosis could also modulate the immune function of tumor cells [15]. Moreover, the ferroptosis tumor cells could release

distinct 'find me' signals to recruit some immune cells like the antigen-presenting cells (APCs) to the site of the malignant cells [38]. A few important steps that take place during the interaction between the immune and ferroptosis malignant cells are observed to be phagocytosis and migration, maturation, antigen-processing, and the cross-presentation by DCs [39, 40]. Interestingly, the results of GO enrichment analyses between the 2 risk groups revealed a few unexpected immune-linked biological processes and pathways such as immune cell activation, antigen processing and presenting, and the IFN $\gamma$ -mediated signaling pathways, which were seen to be especially enriched in the low-risk category. Furthermore, the analysis of the immune system suggested that immune-linked activities in the low-risk category were significantly higher than those in the high-risk category, which contributed to a better prognosis in the low-risk group. Taken together, these findings revealed that ferroptosis could be associated with the immune function of the OS patients, benefitting the prognoses of OS patients and indicating that therapeutic strategies that targeted the FRGs could offer a new treatment scheme for OS patients.

Furthermore, the prognostic model that was constructed in this study included 5 FRGs (ATG7, SOCS1, PEBP1, CBS, and MUC1). ATG7 was reported to suppress tumor cell growth in glioma by promoting ferroptosis [41]. The suppressor of cytokine signaling (SOCS) family members are regarded as cytokine signaling inhibitors that regulate cell growth and differentiation. SOCS1 was known as an inhibitor of tumor cell growth [42]. Studies have shown that P53 promoted ferroptosis in tumor cells by blocking the transcription of SLC7A11 and SOCS1 sensitized cells to ferroptosis by controlling P53 target gene expression [43]. Meanwhile, SOCS1 was also a protective FRG and helped in predicting the prognosis of head and neck squamous cell carcinoma patients [44, 45]. In addition, Phosphatidylethanolamine Binding Protein 1 (PEBP1) induced ferroptosis in epithelial cells by generating hydroperoxyphosphatidylethanolamine [46] and was involved in the cell death process in hepatocellular carcinoma by regulating ferroptosis [47]. PEBP1 was also a robust prognostic marker associated with good outcomes in lung adenocarcinoma [48, 49]. The system Xc<sup>-</sup>/glutathione- (GSH-) GPX4 axis has been considered a primary system in protecting cells from lipid peroxidation-mediated ferroptosis owing to its involvement in eliminating ROS [10]. CBS is the biosynthetic enzyme for cysteine, which is the major component of GSH. CBS overexpression induces ferroptosis resistance in ovarian cancer cells [50]. Additionally, ferroptosis was triggered in hepatocellular carcinoma by suppressing the expression of CBS [51]. Similarly, MUC1 mediates triple-negative breast cancer cells' self-renewal capacity and tumorigenicity by stabilizing system Xc<sup>-</sup> and inhibits erastin-induced ferroptosis [52]. Moreover, MUC1 was a ferroptosis-related disease marker in nontumor diseases like idiopathic pulmonary fibrosis and ulcerative colitis [53, 54]. In summary, 3 genes in the prognostic signature (ATG7, SOCS1, and PEBP1) were reported to facilitate ferroptosis in tumor cells, while the remaining two genes (CBS, MUC1) are the opposite. Furthermore, the prognoses in

the high expressing proferroptotic genes group were better than those in the low-expression group, which were also dramatically opposed to anti-ferroptotic genes. Therefore, these results provided a significant theoretical basis for the novel FRGs-based prognostic model.

Although ferroptosis was distinct from other RCD processes, the potential relationships among them could not be ignored. Autophagy contributes to ferroptosis in cancer cells by ferritin degradation, providing novel insights into the interplay between autophagy and ferroptosis [55]. Notably, autophagy played an essential role in OS chemoresistance, resulting in treatment failure and poor prognosis for OS patients [55–58]. The role of ferroptosis (antitumor) and autophagy (protumor) in OS seem contradictory. Meanwhile, ATG7, as an autophagy-related gene, is critical for the formation of autophagosomes [55]. Hence, the ATG7 gene was selected as a candidate gene to explore its specific function in the development of OS cells, specifically the role of ATG7 in affecting the oxidative stress reaction and ferroptosis process in OS cells.

Notably, the role of ATG7 in regulating tumor progression might be controversial. For example, ATG7's antineoplastic role could suppress tumorigenesis by accelerating tumor cell death in non-small-cell lung cancer and colorectal cancer [59, 60]. ATG7 was linked to better outcomes in renal carcinoma and triple-negative breast cancer [61, 62] while promoting the progression of hepatocellular carcinoma and myeloid leukemia instead [63, 64]. The findings in this study showed that the downregulation of ATG7 significantly enhanced the malignancy of the OS cells, and high ATG7 expression was linked to better survival outcomes, suggesting the protective function of ATG7 in OS patients.

Studies have reported that cellular stress modalities like oxidative stress could induce autophagy [65]. As a key gene of autophagy, ATG7 plays a crucial role in regulating the response to oxidative stress and oxidative stress-induced cell death [66, 67]. Moreover, it was found that ferritin degradation driven by autophagy led to iron accumulation, inducing oxidative stress by the Fenton reaction in cells [15, 68]. Meanwhile, excessive iron accumulation resulted in oxidative damage membrane, triggering the ferroptosis process in cells [14]. The results of the study indicated that silencing ATG7 might inhibit the increase in the oxidizing materials and promote the production of antioxidants, endowing OS cells with a stronger antioxidant capacity when they face oxidative stress. Meanwhile, it also suppressed ferroptosis in OS cells by decreasing the levels of Fe<sup>2+</sup>. These results implicate that ATG7 might promote the ferroptosis of OS cells by modulating oxidative stress. Therefore, ATG7 may be a novel therapeutic target for OS. In addition, autophagy may result in chemotherapy resistance in OS treatment and might serve as a promoter of ferroptosis, while OS patients might benefit from ferroptosis. As the contradictory role of ferroptosis (antitumor) and autophagy (protumor) in OS cells, we believe that using a combination of ferroptosis inducers and autophagy inhibitors might not be advisable when treating OS.

Although one similar study based on 12 FRGs was previously reported [69], differences between the two were as

follows: Firstly, the AUC of the previous gene signature was lower than that determined in this study, indicating that the novel FRG signature constructed here has higher accuracy in forecasting the prognosis of the OS patients. Additionally, the number of FRGs was narrowed down to develop a signature (from 12 to 5 FRGs) and improve the predictive ability of the signature, which makes the examination more convenient for clinicians and decreases patient costs. Moreover, all studies constructing predictive FRG signatures for OS patients were only based on bioinformatics methods without any experimental validations, which may make their conclusions less convincing. Finally, the role exerted by the ATG7 gene in oxidative stress and ferroptosis in OS cells was highlighted in this study, which depicted the potential relationship between autophagy and ferroptosis in OS.

This study constructed and validated an FRG prognostic signature for OS patients and proposed that ATG7 might promote ferroptosis by regulating oxidative stress in OS. However, it still had some limitations. Firstly, the training and validation cohort sample size was still small, potentially due to the low incidence of OS compared with other tumors. Secondly, this study only focused on ATG7 and explored its specific role in OS, but the effects of the other four genes in OS are still unclear. The function of the remaining 4 genes and their ferroptosis mechanisms in OS cells will be investigated in the future. Therefore, larger sample size and prospective mechanistic studies are needed to validate the results and conclusions of the present study.

## 5. Conclusions

In summary, a novel FRG signature with good accuracy and effectiveness in predicting prognosis for OS patients was constructed. Our results suggested that ATG7 might influence the regulation of oxidative stress, promote ferroptosis in OS cells, and act as a protectively therapeutic target for OS patients. Further studies are warranted to confirm these findings and investigate the fundamental mechanisms of ferroptosis in OS.

## Data Availability

The data used in this study can be found in public databases online. The websites and accession number(s) of the data can be found in the article.

## Disclosure

The funding sources had no role in the study design, data gathering, analysis, interpretation, writing of the report, or the decision to submit the report for publication.

## Conflicts of Interest

The authors declare that the research was conducted without any commercial or financial relationships that could be construed as a potential conflict of interest.

## Authors' Contributions

XJR, XW, WHF, and HSH conceived and designed the original ideas of this manuscript, as well as executed and supervised them throughout the process. JRY, HSH, and GHY collected the data and did the analysis. JRY, LHSC, and JSY prepared the figures and tables. JRY, HSH, and WY did molecular biology experiments. WW, CJ, YC, and HJB collected related literature. JRY drafted the initial manuscript, and XJR, XW, WHF, and HSH reviewed and edited the initial manuscript. All authors have read and approved the manuscript. Runyi Jiang, Shaohui He, Haiyi Gong, and Yao Wang contributed equally to this work and share the first authorship.

## Acknowledgments

We acknowledge all researchers and individuals participating in the TARGET and GEO database study. This work was supported by grants from the National Natural Science Foundation of China (81402417, 82072971, and 82203401), Shanghai Science and Technology Committee Program (17411950300 and 17411950301), and Shanghai excellent medical talents funding (2018YQ56).

## Supplementary Materials

Supplementary Figure S1: the flow chart of this study. Supplementary Figure S2: selecting the best  $k$  value to classify OS patients into two clusters by NMF method. Supplementary Figure S3: KM curves of another 14 candidate ferroptosis-related genes ( $p \leq 0.01$ ) that were not included in the prognostic signature. Supplementary Figure S4: identification of risk level as an independent risk factor. Supplementary Table S1: a total of 200 ferroptosis-related genes. (*Supplementary Materials*)

## References

- [1] Y. Deng, W. Yuan, E. Ren, Z. Wu, G. Zhang, and Q. Xie, "A four-methylated LncRNA signature predicts survival of osteosarcoma patients based on machine learning," *Genomics*, vol. 113, no. 1, pp. 785–794, 2021.
- [2] P. A. Meyers, C. L. Schwartz, M. Krailo et al., "Osteosarcoma: a randomized, prospective trial of the addition of ifosfamide and/or muramyl tripeptide to cisplatin, doxorubicin, and high-dose methotrexate," *Journal of Clinical Oncology*, vol. 23, no. 9, pp. 2004–2011, 2005.
- [3] S. Ferrari, S. Smeland, M. Mercuri et al., "Neoadjuvant chemotherapy with high-dose Ifosfamide, high-dose methotrexate, cisplatin, and doxorubicin for patients with localized osteosarcoma of the extremity: a joint study by the Italian and Scandinavian Sarcoma Groups," *Journal of Clinical Oncology*, vol. 23, no. 34, pp. 8845–8852, 2005.
- [4] B. Kempf-Bielack, S. S. Bielack, H. Jürgens et al., "Osteosarcoma relapse after combined modality therapy: an analysis of unselected patients in the Cooperative Osteosarcoma Study Group (COSS)," *Journal of Clinical Oncology*, vol. 23, no. 3, pp. 559–568, 2005.
- [5] W. Yu, Y. Wang, J. Zhu et al., "Autophagy inhibitor enhance ZnPc/BSA nanoparticle induced photodynamic therapy by



- suppressing PD-L1 expression in osteosarcoma immunotherapy,” *Biomaterials*, vol. 192, pp. 128–139, 2019.
- [6] D. Yang, T. Xu, L. Fan, K. Liu, and G. Li, “MicroRNA-216b enhances cisplatin-induced apoptosis in osteosarcoma MG63 and SaOS-2 cells by binding to JMJD2C and regulating the HIF1 $\alpha$ /HES1 signaling axis,” *Journal of Experimental & Clinical Cancer Research: CR*, vol. 39, no. 1, p. 201, 2020.
- [7] D. Hanahan and R. A. Weinberg, “Hallmarks of cancer: the next generation,” *Cell*, vol. 144, no. 5, pp. 646–674, 2011.
- [8] S. Cogo, A. Ferino, G. Miglietta, E. B. Pedersen, and L. E. Xodo, “The regulatory G4 motif of the Kirsten ras (KRAS) gene is sensitive to guanine oxidation: implications on transcription,” *Nucleic Acids Research*, vol. 46, no. 2, pp. 661–676, 2018.
- [9] J. D. Hayes, A. T. Dinkova-Kostova, and K. D. Tew, “Oxidative stress in cancer,” *Cancer Cell*, vol. 38, no. 2, pp. 167–197, 2020.
- [10] S. S. Sabharwal and P. T. Schumacker, “Mitochondrial ROS in cancer: initiators, amplifiers or an Achilles' heel?,” *Nature Reviews Cancer*, vol. 14, no. 11, pp. 709–721, 2014.
- [11] E. Obrador, R. Salvador, R. López-Blanch et al., “Melanoma in the liver: oxidative stress and the mechanisms of metastatic cell survival,” *Seminars in Cancer Biology*, vol. 71, pp. 109–121, 2021.
- [12] M. P. Murphy, A. Holmgren, N. G. Larsson et al., “Unraveling the biological roles of reactive oxygen species,” *Cell Metabolism*, vol. 13, no. 4, pp. 361–366, 2011.
- [13] M. Redza-Dutordoir and D. A. Averill-Bates, “Activation of apoptosis signalling pathways by reactive oxygen species,” *Biochimica et Biophysica Acta*, vol. 1863, no. 12, pp. 2977–2992, 2016.
- [14] S. J. Dixon, K. M. Lemberg, M. R. Lamprecht et al., “Ferroptosis: an iron-dependent form of nonapoptotic cell death,” *Cell*, vol. 149, no. 5, pp. 1060–1072, 2012.
- [15] X. Chen, R. Kang, G. Kroemer, and D. Tang, “Broadening horizons: the role of ferroptosis in cancer,” *Nature Reviews Clinical Oncology*, vol. 18, no. 5, pp. 280–296, 2021.
- [16] H. Lin, X. Chen, C. Zhang et al., “EF24 induces ferroptosis in osteosarcoma cells through HMOX1,” *Biomedicine & pharmacotherapy = Biomedecine & pharmacotherapie*, vol. 136, article 111202, 2021.
- [17] Q. Liu and K. Wang, “The induction of ferroptosis by impairing STAT3/Nrf2/GPx4 signaling enhances the sensitivity of osteosarcoma cells to cisplatin,” *Cell Biology International*, vol. 43, no. 11, pp. 1245–1256, 2019.
- [18] Y. Luo, X. Gao, L. Zou, M. Lei, J. Feng, and Z. Hu, “Bavachin induces ferroptosis through the STAT3/P 53/SLC7A11 axis in osteosarcoma cells,” *Oxidative Medicine and Cellular Longevity*, vol. 2021, Article ID 1783485, 14 pages, 2021.
- [19] Y. Pignochino, G. Grignani, G. Cavalloni et al., “Sorafenib blocks tumour growth, angiogenesis and metastatic potential in preclinical models of osteosarcoma through a mechanism potentially involving the inhibition of ERK1/2, MCL-1 and ezrin pathways,” *Molecular Cancer*, vol. 8, no. 1, p. 118, 2009.
- [20] X. Niu, L. Chen, Y. Li, Z. Hu, and F. He, “Ferroptosis, necroptosis, and pyroptosis in the tumor microenvironment: perspectives for immunotherapy of SCLC,” *Seminars in Cancer Biology*, 2022.
- [21] P. Liu and W. Wang, “Ferroptosis: a new regulatory mechanism in osteoporosis,” *Oxidative Medicine and Cellular Longevity*, vol. 2022, Article ID 2634431, 10 pages, 2022.
- [22] Y. Peng, L. Shui, J. Xie, and S. Liu, “Development and validation of a novel 15-CpG-based signature for predicting prognosis in triple-negative breast cancer,” *Journal of cellular and molecular medicine*, vol. 24, no. 16, pp. 9378–9387, 2020.
- [23] X. Sui, R. Zhang, S. Liu et al., “RSL3 drives ferroptosis through GPX4 inactivation and ROS production in colorectal cancer,” *Frontiers in Pharmacology*, vol. 9, p. 1371, 2018.
- [24] J. Wu, A. M. Minikes, M. Gao et al., “Intercellular interaction dictates cancer cell ferroptosis via NF2-YAP signalling,” *Nature*, vol. 572, no. 7769, pp. 402–406, 2019.
- [25] R. Gaujoux and C. Seoighe, “A flexible R package for nonnegative matrix factorization,” *BMC Bioinformatics*, vol. 11, no. 1, p. 367, 2010.
- [26] C. Holze, C. Michaudel, C. Mackowiak et al., “Oxeiptosis, a ROS-induced caspase-independent apoptosis-like cell-death pathway,” vol. 19, no. 2, pp. 130–140, 2018.
- [27] X. Jiang and B. R. Stockwell, “Ferroptosis: mechanisms, biology and role in disease,” *Nature Reviews Molecular Cell Biology*, vol. 22, no. 4, pp. 266–282, 2021.
- [28] G. Lei and Y. Zhang, “The role of ferroptosis in ionizing radiation-induced cell death and tumor suppression,” *Cell Research*, vol. 30, no. 2, pp. 146–162, 2020.
- [29] Y. Hu, N. Guo, T. Yang, J. Yan, W. Wang, and X. Li, “The potential mechanisms by which artemisinin and its derivatives induce ferroptosis in the treatment of cancer,” *Oxidative Medicine and Cellular Longevity*, vol. 2022, Article ID 1458143, 12 pages, 2022.
- [30] X. Sun, Z. Ou, R. Chen et al., “Activation of the p62-Keap1-NRF2 pathway protects against ferroptosis in hepatocellular carcinoma cells,” *Hepatology (Baltimore, Md)*, vol. 63, no. 1, pp. 173–184, 2016.
- [31] E. Lachaier, C. Louandre, C. Godin et al., “Sorafenib induces ferroptosis in human cancer cell lines originating from different solid tumors,” *Anticancer Research*, vol. 34, no. 11, pp. 6417–6422, 2014.
- [32] S. J. Dixon, D. N. Patel, M. Welsch et al., “Pharmacological inhibition of cystine-glutamate exchange induces endoplasmic reticulum stress and ferroptosis,” vol. 3, Article ID e02523, 2014.
- [33] J. S. Whelan, S. S. Bielack, N. Marina et al., “EURAMOS-1, an international randomised study for osteosarcoma: results from pre-randomisation treatment,” *Annals of oncology: official journal of the European Society for Medical Oncology*, vol. 26, no. 2, pp. 407–414, 2015.
- [34] D. Wang, G. Wei, J. Ma et al., “Identification of the prognostic value of ferroptosis-related gene signature in breast cancer patients,” *BMC Cancer*, vol. 21, no. 1, p. 645, 2021.
- [35] Y. Dong, T. Shang, H. Ji, X. Zhou, and Z. Chen, “Identification of distinct molecular patterns and a four-gene signature in colon cancer based on invasion-related genes,” *Frontiers in Genetics*, vol. 12, p. 685371, 2021.
- [36] N. Shao, H. Tang, Y. Mi, Y. Zhu, F. Wan, and D. Ye, “A novel gene signature to predict immune infiltration and outcome in patients with prostate cancer,” *Oncoimmunology*, vol. 9, no. 1, p. 1762473, 2020.
- [37] W. Wang, M. Green, J. E. Choi et al., “CD8<sup>+</sup> T cells regulate tumour ferroptosis during cancer immunotherapy,” *Nature*, vol. 569, no. 7755, pp. 270–274, 2019.
- [38] J. P. Friedmann Angeli and D. V. Krysko, “Ferroptosis at the crossroads of cancer-acquired drug resistance and immune evasion,” *Nature Cell Biology*, vol. 19, no. 7, pp. 405–414, 2019.

## Retraction

# Retracted: Macrophage-Derived Exosomes in TLR9-/- Mice Ameliorate Sepsis-Induced Mitochondrial Oxidative Stress and Apoptosis in Cardiomyocytes

### Oxidative Medicine and Cellular Longevity

Received 20 June 2023; Accepted 20 June 2023; Published 21 June 2023

Copyright © 2023 Oxidative Medicine and Cellular Longevity. This is an open access article distributed under the Creative Commons Attribution License, which permits unrestricted use, distribution, and reproduction in any medium, provided the original work is properly cited.

This article has been retracted by Hindawi following an investigation undertaken by the publisher [1]. This investigation has uncovered evidence of one or more of the following indicators of systematic manipulation of the publication process:

- (1) Discrepancies in scope
- (2) Discrepancies in the description of the research reported
- (3) Discrepancies between the availability of data and the research described
- (4) Inappropriate citations
- (5) Incoherent, meaningless and/or irrelevant content included in the article
- (6) Peer-review manipulation

The presence of these indicators undermines our confidence in the integrity of the article's content and we cannot, therefore, vouch for its reliability. Please note that this notice is intended solely to alert readers that the content of this article is unreliable. We have not investigated whether authors were aware of or involved in the systematic manipulation of the publication process.

Wiley and Hindawi regrets that the usual quality checks did not identify these issues before publication and have since put additional measures in place to safeguard research integrity.

We wish to credit our own Research Integrity and Research Publishing teams and anonymous and named external researchers and research integrity experts for contributing to this investigation.

The corresponding author, as the representative of all authors, has been given the opportunity to register their agreement or disagreement to this retraction. We have kept a record of any response received.

### References

- [1] X. Li, J. Luo, Y. Li et al., "Macrophage-Derived Exosomes in TLR9-/- Mice Ameliorate Sepsis-Induced Mitochondrial Oxidative Stress and Apoptosis in Cardiomyocytes," *Oxidative Medicine and Cellular Longevity*, vol. 2022, Article ID 5719974, 13 pages, 2022.

## Research Article

# Macrophage-Derived Exosomes in TLR9<sup>-/-</sup> Mice Ameliorate Sepsis-Induced Mitochondrial Oxidative Stress and Apoptosis in Cardiomyocytes

Xiang Li <sup>1</sup>, Junyu Luo,<sup>1</sup> Yanmei Li,<sup>2</sup> Lu Jia,<sup>2</sup> Yuejin Li,<sup>3</sup> Shili Ye,<sup>4</sup> Lanlan Liu,<sup>5</sup> Yanxuan Yu,<sup>5</sup> Yonggang Lu,<sup>6</sup> and Yunpeng Luan <sup>1,5</sup>

<sup>1</sup>The First Affiliated Hospital of Yunnan University of Traditional Chinese Medicine, Kunming 650021, China

<sup>2</sup>Department of Life Technology Teaching and Research, College of Life Sciences, Southwest Forestry University, Kunming 650224, China

<sup>3</sup>The General Surgery Department, The First People's Hospital of Yunnan Province, Kunming 650000, China

<sup>4</sup>Faculty of Mathematics and Physics, Southwest Forestry University, Kunming 650224, China

<sup>5</sup>Key Laboratory for Forest Resources Conservation and Utilization in the Southwest Mountains of China, Ministry of Education, Southwest Forestry University, Kunming 650224, China

<sup>6</sup>Clinical Laboratory, Hebei General Hospital, Shijiazhuang 050000, China

Correspondence should be addressed to Yunpeng Luan; [yunpeng@swfu.edu.cn](mailto:yunpeng@swfu.edu.cn)

Received 7 July 2022; Revised 24 August 2022; Accepted 9 September 2022; Published 3 October 2022

Academic Editor: Tian Li

Copyright © 2022 Xiang Li et al. This is an open access article distributed under the Creative Commons Attribution License, which permits unrestricted use, distribution, and reproduction in any medium, provided the original work is properly cited.

**Objective.** To explore the mechanisms of TLR9 from macrophages on mitochondrial apoptosis in cardiomyocytes at early stage of sepsis. **Methods.** The *in vivo* and *in vitro* sepsis mice were bone marrow transplantation (BMT) with wild type (WT) or (toll-like receptor 9) TLR9 knockout (<sup>-/-</sup> or KO) myeloid cells and then constructed by cecum ligation and puncture (CLP) as *in vivo* experiment and cardiomyocytes cocultured with WT or TLR9-deficient macrophages treated with LPS as *in vitro* experiment, respectively. Sepsis model were performed by CLP. The expression levels of exosome, PI3K/AKT, and ERK1/2, inflammatory factors, and apoptotic proteins were tested by western blot *in vivo*. Besides, associated apoptotic proteins and JC-1 fluorescence assay were tested *in vitro*. **Results.** The expressions of p-PI3K, p-AKT, exosome markers (CD9, CD63, and TSG101), p-ERK1/2, TNF- $\alpha$ , IFN- $\gamma$ , IL-1 $\beta$ , and cleaved-caspase-3/-9 were significantly increased in septic mice vs. control mice, and these proteins were declined dramatically in TLR9<sup>-/-</sup> BMT mice vs. WT BMT mice in sepsis mice models. Meanwhile, the protein expression of cytochrome C, cleaved-caspase-3, and cleaved-caspase-9 increased significantly in primary mouse myocardial cells cocultured with TLR9<sup>-/-</sup> or WT macrophages stimulated with LPS, and these mitochondrial apoptotic proteins as well as the green 5,5',6,6'-tetrachloro-1,1',3,3'-tetraethylbenzimidazolcarbocyanine iodide (JC-1) fluorescence were dramatically lower in LPS-stimulated cardiomyocytes cocultured with TLR9<sup>-/-</sup> than with WT macrophages. **Conclusion.** TLR9<sup>-/-</sup> in macrophages suppressed the inflammatory reaction as well as the exosome secretion and resulted in the inhibition of apoptosis and oxidative stress in sepsis-induced cardiomyopathy.

## 1. Introduction

Sepsis, a clinical syndrome with host response disorder caused by infection, is a life-threatening organ dysfunction [1]. It is usually secondary to severe infection, ischemia-reperfusion injury, trauma, and shock [2]. Sepsis often induces varying degrees of cardiac dysfunction, thereby

resulting in a poor prognosis [3]. In 1984, Parker et al. [4] discovered reversible cardiac dysfunction in septic patients and proposed the concept of sepsis-induced cardiomyopathy (SIC), the major cause of death in septic patients [5]. To date, the pathogenesis of SIC remains elusive [6], which involves a few of factors such as inflammatory damage, myocardial mitochondrial dysfunction, and oxidative stress

injury [7, 8]. Hence, deep exploring the mechanisms of cardiomyocyte injury in sepsis is of important significance for ameliorating the prognosis of sepsis.

During the initiation of sepsis, the obvious change is that monocyte/macrophage injury in patients will cause “endo-toxin tolerance,” thus leading to adverse consequences [9]. Monocytes and macrophages are the main components of the innate immune system, which participate in the host’s innate immune response by recognizing and presenting antigens, releasing cytokines, and relieving inflammation [10]. However, an excessive immune response may trigger systemic inflammatory response syndrome and compensatory anti-inflammatory response syndrome to protect the human body from sepsis injury. PI3K signal is the major negative and braking mechanism for innate immune reactions. Exosomes are extracellular vesicles secreted by late endosomes; initially, exosomes were considered to be involved in the mechanisms by which reticulocytes transport discarded membrane proteins [11]. Generally, exosomes serve as carriers of informatory molecules that mediate cell-to-cell communication [12]. Macrophage-derived exosomes can participate in innate immune response-induced inflammation through synergistic action with toll-like receptors (TLR) [13]. TLR are regarded as an integral part of the innate immune system [14], among which TLR9 can recognize microbial DNA [15]. Moreover, it has been found that macrophage-derived exosomes can recognize long-chain fatty acids, activate the downstream ERK signaling pathway, and promote the secretion of inflammatory factors [16] and proinflammatory cytokines such as TNF- $\alpha$  and L-1 $\beta$ , thus inducing the systemic inflammatory cascade response and causing myocardial injury, apoptosis, and cardiac dysfunction [17]. Excessive immune responses are detrimental to the host and negative feedback regulation, and PI3K plays as a primary endogenous suppressor for TLR-induced inflammatory signals in macrophages, which is crucial for the maintenance of immune system as well as cellular structure integrity [18–20]. Previously, much studies were focused on the inflammatory responses and TLR9 signals, whereas the relationship between the PI3K signal-induced exosome secretion and TLR9 activation remains unclear and ambiguous [15, 21]. Therefore, this study was carried on to elaborate on these mechanisms.

In this study, sepsis animal models were constructed in TLR9<sup>-/-</sup> mice and WT mice by CLP to explore the influencing mechanism of myeloid TLR9 on sepsis-induced inflammatory response *in vivo*, and we also investigate the mechanisms of macrophage-derived exosomes of TLR9<sup>-/-</sup> mice on sepsis-induced mitochondrial apoptosis in cardiomyocytes *in vitro*.

## 2. Materials and Methods

**2.1. Experimental Animals and Bone Marrow Transplantation.** A total of 48 male C57/BL mice (8–10 weeks old, 22  $\pm$  3 g) were purchased from Beijing Huafukang Biotechnology Co., Ltd. In addition, 48 male C57BL/6J mice (8–10 weeks old, 24 TLR9<sup>-/-</sup> mice and 24 WT mice) were purchased from the Henan Skbex Biotechnology Company.

The TLR9<sup>-/-</sup> and WT mice were used as donor mice and euthanized with isoflurane, and the myeloid or bone marrow cells were acquired from femur and tibia bones, then the C57/BL mice were irradiated with 5.5 GY, and 6  $\times$  10<sup>7</sup> donor cells [22, 23] dissolved in RPMI-1640 were injected via caudal veins for the recipient mice. The recipient mice were administrated with acidified water with 100 mg/L neomycin and 10 mg/L polymyxin B sulfate. The BMT animals were placed in a suitable environment at 20  $\pm$  2°C and 55  $\pm$  5% relative humidity, with a 12/12 h light/dark cycle [24]. They had free access to a standard diet and distilled water. The mice BMT with TLR9<sup>-/-</sup> myeloid cells (TLR9<sup>-/-</sup> BMT mice) and WT myeloid cells (WT BMT mice) were randomly divided into control and CLP group (subjected to ligation at 1 cm away from the colon end, and the abdominal cavity was closed after two holes were pierced with a 21 gauge needle) and sham operation group (sham group, subjected to laparotomy and cecum exposure, followed by abdominal cavity closure). The heart tissues of mice were sampled and stored at -80°C or 4% paraformaldehyde for subsequent experiments. All studies were approved by the Laboratory Animal Welfare and Ethics Committee.

**2.2. Extraction and Identification of Exosomes in Sepsis-Cardiomyocyte of Mice.** Cardiomyocytes from control or septic mice were ground, and the supernatant fluid was collected and centrifuged at 4°C and 1000 g for 10 min to remove cells and cell debris and then at 4°C and 12000 g for 30 min to remove small particles such as organelles. Later, the supernatant was harvested and filtered by a 0.22  $\mu$ m filter membrane to remove particles with a size larger than 200 nm. Finally, the filtrate was centrifuged at 4°C and 120000  $\times$  g for 90 min, and the precipitate obtained after centrifugation was the exosomes. The exosomes were resuspended in PBS buffer (pH = 7.4) and then stored in a refrigerator at -80°C for later use. After the culture is complete, the medium is collected and centrifuged (10,000  $\times$  g, 30 min, 4°C). The supernatant was then centrifuged at 4°C (110,000  $\times$  g for 70 min). Wash the precipitate with PBS and centrifuge again at 150,000 g for 120 min at 4°C [25]. TEM was used to detect exosome morphology: the exosomes were dropped on a 2 mm copper grid and left for 1 min before adding uranyl acetate staining for 1 min. After drying, the morphology of cellular exosomes was determined by TEM [26].

**2.3. Isolation and Culture of Bone Marrow-Derived Macrophages.** The bone marrow of TLR9<sup>-/-</sup> mice and WT mice were aseptically harvested in an ultraclean bench, pipetted into a 100 mm<sup>2</sup> culture dish with 10 mL of induction medium using a sterile syringe, and then pipetted evenly with a pipette tip. On the 3<sup>rd</sup> day [27, 28], 7 mL of culture supernatant was gently discarded, which was replaced with a fresh induction medium. On the evening of the 6<sup>th</sup> day, the culture supernatant was discarded and replaced with DMEM containing 10% FBS and double antibody, and the cells were cultured overnight. On the 7<sup>th</sup> day, after the samples were washed with phosphate-buffered saline (PBS) 3 times, the nonadherent cells were removed, and the

macrophages were digested with trypsin for later tests, according to the previous method [29].

**2.4. Culture and Grouping of Primary Cardiomyocytes.** The neonatal mice were collected using sterile tweezers and soaked in 75% alcohol for skin disinfection under a relatively sterile environment. Their hearts were cut into small pieces and rinsed repeatedly with PBS until the rinsing solution was clear. Later, the heart tissues were collected and transferred into a culture flask, which were then added with an appropriate amount of trypsin digest cardiomyocytes for 2-3 minutes, and then left to stand at 4°C overnight. Then, it was added with an appropriate amount of low-glucose DEME complete medium and shaken in a constant temperature water bath box at 37°C at a uniform speed for 5 min. Thereafter, the supernatant was discarded. The tissues were added with 1 mL of collagenase type II and shaken gently in a water bath at 37°C for 30 s, and then, the supernatant was discarded to remove blood cells. Next, 1 mL of collagenase type II was added into the culture flask again. After shaking at 37°C for 15 min in a constant temperature water bath box, the supernatant was collected into a centrifuge tube. The digestion could be repeated many times. After the collected supernatant was centrifuged at 1,000 rpm for 3 min, the supernatant was discarded, and the precipitate obtained was cardiomyocytes. Later, the cell suspension was inoculated into a petri dish and incubated in a 5% CO<sub>2</sub> incubator at 37°C, and the culture medium was replaced after 24 h, according to the previous method of primary cardiomyocyte culture [30]. Thereafter, the bone marrow-derived macrophages of TLR9<sup>-/-</sup> mice and WT mice were added into or cocultured with cardiomyocytes, and sepsis-induced cardiomyocyte injury was induced with lipopolysaccharides purchased from Solarbio No. L8880 (LPS: 1 mg/L for 24 h) [31]. The cardiomyocytes were divided into four groups: WT group, TLR9<sup>-/-</sup> group, WT+LPS group, and TLR9<sup>-/-</sup>+LPS group.

**2.5. Western Blotting.** Total proteins were extracted from macrophages and cardiomyocytes using radioimmunoprecipitation assay (RIPA) lysis buffer and phenylmethanesulfonyl fluoride (PMSF). The protease inhibitor PMSF was added to fully lyse the cells (PMSF : RIPA = 1 : 100). The cells were centrifuged at 4°C and 12000 g for 15 min. The supernatant was harvested into a 200 μL EP tube and stored at -20°C. The protein concentration in the supernatant was determined using the BCA kit. After SDS-PAGE, the target proteins were transferred onto the PVDF membrane and sealed with 5% skim milk powder at room temperature for 2 h, followed by incubation with primary antibodies (p-phosphatidylinositol 3-kinase (PI3K), p-protein kinase B (AKT), t-PI3K, t-AKT, cluster of differentiation 9 (CD9), CD63, tumor susceptibility gene 101 (TSG101), p-extracellular signal-regulated kinases 1/2 (ERK1/2), t-ERK1/2, TNF-α, IFN-γ, IL-1β, cytochrome C, cleaved-Caspase-3, Caspase-3, cleaved-Caspase-9, Caspase-9, and GAPDH at 4°C overnight. After that, the membrane was incubated again with HRP-labeled secondary antibodies at room temperature for 2 h. Finally, high-sensitivity ECL kits

and the FluorChem Q system were used for exposure, and quantitative analysis of protein was conducted in the Alpha-View software.

**2.6. JC-1 Fluorescence Labeling Assay.** After the cells were washed twice with PBS and centrifuged at 2000 g for 5 min, 2 × 10<sup>6</sup> cells were collected, added with 1 mL of 1 × incubation buffer and 2 μL of JC-1, mixed evenly, and incubated in a 5% CO<sub>2</sub> incubator at 37°C for 15 min. Later, the supernatant was discarded after centrifugation, and the cells were resuspended with 1 mL of 1 × incubation buffer, followed by detection using a flow cytometer. The above specimens were stained with fluorescence, the different fluorescence colors in 200 cells were observed and counted under a fluorescence microscope, and their percentages were calculated.

**2.7. Statistical Analysis.** CellQuest Pro software was utilized for image analysis, and SPSS 11.5 software was employed for data analysis. The measurement data were expressed as mean ± standard deviation. The experiment was performed 3 times in each group, and the images displayed representative results. One-way ANOVA was used for intergroup comparison, and *t*-test was adopted for comparison between groups. *P* < 0.05 indicated that the difference was statistically significant.

### 3. Results

**3.1. Myeloid TLR9 Deficiency Improved Structure and Morphology of Myocardium Under Sepsis.** Excessive host responses to infection result into sepsis, which induced structural damage of cardiomyocytes and eventually lead to the sepsis-induced cardiac dysfunction, thereby the pathological morphology of cardiomyocytes was firstly observed in this study. We found that in control mice, there were no significant abnormal changes in the heart, mainly exhibited the healthy tissue' morphological structure, whereas in sepsis mice, the WT BMT mice' myocardium showed relatively extensive cellular shrinkage, chromatin condensation, and nuclear fragmentation, and in TLR9<sup>-/-</sup> BMT mice, these pathological changes were relieved; all these observation indicated that myeloid TLR9 could accelerate the progression of SIC by destroying structures of cell and organelle; all results are shown in Figure 1.

**3.2. Myeloid TLR9 Knockout Inhibited the Expression of Apoptotic Protein Expressions of Cardiomyocyte in Septic Mice.** Cardiomyocytes hardly regenerate and thereby their apoptosis or death is the key and typical characteristics for SIC, and the progression of apoptosis results into the cardiac dysfunction. Prevention of cardiomyocyte death is a pivotal therapeutic strategy for sepsis. In this study, we found in SIC that the myocardial apoptotic proteins of cleaved-caspase-3 and -9 were remarkably increased vs. control groups. Identifying the death or apoptosis was common phenomenon in sepsis-induced cardiac injury. These proteins in TLR9<sup>-/-</sup> BMT mice cardiomyocytes were significantly decreased compared with WT BMT mice under sepsis inhibited, and all results are shown in Figure 2, which preliminary confirmed the deteriorated effects of myeloid or macrophages' TLR9 in SIC.

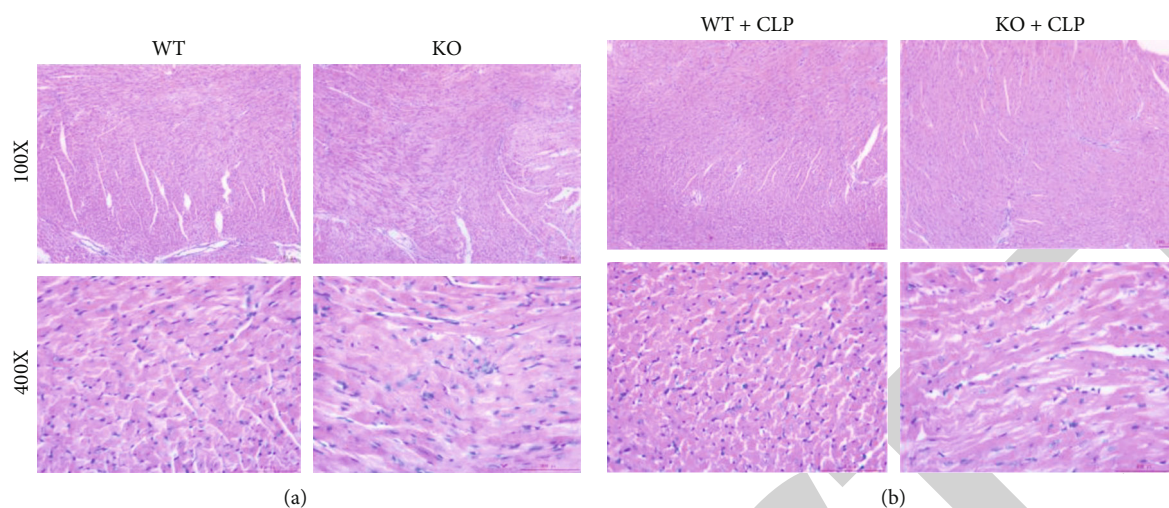


FIGURE 1: Myeloid deficiency of TLR9 improved morphology of cardiomyocytes in septic mice. (a) WT and TLR9<sup>-/-</sup> BMT mice in the control group showed health characteristics of cardiac cell structure. (b) TLR9<sup>-/-</sup> BMT mice improved or inhibited the extensive cellular shrinkage, chromatin condensation, and nuclear fragmentation compared with WT BMT mouse heart. Scar bar: 100  $\mu$ m.

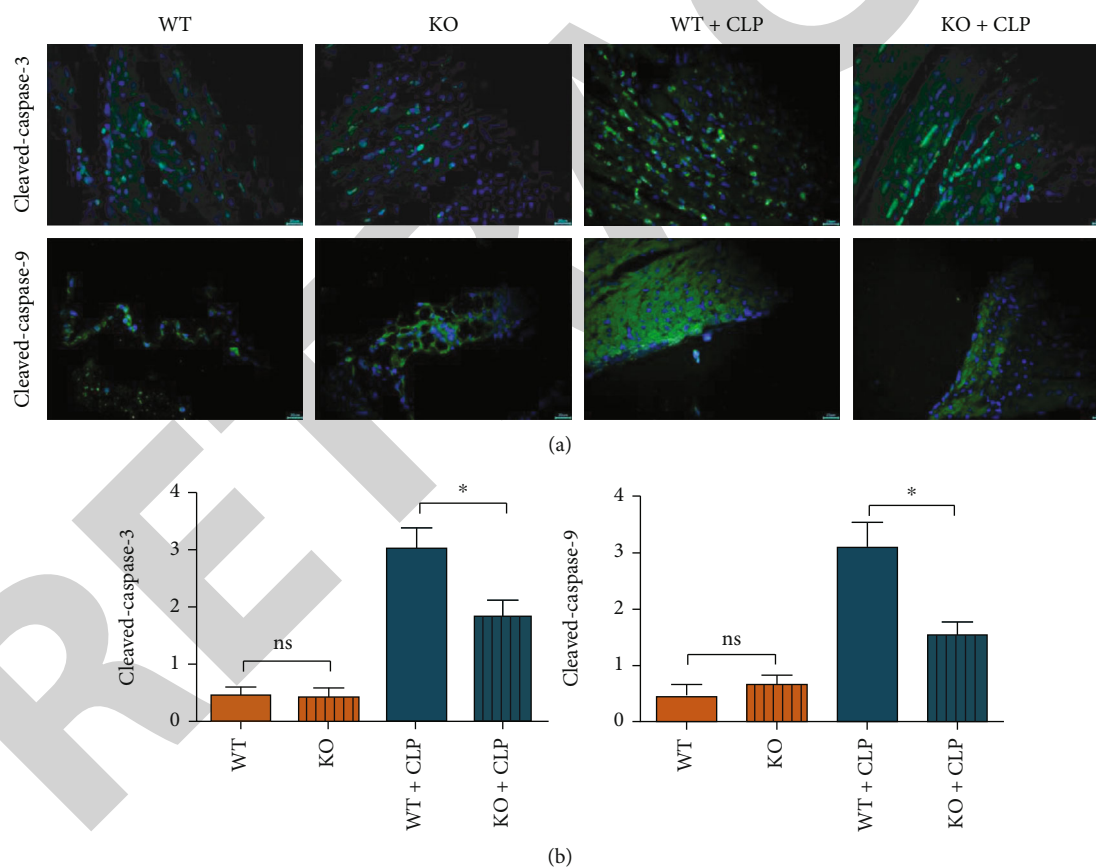


FIGURE 2: Myeloid deletion of TLR9 suppressed the expression of apoptotic associated proteins in septic mice. (a) The expression of cleaved-caspase-3 and cleaved-caspase-9 of WT and TLR9<sup>-/-</sup> BMT mice in control and sepsis status. Statistic data of the relative fluorescence intensity of cleaved-caspase-3 and -9 in each group. \* < 0.05 and \*\* < 0.01 vs. septic mice BMT WT myeloid cells.

**3.3. TLR9 Deletion Suppressed the Secretion of Exosomes and Activation of the PI3K/AKT in Septic Mice.** In the initiation of CLP, PI3K is a powerful inflammation suppressor for avoiding excessive inflammatory response-induced organ

damage and dysfunction, and TLR-9 in macrophages is an important inducer for inflammatory responses in sepsis. Therefore, it was found in the CLP experiment that the expressions of p-PI3K, p-AKT, CD9, CD63, and TSG101

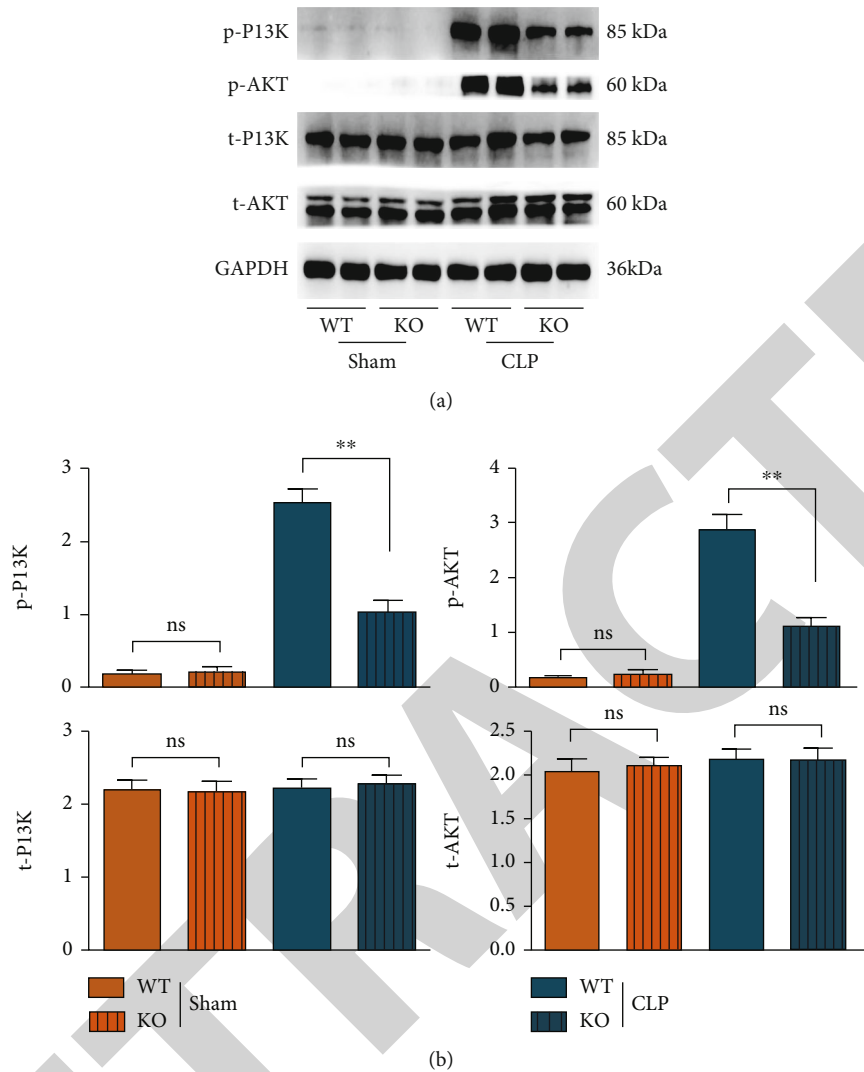


FIGURE 3: The PI3K signals were lower activated in septic mice BMT TLR9-deficient myeloid cells in early stage of sepsis. (a) The protein levels of phosphorylated and total levels of PI3K and AKT from the heart were WT and TLR9<sup>-/-</sup> BMT mice in control and sepsis status. (b) Statistic data of western blot were shown. \* < 0.05 and \*\* < 0.01 vs. septic mice BMT WT myeloid cells.

in bone marrow-derived macrophages of WT and TLR-9 KO mice increased significantly, while the expressions of t-PI3K and t-AKT were not significantly changed. In the CLP group, the expressions of p-PI3K, p-AKT (Figure 3), and exosome markers (CD9, CD63, and TSG101) (Figure 4) in macrophages of KO mice were significantly lower than those of WT mice, and moreover, the morphology of exosome was observed by TEM, to ensure the exosomes were correctly obtained in this study and shown in S3. In the sham group, there were no obvious differences in the expressions of these proteins between KO mice and WT mice. Considering that the PI3K signal is a primary and powerful promotor for exosome secretion, the findings above indicated that the TLR9 deficiency in macrophages suppresses exosome secretion, which is dependent on its inflammatory inhibition and decreased activation of PI3K signal in sepsis. The suppression of PI3K signal and exosomes in TLR9-deficient mice indicated mild rather than violent inflammation.

**3.4. TLR9 Deletion Could Repress the Activation of ERK1/2-Induced Inflammatory Factors in Septic Mice.** Sepsis is characterized by acute release of multiple inflammatory mediators (such as TNF- $\alpha$ , IL-6, and IL-1 $\beta$ ); excessive release of inflammatory mediators damage tissue and organs. There is increasing evidence that explosive inflammation is associated with cardiac cell death. In innate immune responses, TLR9 is a powerful inducer for the activation of ERK and its downstream inflammatory factors in macrophages, and macrophage-induced inflammation is key for myocardial damage and injury caused by sepsis, thereby the relationship between TLR9-ERK1/2 and inflammatory reactions was next evaluated and studied. Compared with those in the sham group, the expressions of p-ERK1/2, TNF- $\alpha$ , IFN- $\gamma$ , and IL-1 $\beta$  in macrophages of mice in the CLP group rose significantly, while the protein expression of t-ERK1/2 displayed no evident change. In the CLP group, the expressions of p-ERK1/2, TNF- $\alpha$ , interferon-gamma (IFN- $\gamma$ ), and IL-1 $\beta$  in macrophages of KO mice were significantly lower than

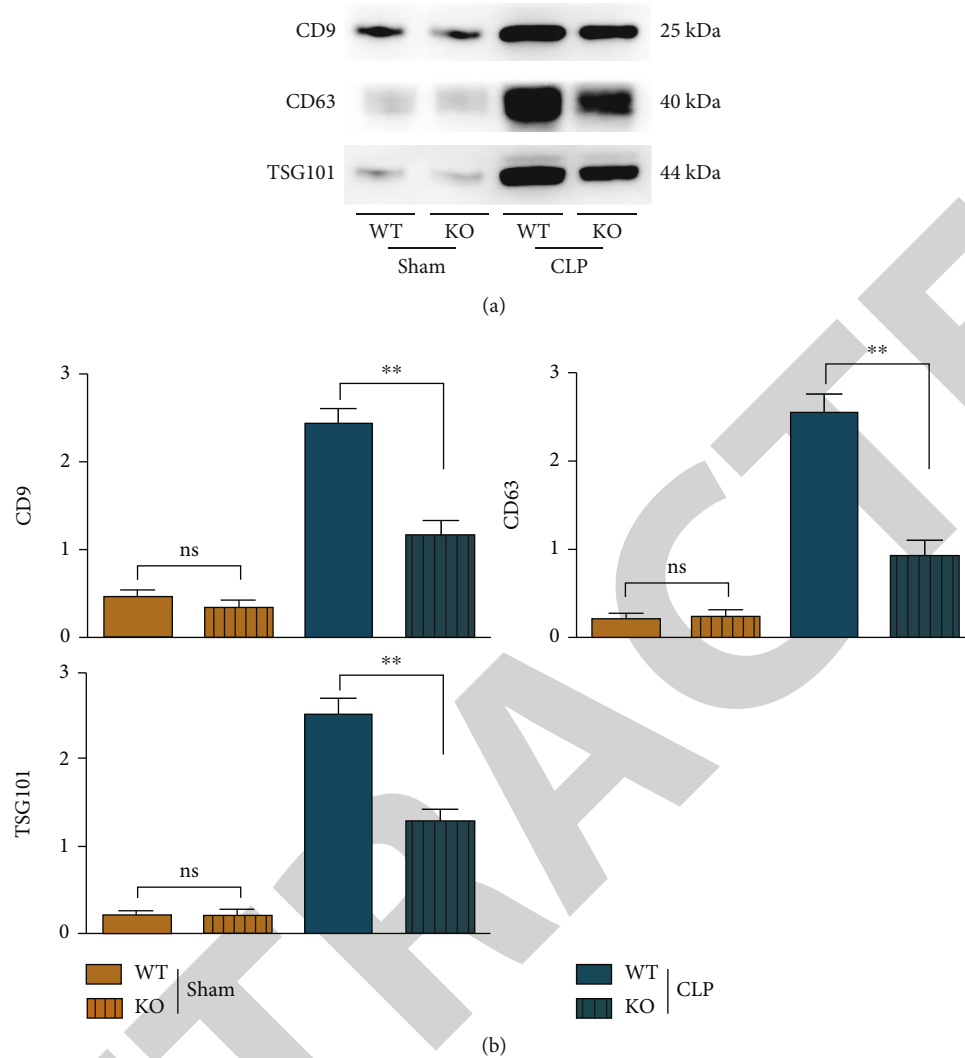


FIGURE 4: The exosome secretion was suppressed in septic mice BMT TLR9-deficient myeloid cells in early stage of sepsis. (a) The exosomes' marker of CD9, CD63, and TSG101 were tested by western blot in WT and TLR9<sup>-/-</sup> BMT mice of control and sepsis. (b) The statistic data tested by western blot in each group. \* <math><0.05</math> and \*\* <math><0.01</math> vs. septic mice BMT WT myeloid cells.

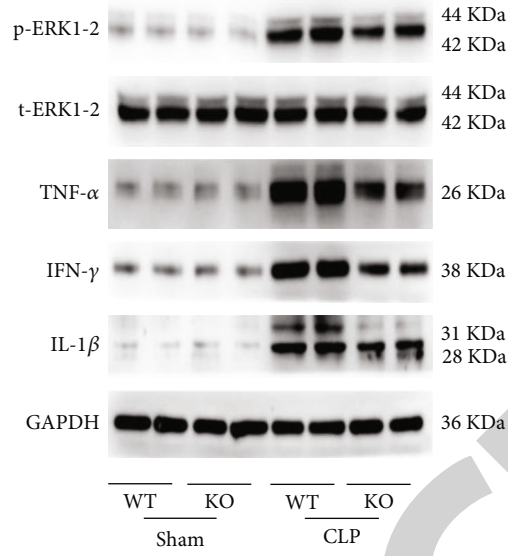
those of WT mice, while the protein expression of t-ERK1/2 displayed no marked difference. In the sham group, no significant differences were found in the expressions of these proteins between KO mice and WT mice, as shown in Figure 5. These results indicated that sepsis-induced inflammatory responses in macrophages are largely dependent on the TLR9 signal.

**3.5. TLR9 Deletion Could Inhibit Myocardial Mitochondrial Apoptosis in Myocardial Tissues of Septic Mice.** Apoptosis or death is a salient characteristic of myocardial damage in sepsis, so the relevant indicators were evaluated in sepsis mice. Macrophage-induced inflammation is a major and important factor for myocardial death in sepsis. Compared with those in the sham group, the protein expressions of cytochrome C, cleaved-Caspase-3, and cleaved-Caspase-9 in myocardial tissues of mice in CLP group were significantly increased. In CLP group, the protein expressions of

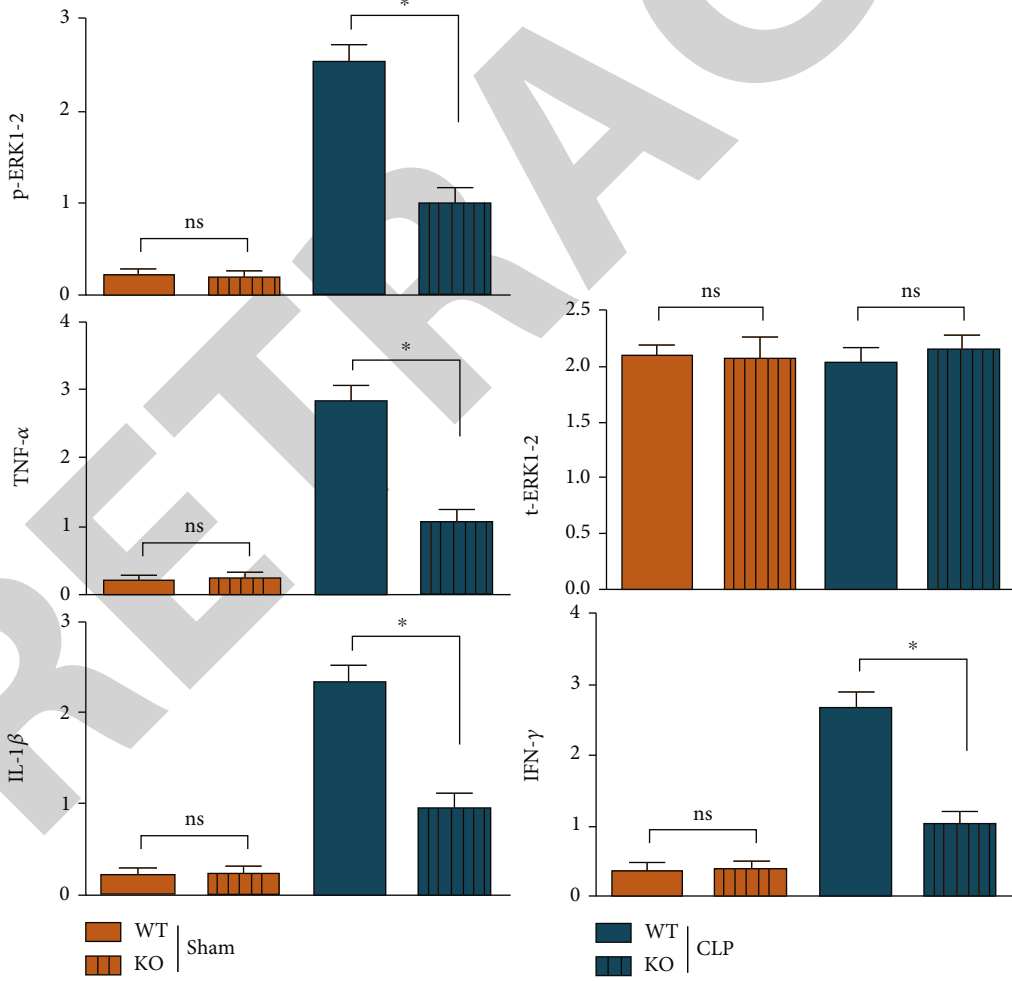
cytochrome C, cleaved-Caspase-3, and cleaved-Caspase-9 in KO mice declined markedly compared with those in WT mice, while the protein expressions of Caspase-3 and Caspase-9 displayed no significant changes. The results indicated that sepsis significantly induces apoptosis and TLR9 deficiency relieves apoptosis or death, which may depend on its inflammatory inhibition.

**3.6. Macrophages from TLR9<sup>-/-</sup> Mice Weakened Apoptosis of Primary Cardiomyocytes In Vitro Experiments.** The primary cardiomyocytes cocultured with macrophages from WT or TLR9<sup>-/-</sup> mice were treated with or without LPS to imitate the sepsis cellular model. After LPS stimulation, the protein expressions of cytochrome C, cleaved-Caspase-3, and cleaved-Caspase-9 in mouse cardiomyocytes increased remarkably, while the protein expressions of Caspase-3 and Caspase-9 displayed no obvious changes. Compared with those in the WT+LPS group, the protein expressions of





(a)



(b)

FIGURE 5: Continued.

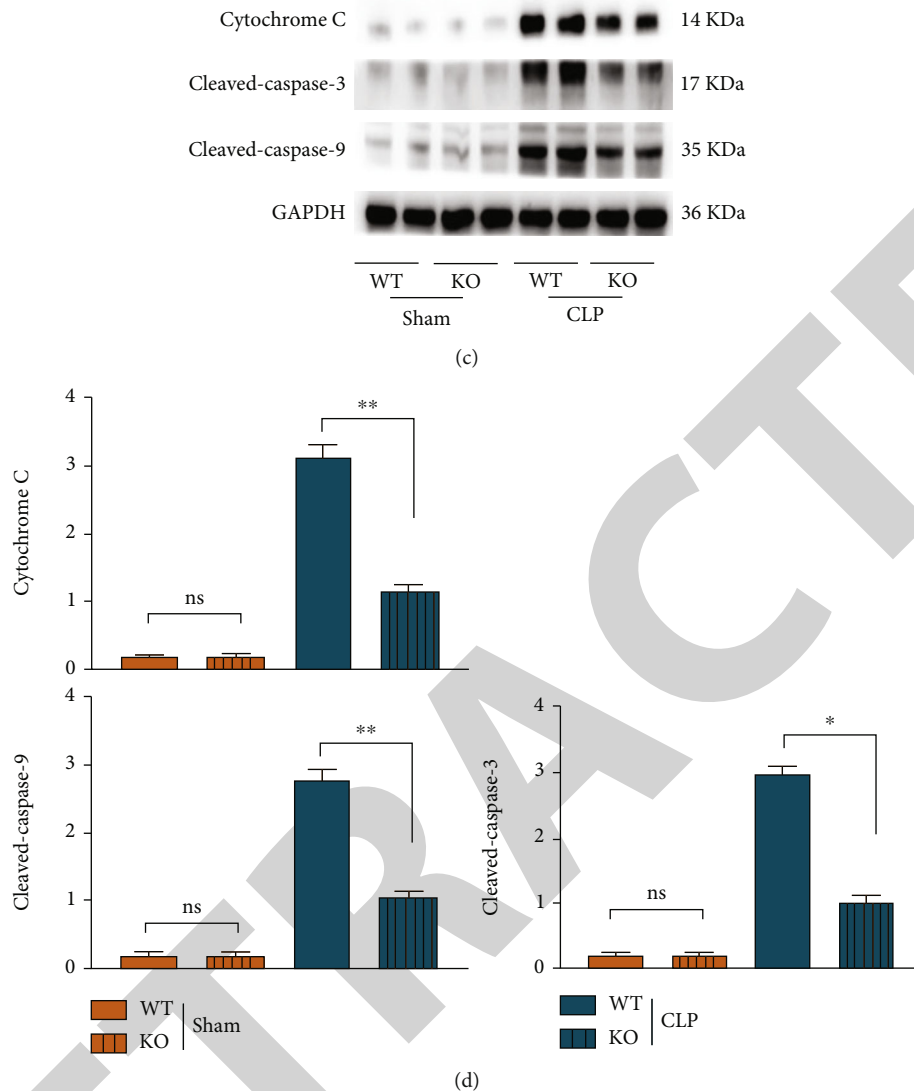


FIGURE 5: The expressions of ERK-associated inflammatory factors were inhibited in septic mice BMT TLR9-deficient myeloid cells. (a) The cardiac protein levels of phosphorylated levels of ERK1/2 and downstream TNF- $\alpha$ , IFN- $\gamma$ , and IL-1 $\beta$  as well as the apoptotic associated proteins: cytochrome C and cleaved-caspase-3/-9 were tested by western blot in WT and TLR9<sup>-/-</sup> BMT mice of control and sepsis groups. (b) The statistic data tested by western blot in each group. \* < 0.05 and \*\* < 0.01 vs. septic mice BMT WT myeloid cells.

cytochrome C, cleaved-Caspase-3, and cleaved-Caspase-9 in the TLR9<sup>-/-</sup>+LPS group declined dramatically, while the protein expressions of Caspase-3 and Caspase-9 had no significant changes (Figure 6). These results suggested that TLR9 promotes the sepsis-induced myocardial damage or apoptosis, which may depend on the raised level of exosomes carrying inflammatory cytokines.

**3.7. Variation of Mitochondrial Membrane Potential in Cardiomyocytes In Vitro Experiments.** It was observed under the fluorescence microscope that JC-1 formed aggregates in normal cells and emitted orange-red fluorescence. In apoptotic cells, JC-1 existed in the form of monomers and emitted green fluorescence. When the mitochondrial membrane potential is high, JC-1 aggregates in the matrix of mitochondria, forming a polymer that can generate red fluorescence.

When the mitochondrial membrane potential is low, JC-1 cannot aggregate in the matrix of mitochondria. At this time, JC-1 is a monomer that can generate green fluorescence. Therefore, the decrease of mitochondrial membrane potential is a landmark event in the early stage of apoptosis. The decrease of cell membrane potential can be easily detected by the change of JC-1 from red fluorescence to green fluorescence. At the same time, the change of JC-1 from red fluorescence to green fluorescence can also be used as an indicator for early apoptosis. After induction with LPS, the number of green fluorescent cells in cardiomyocytes of mice increased, and the  $\Delta\psi_m$  increased. The number of cells emitting green fluorescence declined, and the  $\Delta\psi_m$  decreased in primary cardiomyocytes cocultured with the TLR9<sup>-/-</sup> macrophages+LPS group compared with those in the WT+LPS group (Figure 7).

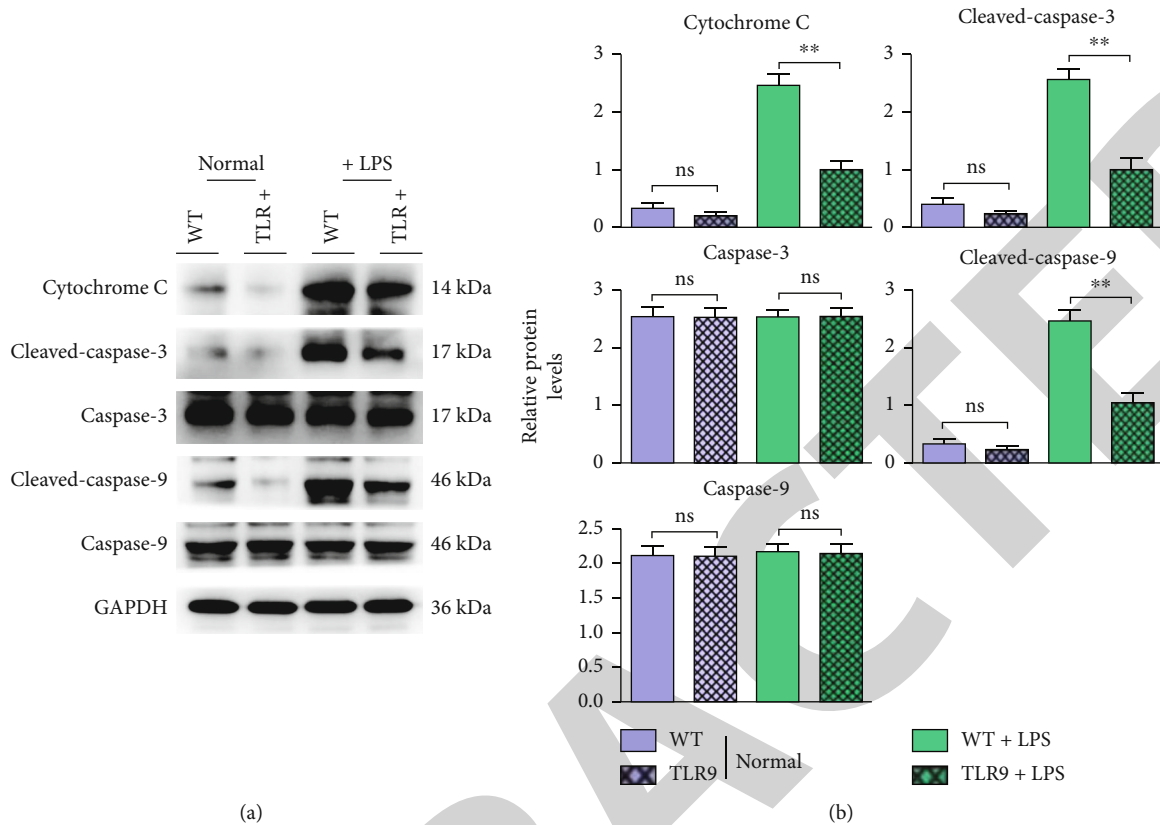


FIGURE 6: The apoptotic associated proteins were suppressed in cardiomyocytes cocultured with macrophages' TLR9 deficiency. (a) The protein levels of cytochrome C and cleaved-caspase-3/-9 were tested by western blot in WT and TLR9<sup>-/-</sup> BMT mice of control and sepsis groups. (b) The statistic data tested by western blot in each group. \* < 0.05 and \*\* < 0.01 vs. primary cardiomyocytes cocultured with WT macrophages.

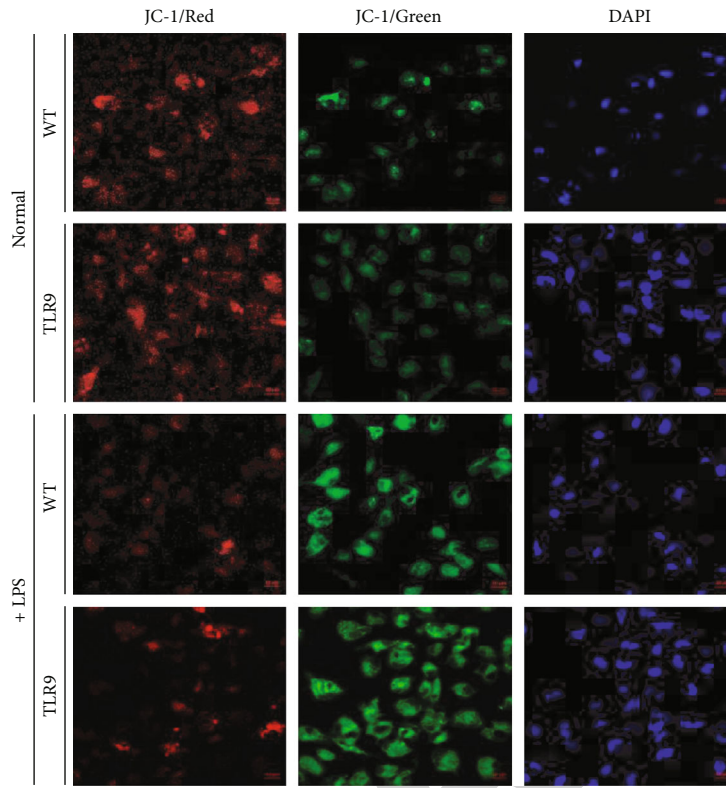
#### 4. Discussion

As one of the most common critical diseases in clinic, sepsis will induce multiple organ failure, posing a heavy burden on the healthcare system. Starting with infection, this life-threatening disease activates systemic inflammatory response through the production of proinflammatory factors [32]. A cytokine-induced excessive inflammatory response will result in the initial inflammatory "cytokine storm," which triggers myocardial injury and cardiac dysfunction, dramatically elevating the mortality of patients [33]. The results of this study manifested that (1) TLR9 deletion could inhibit the activation of the PI3K/AKT signaling pathway in bone marrow-derived macrophages of septic mice, thereby suppressing the secretion of exosomes. (2) TLR9 deletion could repress the activation of ERK in bone marrow-derived macrophages of septic mice, thereby reducing the secretion of inflammatory factors. (3) TLR9 deletion attenuated the mitochondrial apoptosis in mouse cardiomyocytes by interfering with the secretion of exosomes from bone marrow-derived macrophages in septic mice.

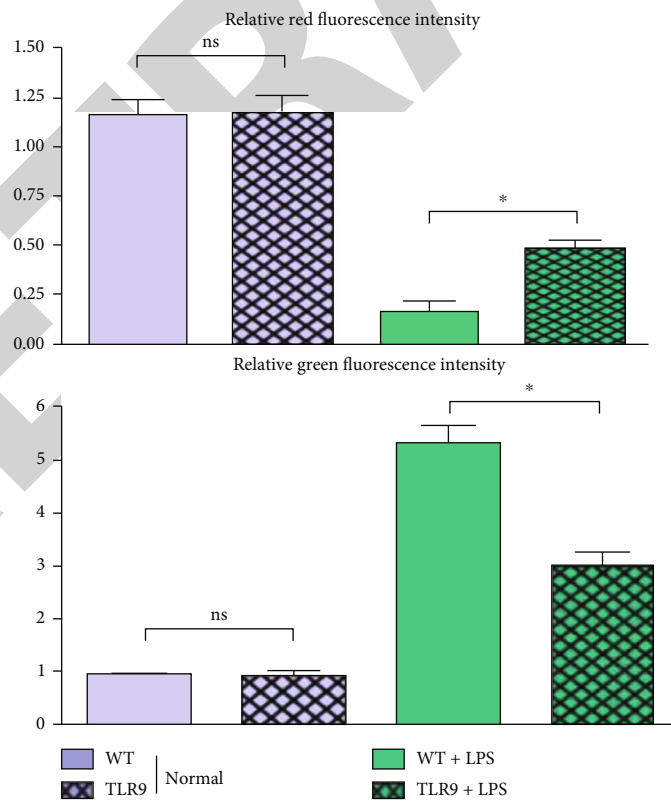
Myeloid cells mainly and especially the macrophages act as the source of inflammation and direct executor for sepsis. Excessive inflammatory responses are major factors for self-injury in the initiation of sepsis, and the host balance in immune responses especially innate immunity appears par-

ticularly important at this stage. Moreover, TLR trigger pro-inflammatory factor burst by recognizing various bacterial sequences and forming a positive feedback loop. Meanwhile, PI3K is activated as a compensatory negative feedback signal to limit excessive inflammatory signaling [34, 35]. Our findings reflected the overall condition of sepsis-induced injury of cardiomyocytes, and TLR9 deficiency-induced inflammatory inhibition was consistent with the lower activation of PI3K; in other words, a forceful anti-inflammatory mechanism of PI3K is not needed under myeloid TLR-9 deletion in septic cardiomyopathy. Considering that the exosome secretion is mainly modulated by PI3K signals and exosomes act as carriers for extreme inflammatory factors, the suppressed or lowered secretion of exosomes from myeloid macrophages also plays a protective role for sepsis. The activation of PI3K and AKT and the expressions of exosomes CD9, CD63, and TSG101 from WT septic mice increased, and the secretion of macrophage exosomes in TLR9<sup>-/-</sup> mice was significantly weaker than that in WT mice, which were all found in our in vivo or mouse experiments. In conclusion, myeloid TLR9 deficiency ameliorates inflammatory, strongly implying the mild rather than violent inflammation in sepsis in myeloid TLR9-deletion environments (Figures 3 and 4).

Additionally, combining with sepsis can activate the ERK signaling pathway and promote the secretion of



(a)



(b)

FIGURE 7: Macrophages' TLR9 deficiency improved cardiomyocytes' mitochondrial membrane potential. (a) The intensity of JC-1 fluorescence in WT and TLR9<sup>-/-</sup> BMT mice of control and sepsis groups. (b) The statistic data tested by JC-1 staining in each group. \* <math><0.05</math> and \*\* <math><0.01</math> vs. primary cardiomyocytes cocultured with WT macrophages.

inflammatory factors, thus resulting in inflammatory response [16]. Hence, the activation of ERK and the expressions of inflammatory factors in macrophages in mice were further detected in this study. Our results revealed that the expressions of p-ERK and inflammatory factors TNF- $\alpha$ , IFN- $\gamma$ , and IL-1 $\beta$  in bone marrow-derived macrophages of KO mice were significantly lower than those in WT mice in sepsis, suggesting that TLR9 deletion can repress the activation of ERK, thereby reducing the inflammatory response. Previous studies focused on TLR-9 and the excessive inflammatory response in cells, such as neutrophils, macrophages, fibroblastic reticular cells, and cardiomyocytes, but the interactions and relationships between two different types of cells in sepsis remain unclear and are urgently needed to clarify [36–39]. This study tried to elaborate on the mechanisms of macrophage TLR-9 in PI3K signal, exosome secretion, inflammatory responses, and myocardial apoptosis in sepsis.

In sepsis, proinflammatory cytokines such as TNF- $\alpha$  and IL-1 $\beta$  trigger the inflammation cascade, inducing a systemic inflammatory cascade response, which can cause myocardial injury, apoptosis, and cardiac dysfunction [17, 40]. The protein expressions of cytochrome C, cleaved-Caspase-3, and cleaved-Caspase-9 rose remarkably in the myocardial tissues of septic mice, and they were significantly lower in TLR9<sup>-/-</sup> mice than those in WT mice. Meanwhile, the exosomes from bone marrow-derived macrophages of TLR9<sup>-/-</sup> mice and WT mice were added into the cardiomyocyte culture medium, respectively, and cardiomyocyte injury was induced with LPS to construct the sepsis models *in vitro*. It was found that in LPS-induced mouse cardiomyocytes, the expressions of mitochondrial apoptosis-related proteins in exosomes from bone marrow-derived macrophages of TLR9<sup>-/-</sup> mice were significantly lower than those in exosomes from bone marrow-derived macrophages of WT mice, which is consistent with the results of *in vivo* experiments. These results suggested that TLR9 deletion attenuates mitochondrial apoptosis in mouse cardiomyocytes by interfering with the secretion of exosomes from bone marrow-derived macrophages of septic mice. Although new findings about the effects of macrophage TLR-9 on sepsis-induced cardiomyocyte apoptosis were obtained, this study had deficiencies. The living cell workstation can be used to observe the interaction between macrophages and cardiomyocytes from the perspective of space and time analysis, transmission electron microscope can be used to observe the structural changes of subcellular organelles in myocardial cells at different times in sepsis, and the inflammatory data of microfluidic single cell proteome and single-cell intracellular phosphorylation proteomics can be obtained by single-cell proteomics for innate immunologic macrophages of TLR-9<sup>-/-</sup> mice, which can be used to evaluate and assess the macrophage status in a panoramic state. Moreover, our research may provide the macrophages' TLR-9 levels may be used as a monitoring marker in clinical practice for evaluating the severity of sepsis.

In summary, in early stage of sepsis, TLR9 deletion can inhibit activation of ERK-associated inflammatory responses and meanwhile improved the PI3K/AKT signals as well as exosome secretion, the key regulators for limitation of inflammation, eventually resulted into the protective roles SIC.

## Abbreviations

CLP:	Cecal ligation and puncture
LPS:	Lipopolysaccharides
PI3K:	Phosphatidylinositol-3-kinase
AKT:	p-protein kinase B
CD9, CD63:	Exosome markers
TSG101:	Tumor susceptibility gene 101
ERK1/2:	p-extracellular signal-regulated kinases 1/2
TNF- $\alpha$ :	Tumor necrosis factor-alpha
IFN- $\gamma$ :	Interferon gamma
IL-1 $\beta$ :	Interleukin-1 beta
BMT:	Bone marrow transplanted
TLR9 <sup>-/-</sup> :	Toll-like receptor 9
WT:	Wild type
TEM:	Transmission electron microscope.

## Data Availability

The data used to support the findings of this study are available from the corresponding author upon request.

## Conflicts of Interest

The authors declare that the research was conducted in the absence of any commercial or financial relationships that could be construed as a potential conflict of interest.

## Authors' Contributions

Xiang Li and Junyu Luo wrote, reviewed, and revised the manuscript. Xiang Li and Junyu Luo contributed equally to this work and should be considered co-first authors. Xiang Li, Junyu Luo, Yanmei Li, and Yunpeng Luan conceived and designed the study. Yanmei Li, Lu Jia, Yuejin Li, Shili Ye, and Lanlan Liu analyzed and interpreted the data. Yanxuan Yu and Yonggang Lu developed the methodology.

## Acknowledgments

This work is supported by the National Natural Science Foundation of China (NSFC) (32160223) and Young Academic and Technical Leaders of Yunnan Province (202105AC160047) and Joint Specific Project of Basic Research of TCM Application of Yunnan Province (30370103808).

## References

- [1] M. Shankar-Hari, G. S. Phillips, M. L. Levy et al., "Developing a new definition and assessing new clinical criteria for septic shock: for the Third International Consensus Definitions for Sepsis and Septic Shock (Sepsis-3)," *Jama*, vol. 315, no. 8, pp. 775–787, 2016.
- [2] C. Fleischmann, A. Scherag, N. K. Adhikari, C. S. Hartog, and K. J. A. J. R. C. C. M. Reinhart, "Assessment of global incidence and mortality of hospital-treated sepsis Current Estimates and Limitations," *American Journal of Respiratory and Critical Care Medicine*, vol. 193, no. 3, pp. 259–272, 2016.

- [3] M. Proietti and G. F. J. C. Romiti, "Management of ventricular heart rate in atrial fibrillation patients with sepsis," *Chest*, vol. 159, no. 4, pp. 1315–1316, 2021.
- [4] M. M. Parker, J. H. Shelhamer, S. L. Bacharach et al., "Profound but reversible myocardial depression in patients with septic Shock," *Annals of Internal Medicine*, vol. 100, no. 4, pp. 483–490, 1984.
- [5] W. Wang, H. Xu, H. Lin, M. Molnar, and H. J. I. I. Ren, "The role of the cholinergic anti-inflammatory pathway in septic cardiomyopathy," *International Immunopharmacology*, vol. 90, article 107160, 2020.
- [6] R. Wang, Y. Xu, Y. Fang et al., "Pathogenetic mechanisms of septic cardiomyopathy," *Journal of Cellular Physiology*, vol. 237, no. 1, pp. 49–58, 2022.
- [7] I. A. Hobai, J. Edgecomb, K. Labarge, and W. S. J. S. Colucci, "Dysregulation of intracellular calcium transporters in animal models of sepsis-induced cardiomyopathy," *Shock*, vol. 43, no. 1, pp. 3–15, 2015.
- [8] P. R. Kvietyts, D. N. J. F. R. B. Granger, and Medicine, "Role of reactive oxygen and nitrogen species in the vascular responses to inflammation," *Free Radical Biology and Medicine*, vol. 52, no. 3, pp. 556–592, 2012.
- [9] M. Sun, X. Han, D. I. Zhou et al., "BIG1 Mediates Sepsis-Induced Lung Injury by Modulating Lipid Raft-Dependent Macrophage Inflammatory Responses," *Acta Biochimica et Biophysica Sinica*, vol. 53, no. 8, pp. 1088–1097, 2021.
- [10] Y.-L. Gu, L.-L. Xiao, D.-J. Li, Y.-N. Liu, C.-J. Zhu, and S.-J. Zhang, "Gene knockout or inhibition of macrophage migration inhibitory factor alleviates lipopolysaccharide-induced liver injury via inhibiting inflammatory response," *Hepatobiliary & Pancreatic Diseases International*, vol. 20, no. 5, pp. 469–477, 2021.
- [11] J. S. Schorey and S. J. T. Bhatnagar, "Exosome function: from tumor immunology to pathogen biology," *Traffic*, vol. 9, no. 6, pp. 871–881, 2008.
- [12] C. Gutiérrez-Vázquez, C. Villarroya-Beltri, M. Mittelbrunn, and F. Sánchez-Madrid, "Transfer of extracellular vesicles during immune cell-cell interactions," *Immunological Reviews*, vol. 251, no. 1, pp. 125–142, 2013.
- [13] D. Patsouris, P. P. Li, D. Thapar, J. Chapman, J. M. Olefsky, and J. G. J. C. M. Neels, "Ablation of CD11c-positive cells normalizes insulin sensitivity in obese insulin resistant animals," *Cell Metabolism*, vol. 8, no. 4, pp. 301–309, 2008.
- [14] R. Medzhitov, "Toll-like receptors and innate immunity," *Nature Reviews Immunology*, vol. 1, no. 2, pp. 135–145, 2001.
- [15] N. Atalan, L. Acar, N. Yapici et al., "The relationship between sepsis-induced immunosuppression and serum Toll-like receptor 9 Level," *In Vivo*, vol. 32, no. 6, pp. 1653–1658, 2018.
- [16] R. Hashimoto, R. Kakigi, K. Nakamura et al., "LPS enhances expression of CD204 through the MAPK/ERK pathway in murine bone marrow macrophages," *Atherosclerosis*, vol. 266, pp. 167–175, 2017.
- [17] M. Xu, Z. Ye, X. Zhao, H. Guo, and R. J. C. S. Huang, "Deficiency of tenascin-C attenuated cardiac injury by inactivating TLR4/NLRP3/caspase-1 pathway after myocardial infarction," *Cellular Signalling*, vol. 86, article 110084, 2021.
- [18] T. Fukao and S. Koyasu, "PI3K and negative regulation of TLR signaling," *Trends in Immunology*, vol. 24, no. 7, pp. 358–363, 2003.
- [19] S. C. Kim, S. Wu, X. Fang et al., "Postconditioning with a CpG containing oligodeoxynucleotide ameliorates myocardial infarction in a murine closed-chest model," *Life Sciences*, vol. 119, no. 1–2, pp. 1–8, 2014.
- [20] M. Tong, A. H. Smith, and V. M. Abrahams, "Activated neutrophils propagate fetal membrane inflammation and weakening through ERK and neutrophil extracellular trap-induced TLR-9 signaling," *The Journal of Immunology*, vol. 206, no. 5, pp. 1039–1045, 2021.
- [21] Z. Cheng, S. T. Abrams, J. Austin et al., "The Central Role and Possible Mechanisms of Bacterial DNAs in Sepsis Development," *Mediators of Inflammation*, vol. 2020, Article ID 7418342, 11 pages, 2020.
- [22] X. Chen, S. Xing, Y. Feng et al., "Early stage transplantation of bone marrow cells markedly ameliorates copper metabolism and restores liver function in a mouse model of Wilson disease," *BMC Gastroenterology*, vol. 11, no. 1, pp. 1–8, 2011.
- [23] Y. Yang, N. L. Jorstad, C. Shiao et al., "Perivascular, but not parenchymal, cerebral engraftment of donor cells after non-myeoablative bone marrow transplantation," *Experimental and Molecular Pathology*, vol. 95, no. 1, pp. 7–17, 2013.
- [24] Q. M. He, F. F. Yu, X. Sun et al., "Establishment of A mixed chimeric mouse model of allogeneic bone marrow transplantation and its influencing factors," *Zhongguo Shi Yan Xue Ye Xue Za Zhi*, vol. 29, no. 2, pp. 603–609, 2021.
- [25] R. A. Dragovic, G. P. Collett, P. Hole et al., "Isolation of syncytiotrophoblast microvesicles and exosomes and their characterisation by multicolour flow cytometry and fluorescence nanoparticle tracking analysis," *Methods*, vol. 87, pp. 64–74, 2015.
- [26] G. Wang, H. Li, H. Long, X. Gong, S. Hu, and C. Gong, "Exosomes derived from mouse adipose-derived mesenchymal stem cells alleviate benzalkonium chloride-induced mouse dry eye model via inhibiting NLRP3 inflammasome," *Ophthalmic Research*, vol. 65, no. 1, pp. 40–51, 2022.
- [27] G. Toda, T. Yamauchi, T. Kadowaki, and K. Ueki, "Preparation and culture of bone marrow-derived macrophages from mice for functional analysis," *STAR Protocols*, vol. 2, no. 1, article 100246, 2021.
- [28] I. Pineda-Torra, M. Gage, A. de Juan, and O. M. Pello, "Isolation, culture, and polarization of murine bone marrow-derived and peritoneal macrophages," *Methods in Molecular Biology*, vol. 1339, pp. 101–109, 2015.
- [29] A. Assouvie, L. P. Daley-Bauer, and G. Rousselet, "Growing murine bone marrow-derived macrophages," *Methods in Molecular Biology*, vol. 1784, pp. 29–33, 2018.
- [30] E. Ehler, T. Moore-Morris, and S. Lange, "Isolation and culture of neonatal mouse cardiomyocytes," *Journal of Visualized Experiments*, vol. 79, article e50154, 2013.
- [31] Y. Qiao, L. Wang, T. Hu, D. Yin, H. He, and M. He, "Capsaicin protects cardiomyocytes against lipopolysaccharide-induced damage via 14-3-3 $\gamma$ -mediated autophagy augmentation," *Frontiers in Pharmacology*, vol. 12, article 659015, 2021.
- [32] J. Han, Y. Shi, G. Willis et al., "Mesenchymal stromal cell-derived syndecan-2 regulates the immune response during sepsis to foster bacterial clearance and resolution of inflammation," *The FEBS Journal*, vol. 289, no. 2, pp. 417–435, 2022.
- [33] P. G. Czaikoski, J. M. Mota, D. C. Nascimento et al., "Neutrophil extracellular traps induce organ damage during experimental and clinical sepsis," *PLoS One*, vol. 11, no. 2, article e0148142, 2016.
- [34] M. C. Manukyan, B. R. Weil, Y. Wang et al., "The phosphoinositide-3 kinase survival signaling mechanism in sepsis," *Shock*, vol. 34, no. 5, pp. 442–449, 2010.

## Retraction

# Retracted: Oxidative-Damaged Mitochondria Activate GABARAPL1-Induced NLRP3 Inflammasomes in an Autophagic-Exosome Manner after Acute Myocardial Ischemia

### Oxidative Medicine and Cellular Longevity

Received 1 August 2023; Accepted 1 August 2023; Published 2 August 2023

Copyright © 2023 Oxidative Medicine and Cellular Longevity. This is an open access article distributed under the Creative Commons Attribution License, which permits unrestricted use, distribution, and reproduction in any medium, provided the original work is properly cited.

This article has been retracted by Hindawi following an investigation undertaken by the publisher [1]. This investigation has uncovered evidence of one or more of the following indicators of systematic manipulation of the publication process:

- (1) Discrepancies in scope
- (2) Discrepancies in the description of the research reported
- (3) Discrepancies between the availability of data and the research described
- (4) Inappropriate citations
- (5) Incoherent, meaningless and/or irrelevant content included in the article
- (6) Peer-review manipulation

The presence of these indicators undermines our confidence in the integrity of the article's content and we cannot, therefore, vouch for its reliability. Please note that this notice is intended solely to alert readers that the content of this article is unreliable. We have not investigated whether authors were aware of or involved in the systematic manipulation of the publication process.

In addition, our investigation has also shown that one or more of the following human-subject reporting requirements has not been met in this article: ethical approval by an Institutional Review Board (IRB) committee or equivalent, patient/participant consent to participate, and/or agreement to publish patient/participant details (where relevant).

Wiley and Hindawi regrets that the usual quality checks did not identify these issues before publication and have since put additional measures in place to safeguard research integrity.

We wish to credit our own Research Integrity and Research Publishing teams and anonymous and named external researchers and research integrity experts for contributing to this investigation.

The corresponding author, as the representative of all authors, has been given the opportunity to register their agreement or disagreement to this retraction. We have kept a record of any response received.

### References

- [1] T. Zhang, D. Hou, J. He et al., "Oxidative-Damaged Mitochondria Activate GABARAPL1-Induced NLRP3 Inflammasomes in an Autophagic-Exosome Manner after Acute Myocardial Ischemia," *Oxidative Medicine and Cellular Longevity*, vol. 2022, Article ID 7958542, 19 pages, 2022.

## Research Article

# Oxidative-Damaged Mitochondria Activate GABARAPL1-Induced NLRP3 Inflammasomes in an Autophagic-Exosome Manner after Acute Myocardial Ischemia

Tiechun Zhang,<sup>1,2</sup> Dongyao Hou,<sup>1</sup> Jianrong He,<sup>1</sup> Xue Zeng,<sup>1</sup> Ruixue Liu,<sup>1</sup> Liangming Liu,<sup>3</sup> Tao Li,<sup>3</sup> Yingbin Xiao,<sup>4</sup> Ruiyan Ma ,<sup>4</sup> He Huang ,<sup>1</sup> and Chenyang Duan <sup>1</sup>

<sup>1</sup>Department of Anesthesiology, The Second Affiliated Hospital of Chongqing Medical University, Chongqing 400010, China

<sup>2</sup>Department of Rehabilitation, the Fifth People's Hospital of Chongqing, Chinese Academy of Sciences, Chongqing 400062, China

<sup>3</sup>Department of Shock and Transfusion, State Key Laboratory of Trauma, Burns and Combined Injury, Daping Hospital, Army Medical University, Chongqing 400042, China

<sup>4</sup>Department of Cardiovascular Surgery, Xinqiao Hospital, Army Medical University, Chongqing 400037, China

Correspondence should be addressed to Ruiyan Ma; [ruiyanma@tmmu.edu.cn](mailto:ruiyanma@tmmu.edu.cn), He Huang; [huanghe@cqmu.edu.cn](mailto:huanghe@cqmu.edu.cn), and Chenyang Duan; [duanchenyang1991@cqmu.edu.cn](mailto:duanchenyang1991@cqmu.edu.cn)

Received 1 July 2022; Accepted 12 September 2022; Published 30 September 2022

Academic Editor: Tian Li

Copyright © 2022 Tiechun Zhang et al. This is an open access article distributed under the Creative Commons Attribution License, which permits unrestricted use, distribution, and reproduction in any medium, provided the original work is properly cited.

**Objective.** This study is aimed at identifying the potential diagnostic markers for circulating endothelial cells (CECs) for acute myocardial ischemia (AMI) and exploring the regulatory mechanisms of the selected biomarker in mitochondrial oxidative damage and vascular inflammation in AMI pathology. **Methods.** Utilizing the Gene Expression Omnibus dataset GSE66360, we scanned for differentially expressed genes (DEGs) in 49 AMI patients and 50 healthy subjects. To discover possible biomarkers, LASSO regression and support vector machine recursive feature elimination examinations were conducted. Using the GSE60993 and GSE123342 datasets and AMI rat models, the expression levels and diagnostic accuracy of the biomarkers in AMI were thoroughly verified. CIBERSORT was employed to evaluate the compositional patterns of 22 distinct immunological cell percentages in AMI according to combined cohorts. The oxidative-damaged mitochondria were detected by confocal microscopy observation of MitoTracker, ROS-DCFH-DA, and mCherry-GFP-LC3B. **Results.** In total, 122 genes were identified. The identified DEGs primarily contributed in arteriosclerosis, arteriosclerotic cardiovascular disorders, bacterial infectious disorder, coronary artery disease, and myocardial infarction. Nine features (NR4A2, GABARAPL1 (GEC1), CLEC4D, ITLN1, SNORD89, ZFP36, CH25H, CCR2, and EFEMP1) of the DEGs were shared by two algorithms, and GABARAPL1 (GEC1) was identified and verified as a diagnostic mitochondrial biomarker for AMI. Confocal results showed that there existed mitochondrial damage and oxidative stress in cardiac CMECs after AMI, and the blocked autophagy flux could be released by exosome burst in cardiac CMECs and blood CECs. Immune cell infiltration testing declared that elevated GEC1 expression in blood CECs was linked to the rise of monocytes and neutrophils. Functional tests revealed that high GEC1 expression in CMECs and CECs could activate the vascular inflammatory response by stimulating NLRP3 inflammasome production after AMI. **Conclusion.** Oxidative-damaged mitochondria in cardiac CMECs activate GEC1-mediated autophagosomes but block autophagy flux after AMI. The exfoliated cardiac CMECs evolve into abnormal blood CECs, and the undegraded GEC1 autophagosomes produce a large number of NLRP3 inflammasomes by exosome burst, stimulating the increase in monocytes and neutrophils and ultimately triggering vascular inflammation after AMI. Therefore, GEC1 in blood CECs is a highly specific diagnostic mitochondrial biomarker for AMI.



## 1. Introduction

Acute myocardial ischemia (AMI) is an inevitable process of most cardiovascular diseases. Presently, early risk assessment of acute myocardial ischemia, myocardial infarction, and the coronary syndrome is primarily based on initial history and physical examination findings and electrocardiogram and cardiac biomarker measurements [1, 2]. Myocardial ischemia involves neuroendocrine hormone activation, myocardial stretch, myocardial injury, cardiac matrix remodeling, inflammation, and other pathophysiological processes, each of which involves related biomarkers, such as cTnT, cTnI, CK-MB, H-FABP, and Hs-CRP [3]. However, the related biomarkers to reflect the mitochondrial damage after AMI have not been studied.

Although the present biomarkers for AMI have been in use, there exist different limitations to some extent. For example, the value of CK-MB is sensitive but has low specificity to AMI. The expressions of cTnT and cTnI usually do not increase until at least 6 h after the onset of symptoms, and their measurements have low sensitivity in the early phase of AMI. After myocardial necrosis, the value of cTnT remains elevated for 10–14 days, and it is hard to detect recurrent myocardial damage [4]. As mitochondria are very sensitive to ischemia and hypoxia injury, evaluation of mitochondrial damage and oxidative stress after AMI by appropriate biomarkers may timely and sensitively reflect the damage of ischemia and hypoxia to cardiac cells.

Approximately one-third of the size of adult cardiac cells is occupied by mitochondria [5]. Besides supplying the vast bulk of the energy consumed by the heart, the mitochondrial role encompasses diverse essential biological and regulating activities, including redox balance [6], biosynthesis, reactive oxygen species signaling, cell proliferation and apoptosis, ion homeostasis [7], protein quality control [8], and inflammatory processes [9]. The dysfunction of mitochondria is closely related to the severity of myocardial damage after acute myocardial ischemia (AMI) [10]. Unbalanced mitochondrial dynamics can activate oxidative stress, and an oxidative stress state can also induce mitochondrial dynamics imbalance and energy metabolism disorder. Therefore, preserving mitochondrial activity and targeting oxidative stress may be crucial for rescuing cardiac function following AMI [11]. However, the detection of mitochondrial cardiac injury in clinical AMI patients and the influence of mitochondrial injury on prognosis are not clear.

Recent studies have identified novel populations of nonhematopoietic blood cells. Hardly observed in healthy blood, circulating endothelial cells (CECs), which are frequently characterized by the expression of membrane glycoprotein CD146, are elevated in a wide variety of clinical diseases, encompassing inflammatory, immunological, contagious, oncogenic, and cardiovascular disorders [12]. Increased CECs were found to anticipate worse cardiovascular outcomes in acute coronary syndromes; however, the underlying processes are still unexamined [13]. This work sought to uncover mitochondrial diagnostic markers in blood CECs that represent mitochondrial damage in cardiac tissue following AMI.

In the current study, we selected acute myocardial infarction as a typical clinical acute myocardial ischemic model to screen for mitochondrial-related genes with diagnostic efficacy in CECs of AMI using a machine learning algorithm and preliminarily explore the regulatory mechanisms of the selected biomarkers to mitochondrial oxidative damage and vascular inflammation in AMI pathology.

## 2. Materials and Methods

**2.1. Materials.** Antibodies against GABARAPL1 (GEC1), CD146, LC3, GAPDH, TSG101, CD63, NLRP3, caspase-1, and interleukin- (IL-)  $1\beta$  were acquired through Abcam (Cambridge, MA, USA). All PE- or FITC-conjugated secondary antibodies, MitoTracker Deep Red, Dynabeads, fetal bovine serum, and penicillin/streptomycin were obtained through Invitrogen (Carlsbad, CA, USA). AdmCherry-GFP-LC3 and ROS-DCFH-DA kit were acquired through Beyotime (Shanghai, China), while adenoviral vectors for GEC1 shRNA and AAV2-GEC1 shRNA were produced by GeneChem Technology (Shanghai, China). The endothelial basal medium EBM-2 medium kit was acquired through Lonza (Bern, Switzerland). Any other material was obtained through Sigma-Aldrich except if another source was mentioned.

**2.2. Animal Model Preparation.** Army Medical University, Research Institute of Surgery (Chongqing, China), supplied 220–270 g of male Sprague–Dawley rats. Left anterior descending (LAD) coronary artery occlusion was used to cause acute myocardial ischemia (AMI) in rats. The rats were sedated with 1% pentobarbital sodium (40 mg/kg, given i.p.) and oxygenated with a rodent ventilator (Shanghai Alcott Biotech Co., Ltd. China), a 6/0 suture, the LAD artery ligation. Effective blockage of the LAD was established by the existence of ST-segment elevation on the ECG (Guangzhou Sanrui Electronics Co., Ltd., China) and a coloration difference from bright red to light red in the ventricle. The musculature and skin were sutured separately for each layer, and the incisions were disinfected following assurance of effective shaping.

To reduce GEC1 expression in a rat model, adeno-associated virus- (AAV2-) shGEC1 was injected ( $5 \times 10^{13}$  v.g/mL, 1 mL/kg) into rats via the tail vein two weeks before LAD.

**2.3. Cell Culture and Hypoxia Treatment.** CMECs were cultivated in an EBM-2 media kit enriched with 100 U/mL penicillin/streptomycin at 37°C in a humidified incubator under typical circumstances (5% CO<sub>2</sub>, 21% O<sub>2</sub>, and 74% N<sub>2</sub>). For hypoxic trials, CMECs were cultivated in serum-free Dulbecco's modified Eagle's media and then transmitted to a hypoxic culture compartment (MIC-101, Billups-Rothenberg, Del Mar, CA, USA) saturated with 94% N<sub>2</sub>, 5% CO<sub>2</sub>, and 1% O<sub>2</sub> for 24 h.

**2.4. Isolation of CECs, CMECs, and Monocytes.** To isolate CECs and monocytes, 5 mL of blood from the abdominal aorta of rats including retrieved in a tube with ethylenediamine tetraacetic acid, diluted with 5 mL phosphate-buffered saline (PBS), and separated with rat peripheral blood

lymphocyte isolation buffer (Solarbio, China) to retrieve mononuclear cell suspensions. Mononuclear cells were further separated by density gradient centrifugation to obtain monocytes or used to isolate CECs by magnetic-activated cell sorting (MACS). To isolate CECs by MACS, the mononuclear cell suspensions were first incubated with Dynabeads conjugated to anti-rat CD45 for 30 min at 4°C to deplete the cells and platelets expressing CD45. Next, the cell suspensions were incubated with Dynabeads conjugated to anti-rat CD146 for 30 min at 4°C for positive selection of CECs.

To isolate the CMECs, the hearts of rats were first minced, digested with 0.2% collagenase type II in Hank's basal salt solution for 45 min at 37°C with rotation, and filtered with a 70  $\mu$ m cell strainer to obtain single-cell suspensions. The CMECs were sorted positively from the suspension by MACS using Dynabeads conjugated to anti-rat CD146.

**2.5. Screening of Differentially Expressed Genes (DEGs) and Diagnostic Value of Featured Biomarkers.** The GSE66360, GSE60993, and GSE123342 datasets' matrix files were downloaded at <http://www.ncbi.nlm.nih.gov/geo/>. The GSE66360 dataset was utilized for DEG scanning, while the GSE60993 and GSE123343 databases were utilized to validate the expression patterns of the identified genes. The GSE66360 data were evaluated and represented using R/Bioconductor [14]. Individual gene expression was deemed to be altered when  $|\log \text{ fold change}| > 1.5$ ; Welch's analysis of variance revealed a  $p$  value of 0.05 when comparing the mean normalized signal levels with the Bioconductor tool *genefilter*. To examine the role of DEGs, Bioconductor assessments of disease ontology (DO) enrichment, gene ontology (GO), and Kyoto Encyclopedia of genes and genomes (KEGG) were performed [15].

As described earlier [15], two distinct machine learning techniques, the least absolute shrinkage, and selection operator (LASSO) regression and the support vector machine recursive feature elimination (SVM-RFE) methods, were used to identify possible biomarkers among the DEGs. The overlapped genes between the two methods were chosen as possible predictive biomarkers, and their expression patterns were validated using the GSE60993 and GSE123343 databases.

Using mRNA expression information from the GEO public database, we developed a receiver operating characteristic (ROC) curve to evaluate the diagnostic accuracy of the chosen biomarkers. Furthermore, the area under the ROC curve (AUC) measure was utilized to estimate the diagnostic performance of distinguishing AMI samples from controls.

**2.6. Discovery of Immune Cell Subtypes.** As initially noted [15, 16], we used the bioinformatics tool (CIBERSORT) to calculate the relative ratios of immunological cell infiltration utilizing gene expression patterns in AMI to investigate immunity cell infiltration. Employing the "corrplot" R program, correlation analyses and visualization of 22 kinds of infiltrating immunological cells were done. Utilizing the

"vioplot" tool in R, the variations in immunological cell infiltration between AMI and control samples were visualized using violin graphs.

**2.7. Flow Cytometry Analysis.** The cells were preserved and permeabilized for 20 min at 4°C utilizing fixation and permeabilization solution (BD Bioscience, Franklin Lakes, NJ, USA). Following two rinses with perm/wash buffer (BD Bioscience, Franklin Lakes, NJ, USA), the cell pellet was resuspended and blocked with 2% bovine serum albumin (BSA) at room temperature for 15 min, then incubated for 1 h at 4°C with the suggested quantity of antibody (CD146, GABARAPL1, or NLRP3). Before conducting the flow cytometric examination, the cells were treated with fluorochrome-conjugated secondary antibodies, then incubated for 30 min at 4°C in the dark and rinsed two times.

**2.8. Immunofluorescence.** Heart cell specimens were stained with immunofluorescence, as described previously [10]. The slides were preserved in 4% paraformaldehyde for 20 min, permeabilized with 0.1% triton-X 100 in PBS for 5 min, covered with 5% BSA/PBS for 1 h at 37°C, and then incubated for one night at 4°C with primary antibodies against GABARAPL1. The specimens were therefore rinsed with PBS containing 0.1% Tween-20 and incubated for 1 h at room temperature with FITC-conjugated mouse or rabbit secondary antibodies (Invitrogen, Carlsbad, CA, USA). After that, the specimens were rinsed prior to a final rinsing in 1X PBS and incubation with 4',6-diamidino-2-phenylindole dye (BD Biosciences, Franklin Lakes, NJ, USA) (1:50) for 5 min at room setting. Using a confocal laser scanning microscope (Leica SP5, Germany), immunofluorescence was detected.

**2.9. Western Blotting.** The total protein was recovered by lysing the cells in ice-cold RIPA buffer, which was enriched using protease blockers (Beyotime, Shanghai, CHINA). The bicinchoninic acid (BCA) protein testing kit was utilized to get the results for protein contents (Beyotime, Shanghai, CHINA). After that, total protein was utilized for immunoblotting examinations utilizing the related antibodies, as was earlier [17]. The program Quantity One V 4.62 (Bio-Rad, Life Science, CA, USA) was utilized to perform an analysis of the band strengths.

**2.10. Mitochondrial Morphology Observation.** The mitochondrial morphology was observed as previously described [10]. Mitochondria in the CMECs were tagged with Mito-Tracker Deep Red (100 nM) at 37°C for 30 min. This was followed by the observation of the mitochondria employing confocal microscopy (Leica TCS SP5, Wetzlar, Germany) with a 60  $\times$  1.3 NA oil immersion objective. A laser with a wavelength of 633 nm was employed to activate mitochondrial fluorescence, and the emissions were captured at a wavelength range of 558–617 nm. The program ImageJ V1.8.0 was utilized to measure and compute the length of mitochondria as well as their aspect ratios.

**2.11. Measurement of ROS and Oxidative Stress.** The ROS production was detected as previously described [10]. CMECs were incubated with 10  $\mu$ M DCFH-DA at

37°C for 30 min. Using confocal microscopy (Leica TCS SP5, Wetzlar, Germany) with a 40x objective, DCFH-DA fluorescence was observed at an excitation wavelength of 488 nm and an emission wavelength ranging from 501 to 563 nm.

**2.12. Autophagic Flux Assay.** As per our earlier description, for determining the level of autophagy flux, Ad-mCherry-GFP-LC3B (Beyotime, Shanghai, CHINA) was used to transfect CMECs for 24 h [10]. Intense red fluorescent LC3 proteins revealed that autophagosomes became engulfed in the lysosomal acidic microenvironment to produce autolysosomes, which indicated a smooth autophagy flux. Intense yellow fluorescent LC3 proteins, on the other hand, indicated that autophagosomes were unable to be transformed into autolysosomes, which suggested that autophagy was inhibited.

**2.13. Exosome Extraction.** According to an earlier finding [18], the ultracentrifugation technique was employed to extract exosomes successfully. After centrifuging the cell specimens for 24 h at a speed of  $10,000 \times g$  and a temperature of 4°C, the supernatant was passed through a filter membrane with a pore size of 0.22  $\mu\text{m}$ . Then, the filtrate was centrifuged at  $120,000 \times g$  for 2 h at 4°C. After that, the supernatant was collected with care, and the precipitate was rinsed with an equal volume of cold PBS before being centrifuged at a speed of  $120,000 \times g$  for 2 h at 4°C. The sediment was reconstituted in 200  $\mu\text{L}$  of cold PBS and then placed in an ice bath at -80°C for viewing it utilizing transmission electron microscopy (TEM) and detecting proteins. The ZetaView SP2 program (Particle Metrix, Germany) was utilized to conduct an analysis of the exosomes' dimensions as well as their concentrations. To perform immunological blotting testing, identical quantities of exosome supernatant were placed into each well. The number of exosomes that were available was determined with the markers CD63 and TSG101.

**2.14. TEM Imaging.** To identify exosomes, 20  $\mu\text{L}$  of exosome suspension was placed on a fixed carbon mesh and let remain at room temperature for 20 min. After this period of time, the exosome suspension comprising the surplus discharge was carefully eliminated. After that, 20  $\mu\text{L}$  of phosphotungstic acid with a concentration of 2% was poured onto the carbon mesh, and it was allowed to rest for 20 s prior to transferring into a glass plate, which was covered with a filter membrane and maintained there until TEM inspection was carried out.

**2.15. Statistical Analysis.** All statistical calculations were carried out using R (version 3.6.3). Continuous variables were compared using Student's *t*-test for variables with normal distribution or the Mann-Whitney *U*-test for variables with an irregular distribution. In R, the "glmnet" tool was employed for the LASSO regression evaluation, whereas the "e1071" tool was employed for SVM technique assessment. Utilizing ROC curve modeling, the diagnostic accuracy of the included predictive biomarkers was determined. Spearman's correlation was utilized to investigate the connection between gene biomarker expression and immunological cell infiltration. Each statistical test was two-tailed, and  $p < 0.05$  was utilized to determine statistical significance.

### 3. Results

**3.1. Functional Correlation Analysis of the DEGs in AMI.** Blood samples of CECs from 49 AMI patients and 50 healthy controls in the GEO dataset (GSE66360) were examined in this research. A sum of 122 DEGs were obtained: the expressions of 114 genes were significantly upregulated, and that of eight genes were reduced significantly (Figure 1).

To discover the roles of DEGs, enrichment studies of DO pathways were performed. The findings demonstrated that arteriosclerosis, arteriosclerotic cardiovascular illness, bacterial contagious sickness, coronary artery disorder, and myocardial infarction were strongly linked to DEG-enriched disorders (Figure 2(a)). GO studies revealed that the majority of the biological functions were associated with neutrophil stimulation in immunological reaction, cytokine generation, and leukocyte chemotaxis (Figure 2(b)). The IL-17 signaling pathway, lipid and atherosclerosis, tumor necrosis agent signaling pathway, and cytokine-cytokine receptor interactions dominated the enriched KEGG pathways (Figure 2(c)). These outcomes significantly imply that the immunological reaction is a crucial factor in AMI.

**3.2. Identification and Verification of GABARAPL1 (GEC1) Gene as a Diagnostic Mitochondrial Biomarker for AMI.** Two methods were utilized to identify possible biomarkers.

The LASSO regression approach was employed to filter down DEGs, resulting in the discovery of 17 factors as predictive biomarkers for AMI (Figure 3(a)). By using the SVM-RFE technique, a collection of 40 DEG characteristics was identified (Figure 3(b)). Between these two methods, nine overlapped characteristics (NR4A2, GABARAPL1, CLEC4D, ITLN1, SNORD89, ZFP36, CCR2, and EFEMP1) were identified (Figure 3(c)). We observed that GABARAPL1 (GEC1), an essential mitochondrial-related gene, may have a crucial part in AMI (Figure 3(d)). Using the GSE60993 and GSE123342 datasets, the GEC1 expression pattern in the peripheral circulation was validated to give more accurate outcomes. Investigation of the GSE60993 data revealed that the expression pattern of GEC1 was significantly greater in ST-segment elevation myocardial infarction (STEMI) than in non-STEMI, unstable angina (UA), and normal controls (Figure 3(e)). GSE123342 dataset analysis showed that GEC1, as a mitochondrial biomarker, was especially suitable for the acute attack of AMI than for stable coronary artery disease (CAD) and long-term post-MI (Figure 3(f)). Subsequently, GEC1 was utilized to construct predictive modeling employing a logistic regression technique in the metadata cohort, and the diagnostic capacity of GEC1 in differentiating AMI from control cases was found to have a satisfactory predictive value (AUC: 0.936, 95% CI: 0.882–0.977) (Figure 3(g)), suggesting that GEC1 may be a high-diagnostic feature mitochondrial biomarker for AMI.

**3.3. High GEC1 in Blood CECs Is Due to Injured Cardiac CMECs Exfoliation Whose GEC1-Mediated Autophagy Is Overactivated after AMI.** We further verified the expression of GEC1 in AMI rats. CECs were extracted from whole rat

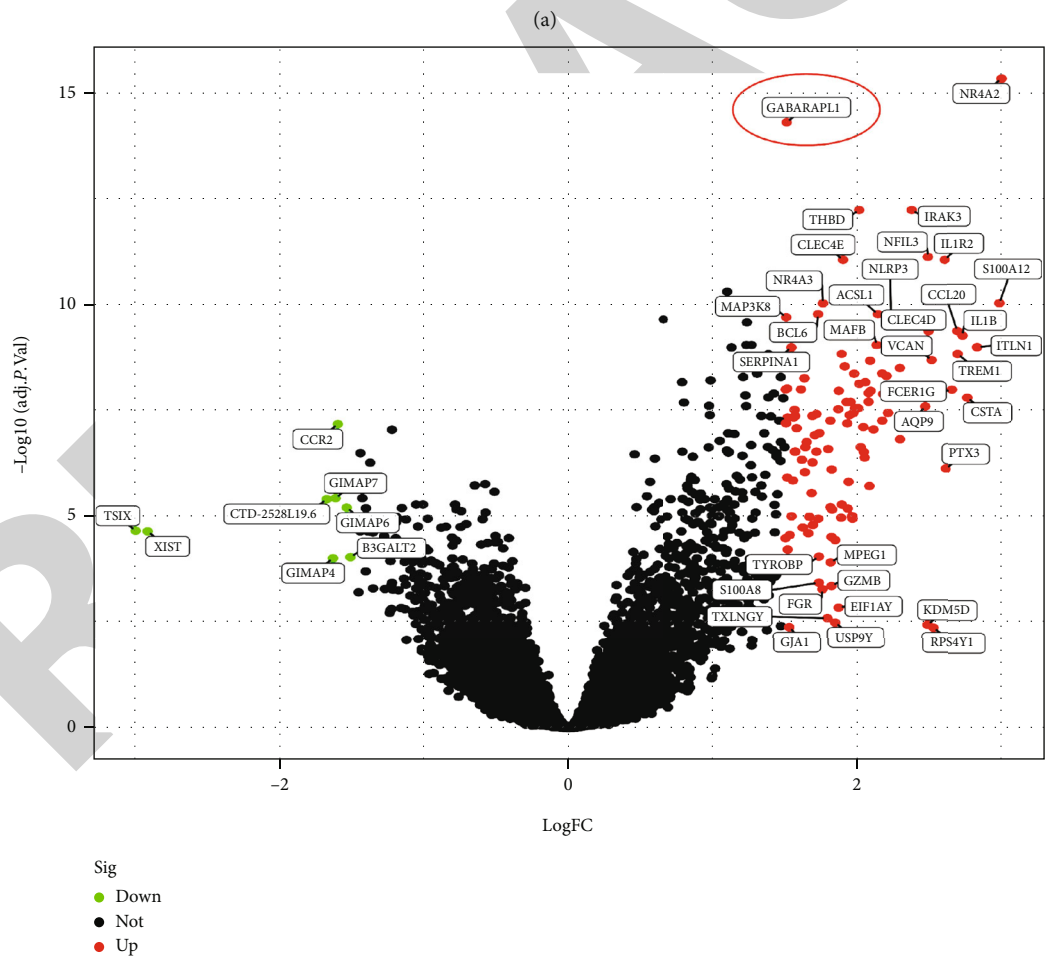
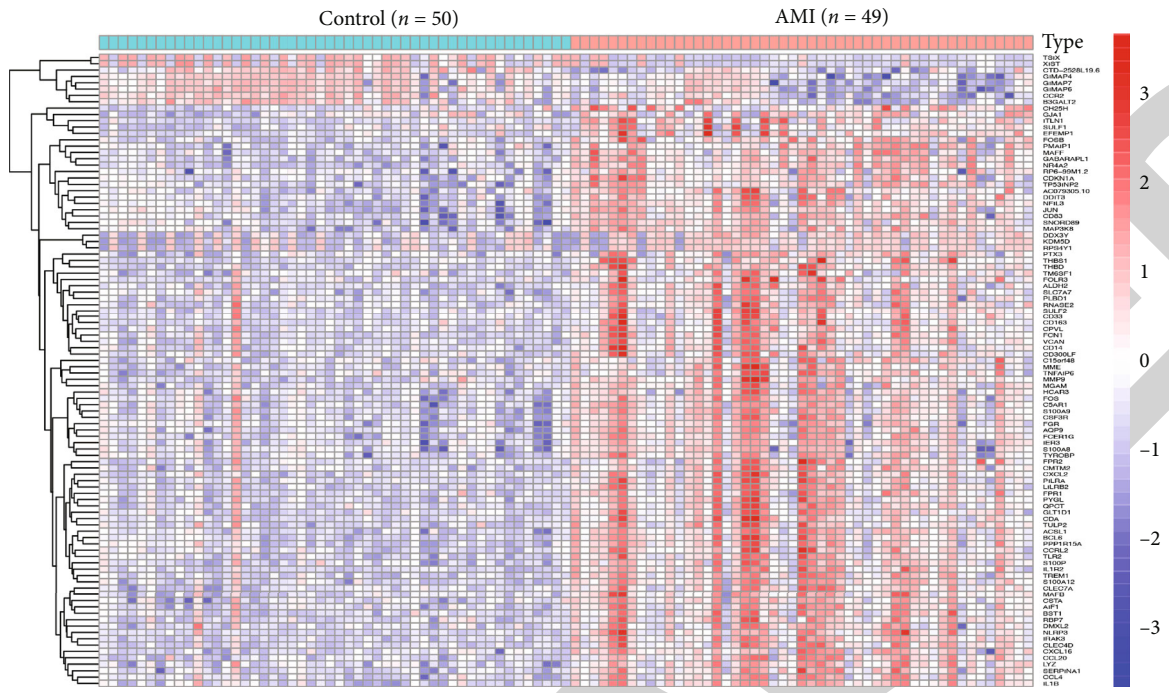


FIGURE 1: DEGs between AMI and control samples. (a) Heatmaps of DEGs between AMI and control samples. (b) Volcanic map showing DEGs between AMI and control samples. Red dots exhibit significantly increased gene expression. Green dots exhibit significantly reduced gene expression. Block dots show non-DEGs.

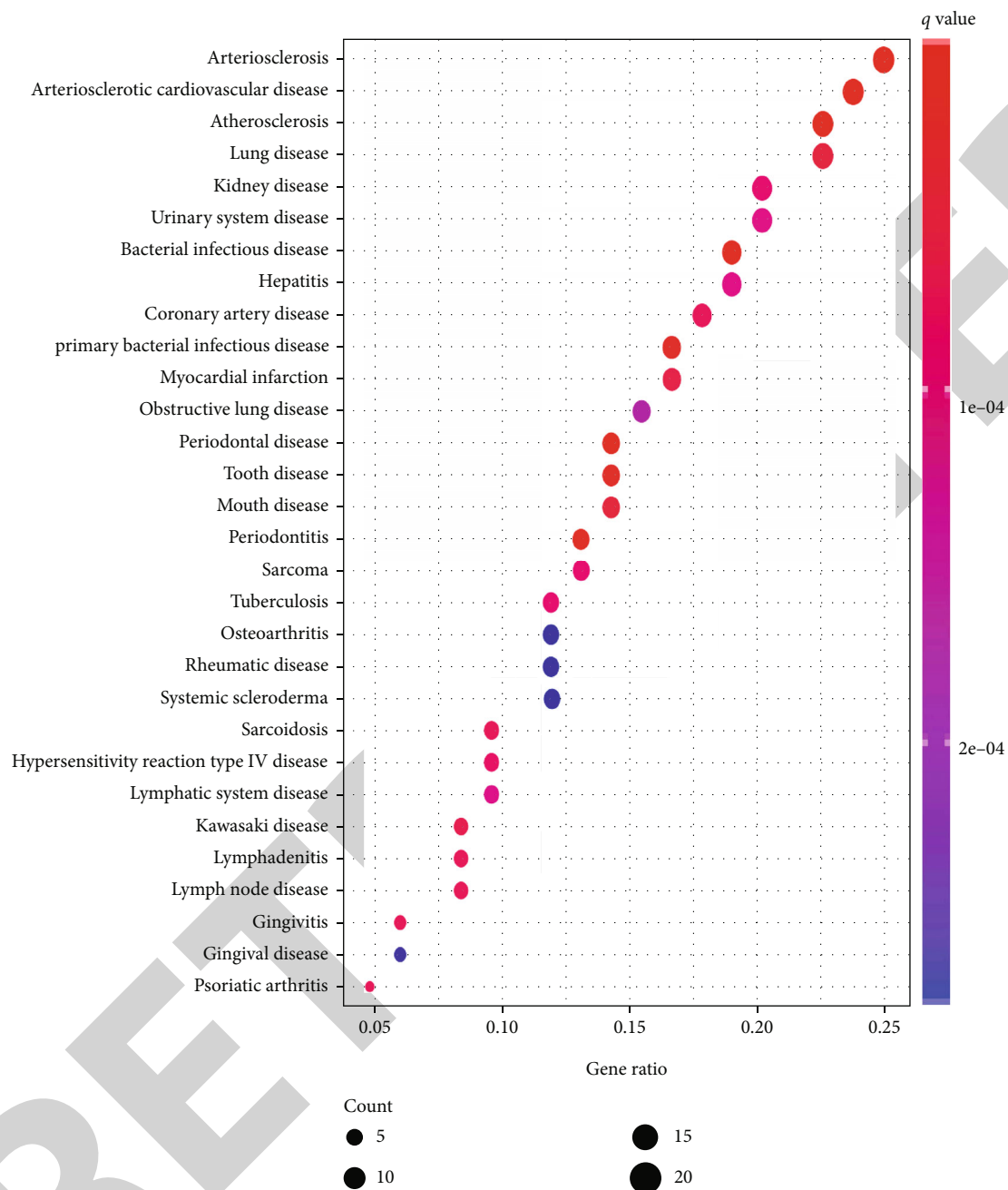
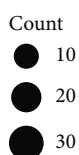
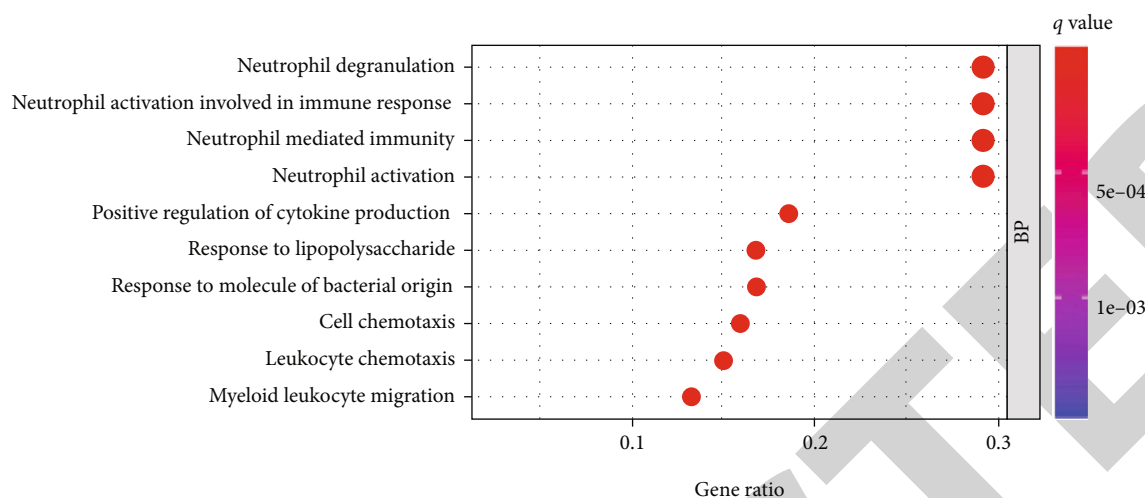
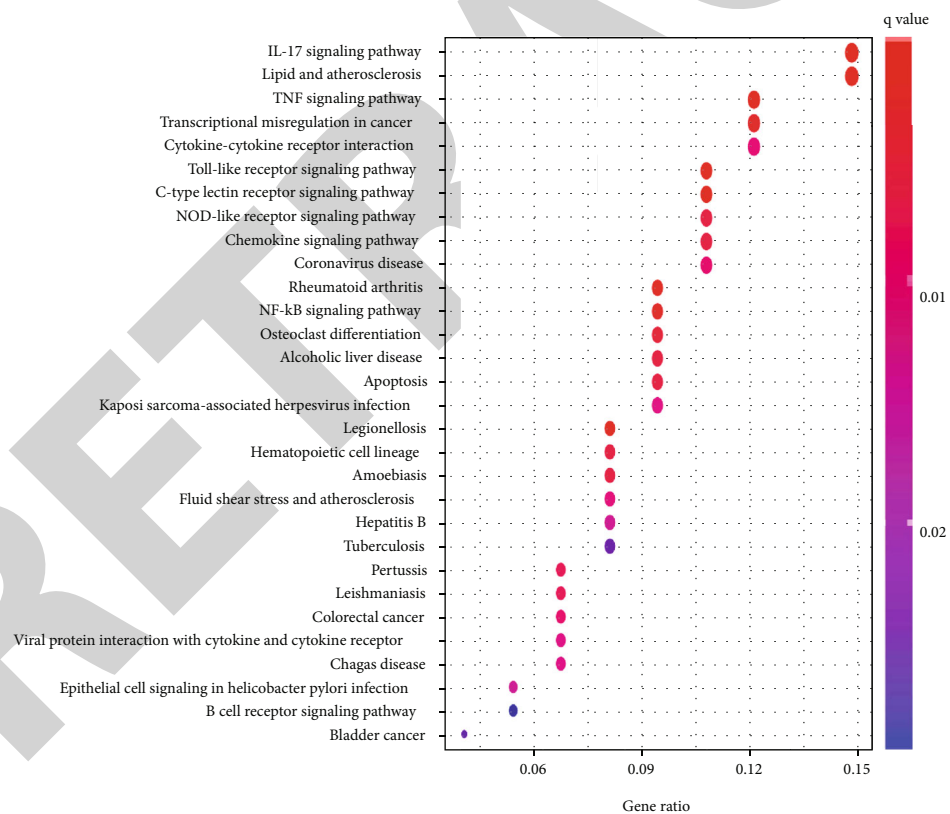


FIGURE 2: Continued.



(b)



(c)

FIGURE 2: Functional enrichment analyses of DEGs between AMI and control samples. Functional enrichment examinations of differentially expressed genes between AMI and control samples via (a) DO pathway enrichment analyses, (b) GO analyses, and (c) KEGG pathway enrichment analyses.

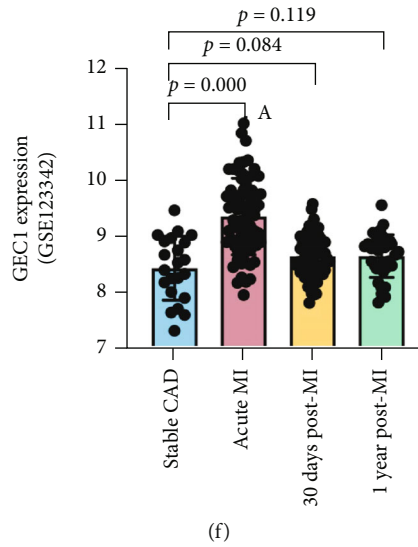
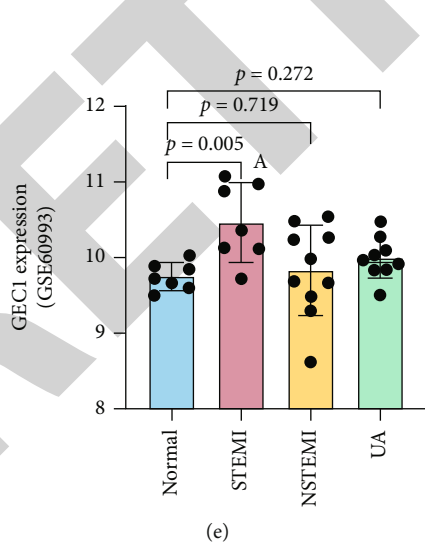
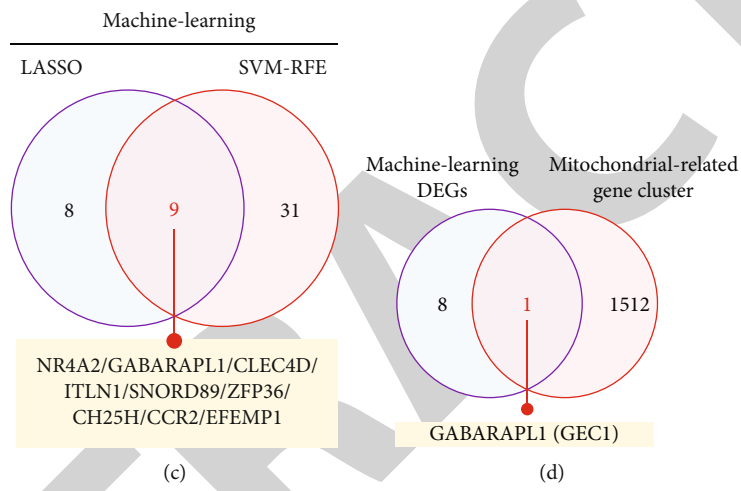
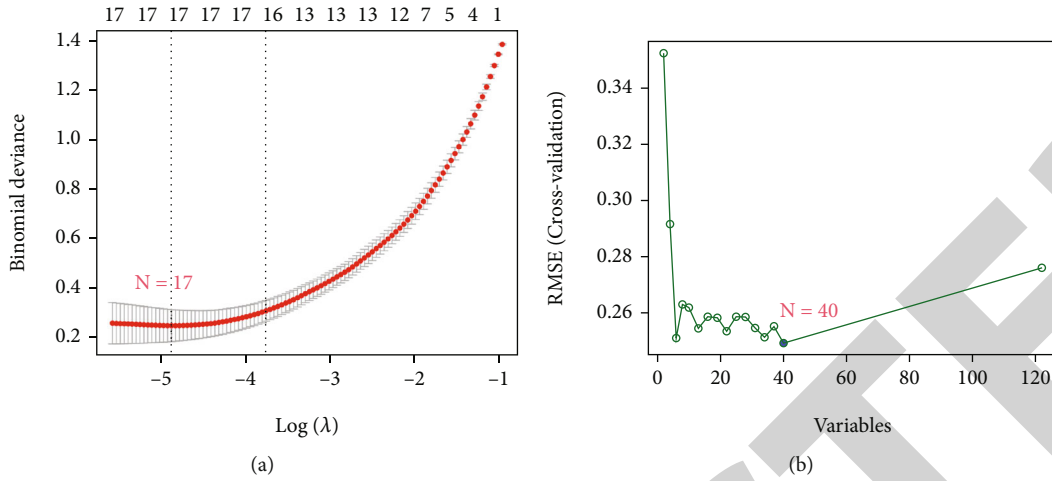


FIGURE 3: Continued.

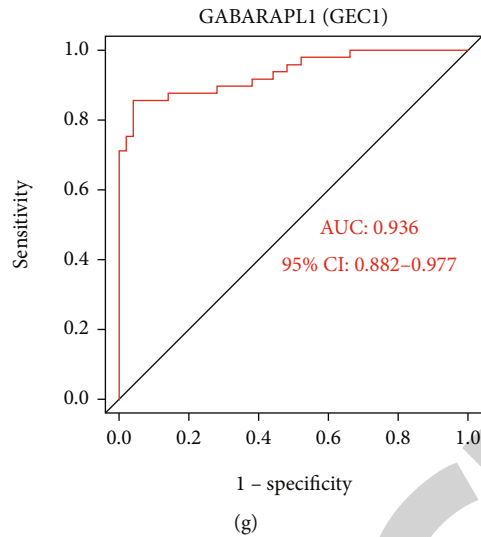


FIGURE 3: Screening process of diagnostic biomarker candidates for AMI diagnosis. Feature selection via (a) the LASSO regression algorithm and (b) SVM-RFE algorithm. (c) The Venn diagram shows nine potential diagnostic markers shared by the LASSO and SVM-RFE algorithms. (d) The Venn diagram demonstrates that GEC1 is the only mitochondria-related gene in the nine potential diagnostic markers. Validation of the expression of GEC1 in the (e) GSE60993 and (f) GSE123342 datasets. (g) The receiver operating characteristic (ROC) curve of GEC1.

blood, and the expression of GEC1 in CECs was detected by flow cytometry. The data showed that the GEC1-positive expressed CECs in the blood of AMI group accounted for 93.47%, which was significantly higher than the 52.42% in the healthy group ( $p < 0.05$ ) (Figure 4(a)). These outcomes were consistent with the bioinformatics analysis of the clinical data (Figure 1).

To explore the internal relationship between high expression of GEC1 in blood CECs and the occurrence of AMI, we detected the expression of GEC1 (labeled with FITC-GABARAPL1) in myocardial microvascular endothelial cells (CMECs, labeled with PE-CD31) in the heart tissue. The findings declared that the expression of GEC1 in cardiac CMECs was significantly elevated in AMI rats ( $p < 0.05$ ) (Figure 4(b)). Immunofluorescence images further confirmed the high expression of GEC1 in the heart of AMI rats (Figure 4(c)). In addition, western blotting findings also declared that the LC3 II/I ratio was significantly upregulated in the hearts of AMI rats (Figure 4(d)), suggesting that GEC1-mediated autophagy might be overactivated in the heart of AMI.

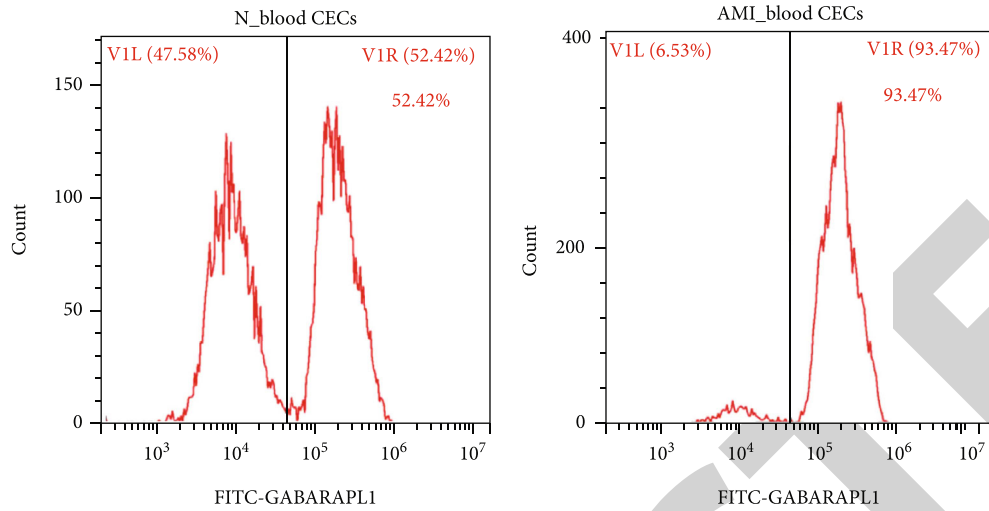
**3.4. The Oxidative-Damaged Mitochondria Block GEC1-Mediated Autophagy Flux and Are Released by Exosomes in Exfoliated Cardiac CMECs and Blood CECs.** We constructed hypoxia-induced CMECs to simulate an AMI model at the cellular level. The confocal images showed that the mitochondrial length, as well as aspect ratio, was significantly decreased after hypoxia in CMECs ( $p < 0.05$ ), and the ROS development in hypoxia-CMECs was also significantly increased ( $p < 0.05$ ) (Figure 5(a)), indicating that hypoxia induced severe mitochondrial damage and oxidative stress in cardiac CMECs. In addition, autophagic flux detection showed that the number of autophagosomes significantly

elevated ( $p < 0.05$ ), but autolysosome number exhibited no increase correspondingly in CMECs that was hypoxia-induced ( $p > 0.05$ ) (Figure 5(b)), implying that damaged lysosomes could not degrade many autophagosomes containing mitochondrial fragments in CMECs after hypoxia. However, autophagic flux was significantly improved after GEC1-shRNA treatment in hypoxia-CMECs ( $p < 0.05$ ) (Figures 5(b)).

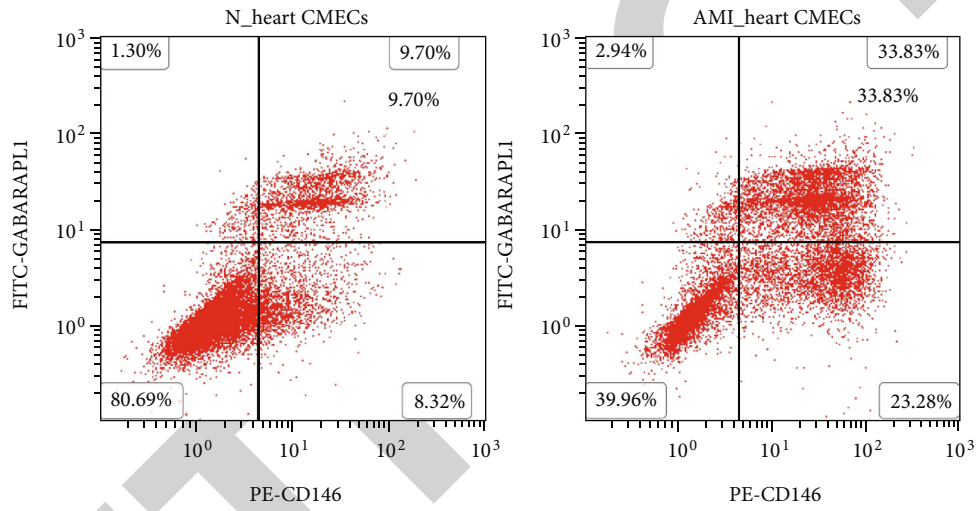
Interestingly, TEM results showed that blood CECs from AMI group released much more exosomes/microvesicles than that in the normal group ( $p < 0.05$ ) (Figure 5(c)). Western blotting results declared that the expression of exosome biomarkers, such as TSG101 and CD63, was significantly increased in hypoxia-induced CMECs ( $p < 0.05$ ), and the GEC1 expression was also increased in exosomes from hypoxia-induced CMECs ( $p < 0.05$ ) (Figure 5(d)). The present findings declare that numerous undegraded autophagosomes containing damaged mitochondrial fragments in exfoliated cardiac CMECs and blood CECs could be released by exosomes in AMI.

**3.5. The Exosome Burst Stimulates NLRP3 Inflammasome Production and Activates Vascular Inflammatory Response after AMI.** To detect the effects of exosome/microvesicle burst in blood CECs after AMI, we explored the immune cell infiltration and found that the percentages of memory B cells ( $p = 0.047$ ), CD4<sup>+</sup> resting memory T cells ( $p < 0.001$ ), gamma-delta T cells ( $p < 0.001$ ), and excited natural killer (NK) cells ( $p < 0.001$ ) significantly decreased after AMI, whereas the proportions of CD4<sup>+</sup>-activated memory T cells ( $p = 0.003$ ), resting NK cells ( $p = 0.001$ ), monocytes ( $p < 0.001$ ), stimulated mast cells ( $p < 0.001$ ), and neutrophils ( $p < 0.001$ ) significantly increased after AMI (Figure 6(a)). We then performed a correlation analysis between GEC1 levels and immunological cell infiltration

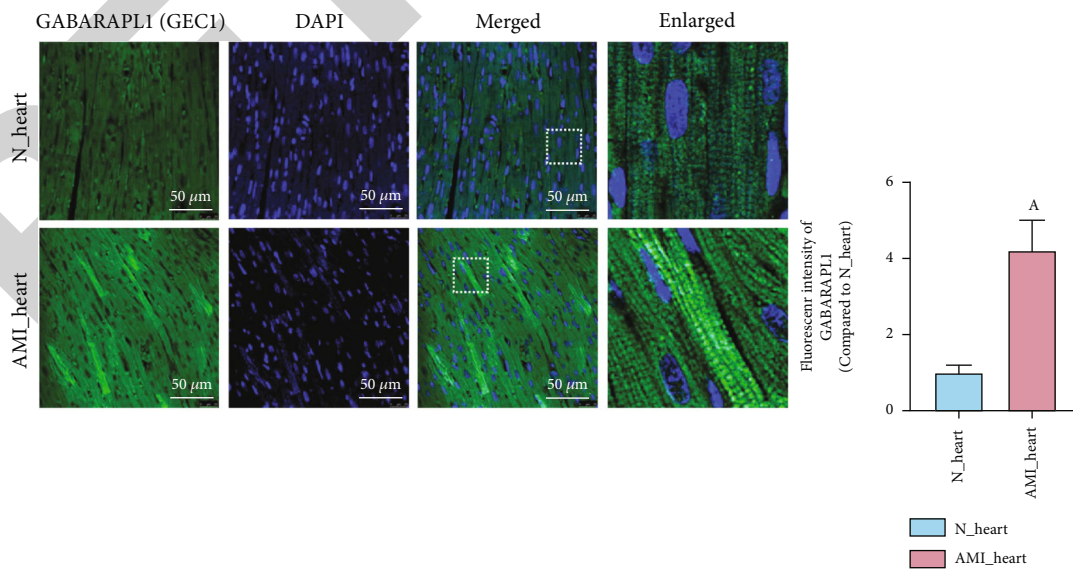




(a)



(b)



(c)

FIGURE 4: Continued.

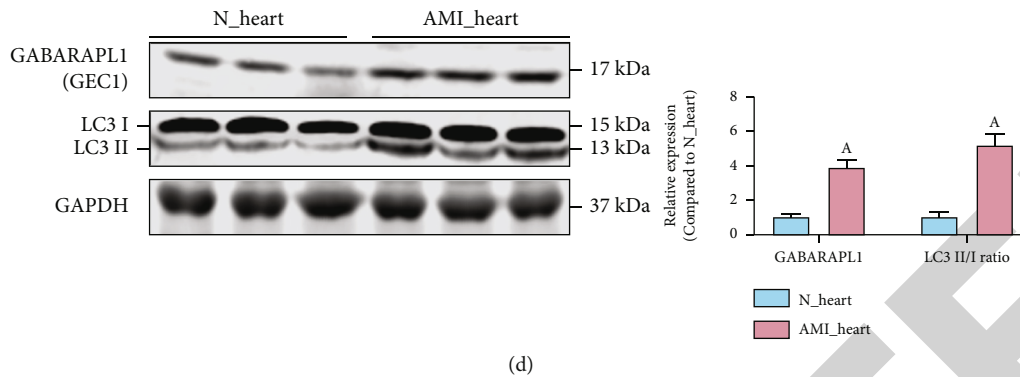


FIGURE 4: The expression of GEC1 in the blood circulating endothelial cells (CECs) and heart cardiac microvascular endothelial cells (CMECs) after AMI. Flow cytometric analysis of the expression of GEC1 (a) in CECs and (b) in CMECs after AMI. (c) Immunofluorescence analysis of the expression of GEC1 in heart tissue after AMI (bar = 50  $\mu$ m). (d) The LC3 II/I ratio and the protein expression of GEC1 in the heart of AMI rats. (a)  $p < 0.05$  compared with the normal group.

after AMI. The results showed that high GEC1 in blood CECs was strongly related to enhanced monocyte ( $R = 0.58$ ,  $p < 0.001$ ), activated mast cells ( $R = 0.41$ ,  $p < 0.001$ ), neutrophils ( $R = 0.40$ ,  $p < 0.001$ ),  $CD4^+$ -activated memory T cells ( $R = 0.31$ ,  $p = 0.002$ ), and resting NK cells ( $R = 0.29$ ,  $p = 0.004$ ) and negatively correlated with the decreased proportion of  $CD4^+$  resting memory T cells ( $R = -0.56$ ,  $p < 0.001$ ), gamma-delta T cells ( $R = -0.48$ ,  $p < 0.001$ ), and stimulated NK cells ( $R = -0.37$ ,  $p < 0.001$ ) after AMI (Figures 6(b) and S1). These results suggest that high GEC1 in blood CECs may be tightly connected with the immune-inflammatory reaction in monocytes as well as neutrophils after AMI.

We further screened DEGs in AMI with immune-related gene clusters and inflammation-related gene clusters. The Venn diagram showed that 23 DEGs were related to the immune-inflammatory response in AMI (Figure 7(a)), including EDN1, CD14, PTAFR, LYN, PLAUR, FPR1, C5AR1, AQP9, CSF3R, ICAM1, TLR2, CCRL2, NFKBIA, NAMPT, CXCL8, CCL20, NLRP3, IL1B, HBEGF, EREG, ADM, FFAR2, and LIF (Figure 7(b)). Notably, NLRP3, a hotspot inflammasome marker, was overactivated in the blood of AMI patients (Figure 7(c)). We further isolated immune monocytes, the proportion of which have been proven to be positively correlated with high GEC1, in AMI rats. The flow cytometry results showed that the NLRP3-positive monocytes in AMI group accounted for 93.18%, implying a significant rise contrasted with that of 54.41% in the healthy group ( $p < 0.05$ ) (Figure 7(d)). Western blotting results showed that the expression of NLRP3 and corresponding inflammation indicators, such as caspase-1 and IL-1 $\beta$ , was significantly increased in blood CECs after AMI ( $p < 0.05$ ) (Figure 7(e)). After tail vein injection with AAV2-shGEC1 to reduce GEC1 expression in cardiac CMECs, the vascular inflammatory response induced by NLRP3 inflammasomes could be markedly inhibited, suggesting the exosome burst with high GEC1 from blood CECs could stimulate NLRP3 inflammasome production and activates vascular inflammatory response after AMI.

#### 4. Discussion

Acute myocardial ischemia (AMI) is the main reason of cardiovascular disease that leads to impairment and mortality all over the world every year [19]. Therefore, quick and correct identification of AMI is the essential stage for improving the prognosis of AMI patients [20]. Recently, with microarray technology and integrated bioinformatics investigation, many studies were conducted to discover unique genes or noncoding RNAs that can be used as diagnostic and prognostic biomarkers of AMI [21, 22]. However, these studies have primarily focused on inflammation and signaling cascade, and few have focused on the aberrantly expressed genes related to oxidative-damaged mitochondria and oxidative stress in AMI. Our study elucidated the process of vascular inflammation caused by myocardial ischemia from the perspective of mitochondrial quality imbalance and preliminarily explained the mechanism through the autophagic-exosome manner [23] in the cardiovascular system.

Mitochondria are essential organelles involved in several processes, such as maintaining cellular ion and energy balance, cell growth and death, etc. Mitochondrial quality imbalance and oxidative stress have been found in many tissues after acute ischemic/hypoxic injury [8]. Our previous study also demonstrated that the number of copies of mitochondrial DNA increased significantly in the superior mesenteric arteries (SMAs) after ischemia, and mitochondrial dynamics changed in primary vascular smooth muscle cells from rat SMAs after hypoxia [10]. In keloid fibroblasts under hypoxia, the mitochondrial complex activities significantly decreased, and the mitochondria were characterized by swelling, cristae effacement, and oxidative stress [24]. In Caco-2 cells, ischemia/reperfusion (I/R) induces severe mitochondrial oxidative damage and apoptosis [25]. In cardiomyocytes, the loss of regularity of mitochondrial striation and membrane integrity were found after I/R [26]. Due to mitochondrial quality imbalance being closely related to the establishment and prognosis of ischemic heart disorder, it is essential to determine possible predictive mitochondrial biomarkers for AMI and examine their roles in AMI.

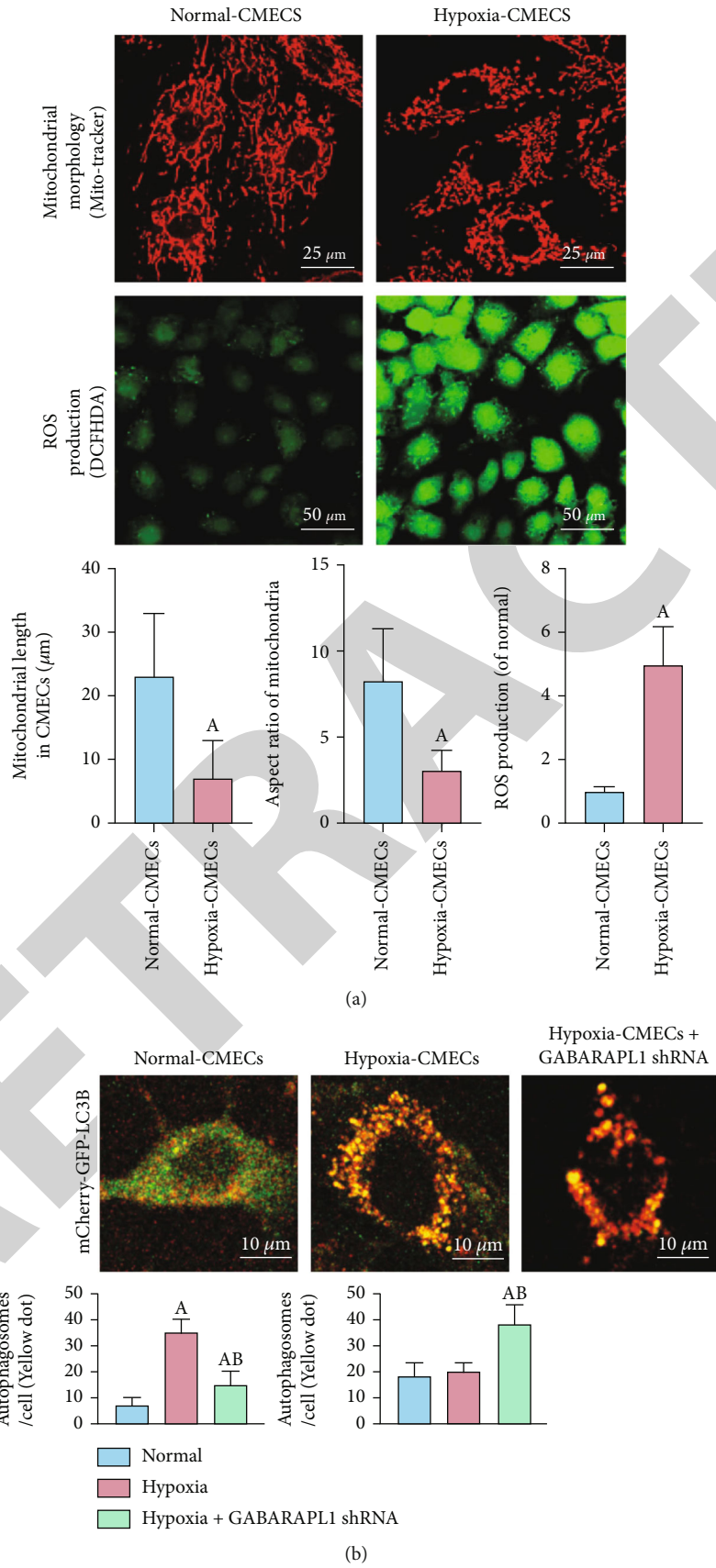


FIGURE 5: Continued.

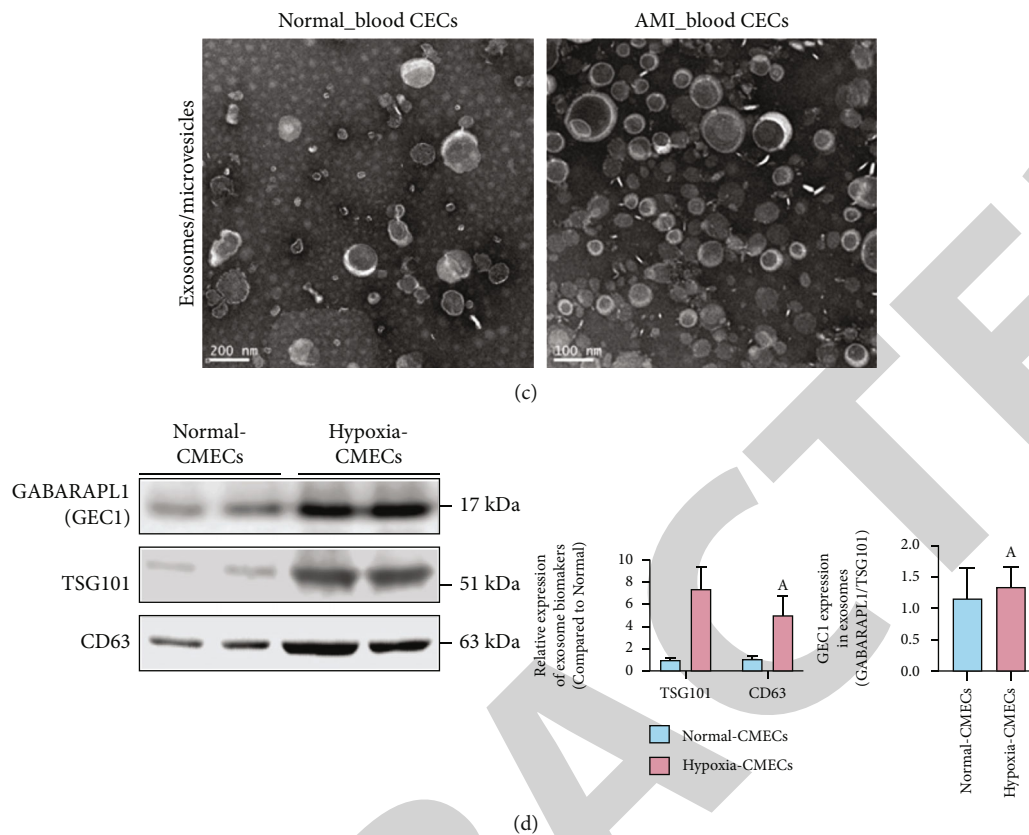


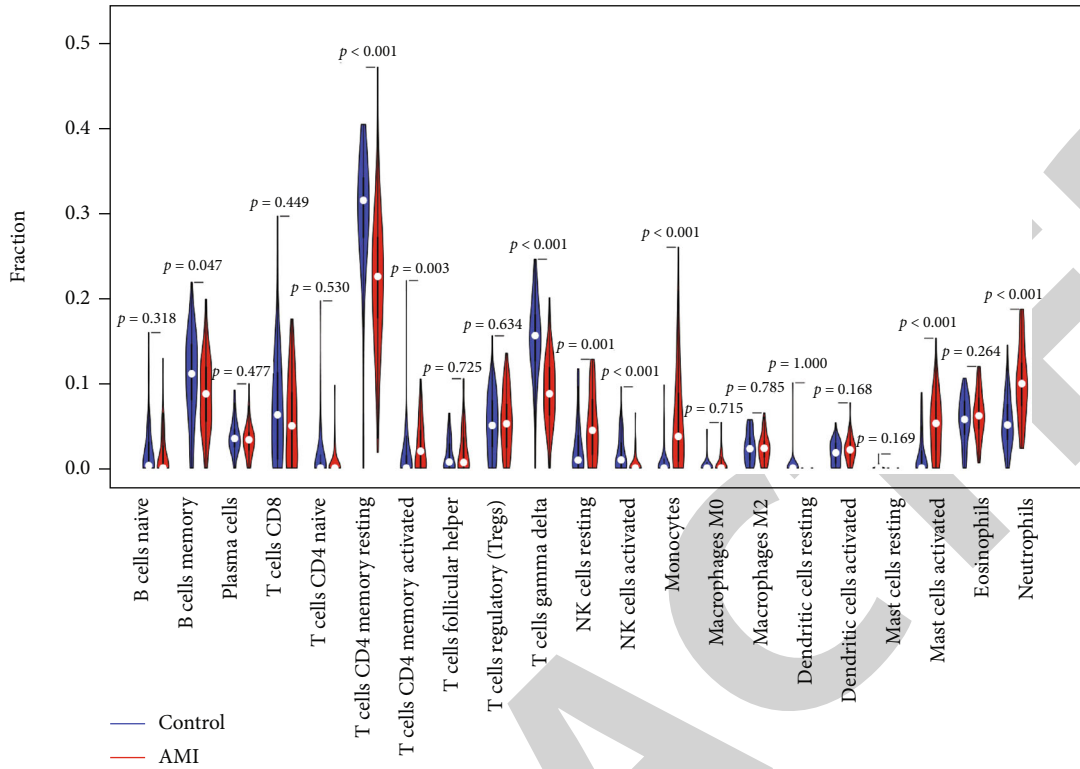
FIGURE 5: The detection of mitochondrial morphology, oxidative stress, autophagy flux, and exosome release in CMECs after AMI. (a) Mitochondrial morphology (bar = 25  $\mu\text{m}$ ) and ROS production (bar = 50  $\mu\text{m}$ ) in normal and hypoxia-CMECs. The length and aspect ratio of mitochondria were analyzed using the ImageJ software. The fluorescence intensity of DCFH-DA reflects the ROS production and oxidative stress. (b) Immunofluorescence images showing autophagy flux labeled by mCherry-GFP-LC3B in CMECs (bar = 10  $\mu\text{m}$ ). (c) Transmission electron microscopic images show more exosomes being released after hypoxia treatment (bar = 100 nm). (d) Western blot analysis shows the effects of hypoxia on the expression of CD63, TSG101, and GEC1. (a)  $p < 0.05$  compared with the normal group, (b)  $p < 0.05$  compared with the hypoxia group.

To detect how markers in the blood can correlate with oxidative-damaged mitochondria in the heart, we selected circulating endothelial cells (CECs) as the target of our study. Meanwhile, cardiac microvascular endothelial cells (CMECs) are among the most abundant cells in the heart and actively participate in cardiac physiology and pathology [27, 28]. Under some pathological conditions, such as atherosclerosis, CMECs in the heart detach from the basement membrane, resulting in increased numbers of CECs within the blood, making CECs an ideal tissue to assess cell damage in the heart from blood [13, 29].

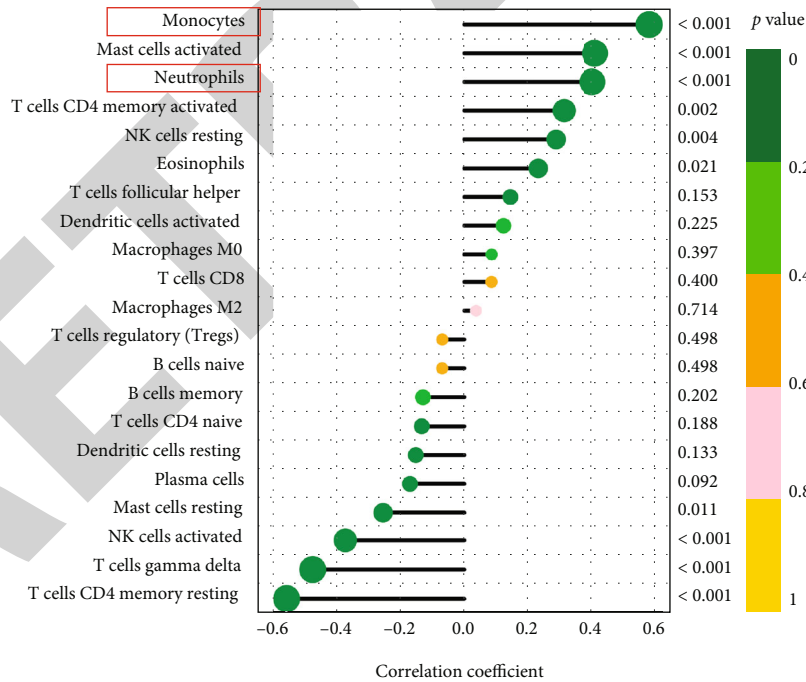
Using the public GEO dataset (GSE66360), 122 DEGs were detected with 114 elevated and eight decreased genes. DO pathway enrichment, GO, and KEGG pathway analyses significantly imply that the immunological reaction takes a key part in AMI, consistent with previous findings, which demonstrated that inflammation and immune responses are involved in AMI [30–32]. Further analysis according to two machine learning methods identified nine genes as potential diagnostic markers, of which GABARAPL1 (GEC1) was the only diagnostic mitochondrial biomarker for AMI. GABARAPL1 (GEC1), similar to GABARAP, engages with the GABAA receptor and tubulin as well as

stimulates tubulin polymerization. Not only are the GABARAP group members (GABARAP, GABARAPL1, and GABARAPL2) and their similar homologs (LC3 and Atg8) engaged in the transportation of proteins or vesicles, but they are also involved in a wide range of mechanisms, including autophagy, apoptosis, cell growth, and tumorigenesis [33]. Nevertheless, in these given parallels, GABARAPL1 (GEC1) shows a control that is distinct from other GABARAP-related members. The study by An et al. [34] showed that GEC1 is essential for autophagosome maturation through the regulation of mitochondrial homeostasis. Boyer-Guittaut et al. [35] also demonstrated that GEC1 is essential for ensuring proper autophagic flux and performs an important function in controlling cell bioenergetics and metabolism, which was similar to our findings.

We found that mitochondria were seriously damaged and presented oxidative stress in hypoxia-induced CMECs, and GEC1 expression and the number of autophagosomes increased significantly, indicating that GEC1-mediated mitophagy was enhanced after hypoxia in CMECs. However, there was no increase in the number of autolysosomes. In contrary, we found that many more exosomes were released in exfoliated cardiac CMECs and blood CECs after AMI or



(a)



(b)

FIGURE 6: The relationship between GEC1 expression in blood CECs and immune cell infiltration after AMI. (a) Comparison of 22 immune cell subtypes between AMI and normal tissues. Blue and red colors represent normal and AMI samples, respectively. (b) Correlation analysis between GEC1 and infiltrating immune cells after AMI.

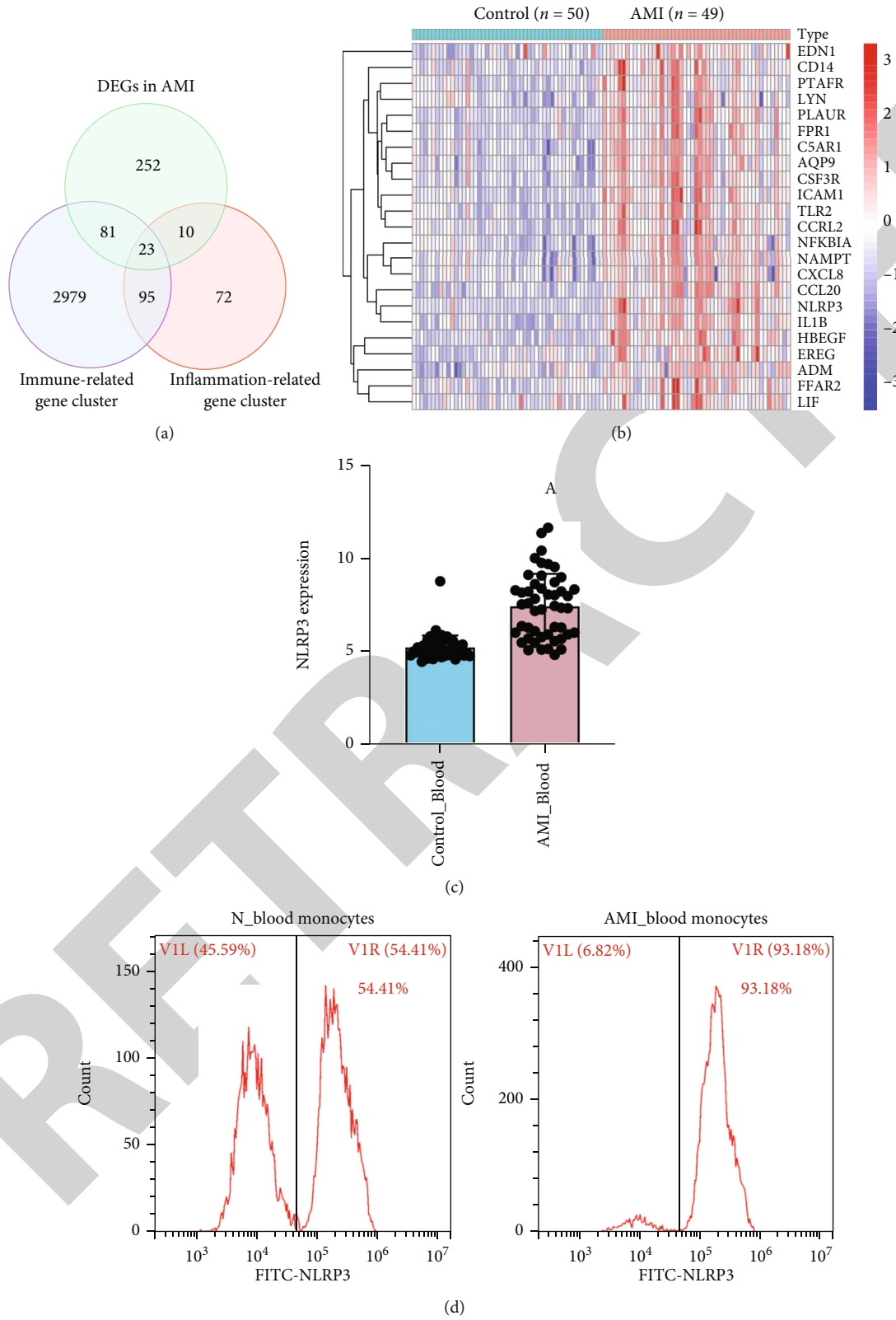


FIGURE 7: Continued.

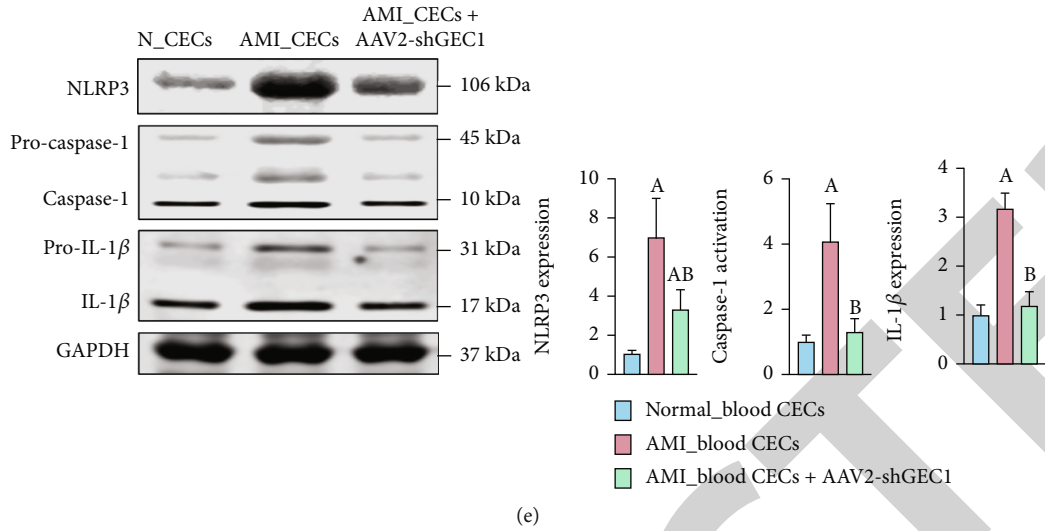


FIGURE 7: The effects of GEC1 in blood CECs on NLRP3 inflammasome production after AMI. (a) Venn diagram showing 23 DEGs shared by immune-related gene cluster and inflammation-related gene cluster in AMI. (b) Heatmaps of the 23 DEGs related to immune and inflammation in AMI. (c) The expression of NLRP3 in blood after AMI is based on GSE66360 database. (d) Flow cytometric analysis of the expression of NLRP3 in blood monocytes after AMI. (e) Western blot analysis shows that the expression of NLRP3 and corresponding inflammatory factors were significantly increased in blood CECs after AMI, which was markedly inhibited by shGEC1. (a)  $p < 0.05$  compared with the normal control group, (b)  $p < 0.05$  compared with the AMI group.

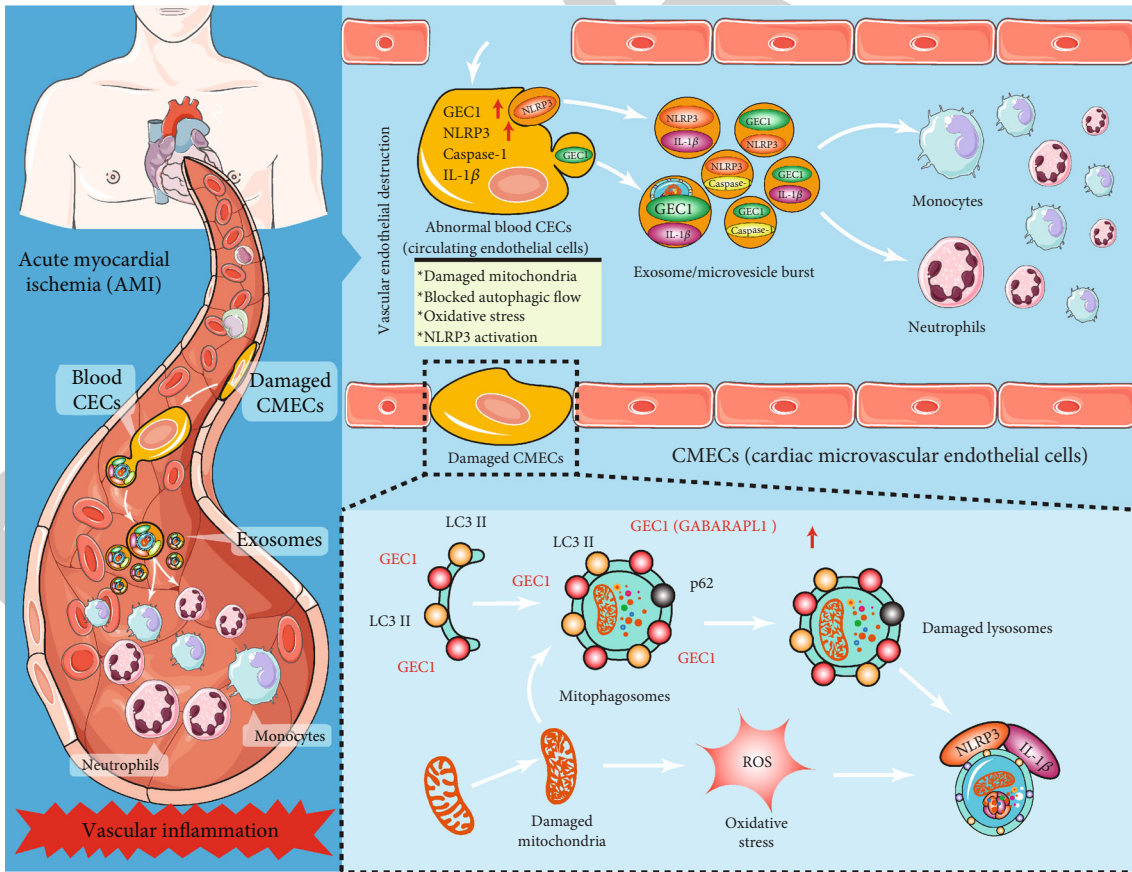


FIGURE 8: Schematic diagram of oxidative-damaged mitochondria activating GEC1-induced NLRP3 inflammasomes in an autophagic-exosome manner after acute myocardial ischemia.

hypoxia. Recently, studies have shown that, in addition to mitophagy, damaged mitochondria can also be packed into extracellular vesicles to be ejected from the cell. The study of Nicolas-Avila et al. [36] showed that dysfunctional mitochondria in cardiomyocytes could be ejected through a process driven by the cardiomyocyte's autophagy machinery and finally be eliminated by macrophages. The research of Crewe et al. [37] declared that adipocytes released secretory extracellular vesicles containing damaged mitochondria into circulation in response to energetic stress, which is taken up by cardiomyocytes and induces transient mitochondrial oxidative stress in cardiac tissue. The research of Souza et al. [37] declared that microvesicles transferred polarized mitochondria to the recipient's brain endothelial cells in culture and neurons in acute mouse brain cortical and hippocampal sections and elevated endothelial cell survivability under ischemic settings. The study of Ikeda et al. [38] showed that mitochondria-rich extracellular vesicles from autologous stem cell-derived cardiomyocytes restored the energetics of the ischemic myocardium. The study of Keulers et al. [39] showed that GEC1 is required for EV cargo loading and secretion. Based on these findings, we hypothesized and confirmed that the oxidative-damaged mitochondria block GEC1-mediated autophagy flux and are released by exosomes in exfoliated cardiac CMECs and blood CECs after AMI.

Inflammation plays an essential role in heart disease progression, and dysfunctional mitochondria are critical players in inflammation [40]. The study of Oka et al. [41] showed that mitochondrial DNA that escapes from autophagy cell-autonomously resulted in Toll-like receptor 9-mediated inflammatory reactions in cardiomyocytes. The study of Zhou et al. [42] showed that blockade of mitophagy caused the accumulation of oxidative-damaged mitochondria and activated the NLRP3 inflammasome, which was consistent with our results in this study. As per the correlation examination between GEC1 and infiltrating immunological cells after AMI, we found that high GEC1 in blood CECs might be closely associated with the immune-inflammatory response after AMI, suggesting that high GEC1 in exfoliated cardiac CMECs and blood CECs could activate vascular inflammatory responses by stimulating NLRP3 inflammasome production after AMI.

The limitations of this study are as follows: (1) In this paper, we only focus on the effects of GEC1-mediated mitochondrial damage and exosome burst in exfoliated cardiac CMECs on NLRP3 inflammasome and vascular inflammatory response after AMI, whether other cell types in heart tissues, such as macrophages and monocytes, participate in this regulation process need further investigation. (2) Due to ethical constraints, the experiments are only verified at the animal and cellular levels. In the next step, we will then collect clinical blood samples for further analysis and exploration.

## 5. Conclusion

In summary, oxidative-damaged mitochondria in cardiac CMECs activate GABARAPL1- (GEC1-) mediated autophagosomes but block autophagy flux after acute myocardial ischemia (AMI). The exfoliated cardiac CMECs evolve into

abnormal blood CECs, and the undegraded GEC1 autophagosomes produce a large number of NLRP3 inflammasomes by exosome/microvesicle burst, stimulating the increase in monocytes and neutrophils and ultimately triggering vascular inflammation after AMI (Figure 8).

## Data Availability

The data that support the findings of this study are available from the corresponding authors upon reasonable request.

## Conflicts of Interest

The authors declare that the research was conducted in the absence of any commercial or financial relationships that could be construed as a potential conflict of interest.

## Authors' Contributions

Tiechun Zhang, Dongyao Hou, and Jianrong He contribute equally to this article.

## Acknowledgments

This work was supported by the National Natural Science Foundation of China (No. 82272252 and 82270378), Chongqing Talents Program (cstc2022ycjh-bgzxm0007), and Kuanren Talents Program of the second affiliated hospital of Chongqing Medical University.

## Supplementary Materials

Figure S1 Correlation analysis between GEC1 expression and (A) monocytes, (B) activated mast cells, (C) neutrophils, (D) CD4 memory-activated T cells, (E) resting NK cells, (F) CD4 memory-resting T cells, (G) gamma delta T cells, and (H) NK cells activated after acute myocardial ischemia. (*Supplementary Materials*)

## References

- [1] A. Kumar and C. P. Cannon, "Acute coronary syndromes: diagnosis and management, part I," *Mayo Clinic Proceedings*, vol. 84, no. 10, pp. 917–938, 2009.
- [2] M. Vafaie, "State-of-the-art diagnosis of myocardial infarction," *Diagnosis*, vol. 3, no. 4, pp. 137–142, 2016.
- [3] A. E. Berezin and A. A. Berezin, "Adverse cardiac remodelling after acute myocardial infarction: old and new biomarkers," *Disease Markers*, vol. 2020, Article ID 1215802, 21 pages, 2020.
- [4] O. Hammarsten, J. Mair, M. Möckel, B. Lindahl, and A. S. Jaffe, "Possible mechanisms behind cardiac troponin elevations," *Biomarkers*, vol. 23, no. 8, pp. 725–734, 2018.
- [5] R. B. Jennings and C. E. Ganote, "Mitochondrial structure and function in acute myocardial ischemic injury," *Circulation Research*, vol. 38, 5 Suppl 1, pp. I80–I91, 1976.
- [6] R. Tian, W. S. Colucci, Z. Arany et al., "Unlocking the secrets of mitochondria in the cardiovascular system: path to a cure in heart failure—a report from the 2018 National Heart, Lung, and Blood Institute Workshop," *Circulation*, vol. 140, no. 14, pp. 1205–1216, 2019.



- [7] T. S. Luongo, J. P. Lambert, P. Gross et al., "The mitochondrial  $\text{Na}^+/\text{Ca}^{2+}$  exchanger is essential for  $\text{Ca}^{2+}$  homeostasis and viability," *Nature*, vol. 545, no. 7652, pp. 93–97, 2017.
- [8] B. Zhou and R. Tian, "Mitochondrial dysfunction in pathophysiology of heart failure," *The Journal of Clinical Investigation*, vol. 128, no. 9, pp. 3716–3726, 2018.
- [9] Q. Zhang, M. Raoof, Y. Chen et al., "Circulating mitochondrial DAMPs cause inflammatory responses to injury," *Nature*, vol. 464, no. 7285, pp. 104–107, 2010.
- [10] C. Duan, L. Wang, J. Zhang et al., "Mdivi-1 attenuates oxidative stress and exerts vascular protection in ischemic/hypoxic injury by a mechanism independent of Drp1 GTPase activity," *Redox Biology*, vol. 37, p. 101706, 2020.
- [11] M. Wang, K. Smith, Q. Yu, C. Miller, K. Singh, and C. K. Sen, "Mitochondrial connexin 43 in sex-dependent myocardial responses and estrogen-mediated cardiac protection following acute ischemia/reperfusion injury," *Basic Research in Cardiology*, vol. 115, no. 1, p. 1, 2019.
- [12] M. Farinacci, T. Krahn, W. Dinh et al., "Circulating endothelial cells as biomarker for cardiovascular diseases," *Research and Practice in Thrombosis and Haemostasis*, vol. 3, no. 1, pp. 49–58, 2019.
- [13] A. D. Blann, A. Woywodt, F. Bertolini et al., "Circulating endothelial cells. Biomarker of vascular disease," *Journal of Thrombosis and Haemostasis*, vol. 93, no. 2, pp. 228–235, 2005.
- [14] G. Yu, L. G. Wang, G. R. Yan, and Q. Y. He, "DOSE: an R/Bioconductor package for disease ontology semantic and enrichment analysis," *Bioinformatics*, vol. 31, no. 4, pp. 608–609, 2015.
- [15] E. Zhao, H. Xie, and Y. Zhang, "Predicting diagnostic gene biomarkers associated with immune infiltration in patients with acute myocardial infarction," *Front Cardiovasc Med*, vol. 7, p. 586871, 2020.
- [16] A. M. Newman, C. L. Liu, M. R. Green et al., "Robust enumeration of cell subsets from tissue expression profiles," *Nature Methods*, vol. 12, no. 5, pp. 453–457, 2015.
- [17] C. Duan, L. Kuang, X. Xiang et al., "Drp1 regulates mitochondrial dysfunction and dysregulated metabolism in ischemic injury via Clec16a-, BAX-, and GSH- pathways," *Cell Death & Disease*, vol. 11, no. 4, p. 251, 2020.
- [18] Y. Song, Z. Li, T. He et al., "M2 microglia-derived exosomes protect the mouse brain from ischemia-reperfusion injury via exosomal miR-124," *Theranostics*, vol. 9, no. 10, pp. 2910–2923, 2019.
- [19] J. A. Ambrose, "Myocardial ischemia and infarction," *Journal of the American College of Cardiology*, vol. 47, no. 11, pp. D13–D17, 2006.
- [20] G. Lippi, M. Franchini, and G. Cervellin, "Diagnosis and management of ischemic heart disease," *Seminars in Thrombosis and Hemostasis*, vol. 39, no. 2, pp. 202–213, 2013.
- [21] L. Li, Y. Cong, X. Gao, Y. Wang, and P. Lin, "Differential expression profiles of long non-coding RNAs as potential biomarkers for the early diagnosis of acute myocardial infarction," *Oncotarget*, vol. 8, no. 51, pp. 88613–88621, 2017.
- [22] H. Meng, X. Wang, J. Ruan, W. Chen, F. Meng, and P. Yang, "High expression levels of the SOCS3 gene are associated with acute myocardial infarction," *Genetic Testing and Molecular Biomarkers*, vol. 24, no. 7, pp. 443–450, 2020.
- [23] X. Zeng, Y. D. Zhang, R. Y. Ma et al., "Activated Drp1 regulates p62-mediated autophagic flux and aggravates inflammation in cerebral ischemia-reperfusion via the ROS-RIP1/RIP3-exosome axis," *Military Medical Research*, vol. 9, no. 1, p. 25, 2022.
- [24] Q. Wang, P. Wang, Z. Qin et al., "Altered glucose metabolism and cell function in keloid fibroblasts under hypoxia," *Redox Biology*, vol. 38, p. 101815, 2021.
- [25] Z. Wang, R. Sun, G. Wang et al., "SIRT3-mediated deacetylation of PRDX3 alleviates mitochondrial oxidative damage and apoptosis induced by intestinal ischemia/reperfusion injury," *Redox Biology*, vol. 28, p. 101343, 2020.
- [26] J. Horstkotte, T. Perisic, M. Schneider et al., "Mitochondrial thioredoxin reductase is essential for early postischemic myocardial protection," *Circulation*, vol. 124, no. 25, pp. 2892–2902, 2011.
- [27] M. A. Forgione, J. A. Leopold, and J. Loscalzo, "Roles of endothelial dysfunction in coronary artery disease," *Current Opinion in Cardiology*, vol. 15, no. 6, pp. 409–415, 2000.
- [28] U. Landmesser, S. Spiekermann, S. Dikalov et al., "Vascular oxidative stress and endothelial dysfunction in patients with chronic heart failure," *Circulation*, vol. 106, no. 24, pp. 3073–3078, 2002.
- [29] J. Quilici, N. Banzet, P. Paule et al., "Circulating endothelial cell count as a diagnostic marker for non-ST-elevation acute coronary syndromes," *Circulation*, vol. 110, no. 12, pp. 1586–1591, 2004.
- [30] W. Chen, A. Spitzl, D. Mathes et al., "Endothelial actions of ANP enhance myocardial inflammatory infiltration in the early phase after acute infarction," *Circulation Research*, vol. 119, no. 2, pp. 237–248, 2016.
- [31] S. M. Davidson, P. Ferdinandy, I. Andreadou et al., "Multitarget strategies to reduce myocardial ischemia/reperfusion injury," *Journal of the American College of Cardiology*, vol. 73, no. 1, pp. 89–99, 2019.
- [32] S. J. Schunk, S. Triem, D. Schmit et al., "Interleukin-1 $\alpha$  is a central regulator of leukocyte-endothelial adhesion in myocardial infarction and in chronic kidney disease," *Circulation*, vol. 144, no. 11, pp. 893–908, 2021.
- [33] J. N. Le Grand, F. Z. Chakrama, S. Seguin-Py et al., "GABAR-APL1 (GEC1): original or copycat?," *Autophagy*, vol. 7, no. 10, pp. 1098–1107, 2011.
- [34] H. K. An, K. M. Chung, H. Park et al., "CASP9 (caspase 9) is essential for autophagosome maturation through regulation of mitochondrial homeostasis," *Autophagy*, vol. 16, no. 9, pp. 1598–1617, 2020.
- [35] M. Boyer-Guittaut, L. Poillet, Q. Liang et al., "The role of GABARAPL1/GEC1 in autophagic flux and mitochondrial quality control in MDA-MB-436 breast cancer cells," *Autophagy*, vol. 10, no. 6, pp. 986–1003, 2014.
- [36] J. A. Nicolas-Avila, A. V. Lechuga-Vieco, L. Esteban-Martínez et al., "A network of macrophages supports mitochondrial homeostasis in the heart," *Cell*, vol. 183, no. 1, pp. 94–109.e23, 2020.
- [37] C. Crewe, J. B. Funcke, S. Li et al., "Extracellular vesicle-based interorgan transport of mitochondria from energetically stressed adipocytes," *Cell Metabolism*, vol. 33, no. 9, pp. 1853–1868.e11, 2021.
- [38] G. Ikeda, M. R. Santoso, Y. Tada et al., "Mitochondria-rich extracellular vesicles from autologous stem cell-derived cardiomyocytes restore energetics of ischemic myocardium," *Journal of the American College of Cardiology*, vol. 77, no. 8, pp. 1073–1088, 2021.

## *Retraction*

# **Retracted: Targeted Diagnosis, Therapeutic Monitoring, and Assessment of Atherosclerosis Based on Mesoporous Silica Nanoparticles Coated with cRGD-Platelets**

### **Oxidative Medicine and Cellular Longevity**

Received 26 December 2023; Accepted 26 December 2023; Published 29 December 2023

Copyright © 2023 Oxidative Medicine and Cellular Longevity. This is an open access article distributed under the Creative Commons Attribution License, which permits unrestricted use, distribution, and reproduction in any medium, provided the original work is properly cited.

This article has been retracted by Hindawi, as publisher, following an investigation undertaken by the publisher [1]. This investigation has uncovered evidence of systematic manipulation of the publication and peer-review process. We cannot, therefore, vouch for the reliability or integrity of this article.

Please note that this notice is intended solely to alert readers that the peer-review process of this article has been compromised.

Wiley and Hindawi regret that the usual quality checks did not identify these issues before publication and have since put additional measures in place to safeguard research integrity.

We wish to credit our Research Integrity and Research Publishing teams and anonymous and named external researchers and research integrity experts for contributing to this investigation.

The corresponding author, as the representative of all authors, has been given the opportunity to register their agreement or disagreement to this retraction. We have kept a record of any response received.

### **References**

- [1] W. Zhang, Z. Lv, Y. Zhang et al., “Targeted Diagnosis, Therapeutic Monitoring, and Assessment of Atherosclerosis Based on Mesoporous Silica Nanoparticles Coated with cRGD-Platelets,” *Oxidative Medicine and Cellular Longevity*, vol. 2022, Article ID 6006601, 19 pages, 2022.

## Research Article

# Targeted Diagnosis, Therapeutic Monitoring, and Assessment of Atherosclerosis Based on Mesoporous Silica Nanoparticles Coated with cRGD-Platelets

Wei Zhang <sup>1</sup>, Zheng Lv,<sup>2</sup> Yupeng Zhang,<sup>2</sup> Subash C. B. Gopinath <sup>3</sup>, Yi Yuan <sup>4</sup>,  
Deyou Huang <sup>5</sup> and Liu Miao <sup>6</sup>

<sup>1</sup>Department of Radiology, Liuzhou People's Hospital Affiliated to Guangxi Medical University, Liuzhou, Guangxi 545006, China

<sup>2</sup>Department of Radiology, Affiliated Hospital of Guilin Medical University, Guilin, Guangxi 541001, China

<sup>3</sup>Faculty of Chemical Engineering & Technology, Micro System Technology, Centre of Excellence (CoE), and Institute of Nano Electronic Engineering, Universiti Malaysia Perlis (UniMAP), Perlis, Malaysia

<sup>4</sup>Institute of Life Sciences, Jiangsu University, Zhengjiang, Jiangsu 212013, China

<sup>5</sup>Department of Radiology, The Affiliated Hospital of Youjiang Medical University for Nationalities, Baise, Guangxi 533000, China

<sup>6</sup>Department of Cardiology, Liuzhou People's Hospital Affiliated to Guangxi Medical University, Liuzhou, Guangxi 545006, China

Correspondence should be addressed to Wei Zhang; zhangwei@glmc.edu.cn, Deyou Huang; fzxyh2012@126.com, and Liu Miao; doc\_miaoliu@163.com

Received 5 May 2022; Accepted 20 August 2022; Published 29 September 2022

Academic Editor: Tian Li

Copyright © 2022 Wei Zhang et al. This is an open access article distributed under the Creative Commons Attribution License, which permits unrestricted use, distribution, and reproduction in any medium, provided the original work is properly cited.

**Objective.** The off-target effects and severe side effects of PPAR $\alpha$  and LXR $\alpha$  agonists greatly limit their application in atherosclerosis (AS). Therefore, this study intended to use mesoporous silica nanoparticles as carriers to generate MnO nanoparticles in situ with T1WI-MRI in mesoporous pores and simultaneously load PPAR $\alpha$  and LXR $\alpha$  agonists. Afterward, cRGD-chelated platelet membranes can be used for coating to construct a new nanotheranostic agent. **Methods.** cRGD-platelet@MnO/MSN@PPAR $\alpha$ /LXR $\alpha$  nanoparticles were synthesized by a chemical method. Dynamic light scattering (DLS) was utilized to detect the size distribution and polydispersity index (PDI) of the nanoparticles. The safety of the nanoparticles was detected by CCK8 in vitro and HE staining and kidney function in vivo. Cell apoptosis was detected by flow cytometry detection and TUNEL staining. Oxidative stress responses (ROS, SOD, MDA, and NOX levels) were tested via a DCFH-DA assay and commercial kits. Immunofluorescence and phagocytosis experiments were used to detect the targeting of nanoparticles. Magnetic resonance imaging (MRI) was used to detect the imaging performance of cRGD-platelet@MnO/MSN@PPAR $\alpha$ /LXR $\alpha$  nanoparticles. Using western blotting, the expression changes in LXR $\alpha$  and ABCA1 were identified. **Results.** cRGD-platelet@MnO/MSN@PPAR $\alpha$ /LXR $\alpha$  nanoparticles were successfully established, with a particle size of approximately 150 nm and PDI less than 0.3, and showed high safety both in vitro and in vivo. cRGD-platelet@MnO/MSN@PPAR $\alpha$ /LXR $\alpha$  nanoparticles showed good targeting properties and better MRI imaging performance in AS. cRGD-platelet@MnO/MSN@PPAR $\alpha$ /LXR $\alpha$  nanoparticles showed better antioxidative capacities, MRI imaging performance, and diagnostic and therapeutic effects on AS by regulating the expression of LXR $\alpha$  and ABCA1. **Conclusion.** In the present study, cRGD-platelet@MnO/MSN@PPAR $\alpha$ /LXR $\alpha$  nanoparticles with high safety and the capacity to target vulnerable plaques of AS were successfully established. They showed better performance on MRI images and treatment effects on AS by promoting cholesterol efflux through the regulation of ABCA1. These findings might address the problems of off-target effects and side effects of nanoparticle-mediated drug delivery, which will enhance the efficiency of AS treatment and provide new ideas for the clinical treatment of AS.

## 1. Introduction

Atherosclerosis (AS) is a chronic disease caused by inflammation in the blood vessel wall, which leads to plaque formation in the endothelial lining in the blood vessel. AS plays a major role in cardiovascular and cerebrovascular-related diseases, which seriously endanger human health [1]. Despite the widespread and successful use of cholesterol-lowering drugs, cardiovascular disease caused by AS is still the leading cause of death worldwide [2]. Kattoor et al. mentioned that reactive oxygen species play a vital role in AS progression [3] and contribute to endothelial injuries [4]. Clarifying the components of AS plaques through auxiliary examinations and assessing the stability of the plaques can provide risk assessment for predicting the occurrence of clinical events. However, the current role of imaging technology is limited to the examination level. The diagnosis of AS still mainly depends on the thickness of the arterial wall and signs of calcification [5]. It is of great significance to identify the components of AS plaques for the targeted treatment of AS.

MRI is a successful imaging technique that is used to diagnose various diseases [6, 7]. With the rapid development of nanoscience and technology, the development of new targeted delivery strategies and new and efficient MRI-T1 contrast agents overcome the cytotoxicity limitations of traditional Gd agents and have pharmacokinetic advantages [8, 9]. This has promoted the successful delivery of the payload to the plaque and realized the diagnosis and treatment of AS [10, 11]. Mesoporous manganese silicate nanoparticles provide a larger surface area for water molecules, and the paramagnetic high-spin metal ions present on the nanoparticle surface have the greatest accessibility to the surrounding water molecules. Therefore, nanoparticles with smaller sizes and larger surface area to volume ratios show a better enhancement effect on T1WI [12]. Therefore, it is necessary to develop a manganese-based MRI-T1 contrast agent to replace the cytotoxic GdIII agent while achieving similar or even better enhancement effects, which has important clinical application value.

The steady state of cholesterol inflow and outflow is of vital importance in the formation of atherosclerosis. With the widespread use of statins, the reduction in cholesterol influx has been clinically successful; however, most cardiovascular-related events still occur due to the plaque load at the beginning of treatment. Therefore, enhancing the cholesterol outflow of atherosclerosis has become the most acceptable treatment to promote AS regression. PPAR and LXR $\alpha$  agonists can upregulate the expression of macrophage ABCA1/ABCG1, promote apoA-I-mediated cholesterol efflux, enhance the burial effect of apoptotic cells in the body, and reduce the formation of atherosclerosis in the body [13, 14] and can already be used as oral preparations. However, due to their systemic off-target effects, such as liver steatosis and heart failure, their clinical application is restricted. Therefore, to achieve safe and efficient treatment of AS, it is necessary to develop new noninvasive, targeted diagnosis and therapeutic drug delivery methods for AS.

Platelets are an important part of blood flow and have the ability to maintain blood circulation integrity and help

to target vascular injury [15]. It has been demonstrated that modification of nanoparticles with platelet membranes can significantly enhance the targeting of the carrier [16]. Compared with uncoated nanoparticles, platelet membrane-coated nanoparticles can avoid complement activation and the uptake of macrophages, provide nanoparticles with immune escape ability, and can be positioned in deep locations [17]. Neovascularization and macrophages in AS plaques overexpress integrin  $\alpha v\beta 3$ , which can be used to detect the early stages of plaques by targeting the arginine-glycine-aspartate polypeptide loop sequence (cRGD) [18, 19]. Therefore, designing cRGD-modified biointerface platelet membrane-modified nanoparticles for targeted drug delivery within AS plaques is important and difficult and needs to be resolved, in order to provide a new strategy for the clinical treatment of AS. Thus, this study is aimed at constructing mesoporous silica nanoparticles coated with cRGD-platelets and evaluate targeted diagnosis and therapeutic monitoring of AS based on mesoporous silica nanoparticles coated with cRGD-platelets.

## 2. Materials and Methods

**2.1. cRGD-Platelet@MnO/MSN@PPAR $\alpha$ /LXR $\alpha$  Nanoparticle Synthesis.** Two grams of cetyltrimethylammonium chloride and 0.02 g of triethanolamine were dissolved in 20 mL of water and stirred vigorously, and then the mixed solution was incubated at 80°C for 1 h. Then, 1.5 mL of tetraethyl orthosilicate was added, and stirring was continued for 1 h. The centrifuged product was washed three times with ethanol to eliminate the remaining reactants after centrifugation. Then, CTAC was removed by adding 1 wt% sodium chloride in methanol for 3 h at room temperature. MnOx nanoparticles were introduced into the pores through a redox reaction, and H<sub>2</sub> (5%)/Ar (95%) MnO/MSN nanoparticles were obtained under high-temperature reduction. The extracted MnO/MSN was thoroughly washed with ethanol and water and vacuum dried at room temperature (RT). Then, 5 mg MnO/MSNs was dispersed into 6 mL PPAR $\alpha$  and LXR $\alpha$  agonist PBS solution and stirred at RT for 24 h in the dark, and MnO/MSN/@PPAR $\alpha$ /LXR $\alpha$  was obtained by centrifugation. The nanoparticles were then added to the platelet membrane and ultrasonicated for 2 min to coat the platelet membrane. The carboxyl-free RGD cyclic peptide molecules were modified to the surface of platelet membrane nanoparticles by the carbodiimide method. Then, the above products and RGD cyclic peptide were mixed in MES buffer and incubated for 30 min. EDC and NHS (0.01 M) were added and placed in a constant temperature shaker at room temperature to react for 24 h. Then, the mixture was centrifuged to remove unreacted RGD cyclic peptide molecules. cRGD-platelet membrane@MnO/MSN@PPAR $\alpha$ /LXR $\alpha$  nanoparticles were obtained by centrifugation and freeze-dried after washing with DMSO. Dynamic light scattering (DLS) was utilized to detect the size distribution of the nanoparticles.

**2.2. Particle Size Measurement.** The hydrodynamic diameter and polydispersity index (PDI) of MnO/MSN, MnO/MSN@PPAR $\alpha$ /LXR $\alpha$ , and cRGD-platelet@MnO/MSN@PP

AR $\alpha$ /LXR $\alpha$  were determined using a nanosize analyzer with a dynamic light scattering (DLS) instrument.

**2.3. Cell Culture and Treatment.** THP-1 cells were ordered from the Global Bioresource Center (ATCC, USA), cultured in RPMI 1640 supplemented with 100 U/mL penicillin, fetal bovine serum (10%), and 100  $\mu$ g/mL streptomycin and placed in a humidified chamber (5% CO<sub>2</sub> at 37°C). The THP-1 cells were differentiated into macrophages by adding 100 ng/mL PMA for 72 h. The macrophages were transformed into foam cells by incubating for 48 h with 50  $\mu$ g/mL oxLDL in serum-free RPMI 1640 medium containing 0.3% BSA [20].

**2.4. CCK-8 Assay.** Endothelial cells were seeded in 96-well plates at a density of  $1 \times 10^4$ /well, and then the nanoparticles at different concentrations (0, 5, 10, 20, 100, 1000  $\mu$ g/mL) were added to the cells and incubated for 24 and 48 h. Culture medium without the nanoparticles was used as a blank control. The viability of endothelial cells was measured using the Cell Counting Kit-8 (Sigma-Aldrich, USA). In brief, a total of 10  $\mu$ l of CCK-8 solution was added to the cells and incubated for 30 min at 37°C. Absorbance was measured by using a microplate reader (Bio-Rad Laboratories, Inc. Ltd., USA) at 450 nm [21].

**2.5. Atherosclerosis Model in Rats.** Eight-week SPF male Sprague Dawley (SD) rats weighing 200~250 g were purchased from Beijing Vital River Co., Ltd. The AS model in rats was established according to a previous report by feeding with a high-fat diet [22]. The high-fat feed was composed of 20% egg yolk, 5% sugar, 8% lard, and 65% basic feed, fed for 12 weeks, and the AS model was successfully established. Feed was prepared daily, and intake was recorded. After the model was established, the relevant *in vivo* experiments were started, and the rats with AS were randomly divided into 3 groups, including the control group injected with saline, the cRGD-platelet @MnO/MSN@PPAR $\alpha$ /LXR $\alpha$  group, and the platelet membrane@MnO/MSN@PPAR $\alpha$ /LXR $\alpha$  group. The injection was performed by tail vein injection, and all samples were within the safe dose range. ICP-AES quantitative methods were used to evaluate the concentration of diagnostic and therapeutic agents in AS plaques.

**2.6. Western Blot Analysis.** The membranes were incubated in 5% skim milk containing Tween-20 and TRIS-buffered saline for 1 hour. After that, the blocked membranes were placed in a solution containing anti-LXR $\alpha$  (1:2,000) and anti-ABCA1 (as a loading control, 1:1,000) antibodies overnight at 4°C. The next day, the membrane was washed with PBS and then placed in a solution with horseradish peroxidase- (HRP-) conjugated secondary antibody (1:5,000) for 1 h. Images were taken by a ChemiDoc MP nucleic acid protein imaging system (Bio-Rad, USA) with enhanced chemiluminescence reagents. Band density was quantified with ImageJ software.

**2.7. Hematoxylin-Eosin (HE) Staining.** Paraffin-embedded tissue samples with nanoparticle treatment were obtained and cut into 4  $\mu$ m-thick sections. Furthermore, the sections

were dipped in hematoxylin staining solution for 3-5 min, and then the slices were rinsed with running water. Subsequently, the slides were dehydrated with 85% and 95% gradient alcohol for 5 min and then stained for 5 min in eosin staining solution. Finally, the cells were washed, images were taken with a microscope (Olympus, Japan) after dehydration, and neutral gum was used to seal the slides.

**2.8. Immunohistochemical Staining.** Paraffin-embedded tissue sections (4  $\mu$ m thickness) were deparaffinized with xylene and rehydrated using graded alcohols. Hydrogen peroxide with 3% in methanol (50%) was used to block endogenous peroxidase for 10 min at RT. The tissue sections were placed in citrate buffer, heated in a microwave oven for 20 min, and then incubated with primary antibody against PCNA (goat polyclonal, Santa Cruz, sc-9857, 1:100 dilution, USA) overnight at 4°C. After that, the slices were washed with PBS and placed in a solution containing biotinylated secondary antibodies, and an avidin-biotinylated peroxidase complex was performed. The color was generated by DAB. Finally, the sections were counterstained with hematoxylin and imaged by a microscope.

**2.9. Terminal Deoxynucleotidyl Transferase-Mediated d-UTP Nick End Labeling (TUNEL) Assay.** Apoptotic cells in tissues were detected by using terminal deoxynucleotidyl transferase-mediated d-UTP nick end labeling (TUNEL). First, sections were immersed in proteinase K (20 min), and deparaffinization and rehydration were conducted. at RT. Then, the sections were placed in TUNEL reaction for 60 minutes at 37°C and washed with PBS thoroughly. Finally, the TUNEL-positive cells labeled with FITC were imaged under fluorescence microscopy (BX-60, Olympus, Japan) with 530 nm emission and 488 nm excitation. Image-Pro Plus 6.0 software was utilized to estimate the number of apoptotic cells [23].

**2.10. Measurement of Oxidative Stress Response Markers.** The levels of ROS in cells and tissues were evaluated using a fluorescent 2',7'-dichlorofluorescein diacetate (DCFH-DA) assay (Beyotime, China). The cells were seeded on a 96-well black plate at  $1 \times 10^5$  cells/mL and incubated. The tissues were homogenized and centrifuged. After removing the medium or the supernatant, 10  $\mu$ M DCFH-DA in PBS was added and maintained for 0.5 h. The fluorescence was measured (ex: 480 nm, em: 530 nm) using a VersaMax microplate reader (MD, USA). The levels of SOD, MDA, and NOX in cells and tissues were measured using commercial detection kits (Beyotime, China) and a VersaMax microplate reader (MD, USA).

**2.11. Statistical Analysis.** The experiments were performed in triplicate and repeated three times. Statistical analyses were performed by utilizing SPSS 21.0 software (SPSS, Inc., USA), and all data were expressed as the means  $\pm$  standard deviations (SD). Differences between two groups or more than two groups were analyzed by Student's unpaired *t*-test and ANOVA followed by an appropriate post hoc test, respectively. *p* < 0.05 was considered as a significant difference.

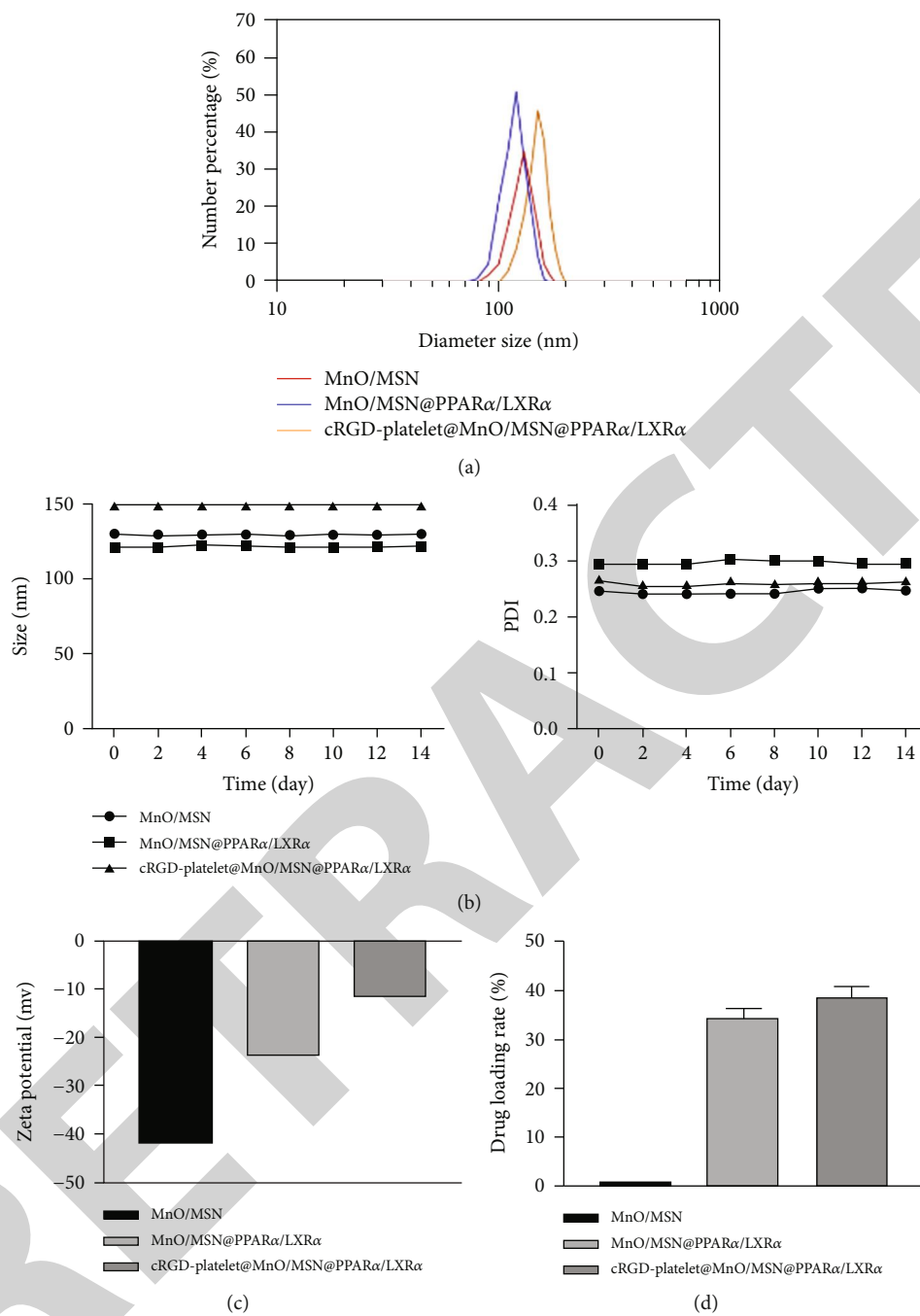


FIGURE 1: Continued.

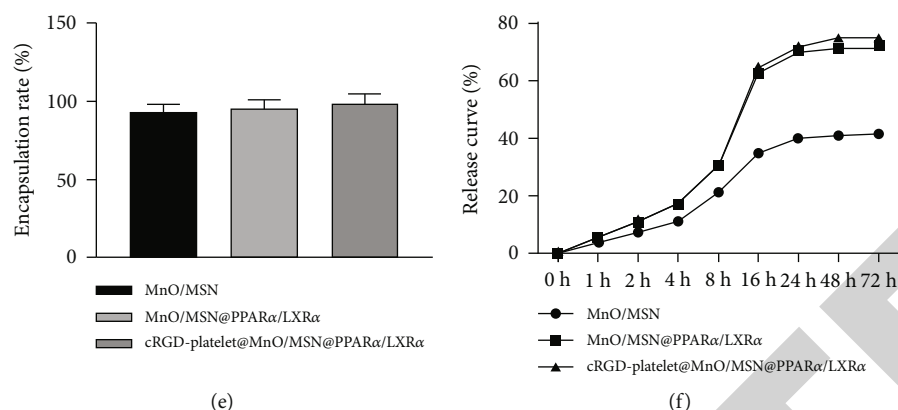


FIGURE 1: Characteristics of cRGD-platelet@MnO/MSN@PPAR $\alpha$ /LXR $\alpha$  nanoparticles. (a) DLS diameters of MnO/MSN, MnO/MSN@PPAR $\alpha$ /LXR $\alpha$ , and cRGD-platelet@MnO/MSN@PPAR $\alpha$ /LXR $\alpha$ . (b) The variations in particle size and PDI of cRGD-platelet@MnO/MSN@PPAR $\alpha$ /LXR $\alpha$  at 4°C for 14 days. (c) The zeta potential of cRGD-platelet@MnO/MSN@PPAR $\alpha$ /LXR $\alpha$ . (d, e) Drug loading rate and the encapsulation rates for cRGD-platelet@MnO/MSN@PPAR $\alpha$ /LXR $\alpha$ , respectively. (f) Drug cumulative release of cRGD-platelet@MnO/MSN@PPAR $\alpha$ /LXR $\alpha$ ;  $n = 1$  for (a)–(c) and (f);  $n = 3$  for (d) and (e).

### 3. Results

**3.1. Characteristics of cRGD-Platelet@MnO/MSN@PPAR $\alpha$ /LXR $\alpha$  Nanoparticles.** MnO/MSN, MnO/MSN@PPAR $\alpha$ /LXR $\alpha$ , and cRGD-platelet@MnO/MSN@PPAR $\alpha$ /LXR $\alpha$  have particle sizes of  $\sim 130$  nm,  $\sim 120$  nm, and  $\sim 150$  nm, respectively, as determined by DLS (Figure 1(a)). When these nanoparticles were incubated at 4°C for 14 days, there were no significant changes in size or PDI, indicating the intrinsic stability of these nanoparticles (Figure 1(b)). Simultaneously, the zeta potentials of MnO/MSN, MnO/MSN@PPAR $\alpha$ /LXR $\alpha$ , and cRGD-platelet@MnO/MSN@PPAR $\alpha$ /LXR $\alpha$  were  $-41.8$  mV,  $-23.4$  mV, and  $-11.8$  mV, respectively. The changing trend of zeta potential suggested that it was reasonable to adopt the synthesis processes (Figure 1(c)). In addition, we found that the drug loading rate was 38.63%, and the encapsulation rate was 98.86% for cRGD-platelet@MnO/MSN@PPAR $\alpha$ /LXR $\alpha$  (Figures 1(d) and 1(e)). The drug cumulative release reached 80% at 10 h, and cRGD-platelet@MnO/MSN@PPAR $\alpha$ /LXR $\alpha$  showed the best drug cumulative release curve (Figure 1(f)).

**3.2. Safety Assessment of cRGD-Platelet@MnO/MSN@PPAR $\alpha$ /LXR $\alpha$  Nanoparticles.** To ensure the safety of the cRGD-platelet@MnO/MSN@PPAR $\alpha$ /LXR $\alpha$  nanoparticles, the cytotoxicity of the nanoparticles was measured in vitro and in vivo. CCK-8 analysis and flow cytometry analysis indicated that the cell proliferation and apoptosis of foam cell cells were not significantly changed when treated with different concentrations of cRGD-platelet@MnO/MSN@PPAR $\alpha$ /LXR $\alpha$  nanoparticles (Figures 2(a) and 2(b)). In vivo, routine blood, liver, and kidney function were not affected in all mice treated with different concentrations of cRGD-platelet@MnO/MSN@PPAR $\alpha$ /LXR $\alpha$  nanoparticles (Figure 2(c)). Meanwhile, no obvious changes were found for the contents of alanine aminotransferase (ALT), aspartate aminotransferase (AST), urea nitrogen (BUN), and creatinine (CREA) in serum injected with different concentrations of cRGD-platelet@MnO/MSN@PPAR $\alpha$ /LXR $\alpha$  nanoparticles compared with the control group

(Figure 2(d)). H&E staining indicated that the tissues presented normal cell morphology, clear boundaries, and orderly tissue structures without inflammation and cell injury treatment with different concentrations of cRGD-platelet@MnO/MSN@PPAR $\alpha$ /LXR $\alpha$  nanoparticles (Figure 2(e)). In addition, TUNEL and PCNA immunohistochemistry suggested that apoptosis and proliferation were not affected by cRGD-platelet@MnO/MSN@PPAR $\alpha$ /LXR $\alpha$  nanoparticles at different concentrations (Figures 2(f) and 2(g)). These results indicated that cRGD-platelet@MnO/MSN@PPAR $\alpha$ /LXR $\alpha$  nanoparticles are safe.

**3.3. Targeting Performance Evaluation of cRGD-Platelet@MnO/MSN@PPAR $\alpha$ /LXR $\alpha$  Nanoparticles.** The targeting performance of cRGD-platelet@MnO/MSN@PPAR $\alpha$ /LXR $\alpha$  nanoparticles was detected by laser confocal microscopy at 0.5, 2 h, 4 h, and 8 h in vitro. As shown in Figure 3(a), the fluorescence signals of both cRGD-platelet@MnO/MSN@PPAR $\alpha$ /LXR $\alpha$  nanoparticles and platelet@MnO/MSN@PPAR $\alpha$ /LXR $\alpha$  nanoparticles increased with increasing time. However, the fluorescence signal was also significantly increased in the cRGD-platelet@MnO/MSN@PPAR $\alpha$ /LXR $\alpha$  nanoparticle group compared with the platelet@MnO/MSN@PPAR $\alpha$ /LXR $\alpha$  group. Furthermore, the T1-MRI signal was enhanced as the concentration of the original nanomaterials increased (Figure 3(b)). The T1-MRI signal was also enhanced in the cRGD-platelet@MnO/MSN@PPAR $\alpha$ /LXR $\alpha$  nanoparticle group compared with the platelet@MnO/MSN@PPAR $\alpha$ /LXR $\alpha$  nanoparticle group (Figure 3(b)). In addition, flow cytometry analysis indicated that decreased phagocytosis was observed in the cRGD-platelet@MnO/MSN@PPAR $\alpha$ /LXR $\alpha$  nanoparticle group compared with the platelet@MnO/MSN@PPAR $\alpha$ /LXR $\alpha$  nanoparticle group (Figure 3(c)). In addition, we found that the nanoparticles were mainly enriched in the arterial plaque after 4 h (Figure 3(d)). These results demonstrated that cRGD-platelet@MnO/MSN@PPAR $\alpha$ /LXR $\alpha$  nanoparticles showed good targeting properties in AS.

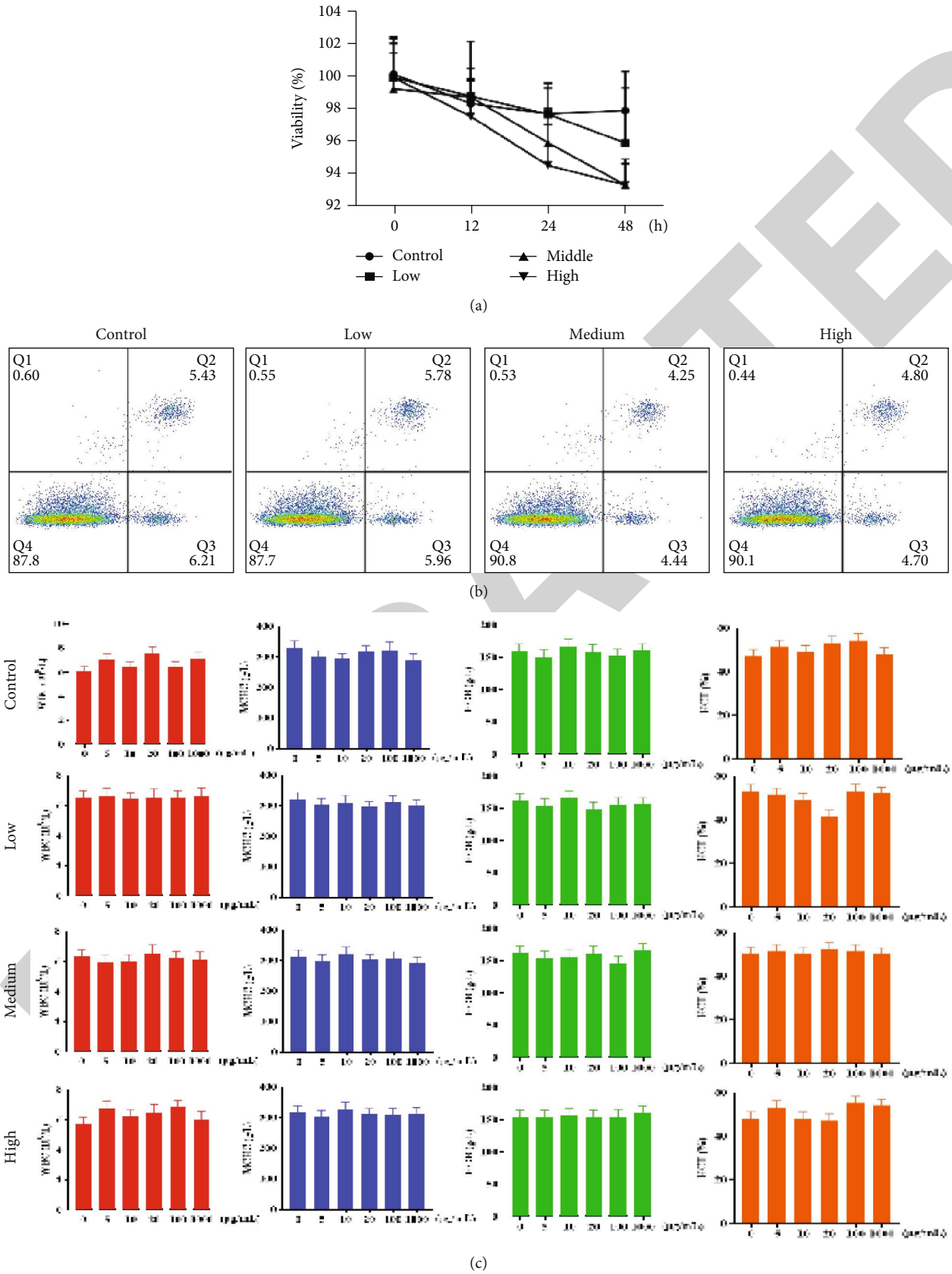
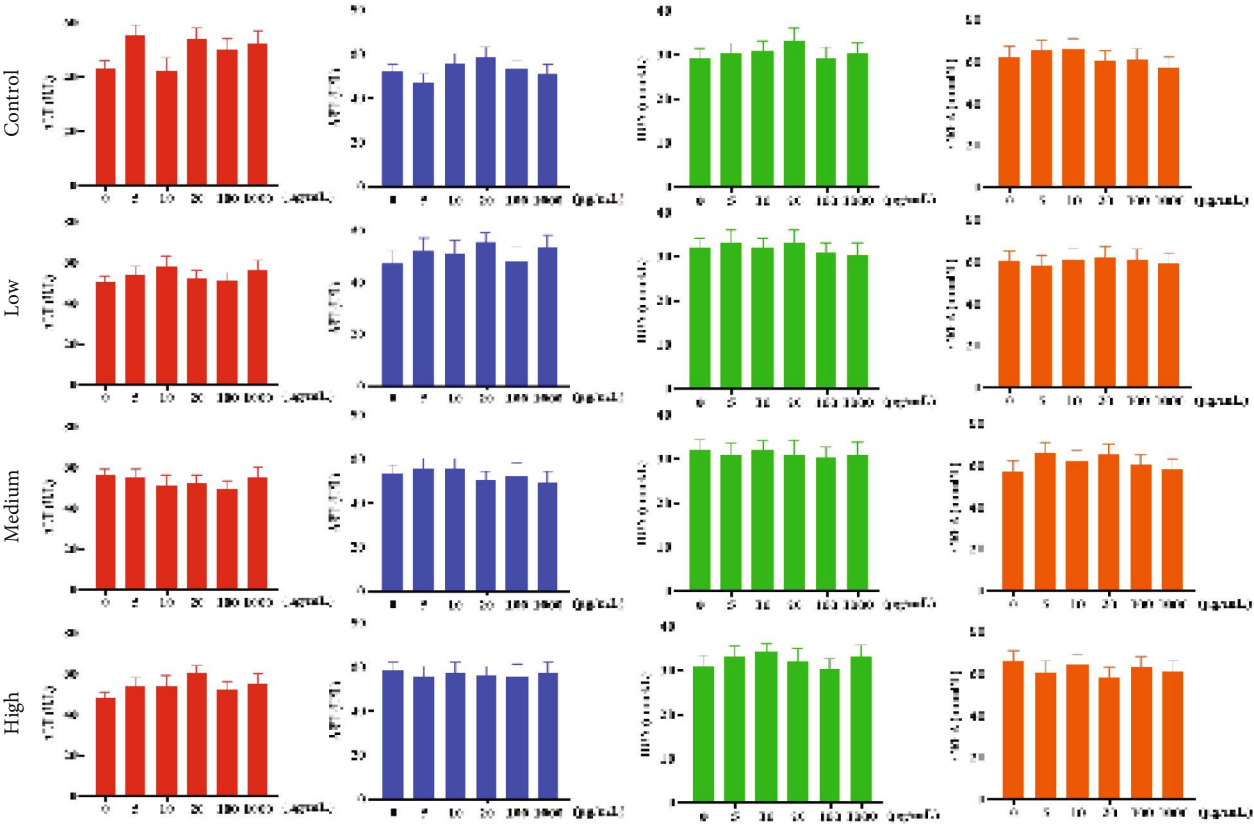
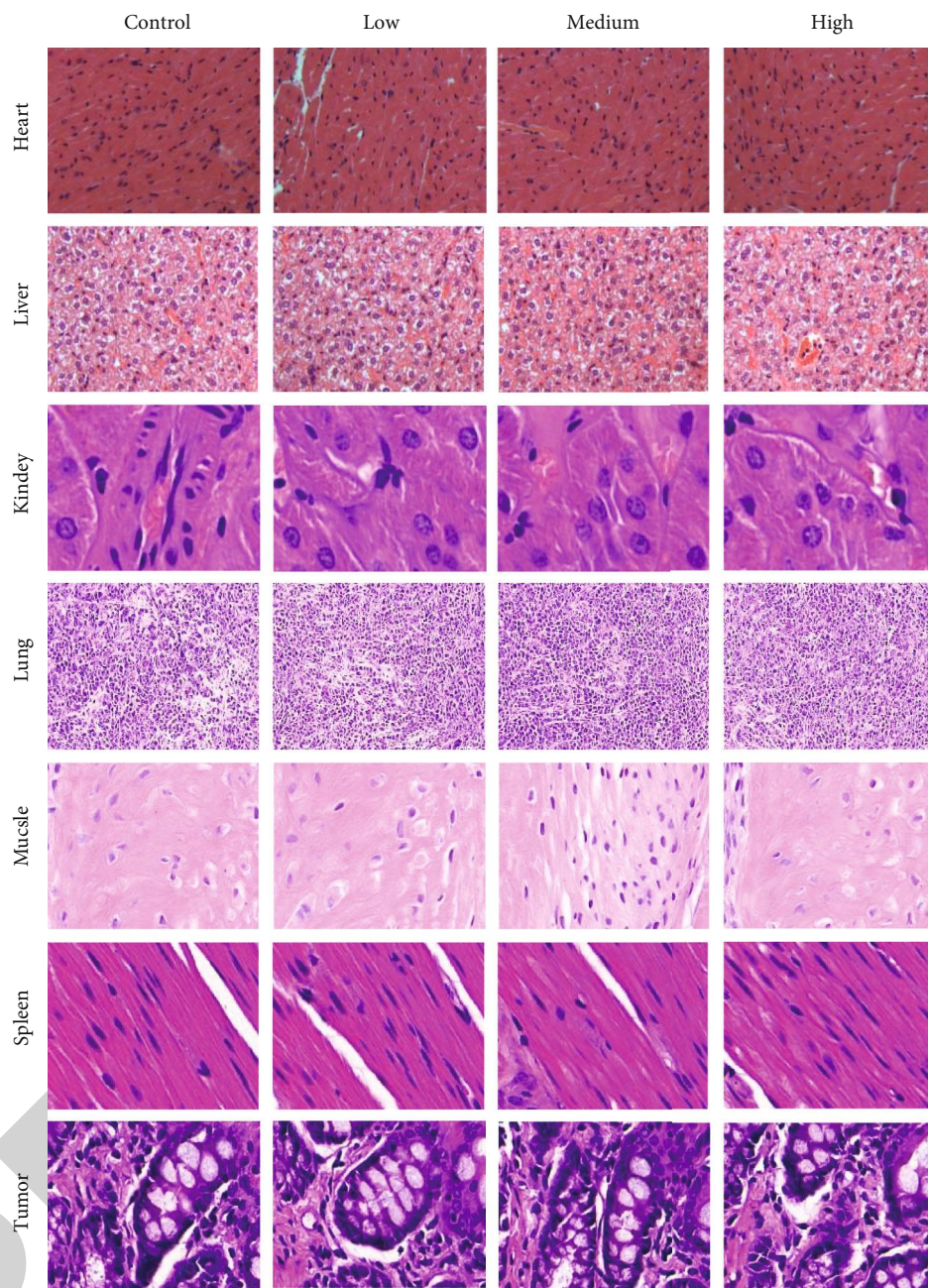


FIGURE 2: Continued.





(d)  
FIGURE 2: Continued.



(e)

FIGURE 2: Continued.

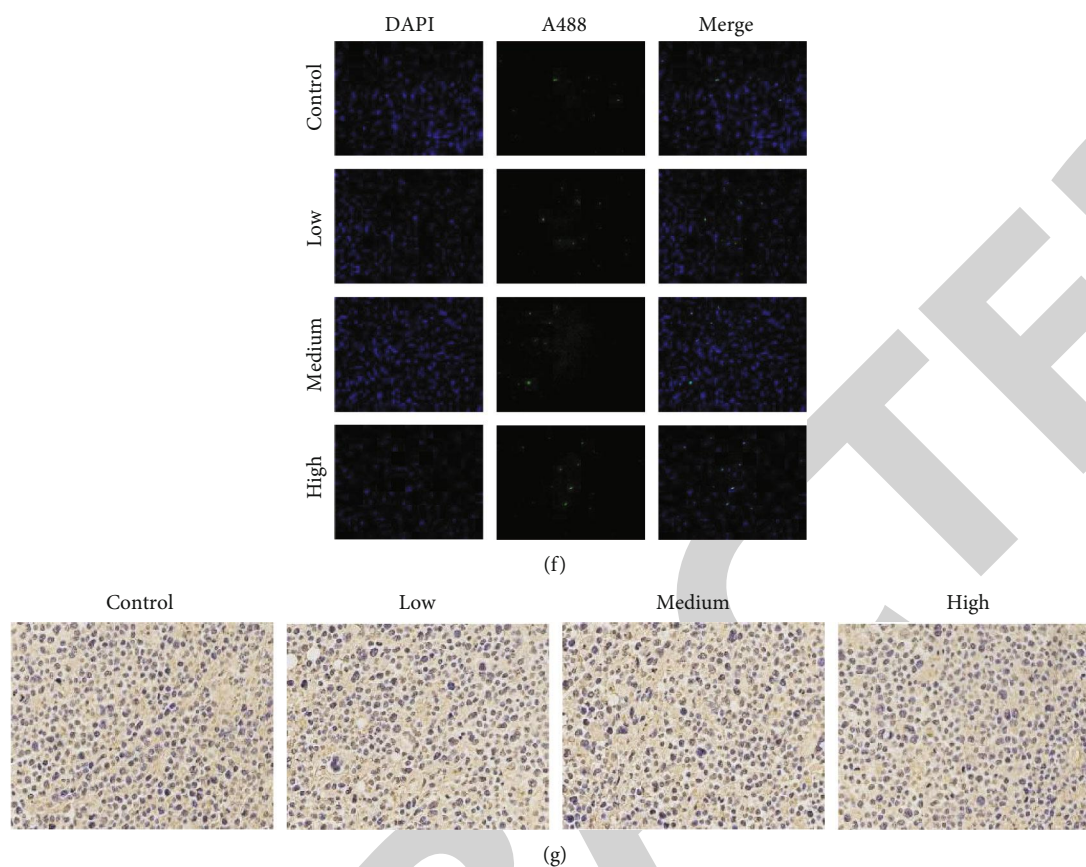
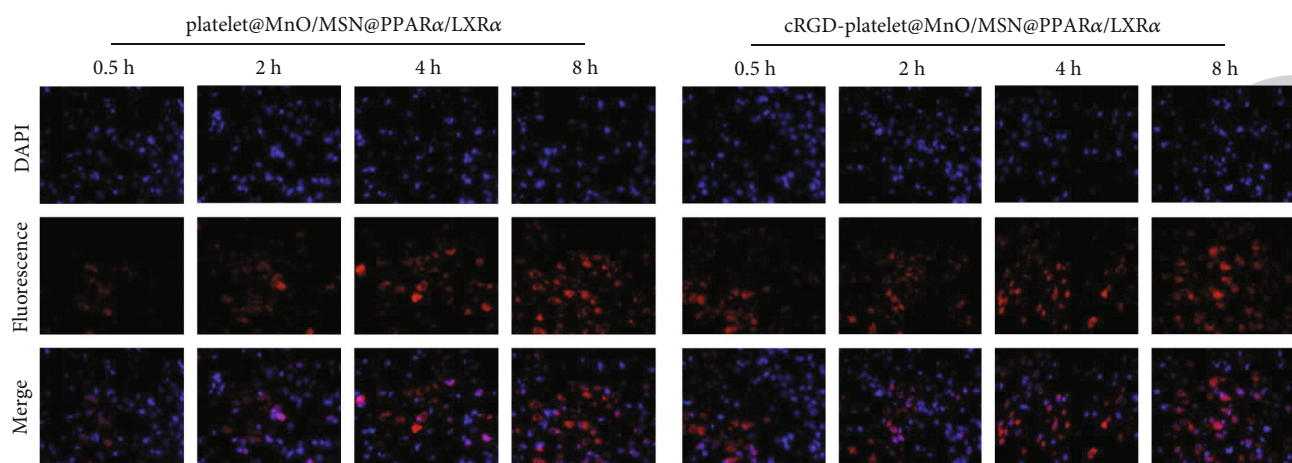


FIGURE 2: Safety assessment of cRGD-platelet@MnO/MSN@PPAR $\alpha$ /LXR $\alpha$  nanoparticles. (a) CCK-8 was used to detect the proliferation of THP-1 cells and foam cells treated with different nanoparticles. (b) Flow cytometry assay was used to detect the apoptosis of foam cells treated with different nanoparticles. (c) The routine blood, liver, and kidney function were detected by ELISA after treatment with different concentrations of nanoparticles. (d) The contents of ALT, AST, BUN, and CREA in serum injected with different concentrations of nanoparticles. (e) H&E staining was utilized to detect the status of the tissue in different organs treated with different concentrations of nanoparticles. (f, g) TUNEL and PCNA immunohistochemistry were used to detect the changes in apoptosis and proliferation after treatment with nanoparticles at different concentrations. Data are shown as the mean  $\pm$  SD.  $n = 1$  for (b) and (e)–(g);  $n = 3$  for (a), (c), and (d).

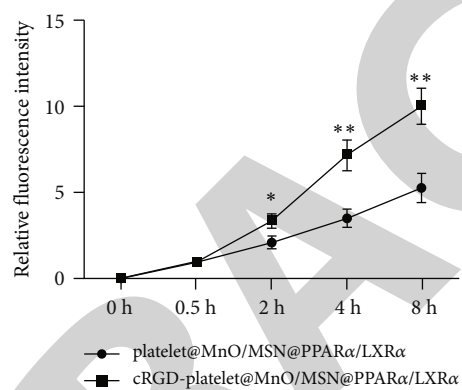
**3.4. Diagnostic and Therapeutic Evaluation of cRGD-Platelet@MnO/MSN@PPAR $\alpha$ /LXR $\alpha$  Nanoparticles.** The effect of cRGD-platelet@MnO/MSN@PPAR $\alpha$ /LXR $\alpha$  nanoparticles on the diagnosis and treatment of AS was assessed. As shown in Figure 4(a), CCK-8 analysis showed that compared with the control group, cell viability was significantly inhibited in both the cRGD-platelet@MnO/MSN@PPAR $\alpha$ /LXR $\alpha$  and platelet@MnO/MSN@PPAR $\alpha$ /LXR $\alpha$  nanoparticle groups when the dose was more than 10  $\mu$ mol/L, and the inhibitory effect was dose-dependent. Flow cytometry and TUNEL assays showed that the apoptosis of cells was significantly elevated when treated with both cRGD-platelet@MnO/MSN@PPAR $\alpha$ /LXR $\alpha$  and platelet@MnO/MSN@PPAR $\alpha$ /LXR $\alpha$  nanoparticles compared with the control group (Figures 4(b) and 4(c)). Moreover, the levels of ROS, SOD, MDA, and NOX were evaluated using a DCFH-DA immunofluorescent assay and commercial assay kits. It was reported that both cRGD-platelet@MnO/MSN@PPAR $\alpha$ /LXR $\alpha$  and platelet@MnO/MSN@PPAR $\alpha$ /LXR $\alpha$  nanoparticles could reduce cellular oxidative stress responses in contrast to the control group, and cRGD-platelet@MnO/

MSN@PPAR $\alpha$ /LXR $\alpha$  nanoparticles exerted better antioxidative effects than platelet@MnO/MSN@PPAR $\alpha$ /LXR $\alpha$  nanoparticles (Figures 4(d) and 4(e)). ELISA analysis indicated that the contents of IL-10 and TGF- $\beta$  were significantly decreased when treated with both cRGD-platelet@MnO/MSN@PPAR $\alpha$ /LXR $\alpha$  and platelet@MnO/MSN@PPAR $\alpha$ /LXR $\alpha$  nanoparticles compared with the control group (Figure 4(f)). The expression changes of ABCA1 and LXR $\alpha$  also confirmed these results (Figure 4(g)). In addition, we found that the diagnostic and therapeutic effects of cRGD-platelet@MnO/MSN@PPAR $\alpha$ /LXR $\alpha$  nanoparticles against AS were dose-dependent, and cRGD-platelet@MnO/MSN@PPAR $\alpha$ /LXR $\alpha$  nanoparticles showed better performance and antioxidative capacities than platelet@MnO/MSN@PPAR $\alpha$ /LXR $\alpha$  nanoparticles (Figures 4(a)–4(g)).

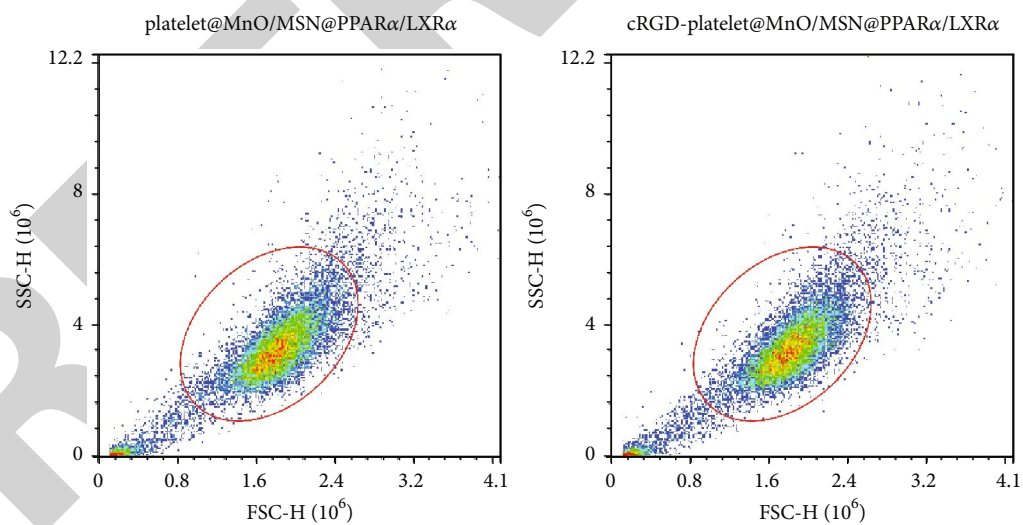
To further confirm the effect of cRGD-platelet@MnO/MSN@PPAR $\alpha$ /LXR $\alpha$  nanoparticles on the diagnosis and treatment of AS, *in vivo* experiments were performed with 30  $\mu$ mol/L cRGD-platelet@MnO/MSN@PPAR $\alpha$ /LXR $\alpha$  nanoparticles. ICP–AES indicated that the cRGD-platelet@MnO/MSN@PPAR $\alpha$ /LXR $\alpha$  nanoparticles were significantly enriched in the plaque



(a)



(b)



(c)

FIGURE 3: Continued.

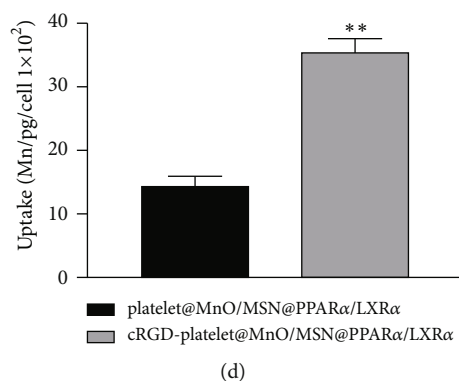


FIGURE 3: Targeting performance evaluation of cRGD-platelet@MnO/MSN@PPAR $\alpha$ /LXR $\alpha$  nanoparticles. (a) The fluorescence signal of nanoparticles detected by laser confocal microscopy at 0.5, 2 h, 4 h, and 8 h in vitro. (b) The T1-MRI signal was enhanced as the concentration of the original nanomaterials increased. (c) Flow cytometry analysis was utilized to detect the phagocytosis affected by nanoparticles. (d) ICP-AES was utilized to detect the enrichment of cRGD-platelet@MnO/MSN@PPAR $\alpha$ /LXR $\alpha$  nanoparticles in the arterial plaque. Data are shown as the mean  $\pm$  SD, \*\* $p < 0.01$  vs. platelet@MnO/MSN@PPAR $\alpha$ /LXR $\alpha$ .  $n = 1$  for (a) and (c);  $n = 3$  for (b) and (d).

area and showed better enrichment than platelet@MnO/MSN@PPAR $\alpha$ /LXR $\alpha$  (Figure 5(a)). HE staining showed that compared with the control group, the area of vascular lesions in the cRGD-platelet@MnO/MSN@PPAR $\alpha$ /LXR $\alpha$  and platelet@MnO/MSN@PPAR $\alpha$ /LXR $\alpha$  model groups was significantly decreased (Figure 5(b)). The TUNEL immunofluorescence assay indicated that the intimal injury area and plaque area were significantly decreased when treated with cRGD-platelet@MnO/MSN@PPAR $\alpha$ /LXR $\alpha$  and platelet@MnO/MSN@PPAR $\alpha$ /LXR $\alpha$  compared with the control group (Figure 5(c)). Moreover, the levels of ROS, SOD, MDA, and NOX were evaluated using a DCFH-DA assay and commercial assay kits. It was reported that both cRGD-platelet@MnO/MSN@PPAR $\alpha$ /LXR $\alpha$  and platelet@MnO/MSN@PPAR $\alpha$ /LXR $\alpha$  nanoparticles could reduce oxidative stress responses in the tissues in contrast to the control group, and cRGD-platelet@MnO/MSN@PPAR $\alpha$ /LXR $\alpha$  nanoparticles exerted a better antioxidative impact than the platelet@MnO/MSN@PPAR $\alpha$ /LXR $\alpha$  nanoparticles (Figures 5(d) and 5(e)). The expression of ABCA1 and LXR $\alpha$  was significantly elevated in the cRGD-platelet@MnO/MSN@PPAR $\alpha$ /LXR $\alpha$  and platelet@MnO/MSN@PPAR $\alpha$ /LXR $\alpha$  groups compared with the control group (Figure 5(f)). These results demonstrated that cRGD-platelet@MnO/MSN@PPAR $\alpha$ /LXR $\alpha$  nanoparticles showed better diagnostic and therapeutic effects on AS.

#### 4. Discussion

Clinical cardiovascular events caused by atherosclerosis (AS) are the leading cause of death worldwide. Efficiently and safely increasing cholesterol efflux and enhancing cell apoptosis have become potential therapeutic methods, but the off-target effects and severe side effects of PPAR $\alpha$  and LXR $\alpha$  agonists have greatly restricted their clinical applications [2]. To overcome this limitation, predict the occurrence of clinical events, and monitor and evaluate the efficacy of drugs, it is necessary to develop new noninvasive, targeted diagnosis and therapeutic drug delivery methods for AS.

AS is a chronic inflammatory disease. It is an abnormal response of the blood vessel wall to various injuries. It has the characteristics of classic inflammatory degeneration, exudation, and hyperplasia. Vulnerable plaque is characterized by a large lipid pool, a large amount of macrophage aggregation, and thin fibrous caps. They are considered to be markers for identifying vulnerable plaques and evaluation parameters for high risk of future adverse events. The components of AS plaques can be analyzed through auxiliary examinations, and the stability of plaques can be evaluated, in order to provide risk assessment for predicting the occurrence of clinical events [24]. MRI technology has high tissue resolution and can accurately reflect the tissue characteristics of carotid atherosclerotic plaques, including fibrous cap, lipid core, intraplaque hemorrhage, and mural thrombus [25]. Enhanced MRI can show neovascularization, and macrophage infiltration has unique advantages in evaluating vulnerable plaques of the carotid artery [26]. Chen and Schilperoot reviewed macrophage-targeted nanoparticles and nanomedicines designed and applied in the diagnosis and treatment of AS [27]. Liang et al. reported a red blood cell biomimetic nanoparticle for AS treatment that exerted anti-inflammatory, antioxidative, and hypolipidemic effects [28]. In addition, Chyu also studied an apoB-100 peptide-linked nanoparticle to activate immunization against AS progression [29]. In recent years, studies have found that the rate of MRI contrast agent transfer from plasma to the interstitial fluid (K<sub>trans</sub> value) and flowing plasma volume (vp value) is significantly and positively correlated with the number of macrophages and new blood vessels [30]. Mesoporous silica has shown great application prospects in biomedicine and other fields due to its ordered mesoporous structure, large specific surface area, good biocompatibility, and easy surface modification, such as in MRI contrast agents, bioimaging, and nanodrug delivery systems [31, 32]. For example, Menard et al. designed hybrid protein-coated magnetic core-mesoporous silica shell nanocomposites that could be used for MRI and drug release in a 3D tumor cell model [33]. Chen et al. established an RGD-

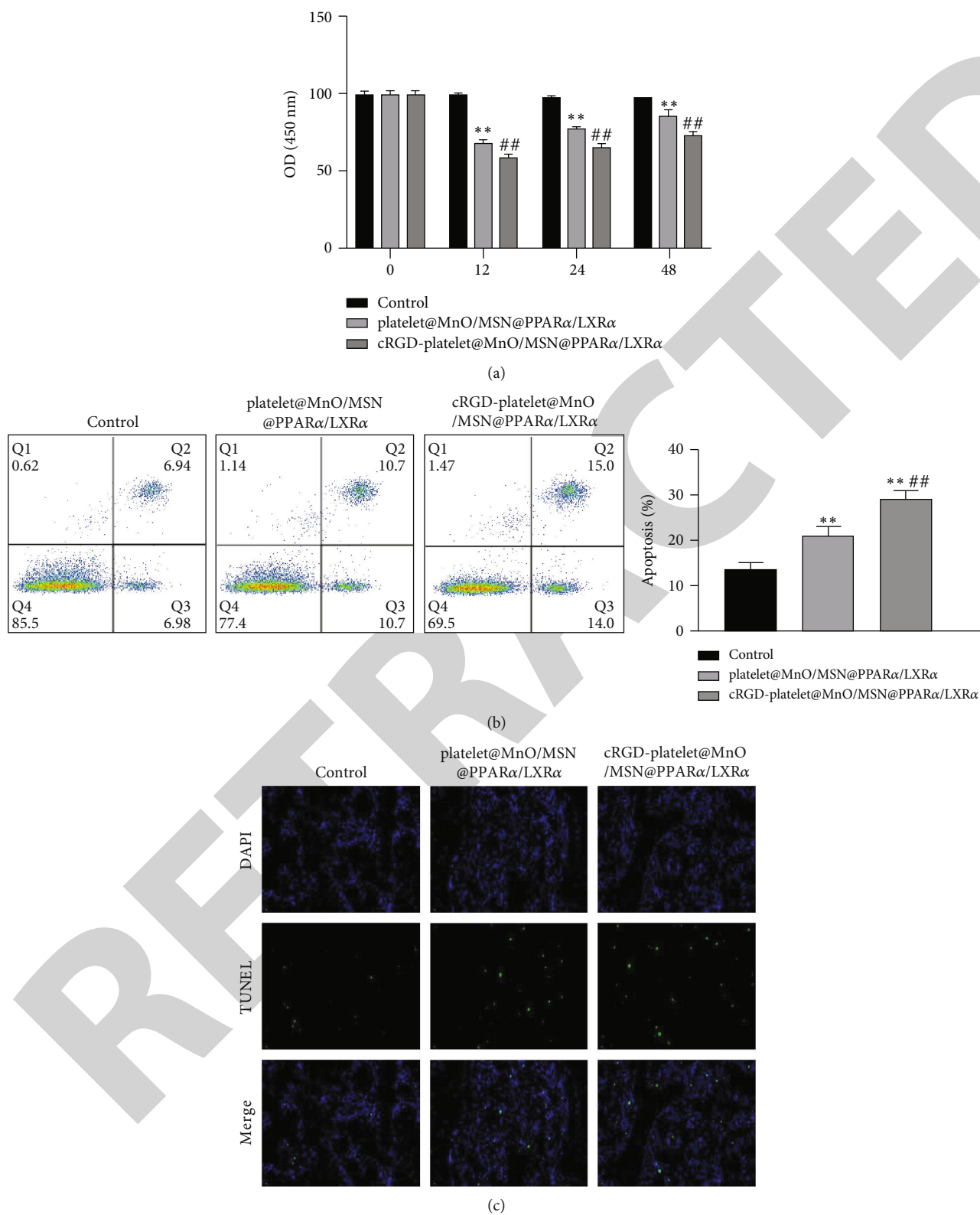


FIGURE 4: Continued.

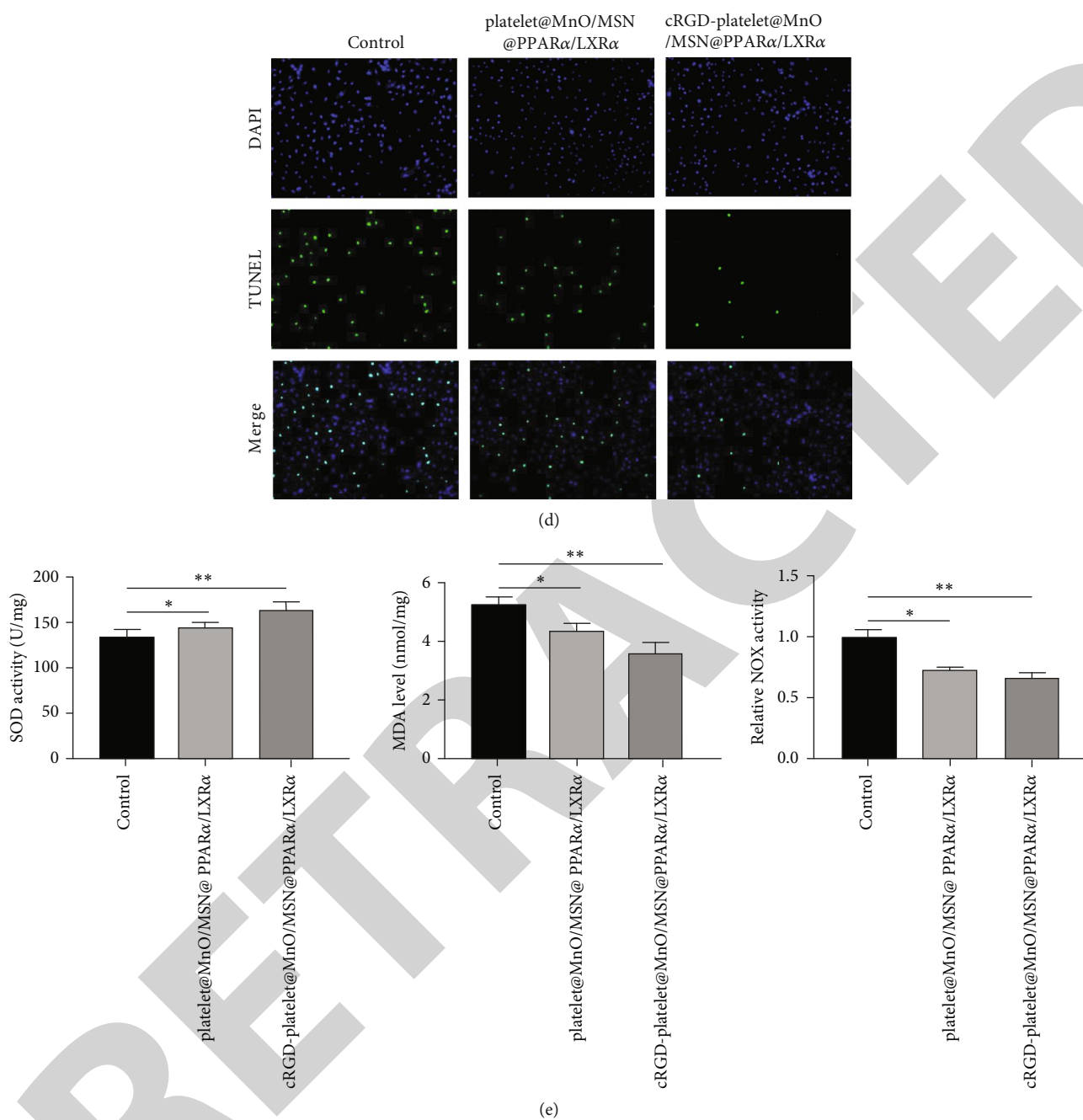


FIGURE 4: Continued.

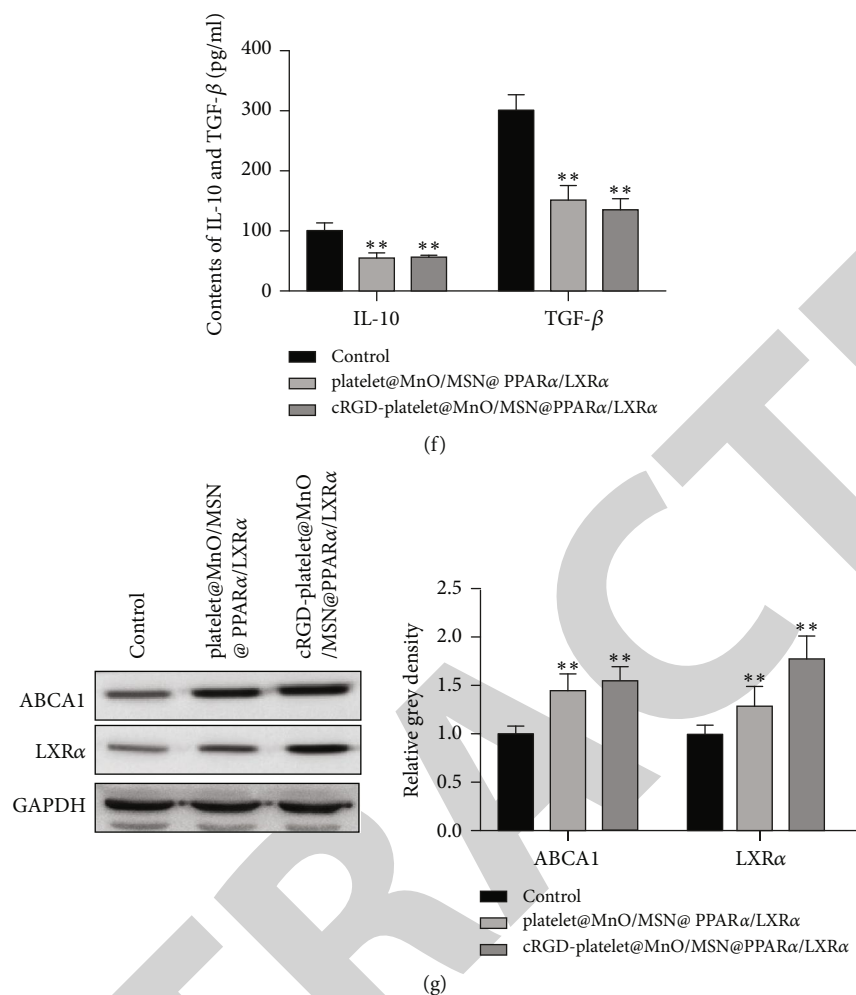


FIGURE 4: Diagnostic and therapeutic evaluation of cRGD-platelet@MnO/MSN@PPAR $\alpha$ /LXR $\alpha$  nanoparticles in vitro. (a) Cell viability was detected by CCK-8 after treatment with different nanoparticles. (b, c) Flow cytometry and TUNEL assays were utilized to determine the apoptosis of cells treated with cRGD-platelet@MnO/MSN@PPAR $\alpha$ /LXR $\alpha$ . (d) The level of ROS was detected by DCFH-DA immunofluorescent assay. (e) The levels of SOD, MDA, and NOX were evaluated using commercial assay kits. (f) ELISA analysis was used to detect the contents of IL-10 and TGF- $\beta$  after treatment with cRGD-platelet@MnO/MSN@PPAR $\alpha$ /LXR $\alpha$ . (g) The expression changes of ABCA1 and LXR $\alpha$  were determined by western blot after treatment with the cRGD-platelet@MnO/MSN@PPAR $\alpha$ /LXR $\alpha$ . Data are shown as the mean  $\pm$  SD, \*\* $p < 0.01$  vs. control.  $n = 1$  for (c) and (d);  $n = 3$  for (a), (b), (e), (f), and (g).

modified and pyroptosis-engineered theranostic agent (PETA) consisting of Fe<sub>3</sub>O<sub>4</sub>-embedded magnetic mesoporous silica nanoparticle (MMSN) vehicles and chlorin e6 (Ce6) photosensitizers to strengthen ROS levels to trigger pyroptosis by a Ce6-mediated photodynamic process [34]. Yang et al. developed a urine microenvironment-responsive 3D-printed hydrogel patch for realizing scarless memory repair, wherein laser-excited reactive oxygen species production and mechanical strength elevation were achieved using chemically crosslinked silicon quantum dots [35]. Kong et al. used a Nb<sub>2</sub>C/Au nanocomposite to demonstrate a microbiome metabolism-engineered phototherapy strategy in the regulation of bacteria [36]. A biomimetic Sim@PMPB theranostic agent designed by Zhang et al. successfully stabilized atherosclerotic plaques, alleviated atherosclerosis, and localized and amplified atherosclerosis, enabling monitoring of H<sub>2</sub>O<sub>2</sub>-related atherosclerotic evolution after treatment [37]. Li et al. indicated that mesoporous

manganese silicate-coated silica nanoparticles could be used as multistimuli-responsive T1-MRI contrast agents and drug delivery carriers [38]. Chen et al. found that mesoporous manganese silicate nanoparticles show better enhancement effects on T1WI due to their smaller size and the higher surface-area-to-volume ratio [12]. Therefore, it is necessary to develop a manganese-based MRI-T1 contrast agent to replace the cytotoxic GdIII agent while achieving similar or even better enhancement effects, which is extremely challenging and has clinical application value. In this study, we developed a cRGD-platelet@MnO/MSN@PPAR $\alpha$ /LXR $\alpha$  nanoparticle that showed high safety both in vitro and in vivo. Further analysis revealed that cRGD-platelet@MnO/MSN@PPAR $\alpha$ /LXR $\alpha$  nanoparticles showed better MRI imaging performance in AS.

In fact, most of the nanoformulations are not sufficiently targeted in vivo and are easily cleared by mononuclear macrophages. Platelets are an important part of blood flow and



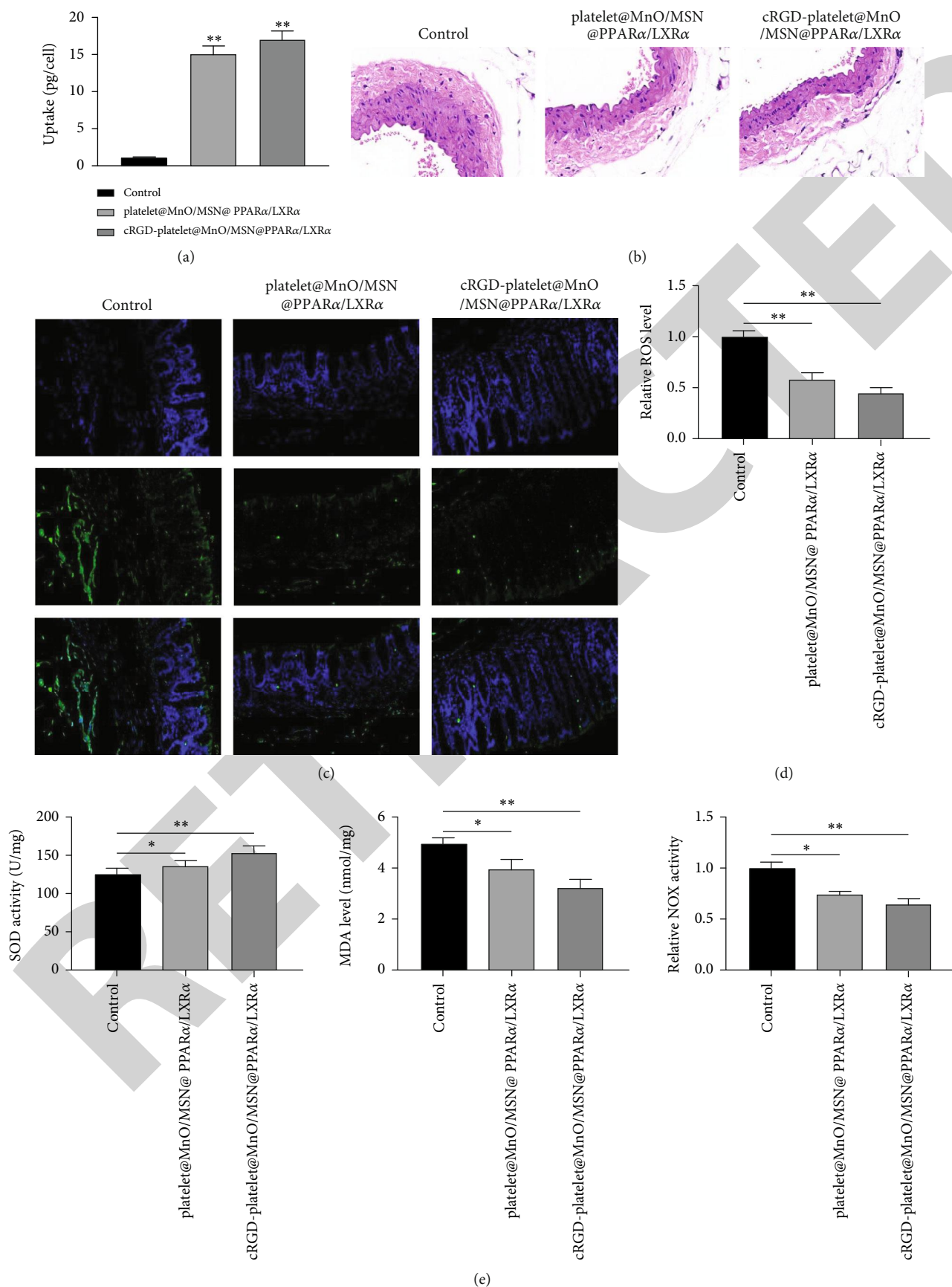


FIGURE 5: Continued.

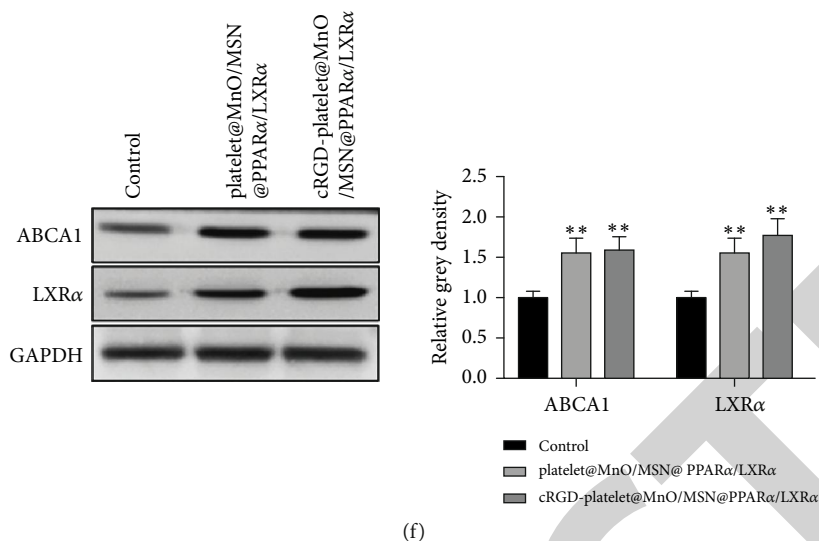


FIGURE 5: Diagnostic and therapeutic evaluation of cRGD-platelet@MnO/MSN@PPAR $\alpha$ /LXR $\alpha$  nanoparticles in vivo. (a) ICP–AES was utilized to determine the enrichment of the cRGD-platelet@MnO/MSN@PPAR $\alpha$ /LXR $\alpha$  nanoparticles in the plaque area. (b) HE staining was used to detect the area of vascular lesions affected by cRGD-platelet@MnO/MSN@PPAR $\alpha$ /LXR $\alpha$ . (c) TUNEL immunofluorescence assay was used to detect the intimal injury area and plaque area when treated with cRGD-platelet@MnO/MSN@PPAR $\alpha$ /LXR $\alpha$ . (d) The level of ROS was detected by DCFH-DA assay. (e) The levels of SOD, MDA, and NOX were evaluated using commercial assay kits. (f) The expression of ABCA1 and LXR $\alpha$  was detected by western blot after treatment with the cRGD-platelet@MnO/MSN@PPAR $\alpha$ /LXR $\alpha$ . Data were displayed as the mean  $\pm$  SD, \*\* $p < 0.01$  vs. control.  $n = 1$  for (b) and (c);  $n = 3$  for (a), (d), (e), and (f).

have the ability to target vascular injury sites and maintain the integrity of blood circulation [39, 40]. Bai et al. wrapped Fe<sub>3</sub>O<sub>4</sub> magnetic nanoparticles with platelet membranes for tumor MRI and photothermal therapy. It was found that platelet membrane-modified magnetic nanoparticles had a longer blood circulation time and better tumor-targeting properties, significantly improved the effects of MRI and photothermal therapy, and had good in vivo safety [41]. Zha et al. used platelet membranes to prepare nanomedicine with photodynamic/photothermal synergistic therapy. Nanomedicine can circulate in the body for a long time, can effectively target tumor cells, and is beneficial to the penetration of deep tumor tissues [42]. These results suggested that the platelet membrane-coated nanoparticles can avoid complement activation and the uptake of macrophages, provide the nanoparticles with immune escape ability, and can be located in deep locations. In addition, integrin  $\alpha v\beta 3$  is an important marker of angiogenesis, and cRGD is currently known to specifically bind to integrin  $\alpha v\beta 3$ . Increasing numbers of RGD probes have been applied by targeting  $\alpha v\beta 3$ . Studies have found that new blood vessels in AS plaques and macrophages overexpress integrin  $\alpha v\beta 3$ , which provides the basis for the application of cRGD in targeting vulnerable plaques by targeting  $\alpha v\beta 3$  [18, 19]. The current investigation demonstrated that cRGD-platelet@MnO/MSN@PPAR $\alpha$ /LXR $\alpha$  nanoparticles showed better performance than platelet@MnO/MSN@PPAR $\alpha$ /LXR $\alpha$  nanoparticles, suggesting that cRGD-platelet@MnO/MSN@PPAR $\alpha$ /LXR $\alpha$  nanoparticles had better diagnostic and therapeutic effects on AS.

In atherosclerotic plaques, cholesterol efflux is reduced, and the continuous accumulation of free cholesterol in foam cells leads to endoplasmic reticulum stress, inflammatory reactions, and finally foam cell apoptosis. If the apoptotic

bodies cannot be effectively cleared by the burial effect, necrosis will occur, leading to the progression of atherosclerosis [43]. Therefore, the steady state of cholesterol inflow and outflow is of vital importance in the formation of atherosclerosis. The PPAR-LXR $\alpha$ -ABCA1/ABCG1 pathway of macrophages plays an important role in regulating cholesterol efflux. In addition to regulating cholesterol homeostasis, PPAR $\alpha$  and LXR $\alpha$  can also exhibit anti-inflammatory functions by preventing the release of inflammatory cytokines [44, 45]. In addition, we also found that the application of platelet@MnO/MSN@PPAR $\alpha$ /LXR $\alpha$  nanoparticles and cRGD-platelet@MnO/MSN@PPAR $\alpha$ /LXR $\alpha$  nanoparticles had antioxidative effects, and that cRGD-platelet@MnO/MSN@PPAR $\alpha$ /LXR $\alpha$  nanoparticles had stronger antioxidative abilities than platelet@MnO/MSN@PPAR $\alpha$ /LXR $\alpha$  nanoparticles. PPAR $\alpha$  is a ligand-activated transcription factor, and its target genes control oxidative stress in rats. The activation of PPAR $\alpha$  mediates oxidative stress responses [46, 47].

In addition, activated LXR $\alpha$  elevates the phagocytosis of apoptotic cells by inducing the expression of the cell surface receptor Mer tyrosine kinase (MerTK) [48]. The expression level of LXR $\alpha$  was also associated with cellular inflammation and oxidative stress responses [49]. All these results indicate that the activation of PPAR $\alpha$  and LXR $\alpha$  improves the prognosis of AS patients. Studies have found that the combination of PPAR $\alpha$  and LXR $\alpha$  agonists can reduce the adverse effects of a single use of agonists. It is speculated that PPAR $\alpha$  agonists may change the plasma TG concentration. Therefore, it is speculated that the combination of PPAR $\alpha$  agonists and LXR $\alpha$  agonists may reduce the risk of AS, which is particularly effective and is considered to be a promising treatment strategy [50, 51]. However, the mechanism of this

strategy for treating AS has not yet been elucidated. Additionally, due to their systemic off-target effects, such as liver steatosis and heart failure, their clinical applications are limited. The current study demonstrated that the cholesterol contents were significantly decreased when treated with cRGD-platelet@MnO/MSN@PPAR $\alpha$ /LXR $\alpha$  nanoparticles compared with the control group. The expression of ABCA1 and LXR $\alpha$  was significantly elevated when treated with cRGD-platelet@MnO/MSN@PPAR $\alpha$ /LXR $\alpha$ . These results suggested that cRGD-platelet@MnO/MSN@PPAR $\alpha$ /LXR $\alpha$  nanoparticles alleviated AS development by promoting cholesterol effluence by regulating the expression of ABCA1 and LXR $\alpha$ . Molecular imaging of atherosclerosis was performed with nanoparticle-based fluorinated MRI contrast agents.

Finally, this study has several limitations; for example, the safety and efficacy of cRGD-platelet@MnO/MSN@PPAR $\alpha$ /LXR $\alpha$  nanoparticles should be monitored long-term. Next, different species of model animals should be used to test the effects of this nanoparticle. Finally, the underlying mechanisms and molecular pathways involved in the therapeutic effects of this nanoparticle should also be investigated.

## 5. Conclusion

In summary, we successfully established cRGD-platelet@MnO/MSN@PPAR $\alpha$ /LXR $\alpha$  nanoparticles with high safety and targeting of vulnerable plaques of AS. Further analysis showed that cRGD-platelet@MnO/MSN@PPAR $\alpha$ /LXR $\alpha$  nanoparticles had better performance on MRI imaging and treatment effects on AS by promoting cholesterol efflux through the regulation of ABCA1.

These findings suggested that the risk prediction, treatment, monitoring, and evaluation of AS might be realized by mesoporous silica nanoparticles coated with cRGD-platelets, which can provide a basis for the clinical diagnosis of AS and has broad application prospects. Our findings provide a reference for solving the off-target and side effects of nanoparticle-mediated drug delivery, improving the efficiency of AS treatment, and providing new ideas for the clinical treatment of AS.

## Data Availability

The datasets used and analyzed in the current study would be available from the corresponding author upon request.

## Conflicts of Interest

The authors declare that they have no competing interests.

## Acknowledgments

The project was supported by the National Natural Science Foundation of China (No. 82060311), Guangxi Science and Technology Department Research Program and Guangxi Natural Science Foundation Program (No. 2019GXNSFAA185031), Baise Science and Technology Department Research Program (No. 20204708), and Liuzhou People's Hospital Program (No. LRYGCC202204).

## References

- [1] A. Milutinovic, D. Suput, and R. Zorc-Pleskovic, "Pathogenesis of atherosclerosis in the tunica intima, media, and adventitia of coronary arteries: an updated review," *Bosnian Journal of Basic Medical Sciences*, vol. 20, no. 1, pp. 21–30, 2020.
- [2] J. Frostegard, "Immunity, atherosclerosis and cardiovascular disease," *BMC medicine*, vol. 11, no. 1, pp. 1–3, 2013.
- [3] A. J. Kattoor, N. V. K. Pothineni, D. Palagiri, and J. L. Mehta, "Oxidative stress in atherosclerosis," *Current Atherosclerosis Reports*, vol. 19, no. 11, p. 42, 2017.
- [4] K. Malekmohammad, R. D. Sewell, and M. Rafieian-Kopaei, "Antioxidants and atherosclerosis: Mechanistic aspects," *Bio-molecules*, vol. 9, no. 8, p. 301, 2019.
- [5] D. Andreini, M. Magnoni, E. Conte et al., "Coronary plaque features on CTA can identify patients at increased risk of cardiovascular events," *JACC: Cardiovascular Imaging*, vol. 13, no. 8, pp. 1704–1717, 2020.
- [6] M. Kocaoglu, B. M. Kline-Fath, M. A. Calvo-Garcia, B. Zhang, and U. D. Nagaraj, "Magnetic resonance imaging of the fetal brain in monochorionic diamniotic twin gestation: correlation of cerebral injury with ultrasound staging and survival outcomes," *Pediatric Radiology*, vol. 50, no. 8, pp. 1131–1138, 2020.
- [7] G. Shukla, G. S. Alexander, S. Bakas et al., "Advanced magnetic resonance imaging in glioblastoma: a review," *Chinese Clinical Oncology*, vol. 6, no. 4, p. 40, 2017.
- [8] T. Yousaf, G. Dervenoulas, and M. Politis, "Advances in MRI methodology," *International Review of Neurobiology*, vol. 141, pp. 31–76, 2018.
- [9] S. Geethanath and J. T. Vaughan Jr., "Accessible magnetic resonance imaging: a review," *Journal of Magnetic Resonance Imaging*, vol. 49, no. 7, pp. e65–e77, 2019.
- [10] A. Phinikaridou, M. E. Andia, S. Lacerda, S. Lorrio, M. Makowski, and R. Botnar, "Molecular MRI of atherosclerosis," *Molecules*, vol. 18, no. 11, pp. 14042–14069, 2013.
- [11] L. Zhou, Y. Yan, H. Du, X. Ni, G. Wang, and Q. Wang, "Plaque features and vascular geometry in basilar artery atherosclerosis," *Medicine (Baltimore)*, vol. 99, no. 18, article e19742, 2020.
- [12] Y. Chen, H. Chen, and J. Shi, "In vivo bio-safety evaluations and diagnostic/therapeutic applications of chemically designed mesoporous silica nanoparticles," *Advanced Materials*, vol. 25, no. 23, pp. 3144–3176, 2013.
- [13] T. Schumacher and R. A. Benndorf, "ABC transport proteins in cardiovascular disease—a brief summary," *Molecules*, vol. 22, no. 4, p. 589, 2017.
- [14] Y. Zeng, Y. Peng, K. Tang et al., "Dihydromyricetin ameliorates foam cell formation via LXR $\alpha$ -ABCA1/ABCG1-dependent cholesterol efflux in macrophages," *Biomedicine & Pharmacotherapy*, vol. 101, pp. 543–552, 2018.
- [15] J. N. Thon and J. E. Italiano, "Platelets: production, morphology and ultrastructure," *Handbook of Experimental Pharmacology*, vol. 210, pp. 3–22, 2012.
- [16] H. Wang, Y. Liu, R. He et al., "Cell membrane biomimetic nanoparticles for inflammation and cancer targeting in drug delivery," *Biomaterials Science*, vol. 8, no. 2, pp. 552–568, 2020.
- [17] B. Choi, W. Park, S. B. Park, W. K. Rhim, and D. K. Han, "Recent trends in cell membrane-cloaked nanoparticles for therapeutic applications," *Methods*, vol. 177, pp. 2–14, 2020.
- [18] M. Kim, A. Sahu, G. B. Kim et al., "Comparison of *in vivo* targeting ability between cRGD and collagen-targeting peptide

- conjugated nano-carriers for atherosclerosis," *Journal of Controlled Release*, vol. 269, pp. 337–346, 2018.
- [19] M. Razavian, R. Marfatia, H. Mongue-Din et al., "Integrin-targeted imaging of inflammation in vascular remodeling," *Arteriosclerosis, Thrombosis, and Vascular Biology*, vol. 31, no. 12, pp. 2820–2826, 2011.
- [20] Y. V. Lomovskaya, M. I. Kobayakova, A. S. Senotov et al., "Macrophage-like THP-1 Cells Derived from High-Density Cell Culture Are Resistant to TRAIL-Induced Cell Death via Down-Regulation of Death-Receptors DR4 and DR5," *Biomolecules*, vol. 12, no. 2, p. 150, 2022.
- [21] L. Liu, H. Guo, A. Song et al., "Progranulin inhibits LPS-induced macrophage M1 polarization via NF- $\kappa$ B and MAPK pathways," *BMC Immunology*, vol. 21, no. 1, p. 32, 2020.
- [22] C. Subramani, A. Rajakannu, S. Gaidhani, I. Raju, and D. V. Kartar Singh, "Glutathione-redox status on hydro alcoholic root bark extract of *Premna integrifolia* Linn in high fat diet induced atherosclerosis model," *Journal of Ayurveda and integrative medicine*, vol. 11, no. 4, pp. 376–382, 2020.
- [23] C. Xie, X. Zhou, C. Liang et al., "Apatinib triggers autophagic and apoptotic cell death via VEGFR2/STAT3/PD-L1 and ROS/Nrf2/p62 signaling in lung cancer," *Journal of Experimental & Clinical Cancer Research*, vol. 40, no. 1, p. 266, 2021.
- [24] A. M. Ruiz-León, M. Lapuente, R. Estruch, and R. Casas, "Clinical advances in immunonutrition and atherosclerosis: a review," *Frontiers in immunology*, vol. 10, no. 837, 2019.
- [25] M. G. Harisinghani, A. O'Shea, and R. Weissleder, "Advances in clinical MRI technology," *Science Translational Medicine*, vol. 11, no. 523, article eaba2591, 2019.
- [26] R. U. Palekar, A. P. Jallouk, G. M. Lanza, H. Pan, and S. A. Wickline, "Molecular imaging of atherosclerosis with nanoparticle-based fluorinated MRI contrast agents," *Nanomedicine (London, England)*, vol. 10, no. 11, pp. 1817–1832, 2015.
- [27] W. Chen, M. Schilperoord, Y. Cao, J. Shi, I. Tabas, and W. Tao, "Macrophage-Targeted Nanomedicine for the Diagnosis and Treatment of Atherosclerosis," *Nature reviews Cardiology*, vol. 19, no. 4, pp. 228–249, 2022.
- [28] X. Liang, H. Li, A. Zhang et al., "Red blood cell biomimetic nanoparticle with anti-inflammatory, anti-oxidative and hypolipidemia effect ameliorated atherosclerosis therapy," *Nanomedicine*, vol. 41, article 102519, 2022.
- [29] K. Y. Chyu, X. Zhao, J. Zhou et al., "Immunization using ApoB-100 peptide-linked nanoparticles reduces atherosclerosis," *JCI insight*, vol. 7, no. 11, 2022.
- [30] J. Wang, H. Chen, J. Sun et al., "Dynamic contrast-enhanced MR imaging of carotid *vasa vasorum* in relation to coronary and cerebrovascular events," *Atherosclerosis*, vol. 263, pp. 420–426, 2017.
- [31] Y. Wang, Q. Zhao, N. Han et al., "Mesoporous silica nanoparticles in drug delivery and biomedical applications," *Nanomedicine*, vol. 11, no. 2, pp. 313–327, 2015.
- [32] C. A. McCarthy, R. J. Ahern, R. Dontireddy, K. B. Ryan, and A. M. Crean, "Mesoporous silica formulation strategies for drug dissolution enhancement: a review," *Expert Opinion on Drug Delivery*, vol. 13, no. 1, pp. 93–108, 2016.
- [33] M. Ménard, F. Meyer, C. Affolter-Zbaraszczuk et al., "Design of hybrid protein-coated magnetic core-mesoporous silica shell nanocomposites for MRI and drug release assessed in a 3D tumor cell model," *Nanotechnology*, vol. 30, no. 17, article 174001, 2019.
- [34] M. Chen, H. Liao, Z. Bu et al., "Pyroptosis activation by photodynamic-boosted nanocatalytic medicine favors malignancy recession," *Chemical Engineering Journal*, vol. 441, no. 136030, article 136030, 2022.
- [35] M. Yang, Y. Zhang, C. Fang et al., "Urine-microenvironment-initiated composite hydrogel patch reconfiguration propels scarless memory repair and reinvigoration of the urethra," *Advanced Materials*, vol. 34, no. 14, article e2109522, 2022.
- [36] F. Kong, C. Fang, Y. Zhang et al., "Abundance and metabolism disruptions of intratumoral microbiota by chemical and physical actions unfreeze tumor treatment resistance," *Advanced Science*, vol. 9, no. 7, article e2105523, 2022.
- [37] Y. Zhang, Y. Yin, W. Zhang et al., "Reactive oxygen species scavenging and inflammation mitigation enabled by biomimetic prussian blue analogues boycott atherosclerosis," *Journal of nanobiotechnology*, vol. 19, no. 1, p. 161, 2021.
- [38] X. Li, W. Zhao, X. Liu et al., "Mesoporous manganese silicate coated silica nanoparticles as multi-stimuli-responsive T<sub>1</sub>-MRI contrast agents and drug delivery carriers," *Acta Biomaterialia*, vol. 30, pp. 378–387, 2016.
- [39] B. Ho-Tin-Noe, Y. Boulaftali, and E. Camerer, "Platelets and vascular integrity: how platelets prevent bleeding in inflammation," *Blood, The Journal of the American Society of Hematology*, vol. 131, no. 3, pp. 277–288, 2018.
- [40] X. Liu, F. Zhang, Q. Wang et al., "Platelet-inspired multiscaled cytophilic interfaces with high specificity and efficiency toward point-of-care cancer diagnosis," *Small*, vol. 10, no. 22, pp. 4677–4683, 2014.
- [41] Y. Bai, Y. Zhang, J. Zhang et al., "Repeated administrations of carbon nanotubes in male mice cause reversible testis damage without affecting fertility," *Nature Nanotechnology*, vol. 5, no. 9, pp. 683–689, 2010.
- [42] Z. Zha, J. Wang, S. Zhang et al., "Engineering of perfluorooctylbromide polypyrrole nano-/microcapsules for simultaneous contrast enhanced ultrasound imaging and photothermal treatment of cancer," *Biomaterials*, vol. 35, no. 1, pp. 287–293, 2014.
- [43] G. J. Koelwyn, E. M. Corr, E. Erbay, and K. J. Moore, "Regulation of macrophage immunometabolism in atherosclerosis," *Nature Immunology*, vol. 19, no. 6, pp. 526–537, 2018.
- [44] S. J. Bensinger and P. Tontonoz, "Integration of metabolism and inflammation by lipid-activated nuclear receptors," *Nature*, vol. 454, no. 7203, pp. 470–477, 2008.
- [45] X. Z. Ruan, J. F. Moorhead, R. Fernando, D. C. Wheeler, S. H. Powis, and Z. Varghese, "PPAR agonists protect mesangial cells from interleukin 1 $\beta$ -induced intracellular lipid accumulation by activating the ABCA1 cholesterol efflux pathway," *Journal of the American Society of Nephrology*, vol. 14, no. 3, pp. 593–600, 2003.
- [46] M. Pawlak, P. Lefebvre, and B. Staels, "Molecular mechanism of PPAR $\alpha$  action and its impact on lipid metabolism, inflammation and fibrosis in non-alcoholic fatty liver disease," *Journal of Hepatology*, vol. 62, no. 3, pp. 720–733, 2015.
- [47] Y. Zhang, Y. Cui, X. L. Wang et al., "PPAR $\alpha$ / $\gamma$  agonists and antagonists differently affect hepatic lipid metabolism, oxidative stress and inflammatory cytokine production in steatohepatic rats," *Cytokine*, vol. 75, no. 1, pp. 127–135, 2015.
- [48] A. C. Doran, L. Ozcan, B. Cai et al., "CAMKII $\gamma$  suppresses an efferocytosis pathway in macrophages and promotes atherosclerotic plaque necrosis," *The Journal of Clinical Investigation*, vol. 127, no. 11, pp. 4075–4089, 2017.

## *Retraction*

# **Retracted: Identification of *MMP9* as a Novel Biomarker to Mitochondrial Metabolism Disorder and Oxidative Stress in Calcific Aortic Valve Stenosis**

### **Oxidative Medicine and Cellular Longevity**

Received 26 December 2023; Accepted 26 December 2023; Published 29 December 2023

Copyright © 2023 Oxidative Medicine and Cellular Longevity. This is an open access article distributed under the Creative Commons Attribution License, which permits unrestricted use, distribution, and reproduction in any medium, provided the original work is properly cited.

This article has been retracted by Hindawi, as publisher, following an investigation undertaken by the publisher [1]. This investigation has uncovered evidence of systematic manipulation of the publication and peer-review process. We cannot, therefore, vouch for the reliability or integrity of this article.

Please note that this notice is intended solely to alert readers that the peer-review process of this article has been compromised.

Wiley and Hindawi regret that the usual quality checks did not identify these issues before publication and have since put additional measures in place to safeguard research integrity.

We wish to credit our Research Integrity and Research Publishing teams and anonymous and named external researchers and research integrity experts for contributing to this investigation.

The corresponding author, as the representative of all authors, has been given the opportunity to register their agreement or disagreement to this retraction. We have kept a record of any response received.

### **References**

- [1] C. Liu, R. Liu, Z. Cao et al., "Identification of *MMP9* as a Novel Biomarker to Mitochondrial Metabolism Disorder and Oxidative Stress in Calcific Aortic Valve Stenosis," *Oxidative Medicine and Cellular Longevity*, vol. 2022, Article ID 3858871, 14 pages, 2022.

## Research Article

# Identification of *MMP9* as a Novel Biomarker to Mitochondrial Metabolism Disorder and Oxidative Stress in Calcific Aortic Valve Stenosis

Cong Liu,<sup>1,2</sup> Ruixue Liu,<sup>3</sup> Zhezhe Cao,<sup>1</sup> Qiao Guo,<sup>3</sup> He Huang<sup>3</sup>,<sup>3</sup> Liangming Liu,<sup>4</sup> Yingbin Xiao<sup>1</sup>,<sup>1</sup> Chenyang Duan<sup>3</sup>,<sup>3</sup> and Ruiyan Ma<sup>1</sup>

<sup>1</sup>Department of Cardiovascular Surgery, Xinqiao Hospital, Army Medical University, Chongqing 400037, China

<sup>2</sup>Department of Ultrasound Medicine, Union Hospital, Tongji Medical College, Huazhong University of Science and Technology, Wuhan 430022, China

<sup>3</sup>Department of Anesthesiology, The Second Affiliated Hospital of Chongqing Medical University, Chongqing 400010, China

<sup>4</sup>Department of Shock and Transfusion, State Key Laboratory of Trauma, Burns and Combined Injury, Daping Hospital, Army Medical University, Chongqing 400042, China

Correspondence should be addressed to Yingbin Xiao; [xiaoyb@vip.sina.com](mailto:xiaoyb@vip.sina.com), Chenyang Duan; [duanchenyang1991@cqmu.edu.cn](mailto:duanchenyang1991@cqmu.edu.cn), and Ruiyan Ma; [ruiyanma@tmmu.edu.cn](mailto:ruiyanma@tmmu.edu.cn)

Received 28 July 2022; Revised 7 September 2022; Accepted 12 September 2022; Published 24 September 2022

Academic Editor: Tian Li

Copyright © 2022 Cong Liu et al. This is an open access article distributed under the Creative Commons Attribution License, which permits unrestricted use, distribution, and reproduction in any medium, provided the original work is properly cited.

Calcific aortic valve stenosis (CAVS) is the most common heart valve disorder among humans. To date, no effective method has been identified to prevent this disease. Herein, we aimed to identify novel diagnostic and mitochondria-related biomarkers of CAVS, based on two machine learning algorithms. We further explored their association with infiltrating immune cells and studied their potential function in CAVS. The GSE12644, GSE51472, and GSE83453 expression profiles were downloaded from the Gene Expression Omnibus (GEO) repository. The GSE12644 and GSE51472 datasets were integrated to identify differentially expressed genes (DEGs). GSE12644 contains 10 normal and 10 CAVS samples, whereas GSE51472 contains 5 normal and 10 CAVS samples. GO and KEGG assays of DEGs were conducted, and the correlation between matrix metalloproteinase 9 (*MMP9*) expression and immune cell infiltration was explored, using CIBERSORT. The LASSO regression model and SVM-RFE analysis were used to identify diagnostic genes. The expression of *MMP9* in CAVS and non-CAVS samples was measured using RT-PCR, western blotting and immunohistochemistry. A series of functional experiments were performed to explore the potential role of *MMP9* in mitochondrial metabolism and oxidative stress during CAVS progression. Twenty-two DEGs were identified, of which six genes (*SCG2*, *PPBP*, *TREMI*, *CCL19*, *WIF1*, and *MMP9*) were ultimately distinguished as diagnostic genes in CAVS. Of these, *MMP9* was indicated as a mitochondria-related gene, the expression and diagnostic value of which were further confirmed in the GSE83453 dataset. Correlation analysis revealed a positive correlation between *MMP9* and infiltrating immune cells. In our cohort, *MMP9* expression was distinctly increased in CAVS samples, and its inhibition attenuated the calcification of valve interstitial cells (VICs) by suppressing mitochondrial damage and oxidative stress. Taken together, our findings suggest *MMP9* as a novel mitochondrial dysfunction biomarker and therapeutic target for CAVS.

## 1. Introduction

Valvular heart disease (VHD) comprises a wide range of common cardiovascular disorders, accounting for 10 to 20% of all cardiac surgical procedures in the United States [1]. Calcific aortic valve stenosis (CAVS) is widely regarded

as the most common form of VHD. It is also a predominant cause of aortic valve stenosis [2], worldwide. Surgical or transcatheter valve replacement is inevitable in the absence of a pharmacological cure for this common and progressive condition. As the most common heart valve condition in developed countries, aortic stenosis affects

approximately 3% of the population aged over 65. The survival rates of asymptomatic patients with aortic stenosis are comparable to those of age- and sex-matched control cases [3]. However, the long-term survival in symptomatic cases without aortic valve replacement is merely 2 to 3 years [4]. Aortic valve calcification remains a mystery despite advancements in drastic therapies, such as valve replacement, and established interventional therapies for treating aortic stenosis. Therefore, it is critical to study the progression of CAVS and identify the molecules that are essential to its development, to facilitate timely identification and treatment of patients.

Mitochondria, the main organelles of aerobic respiration, are of great significance for maintaining the normal physiological function of cells [5, 6]. Under normal conditions, the mitochondrial quality indices—including mitochondrial dynamics, functions, and metabolism—are in dynamic balance [7]. Our previous study [2] confirmed the existence of a severe mitochondrial quality imbalance in calcified valves, which mainly manifests as mitochondrial morphological damage. This includes mitochondrial fragmentation, mitochondrial dysfunction (such as excessive ROS accumulation), reduction of mitochondrial membrane potential, and mitochondrial metabolic disorders, such as the obvious downregulation of glutathione metabolism and the tricarboxylic acid (TCA) cycle. The study of Tandon et al. [8] showed that changes in mitochondrial morphology may lead to the accumulation of collagen matrix in valve interstitial cells (VICs), which can be used as an index to evaluate early CAVS. The study of Morciano et al. [9] showed that mitochondrial dysfunction can promote the synthesis of collagen matrix and alkaline phosphatase of VICs and accelerate the calcification process of CAVS. The study of Khatun et al. [10] indicated that the disorder of mitochondrial metabolism may accelerate the synthesis of alkaline phosphatase and the osteogenic-like changes of VICs. The above researches fully confirmed that the mitochondrial quality imbalance in VICs has important regulatory significance for the occurrence and development of CAVS. Therefore, it is essential to identify an effective mitochondrial marker for severity prediction of CAVS.

In recent years, microarray technology—together with comprehensive assays—has been used to identify new functional genes related to a variety of disorders [11, 12]. These genes could be used as possible markers for the diagnosis and prognosis of various diseases. In the past decade, a growing number of studies have used machine learning algorithms to screen diagnostic genes and potential functional factors of various diseases. However, the application of such machine learning algorithms for screening novel biomarkers for CAVS has rarely been reported.

In this study, we obtained two public microarray datasets (GSE12644 and GSE51472) on CAVS from the Gene Expression Omnibus (GEO) database and screened for differentially expressed genes (DEGs) between CAVS and non-CAVS samples. Moreover, we used machine learning algorithms to identify potential diagnostic mitochondrial genes for CAVS and further performed a series of experiments to confirm our findings.

## 2. Materials and Methods

**2.1. Clinical Samples.** Calcified valve specimens were obtained from 15 patients with CAVS (CAVS group) who had undergone surgical treatment at the Xinqiao Hospital of the Army Medical University (Chongqing, China). Valve samples for the non-CAVS group were obtained from 15 patients with aortic insufficiency but no calcification. This study was approved by the Ethics Committee of the Institute of Biomedicine Research of Xinqiao Hospital of the Army Medical University (No. 2022-YAN187-01).

**2.2. Cell Culture and Calcification.** Noncalcified aortic valves were used for the isolation of human aortic valve interstitial cells (VICs). Primary VICs were isolated, and the quality of the cell preparation was verified in the control media (CM). Osteogenic differentiation was induced in cells from passages 3 to 7 by incubating cells with osteogenic medium (OM) for 28 days. The osteogenic medium included 0.1% fetal bovine serum, 50  $\mu\text{g}/\text{ml}$  ascorbic acid, and 5 mmol/l  $\beta$ -glycerol phosphate (all purchased from Sigma-Aldrich, St. Louis, MO, USA). The medium was changed every 4 days, as previously described [13].

As for inhibiting matrix metalloproteinase 9 (MMP9) expression in OM-VICs, the primary VICs were treated with MMP-9-IN-1 (MMP-9i) accompanied by osteogenic differentiation treatment at a concentration of 100 or 300 nM. MMP-9i was a MMP9-specific inhibitor which was purchased from Selleck (Shanghai, China) [14].

**2.3. Alizarin Red Detection.** The VICs were then fixed in 10% neutral formaldehyde at room temperature for 30 minutes, after the removal of the calcification medium, and washed two to three times with ultrapure water. 3 ml of 0.5% Alizarin Red staining solution (Beyotime, Shanghai, China) was added, and the plate gently shaken on a shaking table for 5–10 minutes, to allow dyeing. Excess dye was removed by pipette suction, and 1 ml ultrapure water was added to each well of the six-well plate. The mixture was shaken for a further 5 minutes before being washed with ultrapure water for four iterations of 5 minutes each. Finally, the preparation was washed with phosphate-buffered saline (PBS) for 15 minutes, excess PBS was absorbed, and the ultrapure water was added to the wells, prior to photography and quantification.

**2.4. Real-Time PCR.** TRIzol reagent (Invitrogen, Carlsbad, CA, USA) was used to extract total RNA from the specimens, according to the manufacturer's instructions. Reverse transcription was executed using HiScript II RT SuperMix for qPCR (+gDNA wiper) (Vazyme Biotech, Nanjing, China) and 1 ng RNA. SYBR Green Master Mix (Vazyme Biotech) was used to conduct real-time PCR according to the following parameters: the reaction mixture was heated to 95°C for 2 minutes, followed by 34 cycles of 94°C denaturation for 50 seconds, annealing for 45 seconds, and 72°C extension for 50 seconds. Glyceraldehyde 3-phosphate dehydrogenase (GAPDH) was used as an internal reference to standardize the expression data. The primer sequences of human MMP-9 and GAPDH were shown as follows: MMP9\_forward: CGTGAACATCTTCGACGCCAT, reverse: CGTCTCTCA

AAGACCGAGTCCA, GAPDH\_ forward: CAACAGCCTCAAGATCATCAGCA, reverse: ATGAGTCCTTCCACGATACCAA. The relative expression was determined using the following equation:

$$2^{-\Delta\Delta Ct} (\Delta Ct = \Delta Ct_{tar} - et - \Delta Ct_{GAPDH}). \quad (1)$$

**2.5. Western Blotting.** Aortic valve tissue was preserved at  $-80^{\circ}\text{C}$ . Sodium dodecyl sulfate-polyacrylamide gel electrophoresis (SDS-PAGE) was used to separate the total protein in a lysis solution, followed by electroblotting to transfer the protein onto polyvinylidene fluoride membranes. Antibodies were incubated on the membrane, overnight at  $4^{\circ}\text{C}$ , after being blocked with the Odyssey blocking buffer (LI-COR, Shanghai, China). Subsequently, the membranes were incubated with a horseradish peroxidase-conjugated secondary antibody, for 1 hour. GAPDH was used as an endogenous control. Mouse anti-human GAPDH polyclonal antibody (1:5000, Abcam, Cambridge, MA, USA) was used to detect GAPDH. The protein level of *MMP9* was examined using a mouse anti-human *MMP9* polyclonal antibody (1:3000, Abcam, Cambridge, MA, USA). Proteins were detected using ECL Plus kits (Thermo Scientific, Waltham, MA, USA), and Image-Pro Plus Version 6.0 was used for analysis.

**2.6. Immunohistochemistry.** For semiquantitative examination, tissue samples were fixed with 10% formalin at room temperature for 24 hours, embedded in paraffin, and cut into  $20\ \mu\text{m}$ -thick sections. Immunohistochemical staining for *MMP9* was also performed. Briefly, sections were washed and blocked using 5% milk in Tris-buffered saline, at room temperature for 2 hours. Primary antibodies were incubated overnight with the tissue slices, at  $4^{\circ}\text{C}$ . The sections were then washed in PBS and incubated for 30 minutes with biotinylated secondary antibodies, prior to treatment with VECTASTAIN ABC reagent (Vector Laboratories, Inc., Burlingame, CA, USA) and 3,3'-diaminobenzidine (Sigma-Aldrich, St. Louis, MO, USA), for 2 minutes at room temperature, followed by counterstaining with hematoxylin. Images were captured using an optical microscope without any filters. Signal quantification was performed using the Image-Pro Plus software.

**2.7. Mitochondrial Morphology Detection.** Mitochondria in VICs were labeled using 100 nmol/l MitoTracker Deep Red (Thermo Fisher Scientific, Waltham, MA, USA) at  $37^{\circ}\text{C}$  for 30 minutes, and observed using confocal microscopy (Leica TCS SP5, Wetzlar, Germany), using a  $\times 60$ , 1.3 NA oil-immersion objective. Mitochondrial fluorophores were excited using a 633 nm laser, and fluorescence emission was recorded at 558–617 nm. Mitochondrial length was determined and calculated using the ImageJ software.

**2.8. FITC-ROS Assay.** VICs were stained with 1% DCFH-DA or dihydroethidium (DHE) fluorescent probes, incubated at  $37^{\circ}\text{C}$  for 20 min, and observed using confocal microscopy (Leica TCS SP5, Wetzlar, Germany), using a  $\times 40$  objective as well as differential and interference contrast (DIC). The ROS fluorescence was excited by a 488 nm laser and emission was collected at 501–563 nm. Quantification for the

ROS assay was conducted using ImageJ to measure the FITC fluorescence intensity [5, 6].

**2.9. Mitochondrial Membrane Potential Assay.** VICs were stained with 0.1% JC-1 fluorescent probes and incubated at  $37^{\circ}\text{C}$  for 20 min. The JC-1 monomer was excited by a 488 nm laser, and emission was collected at 500–650 nm. The JC-1 aggregate fluorescence was excited by a 633 nm laser and emission was collected at 558–617 nm. Quantification for mitochondrial membrane potential was carried out to measure the fluorescence intensity ratio of JC-1 aggregate/JC-1 monomer [5, 6].

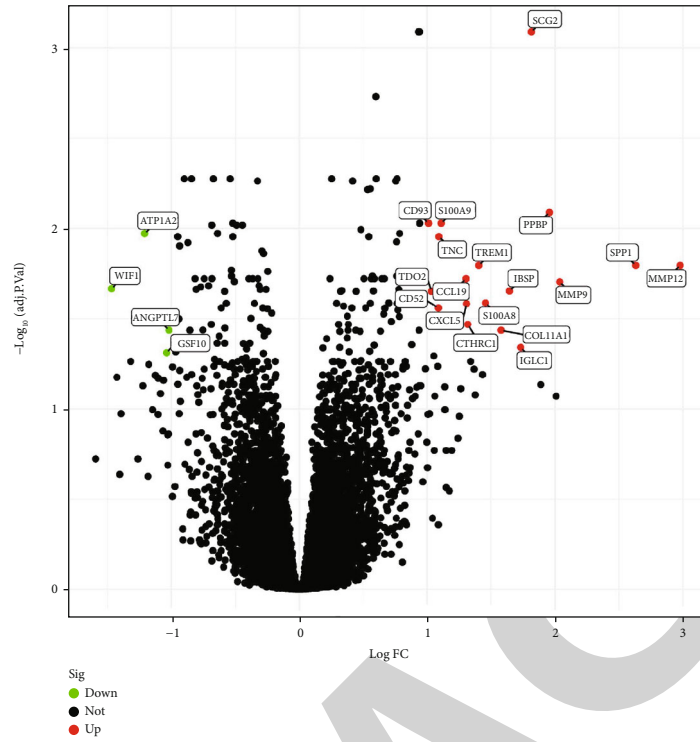
**2.10. Microarray Data.** We retrieved the gene expression profiles, GSE12644 and GSE51472, from the GEO database. These datasets included the expression data of aortic valves—from patients with CAVS, as well as normal controls—which were detected on the GPL570 platform. GSE12644 contains 10 normal and 10 CAVS samples from Canada, whereas GSE51472 contains 5 normal and 10 CAVS samples. In addition, the GSE83453 dataset, which includes 8 normal tricuspid valves, 9 stenotic tricuspid valves, and 10 calcified bicuspid aortic valves, was used as the validation cohort.

**2.11. DEG Analysis.** The data table of the microarray platform was used to annotate the two series matrix files (GSE51472 and GSE12644) with official gene symbols, whereafter gene expression matrix files were obtained. The two datasets were merged into one file, and the “sva” R package was applied to perform batch normalization of the expression data. The DEG analysis was conducted using the “limma” R program. The threshold for DEGs was set as  $|\log_2(\text{fold change})| > 1$  and  $p < 0.05$ .

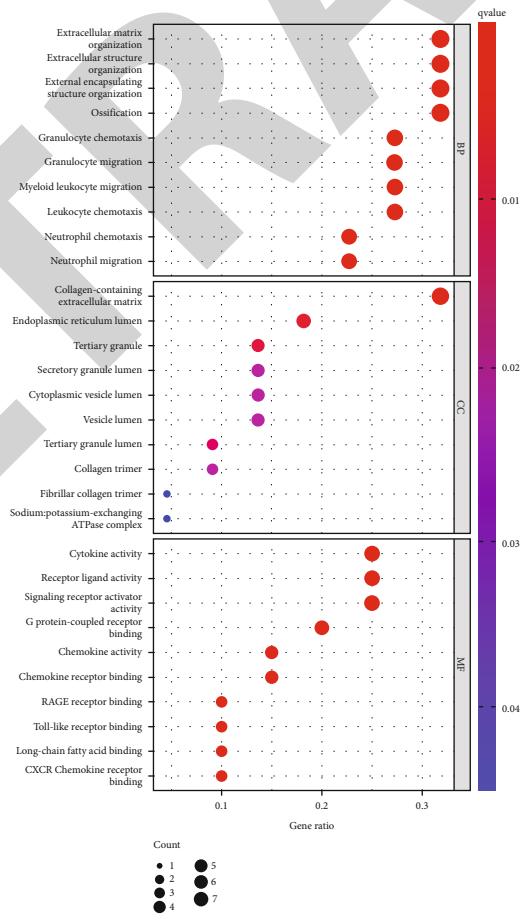
**2.12. Enrichment Analysis of DEGs.** As a predominant bioinformatics tool for the annotation of genes, Gene Ontology (GO) analysis describes three categories of gene functions, namely, biological process (BP), molecular function (MF), and cellular component (CC). Information regarding genomes, biological pathways, diseases, and chemicals were derived from the Kyoto Encyclopedia of Genes and Genomes (KEGG). The clusterProfiler package was applied in RStudio 1.1.456 (RStudio, Boston, MA, USA) to perform GO functional enrichment analysis and KEGG pathway assays on the DEGs.

**2.13. LASSO Model and SVM-RFE Methods.** The diagnostic indicators of CAVS were classified using LASSO logistic regression and the support vector machine (SVM) algorithm. LASSO analysis was conducted using the “glmnet” package, for which the response type was set to binomial and the alpha, to 1. Both classification and regression may benefit from using an SVM. A recursive feature elimination (RFE) method was used to select the best genes from the meta-data cohort, to avoid overfitting. Therefore, support vector machine-recursive feature elimination (SVM-RFE) was used to discover the set of genes with the greatest discriminative ability. A total of 1513 mitochondria-related genes were identified via gene set enrichment analysis.





(a)



(b)

FIGURE 1: Continued.

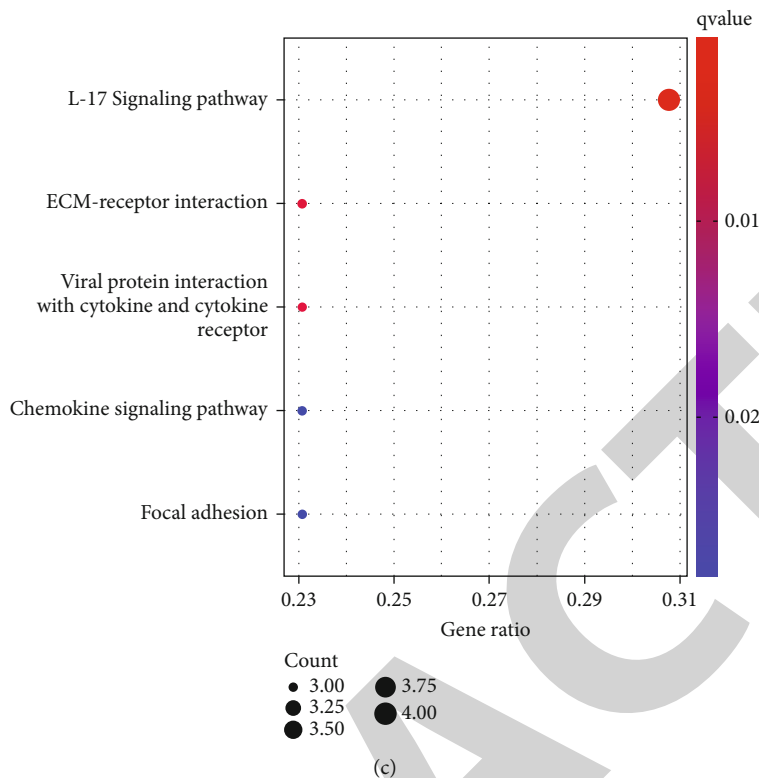


FIGURE 1: Identification of DEGs in CAVS, along with functional enrichment analysis. (a) Volcanic map of identified DEGs between non-CAVS and CAVS samples. (b) GO and (c) KEGG analyses of DEGs.

**2.14. Comprehensive Correlation Analysis of Infiltrating Immune Cells.** Based on normalized gene expression patterns, CIBERSORT can be used to measure infiltrating immune cell fractions [15]. To estimate the abundance of distinct immune cell types in the immunological microenvironment, CIBERSORT employed TPM data from RNA-seq, which were transformed from FPKM data. A total of 100 aligned, default signature matrices were obtained from the CIBERSORT website (<https://cibersort.stanford.edu/index.php>) to conduct gene expression analysis. A correlation analysis in R was performed to examine the relationship between new genes and quantities of invading immune cells. Results were displayed in the form of a chart, constructed using the “ggplot2” program.

**2.15. Statistical Analysis.** All statistical analyses were conducted using R (version 3.6.3) and SPSS 17.0 for Windows (SPSS Inc., Chicago, IL, USA). Comparisons between two independent groups were analyzed using Student’s *t*-test. Statistical significance was set at  $p < 0.05$ .

### 3. Results

**3.1. Identification of DEGs in CAVS and Functional Enrichment Analysis.** Following GSE12644 and GSE51472 dataset analysis, 22 DEGs were identified, which included 4 downregulated and 18 upregulated genes (Figure 1(a)). The KEGG pathway enrichment and GO annotation analysis using clusterProfiler were conducted to gain a better understanding

of the biological roles played by the identified DEGs. The GO and KEGG pathways are shown in Figures 1(b) and 1(c), respectively. BP assays indicated that 22 DEGs were mainly enriched in “extracellular matrix organization,” “extracellular structure organization,” “external encapsulating structure organization,” and “ossification.” For CC assays, the top four distinctly enriched terms were “collagen-containing extracellular matrix,” “endoplasmic reticulum lumen,” “tertiary granule,” and “secretory granule lumen.” The top four distinctly enriched MF terms included “cytokine activity,” “receptor ligand activity,” “signaling receptor activator activity,” and “G protein-coupled receptor binding” (Figure 1(b)). In addition, the data from KEGG assays confirmed that the 22 DEGs were mainly enriched in the “IL-17 signaling pathway,” “ECM-receptor interaction,” “viral protein interaction with cytokine and cytokine receptor,” “chemokine signaling pathway,” and “focal adhesion” (Figure 1(c)).

**3.2. Identification of Diagnostic Genes Using Two Machine Learning Algorithms.** We used two alternative methods to identify biomarkers. CAVS diagnostic biomarkers were reduced using LASSO regression analysis, which resulted in the identification of six genes (Figure 2(a)), whereas nineteen of the twenty-two DEGs were screened using the SVM-RFE algorithm (Figure 2(b)). Six overlapping genes (SCG2, PPBP, TREM1, CCL19, WIF1, and MMP9) were ultimately identified between the two machine learning algorithms (Figure 2(c)). To further identify whether any

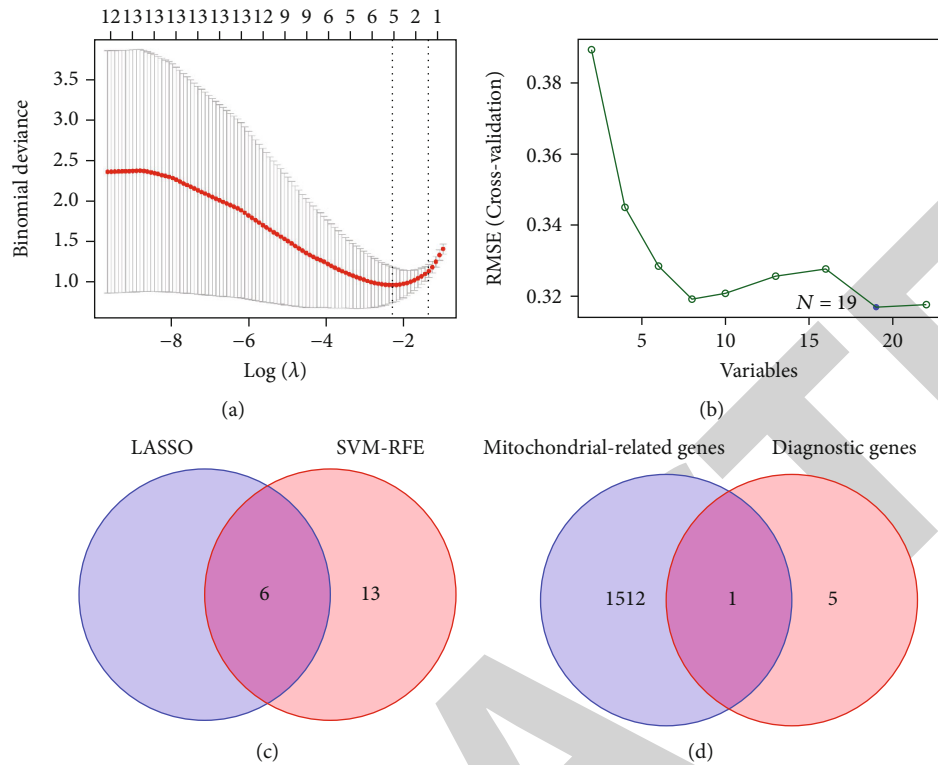


FIGURE 2: Identification of diagnostic genes using two machine learning algorithms. (a) The LASSO regression algorithm was applied to screen diagnostic biomarkers of CAVS. (b) A plot of biomarker selection using the SVM-RFE algorithm. (c) Six diagnostic genes were identified based on the previous two algorithms. (d) A Venn diagram demonstrating mitochondria-related gene, *MMP9*, as a novel biomarker of CAVS.

mitochondria-related genes resided among these six biomarkers, we constructed a Venn diagram and found that *MMP9* met the relevant conditions (Figure 2(d)). Therefore, we focused on *MMP9* expression in this study. We proceeded to analyze the GSE83453 dataset, which also confirmed that *MMP9* expression was distinctly upregulated in CAVS samples compared with normal samples (Figure 3(a)). Moreover, the receiver operating characteristic (ROC) curve analysis revealed that *MMP9* was a potential indicator to distinguish CAVS samples from normal samples, with an area under the curve (AUC) of 0.921 (95% CI, 0.743–0.1000,  $p < 0.001$ ; Figure 3(b)). Furthermore, the results of ROC assays on GSE12644 and GSE51472 exhibited similar results (Figure 3(c)).

**3.3. Relationships between the Expression of *MMP9* and Infiltrating Immune Cells.** The function assays discussed above revealed that the “chemokine signaling pathway,” “viral protein interaction with cytokine and cytokine receptor,” “ECM-receptor interaction,” “IL-17 signaling pathway,” and “focal adhesion” were noticeably enriched. Therefore, we questioned whether *MMP9*’s harmful impact in CAVS was mediated through immune cell infiltration. Accordingly, we used CIBERSORT techniques to investigate the relationship between *MMP9* expression and invading immune cells, in CAVS. Twenty-two types of immune cell profiles identified from CAVS and normal samples are shown in Figures 4(a) and 4(b). In addition, we found that

the levels of M2 macrophages were distinctly decreased in CAVS samples compared with those in normal samples (Figure 4(c)). The results of the correlation analysis showed that *MMP9* was positively correlated with “macrophage M0,” “dendritic cells activated,” and “macrophage M2” (Figures 5(a) and 5(b)). Our findings suggested that *MMP9* expression is substantially correlated with immune cell infiltration in CAVS.

**3.4. Distinct Upregulation of *MMP9* and Its Potential Role in Mitochondrial Metabolism and Oxidative Stress in CAVS Progression.** To determine whether a dysregulated level of *MMP9* was exhibited in CAVS, we collected 15 CAVS and non-CAVS samples, respectively. RT-PCR and western blotting experiments revealed that the expression of *MMP9* was distinctly upregulated in CAVS samples, compared to that in non-CAVS samples (Figures 6(a) and 6(b)). A similar result was also observed using immunohistochemistry (Figure 6(c)). The computed tomography (CT) imaging confirmed the presence of a significantly calcified focus in the CAVS samples. At the same time, we found that the mitochondria in CAVS samples were seriously damaged, with severe vacuolation of the internal cristae (Figure 6(d)). To further explore the possible roles of *MMP9* dysregulation in mitochondrial function, we performed precalcification in VICs with osteogenic medium (OM) and found that the mitochondria were significantly fragmented, confirming the existence of mitochondrial

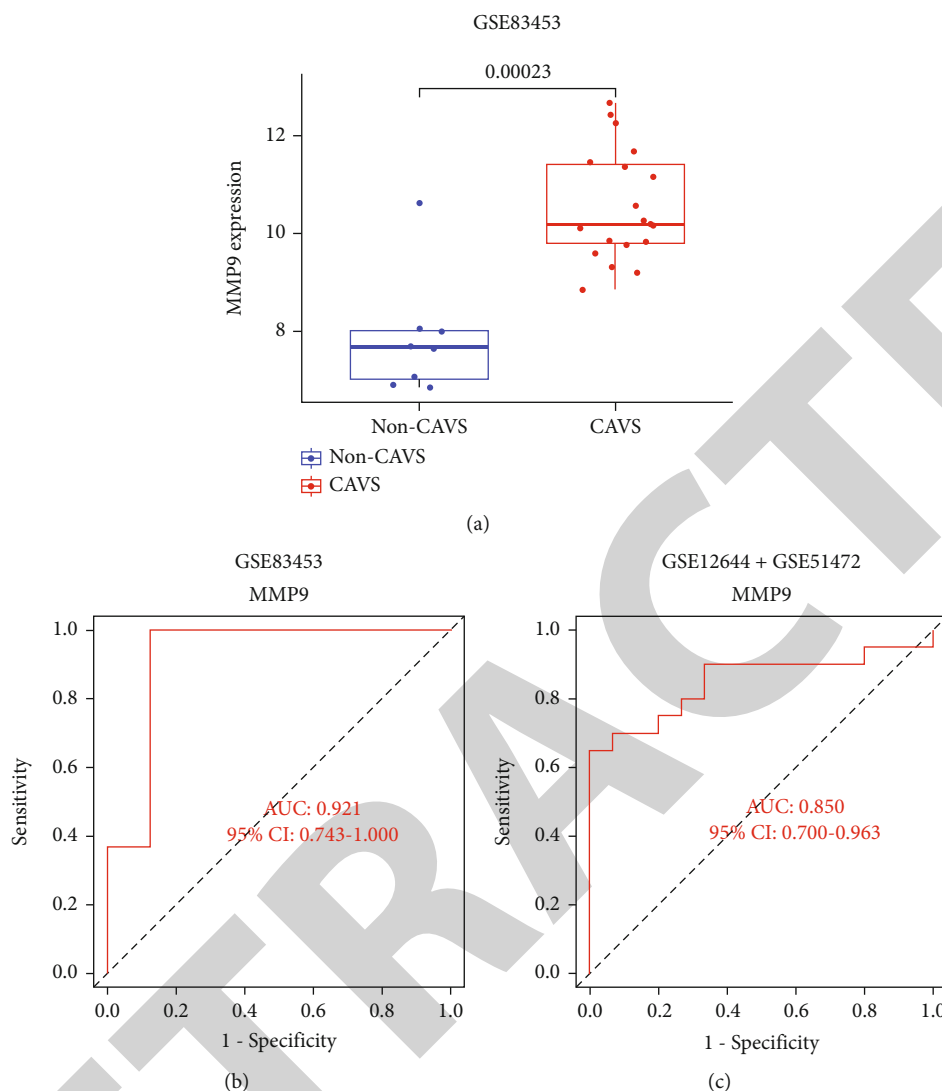


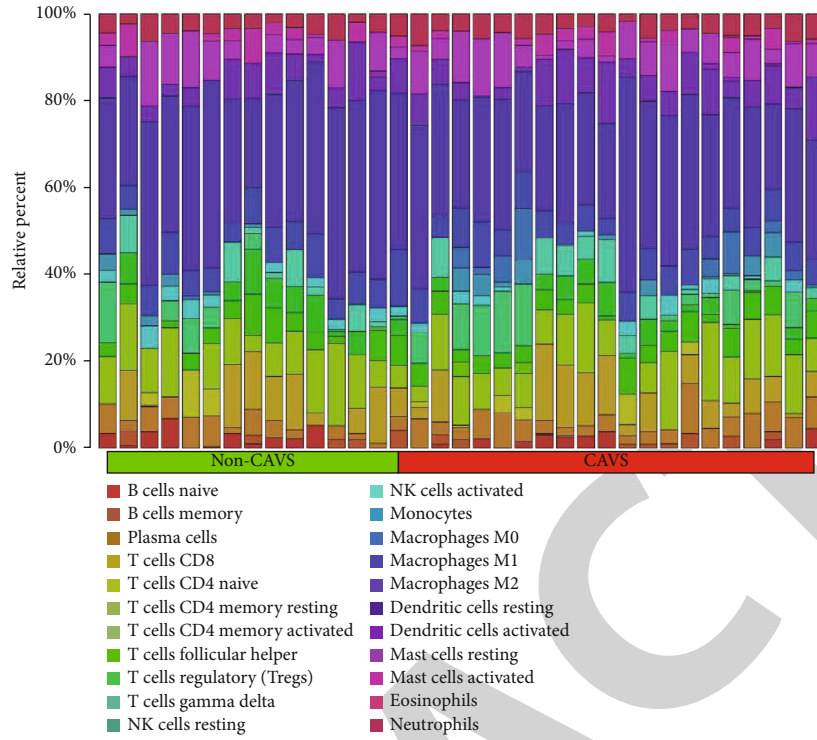
FIGURE 3: Validation of the expression and diagnostic values of *MMP9* in the GSE83453 dataset. (a) *MMP9* expression was distinctly higher in CAVS samples. (b, c) ROC assays of *MMP9* expression based on the GSE83453 and GSE12644 + GSE51472 datasets, respectively.

damage in calcified VICs. *MMP9* inhibition by MMP-9i (Figure S1) could significantly improve mitochondrial morphology in calcified VICs (Figure 7(a)). The fluorescence intensity of FITC-ROS DCFH-DA (Figure 7(b) and S2) and DHE (Figure 7(c)) was significantly increased, indicating that the oxidative stress occurred in calcified VICs. The fluorescence intensity ratio of JC-1 aggregate/JC-1 monomer was markedly decreased (Figure 7(d) and S3), suggesting that the mitochondrial membrane potential reduced in calcified VICs. *MMP9* inhibition by MMP-9i could significantly attenuate mitochondrial dysfunctions (Figures 7(b)–7(d)). Besides, the citrate synthase activity was markedly reduced in calcified VICs (Figure 7(e)), indicating the existence of mitochondrial metabolism disorder in calcified VICs. *MMP9* inhibition by MMP-9i could also enhance the citrate synthase activity of VICs. The above results suggested that inhibiting *MMP-9* may attenuate the mitochondrial quality imbalance of calcified VICs in a dose-dependent manner. In addition, the calcification of VICs was

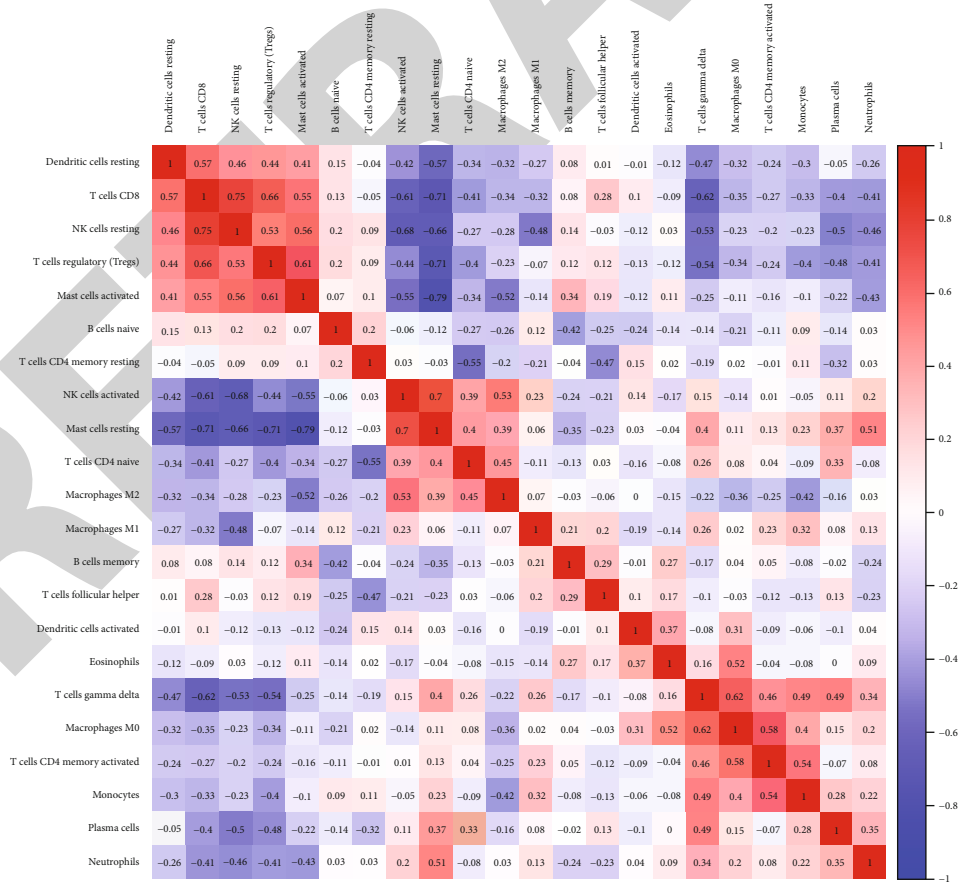
also decreased significantly in a dose-dependent manner (Figures 7(a)–7(e)). Overall, our findings suggested that *MMP9* is highly expressed in CAVS and plays a critical role in the mitochondrial quality imbalance observed in calcified VICs.

#### 4. Discussion

According to our current understanding, CAVS is a dynamic condition characterized by lipid accumulation, persistent inflammation, and active valve leaflet calcification [16]. Valvular degeneration precedes aortic stenosis and is characterized by calcification of the aortic valves, which is initially mild or moderate before worsening, with or without clinical symptoms [17]. CAVS progresses over a lengthy period and its presentation varies greatly from person to person. To date, potential prognostic biomarkers for CAVS have been limited. In recent years, an increasing number of studies have used machine learning techniques to screen novel



(a)



(b)

FIGURE 4: Continued.

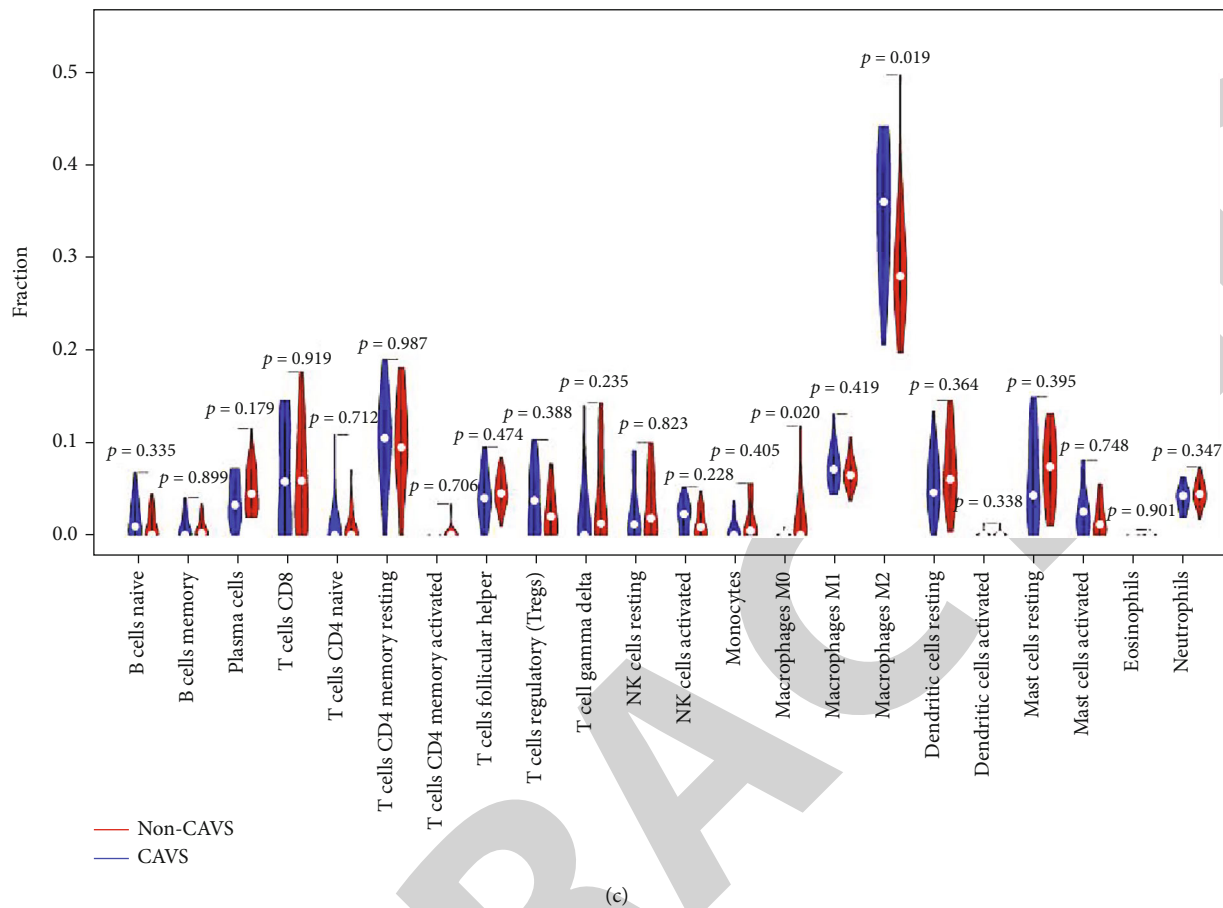


FIGURE 4: CIBERSORT analysis of infiltrating immune cells in non-CAVS and CAVS groups. (a) The distribution of 22 immune cells in the non-CAVS and CAVS groups, respectively, portrayed in a stacked bar chart. (b) Correlation matrix of immune cell proportions. Positive and negative correlations are shown in red and blue, respectively. (c) Violin plot highlighting the differences in immune cell infiltration, between the non-CAVS and CAVS groups.

biomarkers for various diseases, including those of the cardiovascular system [18, 19]. The artificial intelligence sub-field of machine learning makes use of massive datasets to create predictions. Although most algorithms used in machine learning had been developed as far back as the 1950s, this technology has been resurrected over the past two decades [20], owing to the rise of big data and improved computational power.

In our study, we screened DEGs between CAVS and normal samples and identified 22 functionally enriched DEGs. Moreover, we used two machine learning algorithms for the first time, to further screen possible biomarkers of CAVS, identifying *SCG2*, *PPBP*, *TREM1*, *CCL19*, *WIF1*, and *MMP9* as suitable candidates. Mitochondria, known as the “powerhouses” in cells, play essential roles in many cellular activities, including cell growth and death, signal transduction, and energy metabolism. An increasing number of studies have reported the important role of mitochondria in VHD progression. Interestingly, we identified a mitochondria-related gene, *MMP9*, as one of the mitochondrial dysfunction biomarkers for CAVS. Using the GSE83453 dataset, we further demonstrated that *MMP9* expression was distinctly higher in CAVS samples, com-

pared with that in normal samples. In addition, ROC curve analysis revealed *MMP9* as a potential indicator to distinguish CAVS samples from normal samples, with an AUC of 0.921, highlighting its potential use as a novel diagnostic biomarker.

A thorough understanding of disease pathophysiology and basic science is required for drug development. Myofibroblast activation, osteoblastic transition, lipoprotein deposition, and inflammation play important roles in the pathogenesis of CAVS, and accordingly, lymphocytic infiltration is a defining feature thereof. However, most pharmaceutical strategies are absorbed in general cardiovascular health with focus on treatments for dyslipidemia, diabetes, and hypertension [21]. The enrichment analysis conducted herein indicated that the “IL-17 signaling pathway,” “ECM-receptor interaction,” “viral protein interaction with cytokine and cytokine receptor,” “chemokine signaling pathway,” and “focal adhesion” were noticeably enriched; accordingly, we were curious whether immune cell infiltration played a part in the pathogenic role of *MMP9* in CAVS. We found that *MMP9* expression was positively correlated with “macrophage M0,” “dendritic cells activated,” and “macrophage M2” confirming our postulation.

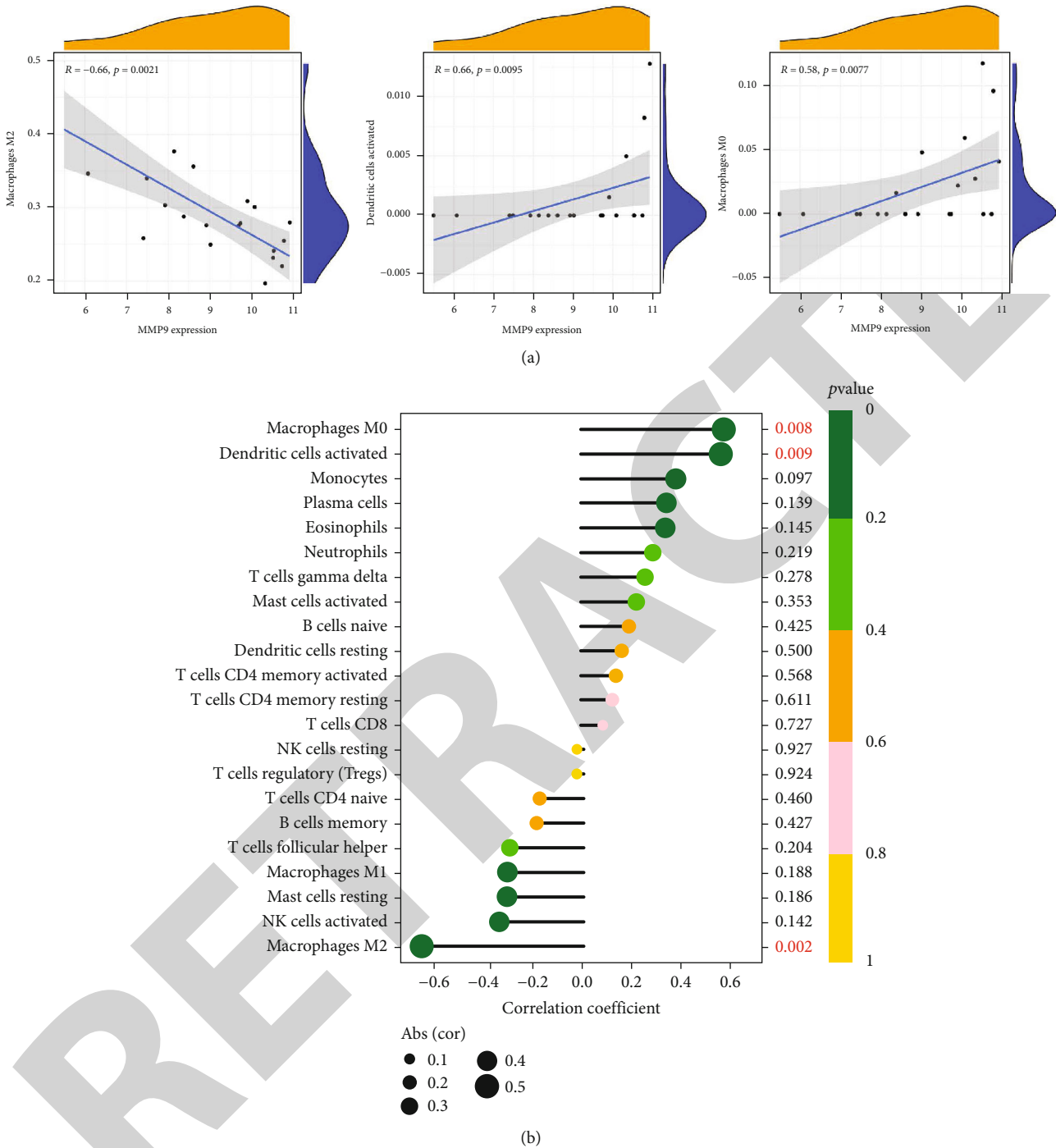


FIGURE 5: Correlations between *MMP9* expression and immune cell infiltration in CAVS. (a) The correlation analysis. (b) The bubble chart.

Finally, to demonstrate the results from online datasets, we performed western blotting and immunohistochemistry, which also confirmed that *MMP9* expression was distinctly increased in CAVS samples, compared to normal samples. Matrix metalloproteinases (MMPs)—a class of approximately 25 zinc-dependent proteinases—are involved in the regulation of several cellular functions, including angiogenesis [22], differentiation, proliferation, and apoptosis [23]. Of these, *MMP9* is reportedly involved in mitochondrial damage, which, in turn, has been confirmed to play an important

role in the progression of CAVS. In this study, we found that the mitochondria of VICs were significantly fragmented, confirming the presence of mitochondrial damage in calcified VICs. However, inhibiting *MMP9* significantly improved mitochondrial morphology, mitochondrial metabolism, and oxidative stress. In addition, the calcification of VICs decreased significantly, in a dose-dependent manner. Our findings highlighted the important role of *MMP9* in the progression of CAVS by inducing an imbalance in mitochondrial quality.

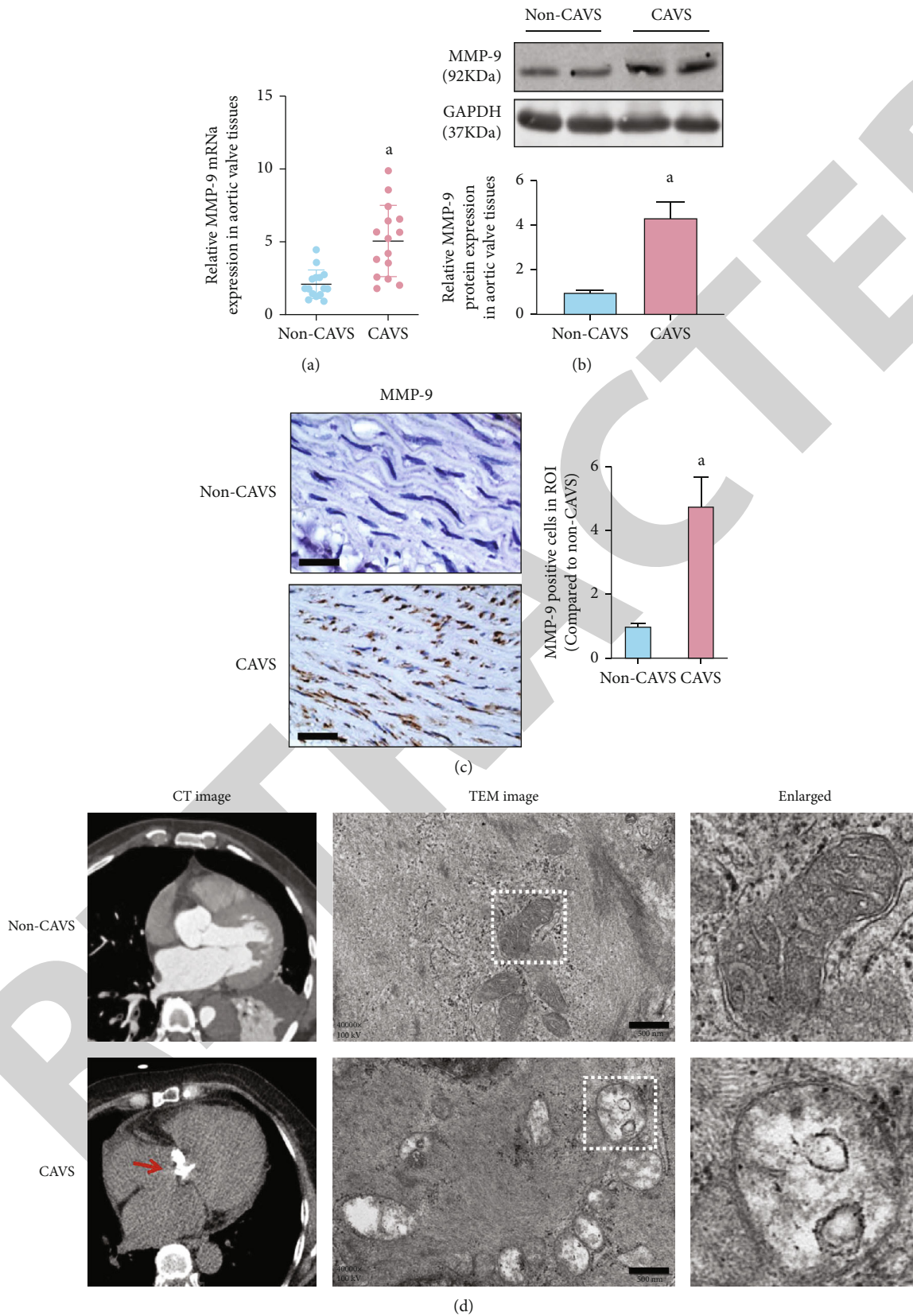
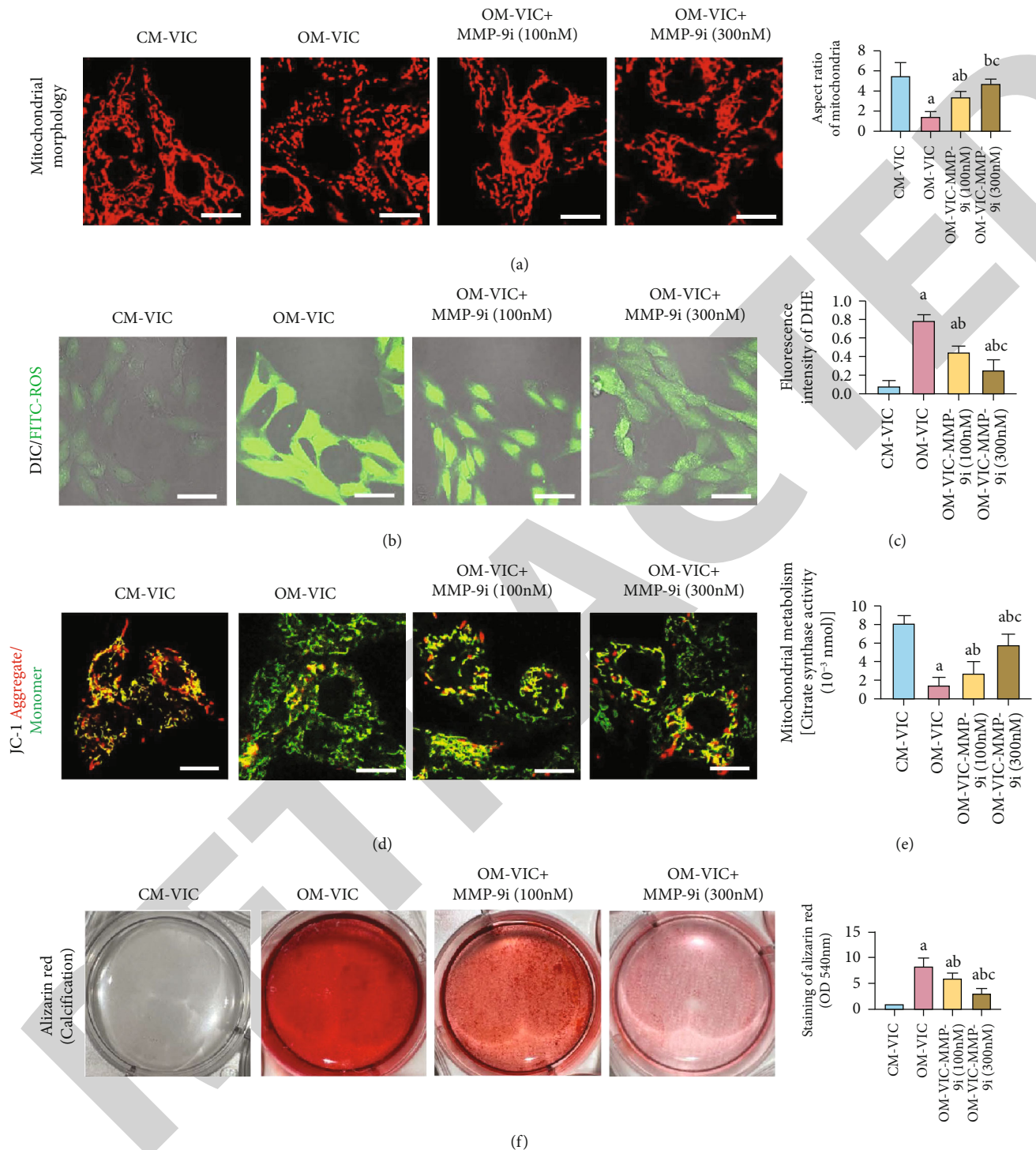


FIGURE 6: *MMP9* was highly expressed in CAVS. (a) RT-PCR, (b) western blotting, and (c) immunohistochemistry were conducted to examine the expression of *MMP9* in non-CAVS and CAVS samples, respectively (bar = 50  $\mu$ m). (d) CT images confirmed an obvious calcified focus in CAVS samples, and TEM images showed mitochondria cristae damage in aortic valve tissues (bar = 500 nm). (a)  $p < 0.05$  compared with non-CAVS group.





**FIGURE 7: MMP9 inhibition attenuated calcification via suppression of mitochondrial quality imbalance.** (a) MitoTracker Red staining immunofluorescence reflected the mitochondrial morphology in VICs. Mitochondrial aspect ratio was quantified by ImageJ (bar = 25  $\mu$ m). (b) FITC-ROS staining immunofluorescence reflected the oxidative stress in VICs (bar = 50  $\mu$ m). (c) The fluorescence intensity of DHE reflected the oxidative stress in VICs. (d) JC-1 aggregate/monomer ratio reflected the mitochondrial membrane potential in VICs (bar = 25  $\mu$ m). (e) Citrate synthase activity was detected to observe the mitochondrial metabolism in VICs. (f) Representative Alizarin Red stain and quantification of calcified VICs, treated with either MMP-9i (100 nM) or MMP-9i (300 nM). CM: control medium, OM: osteogenic medium. (a)  $p < 0.05$  compared with CM-VIC group, (b)  $p < 0.05$  compared with OM-VIC group, (c)  $p < 0.05$  compared with the OM-VIC+ MMP-9i (100 nM) group.

## 5. Conclusion

For the first time, six novel biomarkers (*SCG2*, *PPBP*, *TREM1*, *CCL19*, *WIF1*, and *MMP9*) for CAVS have been identified, based on machine learning algorithms; these may be important regulators of CAVS progression. *MMP9*, a mitochondria-related gene, has been correlated with M0 macrophages, activated dendritic cells, and M2 macrophages, and its inhibition may attenuate cardiovascular calcification by reducing mitochondrial damage. Our findings suggest *MMP9* as a novel mitochondrial dysfunction biomarker and therapeutic target for CAVS.

However, this study has some limitations. First, despite the fact that different datasets were collected to confirm the diagnostic value of *MMP9*, the study has a retrospective design, and additional clinical samples are required to confirm our findings. Second, the potential function of *MMP9* in the immune microenvironment was not demonstrated using either in vitro or in vivo experiment. Third, the molecular mechanisms involved in *MMP9*-mediated mitochondrial quality control need to be further investigated. These factors offer scope for future research.

## Data Availability

The datasets used and/or analyzed during the current study are available from the corresponding authors upon reasonable request.

## Conflicts of Interest

The authors declare that they have no competing interests.

## Authors' Contributions

DCY and MRY designed the whole project. LC and GQ performed most of the bioinformatics analysis in this study. LRX and CZZ performed the in vivo and in vitro experiments. XYB and LLM were responsible for manuscript editing and revision. DCY, MRY, and HH provided scientific research funding support. All authors read and approved the final manuscript.

## Acknowledgments

This work was supported by the National Natural Science Foundation of China (No. 82270378 and 82272252), Chongqing Talents Program (cstc2022ycjh-bgzxm0007), and the Kuanren Talents Program of the Second Affiliated Hospital of Chongqing Medical University. We thank Prof. Tao Li from Army Medical University for the help with experimental equipment.

## Supplementary Materials

*Supplementary 1.* Western blotting result showing the inhibitory effect of MMP-9i to the expression of MMP-9 ( $n = 3$  samples/group). CM: control medium, OM: osteogenic medium. (a)  $p < 0.05$  compared with CM-VIC group, (b)  $p < 0.05$  compared with OM-VIC group, (c)  $p < 0.05$  compared with the OM-VIC+ MMP-9i (100 nM) group.

*Supplementary 2.* The detailed images of FITC-ROS staining in VICs and quantification to Figure 7(b) (bar = 50  $\mu\text{m}$ ). CM: control medium, OM: osteogenic medium. (a)  $p < 0.05$  compared with CM-VIC group, (b)  $p < 0.05$  compared with OM-VIC group, (c)  $p < 0.05$  compared with OM-VIC+ MMP-9i (100 nM) group.

*Supplementary 3.* The detailed images of mitochondrial membrane potential and quantification to Figure 7(d) (bar = 25  $\mu\text{m}$ ). CM: control medium, OM: osteogenic medium. (a)  $p < 0.05$  compared with CM-VIC group, (b)  $p < 0.05$  compared with OM-VIC group, (c)  $p < 0.05$  compared with the OM-VIC+ MMP-9i (100 nM) group.

## References

- [1] C. M. Otto, R. A. Nishimura, R. O. Bonow et al., "2020 ACC/AHA guideline for the management of patients with valvular heart disease: executive summary: a report of the American College of Cardiology/American Heart Association Joint Committee on Clinical Practice Guidelines," *Circulation*, vol. 143, no. 5, pp. e35–e71, 2021.
- [2] C. Duan, Z. Cao, F. Tang et al., "miRNA-mRNA crosstalk in myocardial ischemia induced by calcified aortic valve stenosis," *Aging (Albany NY)*, vol. 11, no. 2, pp. 448–466, 2019.
- [3] A. Adelsheimer, B. Shah, A. Choy-Shan et al., "Gout and progression of aortic stenosis," *The American Journal of Medicine*, vol. 133, no. 9, pp. 1095–1100.e1, 2020.
- [4] I. Okor, T. Bob-Manuel, K. Garikapati, H. Baldawi, C. Gillies, and U. N. Ibebuogu, "Transcatheter aortic valve replacement in rheumatic aortic stenosis: a comprehensive review," *Current Problems in Cardiology*, vol. 46, no. 12, article 100843, 2021.
- [5] X. Zeng, Y. D. Zhang, R. Y. Ma et al., "Activated Drp1 regulates p62-mediated autophagic flux and aggravates inflammation in cerebral ischemia-reperfusion via the ROS-RIP1/RIP3-exosome axis," *Military Medical Research*, vol. 9, no. 1, p. 25, 2022.
- [6] C. Duan, L. Wang, J. Zhang et al., "Mdivi-1 attenuates oxidative stress and exerts vascular protection in ischemic/hypoxic injury by a mechanism independent of Drp1 GTPase activity," *Redox Biology*, vol. 37, article 101706, 2020.
- [7] C. Duan, L. Kuang, X. Xiang et al., "Drp1 regulates mitochondrial dysfunction and dysregulated metabolism in ischemic injury via Clec16a-, BAX-, and GSH- pathways," *Cell Death & Disease*, vol. 11, no. 4, p. 251, 2020.
- [8] I. Tandon, K. P. Quinn, and K. Balachandran, "Label-free multiphoton microscopy for the detection and monitoring of calcific aortic valve disease," *Frontiers in Cardiovascular Medicine*, vol. 8, article 688513, 2021.
- [9] G. Morciano, S. Patergnani, G. Pedriali et al., "Impairment of mitophagy and autophagy accompanies calcific aortic valve stenosis favouring cell death and the severity of disease," *Cardiovascular Research*, vol. 118, no. 11, pp. 2548–2559, 2022.
- [10] S. Khatun, S. Biswas, A. K. Mahanta et al., "Biocompatible fluorescent probe for detecting mitochondrial alkaline phosphatase activity in live cells," *Journal of Photochemistry and Photobiology. B*, vol. 212, article 112043, 2020.
- [11] C. Ren, M. Li, W. Du et al., "Comprehensive bioinformatics analysis reveals hub genes and inflammation state of rheumatoid arthritis," *BioMed Research International*, vol. 2020, Article ID 6943103, 13 pages, 2020.

## Retraction

# Retracted: Decreased Polymorphonuclear Myeloid-Derived Suppressor Cells and ROS Production Correlated Closely with Bronchopulmonary Dysplasia in Preterm Infants

### Oxidative Medicine and Cellular Longevity

Received 20 June 2023; Accepted 20 June 2023; Published 21 June 2023

Copyright © 2023 Oxidative Medicine and Cellular Longevity. This is an open access article distributed under the Creative Commons Attribution License, which permits unrestricted use, distribution, and reproduction in any medium, provided the original work is properly cited.

This article has been retracted by Hindawi following an investigation undertaken by the publisher [1]. This investigation has uncovered evidence of one or more of the following indicators of systematic manipulation of the publication process:

- (1) Discrepancies in scope
- (2) Discrepancies in the description of the research reported
- (3) Discrepancies between the availability of data and the research described
- (4) Inappropriate citations
- (5) Incoherent, meaningless and/or irrelevant content included in the article
- (6) Peer-review manipulation

The presence of these indicators undermines our confidence in the integrity of the article's content and we cannot, therefore, vouch for its reliability. Please note that this notice is intended solely to alert readers that the content of this article is unreliable. We have not investigated whether authors were aware of or involved in the systematic manipulation of the publication process.

In addition, our investigation has also shown that one or more of the following human-subject reporting requirements has not been met in this article: ethical approval by an Institutional Review Board (IRB) committee or equivalent, patient/participant consent to participate, and/or agreement to publish patient/participant details (where relevant).

Wiley and Hindawi regrets that the usual quality checks did not identify these issues before publication and have since put additional measures in place to safeguard research integrity.

We wish to credit our own Research Integrity and Research Publishing teams and anonymous and named external researchers and research integrity experts for contributing to this investigation.

The corresponding author, as the representative of all authors, has been given the opportunity to register their agreement or disagreement to this retraction. We have kept a record of any response received.

### References

- [1] W. Liu, S. Li, Y. Li et al., "Decreased Polymorphonuclear Myeloid-Derived Suppressor Cells and ROS Production Correlated Closely with Bronchopulmonary Dysplasia in Preterm Infants," *Oxidative Medicine and Cellular Longevity*, vol. 2022, Article ID 9010354, 8 pages, 2022.

## Research Article

# Decreased Polymorphonuclear Myeloid-Derived Suppressor Cells and ROS Production Correlated Closely with Bronchopulmonary Dysplasia in Preterm Infants

Wangkai Liu <sup>1</sup>, Sitao Li,<sup>2</sup> Yushan Li,<sup>1</sup> Wei Shen,<sup>3</sup> Haitian Chen,<sup>4</sup> Xiaoyu Li,<sup>1</sup> Linnuan Cai,<sup>1</sup> Fan Wu,<sup>5</sup> Yumei Liu <sup>6</sup>, Qiong Meng <sup>7</sup>, and Xiaoyun Jiang <sup>1</sup>

<sup>1</sup>Department of Pediatrics, The First Affiliated Hospital, Sun Yat-sen University, Guangzhou, China

<sup>2</sup>Department of Pediatrics, The Sixth Affiliated Hospital, Sun Yat-sen University, Guangzhou, China

<sup>3</sup>Department of Pediatrics, Southern Medical University, Guangzhou, Guangdong, China

<sup>4</sup>Department of Obstetrics, The First Affiliated Hospital, Sun Yat-sen University, Guangzhou, China

<sup>5</sup>Department of Pediatrics, Third Affiliated Hospital, Guangzhou Medical University, Guangzhou, China

<sup>6</sup>Department of Neonatology, Guangdong Provincial People's Hospital, Guangdong Academy of Medical Sciences, Guangzhou, China

<sup>7</sup>Department of Pediatrics, Guangdong Second Provincial General Hospital, Guangzhou, China

Correspondence should be addressed to Yumei Liu; 13501519292@139.com, Qiong Meng; mengqiong1969@163.com, and Xiaoyun Jiang; jxiaoy@mail.sysu.edu.cn

Received 25 April 2022; Revised 1 August 2022; Accepted 27 August 2022; Published 20 September 2022

Academic Editor: Tian Li

Copyright © 2022 Wangkai Liu et al. This is an open access article distributed under the Creative Commons Attribution License, which permits unrestricted use, distribution, and reproduction in any medium, provided the original work is properly cited.

**Background.** Bronchopulmonary dysplasia (BPD) is one of the most serious complications in premature infants. Myeloid-derived suppressor cells (MDSCs) have been indicated to promote immune tolerance and induce anti-inflammatory responses during the neonatal stage. However, the role of MDSCs in BPD has not been completely expounded. **Methods.** 130 cases of newborns were collected from six tertiary hospitals in Guangzhou from August 2019 to June 2022. They were divided into BPD group, non-BPD preterm infants group, and term infants group according to gestational age and presence of BPD. The peripheral blood was collected and used to analyze the proportion, phenotypic, and function of MDSCs at 3 to 7 days and 8 to 14 days after birth, respectively. **Results.** We indicated that the number of both MDSCs in premature infants is reduced, and the number of polymorphonuclear myeloid-derived suppressor cells (PMN-MDSCs) in peripheral blood of BPD infants was significantly lower than that of non-BPD infants under 34 weeks of gestational age ( $P < 0.05$ ). Furthermore, PMN-MDSCs from peripheral blood of patients presented inhibitory effect on proliferation of CD4<sup>+</sup>T and CD8<sup>+</sup>T cells in each group. However, PMN-MDSCs from BPD group had obviously weaker inhibitory effect on proliferation of CD4<sup>+</sup>T and CD8<sup>+</sup>T cells than that from non-BPD preterm infants group. In addition, we demonstrated that the expression of NADPH oxidase (Nox2) and reactive oxygen species (ROS) in PMN-MDSCs of BPD children was significantly lower than that in non-BPD preterm infants, suggesting that ROS pathway was affected in BPD in premature infants. **Conclusion.** This study preliminarily revealed the role of PMN-MDSCs in the pathogenesis of BPD in premature infants. The specific immune regulation mechanism of PMN-MDSCs in BPD will provide new ideas and strategies for clinical prevention and treatment of BPD in premature infants.

## 1. Introduction

Preterm birth is not only a common but also a serious disease of newborns with a second-highest mortality rate among children under five [1]. Studies have shown that BPD is the most

prevalent short-term complication of preterm infants [2]. In a study for newborns with a gestational age of 24 to 31 weeks and a birth weight of less than 1500 g in 11 high-income countries indicated that although mortality in early preterm infants decreased in most countries, the incidence of BPD increased

[3]. An analysis of the short-term outcomes of very preterm infants after the discharge from Guangdong Province, China, showed that the neonatal survival rate increased from 36.2% in 2008 to 59.3% in 2017, and the incidence of BPD also significantly increased by more than 50% [4].

MDSCs are a heterogeneous group of cells which have a strong immune inhibitory function [5]. MDSCs are divided into two types according to the expression of surface antigens, including PMN-MDSCs and monocytic MDSCs (M-MDSCs) [6]. M-MDSCs mainly inhibit the function of T cells in an antigen-nonspecific manner by increasing the activity of arginase, while PMN-MDSCs inhibit T cell responses in an antigen-specific manner typically using ROS as immune mediators [7].

Immunosuppression is a major feature of MDSCs, and T cells are their primary targets. Previous studies have shown that MDSCs exert their immunosuppressive effects by regulating multiple pathways, such as regulatory T cell (Treg), iNOS and ARG1, ROS, and peroxynitrite (ONOO<sup>-</sup>) pathways [8]. In our previous research, we found that the oxygen stress pathway related genes were significantly up-regulated in lung tissue, and the transcription of glutathione S-transferase alpha 2 (Gsta2) was also significantly increased in a lung transcriptomic data with an early in the disease course of mouse BPD model. The results suggested that oxygen damage might be one of the important factors that cause early lung inflammation. More importantly, we observed that the MDSCs marker genes S100A8 and S100A9 were significantly down-regulated (unpublished data). We also revealed that MDSCs were significantly deficient in quantity, function, and antibacterial activity in preterm mice, compared with the term mice, suggesting that MDSCs had a protective effect on the development of inflammation in neonatal mice [9].

Taken together, these findings proved that BPD posed a great threat to the quality of life of premature infants. However, its pathogenesis is not fully elucidated. In addition, inflammatory response is an important factor in the development of BPD. It is necessary to find new immune regulation mechanisms related to inflammation to prevent and treat BPD. MDSCs were proved to play an important immunosuppressive role in the early neonatal period and protect the body from anti-inflammatory and anti-infective effects. Thus, this study aims to explore the function of MDSCs in the development of BPD.

## 2. Materials and Methods

**2.1. Human Subjects.** Neonatal cases born in the neonatology department of 6 tertiary hospitals (The First Affiliated Hospital of Sun Yat-sen University, Nanfang Hospital, Guangdong Provincial People's Hospital, Guangdong Second Provincial General Hospital, the Third Affiliated Hospital of Guangzhou Medical University, the Sixth Affiliated Hospital of Sun Yat-sen University) in Guangzhou were collected from August 2019 to June 2022. The inclusion criteria include preterm infants and term infants not included in the exclusion criteria. They were divided into BPD group, non-BPD premature infants group, and non-BPD term infants group based on their gestational age and presence of BPD. The peripheral blood

from all cases was collected at 3-7 days and 8-14 days after birth. 30 premature infants with BPD were collected. In order to analyze the relationship between the occurrence of BPD and the existence of MDSCs, preterm infants and term infants with the same gestational age and sampling age without BPD were collected in a ratio of 1:1:1 as the control group. Exclusion criteria include congenital heart disease (atrial septal defect, ASD; ventricular septal defect, VSD; and patent ductus arteriosus, PDA), persistent pulmonary hypertension in the neonate (PPHN), severe congenital malformations, chromosomal abnormalities, genetic metabolic diseases, anemia, and cases with incomplete data. This project had obtained the ethical exemption of Clinical Research and Animal Trials of the First Affiliated Hospital of Sun Yat-sen University ethics committee (No. [2020]521).

**2.1.1. Collected Data.** According to the 2001 NICHD diagnostic criteria, 30 premature infants with BPD were collected, and the preterm infants and term infants without BPD with the same gestational age were collected as the control group at a ratio of 1:1:1, with total of 90 cases.

**2.1.2. Analyzing the Proportions and Phenotypes of MDSCs by Flow Cytometry.** In order to clarify whether MDSCs can be used as an important predictor of BPD, the correlation analysis was carried out between the levels of MDSCs subtypes and the main indicators related to BPD disease.

**2.1.3. Analyzing the Function of MDSCs in BPD.** The PMN-MDSCs of 5 BPD patients and 5 non-BPD patients were sorted by flow cytometry. Their PMN-MDSCs were co-cultured with CD4<sup>+</sup>/CD8<sup>+</sup> T cells to detect the effect of PMN-MDSCs on the T cell proliferation; In order to figure out whether the PMN-MDSCs of BPD children had immunosuppressive function defects, RT-qPCR was used to detect PMN-MDSCs function-related genes (Arg1, Nos2, and Nox2) and anti-inflammatory factors (IL-10, TGF- $\beta$ , and IFN- $\gamma$ ) in 10 BPD children and 10 non-BPD children.

**2.2. In Vitro Culture of Peripheral Blood MDSCs.** 0.5 ml peripheral blood from patients was collected and the erythrocytes were lysed. Then, it was washed with pre-cooled RPMI medium and resuspended for counting. The cell suspension was laid on 48-well plates at a density of  $1 \times 10^6$  per well or  $2-2.5 \times 10^6$  in 24-well plates. 20 ng/mL human GM-CSF and 20 ng/mL IL-6 were added in the plates to induce the differentiation of cells into human MDSCs. After 3 days of culture, 80% fluid was changed, and phenotypic analysis or functional test was performed until 6 days of culture.

**2.3. Flow Cytometry and Sorting.** Cells ( $1 \times 10^6$  cells) were resuspended in 4 ml  $1 \times$  phosphate buffer saline (PBS) in a 5 ml centrifuge tube then centrifuged at 4,300 rpm/min for 5 min. The supernatant was discarded and then the cells were stained with 100  $\mu$ L antibody (1:400 dilution) at 4°C for 30 min in dark. Then, cells were diluted in PBS to a total volume of 4 ml and centrifuged at 4,300 rpm/min for 5 min. The cells were resuspended with 500  $\mu$ L  $1 \times$  PBS and were analyzed by flow cytometry. Briefly, cells were stained with surface markers HLA-DR, CD1b, CD14, CD15, and LOX-1. The

gating strategy for PMN-MDSCs was CD11b<sup>+</sup>HLA-DR<sup>+</sup>CD15<sup>+</sup>CD14<sup>-</sup> or CD15<sup>+</sup>LOX-1<sup>+</sup>. The proportion of PMN-MDSC cells was detected and sorted by flow cytometry.

**2.4. Co-Culture of MDSC and T Cells.** Labeled CD3<sup>+</sup> T cells were labeled with carboxyfluorescein succinimidyl amino ester (CFSE, 1 $\mu$ M) and were co-cultured at different ratios (8:1, 4:1, and 2:1) with PMN-MDSCs from all the groups in U-bottomed 96-well plate and stimulated with anti-CD3 and anti-CD28 for 3 days. Then, the CD4<sup>+</sup> and CD8<sup>+</sup> T cells were stained and detected CFSE with FITC panel [10].

**2.5. Peripheral Blood Mononuclear Cell (PBMC) Isolation and ROS Analysis.** PBMCs were isolated from whole blood by Ficoll centrifugation and analyzed immediately according to the previous report [11]. Then, cells were incubated with anti-human fluorescence-conjugated antibodies (CD11b-BUV396, HLA-DR-APC-cy7, CD14-APC, and CD15-BV605). And then intracellular ROS levels were determined using dichlorodihydrofluorescein diacetate (DCFH-DA) (Invitrogen). Briefly, cells that were pre-treated with different reagents were incubated with 20 $\mu$ M DCFH-DA in Hanks' balanced salt buffer for 30 min at 37°C. The ROS level was quantified using a FACS flow cytometer ((BD LSR fortessa, BD Biosciences, San Jose, CA, USA).

**2.6. Statistical Analysis.** Statistical analysis was performed with GraphPad Prism version 5.0a and SPSS 22.0. The statistical data are presented as means  $\pm$  standard deviation (SD). Differences between two groups were evaluated by Student's *t*-test. *P* values < 0.05 were considered significant.

### 3. Results

A total of 130 infants were enrolled actually. We collected only 23 patients with BPD, and 107 patients (75 preterm infants and 32 term infants) without BPD. There was no gender difference.

#### 3.1. Correlation between MDSCs and BPD

**3.1.1. Distribution of MDSCs by Gestational Age.** As shown in Figure 1(a), in the absence of infection, BPD premature infants with gestational ages (GA) <28 weeks had lower M-MDSCs (CD11b<sup>+</sup>HLA DR<sup>+</sup>CD14<sup>+</sup>CD15<sup>-</sup>) and PMN-MDSCs (CD11b<sup>+</sup>HLA DR<sup>+</sup>CD14<sup>-</sup>CD15<sup>+</sup>) levels than that in premature infants with GA >28 weeks. Furthermore, the proportion of CD15<sup>+</sup>LOX-1<sup>+</sup> in peripheral blood of late preterm infants with 34-37 weeks GA was significantly higher than that of preterm infants born at 28-32 weeks of GA (*P*=0.0026). However, compared with preterm infants with 32-34 weeks GA, the proportion of CD15<sup>+</sup>LOX-1<sup>+</sup> in peripheral blood of late preterm infants with 34-37 weeks GA was significantly increased (*P*=0.008). These results suggested that the smaller gestational age might contribute to the smaller number of MDSCs, with predominant decrease in PMN-MDSCs.

**3.1.2. Comparative Analysis of MDSCs with Different Phenotypes in Preterm Infants Less Than 34 Weeks Gestational Age.** Since almost all BPD infants in this study had a gestational age <34 weeks, there would be a greater bias if compared with term infants or preterm infants > 34 weeks GA. Thus, statistical

analysis was carried out for the control group with GA <34 weeks between the infants with or without infection at different blood sampling time points, etc.

The results showed that there was no difference in the proportion of M-MDSCs (CD11b<sup>+</sup>HLA DR<sup>+</sup>CD14<sup>+</sup>CD15<sup>-</sup>), CD15<sup>+</sup>LOX1<sup>+</sup>, and PMN-MDSCs (CD11b<sup>+</sup>HLA DR<sup>+</sup>CD14<sup>-</sup>CD15<sup>+</sup>) between premature infants with infection (3-7d after birth, GA <34w) and preterm infants with BPD (3-7d after birth, GA <34w) at the same period (*P* > 0.05) (Figure 1(b)). However, the proportion of PMN-MDSCs (CD11b<sup>+</sup>HLA DR<sup>+</sup>CD14<sup>-</sup>CD15<sup>+</sup>) in peripheral blood of children with BPD was significantly lower than that in premature infants without BPD and infection (3-7d after birth, GA <34w) (*P* < 0.05). The proportion of CD15<sup>+</sup>LOX-1<sup>+</sup> and M-MDSCs (CD11b<sup>+</sup>HLA DR<sup>+</sup>CD14<sup>+</sup>CD15<sup>-</sup>) in BPD children also had a downward trend without statistical significance (Figure 1(c)).

The proportion of PMN-MDSCs (CD11b<sup>+</sup>HLA DR<sup>+</sup>CD14<sup>-</sup>CD15<sup>+</sup>), CD15<sup>+</sup>LOX-1<sup>+</sup>, and M-MDSCs (CD11b<sup>+</sup>HLA DR<sup>+</sup>CD14<sup>+</sup>CD15<sup>-</sup>) in peripheral blood of premature was not significantly different between infants without BPD and infection (8-14d after birth, GA <34w) and premature infants with BPD (*P* > 0.05) (Figure 1(d)). Compared with non-BPD preterm infants with infection, both the proportion of M-MDSCs and CD15<sup>+</sup>LOX-1<sup>+</sup> cells of BPD infants with infection (8-14d after birth, GA <34w) increased (Figure 1(e)), and the proportion of PMN-MDSCs decreased without statistical significance (*P* > 0.05).

These data suggested that the decrease of PMN-MDSCs may lead to the suppression of their immune function which will affect BPD development.

#### 3.2. Analysis of PMN-MDSCs Function in Infants with BPD

**3.2.1. Functional Analysis of PMN-MDSCs Inhibiting the Proliferation of CD4<sup>+</sup>/CD8<sup>+</sup> T Cells.** To determine whether MDSCs in preterm infants have an immunosuppressive function and whether there is a defect in the immunosuppressive function of MDSCs in BPD patients, the function of MDSCs was detected. Peripheral blood PMN-MDSCs of BPD infants were sorted and co-cultured with T cells at 2:1, 4:1, and 8:1, while PMN-MDSCs of non-BPD term infants group and non-BPD preterm infants group were co-cultured with T cells as a control group.

Flow cytometry was used to detect the effect of PMN-MDSCs on CD4<sup>+</sup> T cell proliferation. The results in Figure 2(a) showed that, regardless of the ratio, CD4<sup>+</sup> T cells proliferation in BPD group was remarkably higher than that in non-BPD term infants group (*P* < 0.01) when CD4<sup>+</sup> T cells and PMN-MDSCs were co-cultured. Similarly, when CD4<sup>+</sup> T cells and PMN-MDSCs were co-cultured in the ratio of 2:1, 4:1, and 8:1, the CD4<sup>+</sup> T cells proliferation in BPD group was significantly higher than that in non-BPD preterm infants group (*P* < 0.05, *P* < 0.01). The peripheral blood PMN-MDSCs of all the children in each group had an inhibitory effect on the CD4<sup>+</sup> T cells proliferation. However, the inhibition was apparently weaker in the BPD premature infants group than that in the non-BPD preterm infants group, consistent with the reduced proportion of its flow phenotype.

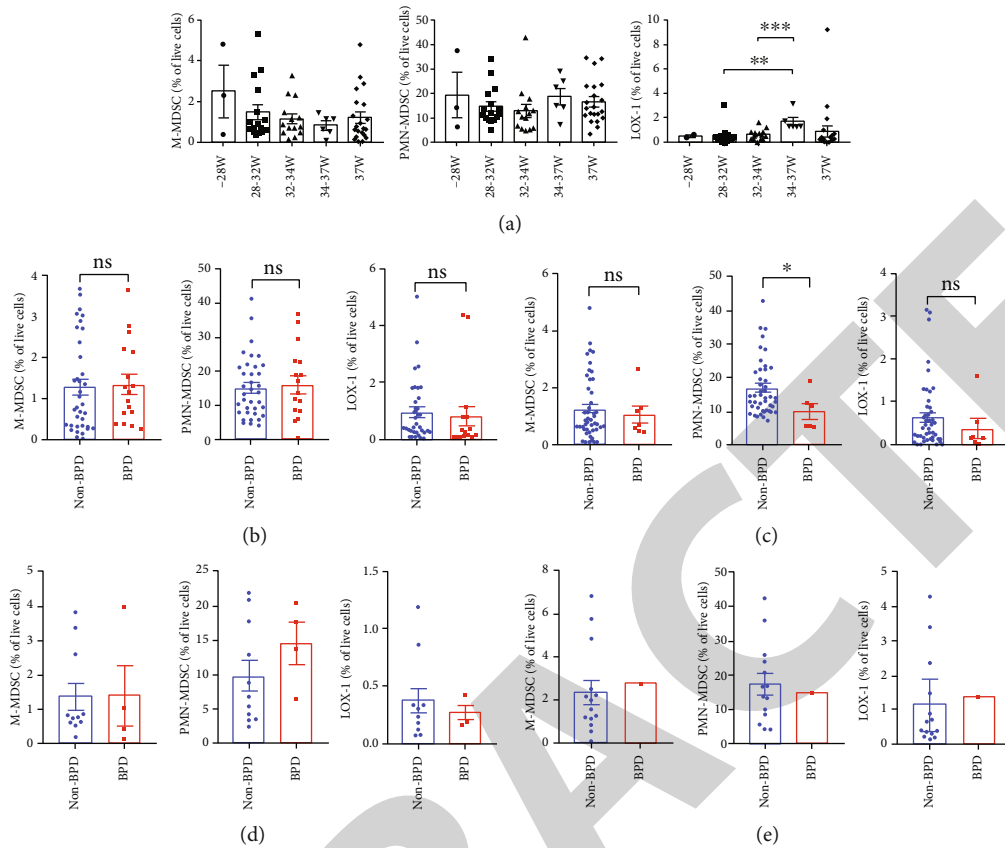


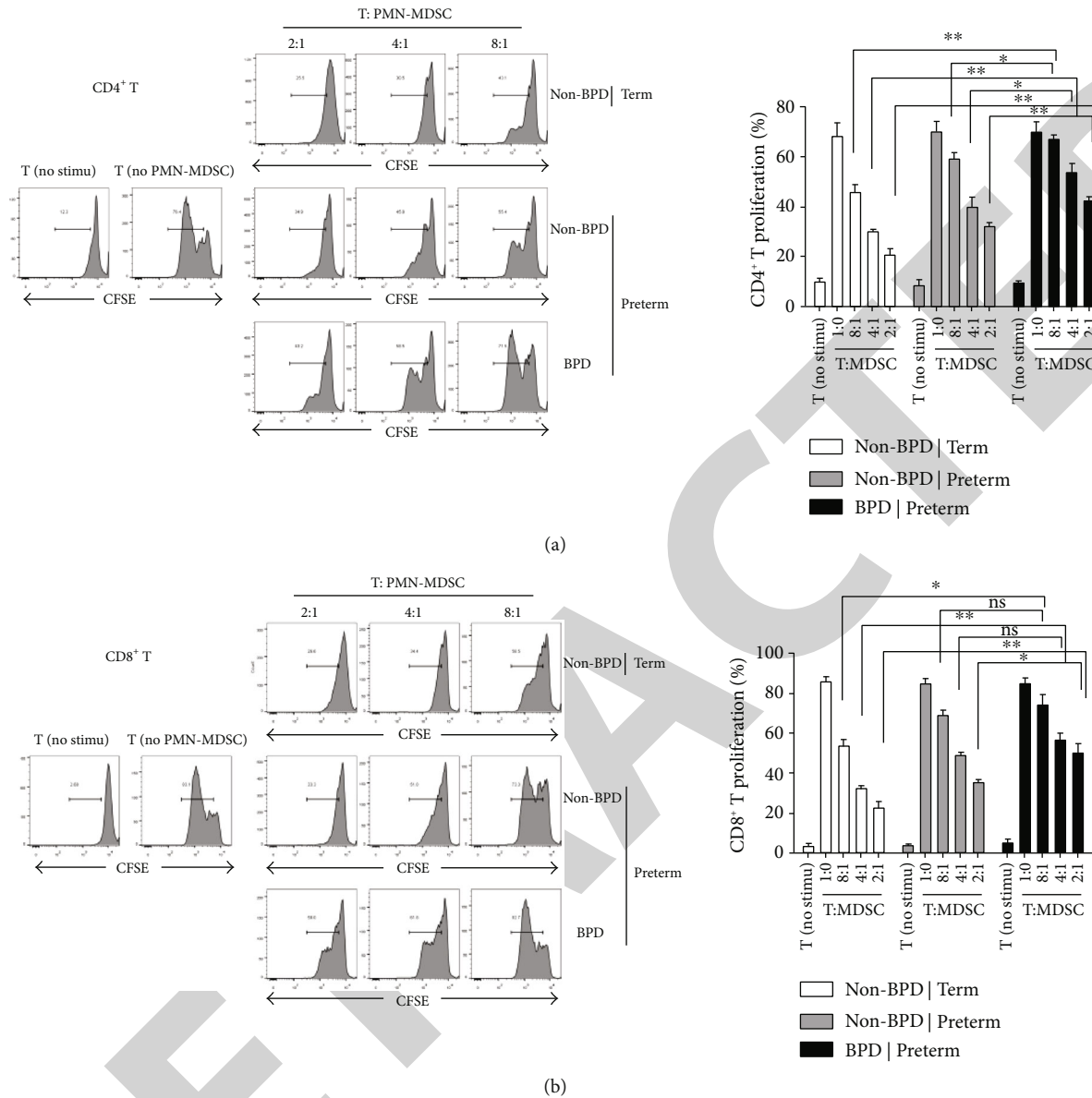
FIGURE 1: Quantification of M-MDSCs, PMN-MDSCs, and LOX-1 in peripheral blood. (a) Quantification of M-MDSCs, PMN-MDSCs, and LOX-1 in peripheral blood of infants (3-7d after birth, without infection) at GA <28W ( $n=3$ ), GA 28~32W ( $n=16$ ), GA 32~34W ( $n=14$ ), GA 34~37w ( $n=6$ ), and GA >37w ( $n=21$ ) (\*\*,  $P < 0.01$ ) (\*\*\*,  $P < 0.001$ ). (b) The proportion of M-MDSCs, PMN-MDSCs, and LOX-1 in peripheral blood of children with BPD ( $n=17$ ) and without BPD (3-7d after birth, gestational age <34w, with infection) ( $n=36$ ). (c) Quantification of M-MDSCs, PMN-MDSCs, and LOX-1 in peripheral blood of children with BPD ( $n=7$ ) and without BPD (3-7d after birth, gestational age <34w, without infection) ( $n=49$ ) (\*,  $P < 0.05$ ). (d) The proportion of M-MDSCs, PMN-MDSCs, and LOX-1 in peripheral blood of children with BPD ( $n=4$ ) and without BPD (8-14d after birth, gestational age <34w, without infection) ( $n=11$ ). (e) The proportion of M-MDSCs, PMN-MDSCs, and LOX-1 in peripheral blood of children with BPD ( $n=1$ ) and without BPD (8-14d, after birth gestational age <34w, with infection) ( $n=14$ ) (\*,  $P < 0.05$ ).

For CD8<sup>+</sup> T cells, the results in Figure 2(b) showed that the CD8<sup>+</sup> T cells multiplication of BPD preterm infant group was markedly higher than that of non-BPD term infants group ( $P < 0.05$ ) when CD8<sup>+</sup> T cells were co-cultured with PMN-MDSCs at 8:1. The propagation of CD8<sup>+</sup> T cells showed the similar result when co-cultured at 4:1 ( $P < 0.01$ ) and 2:1 ( $P < 0.01$ ). The proliferation of CD8<sup>+</sup> T cells in the BPD preterm infants group was significantly higher than that in the non-BPD preterm infant group ( $P < 0.05$ ) when CD8<sup>+</sup> T cells and PMN-MDSCs were co-cultured at 2:1. However, there was no statistical significance when CD8<sup>+</sup> T cells were co-cultured with PMN-MDSCs at a ratio of 8:1 and 4:1 ( $P > 0.05$ ). The PMN-MDSCs of all groups suppressed the proliferation of CD8<sup>+</sup> T cells. Compared with the two other groups, the inhibitory effect was significantly weaker in BPD group, consistent with the reduced proportion of its flow phenotype. These results suggested that although the number of PMN-MDSCs from children with BPD did not decrease, the ability of CD4<sup>+</sup>/CD8<sup>+</sup> T cells proliferation suppression was attenuated.

### 3.3. Screening and Validation of Molecules Related to MDSCs Immunosuppressive Function

**3.3.1. Expression of Arg1, Nos2, and Nox2 in PMN-MDSCs.** The expressions of three classical molecules related to the immunosuppressive function of MDSCs were detected by qRT-PCR, including arginase 1 (Arg1), inducible nitric oxide synthesis (Nos2 or iNos), and Nox2. The results showed that the expression of Arg1 and Nos2 in PMN-MDSCs of BPD infants was not significantly different from that of non-BPD cases. However, the expression of Nox2 in PMN-MDSCs of BPD cases was obviously lower than non-BPD cases ( $P < 0.05$ ) (Figure 3(a)), indicating that PMN-MDSCs have a certain immunosuppressive function in BPD children and the defect was manifested in the low expression of Nox2.

**3.3.2. Expression of IL-10, TGF- $\beta$ , and IFN- $\gamma$  in PMN-MDSCs.** The expression of PMN-MDSCs immunosuppressive function-related cytokines IL-10, TGF- $\beta$ , and IFN- $\gamma$  in BPD and non-BPD premature infants was also detected by RT-



**FIGURE 2: PMN-MDSCs inhibited the proliferation of CD4<sup>+</sup>/CD8<sup>+</sup> T cells.** (a) The proliferation rate of CD4<sup>+</sup> cells was detected by flow cytometry after 3 days. CD4<sup>+</sup> cells and PMN-MDSCs were co-cultured in different proportions. The figure above is typical flow chart and the figure below is statistical chart. PMN-MDSCs inhibited the proliferation of CD8<sup>+</sup> T cells ( $n = 11$ ) ( $*P < 0.05$ ,  $**P < 0.01$ ). (b) Flow cytometry was used to detect the proliferation rate of CD8<sup>+</sup> cells after 3 days. CD8<sup>+</sup> T cells and PMN-MDSCs were co-cultured in different proportions. The figure above is typical flow chart and the figure below is statistical chart ( $n = 11$ ) ( $*P < 0.05$ ,  $**P < 0.01$ ).

qPCR. Compared with non-BPD premature infants, the expressions of IL-10 and TGF- $\beta$  were significantly lower in PMN-MDSCs of BPD children ( $P < 0.05$ ). In contrast, the expression of IFN- $\gamma$  in PMN-MDSCs of BPD children also showed a downward trend, but did not meet statistical significance ( $P > 0.05$ ) (Figure 3(b)).

**3.4. Comparative Analysis of ROS Levels of BPD and Non-BPD Preterm Infants.** ROS levels were measured in the peripheral blood of 14 preterm infants aged 2 to 7 days. They were then grouped according to whether they were diagnosed with BPD at 28 days old. The result showed that ROS level in the peripheral blood from non-BPD preterm infants was significantly higher than that in the BPD infants ( $P < 0.05$ ) (Figure 4).

### 4. Discussion

MDSCs are a class of pathologically activated immature myeloid cells with potent immunosuppressive functions [11, 12]. Recent studies have shown that MDSCs are important to the induction of physiological immune tolerance which could induce individual airway tolerance and prevent asthma attacks [13, 14]. MDSCs have also been found to promote maternal-fetal tolerance and ensure the normal progression of pregnancy [15, 16]. Besides, MDSCs level at birth can predict necrotizing enterocolitis in premature infants [9]. However, whether PMN-MDSC levels are different in peripheral blood of BPD and non-BPD children and whether it can be used as a diagnostic marker of BPD



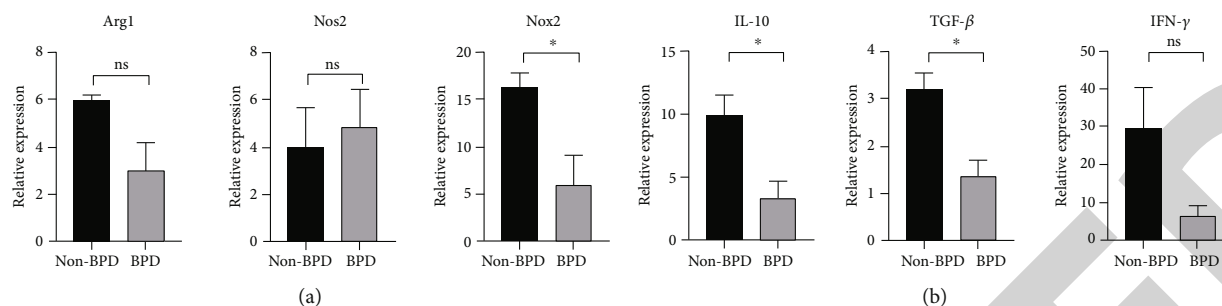


FIGURE 3: Expression of PMN-MDSCs immunosuppressive function-related three classical molecules and cytokines. (a) Expression of Arg1, Nos2, and Nox2 in PMN-MDSCs was detected by RT-qPCR ( $n=3$  per group) ( $*P < 0.05$ ). (b) Expression of IL-10, TGF- $\beta$ , and IFN- $\gamma$  in PMN-MDSCs was detected by RT-qPCR ( $n=3$  per group) ( $*P < 0.05$ ).

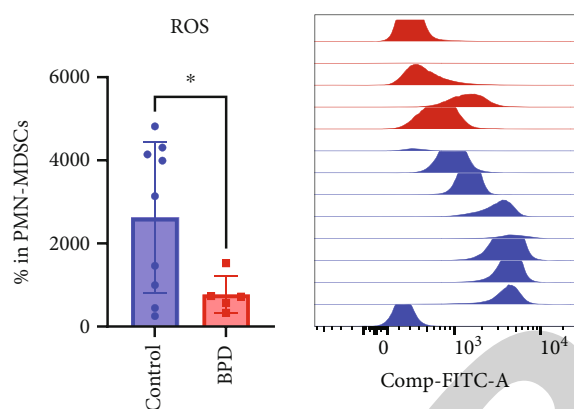


FIGURE 4: ROS levels in BPD infants and non-BPD preterm infants (control,  $n=9$ ; BPD,  $n=5$ ) ( $*P < 0.05$ ).

remains unclear. In the present study, we demonstrated that the number of MDSCs reduced in preterm infants, and on the premise of zero infections in preterm infants with GA  $< 34$ w, the number of PMN-MDSCs from BPD children at 3-7 days after birth was obviously lower than that from non-BPD group. However, there was no statistical difference in the number of PMN-MDSCs, M-MDSCs, and LOX-1 between BPD group and non-BPD group in other groups, especially for sampling time point at 8-14d after birth. These results indicated that BPD might be mainly related to the rapid decline of MDSCs about 10 days after birth.

Co-cultured CD4<sup>+</sup> T cells and CD8<sup>+</sup> T cells with PMN-MDSCs assay is a classic experiment to judge whether the function of MDSCs is defective. Therefore, we speculated that if PMD-MDSCs from the peripheral blood of BPD group have functional defects, the proliferation of CD4<sup>+</sup>T and CD8<sup>+</sup>T cells may also be affected indirectly. In this study, we demonstrated that PMN-MDSCs derived from BPD infants had significantly weaker inhibitory effects on the proliferation of both CD4<sup>+</sup> T and CD8<sup>+</sup>T cells than that derived from the non-BPD premature infants. This finding indicated that there was a certain defect in the immune function of PMN-MDSCs in children with BPD. To be specific, PMN-MDSCs were incapable of taking anti-inflammatory and protective effects and further resulted in the persistence of inflammation, which in turn led to the occurrence and development of BPD.

MDSCs exert immunosuppressive function via regulating multiple pathways. To further verify the specific pathway MDSCs involved in, the expression of three classical molecules related to the immunosuppressive function of MDSCs was detected, including Arg1, Nos2, and Nox2. The results showed that the expressions of Nox2 in PMN-MDSCs from BPD group were significantly lower than that of non-BPD preterm infants group. In contrast, there was no significant difference between BPD group and non-BPD preterm infants group for the expressions of Arg1 and Nos2 in PMN-MDSCs. This result indicated that ROS pathway, as an important pathway for MDSCs to exert immunosuppressive functions, was affected. In addition, we found that ROS level of BPD infants was significantly lower than that of non-BPD preterm infants group, which prompted that low ROS level in first 7 days of life may predict the development of BPD. These results were consistent with the findings reported by Corzo et al. [17] that MDSCs can promote the expression of NOX2 to generate a large amount of ROS, which is considered to be an inhibitor of tumor antigen-specific T cells [17]. In addition, we speculated that low ROS level might be a signal to implement clinical intervention to prevent BPD.

Inflammation is an important factor in the pathogenesis of BPD. MDSCs could affect the function of other immune cells to exert its immunosuppressive and anti-inflammatory effects through secreting anti-inflammatory factors like IL-10 and TGF- $\beta$  [18]. Our results showed that the expressions of IL-10 and TGF- $\beta$  in PMN-MDSCs derived from BPD group were significantly lower than non-BPD preterm infants group, suggesting that the ability to secrete anti-inflammatory cytokines is also decline in peripheral blood PMN-MDSCs of BPD infants with a certain functional defect. These results indicated that the anti-inflammatory effects of PMN-MDSCs were suppressed in premature infants. In addition, our previous study found that lung oxygen damage occurs in the early stage of BPD, and the oxygen stress protein arachidonic acid 15 lipoxygenase (ALOX15) is significantly up-regulated in the early stage of BPD, which catalyzes the production of oxidized low-density lipoprotein (oxLDL) (unpublished data). oxLDL can mediate apoptosis through its receptor LOX-1 which is a signature protein of MDSCs, suggesting that ALOX15 may act on the occurrence of BPD by regulating MDSCs. Based on these findings, we will further validate the scientific hypothesis through in vitro and in vivo experiments which will

hopefully reveal new immune mechanisms in the pathogenesis of BPD and provide new strategies for the clinical treatment of BPD.

In addition, there remain several limitations for the current study. First, although several accurate trends are proven, some statistically significant difference was not observed due to a relative low sample size. Second, some potential influencing factors like birth weight and prophylactic antibiotic use should be included. Third, the specific immunosuppressive function and mechanism of MDSCs in BPD should be verified by establishing BPD animal model for allogeneic intervention.

In conclusion, we revealed that the number of PMN-MDSCs and the levels of anti-inflammatory factors in peripheral blood of BPD premature infants early after birth were significantly lower than those of non-BPD infants, with a defective immunosuppressive function. Besides, we indicated that low ROS level in early postnatal days may be a potential predictor of BPD. These findings suggested that PMN-MDSCs participated in the pathogenesis of BPD in premature infants via regulating the ROS pathway. Our study preliminarily revealed the role of PMN-MDSCs in the pathogenesis of BPD. However, the specific mechanism still needs to be further studied and validated.

### Data Availability

The data used to support the findings of this study are included within the article and figure files.

### Ethical Approval

The authors are accountable for all aspects of the work in ensuring that questions related to the accuracy or integrity of any part of the work are appropriately investigated and resolved. All procedures performed in this study involving human participants were in accordance with the Declaration of Helsinki (as revised in 2013). This retrospective study obtained the ethical exemption of Clinical Research and Animal Trials of the First Affiliated Hospital of Sun Yat-sen University ethics committee (No. [2020]521).

### Conflicts of Interest

The authors declare that they have no competing interest.

### Authors' Contributions

WL, SL, and YL prepared the manuscript. YL, WS, HC, XL, LC, FW, YL, and QM collected the samples. YL and LC performed FACS and cell experiments. WL, SL, XL, and WF performed related bioinformatic analyses. YL, QM, and XJ supervised the experiments and provided essential equipment and infrastructure. WL provided financial support for the experiment. XJ supervised the process of bioinformatic analyses and drafted the final version of the manuscript. All authors read and approved the final manuscript. Wangkai Liu, Sitao Li, and Yushan Li contributed equally to this work and share first authorship.

### Acknowledgments

This work was funded by the Natural Science Foundation of Guangdong Province (2022A1515010031) and the Science and Technology Planning Project of Guangzhou, China (202002020064).

### References

- [1] H. Blencowe, S. Cousens, M. Z. Oestergaard et al., "National, regional, and worldwide estimates of preterm birth rates in the year 2010 with time trends since 1990 for selected countries: a systematic analysis and implications," *Lancet*, vol. 379, no. 9832, pp. 2162–2172, 2012.
- [2] A. A. Fanaroff, B. J. Stoll, L. L. Wright et al., "Trends in neonatal morbidity and mortality for very low birthweight infants," *American Journal of Obstetrics and Gynecology*, vol. 196, no. 2, pp. 147.e1–147.e8, 2007.
- [3] A. Greenough and I. Lingam, "Invasive and non-invasive ventilation for prematurely born infants - current practice in neonatal ventilation," *Expert Review of Respiratory Medicine*, vol. 10, no. 2, pp. 185–192, 2016.
- [4] F. Wu, G. Liu, Z. Feng et al., "Short-term outcomes of extremely preterm infants at discharge: a multicenter study from Guangdong province during 2008–2017," *BMC Pediatrics*, vol. 19, no. 1, p. 405, 2019.
- [5] P. Trikha and W. E. Carson 3rd, "Signaling pathways involved in MDSC regulation," *Biochimica et Biophysica Acta*, vol. 1846, no. 1, pp. 55–65, 2014.
- [6] J. I. Youn, S. Nagaraj, M. Collazo, and D. I. Gabrilovich, "Subsets of myeloid-derived suppressor cells in tumor-bearing mice," *Journal of Immunology*, vol. 181, no. 8, pp. 5791–5802, 2008.
- [7] E. Peranzoni, S. Zilio, I. Marigo et al., "Myeloid-derived suppressor cell heterogeneity and subset definition," *Current Opinion in Immunology*, vol. 22, no. 2, pp. 238–244, 2010.
- [8] D. I. Gabrilovich, S. Ostrand-Rosenberg, and V. Bronte, "Coordinated regulation of myeloid cells by tumours," *Nature Reviews Immunology*, vol. 12, no. 4, pp. 253–268, 2012.
- [9] Y. Liu, M. Perego, Q. Xiao et al., "Lactoferrin-induced myeloid-derived suppressor cell therapy attenuates pathologic inflammatory conditions in newborn mice," *The Journal of Clinical Investigation*, vol. 129, no. 10, pp. 4261–4275, 2019.
- [10] T. Pan, L. Zhong, S. Wu et al., "17 $\beta$ -Oestradiol enhances the expansion and activation of myeloid-derived suppressor cells via signal transducer and activator of transcription (STAT)-3 signalling in human pregnancy," *Clinical and Experimental Immunology*, vol. 185, no. 1, pp. 86–97, 2016.
- [11] A. Qin, W. Cai, T. Pan et al., "Expansion of monocytic myeloid-derived suppressor cells dampens T cell function in HIV-1-seropositive individuals," *Journal of Virology*, vol. 87, no. 3, pp. 1477–1490, 2013.
- [12] W. Cai, A. Qin, P. Guo et al., "Clinical significance and functional studies of myeloid-derived suppressor cells in chronic hepatitis C patients," *Journal of Clinical Immunology*, vol. 33, no. 4, pp. 798–808, 2013.
- [13] J. S. Boomer, A. D. Parulekar, B. M. Patterson et al., "A detailed phenotypic analysis of immune cell populations in the bronchoalveolar lavage fluid of atopic asthmatics after segmental allergen challenge," *Allergy, Asthma and Clinical Immunology*, vol. 9, no. 1, p. 37, 2013.

## Retraction

# Retracted: Knockdown of miR-372-3p Inhibits the Development of Diabetic Cardiomyopathy by Accelerating Angiogenesis via Activating the PI3K/AKT/mTOR/HIF-1 $\alpha$ Signaling Pathway and Suppressing Oxidative Stress

### Oxidative Medicine and Cellular Longevity

Received 20 June 2023; Accepted 20 June 2023; Published 21 June 2023

Copyright © 2023 Oxidative Medicine and Cellular Longevity. This is an open access article distributed under the Creative Commons Attribution License, which permits unrestricted use, distribution, and reproduction in any medium, provided the original work is properly cited.

This article has been retracted by Hindawi following an investigation undertaken by the publisher [1]. This investigation has uncovered evidence of one or more of the following indicators of systematic manipulation of the publication process:

- (1) Discrepancies in scope
- (2) Discrepancies in the description of the research reported
- (3) Discrepancies between the availability of data and the research described
- (4) Inappropriate citations
- (5) Incoherent, meaningless and/or irrelevant content included in the article
- (6) Peer-review manipulation

The presence of these indicators undermines our confidence in the integrity of the article's content and we cannot, therefore, vouch for its reliability. Please note that this notice is intended solely to alert readers that the content of this article is unreliable. We have not investigated whether authors were aware of or involved in the systematic manipulation of the publication process.

Wiley and Hindawi regrets that the usual quality checks did not identify these issues before publication and have since put additional measures in place to safeguard research integrity.

We wish to credit our own Research Integrity and Research Publishing teams and anonymous and named external researchers and research integrity experts for contributing to this investigation.

The corresponding author, as the representative of all authors, has been given the opportunity to register their agreement or disagreement to this retraction. We have kept a record of any response received.

### References

- [1] Z. Han, D. Zhao, M. Han, R. Zhang, and Y. Hao, "Knockdown of miR-372-3p Inhibits the Development of Diabetic Cardiomyopathy by Accelerating Angiogenesis via Activating the PI3K/AKT/mTOR/HIF-1 $\alpha$  Signaling Pathway and Suppressing Oxidative Stress," *Oxidative Medicine and Cellular Longevity*, vol. 2022, Article ID 4342755, 11 pages, 2022.

## Research Article

# Knockdown of miR-372-3p Inhibits the Development of Diabetic Cardiomyopathy by Accelerating Angiogenesis via Activating the PI3K/AKT/mTOR/HIF-1 $\alpha$ Signaling Pathway and Suppressing Oxidative Stress

Zhimin Han,<sup>1</sup> Danyang Zhao,<sup>2</sup> Mengfan Han,<sup>2</sup> Rongjin Zhang,<sup>3</sup> and Yongmei Hao <sup>2</sup>

<sup>1</sup>Academic Affairs Office, The Second Hospital of Hebei Medical University, Shijiazhuang 050000, China

<sup>2</sup>Department of Endocrinology, The Second Hospital of Hebei Medical University, Shijiazhuang 050000, China

<sup>3</sup>Department of Psychosomatic Medicine, The Second Hospital of Hebei Medical University, Shijiazhuang 050000, China

Correspondence should be addressed to Yongmei Hao; [yongmei520@hebmu.edu.cn](mailto:yongmei520@hebmu.edu.cn)

Received 10 June 2022; Accepted 10 August 2022; Published 16 September 2022

Academic Editor: Tian Li

Copyright © 2022 Zhimin Han et al. This is an open access article distributed under the Creative Commons Attribution License, which permits unrestricted use, distribution, and reproduction in any medium, provided the original work is properly cited.

**Background.** DCM is the most common and malignant complication of diabetes. It is characterized by myocardial dilatation, hypertrophy, fibrosis, ventricular remodeling, and contractile dysfunction. Although many studies have demonstrated the function of miRNAs in the progression of DCM, but the specific role of miR-372-3p in DCM remains unknown. **Methods.** C57/BL6J mice were used to construct mouse models of DCM by intraperitoneal injection of STZ (50 mg/kg/d) for 5 consecutive days. Then the mice were randomly divided into model group (intramyocardial injection of empty lentivirus) and miR-372-3p KD group (intramyocardial injection of miR-372-3p KD lentivirus at 10<sup>9</sup>/mouse). Besides, the control group (injection of 0.9% normal saline) was also set up. LY294002, a PI3K inhibitor, was employed in the current study. Western blotting, immunofluorescence staining, quantitative ultrasound method, Masson's trichrome staining, and bioinformatics analysis were performed. **Results.** It was found that miR-372-3p KD significantly improved left ventricular dysfunction and cardiac hypertrophy in DCM mice. Furthermore, it also improved myocardial interstitial fibrosis and remodeling in DCM mice. Immunofluorescence staining and RT-qPCR revealed that miR-372-3p KD might accelerate cardiac remodeling by increasing angiogenesis in DCM mice. Western blotting results revealed that miR-372-3p was an upstream target of the PI3K/AKT-mTOR and HIF-1 $\alpha$  signals, as well as NOX2, NOX4, which were responsible for angiogenesis in DCM mice. Besides, the *in vitro* experiment showed that LY294002 markedly diminished the increased expression levels of p-PI3K, AKT, p-mTOR, p-P70S6K, HIF-1 $\alpha$ , NOX2, and NOX4 in the model group and the miR-372-3p KD group, suggesting that PI3K signaling pathway and oxidative stress are involved in miR-372-3p KD-induced angiogenesis in HG-stimulated C166 cells. **Conclusions.** MiR-372-3p KD inhibits the development of DCM *via* activating the PI3K/AKT/mTOR/HIF-1 $\alpha$  signaling pathway or suppressing oxidative stress. This offers an applicable biomarker for DCM treatment.

## 1. Introduction

DCM, a chronic complication of diabetes mellitus, brings a heavy burden to the patient's family and the society [1, 2]. Some cardiac anomalies are detected in DCM patients, including myocardial dilatation, hypertrophy, fibrosis, ventricular remodeling, contractile dysfunction, and vascular system disorders, which can lead to heart failure and increase the death rate [3–5]. So far, there are no effective

therapeutic regimens to block the pathological changes associated with DCM. Therefore, it is urgent to elucidate the pathogenesis of DCM and determine its therapeutic hallmark.

As reported previously, VEGFs can accelerate angiogenesis, improve myocardial contractility, diminish cardiac hypertrophy effectively constrain ventricular renovation, and improve cardiac functions [6–8]. Angiogenesis plays a crucial role in tissue progression, and homeostasis and impaired

angiogenesis are closely related to several diseases, including DCM [9, 10].

The PI3K is a critical pro-growth cell signal implicated in numerous pathological and physiological processes, which can phosphorylate serine/threonine kinase AKT [11–13]. Additionally, numerous studies have demonstrated that mTOR is a downstream protein complex (mTORC1 and mTORC2) involved in the PI3K/AKT pathway and regulates cell proliferation, protein synthesis, and angiogenesis [14–16]. Furthermore, P70S6K is activated by mTOR and serves as a critical regulator in the progression and functions of blood vessels [17, 18]. Numerous previous studies have highlighted that the PI3K/AKT/mTOR/p70S6K signaling pathway plays a vital role in the development of neovascularization [19–21]. HIF-1 $\alpha$  is another crucial downstream protein of mTOR, which plays a vital role in cell proliferation and angiogenesis [22, 23]. The long-term exposure to hyperglycemia in the heart could produce the amount of oxidative stress induce in the overproduction of ROS, which is derived from NOX, especially NOX2 and NOX4 which are important sources of O $_2^{\cdot-}$  and H $_2$ O $_2$ ; all of these responses result into a serious deteriorating consequence, such as mitochondrial dysfunction, advanced glycation end products, calcium overload, lipotoxicity, and inflammation, all eventually promote the progression of DCM, and moreover, the oxidative stress is also toxic for systolic and endothelial dysfunction and cardiac cell death and necrosis; thereby the reduction of oxidative stress is an attractive target for cure of cardiac diseases. PI3K/AKT signaling pathway has been reported to suppress inflammation and mediate oxidative stress, thereby any interfering factor with anti-inflammatory or antioxidant features may be beneficial for DCM [24–26].

miRNAs are small, noncoding RNAs that act as crucial posttranscriptional regulators of gene expression by binding to the UTRs of large target mRNAs [27, 28]. As an essential member of the miRNA family, miR-372-3p has drawn our attention; it is a highly conserved miRNA among humans and animals [29, 30]. However, the specific role of miR-372-3p in DCM has rarely been reported. Therefore, miR-372-3p expression came into the spotlight of this study. We conducted a series of *in vivo* and *in vitro* experiments to determine the role of miR-372-3p in DCM.

## 2. Materials and Methods

**2.1. Mice.** In this study, 6–8-week-old C57BL/6J mice (Skbex Biotechnology) were used to establish mouse models of diabetes mellitus by intraperitoneal injection of STZ (50 mg/kg/d) for 5 consecutive days. Then the fasting blood glucose (>16.7 mmol/L) was extracted from the tail vein for later use. The mice were randomly divided into model group (intramyocardial injection of empty lentivirus) and miR-372-3p KD group (intramyocardial injection of miR-372-3p KD lentivirus at 10 $^9$ /mouse). Besides, control group (injection of 0.9% normal saline) was also set up. All the mice were kept in SPF-level animal laboratory with a 12:12-h light-dark cycle at 24–26°C, where they were bred adaptively for one week prior to the experiment.

**2.2. Mouse Heart Ultrasound.** db/db mice were anesthetized with isoflurane after chest depilation. The LVIDd and LVIDs of mice in each group were detected by high-resolution small animal ultrasound imaging system. In addition, the LVFS and EF were calculated. Three consecutive cardiac cycles were detected, and the average value was taken.

**2.3. Masson's Trichrome Staining.** The tissues were routinely dehydrated and embedded. Then the obtained tissues were cut into 4- $\mu$ m-thick sections and conventionally dewaxed to water. Next, the sections were mordanted overnight at room temperature, stained with celestine blue staining solution for 2–3 min, with Mayer's hematoxylin staining solution for 2–3 min and with acid ethanol differentiation solution for 2–3 min. After that, the samples were washed by water for 10 min and stained with fuchsin staining solution for 10 min, with molybdophosphoric acid solution for 10 min, and with aniline blue dye for 5 min. After aniline blue solution was rinsed off with weak acid solution, weak acid solution was added again to cover the slices for 2 min. Finally, the sections were sealed using neutral gum. The blue stained parts were the fibrotic areas, and the ratio of these part vs. total myocardial areas was used to calculate the area of fibrosis.

**2.4.  $\alpha$ -SMA, CD31, and Collagen-III Immunofluorescence Staining.** The paraffin-embedded tissues were cut into 4- $\mu$ m-thick sections. After routine dewaxing and dehydration, the antigen was restored at high temperature. Then the sections were incubated with 3% H $_2$ O $_2$  for 30 min and with 3% goat serum for 30 min. Subsequently, the sections were incubated with primary antibody against  $\alpha$ -SMA, CD31 as well as collagen-III diluted in TBS buffer, overnight at room temperature. After that, the secondary antibody was added dropwise, and the nucleus was counterstained with DAPI, washed with acidified water, and sealed with neutral gum. Finally, the fluorescence image was analyzed.

**2.5. Western Blotting.** The total protein was extracted by lysate, and the protein concentration was detected by a protein concentration detection kit and a microplate reader. Then the protein was added to the loading buffer, heated in boiling water for 10 min, and denatured. Next, the protein samples were treated with 12% SDS-PAGE. After SDS-PAGE, the protein samples were transferred onto the membrane, sealed with 0.5% skim milk for 2 h at room temperature, and incubated with primary antibodies (Abcam) at 4°C. The next day, the protein samples were taken out and incubated with secondary antibodies at room temperature. Finally, the optical density of the target strip was analyzed by the gel image processing system. Primary antibodies purchased from abcam, and NOX2, NOX4 (dilution in 1:800), p-PI3K, Total-PI3K, p-AKT, Total-AKT, p-P70S6K, Total-P70S6K, HIF-1 $\alpha$  (dilution in 1:1000), and  $\beta$ -actin (dilution in 1:3000).

**2.6. Mouse C166 Cell Culture and Lentivirus Infection.** The mouse EC line C166 was used as an EC cellular model in our *in vitro* experiment and cultured with the DMEM supplemented with 5% fetal bovine serum and 1% penicillin streptomycin at 37°C and 5% CO $_2$  (v/v). The culture

medium was replaced 2 to 3 days, and the cells were passaged when the cell adherence area reached 80% of the culture dish. Before lentivirus infection, C166 cells were treated with serum-free medium overnight and infected with lentiviruses (MOI = 10.0) (empty lentivirus in the model group and miR-372-3p KD lentivirus in the miR-372-3p KD group), combined with or without tLY294002, a PI3K inhibitor, treatment. When the cell growth density reached 60%, 1/2 volume of the culture medium containing the corresponding infection complex virus was replaced, at 4 h after infection, the culture medium was supplemented, at 24 h after infection, a new culture medium was replaced, and at 48 h after infection, the infection rate was observed under the fluorescence microscope to determine the infection rate.

**2.7. Tube Formation Assay of ECs.** The concentration of ECs in the logarithmic growth phase was adjusted to  $2 \times 10^5$  C166 cells/mL, and high-concentration and low-growth-factor Matrigel was added to a precooled 96-well culture plate. The concentration of LY294002 was 5  $\mu$ M, and the high glucose (HG, 30 mM) concentration was 25.6 mmol/L glucose [31, 32]. After 24 h of incubation, 3 fields of view were randomly selected in each well and photographed (100 $\times$ ). Finally, the differences in the length of the mesh branches and the area of the mesh structure among groups were detected using the ImageJ.

**2.8. Target mRNA Prediction and Pathway Enrichment Analysis.** GSE26887, GSE112556, and GSE146621 datasets were downloaded from the GEO database. The differential analysis between the normal group and DCM group was performed with  $|\text{LogFC}| > 1.5$  and  $\text{adjP} < 0.01$  as the thresholds to obtain the DEGs using the edgeR package in R. In addition, Bayesian method was adopted to analyze differentially expressed miRNAs in the three datasets. To assess the potential target of miR-372-3p, its parental mRNA was obtained using the TargetScan and mirDIP. The function enrichment analysis was carried out according to the GO annotation and the KEGG pathway database using an R-based Bioconductor package data probe.

**2.9. Immunofluorescence Staining for Collagen-III in Mouse Myocardial Sections.** After dewaxed to water by gradient elution, 4- $\mu$ m-thick mouse myocardial tissue sections were firstly incubated overnight at 4°C using collagen-III primary antibody (diluted at 1:100). After the sections were washed 3 times (5 min/each) at room temperature and incubated with a secondary antibody at room temperature for 2 h. Lastly, the sections were observed under an optical microscope, and all data were analyzed with Image-Pro 6.0 software.

**2.10. Q-PCR.** Total RNA was isolated by an RNA extraction kit (Solarbio, China) and reverse transcribed into cDNA by PrimeScript RT Master Mix (Takara Bio). qRT-PCR was performed with a SYBR Green system (Takara) according to the following parameters: 95°C for 10 min, followed by 40 cycles of 95°C for 10 s, and 60°C for 50 s. For miRNA expression, U6 were used as internal reference controls for miRNA expression, respectively, and relative expression was calculated using the  $2^{-\Delta\Delta\text{Ct}}$  method and was used to calculate the relative expression levels of miR-372-3p. Primers:

miR-372-3p, forward 5'-TTT CAC GAC GCT GTA AAC TCG CA-3', reverse 5'-GTG CAG GGT CCG AGG T-3'; U6, forward 5'-GCT TCG GCA GCA CAT ATA CTA A-3', reverse 5'-AAC GCT TCA CGA ATT TGC GT-3'.

**2.11. Statistical Analysis.** GraphPad Prism 6.0 software was used to analyze experimental data. Measurement data were expressed as  $(\bar{x} \pm s)$ . The data were compared between two groups from different countries using the *t*-test method and compared among groups using the univariate analysis of variance (ANOVA).  $P < 0.05$  represented that the difference was statistically significant. All experiments in this study were conducted independently at least three times.

### 3. Results

**3.1. Effect of miR-372-3p KD on Cardiac Dysfunction in DCM Mice.** To validate the effect of miR-372-3p on cardiac dysfunction in DCM mice, we established miR-372-3p KD mouse models of DCM by STZ injection as described in the "Materials and Methods." Quantitative ultrasound methods were employed to investigate the effect of miR-372-3p KD on left ventricular function. The results illustrated that LVFS and LVEF declined in DCM mice, indicating that DCM induces conspicuous cardiac dysfunction and systolic dysfunction (Figures 1(a) and 1(b)). The results also revealed that LVFS and LVEF were elevated in the miR-372-3p KD group compared with those in the model group ( $P < 0.05$ , Figures 1(a) and 1(b)), suggesting that miR-372-3p KD efficiently improves DCM-induced cardiac dysfunction. Furthermore, DCM mice also exhibited a high heart-to-body weight (HW/BW) ratio demonstrating cardiac hypertrophy, which was decreased by miR-372-3p KD. The above findings illustrated that miR-372-3p KD significantly improved left ventricular dysfunction and cardiac hypertrophy in DCM mice,  $n = 7/\text{group}$ .

**3.2. Effect of miR-372-3p KD on Myocardial Interstitial Fibrosis.** Myocardial interstitial fibrosis and hypertrophy are crucial pathophysiological characteristics of DCM. Masson's trichrome staining of mouse myocardial tissues was conducted to evaluate the effect of miR-372-3p KD on cardiac hypertrophy and interstitial fibrosis. As shown in Figure 2(a), the myocardial tissues exhibited significant structural anomalies, excessive fibrosis, and increased collagen fibers in model group. On the contrary, miR-372-3p KD markedly improved these pathological anomalies in myocardial tissues of DCM mice. According to Masson and immunofluorescent analysis results, the ratio of the fibrotic area to the total area as well as fibrotic immunofluorescent intensity in myocardial tissues was increased in the model group compared with that in the miR-372-3p KD group ( $P < 0.05$ , Figure 2(b)). It could be concluded that miR-372-3p KD improved myocardial interstitial fibrosis and remodeling in DCM mice,  $n = 7/\text{group}$ .

**3.3. Effect of miR-372-3p KD on Angiogenesis.** Angiogenesis is a crucial player in tissue growth and homeostasis. Numerous studies have shown that angiogenesis acts as a positive mediator of pathologic cardiac remodeling in DCM. Immunofluorescence staining was performed to investigate the

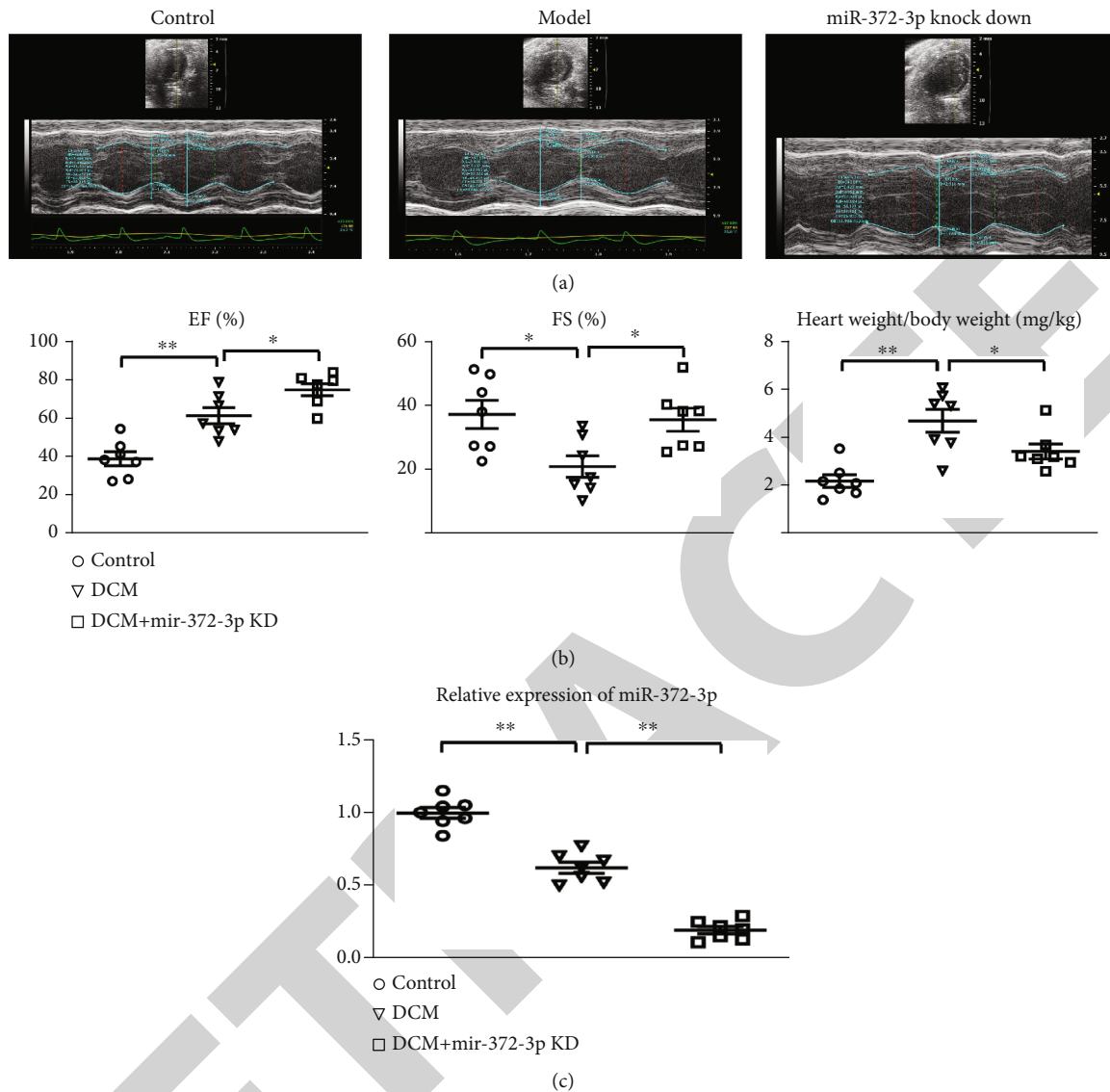


FIGURE 1: Effect of miR-372-3p KD on cardiac dysfunction. (a) Representative echocardiography in the control, model, and miR-372-3p KD groups. (b) Statistical analysis for LVFS, LVEF, and HW/BW ratio in the control, model, and miR-372-3p KD group. (c) RT-qPCR analysis of relative expression of miR-372-3p.  $n = 7/\text{group}$ , \*\* $P < 0.05$ : model group vs. miR-372-3p KD group. HW/BW: heart weight/body weight.

effect of miR-372-3p KD on angiogenesis in myocardial tissues of mice. As revealed by representative staining images in Figure 3(a), angiogenesis was significantly increased in miR-372-3p KD mice at the tissue level, implying a marked increase in the amount of blood vessels and  $\alpha$ -SMA-positive tissues in miR-372-3p KD mice. As shown in Figure 3(b), the neovascularization was notably promoted in comparison with that in model group. The above findings suggested that miR-372-3p KD might accelerate cardiac remodeling by increasing angiogenesis in DCM mice,  $n = 7$ .

**3.4. Effect of miR-372-3p KD on the AKT/mTOR/HIF-1 $\alpha$  Pathway.** Numerous previous studies have highlighted that the PI3K/AKT/mTOR/p70S6K signaling pathway plays a vital role in the development of neovascularization. Phosphorylation of PI3K, P70S6k, mTOR, AKT, and HIF-1 $\alpha$  in the myocardial tissues of mice was determined by

Western blotting. HIF-1 $\alpha$  is another crucial downstream protein of mTOR, which plays a vital role in cell proliferation and angiogenesis. The protein and mRNA expression levels of these molecules were compared among the control, model, and miR-372-3p KD groups. The results manifested that the protein and mRNA expressions of p-PI3K, p-P70S6k, p-mTOR, p-AKT, and HIF-1 $\alpha$  and NADPH oxidase 2 (NOX2) and NOX4 in the miR-372-3p KD group were higher than those in the model and control groups, showing statistically significant differences (Figure 4(a),  $P < 0.01$ ). However, there were no significant differences in the protein and mRNA expressions of these molecules between the control group and the model group (Figure 4(b)). The above findings implied that miR-372-3p is an upstream target of the PI3K/AKT/mTOR/HIF-1 $\alpha$  signaling pathway, regulating the angiogenesis in DM mice,  $n = 4$ .

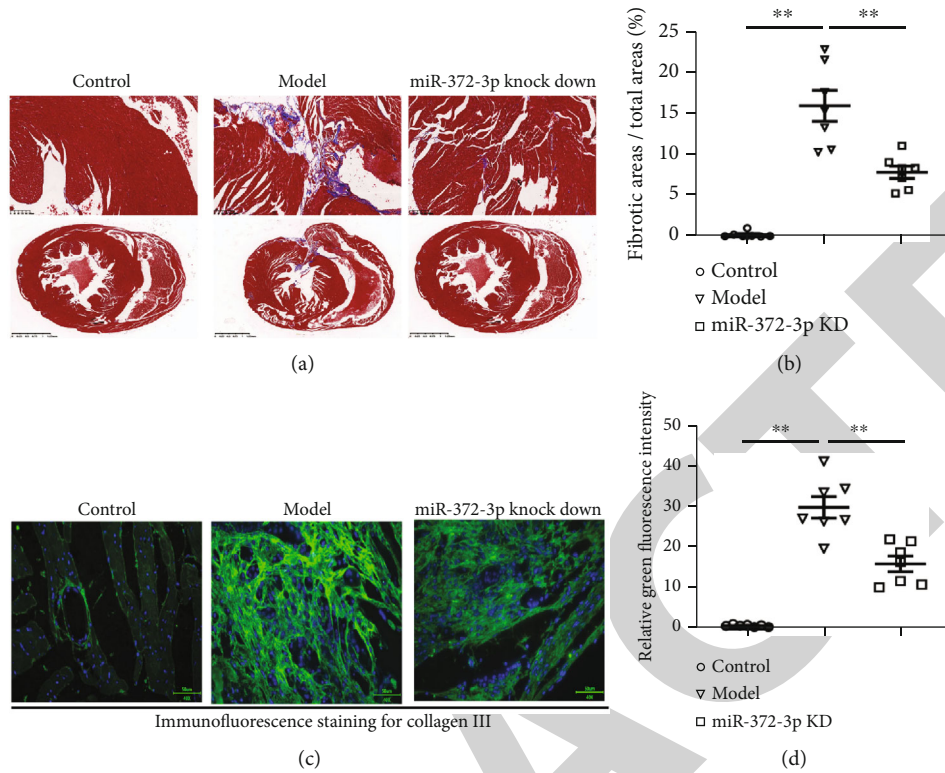


FIGURE 2: Effect of miR-372-3p KD on myocardial interstitial fibrosis. (a) Representative images of Masson's trichrome staining of myocardial tissues. Ratio of fibrotic area to total area. Bar: 1.25 mm; (b) the immunofluorescence staining from collagen-III of mouse myocardial tissues. Bar: 50  $\mu$ M; data were presented as means  $\pm$  SEM.  $n = 7$ /group, \*\* $P < 0.05$ : model group vs. miR-372-3p KD group.

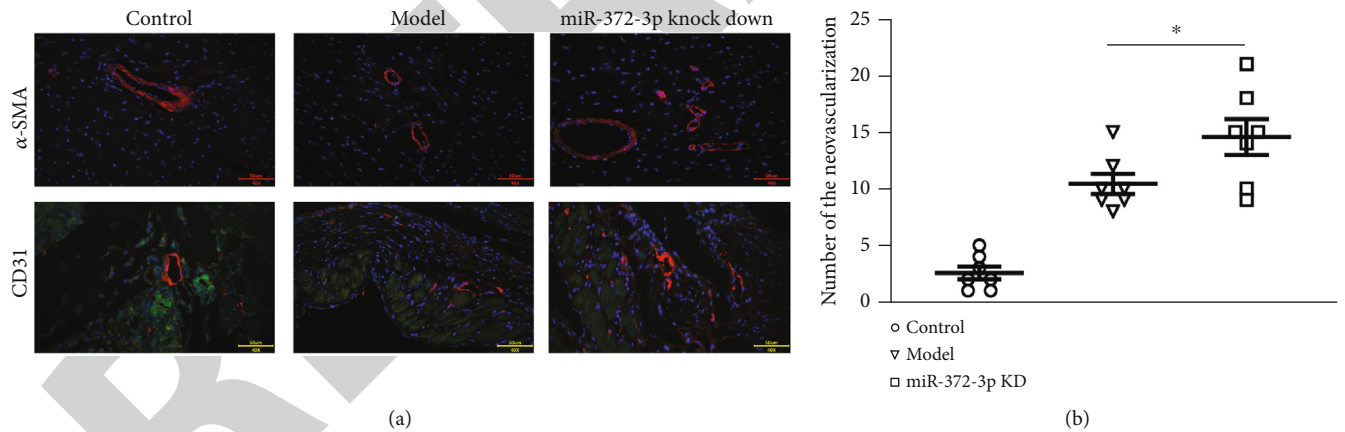


FIGURE 3: Effect of miR-372-3p KD on angiogenesis. (a) Immunofluorescence staining of  $\alpha$ -SMA and CD31 was performed to examine the neovascularization in myocardial tissue sections. (b) Statistical analysis was performed to show the relative amount of new blood vessels in myocardial tissue sections. Bar: 50  $\mu$ M; data were presented as means  $\pm$  SEM.  $n = 7$ /group, \*\* $P < 0.01$ : model group vs. miR-372-3p KD group.

3.5. Involvement of the PI3K Signaling Pathway in miR-372-3p KD-Induced Angiogenesis in HG-Stimulated C166 Cells. Next, we determined whether miR-372-3p KD regulates angiogenesis during DM through activating the PI3K signaling pathway in C166 cells. C166 cells were transfected with miR-372-3p KD lentivirus, and then they were stimulated with or without HG medium for 12 h. LY294002, a PI3K inhibitor, was employed in the current study. To further

confirm the effect of miR-372-3p KD on the AKT/mTOR/HIF-1 $\alpha$  signaling pathway, the expressions of p-PI3K, p-AKT, p-mTOR, p-P70S6K, HIF-1 $\alpha$ , NOX2, and NOX4 in cells were examined by Western blotting. The results exposed that miR-372-3p KD increased the protein and mRNA expressions of p-PI3K, p-AKT, p-mTOR, p-P70S6K, and HIF-1 $\alpha$  in C166 cells (Figures 5(a) and 5(b),  $P < 0.01$ ), indicating that miR-372-3p KD activates the AKT/mTOR/



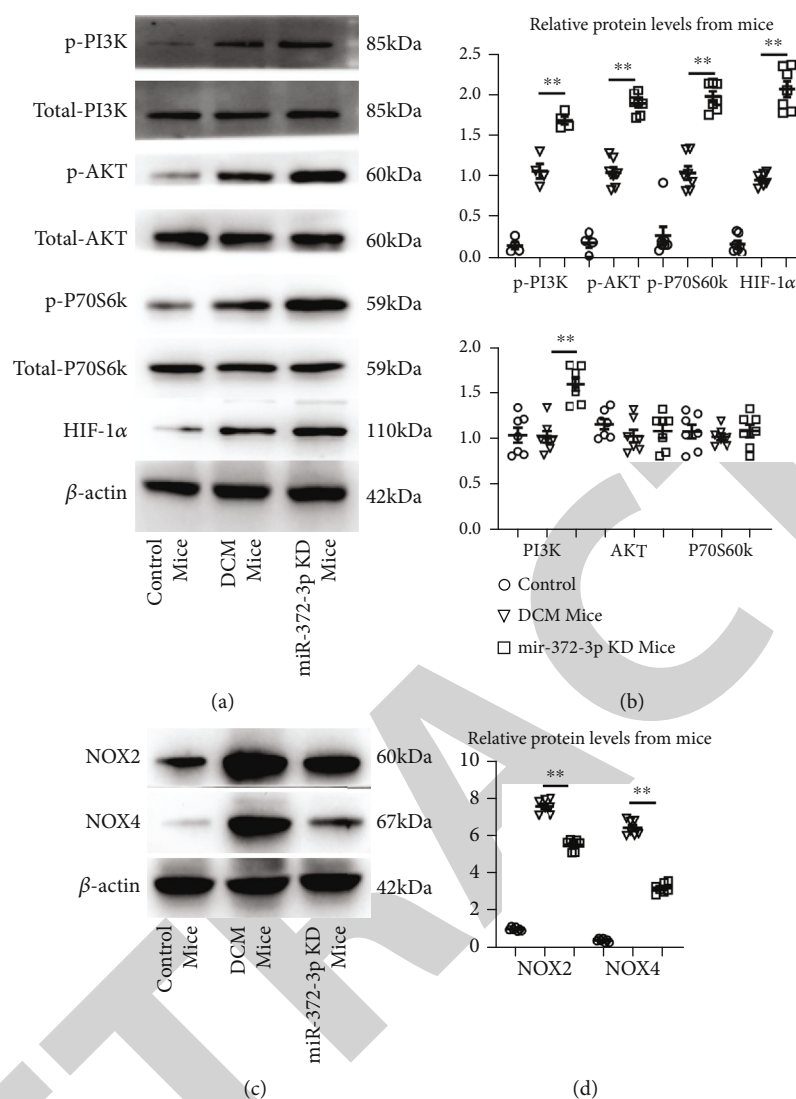
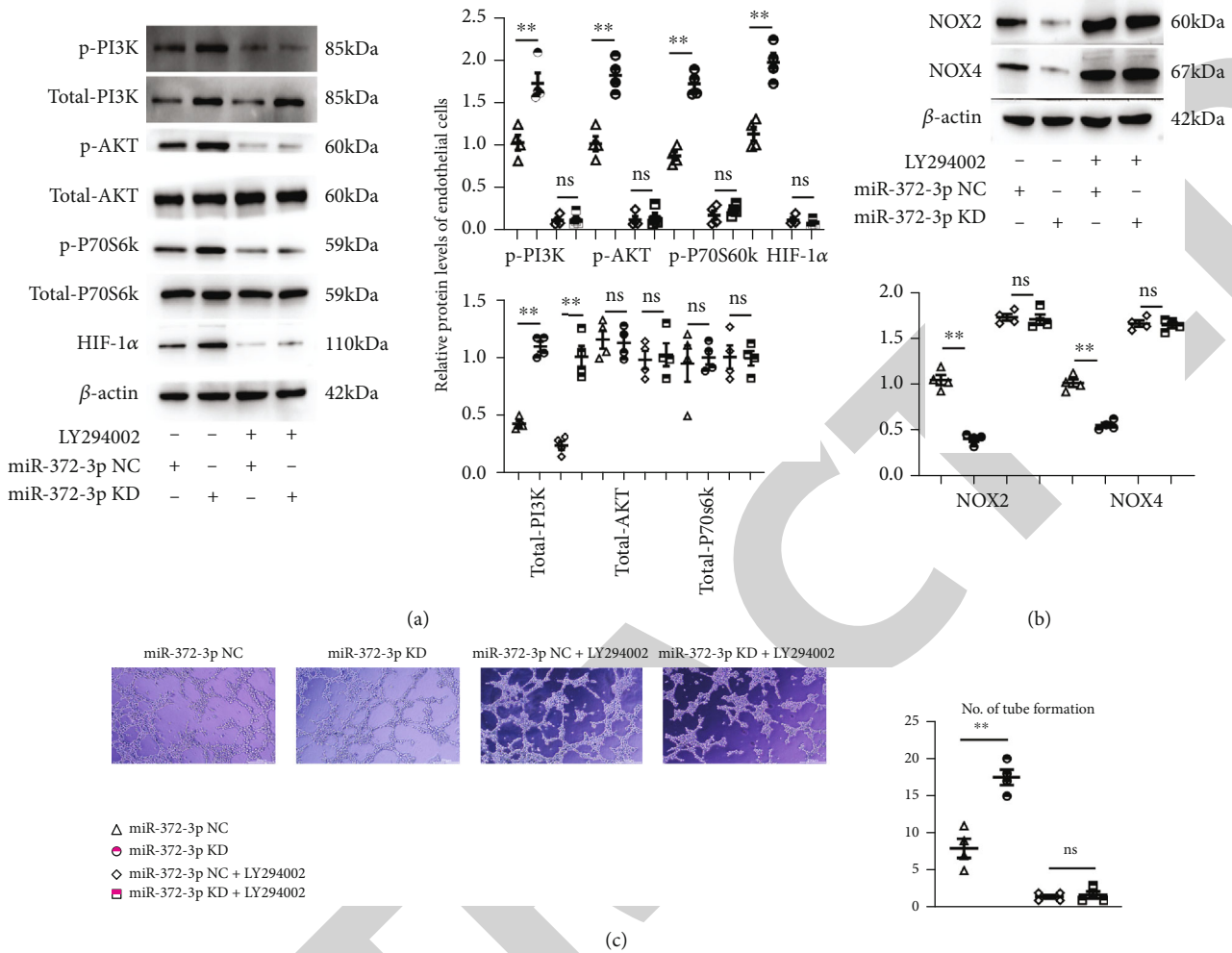


FIGURE 4: Effect of miR-372-3p KD on the AKT/mTOR/HIF-1 $\alpha$  signaling pathway. (a) Protein expressions of p-PI3K, PI3K, p-AKT, AKT, mTOR, p-mTOR, P70S6K, and p-P70S6K HIF-1 $\alpha$  in the control, model, and miR-372-3p KD groups were identified by Western blotting.  $\beta$ -Actin was considered as a loading control. (b) Statistical analysis was performed to examine the expressions of p-PI3K, PI3K, p-AKT, AKT, mTOR, p-mTOR, P70S6K, p-P70S6K, and HIF-1 $\alpha$  in myocardial tissues. (c) Protein expressions of NOX2 and NOX4 in the control, model, and miR-372-3p KD groups were identified by Western blotting.  $\beta$ -Actin was considered as a loading control. (d) Statistical analysis was performed to examine the expressions of NOX2 and NOX4 in myocardial tissues. Data were presented as means  $\pm$  SEM,  $n = 4$ /group,  $^*P < 0.05$  and  $^{**}P < 0.01$ : model group vs. miR-372-3p KD group.

HIF-1 $\alpha$  signaling pathway *in vitro*. Moreover, pretreatment with LY294002 markedly diminished this uptrend in the miR-372-3p KD (Figures 5(a) and 5(b)). Immunofluorescence staining was used to examine the formation of the tubular structure in C166 cells. As shown in Figure 5(c), miR-372-3p KD significantly increased the formation of the tubular structure in C166 cells compared with miR-372-3p NC group ( $P < 0.05$ ). Furthermore, LY294002 weakened the tube formation in the miR-372-3p KD group,  $n = 4$ . However, the number of tubes formed was not significantly different between the miR-372-3p KD+LY294002 group and the miR-372-3p NC+LY294002 group ( $P > 0.05$ , Figure 5(c)). The above findings implied that the PI3K signaling pathway is involved in miR-372-3p KD-induced angiogenesis in HG-stimulated C166 cells.

**3.6. Results of Comprehensive Bioinformatics Analysis of DCM.** The putative target of miR-372-3p was identified to explore the molecular mechanisms of miR-372-3p in DCM. TargetScan and mirDIP were employed for the bioinformatics prediction. Among all the potential target genes of miR-372-3p, PIK3CA was selected (Figures 6(a) and 6(b)). DCM-related gene expression profiles were retrieved from GEO datasets (GSE26887, GSE112556, and GSE146621), from which the DEGs were obtained with  $|\text{Log}(\text{FC})| > 1.5$  and  $\text{adj}P < 0.05$  were obtained. Next, heatmaps were plotted to demonstrate the distribution of significant DEGs in GSE26887 and GSE112556. Additionally, PIK3CA was among the downregulated DEGs (Figures 6(c) and 6(d)). Based on the data from GSE146621, a volcano map was plotted to visualize the DEGs, including PIK3CA (Figure 6(e)).



**FIGURE 5: Involvement of the PI3K signaling pathway in miR-372-3p KD-induced angiogenesis in HG-stimulated C166 cells.** (a) Protein expressions of p-PI3K, PI3K, p-AKT, AKT, mTOR, p-mTOR, P70S6K, p-P70S6K, and HIF-1 $\alpha$  in the control, model, and miR-372-3p KD groups treated with or without LY294002.  $\beta$ -Actin was considered as a loading control, and the statistical analysis was performed to present the p-PI3K, PI3K, p-AKT, AKT, mTOR, p-mTOR, P70S6K, p-P70S6K, and HIF-1 $\alpha$  in the control, model, and miR-372-3p KD groups with or without LY294002. (b) Protein expressions of NOX2 and NOX4 in the control, model, and miR-372-3p KD groups treated with or without LY294002.  $\beta$ -Actin was considered as a loading control, and the statistical analysis was performed to present the NOX2 and NOX4 in the control, model, and miR-372-3p KD groups with or without LY294002. (c) The number of tubes formed in each group. Data were presented as means  $\pm$  SEM, Bar: 200  $\mu$ M,  $n = 4$ /group, \* $P < 0.05$  and \*\* $P < 0.01$ : model group vs. miR-372-3p KD group.

GO enrichment and KEGG pathway enrichment analyses were carried out to investigate the putative function of DEGs in DCM. Most DEGs from GSE26887 and GSE112556 were primarily involved in biological processes, such as angiogenesis, angiogenesis, inflammatory response, nervous system development, patterning of blood vessels, cardiac ventricle morphogenesis, immune system process, protein phosphorylation, cell surface receptor signaling pathway, response to lipopolysaccharide, and negative regulation of Notch signaling pathway (Figures 6(f) and 6(g)). KEGG pathway enrichment analysis for GSE26887 revealed that the DEGs were mainly involved in the PI3K/AKT signaling pathway, HIF-1 $\alpha$  signaling pathway, NOD-like receptor signaling pathway, and NF- $\kappa$ B signaling pathway (Figure 6(h)). To further investigate the interaction of these DEGs in DCM, the interaction PPI network was built using STRING database according to the data from GSE26887. By using the plug-in CytoHubba in Cytoscape soft-

ware, PIK3CA was validated as a hub gene and play a crucial role in DCM (Figures 6(j)–6(i)). The above findings indicated that PIK3CA is a potential target of miR-372-3p, and it is a hub gene crucial for DCM.

#### 4. Discussion

Wide-range studies have shown that angiogenesis plays a critical role in the progression of DCM [33, 34]. miRNAs, small noncoding RNAs, are referred to as negative posttranscriptional regulators of gene expression by binding to the 3'UTR of large target messenger RNAs (mRNAs) [35]. Various studies have confirmed that miRNAs are beneficial diagnostic and therapeutic markers for controlling DCM [36]. As a crucial member of the miRNA family, miR-372-3p has been described to play a significant role in various diseases [37–39]. However, the specific function of miR-372-3p in DCM remains elusive.

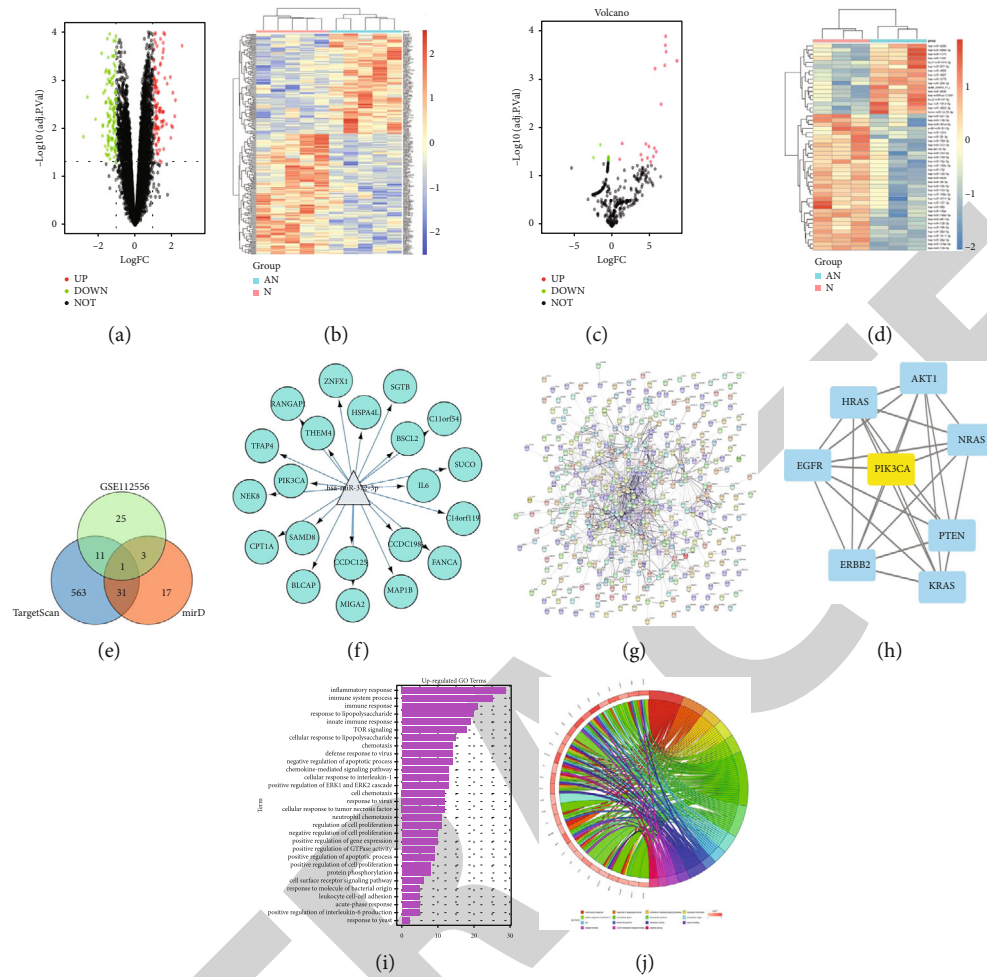


FIGURE 6: Comprehensive bioinformatics analysis in DCM. (a) Identification of mRNAs that hypothetically regulated miR-372-3p based on miRDB and TargetScan databases. (b) Target sequences of miR-372-3p in the 3'-UTR of PIK3CA. (c and d) Heatmaps were sketched to illustrate the DEGs in DCM using microarray GSE26887 and GSE112556 datasets. (e) A volcano plot was sketched to illustrate the DEGs in DCM using microarray GSE146621 dataset. (f and g) GO enrichment analysis for biological processes of DEGs using microarray GSE26887 and GSE112556 datasets.  $P < 0.05$  denotes significant enrichment. (h) Scatter plot of KEGG enrichment analysis of DEGs using microarray GSE26887 dataset.  $P < 0.05$  denotes significant enrichment. (i) The PPI network of DEGs was constructed according to the data from GSE26887. (j) PIK3CA was identified as a hub gene.

Here, we focused on the potential role and mechanism of miR-372-3p in DCM. Firstly, we established miR-372-3p KD mouse models of DCM by injection of STZ. Quantitative ultrasound results showed that DCM reduced the LVFS and LVEF but increased LVIDd and LVIDs, indicating that it induces apparent cardiac dysfunction and systolic dysfunction. However, LVFS and LVEF were elevated by miR-372-3p KD, suggesting that miR-372-3p KD efficiently improves the DCM-induced cardiac dysfunction. Furthermore, miR-372-3p KD also increased the HW/BW ratio, displaying its role in alleviating DCM-induced hypertension resulting in impaired levels of myocardial blood supply, and cardiac hypertrophy correlates with reduced capillary density and may lead to subsequent myocardial ischemia and HF, and the hypoxic environment-induced angiogenesis improves blood flow and revascularization and suppresses and inhibits the fibrotic progression, thereby fortifying myocardial function and promoting cardiac repair and myocardium survival [40–43]. This study was focused on miR-372-3p effects on

the angiogenesis and neovascularization formation and DCM therapy.

It has been previously confirmed that myocardial interstitial fibrosis is a crucial pathophysiological characteristic of DCM [44]. In this study, Masson's trichrome staining and immunofluorescence staining revealed that the myocardial tissues exhibited significant structural anomalies, excessive fibrosis, and increased collagen fibers in model group, but miR-372-3p KD markedly improved these pathological anomalies in myocardial tissues of DCM mice, suggesting that miR-372-3p KD improves myocardial interstitial fibrosis and remodeling in DCM mice. In addition, emerging evidence indicates that hyperglycemia-induced increase in glucose autooxidation, protein glycation, and oxidative degradation of glycated proteins leads to an excessive generation of oxidative stress responses under diabetic conditions, and furthermore, hyperglycemia myocardial metabolism results in ROS overproduction; in conclusion the higher levels of ROS in the heart, the higher the amount of oxidative stress

produced, forming a vicious cycle, and furthermore, ROS has been considered the harmful and deleterious effects for heart remodeling and dysfunction in diabetes [24, 26]. In the pathology of DCM, the angiogenesis is a crucial player or cure in tissue growth and homeostasis and acts as a benefit mediator for cardiac remodeling in DCM [45, 46]; previous studies indicated that excessive mitochondrial ROS generation limits angiogenic capacity or causes defective angiogenesis in microvascular endothelial cells [47, 48]; our immunofluorescence staining showed that angiogenesis was significantly enhanced in the miR-372-3p KD group, implying a marked increase in the number of blood vessels. Furthermore, the neovascularization analysis exposed that the number of new blood vessels was markedly increased in the miR-372-3p KD group compared with that in the model group, suggesting that miR-372-3p KD might accelerate cardiac remodeling by increasing angiogenesis in DCM mice. The PI3K/AKT signals are the major promoter for angiogenesis. They are inhibited by oxidative stress, and in turn, they reversely suppress the burst of oxidative stress [49–52]. Remarkably, it has been shown recently that the PI3K/AKT/mTOR/p70S6K signaling pathway plays a vital role in the development of neovascularization [19]. Moreover, HIF-1 $\alpha$  is another crucial downstream protein of mTOR, which plays a vital role in cell proliferation and angiogenesis [53]. Phosphorylation of PI3K, P70S6k, mTOR, AKT, and HIF-1 $\alpha$  in myocardial tissues of mice was determined by Western blotting. The results revealed that the protein and mRNA expressions of p-PI3K, p-P70S6k, p-mTOR, p-AKT, and HIF-1 $\alpha$  in the miR-372-3p KD group were higher than those in the model and control groups, suggesting that miR-372-3p is an upstream target of the PI3K/AKT/mTOR/HIF-1 $\alpha$  signaling pathway regulating angiogenesis in DCM mice. Furthermore, the oxidative stress could directly destroy the ECs and further inhibits the expression of HIF-1 $\alpha$ , so the suppression of oxidative stress or the activation of PI3K is the key promoter for neovascularization [19, 37, 38, 51, 54]. Additionally, we determined whether miR-372-3p KD regulates angiogenesis during DM through activating the PI3K signaling pathway in C166 cells. Western blotting results exposed that miR-372-3p KD increased the protein and mRNA expressions of p-PI3K, p-AKT, p-mTOR, p-P70S6K, and HIF-1 $\alpha$  in C166 cells. Immunofluorescence staining results demonstrated that miR-372-3p KD significantly increased the tubes formed in C166 cells compared with miR-372-3p NC, but this increase was diminished by LY294002. Besides, LY294002 also markedly diminished the increased expression levels of p-PI3K, p-AKT, p-mTOR, p-P70S6K, and HIF-1 $\alpha$  in the miR-372-3p KD group, suggesting that the PI3K signaling pathway is involved in miR-372-3p KD-induced angiogenesis in HG-stimulated C166 cells.

Furthermore, DCM-related gene expression profiles were retrieved from the GEO datasets (GSE26887, GSE112556, and GSE146621) to obtain DEGs. Heatmaps and volcano map were plotted to screen the DEGs, and it was found that PIK3CA was among the downregulated DEGs. Later, bioinformatics analysis demonstrated that PIK3CA was a potential target of miR-372-3p and a hub gene crucial for DCM. The limitations of this

study lie in the deficiency of single-cell transcriptomics as well as cells communicating signals, such as myocardial fibroblasts and inflammatory cells, so such technology should be replenished, and moreover, the cre-loxP mice should be further established to research the further and precise roles of cell subtypes in DCM, and more mechanisms about myocardial remodeling should be carried on under miR-372-3p KD situation, and furthermore, the levels of miR-372-3p may be used as a clinical indicators to predict the DCM' prognosis.

In conclusion, miR-372-3p KD might protect against DCM by accelerating angiogenesis through activating the PI3K/AKT/mTOR/HIF-1 $\alpha$  signaling pathway or suppressing oxidative stress. Additionally, PIK3CA, a potential target of miR-372-3p, is also a hub gene crucial for DCM. The findings of this study provide a novel evidence for the protective effects of miR-372-3p KD and afford novel potential treatments for patients with DCM.

## Abbreviations

DCM:	Diabetic cardiomyopathy
miRNA:	microRNA
STZ:	Streptozotocin
KD:	Knockdown
PI3K:	Phosphoinositide 3-kinase
AKT:	Protein kinase B
mTOR:	Mammalian target of rapamycin
HIF-1 $\alpha$ :	Hypoxia-inducible factor-1 $\alpha$
VEGFs:	Vascular endothelial growth factors
P70S6K:	p70 ribosomal protein S6 kinase
UTRs:	3' untranslated regions
LVIDd and LVIDs:	Left ventricular internal diameter end diastole and end systole
LVFS:	Left ventricular fractional shortening
EF:	Ejection fraction
$\alpha$ -SMA:	Alpha-smooth muscle actin
ROS:	Reactive oxygen species
NOX:	NADPH oxidase
SDS-PAGE:	Sodium dodecyl sulfate polyacrylamide gel electrophoresis
EC:	Endothelial cell
DMEM:	Dulbecco's modified eagle medium
DEGs:	Differentially expressed genes
NF- $\kappa$ B:	Nuclear factor-kappa B
PPI:	Protein-protein interaction.

## Data Availability

The datasets used and analyzed during the current study are available from the corresponding author on reasonable request.

## Ethical Approval

All animal studies were approved by the Second Affiliated Hospital of Hebei Medical University.

## Conflicts of Interest

All the authors declare that have is no competing interests.

## Authors' Contributions

Zhimin Han was a major contributor in writing the manuscript. Danyang Zhao established Mir-372-3p knockout (KD) mice models. Mengfan Han did the Western blotting experiment. Rongjin Zhang did the immunofluorescence staining. Yongmei Hao did the ultrasound quantification. All authors read and approved the final manuscript.

## Acknowledgments

The study was funded by the Key Research Project of Hebei Provincial Health Commission No. 20210514.

## References

- [1] Y. Chen, Y. Hua, X. Li, I. M. Arslan, W. Zhang, and G. Meng, "Distinct types of cell death and the implication in diabetic cardiomyopathy," *Frontiers in Pharmacology*, vol. 11, 2020.
- [2] S. Khan, S. S. Ahmad, and M. A. Kamal, "Diabetic cardiomyopathy: from mechanism to management in a nutshell," *Endocrine, Metabolic & Immune Disorders - Drug Targets*, vol. 21, no. 2, pp. 268–281, 2021.
- [3] A. S. Jadon, V. Tomar, and P. Kannoja, "Recent molecular events concerned with pathogenesis and management of diabetic cardiomyopathy," *International Journal of Pharmaceutical Research*, vol. 5, no. 1, p. 15, 2013.
- [4] J. Zhao, T. T. Cao, J. Tian et al., "Shengmai san ameliorates myocardial dysfunction and fibrosis in diabetic *db/db* mice," *Evidence-Based Complementray and Alternative Medicine*, vol. 2016, article 4621235, 9 pages, 2016.
- [5] M. H. Bao, X. Feng, Y. W. Zhang, X. Y. Lou, Y. Cheng, and H. H. Zhou, "Let-7 in cardiovascular diseases, heart development and cardiovascular differentiation from stem cells," *International Journal of Molecular Sciences*, vol. 14, no. 11, pp. 23086–23102, 2013.
- [6] J. L. Wallace, M. Dickey, W. McKnight, and G. K. Dudar, "Platelets accelerate gastric ulcer healing through presentation of vascular endothelial growth factor," *British Journal of Pharmacology*, vol. 148, no. 3, pp. 274–278, 2006.
- [7] F. Geiger, H. Bertram, I. Berger et al., "Vascular endothelial growth factor gene-activated matrix (VEGF165-GAM) enhances osteogenesis and angiogenesis in large segmental bone defects," *Journal of Bone & Mineral Research*, vol. 20, no. 11, pp. 2028–2035, 2005.
- [8] C. Qi, B. Li, S. Guo et al., "P-selectin-mediated adhesion between platelets and tumor cells promotes intestinal tumorigenesis in *Apc(min/+)* mice," *International Journal of Biological Sciences*, vol. 11, no. 6, pp. 679–687, 2015.
- [9] X. Zhang, X. Tian, P. Li et al., "Ultrasound-targeted microbubble destruction promotes myocardial angiogenesis and functional improvements in rat model of diabetic cardiomyopathy," *BMC Cardiovascular Disorders*, vol. 21, no. 1, 2021.
- [10] C. Gui, Z. Y. Zeng, Q. Chen, Y. W. Luo, L. Li, and L. L. Chen, "Neuregulin-1 promotes myocardial angiogenesis in the rat model of diabetic cardiomyopathy," *Cellular Physiology and Biochemistry*, vol. 46, no. 6, pp. 2325–2334, 2018.
- [11] M. Zhang, J. Liu, M. Li et al., "Insulin-like growth factor 1/insulin-like growth factor 1 receptor signaling protects against cell apoptosis through the PI3K/AKT pathway in glioblastoma cells," *Experimental & Therapeutic Medicine*, 2018.
- [12] "mTORC1 and mTORC2 regulate EMT, motility, and metastasis of colorectal cancer via RhoA and Rac1 signaling pathways," *Cancer Research*, vol. 71, no. 9, pp. 3246–3256, 2011.
- [13] M. Martini, M. C. de Santis, L. Braccini, F. Gulluni, and E. Hirsch, "PI3K/AKT signaling pathway and cancer: an updated review," *Annals of Medicine*, vol. 46, no. 6, pp. 372–383, 2014.
- [14] R. Margit and H. Markus, "Cytoplasmic and nuclear distribution of the protein complexes mTORC1 and mTORC2: rapamycin triggers dephosphorylation and delocalization of the mTORC2 components rictor and sin1," *Human Molecular Genetics*, vol. 17, no. 19, pp. 2934–2948, 2008.
- [15] Z. Zhe, G. Zhang, X. Xu, W. Su, and B. Yu, "mTOR-rictor is the Ser<sup>473</sup> kinase for AKT1 in mouse one-cell stage embryos," *Molecular and Cellular Biochemistry*, vol. 361, no. 1–2, pp. 249–257, 2012.
- [16] H. Pópulo, J. M. Lopes, and P. Soares, "The mTOR signalling pathway in human cancer," *International Journal of Molecular Sciences*, vol. 13, no. 2, pp. 1886–1918, 2012.
- [17] N. Gao, D. C. Flynn, Z. Zhang et al., "G1 cell cycle progression and the expression of G1 cyclins are regulated by PI3K/AKT/mTOR/p70S6K1 signaling in human ovarian cancer cells," *American Journal of Physiology Cell Physiology*, vol. 287, no. 2, pp. C281–C291, 2004.
- [18] S. Saiki, Y. Sasazawa, Y. Imamichi et al., "Caffeine induces apoptosis by enhancement of autophagy via PI3K/Akt/mTOR/p70S6K inhibition," *Autophagy*, vol. 7, no. 2, pp. 176–187, 2011.
- [19] S.-W. Hong, K. H. Jung, H.-S. Lee et al., "SB365 inhibits angiogenesis and induces apoptosis of hepatocellular carcinoma through modulation of PI3K/Akt/mTOR signaling pathway," *Cancer Science*, vol. 103, no. 11, pp. 1929–1937, 2012.
- [20] S. W. Hong, K. H. Jung, H. S. Lee et al., "Abstract 3747:Pulsatilla saponin D suppresses angiogenesis and induces apoptosis via inhibition of PI3K/Akt/mTOR signaling pathway in hepatocellular carcinoma," *Cancer Research*, vol. 72, Supplement 8, pp. 3747–3747, 2012.
- [21] P. Poyil, A. Budhraj, Y.-O. Son et al., "Quercetin inhibits angiogenesis mediated human prostate tumor growth by targeting VEGFR-2 regulated AKT/mTOR/P70S6K signaling pathways," *PLoS One*, vol. 7, no. 10, article e47516, 2012.
- [22] J. Chen, A. Y. Chen, H. Huang et al., "The flavonoid nobiletin inhibits tumor growth and angiogenesis of ovarian cancers via the Akt pathway," *International Journal of Oncology*, vol. 46, no. 6, pp. 2629–2638, 2015.
- [23] R. Shaw and L. Cantley, "Ras, PI(3)K and mTOR signalling controls tumour cell growth," *Nature*, vol. 441, no. 7092, pp. 424–430, 2006.
- [24] X. Wu, L. Huang, and J. Liu, "Relationship between oxidative stress and nuclear factor-erythroid-2-related factor 2 signaling in diabetic cardiomyopathy (review)," *Experimental and Therapeutic Medicine*, vol. 22, no. 1, p. 678, 2021.
- [25] N. J. Byrne, N. S. Rajasekaran, E. D. Abel, and H. Bugger, "Therapeutic potential of targeting oxidative stress in diabetic cardiomyopathy," *Free Radical Biology & Medicine*, vol. 169, pp. 317–342, 2021.

## Retraction

# Retracted: Exploring the Temporal Correlation of Sarcopenia with Bone Mineral Density and the Effects of Osteoblast-Derived Exosomes on Myoblasts through an Oxidative Stress–Related Gene

### Oxidative Medicine and Cellular Longevity

Received 1 August 2023; Accepted 1 August 2023; Published 2 August 2023

Copyright © 2023 Oxidative Medicine and Cellular Longevity. This is an open access article distributed under the Creative Commons Attribution License, which permits unrestricted use, distribution, and reproduction in any medium, provided the original work is properly cited.

This article has been retracted by Hindawi following an investigation undertaken by the publisher [1]. This investigation has uncovered evidence of one or more of the following indicators of systematic manipulation of the publication process:

- (1) Discrepancies in scope
- (2) Discrepancies in the description of the research reported
- (3) Discrepancies between the availability of data and the research described
- (4) Inappropriate citations
- (5) Incoherent, meaningless and/or irrelevant content included in the article
- (6) Peer-review manipulation

The presence of these indicators undermines our confidence in the integrity of the article's content and we cannot, therefore, vouch for its reliability. Please note that this notice is intended solely to alert readers that the content of this article is unreliable. We have not investigated whether authors were aware of or involved in the systematic manipulation of the publication process.

Wiley and Hindawi regrets that the usual quality checks did not identify these issues before publication and have since put additional measures in place to safeguard research integrity.

We wish to credit our own Research Integrity and Research Publishing teams and anonymous and named external researchers and research integrity experts for contributing to this investigation.

The corresponding author, as the representative of all authors, has been given the opportunity to register their












agreement or disagreement to this retraction. We have kept a record of any response received.

### References

- [1] J. Chen, J. Shen, X. Yang et al., "Exploring the Temporal Correlation of Sarcopenia with Bone Mineral Density and the Effects of Osteoblast-Derived Exosomes on Myoblasts through an Oxidative Stress–Related Gene," *Oxidative Medicine and Cellular Longevity*, vol. 2022, Article ID 9774570, 18 pages, 2022.

## Research Article

# Exploring the Temporal Correlation of Sarcopenia with Bone Mineral Density and the Effects of Osteoblast-Derived Exosomes on Myoblasts through an Oxidative Stress-Related Gene

Jingsong Chen <sup>1</sup>, Jie Shen <sup>2</sup>, Xili Yang <sup>3</sup>, Huiting Tan <sup>1</sup>, Ronghua Yang <sup>4</sup>,  
Cuiying Mo <sup>1</sup>, Ying Wang <sup>5</sup>, Xiaojun Luan <sup>1</sup>, Wenhua Huang <sup>6,7</sup>, Guoqiang Chen <sup>8</sup>,  
and Xuejuan Xu <sup>1</sup>

<sup>1</sup>Department of Endocrinology, The First People's Hospital of Foshan, Foshan, Guangdong 528000, China

<sup>2</sup>Department of Endocrinology, Shunde Hospital of Southern Medical University (The First People's Hospital of Shunde), Foshan, Guangdong 528399, China

<sup>3</sup>Department of Cardiology, The First People's Hospital of Foshan, Guangdong 528000, China

<sup>4</sup>Department of Burn and Plastic Surgery, Guangzhou First People's Hospital, South China University of Technology, Guangzhou, Guangdong, China

<sup>5</sup>Department of Nuclear Medicine, The First People's Hospital of Foshan, Foshan, Guangdong 528000, China

<sup>6</sup>Guangdong Engineering Research Center for Translation of Medical 3D Printing Application, Guangdong Provincial Key Laboratory of Medical Biomechanics, National Key Discipline of Human Anatomy, School of Basic Medical Sciences, Southern Medical University, Guangzhou, Guangdong 510515, China

<sup>7</sup>Guangdong Medical Innovation Platform for Translation of 3D Printing Application, The Third Affiliated Hospital of Southern Medical University, Guangzhou, Guangdong 510000, China

<sup>8</sup>Department of Rheumatology, The First People's Hospital of Foshan, Foshan, Guangdong 528000, China

Correspondence should be addressed to Wenhua Huang; [huangwenhua2009@139.com](mailto:huangwenhua2009@139.com), Guoqiang Chen; [13929981788@139.com](mailto:13929981788@139.com), and Xuejuan Xu; [snowcaressyou@163.com](mailto:snowcaressyou@163.com)

Received 18 May 2022; Revised 30 July 2022; Accepted 5 August 2022; Published 15 September 2022

Academic Editor: Tian Li

Copyright © 2022 Jingsong Chen et al. This is an open access article distributed under the Creative Commons Attribution License, which permits unrestricted use, distribution, and reproduction in any medium, provided the original work is properly cited.

Sarcopenia is an age-related accelerated loss of muscle strength and mass. Bone and muscle are closely related as they are physically adjacent, and bone can influence muscle. However, the temporal association between bone mineral density (BMD) and muscle mass in different regions of the body after adjustment for potential indicators and the mechanisms by which bone influences muscle in sarcopenia remain unclear. Therefore, this study aimed to explore the temporal association between muscle mass and BMD in different regions of the body and mechanisms by which bone regulates muscle in sarcopenia. Here, cross-lagged models were utilized to analyze the temporal association between BMD and muscle mass. We found that low-density lipoprotein (LDL-C) positively predicted appendicular lean mass. Mean whole-body BMD (WBTOT BMD), lumbar spine BMD (LS BMD), and pelvic BMD (PELV BMD) temporally and positively predicted appendicular lean mass, and appendicular lean mass temporally and positively predicted WBTOT BMD, LS BMD, and PELV BMD. Moreover, this study revealed that primary mice femur osteoblasts, but not primary mice skull osteoblasts, induced differentiation of C2C12 myoblasts through exosomes. Furthermore, the level of long noncoding RNA (lncRNA) taurine upregulated 1 (TUG1) was decreased, and the level of lncRNA differentiation antagonizing nonprotein coding RNA (DANCR) was increased in skull osteoblast-derived exosomes, the opposite of femur osteoblast-secreted exosomes. In addition, lncRNA TUG1 enhanced and lncRNA DANCR suppressed the differentiation of myoblasts through regulating the transcription of oxidative stress-related *myogenin* (*Myog*) gene by modifying the binding of myogenic factor 5 (Myf5) to the *Myog* gene promoter via affecting the nuclear translocation of Myf5. The results of the present study may provide novel diagnostic biomarkers and therapeutic targets for sarcopenia.

## 1. Introduction

Sarcopenia is an age-related accelerated loss of muscle strength and mass in older individuals. It increases the risk of falls, fractures, functional decline, and frailty and leads to considerable healthcare costs, poor quality of life, and mortality [1, 2]. Sarcopenia is common among older adults, and the incidence of sarcopenia is increasing rapidly [3]. Although antioxidant and pharmacological agents, including myostatin and activin, have been utilized to treat skeletal muscle atrophy and dysfunction, some studies have reported the off-target effects of these drugs [4, 5]. Thus, research related to age-related (primary) sarcopenia and disease-related (secondary) sarcopenia has focused on improving diagnosis and therapy, with special interest in exploring diagnostic biomarkers and targets for drugs of resistance exercise [3, 6].

In the musculoskeletal system, bone and muscle are closely related as they are physically adjacent. Among age-related diseases, sarcopenia is strongly associated with osteoporosis [7, 8]—a common skeletal disorder caused by a decline in muscle mass [9]. Therefore, bone can exert influence on muscle. Recent studies have focused on the relationship between muscle mass and BMD. For instance, a recent study has revealed that reduced BMD correlates with decreased muscle mass and strength in Chinese subjects with sarcopenia [10]. Our recent study indicated that skull BMD negatively correlates with appendicular skeletal muscle (ASM) mass, whereas BMDs throughout the rest of the body are positively associated with ASM mass in male middle-aged and elderly Chinese individuals [11]. However, the temporal association between sarcopenia (muscle mass) and BMD in different regions of the body after adjustment for potential indicators including albumin, F-box protein 2 (FBXO2/FBS), LDL-C, thyroid-stimulating hormone (TSH), and platelet distribution width remains unclear.

To date, the knowledge on mechanisms by which bone influences muscle is still limited. It is considered that bone and muscle communicate with each other in a paracrine and endocrine manner, and there are various collaborative changes between these two tissues induced by numerous biochemical signals or weight-bearing stimulation [12]. For instance, osteoblast-derived osteoglycin (OGN) may play a role in regulating muscle mass [13]. In addition, the level of prostaglandin E2 secreted by bone cells is much higher than that secreted by damaged muscle cells, which is conducive to muscle regeneration and repair [13]. Extracellular vesicles, including microvesicles and exosomes, are vesicles secreted by cells and mediate the communication among different cells and organs [14]. However, the effect of exosomes derived from osteoblasts on myoblasts is largely unknown.

Exosomes could mediate long-distance communication and cooperative regulatory network among different cells and organs as vectors to carry long noncoding RNAs (lncRNAs) in a variety of diseases [15–17]. Previous studies have shown that lncRNA TUG1 promotes the osteogenic differentiation of osteoblasts through suppressing the Wnt/ $\beta$ -catenin pathway [18]. In contrast, lncRNA DANCR inhibits osteogenic differentiation by activating the Wnt/ $\beta$ -catenin pathway [19]. However, the roles of lncRNA TUG1

and DANCR in myoblasts or muscle have not been reported. Surprisingly, the prediction of RNA–protein binding by RPISEQ (<http://pridb.gdcb.iastate.edu/RPISEQ/index.html>) showed that both lncRNA TUG1 and DANCR had high binding probability with Myf5 (Supplementary Figure S1), suggesting that lncRNA TUG1 and DANCR in osteoblasts-derived exosomes might play critical roles in myoblasts or muscle.

Our latest study has revealed that the relationships between muscle mass and different bone tissues are different [9], suggesting that exosomal lncRNAs derived from different osteoblasts might exert different regulatory effects on muscle mass. Therefore, this study aimed to explore the temporal association between sarcopenia (muscle mass) and BMD in different regions of the body and the effects of exosomal lncRNA TUG1 and DANCR derived from different osteoblasts on myoblasts.

## 2. Methods and Materials

**2.1. Participants.** A total of 3179 male individuals (30–100 years old) with complete body composition and data whole-body BMD detected by the Health Care Department of Foshan First People's Hospital from 2014 to 2016 were recruited for this study. Based on medical history and examination results, we excluded individuals with complete loss of walking ability; alcoholism (more than 210 g per week); other chronic liver diseases; viral or autoimmune hepatitis; severe cardiac or renal insufficiency or severe dementia (MMSE <18 points); use of steroids or immunosuppressants; autoimmune diseases; use of drugs or items that may affect body weight and body composition; pathological obesity; uncontrolled diabetes; or hypothyroidism and other endocrine/metabolic diseases diagnosed in the past five years. The current study was approved by the Ethics Committee of Foshan First People's Hospital, and written informed consent was obtained from each participant.

**2.2. Measurement of BMD.** BMD of the whole body (mean value), head, femoral neck, thoracic spine, left upper arm, right upper arm, lumbar spine, left leg, right leg, left rib, right rib, pelvis, and hip was measured using dual-energy X-ray absorptiometry (DXA, HOLOGIC, Marlborough, MA, USA). The absorptiometry was calibrated daily utilizing the model provided by the manufacturer to maintain the stability of measurement. The coefficient of variation (percentage) of repeated measurements met the accurate criteria of femoral neck (2.5%), lumbar spine (<1.9%), and total femur (<1.8%). Moreover, the values of total and regional BMD ( $\text{g}/\text{cm}^2$ ) were identified by DXA using standard procedures. Next, BMD values were classified by WHO criteria based on  $T$  values of femoral neck and/or lumbar spine and/or hip as follows: normal population ( $T$  value >  $-1.0$  SD), bone mass reduction ( $-1.0$  SD  $\leq T$  value  $\leq -2.5$  SD), and osteoporosis ( $T$  value  $\leq -2.5$  SD).

**2.3. Detection of Muscle Mass.** Muscle mass was detected using DXA (HOLOGIC), and sarcopenia was diagnosed according to two definitions: (1) appendicular skeletal



muscle index (ASMI): the mass of appendicular skeletal muscle divided by the square of height ( $\text{kg}/\text{m}^2$ ), with the threshold of  $7.0 \text{ kg}/\text{m}^2$  in males; and (2) skeletal muscle index (SMI): the percentage of skeletal muscle mass of limbs in body weight, with the threshold of 29.9% in males. In this study, male subjects with ASMI  $<0.7$  or SMI  $<29.9\%$  were defined as “early sarcopenia” and recruited.

**2.4. Measurement of Blood Biochemical Metabolic Indexes.** After more than 8 hours of fasting, forearm venous blood was taken from the subjects between 8 a.m. and 10 a.m., and the subjects sat. Blood processing and collection were performed under strictly standardized conditions. Subsequently, serum albumin was analyzed by turbidimetry, and the coefficient of variation was 2%. FBS, LDL-C, TSH, and platelet distribution width were evaluated using an Olympus AU5400 Automatic Biochemical Analyzer (Tokyo, Japan).

**2.5. Analytic Plan.** Continuous variables were presented using means  $\pm$  standard deviation (SD), and categorical variables were described as a percentage (%). We used a *t* test or ANOVA to estimate the differences in BMDs depending on demographic characteristics and other variables. Pearson correlation analyses were used to analyze the intercorrelations among muscle mass and BMDs across different investigations. A series of structural equation models with autoregressive cross-lagged design (ACLD) were used to estimate the temporal associations among muscle mass and BMDs after adjustment for potential confounders, including albumin, FBS, LDL-C, TSH, and platelet distribution width. ACLD has been demonstrated to be a useful method for examining potential associations between two variables over time (<https://www.tandfonline.com/loi/wean20>). Here, we hypothesized the bidirectional relation of BMDs and muscle mass, that is, that higher BMDs may lead to more muscle mass and that more muscle mass may reversely result in higher BMDs. To test our hypotheses, three models were developed. Model 1 was applied to examine the temporal effects of BMDs or muscle mass at time *T*-1 on BMDs or muscle mass at time *T*; model 2 was applied to test the effects of BMDs at time *T*-1 on muscle mass at time *t* and the effects of muscle mass at time *T*-1 on BMDs at time *T*; and model 3 was a combination of model 1 and model 2. We reported standardized regression coefficients in all structural equation models. Associations were analyzed by Package for the Social Sciences software (v 20.0) (SPSS Inc., Chicago, Illinois, USA) and Analysis of Moment Structures (AMOS) (v 20.0). All of the tests that were conducted were two-sided. The overall model fit was evaluated using the root-mean-square error of approximation (RMSEA,  $<0.08$ ) and the comparative fit index (CFI,  $>0.90$ ).

**2.6. Cell Culture.** Primary mice osteoblasts of skull, primary mice osteoblasts of femur, and C2C12 cells were purchased from LANDM Biotech (Guangzhou, Guangdong, China). All cells were cultured with DMEM high glucose medium (Hyclone, Logan, UT, USA) containing 100 units/mL penicillin (Hyclone) and 10% fetal bovine serum (Hyclone) in a  $37^\circ\text{C}$  atmosphere filled with 5%  $\text{CO}_2$  [20].

**2.7. Cell Treatment.** The differentiation of C2C12 cells was induced by DMEM high glucose medium (Hyclone) with 2% horse serum (Bioind, Kibbutz Beit Haemek, Israel) (differentiation medium). To identify the effect of osteoblasts on myoblasts, culture media of primary mice osteoblasts of skull and primary mice osteoblasts of femur were collected to culture C2C12 cells combined with C2C12 cell culture medium (0%, 50%, or 100%). Moreover, C2C12 cells were incubated with exosomes isolated from the culture media to identify the effects of exosomes derived from osteoblasts on C2C12 cells. In addition, transfection of vectors was performed using Lipofectamine 2000 (Invitrogen, Carlsbad, CA, USA).

**2.8. Cell Counting Kit-8 (CCK8) Assay.** First, C2C12 cells were seeded in 96-well plates at the concentration of  $1 \times 10^4/\text{mL}$ . After the indicated treatments,  $10 \mu\text{L}$  CCK8 solution (Beyotime, Shanghai, China) at a 1/10 dilution was added to incubate C2C12 cells at  $37^\circ\text{C}$  for 1.5 h [21]. Then, absorbance at 450 nm was assayed using a Multiscan MK3 (Thermo Fisher Scientific, Waltham, MA, USA). The means of the optical density (OD) were used to calculate the cell proliferation rate according to the following formula: Cell proliferation rate (%) = (OD treatment group/OD control group)  $\times$  100%.

**2.9. Apoptosis Assay.** A total of  $1 \times 10^6$  C2C12 cells of each group were collected and washed twice using the incubation buffer containing 10 mmol/L HEPES/NaOH (pH 7.4), 140 mmol/L NaCl, and 5 mmol/L  $\text{CaCl}_2$  [22]. Next, C2C12 cells were resuspended in  $150 \mu\text{L}$  of phosphate-buffered solution (PBS) including  $1.5 \mu\text{g}/\text{mL}$  Annexin V (KeyGen, Nanjing, Jiangsu, China) and propidium iodide (PI) (Thermo Fisher Scientific). Then, the cells were incubated with Annexin V and PI in dark at room temperature (RT) for 15 min. After washing with PBS, C2C12 cells were resuspended again in  $400 \mu\text{L}$  incubation buffer and analyzed using flow cytometry (BD FACSCalibur, BD Biosciences, San Jose, CA, USA).

**2.10. Detection of Oxidative Stress.** To detect oxidative stress in C2C12 cells, the levels of malondialdehyde (MDA), L-glutathione (GSH), and superoxide dismutase (SOD) were identified. MDA level was identified using Lipid Peroxidation MDA Assay Kit (#S0131S) purchased from Beyotime. GSH level was tested by Micro Reduced Glutathione (GSH) Assay Kit (#BC1175) obtained from Solarbio (Beijing, China). SOD level was measured utilizing Superoxide Dismutase Activity Assay Kit (#BC0170) from Solarbio. Detections were performed in accordance with the manufacturers' instructions.

**2.11. Western Blot (WB).** Total proteins were first extracted from C2C12 cells or exosomes. Then, the same amount of protein ( $40 \mu\text{g}$ ) was loaded into SDS-polyacrylamide gel and separated using electrophoresis. Next, the proteins were transferred onto PVDF membranes (Millipore, Bedford, MA, USA) and blocked with 5% nonfat milk for 1 h at RT. Subsequently, the membranes were incubated with primary antibodies at  $4^\circ\text{C}$  overnight with gentle shaking [11, 23].

After incubation with primary antibodies, the membranes were washed with Tris-buffered saline containing 0.1% Tween20 (TBST) and then incubated with corresponding secondary antibodies (1:5000, Southern Biotech, Birmingham, AL, USA) at RT for 1 h [9, 23]. Finally, signals of the targeted proteins were detected using Immobilon Western Chemilum HRP Substrate (Millipore). The primary antibodies used in this study included MYH6 antibody (1:500, Abcam, Cambridge, MA, USA), Myog antibody (1:200, Abcam), myHC antibody (1:500, Abcam), CD63 antibody (bs-1523R, Bioss, Beijing, China), CD81 antibody (bs-6934R, Bioss), and GAPDH antibody (1:3000, Kangcheng, Shanghai, China).

**2.12. Isolation and Analysis of Exosomes.** GS™ Exosome Isolation Kit (for cell culture media) (E5001, Genesee, Guangzhou, Guangdong, China) was used to isolate exosomes in accordance with the manufacturer's instruction. To further confirm that exosomes were isolated, their morphology was detected utilizing transmission electron microscopy (TEM) (HT-7700, Hitachi, Tokyo, Japan), and the size was identified using nanoparticle tracking analysis (N30E, NanoFCM, Nottingham, UK). Moreover, the markers of exosomes, including CD63 and CD81, were detected by WB.

**2.13. Quantitative Real-Time PCR (qPCR).** Total RNA from C2C12 cells or exosomes was extracted by TRIzol (Invitrogen). Then, RNA was reverse-transcribed to cDNA using PrimeScript II 1st Strand cDNA Synthesis Kit (Takara Biotechnology, Dalian, Liaoning, China). Next, qPCR was performed by CFX96 Touch Real-Time PCR (Bio-Rad, Hercules, CA, USA) utilizing SYBR Premix Ex Taq II (Takara Biotechnology). Subsequently, the amount of target RNA was normalized to that of GAPDH (internal control), and the fold change of target RNA was identified by  $2^{-\Delta\Delta Ct}$  relative to the control group [11, 23]. The sequences of primers used for qPCR were as follows: Myf5 forward: 5'-GCATCTACTGTCCTGATGTA-3', reverse: 5'-CATCGGGAGAGAGTTCATAA-3'; lncRNA TUG1 forward: 5'-TATTGGTATGGCTGGCCTTTC-3', reverse: 5'-TGGGTGAGGTGTGGGTTGTT-3'; lncRNA DANCR forward: 5'-CAGTTCCTTAGCGCAGGTTGA-3', reverse: 5'-AGCATTGTCACTGCTCTAGCT-3'; GAPDH forward: 5'-GGCTCAAGGAGTAAGAAA-3', reverse: 5'-GCCCTCCTGTATTATGG-3'.

**2.14. RNA Immunoprecipitation (RIP) Assay.** The RIP assay was performed using an EZ-Magna RIP kit (Millipore). Lysates were obtained from  $1 \times 10^7$  C2C12 cells using complete RIP lysis buffer and then immunoprecipitated with RIP buffer containing conjugated magnetic beads (Abcam) and anti-Myf5 antibody. Next, the precipitated RNAs with Myf5 protein were detected by qPCR. Rabbit IgG was used as the negative control.

**2.15. Luciferase Reporter Gene System.** First, the Myog gene promoter was cloned into the luciferase reporter gene plasmid. Then, C2C12 cells were cotransfected with the luciferase reporter gene plasmid and the lncRNA TUG1

expression vector or the lncRNA DANCR expression vector. After transfection for 48 h, C2C12 cells were collected to detect the relative luciferase activity using a dual-luciferase reporter assay system (Promega, Fitchburg, Wisconsin, USA).

**2.16. Chromatin Immunoprecipitation (ChIP).** A ChIP kit obtained from Thermo Fisher Scientific was utilized to assess ChIP. In brief, C2C12 cells were cross-linked by 1% formaldehyde at RT for 15 min and then stopped by glycine. Then, C2C12 cells were sonicated to shear DNA. Next, 25 mg DNA chromatin sample was diluted by 450 mL dilution buffer with protease inhibitors. Subsequently, chromatin samples were incubated with 1  $\mu$ g Myf5 antibody (Abcam)/antirabbit IgG antibody (Abcam) and magnetic protein A/G beads at 4°C with gentle rotation overnight. After incubation, the magnetic beads were collected using magnetic separation device (Thermo Fisher Scientific) and cleaned. Subsequently, 100  $\mu$ L elution buffer containing proteinase K was utilized to elute immunoprecipitated DNAs at 62°C for 2 h. Then, the immunoprecipitated DNAs were purified using the spin columns. Finally, chromatin DNAs were analyzed by qPCR. Primers used for ChIP-qPCR in the present study were as follows: Myog ChIP1 forward: 5'-CTGTTGCCCGTGCCGGAGCG-3', reverse: 5'-AGAATTTGGCCAGATGCAGTG-3'; Myog ChIP2 forward: 5'-GCCCAAACCTTCATGATGTCTC-3', reverse: 5'-AAGAATTTTCCAGGCAGGCC-3'; Myog ChIP3 forward: 5'-CGTCTCCCAATACGATGTTATG-3', reverse: 5'-CTCCCCTCCAAGAAAGGGCCAC-3'; Myog ChIP4 forward: 5'-ATCATGGTTCATTGGCAGCC-3', reverse: 5'-CAGGCACAGTGACTCATGCC-3'.

### 3. Statistical Analysis

All quantitative data were presented as mean  $\pm$  SD. Experiments in this study were repeated three times ( $n = 3$ ). Next, statistical differences were analyzed by SPSS 20 software (SPSS Inc., Chicago, IL, USA). Briefly, the unpaired Student's *t*-test was used to compare two groups, while one-way ANOVA was utilized for comparisons among multiple groups.  $P < 0.05$  was considered statistically significant.

### 4. Results

**4.1. Clinicopathological Features of Patients with Sarcopenia.** The clinicopathological features of 384 male patients with sarcopenia are described in Table 1. Briefly, their median age was 51.6 years (33–93 years); median weight was 72.7 kg (51.9–102.6 kg); median height was 170.5 cm (145–184 cm); and median body mass index (BMI) was 25.0 (16.8–33.6) at T1 (the first year of this study). These clinicopathological features were consistent at each measurement time, including T1 (the first year of this study), T2 (the second year of this study), and T3 (the third year of this study).

**4.2. Descriptive Statistics.** The mean values for the analyzed variables at each measurement time are presented in Table 2. The average values of appendicular lean mass, mean whole-body BMD (WBTOT BMD), skull BMD (HEAD BMD), lumbar spinal BMD (LS BMD), and pelvic BMD

TABLE 1: Clinicopathological characteristics of patients with sarcopenia.

Characteristics	Mean value		
	T1	T2	T3
Age (years)	51.57 ± 8.88	52.61 ± 8.88	53.65 ± 8.90
Weight (kg)	72.70 ± 8.39	72.53 ± 8.3	72.67 ± 8.63
Height (cm)	170.50 ± 5.70	170.48 ± 5.69	170.34 ± 5.62
Body mass index (BMI kg/m <sup>2</sup> )	25.00 ± 2.56	24.95 ± 2.54	25.03 ± 2.60

TABLE 2: Descriptive statistics.

Characteristics	Mean value		
	T1	T2	T3
Appendicular lean mass	8.07 ± 0.79	7.96 ± 0.79	7.92 ± 0.78
WBTOT BMD	1.12 ± 0.09	1.12 ± 0.09	1.11 ± 0.091
Head BMD	2.19 ± 0.27	2.17 ± 0.26	2.11 ± 0.32
LS BMD	1.00 ± 0.14	1.00 ± 0.15	1.00 ± 0.15
PELV BMD	1.24 ± 0.17	1.24 ± 0.17	1.22 ± 0.17
Albumin-1 (μg/mL)	43.47 ± 2.23		
FBS (μg/mL)	5.29 ± 1.10		
LDL-C (μg/mL)	2.94 ± 0.74		
TSH (μg/mL)	1.77 ± 1.18		
Platelet distribution width	13.44 ± 2.23		

(PELV BMD) were 8.07 (5.93–10.52), 1.12 (0.91–1.42), 2.19 (1.44–3.01), 1.00 (0.65–1.52), and 1.24 (0.91–2.08) at T1, respectively. Moreover, the median values at T1 of albumin-1, FBS, LDL-C, TSH, and platelet distribution width were 43.47 μg/mL (35.9–45.7 μg/mL), 5.29 μg/mL (3.69–13.72 μg/mL), 2.94 μg/mL (0.77–5.2 μg/mL), 1.77 μg/mL (0.01–13.26 μg/mL), and 13.44 (8.88–21.2), respectively. Except for platelet distribution width, other clinicopathological features were consistent from T1 to T3. Appendicular lean mass, WBTOT BMD, HEAD BMD, LS BMD, and PELV BMD were consistent at each measurement time (T1 to T3).

**4.3. Cross-Lagged Paths between WBTOT BMD and Appendicular Lean Mass.** Albumin-1, FBS, LDL-C, TSH, and platelet distribution width were used as covariates. The model including cross-lagged paths between WBTOT BMD and appendicular lean mass did not fit the data well (RMSEA = 0.45; CFI = 0.04). As shown in Figure 1(a), LDL-C at T1 positively predicted T1 appendicular lean mass. WBTOT BMD at T1 positively predicted T2 appendicular lean mass, while WBTOT BMD at T2 positively predicted T3 appendicular lean mass (Figure 1(a)). Furthermore, appendicular lean mass at T1 positively predicted T2 WBTOT BMD, and appendicular lean mass at T2 positively predicted T3 WBTOT BMD (Figure 1(a)).

**4.4. Cross-Lagged Paths between HEAD BMD and Appendicular Lean Mass.** The model including cross-lagged paths between HEAD BMD and appendicular lean mass did not fit the data well (RMSEA = 0.406; CFI = 0.002).

Platelet distribution width at T1 negatively predicted T1 HEAD BMD (Figure 1(b)). However, HEAD BMD did not predict appendicular lean mass (Figure 1(b)).

**4.5. Cross-Lagged Paths between LS BMD and Appendicular Lean Mass.** The model including cross-lagged paths between LS BMD and appendicular lean mass did not show a good fit (RMSEA = 0.424; CFI = 0.03). As shown in Figure 2(a), LDL-C at T1 positively predicted T1 appendicular lean mass. LS BMD at T1 positively predicted T2 appendicular lean mass, while LS BMD at T2 positively predicted T3 appendicular lean mass (Figure 2(a)). Furthermore, appendicular lean mass at T1 positively predicted T2 LS BMD, and appendicular lean mass at T2 positively predicted T3 LS BMD (Figure 2(a)).

**4.6. Cross-Lagged Paths between PELV BMD and Appendicular Lean Mass.** The model including cross-lagged paths between PELV BMD and appendicular lean mass did not show a good fit (RMSEA = 0.417; CFI = 0.092). The results showed that PELV BMD at T1 positively predicted T2 appendicular lean mass, while PELV BMD at T2 positively predicted T3 appendicular lean mass (Figure 2(b)). Moreover, appendicular lean mass at T1 positively predicted T2 PELV BMD, and appendicular lean mass at T2 positively predicted T3 PELV BMD (Figure 2(b)).

**4.7. Skull Osteoblasts and Femur Osteoblasts Exert Different Influences on Myoblasts.** Myoblasts, such as murine C2C12 myoblasts, are usually utilized for *in vitro* studies of muscle mass in sarcopenia [24]. However, osteoblasts are critical in maintaining BMD [25, 26]. Therefore, the correlation of BMD and muscle mass (sarcopenia) could involve the interaction of osteoblasts and myoblasts.

Our recent study has indicated that skull BMD negatively correlates with ASM mass, whereas BMDs throughout the rest of the body are positively associated with ASM mass in male middle-aged and elderly Chinese individuals [9]. Our current study indicated that WBTOT BMD could temporally and positively predict appendicular lean mass. Femur is the longest and strongest bone of the body [27], suggesting that the BMD of the femur plays a crucial role in WBTOT BMD except skull BMD. Thus, the effects of skull osteoblasts and femur osteoblasts on myoblasts were investigated.

To identify the effects of different osteoblasts on myoblasts, we detected the proliferation, apoptosis, and differentiation of myoblasts. The results showed that a culture medium of primary mice skull osteoblasts enhanced the

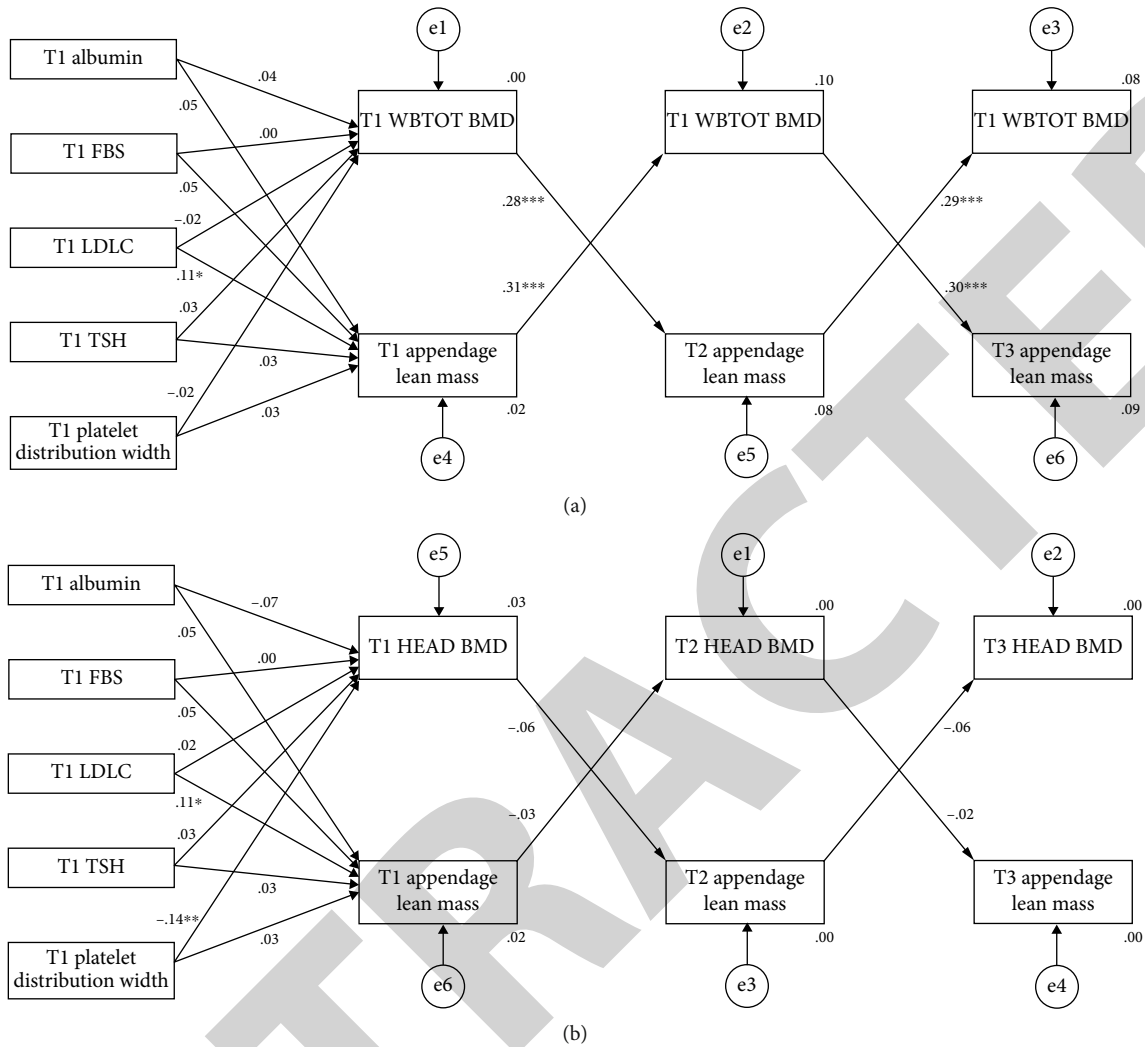


FIGURE 1: Cross-lagged paths between WBTOT BMD and appendicular lean mass (a) and HEAD BMD and appendicular lean mass (b).

proliferation of C2C12 cells, while a culture medium of primary mice femur osteoblasts had no effect on the proliferation of C2C12 cells (Figure 3(a)). Treatments of a culture media of primary mice femur osteoblasts and a culture medium of primary mice skull osteoblasts only slightly induced the apoptosis of C2C12 cells (Figure 3(b)), suggesting that the culture medium of primary mice femur osteoblasts and the culture medium of primary mice skull osteoblasts also had no effect on C2C12 cell apoptosis.

Next, the effects of skull osteoblasts and femur osteoblasts on the differentiation of myoblasts were explored. qPCR analysis showed that mRNA levels of myoblast differentiation makers Myog and Myf5 were increased in C2C12 cells cultured with differential medium (DM) compared with those in C2C12 cells cultured with normal culture medium (CM) (Figure 4(a)). Moreover, treatment with a culture medium of primary mice femur osteoblasts increased the mRNA levels of Myog and Myf5 in C2C12 cells, and the addition of culture medium of primary mice femur osteoblasts to DM further enhanced the effect of DM on Myog and Myf5 mRNA expression (Figure 4(a)). In contrast, treatment with a culture medium of primary mice skull osteo-

blasts reduced the mRNA levels of Myf5 and Myog, and the addition of a culture medium of primary mice skull osteoblasts to DM abolished the effect of DM on Myog and Myf5 mRNA expression (Figure 4(a)).

Similarly, protein levels of the myoblast differentiation makers Myog and myosin heavy chain 6 (MYH6) were increased in C2C12 cells cultured with DM compared with those in C2C12 cells cultured with CM (Figure 4(b)). Treatment with a culture medium of primary mice femur osteoblasts upregulated the protein expression levels of Myog and MYH6, while the addition of a culture medium of primary mice femur osteoblasts to DM further enhanced the effect of DM on Myog and MYH6 protein expression levels (Figure 4(b)). However, treatment with a culture medium of primary mice skull osteoblasts reduced the protein levels of Myog and MYH6, and the addition of a culture medium of primary mice skull osteoblasts to DM abolished the effect of DM on Myog and MYH6 protein expression (Figure 4(b)).

As Myog is associated with oxidative stress, the markers of oxidative stress, including MDA, GSH, and SOD, were detected in C2C12 cells. We showed that the MDA level

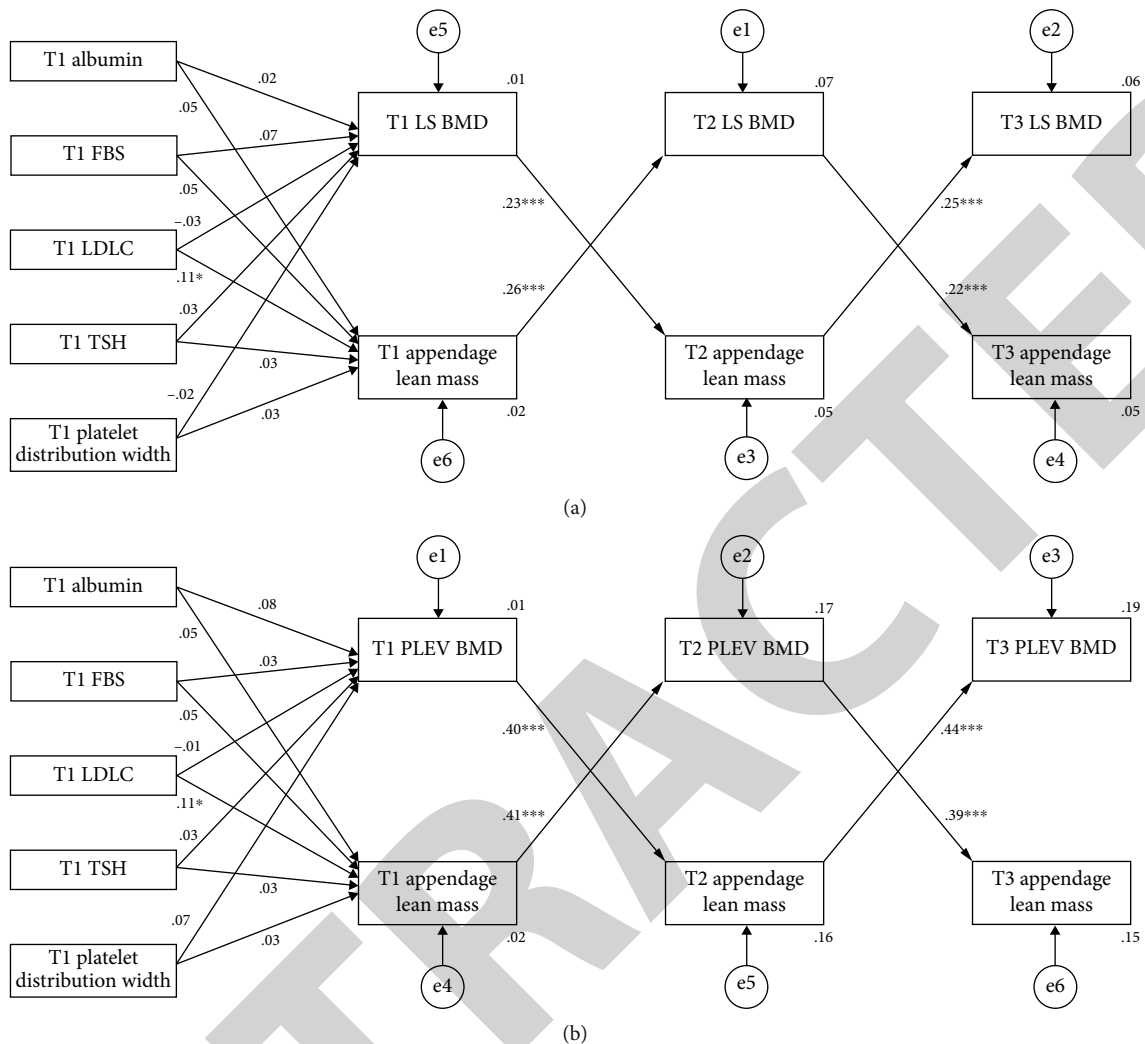


FIGURE 2: Cross-lagged paths between LS BMD and appendicular lean mass (a) and PELV BMD and appendicular lean mass (b).

was decreased, whereas the levels of GSH and SOD were increased, in C2C12 cells cultured with DM compared with those in C2C12 cells cultured with CM (Figures 4(c)–4(e)). Moreover, treatment with a culture medium of primary mice femur osteoblasts reduced the MDA level but elevated the levels of GSH and SOD, while the addition of culture medium of primary mice femur osteoblasts to DM further enhanced the effect of DM on the levels of MDA, GSH, and SOD (Figures 4(c)–4(e)). Nevertheless, treatment with a culture medium of primary mice skull osteoblasts increased the MDA level but decreased the levels of GSH and SOD, and the addition of culture medium of primary mice skull osteoblasts to DM abolished the effect of DM on the levels of MDA, GSH, and SOD (Figures 4(c)–4(e)). These data suggested that primary mice femur osteoblasts, but not primary mice skull osteoblasts, induce the differentiation of C2C12 cells.

**4.8. Exosomes Derived from Skull Osteoblasts or Femur Osteoblasts Exert Different Effects on Myoblasts.** As exosomes mediate the communication among different cells and

organs, the effects of exosomes derived from different osteoblasts on myoblasts were examined. Both skull osteoblast-derived exosomes and femur osteoblast-derived exosomes had a cup-shaped morphology with a size of 50–150 nm as detected by TEM and NanoSight analysis (Figures 5(a) and 5(b)). Detection of exosomal markers CD63 and CD81 by WB confirmed that extracellular vesicles isolated from the culture medium of skull osteoblasts or femur osteoblasts were exosomes (Figure 5(c)). Next, C2C12 cells were incubated with exosomes derived from skull osteoblasts or femur osteoblasts, and cell proliferation, apoptosis, and differentiation were recorded. Compared with C2C12 cells culture without exosomes, both skull osteoblast-derived exosomes and femur osteoblast-derived exosomes had no effect on the proliferation and apoptosis of C2C12 cells (Figures 5(d) and 5(e)). Femur osteoblast-derived exosomes increased the protein levels of Myog and MYH6 in C2C12 cells cultured with DM (Figure 5(f)). In contrast, skull osteoblast-derived exosomes decreased the protein levels of Myog and MYH6 in C2C12 cells cultured with DM (Figure 5(f)). These results suggested that femur

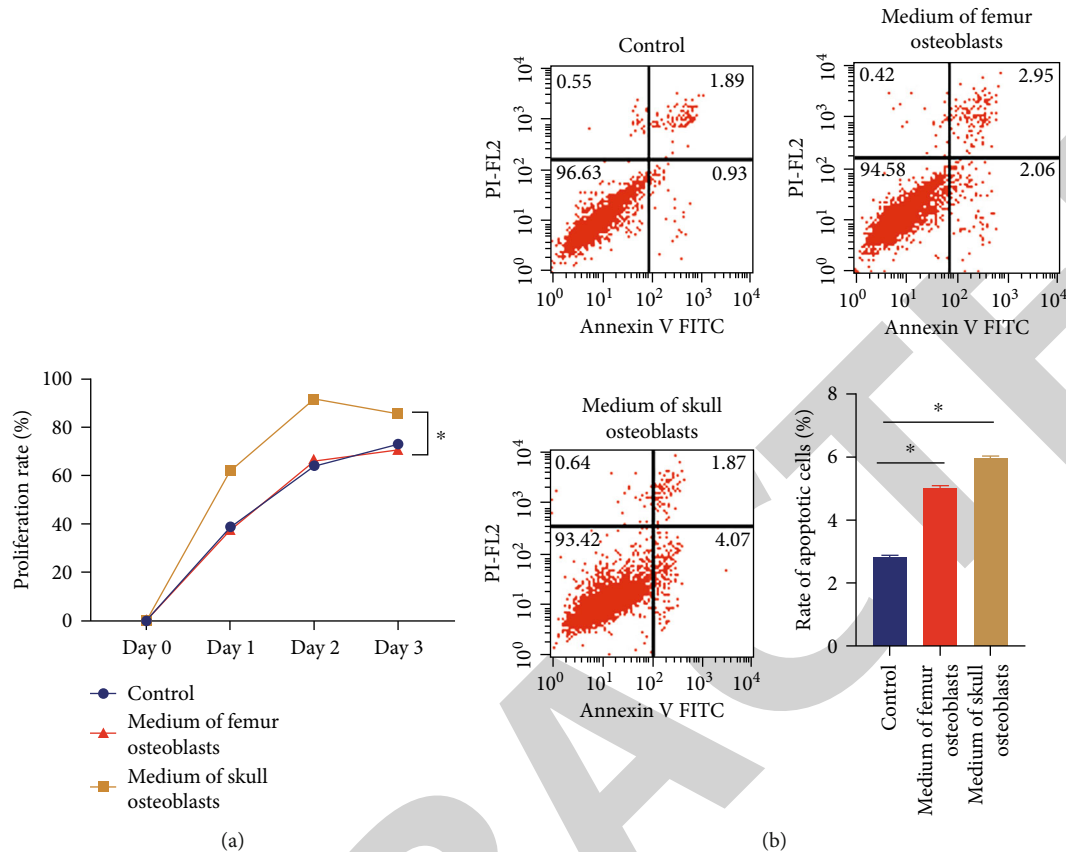


FIGURE 3: Skull osteoblasts and femur osteoblasts exert different influences on the proliferation and apoptosis of myoblasts. (a) The proliferation rate of C2C12 cells detected by CCK8 array. (b) Representative images of flow cytometric apoptosis assay in C2C12 cells. The bar graph shows the quantification of apoptotic cell number in each group.  $N = 3$ .  $*P < 0.05$ .

osteoblast-derived exosomes enhanced the differentiation of myoblasts, whereas skull osteoblast-derived exosomes suppressed this process.

**4.9. Levels of lncRNA TUG1 and DANCR in Skull and Femur Osteoblast-Secreted Exosomes.** So far, the role of exosomal lncRNA TUG1 and DANCR from osteoblasts in myoblasts has been unclear. First, the levels of lncRNA TUG1 and DANCR in osteoblast-secreted exosomes and osteoblasts were detected by qPCR. We found that the level of lncRNA TUG1 in skull osteoblast-secreted exosomes was lower than that in femur osteoblast-secreted exosomes (Figure 6(a)). In contrast, the level of lncRNA DANCR in skull osteoblast-secreted exosomes was higher than that in femur osteoblast-secreted exosomes (Figure 6(b)). Moreover, the level of lncRNA TUG1 in skull osteoblasts was higher than that in femur osteoblasts, while the level of lncRNA DANCR in skull osteoblasts was lower than that in femur osteoblasts (Figures 6(c) and 6(d)), suggesting that the enrichment of lncRNA TUG1 or DANCR in osteoblast-secreted exosomes was negatively related to its expression in osteoblasts. These data indicated that osteoblast-secreted exosomes might exert different influences on myoblasts depending on the levels of exosomal lncRNA TUG1 and DANCR.

**4.10. Skull and Femur Osteoblast-Secreted Exosomes Alter the Levels of lncRNA TUG1 and DANCR in Myoblasts.** To identify whether osteoblast-derived exosomes regulate the levels of lncRNA TUG1 and DANCR in myoblasts, the levels of lncRNA TUG1 and DANCR in C2C12 cells were detected by qPCR after the incubation with osteoblast-derived exosomes. The results revealed that skull osteoblast-secreted exosomes increased the level of lncRNA DANCR in C2C12 cells, while femur osteoblast-secreted exosomes upregulated the level of lncRNA TUG1 in C2C12 cells (Figures 7(a) and 7(b)). These results suggested that lncRNA TUG1 and DANCR in osteoblast-secreted exosomes might contribute to myoblast functions.

**4.11. lncRNA TUG1 and DANCR Play Different Roles in Myoblasts.** To determine the effects of lncRNA TUG1 and DANCR on myoblasts, lncRNA TUG1 and DANCR were overexpressed by transfection of expression vectors into C2C12 cells followed by detections of cell proliferation, apoptosis, and differentiation. Consistent with the results of exosomes incubation, overexpression of lncRNA TUG1 or DANCR had no effect on C2C12 cell proliferation and apoptosis (Figures 8(a) and 8(b)). lncRNA TUG1 overexpression increased and overexpression of lncRNA DANCR reduced the protein levels of Myog and MYH6 in differential

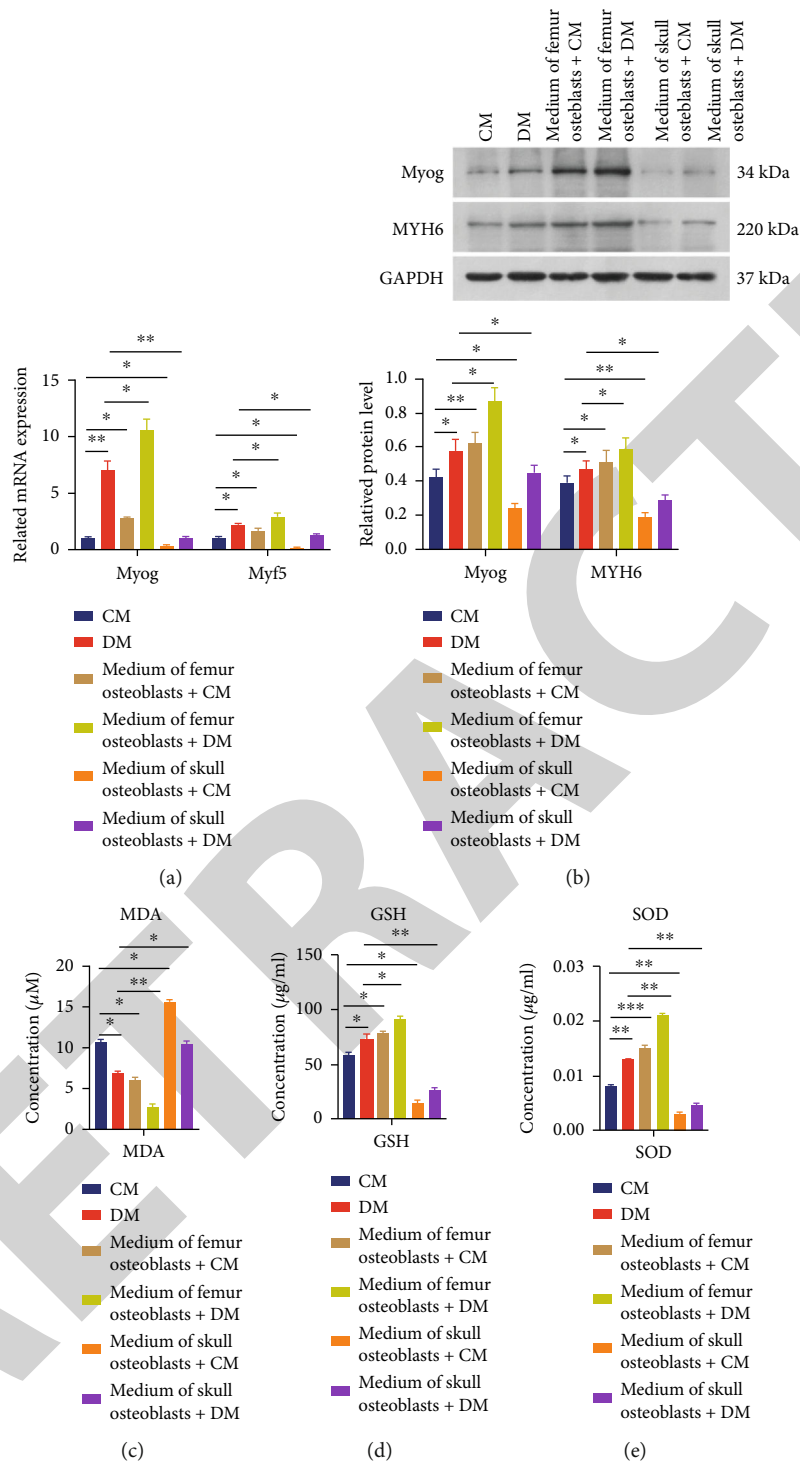


FIGURE 4: Skull osteoblasts and femur osteoblasts exert different influences on the differentiation of myoblasts. (a) The levels of Myog and Myf5 mRNA in C2C12 cells detected by qPCR. (b) The protein levels of Myog and MYH6 in C2C12 cells detected using WB. The bar graph shows the relative levels of Myog and MYH6 in each group. (c) The level of MDA in C2C12 cells. (d) The level of GSH in C2C12 cells. (e) The level of SOD in C2C12 cells. CM: C2C12 cell culture medium; DM: differential medium.  $N = 3$ . \* $P < 0.05$  and \*\* $P < 0.01$ .

C2C12 cells (Figure 8(c)). These results suggested that lncRNA TUG1 enhanced the differentiation of myoblasts, whereas lncRNA DANCR suppressed this process.

**4.12. lncRNA TUG1 and DANCR Exert Different Effects on Myog Expression via Myf5 in Myoblasts.** The prediction of RNA–protein binding by RPISEQ showed that both lncRNA TUG1 and DANCR had high binding probability with myogenic transcription factor Myf5 (Supplementary Figure S1). Thus, RIP assay was performed to identify the interaction between Myf5 and lncRNA TUG1 or DANCR. The results of RIP showed the enrichment of lncRNA TUG1 and DANCR by Myf5 protein, suggesting that lncRNA TUG1 and DANCR were associated with Myf5 protein in C2C12 cells (Figure 9(a)).

Furthermore, luciferase reporter gene assay demonstrated that the luciferase activity of C2C12 cells transfected with plasmids containing the *Myog* gene promoter was increased by the transfection of the lncRNA TUG1 expression vector compared with that of cells cotransfected with plasmids containing the *Myog* gene promoter and a blank expression vector, and transfection of the Myf5 expression vector enhanced the effect of the lncRNA TUG1 expression vector (Figure 9(b)). The luciferase activity of C2C12 cells transfected with plasmids containing the *Myog* gene promoter was decreased by the transfection of the lncRNA DANCR expression vector compared with that of cells cotransfected with plasmids containing the *Myog* gene promoter and a blank expression vector, and transfection of the Myf5 expression vector reversed the effect of the lncRNA DANCR expression vector (Figure 9(b)). These data suggested that lncRNA TUG1 promoted the transcription of the *Myog* gene by Myf5, whereas lncRNA DANCR suppressed the transcription of the *Myog* gene via Myf5.

**4.13. lncRNA TUG1 and DANCR Regulate Myog Expression via Modifying Nuclear Translocation of Myf5 in Myoblasts.** As Myf5 is a transcription factor, lncRNA TUG1 and DANCR might affect the binding between Myf5 and the *Myog* gene promoter. To prove this hypothesis, CHIP followed by qPCR was performed using Myf5 antibody. The results indicated that Myf5 bound to the *Myog* gene promoter in C2C12 cells (Figures 9(c) and 9(d)). Furthermore, overexpression of lncRNA TUG1 dramatically facilitated the binding of Myf5 to the *Myog* gene promoter in C2C12 cells (Figure 9(c)). In contrast, lncRNA DANCR overexpression suppressed the association of Myf5 with the *Myog* gene promoter in C2C12 cells (Figure 9(c)). These results suggested that lncRNA TUG1 and DANCR exerted opposite effects on the transcription of *Myog* gene through modifying the binding of Myf5 to the *Myog* gene promoter.

In addition, the results of IHC showed that overexpression of lncRNA TUG1 enhanced the nuclear translocation of Myf5, whereas lncRNA DANCR overexpression inhibited the nuclear translocation of Myf5 in C2C12 cells (Figure 9(d)). Thus, lncRNA TUG1 might transport Myf5 into the nucleus, while lncRNA DANCR is mainly located in the cytoplasm after associating with Myf5. These data suggest that lncRNA TUG1 and DANCR regulate the tran-

scription of *Myog* gene through modifying the binding of Myf5 to the *Myog* gene promoter by affecting the nuclear translocation of Myf5 as transporters in C2C12 cells.

## 5. Discussion

In this study, the cross-lagged models indicated that LDL-C positively predicted appendicular lean mass and negatively predicted HEAD BMD, WBTOT BMD, LS BMD, and PELV BMD temporally and positively predicted appendicular lean mass, while appendicular lean mass temporally and positively predicted WBTOT BMD, LS BMD, and PELV BMD. In addition, the present study investigated mechanisms by which different osteoblasts exerted different influences on muscle. First, primary mice femur osteoblasts, but not primary mice skull osteoblasts, induced the differentiation of C2C12 cells through exosomes. Second, the level of lncRNA TUG1 was decreased, and the level of lncRNA DANCR was increased in skull osteoblast–secreted exosomes, whereas the level of lncRNA TUG1 was increased and the level of lncRNA DANCR was decreased in femur osteoblast–secreted exosomes. Moreover, lncRNA TUG1 enhanced the differentiation of myoblasts, whereas lncRNA DANCR suppressed this process through regulating *Myog* expression via modifying the nuclear translocation of Myf5.

Several studies have indicated that albumin, LDL-C, and TSH are related to sarcopenia or muscle mass. For instance, serum albumin level is significantly lower in patients with sarcopenia than in healthy controls [28, 29]. Sarcopenia is associated with urinary albumin level in diabetic patients [30]. Moreover, serum albumin is positively related to lean mass and appendicular lean mass in healthy young individuals [31]. Meanwhile, the LDL-C level is reduced in older people with low muscle mass [32], and serum TSH level has a U-shaped correlation with sarcopenia in older adults [33]. In addition, albumin, LDL-C, and platelet distribution are associated with BMD. A recent study has demonstrated that BMD is negatively related to urine albumin [34]. LDL-C is negatively associated with BMD [35, 36]. Furthermore, TSH suppression leads to a decrease in BMD [37, 38]. Our results indicated that LDL-C positively predicted appendicular lean mass. Thus, bone may exert influences on muscle, combined with LDL-C, in sarcopenia.

The temporal association between sarcopenia or muscle mass with BMD remains unknown. To date, few studies have shown the temporal correlation of sarcopenia or muscle mass and BMD. For example, the increase in appendicular lean mass is temporally associated with increased total hip BMD over 5 years [39]. For the first time, the current study demonstrated that WBTOT BMD, LS BMD, and PELV BMD were able to temporally and positively predict appendicular lean mass. In turn, appendicular lean mass was also able to temporally and positively predict WBTOT BMD, LS BMD, and PELV BMD. Therefore, the present study expanded the knowledge of the temporal association between sarcopenia and muscle mass with BMD.

To date, the knowledge on mechanisms by which bone tissues/osteoblasts exert influence on muscle tissues/



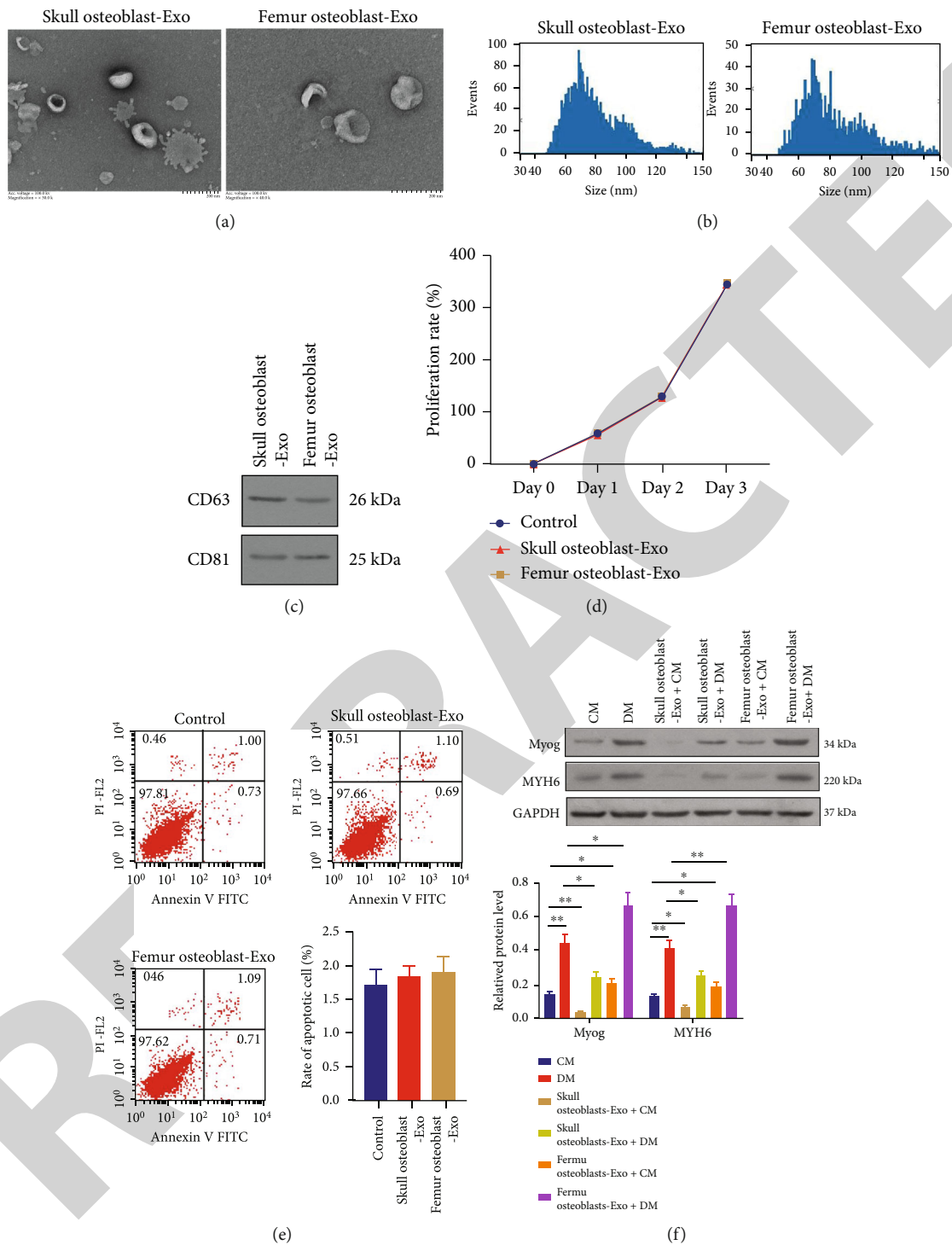


FIGURE 5: Exosomes derived from skull osteoblasts or femur osteoblasts exert different effects on myoblasts. (a) Representative images of purified skull osteoblast- or femur osteoblast-derived exosomes detected by TEM. Scale bars: 100 nm. (b) Purified exosomes derived from skull osteoblasts or femur osteoblasts were identified by nanoparticle tracking analysis. (c) WB analysis of exosomal markers CD63 and CD81 in exosomes derived from skull osteoblasts or femur osteoblasts. (d) The proliferation rate of C2C12 cells detected by CCK8 array. (e) Representative images of flow cytometric apoptosis assay in C2C12 cells. The bar graph shows the quantification of apoptotic cell number in each group. (f) The protein levels of Myog and MYH6 in C2C12 cells detected using WB. The bar graph shows the relative levels of Myog and MYH6 in each group. CM: C2C12 cell culture medium; DM: differential medium; Exo, exosomes.  $N = 3$ . \* $P < 0.05$  and \*\* $P < 0.01$ .

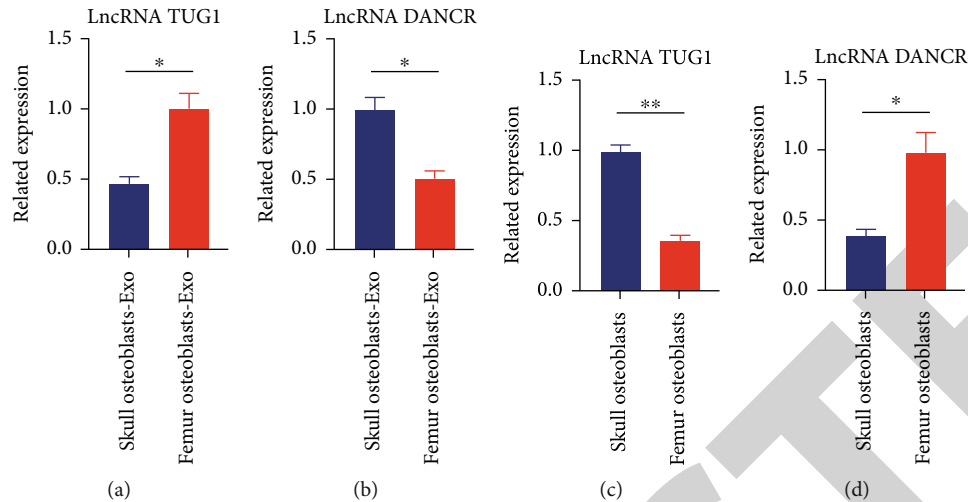


FIGURE 6: Levels of lncRNA TUG1 and DANCR in skull and femur osteoblast-secreted exosomes. (a) The level of lncRNA TUG1 in exosomes derived from skull osteoblasts or femur osteoblasts. (b) The level of lncRNA DANCR in exosomes derived from skull osteoblasts or femur osteoblasts. (c) The level of lncRNA TUG1 in skull osteoblasts or femur osteoblasts. (d) The level of lncRNA DANCR in skull osteoblasts or femur osteoblasts. Exo: exosomes.  $N = 3$ . \* $P < 0.05$  and \*\* $P < 0.01$ .

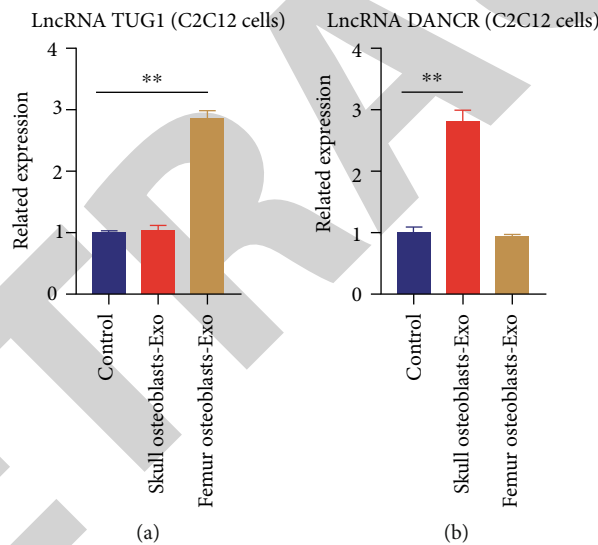


FIGURE 7: Skull and femur osteoblast-secreted exosomes alter the levels of lncRNA TUG1 and DANCR in myoblasts. (a) The level of lncRNA TUG1 in C2C12 cells treated with exosomes derived from skull osteoblasts or femur osteoblasts. (b) The level of lncRNA DANCR in C2C12 cells treated with exosomes derived from skull osteoblasts or femur osteoblasts. Exo: exosomes.  $N = 3$ . \*\* $P < 0.01$ .

myoblasts is still limited. Exosomes mediate the communication among different cells and organs [14]. A previous study has demonstrated that C2C12 myoblasts-derived exosomes facilitate osteogenic differentiation of MC3T3-E1 cells through delivering miR-27a-3p [40]. Nevertheless, the role of exosomes derived from osteoblasts in myoblasts is largely unknown. Several studies have revealed the influences of osteoblast-derived exosomes on other cells or organs. For example, osteoblast-derived exosomes enhance the calcification of vascular smooth muscle cells (VSMCs) [41]. miR-139-5p in senescent osteoblast-secreted exosomes promotes senescence and apoptosis of vascular endothelial cells through targeting T-box transcription factor 1 (TBX1) in

endothelial cells [42]. Moreover, exosomes from osteoblasts inhibit T-cell activity [43]. Previous studies have also revealed the effect of osteoblast secretions on myoblasts or muscle cells. For instance, osteoblast-derived OGN may play a role in regulating muscle mass [13]. Furthermore, osteoblasts secrete active osteocalcin to indirectly regulate myoblast functions [44]. However, the role of osteoblast-derived exosomes in myoblasts or muscle cells has not been reported. Therefore, this study revealed the effects of osteoblast-derived exosomes on myoblast differentiation for the first time.

Exosomes could mediate long-distance communication and cooperative regulatory network among different cells

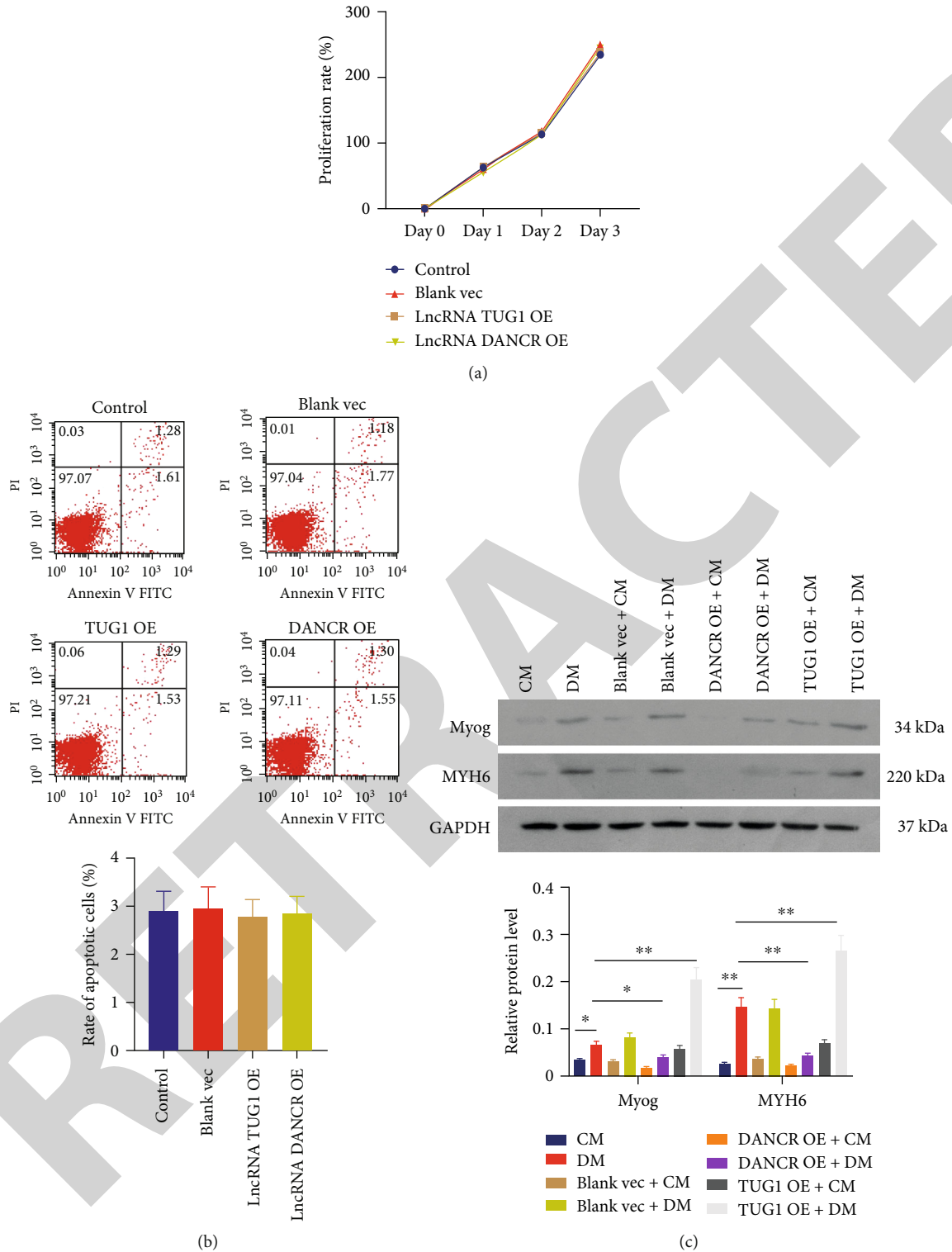


FIGURE 8: lncRNA TUG1 and DANCRCR play different roles in myoblasts. (a) The proliferation rate of C2C12 cells detected by CCK8 array. (b) Representative images of flow cytometric apoptosis assay in C2C12 cells. The bar graph shows the quantification of apoptotic cell number in each group. (c) The protein levels of Myog and MYH6 in C2C12 cells detected using WB. The bar graph shows the relative levels of Myog and MYH6 in each group. CM: C2C12 cell culture medium; DM: differential medium; Vec: expression vector; OE: overexpression.  $N = 3$ . \* $P < 0.05$  and \*\* $P < 0.01$ .

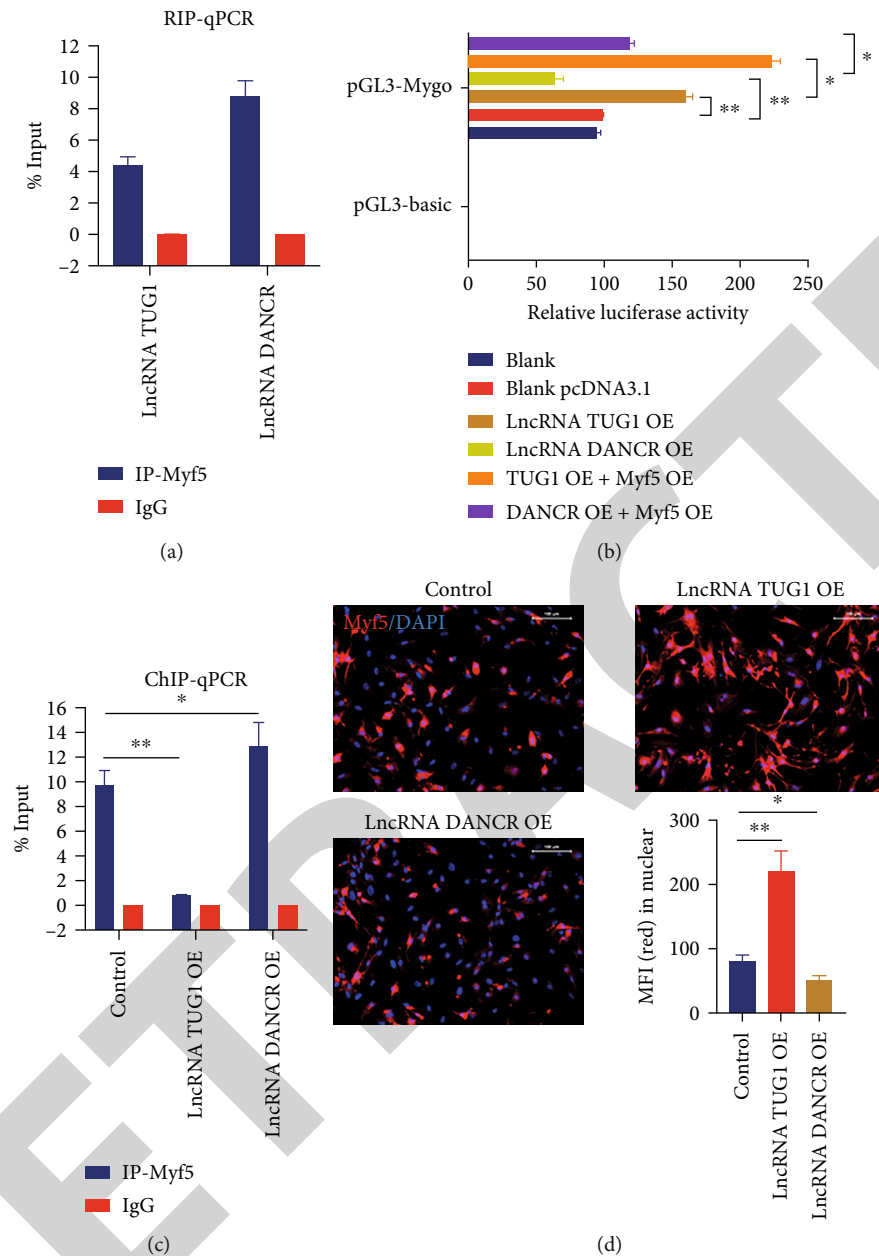


FIGURE 9: lncRNA TUG1 and DANCR regulate Myf5 expression via modifying nuclear translocation of Myf5 in myoblasts. (a) The level of lncRNA TUG1 and DANCR binding to Myf5 protein detected by RIP assay. (b) *Myog* gene promoter activity analyzed by relative luciferase reporter activities in C2C12 cells transfected with lncRNA TUG1 expression vector, lncRNA DANCR expression vector, or Myf5 expression vector. (c) Quantification of Myf5 occupancy on the *Myog* gene promoter by ChIP-qRT-PCR in C2C12 cells transfected with lncRNA TUG1 expression vector or lncRNA DANCR expression vector. (d) Representative images of C2C12 cells staining by Myf5 antibody using IF. The bar graph shows the quantification of mean fluorescence intensity (MFI) of red in the nucleus. Bar = 100  $\mu$ m. OE: overexpression.  $N = 3$ . \* $P < 0.05$  and \*\* $P < 0.01$ .

and organs as vectors to carry lncRNA in a variety of diseases. For example, bladder cancer cell-derived exosomal lncRNA lymph node metastasis-associated transcript 2 (LNMAT2) enhances lymphatic metastasis through upregulating prospero homeobox 1 (PROX1) expression in lymphatic endothelial cells [45]. In addition, carcinoma-associated fibroblast-secreted exosomal lncRNA H19

improves the stemness and chemoresistance of colorectal cancer (CRC) by targeting miR-141 in CRC cells [46]. However, knowledge on the roles of exosomal lncRNA TUG1 and DANCR is limited. Only one study has indicated that exosomal lncRNA TUG1 derived from cervical cancer cell suppresses apoptosis of vascular endothelial cells [47]. To date, no studies have demonstrated the effect of exosomal

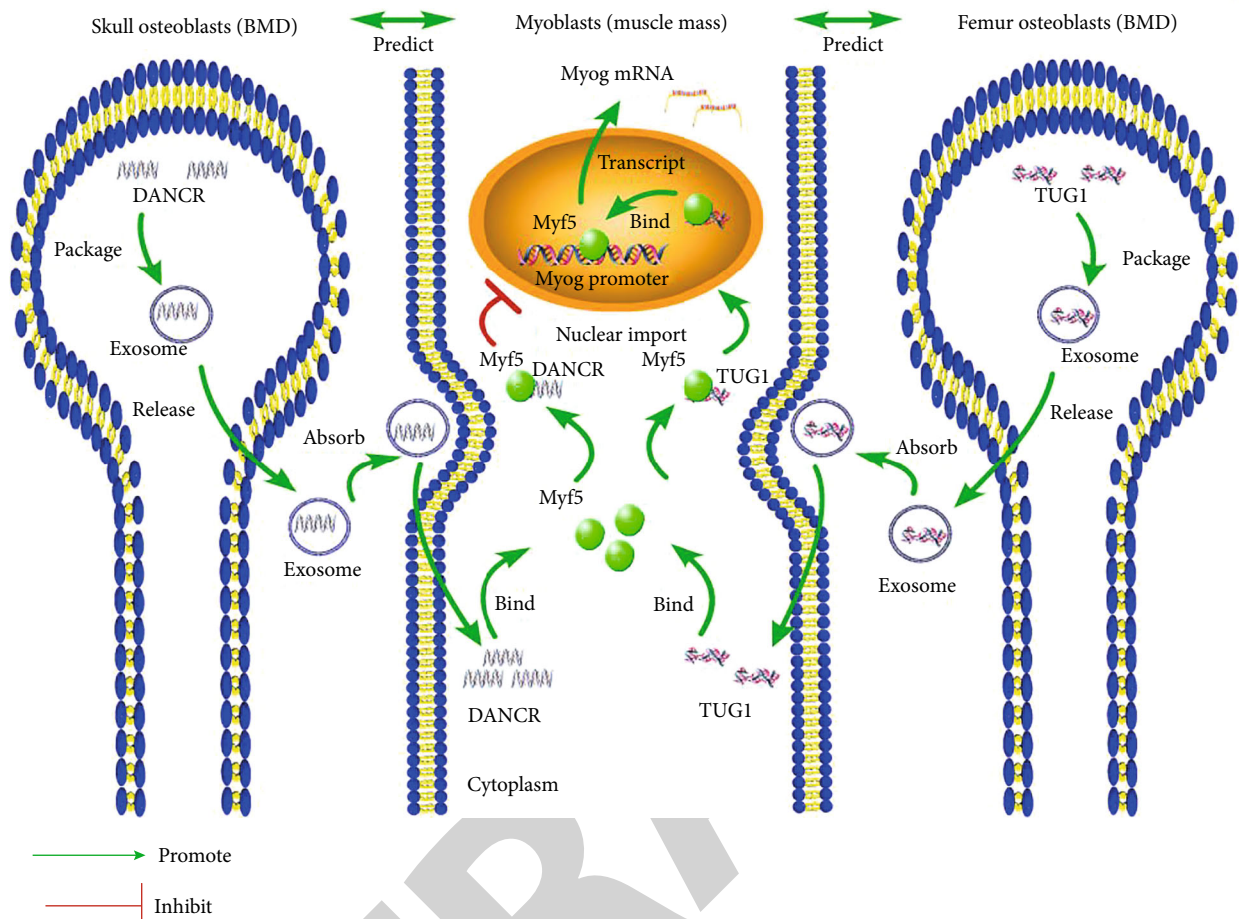


FIGURE 10: Schematic diagram of molecular mechanisms. The cross-lagged models indicated that LDL-C positively predicted appendicular lean mass. WBOT BMD, LS BMD, and PELV BMD temporally and positively predicted appendicular lean mass, while appendicular lean mass in turn temporally and positively predicted WBOT BMD, LS BMD, and PELV BMD. Moreover, this study revealed that femur osteoblast-derived exosomal lncRNA TUG1 and skull osteoblast-derived exosomal DANCR exerted opposite effects on myoblast differentiation through regulating the transcription of *Myog* gene by modifying the binding of Myf5 to the *Myog* gene promoter via affecting the nuclear translocation of Myf5 as transporters.

lncRNA DANCR. Thus, the results of this study could expand the knowledge on the roles of exosomal lncRNA TUG1 and DANCR.

Previous studies have found that lncRNA TUG1 promotes the osteogenic differentiation, whereas lncRNA DANCR inhibits osteogenic differentiation via the Wnt/ $\beta$ -catenin pathway [18, 19]. lncRNA TUG1 upregulates fibroblast growth factor 1 (FGF1) expression to enhance endothelial differentiation via sponging miR-143 in adipose-derived stem cells [48]. In contrast, lncRNA DANCR suppresses odontoblast differentiation through increasing c-Cbl level by sponging miR-216a [15]. Therefore, both lncRNA TUG1 and DANCR play critical roles in cell differentiation. However, the roles of lncRNA TUG1 and DANCR in myoblasts differentiation have not been reported. This study revealed the effects of lncRNA TUG1 and DANCR on the differentiation of myoblasts, which were consistent with previous studies.

Our study indicated that lncRNA TUG1 regulated the transcription of *Myog* gene through modifying the binding of Myf5 to the *Myog* gene promoter by affecting the nuclear

translocation of Myf5 as a transporter. Except as a transporter of Myf5 to regulate the binding of Myf5 to the *Myog* gene promoter, lncRNA TUG1 might modify the binding of Myf5 to the *Myog* gene promoter directly. Numerous studies have revealed that lncRNAs could regulate the transcription of target genes through recruiting transcription factors to the promoter of target genes [49, 50]. A previous study demonstrated that lncRNA TUG1 represses Kruppel-like factor 2 (KLF2) expression by interacting with polycomb repressive complex 2 (PRC2) and recruiting it to the *KLF2* gene promoter [51]. Thus, we assume that lncRNA TUG1 might facilitate the binding between Myf5 and the *Myog* gene promoter through recruiting Myf5 to the *Myog* promoter after transporting Myf5 into nucleus.

However, there are several limitations in the current study. First, more patients should be recruited to improve the accuracy of the cross-lagged models utilized for analyzing the temporal association between BMD and muscle mass. Second, data on the grip strength and walking speed of patients should be collected in a future study. Third, in vivo experiments should be performed to certify

mechanisms by which exosomal lncRNA TUG1 and DANCR derived from different osteoblasts regulate myoblasts.

## 6. Conclusions

In summary, cross-lagged models indicated that LDL-C positively predicted appendicular lean mass. WBTOT BMD, LS BMD, and PELV BMD temporally and positively predicted appendicular lean mass, while appendicular lean mass in turn temporally and positively predicted WBTOT BMD, LS BMD, and PELV BMD. Moreover, this study revealed that femur osteoblast-derived exosomal lncRNA TUG1 and skull osteoblast-derived exosomal DANCR exerted opposite effects on myoblast differentiation through regulating the transcription of the *Myog* gene by modifying the binding of Myf5 to the *Myog* gene promoter via affecting the nuclear translocation of Myf5 as transporters (Figure 10). Therefore, the results of the present study may provide novel diagnostic biomarkers and therapy targets for sarcopenia.

## Data Availability

Data and material are available upon request.

## Ethical Approval

This study was approved by the Ethics Committee of Foshan First People's Hospital.

## Consent

Informed consent was obtained from all individual participants included in the study. The authors affirm that human research participants provided informed consent for publication.

## Conflicts of Interest

The authors declare that they have no competing interests.

## Authors' Contributions

All authors contributed to the study conception and design. Material preparation, data collection, and analysis were performed by Jingsong Chen, Jie Shen, Xili Yang, Huiting Tan, Ronghua Yang, Cuiying Mo, Ying Wang, Xiaojun Luan, and Xuejuan Xu. The first draft of the manuscript was written by Xuejuan Xu, and all authors commented on previous versions of the manuscript. All authors read and approved the final manuscript. Jingsong Chen, Jie Shen, and Xili Yang contributed equally to this work.

## Acknowledgments

This work was supported by the Guangdong Basic and Applied Basic Research Foundation (2019A1515110463), the National Natural Science Foundation of China

(82102526, 21773199, and 31972915), and the Foshan 14th Fifth High-Level Key Specialty Construction Project.

## Supplementary Materials

Supplementary Figure S1: prediction of binding probability between lncRNA TUG1 or DANCR and Myf5. Prediction of binding probability between lncRNA TUG1 (A) or DANCR (B) and Myf5 using RPISEQ (<http://pridb.gdcb.jiastate.edu/RPISeq/index.html>). (Supplementary Materials)

## References

- [1] A. J. Cruz-Jentoft, G. Bahat, J. Bauer et al., "Sarcopenia: revised European consensus on definition and diagnosis," *Age and Ageing*, vol. 48, no. 1, pp. 16–31, 2019.
- [2] J. Woo, "Sarcopenia," *Clinics in Geriatric Medicine*, vol. 33, no. 3, pp. 305–314, 2017.
- [3] A. J. Cruz-Jentoft and A. A. Sayer, "Sarcopenia," *Lancet*, vol. 393, no. 10191, pp. 2636–2646, 2019.
- [4] M. Ristow, K. Zarse, A. Oberbach et al., "Antioxidants prevent health-promoting effects of physical exercise in humans," *Proceedings of the National Academy of Sciences of the United States of America*, vol. 106, no. 21, pp. 8665–8670, 2009.
- [5] R. C. Smith and B. K. Lin, "Myostatin inhibitors as therapies for muscle wasting associated with cancer and other disorders," *Current Opinion in Supportive and Palliative Care*, vol. 7, no. 4, pp. 352–360, 2013.
- [6] C. C. Sieber, "Malnutrition and sarcopenia," *Aging Clinical and Experimental Research*, vol. 31, no. 6, pp. 793–798, 2019.
- [7] E. Marty, Y. Liu, A. Samuel, O. Or, and J. Lane, "A review of sarcopenia: enhancing awareness of an increasingly prevalent disease," *Bone*, vol. 105, pp. 276–286, 2017.
- [8] R. Patil, K. Uusi-Rasi, M. Pasanen, P. Kannus, S. Karinkanta, and H. Sievanen, "Sarcopenia and osteopenia among 70-80-year-old home-dwelling Finnish women: prevalence and association with functional performance," *Osteoporosis International*, vol. 24, no. 3, pp. 787–796, 2013.
- [9] X. Xu, N. Xu, Y. Wang et al., "The longitudinal associations between bone mineral density and appendicular skeletal muscle mass in Chinese community-dwelling middle aged and elderly men," *PeerJ*, vol. 9, p. e10753, 2021.
- [10] H. Qi, Y. Sheng, S. Chen et al., "Bone mineral density and trabecular bone score in Chinese subjects with sarcopenia," *Aging Clinical and Experimental Research*, vol. 31, no. 11, pp. 1549–1556, 2019.
- [11] X. Xu, J. Yang, Y. Ye et al., "SPTBN1 prevents primary osteoporosis by modulating osteoblasts proliferation and differentiation and blood vessels formation in bone," *Frontiers in Cell and Development Biology*, vol. 9, p. 653724, 2021.
- [12] J. Y. Reginster, C. Beaudart, F. Buckinx, and O. Bruyere, "Osteoporosis and sarcopenia: two diseases or one?," *Current Opinion in Clinical Nutrition and Metabolic Care*, vol. 19, no. 1, pp. 31–36, 2016.
- [13] J. Isaacson and M. Brotto, "Physiology of mechanotransduction: how do muscle and bone "talk" to one another," *Clinical Reviews in Bone and Mineral Metabolism*, vol. 12, no. 2, pp. 77–85, 2014.
- [14] G. van Niel, G. D'Angelo, and G. Raposo, "Shedding light on the cell biology of extracellular vesicles," *Nature Reviews. Molecular Cell Biology*, vol. 19, no. 4, pp. 213–228, 2018.

- [15] C. Chen, Y. Luo, W. He et al., "Exosomal long noncoding RNA LNMAT2 promotes lymphatic metastasis in bladder cancer," *The Journal of Clinical Investigation*, vol. 130, no. 1, pp. 404–421, 2020.
- [16] L. Gan, D. Xie, J. Liu et al., "Small extracellular microvesicles mediated pathological communications between dysfunctional adipocytes and cardiomyocytes as a novel mechanism exacerbating ischemia/reperfusion injury in diabetic mice," *Circulation*, vol. 141, no. 12, pp. 968–983, 2020.
- [17] B. Zhang, Y. Yang, L. Xiang, Z. Zhao, and R. Ye, "Adipose-derived exosomes: a novel adipokine in obesity-associated diabetes," *Journal of Cellular Physiology*, vol. 234, no. 10, pp. 16692–16702, 2019.
- [18] S. C. Liu, Q. Z. Sun, X. F. Qiao et al., "LncRNA TUG1 influences osteoblast proliferation and differentiation through the Wnt/ $\beta$ -catenin signaling pathway," *European Review for Medical and Pharmacological Sciences*, vol. 23, no. 11, pp. 4584–4590, 2019.
- [19] S. Y. Jiang, Y. X. Miao, T. Hirokazu, S. Z. Zhu, and J. S. Lu, "Effects of lncRNA DANCR on proliferation and differentiation of osteoblasts by regulating the Wnt/ $\beta$ -catenin pathway," *European Review for Medical and Pharmacological Sciences*, vol. 23, no. 13, pp. 5558–5566, 2019.
- [20] K. R. Matee, A. M. Akinnuga, A. Siboto, P. Ngubane, and A. Khathi, "Bredemolic acid restores glucose utilization and attenuates oxidative stress in palmitic acid-induced insulin-resistant C2C12 cells," *Endocrine Regulations*, vol. 56, no. 2, pp. 126–133, 2022.
- [21] X. Wang, X. Liu, and H. Wang, "Combination regimen of granulocyte colony-stimulating factor and recombinant human thrombopoietin improves the curative effect on elderly patients with leukemia through inducing pyroptosis and ferroptosis of leukemia cells," *Cancer Gene Therapy*, pp. 1–9, 2022.
- [22] X. Chen, J. Zhong, D. Dong, G. Liu, and P. Yang, "Endoplasmic reticulum stress-induced CHOP inhibits PGC-1 $\alpha$  and causes mitochondrial dysfunction in diabetic embryopathy," *Toxicological Sciences*, vol. 158, no. 2, pp. 275–285, 2017.
- [23] J. X. Zhong, L. Zhou, Z. Li, Y. Wang, and J. F. Gui, "Zebrafish Noxa promotes mitosis in early embryonic development and regulates apoptosis in subsequent embryogenesis," *Cell Death and Differentiation*, vol. 21, no. 6, pp. 1013–1024, 2014.
- [24] D. J. Ham, A. Borsch, S. Lin et al., "The neuromuscular junction is a focal point of mTORC1 signaling in sarcopenia," *Nature Communications*, vol. 11, no. 1, p. 4510, 2020.
- [25] S. Moverare-Skrtec, K. H. Nilsson, P. Henning et al., "Osteoblast-derived NOTUM reduces cortical bone mass in mice and the NOTUM locus is associated with bone mineral density in humans," *The FASEB Journal*, vol. 33, no. 10, pp. 11163–11179, 2019.
- [26] X. Zhou, L. F. Wu, W. Y. Wang et al., "Anxa2 attenuates osteoblast growth and is associated with hip BMD and osteoporotic fracture in Chinese elderly," *PLoS One*, vol. 13, no. 3, p. e0194781, 2018.
- [27] D. D. Davis, J. G. Ginglen, Y. H. Kwon, and C. I. Kahwaji, *EMS Traction Splint*, In StatPearls, Treasure Island (FL), 2022.
- [28] F. Firat Ozer, S. Akin, T. Soysal, B. M. Gokcekuyu, and G. Erturk Zararsiz, "Relationship between dysphagia and sarcopenia with comprehensive geriatric evaluation," *Dysphagia*, vol. 36, no. 1, pp. 140–146, 2021.
- [29] Y. D. Rong, A. L. Bian, H. Y. Hu, Y. Ma, and X. Z. Zhou, "Study on relationship between elderly sarcopenia and inflammatory cytokine IL-6, anti-inflammatory cytokine IL-10," *BMC Geriatrics*, vol. 18, no. 1, p. 308, 2018.
- [30] S. Ida, R. Kaneko, K. Imataka, and K. Murata, "Association between sarcopenia and renal function in patients with diabetes: a systematic review and meta-analysis," *Journal Diabetes Research*, vol. 2019, article 1365189, 11 pages, 2019.
- [31] E. M. Reijnierse, M. C. Trappenburg, M. J. Leter et al., "Serum albumin and muscle measures in a cohort of healthy young and old participants," *Age (Dordrecht, Netherlands)*, vol. 37, no. 5, p. 88, 2015.
- [32] V. R. D. Santos, D. G. D. Christofaro, I. C. Gomes, J. Viezel, I. F. Junior Freitas, and L. A. Gobbo, "Analysis of relationship of high fat mass and low muscle mass with lipid profile in Brazilians aged 80 years or over," *Diabetes and Metabolic Syndrome: Clinical Research and Reviews*, vol. 11, Supplement 1, pp. S115–S120, 2017.
- [33] C. Szejf, C. K. Suemoto, S. M. Ccps Janovsky, M. D. Barreto, P. A. Lotufo, and I. M. Bensenor, "Thyroid function and sarcopenia: results from the ELSA-Brasil study," *Journal of the American Geriatrics Society*, vol. 68, no. 7, pp. 1545–1553, 2020.
- [34] X. Zhao, X. M. Zhang, N. Yuan, X. F. Yu, and L. N. Ji, "Associations of bone mineral density and bone metabolism indices with urine albumin to creatinine ratio in Chinese patients with type 2 diabetes," *Experimental and Clinical Endocrinology & Diabetes*, vol. 127, no. 1, pp. 50–55, 2019.
- [35] G. H. Li, C. L. Cheung, P. C. Au, K. C. Tan, I. C. Wong, and P. C. Sham, "Positive effects of low LDL-C and statins on bone mineral density: an integrated epidemiological observation analysis and Mendelian randomization study," *International Journal of Epidemiology*, vol. 49, no. 4, pp. 1221–1235, 2020.
- [36] Y. Zhang, Y. X. Huang, D. L. Wang et al., "LncRNA DSCAM-AS1 interacts with YBX1 to promote cancer progression by forming a positive feedback loop that activates FOXA1 transcription network," *Theranostics*, vol. 10, no. 23, pp. 10823–10837, 2020.
- [37] A. Brancatella and C. Marcocci, "TSH suppressive therapy and bone," *Endocrine Connections*, vol. 9, no. 7, pp. R158–R172, 2020.
- [38] M. Y. Wang, Z. Q. Han, X. W. Gong, Q. Li, and J. Ma, "TSH-suppressive therapy can reduce bone mineral density in patients with differentiated thyroid carcinoma: a meta-analysis," *European Review for Medical and Pharmacological Sciences*, vol. 24, no. 2, pp. 922–929, 2020.
- [39] D. Scott, M. Seibel, R. Cumming et al., "Sarcopenic obesity and its temporal associations with changes in bone mineral density, incident falls, and fractures in older men: the concord health and ageing in men project," *Journal of Bone and Mineral Research*, vol. 32, no. 3, pp. 575–583, 2017.
- [40] Q. Xu, Y. Cui, J. Luan, X. Zhou, H. Li, and J. Han, "Exosomes from C2C12 myoblasts enhance osteogenic differentiation of MC3T3-E1 pre-osteoblasts by delivering miR-27a-3p," *Biochemical and Biophysical Research Communications*, vol. 498, no. 1, pp. 32–37, 2018.
- [41] A. N. Kapustin, M. L. Chatrou, I. Drozdov et al., "Vascular smooth muscle cell calcification is mediated by regulated exosome secretion," *Circulation Research*, vol. 116, no. 8, pp. 1312–1323, 2015.

## Retraction

# Retracted: ZFP36 Inhibits Tumor Progression of Human Prostate Cancer by Targeting CDK6 and Oxidative Stress

### Oxidative Medicine and Cellular Longevity

Received 20 June 2023; Accepted 20 June 2023; Published 21 June 2023

Copyright © 2023 Oxidative Medicine and Cellular Longevity. This is an open access article distributed under the Creative Commons Attribution License, which permits unrestricted use, distribution, and reproduction in any medium, provided the original work is properly cited.

This article has been retracted by Hindawi following an investigation undertaken by the publisher [1]. This investigation has uncovered evidence of one or more of the following indicators of systematic manipulation of the publication process:

- (1) Discrepancies in scope
- (2) Discrepancies in the description of the research reported
- (3) Discrepancies between the availability of data and the research described
- (4) Inappropriate citations
- (5) Incoherent, meaningless and/or irrelevant content included in the article
- (6) Peer-review manipulation

The presence of these indicators undermines our confidence in the integrity of the article's content and we cannot, therefore, vouch for its reliability. Please note that this notice is intended solely to alert readers that the content of this article is unreliable. We have not investigated whether authors were aware of or involved in the systematic manipulation of the publication process.

Wiley and Hindawi regrets that the usual quality checks did not identify these issues before publication and have since put additional measures in place to safeguard research integrity.

We wish to credit our own Research Integrity and Research Publishing teams and anonymous and named external researchers and research integrity experts for contributing to this investigation.

The corresponding author, as the representative of all authors, has been given the opportunity to register their agreement or disagreement to this retraction. We have kept a record of any response received.




### References

- [1] D. Yuan, Y. Fang, W. Chen et al., "ZFP36 Inhibits Tumor Progression of Human Prostate Cancer by Targeting CDK6 and Oxidative Stress," *Oxidative Medicine and Cellular Longevity*, vol. 2022, Article ID 3611540, 24 pages, 2022.



## Research Article

# ZFP36 Inhibits Tumor Progression of Human Prostate Cancer by Targeting CDK6 and Oxidative Stress

Dongbo Yuan,<sup>1,2</sup> Yinyi Fang,<sup>1</sup> Weiming Chen,<sup>1</sup> Kehua Jiang,<sup>2</sup> Guohua Zhu,<sup>2</sup> Wei Wang,<sup>2</sup> Wei Zhang,<sup>2</sup> Ganhua You ,<sup>3</sup> Zhenyu Jia ,<sup>4</sup> and Jianguo Zhu <sup>1,2</sup>

<sup>1</sup>Medical College of Guizhou University, Guiyang, Guizhou Province 550025, China

<sup>2</sup>Department of Urology, Guizhou Provincial People's Hospital, The Affiliated Hospital of Guizhou Medical University, Guiyang, Guizhou Province 550002, China

<sup>3</sup>The Second People's Hospital of Guizhou Province, Guiyang, Guizhou Province 550000, China

<sup>4</sup>Department of Plant and Botany Sciences, University of California of Riverside, Riverside, CA 92521, USA

Correspondence should be addressed to Ganhua You; [ygh0851@163.com](mailto:ygh0851@163.com), Zhenyu Jia; [arthur.jia@ucr.edu](mailto:arthur.jia@ucr.edu), and Jianguo Zhu; [doctorzhujianguo@163.com](mailto:doctorzhujianguo@163.com)

Received 13 June 2022; Revised 26 July 2022; Accepted 4 August 2022; Published 6 September 2022

Academic Editor: Tian Li

Copyright © 2022 Dongbo Yuan et al. This is an open access article distributed under the Creative Commons Attribution License, which permits unrestricted use, distribution, and reproduction in any medium, provided the original work is properly cited.

**Background.** The expression of ZFP36 in previous study was reduced in prostate cancer (PCa) tissues as compared to benign prostate tissues, indicating the potential of ZFP36 as an auxiliary marker for PCa. Further evaluation was conducted in clinical samples for in vitro and in vivo experiments, to prove the potential possibility that ZFP36 dysregulation participated in the malignant phenotype of PCa, to determine its potential mechanism for tumor regulation, and to provide a new theoretical basis for gene therapy of PCa. **Methods.** First, the expression of ZFP36 in prostate tissue and PCa tissue was explored, and the relationship between ZFP36 and clinical features of PCa patients was illustrated. Subsequently, the impact of ZFP36 on the biology of PCa cells and relevant downstream pathways of ZFP36's biological impact on PCa were elucidated. Finally, whether oxidative stress mediated the regulation of ZFP36 in PCa was verified by the determination of oxidative stress-related indicators and bioinformatics analysis. **Results.** The downregulation of ZFP36 in PCa tissue had a positive correlation with high Gleason scores, advanced pathological stage, and biochemical recurrence. ZFP36 was identified as an independent prognostic factor for PCa patients' BCR-free survival ( $P = 0.022$ ) by survival analysis. Following a subsequent experiment of function gain and loss, ZFP36 inhibited the proliferation, invasion, and migration in DU145 and 22RV1 cells and inhibits tumor growth in the mouse model. Additionally, high-throughput sequencing screened out CDK6 as the downstream target gene of ZFP36. Western blot/Q-PCR demonstrated that overexpression of ZFP36 could reduce the expression of CDK6 at both cellular and animal levels, and the dual-luciferase experiment and RIP experiment proved that CDK6 was the downstream target of ZFP36, indicating that CDK6 was a downstream target of ZFP36, which mediated tumor cell growth by blocking cell cycle at the G1 stage. Furthermore, ZFP36 inhibited oxidative stress in PCa cells. **Conclusions.** In PCa, ZFP36 might be a tumor suppressor that regulated growth, invasion, and migration of PCa cells. The lately discovered ZFP36-CDK6 axis demonstrated the molecular mechanism of PCa progression to a certain extent which might act as a new possible therapeutic target of PCa therapy.

## 1. Introduction

The proteins controlling multiple cellular phenotypes of proliferation, differentiation, apoptosis, cell invasion, cell cycle, and angiogenesis, once with abnormal expression, can cause the exacerbation of cancer initiation and progression [1]. The influential factor for such protein synthesis is

positively correlated with the cytoplasmic concentrations of the corresponding mRNAs and consequently depends on the kinetics of mRNA synthesis and degradation. It has been recognized that 2 in 3 of the variation in protein abundance of mammalian cells are accounted for the mechanism of posttranscription [2]. Posttranscriptional regulation is critical for biological processes and pathologies [3–5]. Both

miRNAs and RNA-binding proteins (RBPs) have been identified as the principal decisive factors for posttranscriptional control [6]. As noncoding protein RNAs, miRNAs are known as small as 22 nt, and they negatively mediate the expression of genes on posttranscription, cleavage the target mRNAs by primarily binding to the 3'-untranslated regions (UTRs) of targets, and inhibit translation process when complementary sites are insufficient [7]. Through participating in the whole processes of posttranscriptional regulation, the RBPs determine cell fate and function of transcripts and ensure cellular homeostasis. These proteins can create frequent dynamic interactions with coding and noncoding RNAs and additional proteins, thereby mediating RNA shearing, translation, stability, and degradation [8, 9]. In different cancer types, RBPs are dysregulated, thereby affecting the expression of both oncoproteins and tumor suppressor proteins as well as corresponding functions. Therefore, investigation of interrelationship between RBPs and the corresponding targets of cancer-associated RNA can benefit a lot in tumor biology recognition and it may identify potential targets for cancer management.

The best phenotype of RNA-binding protein is Tristetraprolin (TTP) and recognized as ZFP36, G0S24, Nup475, and TIS11. The property of the TTP family includes three cysteine (C) residues and one histidine (H) residues. ZFP36 or TTP, ZFP36L1, and ZFP36L2 are the human members in the family [10]. The TTP family binds to AREs with a specific sequence and structure via the zinc finger domain. Meanwhile, it can catalyze poly (a) tail removal, as a result of mRNA attenuation. It has been revealed by genomic analysis that AREs present in at least 11% of human genes, and all ten molecular mechanisms defined as "cancer hallmarks" include ARE-containing genes [11, 12]. AREs can bind to proteins, namely, TTPs, and they ensure the stability of transcripts or the direct damage of them [13]. As commonly seen in various mRNAs encoding cancer-related proteins, the expression and/or activity of ARE-BPs is associated with tumorigenesis or progression of tumors. Some studies have reported that model mice with TTP knockout perform normal behaviors at birth, but develop a systemic inflammatory syndrome within 2-3 weeks, including cachexia, arthritis, myeloid hyperplasia, and autoimmune diseases [14]. TTP can directly mediate zinc finger E-box-binding homeobox 1 (ZEB1), SRY gene 9 (SOX9), EMT regulators, and colon cancer metastasis-associated 1 (MACC1); all of these factors are downregulated in colorectal cancer [15]. TTPs play an important role as tumor suppressors; it has been found that MYC oncoprotein can directly inhibit the transcription of TTP; the inhibition of which may be a feature of MYC-involved malignancies [16]. Taken together, the previously described studies have demonstrated the intimate and complicated relationship between ARE-BPs and cell growth, apoptosis, angiogenesis, and the development stages of tumors.

Prostate cancer (PCa) ranks the fifth of malignant tumors in global tumor incidence and the second mortal malignant tumor in the world (after lung cancer) [17-19]. Despite multiple mRNAs encoding tumorigenic products being possibly mediated by AREBPs, dysregulation of

ARE-BP expression and/or activity in PCa development remains unknown. Our previous study indicated a marked decrease of ZFP36 protein expression in PCa tissues versus non-PCa tissues, which indicated that this protein was involved in PCa progression [20].

To address this issue, we employed a database to analyze ZFP36 expression in PCa. Meanwhile, the association between clinicopathological features and prognosis was also explored. Given that we observed expression of ZFP36 was reduced in many cancers, we predicted that reducing ZFP36 levels might increase the tumorigenic phenotype. To validate this model, experiments were performed at the cell and animal levels. Further, high-throughput sequencing and bioinformatics methods were conducted to determine the specific mechanism by which ZFP36 was involved in tumors. These results would help to provide personalized and precise treatment for PCa patients.

## 2. Materials and Methods

**2.1. Patient Enrollment and Sample Collection.** The experiments of the present study have gained the approval of human study ethics committees at MGH, Boston, MA, and Ministry of Public Health of P.R. China. The recruited patients have signed written informed consent. And the specimens have been collected anonymously as per the ethical and legal laws and regulations.

**2.2. Cell Preparation.** Human PCa cell lines DU145, PC-3, 22RV1, and LNCap were from the American Type 6 Culture Collection. By the addition of 10% fetal bovine serum and relevant agents, the cells were cultured in RPMI 1640 medium (Hyclone, USA). Following cell line resuscitation and characterization, passage culture was performed in the laboratory for around 3 months. Reauthentication was not conducted to the cell lines. Short Tandem Repeat (STR) profiling was employed for detection of misidentification, cross-contamination, and genetically drifted cells. The amplification of 17 STR loci plus amelogenin was conducted using the Promega's PowerPlex® 18D System before being kept in a humidified chamber at 37°C with 5% CO<sub>2</sub>.

**2.3. Animals.** All tests followed guidelines of Laboratory Animal Research of Guangzhou Medical University. Twenty male BALB/c nude mice aged 4~5 weeks were from Guangdong Medical Laboratory Animal Center. They were raised in wire-top, sawdust-bedding cages with five in each. The animal room was isolated and clean, with an air conditioner, and the room temperature was set at 25-26°C, relative humidity around 50%, and photoperiod 12:12 h.

**2.4. Cell Line Construction and Transfection.** Virus particles were harvested based on instructions of the SBI packaging protocol of Lenti-Concentin Virus Precipitation Solution (Cat No. LV810A-1). Both cells DU145 and LNCap were infected using the TransDux virus transduction reagent (Cat No. LV850A-1) (SBI, USA). The following isolation used a flow cytometer, and the infected cells were cultured in 96-well plates [21].

**2.5. qRT-PCR.** Expression levels of ZFP36, TGFBR2, LAMC1, CDK6, NKX3-1, PCDH7, PARVA, and KRT14 mRNA in xenograft tumors, clinical PCa tissues, and cell lines were determined via qRT-PCR assays as per procedures of our previous study [22].

**2.6. Western Blot Analysis.** Expression of PCa cell line proteins, xenograft tumors, and PCa tissues was determined using western blot as per procedures of our previous study [22].

**2.7. Immunohistochemistry.** Immunohistochemistry was conducted to examine the expression patterns of MMP9, vimentin, Ki-67, E-cadherin, and caspase-3 proteins and their subcellular locations in subcutaneous tumors of animals. Meanwhile, immunoreactivity score (IRS) of vimentin was obtained based on previously described procedures in our study.

**2.8. Xenograft Model Construction In Vivo.** We subsequently performed tumor formation assay in vivo. After transfection of DU145 or 22RV1 cells with ZFP36, NC lentivectors were trypsinized for suspension in phosphate-buffered saline (PBS). Each nude mouse was subcutaneously injected with the following cells (5 per group): DU145 at a concentration of  $1 \times 10^6$ , 22RV1 at a mixture of  $2 \times 10^6$  of 10 mg/mL. In a 4-day interval, the tumor sizes were measured when available for measurement. The calculation of tumor volume was as per  $V(\text{mm}^3) = \text{width}^2 (\text{mm}^2) \times \text{length} (\text{mm}) / 2$ . The animals were sacrificed for the experiments on days 36 and 44 for DU145 and 22RV1, respectively. They were fed in accordance with the protocols of Laboratory Animal Research at Guangzhou Medical University [23].

**2.9. Luciferase Reporter Assay.** ZFP36 targeted gene expression in DU145 cells was determined through luciferase reporter assays. Putative complementary site of ZFP36 at CDK6 mRNA 3'-UTR or mutant sequence was cloned into the luciferase reporter vector psiCHECK-2 (Promega, USA). DU145 cells were cotransfected with 50 nM ZFP36 mimic or the negative control and 0.5  $\mu\text{g}$  of psiCHECK-2-ZFP36-3'-UTR-WT or psiCHECK-2-ZFP36-3'-UTR-MUT. Following 48 h, cells were harvested for analysis using Dual-Luciferase Reporter Assay System (Promega, USA). Simultaneously, the GloMax fluorescence reader (Promega, USA) was employed to generate firefly and renilla luciferase signals, and the latter was normalized the firefly luciferase signals [24].

**2.10. Transwell Assays.** To further determine invasion and migration of cells, Transwell and scratch wound-healing motility was performed following procedures described previously.

**2.11. RNA Immunoprecipitation Assay.** Cells were scraped from the Petri dish and collected into a 1.5 mL tube, resuspended the magnetic beads, suck 50  $\mu\text{L}$  of the resuspended magnetic bead suspension into each Eppendorf tube, resuspend the magnetic beads with 100  $\mu\text{L}$  of RIP wash buffer, add about 5  $\mu\text{g}$  of the corresponding antibody into each sample, put the Eppendorf tube on the magnetic rack, remove

the supernatant, add RIP immunoprediction buffer into each tube, take 50  $\mu\text{L}$  of supernatant as input for RNA, and put the remaining supernatant into the magnetic bead antibody complex. The total volume was 1 mL and incubated at 4°C for 3. Add 500  $\mu\text{L}$  RIP wash buffer, place the Eppendorf tube on the magnetic frame after vortex vibration, discard the supernatant, and repeat cleaning 6 times; after rinsing, resuspend the magnetic beads with 100  $\mu\text{L}$  RIP immunoprediction buffer, take 20  $\mu\text{L}$  magnetic beads for each group, add loading buffer to cook the sample, centrifuge at 12000 rpm/min and 4°C for 3 min, and do western blot, and the rest is used to extract RNA.

**2.12. Apoptosis Assay.** Apoptosis of the cells was ultimately examined utilizing the APC-conjugated Annexin V Kit (BD Biosciences, USA) and 7-aminoactinomycin D (Multi-sciences, China) as per the procedures described in our previous studies.

**2.13. Enzyme-Linked Immunosorbent Assay (ELISA).** ELISA was conducted to detect SOD, MDA, and ROS of DU145 cell as per instructions of use. Briefly, ELISA kits were equilibrated at room temperature; 50  $\mu\text{L}$  of standard solution and sample was supplied to the sample plates. After being added with 100  $\mu\text{L}$  detection antibody, the well plate was sealed with sealing film and cultured at 37°C for 60 min. 50  $\mu\text{L}$  substrate was provided to each well and incubated in the dark for 15 min. After incubation, stop solution at 50  $\mu\text{L}$  was supplemented, and the OD values at 450 nm were measured for each well.

**2.14. Data Download and PPI Network Construction.** Data related to prostate cancer and oxidative stress were obtained from the database <https://www.ncbi.nlm.nih.gov/geo/query/acc.cgi?acc=GSE119005>, and PPI diagram was constructed using STRING (<http://string-db.org>).

**2.15. GO Enrichment Analysis.** Obtained DEGs were subjected to Gene Ontology (GO) analysis with the help of the R software packages clusterProfiler, enrichplot, and ggplot2. Only pathways with both *P* and *Q* values less than 0.05 were regarded as high enrichment.

**2.16. Statistical Analysis.** SPSS and SAS 9.1 were employed for statistical analysis of the obtained data. Continuous variables were expressed as  $\bar{X} \pm s$ . Wilcoxon signed-rank tests were employed for statistically analyzing qRT-PCR and western blot. Fisher's exact tests were conducted for all  $2 \times 2$  tables and Pearson  $\chi^2$  tests for non- $2 \times 2$  tables. Such tests were carried out by two biostatisticians independently. Kolmogorov-Smirnov (K-S) was conducted to test whether the ZFP36 expression was normally distributed. The interrelationship between ZFP36 expression and clinical pathology features of PCa patients in the Taylor dataset was detected using Mann-Whitney *U* tests and Kruskal-Wallis *H* tests. Survival analysis utilized the Kaplan-Meier method, and Cox regression was conducted for univariate and multivariate analyses,  $n = 3$ . *P* values less than 0.05 were regarded as significant statistical difference.

### 3. Results

**3.1. ZFP36 Expression Is Decreased in Human PCa Cells and Tissues.** First, ZFP36 mRNA expression in all tumors and corresponding healthy tissues was assessed via TCGA database, implying that ZFP36 mRNA expression of most normal tissues in this database was elevated compared to the corresponding cancer tissues (Figure 1(a)); this also fully demonstrated that ZFP36 played a tumor suppressor role in most tumors. Then, the mRNA expression of ZFP36 was evaluated in PCa and normal tissues in TCGA and Taylor public databases (TCGA contains 498 PCa and 52 normal tissues; Taylor contains 150 PCa and 29 normal tissues). The level of ZFP36 mRNA in TCGA database was increased in the normal prostate tissue as compared with PCa (normal:  $13.04 \pm 1.35$ ; cancer:  $12.49 \pm 1.52$ ,  $P = 0.012$ ) (Figure 1(b)), while via Taylor database, the expression of ZFP36 mRNA in normal prostate tissue was lower than that in PCa (normal:  $9.03 \pm 0.76$ ; cancer:  $9.47 \pm 0.97$ ,  $P = 0.024$ ) (Figure 1(c)). The results in the two databases were inconsistent, but TCGA database included larger sample size, more convincing, and greater reliability. We further tested the expression level of ZFP36 in healthy prostate epithelial cells (RWPE-1), prostate hyperplastic cells (BPH-1), and four PCa cell lines (LNCap, DU145, 22RV1, and PC3). The findings revealed that ZFP36 in RWPE-1 and BPH-1 were highly expressed, but were down-regulated in PCa cell lines (Figure 1(d)). We used DU145 and 22RV1 cells for the next experiment.

**3.2. Decreased Expression of Zn in Human PCa Tissues.** Zinc finger proteins refer to a class of proteins that contain short, self-folding “finger” structures that are stabilized by binding  $Zn^{2+}$ . Human prostates contain higher levels of zinc than most tissues [25]. Unluckily, cellular metabolic alteration exerts an important role in prostate malignancy and has been greatly neglected. Several important factors including zinc have been identified and involved in PCa progression. We reviewed the previous literature summary as shown in Table 1, and we drew the following conclusions: the zinc concentration in healthy prostate tissues and benign prostatic hyperplasia tissue was markedly higher than that in PCa. The marked reduction of zinc concentration in malignant cells represents the biochemical feature of PCa, which is consistent with our findings above that observed decreased expression of zinc finger proteins in PCa.

**3.3. The Correlation between ZFP36 Expression and Pathological Features of PCa Patients.** Furthermore, we used TCGA and Taylor public databases to analyze the correlation between ZFP36 mRNA expression and PCa patients' clinical features. As shown in Table 2 via TCGA database, ZFP36 mRNA level was negatively correlated with Gleason score ( $P = 0.002$ ), pathological stage ( $P = 0.002$ ), and biochemical recurrence ( $P = 0.003$ ); Taylor database indicated that ZFP36 mRNA expression was negatively correlated with Gleason score ( $P < 0.001$ ), pathological stage ( $P = 0.016$ ), distant metastasis ( $P < 0.001$ ), overall survival rate ( $P < 0.001$ ), and biochemical recurrence ( $P < 0.001$ ). Both sug-

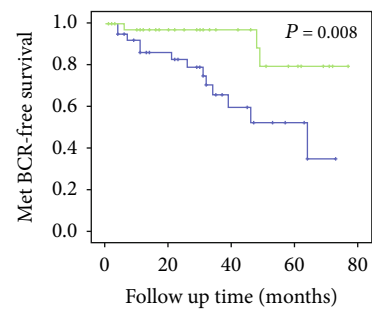
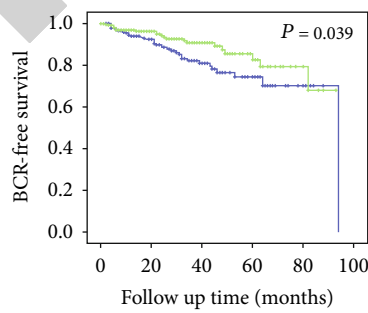
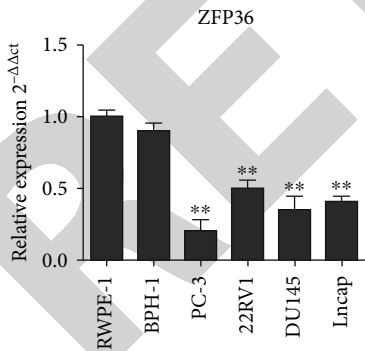
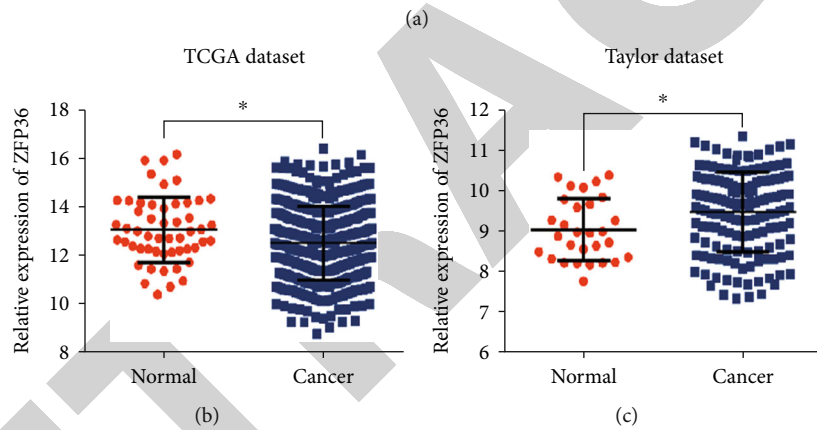
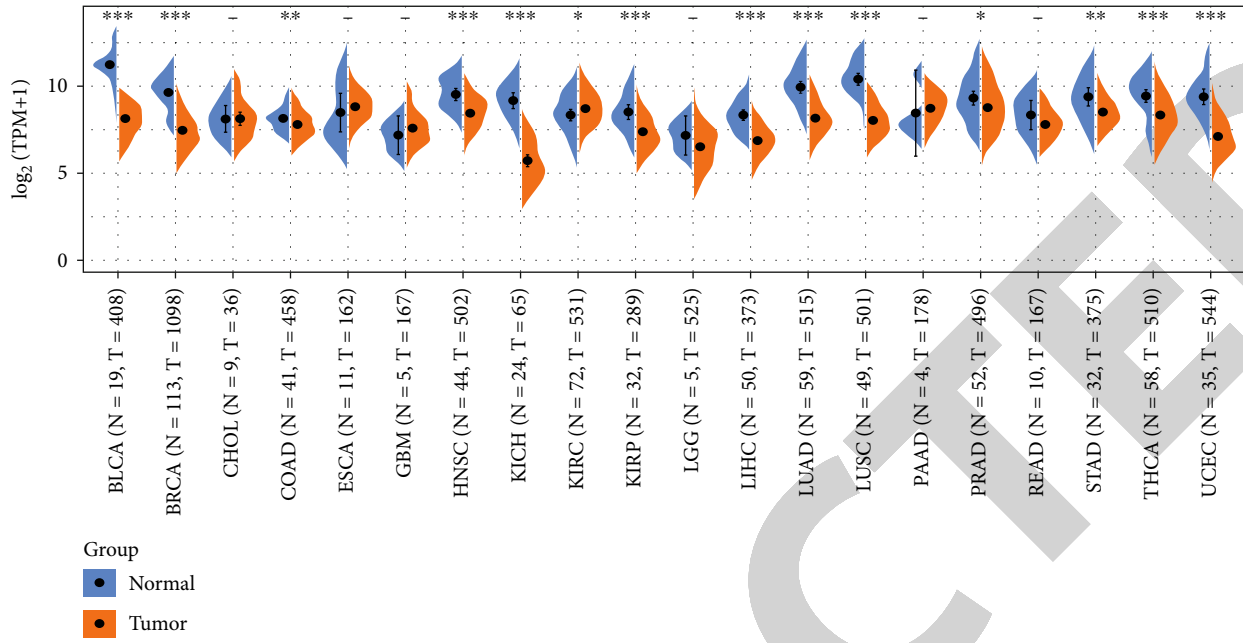
gested that ZFP36 expression had a negative correlation with biological characteristics of malignant prostate tumors.

**3.4. Decreased mRNA Expression Level of ZFP36 Indicates Poor Prognosis of Clinical PCa Patients.** Based on TCGA and Taylor clinical PCa databases, we divided the ZFP36 mRNA expression levels into groups of highly and poorly expressed, respectively, based on median, and analyzed expression level of ZFP36 by Kaplan-Meier survival curve and log-rank tests. TCGA database findings indicated that the ZFP36 high expression group had markedly high survival rates free from postoperative biochemical recurrence and metastasis biochemical recurrence than the ZFP36 low expression group (Figure 1(e),  $P < 0.05$ ); in the Taylor database and the ZFP36 high expression group, the postoperative biochemical recurrence-free survival and metastasis-free survival were markedly higher compared with the ZFP36 low expression group (Figure 1(f),  $P < 0.05$ ), indicating that ZFP36 could suppress cancer in prostate tumors.

**3.5. The mRNA Expression Level of ZFP36 May Serve as an Independent Indicator for Predicting PCa Patients' Prognosis.** Furthermore, we used the COX regression model and analyzed predictive ZFP36 mRNA levels in TCGA database on the risk of postoperative biochemical recurrence in PCa patients. The results of univariate analysis revealed that ZFP36 expression, Gleason score, pathological stage, clinical stage, and positive margins might be important predictors of biochemical recurrence in PCa patients (Table 3). Multivariate analysis suggested that ZFP36 expression, Gleason score, and clinical stage might be independent predictors of biochemical recurrence in PCa patients. Consistent with the above-mentioned Kaplan Meier detection and log-rank methods, ZFP36 expression might be a potential prognostic indicator used in predicting patient survival and biochemical recurrence after PCa surgery, further revealing the clinical significance of ZFP36 for PCa patients. Based on the above results, we will further explain the biological function and potential molecular mechanism of ZFP36 on PCa development through experiments in vitro and in vivo.

**3.6. ZFP36 Can Mediate Proliferation, Migration, and Invasion of PCa Cells In Vitro.** We used lentiviral infection technology to construct ZFP36 overexpression and knockdown DU145 and 22RV1 cell lines and their corresponding blank control (negative control (NC)) and used western blot to detect the overexpression and knockdown efficiency of ZFP36. As shown in Figures 2(a)–2(d), ZFP36 overexpressed DU145 and 22RV1, the protein expression of ZFP36 was markedly elevated compared with the NC group, while following ZFP36 knockdown DU145 and 22RV1, the protein expression of ZFP36 was greatly reduced compared with the NC group, indicating that the cell line was successfully constructed and could be used for the next experiment.

In the DU145 and 22RV1 cell lines overexpressing ZFP36, the corresponding cell function experiments were performed. The cell proliferation test results (CCK-8 assay) indicated that tumor cells were significantly decreased after ZFP36 overexpression versus control, implying that ZFP36



(d)

(e)

FIGURE 1: Continued.

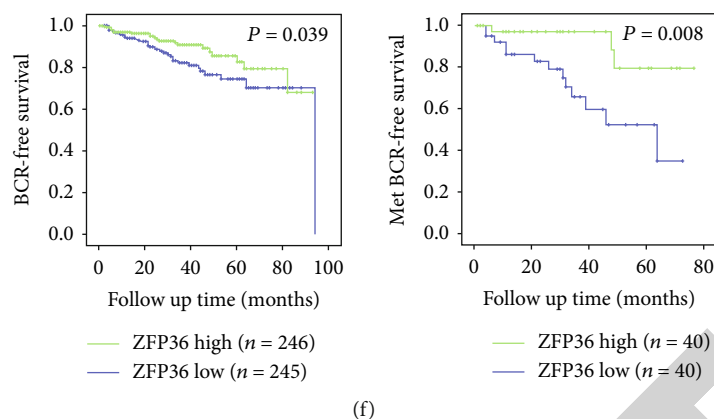


FIGURE 1: (a) ZFP36 expressed higher in normal tissues than cancer tissues based on TCGA database. (b–d) ZFP36 expression in prostate cancer and normal tissues. (e, f) Correlation between ZFP36 expression and PCa patients' survival (\* $P < 0.05$ , \*\* $P < 0.01$ , and \*\*\* $P < 0.001$ ). Note: the sample messages in (b) and (c): TCGA contains 498 PCa and 52 normal tissues; Taylor contains 150 PCa and 29 normal tissues. Sample replicate value  $n = 3$  in (d).

TABLE 1: Zinc in normal, benign prostatic hyperplasia, and PCa tissues (reference data).

Author	Year	Methods	N	Zn ( $\mu\text{g/g}$ dry tissue)				
				Normal Mean	N	BPH Mean	Prostate cancer Mean	
Mawson et al.	1952	SAS	7	895 $\pm$ 96 SE	20	772 $\pm$ 93 SE	5	190 $\pm$ 61 SE
Hoare et al.	1956	SAS	19	744 $\pm$ 124 SE	52	486 $\pm$ 26 SE	18	273 $\pm$ 52 SE
Shirakawa et al.	1961	—	—	790	—	751	—	390
Schrodt et al.	1964	XRF	—	540 $\pm$ 100 SE	9	1902 $\pm$ 395 SE	10	282 $\pm$ 32 SE
GyOrkey et al.	1967	AAS	10	1055 $\pm$ 420	10	3800 $\pm$ 65 SD	10	230 $\pm$ 6 SD
Hienzsich et al.	1970	AAS	60	438	34	855	4	78
GyOrkey et al.	1973	AAS	3	263 $\pm$ 15 SE	8	607 $\pm$ 45 SE	3	80 $\pm$ 7 SE
Mukhitdinov et al.	1975	AES	82	107 $\pm$ 14 SE	61	215 $\pm$ 5 SE	4	147 $\pm$ 11 SE
Wallace et al.	1975	AES	—	—	13	1210 $\pm$ 901 SD	3	432 $\pm$ 238 SD
Habib et al.	1976	AAS	9	447 $\pm$ 79 SE	23	452 $\pm$ 78 SE	9	171 $\pm$ 29 SE
Dunchik et al.	1977	XRF	11	1330 $\pm$ 156 SE	18	1467 $\pm$ 539 SE	23	442 $\pm$ 58 SE
Jafa et al.	1980	AAS	10	2734 $\pm$ 12 SE	10	3770 $\pm$ 13 SE	10	814 $\pm$ 17 SE
Feustel et al.	1982	AAS	16	348 $\pm$ 269 SD	24	774 $\pm$ 524 SD	36	147 $\pm$ 103 SD
Marezyfiska et al.	1983	AAS	8	965 $\pm$ 435 SD	43	851 $\pm$ 410 SD	12	320 $\pm$ 147 SD
Lahtonen et al.	1985	AAS	—	—	15	904 $\pm$ 111 SE	3	160 $\pm$ 57 SE
Feustel et al.	1987	AAS	5	488 $\pm$ 190 SD	10	1177 $\pm$ 485 SD	9	413
Zaichick et al.	1997	XRF	37	1018 $\pm$ 124 SE	50	1142 $\pm$ 77 SE	59	146 $\pm$ 10 SE
Pamela et al.	2011	AAS	20	1009 $\pm$ 155 SD	45	387 $\pm$ 86.1 SD	18	175 $\pm$ 58.6 SD

AES: atomic emission spectrometry; SAS: solution absorption spectrometry; XRF: X-ray fluorescent spectrometry; AAS: atomic absorption spectrometry; SD: standard deviation; SE: standard error of the mean.

could regulate proliferation of PCa tumor cells (Figures 2(e) and 2(h)); then, we performed cell scratch and cell invasion experiments, indicating that overexpression of ZFP36 could greatly suppress migration and invasion of tumor cells versus control (Figures 2(f), 2(i), 2(g), and 2(j)). In general, ZFP36 overexpression could significantly mediate proliferation, invasion, and migration of tumor cells. However, following the inhibition of DU145 and 22RV1 cell lines by

ZFP36, the opposite experimental results were revealed: after ZFP36 inhibition, the number of tumor cells increased significantly, and the migration and invasion capabilities of tumor cells were apparently enhanced.

**3.7. ZFP36 Can Inhibit PCa Growth In Vivo.** In the next step, bilateral armpits of nude mice were injected the constructed ZFP36 stable overexpression cell DU145 and corresponding

TABLE 2: Correlation between ZFP36 mRNA expression and clinical characteristics of PCa patients.

Clinical characteristics	ZFP36 expression in TCGA dataset			ZFP36 expression in Taylor dataset		
	Cases	Mean $\pm$ SD	<i>P</i> value	Cases	Mean $\pm$ SD	<i>P</i> value
<i>ZFP36 expression</i>						
Benign	52	13.04 $\pm$ 1.35	0.012	29	9.03 $\pm$ 0.76	0.024
Cancer	498	12.49 $\pm$ 1.52		150	9.47 $\pm$ 0.97	
<i>Age (years)</i>						
<60	201	12.47 $\pm$ 1.45	0.839	93	9.55 $\pm$ 0.92	0.157
$\geq$ 60	296	12.50 $\pm$ 1.55		57	9.32 $\pm$ 1.05	
<i>Serum PSA (ng/mL)</i>						
<4	—	—	—	24	9.78 $\pm$ 0.92	0.091
$\geq$ 4	—	—	—	123	9.41 $\pm$ 0.98	
<i>Gleason scores</i>						
<8	292	12.66 $\pm$ 1.49	0.002	117	9.72 $\pm$ 0.86	<0.001
$\geq$ 8	206	12.24 $\pm$ 1.52		22	8.74 $\pm$ 0.84	
<i>Clinical stage</i>						
<T2A	177	12.60 $\pm$ 1.49	0.073	80	9.44 $\pm$ 0.96	0.261
$\geq$ T2A	229	12.34 $\pm$ 1.44		65	9.61 $\pm$ 0.93	
<i>Pathological stage</i>						
<T3A	186	12.73 $\pm$ 1.48	0.002	86	9.70 $\pm$ 0.90	0.016
$\geq$ T3A	304	12.31 $\pm$ 1.48		55	9.31 $\pm$ 0.96	
<i>Metastasis</i>						
No	416	12.53 $\pm$ 1.51	0.143	122	9.66 $\pm$ 0.87	<0.001
Yes	82	12.27 $\pm$ 1.56		28	8.61 $\pm$ 0.96	
<i>Overall survival</i>						
Alive	487	12.49 $\pm$ 1.51	0.599	131	9.57 $\pm$ 0.93	<0.001
Die	10	12.23 $\pm$ 1.45		19	8.74 $\pm$ 1.02	
<i>PSA failure</i>						
Negative	439	12.56 $\pm$ 1.51	0.003	104	9.74 $\pm$ 0.88	<0.001
Positive	59	11.95 $\pm$ 1.46		36	9.01 $\pm$ 0.89	
<i>Surgical margin status</i>						
Negative	314	12.52 $\pm$ 1.52	0.727	—	—	—
Positive	153	12.47 $\pm$ 1.49		—	—	

TABLE 3: Correlation between clinicopathological characteristics and biochemical recurrence-free survival of PCa patients.

Parameters	Univariate analysis		Multivariate analysis	
	HR (95% CI)	<i>P</i>	HR (95% CI)	<i>P</i>
ZFP36	0.764 (0.630-0.926)	0.006	0.767 (0.625-0.942)	0.012
Age	1.019 (0.979-1.061)	0.351	1.012 (0.969-1.057)	0.580
Gleason score	2.074 (1.583-2.717)	<0.001	1.842 (1.320-2.572)	<0.001
Pathological stage (T2 vs. T3)	5.110 (2.189-11.928)	<0.001	2.145 (0.839-5.481)	0.111
Clinical stage (<T2A vs. $\geq$ T2A)	3.378 (1.688-6.759)	0.001	2.284 (1.112-4.692)	0.025
Surgical margin (+ vs -)	1.856 (1.087-3.166)	0.023	1.044 (0.554-1.970)	0.893

Note: HR: hazard ratio; CI: confidence interval.

empty vector control cells to construct xenograft tumor models and to remove the tumors from the nude mice subcutaneously after 48 days to measure the tumor size and

weight. The results are shown in Figures 3(a) and 3(b). ZFP36-overexpressed DU145 cells could significantly inhibit subcutaneous tumor growth versus control. We also found

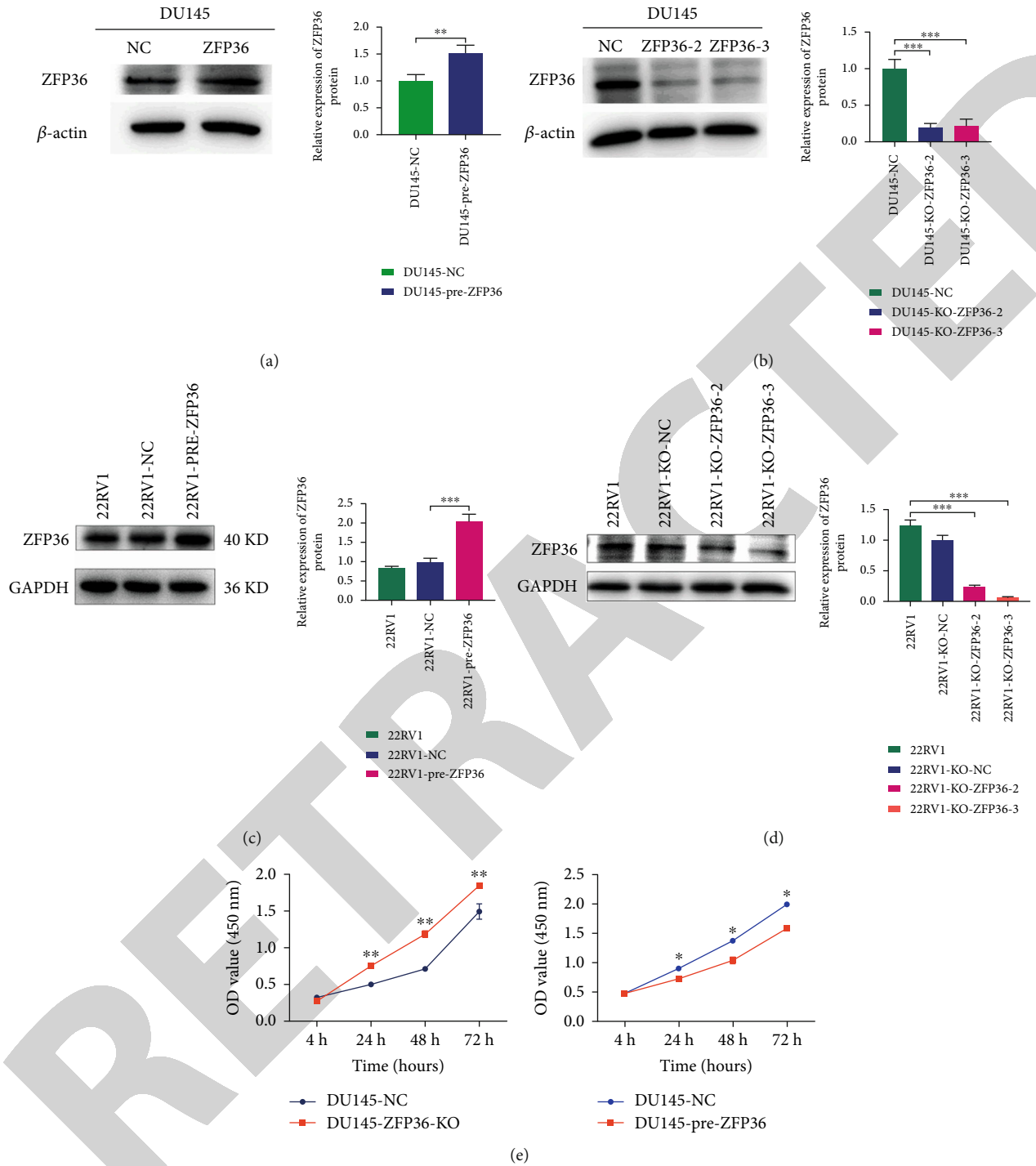
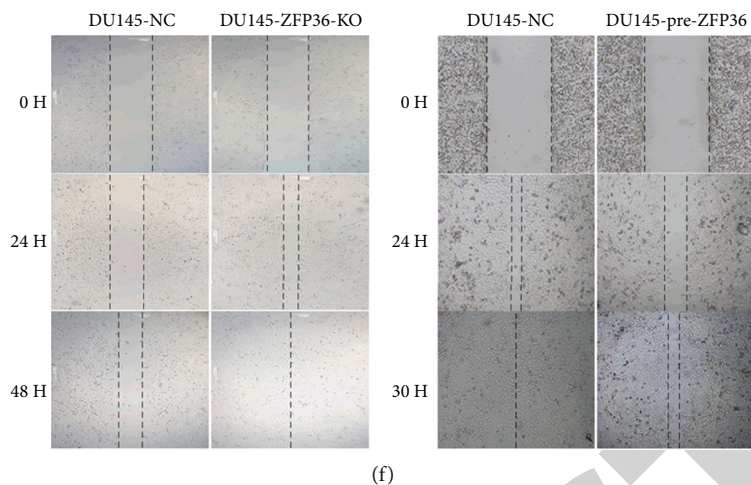
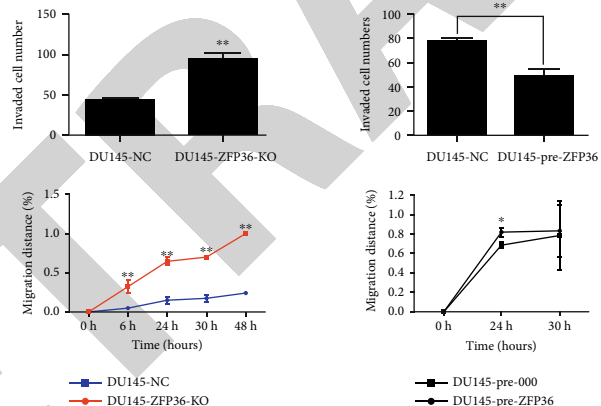
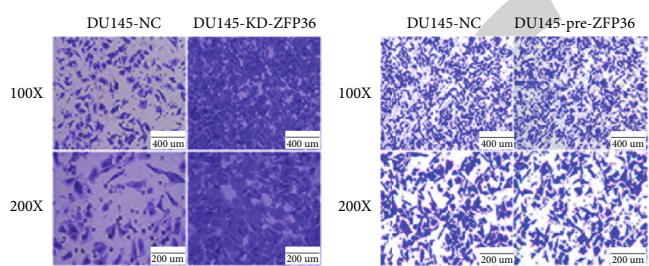


FIGURE 2: Continued.

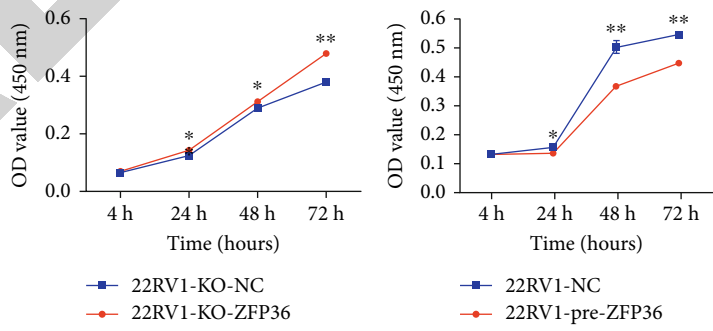




(f)



(g)



(h)

FIGURE 2: Continued.

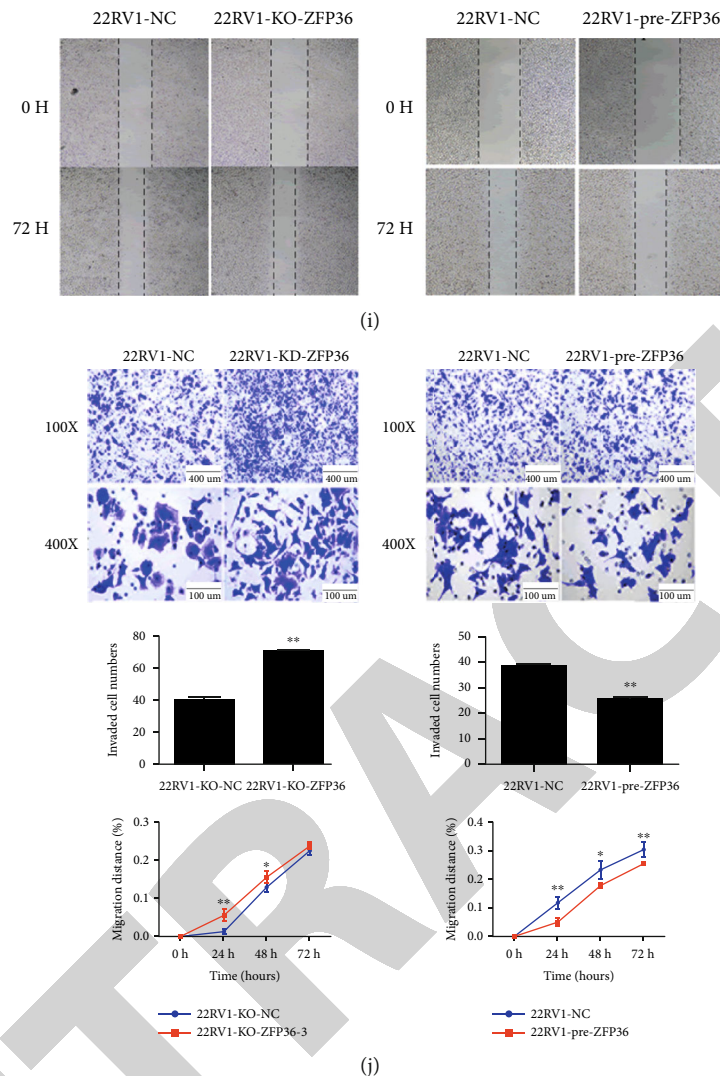


FIGURE 2: (a–d) Western blot verification of ZFP36 overexpression and knockdown models (DU145 and 22RV1). Effects of overexpression and inhibition of ZFP36 on tumor cell (e, h) proliferation (DU145 and 22RV1), (f, i) migration (DU145 and 22RV1), and (g, j) and invasion (DU145 and 22RV1). \*  $P < 0.05$ , \*\*  $P < 0.01$ , and \*\*\*  $P < 0.001$ . Scar bar:  $400 \mu\text{m}$  in the 100x figure and  $200 \mu\text{m}$  in the 200x figure.  $n = 3$ .

that ZFP36 overexpression was consistent in 22RV1 cells (Figures 3(c) and 3(d)); in comparison to the control, overexpressing ZFP36 in 22RV1 markedly inhibited tumor growth of nude mice.

In summary, we carried out in vitro experiments using PCa cell lines implying that ZFP36 could mediate proliferation, invasion, and migration of tumor cells. Meanwhile, in vivo tests have confirmed that ZFP36 inhibited tumor growth. From a cellular perspective, the biological characteristics of ZFP36 were preliminary discovered that might inhibit PCa development.

**3.8. ZFP36 Regulates Prostate Proliferation, Invasion, and Metastasis.** To further understand the molecular biological functions of ZFP36 on PCa, we constructed a DU145-ZFP36-overexpressing PCa subcutaneous xenograft model in nude mice. Tissues were collected and immunohistochemical analysis was conducted, indicating that expression of MMP9, vimentin, and Ki-67 was downregulated after

ZFP36 overexpression compared with the control group, and so as E-cadherin protein expression, whereas it had no obvious effect on the activation of caspase-3 (Figure 3(e)). As a zinc- and calcium-dependent protease family, matrix metalloproteinases (MMPs) can target numerous proteins in the extracellular matrix and promote their degradation. The extracellular matrix and base together constitute the first barrier in the process of tumor metastasis. Therefore, the degradation of the extracellular matrix often intimately links to the malignant invasion and metastasis of tumors. Vimentin expression can promote the decomposition of intercellular junction proteins and reduce the adhesion between epithelial cells. Vimentin's activation of tumor cell microfilaments and tubulin can improve the deformation and infiltration capacity of epithelial cells. Ki67 is a nuclear antigen that exists in proliferating cells. Its expression and function are linked to chromatin and related to cell mitosis, so it is an extensively applied proliferating cell marker. E-cadherin is an important part of maintaining normal

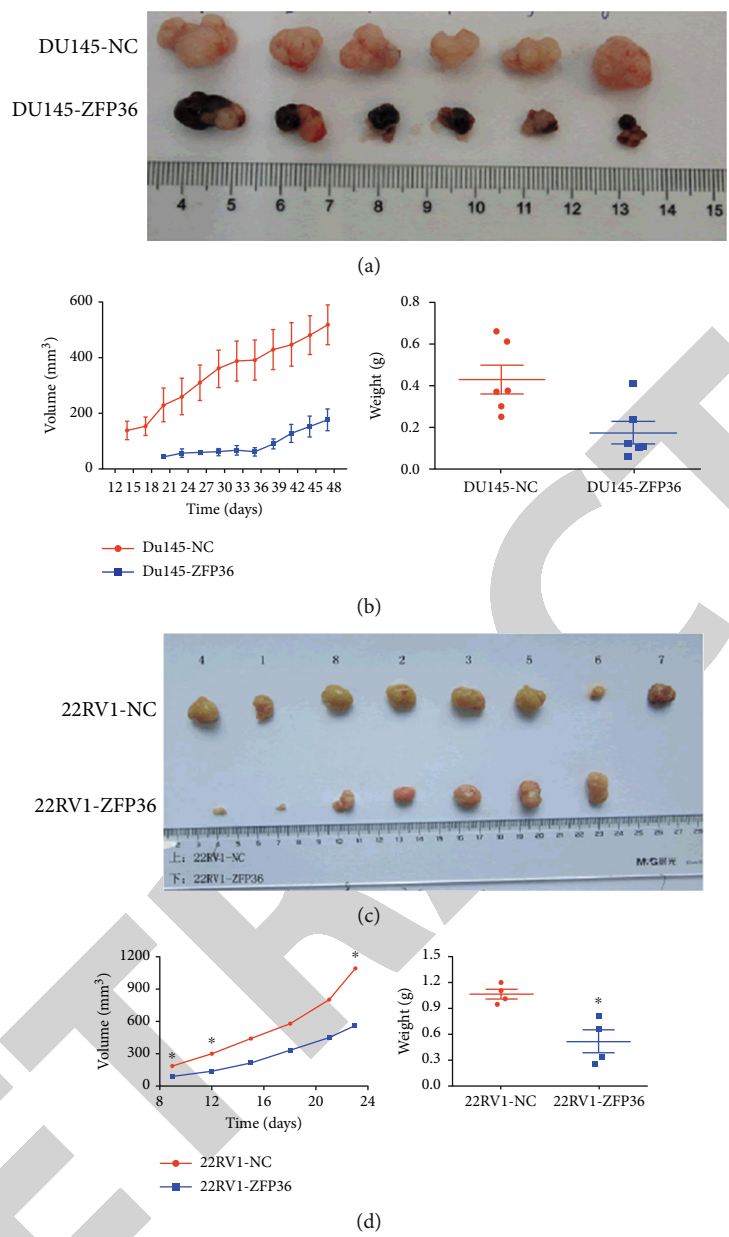


FIGURE 3: Continued.

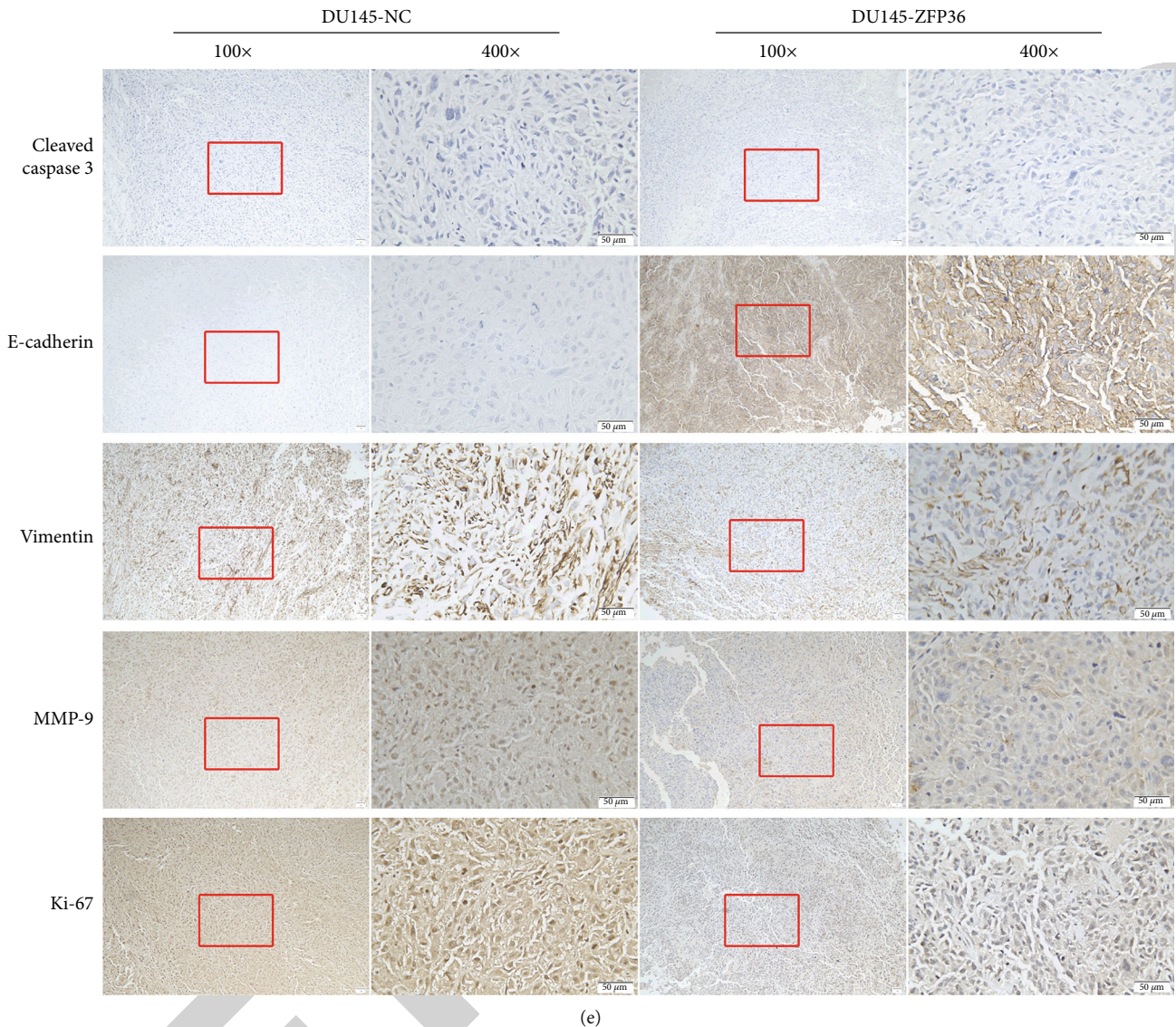


FIGURE 3: (a–d) The nude mouse tumor-bearing model suggests that overexpression of ZFP36 inhibits the growth of prostate cancer xenografts. (e) Immunohistochemistry detection of related protein expression in PCa transplanted tumor tissues (\* $P < 0.05$ , \*\* $P < 0.01$ ). Scar bar: 50  $\mu\text{m}$ . Note: sample replicate values for each time point  $n = 6$  in (b) and  $n = 4$  in (d). Sample replicate value  $n = 3$  in (e).

epithelial cell morphology and cell tissue integrity. It can inhibit tumor cell metastasis and invasion and affect tumor growth and proliferation. When E-cadherin protein expression is downregulated, cells lose their ability to adhere to each other; the tumor cells detach from its original site and then metastasize to lymph nodes or far away. Caspase-3 is a protease and well recognized as the most essential terminal splicing enzyme during apoptosis. Meanwhile, it can regulate CTL cell killing mechanism. Our research results suggest that overexpression of ZFP36 can reduce the expression of MMP9, vimentin, and Ki-67 and promote the expression of E-cadherin, thereby mediating various tumor cell processes, which conforms to our above-mentioned cell function experiments. However, it has no obvious effect on the activation of caspase-3, indicating that it may have no effect on tumor cell apoptosis.

**3.9. Pathways Related to ZFP36 in PCa.** DEGs between ZFP36 inhibition and control DU145 were determined by NGS RNA technique to clarify potential mechanism of ZFP36 in the progression of PCa. Consequently, in DU145 cells inhibited by ZFP36, based on  $|\log_{2}FC| > 1$  of the differential gene, we identified a total of 341 dysregulated genes with 229 upregulated and 112 downregulated (Figure 4(a)). The KEGG enrichment analysis shown in Figure 4(b) shows that the target genes regulated by ZFP36 are mainly related to PI3K-Akt signaling pathway, circadian rhythm, cell matrix adhesion, HIF-1 and Rap1 signaling pathways, and cancer pathway. Meanwhile, GO analysis (Figure 4(c)) revealed that the protein altered by ZFP36 significantly controls multiple biological processes directly related to cancer, namely, cell growth, regulation of cell growth, extracellular matrix tissue, and extracellular structural tissue, involving

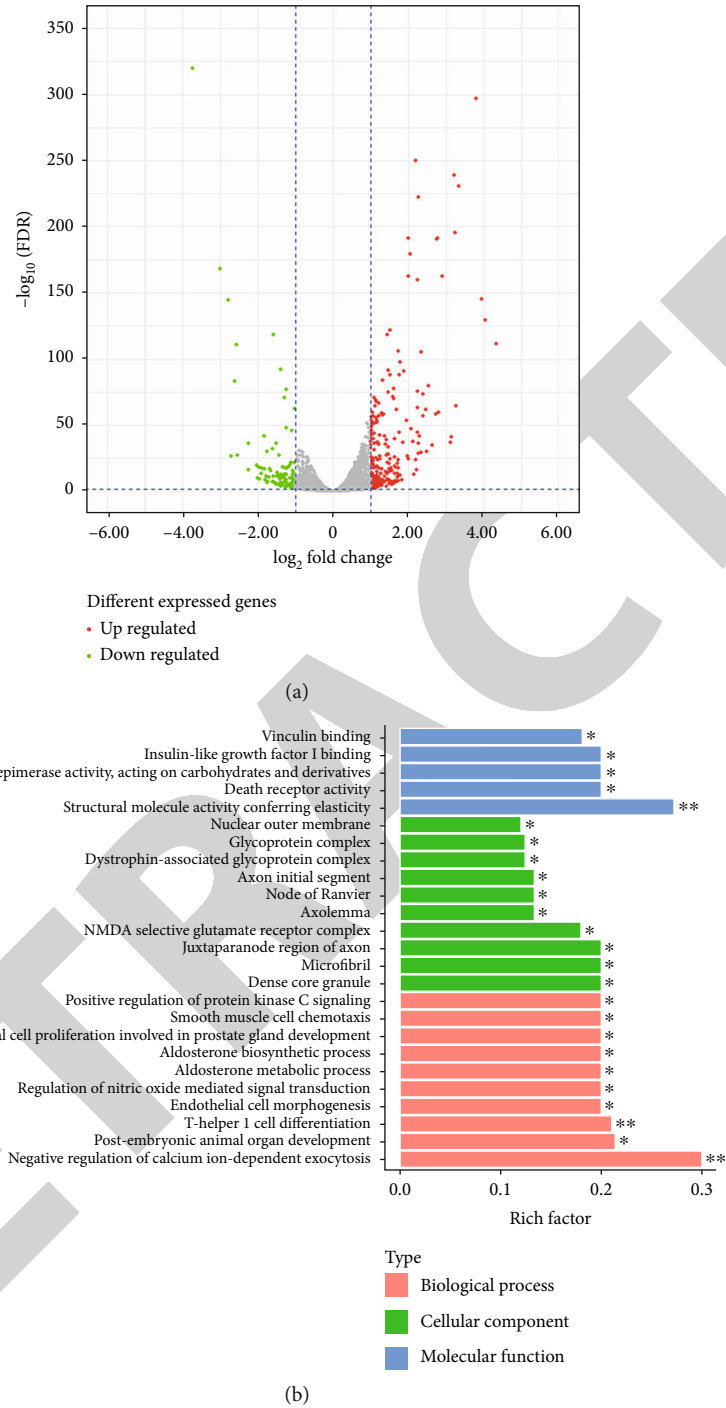


FIGURE 4: Continued.

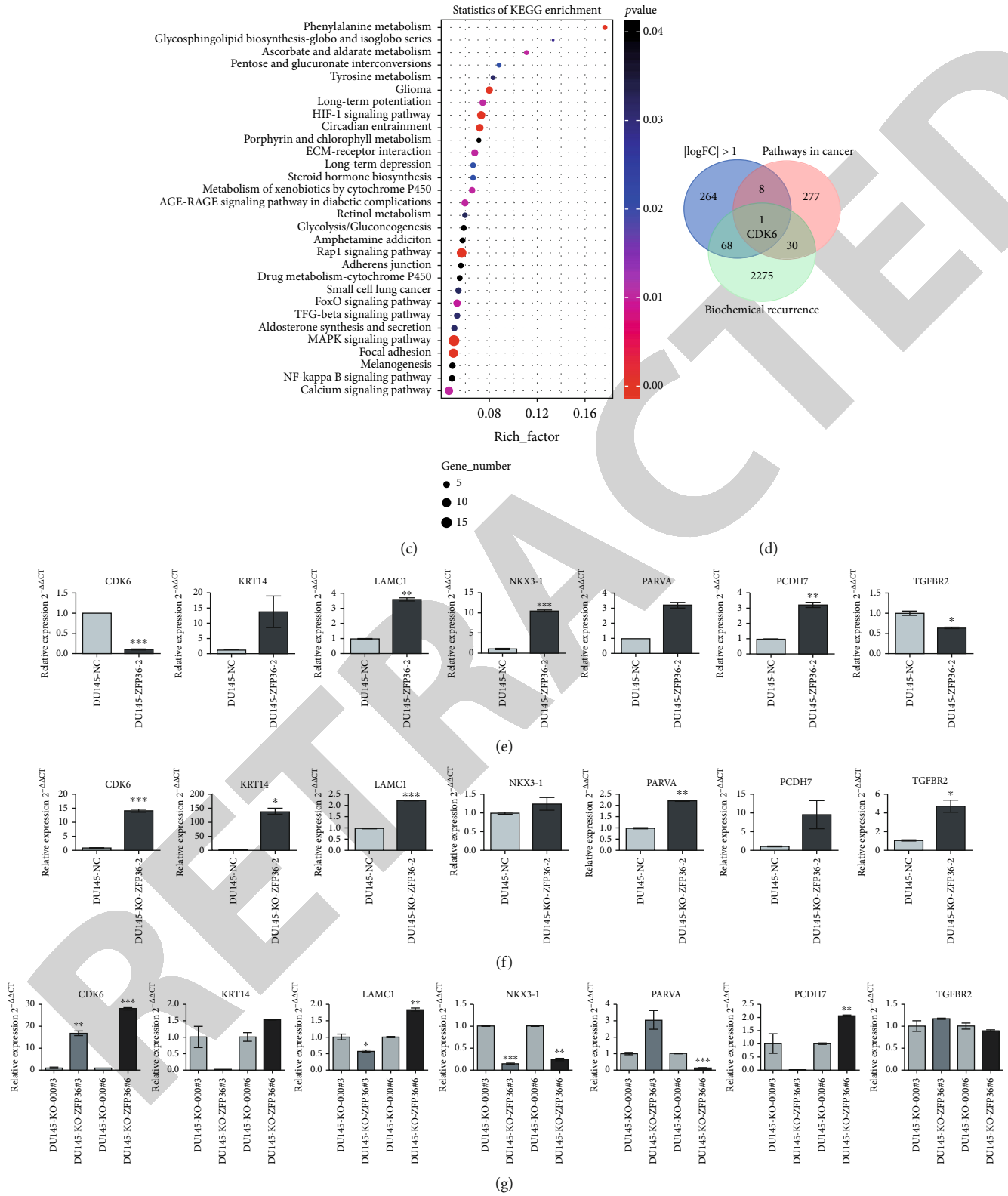


FIGURE 4: Continued.

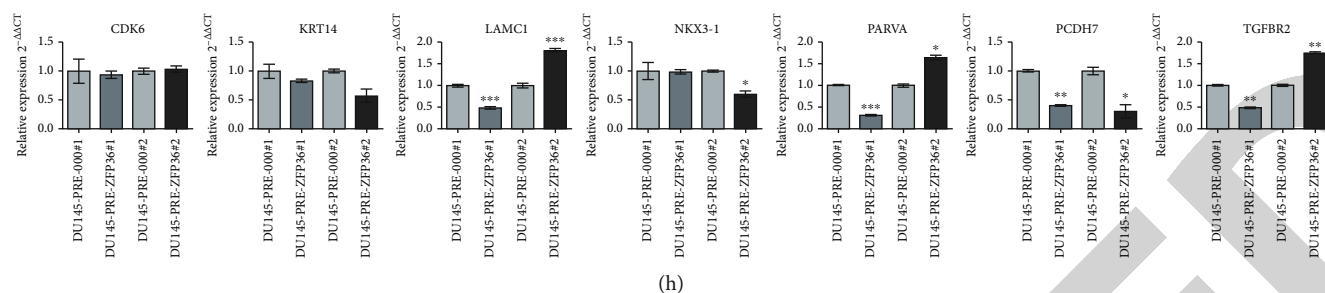


FIGURE 4: The related pathways of ZFP36 in prostate cancer: (a) Volcano diagram, (b) GO, and (c) KEGG pathway enrichment analysis of ZFP36-related genes. (d) Screening map of downstream genes. (e, f) Effects of ZFP36 on the downstream gene (DU145 cell line) mRNA expression and (g, h) animal transplanted tumor tissue (\* $P < 0.05$ , \*\* $P < 0.01$ , and \*\*\* $P < 0.001$ ).  $n = 3$ .

several processes of cell viability and growth, and there is evidence indicating that abnormal regulation of cell viability and growth components may be the cause of tumor formation. Generally, ZFP36 candidate target is associated with a wide range of biological functions related to PCa.

**3.10. CDK6 Is the Direct Target of ZFP36.** According to  $|\log_{2}FC| > 1$  of the differential gene in the DU145-KO-ZFP36 sequencing results, the oncogenes in the KEGG database or the biochemical recurrence meaningful genes in the comprehensive Taylor database were jointly screened for related genes downstream of ZFP36 (TGFBR2, LAMC1, CDK6, NKX3-1, PCDH7, PARVA, and KRT14), but only CDK6 screened for all three of them presented meaningful target genes (Figure 4(d)).

In order to verify this screening, real-time fluorescent quantitative PCR was conducted to detect downstream genes screened in the DU145 cell line after ZFP36 overexpression and knockout. mRNA expression of all genes in DU145 cells knocked out ZFP36 elevated markedly. In DU145 cells that overexpressed ZFP36, CDK6 and TGFBR2 mRNA expression was substantially reduced, but CDK6 reduction was more significant (Figures 4(e) and 4(f)). (CDK6 mRNA expression in the ZFP36 overexpression group decreased significantly, about 0.1144 times as low as control; however, CDK6 mRNA expression increased significantly in the ZFP36 knockout group, about 14.1777 times that of the control group).

Additionally, mRNA levels of downstream genes in nude mouse-transplanted tumor tissues were also determined. The results showed that in the ZFP36 knockout group, the expression of CDK6 was approximately 16.6771 times and 27.7519 times of the control, respectively, with an evident increase (Figure 4(g)), no apparent change was revealed in CDK6 expression in the ZFP36 overexpression group (Figure 4(h)). Furthermore, CDK6 was of vital importance in both PI3K-Akt and cell cycle signaling pathways involved in differentially expressed proteins after ZFP36 inhibition. Therefore, we further verified biological roles of the ZFP36-CDK6 axis in PCa progression in our experiments.

To further illustrate the effect of ZFP36 on the level of CDK6 protein, we detected relative changes in CDK6 protein expression in the ZFP36 overexpression cell line via western blot. The expression of CDK6 protein greatly

reduced in the DU145-ZFP36 group versus DU145-NC (control group) (Figure 5(a)), whereas that of CDK6 was greatly elevated in the DU145-KO-ZFP36 group (Figure 5(b)), indicating that ZFP36 could negatively mediate CDK6 protein expression.

To confirm that ZFP36 targeted CDK6, we constructed the 3'-UTR AU region of CDK6 mRNA. It contains complementary sequence of ZFP36 luciferase reporter gene (wild type). Meanwhile, the 3'-UTR AU region of CDK6 mRNA was deleted and the complementary sequence of ZFP36 (DEL type) luciferase reporter gene (Figures 5(c) and 5(d)). The determination of luciferase activity indicated a great reduction of the expression of CDK6 reporter gene following cotransfection with ZFP36 mimic. Conversely, CDK6 reporter gene changed little with sequence deletion of the same fragment after cotransfection with the ZFP36 mimic (Figure 5(e)). The results revealed that the 3'-UTR AU region ARE sequence of CDK6 mRNA was the complementary site of ZFP36, indicating that CDK6 might be a direct target of ZFP36.

We subsequently employed RNA immunoprecipitation (RIP) to further demonstrate whether there was a direct interaction between ZFP36 protein and CDK6 mRNA. In this experiment, the transfection target protein group was used as the RIP experimental group, and the transfected empty plasmid group was used as the RIP-negative control group. CDK6 was greatly enriched in the experimental group versus control, indicating an interaction between ZFP36 and CDK6 (Figures 5(f) and 5(g)). All of the described results revealed that ZFP36 mediated CDK6 expression negatively by binding to AREs of CDK6.

**3.11. ZFP36 Regulates Prostate Cancer Cell Cycle.** We have shown that ZFP36 can target and negatively regulate CDK6 expression, and CDK6 acts as an essential component of cell cycle signal regulation pathway. Therefore, we further verified whether ZFP36 overexpression and knockout affected PCa cell cycle. Compared with the NC group, DU145 cells at the S+G2 phases were significantly increased following ZFP36 knockout, and the G1 phase was significantly decreased (Figure 6(a)); on the contrary, DU145-pre-ZFP36 at the S+G2 phases were greatly decreased, but increased significantly at the G1 phase (Figure 6(b)), and

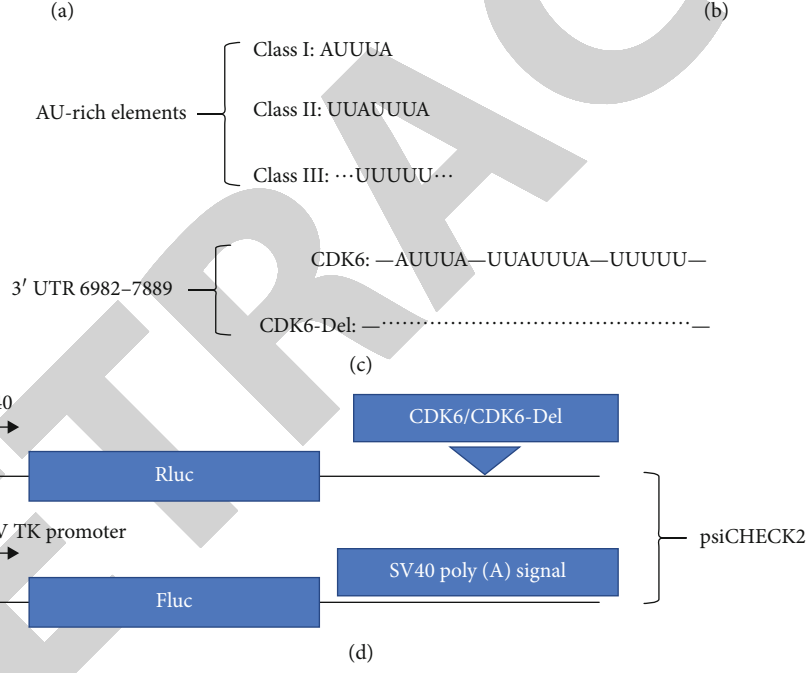
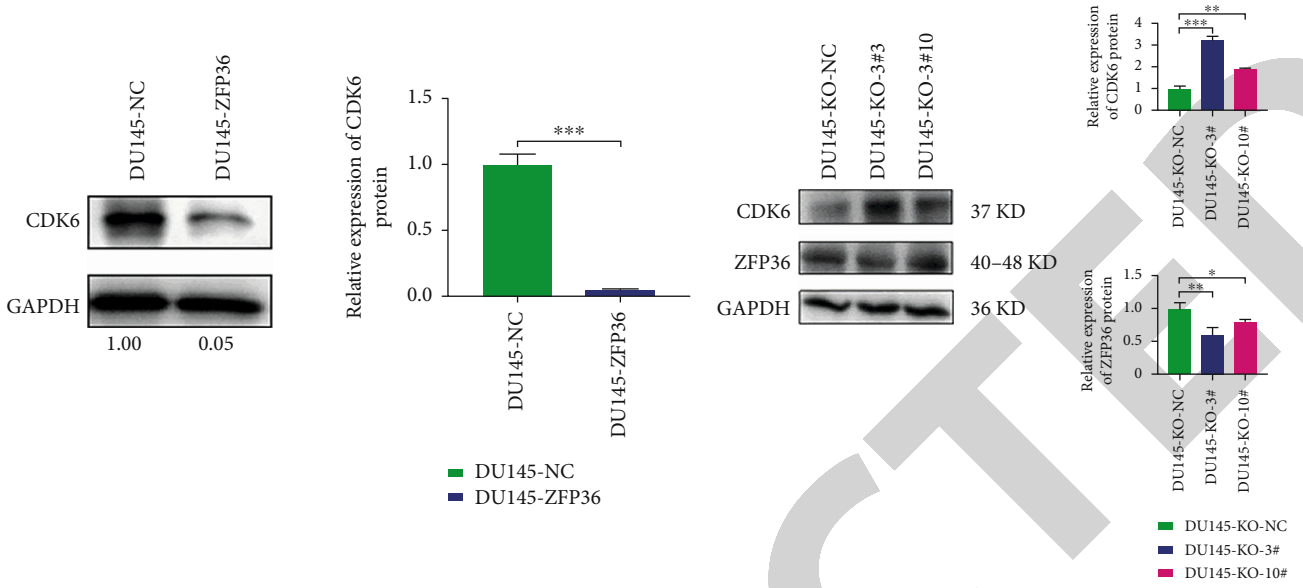


FIGURE 5: Continued.



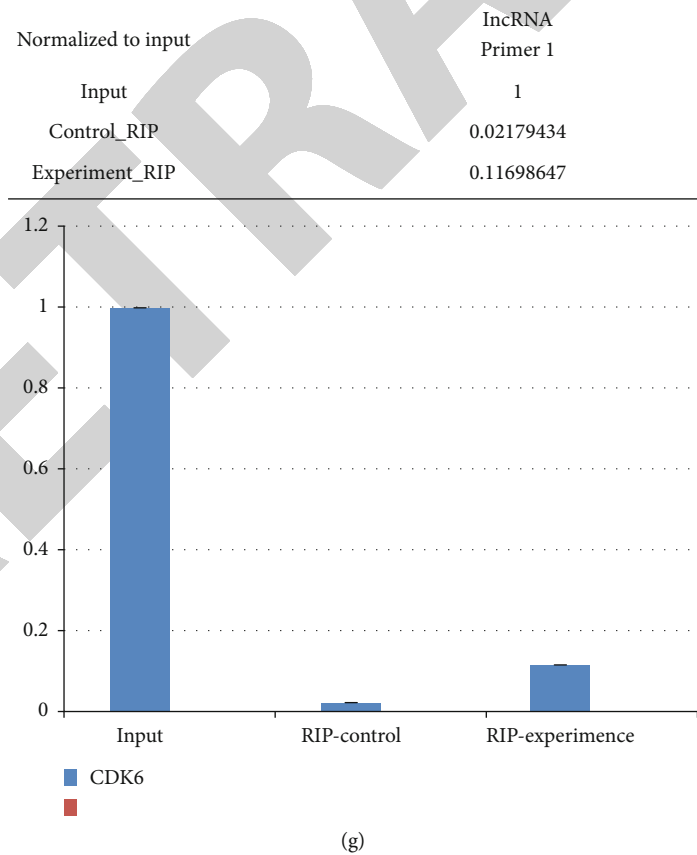
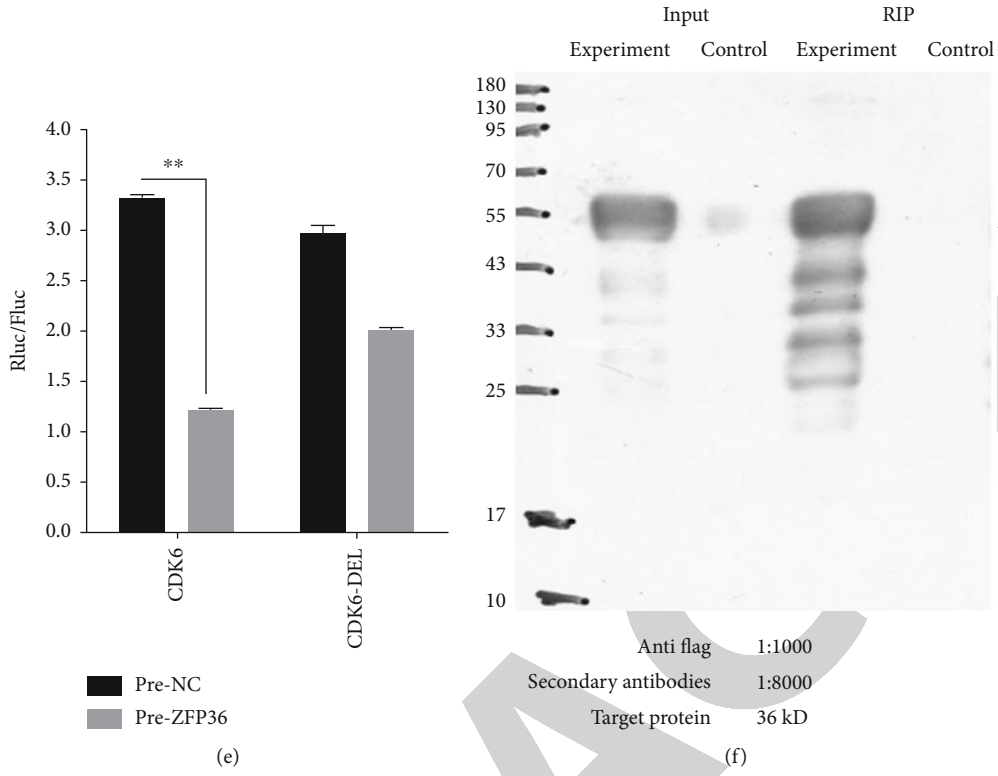


FIGURE 5: (a, b) Negative regulation of ZFP36 on the downstream gene CDK6. (c–e) ZFP36 targeting downstream gene CDK6. (f, g) ZFP36 targeting downstream gene CDK6. \* $P < 0.05$ , \*\* $P < 0.01$ , and \*\*\* $P < 0.001$ .  $n = 3$ . (f) Input is the total cell protein, the control group is the RIP-negative control group, the experimental group is the RIP experimental group, the picture is the WB result of the product during the RIP process, the experimental result is positive, indicating that this experiment is based on the ZFP36 protein Bait protein, and the experiment of obtaining ZFP36-RNA complex is successful. (g) The result of qPCR detection of CDK6 gene expression level of the product obtained by RIP.

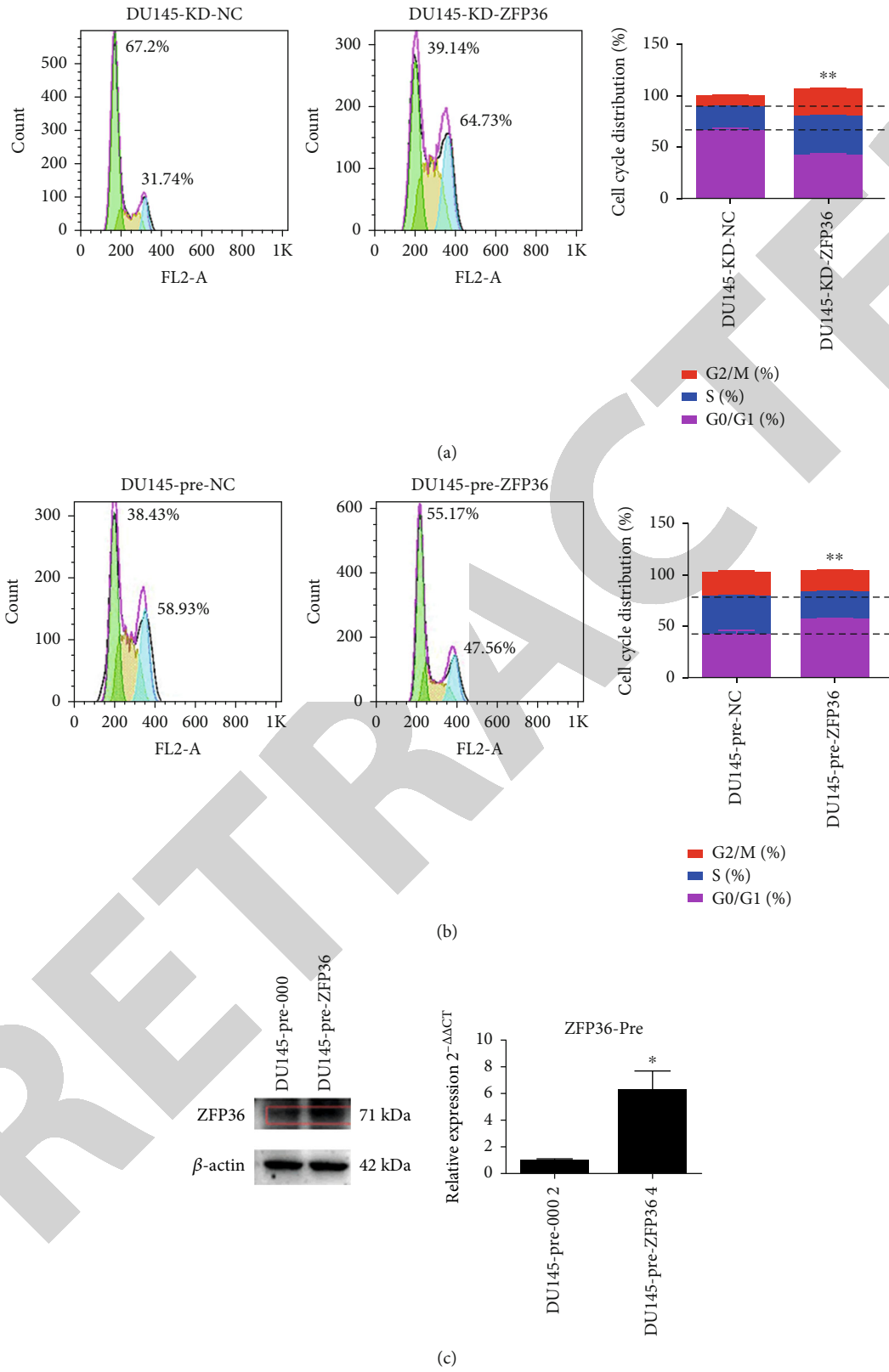


FIGURE 6: Continued.

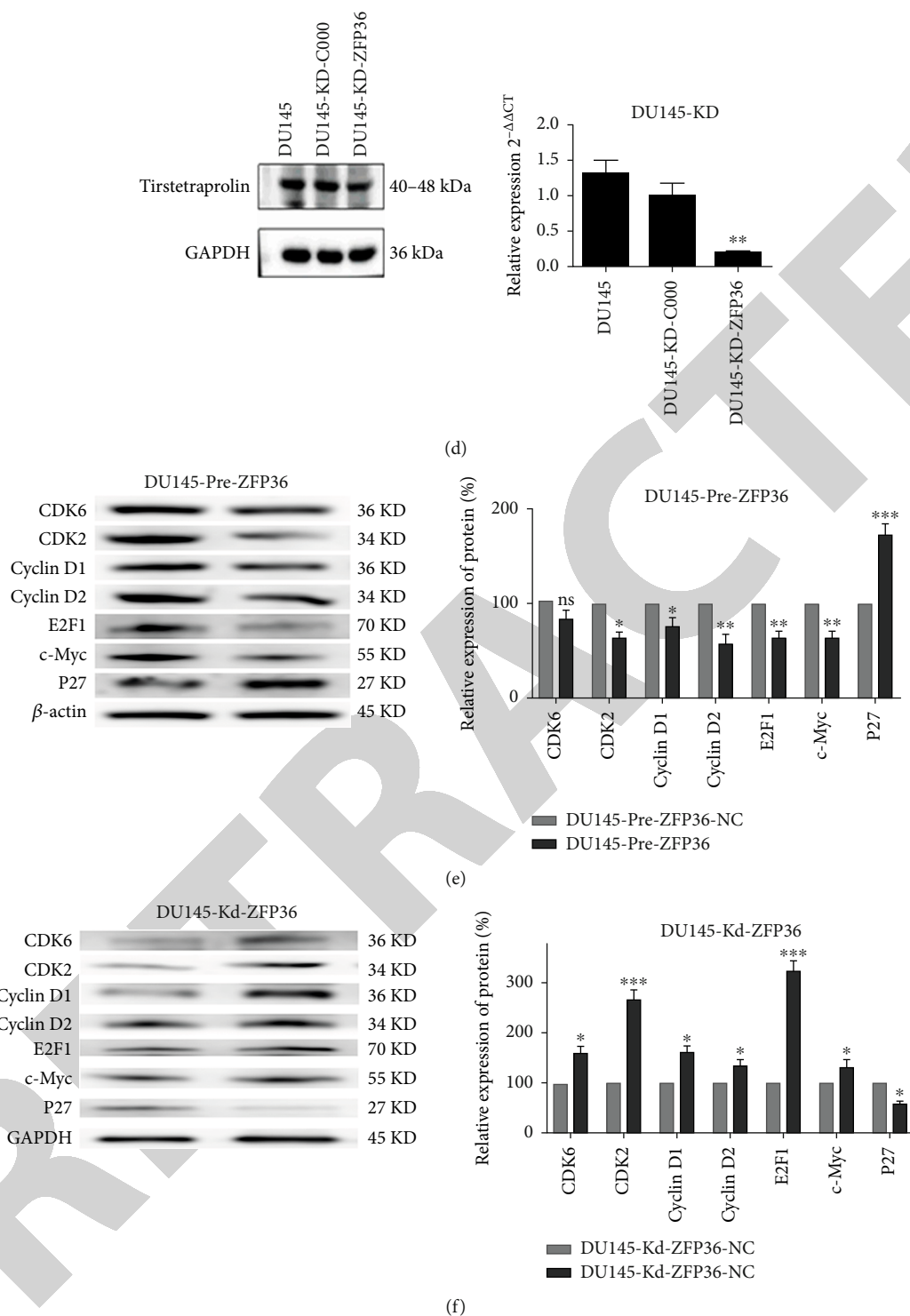


FIGURE 6: (a, b) The effect of ZFP36 on prostate cancer cell cycle. (c, d) Western blot identification of DU145 cell lines. (e, f) Effects of ZFP36 on the cycle-related proteins in PCa cells (\* $P < 0.05$ , \*\* $P < 0.01$ , and \*\*\* $P < 0.001$ ).  $n = 3$ .

both revealed significant differences. It is suggested that ZFP36 blocked the tumor cell cycle in the G1 phase, thereby inhibiting tumor growth.

**3.12. ZFP36 Affects Cell Cycle Progression and Regulates Gene Expression in PCa Cells.** In order to further clarify its

potential mechanism, we tested many cell cycle-related regulators downstream of CDK6. The DU145 cell line with overexpression and knockdown of ZFP36 was constructed and verified. The cell line was identified by western blot (Figures 6(c) and 6(d)). The identification results showed that the cell construction was successful. Relevant proteins

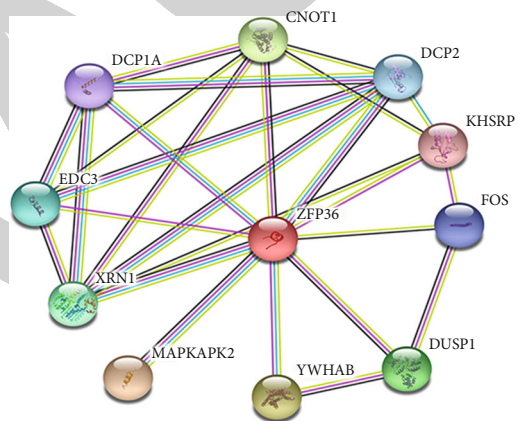
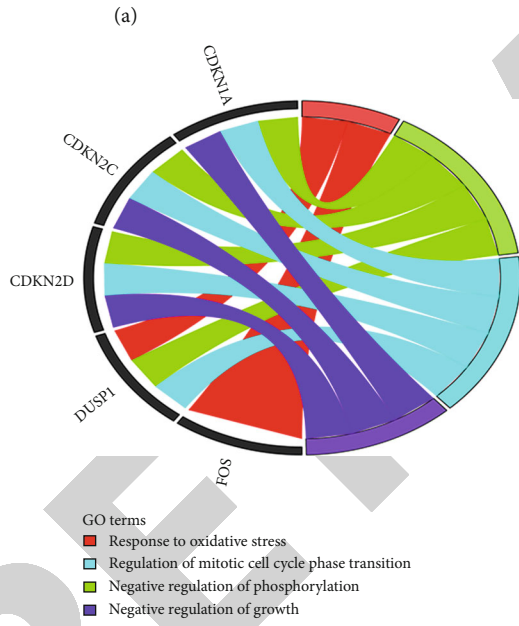
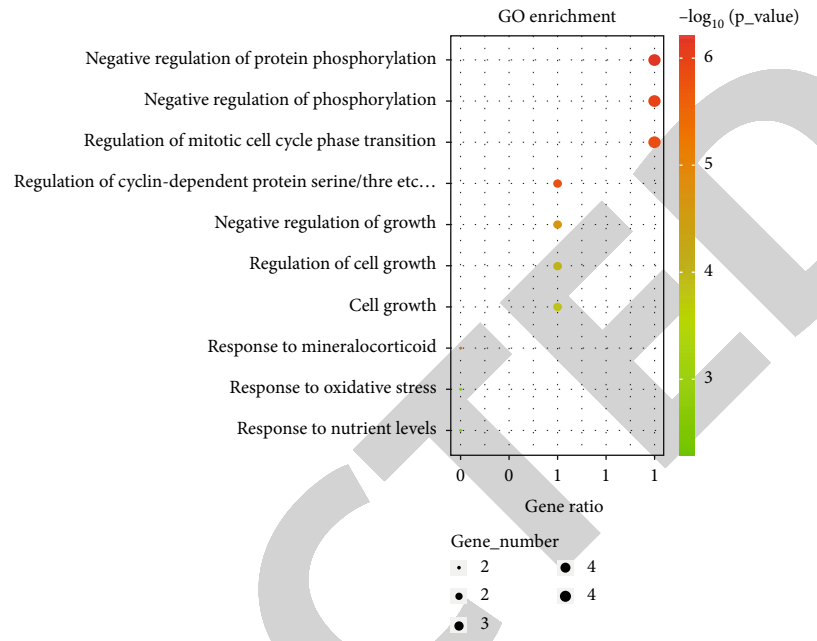
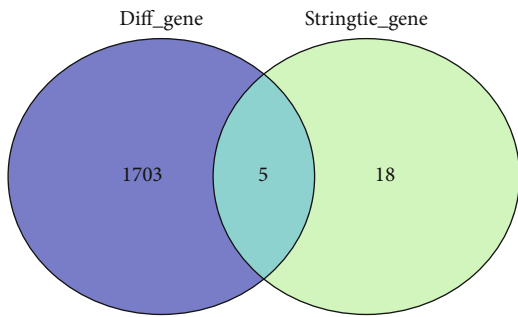


FIGURE 7: Continued.

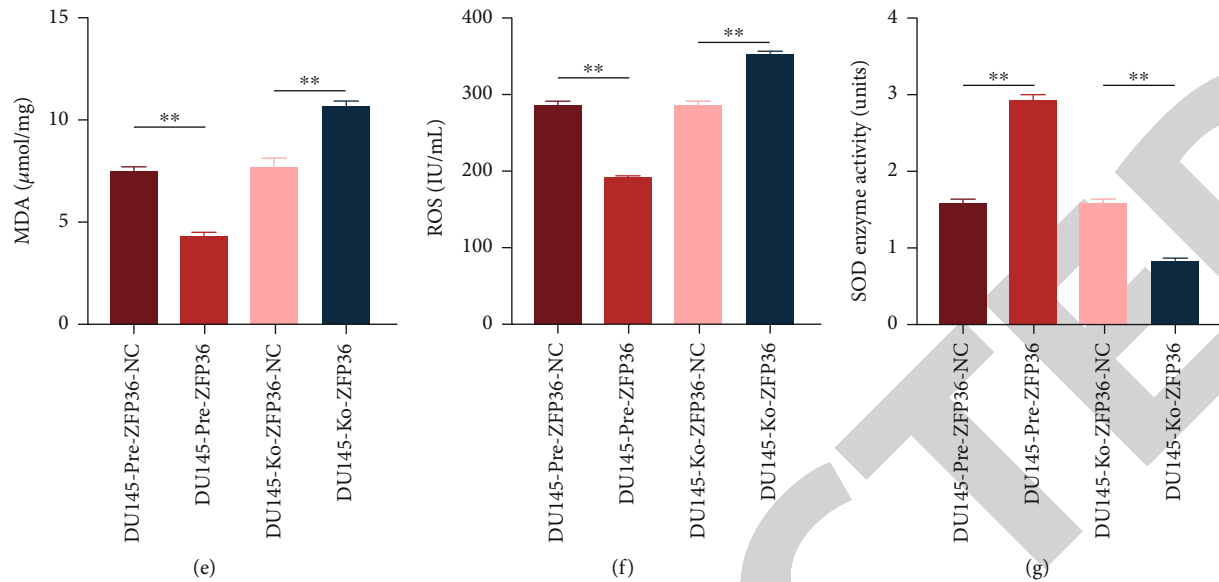


FIGURE 7: (a) Screening map of the intersection gene. (b, c) GO enrichment analysis of 5 intersection genes. (d) PPI network map. (e, f) Determination of MDA and ROS content and SOD enzyme activity by enzyme-linked immunosorbent assay (\*\* $P < 0.01$ ).  $n = 3$ .

were further identified using western blot analysis, suggesting that CDK2, CDK6, cyclin D1, cyclin D2, E2F1, and c-Myc levels in DU145 cells overexpressed by ZFP36 continued to decrease, while the level of P27 was significantly elevated (Figure 6(e)). The knockout DU145 cell line showed the opposite result (Figure 6(f)). Therefore, ZFP36 prevented the growth of the G1 phase by negatively regulating CDK6 and cyclin.

**3.13. Oxidative Stress Mediates ZFP36 Regulation in Prostate Cancer.** To explore whether oxidative stress is related to ZFP36 regulation in PCa, we screened 1708 DEGs related to oxidative stress in PCa patients and used STRING to find 23 genes related to ZFP36 or CDK6. The Venn diagram presented five overlapped genes in the intersection set (Figure 7(a)). GO enrichment showed that the genes associated with response to oxidative stress are DUSP1 and FOS (Figures 7(b) and 7(c)). Importantly, DUSP1 and FOS interacted directly with ZFP36 (Figure 7(d)). Therefore, we guessed oxidative stress mediated the regulation of ZFP36 in PCa by DUSP1 or FOS.

In addition, we verified whether it was involved in the regulatory process of ZFP36 by measuring oxidative stress-related indicators in DU145 cells. Compared with control, MDA and ROS contents were significantly decreased following ZFP36 overexpression, but significantly increased in the knockout of ZFP36 (Figures 7(e) and 7(f)). The SOD enzyme activity was markedly increased in the ZFP36 overexpression group but greatly decreased after ZFP36 knockout (Figure 7(g)). Oxidative stress exerted certain effects on the regulation of PCa by ZFP36.

#### 4. Discussion

It is well recognized that PCa is a heterogeneous cancer; some tumors are indeed very aggressive and can progress

rapidly, while others do not develop for years or decades, ideally requiring only monitoring and no treatment. Because of this heterogeneity, it is difficult to determine which genetic abnormality contributes to prostate cancer initiation, progression, and ultimately treatment resistance [26, 27]. Therefore, in order to improve the diagnostic ability of prostate cancer, find more accurate molecular markers, and provide personalized treatment services, it has always been a hot spot in urological research. The role of RNA has been demonstrated in PCa. For example, PCa progression can be promoted by long noncoding RNA BCYRN1 through elevated HDAC11 [22–28] and by circular RNA circFOXO3 via miR-29a-3p [29]. However, there are fewer studies on ZFP36 in PCa, and this study validated the regulatory role of ZFP36 in PCa based on TCGA database and experiments.

mRNAs encode many proteins involved in tumorigenesis and progression, and their 3'-UTRs contain ARE-like sequences, and therefore, they are likely to be regulated by one or more ARE-BPs through posttranscription. Through TCGA and Taylor databases, we found that ZFP36 expression, a RNA-binding protein, links intimately to PCa biochemical recurrence, and the lower the expression of ZFP36, the lower the survival of PCa patients; the higher the degree of malignancy, and the higher occurrence of distant metastasis, and so the probability. These data suggest that ZFP36, a protein with mRNA binding and instability, is of great significance in PCa growth and tumorigenesis.

The current study determined that elevated levels of ZFP36 expression were inversely correlated with aggressive progression and limited survival time in PCa patients, and it was recognized as a novel PCa suppressor. Significantly, the findings or the present research demonstrated that ZFP36 functioned as a PCa tumor suppressor. By upregulating ZFP36 expression in PCa cells, we demonstrated that ZFP36 could impair the in vitro proliferation, migration, and invasion of PCa cells. Furthermore, ZFP36 activation

hindered the use as subcutaneous xenografts in the ability to grow in the body in DU145 and 22RV1 cells. These results are consistent with those of B cell lymphoma in a mouse model driven by myc cells, where enhanced ZFP36 expression in B cells impedes lymphoma maintenance in an allograft model [16]. Interestingly, a recent study has revealed that ZFP36 can directly bind interleukin- (IL-) 23, cyclooxygenase- (COX-) 2, and VEGF in the 3'-UTRs, thereby reducing the stability and expression in colon cancer and ZFP36 depletion results in colon cancer cell proliferation [30]. As for breast cancer, ZFP36 deletion can upregulate cytokines IL-16, COX-2, and VEGF, which are intimately associated with cell proliferation [31]. ZFP36 is also predicted to be a promising upstream inhibitor of the NF- $\kappa$ B pathway, with a role in reversing the growth of PCa [32]. Taken together, novel therapeutic approaches that specifically stimulate ZFP36 expression can be a potential way to treat tumors with low ZFP36 expression.

In addition, RNA-Seq analysis was conducted to determine whether there were biological pathways directly influenced by ZFP36 expression in PCa. Over 300 genes with changes in expression were identified due to ZFP36. Surprisingly, ZFP36-induced differentially expressed gene pathway analysis in PCa cells identified genes involved in tumorigenesis, including PI3K-Akt signaling, Rap1 signaling, circadian rhythm, cell-matrix adhesion, and HIF-1 signaling pathway, and the cancer pathway was significantly correlated. Most importantly, CDK6 was recognized as a downstream target gene of ZFP36. The cell cycle kinase CDK6 is a cell cycle-dependent kinase and transcriptional regulator. Cell cycle disorder is an important mechanism affecting tumorigenesis. During the regulation process of cell cycle, cyclin and cyclin-dependent kinase abnormalities can lead to tumorigenesis, such as Polo-like. The mRNA of protein kinase 3 consists of 3 AREs in the 3'-UTR, and ZFP36 affects cell cycles via modulating mRNA degradation. In lung cancer, ZFP36 destabilizes cyclin B1 mRNA and reduces its expression [33]. As a tumor suppressor gene, large tumor suppressor kinase 2 (LATS2) is essential for cell cycle inhibition [34]. An ARE has been identified containing in the 3'-UTR of its mRNA, so ZFP36 reduces cyclin B1 and LATS2 by reducing cyclin B1 and LATS2 expression to regulate the lung cancer cell cycle. Transcription factor C-Jun is regarded as a protooncogene of breast cancer. Being a key member of activator protein- (AP-) 1 complex, it can accelerate the cell cycle [35]. The interaction between AP-1 and c-Jun can realize induced cell cycle arrest in breast cancer. TTP has been indicated to have the ability of binding to c-Myc and cyclin D1 mRNA AREs and downregulating their expression levels in glioma [36], which can precisely regulate the glioma cell cycle.

Here, we expressed interest in whether CDK6 has a biological function as the downstream target of ZFP36, and for further validation, we found CDK6 at mRNA level and protein levels in PCa cells and tumor xenografts with enhanced and depleted ZFP36 expression decreased and increased, respectively, demonstrating the negative regulatory effect of ZFP36 on CDK6, which was further confirmed using luciferase reporter and RNA coimmunoprecipitation assays.

Meanwhile, CDK6 was newly discovered as a direct target of ZFP36. It can mediate cell cycle progression at the G1 stage and transition at the G1/S stages [37]. Therefore, we also confirmed in cell cycle experiments that ZFP36 blocks tumor cell cycle in the G1 phase, thereby inhibiting tumor growth. In mammalian cells, CDK6 activates the cell cycle via several interactions with cyclins D1, D2, and D3 during early G1 [38]. As it is related to cell proliferation, CDK6 is reported to be abnormally expressed in lymphoma, medulloblastoma, leukemia, and melanoma due to chromosomal rearrangements [39, 40]. We further identified the downstream effectors of the ZFP36-CDK6 axis and found that the levels of CDK2, CDK6, cyclin D1, cyclin D2, E2F1, and c-Myc were all decreased, while the level of P27 was significantly increased in ZFP36-overexpressing DU145 cells. This data is consistent with the report of Lee et al. in prostate cancer [41], which more fully demonstrates that ZFP36 prevents tumor cell growth in the G1 phase by negatively regulating CDK6 and cyclins. Some researchers have also pointed out that CDK6 is related to the occurrence of tumors, and clinical trials of its inhibitors have shown good safety and efficacy, suggesting that CDK6 can be a promising target for cancer management, which confirms the anticancer potential of ZFP36 from the side.

A central finding of the current research is that suppressed ZFP36 expression usually occurs in human cancer, of which the functional reduction can modulate distinct tumorigenic phenotypes. Reduced expression of ZFP36 in PCa patients might be an indicator of negative prognosis, since low ZFP36 mRNA may develop more advanced tumors, increasing their risks of cancer recurrence and death. In addition, the encouraging finding of this study is that some studies have reported that average level of zinc in PCa tissues is evidently decreased compared with BPH and normal prostate, and zinc is an essential element for zinc finger protein generation; therefore, it is a bold guess that the reduction or absence of zinc may be an important reason for the decreased expression of ZFP36. The aggressive development of PCa might result from a fundamental metabolic transformation that prevents malignant cells from accumulating zinc [42]. This study presented clinical and biochemical evidence, suggesting that alterations in zinc metabolism may be of vital importance in PCa pathogenesis, and timely zinc supplementation may improve ZFP36 expression levels, thereby inhibiting prostate cancer development, which needs to be further confirmed in follow-up studies.

In addition, oxidative stress has an association with PCa [43]. Normal physiological levels of androgens can maintain the balance between ROS and antioxidant enzymes, apoptosis, and proliferation in the prostate [44]. Androgen deprivation therapy (ADT) disrupts normal androgen status by blocking androgen receptor (AR) signaling and increases mRNA levels of three reduced nicotinamide adenine dinucleotide phosphate (NADPH) oxidases in vivo, such as Nox1, Nox2 (gp91phox), and Nox4, while also decreasing the expression levels of antioxidant enzymes, namely, thioredoxin1, manganese superoxide dismutase, and glutathione peroxidase1, leading to excessive ROS production and exacerbating oxidative stress [45]. In this study, bioinformatics

analysis revealed that oxidative stress may mediate the regulation of ZFP36 in PCa. Through experimental validation, it was found that after overexpression of ZFP36 in DU145 cells, MDA and ROS levels, indicators related to oxidative stress, were decreased and SOD enzyme activity was increased as measured, implying that oxidative stress can regulate PCa by ZFP36.

Although this study demonstrated a significant role of ZFP63 in PCa, some limitations are also needed to be further improved. For example, despite reduced zinc expression in human PCa tissues, we did not further elucidate the direct correlation between this result and the role of ZFP63. In addition, we only analyzed the possible role of oxidative stress in this process through bioinformatics but did not further verify it through experiments.

In conclusion, our data provide compelling evidence that strongly supports the proposal that ZFP36 acts as a potential prognostic biomarker. Deregulation of ZFP36 is responsible for cell proliferation and promotes PCa migration and invasion via regulating CDK6 signaling pathway. Meanwhile, the ZFP36-CDK6 axis which has been lately discovered elucidates the molecular mechanism of PCa progression and a novel therapeutic target of PCa therapy. Furthermore, it is exciting that supplemental intake of zinc may be another breakthrough point in ZFP36 expression. In the future, we can effectively provide new strategies and targets for PCa treatment by deeply investigating oxidative stress in regulating PCa by ZFP36 and related signaling pathways.

## Data Availability

All data, models, and code generated or used during the study appear in the submitted article.

## Conflicts of Interest

The authors declare that they have no conflicts of interest.

## Authors' Contributions

Dongbo Yuan, Yinyi Fang, and Weiming Chen contributed equally to this article.

## Acknowledgments

This work was supported by grants from the High-Level Innovative Talent Project of Guizhou Province in 2018 ([2018]5639), the Science and Technology Plan Project of Guiyang in 2019 [2019]2-15, the Science and Technology Projects of Guizhou Province in 2019 ([2019]1203), the National Natural Science Foundation of China (81660426 and 82160551), and the Guizhou Administration of Traditional Chinese Medicine (QZYY-2021-168).

## References

- [1] D. Hanahan and R. A. Weinberg, "The hallmarks of cancer," *Cell*, vol. 100, no. 1, pp. 57–70, 2000.
- [2] C. Vogel, R. de Sousa Abreu, D. Ko et al., "Sequence signatures and mRNA concentration can explain two-thirds of protein abundance variation in a human cell line," *Molecular Systems Biology*, vol. 6, no. 1, p. 400, 2010.
- [3] J. Ye and R. Blelloch, "Regulation of pluripotency by RNA binding proteins," *Cell Stem Cell*, vol. 15, no. 3, pp. 271–280, 2014.
- [4] V. M. Weake, J. O. Dyer, C. Seidel et al., "Post-transcription initiation function of the ubiquitous SAGA complex in tissue-specific gene activation," *Genes & Development*, vol. 25, no. 14, pp. 1499–1509, 2011.
- [5] A. Castello, B. Fischer, K. Eichelbaum et al., "Insights into RNA biology from an atlas of mammalian mRNA-binding proteins," *Cell*, vol. 149, no. 6, pp. 1393–1406, 2012.
- [6] S. A. Ciafrè and S. Galardi, "microRNAs and RNA-binding proteins: a complex network of interactions and reciprocal regulations in cancer," *RNA Biology*, vol. 10, no. 6, pp. 935–942, 2013.
- [7] D. P. Bartel, "MicroRNAs: genomics, biogenesis, mechanism, and function," *Cell*, vol. 116, no. 2, pp. 281–297, 2004.
- [8] G. Dreyfuss, V. N. Kim, and N. Kataoka, "Messenger-RNA-binding proteins and the messages they carry," *Nature Reviews. Molecular Cell Biology*, vol. 3, no. 3, pp. 195–205, 2002.
- [9] S. F. Mitchell and R. Parker, "Principles and properties of eukaryotic mRNPs," *Molecular Cell*, vol. 54, no. 4, pp. 547–558, 2014.
- [10] M. Fu and P. J. Blackshear, "RNA-binding proteins in immune regulation: a focus on CCCH zinc finger proteins," *Nature Reviews. Immunology*, vol. 17, no. 2, pp. 130–143, 2017.
- [11] A. S. Halees, R. el-Badrawi, and K. S. A. Khabar, "ARED organism: expansion of ARED reveals AU-rich element cluster variations between human and mouse," *Nucleic Acids Research*, vol. 36, Database, pp. D137–D140, 2007.
- [12] D. Hanahan and R. A. Weinberg, "Hallmarks of cancer: the next generation," *Cell*, vol. 144, no. 5, pp. 646–674, 2011.
- [13] C. Y. A. Chen and A. B. Shyu, "AU-rich elements: characterization and importance in mRNA degradation," *Trends in Biochemical Sciences*, vol. 20, no. 11, pp. 465–470, 1995.
- [14] G. A. Taylor, E. Carballo, D. M. Lee et al., "A pathogenetic role for TNF $\alpha$  in the syndrome of cachexia, arthritis, and autoimmunity resulting from tristetraprolin (TTP) deficiency," *Immunity*, vol. 4, no. 5, pp. 445–454, 1996.
- [15] L. Montorsi, F. Guizzetti, C. Alecci et al., "Loss of ZFP36 expression in colorectal cancer correlates to wnt/ $\beta$ -catenin activity and enhances epithelial-to-mesenchymal transition through upregulation of ZEB1, SOX9 and MACC1," *Oncotarget*, vol. 7, no. 37, pp. 59144–59157, 2016.
- [16] R. J. Rounbehler, M. Fallahi, C. Yang et al., "Tristetraprolin impairs myc-induced lymphoma and abolishes the malignant state," *Cell*, vol. 150, no. 3, pp. 563–574, 2012.
- [17] H. Sung, J. Ferlay, R. L. Siegel et al., "Global cancer statistics 2020: GLOBOCAN estimates of incidence and mortality worldwide for 36 cancers in 185 countries," *CA: a Cancer Journal for Clinicians*, vol. 71, no. 3, pp. 209–249, 2021.
- [18] A. Rizzo, M. Santoni, V. Mollica, M. Fiorentino, G. Brandi, and F. Massari, "Microbiota and prostate cancer," *Seminars in Cancer Biology*, 2021.
- [19] B. Ma, A. Wells, L. Wei, and J. Zheng, "Prostate cancer liver metastasis: dormancy and resistance to therapy," *Seminars in Cancer Biology*, vol. 71, pp. 2–9, 2021.
- [20] J. G. Zhu, D. B. Yuan, W. H. Chen et al., "Prognostic value of ZFP36 and SOCS3 expressions in human prostate cancer,"

## Retraction

# Retracted: Siglec-15 Regulates the Inflammatory Response and Polarization of Tumor-Associated Macrophages in Pancreatic Cancer by Inhibiting the cGAS-STING Signaling Pathway

### Oxidative Medicine and Cellular Longevity

Received 20 June 2023; Accepted 20 June 2023; Published 21 June 2023

Copyright © 2023 Oxidative Medicine and Cellular Longevity. This is an open access article distributed under the Creative Commons Attribution License, which permits unrestricted use, distribution, and reproduction in any medium, provided the original work is properly cited.

This article has been retracted by Hindawi following an investigation undertaken by the publisher [1]. This investigation has uncovered evidence of one or more of the following indicators of systematic manipulation of the publication process:

- (1) Discrepancies in scope
- (2) Discrepancies in the description of the research reported
- (3) Discrepancies between the availability of data and the research described
- (4) Inappropriate citations
- (5) Incoherent, meaningless and/or irrelevant content included in the article
- (6) Peer-review manipulation

The presence of these indicators undermines our confidence in the integrity of the article's content and we cannot, therefore, vouch for its reliability. Please note that this notice is intended solely to alert readers that the content of this article is unreliable. We have not investigated whether authors were aware of or involved in the systematic manipulation of the publication process.

Wiley and Hindawi regrets that the usual quality checks did not identify these issues before publication and have since put additional measures in place to safeguard research integrity.

We wish to credit our own Research Integrity and Research Publishing teams and anonymous and named external researchers and research integrity experts for contributing to this investigation.

The corresponding author, as the representative of all authors, has been given the opportunity to register their agreement or disagreement to this retraction. We have kept a record of any response received.

### References

- [1] H. Li, R. Zhu, X. Liu, K. Zhao, and D. Hong, "Siglec-15 Regulates the Inflammatory Response and Polarization of Tumor-Associated Macrophages in Pancreatic Cancer by Inhibiting the cGAS-STING Signaling Pathway," *Oxidative Medicine and Cellular Longevity*, vol. 2022, Article ID 3341038, 14 pages, 2022.



## Research Article

# Siglec-15 Regulates the Inflammatory Response and Polarization of Tumor-Associated Macrophages in Pancreatic Cancer by Inhibiting the cGAS-STING Signaling Pathway

HuaGen Li,<sup>1,2</sup> RongXuan Zhu,<sup>3</sup> XiaoLong Liu,<sup>2</sup> Kai Zhao,<sup>1,2</sup> and DeFei Hong<sup>2</sup> 

<sup>1</sup>School of Medicine, Zhejiang University, 866 Yuhangtang Road, Hangzhou, 310058 Zhejiang, China

<sup>2</sup>Department of General Surgery, Sir Run Run Shaw Hospital, The Medicine School of Zhejiang University, Hangzhou, China

<sup>3</sup>Department of Thoracic Surgery, National Cancer Center, National Clinical Research Center for Cancer, Cancer Hospital, Chinese Academy of Medical Sciences and Peking Union Medical College, Beijing, China

Correspondence should be addressed to DeFei Hong; hongdefei@163.com

Received 7 April 2022; Revised 12 August 2022; Accepted 22 August 2022; Published 5 September 2022

Academic Editor: Tian Li

Copyright © 2022 HuaGen Li et al. This is an open access article distributed under the Creative Commons Attribution License, which permits unrestricted use, distribution, and reproduction in any medium, provided the original work is properly cited.

Tumor-associated macrophages especially M2 phenotype macrophages play an important role in tumor progression and the formation of immunosuppressive tumor microenvironment. Previous studies indicated that infiltration of a large number of M2-macrophages was positively associated with a low survival rate and poor prognosis of patients with pancreatic ductal cancer. However, the mechanisms responsible for M2-macrophage polarization remain unclear. Recently, Siglec-15 appears as an emerging target for the normalization of the tumor immune microenvironment. Hence, we detected the Siglec-15 expression on macrophages by using qPCR and Western blot assay and found that the expression of Siglec-15 was upregulated on M2 macrophages induced by IL-4 and conditioned media from pancreatic ductal cancer. In addition, after knocking out Siglec-15, the expression of M2 phenotype macrophage biomarkers such as Arg1 and CD206 was significantly downregulated. Besides, in our study we also found that Siglec-15 could upregulate the glycolysis of macrophage possibly by interacting with Glut1 to regulate the M2-macrophage polarization. The regulation was also partly dependent on STING, and Glut1-related glycolysis metabolism was involved in regulating cGAS/STING signaling. When utilizing a subcutaneous transplantation mouse model, we observed that knocking out of Siglec-15 or co-injecting tumor cells with macrophage from Siglec-15 KO mice could significantly inhibit the growth of subcutaneous tumors in mice. Taken together, these findings suggest that Siglec-15 is essential for the M2-macrophage polarization to shape an immune suppressive tumor microenvironment in pancreatic cancer and makes it an attractive target for pancreatic cancer immunotherapy.

## 1. Introduction

Pancreatic ductal cancer (PDAC) is one of the most lethal malignancies with a poor prognosis and short overall survival [1]. According to the most recent global tumor statistics, the number of new cases and death cases of PDAC exceeded 400,000 last year. The fact that its occurrence is rising among younger people has a significant negative effect on the quality of life of individuals [2, 3]. Despite the modest improvement in surgical and adjuvant treatment for PDAC, the overall survival of PDAC is only minimally improved

with a 5-year survival rate of 8% [4]. Hence, the effective treatments for pancreatic cancer are still urgently needed.

In recent years, multiple studies have demonstrated that the tumor-immunosuppressive microenvironment had an indispensable impact on the occurrence and development of pancreatic cancer and immunotherapy for PDAC [4–6]. Tumor-associated macrophages (TAMs) which are the most abundant infiltrative immune cells in the tumor microenvironment (TME) play an important role in tumor progression [7]. Generally, macrophages could be polarized into M1 or M2-like phenotype macrophages depending on

different environments around it [8]. M1-macrophages are proinflammatory and tumor suppressive, while M2-macrophages are anti-inflammatory and promote tumorigenesis and immunosuppression. However, macrophages located in the tumor microenvironment of PDAC are preferentially polarized into the M2-like phenotype to promote the tumor progression and formation of the immunosuppressive TME [9, 10]. Additionally, it was observed that the infiltration of M2 macrophages was substantially related with tumor metastasis, chemoresistance, and a poor prognosis in a variety of malignancies, including PDAC [11, 12]. Therefore, polarization mechanisms of TAMs have emerged as a focus of intense attention in the field of cancer research and offer the potential for an effective immunotherapy strategy for PDAC.

Siglec-15 is indicated highly expressed in M2 macrophages and appears as an emerging target for tumor immunotherapy. However, its biological function in TAMs of PDAC remains to be determined. In this study, we found that sialic acid-binding immunoglobulin-like lectin 15 (Siglec-15), which could enhance tumor immune escape in TME without an association with the PD-1/PD-L1 pathway [13–15], played an important role in the polarization of TAMs. Our findings suggest that within the TME of pancreatic cancer, Siglec-15 could promote TAMs to polarize into M2 macrophages and contribute to shaping an immunosuppressive TME to promote tumor progression. In addition, we also found that Siglec-15 regulates polarization of TAMs by upregulating glycolysis of macrophages and the cyclic GMP-AMP synthase (cGAS)-stimulator of interferon genes (STING) signaling pathway as well as Glut1-related glucose metabolism was involved in polarization mechanisms.

## 2. Methods

**2.1. Cell Culture and Transfection.** Mouse-derived macrophages RAW264.7; pancreatic ductal cancer cell lines BxPC-3, SW1990, and PANC-1; and normal pancreas cell lines H6C7 were purchased from the American Type Culture Collection (ATCC). Bone marrow-derived macrophages (BMDMs) are extracted from mouse bone marrow cells and induced by adding L929-conditioned medium [16]. When the experimental cell density was about 70%, the serum-containing DMEM medium was replaced with a serum-free Opti-MEM medium. Lipofectamine™ 2000 Reagent (Invitrogen) and plasmid were configured using a transfection system based on plasmid DNA quality and Lipofectamine™ 2000 volume 1:1. Then, the transfection system was added to the cell culture medium. After six hours, the Opti-MEM medium was replaced with a serum-containing DMEM medium and was cultured at 37°C for one day before further processing.

**2.2. Polarization of Bone Marrow-Derived Macrophages (BMDMs).** BMDMs with a maturation rate greater than 90% were used in this study. After stimulation with 100 ng/mL LPS and 20 ng/mL IFN- $\gamma$  for 12 h, BMDMs were induced into M1 macrophages [17], while stimulation with 20 ng/mL IL-4 for 24 h induced BMDMs polarized into M2

macrophages. Tumor cell supernatant and DMEM complete medium were made into conditioned medium at 1:1 and stimulated BMDMs. The phosphorylation level of biomarkers was detected at different time points.

**2.3. Real-Time Quantitative PCR (qPCR).** Routinely culture mouse macrophages RAW264.7, adjust the cell density to  $2.5 \times 10^5$  cells/mL, and maintain them in a 37°C 5% CO<sub>2</sub> incubator for 24 h. Total RNA was extracted using TRIzol Reagent (Invitrogen, Thermo Fisher Scientific, Inc.) according to the manufacturer's instructions. The mRNA expression was assayed by RT-qPCR. For each sample, 1  $\mu$ g of RNA was taken for reverse transcription reaction. The reverse transcription product was collected to perform a PCR reaction. RT-qPCR was performed using the Bio-Rad CFX96 real-time system, and the PCR reaction conditions were as follows: 95°C for 30 s, 95°C for 5 s, 60°C for 30 s, 40 cycles [18]. For the analysis of gene expression, gene expression levels were normalized to the expression of GAPDH to calculate the  $2^{-\Delta\Delta Ct}$  value. The primer sequences are shown in Table 1.

**2.4. Western Blotting.** Proteins from cells were extracted with RIPA buffer with 0.1 mmol/L PMSF (Beyotime Biotechnology, Shanghai) and quantified using the BCA kit (Beyotime Biotechnology, Shanghai) [19]. The total protein (20  $\mu$ g/lane) was separated on 10% SDS-PAGE gel followed by transfer to the PVDF membrane (EMD Millipore, MA, USA). The membrane was blocked in 5% skimmed milk powder at room temperature for 2 h, then incubated with a primary antibody (1:1000) overnight at 4°C. After incubating with the primary antibody, the membrane was washed three times with TBST and incubated with a secondary antibody (1:2500) for 1 h at room temperature. Protein bands were visualized using the ECL kit (Millipore, USA), and the blots were developed and exposed using a ChemiDoc™ Touch Imaging System. Commercial antibodies used in vitro cultures, and western blots were purchased from Abcam, BD Biosciences, or R&D Systems.

**2.5. Bioenergetic Study.** The glycolytic function of macrophages was measured using a Seahorse XF96 Analyzer (Agilent Technologies, USA) following the manufacturer's instructions. Extracellular acidification rates (ECAR) and oxygen consumption rates (OCR) were assessed by using Seahorse XF Glycolysis Stress Test Kit and Seahorse XF Cell Mito Stress Test Kit, respectively. Briefly, the treated macrophages were seeded at a density of  $3 \times 10^6$  cells per well into a Seahorse XF 96 cell culture microplate for 2 h prior to the assay. After baseline measurements, glucose, oligomycin (oxidative phosphorylation inhibitor), and 2-DG (glycolytic inhibitor) were sequentially injected into each well at indicated time points for ECAR, and oligomycin, FCCP (p-trifluoromethoxy carbonyl cyanide phenylhydrazone), and rotenone plus the antimycin A (Rote/AA) were sequentially injected for OCR. Data were assessed by Seahorse XF-96 Wave software and expressed as picomoles per minute (OCR) or miles per hour per minute (ECAR).

TABLE 1: The primer sequences included in this study.

Name	Primer sequences (5'-3')
Siglec-15: forward	GTTCTCGGGCACCTTGG
Siglec-15: reverse	AGCTCCGAAATGGTTGTCC
NOS2: forward	TTCAGTATCACAACTCAGCAAG
NOS2: reverse	TGGACCTGCAAGTAAAATCCC
IL-6: forward	TCCATCCAGTTGCCTTCTTGG
IL-6: reverse	CCACGATTTCCCAGAGAACATG
Arg-1: forward	CTTCAGAGAAGTGGCCCAAC
Arg-1: reverse	GGTGGTGGGTATCACAGGAC
TNF- $\alpha$ : forward	AG CAAACCACCAAGTGGAGGA
TNF- $\alpha$ : reverse	GCTGGCACCAGTGTGGTTGT
GAPDH: forward	ACCCAGAAGACTGTGGATGG
GAPDH: reverse	CACATTGGGGGTAG GAACAC
U6: forward	GCGCGTCGTGAAGCGTTC
U6: reverse	GTGCAGGGTCCGAGGT

**2.6. Co-Immunoprecipitation.** Cells were lysed on ice by adding NP-40 Lysis Buffer for 30 min. After then, the cells were lysed at 12,000 r/min and centrifuged at 4°C for 30 min. The supernatant was collected and added with IgG and Protein A/G Plus Agarose for prewashing. The protein concentration was detected using the BCA kit (Beyotime Biotechnology, Shanghai). The lysate was divided into 2 groups, each with 1 mg protein. The IgG antibody was used as a negative control, and the Flag antibody was used as the experimental group. The cell lysate was incubated with the antibody overnight at 4°C. After 18 hours, Protein A/G agarose beads were added to incubate for 4 hours, followed by washing 5 times with NP-40 and adding to the sample. The precipitated proteins were examined using western blot analysis with the specified antibodies after the addition of 2× SDS loading buffer.

**2.7. GST Fusion Protein Purification.** The GST fusion protein pellet was transformed into *E. coli* Rosetta competent cells and streaked on a plate containing ampicillin antibiotics. After being cultured at 37°C overnight, a single colony was picked and inoculated in 100 mL LB liquid medium. When the OD600 absorbance reached 0.6–0.8, IPTG was added to a final concentration of 0.2 mmol/L and induced at room temperature for 4–6 h. The cells were collected by centrifugation, and the cells were lysed on ice with the lysis buffer containing protease inhibitors for 10 min, followed by ultrasonic disruption for 20 min. The supernatant was collected by centrifugation at 4°C, and DTT was added to a final concentration of 1 mmol/L according to GST Fusion Protein Spin Purification Kit (GE).

**2.8. Glutathione S Transferase (GST) Pulldown.** Cells were lysed in the lysate (containing protease inhibitors) for 30 minutes on ice and centrifuged at 4°C, 12,000 r/min for 30 minutes. After then, the supernatant was collected and the protein concentration was detected using the BCA kit (Beyotime Biotechnology, Shanghai, China). The purified GST fusion protein was combined with the whole-cell lysate

mix and incubated overnight at 4°C with rotation. The beads were washed 5 times with lysate, followed by adding 2× SDS buffer to the sample, and then western blotting assay was used to detect the bound proteins.

**2.9. GEPIA Database Analysis.** The co-expression level of Siglec15 and the metabolism-related gene mRNA in PDAC were analyzed by using the GEPIA database (<http://gepia.cancer-pku.cn>) which integrates database information such as TCGA and GTEx [20]. | log2FC | The cutoff value was set to 1, and the *p* cutoff value was 0.01. The database was also used to verify the correlation between expressions of Siglec15 and overall survival (OS) of pancreatic cancer.

**2.10. Mice and Tumor Study.** For tumor study in vivo, a single-cell suspension of Pan-02 cells ( $5 \times 10^6$  cells) in 0.2 mL of PBS was subcutaneously injected into the right back of female WT or Siglec15 KO C57/BL6 mice aged 6 to 8 weeks. Mice were raised under specific pathogen-free (SPF) conditions at the Sir Run Run Shaw Hospital, Zhejiang University School of Medicine. Tumor growth was monitored using a vernier caliper every 5 days, and tumor volume was calculated as follows:  $V (\text{mm}^3) = (\text{length} \times \text{width}^2) \times 0.5$ . After four weeks, the mice were sacrificed and dissected. The overall survival of WT or Siglec-15 ko mice were presented as days, and the survival curve was drawn. The log-rank (Mantel-Cox) test in GraphPad Prism was used for analysis. For macrophage and tumor cell co-injection model, bone marrow-derived macrophages from wild-type and Siglec-15 KO mice were extracted and cultured in vitro, followed by mixing with Pan-02 cells in single-cell suspension with a total of  $1 \times 10^6$  cells (mixing ratio: 1:1). Female wild-type mice aged 6–8 weeks were selected, and 200  $\mu\text{L}$  of single-cell suspension was injected into the right back subcutaneously. Subsequently, the volume of tumor was monitored every 5 days. All animal experiments in this experiment have been reviewed and approved by the animal care committee of Sir Run Run Shaw Hospital, Zhejiang University.

**2.11. Statistical Analysis.** Quantitative data were expressed as means with standard deviations. Means between two groups are compared using Student's *t*-test, whereas means between multiple groups are compared using one-way analysis of variance (ANOVA) with Bonferroni's post hoc test. The SNK or LSD method was used for multiple comparisons. The Kaplan-Meier method was used to generate survival curves, and the long-rank test was utilized to compare different survival rates. These analyses of overall survival were carried out. The hazard ratios (HR) and 95% confidence intervals (CIs) were calculated using a Cox regression model with two-sided Wald tests. The GraphPad Prism5 software (version 5.02, GraphPad Software, USA) was used for statistical analysis and graphing.  $p < 0.05$  was considered statistically significant.

### 3. Results

**3.1. Siglec-15 Is Expressed Differently in M1 and M2 Macrophages.** IL-4 was used to polarize bone marrow-

derived macrophages (BMDMs) into M2-type macrophages. Then, qPCR assay was performed for detecting Siglec family members, such as CD169, CD22, CD33, Siglec-7, Siglec-G (Siglec10), and Siglec-15, in M2-type macrophages. The results indicated that Siglec-15 was the most significantly upregulated in M2-type macrophage cells (Figure 1(a)). In addition to infiltrating many immune cells in the tumor microenvironment, the most abundant one is the tumor cells themselves. Therefore, we used qPCR assay to detect Siglec-15 expression in H6C7, SW1990, PANC-1, BXPC-3, and M2-macrophage cell lines. The results suggested that compared with pancreatic cancer cells and normal pancreatic epithelial cells, the expression of Siglec-15 was relatively much higher in M2 phenotype TAMs (Figure 1(b)), further indicating that Siglec-15 may be more important for the regulation of TAMs in human pancreatic cancer than tumor cell themselves. In addition, when using Kaplan-Meier (KM) method for univariate analysis based on TCGA data, patients with low Siglec-15 expression levels have longer overall survival (Figure 1(c)), indicating that Siglec-15 expression levels are an independent prognostic factor for the overall survival of patients with pancreatic cancer. Besides, in terms of RNA level, Siglec-15 was downregulated in M1 macrophages induced by LPS+IFN $\gamma$  while it was upregulated in M2 macrophages induced by IL-4 or tumor supernatant (Figures 1(d)–1(f)). Simultaneously, at the protein level, the expressions of Siglec-15 as well as M2-macrophage biomarkers (CD206, Arg1) were upregulated in BMDM cells which were induced with IL-4 (Figure 1(e)). Taken together, these findings suggested that Siglec-15 might be involved in the regulation of TAMs in the TME of pancreatic cancer.

**3.2. Deletion of Siglec-15 Inhibits the Polarization of Macrophages towards M2 Macrophages.** The main focus of research on TAMs in the tumor microenvironment was the polarization and phagocytosis of tumor cells, which are regulated by related genes or receptors. Previously, we found that Siglec-15 is highly expressed in M2 macrophages. Therefore, we hypothesized whether Siglec-15 is involved in the regulation of TAM polarization. For further verification, we extracted BMDMs from WT and Siglec-15 KO mice and induced them into M1 or M2 phenotype macrophages by using LPS plus IFN- $\gamma$  or IL-4 stimulation. In addition, for the better simulation of the effect caused by cytokines which are secreted by tumor cells on TAMs in the TME, we also collected the supernatant of pan02 cells and stimulated macrophages with tumor supernatant conditioned medium. After then, qPCR assay was performed to detect the inflammatory factors and chemokines expressed by M1 macrophages and biomarkers expressed by M2 macrophages. The results showed that knocking out Siglec-15 in macrophages does not affect biomarker genes of M1 macrophages (Figures 2(a)–2(c)) while significantly inhibiting the IL-4 (Figures 2(d)–2(f)) or Pan02 supernatant-induced M2 macrophage marker genes (Figures 2(g)–2(i)).

**3.3. The Effect of Siglec-15 on the Glycolytic Pathway of RAW264.7 Macrophages.** Metabolic changes play an impor-

tant role in the activation phenotype of immune cells by regulating critical transcription and posttranscriptional events. Hence, we detected the influence of Siglec-15 on the metabolism level of RAW264.7 macrophages, hexokinase activity, and lactic acid production. The results showed that both hexokinase activity and lactate production of macrophages were significantly reduced in the macrophages which were induced with IL-4 or Pan02 supernatant (Figures 3(a)–3(d)), while knocking out Siglec-15 could significantly inhibit this phenomenon. Besides, when performing qRT-PCR (qPCR) assay to detect the changes in the mRNA transcription level of metabolic enzymes related to the glycolysis pathway, we also found that knocking down Siglec-15 significantly reduced the relative expression of metabolic enzymes which are related to the glycolysis pathway of macrophages (Figure 3(e)). These findings suggest that Siglec-15 might upregulate the glycolysis pathway of macrophage.

**3.4. Siglec-15 Could Interact with Glut1 Directly to Regulate Macrophage Polarization.** For further validation of the interaction between Siglec-15 and related downstream genes, Siglec-15 and Glut1 in RAW265.7 cells were co-expressed, followed by a immunoprecipitation experiment (Co-IP). The results revealed that Siglec-15 could interact with Glut1 (Figure 4(a)). Furthermore, we also performed a GST pull-down assay in vitro and found that Siglec-15 could directly combine with Glut1 (Figure 4(b)). That means Siglec-15 might directly interact with Glut1 to regulate the glucose metabolism. To confirm whether Siglec-15-mediated M2-type polarization of macrophages is affected by Glut1, we detected the expression of M2-type macrophage biomarkers such as Arg-1 and iNOS using qPCR and WB assay. The experimental results indicated that knocking down Glut1 could significantly overexpress the upregulated expression of Arg-1 and iNOS induced by Siglec-15 (Figure 4(c)). Taken together, these results above suggest that a direct interaction between Siglec-15 and Glut1 is involved in the regulation mechanisms of M2 phenotype macrophage polarization.

**3.5. Siglec-15 Regulates Macrophage Inflammatory Factors Partly Dependent on STING.** Glut1 is associated with the regulation of glycolysis metabolism and involved in response to oxidative stress. Furthermore, oxidative stress could disrupt the original balance of cytoplasmic nucleic acid metabolism and increase the nuclease tolerance of cytoplasmic DNA. These could result in DNA accumulation in the cytoplasm and activate the cGAS-STING signaling pathway to express and release associated inflammatory factors. Therefore, we continue to explore the influence of Siglec-15 on macrophage polarization regulation and the role of the cGAS-STING signaling pathway. We extracted the primary generation of peritoneal macrophages from Siglec-15-KO and wild-type mice and stimulated them with IL-4 or Pan-02 supernatant. The results show that at different time points of IL-4 stimulation, the expression of cGAS protein and phosphorylated STING in the wild-type group gradually decreased, while there was no change in the siglec-15-KO group. Besides, the stimulation of Pan-02 supernatant also

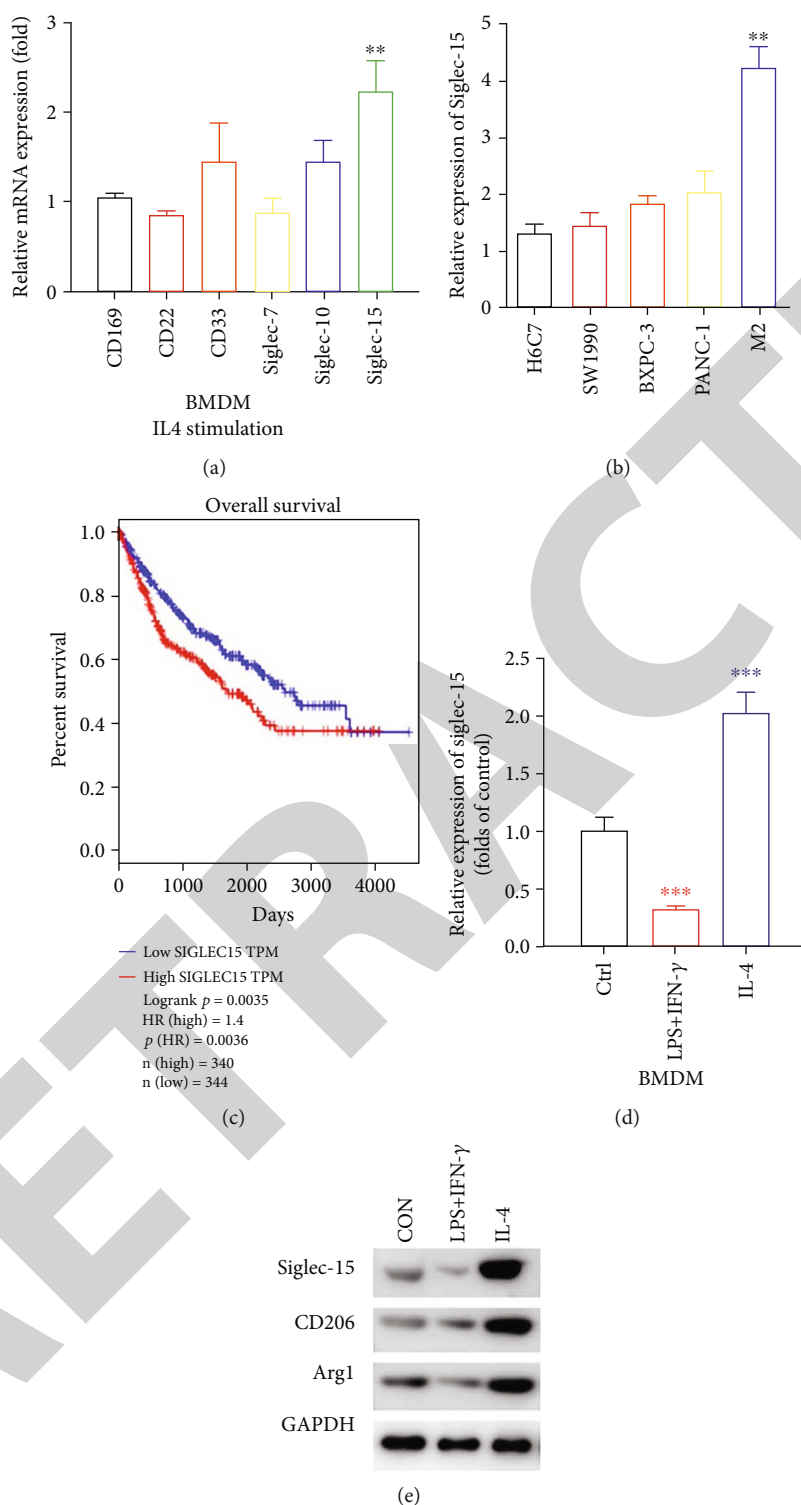


FIGURE 1: Siglec-15 was expressed differently in M1 and M2 macrophages. (a) 20 ng/mL IL-4 was used to induce MΦ into M2 type. The expression of the Siglec family in M2-type MΦ was detected by qPCR. (b) Extract the total RNA of different tumor cells and TAMs and use qPCR assay to detect the expression level of Siglec-15. (c) Correlation analysis between the expression level of Siglec-15 and the overall survival (OS) of pancreatic tumors. (d) Siglec-15 transcription level of BMDMs stimulated by 100 ng/mL LPS and 20 ng/mL IFN-γ, or 20 ng/mL IL-4. (e) Siglec-15 protein level of BMDMs stimulated by 100 ng/mL LPS and 20 ng/mL IFN-γ, or 20 ng/mL IL-4. The experiments were repeated three times, and each experiment was triplicated.

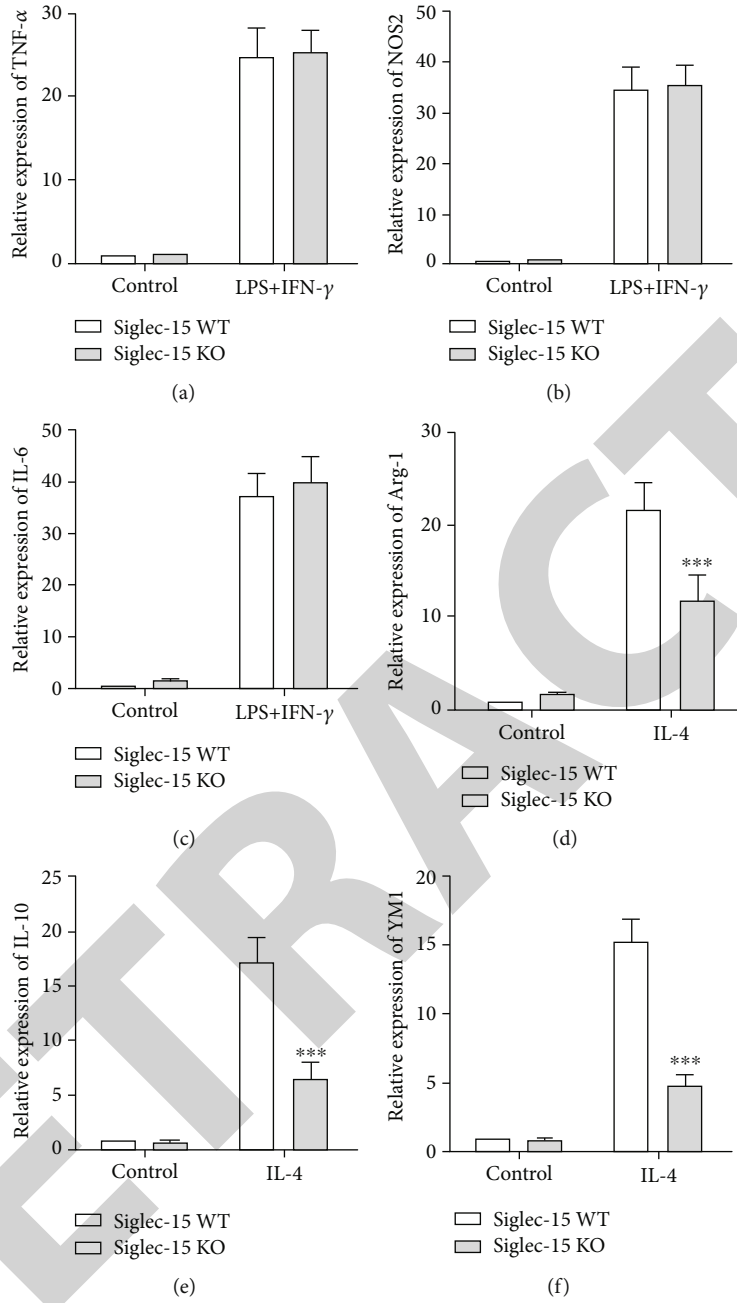


FIGURE 2: Continued.

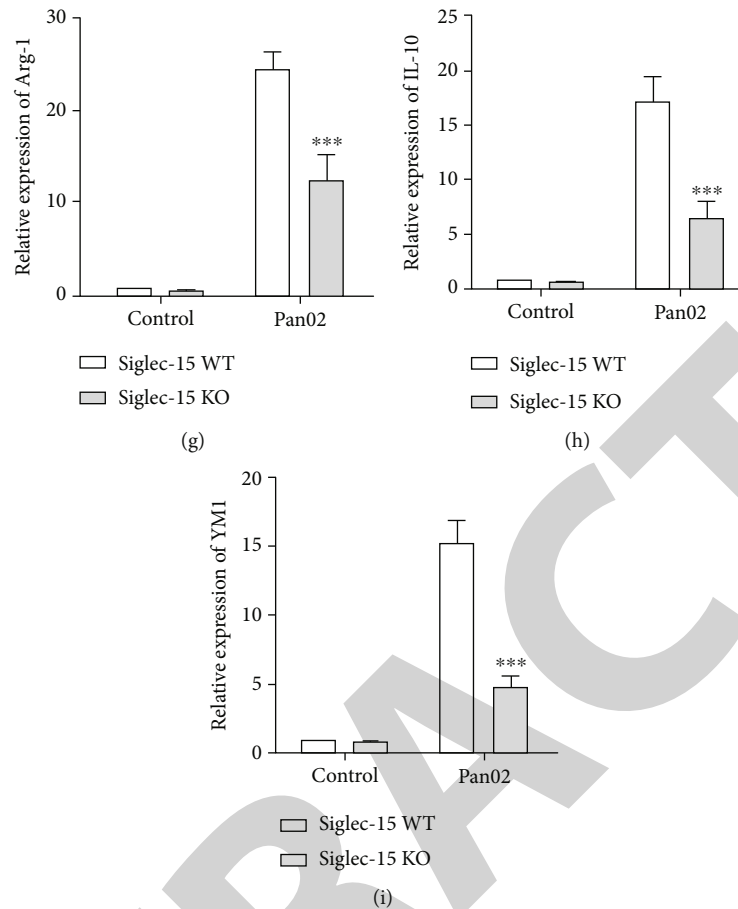


FIGURE 2: Deletion of Siglec-15 inhibits the polarization of macrophages towards M2. (a–c) Bone marrow cells from wild-type and Siglec-15 knockout mice were extracted *in vitro* and induced into bone marrow-derived macrophages (BMDMs). 100 ng/mL LPS and 20 ng/mL IFN- $\gamma$  to stimulate for 12 hours; induce them into M1-type macrophages and detect the inflammatory factors expressed by M1-type macrophages by qPCR. (d–f) 20 ng/mL IL-4 to stimulate BMDMs cells for 24 h or 48 h to induce into M2-type macrophages. qPCR detects the marker genes expressed by M2-type macrophages. (g–i) Tumor supernatant conditioned medium to stimulate BMDM cells for 24 h or 48 h to induce into M2-type macrophages, and qPCR to detect the marker genes expressed by M2-type macrophages. The experiments were repeated three times, and each experiment was triplicated.

had similar results (Figures 5(a) and 5(b)). In addition, cisplatin, which had been confirmed to cause the cGAS-STING signaling pathway activation in macrophages, was employed again in primary macrophages of mice with Siglec-15 overexpression and knockout. Then, we found that overexpression of Siglec-15 could reduce the activation of the cGAS-STING signaling pathway induced by cisplatin in primary macrophages, while deletion of Siglec-15 rescued the downregulated cGAS-STING signaling induced by IL-4 (Figures 5(c) and 5(d)).

**3.6. Glut1-Related Oxidative Stress Is Involved in the Regulation of Macrophage Inflammatory Factors.** To confirm whether Glut1-related oxidative stress plays a role in the cGAS-STING pathway, we used BAY-876 (an inhibitor of Glut1) in further study. The results showed that in the primary peritoneal macrophages of wild-type or STING-KO mice, the phosphorylation of TBK1 decreased significantly with the stimulation of IL-4 or Pan-02, while BAY-876 could inhibit this phenomenon (Figures 6(a) and 6(b)). In addition,

the transcription and released levels of M1-macrophage-related inflammatory factors such as TNF- $\alpha$ , IL-1 $\beta$ , and IL-6 were significantly decreased in either the WT or STING KO macrophage treated with IL-4 (Figure 6(c)), while BAY-876 could significantly inhibit this phenomenon (Figure 6(d)). These findings suggest that Siglec-15 might participate in regulating the cGAS-STING signaling pathway through Glut1-related oxidative stress.

**3.7. Siglec-15 Knockout Inhibits the Growth of Subcutaneous Transplanted Tumors in Mice.** For tumor study *in vivo*, we first selected 6–8-week-old WT and Siglec-15-KO C57/BL6 mice and injected Pan-02 cells subcutaneously on the back. Then, we tracked tumor growth at different time points over time and peeled off tumors and took pictures after 25 days. The results showed that the volume of subcutaneously transplanted tumors in Siglec-15 knockout mice is significantly smaller than that of WT mice (Figures 7(a) and 7(b)). Simultaneously, after constructing the animal model, we also observe the 20th day and drew a survival curve. The results

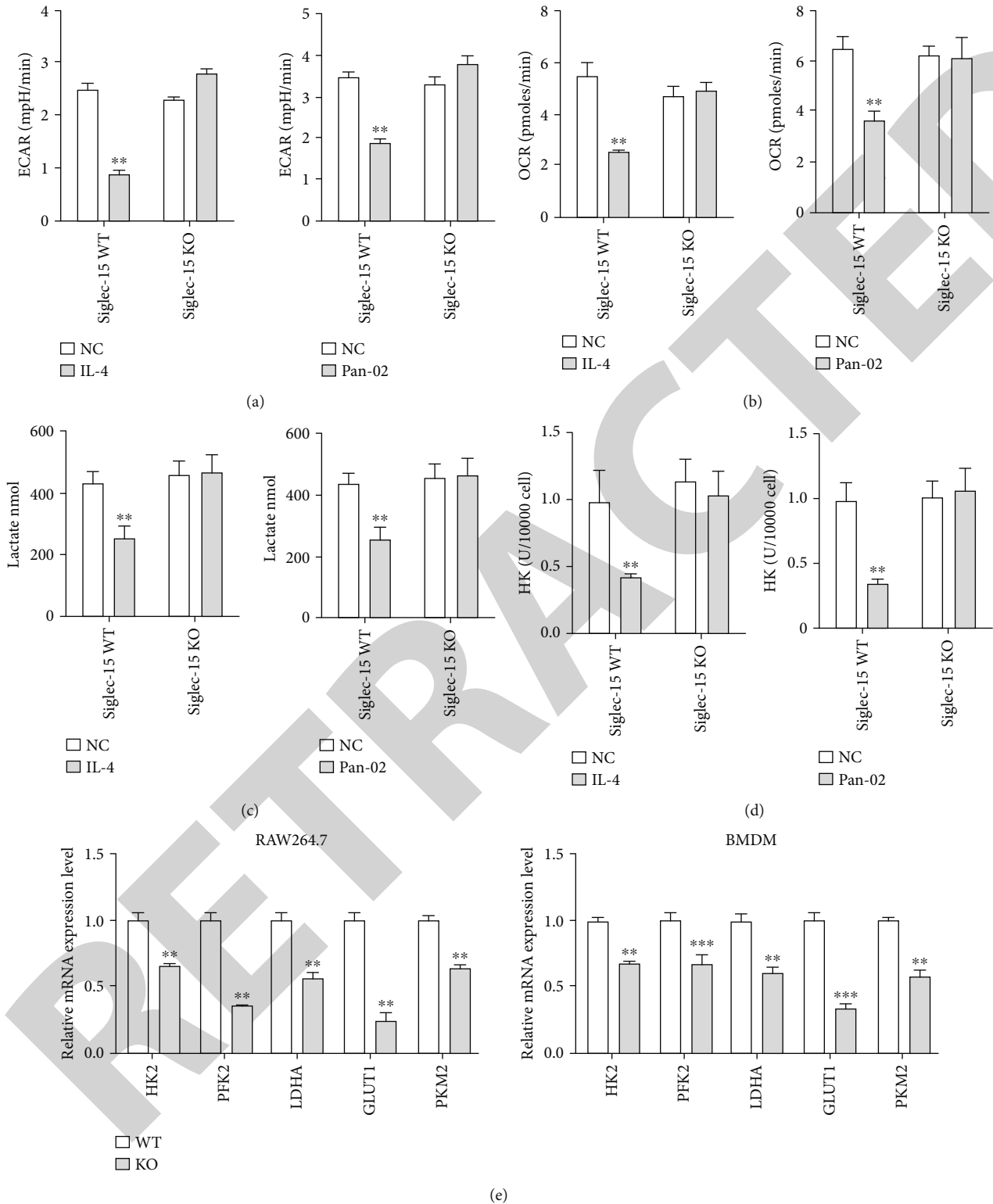


FIGURE 3: The effect of Siglec-15 on the glycolytic pathway of RAW264.7 macrophages. (a) Bone marrow cells from wild-type and Siglec-15 knockout mice were extracted in vitro and induced into bone marrow-derived macrophages (BMDMs). The effect of IL-4 stimulation on ECAR of BMDMs cells. (B) The effect of IL-4 stimulation on the ECAR of BMDMs cells. (c) The effect of IL-4 stimulation on the lactic acid production of BMDMs cells. (d) The effect of IL-4 stimulation on HK enzyme activity. (e) The effect of Siglec-15 knockout of RAW264.7 and BMDMs on the transcription level of glycolysis-related genes.



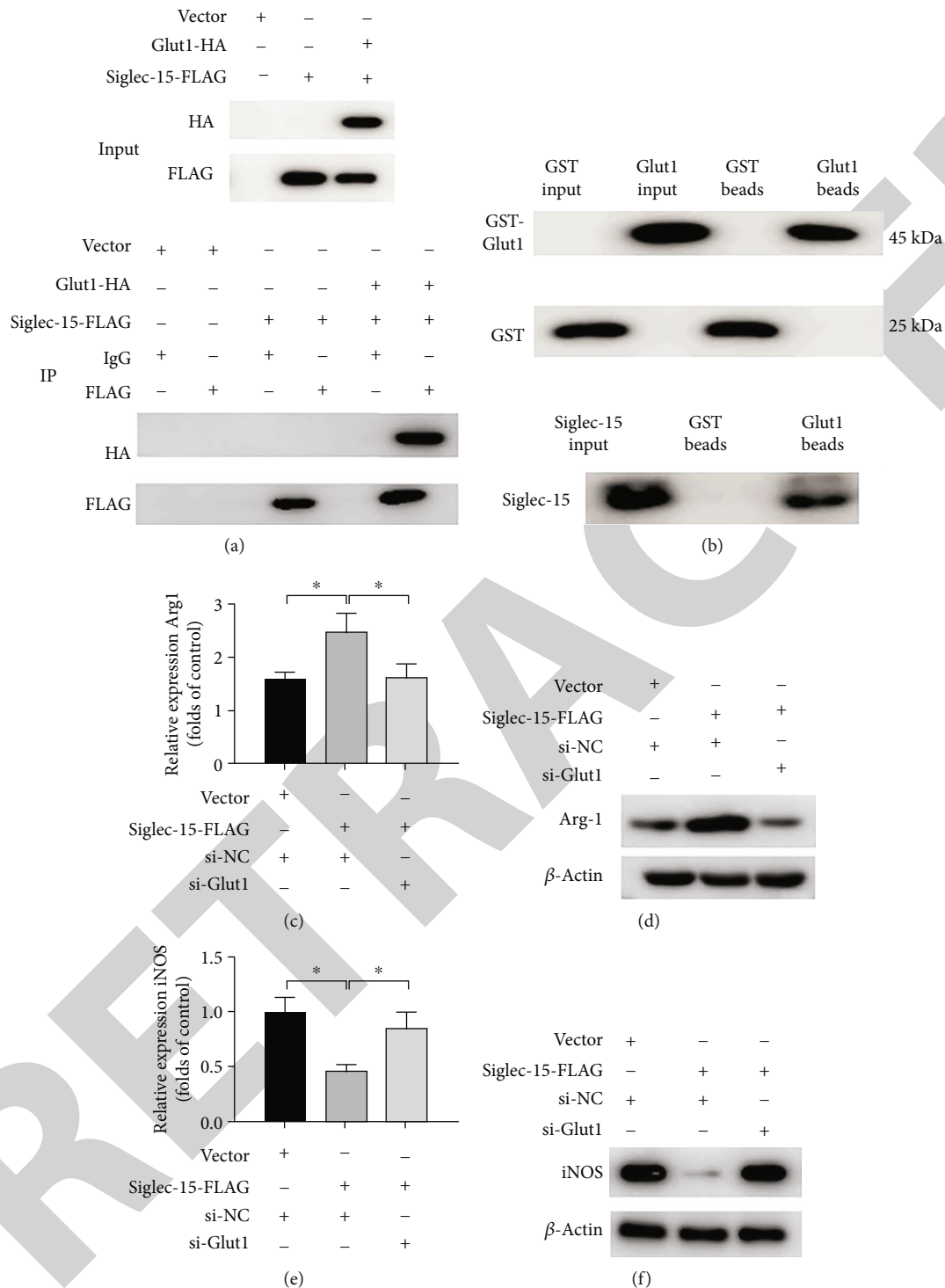
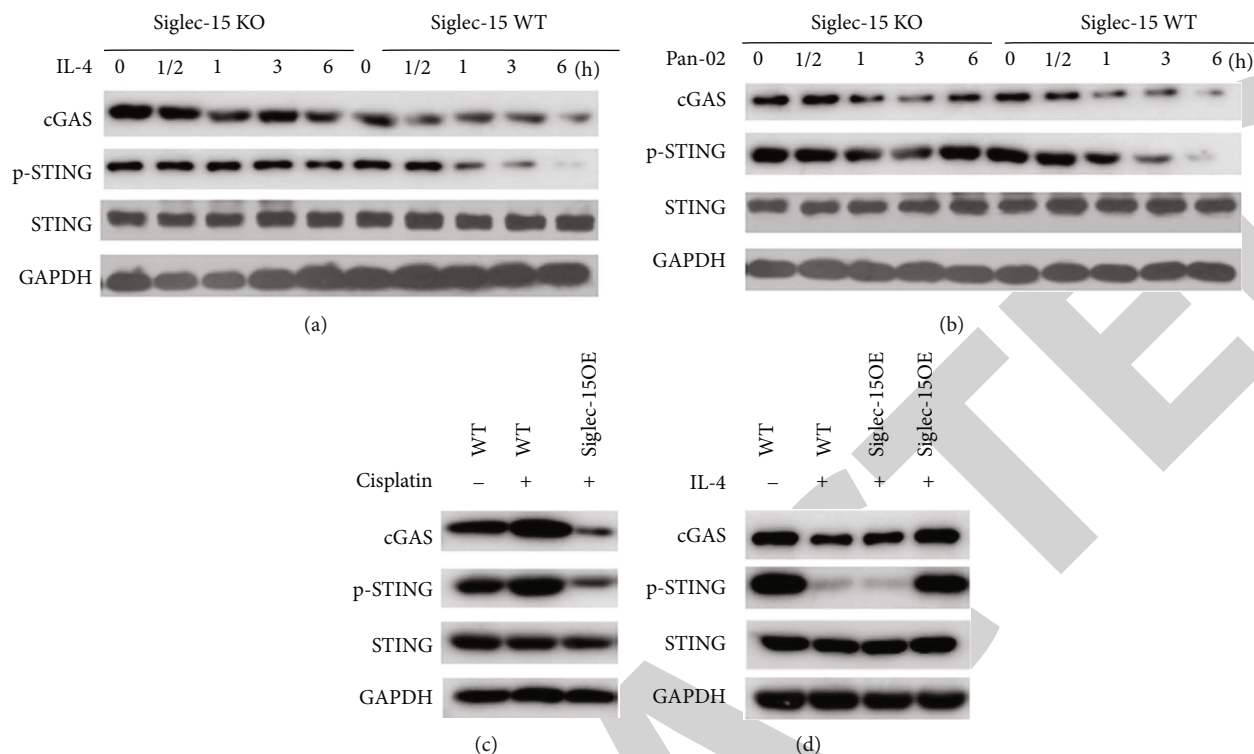


FIGURE 4: Siglec-15 interacts with Glut1 to regulate macrophage polarization. (a) Immunoblotting of cell lysate co-transformed with Siglec-15-FLAG+Glut1-HA with FLAG antibody immunoprecipitation. (b) GST protein pull-down results of GST/GST-Glut1 protein and Glut1 protein. (c) qPCR assay indicated that knocking down Glut1 can overexpress Siglec-15-induced upregulation of Arg1 expression which was a biomarker of M2 phenotype macrophage. (d) Western blotting assay indicated that knocking down Glut1 can overexpress Siglec-15-induced upregulation of Arg1 expression which was a biomarker of M2 phenotype macrophage. (e) qPCR assay indicates that knocking down Glut1 can overexpress Siglec-15-induced upregulation of iNOS which is another biomarker of M2 phenotype macrophage. (f) Western blotting assay indicate that knocking down Glut1 can overexpress Siglec-15-induced upregulation of iNOS which is another biomarker of M2 phenotype macrophage. The experiments were repeated three times, and each experiment was triplicated.



**FIGURE 5:** Siglec-15 regulates macrophage inflammatory factors partly dependent on STING. (a) BMDMs of bone marrow-derived macrophages from WT and Siglec-15 KO mice were extracted, and 50 ng/mL IL-4 stimulated the cells. The proteins were collected according to different experimental time points, and the cGAS-STING signaling pathway was detected by western blot. (b) BMDMs of bone marrow-derived macrophages from WT and Siglec-15 KO mice were extracted, and conditioned medium containing Pan-02 supernatant stimulated the cells. The proteins were collected according to different experimental time points, and the cGAS-STING signaling pathway was detected by western blot. (c) After extracting Siglec-15 KO mouse peritoneal primary macrophages, stimulated with cisplatin for 24 hours, the protein expression of the cGAS-STING signaling pathway conditioned medium containing Pan-02 supernatant was as shown in the figure. (d) After extracting Siglec-15 KO or Siglec-15 OE mouse peritoneal primary macrophages, after IL-4 stimulation, the expression of cGAS-STING signaling pathway molecule protein-conditioned medium containing Pan-02 supernatant was as shown. The experiments were repeated three times, and each experiment was triplicated.

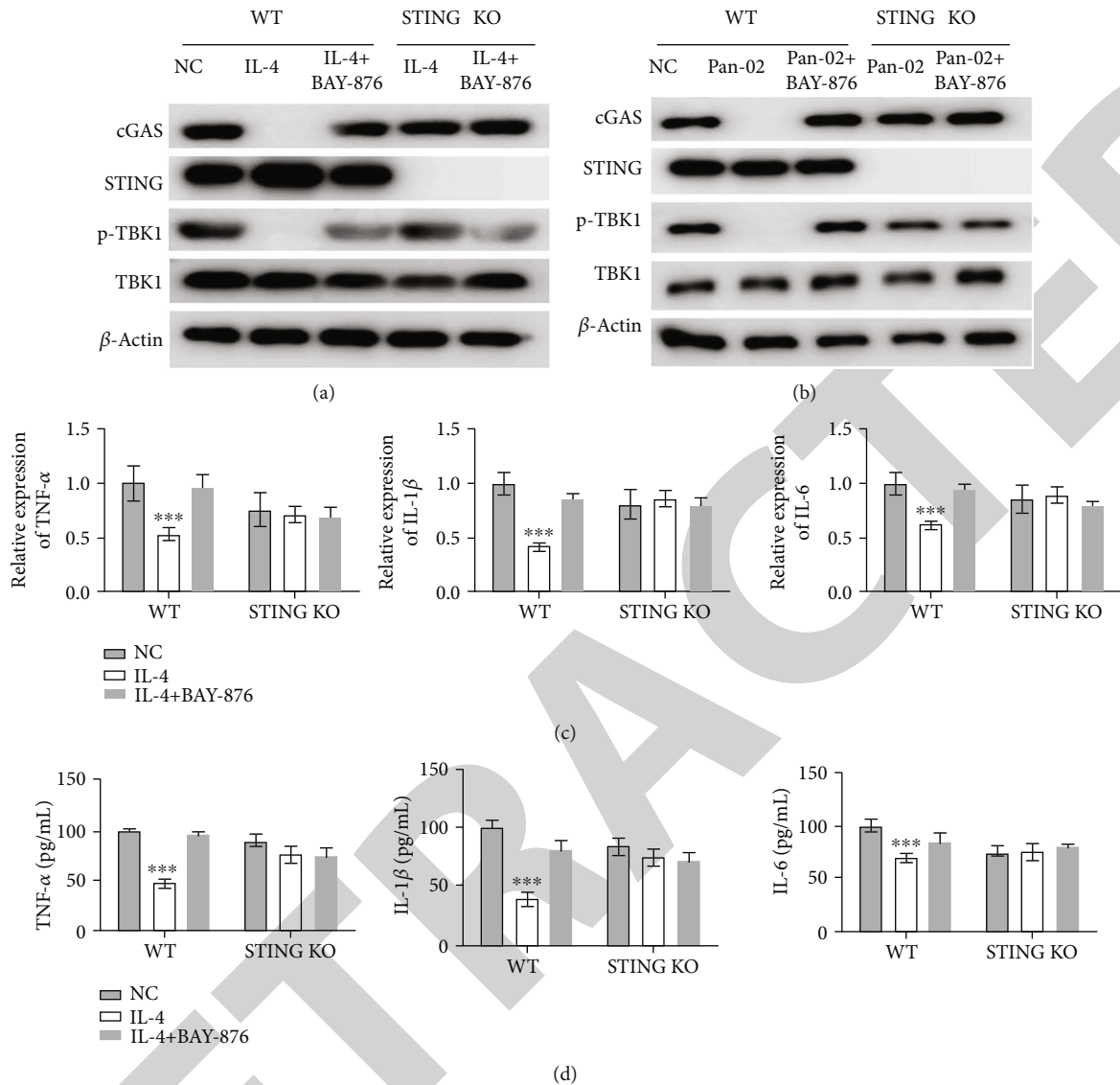
revealed that absence of Siglec-15 significantly increased the survival rate of subcutaneous tumor-bearing mice (Figure 7(d)) and reduced the number of metastatic lymph nodes (Figure 7(d)). For the purpose of eliminating the interference of other cell regulations involved in Siglec-15, we mixed macrophages from WT or Siglec-15 KO mice with Pan-02 at the 1:1 ratio, followed by co-injecting into wild-type C57/BL6 mice on the back subcutaneously. Interestingly, we observed that the growth of tumor volume was significantly slow in the Pan-02 + Siglec-15 KO macrophage co-injecting model (Figures 7(e) and 7(f)). These finds further suggest that Siglec-15 affects the tumor progression by regulating TAMs in the TME of pancreatic cancer.

#### 4. Discussion

It is generally accepted that the TME plays an important role in the regulation of antitumor immunity and tumor progression including pancreatic cancer. Tumor-associated macrophages (TAMs) which are the most abundant infiltrative immune cells in the TME have a tremendous impact in the formation of an immunosuppressive tumor microenvironment [7]. Although TAMs exhibit dual functions of inducing

tumors or inhibiting tumor progression according to different factors existing in the TME, they preferentially polarized into M2-like phenotype macrophages and contributed to tumor progression in various cancers, including PDAC [9–12]. In addition, it was also reported that M2-macrophage infiltration was significantly associated with chemoresistance and poor prognosis of PDAC [11, 12]. However, the mechanisms of TAM polarization are still unclear.

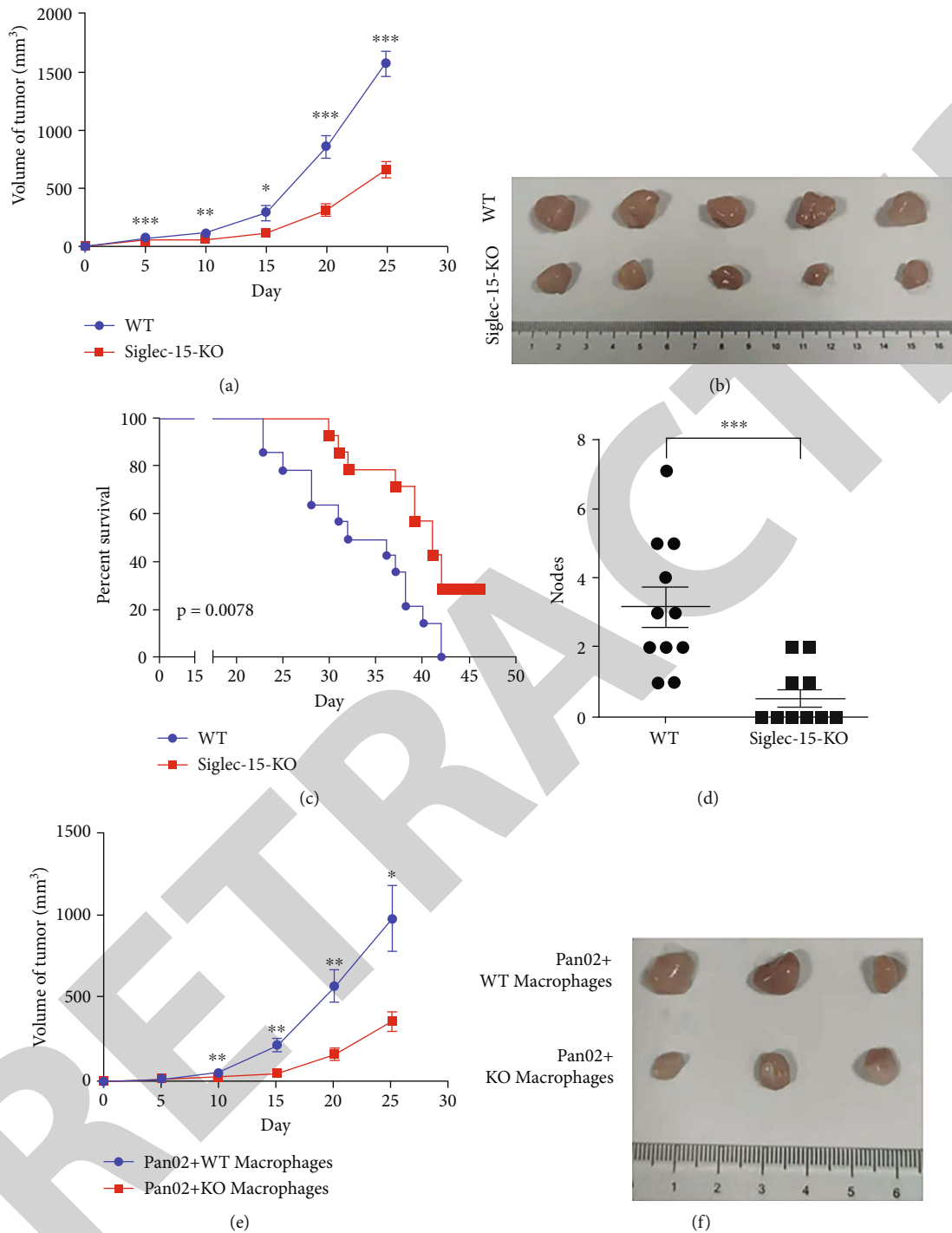
In recent years, members of the sialic acid-binding immunoglobulin-like lectin (Siglecs) family are reported to play a critical role in regulation of immune tolerance, inflammatory response, and tumor progression of various tumors [21–23]. Among them, Siglec-15 appears as an emerging target for tumor immunotherapy especially for patients who do not respond to PD-1/PD-L1 inhibitor treatment. Previous studies indicated that Siglec-15 is highly expressed in M2 macrophages and mainly regulates the effector T cell growth relying on the interleukin 10 (IL-10) level in the TME [24]. In addition, it was also suggested that Siglec-15 could enhance tumor immune escape in the TME without an association with the PD-1/PD-L1 pathway [13–15]. However, whether it is involved in functional



**FIGURE 6:** Glut1-related glycolysis is involved in regulating macrophage inflammatory factors. (A) The peritoneal macrophages of wild-type and STING-KO mice were separately extracted and pre-incubated with Bay-876 for 30 minutes. After stimulation with IL-4, the expression of the cGAS-STING signaling pathway molecules changed. (b) The peritoneal macrophages of wild-type and STING-KO mice were extracted separately and pre-incubated with Bay-876 for 30 minutes. After stimulation with Pan-02 supernatant, the expression of cGAS-STING signaling pathway molecules changed. (c, d) After the above stimulation, the transcription level and release changes of inflammatory factors related to M1-macrophage were detected. The experiments were repeated three times, and each experiment was triplicated.

regulation of macrophages in pancreatic cancer is still unclear. To address this issue, we used LPS and IFN- $\gamma$  to induce BMDMs derived from WT or Siglec-15-KO mice into M1-type macrophages, while using IL-4 or supernatant from PANC-1 tumor cells to induce BMDMs into M2-type macrophages. Then, we performed qPCR assay to detect the expression of different biomarker genes related to macrophages. Interestingly, we found that in BMDMs derived from Siglec-15 KO mice, the expression of M2-type macrophage biomarkers such as Arg1 and CD206 was significantly decreased. These results suggest that Siglec-15 participates in the polarization process of M2-type macrophages in the TME of PDAC.

For the purpose of further investigating the biological function of Siglec-15 on macrophage and tumor progression of PDAC, we then established a series of tumor studies on mice. Then, we found that when knocking out Siglec-15 in mice, it could significantly inhibit the tumor progression of PDAC transplanted subcutaneously and improve the survival time of tumor model mice. In addition, to confirm the specific regulation of TAMs caused by Siglec-15 in PDAC, we further co-injected macrophages from WT or Siglec-15 KO mice and PANC-1 cells into WT mice aged 6–8 weeks. The experimental results showed that co-injection with macrophage from WT mice could significantly promote the tumor growth, while co-injection with



**FIGURE 7: Siglec-15 knockout inhibits the growth of subcutaneous transplanted tumors in mice.** (a, b) Six to eight weeks of wild-type and Siglec-15 KO mice, 200  $\mu$ L of tumor cells was injected subcutaneously, the tumor volume was calculated and statistics ( $n = 10$ ), and the tumor was peeled off and photographed. (c) In the survival curve experiment, the survival of mice was observed and recorded every day from the 20th day ( $n = 14$ ). (d) Take mouse lymph nodes and count the tumor nodules in the lymph nodes. (e, f) Six- to eight-week-old wild-type mice were selected for macrophage and tumor cell co-injection model (200  $\mu$ L, 1:1). The tumor was measured once in 5 days for recording and stripped and photographed. \* $p < 0.05$ ; \*\* $p < 0.01$ ; \*\*\* $p < 0.001$ . The experiments were repeated three times, and each experiment was triplicated.

Siglec-15 KO macrophages showed opposite results. Therefore, we believe that Siglec-15 could inhibit tumor progression of PDAC by regulating TAMs located in the TME.

After establishing that Siglec-15 has a regulatory influence on macrophage polarization both in vitro and in vivo, we proceeded to investigate the cellular and molecular

mechanisms by which Siglec-15 exerts this effect, as well as the specific role it plays in the progression of tumors. Glut1 is an important member of the glucose transporter family, which regulates glucose transport and metabolism [25]. Numerous studies have shown that a high expression of Glut1 is associated with tumor progression and poor prognosis in multiple cancer types including PDAC [26–29]. Simultaneously, it is also reported that Glut1 is involved in oxidative stress response [30]. Interestingly, in our further study we also found that deficiency of Siglec-15 could inhibit the polarization of macrophages toward M2 phenotype macrophages by downregulating metabolism-related enzymes and the extracellular acidification rate (ECAR) and oxygen consumption rate (OCR) were also significantly higher in Siglec-15 KO macrophages. That means glycolysis or metabolism-related pathway and genes might be involved in polarization-regulating mechanisms. Therefore, we further analyzed the clinical correlation between Siglec-15 and co-expressed metabolic genes using TCGA database and found that Glut1 has a strong correlation with Siglec-15. These results suggest that Glut1 might play a role in M2 phenotype macrophage polarization regulated by Siglec-15. For further validation, we also conducted the CO-IP, GST-pulldown assay, and M2 phenotype macrophage biomarkers and confirmed that Siglec-15 could increase the glycolysis by interacting with Glut1 to regulate the polarization of TAMs in PDAC.

Another interesting finding of this study was that the cGAS-STING pathway was partly involved in the regulation of macrophage inflammatory factor secretion. Cyclic GMP-AMP synthase (cGAS) was a cytosolic dsDNA sensor that triggers innate immune response via production of cGAMP, which is the adaptor protein of STING. Activation of the cGAS-STING signal pathway could promote the expression and secretion of type I interferon and inflammatory factors such as TNF- $\alpha$  and IL-6 [31]. Besides, studies have also shown that the cGAS-STING signaling pathway was critical in acute pancreatitis, autoimmune diseases, and tumors [32]. In our study, we confirmed that Siglec-15 could partly inhibit the activation of cGAS-STING and the regulation of glycolysis related to Glut1 plays a role in this process.

However, the present study had several limitations. First, the expression of Siglec-15 in PDAC patients was not confirmed and further confirmation using more tumor samples is needed to confirm the expression and diagnostic value of Siglec-15 in PDAC patients. Second, although we found that a high Siglec-15 expression was associated with poor prognosis in PDAC patients based on TCGA datasets, its prognostic value in other cohort was not confirmed. Third, the potential mechanisms involved in the function of Siglec-15 regulating the inflammatory response needed to be further studied.

Taken together, our data suggested that Siglec-15 was critical for the polarization of TAMs in PDAC. It could interact with Glut1 and inhibit the cGAS-STING pathway in regulation of TAM polarization and release of the macrophage inflammatory factor to promote the tumor progression of PDAC. Hence, our findings were expected to provide a novel immunotherapy strategy for the patients with PDAC.

## Data Availability

The authors declare that all the other data supporting the findings of this study are available within the article and from the corresponding author upon reasonable request.

## Conflicts of Interest

The authors declare no competing interests.

## Authors' Contributions

Huagen Li and RongXuan Zhu contributed equally to this work.

## Acknowledgments

This study was supported by the Key Research and Development Program of Zhejiang Province (2020C03024).

## References

- [1] R. L. Siegel, K. D. Miller, H. E. Fuchs, and A. Jemal, "Cancer statistics, 2021," *CA: a Cancer Journal for Clinicians*, vol. 71, no. 1, pp. 7–33, 2021.
- [2] A. McGuigan, P. Kelly, R. C. Turkington, C. Jones, H. G. Coleman, and R. S. McCain, "Pancreatic cancer: a review of clinical diagnosis, epidemiology, treatment and outcomes," *World Journal of Gastroenterology*, vol. 24, no. 43, pp. 4846–4861, 2018.
- [3] J. X. Hu, C. F. Zhao, W. B. Chen et al., "Pancreatic cancer: a review of epidemiology, trend, and risk factors," *World Journal of Gastroenterology*, vol. 27, no. 27, pp. 4298–4321, 2021.
- [4] M. B. Lankadasari, P. Mukhopadhyay, S. Mohammed, and K. B. Harikumar, "TAMing pancreatic cancer: combat with a double edged sword," *Molecular Cancer*, vol. 18, no. 1, p. 48, 2019.
- [5] W. J. Ho, E. M. Jaffee, and L. Zheng, "The tumour microenvironment in pancreatic cancer - clinical challenges and opportunities," *Nature Reviews. Clinical Oncology*, vol. 17, no. 9, pp. 527–540, 2020.
- [6] M. Huber, C. U. Brehm, T. M. Gress et al., "The immune microenvironment in pancreatic cancer," *International Journal of Molecular Sciences*, vol. 21, no. 19, p. 7307, 2020.
- [7] Y. Komohara, M. Jinushi, and M. Takeya, "Clinical significance of macrophage heterogeneity in human malignant tumors," *Cancer Science*, vol. 105, no. 1, pp. 1–8, 2014.
- [8] S. Gordon and F. O. Martinez, "Alternative activation of macrophages: mechanism and functions," *Immunity*, vol. 32, no. 5, pp. 593–604, 2010.
- [9] A. Mantovani, P. Allavena, and A. Sica, "Tumour-associated macrophages as a prototypic type II polarised phagocyte population: role in tumour progression," *European Journal of Cancer*, vol. 40, no. 11, pp. 1660–1667, 2004.
- [10] L. Cassetta and T. Kitamura, "Targeting tumor-associated macrophages as a potential strategy to enhance the response to immune checkpoint inhibitors," *Frontiers in Cell and Development Biology*, vol. 6, p. 38, 2018.
- [11] K. Yoshikawa, S. Mitsunaga, T. Kinoshita et al., "Impact of tumor-associated macrophages on invasive ductal carcinoma

## Retraction

# Retracted: Leukemia Inhibitory Factor Facilitates Self-Renewal and Differentiation and Attenuates Oxidative Stress of BMSCs by Activating PI3K/AKT Signaling

### Oxidative Medicine and Cellular Longevity

Received 20 June 2023; Accepted 20 June 2023; Published 21 June 2023

Copyright © 2023 Oxidative Medicine and Cellular Longevity. This is an open access article distributed under the Creative Commons Attribution License, which permits unrestricted use, distribution, and reproduction in any medium, provided the original work is properly cited.

This article has been retracted by Hindawi following an investigation undertaken by the publisher [1]. This investigation has uncovered evidence of one or more of the following indicators of systematic manipulation of the publication process:

- (1) Discrepancies in scope
- (2) Discrepancies in the description of the research reported
- (3) Discrepancies between the availability of data and the research described
- (4) Inappropriate citations
- (5) Incoherent, meaningless and/or irrelevant content included in the article
- (6) Peer-review manipulation

The presence of these indicators undermines our confidence in the integrity of the article's content and we cannot, therefore, vouch for its reliability. Please note that this notice is intended solely to alert readers that the content of this article is unreliable. We have not investigated whether authors were aware of or involved in the systematic manipulation of the publication process.

Wiley and Hindawi regrets that the usual quality checks did not identify these issues before publication and have since put additional measures in place to safeguard research integrity.

We wish to credit our own Research Integrity and Research Publishing teams and anonymous and named

external researchers and research integrity experts for contributing to this investigation.

The corresponding author, as the representative of all authors, has been given the opportunity to register their agreement or disagreement to this retraction. We have kept a record of any response received.

### References

- [1] Y. Liang, R. Zhou, X. Liu et al., "Leukemia Inhibitory Factor Facilitates Self-Renewal and Differentiation and Attenuates Oxidative Stress of BMSCs by Activating PI3K/AKT Signaling," *Oxidative Medicine and Cellular Longevity*, vol. 2022, Article ID 5772509, 28 pages, 2022.

## Research Article

# Leukemia Inhibitory Factor Facilitates Self-Renewal and Differentiation and Attenuates Oxidative Stress of BMSCs by Activating PI3K/AKT Signaling

Youde Liang<sup>1</sup>, Ruiping Zhou<sup>1</sup>, Xin Liu<sup>1</sup>, Lin You<sup>1</sup>, Chang Chen<sup>1</sup>, Xiaoling Ye<sup>1</sup>, Wei Wei<sup>1</sup>, Jie Liu<sup>1</sup>, Jiawei Dai<sup>1</sup>, Kaixiong Li<sup>1</sup>, and Xiangxiang Zhao<sup>2</sup>

<sup>1</sup>Department of Stomatology, Southern University of Science and Technology Yantian Hospital, Shenzhen, Guangdong, China

<sup>2</sup>Department of Neurology, Changhai Hospital, Naval Medical University, Shanghai, China

Correspondence should be addressed to Youde Liang; [liangyoude1229@sina.com](mailto:liangyoude1229@sina.com) and Xiangxiang Zhao; [userzhaoux@foxmail.com](mailto:userzhaoux@foxmail.com)

Received 2 May 2022; Revised 9 July 2022; Accepted 15 July 2022; Published 5 September 2022

Academic Editor: Tian Li

Copyright © 2022 Youde Liang et al. This is an open access article distributed under the Creative Commons Attribution License, which permits unrestricted use, distribution, and reproduction in any medium, provided the original work is properly cited.

**Objective.** Transplantation of bone marrow-derived mesenchymal stem cells (BMSCs) remains a hopeful therapeutic approach for bone defect reconstruction. Herein, we investigated the effects and mechanisms of leukemia inhibitory factor (LIF) in the function and viability of hypoxic BMSCs as well as bone defect repair. **Methods.** The effects of LIF on apoptosis (flow cytometry, TUNEL staining), mitochondrial activity (JC-1 staining), proliferation (colony formation, EdU staining), and differentiation (CD105, CD90, and CD29 via flow sorting) were examined in hypoxic BMSCs. LIF, LIFR, gp130, Keap1, Nrf2, antioxidant enzymes (SOD1, catalase, GPx-3), bone-specific matrix proteins (ALP, BSP, OCN), PI3K, and Akt were detected via immunoblotting or immunofluorescent staining. BMSCs combined with biphasic calcium phosphate scaffolds were implanted into calvarial bone defect mice, and the therapeutic effect of LIF on bone defect was investigated. **Results.** Hypoxic BMSCs had increased apoptosis and oxidative stress and reduced mitochondrial activity. Additionally, LIF, LIFR, and gp130 were upregulated and PI3K/Akt activity was depressed in hypoxic BMSCs. Upregulated LIF alleviated apoptosis and oxidative stress and heightened mitochondrial activity and PI3K/Akt signaling in hypoxic BMSCs. Additionally, LIF overexpression promoted self-renewal and osteogenic differentiation of BMSCs with hypoxic condition. Mechanically, LIF facilitated self-renewal and differentiation as well as attenuated oxidative stress of BMSCs through enhancing PI3K/AKT signaling activity. Implantation of LIF-overexpressed BMSC-loaded BCP scaffolds promoted osteogenesis as well as alleviated oxidative stress and apoptosis through PI3K/Akt signaling. **Conclusion.** Our findings demonstrate that LIF facilitates self-renewal and differentiation and attenuates oxidative stress of BMSCs by PI3K/AKT signaling.

## 1. Introduction

Bone defects caused by various traumas and diseases have become one of the most common clinical diseases [1]. At present, bone transplantation is the main method to solve the repair of bone defects [2]. Small-scale bone defects can achieve favorable clinical efficacy, but the treatment of large-scale bone defects, especially those complicated by infection, tumor, systemic metabolic, and vascular diseases, is still a clinical issue [3]. Therefore, to reduce surgical complexity and accelerate bone healing, innovative therapies are urgently needed. Tissue engineering techniques consisting of

seed cells, scaffold materials, and growth factors play a key role in inducing regenerative repair of damaged tissues and organs [4]. Among the three basic elements of tissue engineering techniques, seed cells are essential for initiating tissue regeneration [5]. With the deepening of tissue engineering research, the importance of mesenchymal stem cells in tissue regeneration has received more and more attention [6]. However, stem cells or transplanted cells chemotactically derived from blood or bone marrow undergo apoptosis due to the release of a large number of inflammatory mediators and proapoptotic factors (local hypoxia, acidosis, accumulation of metabolites, tissue necrosis, oxidative

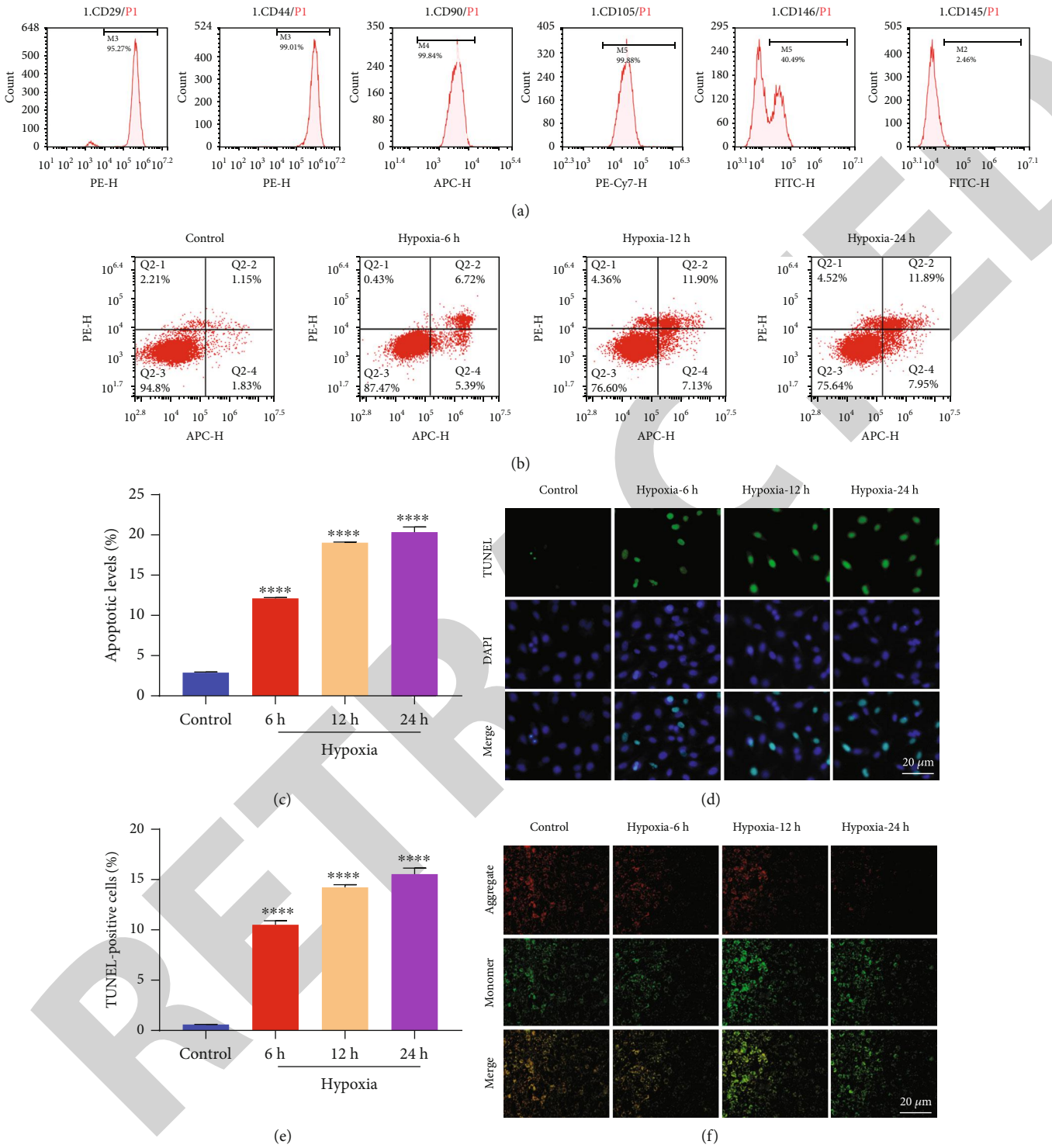


FIGURE 1: Continued.



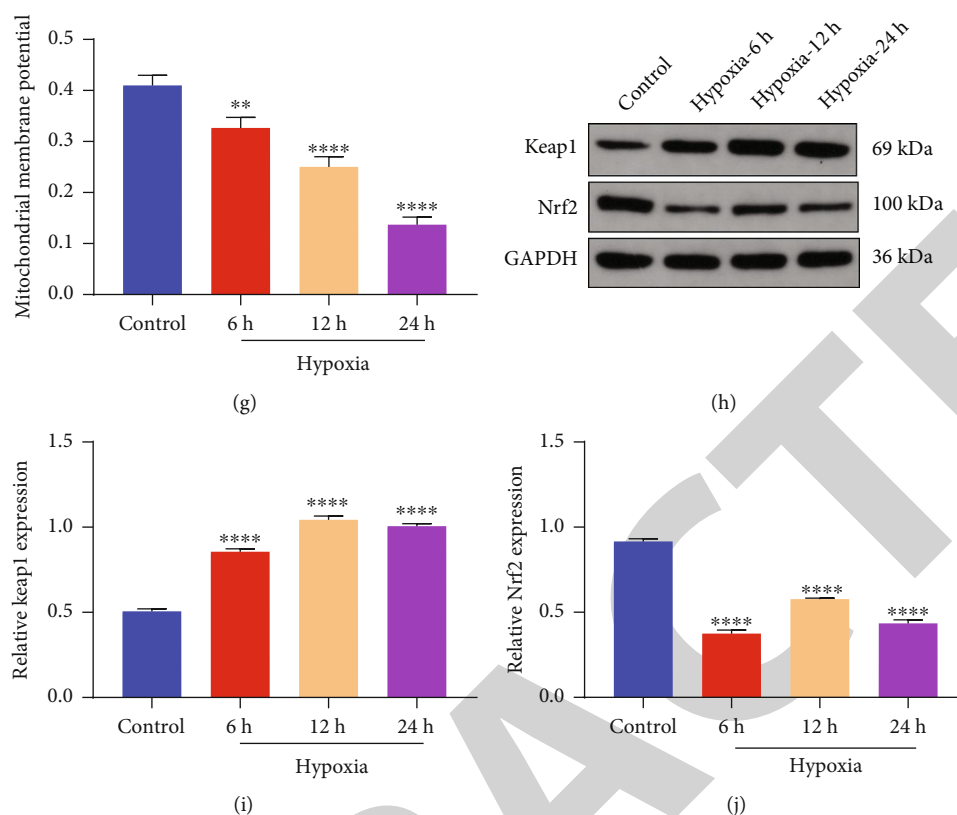


FIGURE 1: BMSCs exhibit increased apoptosis and oxidative stress along with reduced mitochondrial membrane potential in hypoxic condition. (a) Isolation and identification of BMSCs by detecting cell surface antigens via flow sorting. (b, c) Flow cytometry and (d, e) TUNEL staining for examining apoptosis of BMSCs under exposure to hypoxia for 6, 12, and 24 h. Bar, 20  $\mu$ m. (f, g) JC-1 staining for detecting mitochondrial membrane potential of hypoxic BMSCs. Bar, 20  $\mu$ m. (h–j) Immunoblotting of the activity of Keap1 and Nrf2 in hypoxia-exposed BMSCs.

stress, etc.) [7]. Bone marrow-derived mesenchymal stem cells (BMSCs) are one of the important cells involved in bone formation and angiogenesis. Studies have shown that human mesenchymal stem cells implanted in healthy adult nude mice can survive and maintain their own activity for at least 6 weeks [8]. However, Zhang et al. found that BMSCs die on a large scale after 3 days in hypoxic environment [9]. Yuan et al. also observed a sharp decrease in the number of BMSCs within 1 month after composite implantation with a stent [10]. BMSCs begin to die within 3 days of implantation into the ectopic osteogenic site and are barely detectable at 14 days [11]. Our previous study also found that BMSCs undergo significant apoptosis under hypoxic environment [12]. Therapeutic applications of BMSCs are limited due to the sensitivity to oxidative stress, leading to apoptosis of transplanted BMSCs in damaged bone areas [13]. Activation of PI3K/Akt signaling protects the survival and differentiation of BMSCs from oxidative stress [13]. RNA modification is a posttranscriptional mechanism, which controls gene expression and RNA metabolism [14]. The crosstalk between RNA modification and oxidative stress has been investigated in various human diseases [15]. Additionally, RNA modification exerts a crucial role in differentiation of BMSCs [16]. Enhancing BMSC function is a critical step in

optimizing stem cell-mediated bone repair. The enhanced proliferative capacity enables BMSCs to expand in vitro to sufficient numbers for clinical transplantation. Additionally, after transplantation, BMSCs continue to proliferate and migrate to the injury site and differentiate into osteoblasts or secrete trophic factors to stimulate target cells. Hence, to modify BMSCs in enhancing their functions remains the main focus of recent studies on stem cell-mediated bone defect repair.

Leukemia inhibitory factor (LIF) belongs to the IL-6 family and is a natural multifunctional cytokine in the body [17]. Many tissues and cells in the human body can secrete LIF spontaneously or be induced to do so [18]. Studies have shown that LIF is an important factor in maintaining the survival and self-renewal of stem cells [19]. In vivo experiments found that LIF in a hypoxic microenvironment promotes bone development and bone repair [20]. In the study of myocardial infarction by Berry et al., they found that in the process of fighting myocardial ischemia, LIF maintains the survival and antiapoptosis of myocardial cells by activating downstream signaling pathways, related to the protection of bone marrow stem cell chemotaxis to the infarcted area [20]. The exogenous injection of LIF at the site of myocardial infarction reduces the apoptosis index of

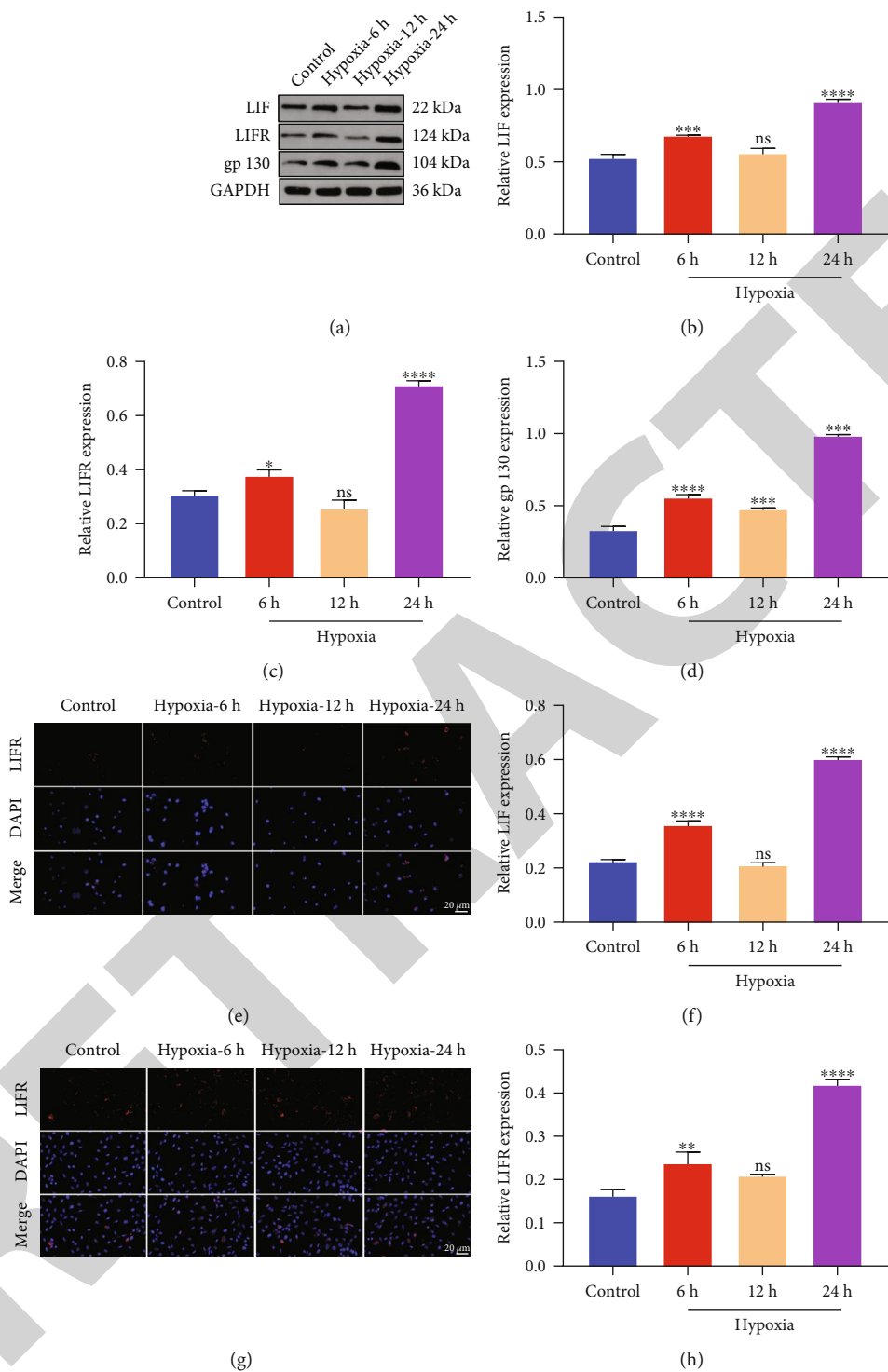


FIGURE 2: Continued.

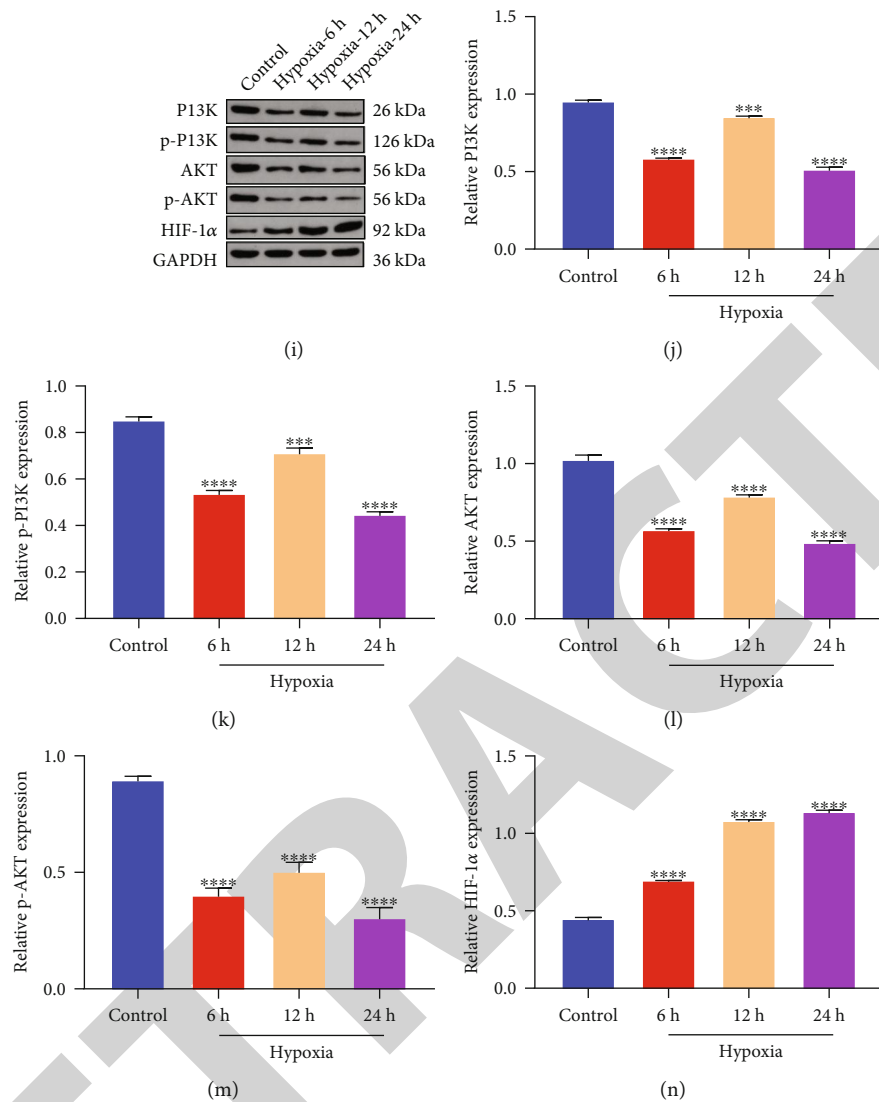


FIGURE 2: Increased LIF/LIFR/gp130 activity and reduced PI3K/Akt activity in hypoxic BMSCs. (a–d) Immunoblotting of LIF, LIFR, and gp130 activity in BMSCs when exposed to hypoxia for 6, 12, and 24 h. (e–h) Immunofluorescent staining of LIF and LIFR activity in BMSCs under hypoxic condition. Bar, 20  $\mu$ m. (i–n) Immunoblotting of PI3K, p-PI3K, AKT, p-AKT, and HIF-1 $\alpha$  expression in hypoxic BMSCs.

myocardial cells and protects the structure and function of cardiac tissue. LIF inhibits myocardial cell apoptosis by activating the myocardial LIF/LIFR/STAT3 signaling pathway in myocardial infarction rats [21]. In bone repair studies, after knocking out the LIF gene, fetal bone mass is reduced by 40% [22]. Our previous study found that hypoxia can induce upregulation of LIF expression in alveolar bone formation in a rat periodontal augmentation animal model (a classic model of persistent hypoxia) [23]. In addition, limited evidence demonstrates that LIF protects photoreceptor cone cells from oxidative stress injury via activation of the JAK/STAT3 pathway [24].

In this study, we found that in the bone defect environment, hypoxia activated LIF and thus activated the downstream signaling pathway PI3K/AKT, ameliorated the

inhibitory effect of hypoxia-induced internal environment disturbance on bone growth, maintained BMSC survival and self-renewal and inhibited oxidative stress, and promoted osteogenic differentiation.

## 2. Materials and Methods

**2.1. Isolation and Culture of BMSCs.** C57BL/6 male mice aged 4–5 weeks weighing  $16 \pm 2$  g (Laboratory Animal Center of Sun Yat-sen University, China) were utilized for isolating BMSCs. After the mice were sacrificed, the bilateral femurs of the rats were taken out under sterile conditions. The obtained femur was placed in PBS solution containing penicillin-streptomycin to remove residual blood and soft tissue fragments. The muscles and aponeurosis attached to

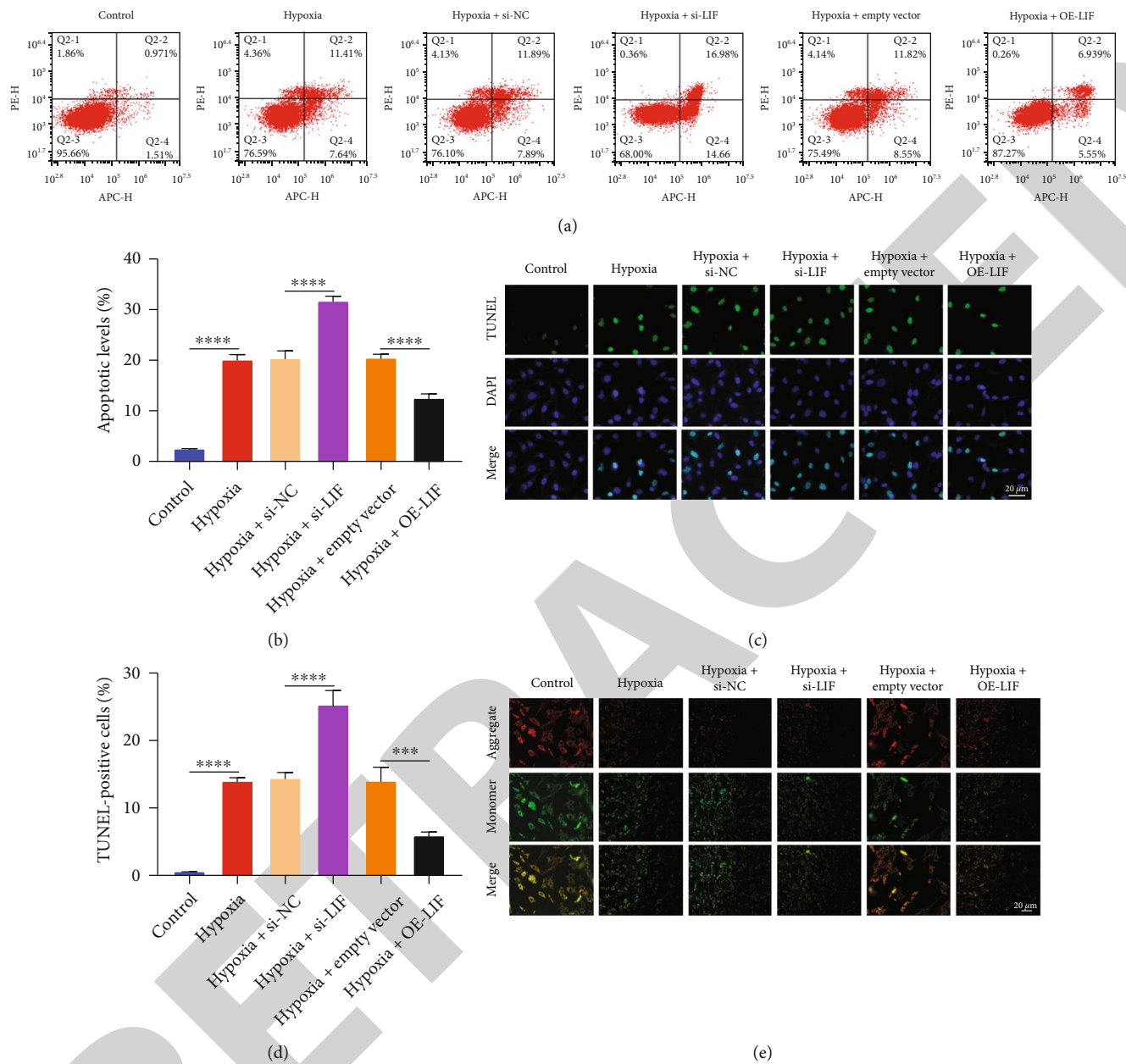


FIGURE 3: Continued.

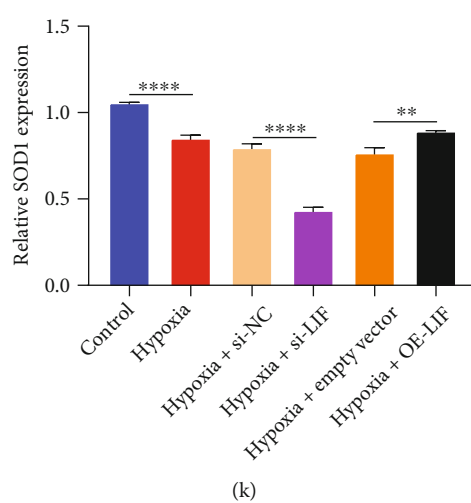
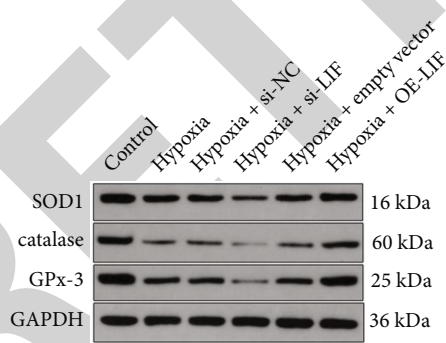
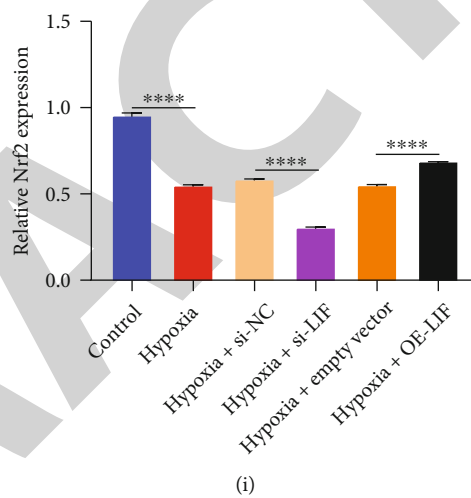
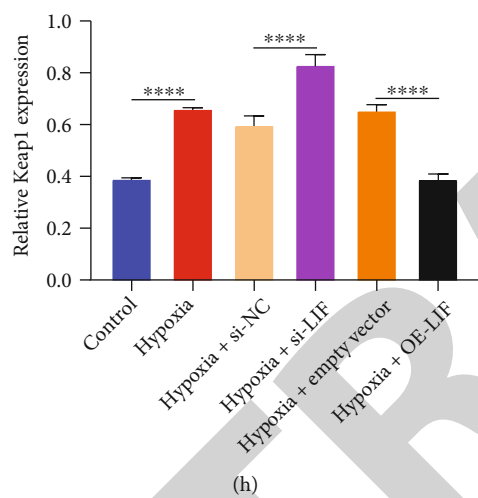
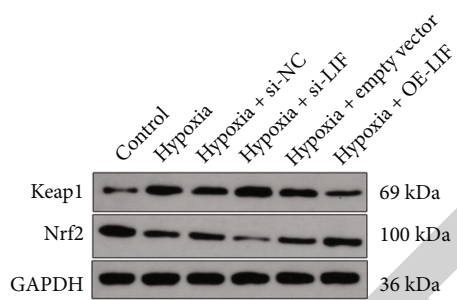
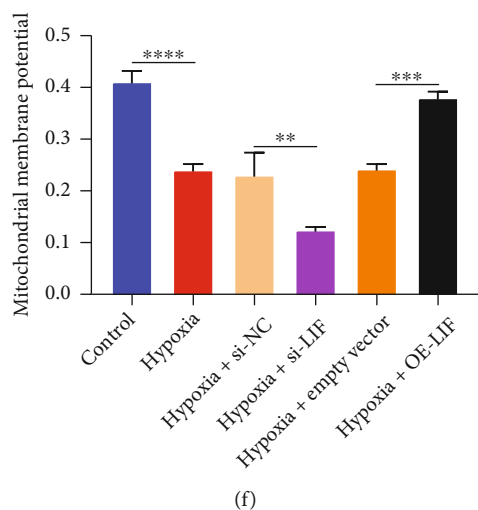


FIGURE 3: Continued.

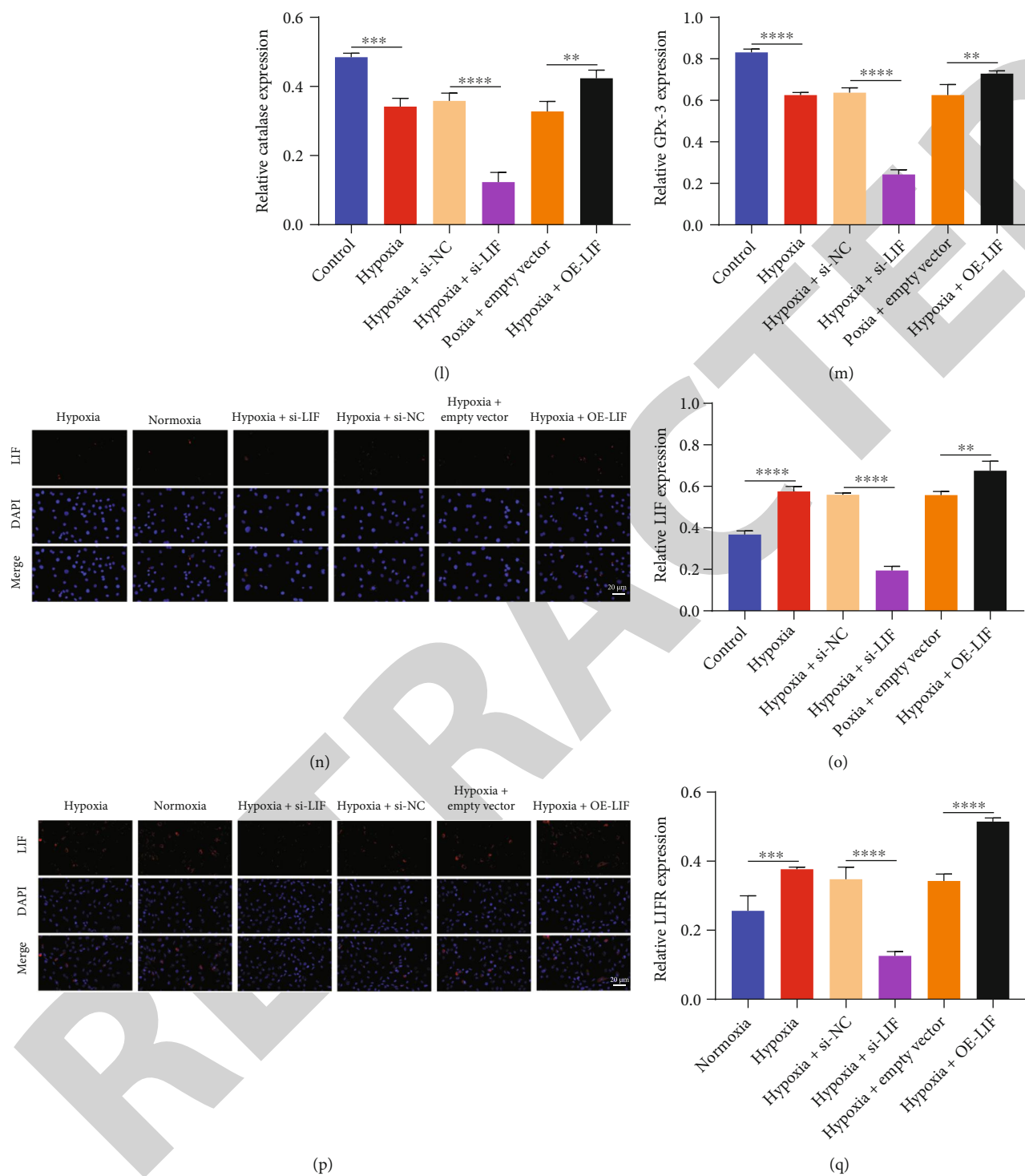


FIGURE 3: Continued.

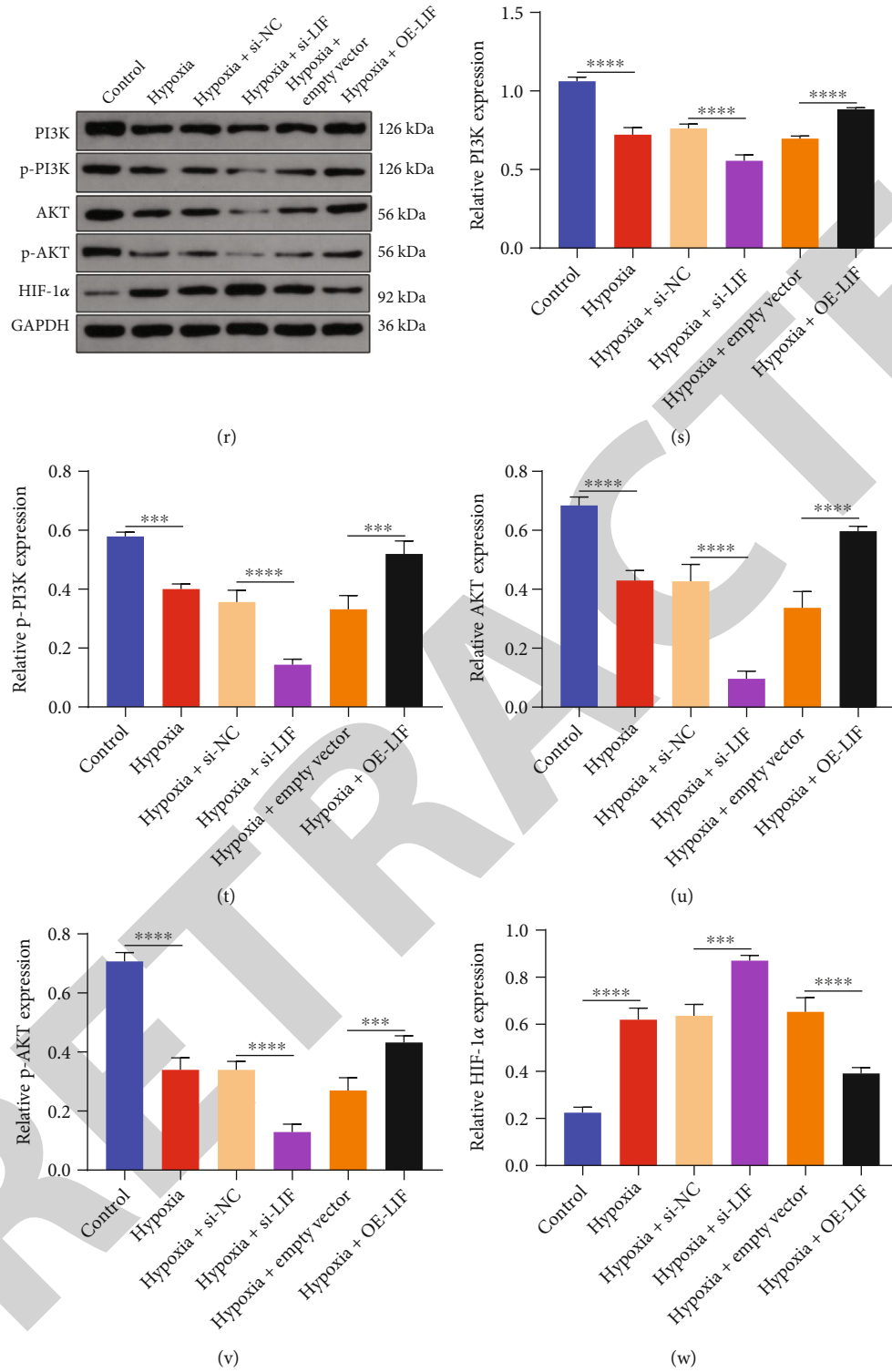


FIGURE 3: Upregulated LIF alleviates apoptosis and oxidative stress and heightens mitochondrial activity and PI3K/Akt signaling in hypoxic BMSCs. (a, b) Flow cytometry and (c, d) TUNEL staining for BMSC apoptosis with hypoxic exposure, along with knockout or overexpressed LIF. Bar, 20  $\mu$ m. (e, f) JC-1 staining for examining mitochondrial membrane potential of hypoxic BMSCs with knockout or overexpressed LIF. Bar, 20  $\mu$ m. (g–m) Immunoblotting of the activity of Keap1, Nrf2, SOD1, catalase, and GPx-3 in hypoxic BMSCs with knockout or overexpressed LIF. (n–q) Immunofluorescent staining of LIF and LIFR activity in BMSCs with hypoxic exposure, along with knockout or overexpressed LIF. Bar, 20  $\mu$ m. (r–w) Immunoblotting of the activity of PI3K, p-PI3K, AKT, p-AKT, and HIF-1 $\alpha$  in hypoxic BMSCs with knockout or overexpressed LIF.

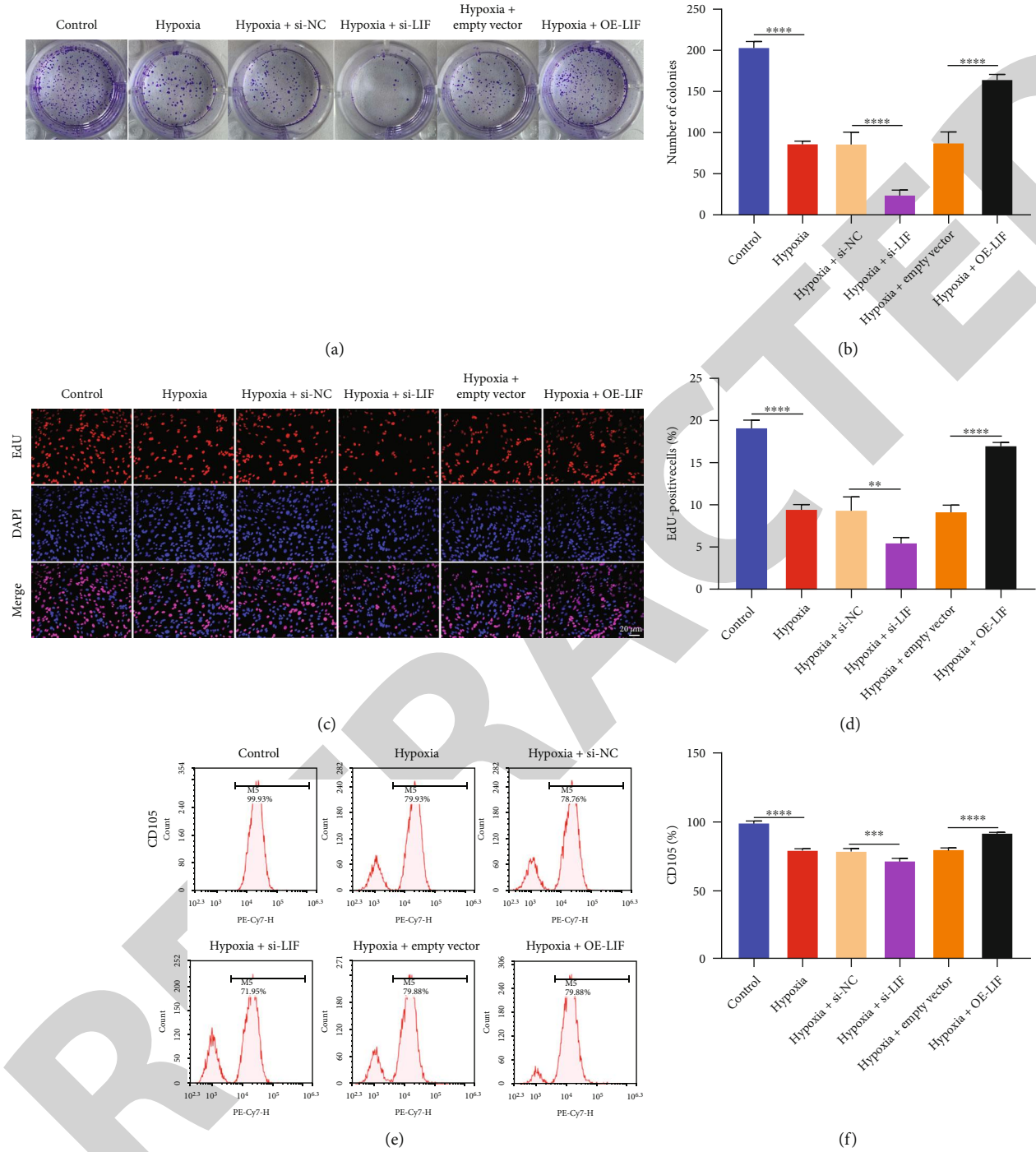


FIGURE 4: Continued.



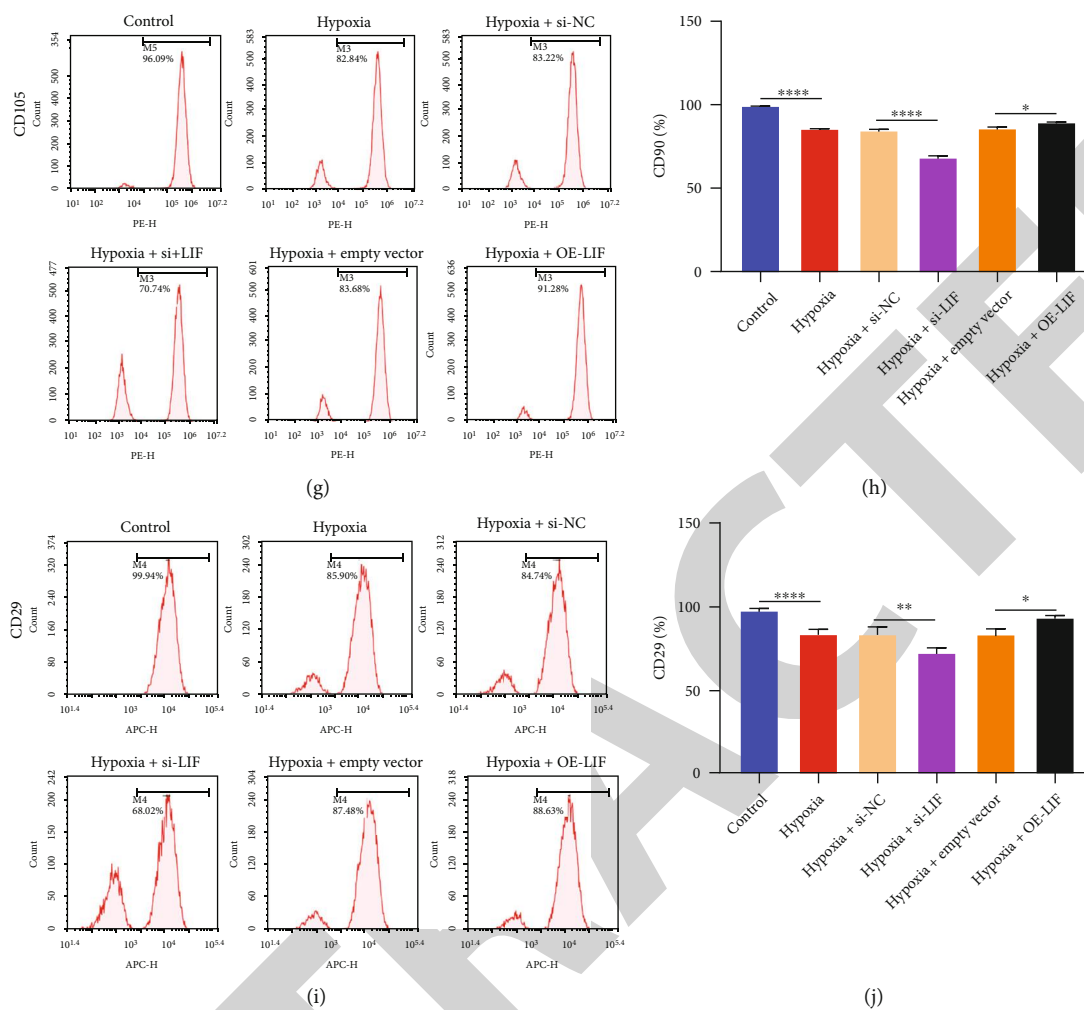


FIGURE 4: Upregulated LIF promotes self-renewal and differentiation of hypoxic BMSCs. (a, b) Colony formation and (c, d) EdU staining for examining BMSC proliferation with exogenous interference or overexpression of LIF under hypoxic condition. Bar, 20  $\mu\text{m}$ . (e–j) Flow sorting for detecting cell surface antigens (CD105, CD90, and CD29) in hypoxic BMSCs with LIF loss or overexpression.

the bone surface were carefully removed with a sterile scalpel and ophthalmic forceps. Ophthalmic scissors were used to remove the sacrum at both ends to expose the medullary cavity. The cells in the bone marrow cavity were washed out with  $\alpha$ -MEM (Sigma-Aldrich, USA). The cell suspension was collected in a 15 mL centrifuge tube, centrifuged at 1000 rpm for 5 min at room temperature, and the supernatant was discarded after centrifugation. 7 mL freshly prepared  $\alpha$ -MEM with 10% FBS was used for resuspending a single cell suspension that was inoculated into a 75  $\text{cm}^2$  cell culture flask. BMSCs were placed in a 5%  $\text{CO}_2$ , 95% air, and 100% humidity incubator at 37°C. After 72 h, the medium was changed to remove nonadherent cells every 2 days. BMSCs were passaged when they reached 80%–90% confluence. The third-generation BMSCs were used for subsequent experiments.

**2.2. Flow Sorting.** BMSCs were digested with 0.25% trypsin to collect  $4 \times 10^5$  cells, centrifuged at 1000 rpm for 4 min at room temperature. After discarding the supernatant, single

cell suspension was prepared. Afterwards, BMSCs were incubated with monoclonal antibodies of cell surface antigens containing CD29-PE (ab218273, Abcam, USA), CD44-PE (ab23396), CD90-APC (ab25322), CD105-PE/Cy7 (ab272352), CD146-FITC (ab78451), and CD45-FITC (ab27287) on the ice in the dark for 30 min. After centrifuging at 1000 rpm for 5 min, the supernatant was discarded. Afterwards, the cells were resuspended in 500  $\mu\text{L}$  PBS and examined utilizing a FACSCalibur flow cytometer (BD Biosciences, USA).

**2.3. Hypoxic Treatment and Transfection.** For hypoxic treatment, BMSCs were cultured in an environment of 5%  $\text{CO}_2$ , 1%  $\text{O}_2$ , and 94%  $\text{N}_2$  for 10 days, with normoxia as controls. BMSCs that stably overexpressed LIF were conducted through transducing retroviral LIF expression vectors (Promega, USA). To construct BMSCs that stably depleted LIF, lentiviral siRNA vectors (Promega) targeting LIF were transduced into BMSCs. The infected BMSCs were chosen utilizing 2 mg/L puromycin for 14 days. PI3K/Akt signaling was

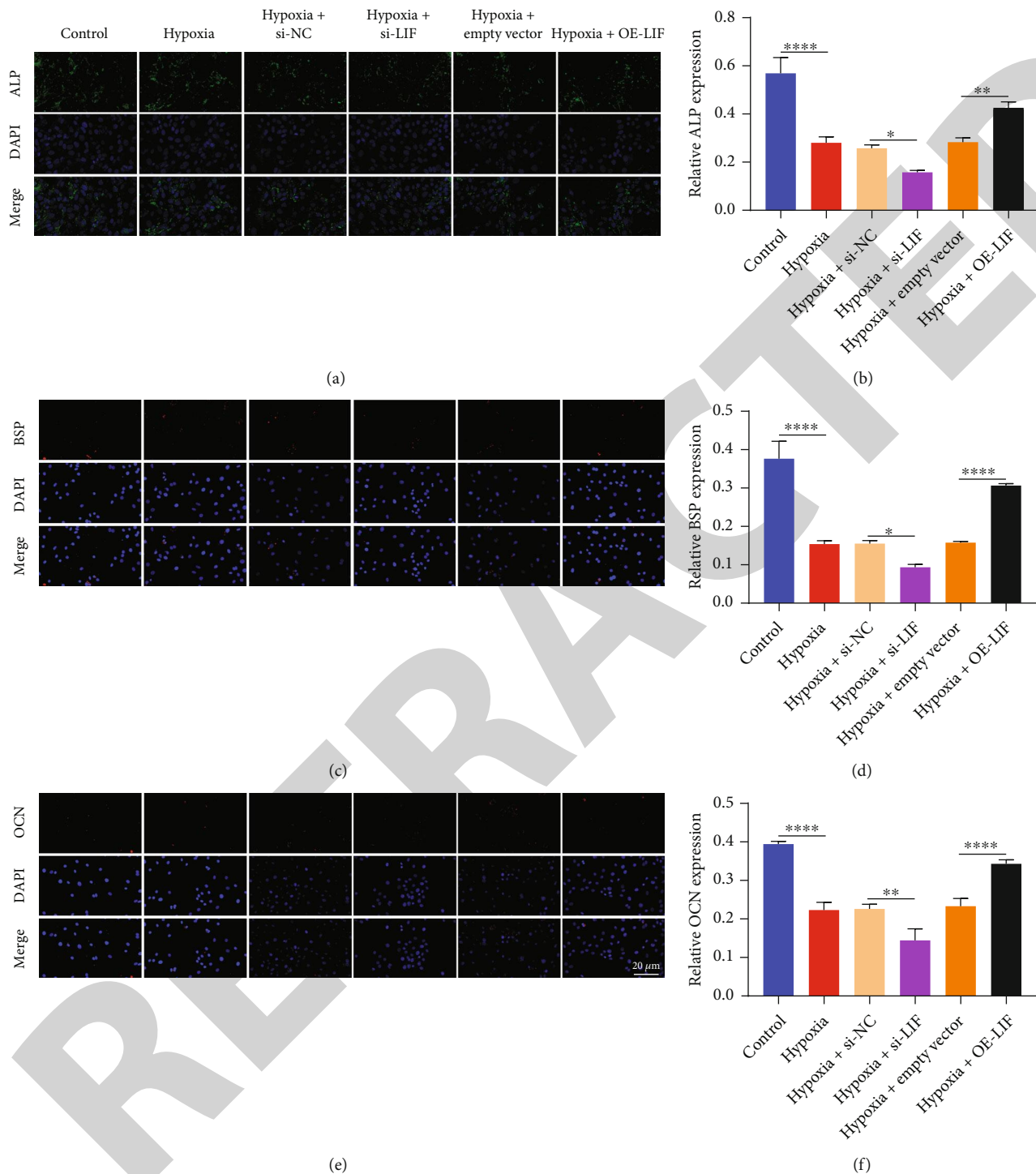


FIGURE 5: LIF upregulation heightens the osteogenic differentiation of hypoxic BMSCs. (a–f) Immunofluorescent staining for ALP, OCN, and BSP activity in hypoxic BMSCs with exogenous interference or overexpression of LIF. Bar, 20  $\mu\text{m}$ .

activated by 30  $\mu\text{M}$  agonist 740Y-P (R&D Systems, UK) and blocked by 50  $\mu\text{M}$  inhibitor LY294002 (R&D Systems).

**2.4. Flow Cytometry.** BMSCs were washed with PBS as well as resuspended in 500  $\mu\text{L}$  of 1x Annexin-binding buffer (Beyotime). Afterwards, incubation with Annexin V-FITC and PI staining was implemented at room temperature in

the dark for 10 min. The samples were immediately analyzed using flow cytometry. Apoptotic cells were examined with a FACSCalibur flow cytometer (BD Biosciences, USA).

**2.5. TUNEL Staining.** BMSCs were immersed utilizing 50  $\mu\text{L}$  TUNEL reaction reagent (Solarbio, China) at 37°C for 1 h. Afterwards, incubation with DAPI was conducted at 37°C

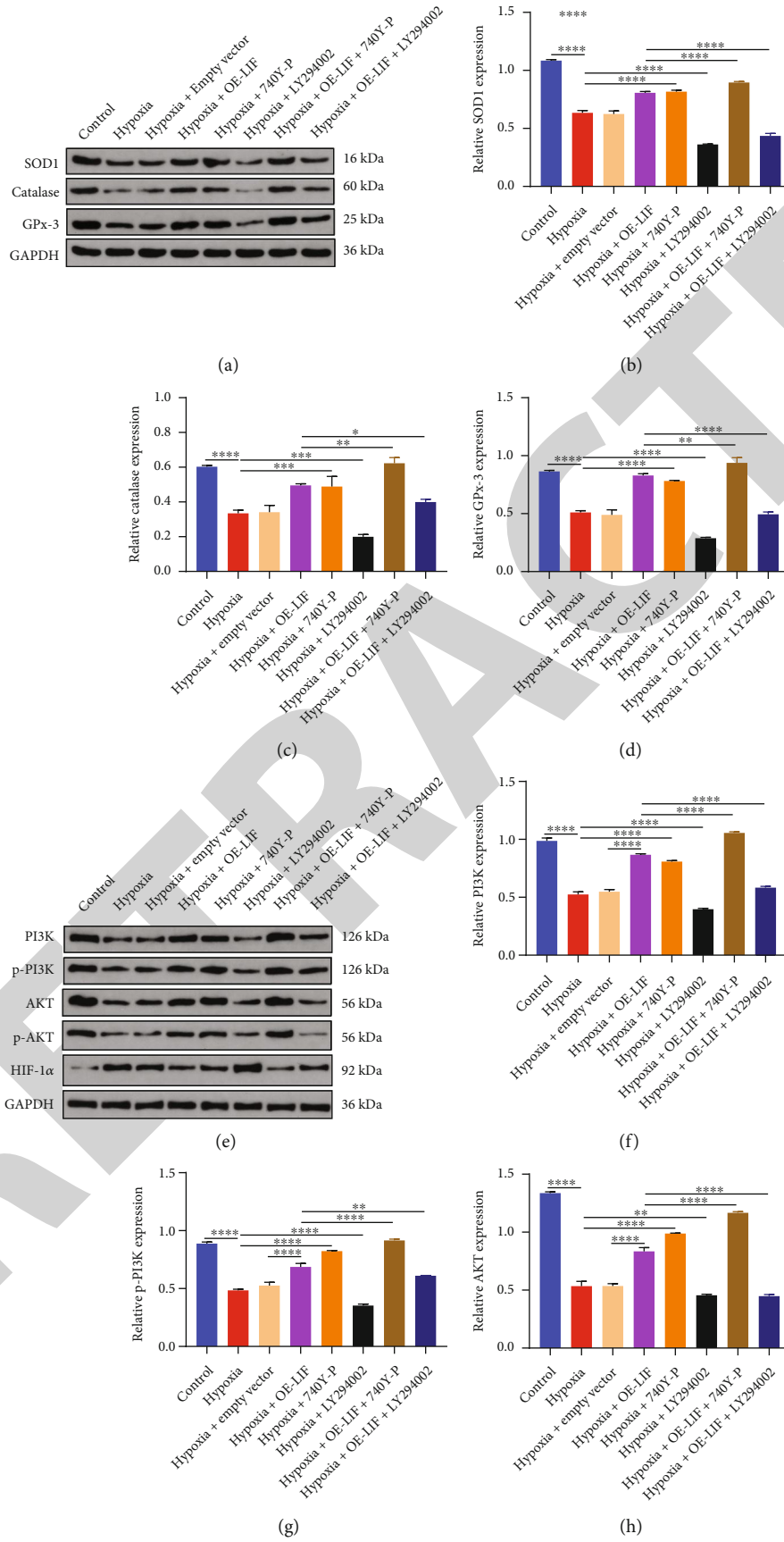


FIGURE 6: Continued.

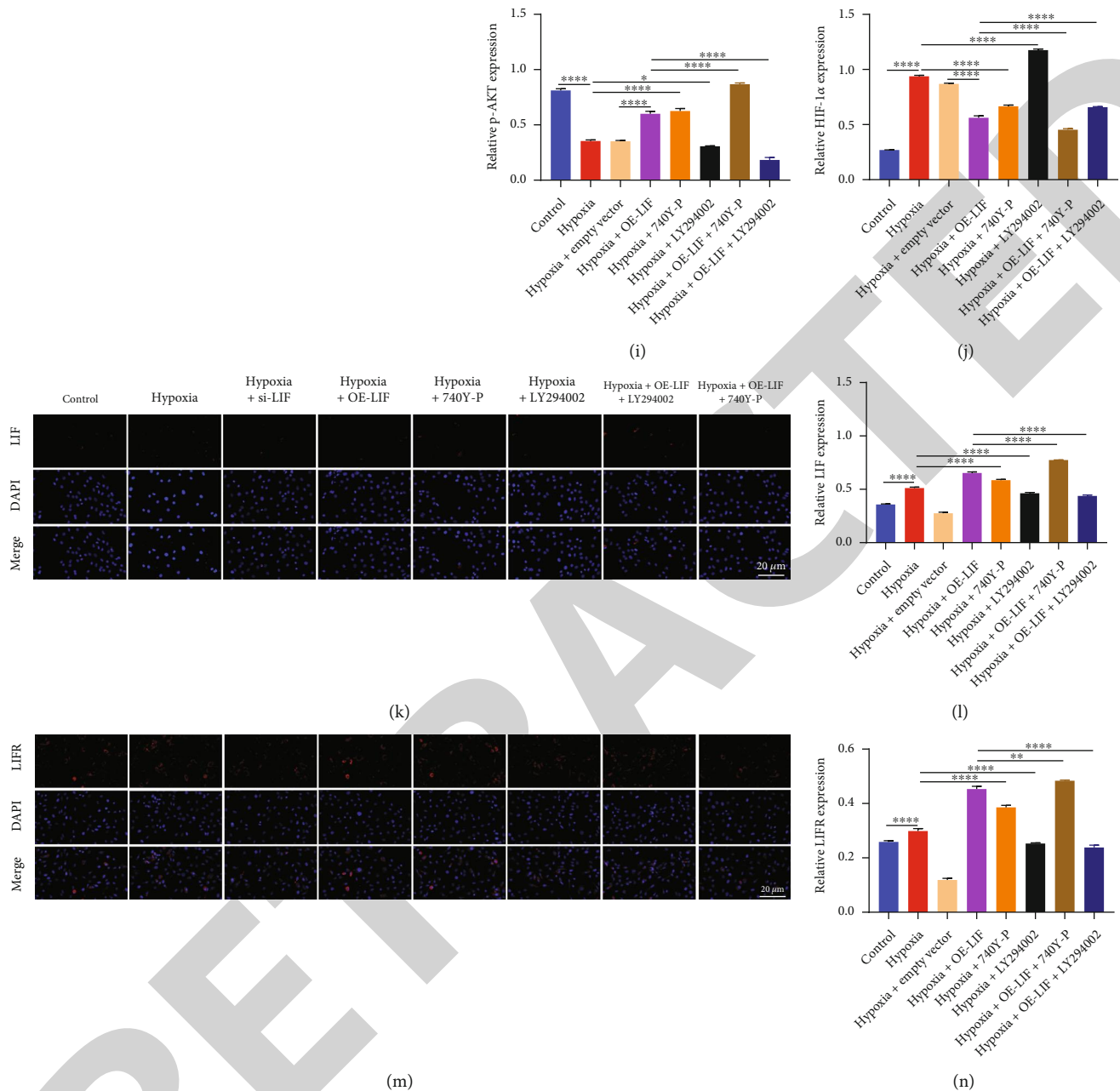
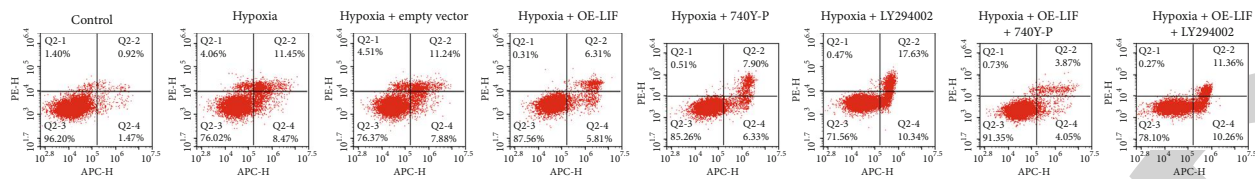


FIGURE 6: LIF upregulation alleviates oxidative stress in hypoxic BMSCs through activating PI3K/Akt signaling. (a–d) Immunoblotting for SOD1, catalase, and GPx-3 activity in hypoxic BMSCs with LIF overexpression as well as PI3K/Akt signaling agonist 740Y-P or inhibitor LY294002. (e–j) Immunoblotting for PI3K, p-PI3K, AKT, p-AKT, and HIF-1 $\alpha$  activity in hypoxic BMSCs with LIF overexpression as well as PI3K/Akt signaling agonist 740Y-P or inhibitor LY294002. (k–n) Immunofluorescent staining for LIF and LIFR in hypoxic BMSCs with LIF overexpression as well as PI3K/Akt signaling agonist 740Y-P or inhibitor LY294002. Bar, 20  $\mu$ m.

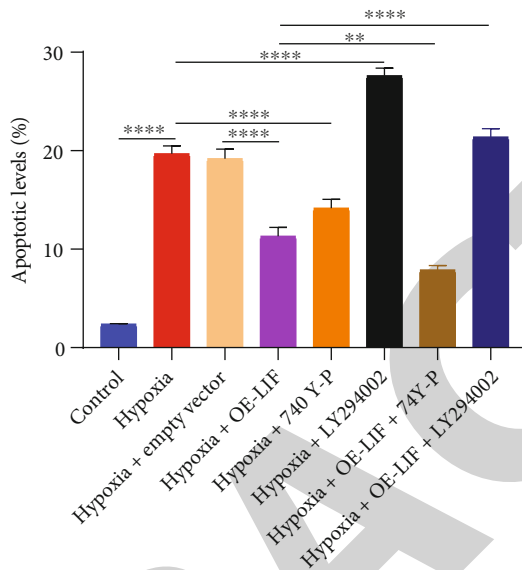
for 30 min. Being washed with PBS, TUNEL-positive cells were captured under a fluorescence microscope (Olympus).

**2.6. JC-1 Staining.** Mitochondrial membrane potential was examined with a JC-1 kit (Merck, Germany). BMSCs were exposed to 2  $\mu$ M of JC-1 for 30 min in the dark at 37°C. Being washed with PBS, images were captured utilizing a fluorescence microscope (Olympus).

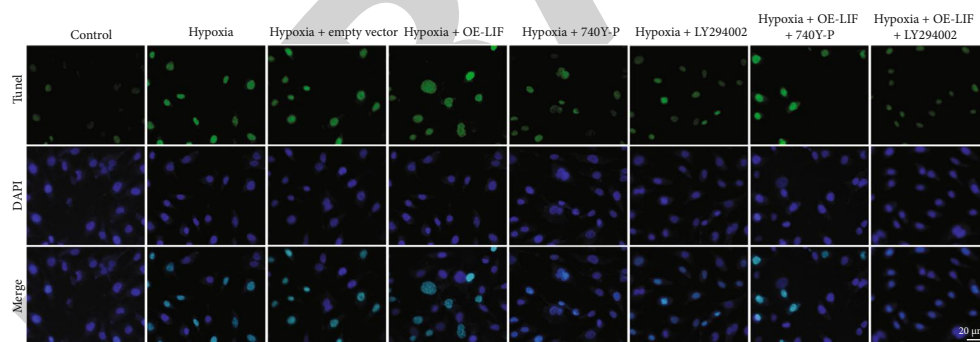
**2.7. Immunoblotting.** Protein separation was implemented through 12% SDS-PAGE, along with transference to PVDF membrane (Millipore, USA) as well as incubation with defatted milk. Afterwards, the PVDF membrane was subjected to immunoblotting following the indicated primary antibodies: Kelch-like ECH-associated protein 1 (Keap1; 1:500; ab119403; Abcam), nuclear factor-erythroid 2-related factor 2 (Nrf2; 1:200; ab62352), LIF (1:1000;



(a)



(b)



(c)

FIGURE 7: Continued.

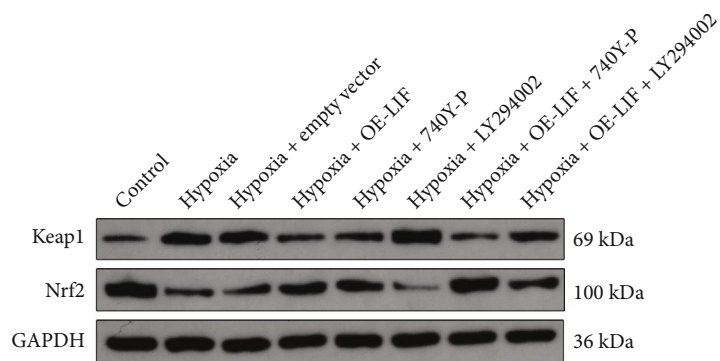
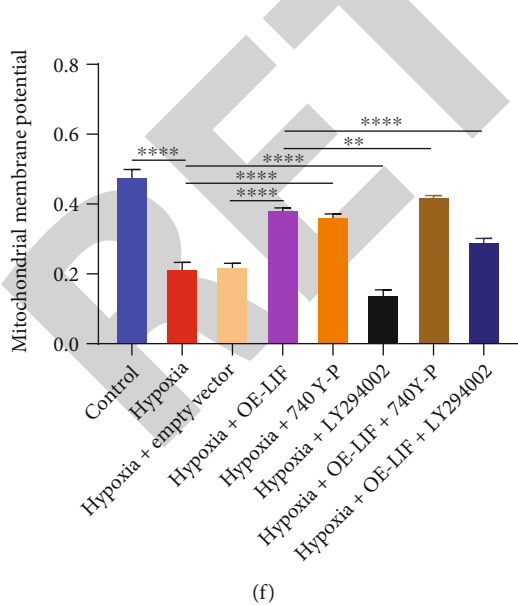
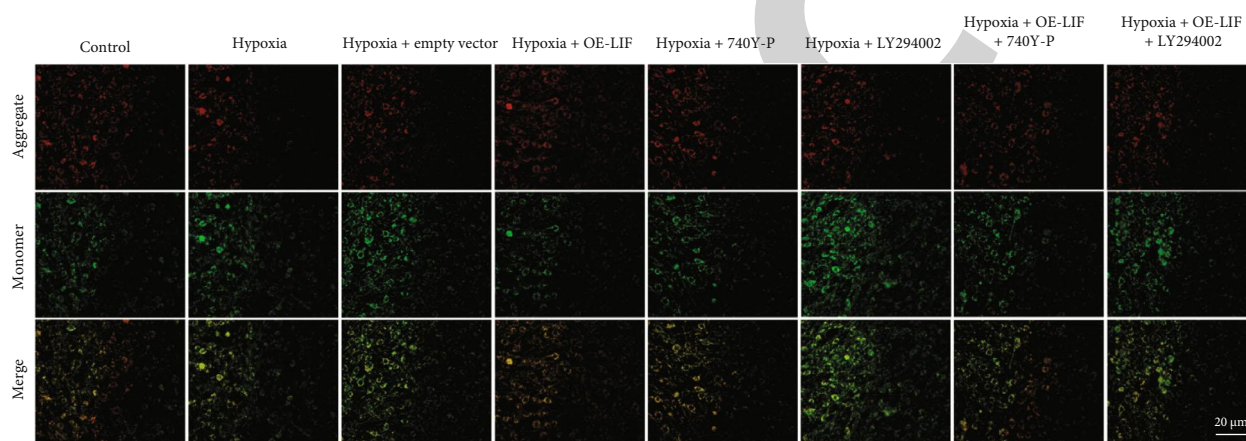
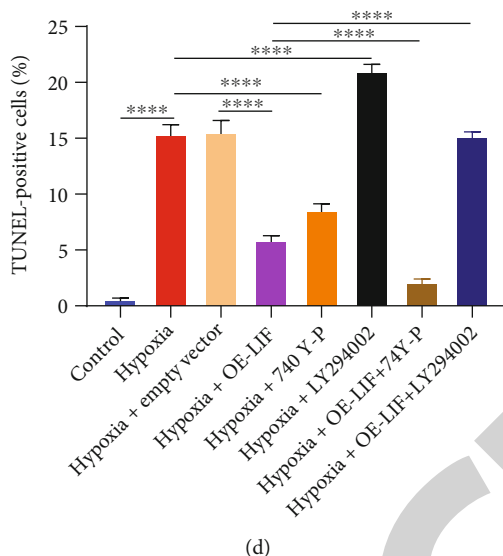


FIGURE 7: Continued.

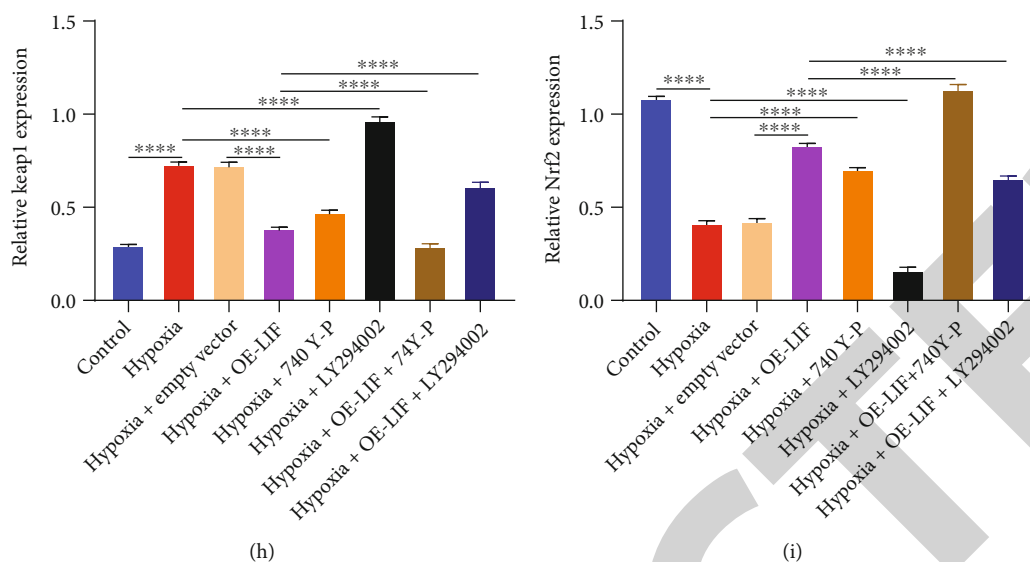
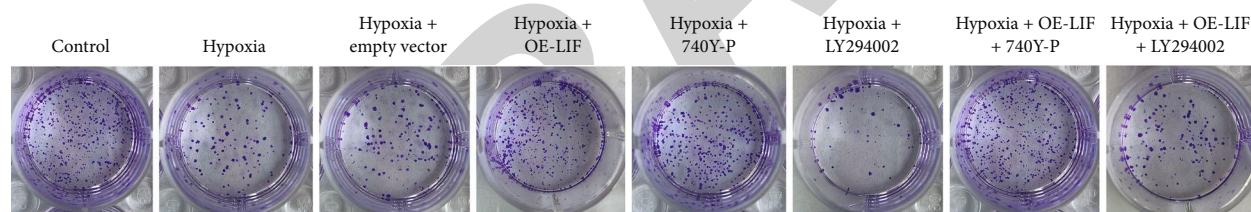
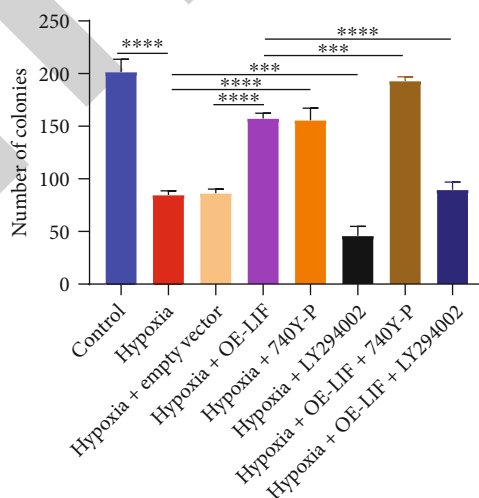


FIGURE 7: LIF upregulation weakens apoptosis and ameliorates mitochondrial activity in hypoxic BMSCs by activating PI3K/Akt signaling. (a, b) Flow cytometry and (c, d) TUNEL staining for BMSC apoptosis in hypoxic environment with LIF overexpression as well as PI3K/Akt signaling agonist 740Y-P or inhibitor LY294002. Bar, 20  $\mu$ m. (e, f) JC-1 staining for detecting mitochondrial membrane potential of hypoxic BMSCs with LIF overexpression as well as PI3K/Akt signaling agonist 740Y-P or inhibitor LY294002. Bar, 20  $\mu$ m. (g-i) Immunoblotting for Keap1 and Nrf2 activity in hypoxic BMSCs with LIF overexpression as well as PI3K/Akt signaling agonist 740Y-P or inhibitor LY294002.

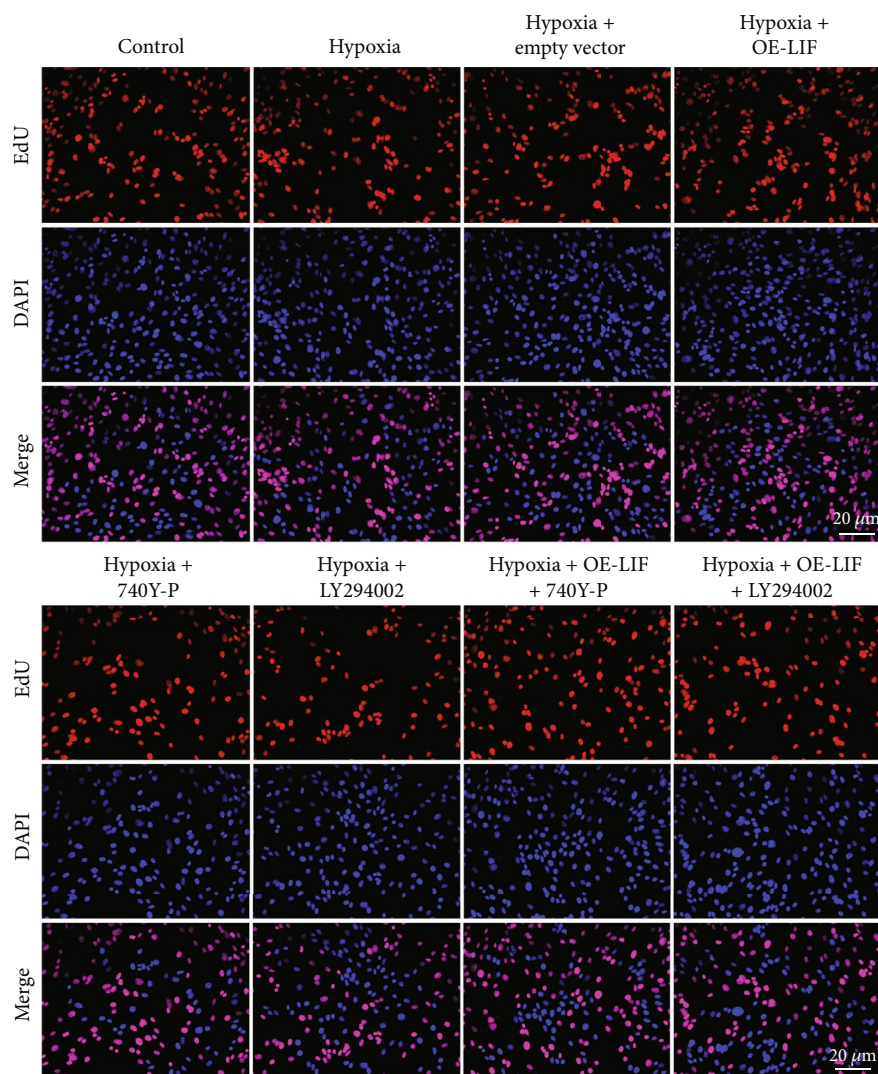


(a)

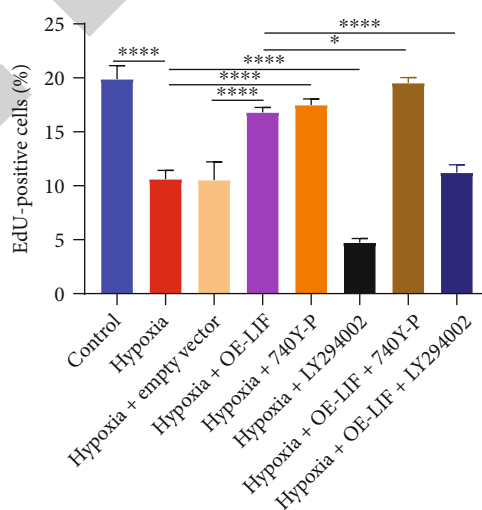


(b)

FIGURE 8: Continued.



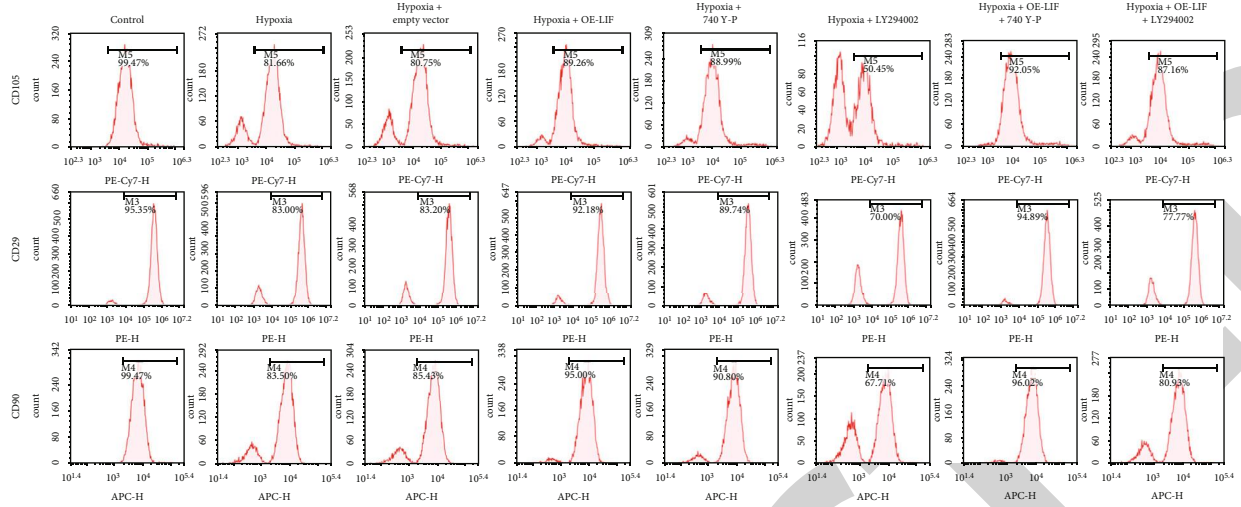
(c)



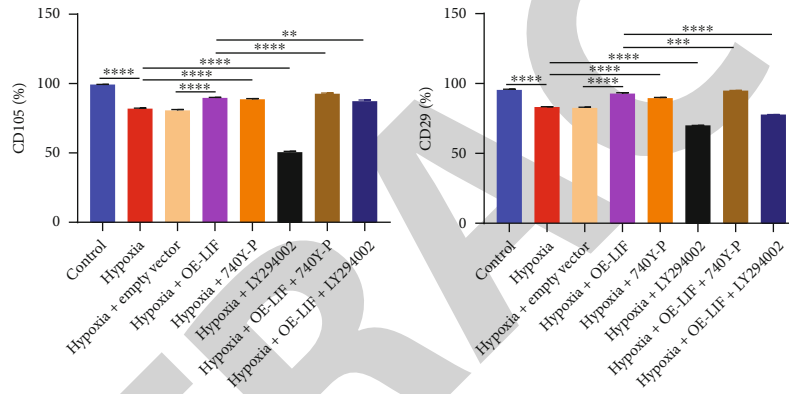
(d)

FIGURE 8: LIF improves proliferative capacity of hypoxic BMSCs by activating PI3K/Akt signaling. (a, b) Colony formation and (c, d) EdU staining for examining BMSC proliferation in hypoxic BMSCs with LIF overexpression as well as PI3K/Akt signaling agonist 740Y-P or inhibitor LY294002. Bar, 20  $\mu$ m.



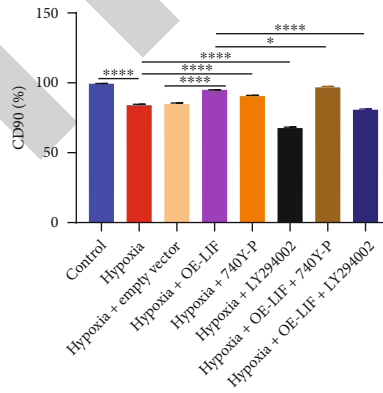


(a)



(b)

(c)



(d)

FIGURE 9: Continued.

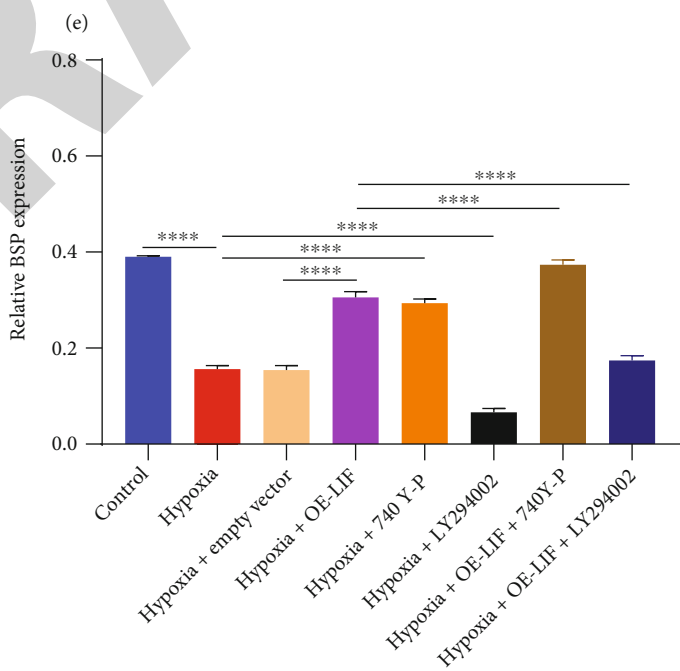
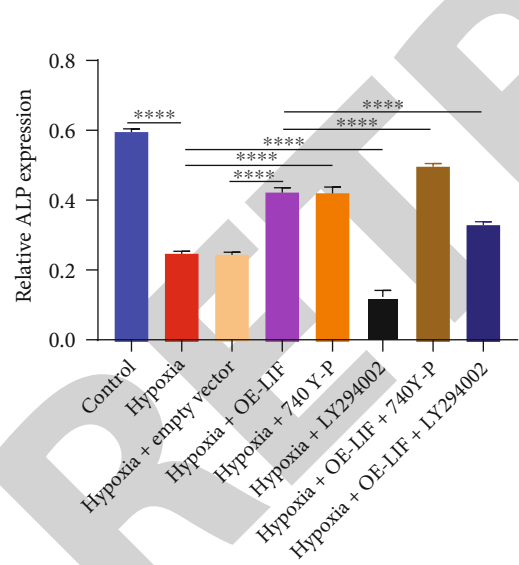
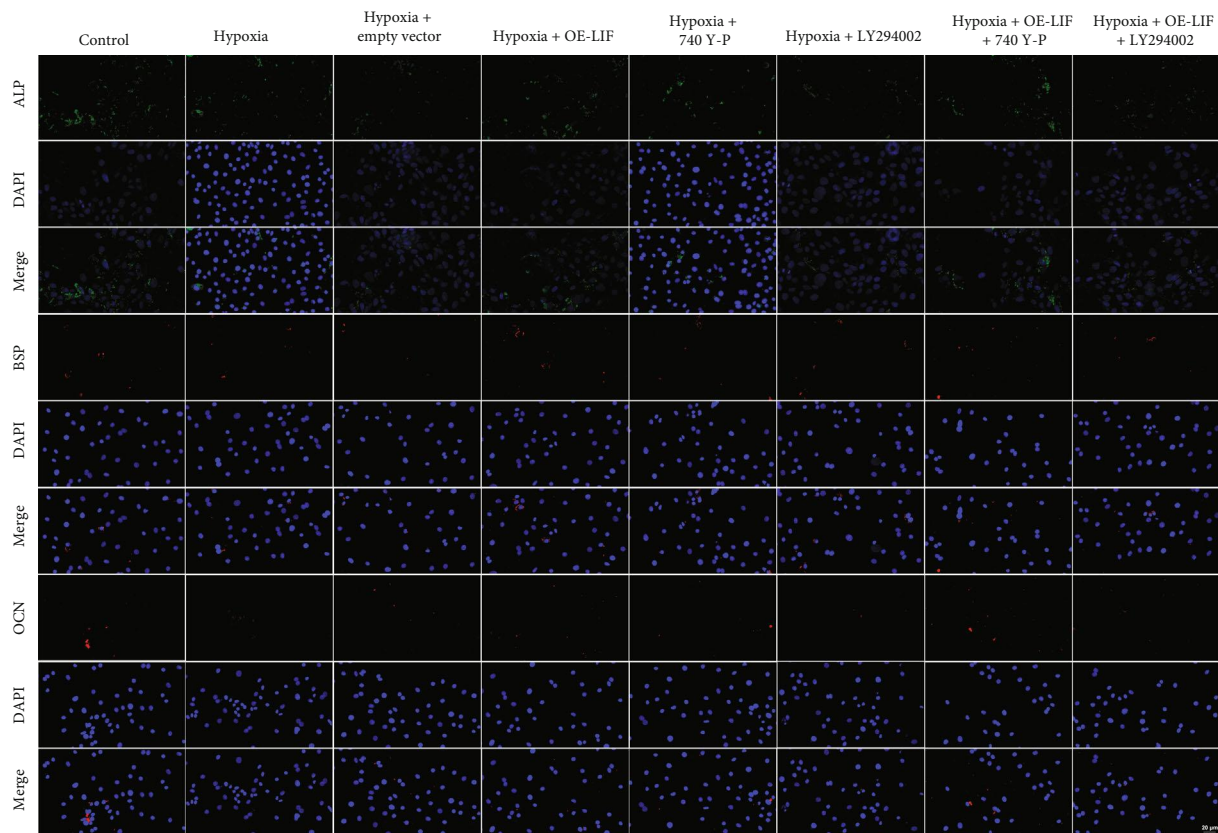


FIGURE 9: Continued.

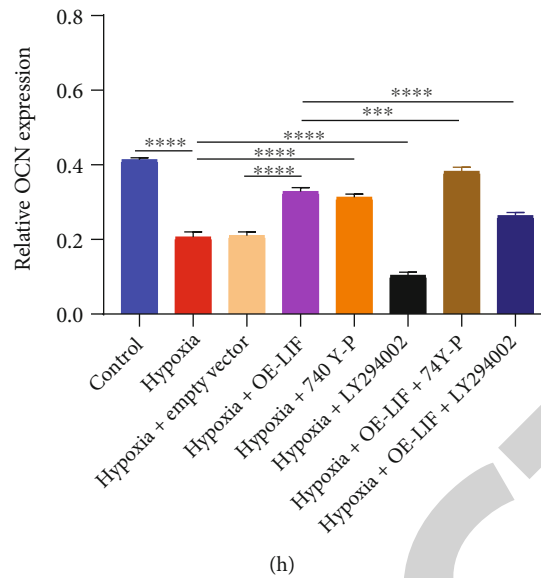


FIGURE 9: LIF improves the self-renewal and differentiation of hypoxic BMSCs by activating PI3K/Akt signaling. (a–d) Flow sorting for detecting cell surface antigens (CD105, CD90, and CD29) in hypoxic BMSCs with LIF overexpression as well as PI3K/Akt signaling agonist 740Y-P or inhibitor LY294002. (e–h) Immunofluorescent staining for ALP, BSP, and OCN expressions in hypoxic BMSCs with LIF overexpression as well as PI3K/Akt signaling agonist 740Y-P or inhibitor LY294002. Bar, 20  $\mu$ m.

ab113262), LIFR (1:1000; ab232877), gp130 (1:1000; ab259927), PI3K (1:1000; ab32089), p-PI3K (1:500; ab182651), AKT (1:500; ab8805), p-AKT (1:500; ab38449), hypoxia-inducible factor 1 $\alpha$  (HIF-1 $\alpha$ ; 1:100; ab51608), superoxide dismutase 1 (SOD1; 1:5000; ab51254), catalase (1:1000; ab52477), glutathione peroxidase 3 (GPx-3; 1:1000; ab256470), and GAPDH (1:2000; ab59164). Incubation with a secondary antibody was implemented for 1 h. Protein was developed with an enhanced chemiluminescence approach.

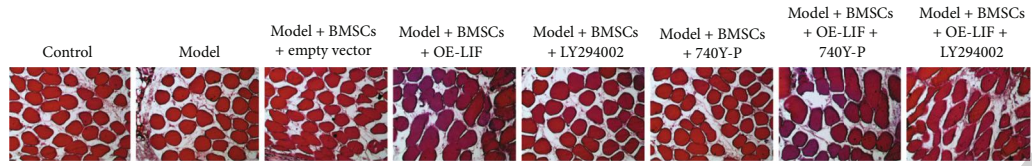
**2.8. Immunofluorescent Staining.** BMSCs were washed with precooled PBS, followed by fixation with 4% paraformaldehyde for 10 min as well as permeability with 0.25% Triton-X100 for 15 min at room temperature. Afterwards, blockage with 1% bovine serum albumin was implemented for 60 min, along with incubation with primary antibody of LIF (1:100; ab113262; Abcam), LIFR (1:100; ab232877), alkaline phosphatase (ALP; 1:200; ab224335), bone sialoprotein (BSP; 1:200; ab270605), and osteocalcin (OCN; 1:200; ab198228) at 4°C overnight as well as Alexa Fluor® 488- (1:200; ab150077; Abcam) or Alexa Fluor® 594- (1:200; ab150080; Abcam) conjugated secondary antibody for 1 h. Thereafter, BMSCs were stained with DAPI for 15 min. Images were captured utilizing a fluorescence microscope (Olympus, Japan).

**2.9. Colony Formation Assay.** BMSCs were seeded onto 6-well culture plates ( $5 \times 10^5$  cells/well).  $\alpha$ -MEM was changed every 2 days. Colonies were fostered for 14 days in  $\alpha$ -MEM. Being fixed by 4% paraformaldehyde, the medium was discarded and BMSCs were stained utilizing 0.1% crystal violet.

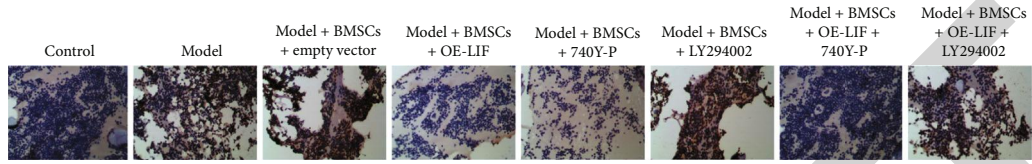
**2.10. EdU Staining.** Incubation of BMSCs with 50  $\mu$ M EdU-labeling medium was implemented for 2 h, along with fixation utilizing 4% paraformaldehyde for 30 min. Thereafter, BMSCs were exposed to 2 mg/mL glycine for 5 min, followed by staining with 100  $\mu$ L Apollo® staining reagent for 30 min. After permeabilizing by 0.5% Triton X-100 for 10 min, incubation with DAPI staining was conducted. EdU-labeled BMSCs were captured utilizing a fluorescence microscope (Olympus, Japan).

**2.11. Establishment of Calvarial Bone Defect Murine Models.** Eight-week-old C57BL/6 male mice weighing 20–25 g (Laboratory Animal Center of Sun Yat-sen University) were randomized to eight groups (10 each group). After making a 1.0 cm sagittal incision, the calvarium was exposed, and two defects were made on the skull through drilling a 4 mm hole with a trephine burr. The control mice did not receive any treatment. Bone defect mice were implanted by BCP scaffolds with LIF-overexpressed, 740Y-P, or LY294002 BMSCs. The incisions were closed with 5–0 resorbable suture. Cranial bones were collected at eight weeks following surgery. Our animal experiments were approved by the Southern University of Science and Technology Yantian Hospital.

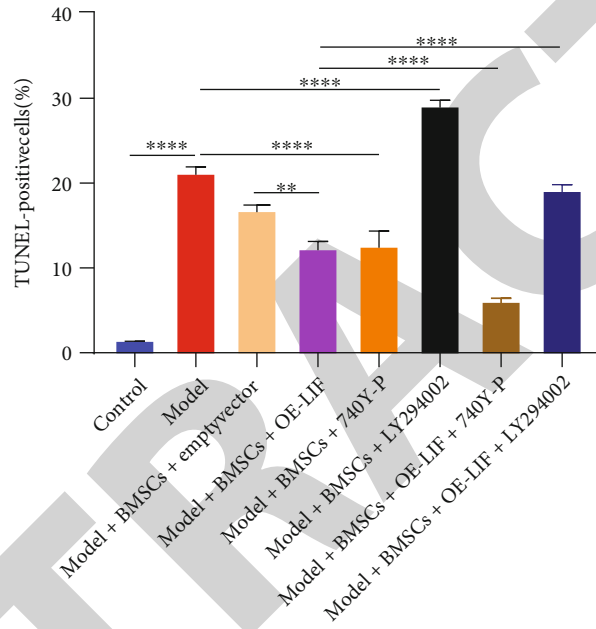
**2.12. Histological Assessment.** Mice were euthanized via injecting excessive pentobarbital sodium. The cranial bone defect specimens were fixed, decalcified, and dehydrated. Thereafter, the specimens were embedded in paraffin and sectioned into 5  $\mu$ m, followed by methylene blue and basic fuchsin staining. Sections were immunohistochemically or immunofluorescently stained, and antibodies included CD34 (1:100; ab81289; Abcam), LIF (1:100; ab113262),



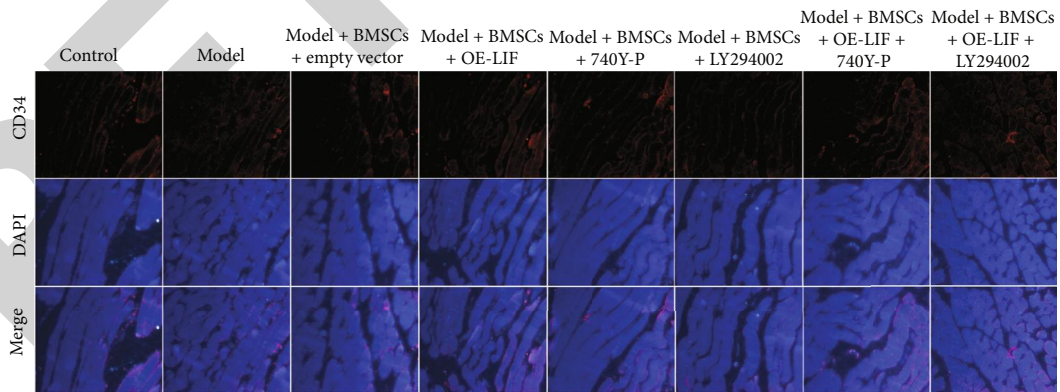
(a)



(b)



(c)



(d)

FIGURE 10: Continued.

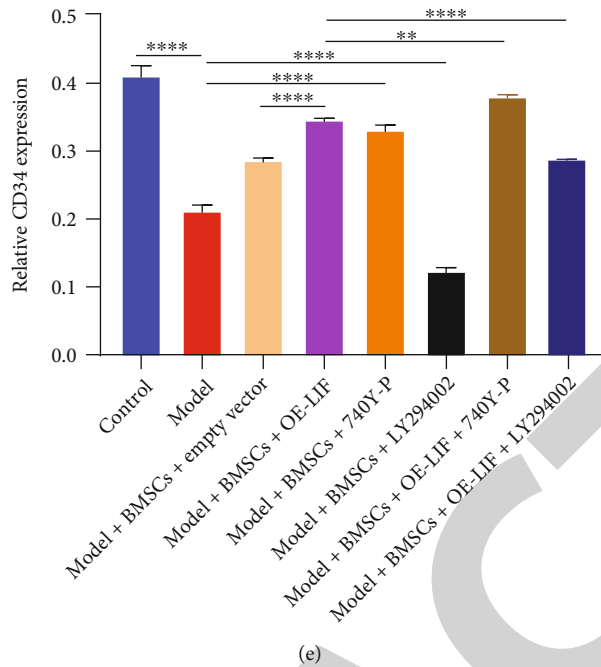


FIGURE 10: Implantation of LIF-overexpressed BMSC-loaded BCP scaffolds increases bone volume and bone density and alleviates apoptosis via PI3K/Akt signaling. (a) Methylene blue and basic fuchsin staining for examining the bone volume and bone density of the murine calvarial bone defect with LIF-overexpressed, PI3K/Akt signaling agonist 740Y-P or inhibitor LY294002 BMSC-loaded BCP scaffolds. Bar, 20  $\mu$ m. (b, c) TUNEL for apoptosis in the murine calvarial bone defect with implantation of LIF-overexpressed, PI3K/Akt signaling agonist 740Y-P or inhibitor LY294002 BMSC-loaded BCP scaffolds. Bar, 20  $\mu$ m. (d, e) Immunofluorescent staining for CD34 in the murine calvarial bone defect with implantation of LIF-overexpressed, PI3K/Akt signaling agonist 740Y-P or inhibitor LY294002 BMSC-loaded BCP scaffolds. Bar, 20  $\mu$ m.

LIFR (1:100; ab232877), gp130 (1:100; ab259927), PI3K (1:100; ab32089), p-PI3K (1:100; ab182651), AKT (1:100; ab8805), p-AKT (1:100; ab38449), Nrf2 (1:200; ab62352), and GPx-3 (1:100; ab256470).

**2.13. Statistical Analyses.** Data were expressed as mean  $\pm$  standard deviation. All analyses were conducted with SPSS 23.0 software. All experiments were repeated at least three times. Statistical difference between groups was determined with one-way analysis of variance. *P* values were labeled as follows: Ns: no significance, \**P* < 0.05, \*\**P* < 0.01, \*\*\**P* < 0.001, and \*\*\*\**P* < 0.0001.

### 3. Results

**3.1. BMSCs Display Increased Apoptosis and Oxidative Stress and Reduced Mitochondrial Membrane Potential in Hypoxic Condition.** To identify murine BMSCs, we examined cell surface antigens via flow sorting. In Figure 1(a), CD29-, CD44-, CD90-, CD105-, CD146-, and CD45-positive cells accounted for 95.27%, 99.01%, 99.84%, 99.88%, 40.49%, and 2.46%, respectively, suggesting that the isolated cells were BMSCs with high purity. Thereafter, BMSCs were exposed to 6h-, 12h-, and 24h-hypoxic conditions for establishing hypoxic models. Both flow cytometry and TUNEL staining demonstrated that hypoxic BMSCs exhibited elevated apoptosis (Figures 1(b)–1(e)). Mitochondrial membrane potential was examined through by a JC-1 fluo-

rescent dye, showing red fluorescence under aggregation condition in normal mitochondria as well as green fluorescence in decreased mitochondrial membrane potential. We noted that green fluorescence was increased as well as red fluorescence reduced in the hypoxic condition (Figures 1(f) and 1(g)). This conversion from red to green fluorescence indicated the reduction in mitochondrial membrane potential of BMSCs. Inactivation of Keap1/Nrf2 protects BMSCs from oxidative stress [25]. In the hypoxic environment, BMSCs displayed elevated Keap1 as well as reduced Nrf2 activity (Figures 1(h)–1(j)), indicating hypoxia-induced oxidative stress in BMSCs.

**3.2. Increased LIF/LIFR/gp130 Activity and Reduced PI3K/Akt Activity in Hypoxic BMSCs.** In the hypoxic condition, we examined the activity of LIF, LIFR, and gp130 in BMSCs. Under 6h and 24h hypoxic treatment, LIF, LIFR, and gp130 exhibited upregulation in BMSCs (Figures 2(a)–2(h)). Additionally, the reduction in PI3K, p-PI3K, AKT, and p-AKT activity was investigated in hypoxic BMSCs (Figures 2(i)–2(m)), indicating that hypoxia inactivated PI3K/Akt signaling in BMSCs. As expected, HIF-1 $\alpha$  was upregulated in BMSCs with hypoxia exposure (Figure 2(n)). 6h hypoxic exposure was utilized for subsequent experiments.

**3.3. Upregulated LIF Alleviates Apoptosis and Oxidative Stress and Heightens Mitochondrial Activity and PI3K/Akt Signaling in Hypoxic BMSCs.** LIF deficiency aggravated

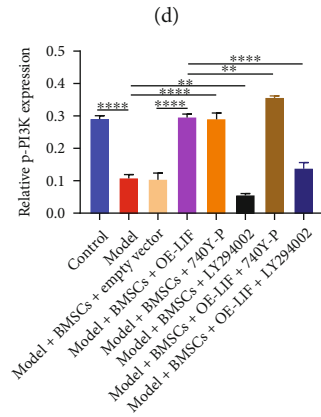
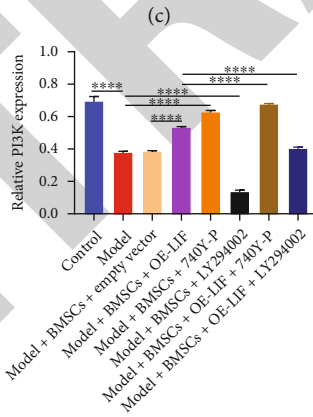
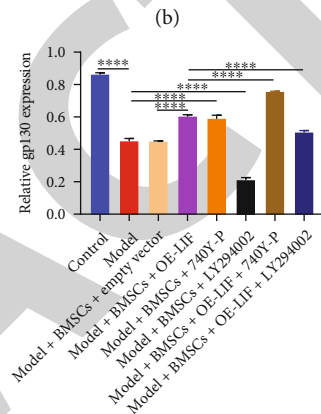
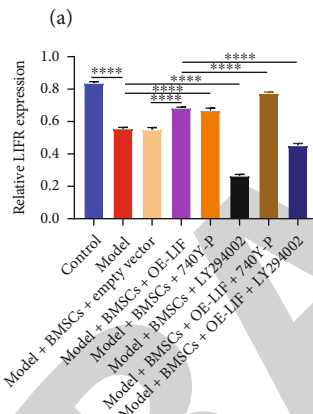
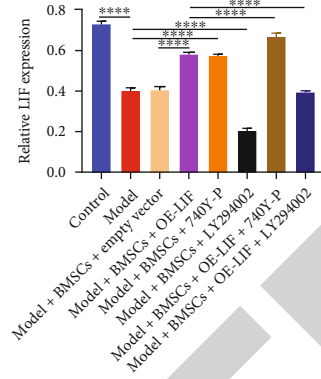
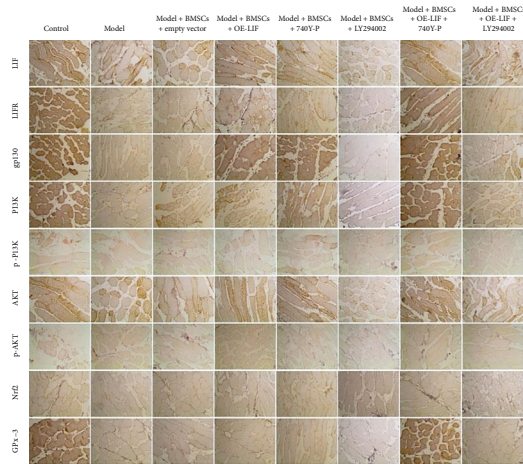


FIGURE 11: Continued.

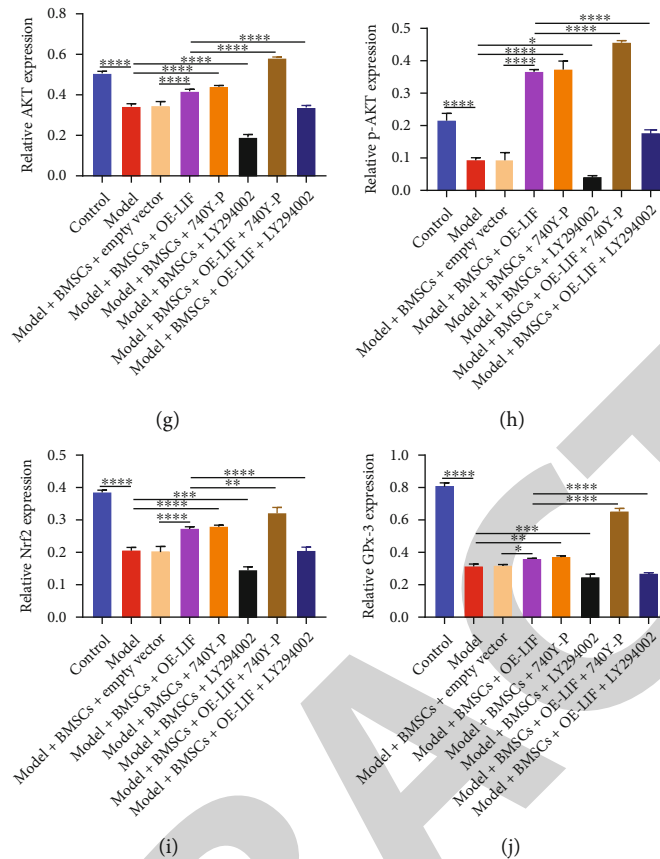


FIGURE 11: Implantation of LIF-overexpressed BMSC-loaded BCP scaffolds alleviates oxidative stress through PI3K/Akt signaling. (a–j) Immunohistochemical staining for LIF, LIFR, gp130, PI3K, p-PI3K, AKT, p-AKT, Nrf2, and GPx-3 expressions in the murine calvarial bone defect with LIF-overexpressed, PI3K/Akt signaling agonist 740Y-P or inhibitor LY294002 BMSC-loaded BCP scaffolds. Bar, 20  $\mu\text{m}$ .

BMSC apoptosis with hypoxic condition; oppositely, LIF upregulations alleviated hypoxia-induced apoptosis in BMSCs (Figures 3(a)–3(d)). Moreover, further reduction in mitochondrial membrane potential of hypoxic BMSCs was found when LIF was knocked out (Figures 3(e) and 3(f)). Conversely, overexpressed LIF ameliorated mitochondrial activity of hypoxic BMSCs. Additionally, hypoxic BMSCs presented the increase in Keap1 as well as the reduction in Nrf2, SOD1, catalase, and GPx-3, which was exacerbated by LIF loss (Figures 3(g)–3(m)). LIF overexpression decreased Keap1 as well as heightened Nrf2, SOD1, catalase, and GPx-3 activity in hypoxic BMSCs, demonstrating that LIF enabled alleviating hypoxia-induced oxidative stress. Moreover, LIF and LIFR expression was further lessened in hypoxic BMSCs with LIF knockdown (Figures 3(n)–3(q)). Inversely, their expression was upregulated in hypoxic BMSCs when LIF was overexpressed. We also found that LIF loss further decreased the activity of PI3K, p-PI3K, AKT, and p-AKT but elevated HIF-1 $\alpha$  expression in hypoxic BMSCs, with the opposite findings when LIF was overexpressed (Figures 3(r)–3(w)), demonstrating that LIF heightened PI3K/Akt signaling activation in hypoxic BMSCs.

**3.4. Upregulated LIF Promotes Self-Renewal and Differentiation of Hypoxic BMSCs.** Exogenous interference

with LIF expression further impaired the proliferative capacity of BMSCs under hypoxia, while overexpressed LIF ameliorated the inhibitory effect of hypoxia on BMSC proliferation (Figures 4(a)–4(d)). In the hypoxic condition, cell surface antigens CD105, CD90, and CD29 presented decreased levels in BMSCs (Figures 4(e)–4(j)). The reduction in CD105, CD90, and CD29 levels was further aggravated by LIF knockdown. Nevertheless, upregulated LIF elevated their activity in hypoxic BMSCs. Hence, LIF motivated self-renewal and differentiation of hypoxic BMSCs.

**3.5. LIF Upregulation Heightens the Osteogenic Differentiation of Hypoxic BMSCs.** The activity of ALP, OCN, and BSP presented reduction in hypoxic BMSCs, while exogenous interference with the expression of LIF further reduced their activity (Figures 5(a)–5(f)). Overexpressed LIF alleviated the inhibitory effect of hypoxia on ALP, OCN, and BSP activity in BMSCs. Thus, LIF enabled heightening the osteogenic differentiation of BMSCs under hypoxic environment.

**3.6. LIF Upregulation Alleviates Oxidative Stress in Hypoxic BMSCs through Activating PI3K/Akt Signaling.** In the hypoxic condition, PI3K/Akt signaling agonist 740Y-P further elevated the levels of SOD1, catalase, and GPx-3 in BMSCs,

with the opposite findings for PI3K/Akt signaling inhibitor LY294002 (Figures 6(a)–6(d)). Additionally, 740Y-P heightened the promoting effect of upregulated LIF on SOD1, catalase, and GPx-3 levels in hypoxic BMSCs; inversely, LY294002 impaired the promoting effect of upregulated LIF on their expression, demonstrating that LIF enabled alleviating oxidative stress in hypoxic BMSCs via heightening PI3K/Akt signaling activity. Our findings also demonstrated that PI3K, p-PI3K, AKT, and p-AKT expressions were activated by PI3K/Akt signaling agonist 740Y-P as well as lessened by inhibitor LY294002 in hypoxic BMSCs in the presence of LIF overexpression (Figures 6(e)–6(i)). Additionally, 740Y-P lessened HIF-1 $\alpha$  activity in hypoxic BMSCs, with the opposite findings for LY294002 (Figure 6(j)). 740Y-P heightened the inhibitory effect of LIF on HIF-1 $\alpha$  in hypoxic BMSCs, with the opposite findings for LY294002. Immunofluorescent staining demonstrated that LIF and LIFR expression was elevated by 740Y-P as well as decreased by LY294002 in hypoxic BMSCs (Figures 6(k)–6(n)).

**3.7. LIF Upregulation Weakens Apoptosis and Ameliorates Mitochondrial Activity in Hypoxic BMSCs by Activating PI3K/Akt Signaling.** In hypoxic environment, PI3K/Akt pathway agonist 740Y-P enhanced the inhibitory effect of LIF overexpression on BMSC apoptosis, while PI3K/Akt pathway-specific inhibitor LY294002 weakened the inhibitory effect of LIF overexpression on BMSC apoptosis (Figures 7(a)–7(d)). Furthermore, 740Y-P synergistically increased the mitochondrial membrane potential with LIF overexpression, while LY294002 attenuated the promoting effect of LIF overexpression on mitochondrial activity (Figures 7(e) and 7(f)). 740Y-P synergized with LIF overexpression to enhance Keap1 expression and decrease Nrf2 expression, with the opposite findings for LY294002 (Figures 7(g)–7(i)). Hence, LIF alleviated apoptosis and improved mitochondrial activity in hypoxic BMSCs via activating PI3K/Akt signaling.

**3.8. LIF Improves Proliferation, Self-Renewal, and Differentiation of Hypoxic BMSCs by Activating PI3K/Akt Signaling.** PI3K/Akt signaling agonist 740Y-P and LIF overexpression synergistically enhance BMSC proliferation under hypoxic conditions, with the opposite findings for inhibitor LY294002 (Figures 8(a)–8(d)). Moreover, the combination of 740Y-P and LIF upregulation heightened CD105, CD90, and CD29 levels in hypoxic BMSCs (Figures 9(a)–9(d)). Nevertheless, LY294002 impaired the promoting effect of LIF on their levels. It was also found that 740Y-P and LIF upregulation synergistically heightened ALP, BSP, and OCN activity in hypoxic BMSCs, with the opposite findings for LY294002 (Figures 9(e)–9(h)). Hence, LIF was capable of improving the proliferative capacity of hypoxic BMSCs by activating PI3K/Akt signaling.

**3.9. Implantation of LIF-Overexpressed BMSC-Loaded BCP Scaffolds Increases Osteogenesis and Alleviates Oxidative Stress and Apoptosis through PI3K/Akt Signaling.** We constructed a murine calvarial bone defect model that was implanted by LIF-overexpressed, PI3K/Akt signaling agonist

740Y-P or inhibitor LY294002 BMSC-loaded BCP scaffolds. After eight weeks, LIF-overexpressed BMSC-loaded BCP scaffolds remarkably increased the bone volume and bone density, which was synergistically enhanced by 740Y-P (Figure 10(a)). Nevertheless, LY294002 BMSC-loaded BCP scaffolds decreased the bone volume and bone density. Implantation of LIF-overexpressed or 740Y-P BMSC-loaded BCP scaffolds presented lower apoptosis, with the opposite findings for LY294002 BMSC-loaded BCP scaffolds (Figures 10(b) and 10(c)). Additionally, CD34 was upregulated when LIF-overexpressed or 740Y-P BMSC-loaded BCP scaffolds were implanted (Figures 10(d) and 10(e)). Oppositely, its expression was downregulated by implantation of LY294002 BMSC-loaded BCP scaffolds. It was also found that LIF, LIFR, gp130, PI3K, p-PI3K, AKT, p-AKT, Nrf2, and GPx-3 were upregulated following implanting LIF-overexpressed BMSC-loaded BCP scaffolds, which were synergistically enhanced by 740Y-P as well as weakened by LY294002 (Figures 11(a)–11(j)). Hence, implantation of LIF-overexpressed BMSC-loaded BCP scaffolds may elevate bone volume and bone density and alleviate apoptosis and oxidative stress via enhancing PI3K/Akt signaling activity.

## 4. Discussion

BMSC transplantation remains an available therapeutic regimen for bone defect restoration [26]. Nevertheless, during the transplantation process, the function and viability of BMSCs can be damaged because of extended duration of the *in vitro* culture, ageing, as well as patients' disease condition, etc. [27]. Severe hypoxia usually suppresses proliferation and osteogenic differentiation of BMSCs and impedes bone defect reconstruction [28]. In the treatment of large bone defects, ischemia and hypoxia in the bone defect area remain a thorny issue [29]. Here, hypoxic BMSCs presented increased apoptosis and oxidative stress and reduced mitochondrial activity. Enhanced mitochondrial activity triggers proliferative and migratory capacities along with osteogenic differentiation of BMSCs and thus facilitates bone defect repair [27]. In the hypoxic environment, BMSCs exhibited increased HIF-1 $\alpha$  activity. Severe hypoxia induces HIF-1 $\alpha$  accumulation and transfers into the nucleus, thereby reducing cellular proliferation and osteogenic differentiation of BMSCs [30]. Additionally, BMSC-exosomes carrying mutant HIF-1 $\alpha$  can improve angiogenesis as well as osteogenesis in critical-size calvarial defects [31].

Our study demonstrated that LIF, LIFR, and gp130 were upregulated in hypoxic BMSCs. Upregulated LIF alleviated apoptosis and oxidative stress and heightened mitochondrial activity and PI3K/Akt signaling in hypoxic BMSCs. Controlling oxidative stress by activating antioxidant signaling is essential for bone homeostasis [32]. Keap1 can bind to nuclear factor Nrf2, a redox-sensitive transcription factor, thereby suppressing Nrf2 activation [33]. Nrf2 enhances the expression of multiple antioxidant and detoxification genes (SOD1, catalase, GPx-3) via antioxidant response elements [33]. Its loss triggers oxidative stress as well as facilitates RANKL-induced osteoclast differentiation [34]. Additionally, activated Nrf2 enhances the osteogenic ability



of human dental pulp stromal cells via alleviating oxidative stress [35]. Our study showed the increase in Keap1 as well as the reduction in Nrf2, SOD1, catalase, and GPx-3 in hypoxic BMSCs, demonstrating that hypoxia induced oxidative stress in BMSCs. Upregulated LIF alleviated hypoxia-induced oxidative stress in BMSCs. Activated PI3K/Akt signaling also decreased Keap1 as well as elevated Nrf2, SOD1, catalase, and GPx-3 in hypoxic BMSCs, demonstrating that PI3K/Akt signaling activation enabled alleviating hypoxia-induced oxidative stress in BMSCs. Evidence suggests that PI3K/Akt-triggered Nrf2 signaling is capable of suppressing oxidative stress along with apoptosis in hepatic damage [36]. Suppressing PI3K/Akt signaling reversed the antioxidative stress of LIF in hypoxic BMSCs. Activated PI3K/Akt signaling heightens bone regeneration in critical-size defects [37]. Herein, LIF overexpression promoted self-renewal and osteogenic differentiation of BMSCs with hypoxic condition. Further, LIF enhanced self-renewal and differentiation as well as attenuated oxidative stress of BMSCs through upregulating PI3K/AKT signaling. In calvarial bone defect models, implantation of LIF-overexpressed BMSC-loaded BCP scaffolds enabled facilitating osteogenesis as well as alleviating oxidative stress and apoptosis through PI3K/Akt signaling.

Nonetheless, a few limitations should be pointed out. First, this study adopted BCP scaffolds, and other types of scaffolds for BSMCs will be considered in our future research, thereby improving the BMSC-mediated bone defect repair potential of LIF. Second, future research might extend the investigating duration to verify the beneficial effect of LIF on self-renewal and differentiation of BMSCs.

## 5. Conclusion

In conclusion, our work suggested the crucial role of LIF in promoting bone regeneration. Upregulated LIF might be a feasible approach for enhancing self-renewal and differentiation and attenuating oxidative stress of BMSCs in vitro via activating PI3K/AKT signaling, as well as bone defect repair in vivo. Thus, upregulated LIF in BMSCs offers great therapeutic promise for improving BMSC function and bone defect reconstruction.

## Abbreviations

BMSCs: Bone marrow-derived mesenchymal stem cells  
 LIF: Leukemia inhibitory factor  
 Keap1: Kelch-like ECH-associated protein 1  
 Nrf2: Nuclear factor-erythroid 2-related factor 2  
 HIF-1 $\alpha$ : Hypoxia-inducible factor 1 $\alpha$   
 SOD1: Superoxide dismutase 1  
 GPx-3: Glutathione peroxidase 3  
 ALP: Alkaline phosphatase  
 BSP: Bone sialoprotein  
 OCN: Osteocalcin.

## Data Availability

The datasets analyzed during the current study are available from the corresponding authors on reasonable request.

## Conflicts of Interest

The authors declare no conflicts of interest.

## Authors' Contributions

Youde Liang and Ruiping Zhou contributed equally to this work.

## Acknowledgments

This work was funded by the Shenzhen Science and Technology Innovative Project (JCYJ20180302144621755) and the Project of Yantian District in Shenzhen City, Guangdong Province, China (20190106).

## References

- [1] H. Hirata, N. Zhang, M. Ueno et al., "Ageing attenuates bone healing by mesenchymal stem cells in a microribbon hydrogel with a murine long bone critical-size defect model," *Immunity & Ageing*, vol. 19, no. 1, p. 14, 2022.
- [2] D. Wu, X. Chang, J. Tian et al., "Bone mesenchymal stem cells stimulation by magnetic nanoparticles and a static magnetic field: release of exosomal miR-1260a improves osteogenesis and angiogenesis," *Journal of Nanobiotechnology*, vol. 19, no. 1, p. 209, 2021.
- [3] M. N. Hsu, K. L. Huang, F. J. Yu et al., "Coactivation of endogenous Wnt10b and Foxc2 by CRISPR activation enhances BMSC osteogenesis and promotes calvarial bone regeneration," *Molecular Therapy*, vol. 28, no. 2, pp. 441–451, 2020.
- [4] Y. Song, H. Wu, Y. Gao et al., "Zinc silicate/nano-hydroxyapatite/collagen scaffolds promote angiogenesis and bone regeneration via the p38 MAPK pathway in activated monocytes," *ACS Applied Materials & Interfaces*, vol. 12, no. 14, pp. 16058–16075, 2020.
- [5] Z. Wan, P. Zhang, Y. Liu, L. Lv, and Y. Zhou, "Four-dimensional bioprinting: current developments and applications in bone tissue engineering," *Acta Biomaterialia*, vol. 101, pp. 26–42, 2020.
- [6] C. Zhang, D. Xia, J. Li et al., "BMSCs and osteoblast-engineered ECM synergetically promotes osteogenesis and angiogenesis in an ectopic bone formation model," *Frontiers in Bioengineering and Biotechnology*, vol. 10, article 818191, 2022.
- [7] D. Li, Z. Yang, X. Zhao et al., "A bone regeneration strategy via dual delivery of demineralized bone matrix powder and hypoxia-pretreated bone marrow stromal cells using an injectable self-healing hydrogel," *Journal of Materials Chemistry B*, vol. 9, no. 2, pp. 479–493, 2021.
- [8] H. Tao, Z. Han, Z. C. Han, and Z. Li, "Proangiogenic features of mesenchymal stem cells and their therapeutic applications," *Stem Cells International*, vol. 2016, Article ID 1314709, 11 pages, 2016.
- [9] Y. Zhang, J. Lv, H. Guo, X. Wei, W. Li, and Z. Xu, "Hypoxia-induced proliferation in mesenchymal stem cells and angiotensin II-mediated PI3K/AKT pathway," *Cell Biochemistry and Function*, vol. 33, no. 2, pp. 51–58, 2015.
- [10] X. Li, Z. Yuan, X. Wei et al., "Application potential of bone marrow mesenchymal stem cell (BMSCs) based tissue-engineering for spinal cord defect repair in rat fetuses with

## *Retraction*

# **Retracted: Inflammation and Oxidative Stress Role of S100A12 as a Potential Diagnostic and Therapeutic Biomarker in Acute Myocardial Infarction**

### **Oxidative Medicine and Cellular Longevity**

Received 26 December 2023; Accepted 26 December 2023; Published 29 December 2023

Copyright © 2023 Oxidative Medicine and Cellular Longevity. This is an open access article distributed under the Creative Commons Attribution License, which permits unrestricted use, distribution, and reproduction in any medium, provided the original work is properly cited.

This article has been retracted by Hindawi, as publisher, following an investigation undertaken by the publisher [1]. This investigation has uncovered evidence of systematic manipulation of the publication and peer-review process. We cannot, therefore, vouch for the reliability or integrity of this article.

Please note that this notice is intended solely to alert readers that the peer-review process of this article has been compromised.

Wiley and Hindawi regret that the usual quality checks did not identify these issues before publication and have since put additional measures in place to safeguard research integrity.

We wish to credit our Research Integrity and Research Publishing teams and anonymous and named external researchers and research integrity experts for contributing to this investigation.

The corresponding author, as the representative of all authors, has been given the opportunity to register their agreement or disagreement to this retraction. We have kept a record of any response received.

### **References**

- [1] J. Xie, C. Luo, B. Mo et al., "Inflammation and Oxidative Stress Role of S100A12 as a Potential Diagnostic and Therapeutic Biomarker in Acute Myocardial Infarction," *Oxidative Medicine and Cellular Longevity*, vol. 2022, Article ID 2633123, 19 pages, 2022.

## Research Article

# Inflammation and Oxidative Stress Role of S100A12 as a Potential Diagnostic and Therapeutic Biomarker in Acute Myocardial Infarction

Jian Xie <sup>1</sup>, Changjun Luo <sup>1</sup>, Binhai Mo <sup>2</sup>, Yunhua Lin <sup>3</sup>, Guoqing Liu <sup>3</sup>,  
Xiantao Wang <sup>1</sup> and Lang Li <sup>1,4</sup>

<sup>1</sup>Department of Cardiology, The First Affiliated Hospital of Guangxi Medical University, Guangxi Cardiovascular Institute, Nanning, 530021 Guangxi, China

<sup>2</sup>Department of Cardiology, The First People Hospital of Nanning & The Fifth Affiliated Hospital of Guangxi Medical University, Nanning, 530016 Guangxi, China

<sup>3</sup>The First Clinical Medical College, Guangxi Medical University, Nanning 530021, China

<sup>4</sup>Guangxi Key Laboratory of Precision Medicine in Cardio-Cerebrovascular Diseases Control and Prevention, Nanning, 530021 Guangxi, China

Correspondence should be addressed to Lang Li; [drililang@126.com](mailto:drililang@126.com)

Received 20 May 2022; Revised 20 July 2022; Accepted 9 August 2022; Published 25 August 2022

Academic Editor: Tian Li

Copyright © 2022 Jian Xie et al. This is an open access article distributed under the Creative Commons Attribution License, which permits unrestricted use, distribution, and reproduction in any medium, provided the original work is properly cited.

Acute myocardial infarction (AMI) is one of the most serious cardiovascular diseases with high morbidity and mortality. Numerous studies have indicated that S100A12 may have an essential role in the occurrence and development of AMI, and in-depth studies are currently lacking. The purpose of this study is to investigate the effect of S100A12 on inflammation and oxidative stress and to determine its clinical applicability in AMI. Here, AMI datasets used to explore the expression pattern of S100A12 in AMI were derived from the Gene Expression Omnibus (GEO) database. The pooled standard average deviation (SMD) was calculated to further determine S100A12 expression. The overlapping differentially expressed genes (DEGs) contained in all included datasets were recognized by the GEO2R tool. Then, functional enrichment analyses, including Gene Ontology (GO) and Kyoto Encyclopedia of Genes and Genomes (KEGG) analyses, were carried out to determine the molecular function of overlapping DEGs. Gene set enrichment analysis (GSEA) was conducted to determine unrevealed mechanisms of S100A12. Summary receiver operating characteristic (SROC) curve analysis and receiver operating characteristic (ROC) curve analysis were carried out to identify the diagnostic capabilities of S100A12. Moreover, we screened miRNAs targeting S100A12 using three online databases (miRWalk, TargetScan, and miRDB). In addition, by comprehensively using enzyme-linked immunosorbent assay (ELISA), real-time quantitative PCR (RT-qPCR), Western blotting (WB) methods, etc., we used the AC16 cells to validate the expression and underlying mechanism of S100A12. In our study, five datasets related to AMI, GSE24519, GSE60993, GSE66360, GSE97320, and GSE48060 were included; 412 overlapping DEGs were identified. Protein-protein interaction (PPI) network and functional analyses showed that S100A12 was a pivotal gene related to inflammation and oxidative stress. Then, S100A12 overexpression was identified based on the included datasets. The pooled standard average deviation (SMD) also showed that S100A12 was upregulated in AMI (SMD = 1.36, 95% CI: 0.70-2.03,  $p = 0.024$ ). The SROC curve analysis result suggested that S100A12 had remarkable diagnostic ability in AMI (AUC = 0.90, 95% CI: 0.87-0.92). And nine miRNAs targeting S100A12 were also identified. Additionally, the overexpression of S100A12 was further confirmed that it may promote inflammation and oxidative stress in AMI through comprehensive in vitro experiments. In summary, our study suggests that overexpressed S100A12 may be a latent diagnostic biomarker and therapeutic target of AMI that induces excessive inflammation and oxidative stress. Nine miRNAs targeting S100A12 may play a crucial role in AMI, but further studies are still needed. Our work provides a positive inspiration for the in-depth study of S100A12 in AMI.

## 1. Introduction

As a serious heart disease, acute myocardial infarction (AMI) has the characteristics of high mortality and a poor prognosis; and it is easy to induce severe cardiovascular events, such as ventricular remodeling and heart failure, which seriously threaten people's lives and cause great pain and financial burden in patients [1–3]. The early diagnosis and treatment of AMI are essential for reducing myocardial injury and malignant consequences, reducing mortality and improving patient prognosis to some extents [4–6]. Currently, the levels of myocardial enzyme (CKMB) and cardiac troponin I (cTnI) are still the gold standards for the clinical diagnosis of AMI, but they are not specific for AMI. Previous studies indicated that patients with heart failure, chronic kidney disease, and septicemia also have elevated cardiac troponin I (cTnI) levels, which may lead to false-positive results in AMI diagnosis [7, 8]. Current studies have suggested that the circulating miRNAs, such as miRNA-499, miRNA-22, miR-223-3p, and miR-483-5p, could be used as potential biomarkers of AMI [9–11]. However, there are still few biomarkers available in the clinic; thus, identifying new biomarkers that can be used in the diagnosis and treatment of AMI is still imperative.

AMI can lead to cardiomyocyte death, often followed by a robust inflammatory response in myocardial tissue. Previous studies have demonstrated that the activation of complement and Toll-like receptor (TLR)/interleukin-1 (IL-1) signaling is involved in the onset and development of inflammation [12–14]. A suitable inflammatory response is beneficial for the healing of injured myocardial tissue, indicating that the body performs the function of self-repair. However, a persistent excessive inflammatory response further aggravates cardiomyocyte apoptosis and may lead to serious adverse events, such as arrhythmia, which seriously affect patient prognosis [15, 16]. In addition, the pathogenesis of AMI is associated with the excessive production of reactive oxygen species (ROS), which induce oxidative stress. Oxidative stress is the main cause of the poor prognosis of ischemic myocardial injury in AMI [17]. Several other studies have also identified oxidative stress as a key factor in AMI [18–20]. Therefore, therapy that targets inflammation and oxidative stress may become a potential treatment strategy for patients with AMI.

S100 calcium-binding protein A12 (S100A12) is a calcium-binding protein that plays a vital role in various diseases [21]. In ischemia-reperfusion (I/R) injury, S100A12 promotes inflammation, oxidative stress, and apoptosis by activating ERK signaling *in vitro* [22]. In addition, S100A12 was identified to be involved in the development of atherosclerosis through the S100A12-CD36 axis, and its expression was upregulated in unstable plaques [23]. It was also previously reported that tumor necrosis factor alpha (TNF- $\alpha$ )+S100A12 treatment stimulated nicotinamide adenine dinucleotide phosphate (NADPH) oxidase activity and the production of hydrogen peroxide (H<sub>2</sub>O<sub>2</sub>) in human aortic smooth muscle cells (HASMCs) [24]. The above evidence suggests that S100A12 plays an essential part in inflammation and oxidative stress in numerous diseases.

However, few existing reports concern the expression, potential mechanism, and clinical significance of S100A12 in AMI. Tong et al. identified 10 gene signatures, including S100A12, as effective markers for diagnosing AMI [25]. Zhang et al. reported S100A12 was a novel diagnostic biomarker for the identification of patients with ST-elevation myocardial infarction (STEMI) [26]. In addition, Gobbi et al. constructed a logical regression model containing five platelet gene expression datasets (FKBP5, S100P, SAMS1N1, CLEC4E, and S100A12) that can identify STEMI and healthy donors [27]. But the above studies did not elucidate the underlying mechanism of S100A12 in AMI, especially those related to inflammation and oxidative stress, and the reliability of some studies was limited by insufficient sample sizes. Therefore, our study is the first to integrate public data and *in vitro* experiments to comprehensively explore its potential mechanism in inflammation and oxidative stress and its clinical application value in AMI.

In our current study, the expression pattern, potential mechanism, and clinical significance of S100A12 in AMI were probed using public datasets. Based on bioinformatics methods, potential miRNAs targeting S100A12 were predicted via three online databases (miRWalk, TargetScan, and miRDB). Furthermore, a series of *in vitro* experiments were carried out to elucidate the effect of S100A12 on inflammation and oxidative stress in AMI. In summary, this study reveals that overexpressed S100A12 is involved in inducing excessive inflammation and oxidative stress and could be applied as a feasible diagnostic biomarker and prospective therapeutic target related to inflammation and oxidative stress in AMI.

## 2. Materials and Methods

**2.1. Overall Study Design and Flow.** Here, we first explored the expression pattern and clinical significance of S100A12 in AMI using public data and conducted Gene Ontology (GO) analysis, Kyoto Encyclopedia of Genes and Genomes (KEGG) analysis, and Gene set enrichment analysis (GSEA) to explore its possible mechanism. Furthermore, real-time quantitative PCR (RT-qPCR), enzyme-linked immunosorbent assay (ELISA), Western blotting (WB) methods, and other *in vitro* experiments were carried out to verify the effect of S100A12 in AMI. The overall design and flow diagram of this study are presented in Figure 1.

**2.2. GEO Dataset Downloading and Data Preprocessing.** All AMI expression profile datasets were obtained through the Gene Expression Omnibus (GEO) database (<https://www.ncbi.nlm.nih.gov/geo/>). We searched for the gene expression profile data of AMI in the GEO database and screened the identified datasets according to the inclusion and exclusion criteria. The inclusion criteria were as follows: (1) including three or more pairs of samples from an AMI group and a non-AMI group and (2) derived from a human source. The exclusion criteria were as follows: (1) that data could not be downloaded and (2) no complete gene expression profile data were provided. Finally, five datasets (GSE24519, GSE60993, GSE66360, GSE97320, and

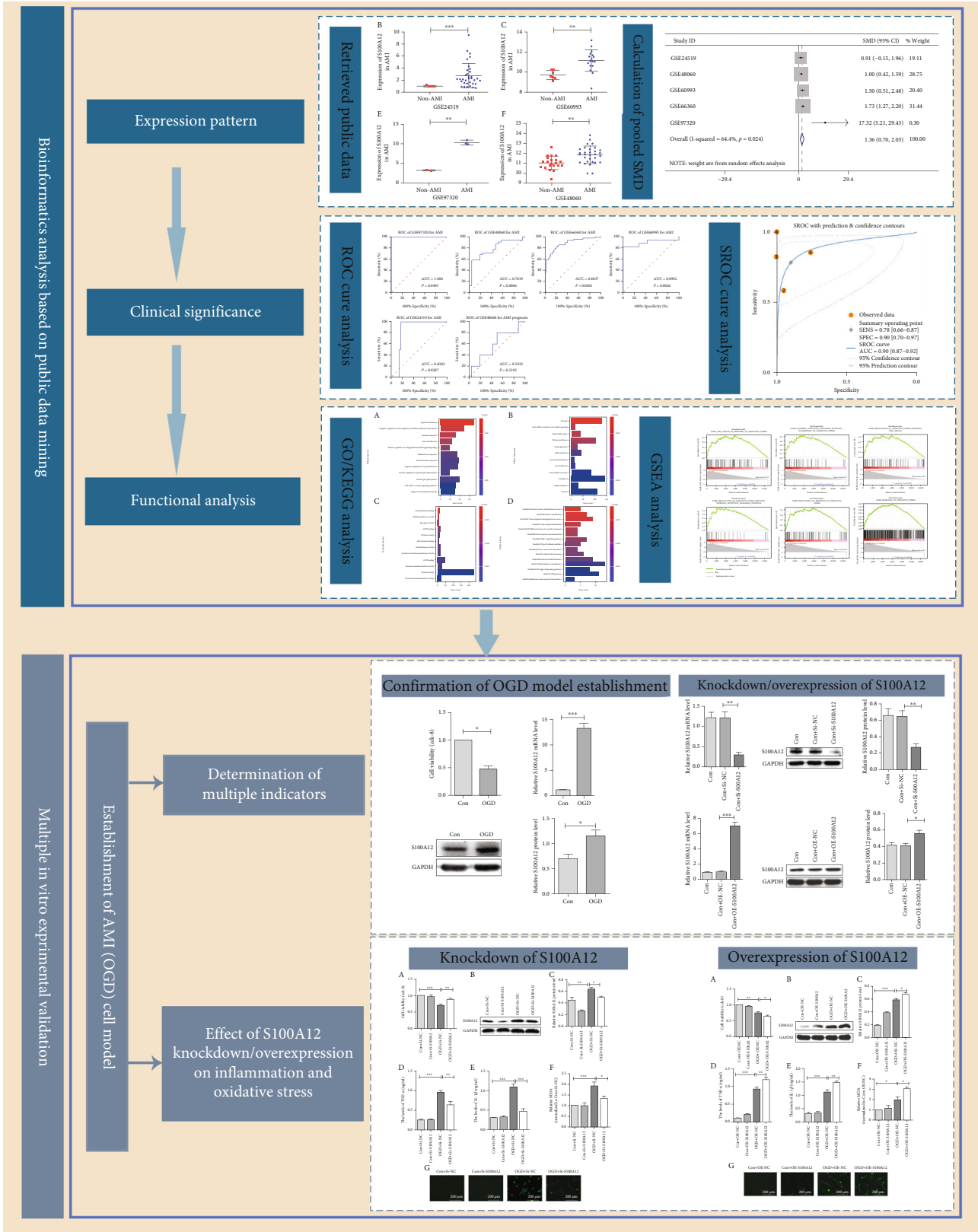


FIGURE 1: Overall design and flow chart of this study. Notes: AMI: acute myocardial infarction; S100A12: S100 calcium-binding protein A12; KEGG: Kyoto Encyclopedia of Genes and Genomes; GO: Gene Ontology; SMD: standardized mean difference; ROC: receiver operating characteristic; SROC: summary receiver operating characteristic; GSEA: gene set enrichment analysis; RT-qPCR: real-time quantitative PCR; ELISA: enzyme-linked immunosorbent assay; WB: Western blotting; OGD: oxygen-glucose deprivation.

TABLE 1: The datasets of AMI in GEO database.

Accession	Author	Year	Country	Platform	Non-AMI	AMI
GEO: GSE24519	Bellin M	2017	Italy	GPL2895	4	34
GEO: GSE48060	Suresh R	2014	USA	GPL570	21	31
GEO: GSE60993	Eun JW	2015	South Korea	GPL6884	7	17
GEO: GSE66360	Kramer ER	2015	USA	GPL570	50	49
GEO: GSE97320	Meng F	2017	China	GPL570	3	3

Notes: AMI: acute myocardial infarction; GEO: Gene Expression Omnibus.

GSE48060) that were included in the standard and did not meet the exclusion criteria were included in this study. The dataset information was described in detail in Table 1. Furthermore, all data downloaded from the GEO database were transformed into  $\log_2$  values for further analysis. And we integrated all included datasets using the “sva” R package and removed batch effects to form a merged dataset.

**2.3. Screening of Overlapping Differentially Expressed Genes (DEGs) via GEO2R.** GEO2R, a web page interaction tool provided by the GEO database, was applied to analyze the differential expression level of genes between the AMI group and non-AMI group. In this study, four datasets, GSE24519, GSE60993, GSE66360, and GSE97320, were used as the discovery datasets to screen the overlapping DEGs using the online web tool GEO2R. Only those genes with  $p < 0.05$  and  $\log_2 \text{FC} < 0$  were defined as downregulated DEGs. In contrast, those genes with  $p < 0.05$  and  $\log_2 \text{FC} > 0$  were defined as upregulated DEGs. Then, the DEGs in each dataset were intersected and defined the overlapping genes as the final overlapping DEGs. Notably, the GSE48060 dataset contained information regarding the recurrence condition of AMI patients; thus, this dataset was not included in the discovery dataset, which was used to evaluate the ability of S100A12 to distinguish between recurrent and nonrecurrent patients.

**2.4. Functional Analysis of Overlapping DEGs and S100A12.** KEGG and GO analyses were carried out through the Database for Annotation, Visualization, and Integrated Discovery (DAVID) (version 6.8, <https://david.ncifcrf.gov/>) to comprehensively understand the potential biological functions and pathways of the overlapping DEGs. To visualize the analysis results, the enrichment results of the top 12 genes (based on the number of enrichment genes) in the KEGG and GO enrichment analyses were intuitively presented as bar charts. Furthermore, the merged dataset was divided into high and low expression groups based on the median expression value of S100A12, and then, a GSEA analysis was carried out using GSEA software (version 4.1.0) to clarify its potential mechanism in AMI (an FDR  $< 0.25$  and nominal  $p < 0.05$  were used as the screening criteria for enriched pathways, and “c5.go.bp.v7.5.symbols.gmt” was chosen as the reference gene set used for this analysis).

**2.5. PPI Network Analysis and Identification of Hub Genes.** Protein-protein interaction (PPI) analysis is usually performed using the online tool STRING (release 11.0, [\[string-db.org/\]\(http://string-db.org/\)\). Based on STRING, we analyzed the PPIs of the selected overlapping DEGs and constructed a PPI network using Cytoscape 3.6.1 software. Using the cytoHubba plug-in, the overlapping DEGs with a degree of not less than 12 and ranking in the top 40 were identified as hub genes.](http://www</a></p>
</div>
<div data-bbox=)

**2.6. Identification of S100A12 Expression Levels in Five Datasets.** By mining the online database, we obtained five datasets that provided the S100A12 gene expression profile data of AMI patients and non-AMI patients. To determine the expression pattern of S100A12 in AMI, we first explored the expression levels of S100A12 in each separate dataset, and the results were shown in the form of a scatter plot. Then, we integrated all included dataset expression profile data to comprehensively evaluate the expression levels of S100A12. As the included data were continuous variables, Stata 14 software was applied to calculate the pooled standard mean deviation (SMD). Egger’s test was applied to estimate the publication bias, and  $p > 0.05$  indicated no publication bias. The Q test and  $I^2$  statistics were used to evaluate the heterogeneity of the analysis using the random effect model under the premise of  $I^2 > 50\%$ . Otherwise, the fixed effect model was applied for nonsignificant heterogeneity.

**2.7. Clinical Significance of S100A12 in AMI.** To test the diagnostic ability of S100A12 in AMI, receiver operator characteristic (ROC) curves were constructed by GraphPad Prism 8 software, and the area under the curve (AUC) was calculated to assess the diagnostic ability of S100A12. Moreover, using Stata 14 software, we plotted a summary receiver operating characteristic (SROC) curve and then calculated the AUC to further identify the diagnosability of S100A12 in AMI.

**2.8. Prediction of miRNAs Targeting S100A12 via Multiple Databases.** We used miRWalk3.0 (<http://mirwalk.umm.uni-heidelberg.de/>), miRDB (<http://mirdb.org/>), and TargetScan7.0 (<http://www.targetscan.org>) for the prediction of miRNAs targeting S100A12 and then obtained the chiasm of the three database predictions. Finally, S100A12 was defined as the target gene of overlapping miRNAs.

**2.9. Verification of the Role of S100A12 Expression through In Vitro Experiments**

**2.9.1. Model Establishment.** We constructed an oxygen-glucose deprivation (OGD) model using the AC16 cells (purchased from Tongpai, Shanghai, China) as previously reported to mimic the state of cardiomyocytes in AMI in vitro [28]. Briefly, AC16 cells were initially cultured in

Dulbecco's modified Eagle's medium (DMEM) (Gibco, Grand Island, NY, USA) for 24 h in a 37°C and 20% O<sub>2</sub> incubator. Then, the cells were washed 3 times with phosphate-buffered saline (PBS) and incubated with glucose- and serum-free DMEM for 6 h at 37°C and 2% O<sub>2</sub> to induce AMI in vitro.

**2.9.2. Knockdown and Overexpression of S100A12.** AC16 cells were transfected with small interfering RNAs (siRNAs) specific for S100A12 and nontargeting siRNAs (Shenggong, Shanghai, China) as a negative control (Si-NC) using Lipofectamine 3000 reagent (Invitrogen, Carlsbad, CA, USA). The transfection time was 48 hours, and the concentration of siRNAs used was 50 nM [29]. In addition, S100A12 overexpression and negative control overexpression (OE-NC) plasmids (3 μg) were transfected into AC16 cells. Supplementary table 1 presented the sequences of small interfering RNAs (siRNAs) and overexpression plasmids. The above experiments were carried out following the instructions supplied by the manufacturer.

**2.9.3. Cell Counting Kit-8 (CCK-8) Assay.** CCK-8 assay was applied to determine the cell viability following the instructions provided by the manufacturer of the CCK-8 kit (Dojindo, Japan). And a microplate reader was used to read the optical density (OD) value at 490 nm.

**2.9.4. Quantitative Real-Time Polymerase Chain Reaction (qRT-PCR).** Total RNA was extracted from AC16 cells using TRIzol reagent (Invitrogen) based on the manufacturer's instructions. Then, the mRNA expression of S100A12 in different groups of AC16 cells was detected by RT-qPCR using the TB Green® Premix Ex Taq™ II (TaKaRa, Japan). The primer sequences used in our study were listed as follows: S100A12: upstream: 5'-TCCACCAATACTCAGTTCGGAAG-3', downstream: 5'-ACTCTTTGTGGGTGTGGTAATGG-3', and GAPDH: upstream: 5'-GGAGTCCACTGGCGTCTTCA-3', downstream: 5'-GTCATGAGTCCTTCCACGATACC-3'.

**2.9.5. Western Blotting (WB) Analysis.** To determine the protein expression level of S100A12, we used sodium dodecyl sulfate-polyacrylamide gel electrophoresis (SDS-PAGE) at a constant voltage of 100 V to separate the total protein of each group of AC16 cells, which was then transferred to polyvinylidene fluoride membranes (PVDF, Millipore, Atlanta, Georgia, United States). Subsequently, the membranes were blocked with bovine serum albumin (BSA) for 1 hour at 25°C, followed by incubation with the corresponding primary antibody (anti-S100A12, 1:1000, Abcam) overnight at 4°C. After 24 h, the membrane was washed five times and incubated with an enzyme-conjugated secondary antibody (1:1000, Abcam) for 2 h. GAPDH was used as a normalized control.

**2.9.6. Inflammatory Indicator Assessment.** The ELISA was used to detect the expression levels of inflammation-related genes, including interleukin 1β (IL-1β) and tumor necrosis factor alpha (TNF-α), in each group of samples.

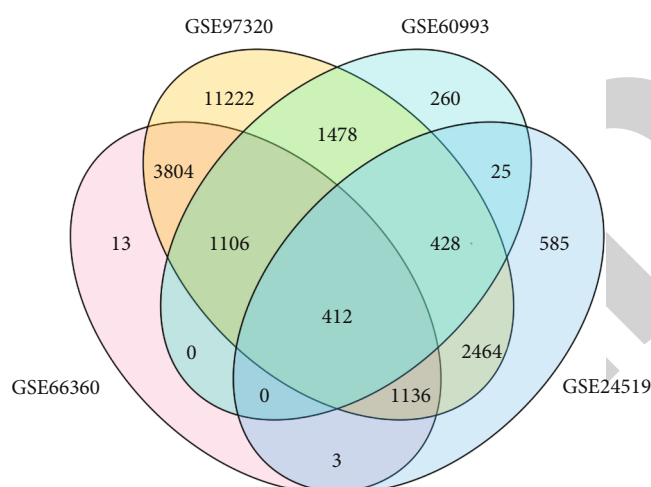


FIGURE 2: Identification of overlapping DEGs. The Venn diagram of DEGs among GSE24519, GSE60993, GSE66360, and GSE97320. The coincident part represents the DEGs shared by the four datasets. Notes: DEGs: differentially expressed genes.

**2.9.7. Oxidative Stress Indicator Assessment.** The malondialdehyde (MDA) expression levels in each group of samples were detected using an MDA assay kit (A003-1-2; Nanjing Jiancheng Bioengineering Institute, Nanjing, China) according to the manufacturer's instructions; and the intracellular reactive oxygen species (ROS) levels were determined with dichlorodihydrofluorescein diacetate (DCFH-DA) (Sigma, USA). Specifically, 50 μM DCFH-DA was applied to incubate the samples for 30 min at 37°C in the dark. Then, the samples were washed twice with cold phosphate buffer (Servicebio, Wuhan, China). Immediately thereafter, a fluorescence microscope (Olympus IX51, Japan) was conducted to capture intracellular ROS fluorescence images.

**2.10. Statistical Analysis.** The comparisons between two and multiple groups were carried out using an independent samples *t*-test and a one-way analysis of variance (ANOVA), respectively. Unless otherwise specified, the number of samples per group was equal to 3 ( $n = 3$ ). The ROC curves and scatter plots were drawn with GraphPad Prism 8 software. The SROC curve and Egger's test were performed by Stata 14 software. In R software (version 3.6.3), the visualization of the functional enrichment analyses results was performed with the application of the R package ggplot2.

### 3. Results

**3.1. Screening of Overlapping Differentially Expressed Genes (DEGs) via GEO2R.** The differential expression levels of genes in the included datasets were analyzed through the online web tool GEO2R, and the overlapping DEGs screened from 4 separate datasets (GSE24519, GSE60993, GSE66360, and GSE97320) were intersected. Ultimately, we screened a total of 412 overlapping DEGs, all of which were used for further analysis (Figure 2).

### 3.2. Functional Analysis of Overlapping DEGs and S100A12.

To reveal the possible biological function and enrichment pathways of the overlapping DEGs, the KEGG pathway analysis and GO analysis were carried out. Among them, GO analysis consisted of three categories: biological process (BP), cellular component (CC), and molecular function (MF). In the BP category, the overlapping DEGs were mainly enriched in signal transduction, positive regulation of I-kappaB kinase/NF-kappaB signaling, inflammatory response, etc. (Figure 3(a)). For the CC category, the overlapping DEGs were enriched in many aspects, such as cytoplasm, cytosol, and nucleus (Figure 3(b)). For the MF category, the overlapping DEGs were significantly enriched in protein binding, ATP binding, and protein homodimerization activity (Figure 3(c)). In addition, these genes were particularly associated with butirosin and neomycin biosynthesis, the phagosome, the NF-kappaB signaling pathway, and the biosynthesis of antibiotics in the KEGG enrichment analysis (Figure 3(d)). Notably, S100A12 was the only overlapping DEGs enriched in all three aspects that were closely associated with the onset and development of inflammation, including GO:0043406~positive regulation of MAP kinase activity, GO:0006954~inflammatory response, and GO:0043123~positive regulation of I-kappaB kinase/NF-kappaB signaling (Table 2). Furthermore, the GSEA analysis showed that multiple oxidative stress-related pathways, including the regulation of the oxidative stress response, the response to oxidative stress, and regulation of oxidative stress-induced cell death, were significantly activated in the samples with high S100A12 expression (Figure 3(e)).

### 3.3. PPI Network Analysis and Identification of Hub Genes.

We obtained 40 hub genes (contained S100A12; rank = 33, score = 13) according to the criteria that the degree was not less than 12 and ranked in the top 40 (Figure 4(a)). Our above study results showed that S100A12 was enriched in several classical pathways associated with inflammation and oxidative stress. Consequently, we conjectured that high expression of S100A12 may play an essential role in the occurrence and development of AMI and promote myocardial inflammation and oxidative stress, which deserves further experimental verification.

### 3.4. The Expression Levels of S100A12 in AMI.

Based on the GEO database, we screened five datasets, including GSE24519, GSE60993, GSE66360, GSE97320, and GSE48060, and then, we extracted the expression level of S100A12 from five above separate datasets, and the outcomes are shown in Table 3. In addition, we intuitively showed the expression level of S100A12 in five datasets between AMI group and non-AMI group in the form of a scatter plot (Figures 4(b)–4(f)). Because of the large heterogeneity ( $I^2 = 64.4\%$ ,  $p = 0.024$ ; Figure 5(a)), the random effect model was carried out to calculate the SMD. The pooled SMD of S100A12 was 1.36 (95% CI: 0.70–2.03,  $p = 0.024$ ; Figure 5(a)), indicating that the expression of S100A12 was significantly upregulated in the AMI group compared with that in the non-AMI group. Egger's test showed that there was no obvious publication bias of overex-

pressed S100A12 in AMI ( $p = 0.448$ , Figure 5(b)). In summary, all the results we obtained thus far confirmed that S100A12 was overexpressed in AMI.

**3.5. Clinical Significance of S100A12 in AMI.** We used GraphPad Prism 8 and Stata 14 software to draw ROC curves and SROC curves, respectively. An AUC value of 0.5 to 0.7 indicates a poor diagnostic value, whereas an AUC value of 0.7 to 0.9 indicates a moderate diagnostic value. A value above 0.9 suggests that the identified biomarkers have good diagnostic value [30]. The ROC results showed that the AUC values were greater than 0.7 in the five separate datasets included in this study, proving that S100A12 has upper-middle diagnostic ability (Figures 6(a)–6(e)). The SROC results indicated that S100A12 had excellent diagnosability (AUC = 0.90, 95% CI: 0.87–0.92; Figure 5(c)). However, our results showed that S100A12 cannot effectively distinguish recurrent patients from nonrecurrent patients (AUC = 0.59,  $p = 0.52$ ; Figure 6(f)). Nevertheless, our findings suggested that S100A12 could be used to distinguish the AMI group samples from the non-AMI group samples. S100A12 may be a diagnostic marker of AMI and has certain clinical application value.

### 3.6. Prediction of miRNAs Targeting S100A12 via Multiple Databases.

After taking the intersection of the prediction results of the three databases (miRWalk, miRDB, and TargetScan), 9 miRNAs were identified, including hsa-miR-4710, hsa-miR-7855-5p, hsa-miR-5589-5p, hsa-miR-4505, hsa-miR-5004-5p, hsa-miR-6858-5p, hsa-miR-1224-5p, hsa-miR-3667-5p, and hsa-miR-5787 (Figure 6(g)).

### 3.7. Validation of S100A12 Overexpression In Vitro.

We successfully constructed an OGD model according to the methods described above, and the CCK-8 detection results showed that the cell viability of the OGD group was significantly lower than that of the Con (control) group (Figure 7(a)). The measurement results of the WB and qRT-PCR analyses suggested that both the protein and mRNA expression levels of S100A12 in the OGD group were significantly higher than that in the Con group (Figures 7(b)–7(d)).

### 3.8. Achieving Knockdown and Overexpression of S100A12.

Both the PCR and WB results indicated that the expression of S100A12 in the Con+Si-S100A12 group was lower than that in the Con+Si-NC group (Figures 7(e)–7(g)). In contrast, its expression in the Con+OE-S100A12 group was higher than that in the Con+NC group (Figures 7(h)–7(j)). Overall, the consistent results of the PCR and WB analyses indicate that we successfully achieved knockdown and overexpression of S100A12.

### 3.9. Assessment of the Role of S100A12 Knockdown in Inflammation and Oxidative Stress in the OGD Model.

The results of the CCK-8 assay (Figure 8(a)) suggest that the cell viability of the OGD+Si-S100A12 group was higher compared with the OGD+Si-NC group ( $p < 0.05$ ). In addition, the expression levels of S100A12 (Figures 8(b) and 8(c)), inflammatory indicators (TNF- $\alpha$  and IL1- $\beta$ ) (Figures 8(d)



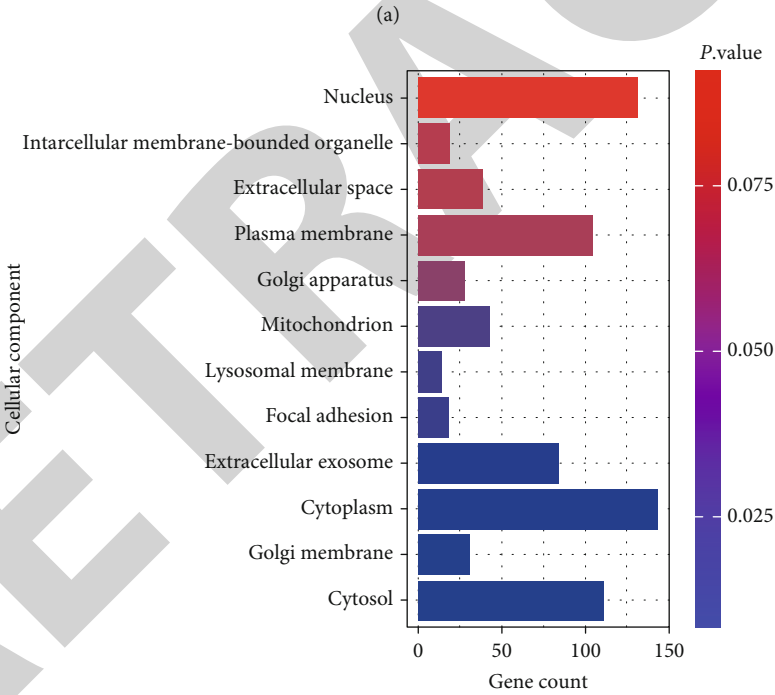
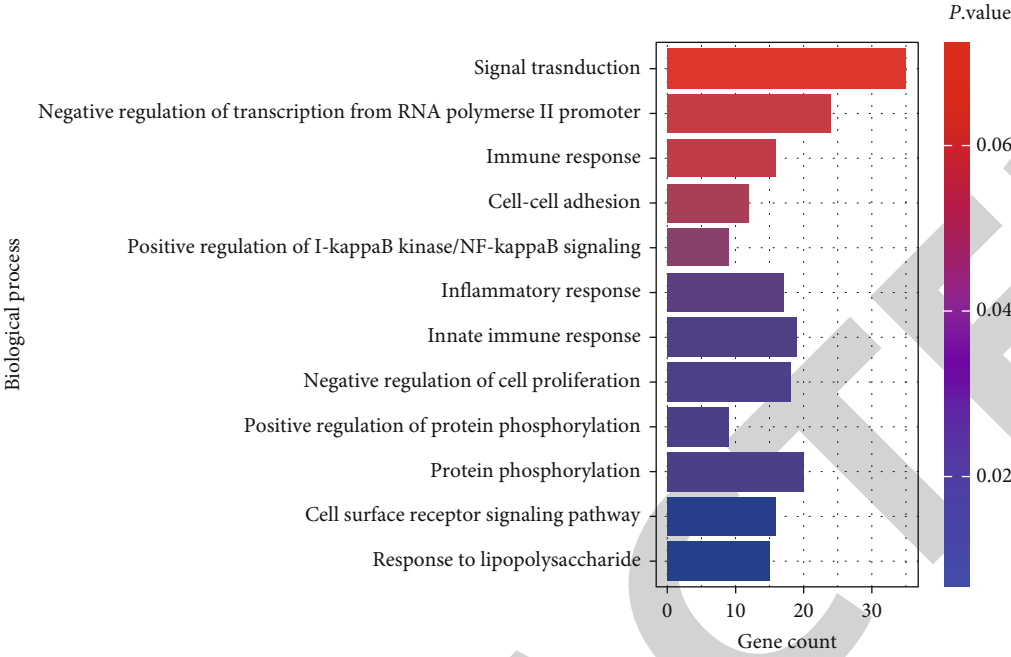
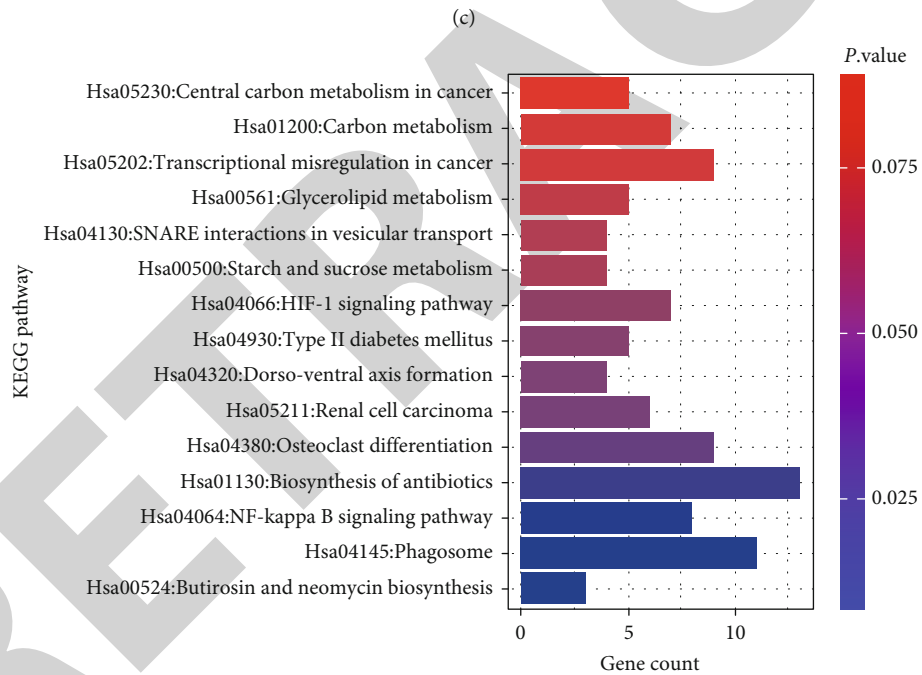
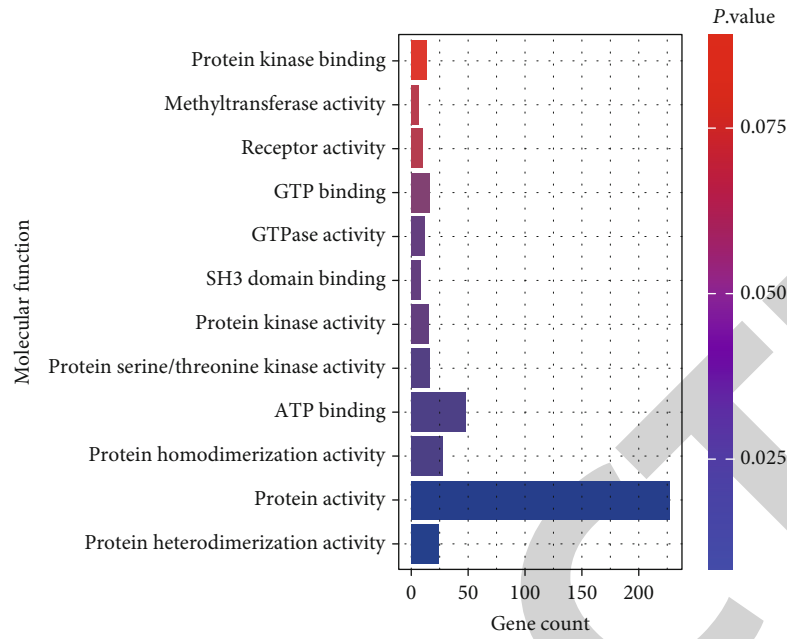


FIGURE 3: Continued.



(d)

FIGURE 3: Continued.

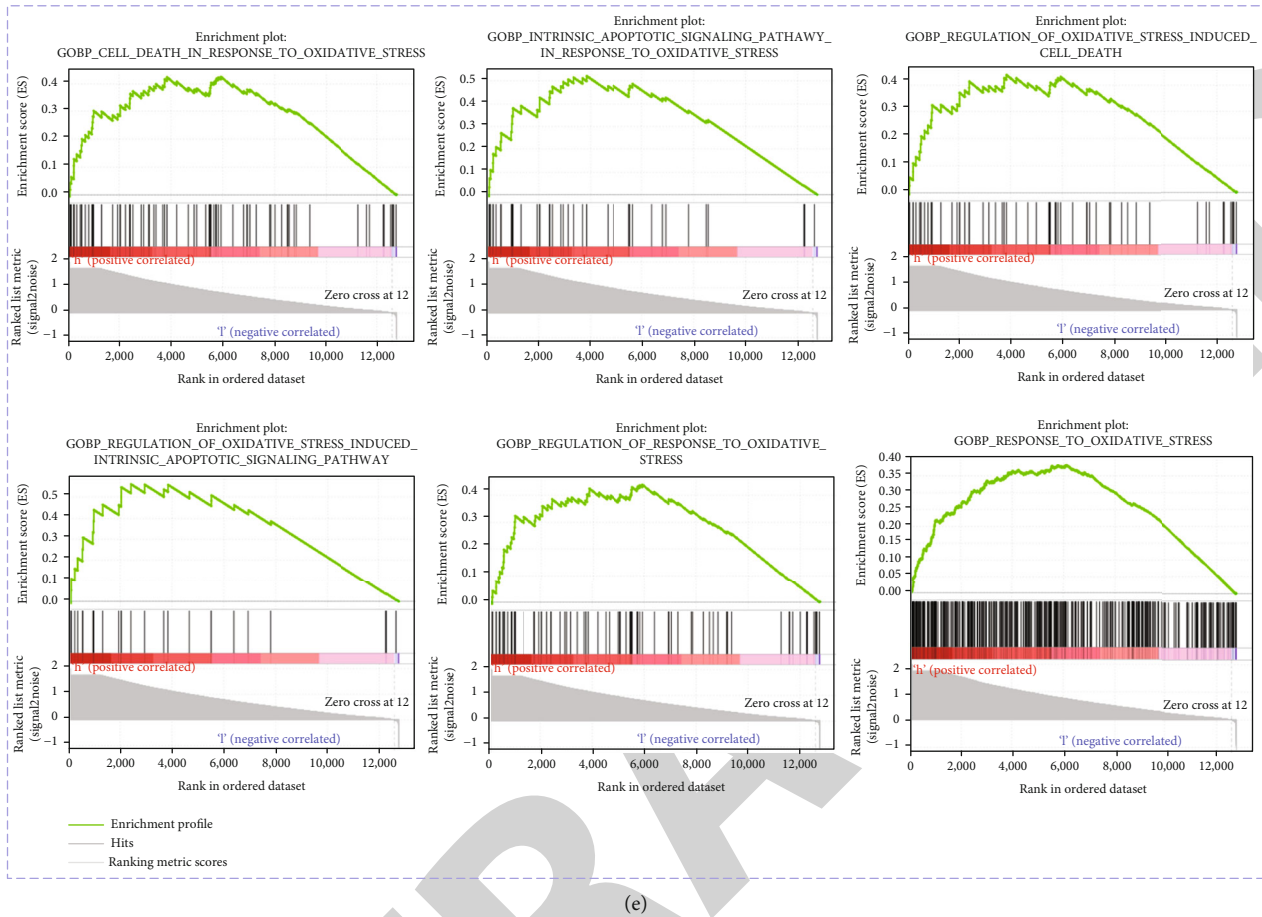


FIGURE 3: GO, KEGG, and GSEA analyses of the DEGs and S100A12 in AMI. (a) Biological process (BP). (b) Cellular component (CC). (c) Molecular function (MF). (d) KEGG pathways. (e) GSEA analysis of S100A12. Notes: S100A12: S100 calcium-binding protein A12; AMI: acute myocardial infarction; DEGs: differentially expressed genes; KEGG: Kyoto Encyclopedia of Genes and Genomes; GO: Gene Ontology; GSEA: gene set enrichment analysis.

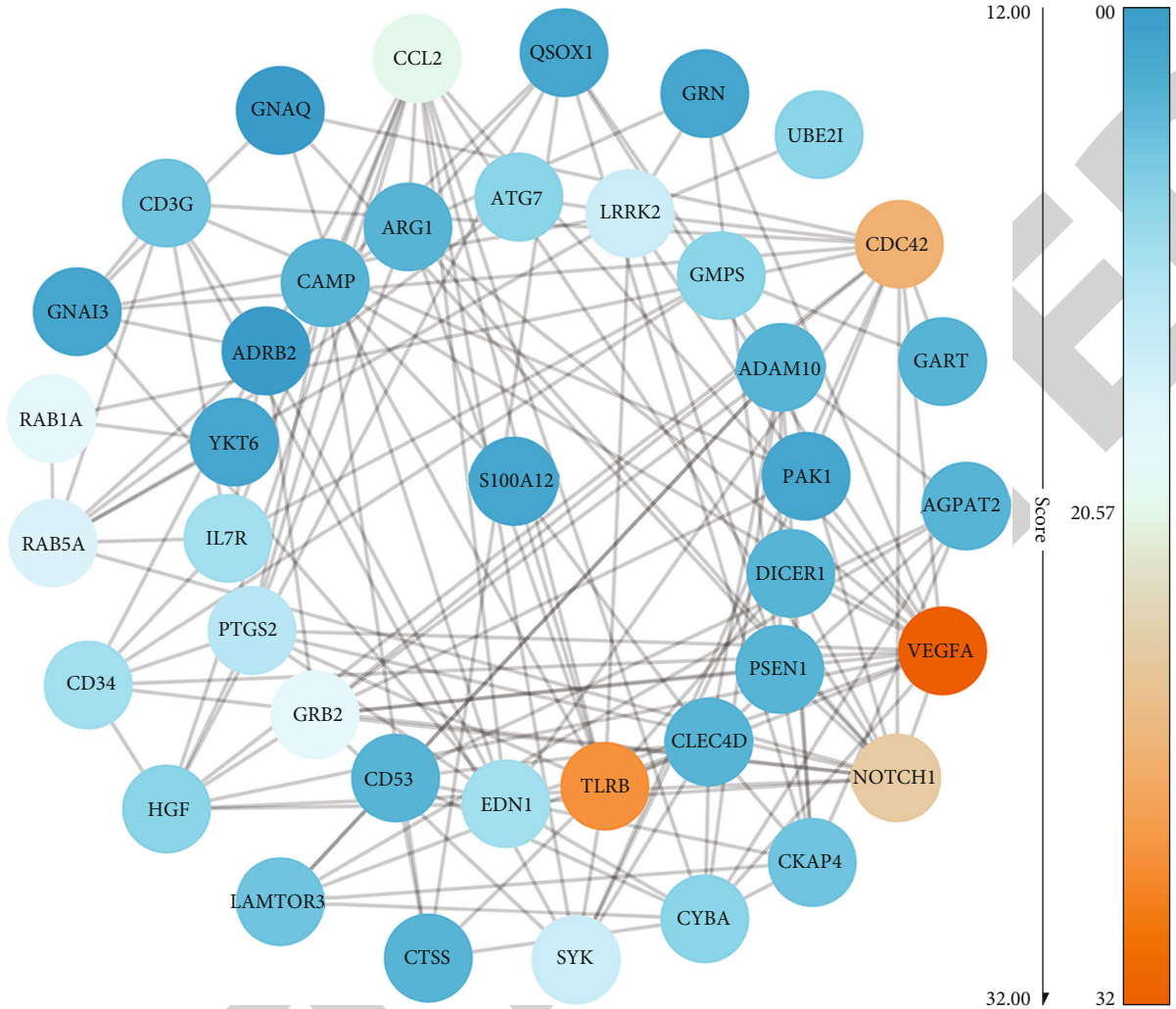
TABLE 2: The significant gene ontology and signal enrichment terms of S100A12 in biological process category.

Term	Count	Genes	<i>p</i> value
GO:0006954~inflammatory response	17	SYK, IL37, GPR68, TNFRSF18, LY96, TNFRSF10B, CYBA, PTGS2, TIRAP, MMP25, NFKBIZ, S100A12, CCL2, TLR8, CD14, LTBR, and KLRG1	0.013
GO:0043123~positive regulation of I-kappaB kinase/NF-kappaB signaling	9	UBE2I, PELI2, MIER1, PELI1, S100A12, TNFRSF10B, LTBR, TIRAP, and LTF	0.031
GO:0043406~positive regulation of MAP kinase activity	5	EDN1, LRRK2, S100A12, PSEN1, and VEGFA	0.045

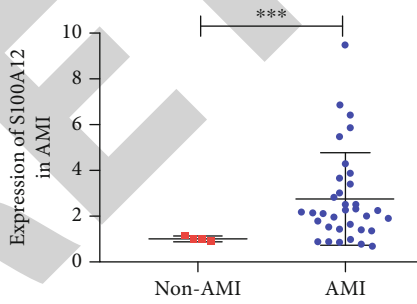
and 8(e)), and oxidative stress indicators (ROS and MDA) in the OGD+Si-NC group were significantly increased compared with the OGD+Si-S100A12 group ( $p < 0.05$ ) (Figure 8(f)–8(g)). Therefore, we concluded that the knock-down of S100A12 expression could alleviate inflammation and oxidative stress in the OGD model and reduce cardiomyocyte injury.

**3.10. Assessment of the Role of S100A12 Overexpression on Inflammation and Oxidative Stress in the OGD Model.** The results of the CCK-8 assay (Figure 9(a)) suggest that the cell

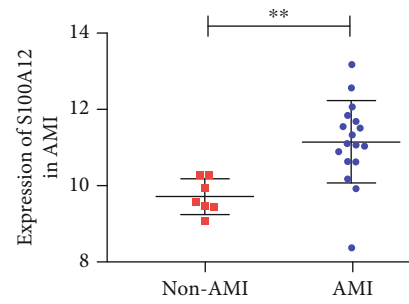
viability of the OGD+OE-S100A12 group samples was lower compared with the OGD+NC group ( $p < 0.05$ ). In addition, the expression levels of S100A12 (Figure 9(b) and 9(c)), inflammatory indicators (TNF- $\alpha$  and IL1- $\beta$ ) (Figures 9(d) and 9(e)), and oxidative stress indicators (ROS and MDA) in the OGD+OE-S100A12 group were significantly increased compared with the OGD+NC group ( $p < 0.05$ ) (Figures 9(f) and 9(g)). The above evidence concluded that S100A12 overexpression aggravated inflammation and oxidative stress in the OGD model, leading to cardiomyocyte injury.



(a)



(b)



(c)

FIGURE 4: Continued.

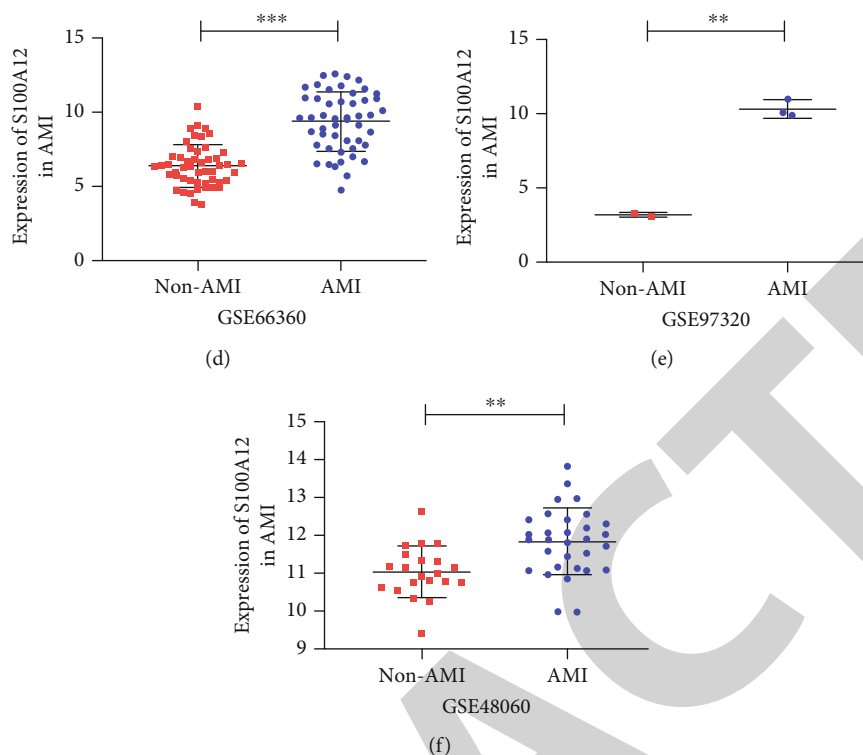


FIGURE 4: Different expression levels of S100A12 in the AMI group and non-AMI group as well as PPI network of the top 40 DEGs. (a) PPI network, (b) GSE24519, (c) GSE60993, (d) GSE66360, (e) GSE97320, and (f) GSE48060. Notes: PPI node color represents DEGs degree (number of connections), where darker orange indicates more degree. Compared with the non-AMI group, \* $p < 0.05$ , \*\* $p < 0.01$ , and \*\*\* $p < 0.001$ . S100A12: S100 calcium-binding protein A12; PPI: protein-protein interaction; AMI: acute myocardial infarction; DEGs: differentially expressed genes.

TABLE 3: Characteristics of the datasets included in the study.

Author (publication year)	Country	Data source	Platform	Non-AMI				AMI	
				N0	M0	SD0	N1	M1	SD1
Bellin M (2017)	Italy	GEO: GSE24519	GPL2895	4	1.020	0.104	34	2.758	2.003
Suresh R (2014)	USA	GEO: GSE48060	GPL570	21	11.025	0.672	31	11.826	0.871
Eun JW (2015)	South Korea	GEO: GSE60993	GPL6884	7	9.728	0.459	17	11.163	1.087
Kramer ER (2015)	USA	GEO: GSE66360	GPL570	50	6.404	1.414	49	9.386	1.984
Meng F (2017)	China	GEO: GSE97320	GPL570	3	3.166	0.102	3	10.224	0.567

Notes: AMI: acute myocardial infarction; N: number; M: mean; SD: standard deviation.

#### 4. Discussion

Acute myocardial infarction (AMI) is one of the most serious cardiovascular diseases, an early diagnosis of AMI is very important, but diagnostic biomarkers and therapeutic targets available in the clinic are lacking [31–33]. Inflammation and oxidative stress are involved in adverse outcomes of AMI [34–37]. As a member of the S100 protein family, S100A12 has been confirmed to play a role in various cardiovascular disease [38–42]. However, there are still few studies systematically exploring the role and potential application value of S100A12 in AMI through integrated means of bioinformatics and experimental validation, especially its effects on inflammation and oxidative stress. Therefore, we attempted to identify a potential diagnostic biomarker and

therapeutic target associated with inflammation and oxidative stress through bioinformatics techniques and multiple in vitro experiments.

Our study suggested that the mitogen-activated protein kinase (MAPK) signaling pathway, NF-kappaB signaling pathway, and inflammatory response pathway, which S100A12 was enriched in, were associated with the occurrence and development of AMI. MAPK can be divided into four subfamilies, extracellular signal-regulated kinase (ERK), p38, c-Jun N-terminal kinase (JNK), and ERK54 that participate in many biological processes, such as cell proliferation, apoptosis, and inflammation [43]. The p38 MAPK signaling pathway played a vital role in the secretion and activity of TNF- $\alpha$ , IL-2, IL-1, and other proinflammatory cytokines in human endothelial cells. ERK1/2 phosphorylation mediates

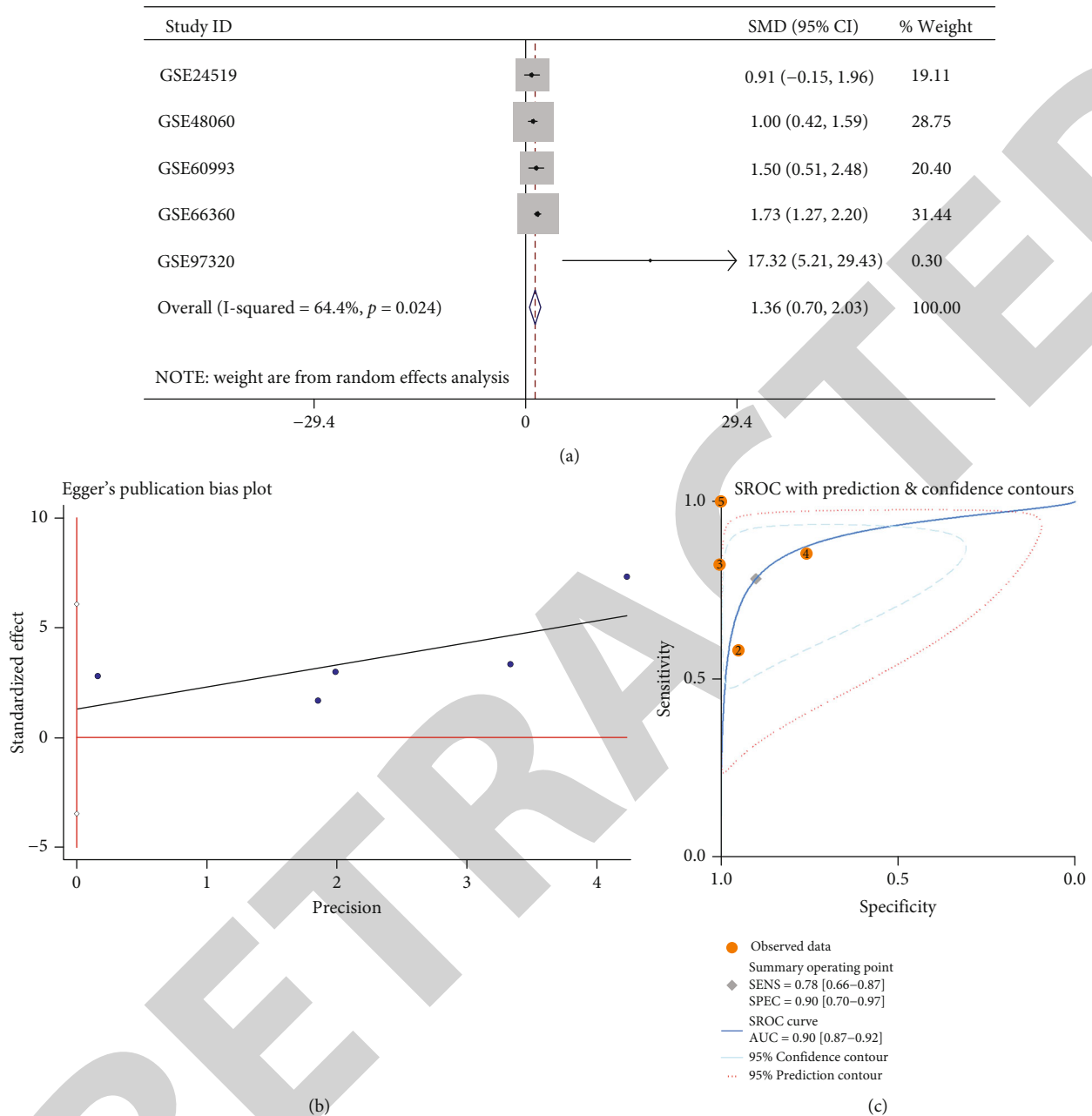


FIGURE 5: Comprehensive analysis of S100A12 in AMI. (a) Forest plot of SMD of the included study. (b) Egger's test. (c) SROC curve. Notes: S100A12: S100 calcium-binding protein A12; AMI: acute myocardial infarction; SMD: standardized mean difference; SROC: summary receiver operating characteristics.

myocardial fibrosis induced by transforming growth factor- $\beta$ 1 by activating Rho kinase1 in myocardial infarction model rats [44]. The JNK-NF-kappaB signal transduction cascade could be inhibited by the intrinsic activation of AMP-activated protein kinase (AMPK), thereby reducing ischemia/reperfusion-induced inflammation [45]. The NF-kappaB signaling pathway was closely related to the occurrence of inflammation. A study reported that adiponectin inhibited the activation of the NF-kappaB signaling pathway and the expression of proinflammatory genes, thereby inhibiting the inflammatory response in atherosclerosis [46]. Moreover, Zhang et al. confirmed that S100A12 could pro-

mote inflammation induced by ischemia-reperfusion injury by activating ERK signal transduction [22]. The GSEA analysis further suggested that overexpressed S100A12 may be associated with excessive oxidative stress. Previous studies have suggested that the oxidative stress levels are significantly elevated in AMI, which could cause myocardial cell dysfunction and damage [47, 48]. In addition, excessive oxidative stress and an inflammatory response could promote the occurrence of heart failure in patients with AMI [49]. Based on the above evidence, we speculated that S100A12 may promote the inflammatory response, oxidative stress, and myocardial damage after AMI.

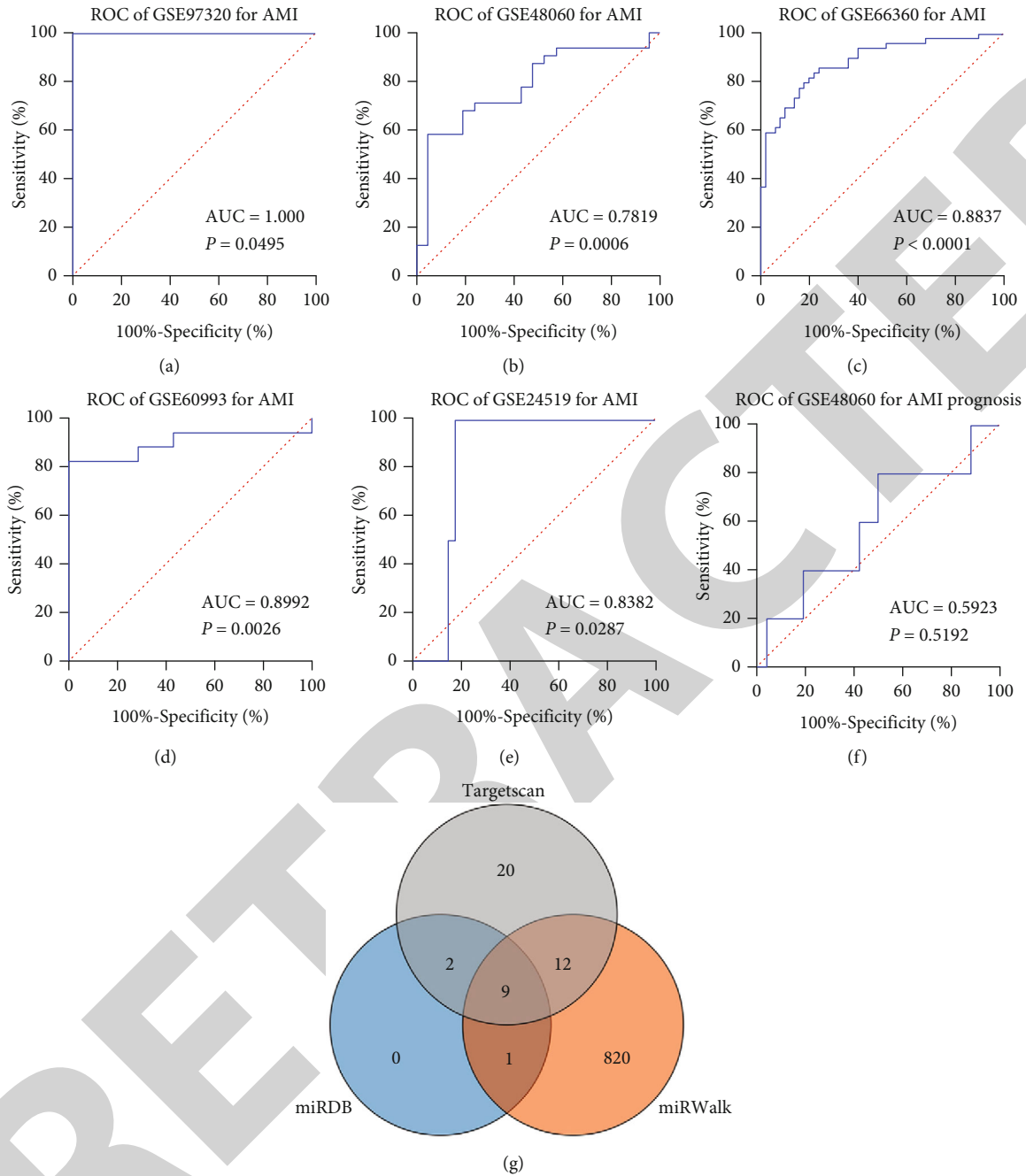


FIGURE 6: ROC curve of S100A12 between AMI patients and non-AMI patients based on 5 datasets included, and prediction of miRNAs targeting S100A12. (a) GSE97320, (b) GSE48060, (c) GSE66360, (d) GSE60993, (e) GSE24519, and (f) GSE48060 for AMI prognosis. (g) Venn diagram for miRNA prediction. Notes: S100A12: S100 calcium-binding protein A12; ROC: receiving operator characteristic; AMI: acute myocardial infarction.

Furthermore, nine miRNAs targeting S100A12, including hsa-miR-4710, hsa-miR-7855-5p, hsa-miR-5589-5p, hsa-miR-4505, hsa-miR-5004-5p, hsa-miR-6858-5p, hsa-miR-1224-5p, hsa-miR-3667-5p, and hsa-miR-5787, were predicted via three online databases (miRWalk, TargetScan, and miRDB). hsa-miR-5787 inhibited inflammation mediated by macrophages in ischemic cerebral infarction through regulating TLR4/NF-kappaB signaling [50]. hsa-miR-4505 aggravated lipopolysaccharide- (LPS-) induced vascular

endothelial cell injury by regulating heat shock proteinA12B (HSPA12B) [51]. Moreover, it was reported that hsa-miR-1224-5p, hsa-miR-4710, and hsa-miR-7855-5p played important roles in various cancers. For example, hsa-miR-1224-5p inhibited the proliferation and invasion of ovarian cancer by targeting staphylococcal nuclease and tudor domain containing 1 (SND1) [52]; hsa-miR-4710 could be used to predict axillary lymph node metastasis of breast cancer [53]. The expression of hsa-miR-7855-5p could be

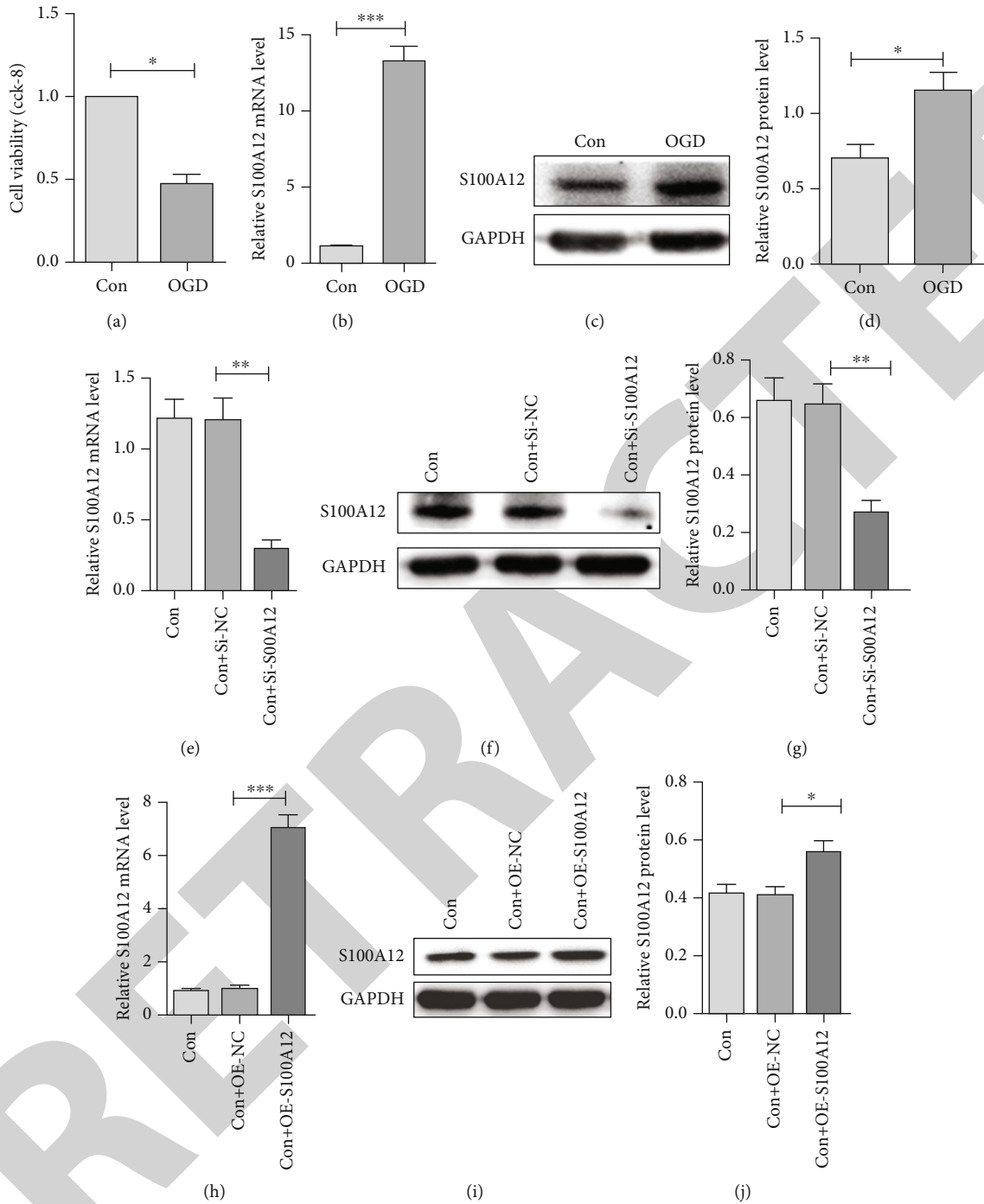


FIGURE 7: Establishment of in vitro model of OGD and implementation of S100A12 knockdown/overexpression. (a) CCK-8 assay was used to gauge AC16 cell viability ( $n = 3$ , per group). (b) The mRNA expression level of S100A12 in Con and OGD groups. (c and d) The protein expression level of S100A12 in Con and OGD groups ( $n = 3$ , per group). (e) The mRNA expression level of S100A12 in Con, Con+Si-NC, and Con+Si-S100A12 groups ( $n = 3$ , per group). (f and g) The protein expression level of S100A12 in Con, Con+Si-NC, and Con+Si-S100A12 groups ( $n = 3$ , per group). (h) The mRNA expression level of S100A12 in Con, Con+OE-NC, and Con+OE-S100A12 groups ( $n = 3$ , per group). (i and j) The protein expression level of S100A12 in Con, Con+OE-NC, and Con+OE-S100A12 groups ( $n = 3$ , per group). Notes: S100A12: S100 calcium-binding protein A12; OGD: oxygen-glucose deprivation; Con: control; Si: small interfering; OE: overexpression; SD: standard deviation. Data were presented as mean  $\pm$  SD based on at least three independent experiments. \* $p < 0.05$ , \*\* $p < 0.01$ , and \*\*\* $p < 0.001$ .

downregulated due to the overexpression of AC006262.5, which ultimately promoted the proliferation and migration of hepatocellular carcinoma [54]. However, few studies focused on hsa-miR-6858-5p, hsa-miR-5004-5p, hsa-miR-

3667-5p, and hsa-miR-5589-5p, especially in cardiovascular diseases. Generally, the molecular mechanism of these nine miRNAs and their relationship with S100A12 in AMI are still unclear and need to be further studied.



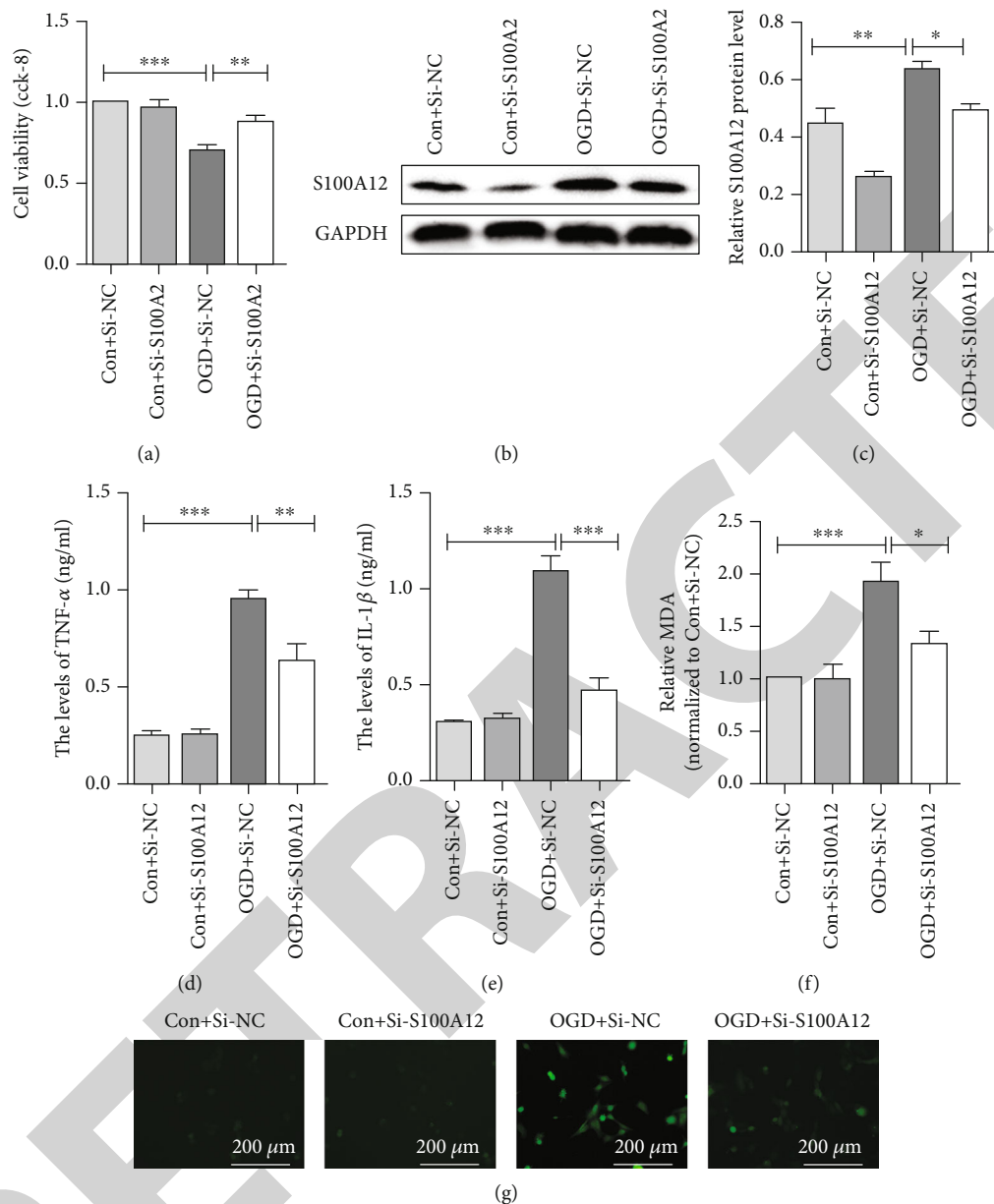


FIGURE 8: The effect of S100A12 knockdown on inflammation and oxidative stress in OGD model. (a) CCK-8 assay was used to gauge AC16 cell viability in Con+Si-NC, Con+Si-S100A12, OGD+Si-NC, and OGD+Si-S100A12 groups ( $n = 3$ , per group). (b and c) The protein expression level of S100A12 in the above four groups ( $n = 3$ , per group). (d) The level of TNF- $\alpha$  in the above four groups ( $n = 3$ , per group). (e) The level of IL-1 $\beta$  in the above four groups ( $n = 3$ , per group). (f) The level of MDA in the above four groups ( $n = 3$ , per group). (g) The ROS production was detected by the DCFH-DA in the above four groups ( $n = 3$ , per group) (magnification  $\times 400$ , scale bar = 200  $\mu$ m). Data were presented as mean  $\pm$  SD based on at least three independent experiments. Notes: S100A12: S100 calcium-binding protein A12; OGD: oxygen-glucose deprivation; Con: control; Si: small interfering; SD: standard deviation; DCFH-DA: dichlorodihydrofluorescein diacetate. \* $p < 0.05$ , \*\* $p < 0.01$ , and \*\*\* $p < 0.001$ .

Moreover, we comprehensively used public data and in vitro experiments of S100A12 expression, its clinical significance, and its effect on inflammation and oxidative stress in AMI. The research based on public data preliminarily showed that S100A12 expression was upregulated in AMI and has a good diagnostic value for AMI. The in vitro experiments confirmed that the expression of S100A12 was significantly upregulated in AMI (OGD model), and its overexpression promoted the occurrence of inflammation and oxidative stress, while the knockdown of its expression

had the opposite effect. Several studies have also shown that inhibiting inflammation and oxidative stress can alleviate myocardial damage caused by myocardial infarction. Zhang et al. demonstrated that the inhibition of death-associated protein kinase 1 (DAPK1) expression inhibited inflammation and oxidative stress and protected rats from myocardial injury caused by myocardial infarction [55]. In addition, a study by Xiao et al. showed that the overexpression of lung cancer associated transcript 1 (LUCAT1) has a protective effect on AMI by inhibiting the effects

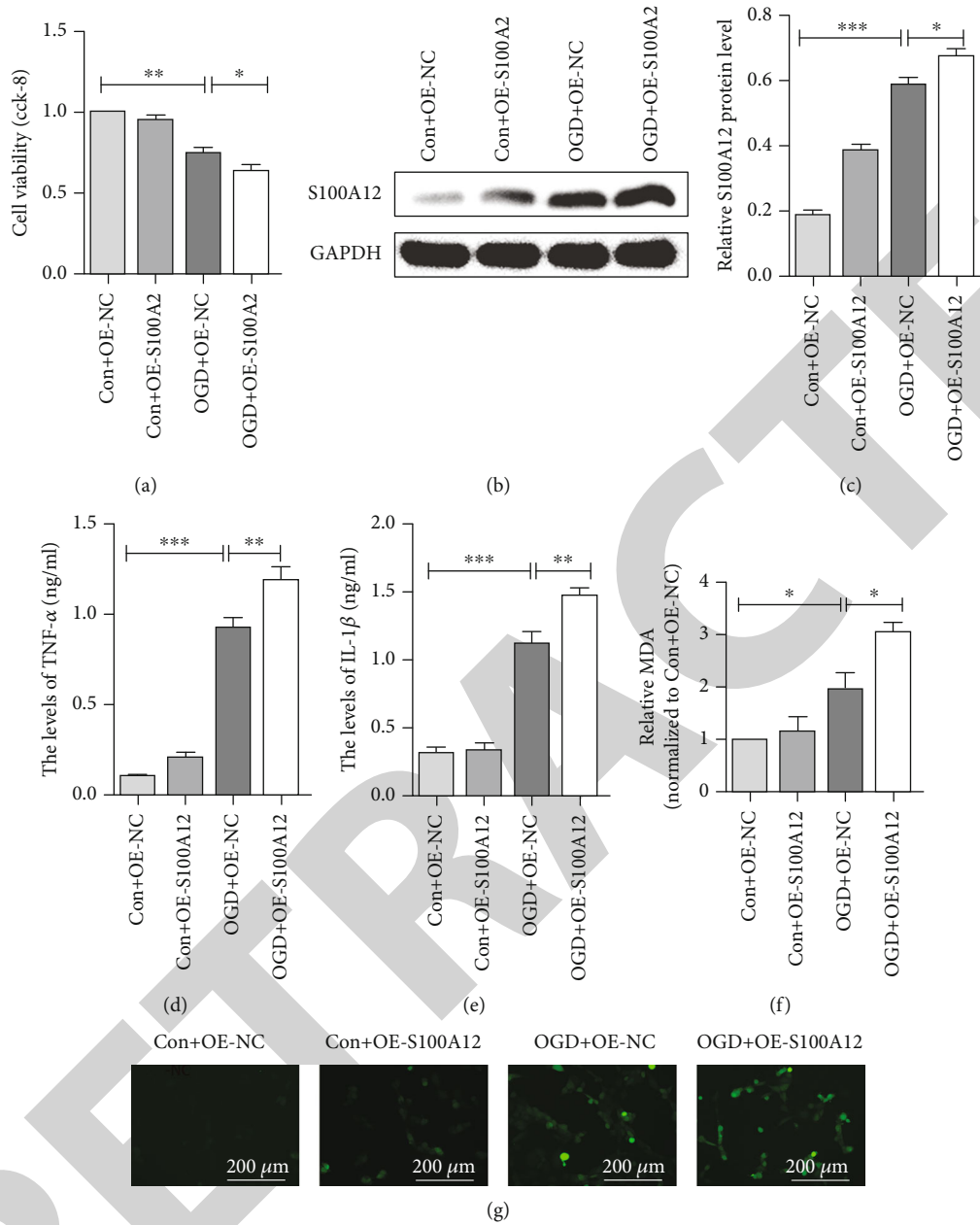


FIGURE 9: The effect of S100A12 overexpression on inflammation and oxidative stress in OGD model. (a) CCK-8 assay was used to gauge AC16 cell viability in Con+OE-NC, Con+Si-S100A12, OGD+OE-NC, and OGD+OE-S100A12 groups ( $n = 3$ , per group). (b and c) The protein expression level of S100A12 in the above four groups ( $n = 3$ , per group). (d) The level of TNF- $\alpha$  in the above four groups ( $n = 3$ , per group). (e) The level of IL-1 $\beta$  in the above four groups ( $n = 3$ , per group). (f) The level of MDA in the above four groups ( $n = 3$ , per group). (g) The ROS production was detected by the DCFH-DA in the above four groups ( $n = 3$ , per group) (magnification  $\times 400$ , scale bar = 200  $\mu$ m). Data were presented as mean  $\pm$  SD based on at least three independent experiments. Notes: S100A12: S100 calcium-binding protein A12; OGD: oxygen-glucose deprivation; Con: control; Si: small interfering; SD: standard deviation; DCFH-DA: dichlorodihydrofluorescein diacetate. \* $p < 0.05$ , \*\* $p < 0.01$ , and \*\*\* $p < 0.001$ .

of H<sub>2</sub>O<sub>2</sub> on oxidative stress, inflammation, viability, and apoptosis in H9c2 cells [56]. Therefore, we speculate that inhibiting the expression of S100A12 could inhibit oxidative stress and inflammation, thereby exerting a similar cardioprotective effect and reducing myocardial injury. S100A12 is expected to serve as a novel target for the diagnosis and treatment of AMI injury, providing clinical benefits to patients.

However, there are some limitations in this study that affect the dependability of our research results. Initially, the AMI dataset was not as easy to obtain as a tumor dataset, and there are few AMI expression profile datasets in the GEO database, leading to a small research sample size and reducing the accuracy of our research. Second, the large sample size difference in some datasets affects the accuracy of our statistical analysis to a certain extent. Third, more

deeper in vivo and in vitro experiments should be carried out to carefully verify our results. Although we conducted in vitro experiments to demonstrate that S100A12 overexpression promotes inflammation and oxidative stress, future in vitro and in vivo experiments with larger sample sizes are still needed to explore the specific molecular mechanisms.

## 5. Conclusion

In summary, our study revealed high expression of S100A12 in AMI and its positive regulation of inflammation and oxidative stress using bioinformatics methods and comprehensive analysis of in vitro experiments. S100A12 may contribute to the early diagnosis of AMI, and inhibiting its expression may reduce myocardial damage and benefit the treatment of AMI patients. And we also identified 9 miRNAs targeting S100A12. Our study can provide certain reference value for further research on the role of S100A12 in the diagnosis and treatment of AMI.

## Abbreviations

AMI:	Acute myocardial infarction
S100A12:	S100 calcium-binding protein A12
GEO:	Gene Expression Omnibus
KEGG:	Kyoto Encyclopedia of Genes and Genomes
GO:	Gene Ontology
SMD:	Standardized mean difference
ROC:	Receiver operating characteristic
SROC:	Summary receiver operating characteristic
GSEA:	Gene set enrichment analysis
RT-qPCR:	Real-time quantitative PCR
ELISA:	Enzyme-linked immunosorbent assay
WB:	Western blotting
OGD:	Oxygen-glucose deprivation.

## Data Availability

The datasets supporting the conclusions of this study are included in the article.

## Conflicts of Interest

The authors report no conflicts of interest in this work.

## Authors' Contributions

Lang Li and Jian Xie conceived the project. Changjun Luo and Binhai Mo designed the study. Yunhua Lin and Guoqing Liu directed the study. Jian Xie, Changjun Luo, and Binhai Mo drafted the manuscript. Yunhua Lin and Guoqing Liu was responsible for all data analysis. Lang Li, Jian Xie, and Xiantao Wang revised the manuscript. All authors have read and agreed to the published version of the manuscript. Jian Xie, Changjun Luo, and Binhai Mo contributed equally.

## Acknowledgments

This work was supported by the Innovative Research Team Project of Guangxi Natural Science Foundation (Grant No.

2018GXNSFGA281006), National Natural Science Foundation of China (Grant Nos. 82170349 and 81900318), Guangxi Natural Science Foundation (Grant No. 2018GXNSFBA050017), and First Affiliated Hospital of Guangxi Medical University.

## Supplementary Materials

Supplementary Table 1: the S100A12-specific sequence of knockdown and overexpression in this study. (*Supplementary Materials*)

## References

- [1] L. Qi, H. Liu, L. Cheng et al., "Prognostic value of the leukoglycemic index in acute myocardial infarction patients with or without diabetes," *Diabetes, metabolic syndrome and obesity: targets and therapy*, vol. 15, pp. 1725–1736, 2022.
- [2] L. Chen, S. Zhou, W. Zhu et al., "Highly sensitive lanthanide-doped nanoparticles-based point-of-care diagnosis of human cardiac troponin I," *International Journal of Nanomedicine*, vol. 17, pp. 635–646, 2022.
- [3] L. Valls-Lacalle, M. Consegal, M. Ruiz-Meana et al., "Connexin 43 deficiency is associated with reduced myocardial scar size and attenuated TGF $\beta$ 1 signaling after transient coronary occlusion in conditional knock-out mice," *Biomolecules*, vol. 10, no. 4, p. 651, 2020.
- [4] R. Ramirez-Carracedo, M. Sanmartin, A. Ten et al., "Therapeutic contribution of extracellular matrix metalloprotease inducer-paramagnetic nanoparticles against acute myocardial infarction in a pig model of coronary ischemia-reperfusion," *Circulation. Cardiovascular Imaging*, vol. 15, no. 6, article e013379, 2022.
- [5] D. Huang, S. Zheng, Z. Liu, K. Zhu, H. Zhi, and G. Ma, "Machine learning revealed ferroptosis features and a novel ferroptosis-based classification for diagnosis in acute myocardial infarction," *Frontiers in Genetics*, vol. 13, article 813438, 2022.
- [6] Q. Wang, B. Liu, Y. Wang, B. Bai, T. Yu, and X.-. Chu, "The biomarkers of key miRNAs and target genes associated with acute myocardial infarction," *PeerJ*, vol. 8, article e9129, 2020.
- [7] J. Zhou, T. Wen, Q. Li et al., "Single-cell sequencing revealed pivotal genes related to prognosis of myocardial infarction patients," *Computational and Mathematical Methods in Medicine*, vol. 2022, Article ID 6534126, 15 pages, 2022.
- [8] H. Ding, W. Chen, and X. Chen, "Serum miR-96-5p is a novel and non-invasive marker of acute myocardial infarction associated with coronary artery disease," *Bioengineered*, vol. 13, no. 2, pp. 3930–3943, 2022.
- [9] L. Chen, J. Bai, J. Liu, H. Lu, and K. Zheng, "A four-MicroRNA panel in peripheral blood identified as an early biomarker to diagnose acute myocardial infarction," *Frontiers in Physiology*, vol. 12, article 669590, 2021.
- [10] X. Wang, L. Tian, and Q. Sun, "Diagnostic and prognostic value of circulating miRNA-499 and miRNA-22 in acute myocardial infarction," *Journal of Clinical Laboratory Analysis*, vol. 34, no. 8, pp. 2410–2417, 2020.
- [11] B. Wang, Y. Li, X. Hao et al., "Comparison of the clinical value of miRNAs and conventional biomarkers in AMI: a systematic review," *Frontiers in Genetics*, vol. 12, article 668324, 2021.

- [12] P. Mohindra and T. Desai, "Micro- and nanoscale biophysical cues for cardiovascular disease therapy," *Medicine*, vol. 34, article 102365, 2021.
- [13] G. Sun, J. Shen, X. Wei, and G. X. Qi, "Circular RNA Foxo3 relieves myocardial ischemia/reperfusion injury by suppressing autophagy via inhibiting HMGB1 by repressing KAT7 in myocardial infarction," *Journal of Inflammation Research*, vol. 14, pp. 6397–6407, 2021.
- [14] N. Pluijmer, R. de Jong, M. de Vries et al., "Phosphorylcholine antibodies restrict infarct size and left ventricular remodelling by attenuating the unperfused post-ischaemic inflammatory response," *Journal of Cellular and Molecular Medicine*, vol. 25, no. 16, pp. 7772–7782, 2021.
- [15] I. M. Seropian, S. Toldo, B. W. Van Tassell, and A. Abbate, "Anti-inflammatory strategies for ventricular remodeling following ST-segment elevation acute myocardial infarction," *Journal of the American College of Cardiology*, vol. 63, no. 16, pp. 1593–1603, 2014.
- [16] S. Huang and N. Frangogiannis, "Anti-inflammatory therapies in myocardial infarction: failures, hopes and challenges," *British Journal of Pharmacology*, vol. 175, no. 9, pp. 1377–1400, 2018.
- [17] D. Yao, B. Shi, S. Wang et al., "Isoliquiritigenin ameliorates ischemia-induced myocardial injury via modulating the Nrf2/HO-1 pathway in mice," *Drug Design, Development and Therapy*, vol. 16, pp. 1273–1287, 2022.
- [18] B. Liang, X. Zhang, R. Li, Y. C. Zhu, X. J. Tian, and N. Gu, "Guanxin V alleviates acute myocardial infarction by restraining oxidative stress damage, apoptosis, and fibrosis through the TGF- $\beta$ 1 signalling pathway," *Phytomedicine: international journal of phytotherapy and phytopharmacology*, vol. 100, article 154077, 2022.
- [19] T. Hao, M. Qian, Y. Zhang et al., "An injectable dual-function hydrogel protects against myocardial ischemia/reperfusion injury by modulating ROS/NO disequilibrium," *advanced science (Weinheim, Baden-Wuerttemberg, Germany)*, vol. 9, no. 15, article e2105408, 2022.
- [20] L. Gao, Z. Ruan, and G. Chen, "MicroRNA-383-5p regulates oxidative stress in mice with acute myocardial infarction through the AMPK signaling pathway via PFKM," *Disease Markers*, vol. 2021, Article ID 8587535, 9 pages, 2021.
- [21] S. Qiu, G. Zheng, C. Ma et al., "High serum S100A12 levels predict poor outcome after acute primary intracerebral hemorrhage," *Neuropsychiatric Disease and Treatment*, vol. 17, pp. 3245–3253, 2021.
- [22] X. Zhang, R. Shen, Z. Shu, Q. Zhang, and Z. Chen, "S100A12 promotes inflammation and apoptosis in ischemia/reperfusion injury via ERK signaling in vitro study using PC12 cells," *Pathology International*, vol. 70, no. 7, pp. 403–412, 2020.
- [23] M. Bao, R. Zhang, X. Huang et al., "Transcriptomic and proteomic profiling of human stable and unstable carotid atherosclerotic plaques," *Frontiers in Genetics*, vol. 12, article 755507, 2021.
- [24] C. Lin, P. Huang, C. Chen et al., "Sitagliptin attenuates arterial calcification by downregulating oxidative stress-induced receptor for advanced glycation end products in LDLR knockout mice," *Scientific Reports*, vol. 11, no. 1, p. 17851, 2021.
- [25] X. Tong, X. Zhao, X. Dang, Y. Kou, and J. Kou, "Predicting diagnostic gene biomarkers associated with immune checkpoints, N6-methyladenosine, and ferroptosis in patients with acute myocardial infarction," *Frontiers in cardiovascular medicine*, vol. 9, article 836067, 2022.
- [26] X. Zhang, M. Cheng, N. Gao et al., "Utility of S100A12 as an early biomarker in patients with ST-segment elevation myocardial infarction," *Frontiers in cardiovascular medicine*, vol. 8, article 747511, 2021.
- [27] G. Gobbi, C. Carubbi, G. Tagliazucchi et al., "Sighting acute myocardial infarction through platelet gene expression," *Scientific Reports*, vol. 9, no. 1, article 19574, 2019.
- [28] X. Guo, Q. Ji, M. Wu, and W. Ma, "Naringin attenuates acute myocardial ischemia-reperfusion injury via miR-126/GSK-3 $\beta$ / $\beta$ -catenin signaling pathway," *Acta chirurgica brasileira*, vol. 37, no. 1, article e370102, 2022.
- [29] K. Ren, B. Li, L. Jiang et al., "circ\_0023461 silencing protects cardiomyocytes from hypoxia-induced dysfunction through targeting miR-370-3p/PDE4D signaling," *Oxidative Medicine and Cellular Longevity*, vol. 2021, Article ID 8379962, 18 pages, 2021.
- [30] S. Hao, M. Ren, D. Li et al., "Fisher linear discriminant analysis for classification and prediction of genomic susceptibility to stomach and colorectal cancers based on six STR loci in a northern Chinese Han population," *PeerJ*, vol. 7, article e7004, 2019.
- [31] F. Zhu, Q. Li, J. Li, B. Li, and D. Li, "Long noncoding Mirt2 reduces apoptosis to alleviate myocardial infarction through regulation of the miR-764/PDK1 axis," *Laboratory investigation; a journal of technical methods and pathology*, vol. 101, no. 2, pp. 165–176, 2021.
- [32] S. Dong, Y. Liu, W. Sun et al., "Analysis of characteristics of patients with non-ST-segment elevation myocardial infarction by cardiac magnetic resonance imaging," *Medical science monitor: international medical journal of experimental and clinical research*, vol. 27, article e933220, 2021.
- [33] X. Zhu, T. Yin, T. Zhang et al., "Identification of immune-related genes in patients with acute myocardial infarction using machine learning methods," *Journal of Inflammation Research*, vol. 15, pp. 3305–3321, 2022.
- [34] P. Christia and N. Frangogiannis, "Targeting inflammatory pathways in myocardial infarction," *European Journal of Clinical Investigation*, vol. 43, no. 9, pp. 986–995, 2013.
- [35] J. Su, C. Gao, R. Wang, C. Xiao, and M. Yang, "Genes associated with inflammation and the cell cycle may serve as biomarkers for the diagnosis and prognosis of acute myocardial infarction in a Chinese population," *Molecular Medicine Reports*, vol. 18, no. 2, pp. 1311–1322, 2018.
- [36] L. Ismail, M. Abdel Rahman, I. Hashad, and S. M. Abdel-Mak-soud, "Contribution of glutathione peroxidase 1 (Pro200Leu) single nucleotide polymorphism and serum homocysteine levels in the risk of acute myocardial infarction in Egyptians," *Journal, Genetic Engineering & Biotechnology*, vol. 20, no. 1, p. 21, 2022.
- [37] E. Michelucci, S. Rocchiccioli, M. Gaggini, R. Ndreu, S. Berti, and C. Vassalle, "Ceramide and cardiovascular risk factors, inflammatory parameters and left ventricular function in AMI patients," *Biomedicine*, vol. 10, no. 2, p. 429, 2022.
- [38] Z. Cai, Q. Xie, T. Hu et al., "S100A8/A9 in myocardial infarction: a promising biomarker and therapeutic target," *Frontiers in cell and developmental biology*, vol. 8, article 603902, 2020.
- [39] L. Gonzalez, K. Garrie, and M. Turner, "Role of S100 proteins in health and disease," *Molecular cell research*, vol. 1867, no. 6, article 118677, 2020.
- [40] S. Aydin, K. Ugur, S. Aydin, İ. Sahin, and M. Yardim, "Biomarkers in acute myocardial infarction: current perspectives,"

## Retraction

# Retracted: Circular RNA hsa\_circ\_0002360 Promotes Proliferation and Invasion and Inhibits Oxidative Stress in Gastric Cancer by Sponging miR-629-3p and Regulating the PDLIM4 Expression

### Oxidative Medicine and Cellular Longevity

Received 20 June 2023; Accepted 20 June 2023; Published 21 June 2023

Copyright © 2023 Oxidative Medicine and Cellular Longevity. This is an open access article distributed under the Creative Commons Attribution License, which permits unrestricted use, distribution, and reproduction in any medium, provided the original work is properly cited.

This article has been retracted by Hindawi following an investigation undertaken by the publisher [1]. This investigation has uncovered evidence of one or more of the following indicators of systematic manipulation of the publication process:

- (1) Discrepancies in scope
- (2) Discrepancies in the description of the research reported
- (3) Discrepancies between the availability of data and the research described
- (4) Inappropriate citations
- (5) Incoherent, meaningless and/or irrelevant content included in the article
- (6) Peer-review manipulation

The presence of these indicators undermines our confidence in the integrity of the article's content and we cannot, therefore, vouch for its reliability. Please note that this notice is intended solely to alert readers that the content of this article is unreliable. We have not investigated whether authors were aware of or involved in the systematic manipulation of the publication process.

In addition, our investigation has also shown that one or more of the following human-subject reporting requirements has not been met in this article: ethical approval by an Institutional Review Board (IRB) committee or equiva-

lent, patient/participant consent to participate, and/or agreement to publish patient/participant details (where relevant).

Wiley and Hindawi regrets that the usual quality checks did not identify these issues before publication and have since put additional measures in place to safeguard research integrity.

We wish to credit our own Research Integrity and Research Publishing teams and anonymous and named external researchers and research integrity experts for contributing to this investigation.


The corresponding author, as the representative of all authors, has been given the opportunity to register their agreement or disagreement to this retraction. We have kept a record of any response received.

### References

- [1] Z. Yu, J. Lan, W. Li et al., "Circular RNA hsa\_circ\_0002360 Promotes Proliferation and Invasion and Inhibits Oxidative Stress in Gastric Cancer by Sponging miR-629-3p and Regulating the PDLIM4 Expression," *Oxidative Medicine and Cellular Longevity*, vol. 2022, Article ID 2775433, 20 pages, 2022.

## Research Article

# Circular RNA hsa\_circ\_0002360 Promotes Proliferation and Invasion and Inhibits Oxidative Stress in Gastric Cancer by Sponging miR-629-3p and Regulating the PDLIM4 Expression

Zhengyuan Yu,<sup>1</sup> Jing Lan,<sup>2</sup> Wei Li,<sup>1</sup> Li Jin,<sup>3</sup> Feng Qi,<sup>4</sup> Chen Yu <sup>5</sup> and Hao Zhu <sup>6</sup>

<sup>1</sup>Department of Medical Oncology, The First Affiliated Hospital of Soochow University, No. 188, Shizi Street, Gusu District, Suzhou 215006 Jiangsu, China

<sup>2</sup>Department of General Surgery, The First Affiliated Hospital of Soochow University, No. 188, Shizi Street, Gusu District, Suzhou 215006 Jiangsu, China

<sup>3</sup>Department of Radiotherapy, Sichuan Cancer Hospital & Institute, Sichuan Cancer Center, School of Medicine, University of Electronic Science and Technology of China, 55# Renmin South Road, 610041 Chengdu, Sichuan, China

<sup>4</sup>Department of Pharmacy, The Fourth Affiliated Hospital of Nantong University, Yancheng City No. 1 Peoples' Hospital, Yancheng, 224006 Jiangsu, China

<sup>5</sup>Department of Integrated TCM & Western Medicine, Jiangsu Cancer Hospital & Jiangsu Institute of Cancer Research & The Affiliated Cancer Hospital of Nanjing Medical University, Nanjing, China

<sup>6</sup>Department of Traditional Chinese Medicine, The First Affiliated Hospital of Soochow University, No. 188, Shizi Street, Gusu District, Suzhou 215006 Jiangsu, China

Correspondence should be addressed to Chen Yu; [yuunique@njmu.edu.cn](mailto:yuunique@njmu.edu.cn) and Hao Zhu; [18409083@masu.edu.cn](mailto:18409083@masu.edu.cn)

Received 6 April 2022; Revised 27 May 2022; Accepted 30 May 2022; Published 9 August 2022

Academic Editor: Tian Li

Copyright © 2022 Zhengyuan Yu et al. This is an open access article distributed under the Creative Commons Attribution License, which permits unrestricted use, distribution, and reproduction in any medium, provided the original work is properly cited.

Many studies have found that circRNA hsa\_0002360 (circ0002360) plays an important role in cancer onset and progression. However, its role in gastric cancer (GC) remains uncertain. Circ0002360 was found to be upregulated in GC cells using QRT-PCR. Furthermore, miR-629-3p, a target miRNA of circ0002360, was the most suppressed miRNA following circ0002360 overexpression. RNA immunoprecipitation (RIP), dual-luciferase reporter analyses, clone formation, transwell, DCFH-DA, and ELISA assays demonstrated that circ0002360-targeted miR-629-3p promotes cell proliferation and migration while inhibiting oxidative stress. GC-related mRNA microarrays from the GEO and TCGA databases, including GSE103236, GSE79973, GSE33429, GSE22804, GSE84437, and TCGA-STAD datasets, were used to find hub biomarkers between normal and gastric cancer samples. WGCNA and uni-Cox analysis were used to identify 27 survival-related risk genes, which were then used to build a risk model for prognosis prediction. Following that, all patients from the GSE84437 and TCGA-STAD datasets with 27 survival-related genes and enough data on survival status and time were randomly assigned to train ( $n = 433$ ) and test ( $n = 375$ ) cohorts. Furthermore, ROC and Kaplan-Meier (KM) analyses were used to validate the risk model for both cohorts. randomForest analysis indicated that PDLIM4 was the target gene of miR-629-3p, whose level was increased by circ0002360 but reversed by miR-629-3p mimics. Finally, this study confirmed that circ0002360 sponged miR-629-3p and then upregulated PDLIM4 expression. As a result, circ0002360 may be a useful marker for predicting GC prognosis and an anti-GC treatment target.

## 1. Introduction

Gastric cancer (GC) is a malignant gastrointestinal (GI) tumor that ranks 5th and 3rd in the world in terms of morbidity and factors contributing to cancer-associated mortality [1].

The data show that GC causes increasing morbidity and mortality in Asian countries, especially in China, Japan, and South Korea [2]. Due to the uneven regional distribution of medical resources in our country, the prevalence of early GC screening remains low. Many GC cases are in an advanced tumor

progression stage at the time of initial diagnosis, making surgical treatment difficult, with a high metastasis rate and poor prognosis [3–5]. Currently, early symptom occurrence and pathologic transformation of GC are considered to be a pathologic process with diverse stages, multiple influencing factors, and slow progression [6, 7]. Changes in gene expression, mutations, and epigenetics are also strongly associated with the progression of GC [8]. Because of increased social and environmental pressures and dietary changes, the incidence of GC has risen in recent years, and the aggressive, differentiated, and bulky tumors of young and middle-aged patients with GC impose a significant mental and physical burden [9, 10]. As a result, it is particularly vital to explore molecular diagnostic markers, prognostic factors, and personalized therapeutic markers that can guide clinical diagnosis.

Circular RNAs (circRNAs) are single-stranded RNAs found in eukaryotes that are specifically expressed in specific tissue types and developmental stages. CircRNAs can be produced by back-splicing precursor mRNA (pre-mRNA) transcripts, resulting in a covalently-closed ring architecture with no 3' poly-A tail or 5'-to-3' polarity [11, 12]. Because of their unique ring architecture, circRNAs are inherently resistant to exonuclease-mediated degradation and exhibit increased stability compared with their corresponding parental genes [13]. Additionally, circRNAs usually display evolutionary conservation in terms of expression levels, and certain circRNAs have significantly increased expression than corresponding parental genes [14]. In recent years, numerous circRNAs have been discovered to participate in GC genesis and development. Zhang et al. had reported that the circRNA circNRIP1 is widely expressed in GC to enhance GC cell growth, invasion, and migration [15]. After that, a few circRNAs were reported to be involved in the progression of GC [15], including circMRPS35, circKIAA1244, and circCUL2 as potential GC biomarkers [16–18]. With recent technological breakthroughs in molecular biology, the ability of circRNAs to regulate tumors has been gradually uncovered. It is now extensively accepted that circRNAs are “molecular sponges” that influence microRNAs (miRNAs) functions by complementary binding to the latter [19]. The adsorption capacity of circRNAs to microRNAs is much stronger than that of linear mRNAs and lncRNAs, and thus, the role of circRNAs as endogenous RNAs has been widely concerned. Luo et al. had reported that circCCDC9 sponged miR-6792-3p for inhibiting GC development [20], circACVR2A sponged miR-1290 to regulate GC progression [21], and circ\_0043691 sponged miR-873-3p to promote GC progression [22]. These studies supported the hypothesis that circRNAs could be new markers for diagnosing GC and anti-GC therapeutic targets. Bai concluded that 285 dysregulated circular transcripts in LUAD tissues using Gene Ontology (GO) and Kyoto Encyclopedia of Genes and Genomes (KEGG) analysis, and interaction analysis showed that hsa\_circ\_0002360 was the most significantly overexpressed in LUAD tissues [23]. The data confirmed that circ\_0002360 could promote LUAD progression. However, its functions and underlying mechanisms is still unclear in GC.

## 2. Materials and Methods

**2.1. Microarray Datasets.** The present study compared gene levels in GEO-derived GC cases to those in matched healthy tissues. Meanwhile, high-throughput sequencing (HTS) datasets, including GSE103236, GSE79973, GSE33429, GSE22804, and GSE84437, were obtained. The GSE22804 dataset contains 14 normal samples, while the GSE103236 dataset contains 10 GC tumor samples and 9 normal samples. The GSE7997 dataset contains GC and matched healthy samples from 20 cases. GSE33429 dataset includes 27 GC tumor samples. GSE84437 dataset includes 433 GC tumor samples.

**2.2. Microarray Data Integration and Differentially Expressed Genes (DEGs) Analysis.** Possible variables and heterogeneity have frequently been identified as the main variability and bias sources. This work collected datasets from several platforms and treated samples at different times by diverse staff or groups. Consequently, using the R software packages *limma* and *sva*, these 4 datasets were integrated by batch normalization to increase sample size (47 cancer along with 33 healthy samples) while avoiding unreliable outcomes. Thereafter, DEGs were identified ( $P < 0.05$ ) between cancer and healthy samples using *limma* package of R. After integration, genes with abnormal expression levels were preserved in subsequent analyses.

**2.3. TCGA Data and Differential Expression Analysis.** This study also obtained clinical information and gene mRNA expression profiles from the TCGA database (<https://portal.gdc.cancer.gov>) for 375 GC and 32 matched noncarcinoma samples. To be specific, the data extracted included age, gender, pathological stage, vital status, grade, and TNM stage. Table 1 presents more detailed patient information. Because all data were obtained from TCGA, there was no need for Ethics Committee approval. Thereafter, DEGs were identified between cancer and healthy samples with *limma* package of R upon the  $\log_{2}FC > 1$  and  $P < 0.05$  thresholds.

**2.4. WGCNA for the GC-Related Data.** Weighted correlation network analysis (WGCNA) was also used in this study to create a weighted gene coexpression correlation network. Meanwhile, “Pearson” correlation coefficients were adopted to determine distances between diverse transcripts. The signless topological overlap matrix (TOM), the minimal module size = 30, and the  $\beta$  – power = 9 were utilized to detect coexpressed gene modules and construct the WGCNA network. The significant tumor group-related modules were identified through assessing the relation of coexpression gene modules with tumor or healthy groups. Thereafter, the most significant tumor-related modules with the highest correlation coefficients were chosen for subsequent analysis.

**2.5. Construction of the GC Model.** Survival analysis was completed using qualified datasets (GSE84437, *module\_bule*) with sufficient survival data. Thereafter, genes that predicted overall survival (OS) for GC cases were evaluated by univariate Cox regression. Thereafter, genes with  $P < 0.05$  upon univariate Cox regression were selected with *glmnet*

TABLE 1: Characteristics of patients with GC from TCGA database.

Characteristics	Variable	Patients (375)	Percentages (%)
Age	<65 years	155	41.33
	≥65 years	216	57.60
	Unknown	4	1.07
Gender	Male	241	64.27
	Female	134	35.73
	G1	10	2.67
Grade	G2	137	36.53
	G3	219	58.40
	GX	9	2.40
	I	53	14.13
Pathological stage	II	111	29.60
	III	150	40.00
	IV	38	10.13
	Unknown	23	6.14
T classification	T1	19	5.07
	T2	80	21.33
	T3	168	44.80
	T4	100	26.67
	TX	8	2.13
	N0	111	29.60
	N1	97	25.87
N classification	N2	75	20.00
	N3	74	19.73
	NX	16	4.27
	Unknown	2	0.53
M classification	M0	330	88.00
	M1	25	6.67
	MX	20	5.33
Vital status	Alive	244	65.07
	Death	131	34.93

GC: gastric cancer. Data are presented as number (%).

package of R by adopting the least absolute shrinkage and selection operator (Lasso) Cox model. Additionally, those as-selected genes with low lambda were later adopted for constructing the GC prognosis prediction model. Typically, the GC formula was developed by determining selected gene expression weighted by related coefficients. To investigate the relationship of prognostic genes in the GC model with the risk score of OS, the risk score distribution, ROC curve, and scatter plot were adopted.

**2.6. Function Enrichment Analysis of DEGs.** GO offers a framework for depicting gene products' roles in living bodies and identifying typical transcriptome data and biological functions of high-throughput genomes. In general, GO annotations are divided into 3 classes, including biological processes (BPs), molecular functions (MFs), and cellular components (CCs). KEGG analysis can be used to analyze the significant pathways enriched by DEGs, and it may be adopted to interpret gene functions and applied in genome

information. Gene functions were analyzed by using the Database for Annotation, Visualization, and Integrated Discovery (DAVID) 6.8 (<https://david.ncifcrf.gov>). By adopting the related DAVID module, data were converted into biological significance, and datasets were rapidly analyzed at genome level. For revealing whether our selected DEGs were significant for HNSCC development, this study utilized DAVID for GO functional annotation as well as KEGG analysis on DEGs by Venn package, with the significance level set at  $FDR < 0.05$ .

**2.7. The Determination of the Biomarkers.** Univariate Cox (uni-Cox) regression was conducted to obtain hazard ratios (HRs) ( $P < 0.05$ ). Thereafter, the "survminer" and "survival" packages were employed to detect critical biomarkers. Additionally, randomSurvivalForest was employed to determine a random forest for ranking survival-associated markers in terms of their importance; finally, markers with the relative importance  $> 0.7$  were selected. Then, the optimal threshold was applied in the survival analysis, survival curves were drawn using the Kaplan-Meier (KM) approach, and differences were assessed by log-rank test. In addition, this study employed the ggrisk package to draw the scatter plot of biomarker levels as a function of GC survival time. Uni-Cox and multivariate Cox (multi-Cox) regression was subsequently performed using forest plot. Furthermore, prognosis prediction ability of the model was evaluated by receiver operating characteristic (ROC) curve analysis as well as concordance index (c-index) value.

**2.8. Actinomycin D and RNase R Treatment.** DMSO (Sigma-Aldrich, St. Louis, MO, USA) or 2 mg/mL actinomycin D was added to the culture medium to inhibit transcription as the control. Thereafter, total RNA (5 mg) was incubated with/without 3 U/mg RNase R (Epicenter Technologies) for a 30-min period at 37°C, while the RNeasy MinElute Cleaning Kit (QIAGEN, Germany) was later utilized to purify the resultant RNA. Afterwards, total RNA was prepared into cDNA through reverse transcription, and qRT-PCR was conducted to measure hsa\_circ\_0002360 and GADPH levels.

**2.9. Dual-Luciferase Reporter Assay.** The circular RNA interactome and TargetScan database were adopted for predicting the miR-629-3p binding sites for circ\_0002360 or PDLIM4. The Dual-Luciferase Assay System Kit (Promega, Madison, WI, USA) was used to detect dual-fluorescein receptor gene in accordance with specific protocols. After amplification, the mutant (MUT) and wild-type (WT) PDLIM4 3'UTR and hsa\_circ\_0002360 UTRs were inserted into the luciferase reporter vector pmirGLO (Promega). Thereafter, miR-629-3p mimics were cotransfected into HEK293T cells with luciferase plasmids for a 48-h period. Thereafter, the Dual-Luciferase Reporter Assay System (Promega) was employed to measure luciferase activities, with Renilla luciferase activity serving as a reference for normalizing firefly activity.

**2.10. RIP Assay.** Magna RIP RNA-Binding Protein Immunoprecipitation Kit (Millipore, Billerica, MA, USA) was used



TABLE 2: The sequences of the primers.

Gene	Forward (5'-3')	Reverse (5'-3')
circRNA_0002360	AGAAACTAAGGCACAGCTAAACA	GGGCGAAAAATGTCCAG
miR-145	AGTCCCTGCAGATATAGCTACAA	AGACGTCAAGGCGGTAGGTAGTT
miR-127-5p	ATGTGTCCGTGTCCGACGTGAAA	CTGTGTTCATGTGTCAATGTCCT
miR-758	TGTGTCCACCATGACGATCGTGTGTC	CTGTGTAAACGTAACGACGACT
miR-629	GCTGTGTAACGCTTGTGAAAGTAA	CGATGTGACGCGCTGGGCAA
miR-1273	AACGCTAACGTGCCATGTGTAA	CCCCATGTAACGTGCAAATGTGT
miR-933	TTGCTAACGCTAAGCTGCAATGG	AACGCTGTAGTGTAGAGATGATA
miR-585	CCGCTAGTGTAAACGTGAAACGCCA	CCATGTGAATGTAGTAGTAACC
PDLIM4	GCAACGCATGTCTGTGTAACA	AATGTGTAAAGTAAACCATGCG
U6	TTCGGCACGCAGTTGACTCGC	ACGAAACCGTCTTGCTAAGG
GAPDH	TTAAATTGCCCCAGCCAATT	ACACACAGGCGGCACCATA

for the RIP assay in line with specific protocols. Anti-immunoglobulin G (IgG) and anti-Ago2 antibodies used in the RIP assays were provided by Millipore. qRT-PCR was conducted to measure circRNA and miRNA levels in the collected total RNA.

**2.11. CircRNA Localization.** This study used the Cytoplasmic and Nuclear RNA Purification Kit (Amyjet) to separate and draw cytoplasmic and nuclear RNAs within GC cells in order to determine circRNA localization. Later, circ\_0002360 expression in cytoplasmic/nuclear RNAs was detected by qRT-PCR, with GAPDH and U5 being the references, separately.

**2.12. Measurement of Intracellular ROS Levels.** The DCFH-DA approach was utilized to measure the relative changes in ROS levels. The cells were incubated for thirty minutes with 10 mmol/L OD DCFH-DA 48 hours after transfection. After three washes, the cells were placed on a fluorescence analyzer (BioTek, USA), and the excitation/emission wavelength was set to 488/525 nm. The results were then analyzed. The values are shown as a percentage of the relative fluorescence of the control group in comparison to the experimental group.

**2.13. ELISA.** Using the appropriate ELISA kits, SOD, CAT, and GSH-PX activities could be measured (Sangon Biotech, Shanghai, China). In a nutshell, the cells were collected before being centrifuged at 1000g for ten minutes. The instructions were followed, and the supernatant was collected and measured. Gather the supernatant and perform the measurements as directed [24].

**2.14. Cell Culture as well as Transfection.** In this study, human GC cells (NCI-N87, SNU-484, MKN-74, SGC-7901, and AGS) were cultivated together with healthy human gastric epithelial GES-1 cells (Cell Bank, Shanghai, China) in RPMI-1640 medium containing penicillin/streptomycin (Invitrogen, Carlsbad, CA, USA) as well as fetal bovine serum (FBS), followed by incubation with 5% CO<sub>2</sub> at 37°C. Thereafter, circ\_0002360/PDLIM4 overexpression (OE circ\_0002360/PDLIM4), shRNA against PDLIM4 (sh PDLIM4), miR-629-3p mimics (miR-629-3p) and inhibitors

(miR-629-3p inhibitor), and controls (RiboBio, Guangzhou, China) plasmids were transfected into cells by the use of Lipofectamine 2000 (Thermo Fisher, Waltham, MA, USA). qRT-PCR was conducted to measure transfection efficiency.

**2.15. qRT-PCR.** TRIzol (Invitrogen) was applied to collect total cellular and tissue RNAs, and later the collected RNAs were prepared into cDNA through reverse transcription using PrimeScript RT Kits (Invitrogen). This work utilized the Mx3000P real-time PCR system (Thermo Fisher) for qRT-PCR using SYBR Green SuperMix (Roche, Basel, Switzerland). PCR conditions were shown below, 15 s under 94°C, 10 s under 60°C, and 20 s under 72°C for altogether 40 cycles. Subsequently, 2<sup>-ΔΔCt</sup> approach was utilized for data analysis, with GAPDH and U6 being the internal references. All primers are listed in Table 2.

**2.16. Colony Formation Analysis.** Cells (2 × 10<sup>4</sup>) were seeded into 6-cm plates and incubated for a 14-day period. Afterwards, methanol was added to fix colonies for a 20-min period (Beyotime, Nanjing, China), followed by 0.1% crystal violet staining (Beyotime), assessment, and count of colonies under the microscope (Olympus, Tokyo, Japan).

**2.17. Transwell Invasion Assay.** Cells (2 × 10<sup>4</sup>) were plated into the Matrigel-coated upper transwell chamber (BD Biosciences) and the RPMI-1640 containing lower chamber. Afterwards, cells were fixed, stained, and observed under the microscope (Olympus).

**2.18. Western Blotting (WB) Analysis.** This work employed RIPA buffer (Beyotime) for extracting total tissue and cell proteins. Thereafter, 12% SDS-PAGE (Beyotime) was performed to separate the extracted proteins, followed by transfer on PVDF membranes (Roche). Then, membranes were blocked using 5% skimmed milk (Beyotime) and incubated with primary antibodies (Abcam, Cambridge, MA, USA) overnight under 4°C, including anti-Ki67 (1:1000), anti-MMP9 (1:1000), and anti-GAPDH (1:5000). Afterwards, the secondary antibody HRP-labeled rabbit IgG (1:50,000, Abcam) was employed to further incubate bands.

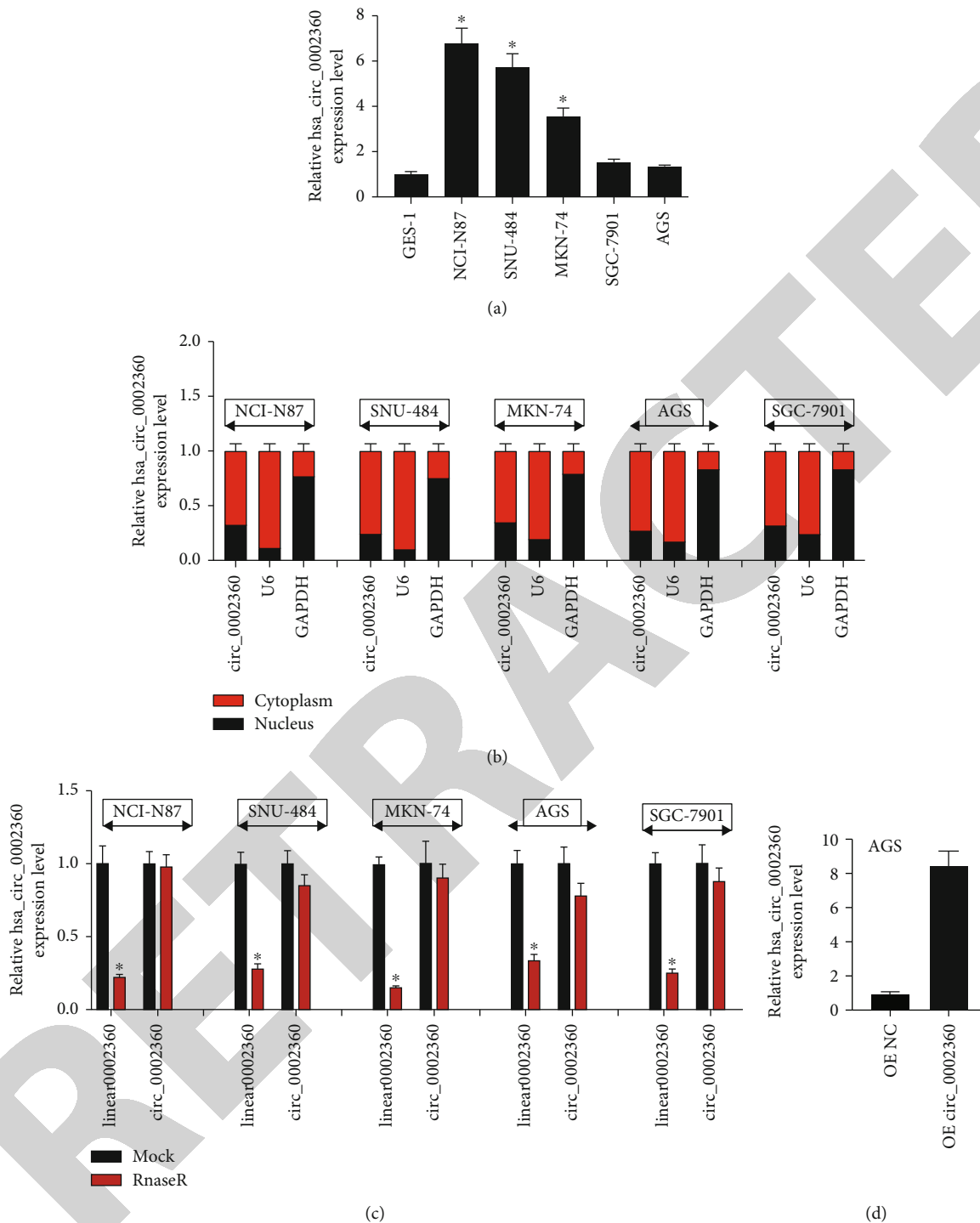


FIGURE 1: Circ\_0002360 was elevated in GC cell lines. (a) The expression of circ\_0002360 in cells was detected by qRT-PCR. (b) qRT-PCR analysis of hsa\_circ\_0002360, GAPDH, and U6 in the cytoplasm and nucleus in LUAD cells. (c) The stability of circ\_0002360 by RNase R assay. (d) QRT-PCR analysis of hsa\_circ\_0002360 expression in cells transfection with circ0002360 overexpression. Data in the represent the mean values  $\pm$  SD from three biological replicates ( $n = 3$ ).  $*P < 0.05$ .

This work adopted enhanced chemiluminescence (ECL, Sangon, Shanghai, China) for protein visualization.

**2.19. Statistical Analysis.** All results were shown in a form of means  $\pm$  SD. Student's *t*-test was adopted to assess differences

in 2 groups, whereas one-way ANOVA was used to assess those among several groups. Significance of difference was analyzed through Spearman correlation. Data were analyzed using SPSS21.0 (IBM, Somers, NY, USA).  $p < 0.05$  suggested statistical significance.

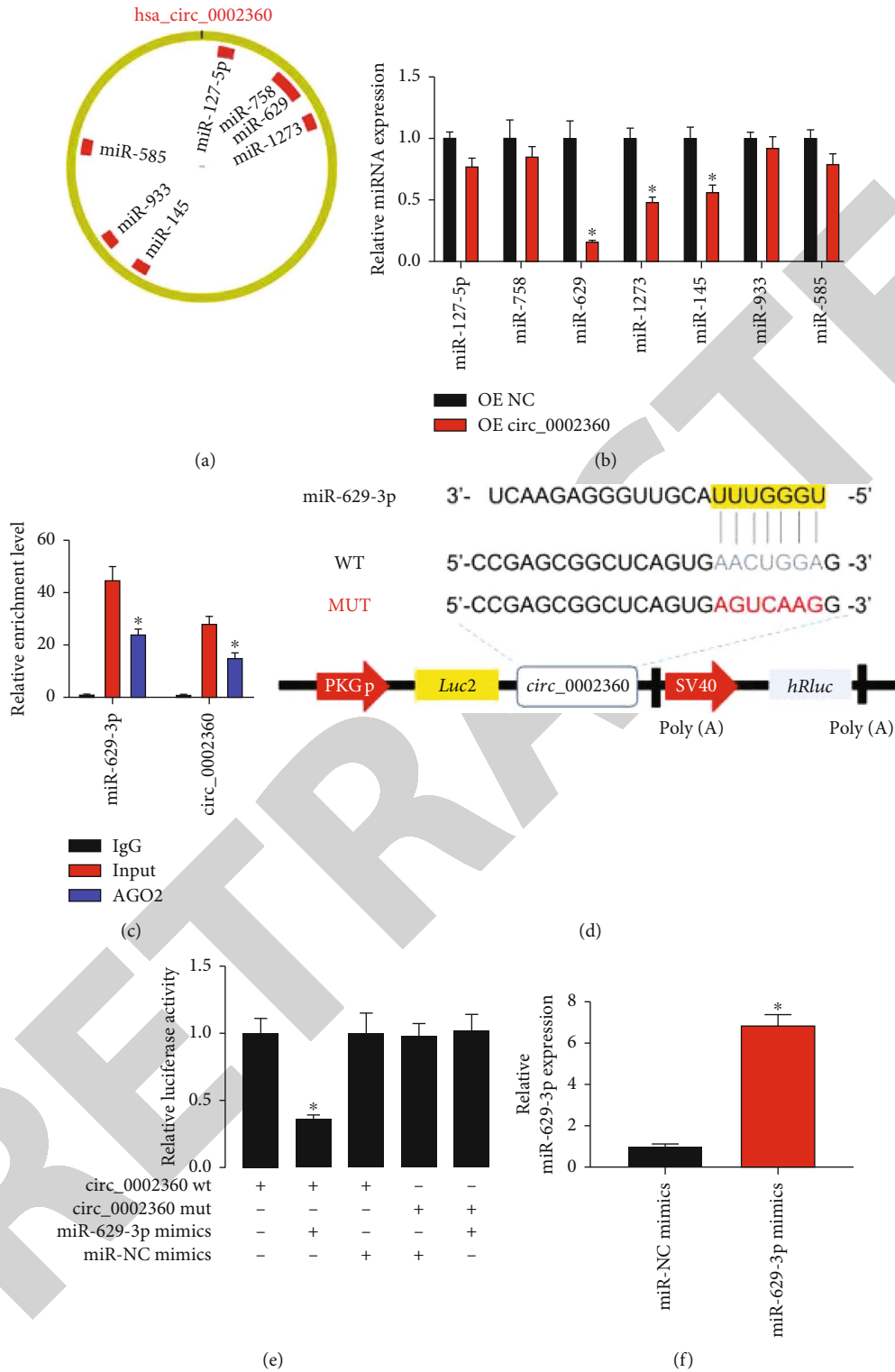


FIGURE 2: Continued.

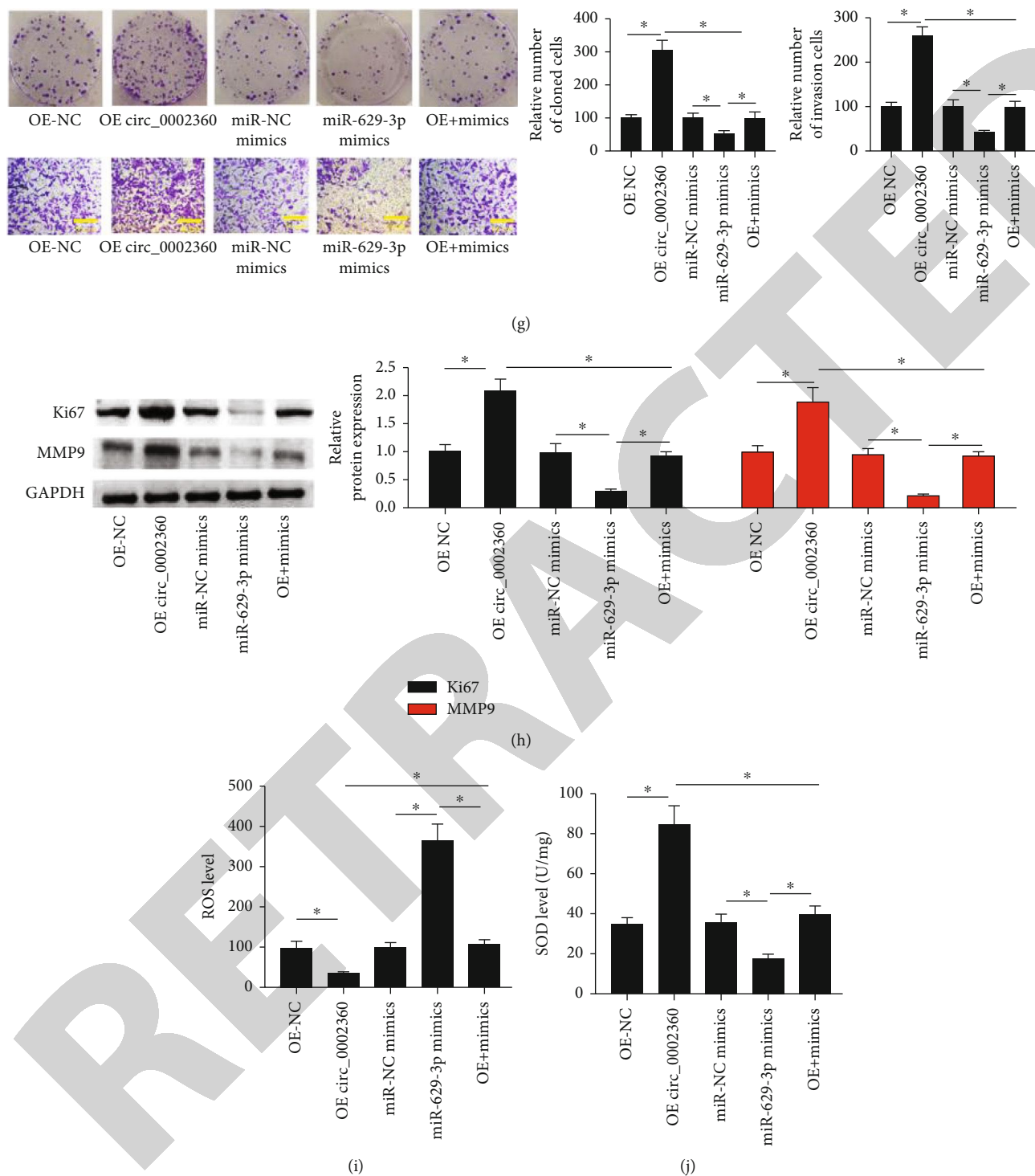
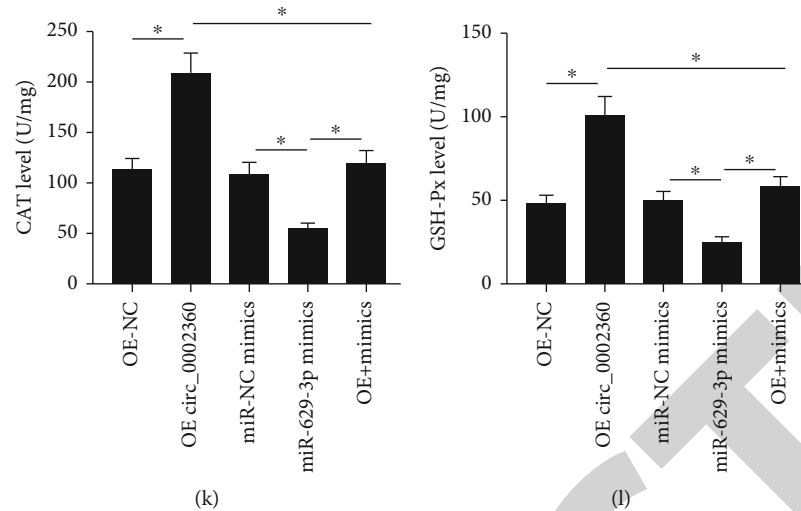


FIGURE 2: Continued.



**FIGURE 2:** Circ\_0002360 sponged miR-145. (a) A schematic illustration demonstrating the putative binding sites of the miRNAs associated with hsa\_circ\_0002360. (b) qRT-PCR data show expressions of the candidate miRNAs after hsa\_circ\_0002360 overexpression in cells. (c) qRT-PCR for the expression of hsa\_circ\_0002360 and miR-145 in cells after pulling down of Ago2 by RIP assay. (d) A schematic of wild-type (WT) and mutant (MUT) hsa\_circ\_0025202 luciferase reporter vectors. (e) The luciferase activity of WT hsa\_circ\_0002360 3' UTR or mutant hsa\_circ\_0002360 30'UTR after transfection with miR-629-3p mimics in cells. (f) The transfection efficiency of miR-145 mimics in cells were evaluated by qRT-PCR. (g) Colony numbers was detected using colony formation assay, and cell invasion was measured with transwell assay. (h) Ki67 and MMP9 expression in cells was detected by western blotting. (i) The production of ROS was measured by DCFH-DA method. (j–l) The activity of SOD, CAT, and GSH-Px was measured by ELISA. Data in (b, c, e, f, g, h, i, j, k, and l) represent the mean values  $\pm$  SD from three biological replicates ( $n = 3$ ). \* $P < 0.05$ .

### 3. Results

#### 3.1. Circ\_0002360 Expression Was Increased in GC Cell Lines.

Firstly, circ\_0002360 expression significantly increased in GC cells in comparison to normal human gastric epithelial cells (Figure 1(a)). Compared with nuclear, cytoplasmic circ\_0002360 expression was increased (Figure 1(b)). The results of RNase R assay are that circ\_0002360 levels remained largely unchanged after RNase R exposure, whereas linear\_0002360 (RUNX1) levels markedly decreased in GC cell lines (Figure 1(c)). As a result, circ\_0002360 overexpression plasmids were transfected into GC cells with a lower expression of circ\_002360 to upregulate circ\_002360 level (Figure 1(d)).

#### 3.2. Circ\_0002360 Sponged miR-145 for Regulating GC Cell Growth, Migration, and Oxidative Stress.

As previously reported, numerous circRNAs are thought to sponge miRNAs; therefore, hsa\_circ\_0002360's miRNA-binding ability needs to be investigated. A CircInteractome website was utilized to predict target miRNAs of circ\_0002360. Among the predicted miRNAs, there were 7 miRNAs (miR-127-5p, miR-758, miR-629, miR-1273, miR-145, miR-933, and miR-585) that were identified according to the score ranked from high to low (Figure 2(a)). miR-629-3p, which was most significantly suppressed following hsa\_circ\_0002360 overexpression, was adopted in the present work for subsequent analyses (Figure 2(b)). Later, the RIP assay was carried out to pull down RNA transcripts that bound to Ago2 in NCI-H1975 cells. The results of qRT-PCR analysis showed that circ\_0002360 and miR-629-3p could be effectively pulled down by anti-Ago2 (Figure 2(c)). Based on luciferase

reporter assay, we constructed dual-luciferase reporter vectors containing either the full length of wild-type (WT) circ0002360 or a version where the miR-629-3p-binding site was mutated (MUT) to determine whether miR-629-3p directly targets circ0002360 (Figure 2(d)). The results showed that luciferase activity remarkably decreased within 293T cells after cotransfection of circ\_0002360-WT with miR-629-3p mimics (Figure 2(e)). Collectively, the above assays suggest that circ\_0002360 can act as miR-629-3p sponges. Next, miR-629-3p mimics was transfected into GC cells to increase its expression (Figure 2(f)). The results of clone formation and transwell assays indicated that the overexpression of circ\_0002360 facilitated colony number and invasion in GC cells, while miR-629-3p mimics abolished the above effects (Figure 2(g)). In addition, the enhancing effect of circ\_0002360 overexpression on the expression of MMP2 and Ki67 in GC cells was also reversed by miR-629-3p mimics (Figure 2(h)). Next, we found that circ\_0002360 overexpression inhibited cellular oxidative stress via reducing ROS level and increasing the levels of SOD, CAT, and GSH-Px (Figure 2(i)–2(l)). However, miR-629-3p mimics abolished the inhibition effects of circ\_0002360 overexpression on oxidative stress.

#### 3.3. Identification of GC-Related Genes from GEO and TCGA Database.

In the present study, we first integrated all samples from GSE103236, GSE22804, GSE33429, and GSE79973 datasets to enlarge the sample size (47 cancer as well as 33 healthy samples; Figure 3(a)). Then, 1874 genes with  $P < 0.05$  from the merged dataset were selected (Figure 3(b)). The heatmap of gene expression from TCGA-STAD dataset

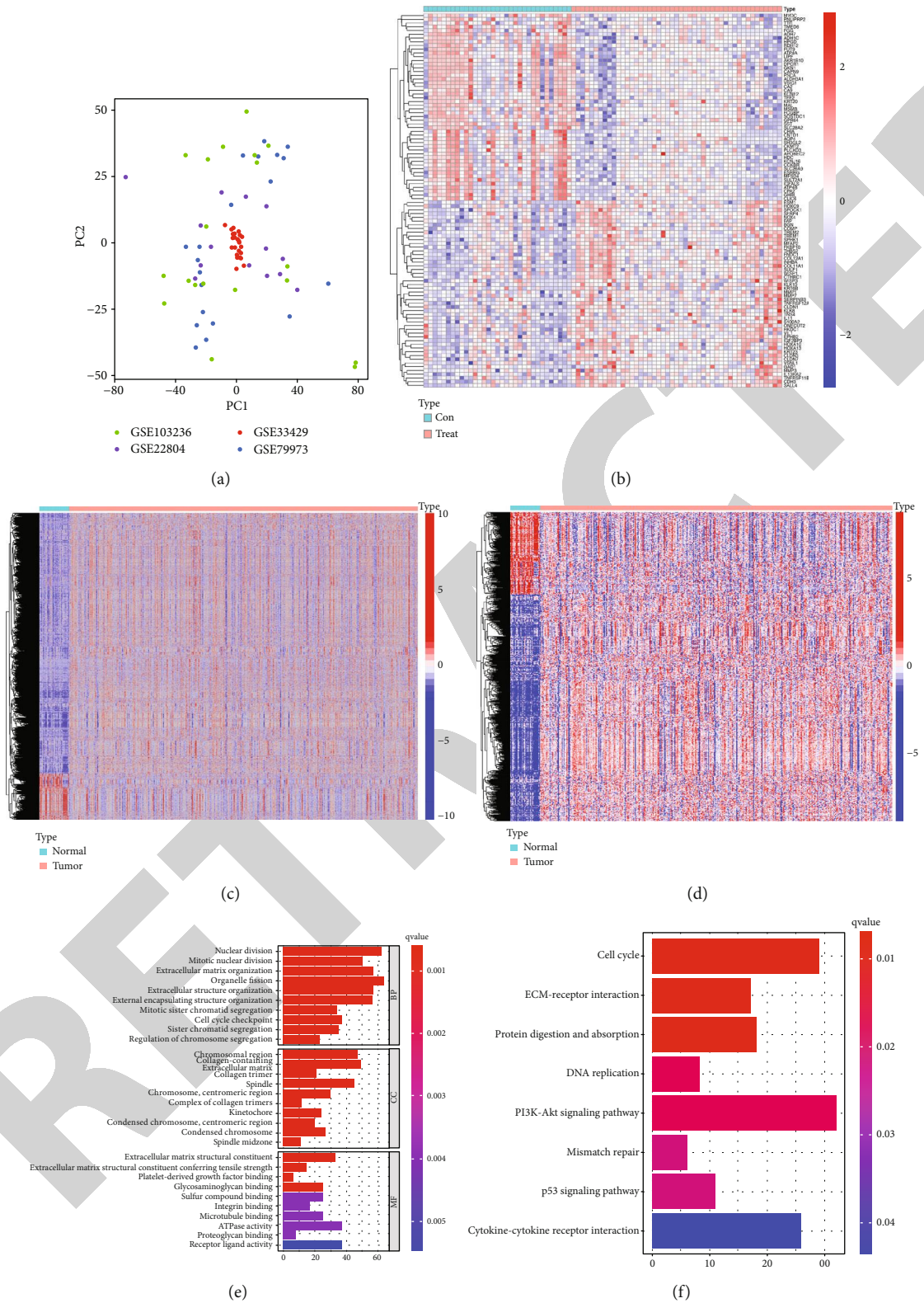


FIGURE 3: Identification of GC-related genes from GEO and TCGA database. (a) Principal component analysis (PCA) of analysis of integrated datasets from GSE103236, GSE22804, GSE33429, and GSE79973 datasets. (b) Heatmap of GEO-derived DEGs with  $P$  value  $< 0.05$ . (c) Heatmap of TCGA-derived DEGs with  $\log_{2}FC > 1$  and  $P$  value  $< 0.05$ . (d) Heatmap of TCGA- and GEO-derived DEGs. GO (e) annotation and KEGG (f) pathways analysis of the DEGs.

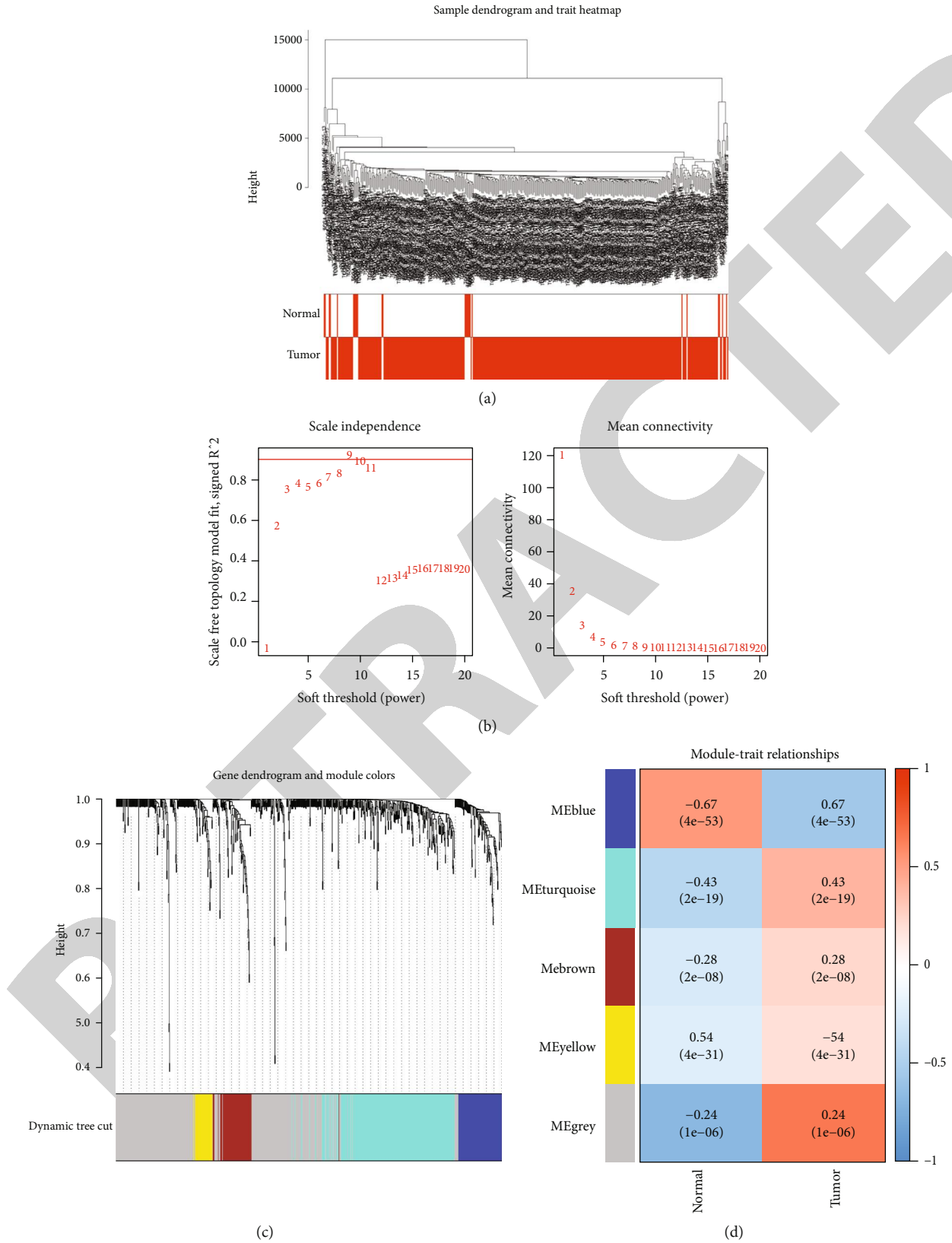


FIGURE 4: WGCNA analysis of hub Modules for the 736 DEGs (a) Clustering dendrogram of 80 samples and excluding two outlier sample. (b) Analysis of the scale-free fit index for various soft-thresholding powers ( $\beta$ ) and analysis of the mean connectivity for various soft-thresholding powers. (c) The dendrogram of all genes is clustered based on a dissimilarity measure (1-TOM). (d) The heatmap shows the correlation among MEs, normal, and tumor. Red represents a positive correlation between modules and clinical characteristics, and blue represents a negative correlation between modules and clinical characteristics.

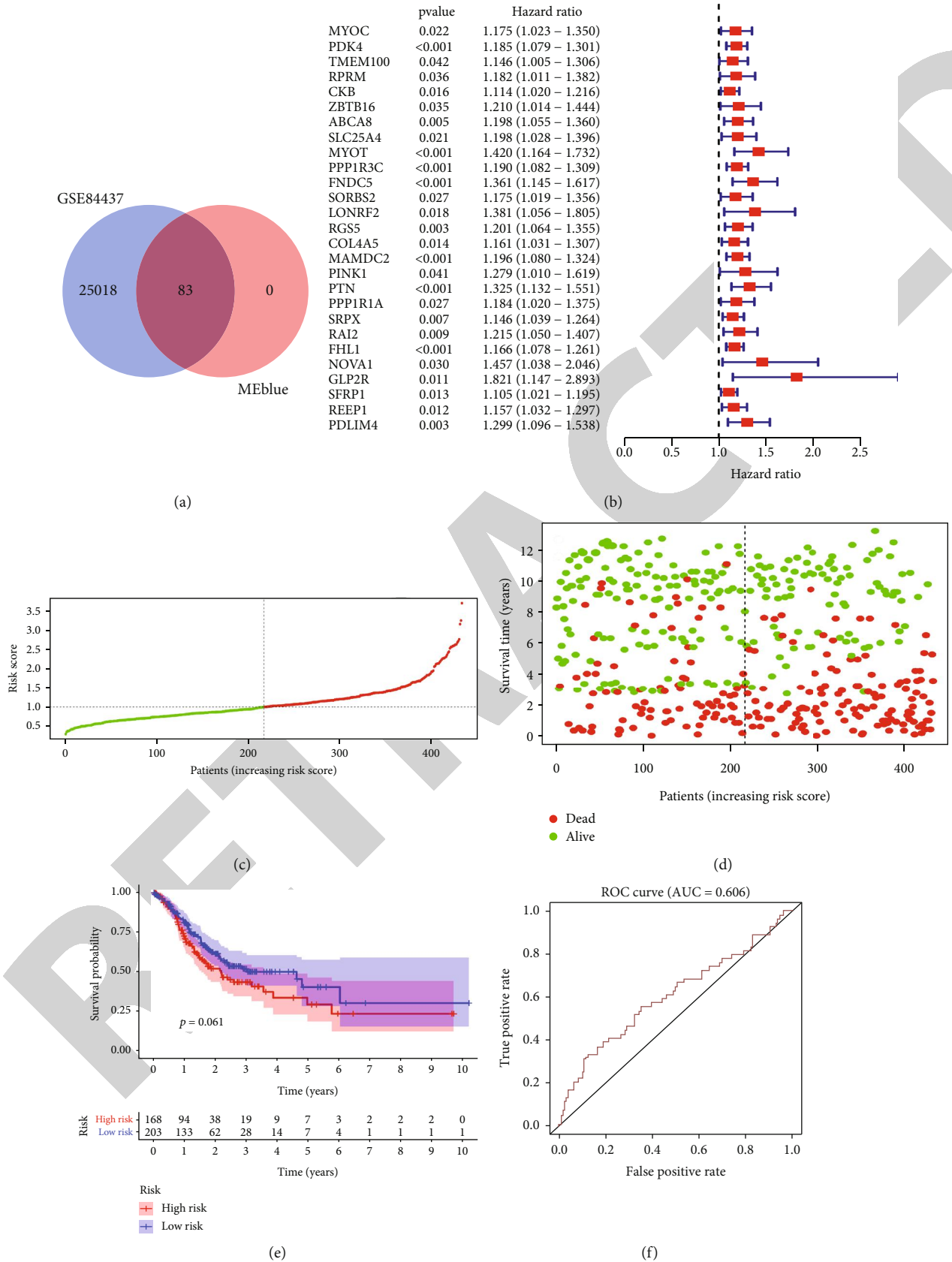


FIGURE 5: Continued.



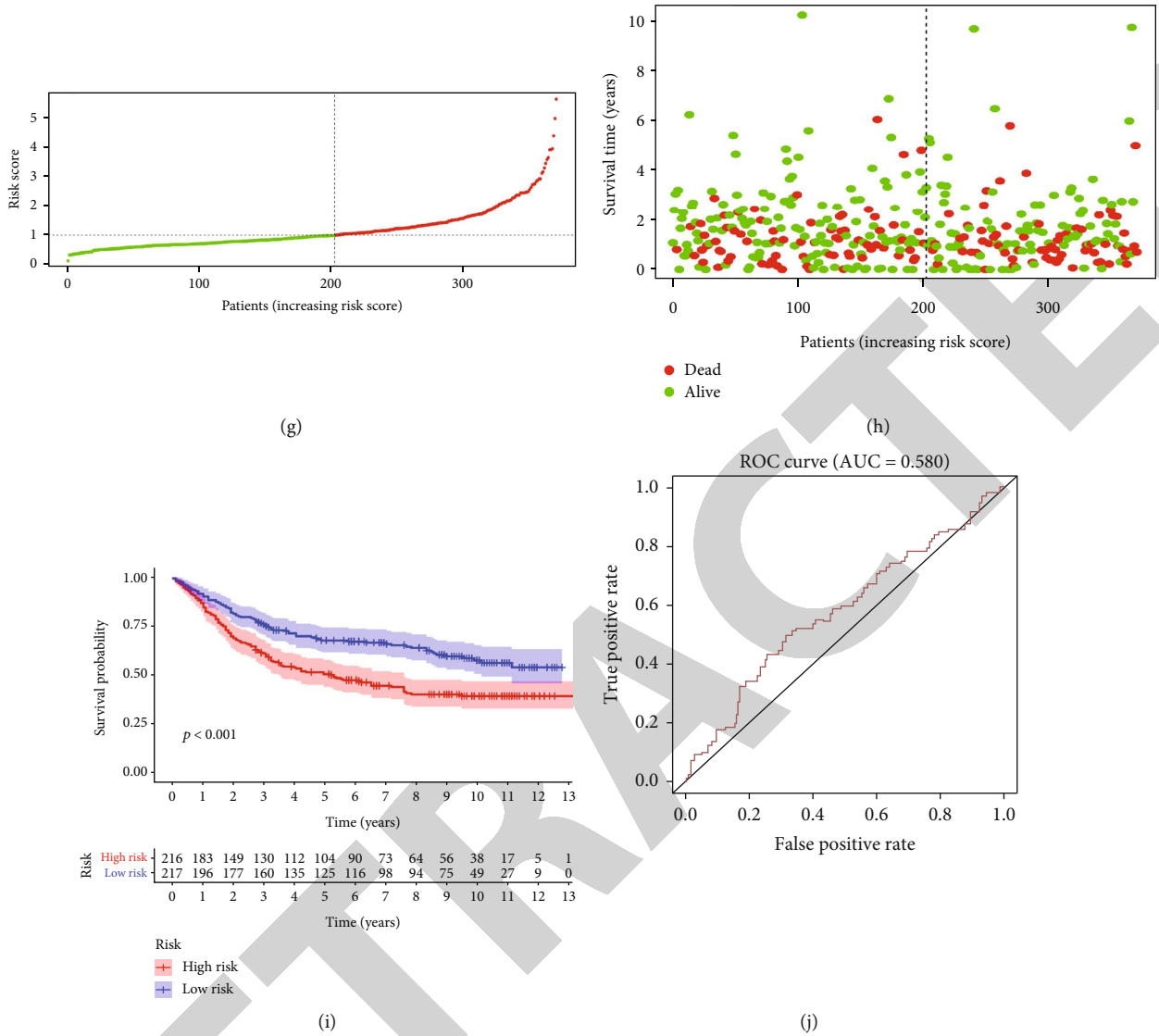


FIGURE 5: Prediction of the mRNA signature for over survival in the train group and test group. (a) Venn analysis of overlapping genes between GSE84437 dataset and blue module. (b) Uni-Cox analysis of the 83 overlapping genes. (c, g) The curve of risk score in training group and testing group; (d, h) survival status by ggrisk in training group and testing group. (e, i) Survival analysis in training group and testing group. (f, j) ROC cure analysis in training group and testing group.

was shown in Figure 3(c). In TCGA-STAD dataset, a total of 736 DEGs were upregulated or downregulated (Figure 3(d)), then these DEGs were employed to perform GO and KEGG analysis (Figures 3(e) and 3(f)). The 736 DEGs were significantly related to the nuclear division of BP, chromosomal region of CC, and extracellular matrix structural constituent of MF (Sup 1), as well as mostly associated with ECM-receptor interaction and cell cycle pathways (Sup 2).

**3.4. WGCNA Analysis of Hub Modules for the 736 DEGs.** To identify some important GC-related genes, WGCNA was performed. The 80 samples were clustered by Pearson correlation analysis and the average linkage approach, and two outlier samples were excluded from further analyses (Figures 4(a)). Thereafter, we conducted a network topology analysis on diverse soft-thresholding powers to achieve relatively balanced scale independence and WGCNA aver-

age connectivity.  $\beta$  power was later raised to 9 to construct a scale-free network, with scale-free  $R^2$  reaching 0.86 (Figure 4(b)). Later, this work obtained altogether 5 different modules within the hierarchical clustering tree by means of tree merged-cut dynamics (Figure 4(c)). We discovered 5 different GC modules after merging modules with <25% dissimilarity (Figure 4(d)). In the present study, the modules associated with tumor were considered to be the most important modules. The modules positively associated with GC were the blue ( $R = 0.67$ ;  $P < 0.0001$ ) module. Finally, a total of 83 blue hub genes were screened for further analysis.

**3.5. Role of mRNA Signature in Predicting OS for Training and Test Cohorts.** In the training and testing groups, high-risk cases were associated with increased mortality compared with low-risk cases based on the median risk score

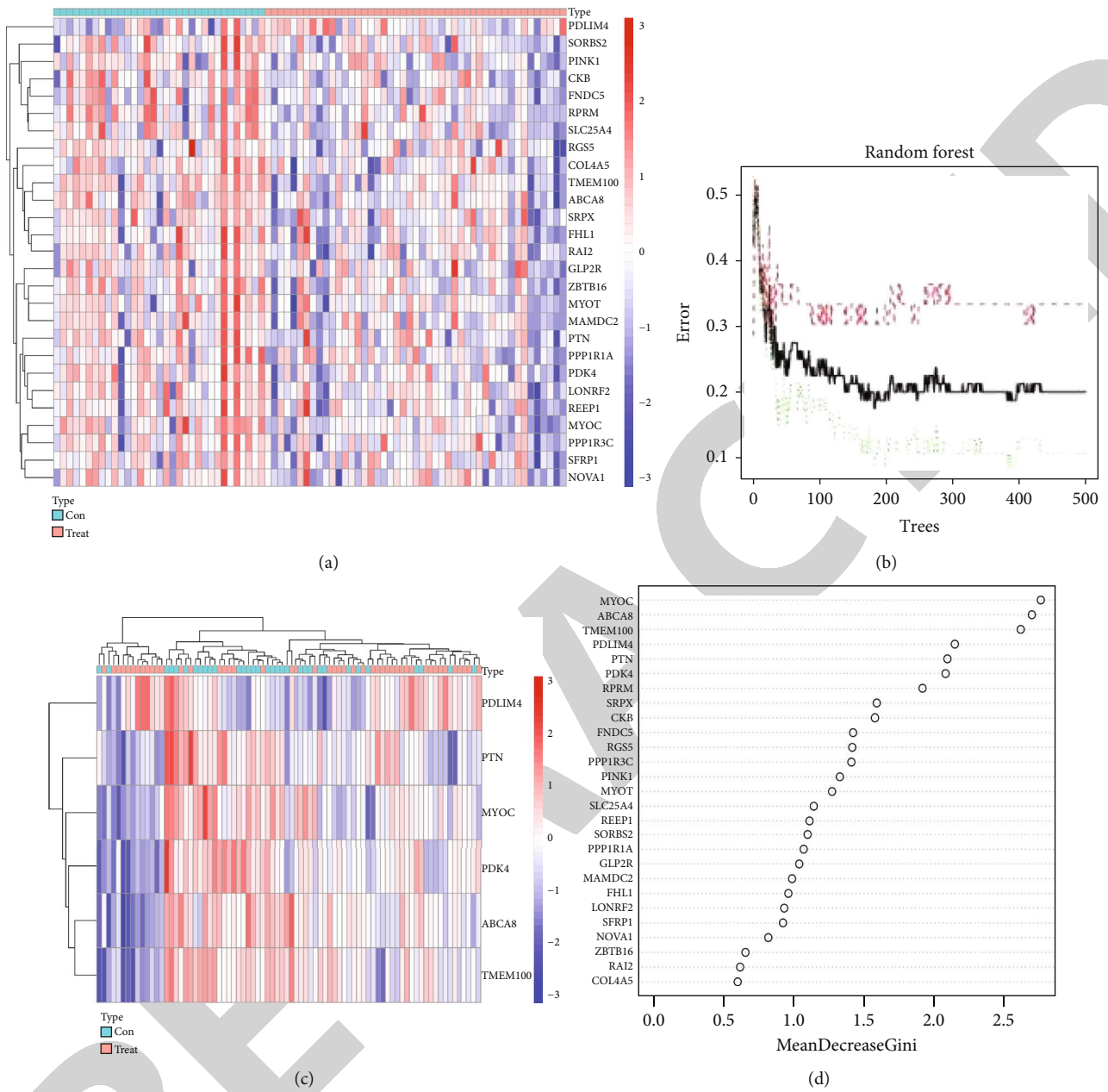


FIGURE 6: The Determination of the Key GC-related genes (a) Heatmap of 27 survival-related risk genes expression in the merged datasets. (b) the tree of randomForest; (c) variable relative importance of randomForest. (d) Heatmap of 6 survival-related risk signatures expression in the merged datasets.

(Figures 5(c), 5(d), 5(g), and 5(h)). As suggested by KM analysis, high-risk patients were associated with dismal OS in comparison with low-risk cases from the training group (Figure 5(e)) and testing group ( $P < 0.001$ ; Figure 5(i)). The AUC values of ROC for our constructed 5-mRNA signature were 0.61 and 0.58, respectively, in the training and testing groups (Figures 5(f) and 5(j)), demonstrating that our constructed model well predicted survival of GC.

**3.6. The Determination of the Key GC-Related Genes.** In the merged datasets, differential expression analysis was performed on 27 survival-related risk genes identified by uni-Cox analysis. According to the findings, the 27 genes

were found to be downregulated in GC tumor samples (Figure 6(a)). By random forest calculation, we found that MYOC, ABCAB, TMEM100, PDLIM4, PTN, and PDK4 were the key GC-related genes (importance  $> 2$ ) (Figures 6(b) and 6(c)), and their expression was presented in Figure 6(d).

**3.7. Circ\_0002360 Acted as a miR-629-3p Sponge to Affect Cell Proliferation, Invasion, and Oxidative Stress in GC Cells via Promoting PDLIM4 Expression.** Firstly, we determined that PDLIM4 was the only one overlapping genes between the six survival-related risk genes and the 5854 target genes of miR-629-3p (Figure 7(a)). The data from GEO and TCGA database verified that GC patients with high

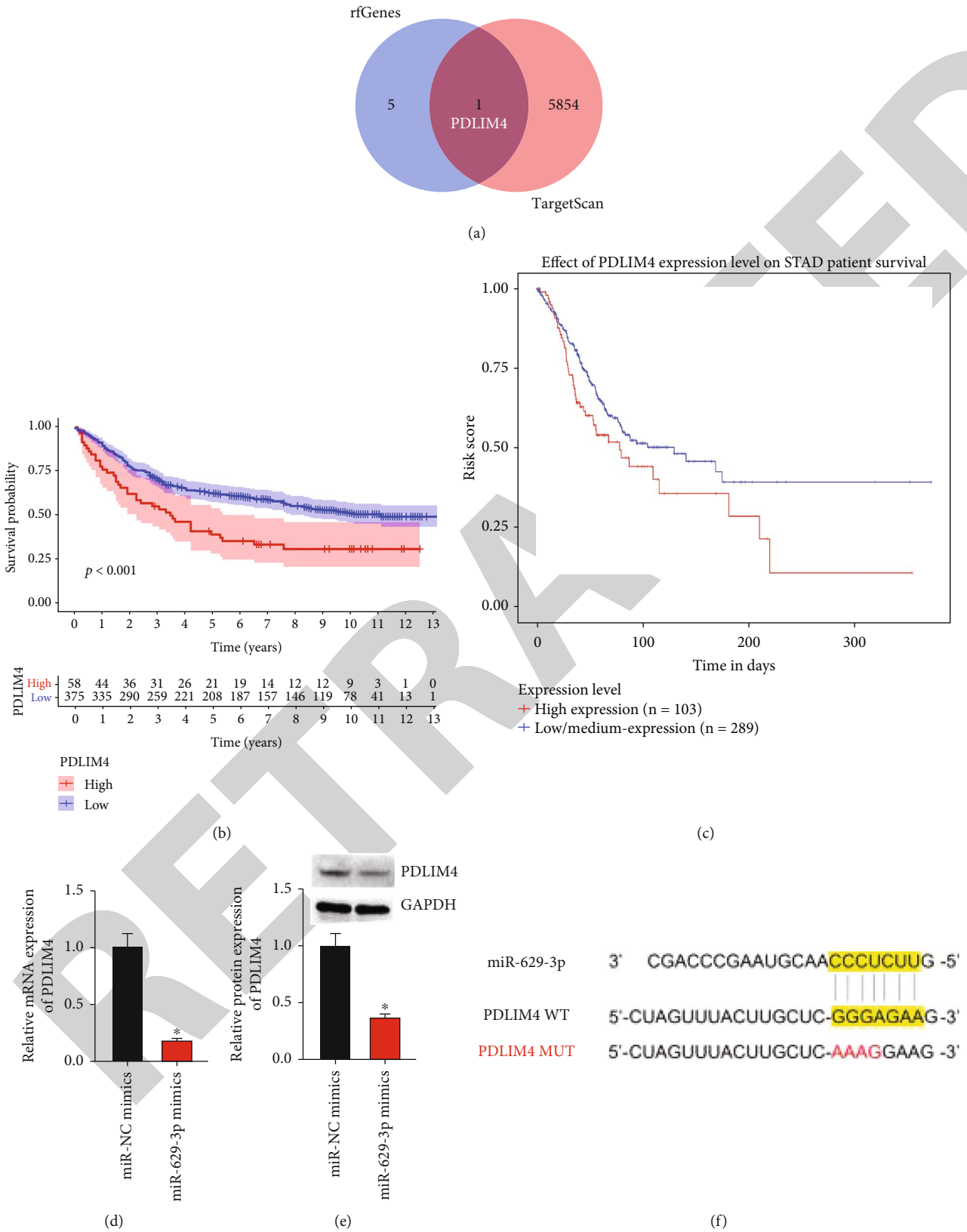


FIGURE 7: Continued.

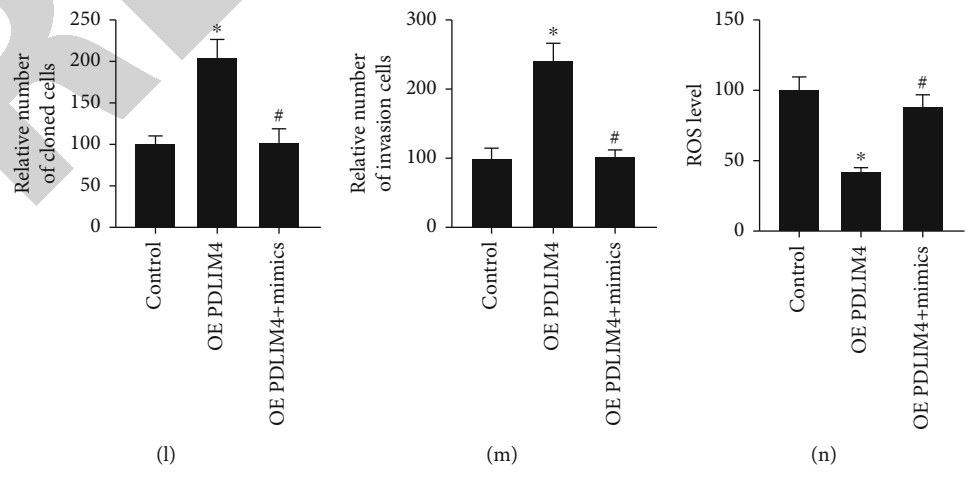
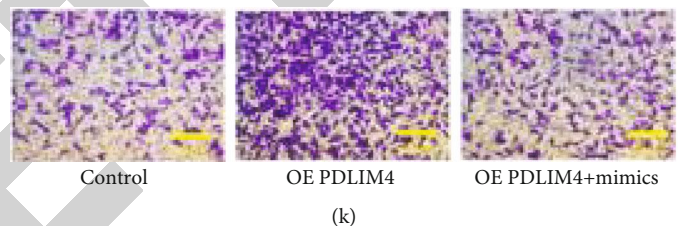
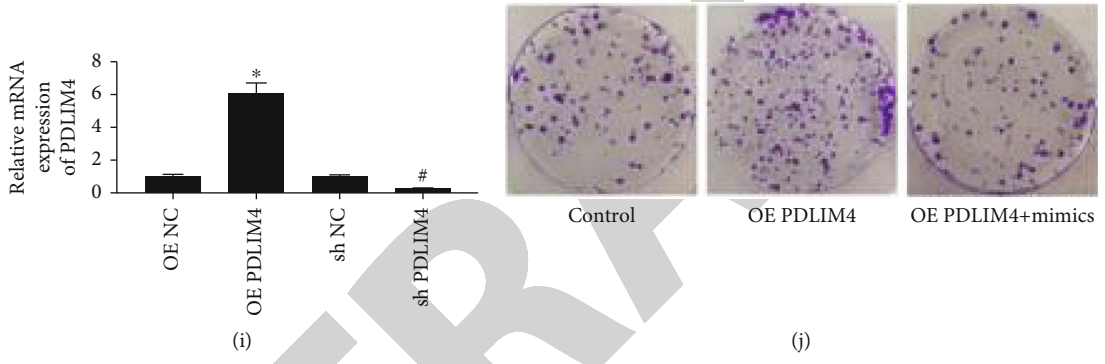
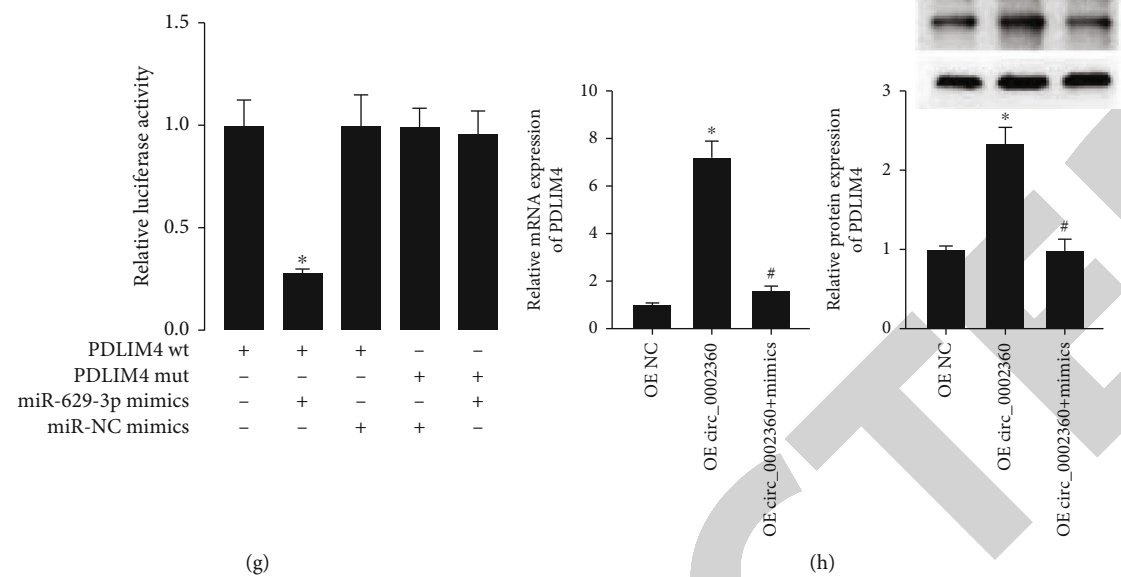


FIGURE 7: Continued.

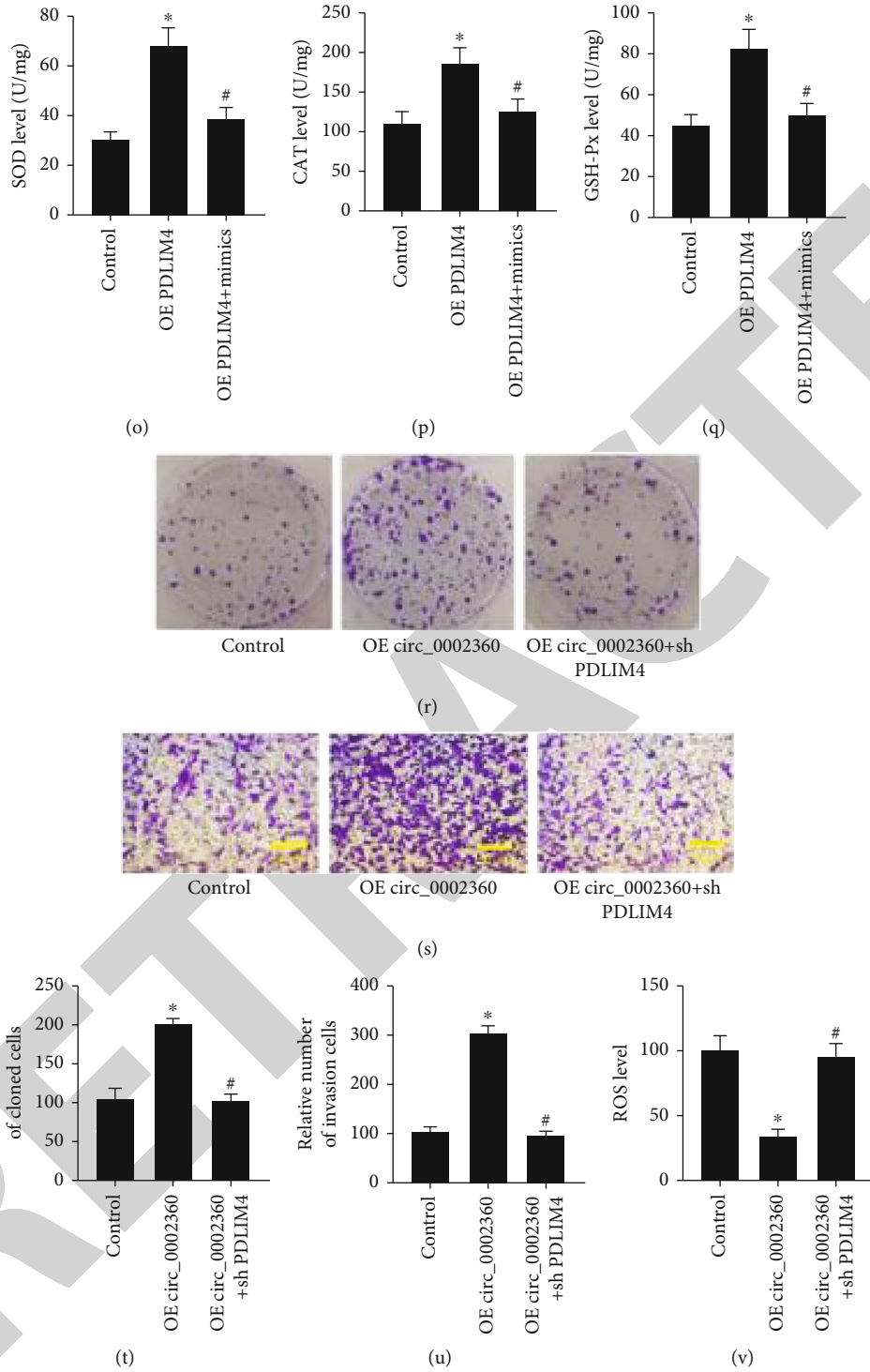


FIGURE 7: Continued.

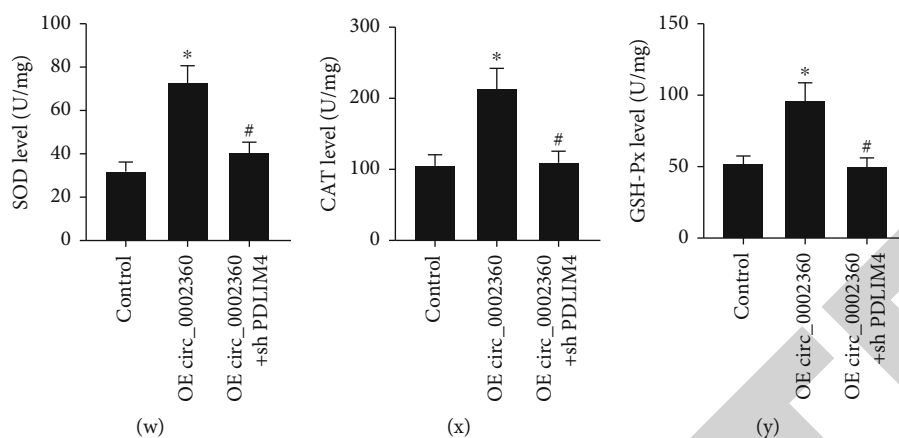


FIGURE 7: Circ\_0002360 acted as a miR-629-3p sponge to affect cell proliferation, invasion, and oxidative stress in GC cells via promoting PDLIM4 expression (a) Venn analysis of overlapping genes between the risk signatures and target genes of miR-629-3p. The survival status between PDLIM4 high expression group and the low expression group in GEO database (b) and TCGA database (c). (d) The transfection efficiency of PDLIM4 overexpression in cells were evaluated by western blotting and qRT-PCR assay. (f) A schematic of wild-type (WT) and mutant (MUT) PDLIM4 luciferase reporter vectors. (g) The luciferase activity of WT PDLIM4 3' UTR or mutant hsa\_circ\_0002360 30' UTR after transfection with miR-629-3p mimics in cells. The PDLIM4 expression (h), cell proliferation (j, l), invasion (k, m), ROS (n), and the levels of SOD, CAT, and GSH-Px (o–q) in cells transfection with circ0002360 overexpression and miR-629-3p mimics were evaluated by western blotting and qRT-PCR assay, colony formation assay, and transwell assay. Cell proliferation (r, t), invasion (s, u), ROS (v), and the levels of SOD, CAT, and GSH-Px (w–y) in cells transfection with circ0002360 overexpression and PDLIM4 knockdown were evaluated by colony formation assay and transwell assay. Data in (d, e, and g–y) represent the mean values  $\pm$  SD from three biological replicates ( $n = 3$ ). \* $P < 0.05$  and # $P < 0.05$ .

expression of PDLIM4 was associated with poor survival in comparison to GC patients with low expression of PDLIM4 (Figures 7(b) and 7(c)). Besides, miR-629-3p mimics suppressed the PDLIM4 level (Figures 7(d) and 7(e)). The results showed that luciferase activity remarkably decreased in 293 T cells subject to cotransfection of PDLIM4-WT with miR-629-3p mimics rather than MUT vector (Figure 7(f)). Then, transfections of OE PDLIM4 and sh PDLIM4 were used to increase PDLIM4 expression and inhibit the expression (Figure 7(i)). Then, circ\_0002360 overexpression promoted PDLIM4 expression; meanwhile, the effect was abolished by transfection of miR-629-3p mimics (Figure 7(h)). In addition, the effects of PDLIM4 overexpression on enhancing proliferation and invasion (Figures 7(j)–7(m)) and inhibiting oxidative stress (Figures 7(n)–7(q)) were reversed by miR-629-3p mimics. Circ\_0002360 obviously promoted cell proliferation and invasion (Figures 7(r)–7(u)) and suppressed oxidative stress (Figure 7(v)–7(y)), while these effects were eliminated by PDLIM4 knockdown.

#### 4. Discussion

CircRNAs can modulate cellular biological behavior to play critical effects on cancer occurrence and development. Because the ring structure is especially stable, circRNAs have been recognized to be the possible targets for tumors diagnosis and prognosis [25]. It reported that circ0002360 expression was upregulated in lung cancer tissues and promoted its progression [23]. Nonetheless, the expression pattern and roles of circ0002360 in GC are still unknown. This work verified that circ0002360 was significantly increased in GC cells in comparison to GES-1 cells, as evi-

denced by qRT-PCR. According to circRNAs serving as the miRNA sponges in various cancers, the possible target miRNAs of circ0002360 was predicted by adopting the bioinformatics methods. A total of 7 targets were obtained from circular RNA Interactome database. According to qRT-PCR and dual-luciferase assays, circNRIP1 sponged miR-629-3p. In addition, miR-629-3p can promote the progression of breast cancer (BRCA), lung cancer (LC), and head and neck cancer (HNC) [26–29], while it affects the growth, invasion, and migration of cervical cancer (CC) cells [30]. However, the roles and mechanism of miR-629-3p had not been reported in GC. Our results showed that circ0002360 promoted GC cell proliferation and invasion. But miR-629-3p inhibited GC cell proliferation and invasion. However, miR-629-3p mimics abolished the functions of circ0002360 in promoting cell growth and metastasis. It demonstrated that circ0002360 promoted GC progression by sponging miR-629-3p.

Current understanding of the etiology of gastric cancer suggests that oxidative stress plays a role in its progression [31]. Tumor cells have a greater oxidative state, which increases the generation of ROS [32]. In addition, large amounts of reactive oxygen species may boost antioxidant activity in patients with stomach cancer [33]. Past studies have found a rise in CAT activity in patients with tumors [34]. In addition, the activities of GSH, xanthine oxidase, catalase, and copper-zinc superoxide dismutase were considerably elevated in the blood of patients with tumors [35]. Antioxidant enzymes in the mitochondria, such as manganese superoxide dismutase (MnSOD) and glutathione-dependent peroxidase (GPX), are the primary mitochondrial defense system against oxidative stress [36]. Therefore,

inhibition of the antioxidant system is therefore a possibility for cancer treatment. In this study, when vectors expressing circ0002360 were transfected into cells, SOD, CAT, and GSH-Px activities rose, while ROS levels dropped. On the other hand, the transfection of miR-629-3p mimics had the opposite effect. Furthermore, miR-629-3p mimics abolished the inhibition of oxidative stress caused by circ0002360 overexpression. Inducing ROS generation to disable the antioxidant defense system has been reported as a novel technique for cancer therapy [37]. Thus, inhibiting circ0002360 decreased gastric cancer cell proliferation and invasion while also increasing the inhibition effects of cell proliferation by promoting ROS generation and decreasing antioxidant activity. This process is inextricably linked to the expression of miR-629-3p.

To determine the target gene of miR-629-3p, we download the GC-related expression profile data from GEO and TCGA database to determine differential expressed genes. Previous studies usually used some target gene prediction websites, such as TargetScan, to screen out target genes of miRNAs [38, 39]. However, we first used WGCNA and uni-Cox analysis to construct a risk model for prognosis prediction. Next, randomForest analysis identify key survival-related risk signatures. Finally, Venn analysis determined a target gene of miR-629-3p from TargetScan database and risk signatures termed PDLIM4. Our results are obtained from multiple databases with different analyses. Therefore, it had a higher degree of confidence.

PDLIM4 (reversion-induced LIM domain) is a tumor suppressor gene located at 31.1 on the long arm of chromosome 5 and can encode one adapter protein, which belongs to ALP/Enigma family and has high conservation degree [40]. Because PDLIM4 has domains (LIM and PDZ), PDLIM4 can be the scaffold that interacts with membrane receptors and cytoplasmic signal molecules, as well as actin-related proteins [41]. PDLIM4 is identified to be a tumor suppressor [42] and shows abnormal expression in different cancer types. For BRCA, the abnormal expression of PDLIM4 is closely related to tumor clinical features, like cell ploidy, tumor size, SPF (S-phase fraction), and differentiation status [43]. Besides, PDLIM4 regulates the expression of proto-oncogene to promote cell proliferation, invasion, and active angiogenesis pathways [44, 45]. Based on cell experiment in this work, miR-629-3p target PDLIM4 and served as the tumor suppressor in GC. It showed that miR-629-3p inhibited the progression GC. Next, we used rescue experiments to verify the relation of circ0002360, miR-629-3p, and PDLIM4 in GC cells. The results showed that miR-629-3p mimics could reverse the effects of circ0002360 and PDLIM4 overexpression on GC cell phenotypes, and PDLIM4 knockdown could abolish the regulated effects of circ0002360 overexpression on GC cell proliferation, invasion, and oxidative stress. Therefore, circ0002360 sponged miR-629-3p to exert its function in GC progression. Besides, circ0002360 positively regulated PDLIM4 to promote cell proliferation and invasion and inhibit oxidative stress. CircRNAs could sponge several miRNAs to regulate cell proliferation and might be the oncogene in several cancer types, which sponged diverse miRNAs (concurrently or not)

because of the certain tissues and cells implicated. In this work, circ0002360 exerted its effects through sponging miR-629-3p in GC cells, at least partly.

**4.1. Limitation.** CircRNAs-mediated effects in cell proliferation, invasion, and so on dependent on the abundance of miRNA and the number of miRNA-binding site. Consequently, the above observations might be change because of the different circ0002360, miRNA targets, and miRNAs expression levels within diverse cells. Therefore, more studies are needed to explore the mechanism of circ0002360 in the action mode in diverse malignancies. Furthermore, this study merely confirmed the role and molecular mechanism of the circ0002360/miR-629-3p/PDLIM4 axis in gastric cancer at the cellular level, with no clinical or animal involvement. Furthermore, bioinformatics approaches were used to examine the stomach cancer-related expression profile data in public databases (TCGA and GEO database), and no comparable clinical cases were obtained for examination, resulting in a lack of clinical guidance. As a result, in the follow-up investigation, we will collect clinical samples and conduct relevant animal studies to clarify the roles and molecular mechanisms of the circ0002360/miR-629-3p/PDLIM4 axis in gastric cancer.

In conclusion, this work suggests the upregulation of circ0002360 in GC cells accelerates GC cell proliferation, invasion, and inhibits oxidative stress through sponging miR-629-3p to increase PDLIM4 expression. This work offers further evidence supporting the roles of circRNAs in sponging miRNAs, which indicates that circ0002360 is the possible marker to predict GC prognosis and the anti-GC therapeutic target.

## Data Availability

Data will be available upon reasonable request.

## Conflicts of Interest

The authors declare that there are no conflicts of interest.

## Authors' Contributions

Zhengyuan Yu and Jing Lan are co-first authors and contributed equally to this work.

## Supplementary Materials

Supplementary Table 1.: GO analysis. Supplementary Table 2: KEGG pathway. (*Supplementary Materials*)

## References

- [1] E. C. Smyth, M. Nilsson, H. I. Grabsch, N. C. van Grieken, and F. Lordick, "Gastric cancer," *Lancet*, vol. 396, no. 10251, pp. 635–648, 2020.
- [2] G. Li, X. Chen, J. Yu, and H. Liu, "Clinical research status of laparoscopic gastric cancer surgery in China, Japan and South Korea," *Zhonghua Wei Chang Wai Ke Za Zhi*, vol. 21, no. 2, pp. 126–131, 2018.

- [3] Y. Cao, H. He, R. Li et al., "Latency-associated peptide identifies immunoevasive subtype gastric cancer with poor prognosis and inferior chemotherapeutic responsiveness," *Annals of Surgery*, vol. 275, no. 1, pp. e163–e173, 2022.
- [4] A. Digkila and A. D. Wagner, "Advanced gastric cancer: current treatment landscape and future perspectives," *World Journal of Gastroenterology*, vol. 22, no. 8, pp. 2403–2414, 2016.
- [5] Y. Zeng and R. U. Jin, "Molecular pathogenesis, targeted therapies, and future perspectives for gastric cancer," *Seminars in Cancer Biology*, 2021.
- [6] T. L. Ang and K. M. Fock, "Clinical epidemiology of gastric cancer," *Singapore Medical Journal*, vol. 55, no. 12, pp. 621–628, 2014.
- [7] G. P. Nagaraju, G. Srivani, B. Dariya et al., "Nanoparticles guided drug delivery and imaging in gastric cancer," *Seminars in Cancer Biology*, vol. 69, p. 69, 2021.
- [8] N. Oue, K. Sentani, N. Sakamoto, N. Uraoka, and W. Yasui, "Molecular carcinogenesis of gastric cancer: Lauren classification, mucin phenotype expression, and cancer stem cells," *International Journal of Clinical Oncology*, vol. 24, no. 7, pp. 771–778, 2019.
- [9] Y. Kono, H. Kanzaki, M. Iwamuro, S. Kawano, Y. Kawahara, and H. Okada, "Reality of gastric cancer in young patients: the importance and difficulty of the early diagnosis, prevention and treatment," *Acta Medica Okayama*, vol. 74, no. 6, pp. 461–466, 2020.
- [10] Q. Li, X. Xu, D. Su, T. Zhou, G. Wang, and Z. Li, "Long-term survival of an elderly patient with advanced gastric cancer after combination therapy: a case report and literature review," *BMC Cancer*, vol. 19, no. 1, p. 459, 2019.
- [11] A. Huang, H. Zheng, Z. Wu, M. Chen, and Y. Huang, "Circular RNA-protein interactions: functions, mechanisms, and identification," *Theranostics*, vol. 10, no. 8, pp. 3503–3517, 2020.
- [12] F. Li, Q. Yang, A. T. He, and B. B. Yang, "Circular RNAs in cancer: limitations in functional studies and diagnostic potential," *Seminars in Cancer Biology*, vol. 75, p. 49, 2021.
- [13] J. Salzman, "Circular RNA expression: its potential regulation and function," *Trends in Genetics*, vol. 32, no. 5, pp. 309–316, 2016.
- [14] S. Qu, X. Yang, X. Li et al., "Circular RNA: a new star of non-coding RNAs," *Cancer Letters*, vol. 365, no. 2, pp. 141–148, 2015.
- [15] X. Zhang, S. Wang, H. Wang et al., "Circular RNA circNRIP1 acts as a microRNA-149-5p sponge to promote gastric cancer progression via the AKT1/mTOR pathway," *Molecular Cancer*, vol. 18, no. 1, p. 20, 2019.
- [16] M. Jie, Y. Wu, M. Gao et al., "CircMRPS35 suppresses gastric cancer progression via recruiting KAT7 to govern histone modification," *Molecular Cancer*, vol. 19, no. 1, p. 56, 2020.
- [17] W. Tang, K. Fu, H. Sun, D. Rong, H. Wang, and H. Cao, "CircRNA microarray profiling identifies a novel circulating biomarker for detection of gastric cancer," *Molecular Cancer*, vol. 17, no. 1, p. 137, 2018.
- [18] L. Peng, H. Sang, S. Wei et al., "circCUL2 regulates gastric cancer malignant transformation and cisplatin resistance by modulating autophagy activation via miR-142-3p/ROCK2," *Molecular Cancer*, vol. 19, no. 1, p. 156, 2020.
- [19] L. S. Kristensen, M. S. Andersen, L. V. W. Stagsted, K. K. Ebbesen, T. B. Hansen, and J. Kjems, "The biogenesis, biology and characterization of circular RNAs," *Nature Reviews Genetics*, vol. 20, no. 11, pp. 675–691, 2019.
- [20] Z. Luo, Z. Rong, J. Zhang et al., "Circular RNA circCCDC9 acts as a miR-6792-3p sponge to suppress the progression of gastric cancer through regulating CAV1 expression," *Molecular Cancer*, vol. 19, no. 1, pp. 1–21, 2020.
- [21] Y. Zhuang, L. Li, H. Wu, and T. Fang, "CircRNA ACVR2A sponges miR-1290 to modulate cell progression in gastric cancer," *Journal of Oncology*, vol. 2022, Article ID 9461054, 13 pages, 2022.
- [22] Y. Zhang, G. Hu, Z. Zhang, Y. Jing, F. Tao, and M. Ye, "CircRNA\_0043691 sponges miR-873-3p to promote metastasis of gastric cancer," *Mammalian Genome*, vol. 32, no. 6, pp. 476–487, 2021.
- [23] S. Bai, Y. Wu, Y. Yan et al., "Construct a circRNA/miRNA/mRNA regulatory network to explore potential pathogenesis and therapy options of clear cell renal cell carcinoma," *Scientific Reports*, vol. 10, article 13659, pp. 1–15, 2020.
- [24] L. Bu, W. Li, Z. Ming, J. Shi, P. Fang, and S. Yang, "Inhibition of TrxR2 suppressed NSCLC cell proliferation, metabolism and induced cell apoptosis through decreasing antioxidant activity," *Life Sciences*, vol. 178, p. 35, 2017.
- [25] X. Chen, T. Yang, W. Wang et al., "Circular RNAs in immune responses and immune diseases," *Theranostics*, vol. 9, no. 2, pp. 588–607, 2019.
- [26] J. Chikuda, K. Otsuka, I. Shimomura et al., "CD44s induces miR-629-3p expression in association with cisplatin resistance in head and neck cancer cells," *Cancers (Basel)*, vol. 12, no. 4, p. 856, 2020.
- [27] J. Wang, C. Song, H. Tang et al., "miR-629-3p may serve as a novel biomarker and potential therapeutic target for lung metastases of triple-negative breast cancer," *Breast Cancer Research*, vol. 19, no. 1, p. 72, 2017.
- [28] B. Li, Y. Q. Meng, Z. Li et al., "MiR-629-3p-induced downregulation of SFTPC promotes cell proliferation and predicts poor survival in lung adenocarcinoma," *Artificial Cells Nanomedicine and Biotechnology*, vol. 47, no. 1, pp. 3286–3296, 2019.
- [29] Z. Jin, Y. Chenghao, and P. Cheng, "Anticancer effect of tanshinones on female breast cancer and gynecological cancer," *Frontiers in Pharmacology*, vol. 12, article 824531, 2021.
- [30] X. Li, N. Ma, Y. Zhang et al., "Circular RNA circNRIP1 promotes migration and invasion in cervical cancer by sponging miR-629-3p and regulating the PTP4A1/ERK1/2 pathway," *Cell Death & Disease*, vol. 11, no. 5, p. 399, 2020.
- [31] S. Wang, Z. Chen, S. Zhu et al., "PRDX2 protects against oxidative stress induced by H. pylori and promotes resistance to cisplatin in gastric cancer," *Redox Biology*, vol. 28, article 101319, 2020.
- [32] S. Y. Lee, E. K. Jeong, M. K. Ju et al., "Induction of metastasis, cancer stem cell phenotype, and oncogenic metabolism in cancer cells by ionizing radiation," *Molecular Cancer*, vol. 16, no. 1, p. 10, 2017.
- [33] M. B. Braga-Neto, D. V. Costa, D. M. Queiroz et al., "Increased oxidative stress in gastric cancer patients and their first-degree relatives: a prospective study from Northeastern Brazil," *Oxidative Medicine and Cellular Longevity*, vol. 2021, Article ID 6657434, 2021.
- [34] R. Lacroix, L. Vallier, A. Bonifay et al., "Microvesicles and cancer associated thrombosis," *Seminars in Thrombosis and Hemostasis*, vol. 45, no. 6, pp. 593–603, 2019.
- [35] K. Danwilai, J. Konmun, B. Sripanidkulchai, and S. Subongkot, "Antioxidant activity of ginger extract as a daily supplement in



## Retraction

# Retracted: Delicaflavone Represses Lung Cancer Growth by Activating Antitumor Immune Response through N6-Methyladenosine Transferases and Oxidative Stress

### Oxidative Medicine and Cellular Longevity

Received 20 June 2023; Accepted 20 June 2023; Published 21 June 2023

Copyright © 2023 Oxidative Medicine and Cellular Longevity. This is an open access article distributed under the Creative Commons Attribution License, which permits unrestricted use, distribution, and reproduction in any medium, provided the original work is properly cited.

This article has been retracted by Hindawi following an investigation undertaken by the publisher [1]. This investigation has uncovered evidence of one or more of the following indicators of systematic manipulation of the publication process:

- (1) Discrepancies in scope
- (2) Discrepancies in the description of the research reported
- (3) Discrepancies between the availability of data and the research described
- (4) Inappropriate citations
- (5) Incoherent, meaningless and/or irrelevant content included in the article
- (6) Peer-review manipulation

The presence of these indicators undermines our confidence in the integrity of the article's content and we cannot, therefore, vouch for its reliability. Please note that this notice is intended solely to alert readers that the content of this article is unreliable. We have not investigated whether authors were aware of or involved in the systematic manipulation of the publication process.

Wiley and Hindawi regrets that the usual quality checks did not identify these issues before publication and have since put additional measures in place to safeguard research integrity.

We wish to credit our own Research Integrity and Research Publishing teams and anonymous and named external researchers and research integrity experts for contributing to this investigation.

The corresponding author, as the representative of all authors, has been given the opportunity to register their agreement or disagreement to this retraction. We have kept a record of any response received.

### References

- [1] X. Wang, D. Xu, B. Chen et al., "Delicaflavone Represses Lung Cancer Growth by Activating Antitumor Immune Response through N6-Methyladenosine Transferases and Oxidative Stress," *Oxidative Medicine and Cellular Longevity*, vol. 2022, Article ID 8619275, 16 pages, 2022.

## Research Article

# Delicaflavone Represses Lung Cancer Growth by Activating Antitumor Immune Response through N6-Methyladenosine Transferases and Oxidative Stress

Xuwen Wang,<sup>1</sup> Dafen Xu,<sup>2</sup> Bing Chen,<sup>2,3</sup> Dandan Huang,<sup>2</sup> Zhijun Li,<sup>4</sup> Yuxia Sui,<sup>5,6</sup> Fei Lin,<sup>3</sup> Hong Yao <sup>2,7</sup>, Huang Yuan Li <sup>1,8</sup> and Xinhua Lin <sup>2,3</sup>

<sup>1</sup>Department of Preventive Medicine, School of Public Health, Fujian Medical University, Fuzhou 350122, China

<sup>2</sup>Department of Pharmaceutical Analysis, School of Pharmacy, Fujian Medical University, Fuzhou 350122, China

<sup>3</sup>Key Laboratory of Nanomedical Technology (Education Department of Fujian Province), School of Pharmacy, Nano Medical Technology Research Institute, Fujian Medical University, Fuzhou 350122, China

<sup>4</sup>School of Pharmacy, Fujian Medical University, Fuzhou, 350122 Fujian, China

<sup>5</sup>Department of Pharmacy, Shengli Clinical Medical College of Fujian Medical University, Fuzhou 350001, China

<sup>6</sup>Department of Pharmacy, Fujian Provincial Hospital, Fuzhou 350001, China

<sup>7</sup>Fujian Key Laboratory of Drug Target Discovery and Structural and Functional Research, Fujian Medical University, Fuzhou 350122, China

<sup>8</sup>Fujian Provincial Key Laboratory of Environment Factors and Cancer, School of Public Health, Fujian Medical University, Fuzhou 350122, China

Correspondence should be addressed to Hong Yao; [yauhung@126.com](mailto:yauhung@126.com), Huang Yuan Li; [lhy@fjmu.edu.cn](mailto:lhy@fjmu.edu.cn), and Xinhua Lin; [lxhfz12345@163.com](mailto:lxhfz12345@163.com)

Received 13 March 2022; Revised 28 April 2022; Accepted 28 May 2022; Published 8 August 2022

Academic Editor: Tian Li

Copyright © 2022 Xuwen Wang et al. This is an open access article distributed under the Creative Commons Attribution License, which permits unrestricted use, distribution, and reproduction in any medium, provided the original work is properly cited.

Our previous studies have shown that delicaflavone (DLL), a biocomponent extracted from *Selaginella doederleinii* Hieron, has antitumor activity. However, the role of DLL in the antitumor immune response is unknown. In this study, we tested the potential roles of DLL in antitumor immune response. An animal tumor model with Lewis lung cancer cell line (3LL) in C57BL/6 mice was established to determine whether DLL induced the tumor-bearing host's antitumor immune response. m6A-MeRIP-qPCR, western blot, and flow cytometry were performed to explore the underlying mechanisms. DLL inhibited the proliferation of 3LL lung cancer cells *in vitro* and *in vivo* and induced tumor cell oxidative stress. DLL significantly inhibited tumor growth in immunocompetent mice compared with nude mice. DLL treatment significantly increased Th1 cytokine production and CD8+ T cell infiltration into tumor tissues in tumor-bearing mice. DLL-mediated antitumor immune effects were reversed by overexpression of the N6-methyladenosine (m6A) transferase *Mettl3/Mettl14*. Mechanistically, DLL upregulated the expression of *Stat1* and *Irf1* and the secretion of cytokines by inhibiting *Mettl3* and *Mettl14* in lung cancer cells. In conclusion, DLL inhibited lung cancer cell growth by suppressing *Mettl3/Mettl14* to activate antitumor immunity. These findings provided an opportunity to enhance lung cancer immunotherapy.

## 1. Introduction

Traditional Chinese medicines have distinct advantages in tumor treatments [1]. They fight cancer by inducing tumor cell apoptosis, inhibiting tumor angiogenesis, reversing multidrug resistance, and regulating the host's immune response [2].

Many biflavonoids have been found to have antitumor activity in recent studies. Natural biflavonoids are widely present in vascular plants such as *Selaginella*. *Selaginella doederleinii* Hieron has a unique antitumor effect and is commonly used clinically to treat nasopharyngeal, esophageal, gastric, liver, lung, choriocarcinoma, and cervical cancer [3]. Lee et al. found

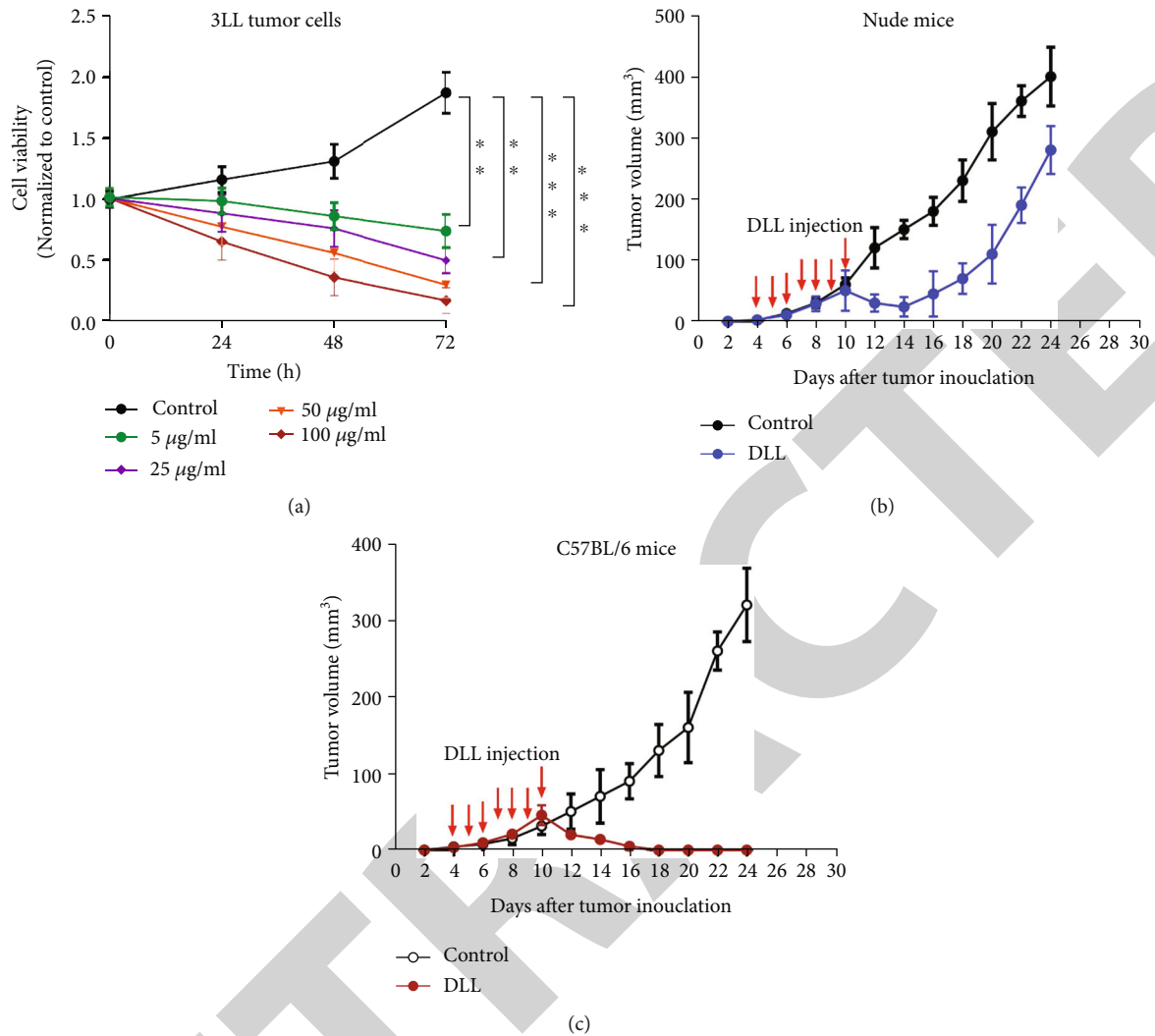


FIGURE 1: DLL inhibited 3LL tumor growth both in vitro and in vivo. (a) 3LL tumor cells were treated for 24, 48, and 72 h in a 96-well plate in the presence of different doses of DLL (0, 5, 25, 50, and 100  $\mu\text{g/ml}$ ). CCK-8 assay was used to estimate the cell viability. Cell viability was decreased with increased DLL concentration. (b, c) Nude mice (b) and C57BL/6 mice (c) were injected subcutaneously with  $5 \times 10^4$  3LL tumor cells per mouse. DLL was injected subcutaneously on day 4 and then once every day for a total of seven injections. Saline was injected subcutaneously as a control. DLL injection significantly inhibited tumor growth in C57BL/6 mice. Data are the mean  $\pm$  SD from three independent experiments. \*\* $P < 0.01$  and \*\*\* $P < 0.001$  by Student's  $t$ -test,  $N = 6$ . DLL: delicaflavone.

that amentoflavone significantly inhibited fatty acid synthase activity, thereby inhibiting tumor cell growth [4]. We previously isolated a new type of biflavonoid compound, delicaflavone (DLL), from *Selaginella doederleinii* Hieron, and discovered that DLL inhibited A549 cell growth via the Akt/mTOR/p70S6K signaling pathway [5]. DLL reduced cisplatin resistance in lung cancer by modulating endoplasmic reticulum stress signaling [6]; however, it is unknown whether DLL can activate an anti-tumor immune response.

Traditional Chinese medicine has been shown in studies to have antitumor activity via oxidative stress and epigenetic mechanisms, such as RNA methylation [7–9]. Reactive oxygen species (ROS) are known to regulate every step of tumorigenesis by acting as second messengers in cancer cells, which play essential roles in the regulation of cancer progression [10]. Traditional Chinese medicine-induced oxidative stress can regulate N6-methyladenosine (m6A)

modification [11]. The interaction of m6A modification and oxidative stress influences tumor growth [12, 13]. m6A modification is an important posttranscriptional modification process that regulates mRNA localization, transcription, and stability [14]. The factors involved in m6A methylation are mainly related to three protein families: methyltransferases (writer) including METL3, METL14, and WTAP; m6A demethylases (eraser) including FTO and ALKBH5; and m6A “readers” including YTHDCs, YTHDFs, and IGF2BPs [15]. Recent research has revealed that m6A plays a role in regulating the tumor immune microenvironment [16]. Increased RNA methylation, for example, reduces the sensitivity of melanoma cells to anticancer immunotherapy [17]. ALKBH5 knockout altered the composition of tumor-infiltrating Treg cells, resulting in changes in the tumor microenvironment [18]. METTL3/14 regulates the immune response of refractory colorectal cancer anti-PD-1 treatment

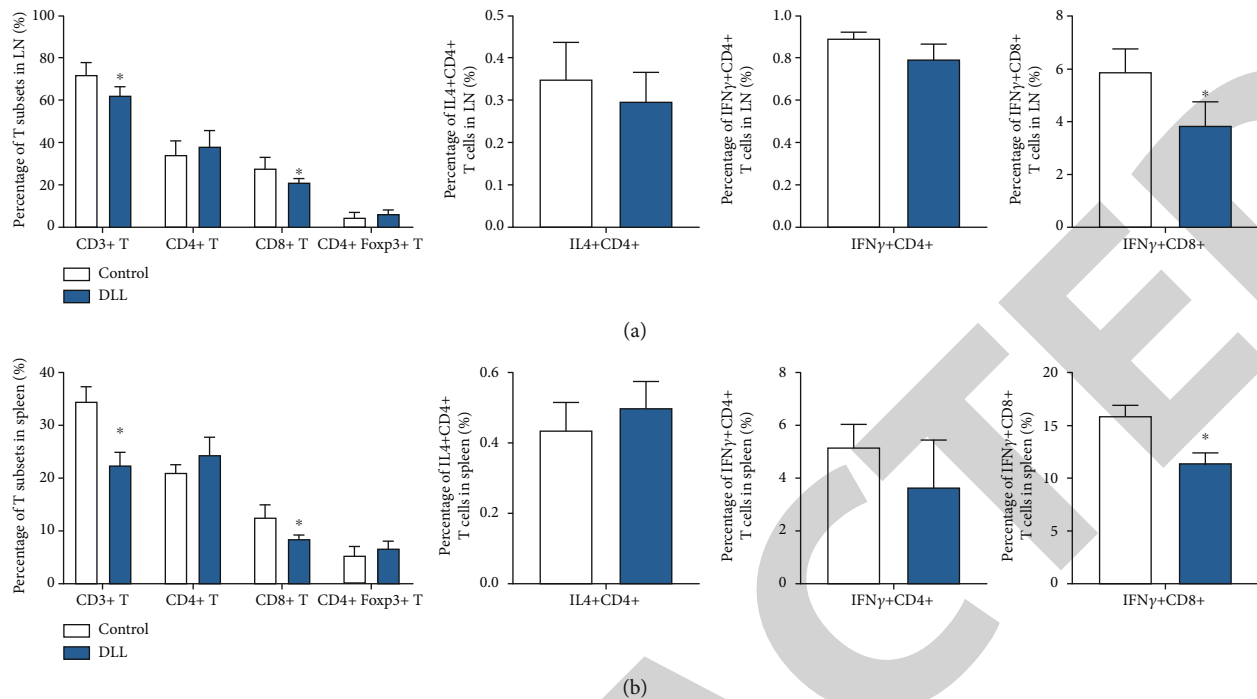


FIGURE 2: DLL slightly reduced the percentage of CD8+ T cells and their IFN- $\gamma$  production in naive mice. (a, b) T cells in the LNs (a) and spleen (b) from naive C57BL/6 mice following treatment with DLL or saline were stained with fluorescent antibodies and detected by FACS. DLL treatment reduced the percentage of CD3+/CD8+ T cells and reduced the percentage of CD8+/IFN- $\gamma$ + cells, while having no effect on the percentage of CD4+/IL4+ T cells and CD4+/IFN- $\gamma$ + T cells, suggesting that DLL treatment mildly suppressed the initial immune response. Data are the mean  $\pm$  SD from three independent experiments. \* $P < 0.05$  by Student's  $t$ -test,  $N = 6$ . IFN: interferon; LN: lymph node; DLL: delicaflavone.

[19]. However, it is still unknown whether DLL can influence tumor immune response via m6A modification and oxidative stress.

In this study, we tested the potential roles of DLL in anti-tumor immune response by establishing a lung cancer model (3LL).

## 2. Experimental Procedures

**2.1. Cell Count Kit 8 Assay.** The murine Lewis lung cancer cell line (3LL) was purchased from ATCC (USA) and was cultured in DMEM medium. The medium was supplemented with 10% FBS (fetal bovine serum).

The cell counting kit 8 (CCK-8) cell proliferation kit (cat no. CA1210, Solarbio, Beijing, China) was used to measure the inhibitory effects of DLL on 3LL cells according to the manufacturer's instructions. 3LL cells were cultured on a 96-well plate at a density of 2000 cells/well. After 24 hours of culture, the cells were exposed to different doses of DLL (0, 5, 25, 50, and 100 mg/ml) for 24, 48, or 72 hours. Then, 10  $\mu$ l of the CCK-8 reagent was added for 2-hour incubation at 37°C. The 450 nm absorbance was recorded.

**2.2. Mice.** C57BL/6 mice (male, 6 weeks, 18–20 g) and nude mice (male, 6 weeks, 18–20 g) were purchased from the Shanghai Experimental Center of the Chinese Academy of Sciences. Animal experiments were ethically approved by the Experimental Animal Ethics Committee of Fujian Medical University.

**2.3. Construction of Tumor-Bearing Mice and DLL Treatment.** Nude mice or immunocompetent C57BL/6 mice were randomly divided into the DLL group ( $n = 6$ ) and the control group (treated with equal volume saline,  $n = 6$ ). Nude mice or immunocompetent C57BL/6 mice were injected subcutaneously with  $5 \times 10^4$  3LL tumor cells (day 0). On day 4, mice in the DLL group were injected with DLL (0.5 mg/kg/day, s.c.) into the subcutaneous tumors, once a day, for a total of 7 times [6]. The tumor size was measured every 2 days to monitor tumor growth in mice.

**2.4. In Vivo Anti-IFN- $\gamma$  Processing.** Four days after subcutaneous injection of 3LL lung tumor cells, DLL was administered intraperitoneally (0.5 mg/kg) into mice once a day, and anti-IFN- $\gamma$  antibody (250  $\mu$ g) was intraperitoneally injected once a day for 7 times [20].

**2.5. Flow Cytometry.** Immune cells were stained with antibodies (anti-CD3, anti-CD4, and anti-CD8, Abcam, USA) for 30 min at 4°C. The Fixation & Permeabilization Kit (Southern Biotech, Birmingham, USA) was used for staining intracellular IFN- $\gamma$ , IL-4, and Foxp3. The fluorescence was determined on BD FACSAria Fusion and analyzed with FlowJo software (v10.8) (Becton, Dickinson and Company, Ashland, OR, USA).

**2.6. Sorting T Cells.** The Dynabeads Untouched Mouse T Cells kit (Life Technologies) was used for isolating T cells from spleen and lymph nodes according to the manufacturer's

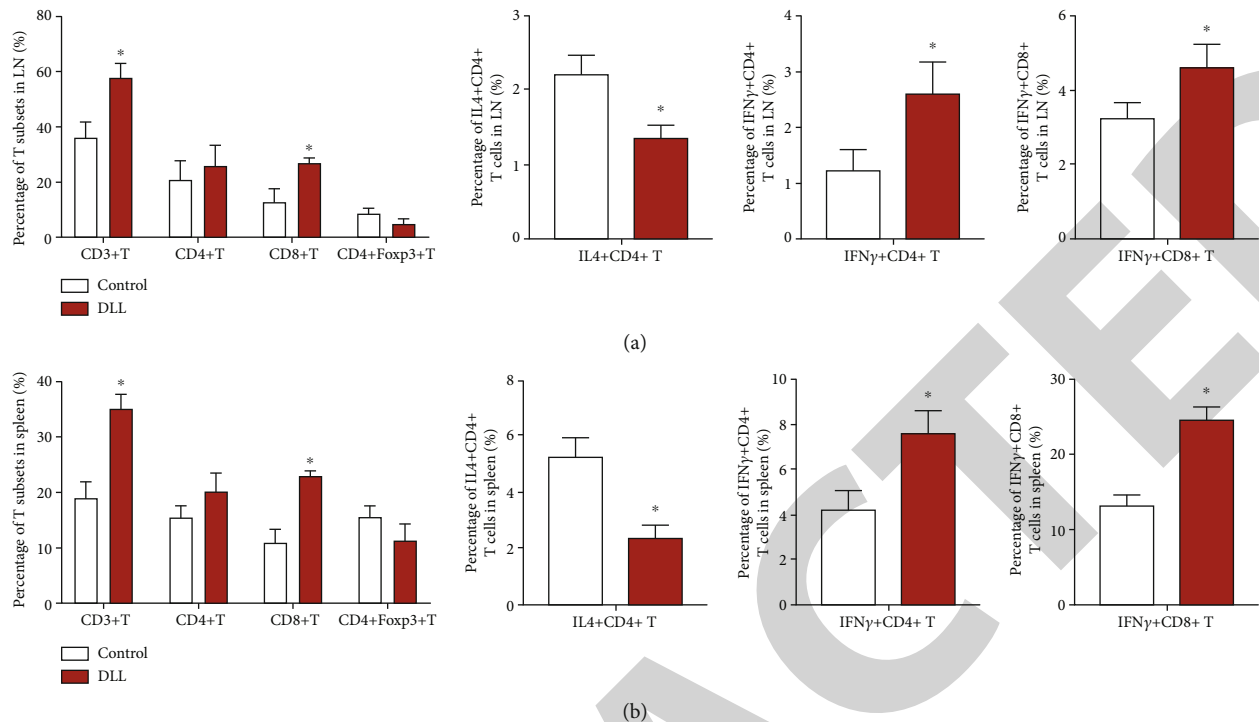


FIGURE 3: DLL increased the percentage of T cells and the cytokine production in tumor-bearing mice. T cells derived from LNs (a) and spleen (b) of DLL-treated tumor-bearing mice were stained with fluorescent antibodies. Foxp3 and cytokine production of CD4+ and CD8+ T cells were also analyzed by detecting intercellular expression. DLL treatment significantly increased the percentage of CD3+ T cells, CD8+ T cells, and IFN- $\gamma$ + T cells in the lymph nodes and spleen and decreased the percentage of Treg T cells and CD4+/IL4+ T cells. Data are the mean  $\pm$  SD from three independent experiments. \* $P < 0.05$  by Student's  $t$ -test,  $N = 6$ . LN: lymph node; DLL: delicaflavone.

instructions. The purified T cells were cultured in a 24-well plate. Effector T cells were activated by CD3 $\epsilon$ /28.

**2.7. Lentiviral Transfection.** To overexpress METTL3 and METTL14 in 3LL cells, lentiviral particles were constructed by Guangzhou Ribo Biological Company (Guangzhou, China). When the cell confluence reached about 80% in a 12-well culture plate, 3LL cells were infected with lentiviral in a 50 multiplicity of infection (MOI) value for 48 h and used for further experiments. The cells infected with negative control virus were used as control.

**2.8. T Cell Proliferation Test In Vitro.** To test the ability of T cells in killing tumor cells, the purified mouse T cells and the treated 3LL cells were cocultured at a ratio of 1:10 for 4 days. The BrdU Cell Proliferation ELISA kit (cat no. ab126556, Abcam) was used to access T cell proliferation in vitro according to the manufacturer's instructions. The data is expressed as the percentage of response T cell proliferation.

**2.9. Real-Time Quantitative Polymerase Chain Reaction (qPCR).** Total RNA was extracted from cells after DLL treatment or transfection using TRIzol. cDNA was then synthesized using Superscript II (ThermoFisher), and qPCR was performed using ChamQ SYBR qPCR Master Mix (cat no. Q311-02, Vazyme, Nanjing, China). The primers are shown in Supplementary Table 1. qPCR was performed as follows: reverse transcription stage: 42°C for 10 min, initial denaturation:

95.0°C for 3 min, denaturation and extension: 38 circles of 95.0°C for 10 s and 60°C for 30 s, and melting curve analysis: 72°C-95.0°C with heating rate 0.5°C/unit time.

**2.10. Commercial Kits.** The Mouse IFN gamma ELISA Kit (ab282874, Abcam), RANTES ELISA Kit (CCL5) (ab100739, Abcam), CXCL9 ELISA Kit (ab203364), IP-10 ELISA Kit (CXCL10), SOD Kit (S0101S, Beyotime, Shanghai), NAD $^{+}$ /NADH Assay Kit (S0175, Beyotime, Shanghai), ATP Assay Kit (S0026, Beyotime, Shanghai), and total Glutathione Peroxidase Assay Kit (S0058, Beyotime, Shanghai) were used for supernatant analysis of the levels of IFN- $\gamma$ , CCL5, CXCL9, CXCL10, SOD, and Gpx according to the manufacturer's instructions.

**2.10.1. Measurement of ROS.** Briefly, after DLL treatment, 3LL cells were collected and incubated with ROS indicator DCFH-DA (10  $\mu$ M) in PBS for 30 min at 37°C. The fluorescence was captured and analyzed using an Accuri C6 plus flow cytometer (BD Biosciences, CA).

**2.11. Western Blotting.** After the indicated treatment, total proteins were extracted using cold RIPA buffer, and the concentrations were determined using a BCA Protein Quantification Kit (cat no. E112-01, Vazyme, Nanjing, China). The protein was separated on SDS-PAGE gel (10%) and transferred to a nitrocellulose membrane. The membranes were blocked with 5% nonfat milk and then incubated with primary antibodies (anti-METTL3, cat no. ab195352; anti-

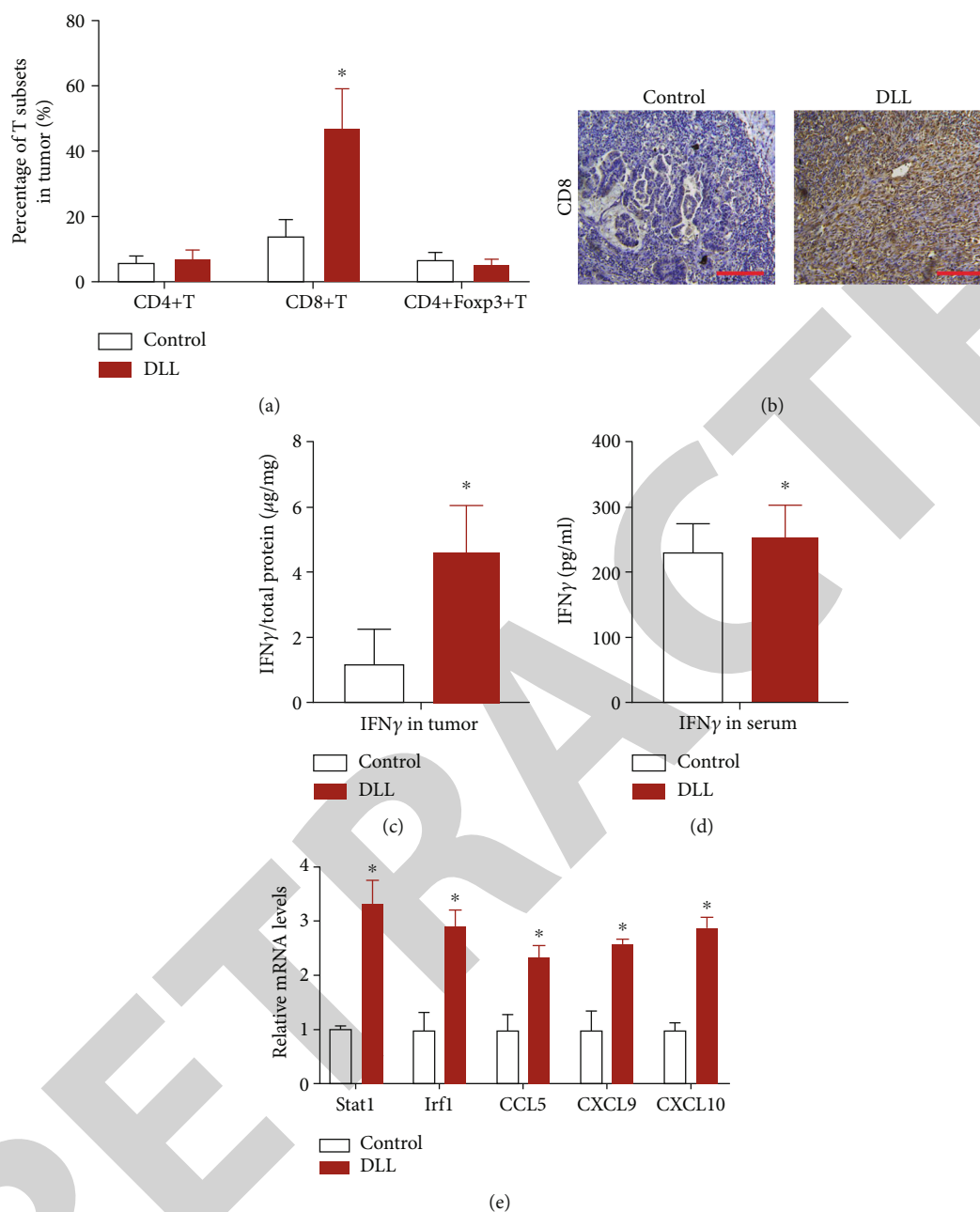
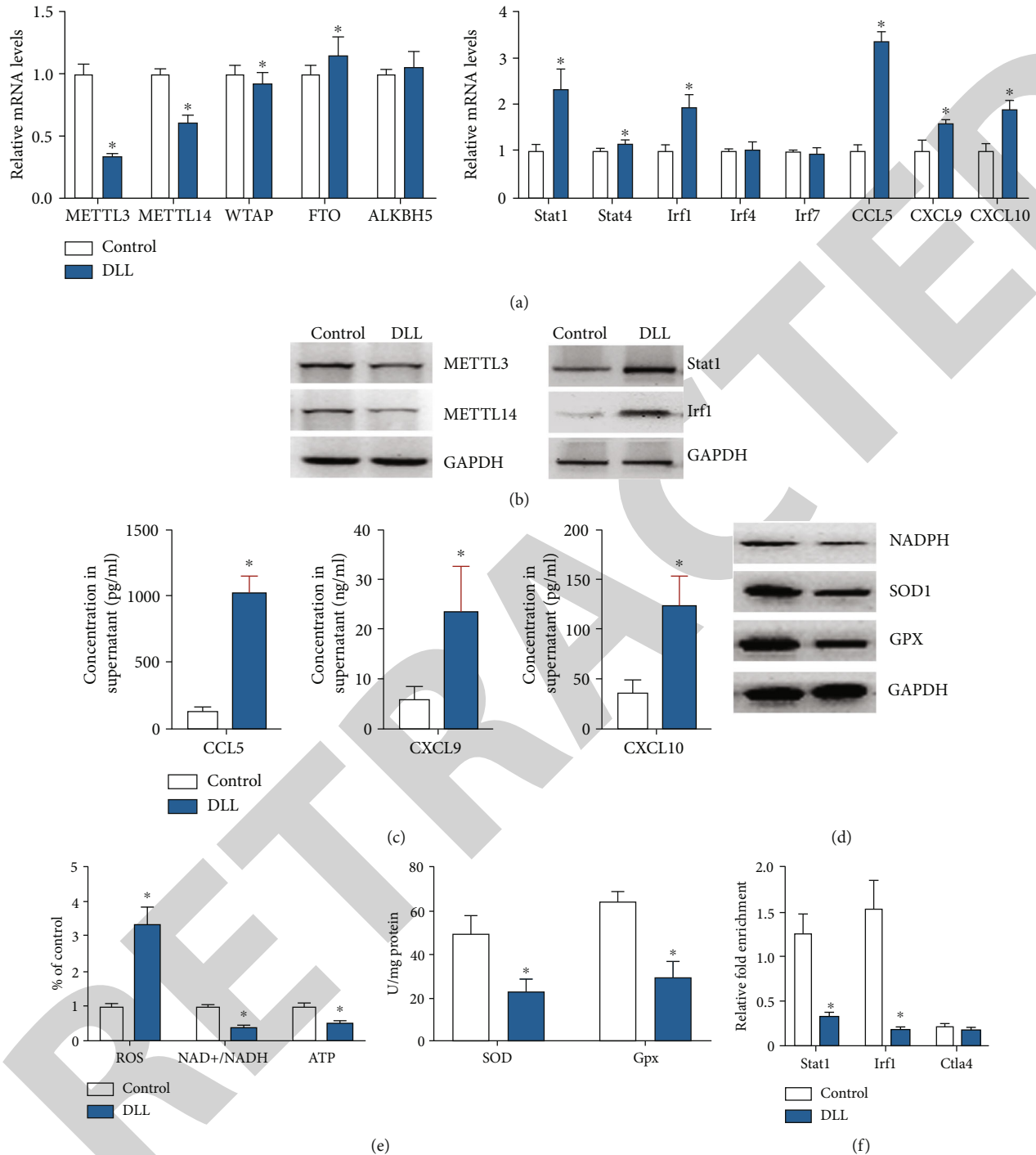


FIGURE 4: DLL enhances tumor-infiltrating CD8+ T cells and cytokine production. (a) Percentage of tumor-infiltrating T cells and Treg cells was identified by flow cytometry from 3LL tumors as indicated. (b) Representative images of CD8 by IHC staining. Tissue sections from BALB/c mice treated with DLL or saline. Scale bars, 200  $\mu\text{m}$ . DLL treatment significantly increased the percentage of CD8+ T cells in tumor. (c, d) IFN- $\gamma$  production in intratumor (c) and serum (d) from BALB/c mice by ELISA. DLL treatment significantly increased IFN- $\gamma$  in tumor but not in serum. (e) Quantitative RT-PCR was performed to identify transcriptional changes of the IFN- $\gamma$  response gene expression in T cells stored from xenografted tumor tissues. DLL treatment significantly upregulated the levels of Stat1, Irf1, CCL5, CXCL9, and CXCL10 in T cells. Data are the mean  $\pm$  SD from three independent experiments. \*  $P < 0.05$  by Student's  $t$ -test,  $N = 6$ . DLL: delicaflavone.

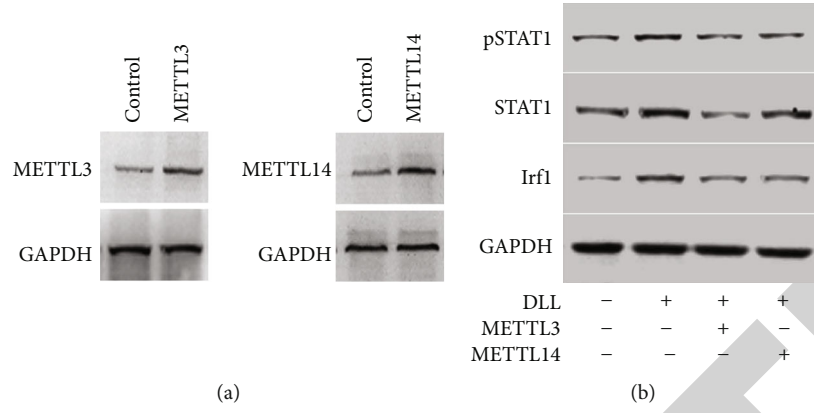
METTL14, cat no. ab220030; anti-stat1, cat no. ab109320; anti-Irf1, cat no. ab243895; anti-STAT1 (phospho S727), cat no. ab278718; and anti-GAPDH, cat no. ab8245. All the antibodies were purchased from Abcam, USA) incubated overnight at 4°C. The next day, after washing with PBS, the membranes were incubated with secondary antibody for 2 h. The positive signal was captured in the gel imaging system. The bands of western blot were quantified by ImageJ,

and the relative protein expression was expressed as the optical density of bands.

**2.12. m6A Methylated RNA Immunoprecipitation Sequencing (MeRIP) qPCR.** A FastPure Cell/Tissue Total RNA Isolation Kit (Vazyme, Nanjing, China) was used to extract total RNA. The RNA was incubated with A/G immunomagnetic beads and m6A antibody premix overnight at

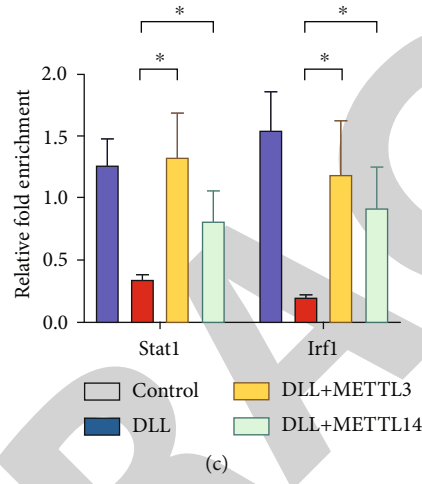


**FIGURE 5: DLL reduces Mettl3/Mettl14-mediated m6A modification on Stat1 and Irf1.** 3LL cells were treated with DLL or saline. (a) Quantitative RT-PCR was performed to identify mRNA levels of the m6A transferases (left) and the IFN- $\gamma$  response gene expression (right). (b) Western blot analysis of Mettl3, Mettl14, Stat1, and Irf1 in DLL-treated 3LL cells. DLL treatment significantly inhibited Mettl3 and Mettl14 expression, while upregulating Stat1 and Irf1 expression in DLL-treated 3LL cells. (c) CCL5, CXCL9, and CXCL10 production in cell culture supernatant by ELISA. DLL treatment significantly upregulated the levels of CCL5, CXCL9, and CXCL10. (d) Western blot analysis of NADPH, SOD1, and GPX in DLL-treated 3LL cells. DLL treatment significantly inhibited NADPH, SOD1, and GPX expression. (e) The ROS, NAD<sup>+</sup>/NADH, and ATP levels were measured. DLL treatment significantly promoted the level of ROS and reduced the levels of NAD<sup>+</sup>/NADH and ATP compared with the control (left). The level of SOD and GPx was measured (right). GAPDH was used as an invariant internal control for calculating protein fold changes. DLL treatment significantly inhibited the activity of SOD and GPx compared with the control. (f) m6A enrichment of Stat1 and Irf1 was examined by m6A RIP-qPCR in control, DLL-treated 3LL cells as indicated. Ctl4 functioned as a m6A negative control. DLL treatment dramatically reduced the m6A methylation on Stat1 and Irf1. Data are the mean  $\pm$  SD from three independent experiments. \* $P < 0.05$  by Student's  $t$ -test,  $N = 6$ . DLL: delicaflavone.

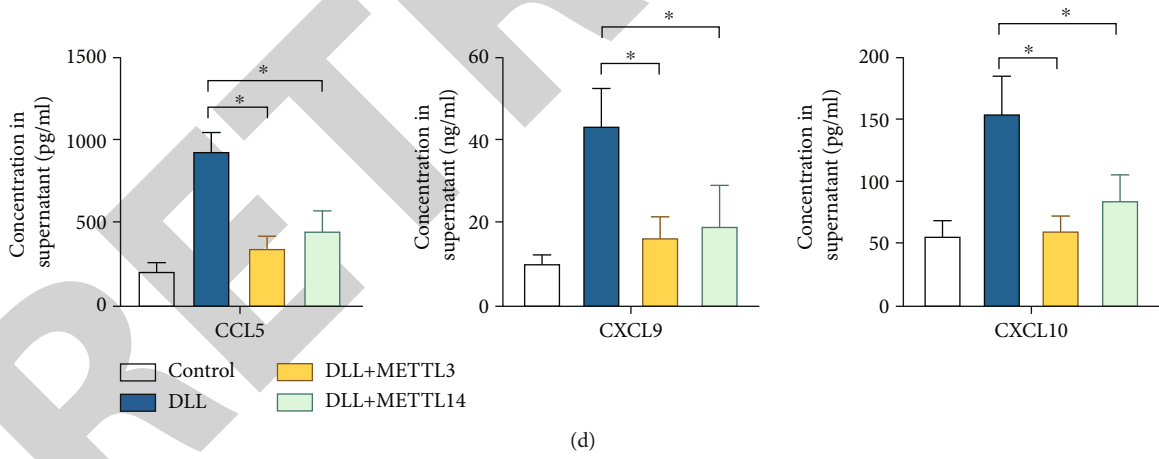


(a)

(b)



(c)



(d)

FIGURE 6: Continued.



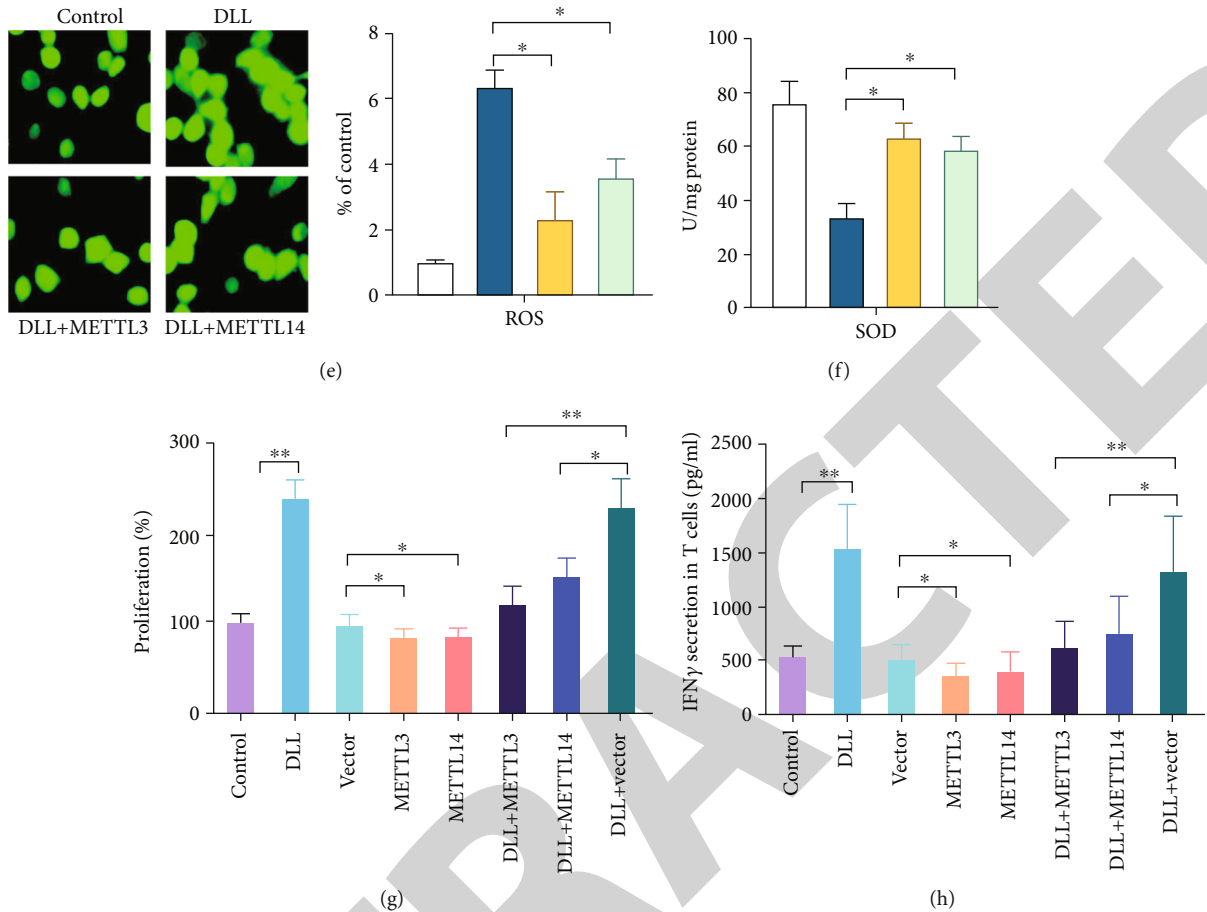


FIGURE 6: Overexpression of Mettl3 or Mettl14 attenuates DLL-mediated IFN- $\gamma$  response. (a) Mettl3 and Mettl14 expression was upregulated in 3LL cells after infection with Mettl3 or Mettl14 expressing lentivirus. (b) The expression of p-Stat1 (phosphorylated), Stat1, and Irf1 was reduced by infection with Mettl3 or Mettl14 expressing lentivirus in DLL-treated 3LL cells. (c) The m6A modification of Stat1 and Irf1 was upregulated by infection with Mettl3 or Mettl14 expressing lentivirus in DLL-treated 3LL cells evaluated by m6A RIP-qPCR. (d) CLL5, CXCL9, and CXCL10 production in cell culture supernatant was reduced by infection with Mettl3 or Mettl14 expressing lentivirus in DLL-treated 3LL cells evaluated by ELISA. (e) The ROS levels were reduced by infection with Mettl3 or Mettl14 expressing lentivirus in DLL-treated 3LL cells. (f) The level of SOD was increased by infection with Mettl3 or Mettl14 expressing lentivirus in DLL-treated 3LL cells. (g) 3LL cells were cocultured for 4 days with T cells acquired from tumor-bearing mice. The specific proliferation of T cells was measured by BrdU incorporation. The proliferation of T cells was inhibited by Mettl3 or Mettl14 expressing 3LL cells, which was reversed by DLL treatment. (h) The secretion of IFN- $\gamma$  was detected by ELISA in cell culture supernatant that 3LL cells cocultured for 4 days with T cells acquired from tumor-bearing mice. The secretion of IFN- $\gamma$  was reduced by coculturing with Mettl3 or Mettl14 expressing 3LL cells, which was reversed by DLL treatment. Data are the mean  $\pm$  SD from three independent experiments. \* $P < 0.05$  and \*\* $P < 0.01$  by Student's *t*-test,  $N = 6$ . DLL: delicaflavone.

4°C. The bounding RNA were eluted from the magnetic beads by adding 30 microliters of RLT buffer. The expression of Stat1 and Irf1 was analyzed by qPCR.

**2.13. Immunohistochemistry.** The paraffin-embedded slides in mouse tumor tissues were deparaffinized and antigen retrieved. After blocking with 5% goat serum (cat no. 5425S, Beyotime, Shanghai, China), the sections were incubated with the primary antibody anti-CD8 (Abcam, ab209775) overnight at 4°C. The sections were incubated with secondary goat anti-mouse IgG antibody (Abcam, ab205719) for 1h. A DAB Horseradish Peroxidase Color Development Kit was used for staining the positive signals and then counterstained with hematoxylin.

**2.14. Statistical Analysis.** All experiments were independently performed three times, and the data were shown as the mean  $\pm$  standard deviation (mean  $\pm$  SD,  $n = 6$ ). Graph-Pad Prism software was used for statistical analysis.  $P < 0.05$  was statistically significant.

### 3. Results

**3.1. DLL Significantly Inhibits Tumor Growth in Immunocompetent Mice.** 3LL cells were exposed to DLL (0, 5, 25, 50, and 100  $\mu$ g/ml). We observed that DLL inhibited 3LL cell viability in a time- and dose-dependent manner (Figure 1(a)). We next injected 3LL cells into immunodeficient nude mice. Four days after injection, DLL (0.5 mg/kg)

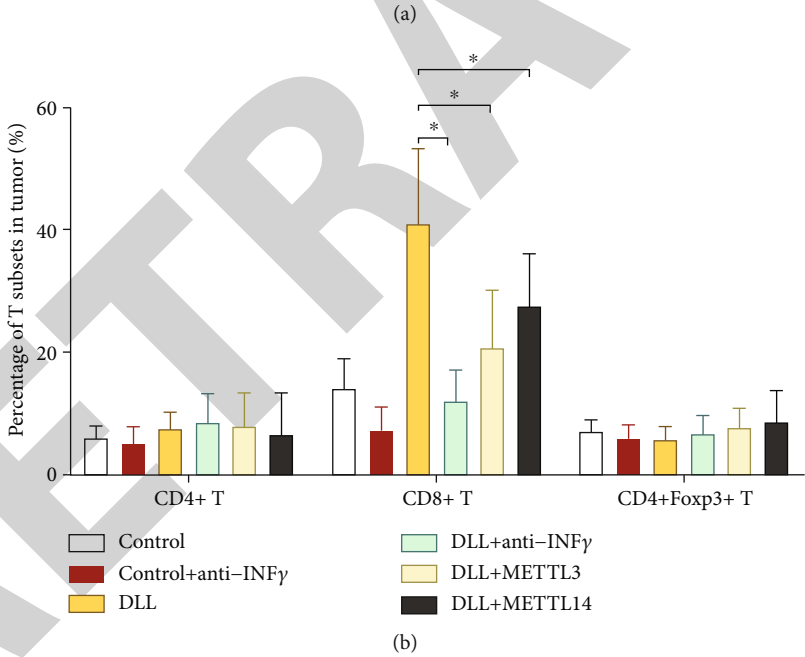
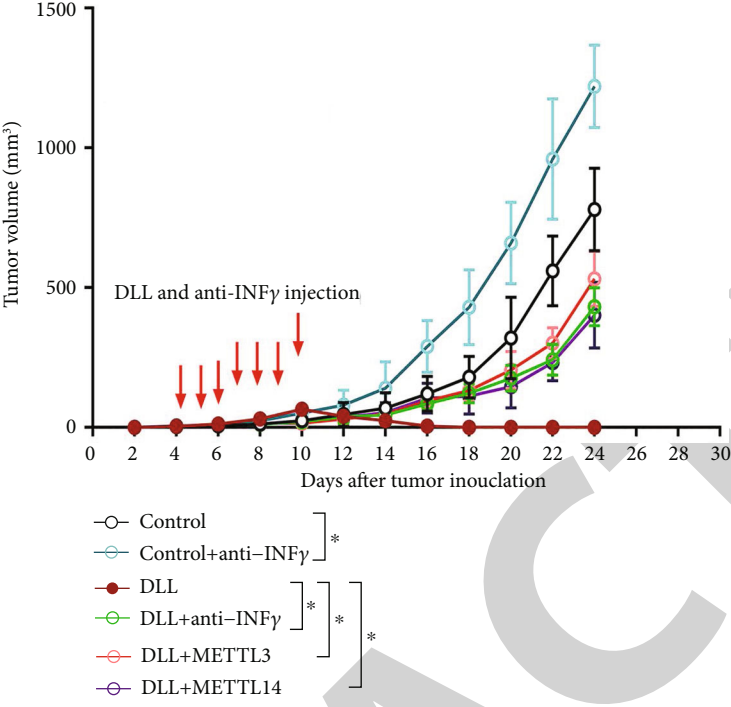
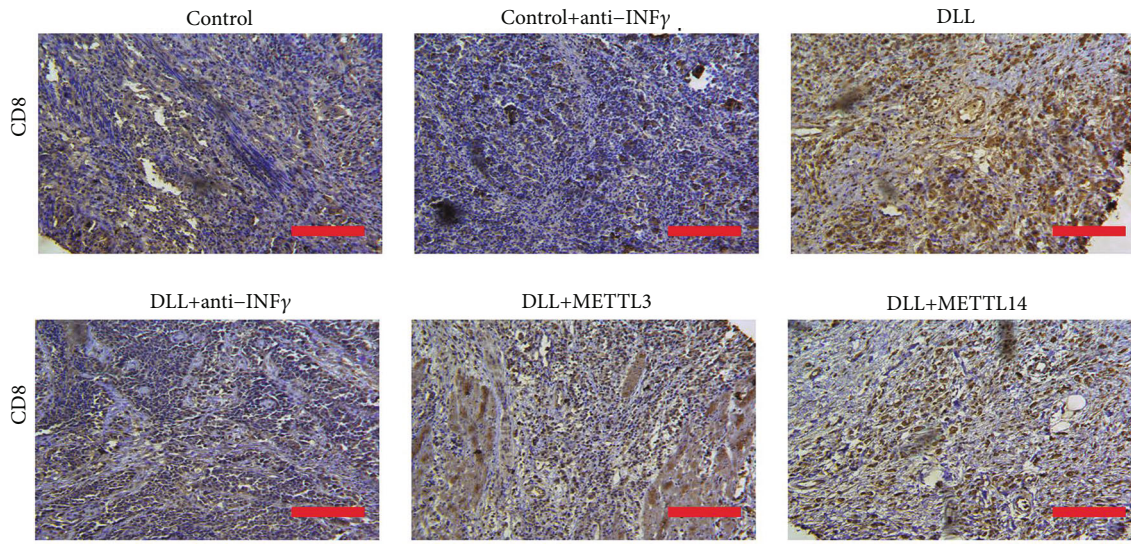
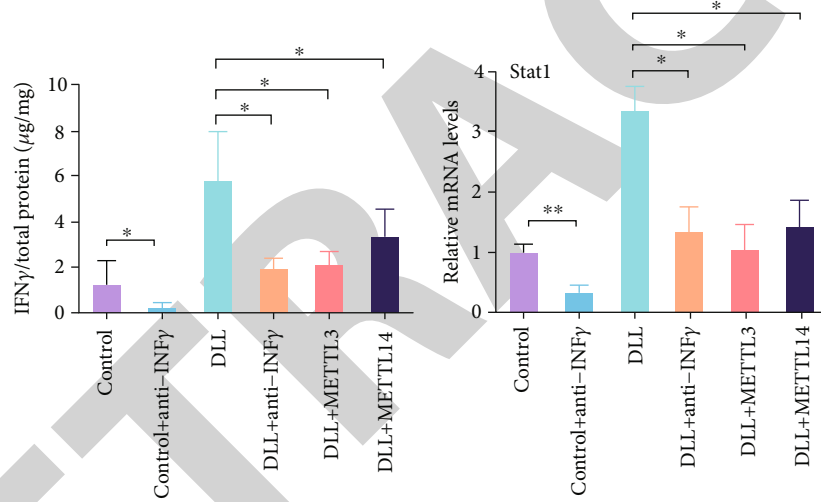


FIGURE 7: Continued.

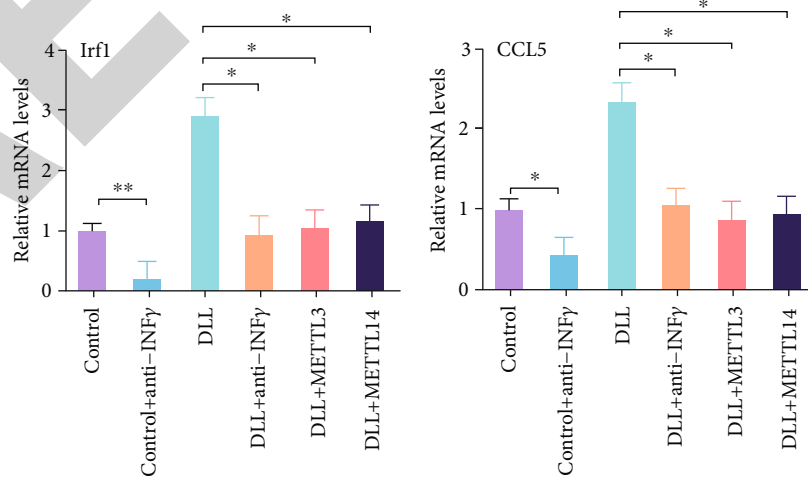


(c)



(d)

(e)



(f)

(g)

FIGURE 7: Continued.

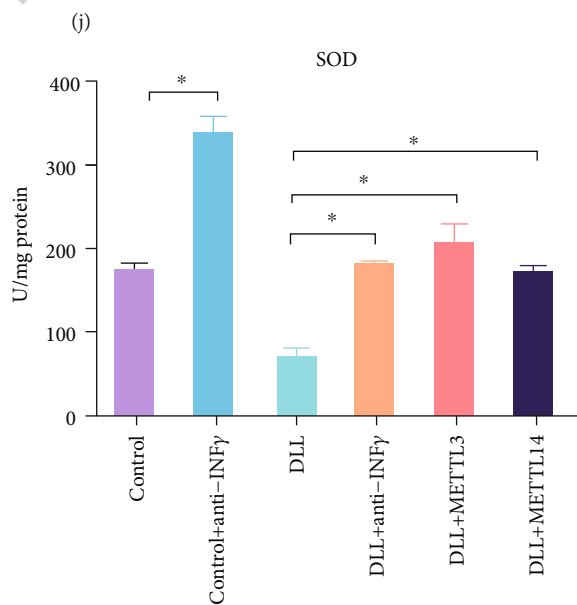
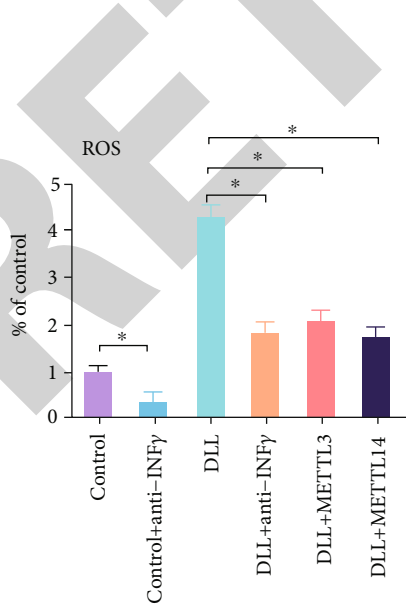
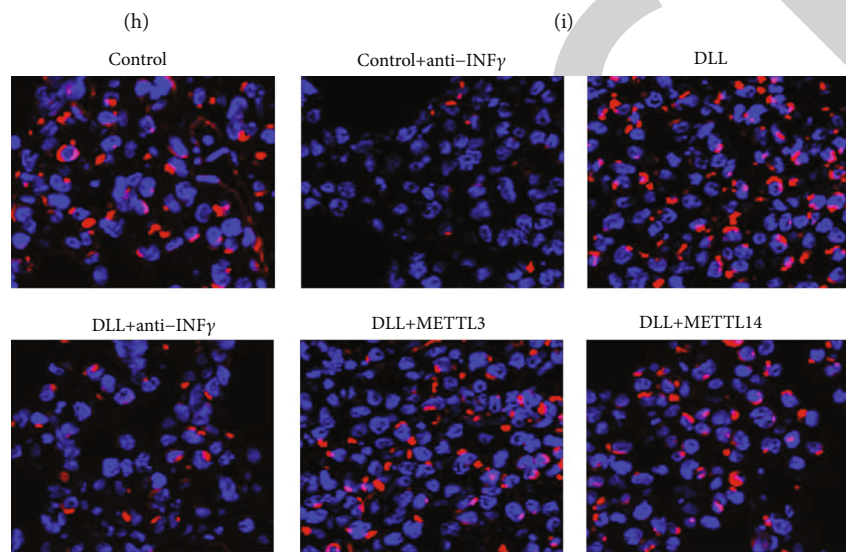
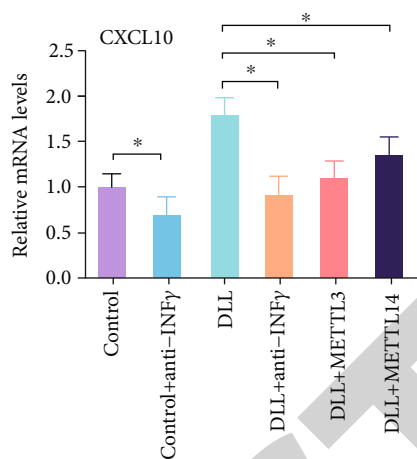
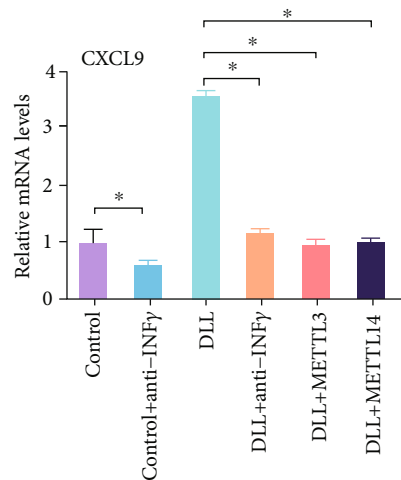


FIGURE 7: Continued.

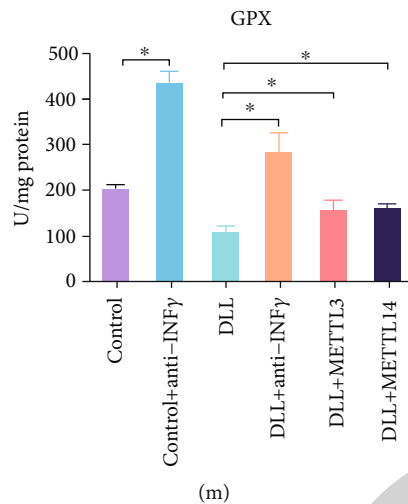


FIGURE 7: Overexpression of Mettl3 or Mettl14 attenuates DLL-mediated tumor-infiltrating CD8<sup>+</sup> T cells and cytokine production. (a) Mice bearing control and Mettl3 or Mettl14 overexpressed tumors were treated with IFN- $\gamma$  blocking antibody and DLL as indicated. Tumor volume was measured over time points. The inhibitory effects of DLL on tumor growth were reversed by Mettl3 or Mettl14 overexpression or IFN- $\gamma$  blocking antibody treatment. (b) Percentage of tumor-infiltrating T cells and Treg cells were identified by flow cytometry from 3LL tumors as indicated. (c) Representative images of CD8 by IHC staining. Tissue sections from BALB/c mice bearing the indicated treatments. DLL-promoted CD8<sup>+</sup> T infiltration was reversed by Mettl3 or Mettl14 overexpression or IFN- $\gamma$  blocking antibody treatment. (d) IFN- $\gamma$  production in intratumor from BALB/c mice by ELISA. DLL-promoted IFN- $\gamma$  secretion was reversed by Mettl3 or Mettl14 overexpression or IFN- $\gamma$  blocking antibody treatment. (e–i) Quantitative RT-PCR was performed to identify transcriptional changes in the IFN- $\gamma$  response gene expression. DLL-enhanced Stat1, Irf1, CLL5, CXCL9, and CXCL10 levels were reversed by Mettl3 or Mettl14 overexpression or IFN- $\gamma$  blocking antibody treatment. (j) The representative images of ROS in tumor. DLL-promoted ROS products were reversed by Mettl3 or Mettl14 overexpression or IFN- $\gamma$  blocking antibody treatment. (k–m) ELISA was performed to measure the concentration of ROS, SOD, and GPX in tumor tissues. DLL-enhanced ROS levels and DLL-reduced SOD and GPX levels were reversed by Mettl3 or Mettl14 overexpression or IFN- $\gamma$  blocking antibody treatment. Data are the mean  $\pm$  SD from three independent experiments. \* $P < 0.05$  by Student's  $t$ -test,  $N = 6$ . DLL: delicaflavone.

was administrated into the tumor site every day for 7 days, and the tumor volumes were detected every two days. Interestingly, the tumor growth of nude mice treated with DLL temporarily slowed down from the 10th to 14th days, but the growth rate increased in the next 10 days (Figure 1(b)), suggesting that DLL not only directly exhibited the antitumor effect on tumor cells but also inhibited tumor cell growth through tumor microenvironment. Next, we injected 3LL cells into the immunocompetent mice (C57BL/6), administrated DLL (0.5 mg/kg) every day for 7 days, and measured tumor volume every two days. Surprisingly, DLL significantly reduced tumor volume in immunocompetent mice compared with nude mice. The tumor almost disappeared on the 16th day in DLL-treated immunocompetent mice (Figure 1(c)). These findings indicate that DLL exhibited the antitumor effect via the host immune system.

**3.2. DLL Slightly Reduces the Percentage of CD8<sup>+</sup> T Cells in Naive Mice.** We tested the roles of DLL on immune response. DLL treatment has no effects on the percentage of CD3<sup>+</sup>/CD4<sup>+</sup> T cells and regulatory T cells. Interestingly, DLL treatment reduced the percentage of CD3<sup>+</sup>/CD8<sup>+</sup> T cells (Figures 2(a) and 2(b)). In addition, DLL treatment significantly reduced the percentage of CD8<sup>+</sup>/IFN- $\gamma$ <sup>+</sup> cells, while having no effect on the percentage of CD4<sup>+</sup>/IL4<sup>+</sup> T cells and CD4<sup>+</sup>/IFN- $\gamma$ <sup>+</sup> T cells (Figures 2(a) and 2(b)). These results revealed that DLL treatment mildly suppressed the initial immune response.

**3.3. DLL Treatment Increases the Percentage of CD8<sup>+</sup> T Cells in Tumor-Bearing Mice.** We next investigated the alterations of immune patterns in DLL-treated immunocompetent tumor-bearing mice. DLL treatment significantly increased the percentage of CD3<sup>+</sup> T cells and CD8<sup>+</sup> T cells in the lymph nodes and spleen and mildly decreased the percentage of Treg T cells (Figures 3(a) and 3(b)). In addition, DLL treatment significantly increased IFN- $\gamma$ <sup>+</sup> T cells, while reducing the percentage of CD4<sup>+</sup>/IL4<sup>+</sup> T cells (Figures 3(a) and 3(b)).

Furthermore, DLL treatment increased significantly the percentage of CD8<sup>+</sup> T cells in tumor tissues, while having no changes in the percentages of CD4<sup>+</sup> T cells and regulatory T cells (Figure 4(a)). The results of immunohistochemistry also confirmed that DLL treatment upregulated the infiltration of CD8<sup>+</sup> T cells (Figure 4(b)). As expected, DLL treatment increased the concentration of the IFN- $\gamma$  factor in the tumor tissue (Figure 4(c)). However, DLL treatment did not alter the concentration of IFN- $\gamma$  in the serum (Figure 4(d)). Additionally, DLL treatment significantly upregulated the IFN- $\gamma$  response gene expression, such as Stat1, Irf1, CCL5, CXCL9, and CXCL10 in T cells stored from xenografted tumor tissue (Figure 4(e)). These findings indicate that the antitumor activity of DLL depends on the induction of Th1-type cell-mediated immune responses.

**3.4. DLL Exerts Antitumor Effects through Mettl3 and Mettl14 and Oxidative Stress.** Studies have shown that traditional Chinese medicine exerts antitumor effects through

epigenetic effects, and m6A methylation modification plays an important role in cancer immunotherapy, but it was not clear whether DLL-mediated antitumor activity was via m6A methylation modification. We used DLL to treat 3LL cells and detected the expression of key enzymes that regulate m6A methylation modification. DLL significantly inhibited *Mettl3* and *Mettl14* expression but had no significant effect on the m6A methylase WTAP and the m6A demethylase FTO and ALKBH5 (Figure 5(a)). Western blot results also showed that DLL significantly inhibited the protein levels of m6A methyltransferases *Mettl3* and *Mettl14* (Figure 5(b)).

IFN- $\gamma$  can stimulate the production of CCL5, CXCL9, and CXCL10 to enhance antitumor immune response [21]. Our results show that DLL mainly exerted antitumor activity by enhancing the CD8<sup>+</sup> T cell recruitment in tumor tissues and the release of IFN- $\gamma$  factors (Figure 4). Stat1, Stat4, Irf1, Irf4, and Irf7 are important transcription factors that regulate the release of cytokines/chemokines. DLL treatment significantly upregulated the levels of Stat1 and Irf1 and the release of cytokines CCL5, CXCL9, and CXCL10 in 3LL cells (Figures 5(a)–5(c)). The balance of oxidation and antioxidation is closely related to the occurrence and development of lung cancer. SOD and GPx are important antioxidative metal enzymes [22, 23]. We tested the level of tumor cell oxidative stress after DLL treatment and found that DLL treatment significantly inhibited the expression of NADPH, SOD1, and GPX and the activity of SOD and GPx, promoted the level of ROS, and reduced the levels of NAD<sup>+</sup>/NADH and ATP compared with the control (Figures 5(d) and 5(e)).

Given that STAT1 and IRF1 play a key role in IFN- $\gamma$  signal transduction and antitumor effects and DLL administration reduced *Mettl3* and *Mettl14* expression, while increasing Stat1 and Irf1 expression, we further analyzed whether DLL played a regulatory role on Stat1 and Irf1 through *Mettl3* and *Mettl14*. The results of MeRIP-qPCR demonstrated that DLL intervention dramatically reduced the m6A methylation levels of Stat1 and Irf1 (Figure 5(f)). Ctla4 functioned as a m6A negative control [24].

We also observed that *Mettl3* or *Mettl14* overexpression significantly attenuated DLL-enhanced Stat1 and Irf1 in 3LL tumor cells (Figures 6(a) and 6(b)), and MeRIP-qPCR results showed that *Mettl3* or *Mettl14* overexpression significantly enhanced the m6A methylation levels of Stat1 and Irf1 that were reduced by DLL treatment (Figure 6(c)). *Mettl3* or *Mettl14* overexpression also significantly reduced the concentration of CCL5, CXCL9, and CXCL10 and inhibited ROS accumulation, while increasing SOD concentration in the supernatant of 3LL cell culture (Figures 6(d)–6(f)). These findings suggest that DLL upregulated the expression of Stat1 and Irf1 and enhanced oxidative stress through inhibiting *Mettl3* and *Mettl14*.

In order to confirm that DLL enhanced T cell activity in tumor-bearing mice through *Mettl3* and *Mettl14*, we purified T cells and cocultured with 3LL cells treated with DLL and/or overexpressed METL3/14 and evaluated T cell proliferation and IFN- $\gamma$  secretion. Compared with the control group, DLL intervention enhanced T cell proliferation, while the overexpression of METL3 and METL14 could signifi-

cantly reduce the effect of DLL (Figure 6(g)). In addition, DLL treatment significantly upregulated cytokine IFN- $\gamma$  secretion, which was eliminated when METL3/14 was overexpressed (Figure 6(h)). These results indicate that DLL increases the production of cytokines and chemokines through the *Mettl3* or *Mettl14* pathway.

**3.5. The Role of DLL Regulating *Mettl3*, *Mettl14*, and IFN- $\gamma$  in Tumor Growth Inhibition.** IFN- $\gamma$  signaling has a significant impact on the antitumor immune response [25]. We next studied the effect of overexpression of *Mettl3* or *Mettl14* and anti-IFN- $\gamma$  antibody on the antitumor activity of DLL *in vivo*. The results of *in vivo* experiments showed that anti-IFN- $\gamma$  antibody administration and overexpression of *Mettl3* or *Mettl14* enhanced tumor growth, which significantly reversed the antitumor activity of DLL (Figure 7(a)). Further analysis of immune cells in tumor tissues found that overexpression of *Mettl3* or *Mettl14* and anti-IFN- $\gamma$  antibodies significantly reduced DLL-mediated CD8<sup>+</sup> T recruitment (Figures 7(b) and 7(c)) and reduced IFN- $\gamma$  secretion in tumor tissues (Figure 7(d)). In addition, *Mettl3* or *Mettl14* overexpression significantly inhibited the expression of closely related genes Stat1, Irf1, CCL5, CXCL9, and CXCL10 in the IFN- $\gamma$  pathway (Figures 7(e)–7(i)). Furthermore, *Mettl3* or *Mettl14* overexpression significantly inhibited the ROS accumulation and increased SOD and GPX levels (Figures 7(j)–7(m)). These results demonstrated that DLL enhanced tumor cell oxidative stress and CD8<sup>+</sup> T cell recruitment, ultimately exerting antitumor activity.

## 4. Discussion

Delicaflavone (DLL) is a hydrophobic component extracted from the plant *Selaginella doederleinii* [26]. DLL inhibited lung cancer growth via the endoplasmic reticular stress pathway and Akt/mTOR/p70S6K signaling pathway [6, 20], induced cervical cancer cell apoptosis via the mitochondrial pathway [27], and induced ROS-mediated colorectal cancer cell apoptosis [5]. In this study, we found that DLL inhibited lung cancer growth both *in vitro* and *in vivo*. Furthermore, DLL effectively inhibited tumor growth in immunocompetent mice.

Tumor cell-released immunosuppressive cytokines cause cancer immunotherapy to fail. Some Chinese medicine extracts, such as Trichosanthin, induce immunosuppressive responses [28]. However, no research has been published on the role of DLL in antitumor immunity. We reported for the first time that DLL treatment reduced CD8<sup>+</sup> T cell percentage in naive mice. Interestingly, in tumor-bearing mice, we observed that DLL significantly upregulated Th1 cytokine production and enhanced CD8<sup>+</sup> T cell infiltration in tumor tissues, thereby enhancing the antitumor immune response.

Phytochemicals have been demonstrated to have the potential to regulate gene expression by modulating m6A modification. Further mechanism investigation found that DLL significantly inhibited *Mettl3* and *Mettl14* expression in 3LL cells. *Mettl3* or *Mettl14* have an oncogene effect on a variety of tumor cells and are closely associated with antitumor immunity [29, 30]. *Mettl3* or *Mettl14* deficiency inhibited tumor

growth in glioblastoma and hepatocellular carcinoma [31–33]. Furthermore, silencing *Mettl3* or *Mettl14* increased the production of cytokines (such as IFN- $\gamma$  and Cxcl9) and the number of CD8+ T cells in colorectal cancer [19]. In this study, we discovered that *Mettl3* or *Mettl14* overexpression reversed DLL's antitumor immune activity, as measured by decreased cytokine and chemokine secretion and downregulation of Stat1-Irf1 expression. These findings suggest that DLL activates the antitumor immune system and alters the tumor microenvironment by inhibiting m6A mRNA transferase. As a result, the dynamic imbalance of m6A modification in lung cancer may control immunotherapy response. However, we could not rule out the possibility of writing and erasing specific RNA modifications through enzymatic translocation under various stress conditions.

IFN- $\gamma$  signal activation and IFN- $\gamma$ -Stat1-Irf1 axis are essential to enhance the sensitivity of tumor cells to immunotherapy. Our findings show that anti-IFN- $\gamma$  antibody treatment can eliminate the antitumor activity of DLL. Mechanistically, we revealed that DLL reduced Stat1 and Irf1 m6A modification abundance by inhibiting *Mettl3* and *Mettl14*, thereby upregulating CCL5, CXCL9, and CXCL10 and inducing oxidative stress. Studies have showed that phytochemicals from natural products induce the accumulation of ROS by damaging DNA biomolecules and triggering cell death-related signaling pathways, including m6A modification [34]. m6A alteration is critical in the creation of tumor immune microenvironment variety and complexity in lung cancer [35]. Reactive oxygen species (ROS) can damage lipids, nucleic acids, and proteins, thereby altering their functions. When a balance between the production of ROS and antioxidative defense is disturbed, the state of oxidative stress occurs [36]. ROS might affect the prognosis of cancer patients through immune response and increase the sensitivity of cancer patients to chemotherapy [37]. The traditional Chinese medicine, Jinfukang, induces lung cancer cell apoptosis through the ROS-mediated ATM/ATR-p53 pathway and DNA damage [38]. Arenobufagin caused apoptosis in the non-small-cell lung cancer (NSCLC) cell line A549 by oxidative stress [39]. Our findings suggest that DLL inhibited lung cancer growth by enhancing ROS-mediated cell death.

CCL5 is a natural adjuvant that can be used to boost anti-tumor immune responses [40, 41]. This finding explained why the antitumor activity of DLL in nude mice was lower than that in immunocompetent mice. Cxcl9 and Cxcl10 extracellular secretion mediates lymphocyte infiltration into tumors and inhibits tumor growth [42, 43]. The activation of chemokine genes in the tumor environment may result in increased levels of CD8+ T and IFN- $\gamma$  in the tumor. Thus, our research provides solid evidence for the use of DLL as an adjuvant drug for lung cancer immunotherapy.

## 5. Limitations

This study uses a mouse-derived cell line and does not involve the analysis of human samples and cells. There may be differences between mouse-derived cells and human cells. Our follow-up research will continue the investigation.

Furthermore, this study did not demonstrate synergy between DLL and existing first-line drugs for lung cancer treatment. If it can be confirmed that DLL can enhance the chemotherapy effect and immunotherapy effect of lung cancer, it will provide a powerful adjuvant drug for lung cancer.

## 6. Conclusion

We found that DLL exerted a tumor suppressor effect by inhibiting m6A transferase and upregulating Stat1 and Irf1 levels to activate antitumor immunity. Our findings provided a potential drug to enhance lung cancer immunotherapy.

## Data Availability

The data that support the findings of this study are available from the corresponding authors upon reasonable request.

## Conflicts of Interest

The authors declare that there is no conflict of interest regarding the publication of this article.

## Authors' Contributions

Xuwen Wang, Dafen Xu, and Bing Chen contributed equally to this work.

## Acknowledgments

The authors thank the Fujian Medical University Ethics Committee for their kind guidance in the animal experiments and the Public Technology Service Center of Fujian Medical University. This work was supported by the National Natural Science Foundation of China (grant numbers: 81973083 and 22074017) and Natural Science Foundation of Fujian Province (grant numbers: 2021J02033, 2021J02034, and 2020J01631).

## Supplementary Materials

Supplementary Table 1: primers used in quantitative polymerase chain reaction. (*Supplementary Materials*)

## References

- [1] Y. Liu, S. Yang, K. Wang et al., "Cellular senescence and cancer: focusing on traditional Chinese medicine and natural products," *Cell Proliferation*, vol. 53, no. 10, article e12894, 2020.
- [2] Y. Fan, Z. Ma, L. Zhao et al., "Anti-tumor activities and mechanisms of traditional Chinese medicines formulas: a review," *Biomedicine & Pharmacotherapy*, vol. 132, article 110820, 2020.
- [3] X. Wang, B. Chen, D. Xu et al., "Molecular mechanism and pharmacokinetics of flavonoids in the treatment of resistant EGF receptor-mutated non-small-cell lung cancer: a narrative review," *British Journal of Pharmacology*, vol. 178, no. 6, pp. 1388–1406, 2021.
- [4] J. S. Lee, J. Y. Sul, J. B. Park et al., "Fatty acid synthase inhibition by amentoflavone suppresses HER2/neu (erbB2)

- oncogene in SKBR3 human breast cancer cells,” *Phytotherapy Research*, vol. 27, no. 5, pp. 713–720, 2013.
- [5] W. Yao, Z. Lin, P. Shi et al., “Delicaflavone induces ROS-mediated apoptosis and inhibits PI3K/AKT/mTOR and Ras/MEK/Erk signaling pathways in colorectal cancer cells,” *Biochemical Pharmacology*, vol. 171, article 113680, 2020.
  - [6] X. Wang, B. Chen, D. Xu, Z. Li, Y. Sui, and X. Lin, “Delicaflavone reverses cisplatin resistance via endoplasmic reticulum stress signaling pathway in non-small cell lung cancer cells,” *Oncotargets and Therapy*, vol. Volume 13, pp. 10315–10322, 2020.
  - [7] X. Q. Hu and S. B. Su, “An overview of epigenetics in Chinese medicine researches,” *Chinese Journal of Integrative Medicine*, vol. 23, no. 9, pp. 714–720, 2017.
  - [8] J. Sivinski, D. D. Zhang, and E. Chapman, “Targeting NRF2 to treat cancer,” *Seminars in Cancer Biology*, vol. 76, pp. 61–73, 2021.
  - [9] T. Efferth and F. Oesch, “Anti-inflammatory and anti-cancer activities of frankincense: targets, treatments and toxicities,” *Seminars in Cancer Biology*, vol. 80, pp. 39–57, 2022.
  - [10] R. Jiao, Y. Liu, H. Gao, J. Xiao, and K. F. So, “The anti-oxidant and antitumor properties of plant polysaccharides,” *The American Journal of Chinese Medicine*, vol. 44, no. 3, pp. 463–488, 2016.
  - [11] N. Chen, J. Tang, Q. Su et al., “Paraquat-induced oxidative stress regulates N6-methyladenosine (m<sup>6</sup>A) modification of circular RNAs,” *Environmental Pollution*, vol. 290, article 117816, 2021.
  - [12] C. Zhuang, C. Zhuang, X. Luo et al., “N6-Methyladenosine demethylase FTO suppresses clear cell renal cell carcinoma through a novel FTO-PGC-1 $\alpha$  signalling axis,” *Journal of Cellular and Molecular Medicine*, vol. 23, no. 3, pp. 2163–2173, 2019.
  - [13] C. Zhang, A. Quinones, and A. Le, “Metabolic reservoir cycles in cancer,” *Seminars in Cancer Biology*, 2022.
  - [14] T. Wang, S. Kong, M. Tao, and S. Ju, “The potential role of RNA N6-methyladenosine in cancer progression,” *Molecular Cancer*, vol. 19, no. 1, p. 88, 2020.
  - [15] L. He, H. Li, A. Wu, Y. Peng, G. Shu, and G. Yin, “Functions of N6-methyladenosine and its role in cancer,” *Molecular Cancer*, vol. 18, no. 1, p. 176, 2019.
  - [16] M. Li, X. Zha, and S. Wang, “The role of N6-methyladenosine mRNA in the tumor microenvironment,” *Cancer*, vol. 1875, no. 2, article 188522, 2021.
  - [17] S. Yang, J. Wei, Y. H. Cui et al., “m<sup>6</sup>A mRNA demethylase FTO regulates melanoma tumorigenicity and response to anti-PD-1 blockade,” *Nature Communications*, vol. 10, no. 1, p. 2782, 2019.
  - [18] N. Li, Y. Kang, L. Wang et al., “ALKBH5 regulates anti-PD-1 therapy response by modulating lactate and suppressive immune cell accumulation in tumor microenvironment,” *Proceedings of the National Academy of Sciences of the United States of America*, vol. 117, no. 33, pp. 20159–20170, 2020.
  - [19] L. Wang, H. Hui, K. Agrawal et al., “m<sup>6</sup>A RNA methyltransferases METTL3/14 regulate immune responses to anti-PD-1 therapy,” *The EMBO Journal*, vol. 39, no. 20, article e104514, 2020.
  - [20] Y. Sui, H. Yao, S. Li et al., “Delicaflavone induces autophagic cell death in lung cancer via Akt/mTOR/p70S6K signaling pathway,” *Journal of Molecular Medicine (Berlin, Germany)*, vol. 95, no. 3, pp. 311–322, 2017.
  - [21] F. Castro, A. P. Cardoso, R. M. Goncalves, K. Serre, and M. J. Oliveira, “Interferon-gamma at the crossroads of tumor immune surveillance or evasion,” *Frontiers in Immunology*, vol. 9, p. 847, 2018.
  - [22] M. W. Park, H. W. Cha, J. Kim et al., “NOX4 promotes ferroptosis of astrocytes by oxidative stress-induced lipid peroxidation via the impairment of mitochondrial metabolism in Alzheimer's diseases,” *Redox Biology*, vol. 41, article 101947, 2021.
  - [23] H. Liu, L. Wang, X. Weng et al., “Inhibition of Brd4 alleviates renal ischemia/reperfusion injury-induced apoptosis and endoplasmic reticulum stress by blocking FoxO4-mediated oxidative stress,” *Redox Biology*, vol. 24, article 101195, 2019.
  - [24] H. Wang, X. Hu, M. Huang et al., “Mettl3-mediated mRNA m<sup>6</sup>A methylation promotes dendritic cell activation,” *Nature Communications*, vol. 10, no. 1, p. 1898, 2019.
  - [25] P. Ramesh, R. Shivde, D. Jaishankar, D. Saleiro, and I. C. Le Poole, “A palette of cytokines to measure anti-tumor efficacy of T cell-based therapeutics,” *Cancers (Basel)*, vol. 13, no. 4, p. 821, 2021.
  - [26] B. Chen, X. Wang, D. Lin et al., “Proliposomes for oral delivery of total biflavonoids extract from *Selaginella doederleinii*: formulation development, optimization, and in vitro-in vivo characterization,” *International Journal of Nanomedicine*, vol. Volume 14, pp. 6691–6706, 2019.
  - [27] W. Yao, Z. Lin, G. Wang et al., “Delicaflavone induces apoptosis via mitochondrial pathway accompanying G2/M cycle arrest and inhibition of MAPK signaling cascades in cervical cancer HeLa cells,” *Phytomedicine*, vol. 62, article 152973, 2019.
  - [28] Y. Cai, S. Xiong, Y. Zheng, F. Luo, P. Jiang, and Y. Chu, “Trichosanthin enhances anti-tumor immune response in a murine Lewis lung cancer model by boosting the interaction between TSLC1 and CRTAM,” *Cellular & Molecular Immunology*, vol. 8, no. 4, pp. 359–367, 2011.
  - [29] C. Zeng, W. Huang, Y. Li, and H. Weng, “Roles of METTL3 in cancer: mechanisms and therapeutic targeting,” *Journal of Hematology & Oncology*, vol. 13, no. 1, p. ???, 2020.
  - [30] Y. Gao, R. Vasic, Y. Song et al., “m<sup>6</sup>A modification prevents formation of endogenous double-stranded rnas and deleterious innate immune responses during hematopoietic development,” *Immunity*, vol. 52, no. 6, pp. 1007–1021.e8, 2020.
  - [31] T. Li, P. S. Hu, Z. Zuo et al., “METTL3 facilitates tumor progression via an m<sup>6</sup>A-IGF2BP2-dependent mechanism in colorectal carcinoma,” *Molecular Cancer*, vol. 18, no. 1, p. ???, 2019.
  - [32] S. Lin, J. Choe, P. Du, R. Triboulet, and R. I. Gregory, “The m<sup>6</sup>A methyltransferase METTL3 promotes translation in human cancer cells,” *Molecular Cell*, vol. 62, no. 3, pp. 335–345, 2016.
  - [33] I. Barbieri, K. Tzelepis, L. Pandolfini et al., “Promoter-bound METTL3 maintains myeloid leukaemia by m<sup>6</sup>A-dependent translation control,” *Nature*, vol. 552, no. 7683, pp. 126–131, 2017.
  - [34] P. Wang, F. Long, H. Lin, S. Wang, and T. Wang, “Dietary phytochemicals targeting Nrf2 to enhance the radiosensitivity of cancer,” *Oxidative Medicine and Cellular Longevity*, vol. 2022, Article ID 7848811, 15 pages, 2022.
  - [35] F. Jiang, Y. Hu, X. Liu, M. Wang, and C. Wu, “Methylation pattern mediated by m<sup>6</sup>A regulator and tumor microenvironment invasion in lung adenocarcinoma,” *Oxidative Medicine and Cellular Longevity*, vol. 2022, 2930315 pages, 2022.



## Retraction

# Retracted: miR-494-3p Promotes Erastin-Induced Ferroptosis by Targeting REST to Activate the Interplay between SP1 and ACSL4 in Parkinson's Disease

### Oxidative Medicine and Cellular Longevity

Received 20 June 2023; Accepted 20 June 2023; Published 21 June 2023

Copyright © 2023 Oxidative Medicine and Cellular Longevity. This is an open access article distributed under the Creative Commons Attribution License, which permits unrestricted use, distribution, and reproduction in any medium, provided the original work is properly cited.

This article has been retracted by Hindawi following an investigation undertaken by the publisher [1]. This investigation has uncovered evidence of one or more of the following indicators of systematic manipulation of the publication process:

- (1) Discrepancies in scope
- (2) Discrepancies in the description of the research reported
- (3) Discrepancies between the availability of data and the research described
- (4) Inappropriate citations
- (5) Incoherent, meaningless and/or irrelevant content included in the article
- (6) Peer-review manipulation

The presence of these indicators undermines our confidence in the integrity of the article's content and we cannot, therefore, vouch for its reliability. Please note that this notice is intended solely to alert readers that the content of this article is unreliable. We have not investigated whether authors were aware of or involved in the systematic manipulation of the publication process.

Wiley and Hindawi regrets that the usual quality checks did not identify these issues before publication and have since put additional measures in place to safeguard research integrity.

We wish to credit our own Research Integrity and Research Publishing teams and anonymous and named external researchers and research integrity experts for contributing to this investigation.

The corresponding author, as the representative of all authors, has been given the opportunity to register their agreement or disagreement to this retraction. We have kept a record of any response received.

### References

- [1] J. Ma, X. Li, Y. Fan et al., "miR-494-3p Promotes Erastin-Induced Ferroptosis by Targeting REST to Activate the Interplay between SP1 and ACSL4 in Parkinson's Disease," *Oxidative Medicine and Cellular Longevity*, vol. 2022, Article ID 7671324, 17 pages, 2022.

## Research Article

# miR-494-3p Promotes Erastin-Induced Ferroptosis by Targeting REST to Activate the Interplay between SP1 and ACSL4 in Parkinson's Disease

Jianjun Ma<sup>1,2,3</sup>, Xiaohuan Li<sup>1,2</sup>, Yongyan Fan<sup>1,2</sup>, Dawei Yang<sup>1,2</sup>, Qi Gu<sup>1,2,3</sup>, Dongsheng Li<sup>1,2,3</sup>, Siyuan Chen<sup>1,2,3</sup>, Shaopu Wu<sup>1,2,3</sup>, Jinhua Zheng<sup>1,2,3</sup>, Hongqi Yang<sup>1,2,3</sup> and Xue Li<sup>1,2,3</sup>

<sup>1</sup>Department of Neurology, Henan Provincial People's Hospital, Zhengzhou, Henan 450003, China

<sup>2</sup>Department of Neurology, Zhengzhou University People's Hospital, Zhengzhou, Henan 450003, China

<sup>3</sup>Department of Neurology, Henan University People's Hospital, Zhengzhou, Henan 450003, China

Correspondence should be addressed to Jianjun Ma; majj1124@163.com

Received 31 March 2022; Revised 28 June 2022; Accepted 18 July 2022; Published 29 July 2022

Academic Editor: Tian Li

Copyright © 2022 Jianjun Ma et al. This is an open access article distributed under the Creative Commons Attribution License, which permits unrestricted use, distribution, and reproduction in any medium, provided the original work is properly cited.

**Background.** Ferroptosis is a type of iron-dependent programmed cell death. Ferroptosis has been shown to be a significant factor for the pathogenesis of Parkinson's disease (PD). However, the mechanism involved in ferroptosis has not been fully elucidated in PD. **Methods.** Repressor element-1 silencing transcription factor (REST) and specificity protein 1 (SP1) expressions were monitored by qRT-PCR. Cell viability, reactive oxygen species (ROS), and mitochondrial injury were validated by CCK-8, flow cytometry, and transmission electron microscope. The levels of neurons-related proteins and ferroptosis-associated proteins were identified by western blot and immunofluorescence assays. The interaction between miR-494-3p and REST or SP1 and ACSL4 was analyzed by luciferase, chromatin immunoprecipitation, or EMSA assay. **Results.** Erastin could dose-dependently induce neuron injury and ferroptosis of LUHMES cells. miR-494-3p overexpression induced ROS production, mitochondrial damage, ferroptosis, and neuron injury in erastin-induced LUHMES cells. Likewise, miR-494-3p inhibition had the opposite effects. We also showed that REST was a target gene of miR-494-3p and could repress erastin-induced ferroptosis, neuron injury, ROS, and mitochondrial injury via SP1 in LUHMES cells. Moreover, we demonstrated that SP1 could interact with ACSL4. We also confirmed that miR-494-3p could aggravate the pathological changes of substantia nigra and corpus striatum in the MPTP-induced PD mouse model. **Conclusion.** miR-494-3p significantly promotes ferroptosis by regulating the REST/SP1/ACSL4 axis in PD. Thus, our results open potential therapeutic targets for PD.

## 1. Introduction

Parkinson's disease (PD) is the second most common neurodegenerative disease after Alzheimer's. The primary pathological features of PD are the degeneration and loss of dopaminergic neurons in substantia nigra pars compacta of the midbrain [1–3]. Studies manifested that PD can cause static tremor, muscle rigidity, sleep disorders, bradykinesia, abnormal attitudinal reflexes, sensory disorders, autonomic nervous dysfunction, and other clinical manifestations [4, 5]. It has been reported that many factors are involved in the occurrence of PD, including the environment, genetics,

aging, oxidative stress, inflammation, mitochondrial dysfunction, lack of neurotrophic factors, and abnormal accumulation of iron [6–8]. Meanwhile, various cell death modes, including apoptosis, autophagy, and necrosis, also participate in the pathological process of PD [9, 10]. However, the pathogenesis of PD is still not fully understood in the existing studies.

Ferroptosis is a new type of cell death caused by iron-dependent oxidative damage, which is different from apoptosis, necrosis, and autophagy in aspects of morphology, biochemistry, and genetics [11]. As a mode of iron-dependent cell death, iron has a significant effect on ferroptosis

[12]. Neuroimaging examination and autopsy pathology report of PD patients confirmed a large amount of iron deposition in the substantia nigra and increased iron content in the remaining dopaminergic neurons. Iron selectively aggregates in the substantia nigra in early PD patients, suggesting that iron can be served as a biomarker and imaging indicator to reflect the progression of PD [13]. Recent researches also verified that ferroptosis could facilitate PD progression [14, 15]. However, the mechanism of ferroptosis involvement in the degeneration of dopaminergic neurons in PD substantia nigra is still unclear. Therefore, a better understanding of the pathogenesis of ferroptosis in PD will aid in providing new ideas for PD therapy.

MicroRNAs (miRNAs) are a class of cellular endogenous, highly conserved, noncoding small RNA molecules, approximately 21-25 nucleotides in length [16]. The main function of miRNAs is to regulate gene expression at the transcriptional level to exert physiological functions [17]. It has been reported that miRNAs can participate in cell proliferation, differentiation, apoptosis, inflammatory response, autophagy, and other biological characteristics [18]. And miRNAs are also associated with neurodegenerative diseases, including PD [19, 20]. Meanwhile, miRNAs, such as miR-137, miR-424-5p, and miR-30-5p, were proven to be relevant to ferroptosis [21]. Moreover, the latest study showed that miR-494-3p could induce PD progression by SIRT3 [22], and pramipexole could prevent neurotoxicity by miR-494-3p in PD [23]. Through literature screening, we also found that miR-494-3p is associated with multiple diseases, including myocardial infarction [24], lung cancer [25], and hepatocellular carcinoma [26]. While the function and mechanism of miR-494-3p in ferroptosis-mediated PD are still broadly unknown.

In the current study, we verified the potential function and mechanism of miR-494-3p in PD through *in vivo* and *in vitro* experiments, especially the regulation of ferroptosis, which may provide a novel target for PD treatment.

## 2. Materials and Methods

**2.1. Cell Treatment.** To establish the ferroptosis cell model, different concentrations (0, 0.25, 0.5, 1, 2, and 4  $\mu\text{M}$ ) of erastin (Tocris, USA) were used to stimulate the LUHMES for 24 hours [27, 28]. Negative control (NC), miR-494-3p mimics, and miR-494-3p inhibitor were purchased from GenePharma (Suzhou, China). Empty vector, REST-overexpressed plasmids, SP1-overexpressed plasmids, REST shRNAs (sh-REST), and sh-NC were acquired from Hanbio Biotechnology (China). In 6-well plates, LUHMES cells ( $5 \times 10^4$  cells/well) were transfected with these oligodeoxynucleotides or overexpressed plasmids using Lipofectamine 3000 (Invitrogen) for 48 hours based on the specification. 100 nM ferroptosis inhibitor (ferrostatin-1, Selleck, USA) or mithramycin was added to the erastin-stimulated LUHMES cells for 1 hour [29].

**2.2. Animal.** Healthy C57BL/6 male mice (weight  $20 \pm 1$  g) were purchased from the Henan Experimental Animal Center and kept in the Henan Experimental Animal Center with

temperature ( $24^\circ\text{C} \pm 2^\circ\text{C}$ ), humidity ( $55\% \pm 5\%$ ), and 12 hours light/12 hours darkness and sterile water. The Ethics Committee of Henan University People's Hospital has approved the animal experiment (No. 2019-76). PD mouse model was established by intraperitoneal injection of 30 mg/kg 1-methyl-4-phenyl-1,2,3,6-tetrahydropyridine (MPTP; Sigma, Cat. no. MO896) for 7 days [30]. Then, PD model mice were randomly divided into 6 groups: sham ( $n = 8$ , mice were intraperitoneally injected with 30 mg/kg normal saline for 7 days), MPTP ( $n = 8$ , mice were intraperitoneally injected with 30 mg/kg MPTP for 7 days), MPTP+NC ( $n = 8$ , a stereotactic catheter was implanted into the right lateral ventricle of MPTP-treated mice through surgery, and NC was injected through the catheter for 5 days), MPTP+miR-494-3p antagomir ( $n = 8$ , 5  $\mu\text{L}$  of saline with 20 nmol/L miR-494-3p antagomir was injected through the catheter for 5 days in the MPTP-treated mice), MPTP+miR-494-3p agomir ( $n = 8$ , 5  $\mu\text{L}$  of saline with 20 nmol/L miR-494-3p agomir was injected through the catheter for 5 days in the MPTP-treated mice) [31, 32], and MPTP+ferrostatin-1 ( $n = 8$ , mice were injected with 2.5 mM ferrostatin-1 via ventricle 1 day before the MPTP intoxication) groups [33]. The mice were sacrificed through cervical dislocation at the end of the experiment, the brain was removed, and substantia nigra and corpus striatum were isolated and stored at  $-80^\circ\text{C}$ .

**2.3. Immunofluorescence Assay.** LUHMES cells in each group were grown on coverslips, fixed with 4% paraformaldehyde for 20 min, and permeated using 0.5% Triton X-100 (Sigma-Aldrich) for 20 min. For the tissue sections, the slices of substantia nigra and corpus striatum were dewaxed with xylene, treated with gradient alcohol, and washed with PBS. Subsequently, the slices were subjected to antigen repair by microwave with citrate. After cooling to room temperature, the slices were treated with 3.3%  $\text{H}_2\text{O}_2$  at  $37^\circ\text{C}$  for 20 min. After washing and blocking, the samples were incubated with anti-ACSL4 (1:50 dilution, Abcam, ab227256) and anti-TH (1:50 dilution, Abcam, ab137721) overnight at  $4^\circ\text{C}$ , then with the corresponding secondary antibody (Abcam) for 1 hour. The nuclei were stained using 10 g/mL DAPI, and the results were immediately photographed under a fluorescence microscope. For details of other experimental methods, please refer to the supplementary materials (available here).

**2.4. Statistical Analysis.** All data were expressed as mean  $\pm$  SD from three independent replicates. The data was calculated using SPSS software 23.0 (SPSS Inc., Chicago, IL, USA) with a one-way analysis of variance (ANOVA) followed by post hoc Newman-Keuls multiple comparisons.  $P < 0.05$  was considered statistically significant.

## 3. Results

**3.1. Different Concentrations of Erastin Induce Ferroptosis and Upregulate miR-494-3p in the LUHMES Cells.** To establish the ferroptosis cell model, we applied different concentrations of erastin (0, 0.25, 0.5, 1, 2, and 4  $\mu\text{M}$ ) to stimulate LUHMES cells for 24 hours. qRT-PCR results showed that

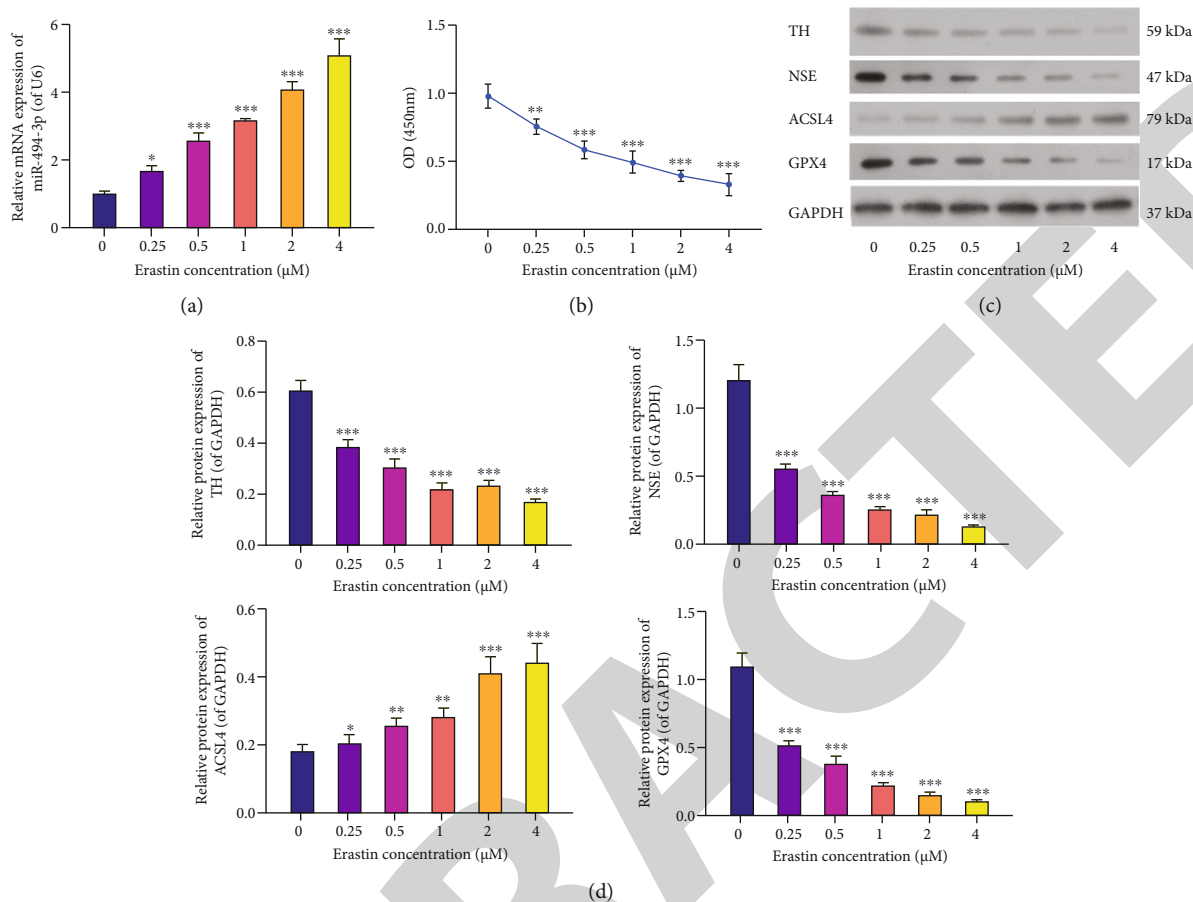


FIGURE 1: Different concentrations of erastin induce ferroptosis and upregulate miR-494-3p in the LUHMES cells. LUHMES cells were stimulated by 0, 0.25, 0.5, 1, 2, and 4  $\mu\text{M}$  erastin for 24 hours. (a) qRT-PCR analysis of miR-494-3p in erastin-stimulated LUHMES cells. (b) Cell proliferation analysis by CCK-8 assay. (c) The levels of TH, NSE, ACSL4, and GPX4 were estimated by western blotting in erastin-stimulated LUHMES cells. (d) Relative protein levels of TH, NSE, ACSL4, and GPX4 based on the western blotting results. Results were representative data from triplicate experiments, and data are means  $\pm$  SD. \* $P < 0.05$ , \*\* $P < 0.01$ , and \*\*\* $P < 0.001$ .

the level of miR-494-3p was gradually elevated in the erastin treatment compared to the control groups. We found a dose-dependent relationship between the upregulation of miR-494-3p and the increase of erastin concentration ( $P < 0.05$ ,  $P < 0.001$ , Figure 1(a)). Meanwhile, CCK-8 data uncovered that the proliferation activity of LUHMES cells gradually decreased with the increase in erastin concentration ( $P < 0.01$ ,  $P < 0.001$ , Figure 1(b)). Moreover, the western blots demonstrated that erastin induction markedly downregulated TH, NSE, and GPX4 and upregulated ACSL4 in LUHMES cells ( $P < 0.05$ ,  $P < 0.01$ ,  $P < 0.001$ , respectively, Figures 1(c) and 1(d)). Thus, the ferroptosis cell model was successfully built through erastin stimulation, and 4  $\mu\text{M}$  erastin had the strongest inducing effect.

**3.2. Inhibition of miR-494-3p Suppresses Ferroptosis, Neuron Injury, and Reactive Oxygen Species (ROS) Production and Induces Viability in Erastin-Induced LUHMES Cells.** Subsequently, we treated erastin-stimulated LUHMES cells with miR-494-3p inhibitor, miR-494-3p mimics, or ferroptosis inhibitor (ferrostatin-1). The qRT-PCR data revealed that relative to the control LUHMES group, the expression level

of miR-494-3p was significantly increased in the erastin-stimulated LUHMES cells ( $P < 0.01$ ). Meanwhile, the increase in miR-494-3p level was substantially reduced by miR-494-3p inhibitor and ferrostatin-1 in the erastin-stimulated LUHMES group ( $P < 0.001$ , Figure 2(a)). Furthermore, CCK-8 data showed that erastin memorably inhibited the proliferation of LUHMES cells, while this inhibition was weakened by miR-494-3p inhibitor and ferrostatin-1 ( $P < 0.05$ ,  $P < 0.01$ , and  $P < 0.001$ , Figure 2(b)). And our results discovered that erastin dramatically enhanced ROS activity in LUHMES cells, while miR-494-3p inhibitor and ferrostatin-1 partially rescued the enhancement of ROS activity in erastin-stimulated LUHMES cells ( $P < 0.01$ ,  $P < 0.001$ , Figures 2(c) and 2(d)). Furthermore, transmission electron microscopy (TEM) results revealed that in the control group, the mitochondrial structure in the LUHMES cells was complete with many mitochondria and visible cristae. In contrast, in the erastin group, the mitochondria had local edema, disordered cristae, and vacuolar degeneration; in the erastin + miR-494-3p inhibitor and erastin + ferrostatin-1 groups, mitochondria were abundant and normal in shape, and cristae are visible; in erastin + miR-494-3p mimics, the degree of

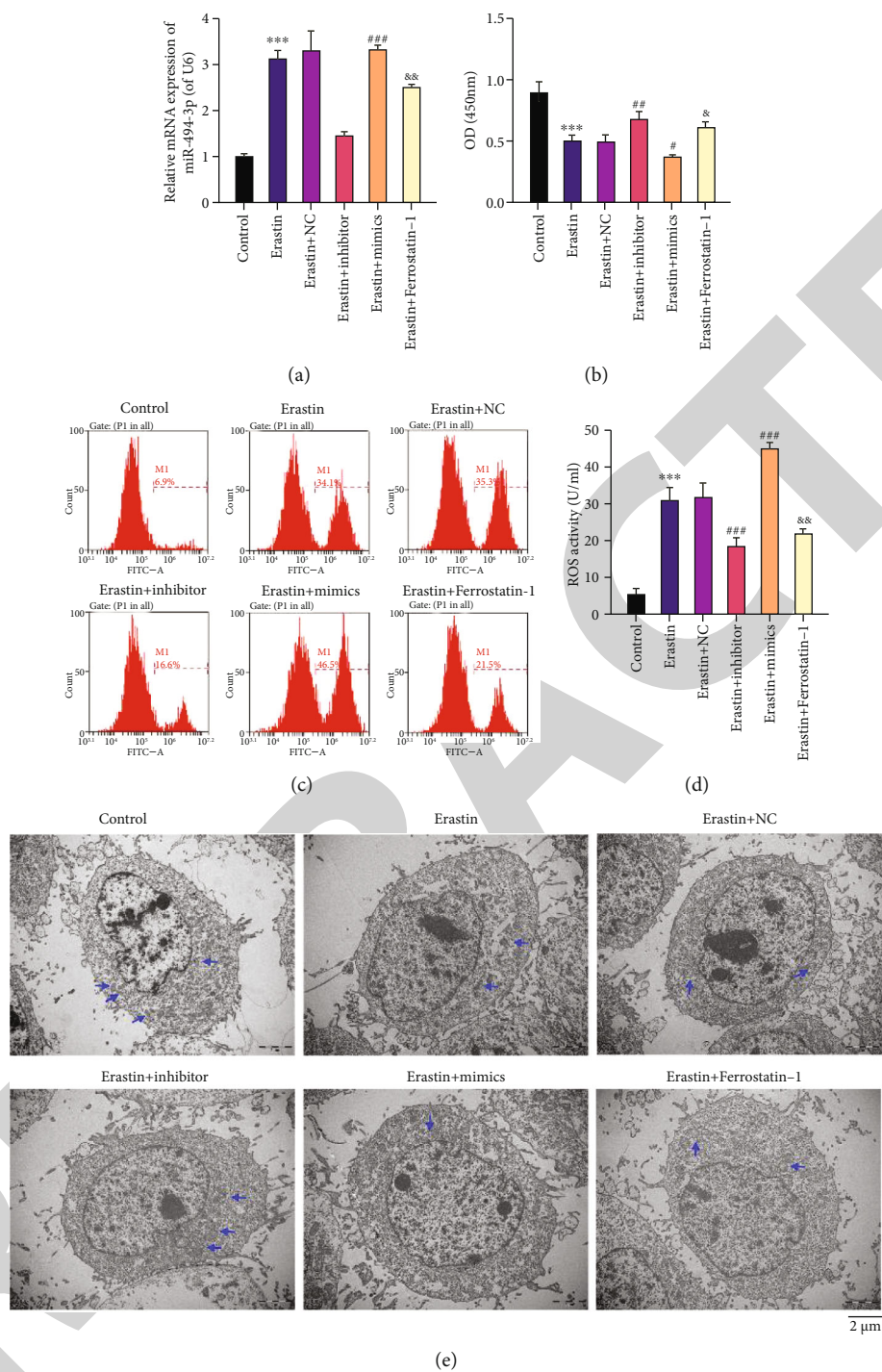
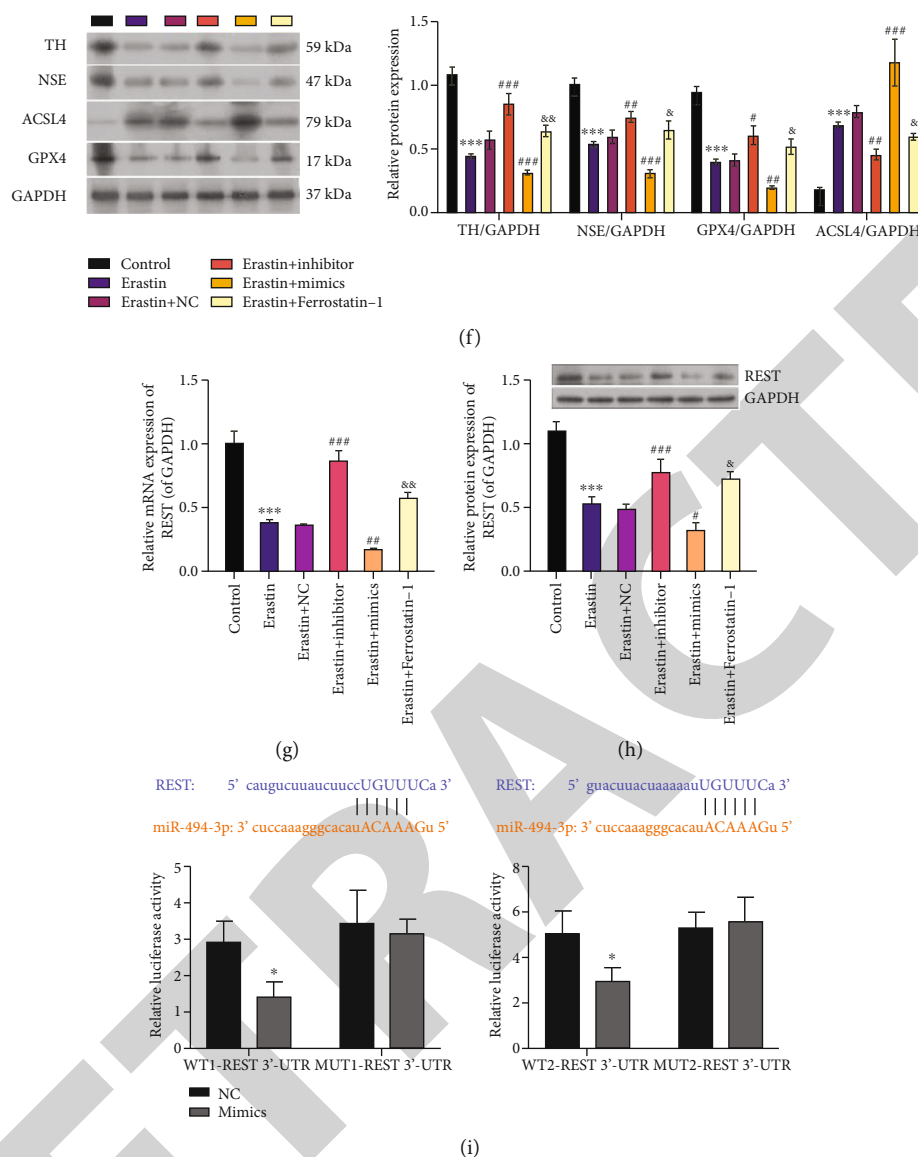


FIGURE 2: Continued.



**FIGURE 2:** The impact of miR-494-3p on viability, ROS, ferroptosis, neuron injury, and REST in erastin-induced LUHMES cells. Erastin-stimulated LUHMES cells were transfected with miR-494-3p inhibitor, miR-494-3p mimics, or NC or treated with ferroptosis inhibitor (ferrostatin-1). (a) The miR-494-3p level was tested by qRT-PCR assay in each group. (b) Cell proliferation was monitored via CCK-8 assay in the above groups. (c and d) ROS activity was identified via a flow cytometer in each group. (e) TEM images showing mitochondrial morphology in each group. Scale bar = 2  $\mu$ m. Mitochondria are marked with blue arrows. (f) Western blotting analysis of TH, NSE, ACSL4, and GPX4 in each group. (g and h) qRT-PCR and western blotting analysis of REST. (i) WT and Mut REST 3'-UTR plasmids were constructed and cotransfected with miR-494-3p mimics into cells, and then, the luciferase activity was tested by dual-luciferase reporter assay. Results were representative data from triplicate experiments, and data are means  $\pm$  SD. \* $P$  < 0.05 and \*\*\* $P$  < 0.001 vs. control or NC group; # $P$  < 0.05, ## $P$  < 0.01, and ### $P$  < 0.001 vs. erastin+NC group; &#math;P < 0.05 and &#math;P < 0.01 vs. erastin group.

mitochondrial injury was more severe than that in the erastin group (Figure 2(e)). Moreover, western blotting data showed that neuron injury-related proteins (TH and NSE) and GPX4 were significantly downregulated, and ACSL4 was strikingly upregulated in erastin-stimulated LUHMES cells compared to that in controls. Meanwhile, the above effect was markedly reversed by miR-494-3p inhibitor or ferrostatin-1 ( $P$  < 0.01,  $P$  < 0.001, Figure 2(f)).

**3.3. REST Is a Target Gene of miR-494-3p.** The underlying mechanism was further identified by which miR-494-3p

inhibition prevents ferroptosis, thus affecting the progression of PD. qRT-PCR and western blot results showed that miR-494-3p inhibition or ferrostatin-1 dramatically upregulated REST, and miR-494-3p overexpression significantly downregulated REST in erastin-induced LUHMES cells ( $P$  < 0.05,  $P$  < 0.001, Figures 2(g) and 2(h)). Moreover, through bioinformatics, we discovered two latent binding sites between miR-494-3p and REST, indicating that REST might be a target gene of miR-494-3p. Then, we constructed the plasmids of WT-REST and Mut-REST and conducted a dual-luciferase reporter assay with miR-494-3p mimics. The

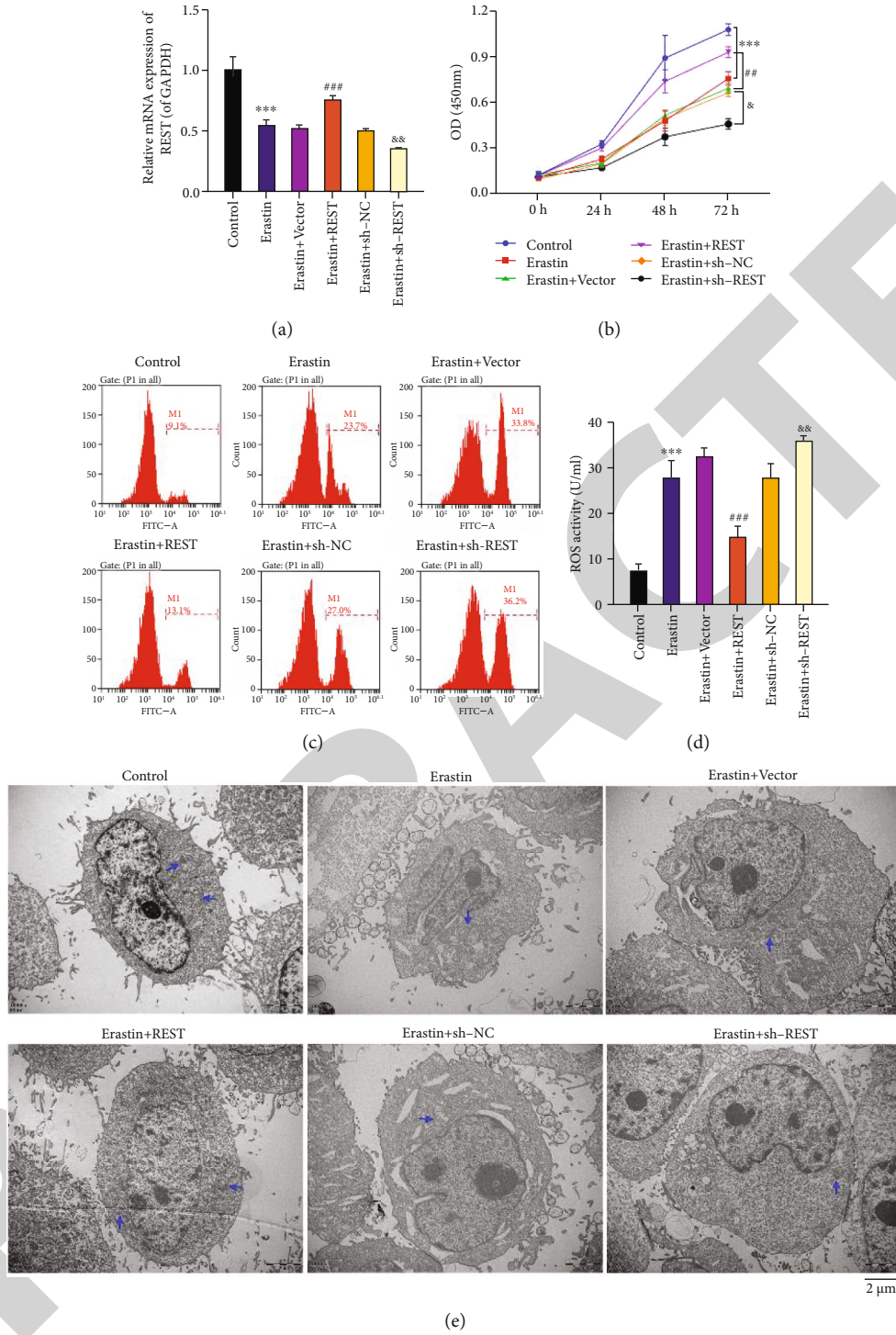


FIGURE 3: Continued.

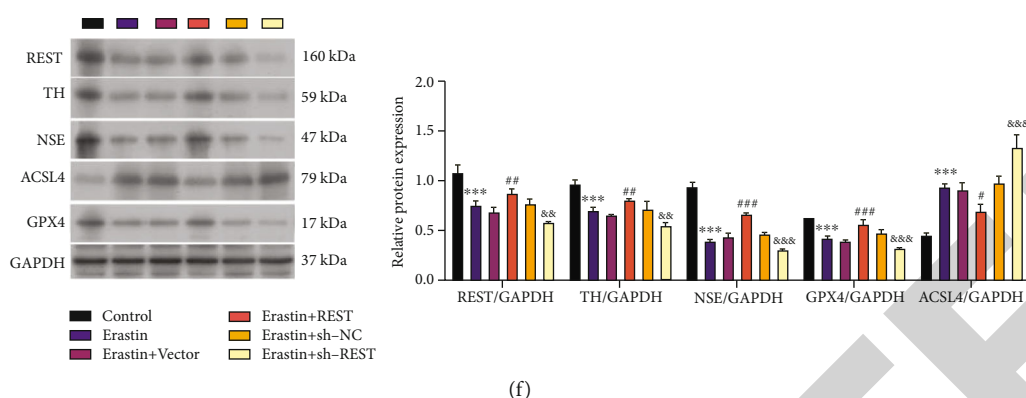


FIGURE 3: Effects of REST on viability, ROS, ferroptosis, and neuron injury in erastin-induced LUHMES. After erastin stimulation, LUHMES were transfected with REST-overexpressed plasmid or sh-REST. (a) The levels of REST were evaluated through qRT-PCR analysis. (b) CCK-8 analyzed the impact of REST on the viability of cells. (c and d) Flow cytometry analyzed the impact of REST on ROS activity in the treated LUHMES cells. (e) TEM shows mitochondrial morphology. Scale bar = 2  $\mu$ m. Mitochondria are marked with blue arrows. (f) Western blotting analysis of REST, TH, NSE, ACSL4, and GPX4, and quantitative analysis of these proteins based on the western blotting results. Results were representative data from triplicate experiments, and data are means  $\pm$  SD. \*\*\* $P$  < 0.001 vs. control group; \* $P$  < 0.05, \*\* $P$  < 0.01, and \*\*\* $P$  < 0.001 vs. erastin+vector group; &#x2013; $P$  < 0.05, &#x2013;&#x2013; $P$  < 0.01, and &#x2013;&#x2013;&#x2013; $P$  < 0.001 vs. erastin+sh-NC group.

luciferase activity of WT-REST was notably attenuated after the cotransfection of miR-494-3p mimics. However, the luciferase activity of Mut-REST did not change, which suggested that REST is a direct target of miR-494-3p ( $P$  < 0.05, Figure 2(i)).

**3.4. REST Inhibits Ferroptosis, Neuron Injury, and ROS Production and Accelerates Viability in Erastin-Induced LUHMES Cells.** Next, we further validated the effects of REST alteration on the related functions of erastin-induced LUHMES cells. The erastin-induced LUHMES cells were transfected with REST-overexpressed plasmid or sh-REST. qRT-PCR analysis validated that REST overexpression increased REST expression, and REST knockdown decreased REST expression in erastin-induced LUHMES cells, indicating the successful transfection of REST-overexpressed plasmid or sh-REST ( $P$  < 0.01,  $P$  < 0.001, Figure 3(a)). CCK-8 data showed that overexpression of REST dramatically enhanced, and knockdown of REST significantly prevented the viability of erastin-induced LUHMES cells ( $P$  < 0.05,  $P$  < 0.01,  $P$  < 0.001, Figure 3(b)). Flow cytometer data showed that overexpression and knockdown of REST significantly reduced and increased the ROS levels, respectively, in erastin-induced LUHMES cells ( $P$  < 0.01,  $P$  < 0.001, Figures 3(c) and 3(d)). Furthermore, TEM images also uncovered that overexpression of REST observably alleviated mitochondrial injury, and knockdown of REST memorably aggravated the mitochondrial injury in erastin-induced LUHMES cells (Figure 3(f)). Moreover, western blotting data highlighted that overexpression of REST upregulated REST, TH, NSE, and GPX4 and downregulated ACSL4 in erastin-induced LUHMES cells. Knockdown of REST exerted the opposite effect of overexpression-mediated expression change of these proteins ( $P$  < 0.05,  $P$  < 0.01,  $P$  < 0.001, Figure 3(f)).

**3.5. REST Attenuates the Effect of miR-494-3p on Viability, ROS, Ferroptosis, and Neuron Injury in Erastin-Induced LUHMES Cells.** Subsequently, we conducted the rescue

experiments to investigate whether REST can be involved in blocking PD mediated by miR-494-3p downregulation by inhibiting ferroptosis. Erastin-stimulated LUHMES cells were first cotransfected with miR-494-3p inhibitor and sh-REST or REST-overexpressed plasmid and miR-494-3p mimics. The qRT-PCR data showed that knockdown of REST upregulated miR-494-3p mediated by miR-494-3p inhibitor, whereas overexpression of REST significantly downregulated miR-494-3p mediated by miR-494-3p mimics in erastin-induced LUHMES cells ( $P$  < 0.05,  $P$  < 0.01, Figure 4(a)). And we also showed that knockdown of REST significantly reduced REST expression mediated by miR-494-3p inhibitor, and overexpression of REST markedly raised REST expression mediated by miR-494-3p mimics in erastin-induced LUHMES cells ( $P$  < 0.01, Figure 4(b)). Likewise, CCK-8 data demonstrated that knockdown of REST dramatically attenuated viability mediated by miR-494-3p inhibitor, whereas overexpression of REST remarkably enhanced viability mediated by miR-494-3p mimics in erastin-induced LUHMES cells ( $P$  < 0.05,  $P$  < 0.01, Figure 4(c)). The flow cytometry results disclosed that REST knockdown significantly elevated ROS level mediated by miR-494-3p inhibitor and REST overexpression significantly lowered ROS level mediated by miR-494-3p mimics in erastin-induced LUHMES ( $P$  < 0.05, Figure 4(d)). Meanwhile, TEM images showed that REST knockdown markedly induced mitochondrial injury mediated by miR-494-3p inhibitor, and REST overexpression prevented mitochondrial damage mediated by miR-494-3p mimics in erastin-induced LUHMES cells (Figure 4(e)). Meanwhile, immunofluorescence assay also uncovered that REST silencing could upregulate ACSL4 and downregulate TH mediated by miR-494-3p inhibitor and downregulate ACSL4 and upregulate TH mediated by miR-494-3p mimics in erastin-induced LUHMES cells (Figures 4(f) and 4(g)). Furthermore, we proved that REST silencing downregulated REST, TH, NSE, and GPX4 and upregulated ACSL4, which were mediated by miR-494-3p inhibitor, and REST overexpression



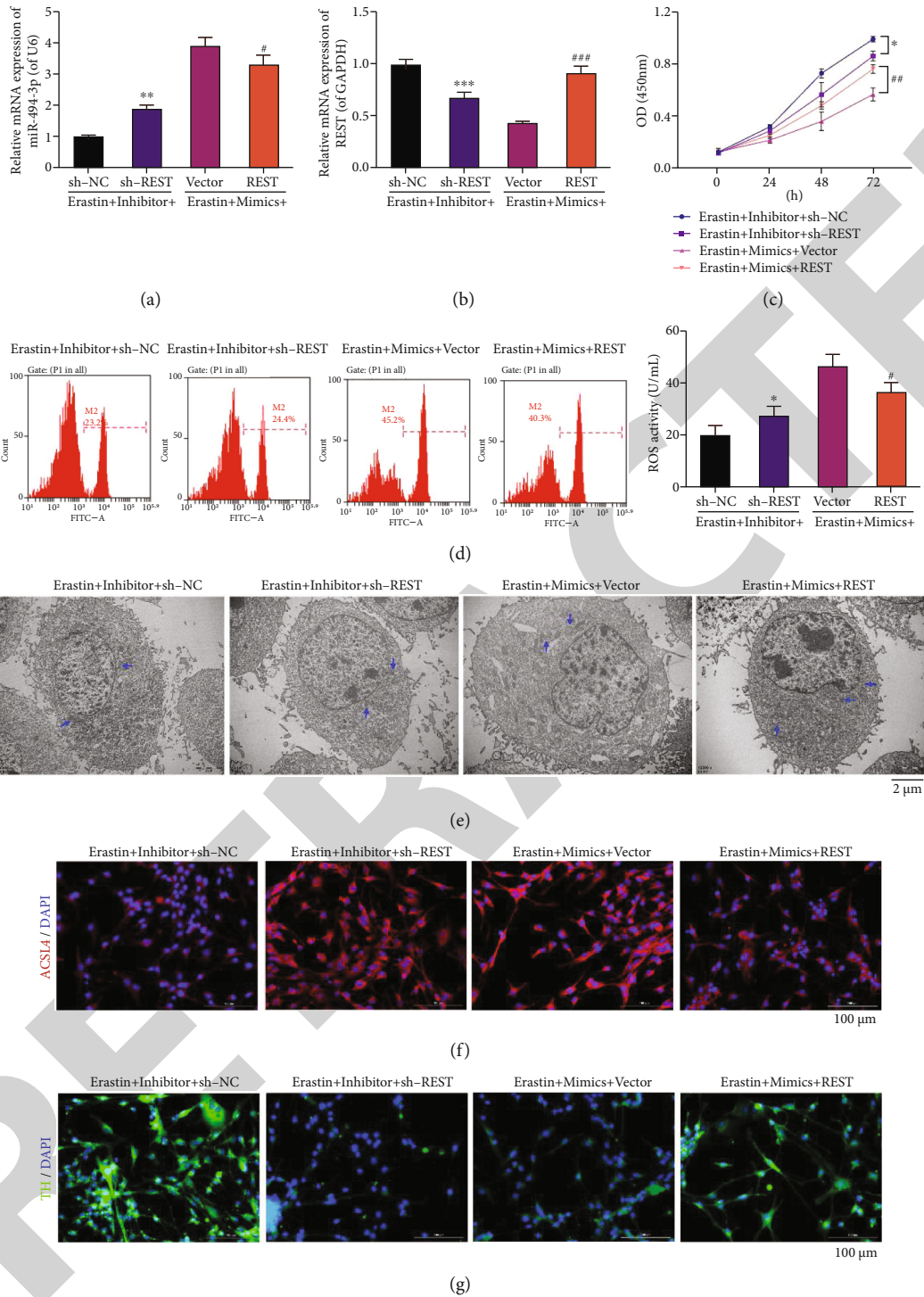


FIGURE 4: Continued.

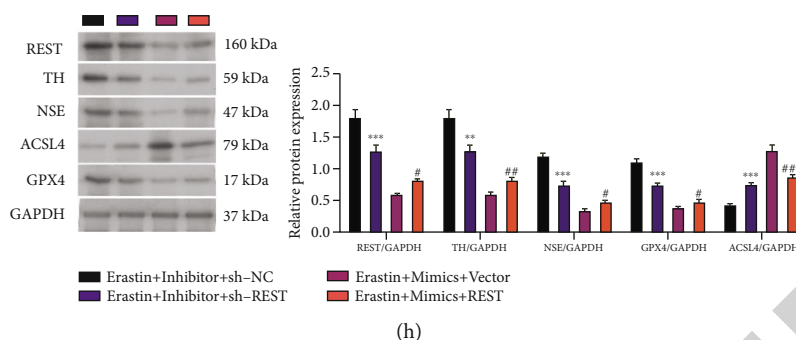


FIGURE 4: REST attenuates the effect of miR-494-3p on viability, ROS, ferroptosis, and neuron injury in erastin-induced LUHMES cells. Erastin-stimulated LUHMES were cotransfected with miR-494-3p inhibitor and sh-REST or REST-overexpressed plasmid and miR-494-3p mimics, respectively. (a and b) qRT-PCR showing the levels of miR-494-3p (a) and REST (b). (c) Cell viability was measured through the CCK-8 assay. (d) A Flow cytometer verified the change in ROS activity. (e) TEM images showing changes in mitochondrial morphology. Scale bar = 2  $\mu$ m. Mitochondria are marked with blue arrows. (f and g) Immunofluorescence images showing ACSL4 (f) and TH (g) expressions. Magnification: 200 $\times$ , scale bar = 100  $\mu$ m. (h) Western blotting analysis showing REST, TH, NSE, ACSL4, and GPX4 levels. Results were representative data from triplicate experiments, and data are means  $\pm$  SD. \* $P$  < 0.05, \*\* $P$  < 0.01, and \*\*\* $P$  < 0.001 vs. inhibitor+sh-NC group; # $P$  < 0.05, ## $P$  < 0.01, and ### $P$  < 0.001 vs. mimics+vector group.

upregulated REST, TH, NSE, and GPX4 and downregulated ACSL4, which were mediated by miR-494-3p mimics in erastin-induced LUHMES ( $P$  < 0.05,  $P$  < 0.01,  $P$  < 0.001, Figure 4(h)).

**3.6. SP1 Reverses the Roles of REST on Viability, ROS, Ferroptosis, and Neuron Injury in Erastin-Induced LUHMES Cells.** Moreover, we further verified whether SP1 could participate in blocking the PD progression mediated by REST by inhibiting ferroptosis and whether SP1 also can participate in the inhibition effect of REST on PD progression. Erastin-stimulated LUHMES cells were coprocessed with REST and SP1 overexpressing plasmids or REST shRNAs (sh-REST) and mithramycin. The results unveiled that overexpression of REST significantly reduced SP1 expression and transcription factor activity in erastin-stimulated LUHMES cells; this expression and transcription factor activity of SP1 mediated by REST overexpression could be notably potentiated by SP1 overexpression. Meanwhile, silencing of REST significantly elevated SP1 expression and transcription factor activity in erastin-stimulated LUHMES cells. This elevation mediated by REST silencing could be observably attenuated by mithramycin ( $P$  < 0.05,  $P$  < 0.01,  $P$  < 0.001, Figures 5(a) and 5(b)). Then, we utilized an SP1 transcription factor assay to identify SP1 activity in REST overexpressed or silenced LUHMES after erastin induction. The data revealed that overexpression of REST markedly lowered SP1 activity, and knockdown of REST prominently lowered SP1 activity in erastin-induced LUHMES ( $P$  < 0.001, Figure 5(c)). Subsequently, we found that overexpression of REST enhanced the viability of erastin-stimulated LUHMES cells, while this enhancement was remarkably weakened by SP1 overexpression. On the other hand, silencing of REST markedly reduced the viability of erastin-stimulated LUHMES cells, while this reduction was significantly reversed by mithramycin (Figure 5(d)). Furthermore, we found that overexpression of REST dramatically diminished ROS activity of erastin-stimulated LUHMES cells, while this reduction was weak-

ened by SP1 overexpression. Silencing of REST markedly improved ROS activity of erastin-stimulated LUHMES cells, while this improvement was markedly reversed by mithramycin ( $P$  < 0.01,  $P$  < 0.001, Figure 5(e)). And the TEM data indicated that REST overexpression prominently mitigated mitochondrial injury of erastin-stimulated LUHMES cells, while this mitigation was weakened by SP1 overexpression. REST silencing memorably accelerated mitochondrial injury of erastin-stimulated LUHMES, while mithramycin significantly reversed this acceleration (Figure 5(f)). Besides, immunofluorescence results demonstrated that SP1 overexpression could reverse the downregulation of ACSL4 and upregulation of TH, mediated by REST overexpression. Similarly, mithramycin also could reverse the upregulation of ACSL4 and downregulation of TH, mediated by REST silencing in erastin-stimulated LUHMES cells (Figures 5(g) and 5(h)). The results also revealed that overexpression of REST downregulated SP1 and ACSL4 and upregulated TH, NSE, and GPX4, which was reversed by SP1 overexpression. Knockdown of REST upregulated SP1 and ACSL4 and downregulated TH, NSE, and GPX4, which was also significantly reversed by mithramycin ( $P$  < 0.05,  $P$  < 0.01,  $P$  < 0.001, Figure 5(i)).

**3.7. SP1 Can Target ACSL4.** The specific mechanism was further understood by which SP1 influences ferroptosis. Bioinformatics analysis suggested that ACSL4 might be the downstream target gene of SP1. We also explored the binding sites between SP1 and ACSL4 (Figure 6(a)). Then, dual-luciferase reporter assay showed that SP1 significantly enhanced the promoter activity of ACSL4 (two binding sites) relative to the respective wild-type ACSL4 promoter, suggesting that SP1 could target ACSL4 ( $P$  < 0.001, Figures 6(b) and 6(c)). A chromatin preparation was precipitated with anti-SP1, and the immunoprecipitated DNA fragments were amplified with the primers, including the ACSL4 binding site. Chromatin immunoprecipitation (CHIP) results suggested that DNA fraction was immunoprecipitated with

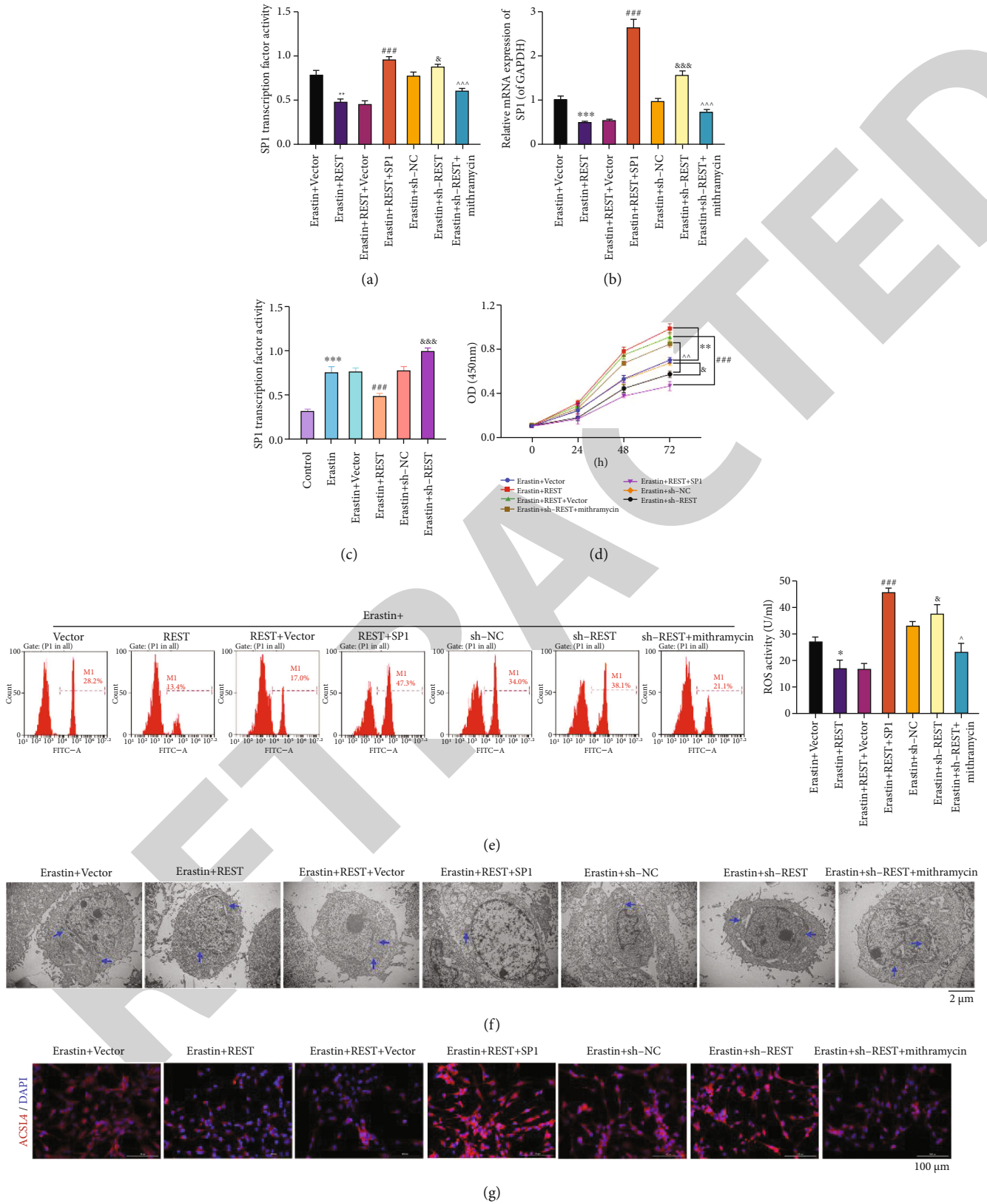


FIGURE 5: Continued.

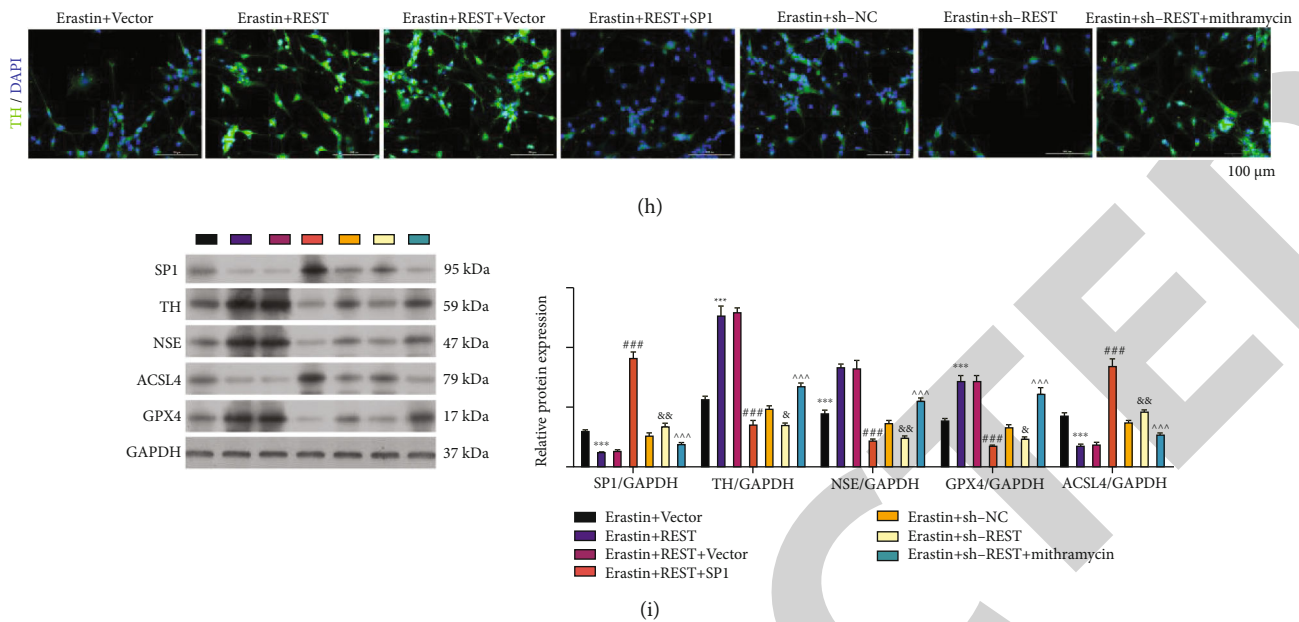


FIGURE 5: SP1 reverses the roles of REST on viability, ROS, ferroptosis, and neuron injury in erastin-induced LUHMES cells. Erastin-stimulated LUHMES cells were coprocessed with REST and SP1 overexpression plasmids or REST shRNAs (sh-REST) and mithramycin. (a and b) The corresponding kit and qRT-PCR assay confirmed the transcription factor activity and expression of SP1. (c) Verification of SP1 transcription factor activity in REST-overexpressed or -silenced LUHMES cells after erastin stimulation. (d) CCK-8 was used to examine the change in cell viability. (e) ROS level was determined by flow cytometry. (f) TEM images showing mitochondrial morphology. Scale bar = 2  $\mu\text{m}$ . Mitochondria are marked with blue arrows. (g and h) Immunofluorescence staining showing ACSL4 (g) and TH (h) expressions. Magnification: 200 $\times$ , scale bar = 100  $\mu\text{m}$ . (i) Western blotting highlights the changes in SP1, TH, NSE, ACSL4, and GPX4 expressions. Results were representative data from triplicate experiments, and data are means  $\pm$  SD. \* $P$  < 0.05, \*\* $P$  < 0.01, and \*\*\* $P$  < 0.001 vs. erastin+vector group; ### $P$  < 0.001 vs. erastin+REST+vector group; ^ $P$  < 0.05, ^^ $P$  < 0.01, and ^^^ $P$  < 0.001 vs. erastin+sh-REST group; & $P$  < 0.05, && $P$  < 0.01, and &&& $P$  < 0.001 vs. erastin+sh-NC group; ^ $P$  < 0.05, ^^ $P$  < 0.01, and ^^^ $P$  < 0.001 vs. erastin+sh-REST group.

the anti-SP1 while none with the IgG (negative control), indicating SP1 could bind to ACSL4 ( $P$  < 0.001, Figure 6(d)). Likewise, electrophoretic mobility shift (EMSA) results also showed that SP1 and ACSL4 could interact directly (Figure 6(e)).

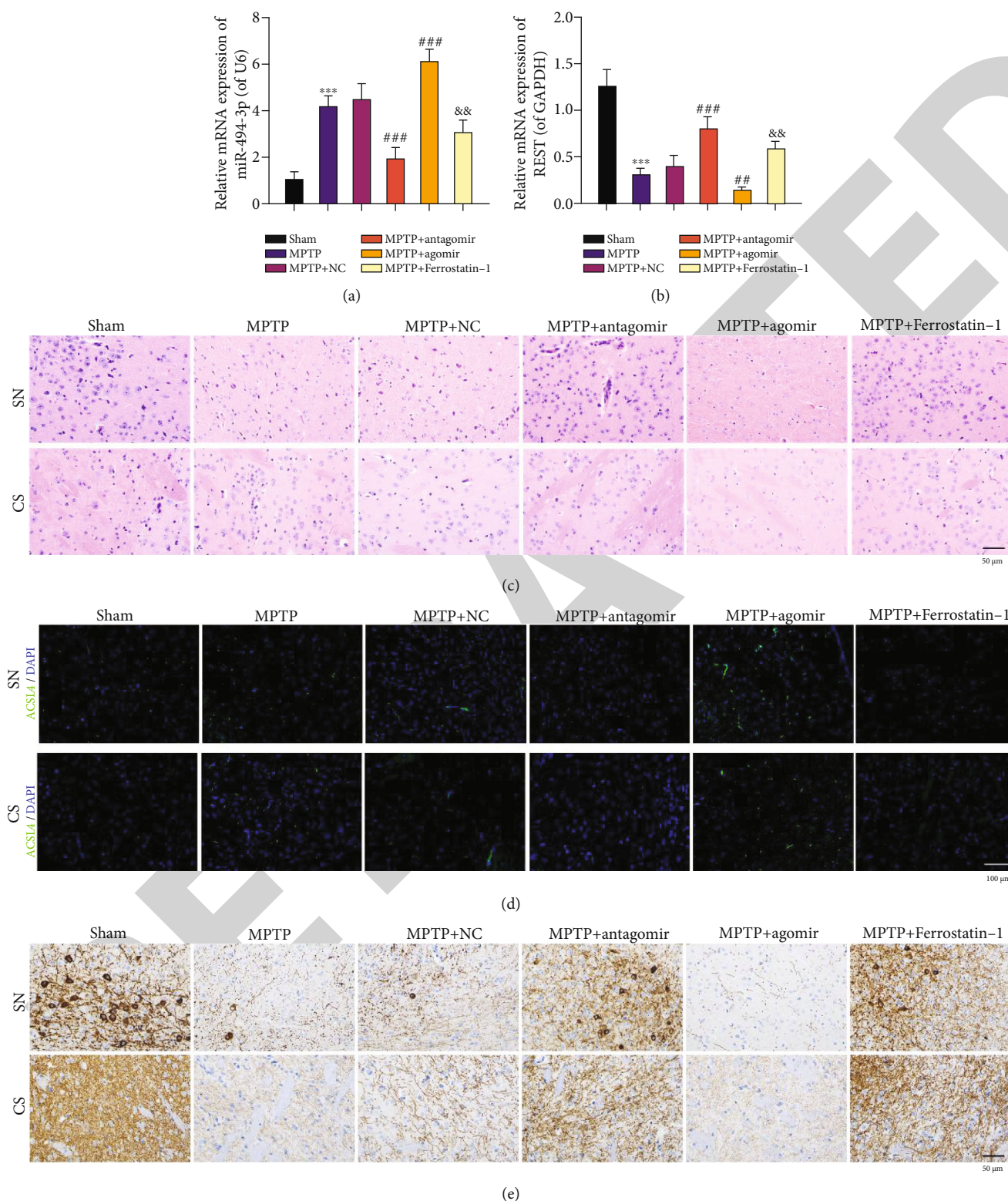
**3.8. miR-494-3p Aggravates Pathological Changes, Upregulates ACSL4, and Downregulates TH in the Substantia Nigra and Corpus Striatum of the MPTP-Induced PD Mouse Model.** Furthermore, we established a PD mouse model through MPTP induction and examined the influence of miR-494-3p and ferrostatin-1 on the pathological changes and ACSL4 and TH expressions in substantia nigra and corpus striatum. The qRT-PCR data showed that relative to sham mice, miR-494-3p was upregulated, and REST was downregulated in the MPTP-induced PD model mice. Inhibition of miR-494-3p or ferrostatin-1 downregulated miR-494-3p and upregulated REST. Further, overexpression of miR-494-3p upregulated miR-494-3p and downregulated REST in MPTP-induced PD model mice, suggesting the successful treatment of the PD mouse model ( $P$  < 0.05,  $P$  < 0.01, Figures 7(a) and 7(b)). Then, hematoxylin and eosin (H&E) staining demonstrated that the number of neurons in the sham group was relatively dense and orderly, and the stroma was clear. However, in the PD model group, the neurons were disordered, the number of neurons was reduced, the contour of the cell body was blurred, the cytoplasm was swol-

len, and some vacuolar degeneration or shrinkage necrosis was observed. These conditions improved in the miR-494-3p antagonist and ferrostatin-1 treatment groups and worsened in the miR-494-3p agomir group (Figure 7(c)). Immunofluorescence results then showed that ACSL4 expression was elevated in the substantia nigra and corpus striatum of the MPTP-induced PD mice compared to sham mice. Inhibiting miR-494-3p or ferrostatin-1 dramatically downregulated ACSL4, and overexpression of miR-494-3p observably upregulated ACSL4 in the MPTP-induced PD model mice (Figure 7(d)). Similarly, immunohistochemistry results showed that TH expression was reduced in the MPTP-induced PD model mice's substantia nigra and corpus striatum relative to that in the sham mice. Inhibition of miR-494-3p or ferrostatin-1 dramatically increased TH expression, and overexpression of miR-494-3p significantly decreased TH expression in MPTP-induced PD model mice (Figure 7(e)).

#### 4. Discussion

PD is one of the most common neurodegenerative diseases of the central nervous system [2]. However, the etiology and pathogenesis of PD are still broadly unknown. Recent studies demonstrated that the midbrain of PD patients is characterized by high iron content, low glutathione, and increased lipid peroxidation, suggesting that the pathogenesis of PD is relevant to ferroptosis [15, 34]. Ferroptosis is a





**FIGURE 7: miR-494-3p aggravates pathological changes, upregulates ACSL4, and downregulates TH in the substantia nigra and corpus striatum of the MPTP-induced PD mouse model.** PD mouse model was established through MPTP induction, and then, PD model mice were addressed with miR-494-3p antagomir, miR-494-3p agomir, or ferrostatin-1. (a and b) qRT-PCR was utilized to analyze miR-494-3p (a) and REST (b) levels. (c) H&E staining determined the pathological changes in the substantia nigra and corpus striatum in the MPTP-induced PD mouse model. Magnification: 400 $\times$ , scale bar = 50  $\mu$ m. (d) ACSL4 expression was assessed using an immunofluorescence assay. Magnification: 200 $\times$ , scale bar = 100  $\mu$ m. (e) TH expression was identified using an immunohistochemistry assay. Magnification: 400 $\times$ , scale bar = 50  $\mu$ m. Results were representative data from triplicate experiments, and data are means  $\pm$  SD. Each group contained eight mice. <sup>\*\*\*</sup> $P < 0.001$  vs. sham group; <sup>##</sup> $P < 0.01$  and <sup>###</sup> $P < 0.001$  vs. MPTP+NC group; <sup>&&</sup> $P < 0.01$  vs. MPTP group.

erastin stimulation. Epidemiological investigation testified that occupational exposures to heavy metals, pesticides, herbicides, and other environmental factors might be a risk factor for PD [43]. Earlier studies also discovered that the injection of 1-methyl-4-phenyl-1,2,3,6-tetrahydropyridine (MPTP) could result in symptoms like PD [44]. As previously reported, iron was significantly increased in the substantia nigra of MPTP-induced PD mice and the remaining dopaminergic neurons [45]. An iron-chelating agent can protect the neurotoxic model induced by MPP<sup>+</sup> [46]. The specific iron deposition in the substantia nigra is a crucial factor in the damage of dopaminergic neurons in PD [8]. We also chose MPTP to generate the chronic PD mouse model in this study. We showed the pathological structure unfavorably changes in the substantia nigra and corpus striatum of PD mice, suggesting that the PD mouse model was successfully generated.

Besides, our results uncovered that miR-494-3p was dramatically upregulated in erastin-induced LUHMES and MPTP-induced PD mice, suggesting that miR-494-3p might participate in the PD process. Downregulation of miR-494-3p could attenuate neurotoxicity of SK-N-SH and CHP 212 cells, suggesting that inhibition of miR-494-3p might be a latent method of PD therapy [23]. In our study, we also showed that inhibition of miR-494-3p could weaken neuron injury and enhance the viability of erastin-induced LUHMES, suggesting the protective effect of miR-494-3p inhibition on PD model cells induced by erastin. We also demonstrated that inhibition of miR-494-3p, consistent with ferrostatin-1, could suppress ferroptosis and ROS production in PD model cells induced by erastin. Moreover, we found that inhibition of miR-494-3p could improve pathological changes and ferroptosis in substantia nigra and corpus striatum of MPTP-induced PD model mice. Thus, our results indicate that inhibition of miR-494-3p might relieve PD by inhibiting ferroptosis.

As a DNA zinc-finger binding protein, REST can induce histone deacetylation and transcriptional inhibition of target genes by binding with neuron-restrictive silencer element (NRSE) [47]. REST, as a key negative transcriptional regulator in the nervous system, is widely involved in neuronal growth and differentiation, axon growth, vesicle transport and release, and ion conduction [47]. Therefore, REST plays a role in regulating various aspects of nerve function, such as cell differentiation, nerve regeneration, nerve protection, and cognitive function [48]. Researchers also discovered that REST plays multiple roles in different neurological diseases, especially PD [49]. REST also has a protective effect on numerous stress stimulations and can maintain neuronal activity through antioxidative stress [50]. In our study, we further confirmed that REST also could inhibit ferroptosis, neuron injury, and ROS production and induce viability of erastin-induced LUHMES cells, suggesting the mitigation role of REST on PD. Moreover, we found that miR-494-3p could bind to REST 3'-UTR through prediction software, suggesting that REST might be the target gene of miR-494-3p. And the results from the dual-luciferase reporter assay verified the same. Meanwhile, the rescue experiments showed that inhibition of

miR-494-3p could alleviate PD by targeting REST to inhibit ferroptosis.

SP1 protein is a member of the SP/KLF transcription factor family [51]. SP1 has 4 parts based on its functions: DNA binding region, SP1 active region, Buttonhead (BTD) box, and SP box [51]. Under normal physiological conditions, SP1 is widely expressed in various tissues and organs in the organism and regulates multiple housekeeping genes [52]. Recently, it has been reported that SP1 is associated with oxidative stress and ferroptosis [53]. Meanwhile, SP1 was confirmed to be relevant to PD by several studies. For instance, miR-375 ameliorates dopaminergic neuronal damage by attenuating SP1 to attenuate PD inflammatory response [54]. miR-126-5p targets SP1 to stop PD progression [55]. miR-29c targets SP1 to inhibit PD inflammation and apoptosis [56]. SP1 is involved in MPTP-induced cell damage in PD [57]. In PD models, SP1 inhibition can exert neuroprotective effects [58]. And our results further demonstrated that SP1 also could reverse the roles of REST on viability, ROS, ferroptosis, and neuron injury in erastin-induced LUHMES cells, suggesting that REST also could alleviate PD by reducing SP1 activity. Thus, we uncovered that SP1 is vital in REST-regulated ferroptosis in PD.

Besides, SP1 can interact with other protein molecules to exert a negative regulation on target genes [59]. Study has shown that SP1 can affect the cell cycle, apoptosis, and angiogenesis [60]. Here, we unexpectedly discovered that ACSL4 might be the downstream target gene of SP1 through bioinformatics analysis. Moreover, our data also disclosed that overexpression of REST could downregulate ACSL4 in erastin-induced LUHMES cells. ACSL4 is a crucial enzyme in fatty acid metabolism and a member of the long-chain lipid coenzyme A synthase (ACSL) family [61]. Study has demonstrated that ACSL4 is closely related to animal fat metabolism [62]. In addition, the expression of ACSL4 can affect cancer cell proliferation, migration, invasion, and apoptosis [63, 64]. It has also been found that mutations in the ACSL4 gene cause altered ACSL4 enzyme activity, affecting neurodevelopment [65]. ACSL4 has also been reported to be one of the essential components for triggering cellular ferroptosis through its involvement in the synthesis of membrane phospholipids that are susceptible to oxidation [66–68]. Therefore, we speculated that ACSL4 is likely to be associated with ferroptosis in PD. The role and mechanism of ACSL4 in PD were broadly unknown. In our study, we further certified that ACSL4 is a target gene of SP1. Overall, we showed that inhibition of miR-494-3p could attenuate ferroptosis and PD progression by the REST/SP1/ACSL4 axis.

However, the current study also has limitations that need further study. (i) The specific mechanism between SP1 and REST is still unclear. (ii) The effects of the miR-494-3p/REST/SP1/ACSL4 axis on other related functions of PD, such as oxidative stress, autophagy, apoptosis, and proliferation, remain unanswered. (iii) Although this study verified the role of the miR-494-3p/REST/SP1/ACSL4 axis, we mainly focused on the cellular level, and further verification is also needed in experimental animal studies. (iv) The

influence of this signaling pathway on PD patients also needs to be further investigated.

## 5. Conclusion

Our results manifested that inhibition of miR-494-3p could prevent ferroptosis and neuron injury by targeting REST to regulate the SP1/ACSL4 axis in PD. These findings demonstrated that miR-494-3p/REST/SP1/ACSL4 pathway is crucial in regulating PD ferroptosis. Overall, this study revealed that miR-494-3p, REST, SP1, and ACSL4 are in the same signaling axis, and there is a clear upstream and downstream regulatory relationship between them. Therefore, it would be of great clinical application to further explore drugs with functional activity to regulate these four genes and validate whether they can improve PD.

## Abbreviations

CHIP:	Chromatin immunoprecipitation
GPX4:	Glutathione peroxidase 4
H&E:	Hematoxylin and eosin
LUHMES:	Lund human mesencephalic cells
miRNAs:	MicroRNAs
MPTP:	1-Methyl-4-phenyl-1,2,3,6-tetrahydropyridine
NC:	Negative control
NSE:	Neuron-specific enolase
PD:	Parkinson's disease
qRT-PCR:	Quantitative real-time polymerase chain reaction
REST:	Repressor element-1 silencing transcription factor
ROS:	Reactive oxygen species
SP1:	Specificity protein 1
TEM:	Transmission electron microscope
TH:	Tyrosine hydroxylase.

## Data Availability

The datasets are available from the corresponding author upon reasonable request.

## Additional Points

**Highlights.** (i) miR-494-3p inhibition prevents erastin-induced ferroptosis and neuron injury. (ii) REST is a target gene of miR-494-3p. (iii) REST inhibits ferroptosis, neuron injury, and ROS in erastin-induced LUHMES cells. (iv) SP1 is a downstream regulatory gene of REST. (v) SP1 can target ACSL4. (vi) miR-494-3p/REST/SP1/ACSL4 axis in Parkinson's disease.

## Ethical Approval

All animal experiments followed the Universal Declaration on Animal Welfare and approved by the Ethics Committee of Henan University People's Hospital (No. 2019-76).

## Conflicts of Interest

The authors declare that they have no competing interest.

## Authors' Contributions

JJM, XL, and HQY designed the experiments; XHL, YYF, and DWY conducted the cell experiments; XHL, QG, and SYC performed the animal experiments; DSL and SPW provided research materials and methods; XHL and JHZ analyzed data; XHL and JJM wrote the manuscript. All authors read and approved the final manuscript.

## Acknowledgments

This study was funded by the Henan Province Medical Science and Technology Research Program (No. SBGJ2021 02035) and the Henan Province Science and Technology Development Plan (No. 192102310085).

## Supplementary Materials

Detailed methods for other experiments. (*Supplementary Materials*)

## References

- [1] O. B. Tysnes and A. Storstein, "Epidemiology of Parkinson's disease," *Journal of Neural Transmission (Vienna)*, vol. 124, no. 8, pp. 901–905, 2017.
- [2] S. N. Rai and P. Singh, "Advancement in the modelling and therapeutics of Parkinson's disease," *Journal of Chemical Neuroanatomy*, vol. 104, article 101752, 2020.
- [3] S. N. Rai, P. Singh, R. Varshney et al., "Promising drug targets and associated therapeutic interventions in Parkinson's disease," *Neural Regeneration Research*, vol. 16, no. 9, pp. 1730–1739, 2021.
- [4] S. G. Reich and J. M. Savitt, "Parkinson's disease," *The Medical Clinics of North America*, vol. 103, no. 2, pp. 337–350, 2019.
- [5] S. N. Rai, V. K. Chaturvedi, P. Singh, B. K. Singh, and M. P. Singh, "Mucuna pruriens in Parkinson's and in some other diseases: recent advancement and future prospective," *Biotech*, vol. 10, no. 12, p. 522, 2020.
- [6] J. Lu, M. Wu, and Z. Yue, "Autophagy and Parkinson's disease," *Advances in Experimental Medicine and Biology*, vol. 1207, pp. 21–51, 2020.
- [7] E. M. Rocha, B. De Miranda, and L. H. Sanders, "Alpha-synuclein: pathology, mitochondrial dysfunction and neuroinflammation in Parkinson's disease," *Neurobiology of Disease*, vol. 109, Part B, pp. 249–257, 2018.
- [8] H. Mochizuki, C. J. Choong, and K. Baba, "Parkinson's disease and iron," *Journal of Neural Transmission (Vienna)*, vol. 127, no. 2, pp. 181–187, 2020.
- [9] P. P. Michel, E. C. Hirsch, and S. Hunot, "Understanding dopaminergic cell death pathways in Parkinson disease," *Neuron*, vol. 90, no. 4, pp. 675–691, 2016.
- [10] T. Kim and R. Vemuganti, "Mechanisms of Parkinson's disease-related proteins in mediating secondary brain damage after cerebral ischemia," *Journal of Cerebral Blood Flow and Metabolism*, vol. 37, no. 6, pp. 1910–1926, 2017.



- [11] Y. Mou, J. Wang, J. Wu et al., "Ferroptosis, a new form of cell death: opportunities and challenges in cancer," *Journal of Hematology & Oncology*, vol. 12, no. 1, p. 34, 2019.
- [12] T. Hirschhorn and B. R. Stockwell, "The development of the concept of ferroptosis," *Free Radical Biology & Medicine*, vol. 133, pp. 130–143, 2019.
- [13] X. Zeng, H. An, F. Yu et al., "Benefits of iron chelators in the treatment of Parkinson's disease," *Neurochemical Research*, vol. 46, no. 5, pp. 1239–1251, 2021.
- [14] S. J. Guiney, P. A. Adlard, A. I. Bush, D. I. Finkelstein, and S. Ayton, "Ferroptosis and cell death mechanisms in Parkinson's disease," *Neurochemistry International*, vol. 104, pp. 34–48, 2017.
- [15] L. Mahoney-Sánchez, H. Bouchaoui, S. Ayton, D. Devos, J. A. Duce, and J. C. Devedjian, "Ferroptosis and its potential role in the pathophysiology of Parkinson's disease," *Progress in Neurobiology*, vol. 196, article 101890, 2021.
- [16] S. Kalayinia, F. Arjmand, M. Maleki, M. Malakootian, and C. P. Singh, "MicroRNAs: roles in cardiovascular development and disease," *Cardiovascular Pathology*, vol. 50, article 107296, 2021.
- [17] Y. Akkoc and D. Gozuacik, "MicroRNAs as major regulators of the autophagy pathway," *Biochimica et Biophysica Acta (BBA) - Molecular Cell Research*, vol. 1867, no. 5, article 118662, 2020.
- [18] K. Saliminejad, H. R. Khorram Khorshid, S. Soleymani Fard, and S. H. Ghaffari, "An overview of microRNAs: biology, functions, therapeutics, and analysis methods," *Journal of Cellular Physiology*, vol. 234, no. 5, pp. 5451–5465, 2019.
- [19] D. Han, X. Dong, D. Zheng, and J. Nao, "MiR-124 and the underlying therapeutic promise of neurodegenerative disorders," *Frontiers in Pharmacology*, vol. 10, article 1555, 2020.
- [20] C. A. Józwiak, S. S. Drake, Y. Zhang et al., "MicroRNA dysregulation in neurodegenerative diseases: a systematic review," *Progress in Neurobiology*, vol. 182, article 101664, 2019.
- [21] M. Luo, L. Wu, K. Zhang et al., "miR-137 regulates ferroptosis by targeting glutamine transporter SLC1A5 in melanoma," *Cell Death and Differentiation*, vol. 25, no. 8, pp. 1457–1472, 2018.
- [22] L. Geng, T. Zhang, W. Liu, and Y. Chen, "miR-494-3p modulates the progression of in vitro and in vivo Parkinson's disease models by targeting SIRT3," *Neuroscience Letters*, vol. 675, pp. 23–30, 2018.
- [23] C. Deng, J. Zhu, J. Yuan, Y. Xiang, and L. Dai, "Pramipexole inhibits MPP(+)-induced neurotoxicity by miR-494-3p/BDNF," *Neurochemical Research*, vol. 45, no. 2, pp. 268–277, 2020.
- [24] H. Liu, Y. Zhang, J. Yuan et al., "Dendritic cell-derived exosomal miR-494-3p promotes angiogenesis following myocardial infarction," *International Journal of Molecular Medicine*, vol. 47, no. 1, pp. 315–325, 2021.
- [25] A. Faversani, S. Amatori, C. Augello et al., "miR-494-3p is a novel tumor driver of lung carcinogenesis," *Oncotarget*, vol. 8, no. 5, pp. 7231–7247, 2017.
- [26] H. Lin, Z. P. Huang, J. Liu et al., "MiR-494-3p promotes PI3K/AKT pathway hyperactivation and human hepatocellular carcinoma progression by targeting PTEN," *Scientific Reports*, vol. 8, no. 1, p. 10461, 2018.
- [27] M. Brüll, A. S. Spreng, S. Gutbier et al., "Incorporation of stem cell-derived astrocytes into neuronal organoids to allow neuroglial interactions in toxicological studies," *ALTEX*, vol. 37, no. 3, pp. 409–428, 2020.
- [28] Y. Yang, M. Luo, K. Zhang et al., "Nedd4 ubiquitylates VDAC2/3 to suppress erastin-induced ferroptosis in melanoma," *Nature Communications*, vol. 11, no. 1, p. 433, 2020.
- [29] S. Gutbier, S. Kyriakou, S. Schildknecht et al., "Design and evaluation of bi-functional iron chelators for protection of dopaminergic neurons from toxicants," *Archives of Toxicology*, vol. 94, no. 9, pp. 3105–3123, 2020.
- [30] M. Campolo, G. Casili, F. Biundo et al., "The neuroprotective effect of dimethyl fumarate in an MPTP-mouse model of Parkinson's disease: involvement of reactive oxygen species/nuclear factor- $\kappa$ B/nuclear transcription factor related to NF-E2," *Antioxidants & Redox Signaling*, vol. 27, no. 8, pp. 453–471, 2017.
- [31] D. Li, H. Yang, J. Ma, S. Luo, S. Chen, and Q. Gu, "MicroRNA-30e regulates neuroinflammation in MPTP model of Parkinson's disease by targeting Nlrp3," *Human Cell*, vol. 31, no. 2, pp. 106–115, 2018.
- [32] Y. B. Hu, Y. F. Zhang, H. Wang et al., "miR-425 deficiency promotes necroptosis and dopaminergic neurodegeneration in Parkinson's disease," *Cell Death & Disease*, vol. 10, no. 8, p. 589, 2019.
- [33] B. Don Van, F. Gouel, A. Jonneaux et al., "Ferroptosis, a newly characterized form of cell death in Parkinson's disease that is regulated by PKC," *Neurobiology of Disease*, vol. 94, pp. 169–178, 2016.
- [34] P. Zhang, L. Chen, Q. Zhao et al., "Ferroptosis was more initial in cell death caused by iron overload and its underlying mechanism in Parkinson's disease," *Free Radical Biology & Medicine*, vol. 152, pp. 227–234, 2020.
- [35] B. R. Stockwell and X. Jiang, "The chemistry and biology of ferroptosis," *Cell Chemical Biology*, vol. 27, no. 4, pp. 365–375, 2020.
- [36] D. Tang, X. Chen, R. Kang, and G. Kroemer, "Ferroptosis: molecular mechanisms and health implications," *Cell Research*, vol. 31, no. 2, pp. 107–125, 2021.
- [37] A. Bruni, A. R. Pepper, R. L. Pawlick et al., "Ferroptosis-inducing agents compromise in vitro human islet viability and function," *Cell Death & Disease*, vol. 9, no. 6, p. 595, 2018.
- [38] S. Doll, F. P. Freitas, R. Shah et al., "FSP1 is a glutathione-independent ferroptosis suppressor," *Nature*, vol. 575, no. 7784, pp. 693–698, 2019.
- [39] X. Chen, J. Li, R. Kang, D. J. Klionsky, and D. Tang, "Ferroptosis: machinery and regulation," *Autophagy*, vol. 17, no. 9, pp. 2054–2081, 2021.
- [40] J. R. Wu, Q. Z. Tuo, and P. Lei, "Ferroptosis, a recent defined form of critical cell death in neurological disorders," *Journal of Molecular Neuroscience*, vol. 66, no. 2, pp. 197–206, 2018.
- [41] Y. Zhao, Y. Li, R. Zhang, F. Wang, T. Wang, and Y. Jiao, "The role of erastin in ferroptosis and its prospects in cancer therapy," *Oncotargets and Therapy*, vol. Volume 13, pp. 5429–5441, 2020.
- [42] F. Gouel, B. Do van, M. L. Chou et al., "The protective effect of human platelet lysate in models of neurodegenerative disease: involvement of the Akt and MEK pathways," *Journal of Tissue Engineering and Regenerative Medicine*, vol. 11, no. 11, pp. 3236–3240, 2017.
- [43] L. G. Gunnarsson and L. Bodin, "Parkinson's disease and occupational exposures: a systematic literature review and meta-

## Retraction

# Retracted: Chrysophanol Ameliorates Hemin-Induced Oxidative Stress and Endoplasmic Reticulum Stress by Regulating MicroRNA-320-5p/Wnt3a Pathway in HT22 Cells

### Oxidative Medicine and Cellular Longevity

Received 1 August 2023; Accepted 1 August 2023; Published 2 August 2023

Copyright © 2023 Oxidative Medicine and Cellular Longevity. This is an open access article distributed under the Creative Commons Attribution License, which permits unrestricted use, distribution, and reproduction in any medium, provided the original work is properly cited.

This article has been retracted by Hindawi following an investigation undertaken by the publisher [1]. This investigation has uncovered evidence of one or more of the following indicators of systematic manipulation of the publication process:

- (1) Discrepancies in scope
- (2) Discrepancies in the description of the research reported
- (3) Discrepancies between the availability of data and the research described
- (4) Inappropriate citations
- (5) Incoherent, meaningless and/or irrelevant content included in the article
- (6) Peer-review manipulation

The presence of these indicators undermines our confidence in the integrity of the article's content and we cannot, therefore, vouch for its reliability. Please note that this notice is intended solely to alert readers that the content of this article is unreliable. We have not investigated whether authors were aware of or involved in the systematic manipulation of the publication process.

Wiley and Hindawi regrets that the usual quality checks did not identify these issues before publication and have since put additional measures in place to safeguard research integrity.

We wish to credit our own Research Integrity and Research Publishing teams and anonymous and named external researchers and research integrity experts for contributing to this investigation.

The corresponding author, as the representative of all authors, has been given the opportunity to register their

agreement or disagreement to this retraction. We have kept a record of any response received.

### References

- [1] X. Zhao, D. Qiao, D. Guan, K. Wang, and Y. Cui, "Chrysophanol Ameliorates Hemin-Induced Oxidative Stress and Endoplasmic Reticulum Stress by Regulating MicroRNA-320-5p/Wnt3a Pathway in HT22 Cells," *Oxidative Medicine and Cellular Longevity*, vol. 2022, Article ID 9399658, 19 pages, 2022.

## Research Article

# Chrysophanol Ameliorates Hemin-Induced Oxidative Stress and Endoplasmic Reticulum Stress by Regulating MicroRNA-320-5p/Wnt3a Pathway in HT22 Cells

Xu Zhao,<sup>1</sup> Dongge Qiao,<sup>2</sup> Dongsheng Guan,<sup>3</sup> Kun Wang,<sup>1</sup> and Yinglin Cui<sup>3</sup> 

<sup>1</sup>Department of Pharmacy, Henan Province Hospital of TCM (The Second Clinical Medical College, Henan University of Traditional Chinese Medicine), Zhengzhou 450002, China

<sup>2</sup>Nursing Department, Henan Province Hospital of TCM (The Second Clinical Medical College, Henan University of Traditional Chinese Medicine), Zhengzhou 450002, China

<sup>3</sup>Department of Encephalopathy, Henan Province Hospital of TCM (The Second Clinical Medical College, Henan University of Traditional Chinese Medicine), Zhengzhou 450002, China

Correspondence should be addressed to Yinglin Cui; [hnszyy001@126.com](mailto:hnszyy001@126.com)

Received 27 April 2022; Accepted 7 July 2022; Published 29 July 2022

Academic Editor: Cornelia Wilson

Copyright © 2022 Xu Zhao et al. This is an open access article distributed under the Creative Commons Attribution License, which permits unrestricted use, distribution, and reproduction in any medium, provided the original work is properly cited.

Oxidative stress, endoplasmic reticulum (ER) stress, and neuronal cell apoptosis have been considered as the main pathogenesis factors of brain injury after intracerebral hemorrhage (ICH). Chrysophanol (CHR) has been proved to have neuroprotective effects, but the role and underlying mechanisms of CHR in ICH remain unclear. HT22 cells were dealt with hemin to mimic an in vitro ICH model and then subjected to treatment with or without CHR. The cell viability, apoptosis, ER stress, and oxidative stress were evaluated by conducting the cell counting kit-8 (CCK-8), TdT-mediated dUTP nick end labeling (TUNEL) staining assays, western blot, and corresponding kit, respectively. Further, microRNA-sequencing, bioinformatic analysis, dual-luciferase reporter method, and rescue experiments were conducted to explore the molecular mechanisms of CHR alleviating hemin-induced ER in HT22 cell. Our data revealed that CHR increased cells viability, antiapoptosis, anti-ER stress, and antioxidative stress under conditions of hemin-induced HT22 cell injury. Mechanically, it was observed that Wnt3a was competitively sponged by miR-320-5p, and CHR activated  $\beta$ -catenin pathway by regulating miR-320-5p/Wnt3a molecular axis. Finally, results from the rescue experiment suggested that CHR inhibited hemin-induced cells apoptosis, ER stress, and oxidative stress through regulating the miR-320-5p/Wnt3a axis in HT22 cells. In conclusion, CHR prevented hemin-induced apoptosis, ER stress, and oxidative stress via inhibiting the miR-320-5p/Wnt3a/ $\beta$ -catenin pathway in HT22 cells. Our results certified that CHR could be served as a promising treatment for brain damage following ICH.

## 1. Introduction

Intracranial hemorrhage (ICH) is a clinically common type of cerebral apoplexy with high disability rate and mortality, accounting for about 10-15% of all stroke types [1]. The overall survival rate of one year after intracerebral hemorrhage is about 40%, and only 12% to 39% of the survivors have the ability to live independently, which seriously threatens the lives and health of residents and brings heavy burden to families and society [2]. Current research has shown that oxidative stress and endoplasmic reticulum

(ER) stress are the prominent contributors in ICH-induced brain injury [3]. Accumulating studies have disclosed that ROS production is enhanced along with the decreasing antioxidant enzyme in the brain following ICH, and the increased oxidative stress aggravates inflammatory reaction, apoptosis, autophagy, and blood-brain barrier destruction, leading to further the aggravation of brain damage, suggesting that antioxidative stress strategies improve ICH-induced brain injury [3, 4]. Deng et al. uncovered that targeted intervention of ERK/Nrf2/HO-1 pathway attenuated neuronal death via attenuating oxidative stress in rats with ICH [5].

Zheng et al. reported that overexpression of Sirt3 inhibited oxidative stress-induced neuronal damage following ICH in rats with hyperglycemia [6]. Wang et al. indicated that the upregulation of SERPINE1 exacerbated cell apoptosis and promoted cell inflammation response in hemin-stimulated HT22 cells, suggesting SERPINE1 as a new mechanism and therapeutic target of brain damage after ICH [7]. Although significant development has been made to explore the mechanisms of brain injury after ICH, there is still no safe and valid clinical therapy method to obviously ameliorate the prognosis of ICH [8]. Therefore, it is important to elucidate the pathophysiology of intracerebral hemorrhage and to discover new therapeutic methods.

Chrysophanol (CHR) is an active component found in *Polygoni multiflori* and *Rhamnus alpinus* L. and is used to prepare Traditional Chinese Medicine [9, 10]. CHR is an anthraquinone that exhibits excellent pharmacokinetic properties that can be used to achieve a good extent of absorption and slow rate of elimination [11]. It has been recently reported that CHR exhibits numerous beneficial pharmacological properties (such as anticancer, anticonvulsant, hepatoprotective, antioxidative, anti-inflammatory, antiulcer, and antimicrobial properties) [11, 12]. Park et al. disclosed that CHR repressed breast cancer cell formation through regulating mitochondrial apoptosis and ER stress by controlling the AKT/MAPK pathway [13]. Lu et al. revealed that CHR ameliorates doxorubicin-induced cardiotoxicity by inhibiting cellular PARylation [14]. CHR could prevent hepatitis B virus X protein- (HBx-) induced hepatic stellate cell activation through the activation of ER stress [15]. It has been recently reported that CHR exhibits neuroprotective properties. For example, Cui et al. reported that CHR could protect against nerve damage by regulating the process of mitochondrial autophagy in mice suffering from cerebral ischemia/reperfusion [16]. Zhao et al. reported that CHR helped reduce oxidative stress and ER stress to alleviate cerebral ischemia/reperfusion-induced neuronal injury in mice [17, 18]. Chu et al. demonstrated that CHR ameliorated cognition dysfunction and neuronal loss by anti-inflammation in mice with diabetic encephalopathy [19]. However, the roles of CHR and the underlying mechanisms associated with treating ICH are still unclear.

MicroRNAs (miRNAs) are a member of noncoding RNAs that contain 18–25 nucleotides, which influence numerous biological and pathological processes through the process of posttranscriptional regulation of gene expression [20]. Numerous researchers demonstrated that miRNAs influence the occurrence and development of ICH [21, 22]. For example, upregulation of miR-126 could protect against ICH. The behavioral performance can be improved, and apoptosis can be inhibited via the upregulation of VEGF-A and downregulation of caspase-3 [23]. Modulation of the miR-124/ferroportin pathway inhibited neuronal cell death by decreasing the extent of apoptosis and ferroptosis realized in aged mice with ICH [24]. Iso-rhynchophylline compactivity sponged TP53 to inhibit its expression by upregulating miR-122-5p. This subsequently prevented the occurrence of ferroptosis-induced nerve injury following ICH [25]. The results revealed that miRNAs

exerted critical roles in the occurrence and development of ICH, which could be used as potential therapeutic targets. However, whether CHR function in ICH are still unclear.

Hemin, a cytotoxic decomposition product released from hemoglobin, is key mediators of neuronal damage during ICH and is widely used to simulate the ICH injury model [26–28]. For example, Wang et al. demonstrated that TGF $\beta$ 1/SERPINE1 axis is a novel mechanism promoting the development of ICH using hemin-induced ICH model in vitro [7]. Chu et al. indicated that inhibition of IL-1RA protected against neuronal necroptosis by decreasing the necrosome complex levels in hemin-induced ICH model in vitro and vivo, suggesting that targeted inhibition of IL-1R1 may be a promising therapeutic strategy for ICH patients [29]. In addition, HT22 cell is an immortalized mouse hippocampal neuronal cell line subcloned from parent HT4 cells that were originally immortalized from cultures of primary mouse hippocampal neurons [30], and HT22 cell is known to phenotypically resemble neuronal precursor cells, which has been used in cell model to study of hemin-induced injury in neuronal cells [7, 29]. Therefore, we used hemin-induced HT22 cell injury to establish an in vitro ICH model to understand the effect exerted by CHR on the hemin-induced HT22 cell injury and to explore the mechanism following which CHR prevented hemin-induced HT22 cell injury. We conducted comprehensive miRNAs-sequencing, bioinformatics prediction, dual-luciferase reporting, and rescue experiments to arrive at the results.

## 2. Materials and Methods

**2.1. Reagents.** CHR (purity  $\geq$  98%) was obtained from Solarbio Life Sciences (Beijing, China) and dissolved in dimethyl sulfoxide (DMSO, purity  $\geq$  99.5.0%, Sigma) to form a stock solution of concentration 40 mM. The solution was stored at  $-20^{\circ}\text{C}$ . The prepared stock solution was diluted to form the corresponding working solutions before conducting each set of experiments. Hemin (purity  $\geq$  96%) was obtained from Sigma-Aldrich (St. Louis, MO, USA). Tunicamycin (TM) was obtained from Shanghai Yuanye Biotechnology Co., Ltd. (Shanghai, China). Dulbecco's modified eagle's medium (DMEM), phosphate-buffered saline (PBS), and penicillin/streptomycin were obtained from Thermo Fisher Scientific (Waltham, MA, USA). The cell counting kit-8 (CCK-8), lactate dehydrogenase (LDH) assay kit, malondialdehyde (MDA) assay kit, superoxide dismutase (SOD) assay kit with WST-8, glutathione peroxidase (GPx) assay kit with DTNB, reactive oxygen species (ROS) assay kit, and One Step TdT-mediated dUTP Nick-End Labeling (TUNEL) apoptosis assay kit were bought from Beyotime (Shanghai, China). Fetal bovine serum (FBS) was bought from Gibco (Thermo Fisher Scientific, USA). The caspase-3 assay kit was purchased from Solarbio Life Sciences (Beijing, China). The Hairpin-itTM miRNA real-time PCR quantification kit was obtained from GenePharma (Shanghai, China). The PrimeScript<sup>TM</sup> RT reagent kit with gDNA eraser and TB Green<sup>®</sup> Fast qPCR Mix were obtained from Takara (Dalian, China). Antibody against phospho-eukaryotic translation initiation factor 2 $\alpha$  (p-Eif2 $\alpha$ , #3398, 1:1000), C/EBP homologous protein (CHOP, #2895, 1:1000), cleaved

caspase-12 (#35965, 1:1000), cleaved caspase-3 (#9661, 1:1000), Bax (#2772, 1:2000), and Bcl-2 (#2870, 1:2000) were bought from Cell Signaling Technology (Beverly, MA, USA). Antibody against glucose-regulated protein 78 (GRP78, ab108315, 1:1000),  $\beta$ -actin (ab179467, 1:5000), Wnt3a (ab219412, 1:1000),  $\beta$ -catenin (ab108315, 1:1000), and Lamin B (ab16048, 0.1  $\mu$ g/ml) were obtained from Abcam (Cambridge, MA, USA).

**2.2. Culture and Treatment of HT22 Cells.** HT22 cell is an immortalized mouse hippocampal neuronal cell line subcloned from parent HT4 cells that were originally immortalized from cultures of primary mouse hippocampal neurons [30]. HT22 cell is known to phenotypically resemble neuronal precursor cells, which has been used in cell model to study of hemin-induced injury in neuronal cells [7, 29]. HT22 cells (Merck, USA) were cultured in DMEM containing 10% FBS and 1% penicillin/streptomycin in an atmosphere with 5% CO<sub>2</sub> at 37°C. After growing to 80% confluence, the HT22 cells were used for experiment. The HT22 cells were dealt with various concentrations of hemin (0, 10, 20, 40, 80, and 100  $\mu$ M) over a period of 6 h to simulate the in vitro ICH model [7]. Subsequent studies were conducted using 20  $\mu$ M of hemin. To evaluate the security of CHR, HT22 cells were dealt with various concentrations of CHR (0, 5, 10, 20, and 40  $\mu$ M). To evaluate the neuroprotective effects of CHR, HT22 cells were dealt with CHR after treating them with 20  $\mu$ M of hemin over a period of 6 h. Following this, they were incubated for 24 h. The negative control groups were dealt with an equal volume of solvent (Figure S1).

**2.3. CCK-8 Assay.** The viability of the HT22 cells was tested by the CCK-8 assay depending on the operating instruction [31]. Briefly, the treated cells were dealt with the CCK-8 reagent at 37°C for 2 hours. Following this, the optical density (OD) of the specimens was detected at 450 nm with a microplate reader (Thermo Fisher Scientific).

**2.4. Lactate Dehydrogenase (LDH) Activity.** The activity of LDH was measured according to the previous report [32]. LDH activity was detected by an LDH Activity Assay Kit (Solarbio, China) on the basis of the operating instruction. Briefly, the obtained supernatants were mixed with various reagents provided in the LDH Activity Assay Kit. Then, the OD of the samples was recorded at 450 nm with a microplate reader (Thermo Fisher Scientific). The LDH activity (U/l) was counted as follows:  $(OD_U - OD_C) \times C_S \times N \times 1000 / (OD_S - OD_B)$ , where OD<sub>U</sub> indicates the OD value of the specimen pipe, OD<sub>C</sub> indicates the OD value of the blank pipe, C<sub>S</sub> indicates the standard concentration (2 mmol/l), N indicates the multiples of dilution of the specimens before testing, OD<sub>S</sub> indicates the OD value of the standard pipe, and OD<sub>B</sub> indicates the OD value of the control pipe.

**2.5. TUNEL Staining.** TUNEL staining was performed according to the previous report [33]. Cell apoptosis rates were assessed by the One Step TUNEL Apoptosis Assay Kit (Beyotime, Shanghai, China) on the base of the operating instruction. In brief, the treated cells were immobilized by using 4% paraformaldehyde for 30 min. Following this, they

were dealt with the TUNEL detection reagent. Subsequently, these cells were coincubated in the dark at 37°C for 60 min. Finally, the TUNEL-positive cells were observed and counted by the fluorescence microscopy.

**2.6. Nuclear Protein Extraction.** The nuclear protein from the treated cells was obtained using the Nuclear and Cytoplasmic Protein Extraction Kit (Beyotime, Shanghai, China) [34]. The protocols outlined by the manufacturer were followed to conduct the experiments. The extracted samples were detected using the western blotting technique in the presence of the anti- $\beta$ -catenin antibody (ab108315, 1:1000). LaminB1 (ab16048, 0.1  $\mu$ g/ml) was served as the internal reference.

**2.7. Western Blot Analysis.** Western blot was operated according to the previous report [35]. The cells were lysed using the precooled radio immune-precipitation assay buffer (RIPA, Beyotime, Shanghai, China) including protease and phosphatase inhibitors (Sigma-Aldrich, USA). The experiments were conducted at 4°C, and the extracted protein specimens were quantified with the BCA Protein Assay Kit (Millipore, US). Equal amounts of protein specimens were dealt with the sodium dodecyl sulfate-polyacrylamide gel electrophoresis (SDS-PAGE) technique. The samples were then transferred to polyvinylidene fluoride (PVDF) membranes (Millipore, USA). Following this, the membranes were sealed with 5% skimmed milk solution at room temperature for 1 h. Subsequently, the specimens were incubated overnight with primary antibodies at 4°C. Finally, the membranes were incubated with the HRP-conjugated secondary antibodies at room temperature (incubation time: 2 h). The samples were visualized using the ECL detection reagent on the ChemiDoc Imaging System (Bio-Rad Laboratories, Inc.). The blot of the membrane was analyzed with ImageJ software (National Institutes of Health, Bethesda, MD) and normalized to  $\beta$ -actin (Abcam, ab179467, 1:5000) or LaminB1 (Abcam, ab16048, 0.1  $\mu$ g/ml). The primary antibodies used to conduct the western blot tests were phospho-eIF2 $\alpha$  (dilution, 1:1000, Cell Signaling Technology, #3398), CHOP (dilution, 1:1000, Cell Signaling Technology, #2895), cleaved caspase-12 (dilution, 1:1000, Cell Signaling Technology, #35965), cleaved caspase-3 (dilution, 1:1000, Cell Signaling Technology, #9661), Bax (dilution, 1:1000, Cell Signaling Technology, #2772), Bcl-2 (dilution, 1:1000, Cell Signaling Technology, #2870), GRP78 (dilution, 1:1000, Abcam, ab108315), Wnt3a (dilution, 1:1000, Abcam, ab219412), and  $\beta$ -catenin (dilution, 1:5000, Abcam, ab108315).

**2.8. Caspase-3 Activity.** The caspase-3 activity was detected following previously reported protocols [33]. The caspase-3 activity was detected with the caspase-3 activity kit (Solarbio, China) according to the manufacturer's instructions. Briefly, the total protein from the collected cells was extracted with the lysis buffer, and the BCA protein assay kit was used for quantification. The specimens were incubated in the presence of the reaction buffer, and the OD value of the specimens was recorded at 405 nm with a microplate reader (Thermo Fisher Scientific).

**2.9. Determination of MDA, SOD, and GPx Levels.** The levels of MDA, SOD, and GPx in HT22 cells were determined using Lipid Peroxidation MDA Assay Kit (Beyotime Biotechnology, #S0131S), Total Superoxide Dismutase Assay Kit (Beyotime Biotechnology, #S0101S), and Total Glutathione Peroxidase Assay Kit with NADPH (Beyotime Biotechnology, #S0058) following the manufacturer's instructions, respectively [36].

**2.10. Measurement of ROS Production.** The ROS levels were assessed with Reactive Oxygen Species Assay Kit (Beyotime Biotechnology, #S0063) according to the manufacturer's operating instruction [37]. Briefly, pretreated cells were incubated with dichlorodihydrofluorescein diacetate (DCFH-DA, 20  $\mu$ M) in Hanks' balanced salt buffer at 37°C for 20 min. The ROS levels were detected with a fluorescence microplate reader (BioTek Synergy 2, USA).

**2.11. MicroRNA-Sequencing.** MicroRNA-sequencing was performed according to the previous report [38]. Briefly, total RNAs were extracted from three independent samples of hemin-induced HT22 cells with or without CHR using the TRIzol reagents (Invitrogen) in accordance with the manufacturer's recommended protocol. Following this, the purified cDNA library was established using an Illumina TruSeq Small RNA Preparation Kit, depending on the manufacturer's recommendations. Subsequently, the samples were subjected to the process of next-generation sequencing (Illumina HiSeq technology) at the Beijing Genomics Institute (BGI, Shenzhen, China) in accordance with the manufacturer's instructions. Subsequently, Illumina's analysis software was used to collect raw sequencing data. Finally, the differentially expressed miRNAs (in hemin-induced HT22 cells and hemin-induced HT22 cells posttreated with CHR) were analyzed using the EBseq R package. The  $|\log F C| > 1$  and  $p$  value  $< 0.05$  served as the screening criteria to obtain the differentially expressed miRNAs.

**2.12. Bioinformatics Analysis.** It has been proved that the function of miRNAs is closely related to its target mRNA [39]. To explore the potential biological function of differentially expressed miRNAs, the miRWalk software was used to predict the potential target genes for these differentially expressed miRNAs. Then, these target genes of miRNAs were analyzed by Kyoto Encyclopedia of Genes and Genomes (KEGG) and Gene Ontology (GO) enrichment analysis.  $p$  values  $< 0.05$  were considered significantly.

**2.13. Quantitative Real-Time PCR (RT-PCR) Analysis.** RT-PCR analysis was performed based on previous report [40]. Total RNAs were extracted from the treated cells by the TRIzol reagent (Invitrogen) according to the operating instructions. For miRNAs, the processes of cDNA synthesis and amplification were conducted by the Hairpin-it™ Real-Time PCR miRNAs kit (GenePharma, Shanghai, China). For mRNAs, cDNA synthesis and amplification were conducted using the PrimeScript™ RT reagent Kit with gDNA Eraser (Takara, Dalian, China) and TB Green® Fast qPCR Mix (Takara, Dalian, China), respectively. All RT-PCR tests were performed using the ABI 7500 Fast Real-Time PCR

system (Applied Biosystems). GAPDH and U6 were served as the internal reference for mRNAs and miRNAs, respectively. RT-PCR tests were performed in triplicate, and the expressions of miRNAs and mRNAs were computed by the  $2^{-\Delta\Delta C_t}$  assay. The primer sequences corresponding to miRNAs or mRNA are shown in Table S1.

**2.14. Cell Transfection.** The miR-320-5p mimics, miR-320-5p inhibitors, and their negative controls (NC inhibitor and NC mimics) were obtained from GenePharma (Suzhou, China). The small hairpin RNA (shRNA) silencing Wnt3a (sh-Wnt3a) and its negative control (sh-NC) were also brought from GenePharma (Shanghai, China). The HT22 cells were transfected by Lipofectamine™ 3000 (Invitrogen) on the base of the operating instructions. Following transfection, the transfection efficiency was confirmed by the RT-PCR technique. The sequences of the miR-320-5p mimics, miR-320-5p inhibitor, and Wnt3a shRNA are listed in Table S1.

**2.15. Dual-Luciferase Reporter Assay.** The dual-luciferase report assay was used to verify the interaction between miR-320-5p and Wnt3a. Dual-luciferase reporter assay was performed according to the previous report [40]. The wild-type or mutant vectors corresponding to Wnt3a 3'UTR were constructed using the pmirGLO dual-luciferase vector. The wild or mutant vectors corresponding to Wnt3a 3'UTR and miR-320-3p mimics (or NC mimics) were cotransfected to HT22 cells using the Lipofectamine™ 3000 reagent (Invitrogen, Carlsbad, CA, USA). Following the process of cotransfection for 48 h, the firefly luciferase and Renilla luciferase activities were detected using the Dual-Luciferase Reporter Assay System. The Renilla luciferase activity was served as an internal reference for the normalization of the firefly luciferase activity.

**2.16. Statistical Analyses.** Data were marked as mean  $\pm$  standard deviation (S.D.). All data were analyzed and charted by the GraphPad Prism 6.0 software (GraphPad Software, CA, USA). Student's  $t$ -test and the one-way ANOVA tests were conducted to compare the characteristics of two groups and more than two groups, respectively. At least three independent experiments were performed for each set. The  $p$  values  $< 0.05$  were considered to be statistically significant.

### 3. Results

**3.1. The Protective Effect of CHR against Hemin-Induced Apoptosis, ER Stress, and Oxidative Stress in HT22 Cells.** It has been reported that hemin is a cytotoxic decomposition product released from hemoglobin during the lysis of erythrocytes, and it mimics the secondary injury observed following ICH [26–28]. To establish an in vitro ICH injury model, HT22 cell was incubated with various concentrations of hemin. Cell viability and cytotoxicity were detected by CCK-8 assay and LDH cytotoxicity assay to confirm an optional condition. The results indicated that HT22 cell viability and cytotoxicity were significantly augmented with increasing hemin concentration in a dose-dependent manner (Figure S2). Dose-response

studies showed that 20  $\mu\text{M}$  hemin efficiently induced HT22 cell damage (half maximal effective concentration [EC50] = 20  $\mu\text{M}$ , Figure S2). Therefore, we selected 20  $\mu\text{M}$  of hemin (optimal condition) to treat HT22 cells for 6 h to construct an in vitro ICH injury model for subsequent experiments.

To understand the neuroprotective effect of CHR, HT22 cells were dealt with or without 20  $\mu\text{M}$  hemin for 6 h followed by CHR (0, 5, 10, 20, and 40  $\mu\text{M}$ ) over a period of 24 h. The results of CCK-8 showed that CHR exhibited no cell viability in the absence of hemin but significantly increased HT22 cell viability in hemin-induced cell injury models (Figure 1(a)), indicating that CHR had a concentration-dependent protective effect on hemin-induced damaged cells, while the result of western blot indicated that 10  $\mu\text{M}$  CHR had no effect on the PCNA expression in HT22 cells without hemin but could markedly reduce the PCNA expression in HT22 cells with hemin (Figure 1(b)). In addition, analysis of the LDH activity indicated that CHR could markedly reduce the level of LDH release in HT22 cells with hemin but had no effect on the LDH release level in HT22 cells devoid of hemin (Figure 1(c)). These data suggested that CHR (10  $\mu\text{M}$ ) could be efficiently used to treat neuronal cells. Hence, it was used for further studies.

It has been recently reported by several research groups that apoptosis and ER stress are the major cause of neuronal injury post ICH, and restraint of neuronal apoptosis and ER stress can potentially ameliorate ICH prognosis [41, 42]. To explore the effect of CHR on HT22 cell apoptosis in hemin-induced cell damage, the level of apoptosis was measured by caspase-3 activity, TUNEL staining assay, and western blot assay. It was observed that the caspase-3 activity increased significantly in the hemin-induced HT22 cells under conditions of injury. It was inhibited significantly by CHR post-treatment (Figure 1(d)). The results obtained from the TUNEL staining assays revealed that hemin effectively induced the apoptosis of HT22 cells, which was remarkably mitigated by CHR treatment (Figure 1(e)). In addition, the protein expressions for the apoptosis-related genes were analyzed by the western blot, and the results that the protein expression of Bax and cleaved caspase-3 was remarkably increased and the protein expression of Bcl-2 was significantly decreased in hemin-stimulated HT22 cells, the phenomenon was obviously ameliorated CHR treatment (Figure 1(f)). All the data indicated that CHR could protect neurons from hemin-induced apoptosis and ER stress. Western blot was used to assess the protein expressions of the ER stress-related genes (GRP78, cleaved caspase-12, p-eIF2 $\alpha$ , and CHOP), the results demonstrated that the levels of protein expressions of GRP78, cleaved caspase-12, p-eIF2 $\alpha$ , and CHOP increased significantly in hemin-induced HT22 cell injury, and the effect was inhibited following the process of CHR treatment (Figure 1(g)). The above results indicated that the process of CHR treatment could reduce hemin-induced ER stress and apoptosis in HT22 cells.

Oxidative stress plays a pivotal role in neuronal apoptosis and ER stress, especially brain damage following ICH [5, 43]. We further investigate whether CHR regulates hemin-induced oxidative stress in HT22 cells. As shown in Figure 2,

the levels of MDA and ROS were significantly increased in hemin-induced HT22 cell injury, the phenomenon was obviously inhibited by CHR treatment. While SOD activity and GPx activity were significantly decreased in hemin-induced HT22 cell injury, the phenomenon was obviously reversed by CHR treatment. These data indicated that CHR inhibited hemin-induced oxidative stress in HT22 cells.

*3.2. CHR Protects against Hemin-Induced Apoptosis, ER Stress, and Oxidative Stress by Restraining the Expression of miR-320-5p in HT22 Cells.* Recently conducted clinical and preclinical studies have revealed that the levels of expressions of various miRNAs get altered in serum or cerebrospinal fluid following ICH, and these miRNAs could be used as potential therapeutic targets for ICH [22, 44–47], suggesting that dysregulation of miRNAs acts as key roles in development and incidence of ICH. To elucidate the neuroprotective mechanism of CHR against hemin-induced HT22 cell injury, the process of miRNA-sequencing was performed using hemin-induced HT22 cells posttreated with or without CHR. It was observed that the levels of expressions of the three miRNAs were outstandingly upregulated in the CHR treatment group, whereas the levels of expressions of the eight miRNAs were markedly downregulated (Figure 3(a) and Table S2). Then, KEGG and GO analyses were performed for the different miRNAs. The GO enrichment revealed that the differential miRNAs were involved in antioxidative activity, nervous system development, neuron differentiation, and so on (Figure S3A). And KEGG analysis showed that the differential miRNAs were centrally enriched in Wnt signaling pathway, Axon guidance, Rap1 signaling pathway, and so on (Figure S3B). Subsequently, we used the RT-qPCR to verify the six significantly altered miRNAs (three upregulated miRNAs and three downregulated miRNAs). The results of the RT-qPCR demonstrated that the changes in the levels of expression of the six miRNAs were consistent with the results obtained using the miRNAs-sequencing, and the difference of the miR-320-5p was the most significant (Figure 3(b)). And we also observed that CHR treatment significantly inhibited hemin-induced miR-320-5p expression in HT22 cells (Figure 3(c)), manifesting that miR-320-5p could be a key target of CHR to protect hemin-induced HT22 cell injury. To further investigate the effect of miR-320-5p on normal or hemin-induced HT22 cells, HT22 cells transfected with miR-320-5p mimics and NC mimics were dealt with or without hemin. We observed that the miR-320-5p expression significantly increased in normal or hemin-induced HT22 cell transfected with miR-320-5p mimics (Figure S4A). Results from CCK-8 uncovered that the miR-320-5p overexpression inhibited cell viability in hemin-induced HT22 cells but had no effect on HT22 cell viability in the absence of hemin (Figure S4B). The caspase-3 activity assay and TUNEL staining showed that miR-320-5p overexpression remarkably increased hemin-induced apoptosis in HT22 cells but had no effect on HT22 cell apoptosis in the absence of hemin (Figure S4C–S4E). Moreover, we found that overexpression of miR-320-5p promoted the relative levels of MDA and ROS and inhibited the activity of SOD and GPx in hemin-induced HT22 cells; but overexpression of miR-320-5p had no effect

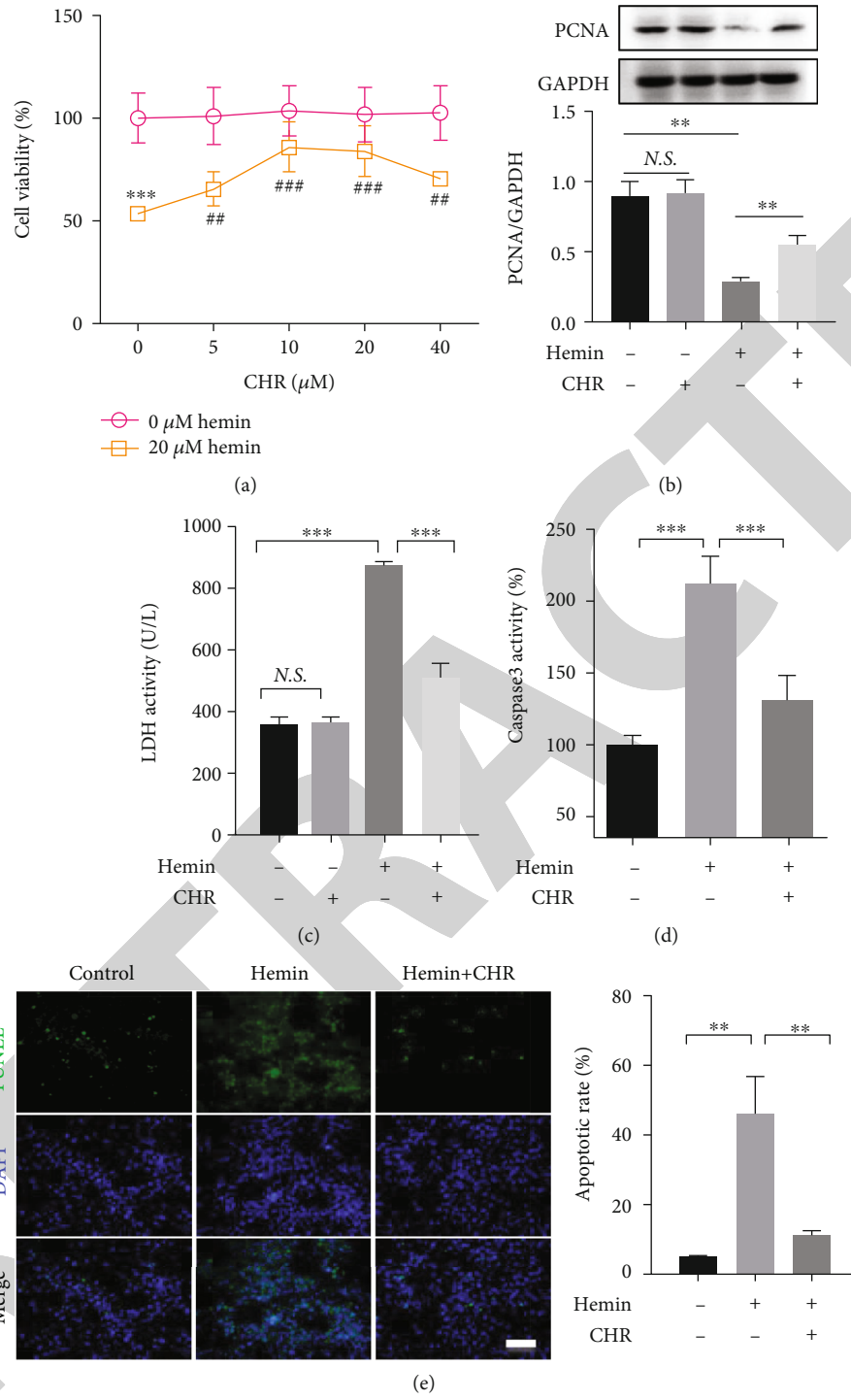
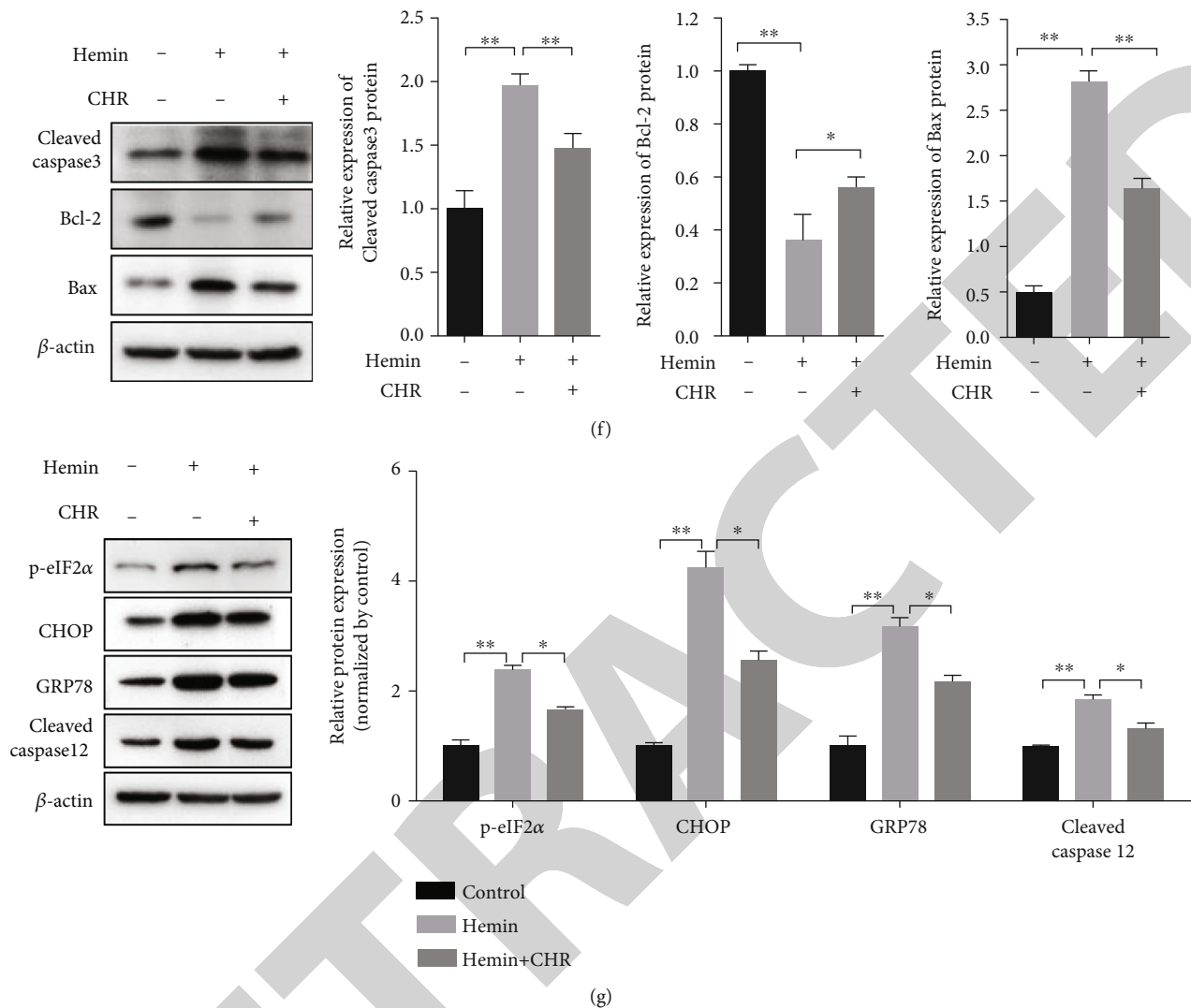


FIGURE 1: Continued.





**FIGURE 1:** Chrysophanol (CHR) prevented HT22 cell survival, antiapoptosis, and anti-ER stress in hemin-induced HT22 cell injury models. (a) Cell viability was studied for nonhemin (0  $\mu$ M) and hemin (20  $\mu$ M)-treated HT22 cells dealt with varying concentrations of CHR (0, 5, 10, 20, and 40  $\mu$ M; treatment time: 24 h) by conducting CCK-8 assays. \*\*\* $p$  < 0.001 vs. nonhemin. ## $p$  < 0.01 and ### $p$  < 0.001 vs. hemin.  $N$  = 3. (b) Expression of PCNA affected by CHR in hemin-induced HT22 cells was detected using the western blot.  $N.S.$   $p$   $\geq$  0.05 and \*\* $p$  < 0.01.  $N$  = 3. (c) LDH release level was analyzed in nonhemin (0  $\mu$ M) and hemin (20  $\mu$ M)-treated HT22 cells in the presence and absence of CHR (0, 5, 10, 20, and 40  $\mu$ M; treatment time: 24 h) by conducting the LDH cytotoxicity assay.  $N.S.$   $p$   $\geq$  0.05 and \*\*\* $p$  < 0.001.  $N$  = 3. (d) Caspase-3 activity was studied in hemin-induced cells in the presence and absence of CHR (10  $\mu$ M). \*\*\* $p$  < 0.001. (e) Rate of cell apoptosis was determined using hemin-induced cells in the presence and absence of CHR (10  $\mu$ M; treatment time: 24 h) by conducting TUNEL staining assays. Bar = 100  $\mu$ m, \*\* $p$  < 0.01.  $N$  = 3. (f) The protein expression levels of apoptosis-related genes (cleaved caspase-3, Bax, and Bcl-2) were analyzed in hemin-induced cells in the presence and absence of CHR (10  $\mu$ M; treatment time: 24 h) using the western blot technique. \* $p$  < 0.05, \*\* $p$  < 0.01, and \*\*\* $p$  < 0.001.  $N$  = 3. (g) Levels of protein expression of ER stress-related genes (p-eIF2 $\alpha$ , CHOP, GRP78, and cleaved caspase-12) were analyzed in hemin-induced cells in the presence and absence of CHR (10  $\mu$ M; treatment time: 24 h) using the western blot technique. \* $p$  < 0.05 and \*\* $p$  < 0.01.  $N$  = 3.

on oxidative stress related indexes (MDA, ROS, SOD, and GPx) in HT22 cells without hemin (Figure S4F). These data indicated that overexpression of miR-320-5p enhances hemin-induced cell survival, ER stress, and oxidative stress in HT22 cell.

Then, we further explored whether the overexpression of miR-320-5p reversed the neuroprotection effect generated by CHR. The results of CCK-8 assays disclosed that CHR treatment outstandingly enhanced cell viability in hemin-induced

HT22 cells, and this enhancement was reduced by overexpression of miR-320-5p (Figure S5A). The results obtained using the TUNEL staining assays also indicated that CHR treatment inhibited hemin-induced cell apoptosis in HT22 cells, and the inhibition was alleviated by the overexpression of miR-320-5p (Figure 3(d)). Consistent with the results of TUNEL staining assays, CHR treatment remarkably inhibited caspase-3 activate of HT22 cells in exist of hemin, and the inhibition was weakened by miR-320-5p

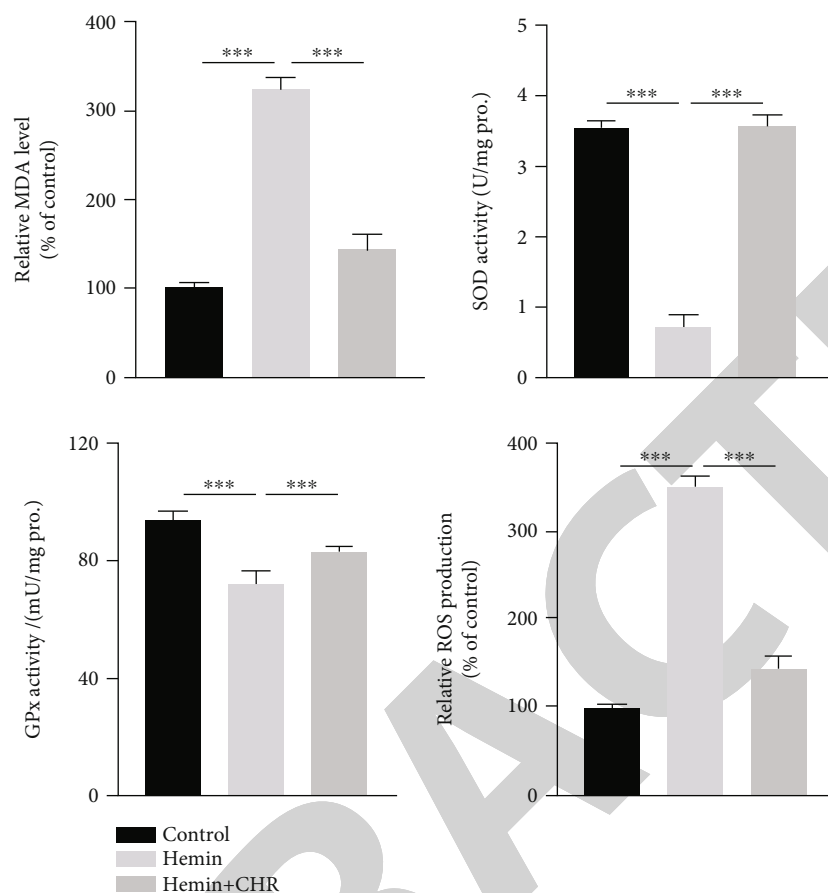


FIGURE 2: Chrysophanol (CHR) inhibited hemin-induced oxidation stress in HT22 cell. The changes of oxidation stress-related indexes (ROS, MDA, SOD, and GPx) were analyzed in the hemin-induced cells with or without CHR (10  $\mu$ M) (treatment time: 24 h) using the western blot. \*\*\* $p < 0.001$ .  $N = 3$ .

overexpression (Figure S5B). Moreover, the western blot was used to assess the protein expression of ER stress-related gene (GRP78, cleaved caspase-12, p-eIF2 $\alpha$ , and CHOP), the results revealed that CHR inhibited the protein expression of GRP78, cleaved caspase-12, p-eIF2 $\alpha$ , and CHOP in the hemin-induced HT22 cells, and the inhibition was alleviated by the overexpression of miR-320-5p (Figure 3(e)). Finally, we examined the changes of oxidative stress-related indicators (MDA, ROS, SOD, and GPx) to evaluate whether CHR affected hemin-induced oxidative stress in HT2 cells through miR-320-5p. As shown in Figure 3(f), CHR inhibited the relative levels of MDA and ROS in the hemin-induced HT22 cells, and the inhibition was obviously alleviated by overexpression of miR-320-5p. While CHR increased the ROS activity and GPx activity in the hemin-induced HT22 cells, the phenomenon was obviously weakened by overexpression of miR-320-5p. Altogether, these data suggested that CHR increased cell survival, antiapoptosis, anti-ER stress, and antioxidative stress by inhibiting miR-320-5p in hemin-induced HT22 cell injury model.

**3.3. CHR Activates the Wnt3a/ $\beta$ -Catenin Pathway by Restraining miR-320-5p Expression.** The miRWalk software was used for predicting the potential target genes of miR-

320-5p, and then, the potential target genes of miR-320-5p were performed by KEGG analysis. We found that these genes mainly enriched in the WNT signaling pathway, neuroactive ligand-receptor interaction, cAMP signaling pathway, and so on (Figure S3C). Meanwhile, we found a highly conserved potential binding site between miR-320-5p and Wnt3a mRNA 3'UTR in the WNT signaling pathway (Figure 4(a)). A dual-luciferase reporter assay system was used to verify the interaction between miR-320-5p and Wnt3a. Fragments of Wnt3a mRNA 3'UTR, containing either the binding site (wild type) for miR-320-5p or the binding site of MUT, were designed (Figure 4(a)). The results of dual-luciferase reporter assay system indicated that the cotransfection of Wnt3a-3'UTR (wild type) with the miR-320-5p mimics resulted in an outstanding reduction in the relative luciferase activity, whereas the cotransfection of the Wnt3a-3'UTR-mutant with the miR-320-5p mimics did not result in a decrease in the luciferase activity (Figure 4(b)). We further confirmed the regulation of Wnt3a by miR-320-5p in HT22 cells. The miR-320-5p mimics inhibited Wnt3a expression by augmenting the expression of miR-320-5p, while the miR-320-5p inhibitor enhanced the level of expression of Wnt3a by restraining miR-320-5p expression (Figure 4(c)),

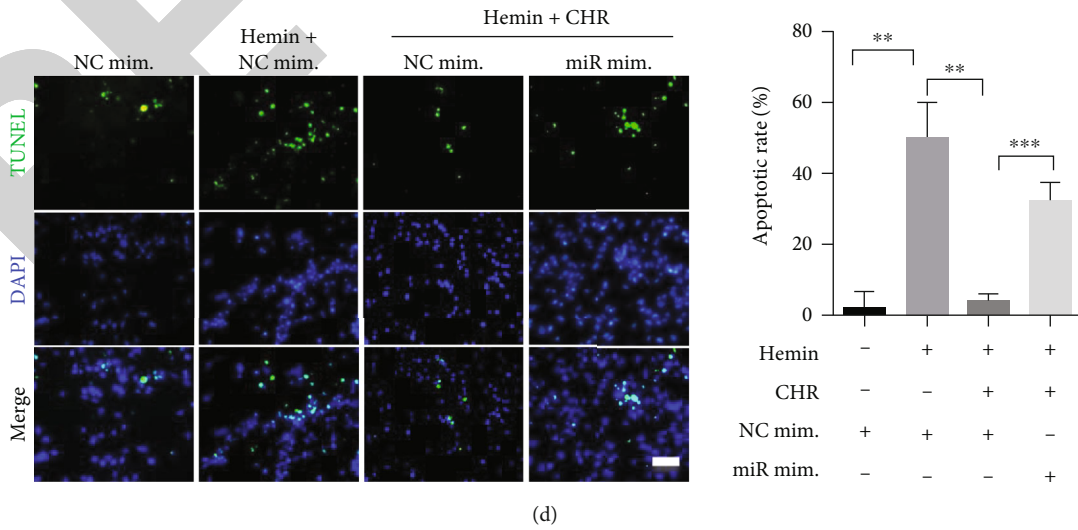
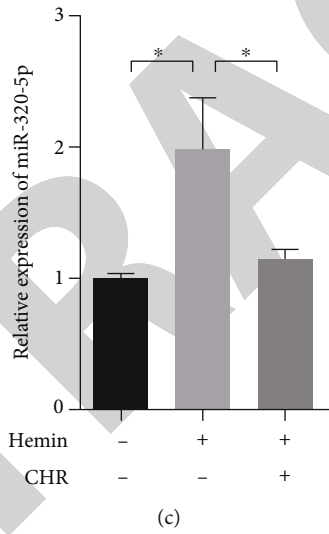
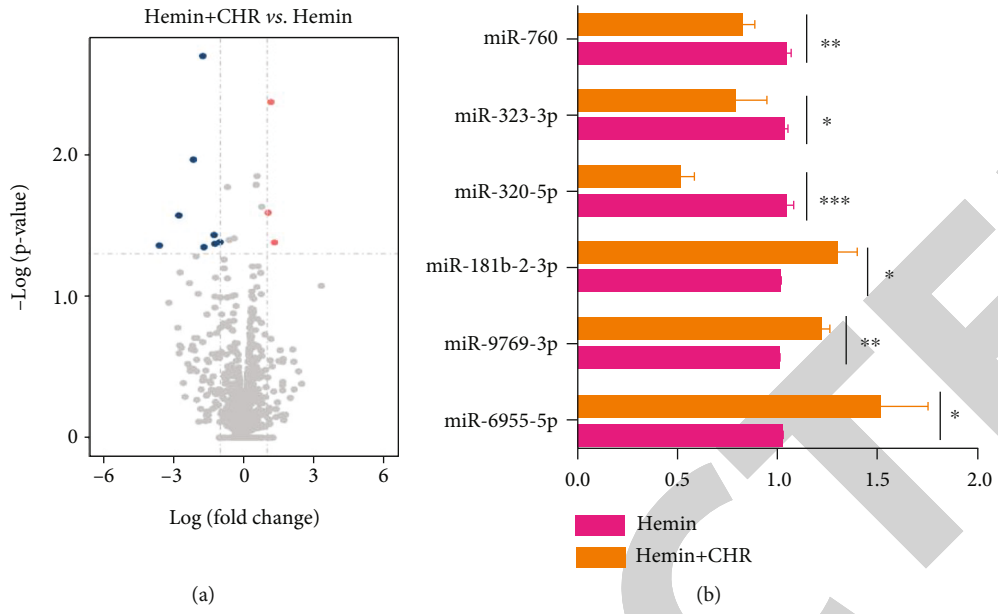
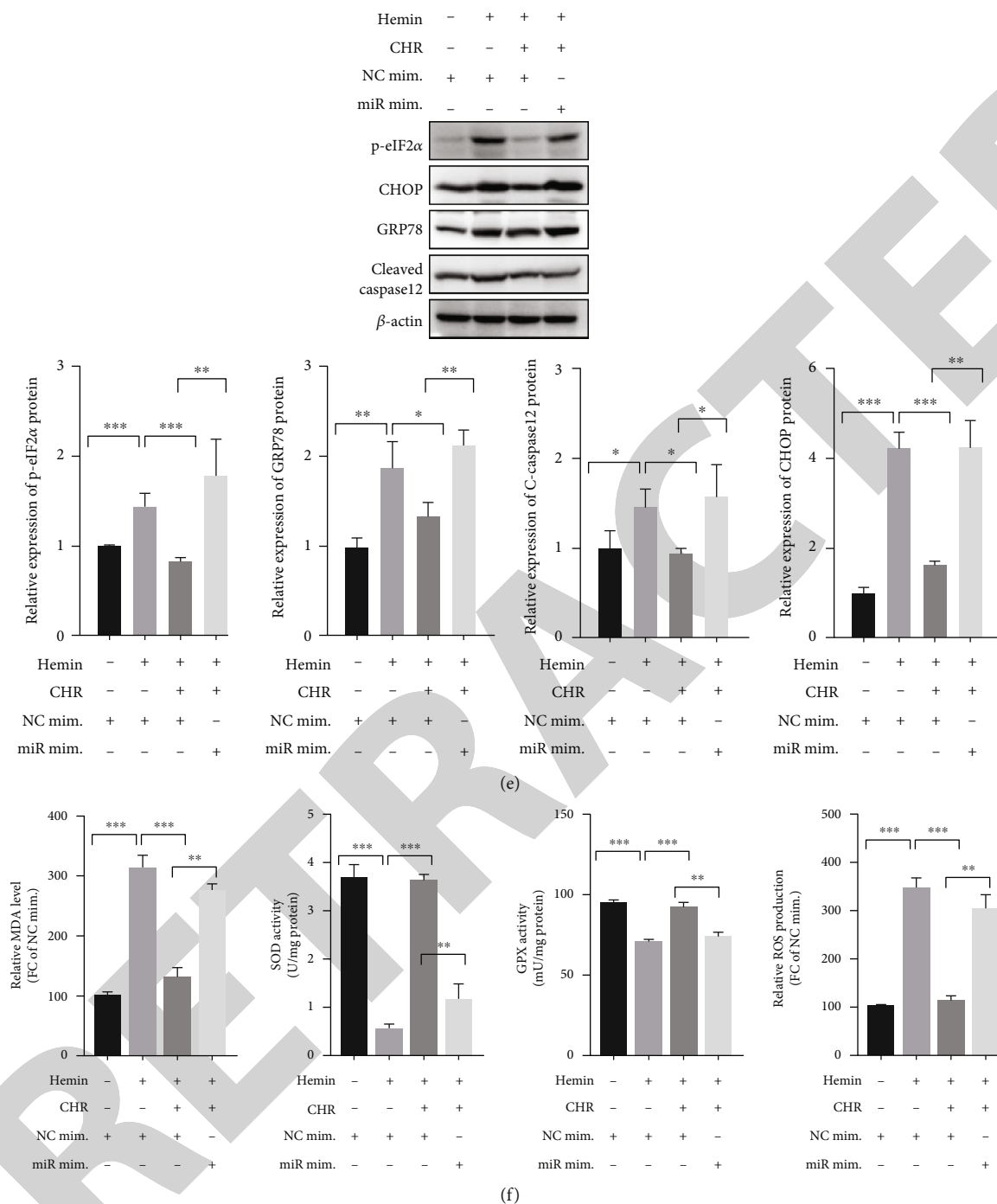


FIGURE 3: Continued.



**FIGURE 3:** CHR inhibited HT22 cell apoptosis, ER stress, and oxidation stress by downregulating miR-320-5p in hemin-induced HT22 cell injury models. NC mim.: negative control mimics; miR mim.: miR-320-5p mimics. (a) Volcano plot generated for the miRNA expression profiles for the hemin-induced HT22 cell injury and CHR treatment groups. (b) Levels of expression of the top six miRNAs with the most significant difference in expression (identified following the sequencing method) were studied using hemin-induced cells in the presence and absence of CHR (10  $\mu$ M; treatment time: 24 h) using the RT-PCR technique. \* $p$  < 0.05, \*\* $p$  < 0.01, and \*\*\* $p$  < 0.001.  $N$  = 3. (c) Level of expression of miR-320-5p was studied using hemin-induced cells in the presence and absence of CHR (10  $\mu$ M; treatment time: 24 h) using the RT-PCR technique. \* $p$  < 0.05.  $N$  = 3. (d) The apoptosis rate in hemin-induced HT22 cells in the presence and absence of CHR (10  $\mu$ M; treatment time: 24 h) or miR-320-5p mimics (treatment time: 24 h) was studied by conducting the TUNEL staining assays. \*\*\* $p$  < 0.001.  $N$  = 3. (e) Protein expression levels of the ER stress-related genes (p-eIF2 $\alpha$ , CHOP, GRP78, and cleaved caspase-12) were analyzed in hemin-induced HT22 cells in the presence and absence of CHR (10  $\mu$ M; treatment time: 24 h) or miR-320-5p mimics (treatment time: 24 h) using the western blot technique. \* $p$  < 0.05, \*\* $p$  < 0.01, and \*\*\* $p$  < 0.001.  $N$  = 3. (f) The changes of oxidation stress-related indexes (ROS, MDA, SOD, and GPx) were analyzed in hemin-induced HT22 cells in the presence and absence of CHR (10  $\mu$ M; treatment time: 24 h) or miR-320-5p mimics (treatment time: 24 h). \*\* $p$  < 0.01 and \*\*\* $p$  < 0.001.  $N$  = 3.

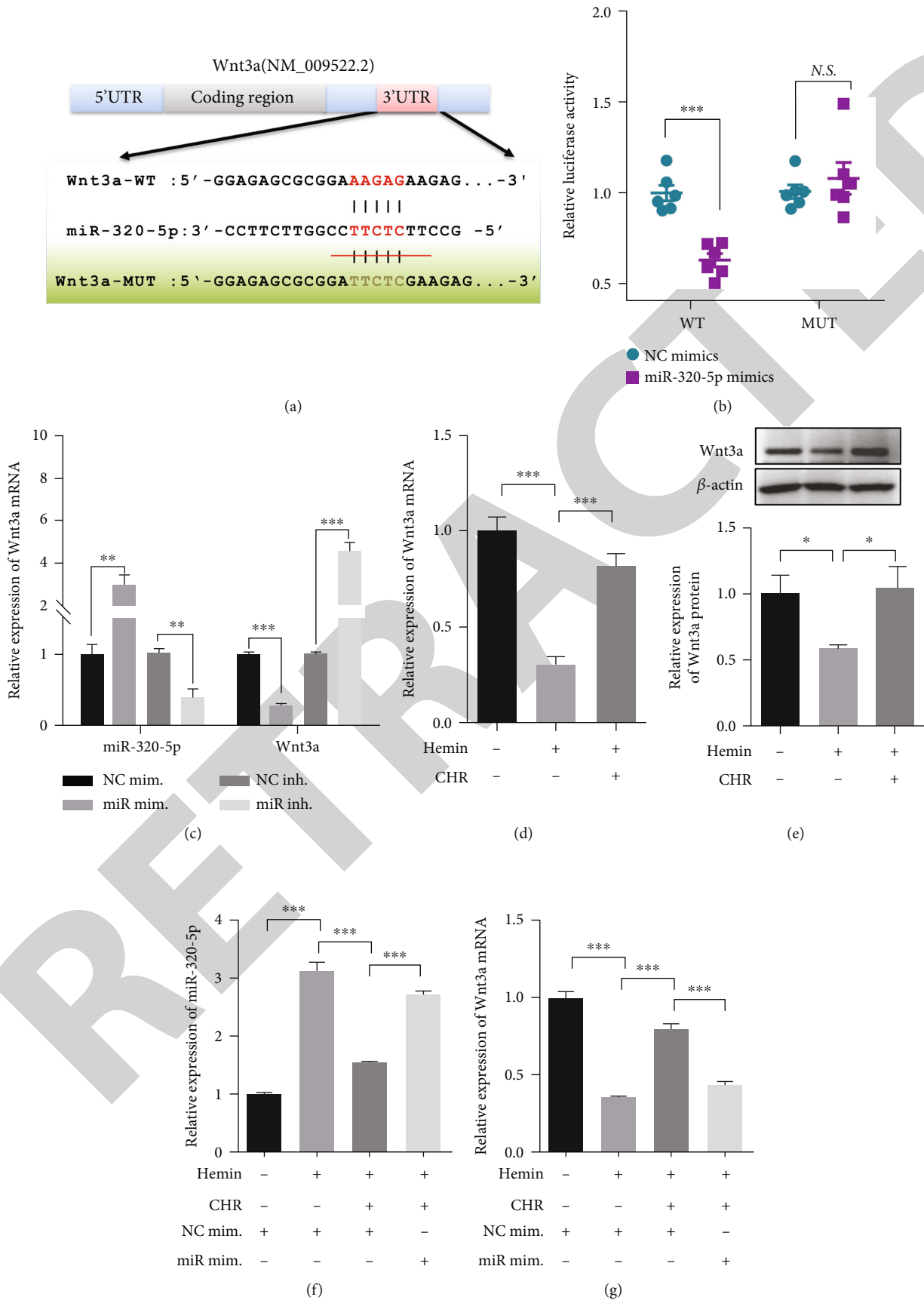


FIGURE 4: Continued.

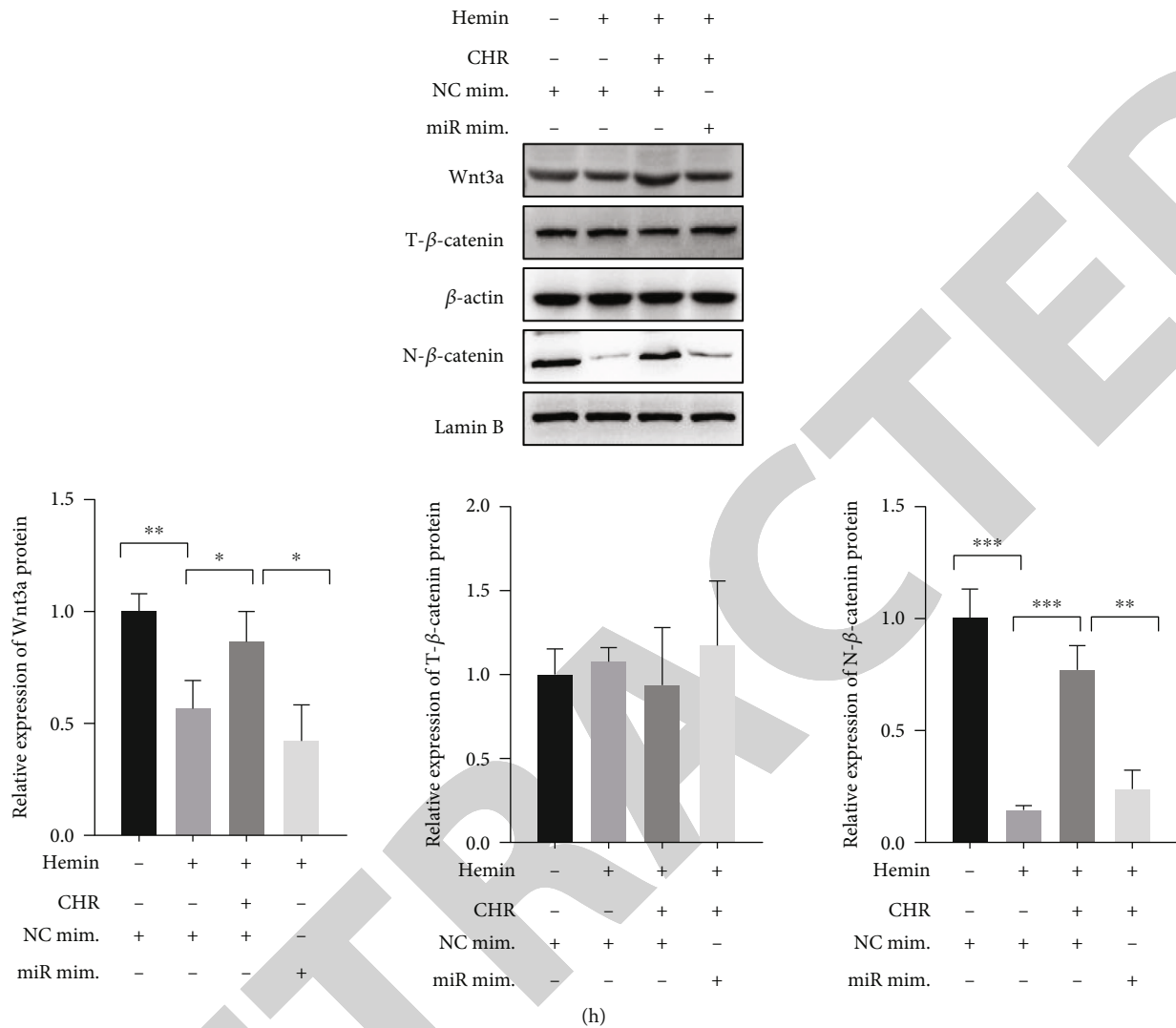


FIGURE 4: CHR activated the Wnt3a/ $\beta$ -catenin signaling pathway by downregulating miR-320-5p in hemin-induced HT22 cell injury models. (a) Potential binding site of miR-320-5p at the 3'-UTR of Wnt3a mRNA is predicted using the miRWalk software. The red color indicates wild-type, and the green color indicates the mutated sequence of Wnt3a at the miR-320-5p-binding site. (b) HT22 cells were cotransfected with miR-320-5p (or NC mimics) and a pmir-GLO vector containing wild-type or mutated miR-320-5p-binding sites (mutated) at Wnt3a 3'-UTR. Luciferase reporter assays were performed 24 h after cotransfection. NC mim.: negative control mimics; miR mim.: miR-320-5p mimics; NC inh.: negative control inhibitor; miR inh.: miR-320-5p inhibitor. <sup>N.S.</sup>  $p > 0.05$ ,  $***p < 0.001$ .  $N = 6$ . (c) HT22 cells were transfected with the miR-320-5p inhibitor or miR-320-5p mimics and their corresponding controls. The expression of miR-320-5p and Wnt3a mRNA was analyzed using the RT-PCR technique.  $***p < 0.001$ .  $N = 3$ . (d and e) Expression levels of mRNA and protein of Wnt3a were analyzed in hemin-induced HT22 cells with or without CHR (10  $\mu$ M; treatment time: 24 h) using the RT-PCR and western blot.  $**p < 0.05$  and  $***p < 0.001$ .  $N = 3$ . (f) Expression of miR-320-5p was analyzed in hemin-induced HT22 cells in the presence and absence of CHR (10  $\mu$ M; treatment time: 24 h) or miR-320-5p mimics (treatment time: 24 h) using the RT-PCR technique.  $***p < 0.001$ .  $N = 3$ . (g) The mRNA expression of Wnt3a was analyzed in hemin-induced HT22 cells with or without CHR (10  $\mu$ M; treatment time: 24 h) or miR-320-5p mimics (treatment time: 24 h) using the RT-PCR technique.  $***p < 0.001$ .  $N = 3$ . (h) The protein expression levels of Wnt3a, total  $\beta$ -catenin (T- $\beta$ -catenin), and nuclear  $\beta$ -catenin (N- $\beta$ -catenin) were analyzed in hemin-induced HT22 cells with or without CHR (10  $\mu$ M; treatment time: 24 h) or miR-320-5p mimics (treatment time: 24 h) using the western blot technique.  $*p < 0.05$ ,  $**p < 0.01$ , and  $***p < 0.001$ .  $N = 3$ .

suggesting that the expression levels of Wnt3a were negatively regulated by miRNA-320-5p present in the HT22 cells. Together, these data revealed that Wnt3a is a direct downstream target of miR-320-5p.

Wnt3a is a naturally occurring protein that exhibits neuroprotective effects [48]. The mRNA and protein expression of the Wnt3a gene was determined using the RT-qPCR and

western blot to explore whether CHR regulated the expression of Wnt3a in the hemin-induced HT22 cell injury group. The results demonstrated that the mRNA and protein expression levels of Wnt3a in hemin-induced HT22 cells were dramatically lower than the levels observed in HT22 cells devoid of hemin. It was also observed that the level of expression of Wnt3a in the hemin-induced HT22 cell injury

group could be remarkably improved following the process of CHR treatment (Figures 4(d) and 4(e)). In addition, we carried out rescue experiments to explore whether CHR effected the Wnt3a by inhibiting miR-320-5p. The results of the RT-PCR and western blot revealed that the mRNA and protein expression of Wnt3a in hemin-induced HT22 cells could be significantly upregulated following CHR treatment, and the regulation was weakened by the overexpression of miR-320-5p (Figures 4(f)–4(h)). These data indicated that CHR could enhance Wnt3a expression in the hemin-induced HT22 cell injury through regulating miR-320-5p expression.

Wnt3a, one of the most important endogenous ligands of Wnt, participates in the typical Wnt/ $\beta$ -catenin pathway. The Wnt/ $\beta$ -catenin pathway is a central signal transduction pathway that can influence numerous biological processes, such as cell apoptosis, survival, and ER stress [49, 50]. It has been recently revealed that the Wnt/ $\beta$ -catenin pathway significantly influences the incidence of neurological diseases [51, 52]. It has been observed that the activation of the Wnt/ $\beta$ -catenin pathway can help achieve neuroprotection [53–56]. Therefore, we transfected sh-Wnt3a (#1, #2, and #3) and the negative control shRNA (sh-NC) to identify the best sh-Wnt3a in the HT22 cells (Figure S6A) and to explore the effect of Wnt3a on  $\beta$ -catenin pathway, cell survival, apoptosis, and oxidative stress under normal or hemin-induced HT22 cells. In normal or hemin-induced HT22 cells transfected with sh-Wnt3a, the expression levels of Wnt3a and nucleus  $\beta$ -catenin observably decreased, but the expression of total  $\beta$ -catenin was not affected (Figure S6B and S6C). Results from the CCK-8 assays indicated that cell viability was significantly inhibited in normal or hemin-induced cells transfected with sh-Wnt3a (Figure S6D). Treatment with silenced Wnt3a outstandingly increased caspase-3 activity in normal or hemin-induced HT22 cells (Figure S6E). The results from the TUNEL assays revealed that silenced Wnt3a could promote apoptosis in normal or hemin-induced HT22 cells (Figure S6F). In addition, treatment with silenced Wnt3a dramatically increased MDA and ROS levels and decreased the activity of SOD and GPx in hemin-induced HT22 cell damage model, but treatment with silenced Wnt3a had no effect on oxidative stress-related indexes (MDA, ROS, SOD, and GPx) in HT22 cells without hemin (Figure S6G). These data showed that silenced Wnt3a inhibited  $\beta$ -catenin pathway, antiapoptosis, and antioxidative stress in hemin-induced HT22 cells.

Based on the above data, we speculated that CHR could regulate the  $\beta$ -catenin pathway by inhibiting miR-320-5p. The rescue experiments suggested that the protein expression of nucleus  $\beta$ -catenin in hemin-induced HT22 cells could be significantly upregulated following CHR treatment; this enhancement was weakened by the overexpression of miR-320-5p. Differences in the total  $\beta$ -catenin expression were not observed among different groups (Figure 4(h)). These data revealed that CHR activated the Wnt3a/ $\beta$ -catenin pathway by restraining the expression of miR-320-5p in the hemin-induced HT22 cell injury.

**3.4. CHR Protects against Hemin-Induced Injury by Activating the Wnt3a/ $\beta$ -Catenin Pathway.** To further explore whether CHR inhibits hemin-induced cell apoptosis, ER stress, and oxidative stress by activating the Wnt3a/ $\beta$ -catenin pathway, the results of western blot revealed that the levels of protein expression corresponding to Wnt3a and nucleus  $\beta$ -catenin in hemin-induced HT22 cells increased significantly following CHR treatment, and the enhancement was partly inhibited by the suppression of Wnt3a (Figure 5(a)). Subsequently, the results obtained by conducting the CCK-8 assays indicated that the cell viability in hemin-induced HT22 cells increased significantly following the process of CHR treatment, and the extent of the increase in the viability of the cells was reduced by the suppression of Wnt3a (Figure S7A). The caspase-3 activity in hemin-induced HT22 cells decreased significantly following the process of CHR treatment, and the extent of decrease in the activity was alleviated by the suppression of Wnt3a (Figure S7B). In addition, the results obtained by conducting the TUNEL staining assays also indicated that the cell apoptosis rates in hemin-induced HT22 cells were significantly restrained under conditions of CHR treatment, and the restraint was alleviated by the suppression of Wnt3a (Figure 5(b)). Further, the results obtained using the western blot revealed that the protein expressions of the ER stress-related genes (GRP78, cleaved caspase-12, p-eIF2 $\alpha$ , and CHOP) in hemin-induced HT22 cells were significantly inhibited under conditions of CHR treatment, and the inhibition was impaired by the suppression of Wnt3a (Figure 5(c)). Finally, we examined the changes of oxidative stress-related indicators (MDA, ROS, SOD, and GPx) to evaluate whether CHR affected hemin-induced oxidative stress in HT2 cells through Wnt3a. As shown in Figure 5(d), CHR inhibited the relative levels of MDA and ROS in the hemin-induced HT22 cells; the inhibition was obviously alleviated by silenced Wnt3a. While CHR increased the ROS activity and GPx activity in the hemin-induced HT22 cells, the phenomenon was obviously weakened by silenced Wnt3a. Altogether, the obtained data suggested that CHR inhibited hemin-induced cell apoptosis, ER stress, and oxidative stress by activating the Wnt3a/ $\beta$ -catenin pathway.

## 4. Discussion

ICH accounts for only 10–15% of all strokes. However, the level of mortality and morbidity recorded is extremely high [57]. In recent years, significant advances have been made in the field, and the results can help explain the causes of ICH. The advancements made in the field help in understanding the pathophysiology associated with the disease. The results can help in developing acute therapy and prevention methods. However, specific clinical treatment methods for ICH are not known. It has been previously reported that CHR exhibits neuroprotective effects during brain damage [16, 58]. However, the role and underlying molecular mechanisms of CHR in ICH are unknown. We demonstrated that the process of CHR posttreatment helped protect against hemin-induced neuronal cell injury in HT22

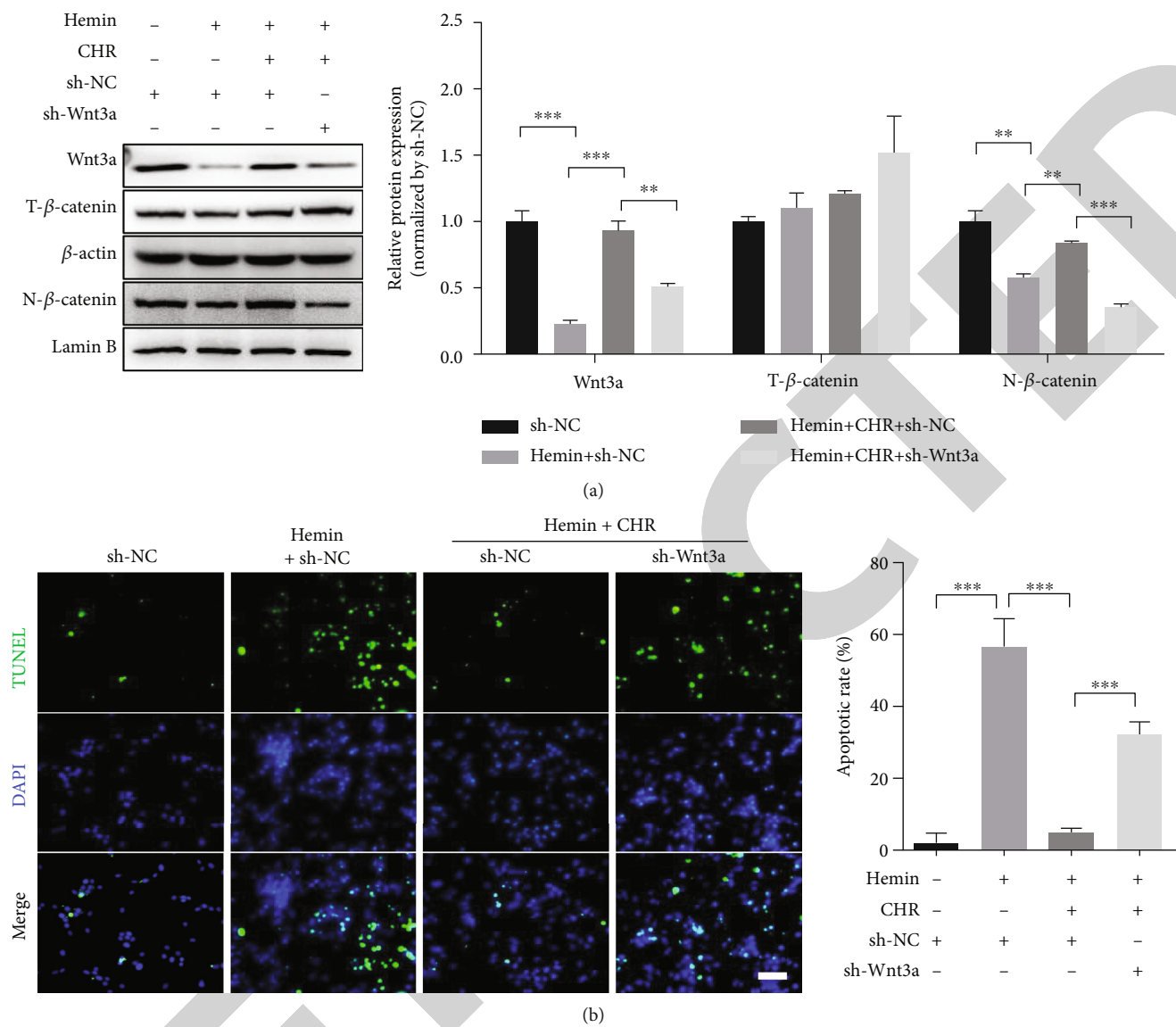


FIGURE 5: Continued.



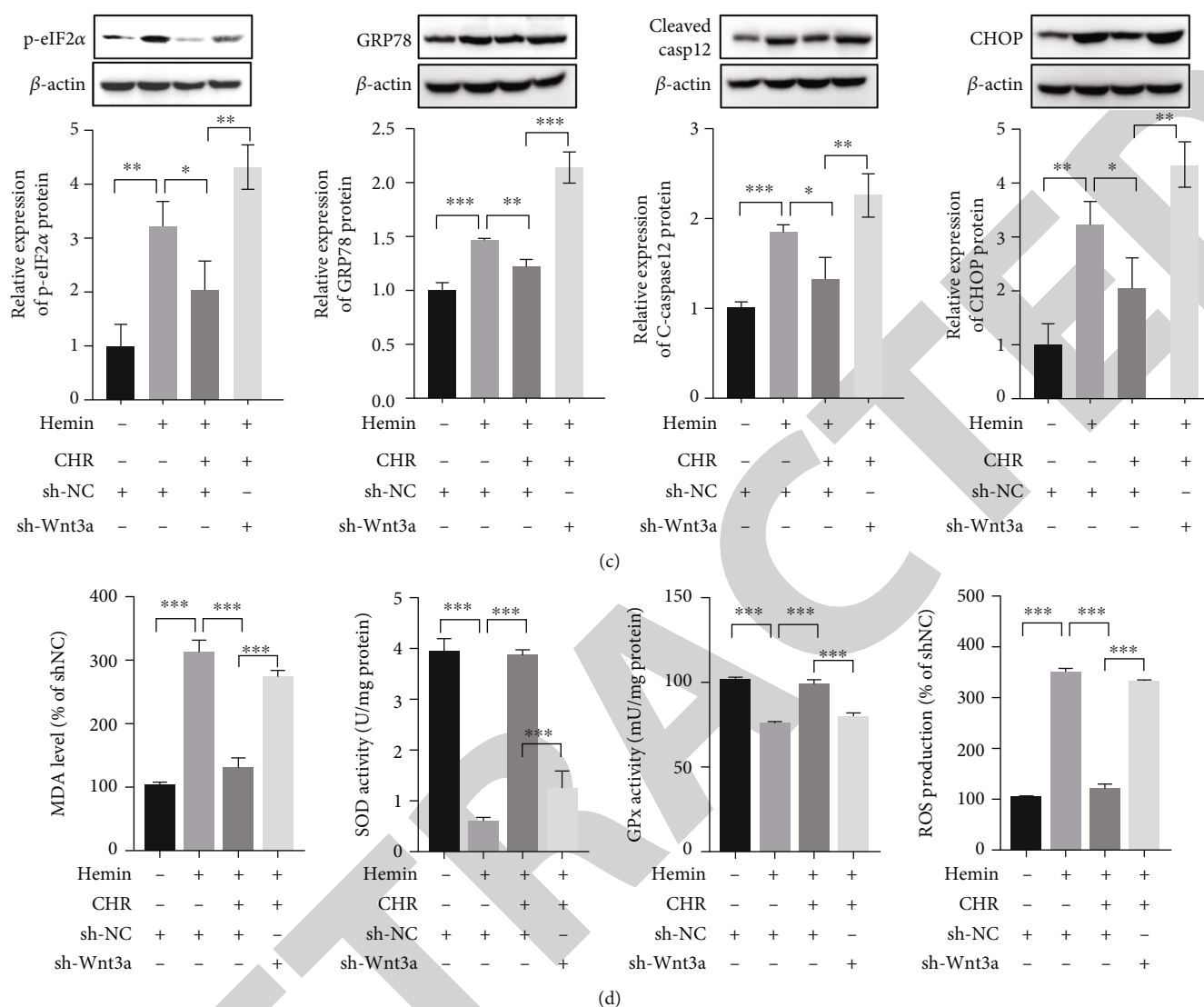


FIGURE 5: CHR inhibited the cell apoptosis, ER stress, and oxidative stress by upregulating Wnt3a in hemin-induced HT22 cell injury models. Sh-NC: negative control shRNA; sh-Wnt3a: Wnt3a shRNA. (a) Protein expression levels of Wnt3a, T- $\beta$ -catenin, and N- $\beta$ -catenin were analyzed in hemin-induced HT22 cells (20  $\mu$ M) with or without CHR (10  $\mu$ M; treatment time: 24 h) or sh-Wnt3a (treatment time: 24 h) following the western blot technique. \*\* $p < 0.01$ , \*\*\* $p < 0.001$ .  $N = 3$ . (b) Apoptosis rate in hemin-induced HT22 cells (20  $\mu$ M) with or without CHR (10  $\mu$ M; treatment time: 24 h) or sh-Wnt3a (treatment time: 24 h) was studied by conducting the TUNEL staining assays. \*\*\* $p < 0.001$ .  $N = 3$ . (c) The protein expression levels of ER stress-related genes (p-eIF2 $\alpha$ , CHOP, GRP78, and cleaved caspase-12) were analyzed in hemin-induced HT22 cells with or without CHR (10  $\mu$ M; treatment time: 24 h) or sh-Wnt3a (treatment time: 24 h) using the western blot technique. \* $p < 0.05$ , \*\* $p < 0.01$ , and \*\*\* $p < 0.001$ .  $N = 3$ . (d) The change of oxidative stress-related indexes (MDA, SOD, GPx, and ROS) were analyzed in hemin-induced HT22 cells with or without CHR (10  $\mu$ M; treatment time: 24 h) or sh-Wnt3a (treatment time: 24 h). \* $p < 0.05$ , \*\* $p < 0.01$ , and \*\*\* $p < 0.001$ .  $N = 3$ .

cells by regulating the miR-320-5p/Wnt3a signaling pathway.

ICH injury consists of two stages: primary brain injury (PBI) and secondary brain injury (SBI). Typically, PBI is followed by SBI, and it negatively affects human health. The severity of SBI depends on the rate of recovery and location of ICH [42]. Hemin is a neurotoxic product generated during the degradation of free hemoglobin (released following ICH) in the presence of heme oxygenase-1 (HO-1). It significantly affects the incidence of SBI [59]. It has been reported that hemin can mimic secondary injury (in vitro) [26–28]. CHR

is one of the most key anthraquinone components extracted from rhubarb, which has broad spectrum of therapeutic potential, such as neuroprotection [12]. Cui et al. reported that CHR suppressed the hippocampus damage by inhibiting the level of mitochondrial autophagy [16]. Chae et al. showed that CHR alleviated hippocampal neuronal cell death via inhibition of Drp1-dependent mitochondrial fission [60]. In addition, our previous studies proved that rhubarb treatments effectively protected nerve cell damage by increasing of the antioxidative stress and anti-inflammatory responses in rat with ICH [61], and studies have shown that CHR is the most abundant-

free anthraquinone component in the rhubarb [12]. Therefore, we hypothesized that CHR extracted from rhubarb has a protective effect on ICH following brain injury. Herein, we reported that CHR could protect HT22 cells from hemin-induced neuronal cell injury by improving cell viability and restricting cell apoptosis. Moreover, it has been elucidated that oxidative stress plays critical roles in determining the extent of ICH damage, and oxidative stress after ICH increases the blood-brain barrier, autophagy, apoptosis, and inflammatory response, thus exacerbating brain injury [3]. Our data revealed that CHR could reduce hemin-induced oxidative stress in HT22 cell; this result is similar to the role of CHR in other diseases. For example, Ma et al. reported that CHR relieves cisplatin-induced nephrotoxicity via concomitant inhibition of oxidative stress and apoptosis [62]. Zhao et al. demonstrated that CHR alleviates nitrosation/oxidative stress injury in focal cerebral ischemia/reperfusion [17]. Lin et al. showed that CHR significantly inhibited lipopolysaccharide-induced oxidative stress in microglia [63]. In addition to oxidative stress, ER stress is also involved in brain injury after ICH [64]. And ER stress after ICH causes excess release of ROS, leading to the increase of oxidative stress response [3]. Our data revealed that CHR could reduce hemin-induced ER stress in HT22 cell; this result is similar to the role of CHR in other diseases. For example, CHR was found to protect against I/R-induced nerve injury by restraining the activation of ER stress [18]. CHR hindered the hepatitis B virus X protein- (HBx-) induced activation of hepatic stellate cells by activating ER stress [15].

It has been reported that miRNAs can be the potential biomarkers for the diagnosis and prognosis of brain damage [65, 66]. Therefore, it is important to explore miRNAs to develop effective treatment methods for ICH. Herein, we found that the expression of miR-320-5p in the hemin-induced HT22 cell was significantly higher than the expression observed in the NC group. A large number of studies have shown that miR-320-5p is involved in the oxidative stress response of different diseases [67–71]. For example, the inhibition of miR-320 inhibited oxidative stress-induced injury in MC3T3-E1 cells [71]. Xiao et al. demonstrated that aerosol inhalation of edaravone suppressed oxidative stress and improved pulmonary function by downregulating miR-320 in rats with smoke inhalation injury [68]. Zhu et al. proved that the inhibition of miR-320 decreased oxidative stress and cell apoptosis by upregulating Nrf2 expression in myocardial ischemia-reperfusion (I-R) injury [69]. Shen et al. indicated that overexpression of miR-320 hindered the ischemic cerebral-induced oxidative stress injury by inhibiting Nox2/ROS signaling pathway [67]. Fu et al. showed that the expression of miR-320 was downregulated in diabetic retinopathy, and overexpression of miR-320 restrained inflammation and ROS production by directly targeting USP14 in HG-stimulated Müller cells [70]. These studies showed that miR-320 plays a dual role in the regulation of oxidative stress, which may be antioxidative stress or promoting oxidative stress. However, the role of miR-320-5p in brain injury after ICH has not been explored. Our data showed that overexpression of miR-320-5p aggravated hemin-induced oxidative stress and ER stress in HT22 cells, suggesting that miR-320-5p intensifies the oxidative stress response of neurons

after ICH. Furthermore, we observed that the overexpression of miR-320-5p in the hemin-induced HT22 cell could be significantly suppressed following CHR treatment, suggesting that the attenuation of miR-320-5p potentially influenced the protective mechanism following which CHR protected against hemin-induced nerve injury. As far as we know, we are the first to report that CHR ameliorated hemin-induced cell damage in HT22 cells by restraining miR-320-5p.

It has been recently reported that miRNAs play important roles in regulating gene expression at the transcriptional or posttranscriptional levels by binding to 3'-UTR of diverse target genes [20]. The results obtained by us demonstrated that miR-320-5p could directly bind with Wnt3a to lower its level of expression. Numerous researchers have reported that Wnt3a functioned as a neuroprotective factor under conditions of traumatic brain injury and ischemic stroke. Matei et al. and Zhang et al. reported that intranasal Wnt3a could protect neurons against apoptosis and ameliorate toxic responses of microglia/macrophages and astrocytes. They studied the middle cerebral artery occlusion model [48, 72]. Wei et al. demonstrated that intranasal Wnt3a exhibited a dual neuroprotective and regenerative role during the treatment of focal ischemic stroke [73]. Ruan et al. reported that intranasal Wnt3a inhibited neuronal apoptosis in the early stages of brain damage post subarachnoid hemorrhage [74]. The data obtained by us indicated that the level of expression of Wnt3a in HT22 cells experiencing hemin-induced injury could be increased under conditions of CHR treatment. This indicated that Wnt3a influenced the protective effect generated by CHR. It has been reported that the Wnt/ $\beta$ -catenin pathway dictates the incidence of neurodegenerative and neuropsychiatric disorders. It also influences the occurrence of brain injury [75–78]. Wnt3a is one of the most critical ligands that participate in the typical Wnt/ $\beta$ -catenin pathway. Herein, we reported that CHR activated the Wnt3a/ $\beta$ -catenin pathway by inhibiting miR-320-5p and ameliorated HT22 cell injury by increasing the level of Wnt3a expression.

However, this study has several limitations. Firstly, the present study lacks the *in vivo* animal experiments to prove that administered CHR has a protective effect on ICH. Secondly, the molecular mechanism of CHR inhibiting miR-320-5p expression has not studied in *in vivo*. Although the hemin-induced ICH model *in vitro* offers a well-characterized injury mode to evaluate the effect and mechanism of drugs on ICH following neurocyte injury, we acknowledge that this injury model does not completely stimulate the clinical ICH microenvironment and pharmacokinetic process of drugs *in vivo* [79]. Therefore, the efficacy and mechanism of CHR on brain injury after ICH need to be further verified *in vivo*. In further study, these parts in our experiment will be designed. Our study suggests that CHR may be a potential drug in clinical treatment of ICH and provides a latest reference for further research and clinical application of CHR in the treatment of ICH.

## 5. Conclusion

The results demonstrated in the present study that posttreatment with CHR prevented hemin-induced cell apoptosis, oxidative stress, and ER stress by modulating the miR-320-

5p/Wnt3a pathway in HT22 cells. Considering this, CHR could be used as a potent agent against ICH.

## Data Availability

The data used to support the findings of this study are included within the article.

## Conflicts of Interest

The authors declare that there is no conflict of interest regarding the publication of this paper.

## Acknowledgments

This research was supported by the National Natural Science Foundation of China (Grant No. 81573919) and the Project of Scientific Research on Traditional Chinese Medicine in Henan Province (No. 20-21ZYZD08, No. 2019ZY2037, and No. 2018ZY2053).

## Supplementary Materials

Figure S1: diagram showing the timeline of the chrysophanol (CHR) posttreatment process conducted using hemin-induced HT22 cells. Figure S2: effects of hemin on HT22 cells. Figure S3: Kyoto Encyclopedia of Genes and Genomes (KEGG) and Gene Ontology (GO) analysis of differential miRNA and potential binding target genes of miR-320. Figure S4: overexpression of miR-320-5p decreased the viability of the HT22 cells and promoted apoptosis in normal or hemin-induced HT22 cell injury models. Figure S5: CHR inhibited HT22 cell viability and apoptosis by downregulating miR-320-5p in hemin-induced HT22 cell injury models. Figure S6: downregulation of Wnt3a promoted the apoptosis of HT22 cells and reduced the level of nuclear  $\beta$ -catenin in hemin-induced HT22 cell injury models. Figure S7: CHR of HT22 cells promoted cell viability and inhibited the apoptosis by upregulating Wnt3a in hemin-induced HT22 cell injury models. Table S1: the primer sequence of RNAs and the sequence of miR-320-5p mimics/inhibitor and Wnt3a shRNA. Table S2: there were significant differences in miRNAs between the hemin-induced HT22 cell injury groups and CHR treatment groups. (*Supplementary Materials*)

## References

- [1] Z. Wang, F. Zhou, Y. Dou et al., "Melatonin alleviates intracerebral hemorrhage-induced secondary brain injury in rats via suppressing apoptosis, inflammation, oxidative stress, DNA damage, and mitochondria injury," *Translational Stroke Research*, vol. 9, no. 1, pp. 74–91, 2018.
- [2] S. Sacco, C. Marini, D. Toni, L. Olivieri, and A. Carolei, "Incidence and 10-year survival of intracerebral hemorrhage in a population-based registry," *Stroke*, vol. 40, no. 2, pp. 394–399, 2009.
- [3] Z. Yao, Q. Bai, and G. Wang, "Mechanisms of oxidative stress and therapeutic targets following intracerebral hemorrhage," *Oxidative Medicine and Cellular Longevity*, vol. 2021, Article ID 8815441, 12 pages, 2021.
- [4] Y. Zhang, S. Khan, Y. Liu, G. Wu, V. W. Yong, and M. Xue, "Oxidative stress following intracerebral hemorrhage: from molecular mechanisms to therapeutic targets," *Frontiers in Immunology*, vol. 13, article 847246, 2022.
- [5] S. Deng, S. Liu, P. Jin et al., "Albumin reduces oxidative stress and neuronal apoptosis via the ERK/Nrf2/HO-1 pathway after intracerebral hemorrhage in rats," *Oxidative Medicine and Cellular Longevity*, vol. 2021, Article ID 8891373, 14 pages, 2021.
- [6] J. Zheng, L. Shi, F. Liang et al., "Sirt3 ameliorates oxidative stress and mitochondrial dysfunction after intracerebral hemorrhage in diabetic rats," *Frontiers in Neuroscience*, vol. 12, p. 414, 2018.
- [7] T. Wang, H. Lu, D. Li, and W. Huang, "TGF- $\beta$ 1-mediated activation of SERPINE1 is involved in hemin-induced apoptotic and inflammatory injury in HT22 cells," *Neuropsychiatric Disease and Treatment*, vol. Volume 17, pp. 423–433, 2021.
- [8] H. Zhu, Z. Wang, J. Yu et al., "Role and mechanisms of cytokines in the secondary brain injury after intracerebral hemorrhage," *Progress in Neurobiology*, vol. 178, p. 101610, 2019.
- [9] Y. Jiao and Y. Zuo, "Ultrasonic extraction and HPLC determination of anthraquinones, aloe-emodin, emodin, rheine, chrysophanol and physcione, in roots of *Polygoni multiflori*," *Phytochemical Analysis*, vol. 20, no. 4, pp. 272–278, 2009.
- [10] S. Genovese, F. Tammaro, L. Menghini, G. Carlucci, F. Epifano, and M. Locatelli, "Comparison of three different extraction methods and HPLC determination of the anthraquinones aloe-emodin, emodin, rheine, chrysophanol and physcione in the bark of *Rhamnus alpinus* L. (Rhamnaceae)," *Phytochemical Analysis*, vol. 21, no. 3, pp. 261–267, 2010.
- [11] M. A. Yusuf, B. N. Singh, S. Sudheer et al., "Chrysophanol: a natural anthraquinone with multifaceted biotherapeutic potential," *Biomolecules*, vol. 9, no. 2, p. 68, 2019.
- [12] S. Su, J. Wu, Y. Gao, Y. Luo, D. Yang, and P. Wang, "The pharmacological properties of chrysophanol, the recent advances," *Biomedicine & pharmacotherapy = Biomedecine & pharmacotherapie*, vol. 125, p. 110002, 2020.
- [13] S. Park, W. Lim, and G. Song, "Chrysophanol selectively represses breast cancer cell growth by inducing reactive oxygen species production and endoplasmic reticulum stress via AKT and mitogen-activated protein kinase signal pathways," *Toxicology and Applied Pharmacology*, vol. 360, pp. 201–211, 2018.
- [14] J. Lu, J. Li, Y. Hu et al., "Chrysophanol protects against doxorubicin-induced cardiotoxicity by suppressing cellular PARylation," *Acta Pharmaceutica Sinica B*, vol. 9, no. 4, pp. 782–793, 2019.
- [15] C. Y. Kuo, V. Chiu, P. C. Hsieh et al., "Chrysophanol attenuates hepatitis B virus X protein-induced hepatic stellate cell fibrosis by regulating endoplasmic reticulum stress and ferroptosis," *Journal of Pharmacological Sciences*, vol. 144, no. 3, pp. 172–182, 2020.
- [16] W. H. Cui, H. H. Zhang, Z. M. Qu, Z. Wang, D. J. Zhang, and S. Wang, "Computed tomographic parameters correlate with coagulation disorders in isolated traumatic brain injury," *The International Journal of Neuroscience*, pp. 1–8, 2020.
- [17] Y. Zhao, Y. Huang, Y. Fang et al., "Chrysophanol attenuates nitrosative/oxidative stress injury in a mouse model of focal cerebral ischemia/reperfusion," *Journal of Pharmacological Sciences*, vol. 138, no. 1, pp. 16–22, 2018.
- [18] Y. Zhao, Y. Fang, H. Zhao et al., "Chrysophanol inhibits endoplasmic reticulum stress in cerebral ischemia and reperfusion mice," *European Journal of Pharmacology*, vol. 818, pp. 1–9, 2018.

- [19] X. Chu, S. Zhou, R. Sun et al., “Chrysophanol relieves cognition deficits and neuronal loss through inhibition of inflammation in diabetic mice,” *Neurochemical Research*, vol. 43, no. 4, pp. 972–983, 2018.
- [20] V. Ambros, “The functions of animal microRNAs,” *Nature*, vol. 431, no. 7006, pp. 350–355, 2004.
- [21] L. Li, P. Wang, H. Zhao, and Y. Luo, “Noncoding RNAs and intracerebral hemorrhage,” *CNS & Neurological Disorders Drug Targets*, vol. 18, no. 3, pp. 205–211, 2019.
- [22] D. Guo, J. Liu, W. Wang et al., “Alteration in abundance and compartmentalization of inflammation-related miRNAs in plasma after intracerebral hemorrhage,” *Stroke*, vol. 44, no. 6, pp. 1739–1742, 2013.
- [23] F. Kong, J. Zhou, W. Zhou, Y. Guo, G. Li, and L. Yang, “Protective role of microRNA-126 in intracerebral hemorrhage,” *Molecular Medicine Reports*, vol. 15, no. 3, pp. 1419–1425, 2017.
- [24] W. D. Bao, X. T. Zhou, L. T. Zhou et al., “Targeting miR-124/ferroportin signaling ameliorated neuronal cell death through inhibiting apoptosis and ferroptosis in aged intracerebral hemorrhage murine model,” *Aging Cell*, vol. 19, no. 11, article e13235, 2020.
- [25] H. Zhao, X. Li, L. Yang et al., “Isorhynchophylline relieves ferroptosis-induced nerve damage after intracerebral hemorrhage via miR-122-5p/TP53/SLC7A11 pathway,” *Neurochemical Research*, vol. 46, no. 8, pp. 1981–1994, 2021.
- [26] X. Shen, L. Ma, W. Dong et al., “Autophagy regulates intracerebral hemorrhage induced neural damage via apoptosis and NF- $\kappa$ B pathway,” *Neurochemistry International*, vol. 96, pp. 100–112, 2016.
- [27] L. Hu, H. Zhang, B. Wang, Q. Ao, J. Shi, and Z. He, “MicroRNA-23b alleviates neuroinflammation and brain injury in intracerebral hemorrhage by targeting inositol polyphosphate multikinase,” *International Immunopharmacology*, vol. 76, p. 105887, 2019.
- [28] S. S. Karuppagounder, L. Alin, Y. Chen et al., “N-acetylcysteine targets 5 lipoxygenase-derived, toxic lipids and can synergize with prostaglandin E2 to inhibit ferroptosis and improve outcomes following hemorrhagic stroke in mice,” *Annals of Neurology*, vol. 84, no. 6, pp. 854–872, 2018.
- [29] X. Chu, X. Wu, H. Feng et al., “Coupling between interleukin-1R1 and necrosome complex involves in hemin-induced neuronal necroptosis after intracranial hemorrhage,” *Stroke*, vol. 49, no. 10, pp. 2473–2482, 2018.
- [30] M. Pascual, B. R. Do Couto, S. Alfonso-Loeches, M. A. Aguilar, M. Rodriguez-Arias, and C. Guerri, “Changes in histone acetylation in the prefrontal cortex of ethanol-exposed adolescent rats are associated with ethanol-induced place conditioning,” *Neuropharmacology*, vol. 62, no. 7, pp. 2309–2319, 2012.
- [31] D. Chen, X. Wu, J. Zhao, and X. Zhao, “MicroRNA-634 functions as a tumor suppressor in pancreatic cancer via directly targeting heat shock-related 70-kDa protein 2,” *Experimental and Therapeutic Medicine*, vol. 17, no. 5, pp. 3949–3956, 2019.
- [32] Y. Guo, Y. Liu, H. Wang, and P. Liu, “Long noncoding RNA SRY-box transcription factor 2 overlapping transcript participates in Parkinson's disease by regulating the microRNA-942-5p/nuclear apoptosis-inducing factor 1 axis,” *Bioengineered*, vol. 12, no. 1, pp. 8570–8582, 2021.
- [33] L. Yuan, H. Xu, R. Guo, T. Lu, and X. Li, “Long non-coding RNA ZFAS1 alleviates bupivacaine-induced neurotoxicity by regulating the miR-421/zinc finger protein564 (ZNF564) axis,” *Bioengineered*, vol. 12, no. 1, pp. 5231–5240, 2021.
- [34] Y. Sun, D. Yang, L. Xi et al., “Primed atypical ductal hyperplasia-associated fibroblasts promote cell growth and polarity changes of transformed epithelium-like breast cancer MCF-7 cells via miR-200b/c-IKK $\beta$  signaling,” *Cell Death & Disease*, vol. 9, no. 2, p. 122, 2018.
- [35] J. Gu, S. Rauniyar, Y. Wang et al., “Chrysophanol induced glioma cells apoptosis via activation of mitochondrial apoptosis pathway,” *Bioengineered*, vol. 12, no. 1, pp. 6855–6868, 2021.
- [36] Z. Liu, H. Wang, C. Hu et al., “Targeting autophagy enhances atezolizumab-induced mitochondria-related apoptosis in osteosarcoma,” *Cell Death & Disease*, vol. 12, no. 2, p. 164, 2021.
- [37] Y. Yang, L. Yang, S. Jiang et al., “HMGB1 mediates lipopolysaccharide-induced inflammation via interacting with GPX4 in colon cancer cells,” *Cancer Cell International*, vol. 20, no. 1, p. 205, 2020.
- [38] K. B. Walsh, K. D. Zimmerman, X. Zhang et al., “miR-181a mediates inflammatory gene expression after intracerebral hemorrhage: an integrated analysis of miRNA-seq and mRNA-seq in a swine ICH model,” *Journal of molecular neuroscience : MN*, vol. 71, no. 9, pp. 1802–1814, 2021.
- [39] T. X. Lu and M. E. Rothenberg, “MicroRNA,” *The Journal of Allergy and Clinical Immunology*, vol. 141, no. 4, pp. 1202–1207, 2018.
- [40] Z. Guo, M. Xie, Y. Zou et al., “Circular RNA Hsa\_circ\_0006766 targets microRNA miR-4739 to regulate osteogenic differentiation of human bone marrow mesenchymal stem cells,” *Bioengineered*, vol. 12, no. 1, pp. 5679–5687, 2021.
- [41] X. Lu, H. Y. Zhang, and Z. Y. He, “MicroRNA-181c provides neuroprotection in an intracerebral hemorrhage model,” *Neural Regeneration Research*, vol. 15, no. 7, pp. 1274–1282, 2020.
- [42] S. I. Mohammed Thangameeran, S. T. Tsai, H. Y. Hung et al., “a role for endoplasmic reticulum stress in intracerebral hemorrhage,” *Cell*, vol. 9, no. 3, article cells9030750, p. 750, 2020.
- [43] X. Hu, C. Tao, Q. Gan, J. Zheng, H. Li, and C. You, “Oxidative stress in intracerebral hemorrhage: sources, mechanisms, and therapeutic targets,” *Oxidative Medicine and Cellular Longevity*, vol. 2016, Article ID 3215391, 12 pages, 2016.
- [44] I. Gareev, G. Yang, J. Sun et al., “Circulating microRNAs as potential noninvasive biomarkers of spontaneous intracerebral hemorrhage,” *World Neurosurgery*, vol. 133, pp. e369–e375, 2020.
- [45] J. Wang, Y. Zhu, F. Jin, L. Tang, Z. He, and Z. He, “Differential expression of circulating microRNAs in blood and haematoma samples from patients with intracerebral haemorrhage,” *The Journal of International Medical Research*, vol. 44, no. 3, pp. 419–432, 2016.
- [46] X. Cheng, B. P. Ander, G. C. Jickling et al., “MicroRNA and their target mRNAs change expression in whole blood of patients after intracerebral hemorrhage,” *Journal of Cerebral Blood Flow and Metabolism*, vol. 40, no. 4, pp. 775–786, 2020.
- [47] H. W. Zheng, Y. L. Wang, J. X. Lin et al., “Circulating microRNAs as potential risk biomarkers for hematoma enlargement after intracerebral hemorrhage,” *CNS Neuroscience & Therapeutics*, vol. 18, no. 12, pp. 1003–1011, 2012.
- [48] N. Matei, J. Camara, D. McBride et al., “Intranasal wnt3a attenuates neuronal apoptosis through Frz1/PIWIL1a/FOXM1 pathway in MCAO rats,” *The Journal of Neuroscience*, vol. 38, no. 30, pp. 6787–6801, 2018.
- [49] O. Silva-Garcia, J. J. Valdez-Alarcon, and V. M. Baizabal-Aguirre, “Wnt/ $\beta$ -catenin signaling as a molecular target by pathogenic bacteria,” *Frontiers in Immunology*, vol. 10, p. 2135, 2019.

## *Retraction*

# **Retracted: Identification of Nine M6A-Related Long Noncoding RNAs as Prognostic Signatures Associated with Oxidative Stress in Oral Cancer Based on Data from The Cancer Genome Atlas**

### **Oxidative Medicine and Cellular Longevity**

Received 26 December 2023; Accepted 26 December 2023; Published 29 December 2023

Copyright © 2023 Oxidative Medicine and Cellular Longevity. This is an open access article distributed under the Creative Commons Attribution License, which permits unrestricted use, distribution, and reproduction in any medium, provided the original work is properly cited.

This article has been retracted by Hindawi, as publisher, following an investigation undertaken by the publisher [1]. This investigation has uncovered evidence of systematic manipulation of the publication and peer-review process. We cannot, therefore, vouch for the reliability or integrity of this article.

Please note that this notice is intended solely to alert readers that the peer-review process of this article has been compromised.

Wiley and Hindawi regret that the usual quality checks did not identify these issues before publication and have since put additional measures in place to safeguard research integrity.

We wish to credit our Research Integrity and Research Publishing teams and anonymous and named external researchers and research integrity experts for contributing to this investigation.

The corresponding author, as the representative of all authors, has been given the opportunity to register their agreement or disagreement to this retraction. We have kept a record of any response received.

## **References**

- [1] L. Shan, Y. Lu, Y. Song et al., "Identification of Nine M6A-Related Long Noncoding RNAs as Prognostic Signatures Associated with Oxidative Stress in Oral Cancer Based on Data from The Cancer Genome Atlas," *Oxidative Medicine and Cellular Longevity*, vol. 2022, Article ID 9529814, 18 pages, 2022.

## Research Article

# Identification of Nine M6A-Related Long Noncoding RNAs as Prognostic Signatures Associated with Oxidative Stress in Oral Cancer Based on Data from The Cancer Genome Atlas

Li Shan <sup>1</sup>, Ye Lu <sup>2</sup>, Yihua Song,<sup>3</sup> Xiaoli Zhu <sup>1</sup>, Cheng-Cheng Xiang,<sup>1</sup> Er-Dong Zuo,<sup>1</sup> and Xu Cheng <sup>1</sup>

<sup>1</sup>Department of Hematology and Oncology, Soochow University Affiliated Taicang Hospital (the First People's Hospital of Taicang), Jiangsu 215400, China

<sup>2</sup>Suzhou Medical College of Soochow University/Soochow University Affiliated Taicang Hospital, China

<sup>3</sup>Department of Stomatology Affiliated Hospital of Nantong University, Nantong University, Nantong, Jiangsu, China

Correspondence should be addressed to Xu Cheng; [chx1029@163.com](mailto:chx1029@163.com)

Received 22 April 2022; Revised 12 June 2022; Accepted 29 June 2022; Published 22 July 2022

Academic Editor: Tian Li

Copyright © 2022 Li Shan et al. This is an open access article distributed under the Creative Commons Attribution License, which permits unrestricted use, distribution, and reproduction in any medium, provided the original work is properly cited.

**Objective.** Although the expression of long noncoding RNAs (lncRNAs) and N6-methyladenosine (M6A) is correlated with different tumors, it remains unclear how M6A-related lncRNA functioning affects the initiation and progression of oral squamous cell carcinoma (OSCC). **Materials and Methods.** Gene expression and clinical data were retrieved from The Cancer Genome Atlas. The prognostic value of M6A-related lncRNAs was determined using univariate Cox regression analyses. Gene set enrichment analysis of OSCC patient clusters revealed the pathways that elucidate the mechanism. Furthermore, a risk-based model was established. The difference in the overall survival (OS) between groups, including low-/high-risk groups, was determined by Kaplan-Meier analysis. Relationships among immune cells, clusters, clinicopathological characteristics, and risk scores were explored. **Results.** Among 1,080 M6A-related lncRNAs, 36 were prognosis-related. Patients with OSCC were divided into two clusters. T stage and the pathological grade were noticeably lower in cluster 2 than in cluster 1. Epithelial-mesenchymal transition showed greater enrichment in cluster 1. Nine hub M6A-related lncRNAs were identified for the model of risk score for predicting OSCC prognosis. The OS was longer in patients with a low-risk score than in patients with a high-risk score. The risk score was an independent prognostic factor of OSCC and was associated with the infiltration of different immune cells. T stages and the American Joint Committee on Cancer (AJCC) stages were more advanced in the high-risk score group than in the low-risk score group. Finally, expression correlation analysis showed that the risk score is associated with the expression of oxidative stress markers. **Conclusion.** M6A-related lncRNAs play an important role in OSCC progression. Immune cell infiltration was related to the risk score model in OSCC and could accurately predict OSCC prognosis.

## 1. Introduction

Approximately 405,000 new oral cancer cases are reported worldwide annually, with the highest incidence reported in Sri Lanka and India [1, 2]. According to the International Classification of Diseases, oral cancer can be categorized into cancers of the tongue, lip, gum, upper jaw, sublingual space, hard palate, buccal mucosa, and retromolar area. The ratio

of the number of cases of oral squamous cell carcinoma (OSCC) to those of other types of oral cancer is almost 90% [2, 3]. OSCC has multiple risk factors, primarily smoking, drinking, chewing betel nut, and human papillomavirus infection [4, 5]. Early diagnosis of OSCC is difficult. As a result, the rate of cure is low and the mortality rate is high, which places a heavy burden on individuals and societal economies.

Research on the induction and progression of OSCC at the molecular level is particularly important owing to a lack of biomarkers for early OSCC prognosis and diagnosis. The present study focused on the screening of prognostic biomarkers for OSCC.

N6-Methyladenosine (M6A) epigenetically modifies RNA molecules. M6A can affect tumor progression by inducing suppressor genes and regulating oncogene expression in tumorigenesis and subsequent tumor development. The M6A regulators are controlled by regulatory proteins with methyltransferase activity (“writers”), signal transducers (“readers”), and demethylases (“erasers”) [6]. M6A is related to the induction and development of hepatocellular carcinoma, cervical cancer, breast cancer, and OSCC [7, 8]. Linear RNAs spanning more than 200 nucleic acids are long noncoding RNAs (lncRNAs) and do not encode proteins. lncRNAs affect gene expression at the transcription and posttranscription levels. The degree of tumor malignancy is strongly associated with the dysregulation of lncRNAs [9]. lncRNAs play significant roles in the progression of OSCC [10]. For example, the level of expression of the HOX transcript antisense intergenic RNA (HOTAIR) is related to the tumor size, AJCC stage, and prognosis of OSCC [11]. RNA1, known as the epidermal growth factor receptor antisense (EGFR-AS1), is strongly upregulated in cervical squamous cell carcinoma and is considered a biomarker of OSCC [12]. Findings from the latest research suggest that lncRNAs are responsible for regulating the modification of M6A and consequently the development of cancers, including gliomas and liver cancer [13, 14]. Meanwhile, the mechanism underlying the action of M6A in the dysregulation of lncRNAs in tumor cells and the process by which M6A-related lncRNAs promote the initiation and progression of OSCC remain elusive. GSEA results showed that the signature may be related to oxidative stress. Information about how M6A-related lncRNAs are responsible for the initiation and progression of OSCC can aid the identification of new biomarkers and therapeutic targets.

Evidence from studies suggests that oxidative stress can increase the infiltration of dendritic cells (DCs) and T cells in the tumor-immune microenvironment and transform cold tumors into hot tumors, thereby promoting a more effective antitumor immune response. Nevertheless, the elimination of oxidative stress increases antitumor immunity and T-lymphocyte infiltration, causing a potent antitumor effect. A previous study showed that, in breast cancer, the removal of oxidative stress in the tumor microenvironment (TME) alleviates immunosuppressive immunogenic cell death induced by oleandrin-based anticancer drugs and induces a more persistent effect on T cells. Collectively, these contradictory results indicate that immunogenic cell death can be induced by modulating oxidative stress to enhance the outcomes of immunotherapy. Hence, further investigations are needed to identify the mechanism underlying oxidative stress and OSCC.

This study investigated M6A-related lncRNAs that could affect OSCC prognosis, based on data from The Cancer Genome Atlas (TCGA). Patients with OSCC were grouped

between the two clusters using consensus clustering, and their characteristics were explored. A risk score model was developed for the prediction of OSCC prognosis using nine major M6A-related lncRNAs identified using least absolute shrinkage and selection operator (LASSO) and Cox regression analyses. These M6A-related lncRNAs were determined to contribute significantly to OSCC progression and the risk score model, which could be used precisely for the prediction of OSCC prognosis.

## 2. Materials and Methods

**2.1. Data Resource.** TCGA gene expression data of 371 patients with OSCC and 32 normal individuals (controls) were retrieved from the database website (accessed in April 2021). The data were obtained from patients with OSCC involving the gum, base of the tongue, general parts of the tongue, lips, sublingual space, general parts of the mouth, tonsil, palate, and poorly defined sites in the oral cavity and lip. Corresponding clinical information was available for 368 patients. TCGA-acquired data also included expression data for 23 M6A-related genes, including eight writer genes (METTL16, METTL3, METTL14, RBM15B, WTAP, RBM15, VIRMA, and ZC3H13), 13 reader genes (FMR1, HNRNPC, HNRNPA2B1, IGF2BP3, IGF2BP2, IGF2BP1, LRPRRC, RBMX, YTHDF3, YTHDF2, YTHDC2, YTHDC1, and YTHDF1), and two eraser genes (ALKBH5 and FTO)<sup>A</sup>. The anatomic stage was determined based on the criteria published by the American Joint Committee on Cancer (AJCC) Staging Manual, 8th edition (2017) [15].

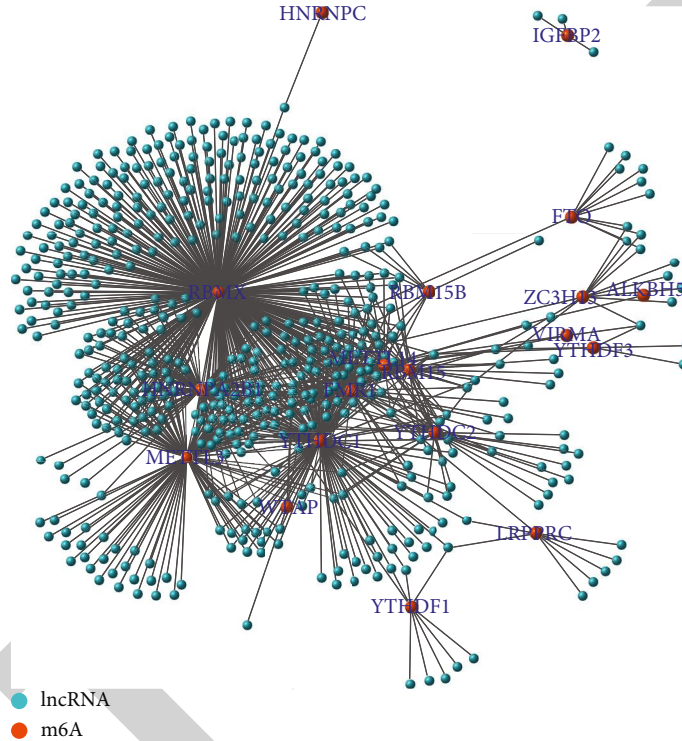
**2.2. Identifying M6A-Related lncRNAs for OSCC Prognosis, Consensus Clustering, Survival Analysis, and Correlations.** Coexpression analysis was performed to screen M6A-related lncRNAs using the Wilcoxon test with the criteria  $p < 0.001$  and correlation  $> 0.4$ . Following this, the coexpression network was developed using the “igraph” R package. Subsequently, univariate Cox regression analysis was used to identify prognostic M6A-related lncRNAs with  $p < 0.01$ . Patients with OSCC were grouped into various clusters by consensus clustering depending on the lncRNA expression levels. OS differences in the different clusters were explored using Kaplan-Meier (KM) analysis. Finally, the “pheatmap” and “ggpubr” R plugins were used to examine changes in the expression levels of M6A-related lncRNAs and clinical characteristics between the clusters [16, 17].

**2.3. Gene Set Enrichment Analysis (GSEA).** To complete the pathway analysis, the GSEA software (v4.0.3) was used. Nominal values (NOM) with ( $p < 0.05$ ) and a false discovery rate ( $q$  value  $< 0.25$ ) were both considered statistically significant [18, 19].

**2.4. Risk Score Model Establishment and Evaluation.** A random distribution of patients was performed among the training and test groups using the R plugin “caret.” Major M6A-associated lncRNAs related to patient prognosis in the training group were identified using LASSO Cox analysis. The minimum standard method (evaluation of penalty parameters by at least ten cross-validations) was used to

TABLE 1: Primer pairs for the target genes.

Gene	Forward primer sequence (5-3)	Reverse primer sequence (5-3)
NOS3	GCCGGAACAGCACAAAGAGTTA	CCCTGCACTGTCTGTGTTACT
NFE2L2	AGGTTGCCACATTCCTCCAAA	ACGTAGCCGAAGAAACCTCA
TP53	ACCTATGGAACTACTTCTGAAA	CTGGCATTCTGGGAGCTTCA
NOS2	GCTTTGTGCGAAGTGTCAGT	TTGTGCTGGGAGTCATGGAG
HMOX1	AGTTCAAGCAGCTCTACCGC	GCAACTCCTCAAAGAGCTGGAT
GAPDH	AATGGGCAGCCGTTAGGAAA	GCCAATACGACCAAATCAGAG

FIGURE 1: Network of N6-methyladenosine (m6A) as red nodes and 1080 long noncoding RNAs (lncRNAs) as blue nodes ( $n = 371$ ).

determine the coefficients. After identifying M6A-correlated lncRNAs and their coefficients, a risk score model was established using the following formula:

$$\text{Risk score} = \sum_{i=1}^n \text{Coef}_i * x_i, \quad (1)$$

where  $\text{Coef}_i$  = coefficient and  $x_i$  = fragments per kilobase of transcript per million (FPKM) value of major M6A-related lncRNAs for OSCC prognosis.

Based on the average risk score, patients were categorized among the high-risk and low-risk score groups. Risk plots, survival analysis, and receiver operating characteristics (ROC) curves were used to assess the efficacy of the risk score model. Additionally, the test group was used to verify the value of the risk score model. Univariate and multivariate Cox analyses revealed the effects of other clinical characteristics and risk scores on the OS. The “survminer” function of R package was used for evaluating the value of the prognostic

risk score in a population with various clinicopathological characteristics [20, 21].

**2.5. Relationships among Risk Scores, Clusters, Immune Cell Populations, and Clinicopathological Characteristics.** For each sample, the number of cells among 22 types of immune cells (resting mast cells, regulatory T cells, M2 macrophages, CD8+ T cells, activated DCs, M0 macrophages, resting DCs, eosinophils, M1 macrophages, plasma cells, resting natural killer (NK) cells, CD4+ memory resting T cells, activated NK cells, monocytes, CD4+ naïve T cells, neutrophils, CD4+ activated memory T cells, memory B cells, gamma delta T cells, naïve B cells, follicular helper T cells, resting DCs, and activated mast cells) was estimated using the “CIBERSOFT” R package. Alternatively, the “ggpubr” R package was used to investigate the associations among the immune cells, risk score, clusters assessed by consensus clustering, and clinicopathological characteristics of patients with OSCC [22, 23].



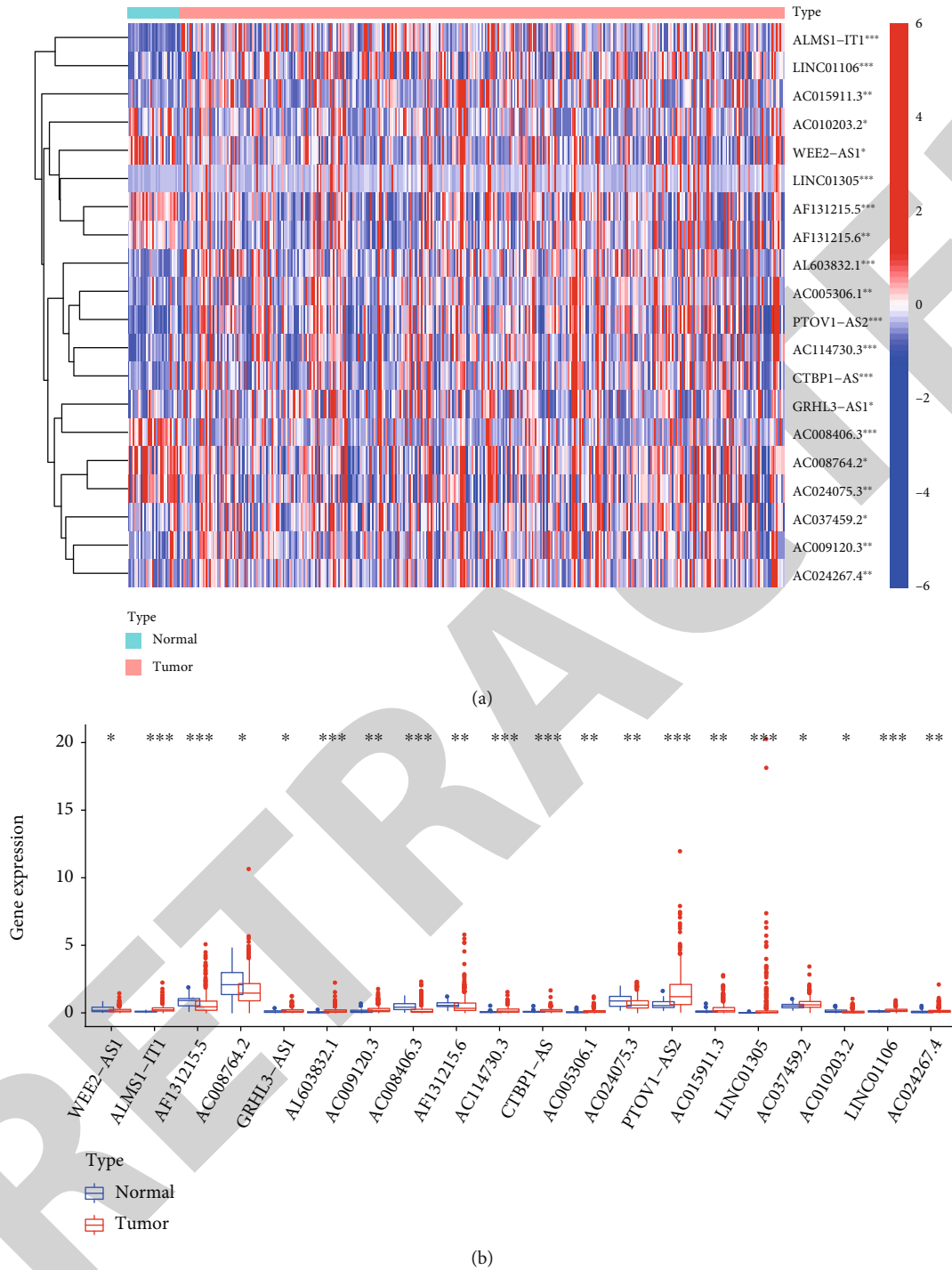


FIGURE 2: Continued.

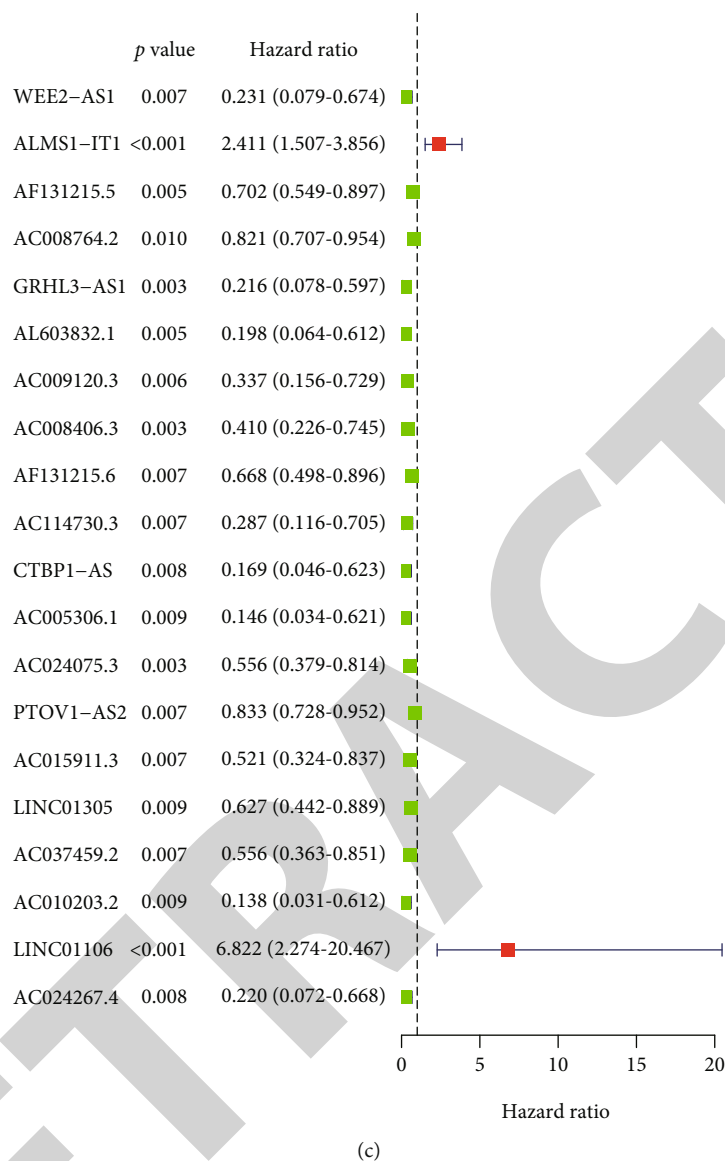


FIGURE 2: Identification of 36 prognostic N6-methyladenosine- (m6A-) relevant lncRNAs using univariate Cox regression analysis. (a) Heatmap of the prognostic expression m6A-relevant lncRNAs ( $n = 371$ ). (b) Vioplot diagram of prognostic expression m6A-relevant lncRNAs ( $n = 371$ ). (c) Forest plot and hazard ratio values obtained from univariate regression analysis ( $n = 368$ ). \* $p < 0.05$ ; \*\* $p < 0.01$ ; \*\*\* $p < 0.01$ .

### 2.6. Validation of Oxidative Stress-Related Genes in OSCC.

Total RNA was isolated from OSCC tissues using TRIzol reagent (Sigma-Aldrich, St. Louis, MO, USA). Next, 2  $\mu\text{g}$  of RNA was isolated from each sample, and quantitative reverse transcription PCR was performed using the FastStart Universal SYBR <sup>®</sup>Green Master (Roche, Germany) on an ABI QuantStudio5 Q5 real-time PCR System (Thermo Fisher Scientific, USA). cDNA was used as a template in a 20  $\mu\text{L}$  reaction volume (10  $\mu\text{L}$  of PCR mixture, 0.5  $\mu\text{L}$  of forward and reverse primers, 2  $\mu\text{L}$  of the cDNA template, and an appropriate volume of water). PCRs were performed as follows: cycling conditions began with an initial DNA denaturation step at 95°C for 30 s, followed by 45 cycles at 94°C for 15 s, 56°C for 30 s, and 72°C for 20 s. Each sample was examined in triplicate. Threshold cycle (CT) readings were

collected and normalized to the glyceraldehyde 3-phosphate dehydrogenase (GAPDH) levels in all samples using the  $2^{-\Delta\Delta\text{CT}}$  method. The mRNA expression levels were compared to those in precancerous tissue controls. The sequences of primer pairs for the target genes are shown in Table 1.

**2.7. Statistical Analyses.** R software (v4.0.5) was used to perform data analysis. Unless specified otherwise, statistical significance was considered at  $p < 0.05$ . The relationship between different clusters and their characteristics was analyzed using the chi-square test ( $n = 368$ ). The relationship between the OS and individual factors was explored by univariate and multivariate Cox analyses ( $n = 368$ ). Data visualization was performed using the “ggplot2” R package.

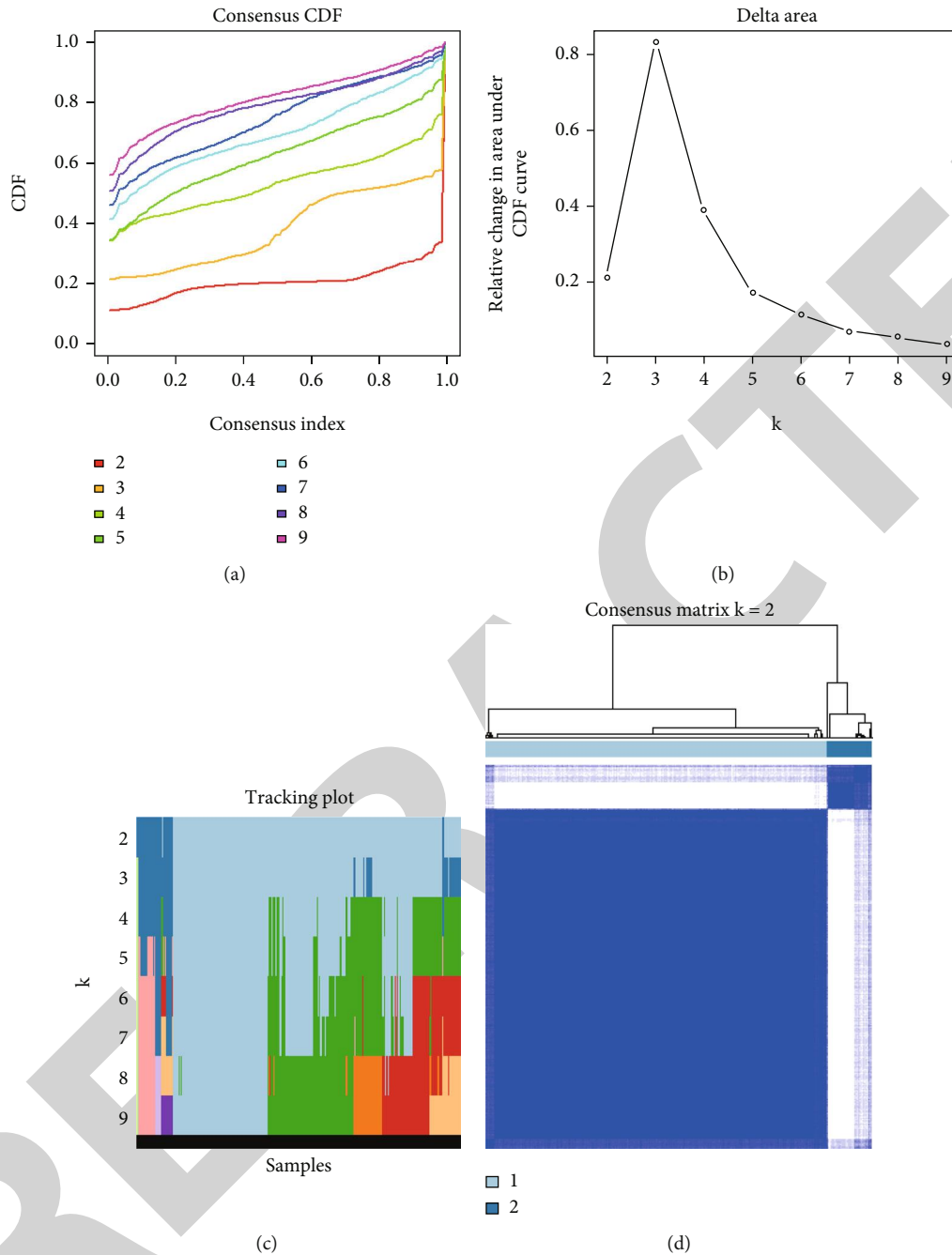


FIGURE 3: Consensus clustering of the OSCC TCGA cohort based on the levels of expression of 36 prognostic m6A-relevant lncRNAs ( $n = 368$ ). (a) CDF for  $k = 2-9$ . (b) Increment in the area under the CDF curve for  $k = 2-9$ . (c) Tracking plot for  $k = 2-9$ . (d) Consensus matrix for the optimal value, i.e.,  $k = 2$ . OSCC: oral squamous cell carcinoma; TCGA: The Cancer Genome Atlas; CDF: consensus clustering distribution function.

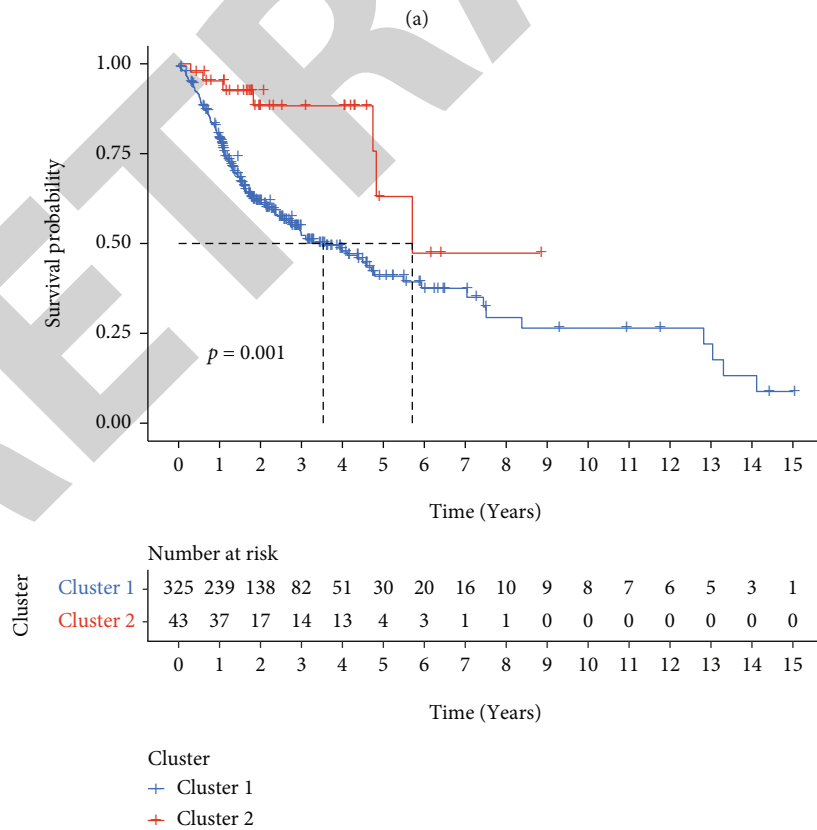
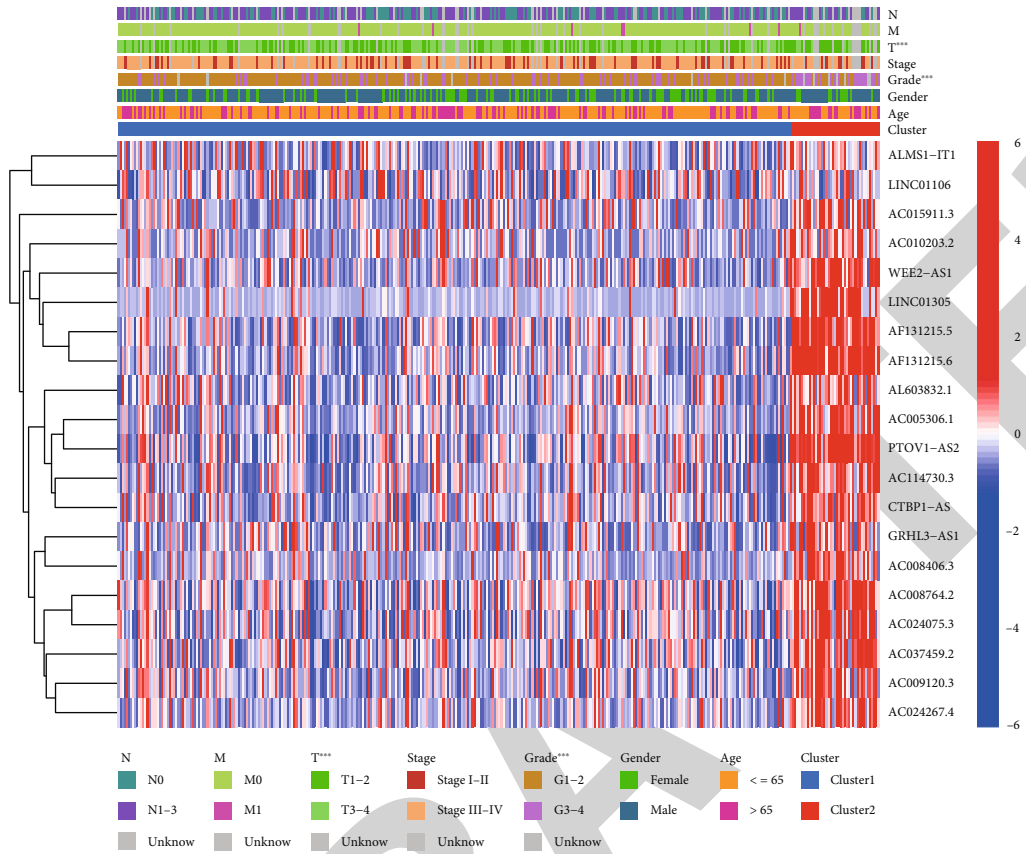
### 3. Results

**3.1. Patient Characteristics.** This work included 368 patients with OSCC. The average follow-up time was 888 days (1–5,480 days).

**3.2. Prognostic M6A-Related lncRNAs in Patients with OSCC.** Coexpression analysis was used to screen 1,080 M6A-related lncRNAs (Figure 1). Univariate Cox regression analysis

identified 36 out of the total number of lncRNAs linked to OSCC prognosis. Figure 2 presents the levels of lncRNAs in normal and OSCC samples as well as the hazard ratios (HRs).

**3.3. Patient Clusters by Consensus Clustering.** The consensus clustering distribution function (CDF) is displayed in Figures 3(a)–3(c), in which  $k = 2$  to  $9$ , along with the increment in the AUC of the CDF and the tracking plot in which



(b)

FIGURE 4: Continued.

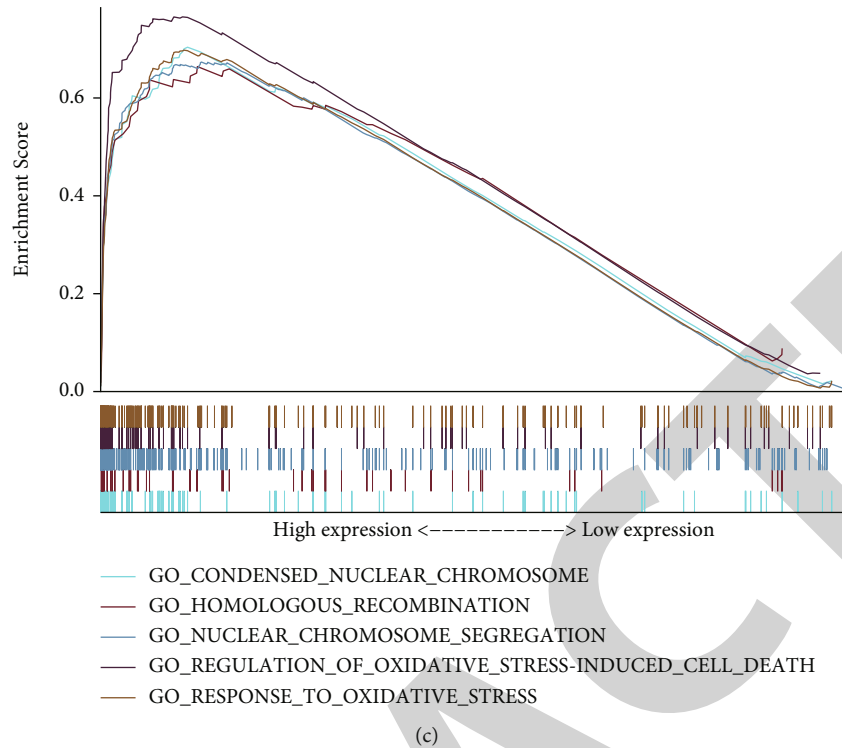


FIGURE 4: Varying prognoses, clinical characteristics, and pathways in different clusters. (a) Clinical characteristics and expression of lncRNAs in different clusters of patients with OSCC. (b) Kaplan-Meier OS curves for the different patients' clusters with OSCC. (c) Pathways enriched in comparison of cluster 1 ( $n = 325$ ) with cluster 2 ( $n = 43$ ). lncRNAs; long noncoding RNAs; OSCC: oral squamous cell carcinoma; OS: overall survival;  $*p < 0.05$ ;  $**p < 0.01$ ;  $***p < 0.01$ .

$k = 2$  to 9, respectively. Based on the largest increment in the AUC and the association of the prognostic expression levels of M6A-correlated lncRNAs in the clusters, two OSCC clusters ( $k = 2$ , clusters 1 and 2) were subsequently identified (Figure 3(d)).

**3.4. Clinical Characteristics and Pathway Analysis of the Different Clusters.** Heat mapping showed that cluster 1 of patients was more advanced than the cluster 2 in terms of the T stage and the pathological grade (Figure 4(a)). Cluster 1 patients showed a dismal outcome ( $p < 0.001$ , Figure 4(b)), as shown by the KM survival analysis. Thereafter, we compared the expression and clinical characteristics of lncRNAs in the various clusters. In addition, the GSEA results suggested that compared with that in cluster 2 samples, certain pathways, such as oxidative stress, showed greater enrichment in cluster 1 samples (Figure 4(c)).

**3.5. Predicting OSCC Prognosis Using the Risk Score Model, Based on 9-Key Prognostic M6A-Related lncRNAs.** From the training group, we identified nine major M6A-related lncRNAs for prognosis. The risk score was determined as follows:  $\text{risk score} = \text{ALMS1} - \text{IT1} * 0.627 + \text{INC01106} * 1.158 - \text{AL603832.1} * 0.280 - \text{AC009120.3} * 0.772 - \text{AC008406.3} * 0.270 - \text{AC114730.3} * 0.071 - \text{LINC01305} * 0.203 - \text{AC037459.2} * 0.130 - \text{AC024267.4} * 0.450$ . In both the test and training groups, the rates of survival of patients with high-risk diseases were lower (Figure 5(a)). The train-

ing group and the test group showed AUCs of the three-year OS curve of 0.75 and 0.69 (Figure 5(b)), respectively. In patients from the low-risk and high-risk score groups, the risk score could be distinguished accurately using survival state and risk plots (Figures 5(c) and 5(d)). In addition, for the survival of the two groups, the risk score was an independent factor, as revealed by the results of the univariate and multivariate analyses (Figures 6). Lastly, in populations with diverse clinicopathological characteristics, the prognostic value of the risk score was evaluated. Our data indicated that the prognosis in all categories, apart from that of patients with distant metastases, might be accurately distinguished using the risk score.

**3.6. Relationship among Risk Scores, Clusters, Immune Cell Populations, Clinicopathological Characteristics, and Oxidative Stress-Associated Biomarker Expression.** The risk score showed a negative correlation with the number of resting mast cells, naïve B cells, and plasma cells, but a positive correlation with the number of resting NK cells, follicular helper T cells, activated mast cells, and M2 macrophages (Figure 7). The risk score was higher for patients included in cluster 1, who had a poor prognosis, as compared to that for patients in cluster 2, who had a good prognosis. Additionally, patients with a high-risk score showed a more advanced AJCC stage and T stage than patients with a low-risk score (Figure 8). The relationship between the risk score and

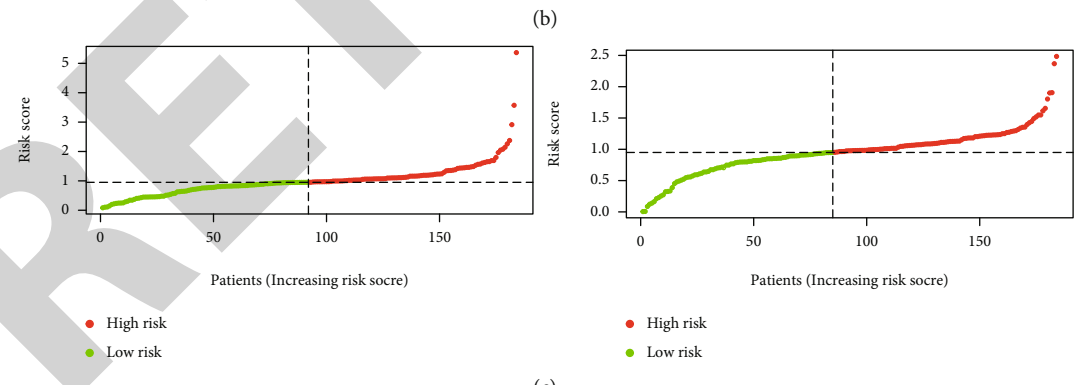
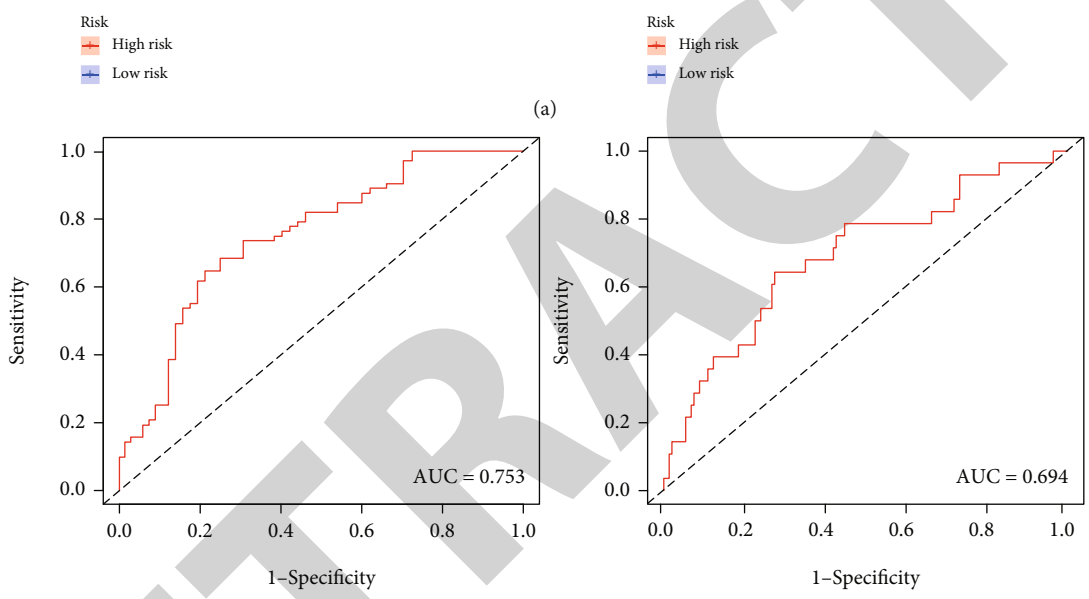
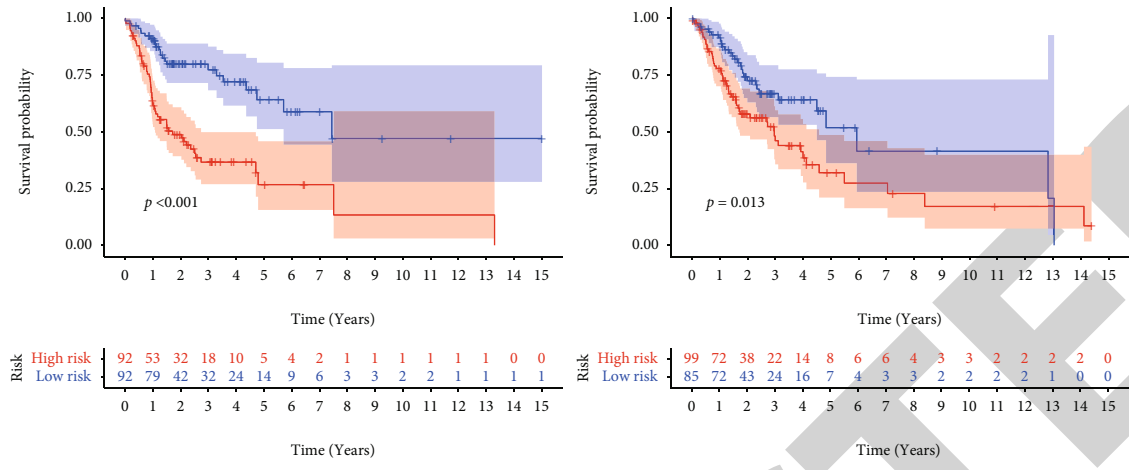


FIGURE 5: Continued.

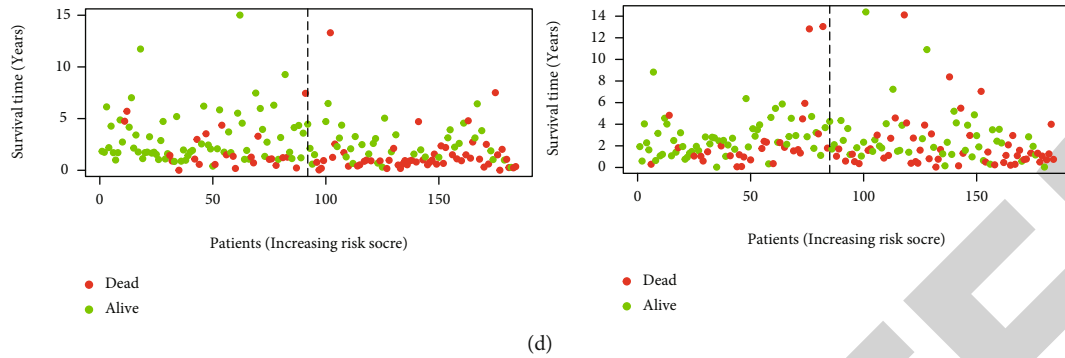


FIGURE 5: (a) The Kaplan-Meier analysis of patients present in the low-risk group and high-risk group in the test and training groups. (b) ROC curves of patients depicting high- and low-risk scores in the training ( $n = 184$ ) and test groups ( $n = 184$ ) (AUC = 0.75 and 0.69, respectively). (c, d) Risk plots and survival state of patients which present in the low-risk group and high-risk group in the test and training groups. ROC: receiver operating characteristic; AUC: area under the curve.

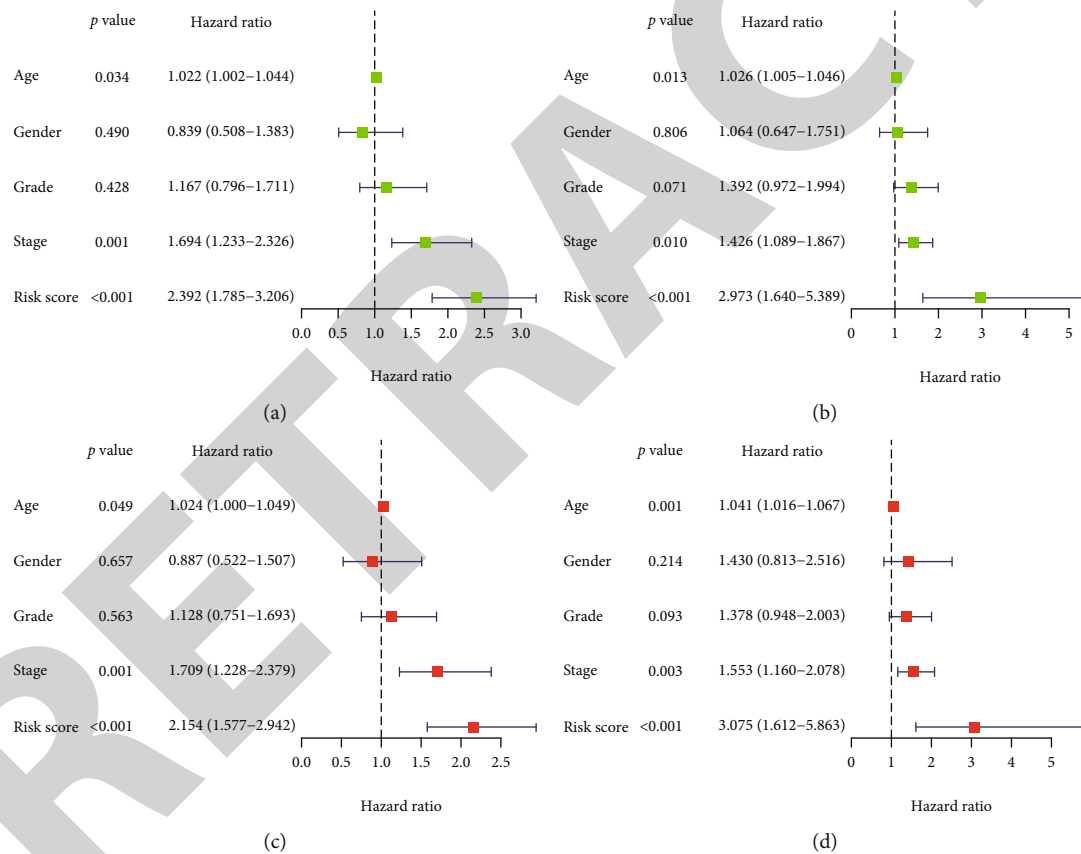


FIGURE 6: Results of the univariate and multivariate Cox regression analysis. (a) Training group of univariate Cox regression analysis. (b) Test group of univariate Cox regression analysis. (c) Training group of multivariate Cox regression analysis. (d) Test group of multivariate Cox regression analysis.  $n = 184$  in both two group.

oxidative stress-associated biomarker expression indicated that the risk score could be affected by oxidative stress.

**3.7. The Oxidative Stress-Related Gene Validation in OSCC Patients.** The results of PCR showed that the biomarkers like HMOX1, NFE2L2, NOS2, NOS3, and TP53 which is associated with oxidative stress was validated that expressed higher in normal tissue (Figures 9 and 10).

## 4. Discussion

Despite recent advances in treatment methods, the 5-year survival in OSCC remains at approximately 60% owing to difficulties in early diagnosis and prognostic determination [24]. Recent studies have identified numerous effective OSCC biomarkers. Previously, based on the expression patterns of seven immunity-related genes, a prognostic model

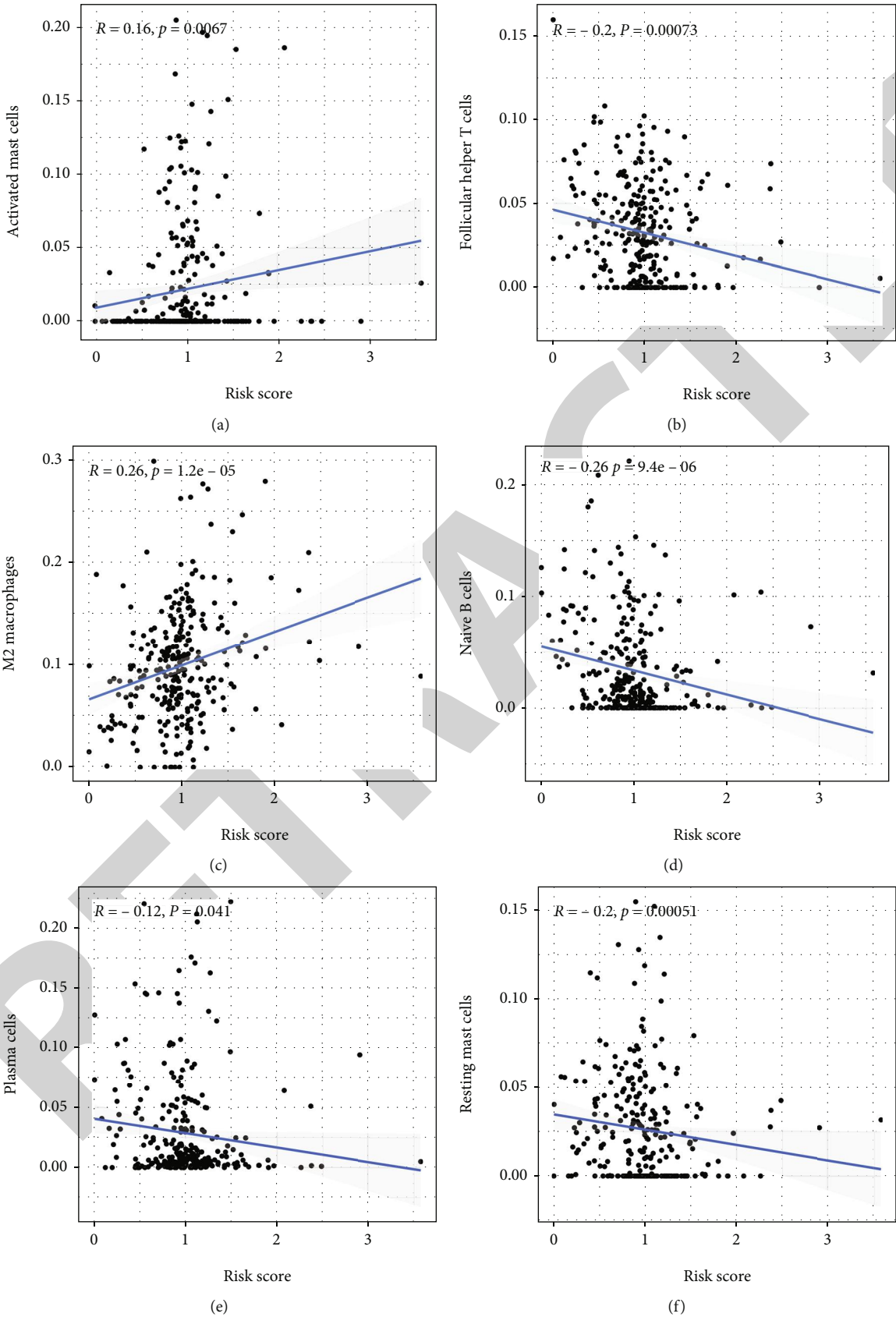


FIGURE 7: Continued.



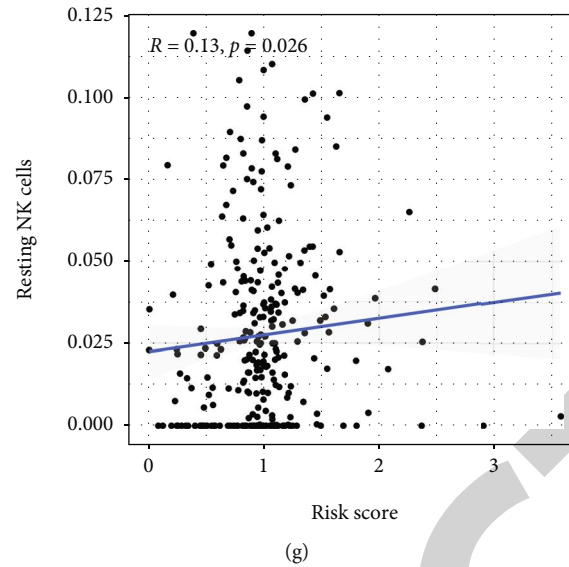


FIGURE 7: Relationship between the risk scores and immune cells ( $n = 368$ ): (a) activated mast cells, (b) follicular helper T cells, (c) M2 macrophages, (d) naïve B cells, (e) plasma cells, (f) resting mast cells, and (g) resting NK cells.

for OSCC was established [25]. We believe that the model developed in this study is critical for identifying useful and specific biomarkers for predicting OSCC outcomes.

Yang et al. developed a model for predicting prognosis based on 16 M6A-related lncRNAs in OSCC. However, only 164 patients were recruited for the study, and not all patients with OSCC who were included in TCGA databases were included. Concurrently, the study did not analyze the relationship between the lncRNAs and oxidative stress, a regulatory pathway involved in the development of oral cancer [26]. For the identification of new biomarkers of OSCC, we investigated the prognostic value of lncRNAs associated with M6A using TCGA data of 371 patients with OSCC and analyzed the relationship between these lncRNAs and oxidative stress pathways. Cox expression analysis was used to identify 1,080 M6A-related lncRNAs. Based on the findings of the univariate Cox regression analysis, 36 lncRNAs were found to be related to prognosis. Oxidative damage accumulates with aging in various species and in different tissues. RNA modification is mobilized to activate or inhibit stress-resistant signaling pathways [27]. Li et al. found that the activities of METTL3/METLL14, p21, and senescence-related  $\beta$ -galactosidase (SA- $\beta$ GAL) increased significantly in oxidative damage-exposed HCT116 p53<sup>-/-</sup> cells, indicating that METTL3/METLL14 may trigger the p53-independent effect of aging in the oxidative damage response, which needs to be tested further [28]. Arsenite et al. stimulated human keratinocytes to induce reactive oxygen species (ROS) production, which thereby increased the WTAP, METTL14, and total M6A expression levels [29]. FTO induces oxidative stress and increases ROS levels by reducing the M6A methylation of peroxisome proliferator-activated receptor-gamma coactivator-1 alpha (PGC1 $\alpha$ ), an important regulator of mitochondrial metabolism that is also affected by the aging process, and increasing PGC1 $\alpha$  mRNA translation efficiency. In our study, the M6A risk score was significantly associated

with oxidative stress. This warrants an investigation of the underlying relationship.

Subsequently, depending upon the variations in the expression level of these prognostic M6A-associated lncRNAs, consensus clustering was used to divide the samples into two clusters. A more advanced pathological grade and T grade and worse outcomes were observed in patients in cluster 1, indicating that the prognosis of patients with OSCC could be accurately distinguished using the proposed method, and the M6A-related lncRNAs could influence the pathogenesis of OSCC. In addition, the findings of the GSEA suggested that “oxidative stress” was less enriched in cluster 2 than in cluster 1. The upregulation of the EMT pathway, which is associated with cancer cell invasion and metastasis, can increase the risk of cancer recurrence and reduce the survival rate [30]. Furthermore, EMT is involved in local recurrence, lymph node metastasis, and low survival rate among patients with OSCC [31]. However, the specific mechanism underlying this upregulation, and particularly its correlation with M6A-related lncRNAs, remains unclear.

Depending upon the results of the LASSO Cox regression analysis in the training group, nine prognostic hub M6A-related lncRNAs were filtered. Among these lncRNAs, ALMS1-IT1 was found to be associated with the poor prognosis of lung cancer and AC114730.3 with the good prognosis of bladder cancer [32, 33]. Reportedly, LINC01305 reduced the metastasis and invasion of ovarian and lung cancer by inhibiting EMT [34]. However, the mechanism underlying the action of the lncRNAs in OSCC, and the roles of AL603832.1, AC0091230.3, AC008406.3, AC037459.2, INC01106, and AC024267.4 in tumorigenesis remain unclear. In particular, their role in the initiation of OSCC requires further elucidation.

A risk score model was developed for the prediction of OSCC prognosis according to the coefficients of major prognosis-related M6A-associated lncRNAs and the FPKM

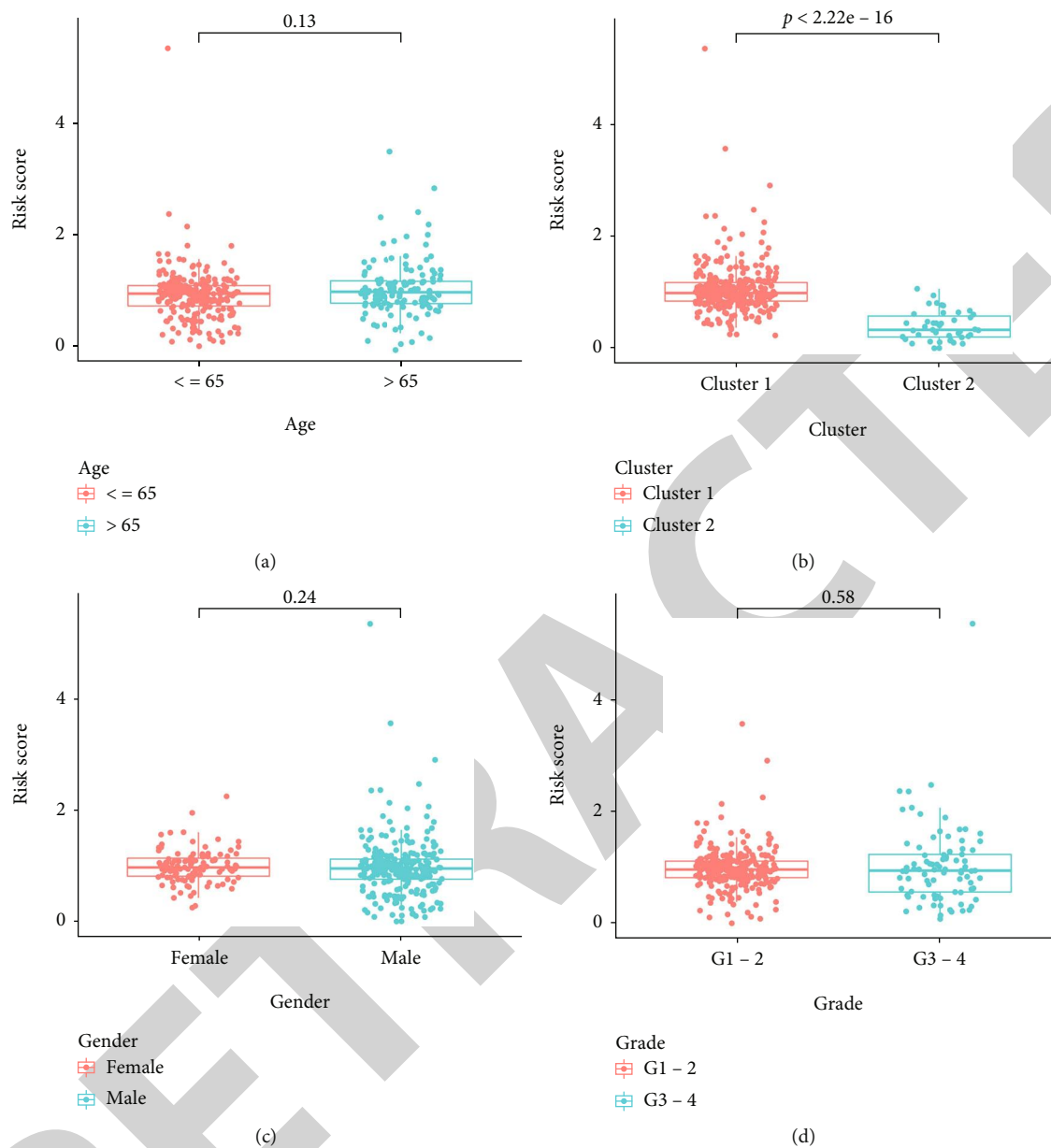


FIGURE 8: Continued.

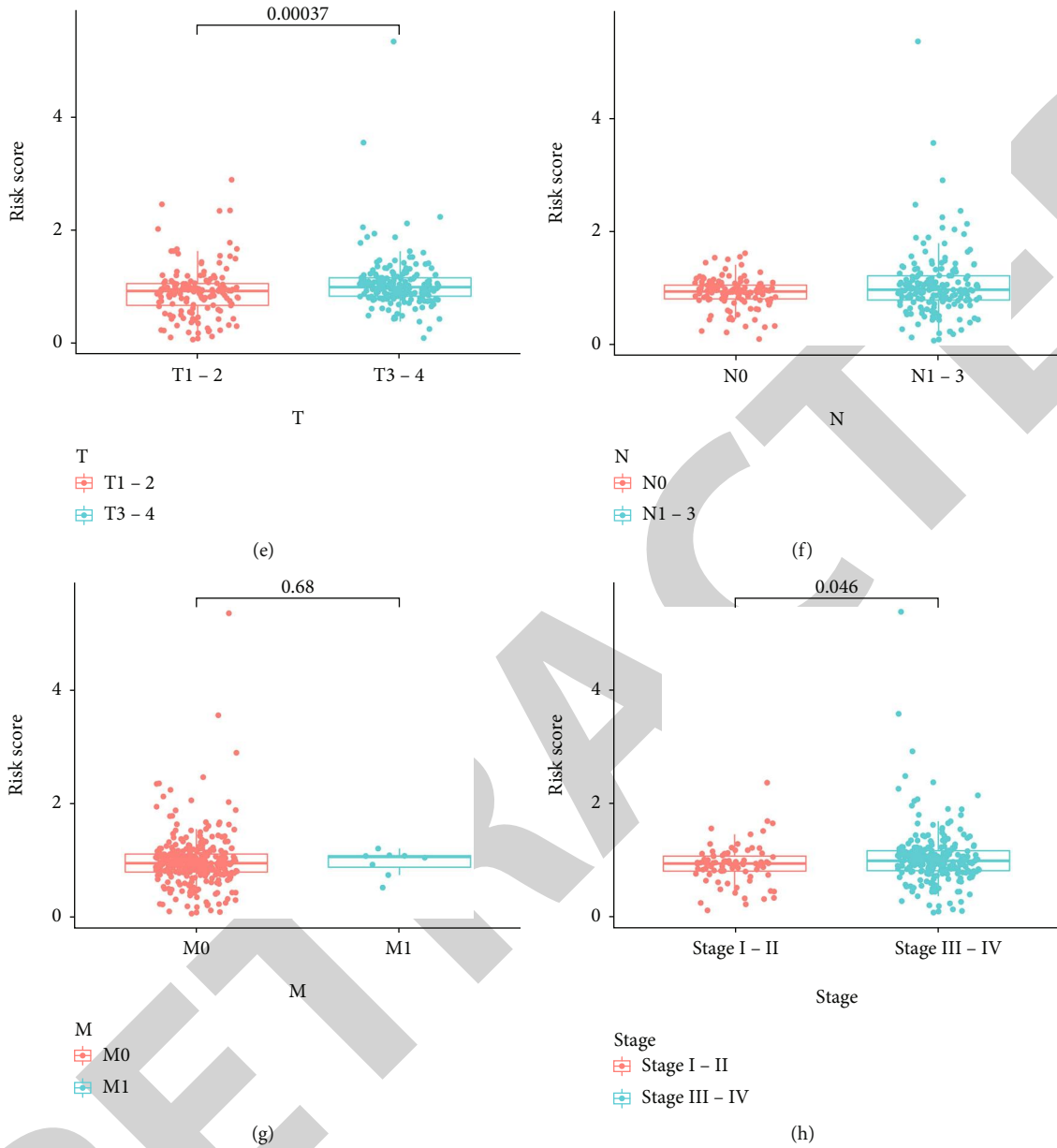


FIGURE 8: Relationship between risk score, clusters, and clinicopathological characteristics ( $n = 368$ ): (a) age, (b) Cluster, (c) gender, (d) grade, (e) tumor, (f) lymph node metastasis, (g) distant metastasis, and (h) stage.

values. We also compared the risk scores of the test and training groups. The risk score served as a reliable independent prognostic factor of OSCC, as indicated in the results obtained from the KM analysis, ROC curves, risk map analysis, and univariate and multivariate Cox regression analyses. Apart from that of patients with distant metastasis, the prognosis of populations with different clinicopathological characteristics could be predicted by the risk score. The risk score probably failed to distinguish among the prognosis of patients with distant metastasis because only eight patients were included in this category. In addition, patients who were present in the high-risk score group showed a more advanced T stage and AJCC stage and a shorter OS, whereas patients present in the low-risk cluster 2 showed a lower risk score than patients in the high-risk cluster 1. These results

indicated that the key prognostic M6A-related lncRNAs identified in this study may be important for the initiation and progression of OSCC. Verification was performed to confirm the risk score accuracy and significance while predicting OSCC prognosis. To further confirm oxidative stress in patients with OSCC, we performed RT-PCR using tissues obtained from patients with OSCC to confirm the relationship between normal and OSCC patient groups. Prognostic data should be collected in the future to confirm the signature.

The risk score showed a negative correlation with the number of resting mast cells, naïve B cells, and plasma cells, but showed a positive correlation with the number of M2 macrophages, follicular helper T cells, NK cells, and activated mast cells. B cells are important in the host response

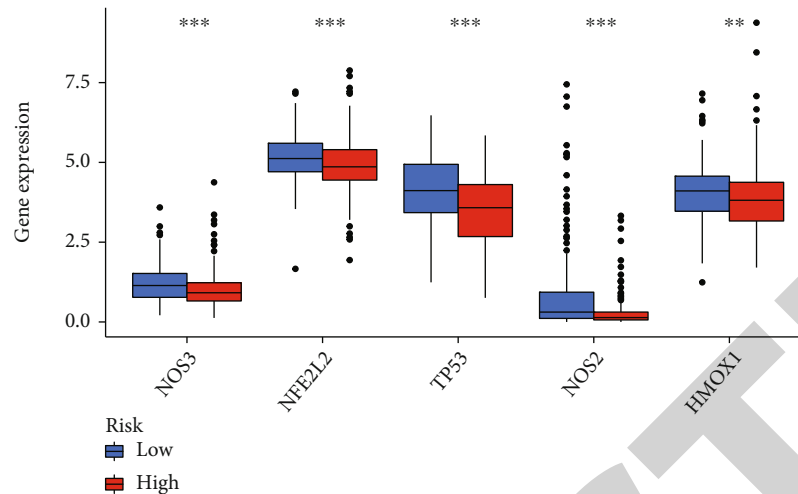


FIGURE 9: Relationship between risk score and oxidative stress expression ( $n = 184$  in both two group).

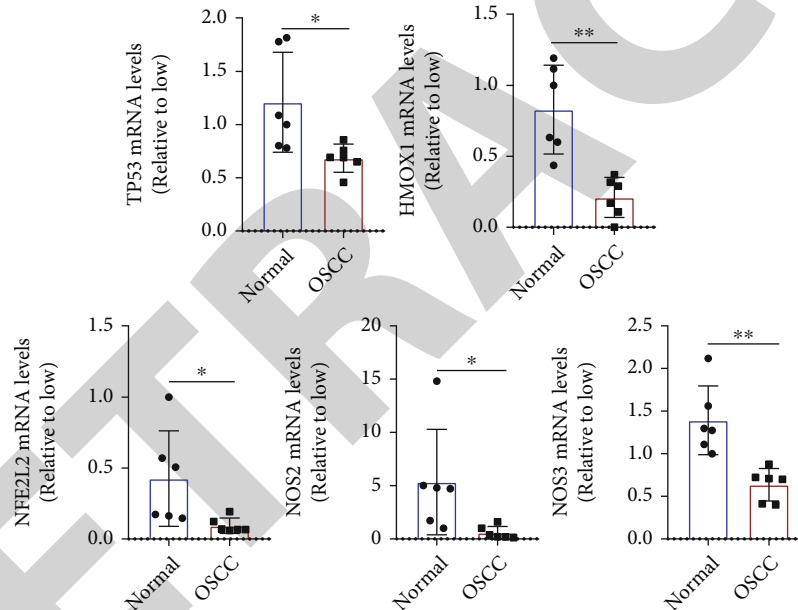


FIGURE 10: The expression of oxidative stress related genes ( $n = 6$ ).

to tumors, and naïve B cells inhibit tumor cell growth and promote good prognosis in prostate cancer and non-small-cell lung cancer [35, 36]. Alternatively, plasma cells can produce tumor-specific antibodies that can bind to tumor cells for inhibiting the activation of their complements and target proteins and/or for promoting antibody-dependent cytotoxicity [37]. The number of plasma cells has been associated with a good prognosis for lung cancer, liver cancer, and other tumors [38]. Similarly, the results of the present study indicated that plasma cells and naïve B cells are potentially associated with a good prognosis of OSCC. In contrast, mast cells undertake distinct functions in different tumors and can either promote or inhibit tumor growth [39]. Increased mast cell infiltration is linked to the poor prognosis of lung and colorectal cancer and good prognosis of breast and prostate cancer [40, 41]. The findings of a study on head and

neck cancer suggested that activated mast cells were linked to a poor prognosis [42]. In the present study, the risk score showed a negative correlation with the number of resting mast cells but a positive correlation with the number of activated mast cells. These findings indicate that the latter can promote the growth of OSCC. Tumor-associated macrophages exhibit two distinct phenotypes: M1 (classically activated macrophages) and M2 (alternatively activated macrophages). M2 macrophages can contribute to tumor growth, angiogenesis, and immunosuppression [43]. The number of M2 macrophages is linked to the poor prognosis of patients with intrahepatic cholangiocarcinoma, renal cell carcinoma, and glioma [44, 45]. NK cells, which exhibit potent cytolytic activity, are important contributors to the host defense against tumors [46]. Although few studies have been conducted on the relationship between the number of

resting NK cells and tumors, the number of resting NK cells was found to be positively correlated with the Gleason score in patients with prostate cancer, which indicates its correlation with prostate cancer malignancy [36]. The involvement of follicular helper T cells in the initiation and progression of tumors has been recognized. The formation and maintenance of the germinal center depend on follicular helper T cells, which represent the key cell type of the latter. These cells can promote B cell proliferation and somatic hypermutation and are linked to the poor prognosis of gastric and lung cancer [47]. In this study, the risk score showed a positive correlation with the number of M2 macrophages, follicular helper T cells, and resting NK cells, indicating the correlation of poor prognosis in OSCC with the population of these immune cell types. However, further research is necessary to understand how these cells interact during the initiation and progression of OSCC. The limitations of this study were the small sample size of adjacent normal tissues and the OSCC RNA sequence FPKM data. Thus, potential statistical errors could not be excluded. Further experiments are needed to explore the efficacy of the proposed prognostic model in the clinical environment to improve its reliability in terms of prognostic prediction in patients with OSCC. Additionally, no experiment was performed to confirm the interaction between the prognostic factors lncRNAs and M6A modulators in OSCC. Further investigation is necessary to confirm the relationship among M6A, oxidative stress, and OSCC.

In conclusion, to our knowledge, this is the first study to verify the expression and prognostic value of M6A-related lncRNAs in OSCC. The expression of M6A-related lncRNAs is closely related to the clinical characteristics and a poor survival rate in OSCC and can be used clinically to predict the prognosis of OSCC. Such findings will inform future investigations on the potential therapeutic targets of OSCC.

## Abbreviations

M6A:	N6-methyladenosine
lncRNA:	Long noncoding RNA
OSCC:	Oral squamous cell carcinoma
TCGA:	The Cancer Genome Atlas
GSEA:	Gene set enrichment analysis
OS:	Overall survival
AJCC:	American Joint Committee on Cancer
HOTAIR:	HOX transcript antisense intergenic RNA
LASSO:	Least absolute shrinkage and selection operator
KM:	Kaplan–Meier
DCs:	Dendritic cells
NK:	Natural killer
ROC:	Receiver operating characteristic
CDF:	Cumulative distribution function
AUC:	Area under the curve.

## Data Availability

The datasets used and/or analyzed during the current study are available from the corresponding author on reasonable request.

## Ethical Approval

The experimental protocol was established, according to the ethical guidelines of the Helsinki Declaration. Ethical permissions were granted by the Human Ethics Committee.

## Consent

Written informed consent was obtained from the individual or guardian participants.

## Conflicts of Interest

The authors declare that the research was conducted in the absence of any commercial or financial relationships that could be construed as a potential conflict of interest.

## Authors' Contributions

Li Shan and Ye Lu contributed equally to this work.

## Acknowledgments

The authors acknowledge the financial grant by the Key Projects of Medical and Health Technology Programme of Taicang Bureau of Science and Technology in Jiangsu Province, PRC (grant number TC2021JCYL30).

## References

- [1] P. H. Montero and S. G. Patel, "Cancer of the Oral Cavity," *Surgical Oncology Clinics of North America*, vol. 24, no. 3, pp. 491–508, 2015.
- [2] I. Chattopadhyay, M. Verma, and M. Panda, "Role of oral microbiome signatures in diagnosis and prognosis of oral cancer," *Technology in Cancer Research Treatment*, vol. 18, p. 153303381986735, 2019.
- [3] H. S. Bawaskar and P. H. Bawaskar, "Oral diseases: a global public health challenge," *The Lancet*, vol. 395, no. 10219, pp. 185–186, 2020.
- [4] J. Podlodowska, J. Szumiło, W. Podlodowski, E. Starosławska, and F. Burdan, "Epidemiology and risk factors of the oral carcinoma," *Polski merkuriusz lekarski : organ Polskiego Towarzystwa Lekarskiego*, vol. 32, no. 188, pp. 135–137, 2012.
- [5] C. U. Hübbers and B. Akgül, "HPV and cancer of the oral cavity," *Virulence*, vol. 6, no. 3, pp. 244–248, 2015.
- [6] Q. Lan, P. Y. Liu, J. Haase, J. L. Bell, S. Hüttelmaier, and T. Liu, "The critical role of RNA m6A methylation in cancer," *Cancer research*, vol. 79, no. 7, pp. 1285–1292, 2019.
- [7] C. Zhang, D. Samanta, H. Lu et al., "Hypoxia induces the breast cancer stem cell phenotype by HIF-dependent and ALKBH5-mediated m6A-demethylation of NANOG mRNA," *Proceedings of the National Academy of Sciences of the United States of America*, vol. 113, no. 14, pp. E2047–E2056, 2016.
- [8] X. Ma, Y. Li, J. Wen, and Y. Zhao, "m6A RNA methylation regulators contribute to malignant development and have a clinical prognostic effect on cervical cancer," *American journal of translational research*, vol. 12, no. 12, pp. 8137–8146, 2020.
- [9] R. Z. He, D. X. Luo, and Y. Y. Mo, "Emerging roles of lncRNAs in the post-transcriptional regulation in cancer," *Genes & diseases*, vol. 6, no. 1, pp. 6–15, 2019.

- [10] L. Zhang, X. Meng, X. W. Zhu et al., “Long non-coding RNAs in oral squamous cell carcinoma: biologic function, mechanisms and clinical implications,” *Molecular cancer*, vol. 18, no. 1, p. 102, 2019.
- [11] J. Wu and H. Xie, “Expression of long noncoding RNA-HOX transcript antisense intergenic RNA in oral squamous cell carcinoma and effect on cell growth,” *Tumour biology : the journal of the International Society for Oncodevelopmental Biology and Medicine*, vol. 36, no. 11, pp. 8573–8578, 2015.
- [12] D. S. W. Tan, F. T. Chong, H. S. Leong et al., “Long noncoding RNA EGFR-AS1 mediates epidermal growth factor receptor addiction and modulates treatment response in squamous cell carcinoma,” *Nature medicine*, vol. 23, no. 10, pp. 1167–1175, 2017.
- [13] Z. Tu, L. Wu, P. Wang et al., “N6-Methyladenosine-related lncRNAs are potential biomarkers for predicting the overall survival of lower-grade glioma patients,” *Frontiers in cell and developmental biology*, vol. 8, p. 642, 2020.
- [14] X. Zuo, Z. Chen, W. Gao et al., “M6A-mediated upregulation of LINC00958 increases lipogenesis and acts as a nanotherapeutic target in hepatocellular carcinoma,” *Journal of hematology & oncology*, vol. 13, no. 1, p. 5, 2020.
- [15] F. Chen, E. Gong, J. Ma et al., “Prognostic score model based on six m6A-related autophagy genes for predicting survival in esophageal squamous cell carcinoma,” *Journal of Clinical Laboratory Analysis*, p. e24507, 2022.
- [16] S. Ren, W. Wang, H. Shen et al., “Development and validation of a clinical prognostic model based on immune-related genes expressed in clear cell renal cell carcinoma,” *Frontiers in oncology*, vol. 10, p. 1496, 2020.
- [17] W. Wang, Q. Wu, Z. Wang et al., “Development of a prognostic model for ovarian cancer patients based on novel immune microenvironment related genes,” *Frontiers in oncology*, vol. 11, p. 647273, 2021.
- [18] X. Ge, Z. Wang, R. Jiang et al., “SCAMP4 is a novel prognostic marker and correlated with the tumor progression and immune infiltration in glioma,” *The international journal of biochemistry & cell biology*, vol. 139, p. 106054, 2021.
- [19] X. Jin, H. Xie, X. Liu et al., “\_RELL1\_ , a novel oncogene, accelerates tumor progression and regulates immune infiltrates in glioma,” *International Immunopharmacology*, vol. 87, p. 106707, 2020.
- [20] X. Chen, S. Mo, L. Zong, S. Yu, Z. Lu, and J. Chen, “A novel signature based on m6A RNA methylation regulators reveals distinct prognostic subgroups and associates with tumor immunity of patients with pancreatic neuroendocrine neoplasms,” *Neuroendocrinology*, 2022.
- [21] H. Xu, L. Yin, Q. Xu, J. Xiang, and R. Xu, “N6-methyladenosine methylation modification patterns reveal immune profiling in pancreatic adenocarcinoma,” *Cancer cell international*, vol. 22, no. 1, p. 199, 2022.
- [22] X. Ge, S. Jiang, Z. Wang et al., “Prognostic biomarker ZNF311 and its correlation with tumor progression and immune infiltrates in glioma,” *World Neurosurgery*, vol. 151, pp. e37–e46, 2021.
- [23] A. M. Newman, C. L. Liu, M. R. Green et al., “Robust enumeration of cell subsets from tissue expression profiles,” *Nature Methods*, vol. 12, no. 5, pp. 453–457, 2015.
- [24] D. K. Zanoni, P. H. Montero, J. C. Migliacci et al., “Survival outcomes after treatment of cancer of the oral cavity (1985–2015),” *Oral oncology*, vol. 90, pp. 115–121, 2019.
- [25] X. T. Zhao, Y. Zhu, J. F. Zhou, Y. J. Gao, and F. Z. Liu, “Development of a novel 7 immune-related genes prognostic model for oral cancer: a study based on TCGA database,” *Oral oncology*, vol. 112, p. 105088, 2021.
- [26] Q. Yang, C. Cheng, R. Zhu et al., “A N6-methyladenosine-related long noncoding RNAs model for predicting prognosis in oral squamous cell carcinoma: association with immune cell infiltration and tumor metastasis,” *Oral oncology*, vol. 127, p. 105771, 2022.
- [27] A. Peters, T. S. Nawrot, and A. A. Baccarelli, “Hallmarks of environmental insults,” *Cell*, vol. 184, no. 6, pp. 1455–1468, 2021.
- [28] Q. Li, X. Li, H. Tang et al., “NSUN2-mediated m5C methylation and METTL3/METTL14-mediated m6A methylation cooperatively enhance p21 translation,” *Journal of Cellular Biochemistry*, vol. 118, no. 9, pp. 2587–2598, 2017.
- [29] T. Zhao, X. Li, D. Sun, and Z. Zhang, “Oxidative stress: one potential factor for arsenite-induced increase of N<sup>6</sup>-methyladenosine in human keratinocytes,” *Environmental Toxicology and Pharmacology*, vol. 69, pp. 95–103, 2019.
- [30] J. M. Lee, S. Dedhar, R. Kalluri, and E. W. Thompson, “The epithelial-mesenchymal transition: new insights in signaling, development, and disease,” *The Journal of cell biology*, vol. 172, no. 7, pp. 973–981, 2006.
- [31] P. Jayanthi, B. R. Varun, and J. Selvaraj, “Epithelial-mesenchymal transition in oral squamous cell carcinoma: an insight into molecular mechanisms and clinical implications,” *Journal of oral and maxillofacial pathology : JOMFP*, vol. 24, no. 1, p. 189, 2020.
- [32] T. Luan, T. Y. Zhang, Z. H. Lv et al., “The lncRNA ALMS1-IT1 may promote malignant progression of lung adenocarcinoma via AVL9-mediated activation of the cyclin-dependent kinase pathway,” *FEBS Open Bio*, vol. 11, no. 5, pp. 1504–1515, 2021.
- [33] Y. Wu, L. Zhang, S. He et al., “Identification of immune-related lncRNA for predicting prognosis and immunotherapeutic response in bladder cancer,” *Aging*, vol. 12, no. 22, pp. 23306–23325, 2020.
- [34] F. Yan, S. W. Liu, X. Y. Li, C. C. Li, and Y. Wu, “Silencing lncRNA LINC01305 inhibits epithelial mesenchymal transition in lung cancer cells by regulating TNXB-mediated PI3K/Akt signaling pathway,” *Journal of biological regulators and homeostatic agents*, vol. 34, no. 2, pp. 499–508, 2020.
- [35] J. Chen, Y. Tan, F. Sun et al., “Single-cell transcriptome and antigen-immunoglobulin analysis reveals the diversity of B cells in non-small cell lung cancer,” *Genome biology*, vol. 21, no. 1, p. 152, 2020.
- [36] Z. Wu, H. Chen, W. Luo et al., “The landscape of immune cells infiltrating in prostate cancer,” *Frontiers in oncology*, vol. 10, p. 517637, 2020.
- [37] M. C. A. Wouters and B. H. Nelson, “Prognostic significance of tumor-infiltrating B cells and plasma cells in human cancer,” *Clinical cancer research : an official journal of the American Association for Cancer Research*, vol. 24, no. 24, pp. 6125–6135, 2018.
- [38] X. Liu, S. Wu, Y. Yang, M. Zhao, G. Zhu, and Z. Hou, “The prognostic landscape of tumor-infiltrating immune cell and immunomodulators in lung cancer,” *Biomedicine & Pharmacotherapy*, vol. 95, pp. 55–61, 2017.
- [39] S. A. Oldford and J. S. Marshall, “Mast cells as targets for immunotherapy of solid tumors,” *Molecular immunology*, vol. 63, no. 1, pp. 113–124, 2015.

## *Retraction*

# **Retracted: ZNF354C Mediated by DNMT1 Ameliorates Lung Ischemia-Reperfusion Oxidative Stress Injury by Reducing TFPI Promoter Methylation to Upregulate TFPI**

### **Oxidative Medicine and Cellular Longevity**

Received 26 December 2023; Accepted 26 December 2023; Published 29 December 2023

Copyright © 2023 Oxidative Medicine and Cellular Longevity. This is an open access article distributed under the Creative Commons Attribution License, which permits unrestricted use, distribution, and reproduction in any medium, provided the original work is properly cited.

This article has been retracted by Hindawi, as publisher, following an investigation undertaken by the publisher [1]. This investigation has uncovered evidence of systematic manipulation of the publication and peer-review process. We cannot, therefore, vouch for the reliability or integrity of this article.

Please note that this notice is intended solely to alert readers that the peer-review process of this article has been compromised.

Wiley and Hindawi regret that the usual quality checks did not identify these issues before publication and have since put additional measures in place to safeguard research integrity.

We wish to credit our Research Integrity and Research Publishing teams and anonymous and named external researchers and research integrity experts for contributing to this investigation.

The corresponding author, as the representative of all authors, has been given the opportunity to register their agreement or disagreement to this retraction. We have kept a record of any response received.

### **References**

- [1] Q. Shi, N. Feng, Q. Ma et al., “ZNF354C Mediated by DNMT1 Ameliorates Lung Ischemia-Reperfusion Oxidative Stress Injury by Reducing TFPI Promoter Methylation to Upregulate TFPI,” *Oxidative Medicine and Cellular Longevity*, vol. 2022, Article ID 7288729, 18 pages, 2022.

## Research Article

# ZNF354C Mediated by DNMT1 Ameliorates Lung Ischemia-Reperfusion Oxidative Stress Injury by Reducing TFPI Promoter Methylation to Upregulate TFPI

Qi Shi,<sup>1,2</sup> Nana Feng,<sup>3</sup> Qingyun Ma,<sup>1</sup> Shaohua Wang,<sup>1</sup> Huijun Zhang,<sup>1</sup> Dayu Huang,<sup>1</sup> Jiayuan Sun <sup>2</sup> and Meng Shi <sup>1</sup>

<sup>1</sup>Department of Thoracic and Cardiovascular Surgery, Huashan Hospital, Affiliated with Fudan University, Shanghai 200040, China

<sup>2</sup>Department of Respiratory Endoscopy, Department of Respiratory and Critical Care Medicine, Shanghai Chest Hospital, Shanghai Jiao Tong University, Shanghai 200030, China

<sup>3</sup>Department of Respiratory and Critical Medicine, Shanghai Eighth People's Hospital Affiliated to Jiang Su University, Shanghai 200030, China

Correspondence should be addressed to Jiayuan Sun; [xkyjyjsun@163.com](mailto:xkyjyjsun@163.com) and Meng Shi; [mengshi@fudan.edu.cn](mailto:mengshi@fudan.edu.cn)

Qi Shi and Nana Feng contributed equally to this work.

Received 16 March 2022; Revised 6 May 2022; Accepted 27 May 2022; Published 19 July 2022

Academic Editor: Tian Li

Copyright © 2022 Qi Shi et al. This is an open access article distributed under the Creative Commons Attribution License, which permits unrestricted use, distribution, and reproduction in any medium, provided the original work is properly cited.

**Background.** Pulmonary ischemia reperfusion- (I/R-) induced dysfunction is a significant clinical problem after lung transplantation. In this study, we aim to explore the molecular mechanism of lung I/R injury (LIRI). **Methods.** Bioinformatic analysis of gene involved in oxidative stress. A HUVEC oxygen glucose deprivation/reoxygenation (OGD/R) model and I/R mouse model were first established via I/R. The cellular proliferation, migration, reactive oxygen species (ROS), and parameters of lung injury were assessed via CCK-8, EdU staining, Transwell, cellular ROS kit, and H&E staining. We also confirmed related gene expressions and protein levels and the interaction between the tissue factor pathway inhibitor (TFPI) promoter and ZNF354C. **Results.** Bioinformatic analysis results showed TFPI contributed to oxidative stress. OGD/R caused a reduction in cell viability and migration, hypermethylation of TFPI, increased ROS, and downregulation of ZNF354C, TFPI, and DNA methyltransferases (DNMTs) in HUVECs. Besides, ZNF354C could directly bind to the TFPI promoter, enhance proliferation and migration, and inhibit ROS in OGD/R-induced HUVECs by upregulating TFPI. More importantly, we discovered that 5-Aza could reduce TFPI methylation, upregulate TFPI, and enhance the binding of ZNF354C to the TFPI promoter in LIRI. Furthermore, DNMT1 silencing could induce proliferation and migration and prevent ROS in OGD/R-induced HUVECs by upregulating ZNF354C. Additionally, we verified that ZNF354C could alleviate LIRI by preventing DNA methylation *in vivo*. **Conclusions.** ZNF354C overexpression induced proliferation and migration, as well as suppressed ROS in OGD/R-induced HUVECs, and alleviated LIRI in mice by inhibiting TFPI promoter methylation to upregulate TFPI. Therefore, ZNF354C and TFPI methylation might be promising molecular markers for LIRI therapy.

## 1. Background

During lung transplantation, acute lung injury (ALI) caused by the insufficient blood supply to the lungs and subsequent perfusion (denoted ischemia-reperfusion (I/R) injury [1] and “LIRI” when specific to the lung) [2] remain a challenging clinical

problem, resulting in the high mortality after lung transplantation [3]. The success rate of lung transplantation is furthermore limited by high rates of primary graft dysfunction (PGD) [4]. LIRI is usually associated with acute, aseptic inflammation, alveolar damage, and vascular permeability [5, 6]. Furthermore, LIRI is also a complex pathophysiological process, which may



be associated with neutrophil infiltration, endothelial cell injury, apoptosis, and necrosis [7, 8]. There are no therapeutic agents clinically utilized to specifically prevent LIRI, with treatment strategies limited to supportive care. Therefore, it is imperative to find effective molecular targets for LIRI therapy.

A tissue factor pathway inhibitor (TFPI), a multidomain and a Kunitz-type protease inhibitor of factor VIIa/tissue factor (TF), is produced primarily by endothelial cells and released after cellular stimulation [9]. Endothelial cells are one of the primary cell types for TFPI synthesis, and the endothelial-bound TFPI contributes to the antithrombotic potential of vascular endothelial cells [10]. Research verified that TFPI can increase the occurrence of autoimmune injury by promoting the overactivation of autoimmune factors or chemokines [11]. Moreover, the elevated TFPI level in sepsis may represent endothelial dysfunction [12]. TFPI also plays a key role in the regulation and function of endothelial permeability, which is associated with the development of sepsis and ALI [13]. Research has also shown that intratracheal TFPI can improve gas exchanges and prevent mortality in ALI model rats that presents with severe sepsis [14]. Importantly, endothelial-specific destruction of TFPI can enhance lung endothelial permeability and promote metastasis in lung metastatic tumor models. TFPI deficiency in endothelial cells also induces pulmonary tumor metastasis with increased vascular permeability and altered lung microenvironment [15]. Despite accumulating research into the effects of TFPI in ALI, the function and mechanism of TFPI in LIRI have not been elucidated.

Zinc finger proteins (ZNF) are a class of transcription factors with multiple functions [16]. Specifically, ZNF354C has been found to have a critical role in bone and tumors [17, 18]. To further investigate the possible mechanisms of TFPI in LIRI, we applied bioinformatic analysis to predict the potential proteins that can bind to the TFPI promoter and concluded that ZNF354C may have a direct targeting regulatory role with the TFPI promoter. We also found that ZNF354C was downregulated in oxygen-glucose deprivation/reperfusion- (OGD/R-) induced human umbilical vein endothelial cells (HUVECs). Therefore, we speculated that ZNF354C may regulate TFPI expression by targeted binding, thus affecting the developmental process of ALI. However, the regulatory mechanism of ZNF354C has not been reported yet.

Epigenetic modifications are reportedly to play a key role in disease progression and are widely involved in biological processes covering cell development, cycle, oxidative stress, and inflammatory responses [19]. Among the processes, DNA methylation is the most intensively studied epigenetic modification, which relies on the catalytic action of DNA methyl transferases (DNMTs) [20]. Therefore, DNMTs are key factors in regulating the methylation levels of target genes. DNA methylation is mainly regulated by three DNMTs, DNMT1, DNMT3a, and DNMT3b [21]. DNMT1 is considered the key enzyme for maintaining normal DNA methylation due to its high affinity for hemimethylated DNA duplexes [22]. Vast evidence suggests that DNMT1 can regulate cell cycle and tumor suppressor gene expression, which is crucial in tumor metastasis and linked

to poor prognosis [23, 24]. Besides, studies have confirmed that DNMT1 is associated with other common diseases, such as type II diabetes [25], Alzheimer's disease [26], and periodontal disease [27]. Recent research also revealed that DNMT1 can mediate the polarization of M1 alveolar macrophages in ALI [28]. Lastly, our preliminary experiment also discovered that DNMT1, DNMT3A, and DNMT3B were memorably upregulated in OGD/R-induced HUVECs. However, the regulatory role between subtypes A and B is not clear.

In the present study, we established an *in vitro* and an *in vivo* I/R model to determine the effects of TFPI on LIRI. We discovered that TFPI was methylated under OGD/R condition in HUVECs. Besides, we further disclosed a protective role of TFPI in OGD/R HUVECs and I/R model mice. More importantly, we found that as a binding partner of TFPI, ZNF354C also could attenuate cell proliferation and migration of OGD/R-induced HUVECs via repressing the methylation of TFPI. These findings suggested that the ZNF354C/TFPI axis might be a potential therapeutic target for LIRI.

## 2. Methods

**2.1. Microarray Data Download and Processing.** We downloaded four different types of stem cells from geo database (<https://www.ncbi.nlm.nih.gov/geo/query/acc.cgi?acc=GSE127003>), including 46 pairs of expression data from peripheral human lung biopsies at the end of cold ischemia and after two hours of reperfusion following transplantation. We extracted the original data with R software package affyio, standardized the data with R software package oligo, and mapped the probe to the gene. When multiple probes are matched to a gene, take the median as the expression level of the gene, remove the multiple matched probes, and conduct single sample gene set enrichment analysis on each sample with R software package GSEA to obtain the enrichment fraction of each sample in different go biological processes. R software package pheatmap is used for heat map visualization.

**2.2. Cell Culture and Treatment.** HUVECs were purchased from ATCC (CRL-1730) and cultured in Dulbecco's modified Eagle's medium (DMEM; Gibco, Billings, MT, USA) supplemented with 10% fetal bovine serum (FBS, Gibco) in a humidified incubator with 5% CO<sub>2</sub> at 37°C. For OGD/R treatment, HUVECs were incubated with glucose-free media in a closed tank with 95% N<sub>2</sub> and 5% CO<sub>2</sub> (replace the gas in the closed tank with 95% N<sub>2</sub>-5% CO<sub>2</sub> (5 L/min flow rate for 15 min), so that the O<sub>2</sub> content in the closed tank is less than 1%) at 37°C for 4 h. Then, after replacing with conventional culture medium, cells were incubated in a 37°C, 5% CO<sub>2</sub>-95% O<sub>2</sub> incubator for 3 h [29]. Cells were then changed to complete media and cultured for 6, 12, 24, 48, or 72 h, respectively, to perform subsequent assays.

**2.3. Cell Transfection.** Control short-hairpin RNAs (shRNAs) (shCTRL), DNMT1 shRNAs (shDNMT1), or ZNF354C shRNAs (sh ZNF354C) were gained from GenePharm (Shanghai, China). The sequence of DNMT1 shRNA was 5'-UGUUAAGCUGUCUCUUCCAAdTdT-3'. The

sequence of ZNF354C shRNA was 5'-AAAUGUAUAAU ACAUUAUUGGGdTdT-3'. HUVECs were cultured in a 6-well plate ( $2 \times 10^5$  cells/well) and transfected with Lipofectamine 2000 based on the manufacturer's instruction. Vector control (OE-CTRL), ZNF354C overexpression plasmids, or DNMT overexpression plasmids were provided by HanBio Biotechnology (Shanghai, China). HUVECs were then transfected with 50  $\mu$ L lentivirus ( $10^7$  IU/mL), which were filtered with 6  $\mu$ g/mL polybrene. Then, cells were incubated for 48 h and collected for further study.

**2.4. Cell Counting Kit-8 (CCK-8).** HUVECs under OGD/R ( $1 \times 10^4$  cells/well) were seeded onto 96-well plate and transfected with the indicated plasmids. After 24, 48, and 72 h, 10  $\mu$ L of CCK-8 was added to HUVECs in each well. After 2 h, the absorbance of 450 nm was measured using by a microplate reader (Infinite M200, Tecan, Männedorf, Switzerland). Data are representatives of three independent experiments.

**2.5. EdU Staining.** The transfected HUVECs ( $2 \times 10^5$  cells/well) were seeded onto a 12-well plate. Then, the EdU solution (10  $\mu$ M) was added to the cells and incubated for 2 h. Cells were fixed by 4% paraformaldehyde for 15 min, disposed of glycine (50  $\mu$ L), and permeabilized by 0.5% Triton X-100 for 15 min. FITC-labeled EdU was added to cells and further incubated for 30 min. Diaminophenylindane (DAPI) was utilized to label the nuclear. Images were taken by using a fluorescence microscope (Olympus IX73, Olympus Corporation, Tokyo, Japan).

**2.6. Transwell Assay.** The processed HUVECs in 6-well plate were digested using trypsin and harvested. Then, HUVECs ( $1 \times 10^5$  cells) were supplemented into the upper chamber of the transwell plate, and a total of 500  $\mu$ L complete medium was positioned into the lower chamber. After 24 h, HUVECs were stained with crystal violet and images were taken by a light microscope (Olympus BX41; Olympus Optical Co. Ltd., Japan). Four images were taken for each condition.

**2.7. Wound Healing.** The processed HUVECs ( $1 \times 10^5$  cells/well) in 12-well plates were incubated and adhered to the wall at 37°C. Then, an artificial gap was generated on the cell monolayer by a 200  $\mu$ L tip, and pictures were taken. After 24 h, the cell movement was tracked via light microscopy. The distance of cell movement was calculated.

**2.8. RNA Extraction and Reverse Transcription Polymerase Chain Reaction (RT-qPCR).** Total RNA was extracted from the HUVECs or tissues by TRIzol reagent (Invitrogen, Carlsbad, CA, USA) according to the instruction of manufacturer. The first-strand cDNA was synthesized using a Bestar qPCR RT kit (DBI® Bioscience, Ludwigshafen, Germany). TFPI and ZNF354C were amplified by SYBR-Green PCR Master Mix (Applied Biosystems, Weiterstadt, Germany). The PCR procedure was 95°C for 2 min, followed by 95°C for 20 sec and 65°C for 1 min, total of 40 cycles. The primer sequences were as follows: GAPDH-F: 5' TGTTTCGTCATG GGTGTGAAC 3' and GAPDH-R: 5' ATGGCATGGAC

TGTGGTCAT 3', TFPI-F: 5' AGTTGCCACCACTGAA ACT 3' and TFPI-R: 5' TCGCACTGTGAGTGAAAAT 3', ZNF354C-F: 5' AAGTCCCTTCAGATACCCGT 3' and ZNF354C-R: 5' TGTCCCAGTGACCATCCTTA 3'. GAPDH was used as a negative control. The relative expression was calculated via the  $2^{-\Delta\Delta Ct}$  method.

**2.9. Western Blot.** The processed HUVECs or lung tissues were lysed by radioimmunoprecipitation assay (RIPA; Sigma-Aldrich, St. Louis, MO, USA) buffer containing protease inhibitor. The protein concentration was determined by a bicinchoninic acid (BCA) protein assay kit. A total of 30-40  $\mu$ g protein was separated using 12% SDS-PAGE and transferred to polyvinylidene fluoride (PVDF; Beyotime, Shanghai, China) membrane. After blocking with 5% nonfat milk at room temperature for 1 h, membranes were incubated with the first antibodies (anti-TFPI antibody, anti-ZNF354C antibody, anti-GAPDH antibody, and anti-DNMT1 antibody) at 4°C overnight. The next day, membranes were washed with 1XTBST for three times and incubated with secondary antibodies for 1 h at room temperature. The results were visualized using ECL and the quantified by ImageJ software (ImageJ 1.32 J, National Institutes of Health, Bethesda, MD, USA).

**2.10. Immunofluorescence.** Following a previous study [30], the processed HUVECs were seeded onto polylysine-coated slides in 24-well plate. After 48 h, cells were fixed with 4% paraformaldehyde and permeabilized by 0.1% Triton X100. Cells were then blocked with 1% bovine serum albumin (BSA) in 1X phosphate-buffered saline (PBS) at room temperature for 30 min followed by incubating with TFPI antibody at 4°C overnight. The next day, cells were washed with PBS for three times and incubated with a secondary antibody for 1 h at room temperature. The nuclear was stained by DAPI. The images were taken with a fluorescence microscope.

**2.11. Methylation-Specific Polymerase Chain Reaction (MS-PCR).** A standard phenol-chloroform protocol was used to extract the genomic DNA from the cultured cells. DNA was treated with sodium bisulfite using an EpiTect Bisulfite kit (Qiagen, Hilden, Germany), and PCR amplification was performed. The PCR reaction condition was as follows: pre-denatured at 95°C for 10 min, followed by 35 cycles of 95°C for 30 s, 56°C for 30 s, and 72°C for 30 s, and with a final extension at 72°C for 5 min. The primer sequences used for methylation analysis of TFPI were 5' ATAATGGGCGG TTAGGTAGAGAC 3' and 5' CCTAAAATACCGAAAT TACAAACGA 3'. The primer sequence set used for unmethylation analysis of TFPI was 5' TAATGGGTGGT TAGGTAGAGATGA 3' and 5' CTAATAACCAAAATT ACAAAACAAA 3'. The PCR products were separated by electrophoresis on the 2% agarose gel.

**2.12. Chromatin Immunoprecipitation (ChIP) Assay.** By referring to a previous study [31], HUVECs were cross-linked by adding formaldehyde at a final concentration of

1% and incubated at room temperature for 10 min. A final concentration of 125 mM glycine was added to cells to stop the cross-linking. Cells were then washed with ice-cold PBS and scraped off in a solution of PBS plus protease inhibitors and centrifuged at 1000 rpm for 4 min. Cell pellets were resuspended in lysis buffer and incubated for 10 min on ice. Nuclei were collected by centrifugation and resuspended in nuclear lysis buffer and sonicated to an average length of 300-600 bp. The supernatant was divided into two fractions: one was for control and the second was incubated with 5  $\mu$ g antibody at 4°C overnight with rotation. The next day, the immune complex was washed consecutively for 5 min with low-salt wash buffer, high-salt wash buffer, and LiCl wash buffer, respectively. Elution was reverse cross-linked by adding 0.3 M NaCl and incubated at 65°C for 1.5 h. DNA was collected and purified by QiaQuick spin columns, and 2  $\mu$ L of DNA was used for PCR reactions. The PCR primers were TFPI-1F: 5' CCATTGAGCACTGAGTGAACC 3' and TFPI-1R: 5' CCTCCCTGCCTGATTCTCC 3', TFPI-2F: 5' CAGGGCATGAGGTAATAGGA 3' and TFPI-2R: 5' ATTTGGTGGTGACTGGAACA 3', TFPI-3F: 5' AAGCAT TCTTTTCAACTGATTACA 3' and TFPI-3R: 5' AGAT CACTGGCAGTTGGGAAT 3', RNA polymerase II-F: 5' ATGCTGGGTCTGCCTTAA 3' and RNA polymerase II-R: 5' ATGCCTCAGTTCCTTTGTTCC 3'.

**2.13. Luciferase Assay.** By referring to the relevant literature [32], HUVECs ( $0.8 \times 10^4$  cells/well) were seeded onto a 24-well plate and transfected with TFPI wild-type (WT) or mutant plasmid (0.8  $\mu$ g/well) by Lipofectamine 2000. After 48 h of transfection, cells were washed twice with PBS and lysed by passive lysis buffer. Cell lysates were collected, and a 100  $\mu$ L LARII working solution was added and mixed. A total of 100  $\mu$ L Stop & Glo reagent was added and mixed, before the absorption was measured at 560 nm.

**2.14. Electrophoretic Mobility Shift Assay (EMSA).** According to a previous reports [33], nuclear DNA was extracted by nuclear and cytoplasmic protein extraction kit (Beyotime, P0028). The reaction mixture contained nuclear protein, antibody, and either the probe or mutant probe and antibody. And the sequence of probe was 5'-CTGTTTCCTTC ATCTGTTTCCTCCACTAAAAAAG-3'. After incubation for 20 min on ice, biotin labeled probe was added to the mixture and incubated for 10 min at room temperature. Non-denaturing TBE-polyacrylamide gel was used to resolve protein-DNA complexes from free DNA. After electrophoresis, the polyacrylamide gel was transferred PVDF membrane and cross-linked by ultraviolet exposure (254 nm, 20 min). The membrane was blocked and washed, and the results were determined by chemiluminescence detection.

**2.15. Enzyme-Linked Immunosorbent Assay (ELISA).** Based on a previous study [34], HUVECs were lysed by RIPA buffer containing proteinase inhibitor on ice for 30 min to 2 h. The cell lysis or serum from mice was centrifuged at 12000 rpm for 10 min at 4°C. The MDA and TFPI content in the supernatant were determined by ELISA kit according

to the manufacturer's instruction. The concentrations of MDA, nitric oxide synthase (NOS), and TFPI in bronchoalveolar lavage fluid (BALF) were quantified using ELISA kits (Elabscience Biotechnology, Wuhan, China) following the manufacturer's instructions. The absorption at OD<sub>450</sub> was measured using a microplate reader.

**2.16. ROS Detection.** Following previous research [35], the level of reactive oxygen species (ROS) was analyzed using a DCFDA/H2DCFDA-Cellular ROS Assay (ab113851; Abcam, Cambridge, UK) according to the manufacturer's instruction.

**2.17. Ischemia/Reperfusion Animal Model.** As described in a previous study [36], total of 120 (6-8 weeks, male) mice were randomly divided into eight groups (five mice/group): control, I/R, I/R plus 5-Aza, I/R plus control lentivirus, I/R plus ZNF354C lentivirus, I/R plus control shRNA, I/R plus ZNF354C silencing, and I/R plus ZNF354C silencing and 5-Aza. For the I/R model, the mice were anesthetized by intraperitoneal injection of 50 mg/kg bodyweight pentobarbital sodium. After tracheotomy, mice were mechanically ventilated by tracheal intubation with a tidal volume of 0.6 ml, a ventilation rate of 120 breaths/min, an inspiration-to-expiration ratio of 1:2, and an inhalation oxygen concentration of 100%. The left chest was debrided, local skin was disinfected, and the 4th and 5th intercostal spaces were bluntly separated to fully expose the left hilum. The mice were injected with 5 U/g bodyweight heparin into the tail vein, and the left hilum was blocked with a vascular clamp at the end of expiration after 5 min, so that the left lung was ischemic for 90 min (the ischemic period). Then, the vascular clamp was removed, and the left lung was reperused for 120 min (the reperfusion period). For 5-Aza treatment, 5-Aza was injected through the tail vein at a concentration of 1 mg/kg bodyweight. For lentivirus treatment, a total of 200  $\mu$ L virus ( $10^8$  pfu/mL) was injected through the tail vein. The mice were sacrificed 3 days after infection, and the left lung tissues were collected.

**2.18. Lung Wet-To-Dry Ratio.** After sacrifice, the wet left lung tissue was weighed, incubated at 60°C for 96 h, and weighed as dry weight [37]. These values were used to calculate the wet-to-dry ratios.

**2.19. Evans Blue Staining.** Evans Blue (1%, 2 mg/kg bodyweight, Sigma-Aldrich) was injected via the tail vein 2 h before sacrifice [38]. Then, the left lung tissue was weighed, homogenized, treated with formamide (100 mg/ml; Sigma-Aldrich, Shanghai, China), incubated at 37°C for 24 h, and centrifuged for 20 min at 10,000 g. The absorbance of the supernatant was measured at 620 nm, and the concentration of Evans Blue was calculated from the absorbance according to a standard curve.

**2.20. FITC Dextran Assay.** FITC dextran (1%, 200  $\mu$ L) was injected via the tail vein 2 h before sacrifice. The left lung tissue was weighed and homogenized. The fluorescence intensity was measured by the fluorescent microplate reader at an excitation of 485 nm and an emission of 538 nm. The FITC-conjugated dextran concentration was calculated with a standard curve.

**2.21. Immunohistochemistry (IHC).** Lung tissue specimens were embedded in paraffin and sliced 4  $\mu\text{m}$  thick. The sections were dewaxed, rehydrated, immersed in 0.01 M citrate buffer (pH 6.0), and boiled in a pressure cooker for 15 min. The sections were blocked with 3% hydrogen peroxide for 10 min and then incubated overnight at 4°C with rabbit monoclonal antibody against TFPI (1:100). The sections were exposed to secondary antibody for 1 h at room temperature. The nuclear was stained by hematoxylin.

**2.22. Haematoxylin and Eosin (H&E) Staining.** Lung tissue specimens were embedded, sliced, dewaxed, and rehydrated for the IHC assay. Slides were stained with hematoxylin solution for 10 sec and washed with tap water for 10 min. The sections were immersed in eosin staining solution for 30 sec and washed with tap water for 10 min. The sections were dehydrated in ascending alcohol concentrations and cleared with xylene.

**2.23. Statistical Analysis.** All data were analyzed using GraphPad Prism v9.0. The data were presented as the mean  $\pm$  standard deviation (SD). One- or two-way ANOVAs followed by Tukey's post hoc test were used to compare the results from multiple groups.  $P < 0.05$  was considered statistically significantly different.

### 3. Results

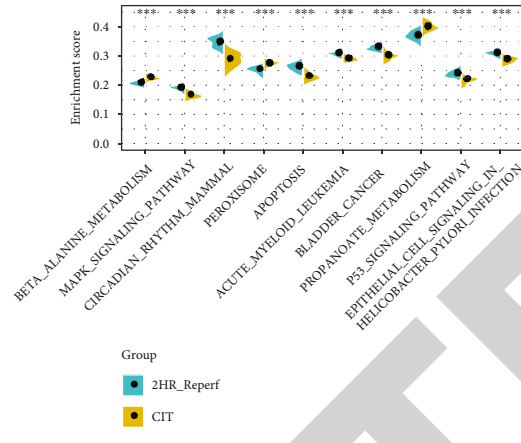
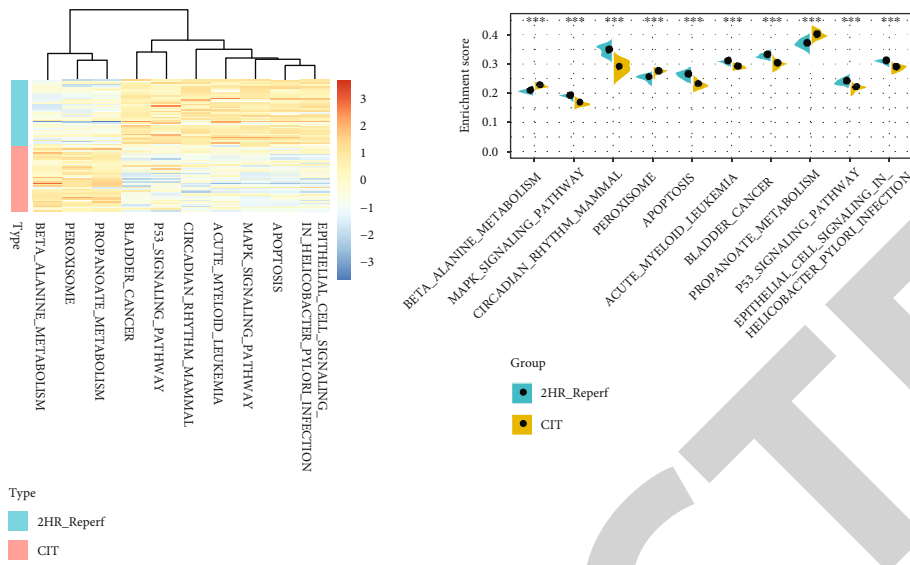
**3.1. TFPI Oxidative Stress.** According to the 46 pair expression data from peripheral human lung biopsies at the end of cold ischemia and after two hours of reperfusion following transplantation, we found 19284 different genes. Compared with the differences of KEGG pathway between the two samples, the top 10 KEGG pathways with the most significant differences were observed, which mainly includes beta alanine metabolism, MAPK signaling pathway, circadian rhythm mammal, and peroxisome (Figure 1(a)). It was worth mentioning that peroxisome, beta alanine metabolism, and propanoate metabolism were significantly activated in end of cold ischemia samples, whereas p53, MAPK signaling pathway, and other pathways were significantly blocked (Figure 1(b)). In addition, lower activity of oxidative stress-related biological processes was observed in the end of cold ischemia samples (Figure 1(c)) and twelve of the 14 oxidative stress-related biological processes were significantly lower in the end of cold ischemia samples (Figure 1(d)). Furthermore, a tissue factor pathway inhibitor (TFPI) was found involved in response to oxidative stress. The role of TFPI in oxidative stress was further analyzed as follows.

**3.2. Impacts of OGD/R on Cell Viability, Migration, DNMT, ROS, and TFPI in HUVECs.** To confirm the possible mechanism and therapeutic method in LIRI, we first established the OGD/R cell model in HUVECs. CCK-8 signified that cell proliferation of HUVECs was notably reduced after 6 h of OGD/R and recovered with extended reoxygenation (Figure 2(a)). The EdU staining results also denoted that OGD/R diminished the proliferation of HUVECs, and with increasing reoxygenation time, cell proliferation was gradually increased (Figures 2(b) and 2(c)). Meanwhile, the trans-

well experiment showed lower cell migration in OGD/R-mediated HUVECs versus that in the control HUVECs, while cell migration was gradually increased with reperfusion time (Figures 2(d) and 2(e)). TFPI is mainly produced by endothelial cells and megakaryocytes [39, 40]. In this regard, we further found that ZNF354C was the predicted transcriptional factor of TFPI. It is known that ZNF354C is a transcriptional factor that can bind short DNA consensus motif [41, 42]. Next, we further investigated the expressions of key genes (TFPI and ZNF354C) in OGD/R treated HUVECs. The results showed that the expression and concentration of TFPI were memorably suppressed by OGD/R and then recovered with the extension time of reoxygenation (Figures 2(f)–2(i)). We also discovered that OGD/R (6 h of reperfusion) could downregulate ZNF354C in HUVECs, which then could be reversed as the reperfusion time increases (Figures 2(f) and 2(i)). Besides, western blot displayed that DNA methyltransferase enzymes (DNMT1, DNMT3a, and DNMT3b) were memorably induced by OGD/R in HUVECs; then, the expressions of these proteins were gradually decreased with the increase of reperfusion time (Figure 2(i)). Likewise, we discovered that the level of ROS was also observably elevated in OGD/R-induced HUVECs; then, ROS level gradually decreased with the increase of reperfusion time (Figures 2(j) and 2(k)). Together, our data revealed that OGD/R could reduce cell viability and migration and increase ROS, which might be relevant to the functions of ZNF354C, TFPI, and DNMTs in HUVECs.

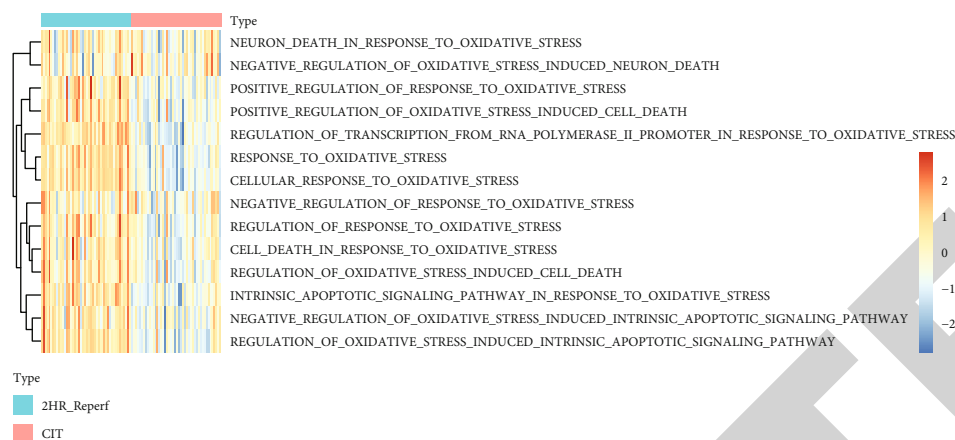
**3.3. OGD/R Induced Hypermethylation of TFPI in HUVECs, and TFPI Could Interact with ZNF354C.** Subsequently, we verified the regulatory relationship between DNA methylation, TFPI and ZNF354C. First, we discovered that OGD/R (6 h of reperfusion) could cause the hypermethylation of TFPI promoter in HUVECs, while the elevation of TFPI promoter methylation could be gradually decreased as the reperfusion time increases (Figures 3(a) and 3(b)). Second, we predicated the binding sites between TFPI and ZNF354C (Figure 3(c)). And the luciferase results indicated that ZNF354C overexpression raised the luciferase activity of the WT-TFPI promoter, while the luciferase activity of the Mut-TFPI promoter was not affected by ZNF354C overexpression in HUVECs (Figure 3(d)). The EMSA results showed that ZNF354C is bound directly to the promoter of TFPI (Figure 3(e)). The CHIP results signified that the level of TFPI promoter was notably lessened in the OGD/R (6 h of reperfusion) group versus that in the control group, which were also prominently restored in HUVECs with the extended perfusion time (Figure 3(f)). Similarly, CHIP results revealed that the association of RNA pol-II with TFPI was most abundant after 6 h of OGD/R in HUVECs (Figure 3(g)). In short, these data uncovered that TFPI was hypermethylated and could interact with ZNF354C in OGD/R-induced HUVECs.

**3.4. ZNF354C Overexpression Induced Proliferation and Migration and Reduced ROS Level through Upregulating TFPI in OGD/R-Induced HUVECs.** Next, we verified the



(c)

FIGURE 1: Continued.



(d)

FIGURE 1: Bioinformatic analysis of gene expression in peripheral human lung biopsies at the end of cold ischemia and after two hours of reperfusion following transplantation. (a) The top 10 KEGG pathways with the most significant differences were observed. (b) Peroxisome, beta alanine metabolism, and propanoate metabolism were significantly activated in the end of cold ischemia samples, whereas p53, MAPK signaling pathway, and pathways were significantly blocked. (c) Lower activity of oxidative stress-related biological processes was observed in the end of cold ischemia samples. (d) Twelve of the 14 oxidative stress-related biological processes were significantly lower in the end of cold ischemia samples.

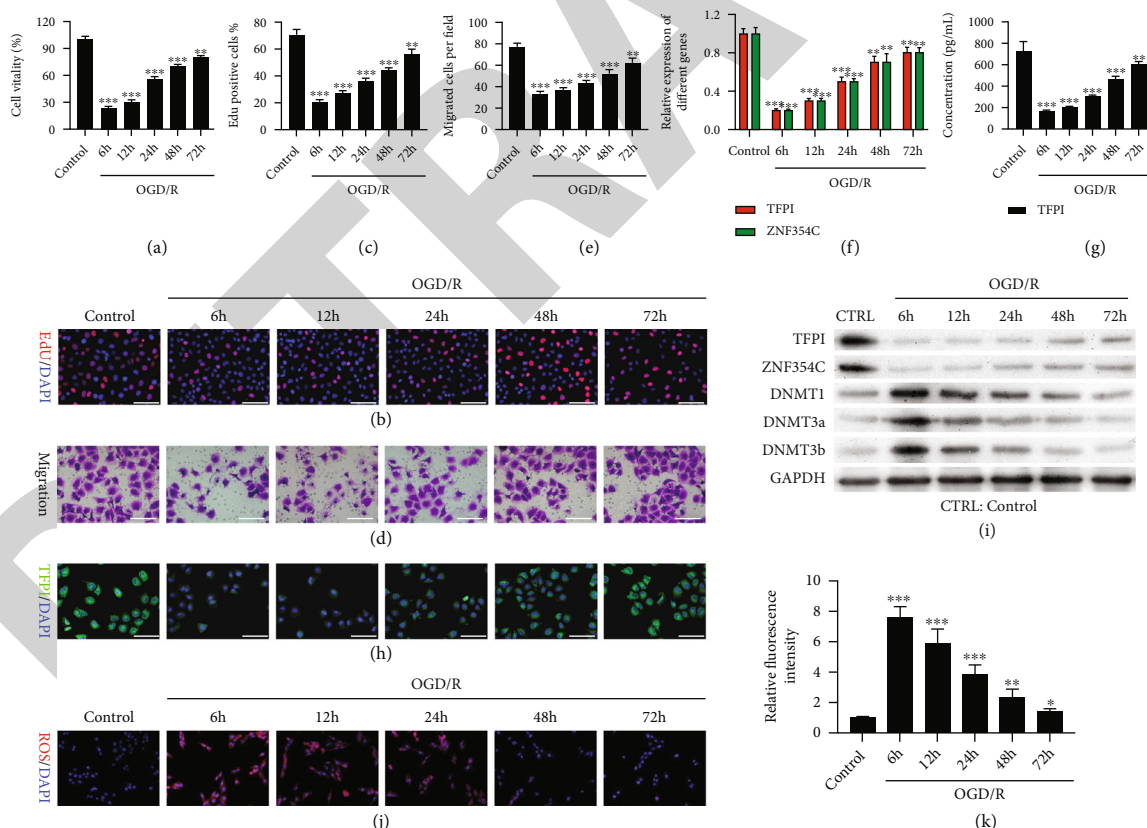


FIGURE 2: The impact of OGD/R on cell viability, migration, DNA methyltransferase, and TFPI in HUVECs. HUVECs were exposed to OGD for 4h and reoxygenated for 6, 12, 24, 48, and 72 h. (a) Cell viability was tested by CCK-8. (b, c) HUVECs were subjected to EdU staining, and EdU-positive cells were calculated in each group. (d, e) Migrated cells were confirmed via Transwell, and five fields were summarized and counted. TFPI level was monitored with (f) RT-qPCR, (g) ELISA, and (h) IF in HUVECs after OGD/R. (i) Western blotting analysis of TFPI, ZNF354C, DNMT1, DNMT3a, and DNMT3b levels. (j) ROS level was tested using DCFDA/H2DCFDA-Cellular ROS Assay in each group. (k) Quantitative analysis of ROS relative fluorescence intensity. The experiments were repeated three times independently.

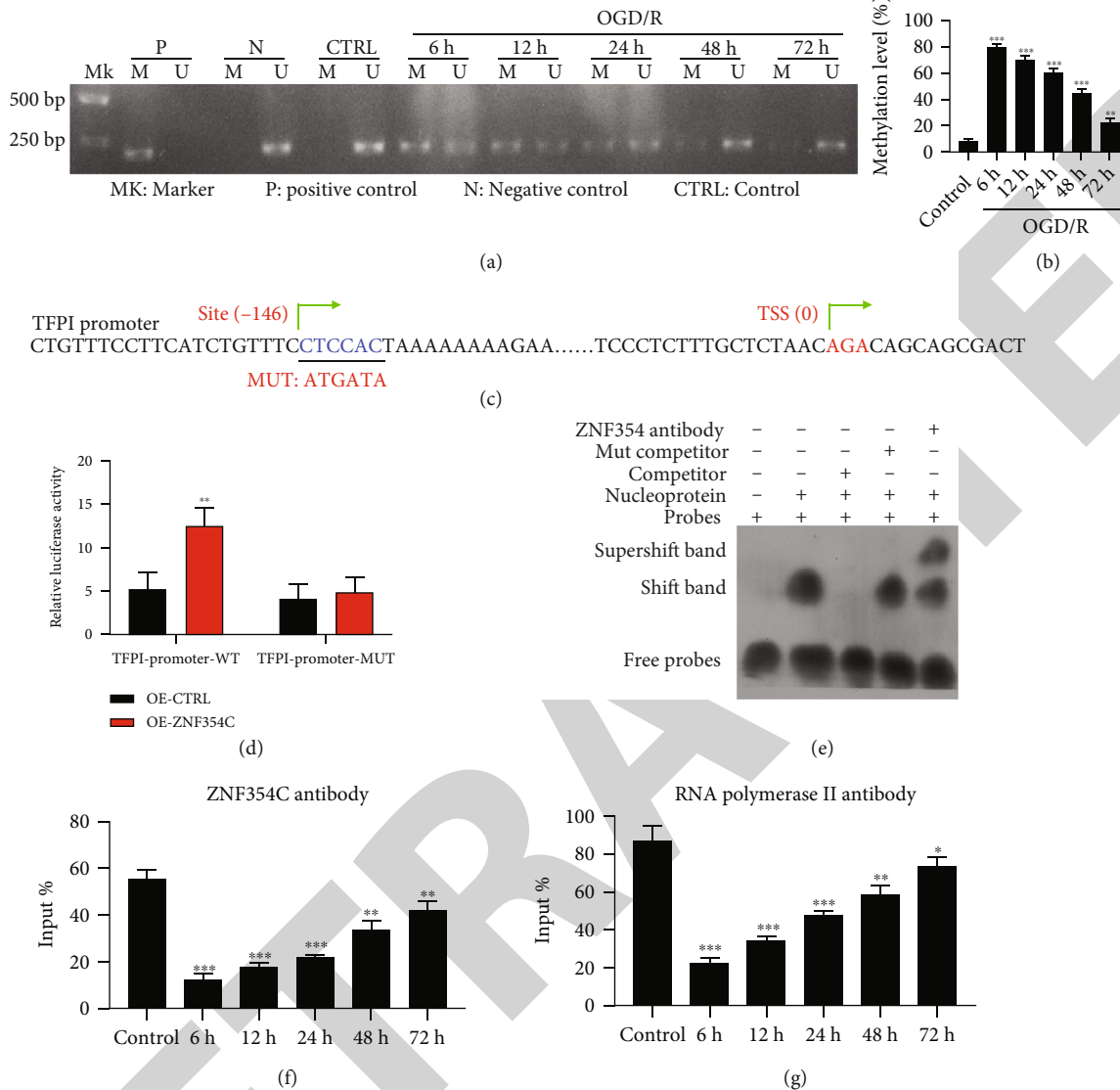
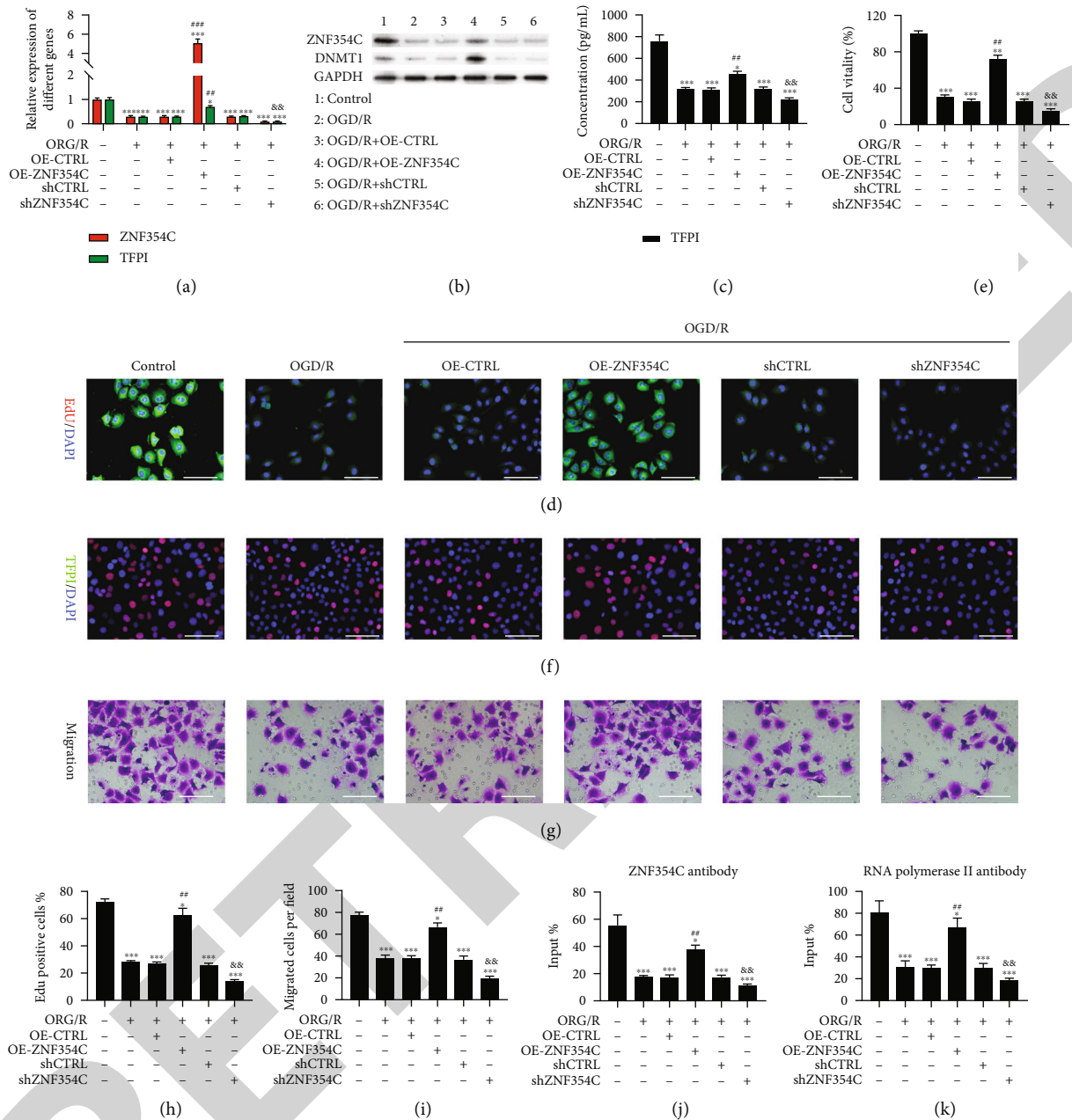


FIGURE 3: OGD/R induced hypermethylation of TFPI in HUVECs, and TFPI could interact with ZNF354C. (a) Methylation level of TFPI promoter was tested with MSP in OGD/R-treated HUVECs. (b) The methylation level was quantified based on MSP results. (c) The predicated binding sites between TFPI and ZNF354C. (d) Luciferase activity of TFPI promoter in ZNF354C-overexpressed HUVECs was determined by applying dual luciferase reporter gene. (e) EMSA was utilized to test the binding of TFPI promoter and ZNF354C. (f) The interaction between ZNF354C antibody and TFPI promoter was confirmed with ChIP in HUVECs under OGD/R. (g) HUVECs were incubated with Poly II antibody and beads, and the binding of RNA polymerase II on TFPI 5'UTR was examined using ChIP in HUVECs under OGD/R. The experiments were repeated three times independently.

underlying roles of ZNF354C and TFPI in the proliferation and migration of OGD/R-induced HUVECs. We first overexpressed and silenced ZNF354C in OGD/R-mediated HUVECs. The results showed that ZNF354C overexpression dramatically reversed the reduction of ZNF354C and TFPI expressions, whereas ZNF354C silencing prominently enhanced the down-regulation of ZNF354C and TFPI expressions in OGD/R-mediated HUVECs (Figures 4(a) and 4(b)). Likewise, the results of ELISA and IF staining denoted that ZNF354C overexpression markedly upregulated TFPI and ZNF354C silencing prominently downregulated TFPI in OGD/R-treated HUVECs (Figures 4(c) and 4(d)). Besides, ZNF354C overexpression dramatically increased cell proliferation, which was inhibited by OGD/R in HUVECs; conversely, suppression of ZNF354C

alleviated the reduction of cell proliferation caused by OGD/R in HUVECs (Figures 4(e), 4(f), and 4(h)). In addition, ZNF354C overexpression also observably reversed the cell migration, which was decreased by OGD/R, whereas ZNF354C silencing markedly promoted the reduction of cell migration caused by OGD/R (Figures 4(g) and 4(i)). The ZNF354C overexpression also markedly reduced the ROS level, which was increased by OGD/R, while ZNF354C silencing memorably promoted the ROS level caused by OGD/R (Figure S1A). Moreover, ChIP data revealed that the binding of ZNF354C to the TFPI promoter was memorably decreased by OGD/R treatment, which could also be recovered by ZNF354C overexpression or further reduced by ZNF354C silencing in HUVECs (Figure 4(j)). The binding of RNA pol II to UTR of



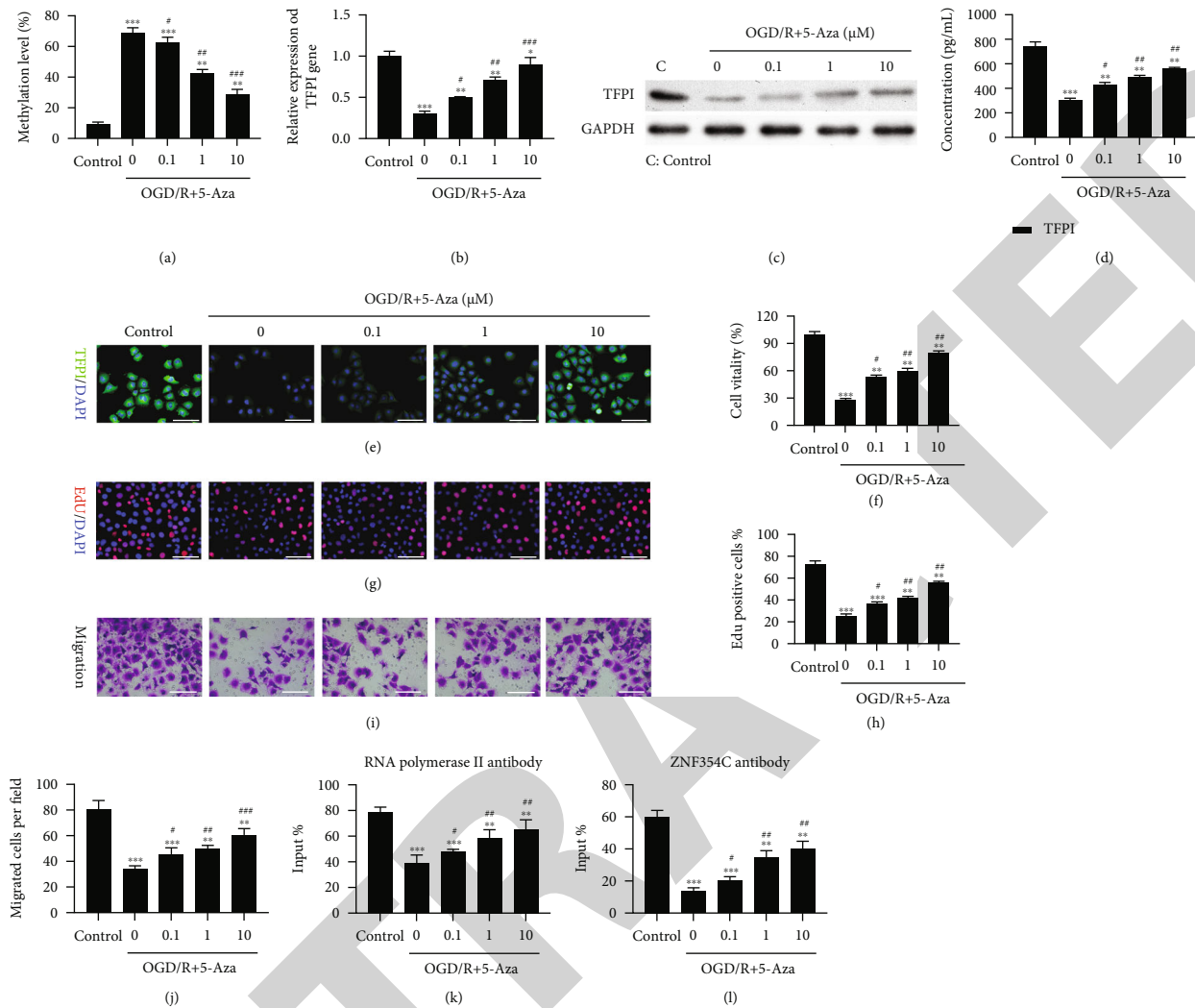
**FIGURE 4:** ZNF354C overexpression induced proliferation and migration through upregulating TFPI in OGD/R-induced HUVECs. OGD/R-treated HUVECs were transfected with ZNF354C overexpression plasmids or shZNF354C, respectively. ZNF354C and TFPI expressions were assessed via (a) RT-qPCR and (b) western blot. (c) TFPI level was analyzed with ELISA kit. (d) IF staining of TFPI in the processed HUVECs. (e) Cell viability was evaluated by CCK-8. (f) HUVECs in each group were subjected to EdU staining. (g) The images of cell migration were obtained using Transwell. (h) EdU-positive cells were quantitated in line with EdU staining results. (i) Quantitative analysis of migratory cells. (j) The binding of ZNF354C and TFPI promoter was confirmed through ChIP in each group. (k) The binding of RNA polymerase II on TFPI 5'UTR was examined via ChIP. The experiments were repeated three times independently.

TFPI was also prominently increased by ZNF3544 overexpression and decreased by ZNF354C silencing in HUVECs (Figure 4(k)). Overall, these findings certified that ZNF354C could enhance the proliferation and migration and decrease the ROS level of OGD/R-induced HUVECs by upregulating TFPI.

**3.5. 5-Aza Decreased TFPI Methylation, Increased TFPI Expression, Accelerated Proliferation and Migration, Attenuated**

*ROS Level, and Enhanced the Combination of TFPI and ZNF354C in OGD/R-Treated HUVECs.* To further confirm whether the methylation of TFPI is involved in the regulation of cell proliferation and migration in HEVCs under OGD/R, we treated HUVECs with 5-Aza, an inhibitor of DNA methylation [43]. The MSP results indicated that elevated methylation level of the TFPI promoter could be notably attenuated by 5-Aza, especially high concentrations of 5-Aza, in OGD/R treated HUVECs (Figure 5(a)). Furthermore, the OGD/R-





**FIGURE 5:** 5-Aza decreased TFPI methylation, increased TFPI expression, accelerated proliferation and migration, and enhanced the combination of TFPI and ZNF354C in OGD/R-treated HUVECs. OGD/R-mediated HUVECs were treated with 5-Aza (low: 0.1  $\mu\text{M}$ , mid: 1  $\mu\text{M}$ , high: 10  $\mu\text{M}$ ) for 24 h. (a) MSP was utilized to identify the methylation level of TFPI promoter. TFPI level was certified by applying (b) RT-qPCR, (c) western blot, (d) ELISA, and (e) IF staining in the processed HUVECs. Cell proliferation was determined with (f) CCK-8 and (g) EdU staining. (i) Migration in HUVECs was tested with Transwell. (h) EdU-positive cells and (j) migrated cells were counted. (k) The impact of 5-Aza on the binding of ZNF354C and TFPI promoter was confirmed by ChIP. (l) ChIP was adopted to analyze the effect of 5-Aza on the binding of RNA polymerase II on TFPI 5'UTR. The experiments were repeated three times independently.

mediated decrease of TFPI expression could also be reversed by 5-Aza, especially high concentrations of 5-Aza, in HUVECs (Figures 5(b)–5(e)). In addition, we found that 5-Aza could also memorably recover the OGD/R-mediated reduction of cell proliferation and migration in HUVECs in a dose-dependent manner (Figures 5(f)–5(j)). Meanwhile, we also revealed that 5-Aza also could notably reverse the elevation of ROS level, which were caused by OGD/R in HUVECs with a dose dependent manner (Figure S1B). Moreover, ChIP results confirmed that OGD/R lowered the binding of the TFPI promoter and ZNF354C antibody in HUVECs, which could be recovered by 5-Aza (Figure 5(k)). The binding of ZNF354C and RNA polymerase II with the promoter of TFPI could be decreased by OGD/R, yet could be partially reversed by 5-Aza in HUVECs (Figure 5(l)). Thus, the results

disclosed that 5-Aza could aggrandize the proliferation and migration of OGD/R-treated HUVECs by reducing TFPI methylation to increase TFPI expression.

**3.6. DNMT1 Suppressed Proliferation and Migration, Increased ROS Levels, and Reduced the Interaction of TFPI and ZNF354C in OGD/R-Induced HUVECs.** Next, we investigated the involvement of DNA methyltransferase (DNMT1) in cell proliferation and migration of OGD/R-induced HUVECs. The MSP results first displayed that the OGD/R-mediated increased methylation of the TFPI promoter could be further potentiated by DNMT1 overexpression, or reversed by DNMT1 silencing in HUVECs (Figure 6(a)). We also verified that the expression and concentration of TFPI were further decreased by DNMT1

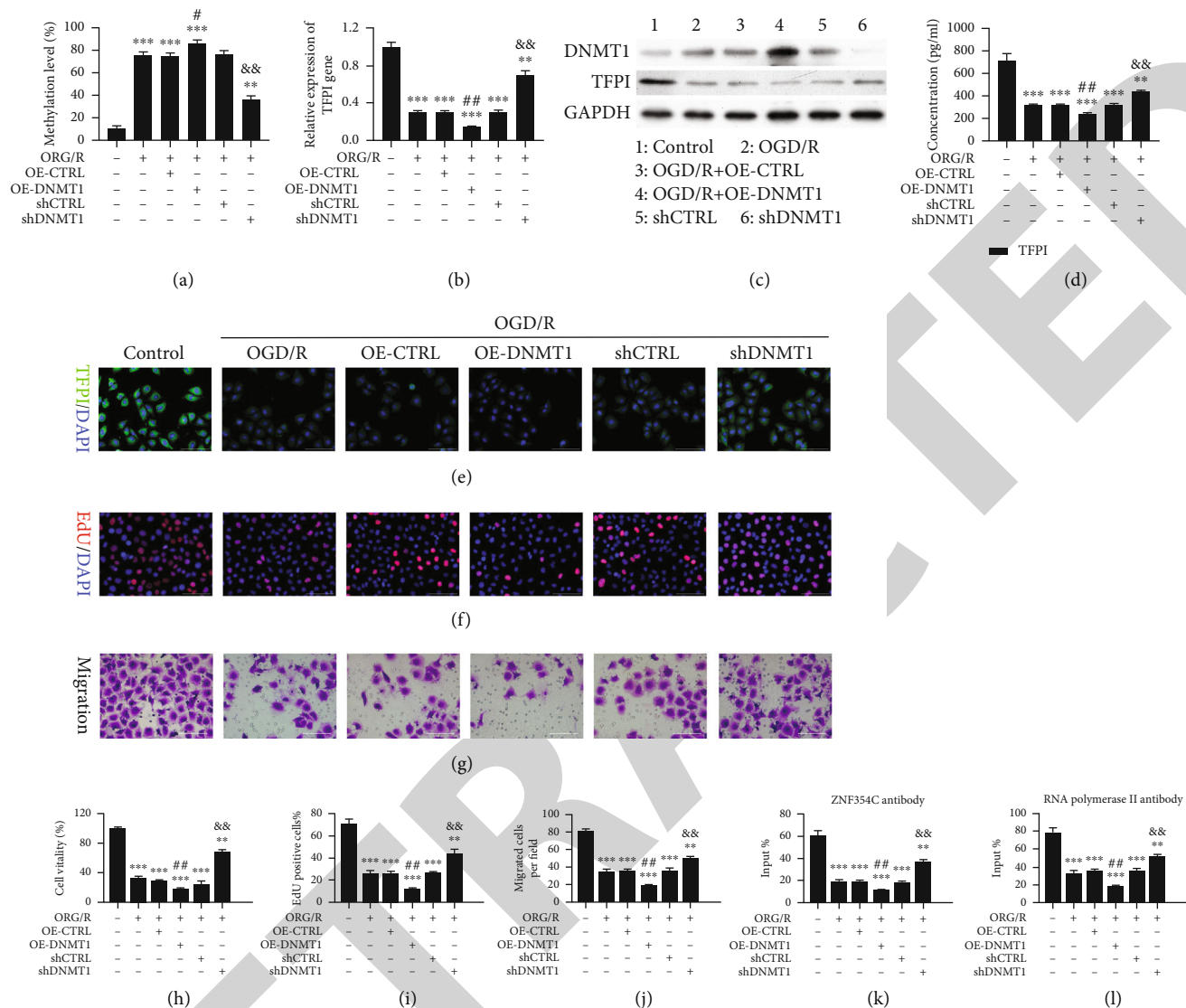


FIGURE 6: DNMT1 suppressed proliferation and migration and reduced the interaction of TFPI and ZNF354C in OGD/R-induced HUVECs. HUVECs under OGD/R were transfected with DNMT1 overexpression plasmids or shDNMT1, respectively. (a) MSP displayed the change in the methylation level of TFPI promoter. The level of TFPI was tested through (b) RT-qPCR and (c) western blot, (d) ELISA, and (e) IF staining. (f) EdU staining was utilized to confirm the change of proliferation. (g) Transwell exhibited the change of cell migration. (h) CCK-8 presented the change in cell viability. (i) Based on the EdU staining data, EdU-positive cells were quantitated. (j) Migratory cells were quantitated in line with Transwell data. (k) ChIP demonstrated the impact of DNMT1 on the binding of ZNF354C and TFPI promoter. (l) ChIP showed the influence of DNMT1 on the binding of RNA polymerase II on TFPI 5'UTR. The experiments were repeated three times independently.

overexpression and increased by DNMT1 silencing in OGD/R-mediated HUVECs (Figures 6(b)–6(e)). Overexpression and silencing of DNMT1 were also verified in western blotting results (Figure 6(c)). As exhibited by CCK-8 and EdU assays, overexpression of DNMT1 observably promoted the OGD/R-mediated inhibitory effects on cell proliferation, and knockdown of DNMT1 by shRNAs partly reversed the OGD/R-mediated inhibitory effects of OGD/R on cell proliferation in HUVECs (Figures 6(f), 6(h), and 6(i)). The results also signified that DNMT1 overexpression memorably enhanced the OGD/R-mediated inductive effects on ROS level, whereas DNMT1 knockdown notably weakened these

effects on the ROS levels in HUVECs (Figure S1C). Meanwhile, OGD/R caused defects of cell migration that could be recovered by DNMT1 silencing, or contrastingly elevated by DNMT1 overexpression in HUVECs (Figures 6(g) and 6(j)). Furthermore, ChIP results uncovered that the binding of the ZNF354C antibody to the TFPI promoter could be markedly depressed by DNMT1 overexpression and heightened by DNMT1 knockdown in OGD/R-induced HUVECs (Figure 6(k)). The binding of ZNF354C and RNA polymerase II to the TFPI promoter was also weakened by DNMT1 overexpression and prominently facilitated by DNMT1 knockdown in OGD/R-induced

HUVECs (Figure 6(l)). These results further indicated suppression of DNMT1 could partly reverse the OGD/R-mediated reduction in proliferation and migration of HUVECs.

**3.7. Silencing of DNMT1 Accelerated Proliferation and Migration and Suppressed ROS Levels by Regulating ZNF354C to Target the TFPI Promoter in OGD/R-Induced HUVECs.** Meanwhile, we tested whether the influences of DNMT1 on the progress of OGD/R-induced HUVECs are mediated by ZNF354C. Our results disclosed that TFPI could be memorably upregulated by DNMT1 silencing, while this upregulation in TFPI expression was blunted by ZNF354C silencing in OGD/R-induced HUVECs (Figures 7(a)–7(d)). We next discovered that cell proliferation and migration could be notably strengthened by DNMT1 silencing, while this enhancement could also be memorably reduced by ZNF354C silencing in OGD/R-induced HUVECs (Figures 7(e)–7(i)). Meanwhile, the results showed that the level of ROS could be lowered by DNMT1 silencing, while this reduction could be dramatically reversed by ZNF354C silencing in OGD/R-induced HUVECs (Figure S1D). Generally, our data verified that DNMT1 silencing could induce proliferation and migration of OGD/R-induced HUVECs through ZNF354C.

**3.8. ZNF354C Alleviated LIRI by Suppressing DNA Methylation In Vivo.** Furthermore, we also demonstrated the influence and mechanism of ZNF354C in a LIRI mouse model. The LIRI mouse model was constructed through ischemia for 90 min and reperfusion for 120 min. Afterwards, the mice were injected with ZNF354C overexpression plasmids, shZNF354C lentivirus, and 5-Aza. As displayed in Figure 7(a), the dry-to-wet ratio of lung tissues was notably enhanced in the I/R mice relative to that in sham mice, and the dry and wet ratio was also signally reduced by 5-Aza or ZNF354C overexpression in I/R mice, while ZNF354C silencing cancelled the protective effects of 5-Aza on lung injury (Figure 8(a)). Meanwhile, we adopted Evans Blue to assess the degree of cerebral thrombosis. And as verified in Figure 7(b), the content of Evans Blue was dramatically strengthened in the I/R group versus that in the sham group, and 5-Aza or ZNF354C overexpression could prominently reduce the content of Evans Blue in I/R mice, and ZNF354C silencing also could weaken the reduction of Evans Blue mediated by 5-Aza in I/R mice (Figure 8(b)). Evans Blue dye and FITC-Dextran which all could be adopted to evaluate the permeability of pulmonary microvasculature. We found that the changing trend of fluorescence intensity of FITC-Dextran was similar to that of Evans Blue in each group of mice (Figure 8(c)). H&E staining results revealed that in the control group, the pulmonary alveoli and interstitium were intact, and the alveolar septum showed uniform thickness without signs of alveolar wall thickening or inflammatory cell infiltration; in the I/R group, lung tissue was severely hyperemic and bleeding, with inflammatory cells; and degree of lung injury in 5-Aza or ZNF354C overexpression groups was lower than that of I/R group; inhibition of ZNF354C also aggravated I/R induced-lung injury mediated by 5-Aza (Figures 8(d) and

8(e)). Moreover, we proved that TFPI expression was markedly lowered in the I/R group versus that in the sham group, and 5-Aza or ZNF354C overexpression could prominently elevate TFPI level in I/R mice, while the elevation of TFPI expression mediated by 5-Aza also could be remarkably attenuated by ZNF354C silencing in the lung tissues of I/R mice (Figures 8(f), 8(g), 8(i), and S2). Similarly, ELISA data also signified that 5-Aza or ZNF354C overexpression prominently upregulated TFPI, and the upregulation of TFPI mediated by 5-Aza also could be reduced by ZNF354C silencing in the serum of I/R mice (Figures 8(f), 8(g), and 8(j)). Furthermore, results showed that the expression change of ZNF354C in each group was consistent with that of TFPI (Figures 8(g) and 8(h)). As I/R injury is directly related to the formation of reactive oxygen species (ROS), endothelial cell injury, increased vascular permeability, and the activation of neutrophils and platelets, cytokines, and the complement system. Our data certified that I/R induced prominent elevation of TFPI, MDA, and NOS levels in BALF, which could be prominently decreased by 5-Aza or ZNF354C overexpression; however, inhibition of ZNF354C again attenuated the decrease in the levels of TFPI, MDA and NOS in BALF (Figures 8(k)–8(m)). Consequently, our results indicate that 5-Aza or ZNF354C could play protective roles in lung LIRI, which is relevant to DNA methylation.

## 4. Discussion

Pulmonary I/R not only maintains lung vitality but also triggers a series of complex cascade reactions, collectively known as LIRI [44]. LIRI has been proved to induce postoperative morbidity in patients undergoing lung transplantation [7]. It is characterized by increased microvascular permeability, elevated pulmonary vascular resistance, pulmonary edema, and pulmonary hypertension [45]. Furthermore, it can cause prolonged mechanical ventilation and pulmonary hypertension, which can seriously affect the prognosis of patients [46]. Therefore, the prevention and mitigation of LIRI are of great practical significance. In our study, we first applied OGD/R to establish an *in vitro* I/R model in HUVECs. In addition, we also constructed an I/R mouse model to investigate the *in vivo* cellular mechanisms involved in LIRI development via genetic overexpression and RNA silencing of crucial genes (i.e., TFPI, ZNF354C, and DNMT1).

The pulmonary endothelial cells play crucial roles in the development of ALI by increasing pulmonary vascular permeability [47]. Endothelial cell apoptosis can also disrupt cell-cell and cell-extracellular matrix interactions and loss of endothelial barrier function, leading to direct or indirect ALI [48]. Furthermore, oxidative stress results from an imbalance in oxidative and antioxidant levels. In this regard, it has been shown that the “respiratory burst” caused by damaging factors can produce large amounts of ROS, which further aggravate lung injury [49]. In our study, we also discovered that OGD/R could suppress cell viability and migration and induce ROS production of HUVECs. A previous study found that during sepsis, lung-associated TFPI antigens, mRNA levels decreased, and TFPI activity suddenly

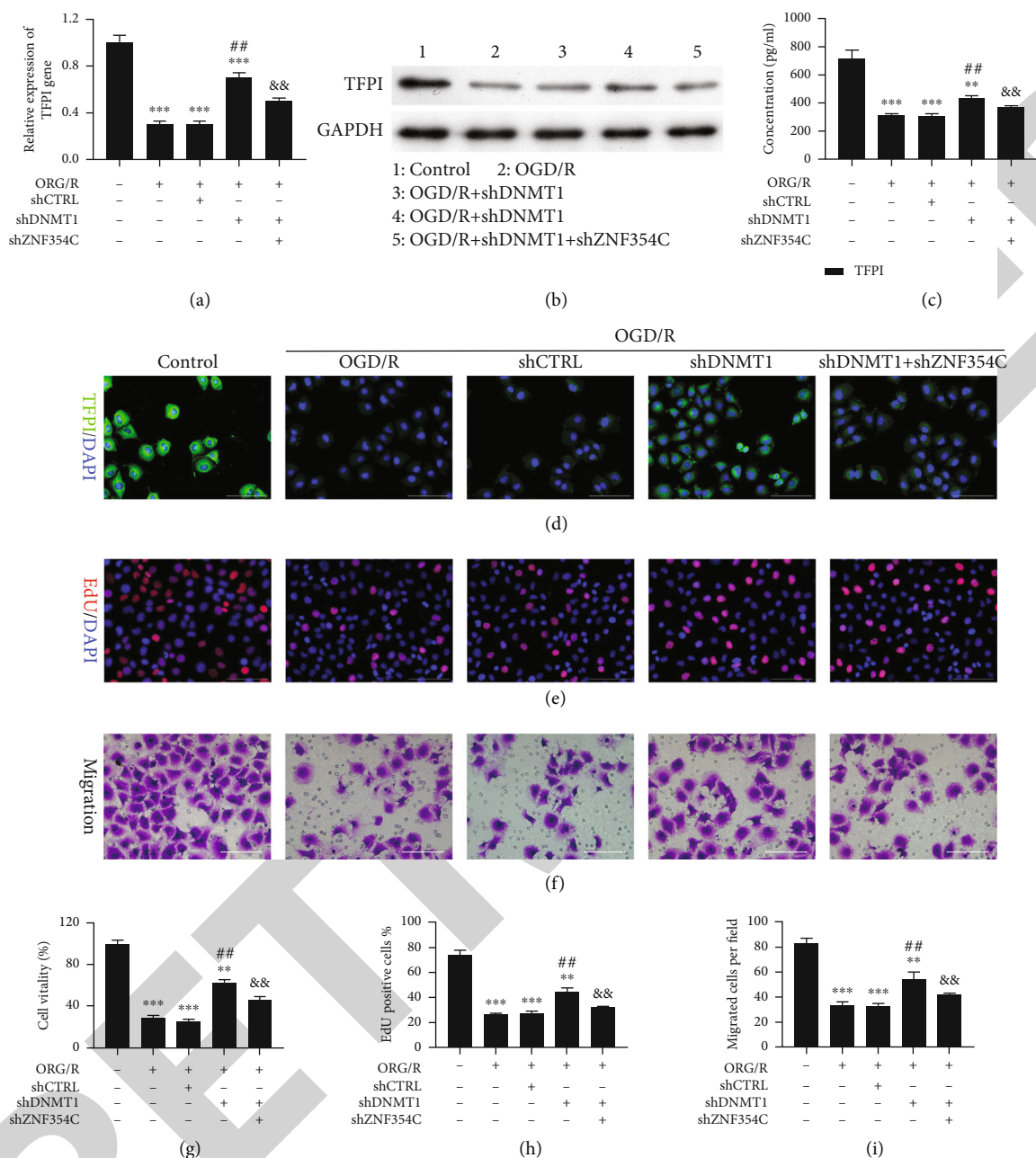
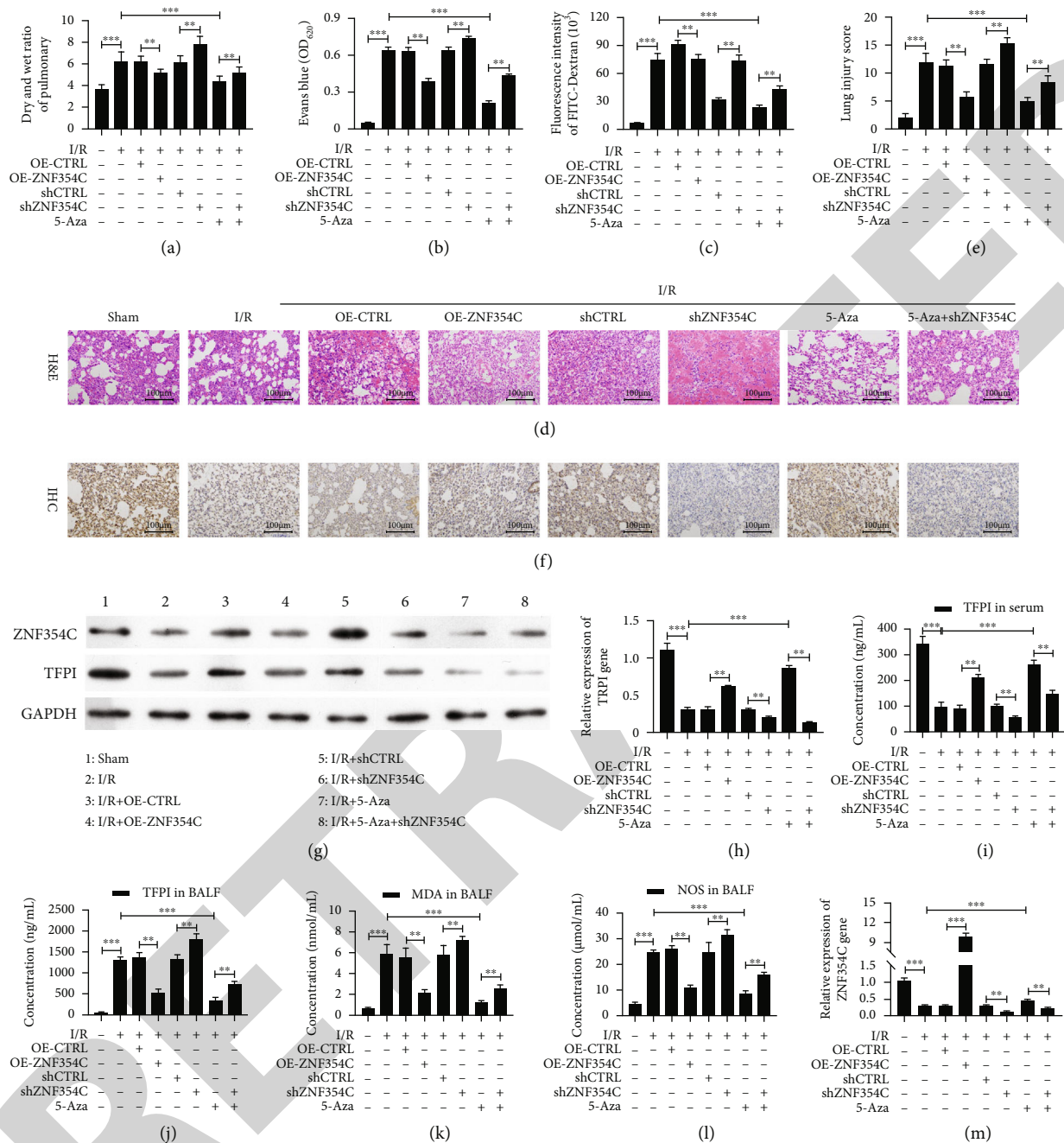


FIGURE 7: Silencing of DNMT1 accelerated proliferation and migration by regulating ZNF354C to target TFPI in OGD/R-induced HUVECs. OGD/R-induced HUVECs were transfected with shDNMT1 or/and shZNF354C. TFPI expression was identified through (a) RT-qPCR and (b) western blot, (c) ELISA, and (d) IF staining. (e, h) The change of cell proliferation was confirmed with EdU staining, and EdU-positive cells were quantitated. (f, i) The change of cell migration was monitored with Transwell, and migratory cells were quantitated. (g) CCK-8 presented the change of cell viability. The experiments were repeated three times independently.

decreased 2 h after bacterial infusion [50]. Tissue factor (TF) and TFPI levels in BALF supernatant are significantly higher in patients with idiopathic pulmonary fibrosis compared to healthy controls [51]. Overexpression of TFPI also results in improved hemodynamic performance and reduced pulmonary vascular remodeling in a murine model of hypoxia-induced pulmonary hypertension [52]. TFPI deficiency in endothelial cells has been linked to pulmonary tumor metastasis with an increased vascular permeability and altered lung microenvironment [15]. Knockdown of

endothelial-specific TFPI exacerbates lipopolysaccharide (LPS) induced ALI via the NF- $\kappa$ B signaling pathway [53]. Local administration of recombinant human TFPI attenuates both pulmonary and systemic coagulopathy. Furthermore, nebulized rh-TFPI modestly reduces the pulmonary inflammatory response and allows increased bacterial clearance in rats with direct lung injury caused by *P. aeruginosa* [54]. Therefore, TFPI may be a beneficial therapeutic agent in intravascular clotting, sepsis, cancer, and ALI to attenuate pathologic clotting. Our results also proved that the TFPI



**FIGURE 8:** ZNF354C alleviated LIRI through suppressing DNA methylation *in vivo*. The I/R model was established and then was disposed of ZNF354C overexpression plasmids, shZNF354C lentivirus, and/or 5-Aza (each group contained 5 mice). (a) After sacrifice, wet and dry lung weights of mice were measured and compared with wet-to-dry ratios. (b) Evans Blue was injected via the jugular vein 1 h before sacrifice, and the absorbance of the supernatant was tested at 620 nm. (c) The fluorescence intensity of FITC-Dextran was confirmed with FITC dextran assay. (d) The pathologic structure of lung tissues was assessed by H&E staining. (e) The lung injury score was also calculated by ImageJ based on the H&E staining results. (f) The expression of TFPI was measured by IHC. (g) The expressions of ZNF354C and TFPI were identified by Western blot. (h, i) And ZNF354C and TFPI expressions were quantified. ELISA kits were adopted to evaluate the levels of (j) TFPI in serum, (l) TFPI in BALF, (l) MDA in BALF, and (m) NOS in BALF.

promoter could be highly methylated under OGD/R in HUVECs, whereas TFPI and DNMT were downregulated in OGD/R-induced HUVECs. Therefore, TFPI methylation might be of vital importance in LIRI.

The pathogenesis of tissue injury induced by I/R involves epigenetic regulation [55]. DNA methylation on CpG dinu-

cleotides is applied to “shut down” gene expression in cells catalyzed by DNMTs [56]. DNA methylation plays a key role in I/R related organ damage, including kidney injury, cerebral ischemia, and ischemic heart disease [55]. In our study, we further certified that the methylation inhibitor (i.e., 5-Aza) could reverse the downregulation of TFPI in

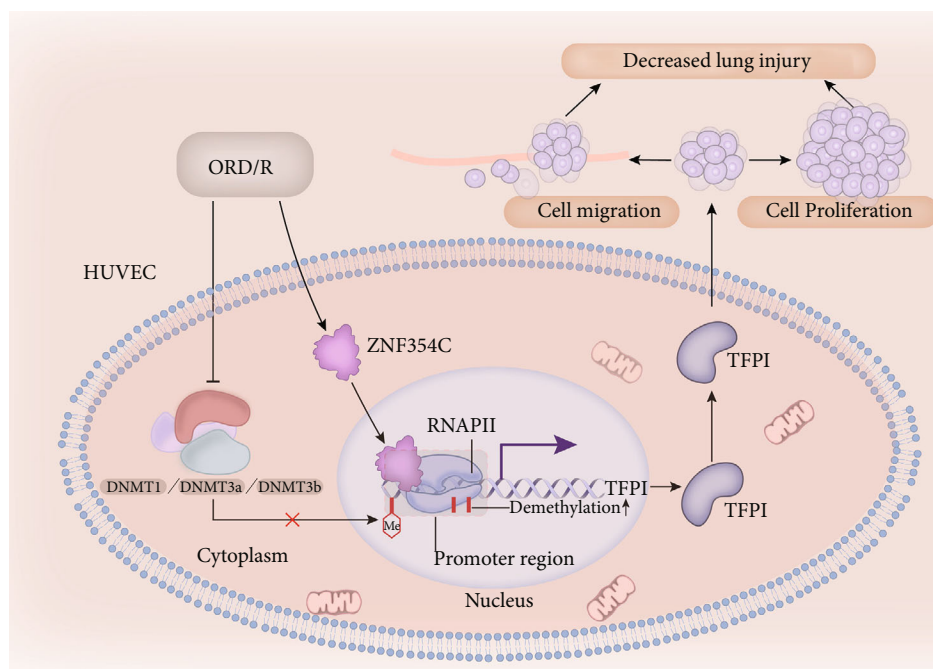


FIGURE 9: Schematic overview of the mechanism between ZNF354C, TFPI, and DNMT1 based on the findings of the study. ZNF354C interacts with TFPI and upregulates TFPI by preventing TFPI promoter methylation in OGD/R-induced HUVECs. DNMT1 reduces the interaction of TFPI and ZNF354C. Functionally, ZNF354C ameliorates LIRI by preventing TFPI methylation to upregulate TFPI.

OGD/R-induced HUVECs by inhibiting TFPI promoter methylation. Besides, 5-Aza also induced proliferation and migration, as well as lowered ROS levels in the OGD/R-induced HUVECs. More importantly, 5-Aza reduced the TFPI methylation, upregulated TFPI, and enhanced the combination of TFPI and ZNF354C in LIRI.

In the ischemic brain, the expression of DNMT1 is upregulated in astrocytes [57]. Another study revealed that after 4 days of transient global cerebral ischemia, the expression of DNMT1 distinctively decreased in the ischemic CA1 region, which may be related to ischemia-induced delayed neuronal death [58]. In addition, the reduction, but not the absence of DNMT1 in post mitotic neurons, protects against ischemic brain injury [59]. However, the functional role of DNMT1 in pulmonary ischemia reperfusion has not been found. In our study, we also verified that DNMT1 was involved in the regulation of OGD/R in HUVECs. Furthermore, DNMT1 silencing accelerated proliferation and migration, as well as prevented ROS production in OGD/R-induced HUVECs, whereas DNMT overexpression aggravated the lung injury induced by OGD/R. Although the methylation of TFPI has not been proven in HUVECs or other cells, hypermethylation in the promoter region of TFPI-2 has been analyzed in various types of cancers, such as non-small cell lung cancer [60], esophageal carcinogenesis [61], gastric cancer [62], acute myeloid leukemia [63], glioblastomas [64], and cervical cancer [65]. Thus, we suggest that the TFPI promoter methylation is a major contributor to LIRI-induced damage.

Zinc finger proteins (ZNF) are a large group of transcription factors with differential functions [66]. A previous study reported that ZNF354C is a key transcriptional factor

in carcinogenesis and the development of esophageal squamous cell carcinoma (ESCC) by regulating target genes [67]. Recently, a study revealed that ZNF354C is expressed in vascular cells, while ZNF354C overexpression inhibits the endothelial sprouting by binding to specific endothelial relevant target gene promoter [18]. In our study, we also proved that ZNF354C, as a transcriptional factor, could directly bind the promoter of TFPI. And ZNF354C also could enhance the proliferation and migration and reduced the ROS level of OGD/R-induced HUVECs through TFPI. Moreover, DNMT1 silencing could accelerate the proliferation and migration, as well as suppress ROS production, of OGD/R-induced HUVECs by regulating ZNF354C. Therefore, we further uncovered the crucial effects of ZNF354C and TFPI methylation in LIRI.

Nevertheless, our study is not without limitations. First, DNMT1 was not involved in the *in vivo* experiments. Second, pulmonary fibrosis and angiogenesis were not explored. Third, the specific regulatory mechanism between ZNF354C and DNMT1 is not completely clear. Fourth, the roles and mechanisms of DNMT3a and DNMT3b in ALI have not been clarified. For future research, Evans Blue Staining should be replaced with Evans Blue-TTC staining.

## 5. Conclusions

Our study showed that ZNF354C could interact with TFPI, and upregulate TFPI by preventing TFPI promoter methylation in OGD/R-induced HUVECs. DNMT1 could also reduce the interaction of TFPI and ZNF354C (Figure 9). Functionally, we discovered that ZNF354C ameliorates LIRI by preventing TFPI methylation to upregulate TFPI. Therefore, our study

verified the key roles of ZNF354C overexpression or inhibition in TFPI promoter methylation of LIRI. This research provides a theoretical basis for further understanding of the molecular mechanism of LIRI development, as well as an experimental basis for the clinical diagnosis and therapeutic biomarkers of patients with ALI.

## Abbreviations

I/R:	Ischemia reperfusion
LIRI:	Lung ischemia-reperfusion injury
ALI:	Acute lung injury
PGD:	Primary graft dysfunction
TFPI:	Tissue factor pathway inhibitor
OGD/R:	Oxygen glucose deprivation/reoxygenation
HUVECs:	Human umbilical vein endothelial cells
shRNA:	Short hairpin RNA
CTRL:	Control
OE:	Overexpression
CCK-8:	Cell Counting Kit-8
FITC:	Fluorescein isothiocyanate
EdU:	5-Ethynyl-2'-deoxyuridine
RT-qPCR:	Real-Time Quantitative PCR
PCR:	Polymerase Chain Reaction
RT:	Reverse transcription
BCA:	Bicinchoninic acid assay
SDS:	Sodium dodecyl sulfate
PAGE:	Polyacrylamide gel electrophoresis
PVDF:	Polyvinylidene fluoride
GAPDH:	Glyceraldehyde-3phosphate dehydrogenase
DAPI:	2-(4-Amidinophenyl)-6-indolecarbamide dihydrochloride
MS-PCR:	Methylation-specific polymerase chain reaction
ChIP:	Chromatin immunoprecipitation
PBS:	Phosphate-buffered saline
min:	Minute
WT:	Wild-type
EMSA:	Electrophoretic mobility shift assay
UV:	Ultraviolet ray
ELISA:	Enzyme-linked immunosorbent assay
MDA:	Malondialdehyde
NOS:	Nitric oxide synthase
BALF:	Bronchoalveolar lavage fluid
IHC:	Immunohistochemistry
H&E:	Hematoxylin and eosin.

## Data Availability

The data and study materials that support the findings of this study will be available to other researchers from the corresponding authors upon reasonable request.

## Ethical Approval

All the experimental protocols involving animals were approved by the Ethics Committee of Fudan University (20210302-117). All animal experiments were carried out in accordance with relevant guidelines and regulations. Furthermore, all the related procedures were consistent with

Ethics Committee regulations. The study was carried out in compliance with the ARRIVE guidelines.

## Conflicts of Interest

The authors declare no conflicts of interest.

## Authors' Contributions

Jiayuan Sun and Meng Shi did the conceptualization. Qi Shi and Meng Shi curated the data. Nana Feng and Jiayuan Sun did the formal analysis. Jiayuan Sun and Meng Shi acquired funding. Meng Shi, Qingyun Ma, and Hauhau Wang did the investigation. Nana Feng, Huijun Zhang, and Dayu Huang are assigned to the methodology. Jiayuan Sun and Meng Shi are responsible for the project administration. Qi Shi and Nana Feng are assigned to the writing—original draft. All authors are assigned to the writing—review and editing. Qi Shi and Nana Feng contributed equally to this work.

## Acknowledgments

This work was sponsored by grants from the National Natural Science Foundation of China (nos. 30800500 and 81900007), the Shanghai Science and Technology Committee (18140903400), the Shanghai Municipal Health Commission (20204Y0082), and the Project of the Xuhui District Science Committee of Shanghai (SHXH201838).

## Supplementary Materials

*Supplementary 1.* Figure S1: quantitative analysis of ROS level. The level of ROS was tested with DCFDA/H<sub>2</sub>DCFDA-Cellular ROS Assay, and relative fluorescence intensity was counted in the corresponding groups. The experiment was repeated three times independently.

*Supplementary 2.* Figure S2: quantitative analysis of TFPI in IHC results. The relative intensity of TFPI was quantitatively analyzed based on the IHC results in Figure 7(f).

## References

- [1] V. E. Laubach and A. K. Sharma, "Mechanisms of lung ischemia-reperfusion injury," *Current Opinion in Organ Transplantation*, vol. 21, no. 3, pp. 246–252, 2016.
- [2] A. V. Ovechkin, D. Lominadze, K. C. Sedoris, T. W. Robinson, S. C. Tyagi, and A. M. Roberts, "Lung ischemia-reperfusion injury: implications of oxidative stress and platelet-arteriolar wall interactions," *Archives of Physiology and Biochemistry*, vol. 113, no. 1, pp. 1–12, 2007.
- [3] J. Tang, L. Xu, Y. Zeng, and F. Gong, "Effect of gut microbiota on LPS-induced acute lung injury by regulating the TLR4/NF- $\kappa$ B signaling pathway," *International Immunopharmacology*, vol. 91, article 107272, 2021.
- [4] R. J. Shah and J. M. Diamond, "Primary graft dysfunction (PGD) following lung transplantation," *Seminars in Respiratory and Critical Care Medicine*, vol. 39, no. 2, pp. 148–154, 2018.
- [5] W. A. den Hengst, J. F. Gielis, J. Y. Lin, P. E. Van Schil, L. J. De Windt, and A. L. Moens, "Lung ischemia-reperfusion injury: a

- molecular and clinical view on a complex pathophysiological process,” *American journal of physiology Heart and circulatory physiology*, vol. 299, no. 5, pp. H1283–H1299, 2010.
- [6] M. K. Porteous, J. M. Diamond, and J. D. Christie, “Primary graft dysfunction: lessons learned about the first 72 h after lung transplantation,” *Current Opinion in Organ Transplantation*, vol. 20, no. 5, pp. 506–514, 2015.
- [7] T. F. Chen-Yoshikawa, “Ischemia–reperfusion injury in lung transplantation,” *Cells*, vol. 10, no. 6, p. 1333, 2021.
- [8] N. Haywood, H. Q. Ta, E. Rotar, Z. Daneva, S. K. Sonkusare, and V. E. Laubach, “Role of the purinergic signaling network in lung ischemia-reperfusion injury,” *Current Opinion in Organ Transplantation*, vol. 26, no. 2, pp. 250–257, 2021.
- [9] M. C. Thomassen, A. C. Heinzmann, L. Herfs et al., “Tissue factor-independent inhibition of thrombin generation by tissue factor pathway inhibitor- $\alpha$ ,” *Journal of thrombosis and haemostasis : JTH*, vol. 13, no. 1, pp. 92–100, 2015.
- [10] S. Kahraman, R. Erdim, F. Helvacioğlu et al., “The impact of TFPI on coronary atherosclerotic burden,” *Bratislavské Lekárske Listy*, vol. 119, no. 6, pp. 385–390, 2018.
- [11] C. Moratz, R. Robbins, J. Eickhoff, J. Edison, H. Lui, and S. Peng, “Regulation of systemic tissue injury by coagulation inhibitors in B6.MRL/ *lpr* autoimmune mice,” *Clinical Immunology*, vol. 197, pp. 169–178, 2018.
- [12] M. S. Bajaj, J. J. Birktoft, S. A. Steer, and S. P. Bajaj, “Structure and biology of tissue factor pathway inhibitor,” *Thrombosis and Haemostasis*, vol. 86, no. 4, pp. 959–972, 2001.
- [13] S. Gando, T. Kameue, Y. Morimoto, N. Matsuda, M. Hayakawa, and O. Kemmotsu, “Tissue factor production not balanced by tissue factor pathway inhibitor in sepsis promotes poor prognosis,” *Critical Care Medicine*, vol. 30, no. 8, pp. 1729–1734, 2002.
- [14] R. C. Rancourt, L. A. Veress, A. Ahmad et al., “Tissue factor pathway inhibitor prevents airway obstruction, respiratory failure and death due to sulfur mustard analog inhalation,” *Toxicology and Applied Pharmacology*, vol. 272, no. 1, pp. 86–95, 2013.
- [15] J. Wang, J. Xiao, D. Wen et al., “Endothelial cell-anchored tissue factor pathway inhibitor regulates tumor metastasis to the lung in mice,” *Molecular Carcinogenesis*, vol. 55, no. 5, pp. 882–896, 2016.
- [16] J. Jen and Y. C. Wang, “Zinc finger proteins in cancer progression,” *Journal of Biomedical Science*, vol. 23, no. 1, p. 53, 2016.
- [17] Z. Li, X. Lu, Y. Liu et al., “Gain of LINC00624 enhances liver cancer progression by disrupting the histone deacetylase 6/tripartite motif containing 28/zinc finger protein 354C corepressor complex,” *Hepatology*, vol. 73, no. 5, pp. 1764–1782, 2021.
- [18] J. A. Oo, B. Irmer, S. Günther et al., “ZNF354C is a transcriptional repressor that inhibits endothelial angiogenic sprouting,” *Scientific Reports*, vol. 10, no. 1, p. 19079, 2020.
- [19] L. Zhang, Q. Lu, and C. Chang, “Epigenetics in health and disease,” *Advances in Experimental Medicine and Biology*, vol. 1253, pp. 3–55, 2020.
- [20] Y. Zeng and T. Chen, “DNA methylation reprogramming during mammalian development,” *Genes*, vol. 10, no. 4, p. 257, 2019.
- [21] K. K. Wong, C. H. Lawrie, and T. M. Green, “Oncogenic roles and inhibitors of DNMT1, DNMT3A, and DNMT3B in acute myeloid leukaemia,” *Biomarker Insights*, vol. 14, p. 117727191984645, 2019.
- [22] Ž. M. Svedružić, “Dnmt1: structure and function,” *Progress in Molecular Biology and Translational Science*, vol. 101, pp. 221–254, 2011.
- [23] K. K. Wong, “DNMT1 as a therapeutic target in pancreatic cancer: mechanisms and clinical implications,” *Cellular Oncology (Dordrecht)*, vol. 43, no. 5, pp. 779–792, 2020.
- [24] K. K. Wong, “DNMT1: a key drug target in triple-negative breast cancer,” *Seminars in Cancer Biology*, vol. 72, pp. 198–213, 2021.
- [25] Y. T. Chen, W. D. Lin, W. L. Liao, Y. C. Tsai, J. W. Liao, and F. J. Tsai, “\_NT5C2\_ methylation regulatory interplay between DNMT1 and insulin receptor in type 2 diabetes,” *Scientific Reports*, vol. 10, no. 1, p. 16087, 2020.
- [26] C. M. Kloske, A. J. Dugan, E. M. Weekman et al., “Inflammatory pathways are impaired in Alzheimer disease and differentially associated with apolipoprotein E status,” *Journal of Neuropathology and Experimental Neurology*, vol. 80, no. 10, pp. 922–932, 2021.
- [27] R. I. F. Assis, A. G. Schmidt, F. Racca et al., “DNMT1 inhibitor restores RUNX2 expression and mineralization in periodontal ligament cells,” *DNA and Cell Biology*, vol. 40, no. 5, pp. 662–674, 2021.
- [28] Y. Wang, X. Wang, H. Zhang et al., “Transforming growth factor- $\beta$ 1 promotes M1 alveolar macrophage polarization in acute lung injury by up-regulating DNMT1 to mediate the microRNA-124/PELI1/IRF5 Axis,” *Frontiers in Cellular and Infection Microbiology*, vol. 11, article 693981, 2021.
- [29] J. Li, C. Yang, and Y. Wang, “miR-126 overexpression attenuates oxygen-glucose deprivation/reperfusion injury by inhibiting oxidative stress and inflammatory response via the activation of SIRT1/Nrf2 signaling pathway in human umbilical vein endothelial cells,” *Molecular Medicine Reports*, vol. 23, no. 2, 2020.
- [30] S. Lai, M. Pan, H. Liao, J. Chen, Y. Jiang, and Y. Li, “The impact of CRMP4 SUMOylation on the Cav1.2 interaction, neurite outgrowth and thermal pain sensitivity,” *Journal of Integrative Neuroscience*, vol. 20, no. 3, pp. 595–603, 2021.
- [31] M. Di, Y. Zhang, R. Zeng et al., “The pro-angiogenesis effect of miR33a-5p/Ets-1/DKK1 signaling in ox-LDL induced HUVECs,” *International Journal of Biological Sciences*, vol. 17, no. 15, pp. 4122–4139, 2021.
- [32] B. Liu, M. Lan, H. Wei, D. Zhang, J. Liu, and J. Teng, “Down-regulated microRNA-133a induces HUVECs injury: potential role of the (pro) renin receptor in angiotensin II-dependent hypertension,” *Molecular Medicine Reports*, vol. 20, no. 3, pp. 2796–2804, 2019.
- [33] X. Liu, S. Yin, Y. Chen et al., “LPS-induced proinflammatory cytokine expression in human airway epithelial cells and macrophages via NF- $\kappa$ B, STAT3 or AP-1 activation,” *Molecular Medicine Reports*, vol. 17, no. 4, pp. 5484–5491, 2018.
- [34] Z. Xin, Z. Tong, J. Tan, and C. Liu, “MicroRNA-145-5p aggravates cell apoptosis and oxidative stress in tongue squamous cell carcinoma,” *Experimental and Therapeutic Medicine*, vol. 21, no. 4, p. 373, 2021.
- [35] A. Alsterda, K. Asha, O. Powrozek et al., “Salubrinal exposes anticancer properties in inflammatory breast cancer cells by manipulating the endoplasmic reticulum stress pathway,” *Frontiers in Oncology*, vol. 11, article 654940, 2021.
- [36] H. Hong, Q. Huang, Y. Cai, T. Lin, F. Xia, and Z. Jin, “Dexametomidine preconditioning ameliorates lung injury induced by pulmonary ischemia/reperfusion by upregulating promoter histone H3K4me3 modification of KGF-2,” *Experimental Cell Research*, vol. 406, no. 2, article 112762, 2021.
- [37] X. Lin, T. Yu, J. Luo et al., “BMSCs mediates endothelial cell autophagy by upregulating miR-155-5p to alleviate ventilator-



## *Retraction*

# **Retracted: Exosomal miR-27b-3p Derived from Hypoxic Cardiac Microvascular Endothelial Cells Alleviates Rat Myocardial Ischemia/Reperfusion Injury through Inhibiting Oxidative Stress-Induced Pyroptosis via Foxo1/GSDMD Signaling**

## **Oxidative Medicine and Cellular Longevity**

Received 26 December 2023; Accepted 26 December 2023; Published 29 December 2023

Copyright © 2023 Oxidative Medicine and Cellular Longevity. This is an open access article distributed under the Creative Commons Attribution License, which permits unrestricted use, distribution, and reproduction in any medium, provided the original work is properly cited.

This article has been retracted by Hindawi, as publisher, following an investigation undertaken by the publisher [1]. This investigation has uncovered evidence of systematic manipulation of the publication and peer-review process. We cannot, therefore, vouch for the reliability or integrity of this article.

Please note that this notice is intended solely to alert readers that the peer-review process of this article has been compromised.

Wiley and Hindawi regret that the usual quality checks did not identify these issues before publication and have since put additional measures in place to safeguard research integrity.

We wish to credit our Research Integrity and Research Publishing teams and anonymous and named external researchers and research integrity experts for contributing to this investigation.

The corresponding author, as the representative of all authors, has been given the opportunity to register their agreement or disagreement to this retraction. We have kept a record of any response received.

## **References**

- [1] B. Zhang, C. Sun, Y. Liu, F. Bai, T. Tu, and Q. Liu, "Exosomal miR-27b-3p Derived from Hypoxic Cardiac Microvascular Endothelial Cells Alleviates Rat Myocardial Ischemia/Reperfusion Injury through Inhibiting Oxidative Stress-Induced Pyroptosis via Foxo1/GSDMD Signaling," *Oxidative Medicine and Cellular Longevity*, vol. 2022, Article ID 8215842, 19 pages, 2022.

## Research Article

# Exosomal miR-27b-3p Derived from Hypoxic Cardiac Microvascular Endothelial Cells Alleviates Rat Myocardial Ischemia/Reperfusion Injury through Inhibiting Oxidative Stress-Induced Pyroptosis via Foxo1/GSDMD Signaling

Baojian Zhang,<sup>1,2</sup> Chao Sun,<sup>2</sup> Yaozhong Liu,<sup>2</sup> Fan Bai,<sup>2</sup> Tao Tu,<sup>2</sup> and Qiming Liu<sup>2</sup> 

<sup>1</sup>Cardiac Care Unit, Affiliated Hospital of Traditional Chinese Medicine, Xinjiang Medical University, Urumqi City, Xinjiang Uygur Autonomous Region, China

<sup>2</sup>Department of Cardiology/Cardiac Catheterization Lab, Second Xiangya Hospital, Central South University, Changsha, Hunan, China

Correspondence should be addressed to Qiming Liu; [qimingliu@csu.edu.cn](mailto:qimingliu@csu.edu.cn)

Received 31 March 2022; Revised 10 May 2022; Accepted 31 May 2022; Published 6 July 2022

Academic Editor: Tian Li

Copyright © 2022 Baojian Zhang et al. This is an open access article distributed under the Creative Commons Attribution License, which permits unrestricted use, distribution, and reproduction in any medium, provided the original work is properly cited.

**Background.** Exosomes derived from cardiac microvascular endothelial cells (CMECs) under hypoxia can mediate cardiac repair functions and alleviate pyroptosis and oxidative stress during ischemia-reperfusion (I/R) injury. This study is aimed at investigating the effect and mechanism of miR-27b-3p underlying hypoxic CMECs-derived exosomes against I/R injury. **Methods.** CMECs were isolated from the left ventricle of Sprague-Dawley rats, followed by culturing under hypoxic conditions or pretreatment with the miR-27b-3p inhibitor. CMECs-derived exosomes were added into H9C2 cells before hypoxia/reoxygenation (H/R) or injected into the rat heart before I/R injury. An *in vivo* I/R injury model was established by ligating and releasing the left anterior descending coronary artery. Expression of pyroptosis-related factors was detected using Western blot, and heart infarcted size was determined by the 2,3,5-triphenyl-2H-tetrazpinolium chloride staining method. Dual-Luciferase Reporter assays were performed to analyze the interactions of nmiR-27b-3p-forkhead box O1 (Foxo1) and Gasdermin D- (GSDMD-) Foxo1. Chromatin-immunoprecipitation (ChIP) assays were performed to validate the interactions between forkhead box O1 (Foxo1) and Gasdermin D (GSDMD) and Foxo1-mediated histone acetylation of GSDMD. **Results.** CMECs were successfully identified from left ventricle of Sprague-Dawley rats. The expressions of Foxo1 and pyroptosis-related proteins (GSDMD, NLRP3, cleaved caspase 1, IL-1 $\beta$ , and IL-18) were upregulated in the rat heart after I/R injury. Treatment of CMEC-derived exosomes, especially that under hypoxic conditions, significantly reduced pyroptosis in the rat heart. miR-27b-3p was significantly upregulated in CMEC-derived exosomes under hypoxic conditions, and miR-27b-3p inhibition in exosomes alleviated its cytoprotection and inhibited oxidative stress in H9C2 cells. Treatment with Foxo1 overexpression plasmids aggravated *in vitro* H/R and *in vivo* I/R injury by upregulating pyroptosis-related proteins. Further experiments validated that miR-27b-3p negatively targeted Foxo1, which bound to the promoter region of GSDMD. **Conclusions.** These results demonstrated a great therapeutic efficacy of miR-27b-3p overexpression in hypoxic CMEC-derived exosomes in preventing the development of myocardial damage post I/R injury through inhibiting Foxo1/GSDMD signaling-induced oxidative stress and pyroptosis.

## 1. Introduction

Myocardial infarction (MI), a life-threatening disease worldwide, is the most common in Europe and the United States. Annually, there are about 1.5 million myocardial infarction

in the United States. In recent years, China has shown an obvious increasing trend, with at least 500000 new cases per year and at least 2 million current cases. The most commonly used treatment for MI in clinical practice is reperfusion therapy, which causes myocardial ischemia-

reperfusion (I/R) injury to produce irreversible damage to cardiomyocytes and myocardial diastolic dysfunction [1]. Therapeutic reperfusion could result in complications through initiating multiple pathophysiological processes, including myocyte necrosis, microvascular obstruction, and microcirculation dysfunction [2–4].

Cardiac microvascular endothelial cells (CMECs) are important cells in the myocardium. Abnormal and detrimental changes in CMECs in responses to I/R include excessive inflammation, apoptosis, and reactive oxygen species (ROS) production, which could contribute to the progression of cardiac dysfunction [2, 4–6]. CMECs constitute the microcirculatory tract and play crucial roles in causing cardiac microvasculature injury in I/R [2, 4]. CMECs secrete a wide range of cytokines, cellular contents, and exosomes that mediate functional interactions between cardiomyocytes, leukocytes, and the circulation [2, 4, 7, 8]. Accordingly, CMECs are commonly used to mimic actual pathological state and I/R injury and have been applied in *in vitro* drug research [6]. NLRP3 inflammasome-induced pyroptosis in CMECs under I/R injury aggravates I/R-induced damage [9, 10]. Under I/R conditions, NLRP3 inflammasome is induced to stimulate caspase-1 cascade, which is responsible for the upregulation of cytokines (including interleukin- (IL-) 1 $\beta$  and IL-18) and the activation of caspase-11/gasdermin-D (GSDMD) cascade [4, 11]. Recent studies showed that exosomes derived from endothelial cells (ECs) and mesenchymal stem cells (MSCs) mediate strong cardiac repair functions of cardiomyocytes, smooth muscle cells, and fibroblasts as well as protecting against NLRP3 inflammasome-induced pyroptosis [11–16].

Exosomes are nanosized and lipid-bilayer-enclosed extracellular vesicles released by all cells that circulate in the blood. Exosomes contain RNA, lipids, and proteins and deliver signals to target cells, which is essential for intercellular communication and exchange of genetic information [17]. Exosomes derived from stem cells could inhibit inflammation and doxorubicin-induced pyroptosis in cardiac cells [11, 18, 19]. Dargani et al. [18] indicated that doxorubicin promotes the expression of IL-1 $\beta$  and IL-18 in exosomes derived from embryonic stem cells. Evidence showed that the abundance of exosomal proteins, mRNA, and miRNA and exosomal therapeutic potential could be enhanced by hypoxia [20–23]. Hypoxia stimulates the expression of miRNAs (including miR-27b-3p, miR-17-1-3p, and miR-217-3p) and proteins in cardiomyocyte or CPC-derived exosomes with cytoprotection, proangiogenic, and antifibrotic effects [20, 22, 24, 25]. However, no studies demonstrated that exosomal-derived miRNAs can protect against damage caused by I/R models; therefore, this study treated I/R model rats with CMEC-derived exosomes to explore the role of CMEC-derived exosomes in I/R model rats. Also, less was known on the effect of hypoxic CMEC-derived exosomes on I/R injury.

Here, in our study, we demonstrated the protective effect of miR-27b-3p on CMEC-derived exosomes against I/R injury. Furthermore, hypoxia treatment increased exosomal miR-27b-3p and showed a higher efficacy in alleviating I/R-induced infarction size and myocardial damage in the

rat heart. The mechanism of miR-27b-3p-forkhead box O1 (Foxo1) in inflammation-induced pyroptosis in the progression of I/R injury was explored in the *in vitro* and *in vivo* rat model of I/R injury. These data confirmed the myocardial protective potential of using CMEC-derived exosomes under hypoxic conditions.

## 2. Materials and Methods

### 2.1. CMEC Isolation, Identification, and Culture Conditions.

The results of the isolation and identification of CMEC cells were provided by Wuhan Procell Life Sci&Tech Co., Ltd. Rat CMECs were dissociated from the left ventricle of Sprague-Dawley rats (3–4 weeks old; Disease Control and Prevention Center of Hubei, Wuhan, China) as previously described [26]. In brief, the left ventricle was isolated, minced into pieces (1 mm<sup>3</sup>), washed in PBS (containing 1% penicillin-streptomycin; Procell, Wuhan, China; PB180120), and digested in 0.1% trypsin (Procell, PB180225). The cells were filtrated and centrifuged at 300  $\times$  g for 5 minutes (min), followed by incubation in complete CMEC medium (Procell, CM-R135) containing 10% fetal bovine serum (FBS; Hyclone; cat. no. 10099-141) and 1% penicillin-streptomycin at 37°C with 95% air plus 5% CO<sub>2</sub>. The medium was replaced medium every three days. The expression of CD31 in CMECs was detected using immunofluorescence assay.

**2.2. Clinical Sample Collection.** We collected the blood samples from 32 clinical patients, including 16 nonmyocardial infarction patients and 16 patients with myocardial infarction (11 women and 21 men aged 12–80 years) and took the mRNA from patient plasma to study the expression of miR-27b-3p in patients with myocardial infarction and nonmyocardial infarction.

**2.3. Cell Transfection and Treatment.** miR-27b-3p inhibitor was purchased from GenePharma (Shanghai, China) and used in cellular transfections according to the manufacturer's recommendation. miRNA inhibitor as a chemically modified RNA single strand can competitively bind with mature miRNA sequence. Moreover, it can specifically target and knock out a single miRNA molecule, weaken the gene silencing effect of endogenous miRNA, improve protein expression, conduct loss of function research, and be used to screen miRNA target sites.  $1.0 \times 10^5$  CMECs were placed into 6-well plates filled with fresh complete medium containing Umibio®Exosome-Free FBS medium (Umibio, Shanghai, China; cat# UR50202) and maintained for 12 hours (h) to reach 80% confluence. Then, the cells were treated with 50 nmol miR-27b-3p or NC inhibitors using Lipofectamine 2000 (Invitrogen, California, USA) for 48 h in triplicate. For hypoxia treatment, the cells were maintained in complete medium in triplicate at 37°C with 5% CO<sub>2</sub> and 95% N<sub>2</sub> (hypoxic conditions) for 12 h in a trigas incubator (HF100, HealForce, Hong Kong).

**2.4. Isolation and Identification of Exosomes.** The isolation of CMEC-derived exosomes was conducted using total exosome-isolation kit (Thermo Fisher, USA), according to the manufacturer's instructions. The treated cell culture

was harvested by centrifugation (3000 rpm at 4°C for 15 min; 15,000 × g for 30 min) twice to remove microvesicles. After filtration (0.22 μm), the exosomes were pelleted twice (100,000 × g, 4°C for 1 h; centrifuged at 120,000 × g, 4°C for 1 h) and then suspended in PBS. Exosome morphology was detected under a transmission electron microscopy (TEM, 120,000x; FEI Tecnai G12, Philips, Netherlands). The size of exosome was measured using NanoSight NS300 nanoparticle tracking analysis (Malvern, UK). Exosomal protein quantification was determined using the BCA methods (Thermo Scientific; Waltham, MA, USA; Cat #23227). The expression of exosomal markers CD63, CD81, and TSG101 were detected in triplicate by Western blotting analysis.

**2.5. H9C2 Cell Culture, Transfection, and Treatments.** The rat origin H9C2 cell line was obtained from ATCC (Manassas, VA, USA) and incubated in high-glucose DMEM (Hyclone, USA; Cat.No.SH30022.01B) containing FBS (Hyclone) and 1% penicillin-streptomycin at 37°C with 95% air and 5% CO<sub>2</sub>. The Foxo1 expressing pcDNA vector (Vipotion, Guangzhou, China) was constructed into EcoRI/*Bam*HI sites of pcDNA 3.0 vector. A total of 1.0 × 10<sup>5</sup> H9C2 cells were placed into 6-well plates to 80% confluence, and the cells were treated with 4.0 μg Foxo1 plasmids using Lipofectamine 2000.

For the construction of cellular hypoxia/reoxygenation (H/R) model, transfected H9C2 cells were incubated under 2 h hypoxic (5% CO<sub>2</sub> and 95% N<sub>2</sub>) plus 4 h normal conditions (H/R condition) at 37°C. Then, the H9C2 cells were incubated in medium supplemented with 50 μg/ml exosomes isolated from CMECs with or without miR-27b-3p inhibitor under hypoxic conditions for 48 h.

**2.6. Cell Proliferation Analysis.** For the cell viability assay, the transfected H9C2 cells (1.0 × 10<sup>5</sup>/ml) were plated into 96-well plate overnight. 50 μg/ml exosomes after subjecting to H/R were added into the plates and incubated for 24, 48, and 72 h. Then, the cells were incubated in CCK8 working solution (10 μl, 5 mg/ml; Beyotime, Shanghai, China) in the dark for 1 h. The absorbance at 450 nm was recorded using a microplate reader (BioTek Instruments, Winooski, VT, USA).

**2.7. I/R Model Construction and Intervention.** Research approval was obtained from the Ethical Committee of Animal Experimentation of the Second Xiangya Hospital, Central South University. Healthy male Wistar rats (300 g-350 g) were randomly assigned into three sections. Forty-eight rats in the first part were grouped into four groups according to the surgery and treatment strategy ( $n = 12$ ). Rats in the I/R model group received I/R surgery. All the animals were anesthetized with pentobarbital sodium (50 mg/kg) via intraperitoneal injection. After disinfection, the heart was exposed. The left coronary artery was ligated for 30 min and released to allow blood reperfusion for 120 min. Before I/R surgery, 12 rats were administrated with exosomes (10 μl, 6 × 10<sup>12</sup> particles; intramyocardial injection) derived from CMECs cultured under normal and hypoxic conditions, respectively. Rats in the control group ( $n = 12$ ) received sham operation without ligation or reperfusion.

Forty-eight rats in the second part were treated with I/R and then injected (intramyocardial injection) with 20 μl lentivirus plasmid carrying Foxo1 ( $n = 24$ ; 1 × 10<sup>8</sup> TU/ml) or lentivirus vector (negative control (NC);  $n = 24$ ) and given with free access to water and food. Forty-eight rats in the third part were injected (intramyocardial injection) with 20 μl lentivirus plasmid carrying Foxo1 ( $n = 24$ ; 1 × 10<sup>8</sup> TU/ml) or lentivirus vector (negative control (NC);  $n = 24$ ) and then treated with I/R. The lentivirus-containing Foxo1 and empty vector were purchased from GenePharma. After 7 days, intramyocardial injection with exosome isolated from CMECs was performed on all the rats. Immediately after 2 h reperfusion, the blood sample was collected from femoral arteries of each rat. Then, all rats were sacrificed using a Quietek CO<sub>2</sub> Delivery Systems (Electron Microscopy Sciences), and the rat hearts were isolated and prepared for the examination of infarcted volume, histological examination, Western blot, and PCR analysis.

**2.8. Enzyme-Linked Immunosorbent Assay (ELISA).** The rat blood serum and the supernatant of H9C2 cells were prepared and used for the examination of creatine kinase (CK). Lactate dehydrogenase (LDH; Nanjing Jiancheng Biological Engineering Institute, Nanjing, China; Cat# A020-2), interleukin (IL)-1β (Elabscience, Wuhan, China; Cat# E-EL-R0012c), and IL-18 (Elabscience; Cat# E-EL-R0567c) were detected using the commercial ELISA kits, according to the manufacturer's recommendation.

**2.9. ROS and SOD Detection in H9C2 Cells.** The level of intracellular ROS was detected using 2',7'-dichlorofluorescein diacetate (DCFH-DA, D6883, Shanghai, Sigma). Cells were harvested after treated with hypoxia/reoxygenation and exosomes and were incubated with 5 μM DCFH-DA for 30 min at 37°C in the dark, and then, DCF fluorescence was assayed using the microplate reader (Biotek, USA) at excitation (488 nm) and emission (525 nm) wavelengths. The SOD in H9C2 cell culture supernatant was detected by SOD kits (BC0170, Solarbio Science and Technology Co., Ltd., Beijing.). After the H9C2 cells were treated with hypoxia/reoxygenation and exosomes, the supernatant of H9C2 cells was collected and tested for SOD by SOD kits. The procedure and result analysis of SOD assays refer to the instruction of SOD kits.

**2.10. Lesion Volume Determination.** The heart was quickly removed, cleaned and squeezed, dipped in dry blood, and rinsed in 4°C normal saline, followed by dipping the heart in dry and freezing in the refrigerator at -20°C for 15 min until the heart hardened. Next, the heart was taken to be cut into 1 mm thick slices using a blade from the apex to the bottom of the heart along the direction of atrioventricular sulcus. Five slices in total was prepared, and then, the slices were quickly placed in 5 ml 37°C 1% in TTC phosphate buffer (Guduo, Shanghai, China) at pH 7.4. The infarct area was white, the infarct border area was brick red, and the normal area was red. The slices were photographed using a camera.

**2.11. Immunofluorescence Assay.** PKH67 labeling of exosomes and exosomal uptake into H9C2 cells was performed as previously reported [27]. Cellular slides were fixed in 4% paraformaldehyde for 15 min and incubated with 5% Triton X-100 in PBS for 20 min, blocked with goat serum (Boster, Wuhan, China) for 30 at room temperature, with F-actin (1: 100; ab205, Abcam, Cambridge, MA, USA) at 4°C overnight, with secondary antibody (Cy3-labeled goat-anti-rabbit IgG; Boster; BA1032) at 37°C for 1 h. DAPI was used for nuclear staining. The cells were also labeled with lipid membrane dye PKH76 (Sigma-Aldrich). An Olympus microscope (Olympus, BX53, Tokyo, Japan) was used for the capturing cellular images.

**2.12. Histological and Immunohistochemistry Examination.** The hearts were fixed (10% formaldehyde; Beyotime), dehydrated, paraffin-embedded, and sectioned (4 μm thick) using a microtome (Leica, Nussloch, Germany). Hematoxylin and eosin (HE) staining (Sigma) was performed on tissue slices according to previously reported methods [28]. For immunohistochemistry analysis of caspase-1, the sections were pretreated in H<sub>2</sub>O<sub>2</sub> solutions, blocked by goat serum (Boster), and incubated with primary antibody against caspase-1 (1: 50; ab74279, Abcam,) at 4°C overnight. Secondary incubation was conducted using goat anti-rabbit IgG (1:1000, Abcam) in the dark for 2 h. The slices were then treated in DAB solution and Harris' hematoxylin. A BX-51 light microscopy (Olympus, Japan) was used for photographing (magnification ×200 and ×400).

**2.13. Western Blot Analysis.** The protein samples were isolated from the exosomes, rat hearts, or H9C2 cells using lysis buffer (Beyotime). The protein lysates were quantified using Bradford protein assay kit (Thermo Fisher Scientific Inc.), followed by protein separation on SDS-PAGE (10%; Beyotime) and transferring onto PVDF membranes (Millipore, Billerica, MA, USA) according to the standard methods. The expression of CD63 (1:1000, GTX37555, GeneTex), CD81 (1:500, ab109201), TSG101 (1:500, ab125011), Foxo1 (1:1000, ab39670), GSDMD (1:1000, ab219800), NOD-like receptor protein 3 (NLRP3; 1:1000, ab263899), caspase-1 (1:1000, ab286125) proteins, and GAPDH (1:10000, ab8245) were detected using specific primary antibodies at 4°C overnight. The primary antibodies were purchased from Abcam. Secondary incubation was conducted using HRP goat anti-rabbit/mouse IgG antibodies (Boster; 1:20000). GAPDH was used as the reference protein. The integral optical density values of proteins were analyzed using Image-Pro Plus 6.0 software.

**2.14. Reverse Transcription Quantitative PCR (RT-qPCR).** Total RNA was extracted from the treated exosomes, cells, or fresh heart tissues using TRIzol according to the manufacturer's instruction (Invitrogen). RNA was reversely transcribed to cDNA templates using 5x primeScript RT Master MIXperfect (TAKARA, Japan). RT-qPCR reaction was performed using Power SYBR Green PCR Master Mix (Thermo Fisher, Germany) using synthesized primers (Table 1). PCR amplification reaction conditions were at

95°C for 4 min, 40 cycles at 95°C for 20s, at 60°C for 30s, and at 72°C for 30s. The 2<sup>-ΔΔct</sup> method was used for calculating the relative expression levels of gene. GAPDH and U6 served as the reference internal gene for mRNA and miRNA, respectively.

**2.15. Luciferase Reporter Assay.** The interaction between miR-27b-3p and Foxo1 target was predicted using TargetScan Human ([http://www.targetscan.org/vert\\_71/](http://www.targetscan.org/vert_71/)) and was validated using the dual-luciferase reporter assay [29]. The interaction between GSDMD and Foxo1 was predicated using JASPAR database (<http://jaspar.binf.ku.dk/>) (updated 2020) [30]. The luciferase vectors containing wild-type and mutant 3'UTR reporters of Foxo1, and the dual-luciferase reporter gene vectors of GSDMD promoter carrying the wild-type binding sites of Foxo1 were purchased from Vipotion (Guangzhou, China) and used for dual-luciferase reporter assay. miR-27b-3p mimics and negative control mimics were purchased from GenePharma and used with Lipofectamine 2000 for cellular transfections. The relative fluorescence intensities were detected 48 h after the cell transfection according to the manufacturer's instruction of luciferase reporting system (Promega, Mannheim, Germany).

**2.16. Methylation-Specific PCR (MSP) Assay.** The effect of miR-27b-3p expression on the promoter methylation level of GSDMD gene was detected using MSP analysis. In brief, the H9C2 cells (1 × 10<sup>5</sup>) were transfected with 50 nmol inhibitor and mimics for 48 h. Cellular DNA was isolated and then sodium bisulfite-modified using EpiTect Bisulfite Kit (Qiagen, CA, USA). The samples were then desulfonated and purified and used for the measurement of methylation level using MSP. The primer sequences for amplifying GSDMD promoter region (between -1700 bp and -2100 bp) are listed in Table 1. PCR was conducted using Phanta® Uc Super-Fidelity DNA Polymerase (1 U/μl; Novozyme Company, Novonordisk, Denmark) under the following reaction conditions: at 95°C for 3 min, 40 cycles of 95°C for 15 seconds (s), at 60°C for 15 s, at 72°C for 30s, and at 72°C for 5 min. The PCR product was detected using 2% agarose gel.

**2.17. Chromatin-Immunoprecipitation (ChIP).** ChIP assay coupled with quantitative PCR (ChIP-qPCR) was conducted to confirm the DNA-binding ability of Foxo1, HDAC2, or H3K9AC protein with GSDMD gene using a Simple ChIP Plus Enzymatic Chromatin IP Kit (CST) according to the manufacturer's protocol. The H9C2 cells were treated with protease inhibitor cocktail coupled with gradually decreased formaldehyde (37% ~1.5%) for 20 min and then blocked by glycine solution for 5 min at room temperature. Cross-linked chromatin was broken into DNA fragments using DNA micrococcal nuclease at 37°C for 20 min. ChIP reaction was conducted using 5 μg of antibody against Foxo1 (1:30, ab39670, Abcam), H3K9AC (ab32117, 20 μg/ml), HDAC2 (1:60, ab32117), or 1-2 μl IgG (negative control) enriched in protein G magnetic beads (Invitrogen) at 4°C overnight. The immunoprecipitated complexes were then

TABLE 1: The sequences of primers that were used in this study.

Name of gene	Primer	Sequence (5'-3')
GAPDH	Forward	CCTCGTTCATAGACAAGATGGT
	Reverse	GGGTAGAGTCATACTGGAACATG
U6	Forward	CTCGCTTCGGCAGCACA
	Reverse	AACGCTTCACGAATTTGCGT
All miRNA	Reverse	CTCAACTGGTGTCTGTGGA
FOXO1	Forward	CAGCCAGGCACCTCATAACA
	Reverse	TCAAGCGTTTCATGGCAGAT
rno-miR-27b-3p	Reverse transcription	CTCAACTGGTGTCTGTGGAGTCGGCAATTCAGTTGAGGCAGAACT
	Forward	ACACTCCAGCTGGGTTACAGTGGCTAAGTT
rno-miR-17-1-3p	Reverse transcription	CTCAACTGGTGTCTGTGGAGTCGGCAATTCAGTTGAGCCACAAGT
	Forward	ACACTCCAGCTGGGACTGCAGTGAAGGCACCTT
rno-miR-217-5p	Reverse transcription	CTCAACTGGTGTCTGTGGAGTCGGCAATTCAGTTGAGCCAGTCAG
	Forward	ACACTCCAGCTGGGTTACTGCATCAGGAACTGA
Foxo1-GSDMD-ChIP	Forward	AGAGGCAGAGGCAGGTGAAT
	Reverse	GCCAATGGCTAAAGGACAAA
GSDMD (MSP)	M-F	TTCAGATCTTTTACTATGGCCCC
	M-R	CAGCCTGCCCTAGCCTTCTC
	U-F	TTTAGATTTTTTATTATGGTTTTGGTGT
	U-R	CAACCTACCCTAACCTTCTCCTC

eluted using ChIP elution buffer at 65°C for 30 min, and DNA were decross-linked from proteins using proteinase K (Cell Signaling Technology) at 65°C for 2 h. The products were used for PCR of GSDMD gene using the primer pairs listed in Table 1. PrimeSTAR® HS DNA Polymerase (Takara) and a SYBR Green qPCR SuperMix kit (DBI Bioscience, Shanghai, China) were employed for PCR amplification. The DNA samples obtained were purified and subjected to PCR analysis and 2% agarose gel (Biowest, Nuaille, France). All the reactions were performed in triplicate.

**2.18. Statistical Analyses.** All the data were expressed as mean ± standard deviation. Statistical analysis was performed using GraphPad Prism 8.0 (San Diego, CA, USA). Unpaired *t*-test or one-way ANOVA followed by Tukey's post hoc test was used to analyze differences between two groups and among more than three groups, respectively. Difference at  $p < 0.05$  was considered as statistically significant.

### 3. Results

**3.1. Isolation and Identification of CMEC and Exosomes.** The isolated CMECs from the rat left ventricle were CD31-positive with a purity of >90% (SupplementaryFigure 1). TEM images showed exosomes isolated from CMEC under normal and hypoxic conditions were of the expected structure and size ranging from 50 to approximately 150 nm (Figure 1(a)). NanoSight NTA showed that hypoxic conditions induced a fraction of exosomes in a range of 200~300 nm (Figure 1(b)). Western blot analysis validated high expressions of exosomal biomarkers (CD63,

CD81, and TSG101 proteins) in the isolated vesicles (Figure 1(c)).

**3.2. Hypoxic CMEC-Derived Exosomes Prevent I/R Injury and Pyroptosis and Increases miR-27b-3p Expression.** To investigate the effect of hypoxic CMEC-derived exosomes on I/R injury, we injected exosomes into the heart of rats before I/R surgery. Significant MI area in the rat heart in the I/R group was seen (Figure 2(a)). The pretreatment with CMEC-derived exosomes (normal and hypoxic conditions) significantly reduced infarct area (Figure 2(a)). Western blot confirmed that the expression of Foxo1, GSDMD, NLRP3, and caspase-1 proteins were upregulated in peri-infarct tissues after I/R injury (Figure 2(b)), while pretreatment with hypoxic CMECs-derived exosomes significantly attenuated these changes (Figure 2(b)). I/R injury increased the secretion of CK, LDH, IL-1 $\beta$ , and IL-18 ( $p < 0.01$  vs. sham, Figure 2(c)). However, these changes were greatly prevented by intramyocardial injection of CMEC-derived exosomes, especially that from hypoxic CMECs. As for the effect of hypoxic exosomes on miRNAs, we found that the expression of miR-27b-3p, miR-17-1-2p, and miR-217-3p were downregulated in the periphery of the infarct zone after I/R injury (Figure 2(d)). However, the administration of CME-derived exosomes significantly reversed their expression ( $p < 0.05$ ). As expected, the stimulation of hypoxic conditions was photographically confirmed by PCR analysis on the expression of miR-27b-3p, miR-17-1-2p, and miR-217-3p in CMECs (Figure 2(e)). miR-27b-3p expression was upregulated by hypoxia by 6-fold compared to normal condition ( $p < 0.0001$ ); therefore, miR-27b-3p was selected to further study.

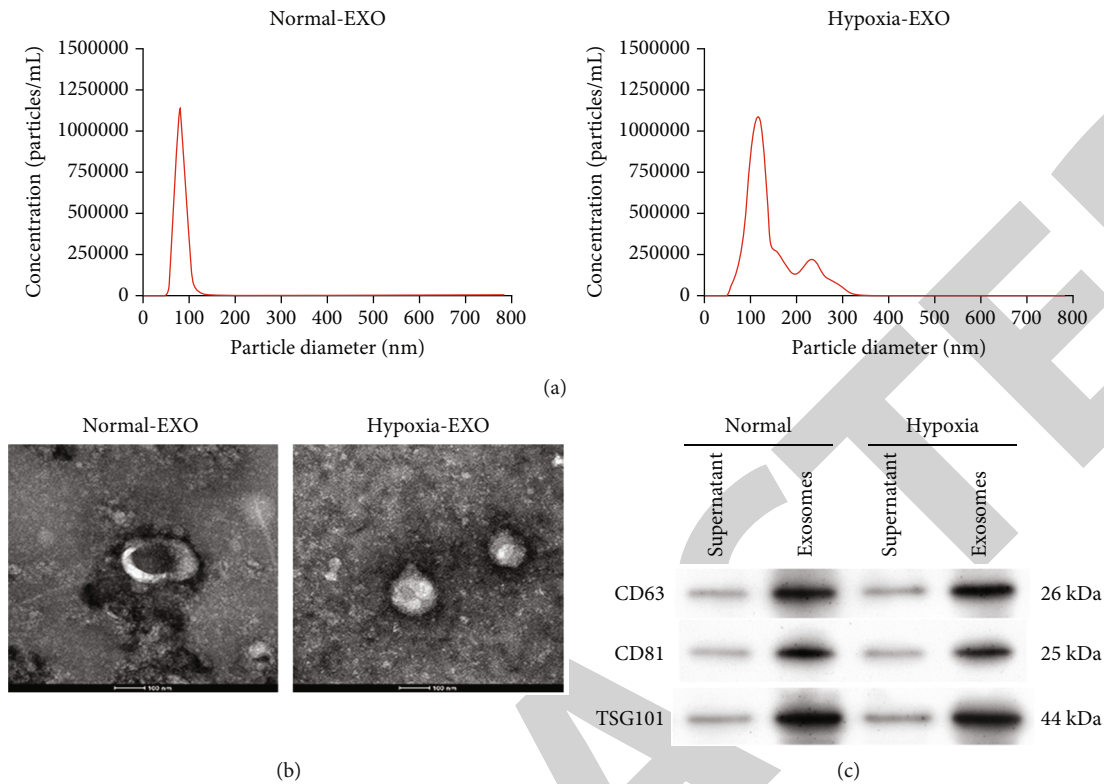


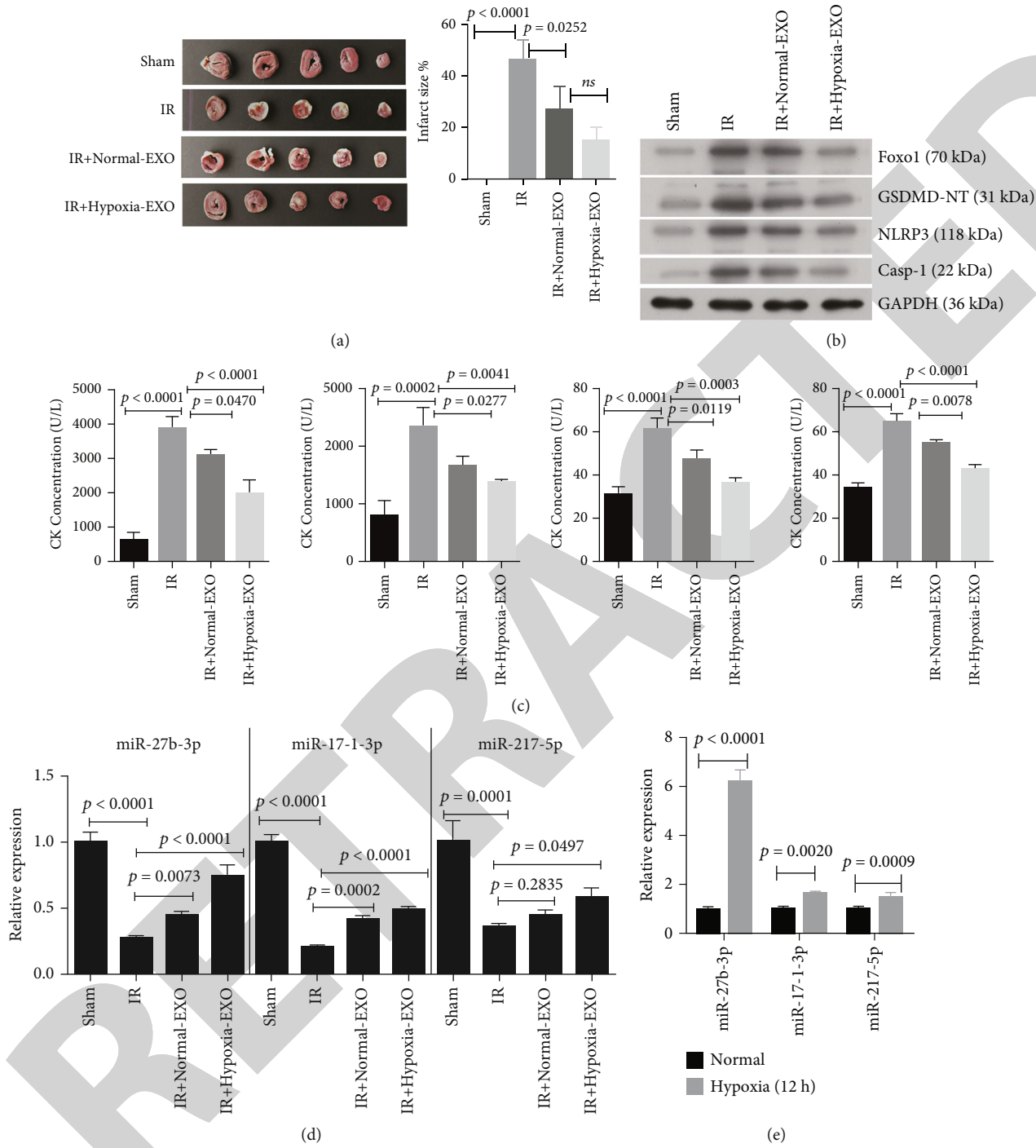
FIGURE 1: The extraction and identification of exosomes. (a) The size of exosomes derived from CMECs in normal and hypoxic conditions. (b) The transmission electron microscopy (TEM) result for determining the exosomal morphology (scale bar = 100 nm). The figures are generated from NanoSight nanoparticle tracking analysis (NTA). (c) The expression of exosomal markers CD63, CD81, and TSG101 by Western blot analysis. EXO: exosomes.

**3.3. Hypoxic CMEC-Derived Exosomes Protect H9C2 Cells against H/R Injury via miR-27b-3p.** We found that the expression of miR-27b-3p in patients' plasma was significantly higher than that in normal people (Figure 3(a)). To confirm whether the effect of CMEC-derived exosomes on I/R injury was mediated by the upregulation of miR-27b-3p, the expression of miR-27b-3p was inhibited in CMECs. After transfection with miR-27b-3p inhibitor, the expression of miR-27b-3p was significantly inhibited in normal and hypoxic CMEC-derived exosomes (Figure 3(b)). In addition, the repair ability of hypoxic CMEC-derived exosomes on miR-27b-3p expression in the H9C2 H/R model was weakened by miR-27b-3p inhibitor compared to negative control (NC,  $p = 0.0138$ ; Figure 3(c)). Immunofluorescence analysis showed the F-actin cytoskeleton was obviously reduced in H9C2 cells after H/R injury (Figure 3(d)). By contrast, the addition of CMEC-derived exosomes greatly upregulated F-actin expression, which was then downregulated by miR-27b-3p inhibitor (Figure 3(d)). The cellular uptake of PKH67-labeled exosomes into H9C2 cells was confirmed (Figure 3(d)), indicating that H9C2 cells successfully absorbed and integrated CMEC-derived exosomes.

We also confirmed that H/R injury significantly reduced the cell proliferation of H9C2 cells ( $p < 0.0001$ , Figure 3(g)). However, the addition of hypoxic CMEC-derived exosomes significantly rescued H/R injury-inhibited H9C2 cell proliferation. In comparison with exosomes with normal miR-

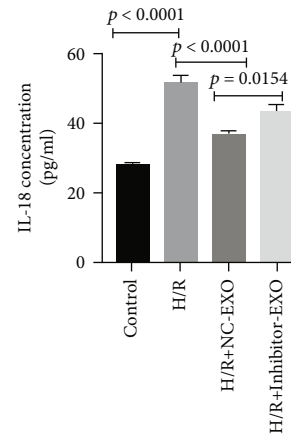
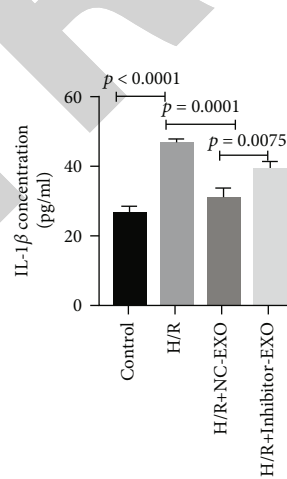
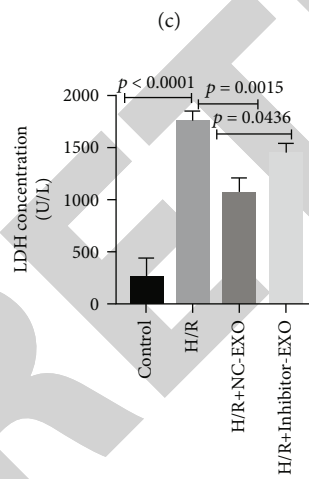
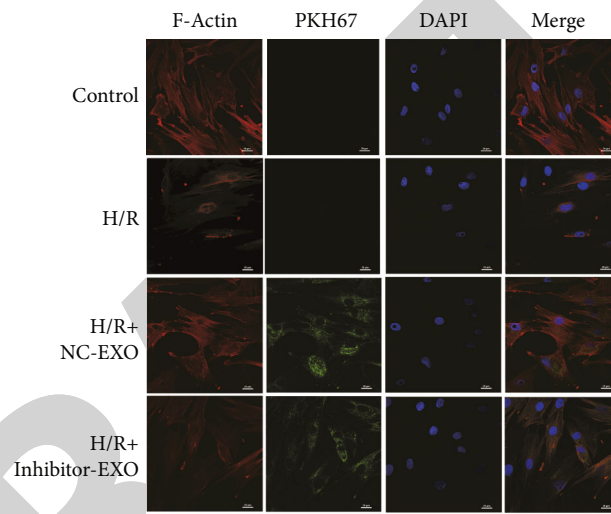
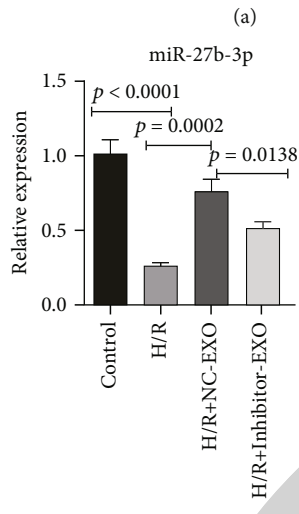
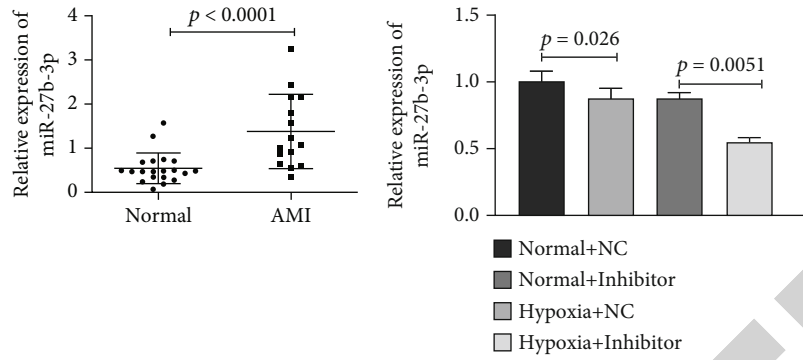
27b-3p expression, those with inhibited miR-27b-3p expression had a significant lower effect on rescuing H9C2 cell proliferation from H/R injury ( $p = 0.0117$ , Figure 3(g)). Reverse results were found in the production of cellular LDH and cytokines (IL-1 $\beta$  and IL-18, Figure 3(e)). The productions of LDH, IL-1 $\beta$ , and IL-18 in H9C2 cell culture medium and the expressions of Foxo1, GSDMD, NLPR3, and caspase-1 proteins in H9C2 cells were significantly promoted by H/R injury ( $p < 0.0001$ , Figure 3(f)). Treatment with hypoxic CMEC-derived exosomes significantly reduced their elevation in the H9C2 H/R model. However, the inhibition of miR-27b-3p showed a weaker effect on reducing H/R-induced changes ( $p < 0.05$ , Figure 3(f)). By detecting the expression of oxidative stress-related factors of ROS and SOD in H9C2 cells after hypoxia-reoxygenation treatment, the results showed that hypoxia treatment induced the increase of ROS and the decrease of SOD secretion, CMEC-derived exosomes greatly upregulated ROS expression, which was then downregulated by miR-27b-3p inhibitor; however, the expression of extracellular SOD was the opposite (Figure 3(h)). These results indicated that miR-27b-3p played a role in promoting the protective effect of CMEC-derived exosomes against H/R injury.

**3.4. miR-27b-3p in Hypoxic CMEC-Derived Exosomes Attenuates H/R-Induced Injury and Pyroptosis in H9C2 Cells by Targeting Foxo1.** We also found there were opposite



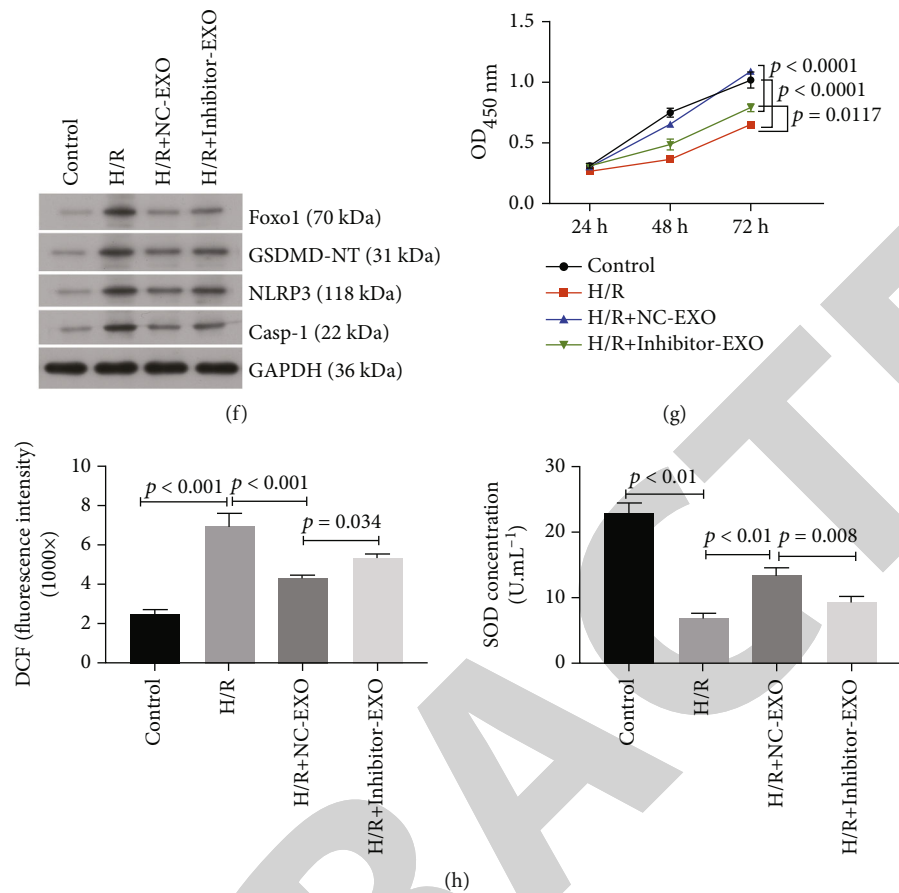
**FIGURE 2: CMEC-derived exosomes prevent I/R injury and pyroptosis in the rat heart.** Exosomes (EXO) were injected into the rat heart (intramyocardial injection). (a) TTC staining was used for the indication of the infarcted size in the rat heart. (b) The expression of Foxo1 protein and pyroptosis-related proteins in heart of rat with different treatments ( $n = 3$ ). (c) The production of serum creatine kinase (CK), lactate dehydrogenase (LDH), interleukin- (IL-) 1 $\beta$ , and IL-18 by ELISA assay ( $n = 5$ ). (d) The relative expression of miR-27b-3p, miR-17-1-2p, and miR-217-3p in heart of rat with different treatments ( $n = 5$ ). (e) The relative expression of miR-27b-3p, miR-17-1-2p, and miR-217-3p in exosomes from CMECs cultured under normal and hypoxic conditions, respectively ( $n = 3$ ). The sham group ( $n = 5$ ), without ligation and reperfusion; the I/R group ( $n = 5$ ), ischemia-reperfusion injury. The I/R+normal-EXO group ( $n = 5$ ), exosomes, rats were administrated with exosomes ( $10 \mu\text{l}$ ,  $6 \times 10^{12}$  particles; intramyocardial injection) derived from CMECs cultured under normal conditions; the I/R+hypoxia-EXO group ( $n = 5$ ), rats were administrated with exosomes ( $10 \mu\text{l}$ ,  $6 \times 10^{12}$  particles; intramyocardial injection) derived from CMECs cultured under hypoxic conditions.





(e)

FIGURE 3: Continued.



**FIGURE 3:** miR-27b-3p is necessary for the cytoprotection of exosomes derived from CMECs in H9C2 cells. (a) The relative expression level of miR-27b-3p in patients and normal people ( $n = 16$ ). (b) The relative expression level of miR-27b-3p in exosomes derived from CMECs cultured under hypoxic conditions with and without miRNA inhibitors ( $n = 3$ ). (c) The relative expression level of miR-27b-3p in H9C2 cells with different treatments ( $n = 3$ ). (d) Fluorescence analysis for the effect of the uptake of PKH67-labeled exosomes to the cytoskeleton of H9C2 cells. Scale bar = 20  $\mu\text{m}$ . (e) ELISA assay of the lactate dehydrogenase (LDH), interleukin- (IL-) 1 $\beta$ , and IL-18 in H9C2 cell culture medium ( $n = 3$ ). (f) The expression of Foxo1 protein and pyroptosis-related proteins in H9C2 cells with different treatments. (g) Result of cell viability using CCK8 assay ( $n = 3$ ). (h), the expression of ROS and SOD in H9C2 cells after different treatments. H/R: hypoxia/reoxygenation condition (2 h hypoxia: 5%  $\text{CO}_2$ , and 95%  $\text{N}_2$ ; and 4 h normal conditions: 95% air plus 5%  $\text{CO}_2$ ). EXO: exosomes. NC-EXO or inhibitor-EXO indicated exosomes were derived from CMECs with pretreatment of negative control (NC) or miR-27b-3p inhibitor in hypoxic conditions.

expression pattern between miR-27b-3p and Foxo1 at the gene level (Figure 4(a)). The target pair between miR-27b-3p and Foxo1 gene was predicted using TargetScan database (Figure 4(b)) and then validated using the dual-Luciferase Reporter assay (Figure 4(c)). *In vitro* experiments were performed and H9C2 cells were treated with Foxo1 transfection, followed by transfection with miR-27b-3p inhibitor, H/R, and incubation with hypoxic CMEC-derived exosomes. The expression levels of miR-27b-3p and Foxo1 were found to be correlated in H9C2 cells. The expression of Foxo1 mRNA in the H9C2 H/R cell model was upregulated by the transfection with Foxo1 plasmid ( $p < 0.0001$  for H/R+vector+NC-EXO versus H/R+Foxo1+NC-EXO, or H/R+vector+inhibitor-EXO versus H/R+Foxo1+inhibitor-EXO; Figure 4(d)), and this change was further enhanced by the miR-27b-3p inhibitor ( $p = 0.0003$  for H/R+vector+inhibitor-EXO versus H/R+vector+NC-EXO, and  $p = 0.0002$  for H/R+Foxo1+inhibitor-EXO versus H/R+Foxo1+NC-EXO).

We observed a negative feedback loop between miR-27b-3p and Foxo1, as the expression of miR-27b-3p in H9C2 cells was downregulated by its inhibitors and Foxo1 overexpression ( $p < 0.01$ , Figure 4(e)).

Following Foxo1 overexpression, the expressions of F-actin and cell proliferation of H9C2 cells were inhibited (Figures 4(f) and 4(g)). The fluorescence intensity of F-actin protein and cell viability of H9C2 cells were reduced by Foxo1 expression (H/R+vector+NC-EXO>H/R+vector+inhibitor-EXO>H/R+Foxo1+NC-EXO>H/R+Foxo1+inhibitor-EXO). In addition, the expression of GSDMD, NLRP3, and caspase-1 proteins and the production of LDH, IL-1 $\beta$ , and IL-18 in H9C2 cells were increased accompanied with Foxo1 expression level (Figures 4(h) and 4(i)). These factors were increased by all treatments, especially by H/R+Foxo1+inhibitor-EXO. These results indicated that the overexpression of Foxo1 impaired the protective effect of hypoxic CMEC-derived exosomes in H9C2 cells and that

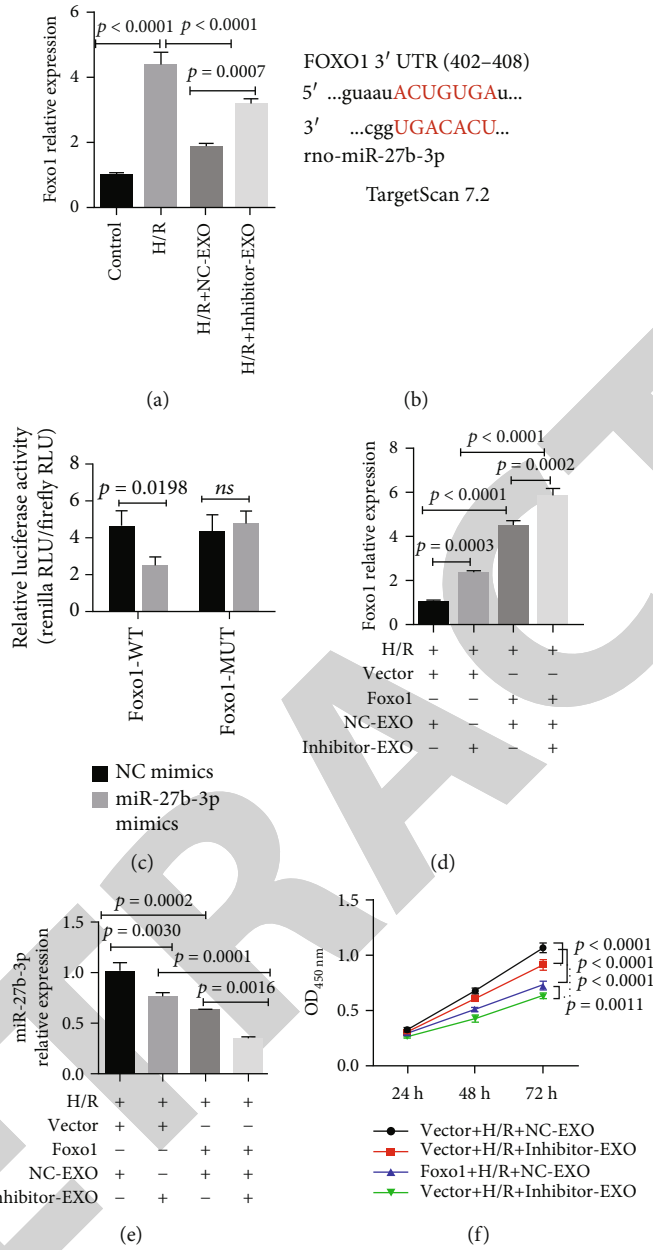
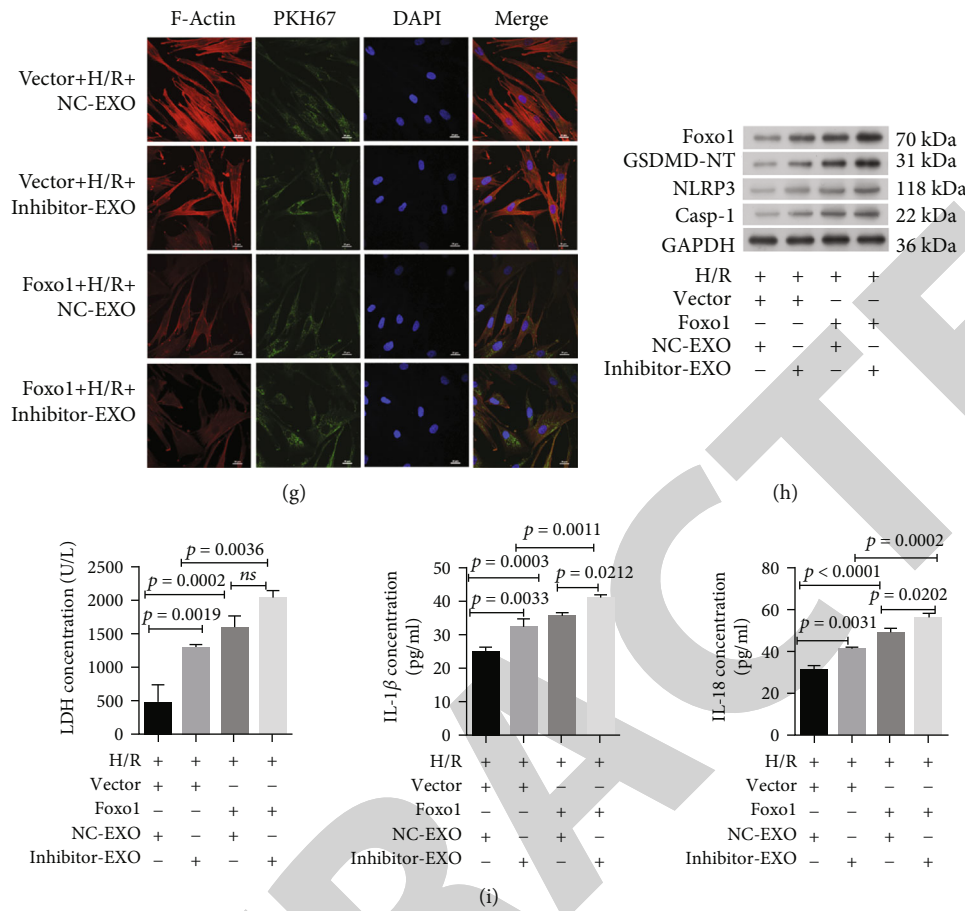


FIGURE 4: Continued.



**FIGURE 4:** miR-27b-3p in hypoxic CMEC-derived exosomes attenuates H/R-induced injury and pyroptosis in H9C2 cells by targeting Foxo1. (a) The relative expression of Foxo1 in H9C2 cellular model under different treatments ( $n = 3$ ). (b) The predictive targeting site of miR-27b-3p at the 3'UTR region of Foxo1 gene. Prediction was conducted in Targetscan Human database. (c) The Dual-Luciferase Reporter assay reported the interaction between Foxo1 and miR-27b-3p ( $n = 3$ ). (d) The relative expression of Foxo1 in H9C2 cellular model in response to Foxo1 overexpression ( $n = 3$ ). (e) Overexpression of Foxo1 decreased miR-27b-3p expression in the H9C2 H/R cell model ( $n = 3$ ). This result shows a negative feedback between miR-27b-3p and Foxo1. (f) Overexpression of Foxo1 decreased the protective effects of exosomes on the cell viability of the H9C2 H/R cell model ( $n = 3$ ). (g) Fluorescence analysis for the effect of the uptake of PKH67-labeled exosomes to the cytoskeleton of the H9C2 cell model with pretreatment of Foxo1 plasmids. Scale bar = 20  $\mu$ m. (h) Western blot analysis of the expression of Foxo1 protein and pyroptosis-related proteins. (i) Overexpression Foxo1 upregulated the production of lactate dehydrogenase (LDH), interleukin- (IL-) 1 $\beta$ , and IL-18 in the supernatant fluid of the H9C2 H/R cell model in response to exosomes ( $n = 3$ ). H/R: hypoxia/reoxygenation (2 h hypoxia: 5% CO<sub>2</sub> and 95% N<sub>2</sub> and 4 h normal condition: 95% air plus 5% CO<sub>2</sub>). Caspase-1, EXO: exosomes. NC-EXO or inhibitor-EXO indicated exosomes were derived from CMECs with pretreatment of negative control (NC) or miR-27b-3p inhibitor in hypoxic conditions.

the protective effects of miR-27b-3p in hypoxic CMEC-derived exosomes against H/R injury in H9C2 cells were mediated partially through decreasing Foxo1.

**3.5. Foxo1 Expression Impairs the Protective Effect of Hypoxic CMEC-Derived Exosomal miR-27b-3p against In Vivo I/R Injury and Promotes Pyroptosis.** We first determined that the treatments with injection of lentiviral plasmid carrying Foxo1 and hypoxic CMEC-derived exosomes with the miR-27b-3p inhibitor obviously suppressed the protective effect of hypoxic CMEC-derived exosomes against I/R injury (Figure 5). The results showed that the expression of miR-27b-3p in the peri-infarct tissues in the rat heart was obviously decreased by injection of lentiviral plasmid carrying Foxo1 and hypoxic CMEC-derived exosomes transfected

with miR-27b-3p inhibitors (Figure 5(a)). The expression level of miR-27b-3p in the rat heart was decreased sequentially from the greatest to the lowest by I/R+vector+NC-EXO, I/R+vector+inhibitor-EXO, I/R+Foxo1+NC-EXO, and I/R+Foxo1+inhibitor-EXO. After the I/R model was established, lentiviral plasmid expressing Foxo1 and exosomes (EXO) were injected into the rat heart. We found that the infarct area in rat hearts were increased by Foxo1 expression ( $p = 0.0302$  between I/R+Foxo1+NC-EXO and I/R+vector+NC-EXO, and  $p < 0.01$  between I/R+Foxo1+inhibitor-EXO and I/R+vector+inhibitor-EXO; Figure 5(b)). Lentiviral plasmid expressing Foxo 1 and exosomes (EXO) were injected into the rat heart, and then, the I/R model was established. The results showed that the ischemic areas in rat hearts were increased by Foxo1 expression

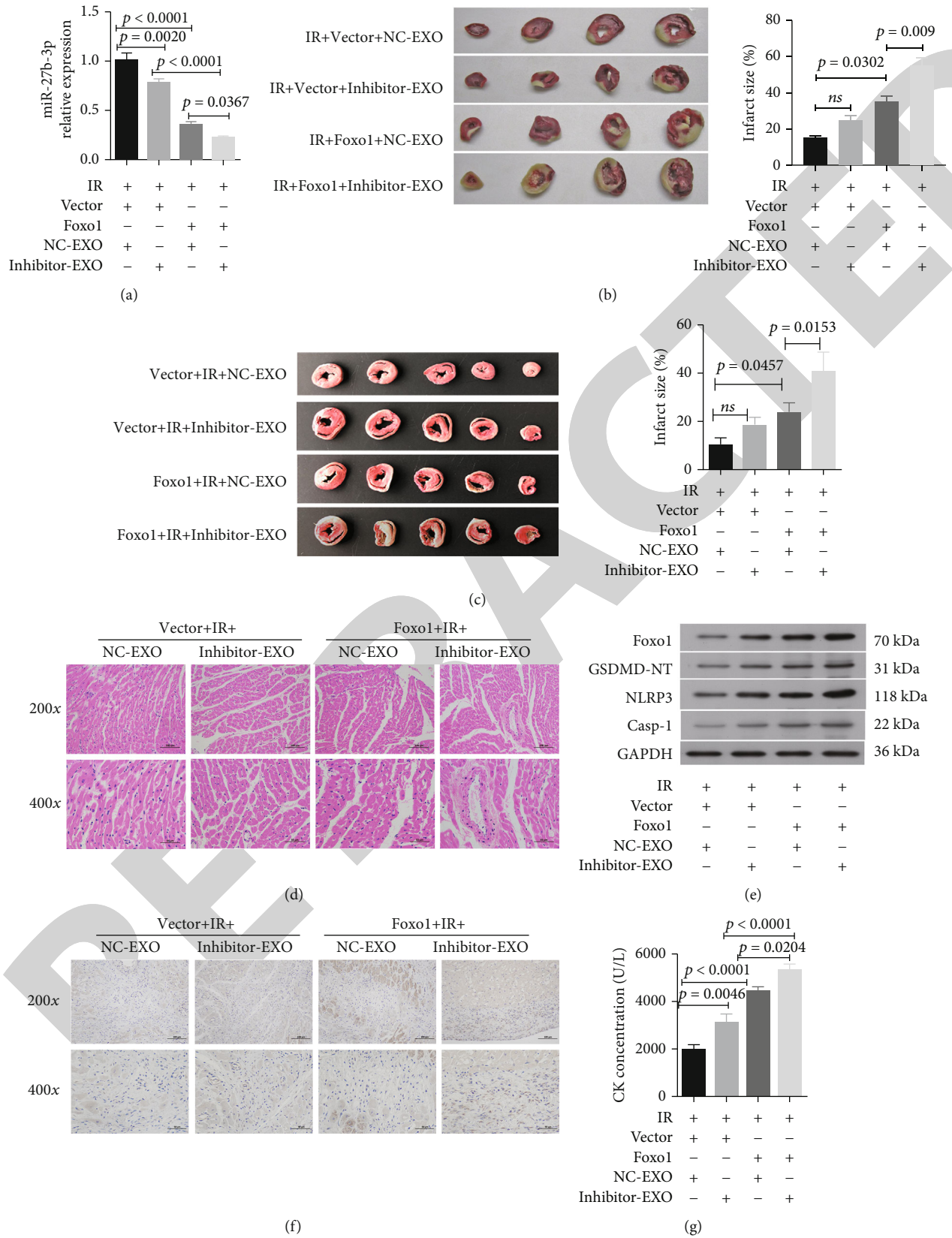


FIGURE 5: Continued.

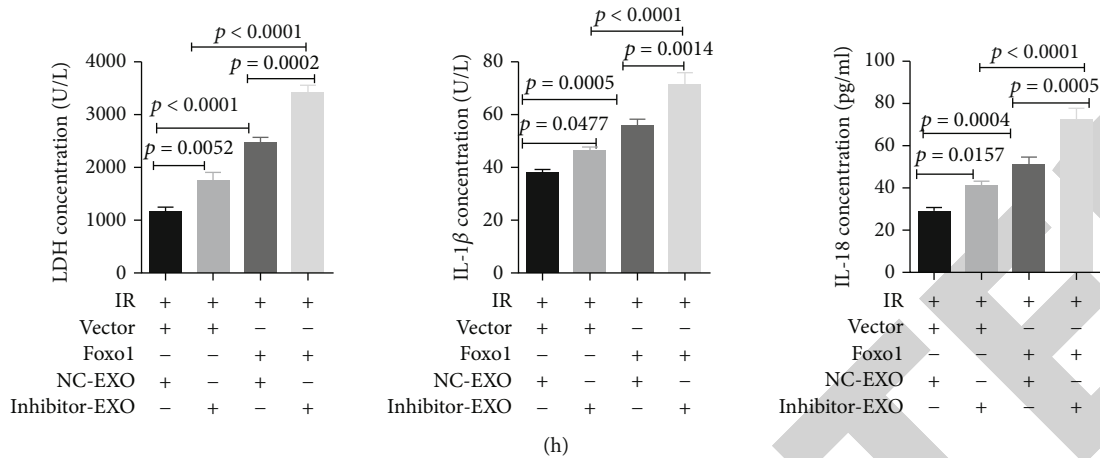


FIGURE 5: miR-27b-3p inhibition and Foxo1 expression synergistically promotes I/R injury in rat heart. (a) The relative expression level of miR-27b-3p in peri-infarct heart tissues after I/R injury ( $n = 4$ ). (b) The images and statistical results of infarcted sizes in rat heart (after the I/R model was established, lentiviral plasmid expressing Foxo 1 and exosomes (EXO) were injected into rat heart) ( $n = 4$ ). (c) The images and statistical results of infarcted sizes in the rat heart (lentiviral plasmid expressing Foxo 1 and exosomes (EXO) were injected into rat heart; then, I/R model was established) ( $n = 5$ ). (d) The representative images of histology (HE staining) of rat heart tissues (magnification,  $\times 200$ ,  $\times 400$ ; scale bar: 100, 50  $\mu\text{m}$ , respectively). (e) Western blot analysis of Foxo1 and pyroptosis-related proteins in the rat heart in response to different treatments. (f) The representative images of Foxo1 immunohistochemistry (magnification,  $\times 200$  and  $\times 400$ ; scale bar = 100 and 50  $\mu\text{m}$ , respectively). (g, h) The serum level of creatine kinase (CK), lactate dehydrogenase (LDH), interleukin- (IL-) 1 $\beta$ , and IL-18 in the rat heart ( $n = 5$ ).

( $p = 0.0457$  between Foxo1+I/R+NC-EXO and vector+I/R+NC-EXO, and  $p < 0.01$  between Foxo1+I/R+inhibitor-EXO and vector+I/R+inhibitor-EXO; Figure 5(c)). The miR-27b-3p inhibitor in hypoxic CMEC-derived exosomes showed a significant contribution to ischemic areas ( $p = 0.153$  between Foxo1+I/R+NC-EXO and Foxo1+I/R+inhibitor-EXO). HE staining of rat heart tissues indicated that pretreatment with Foxo1 plasmids counteracted the proactive effect of hypoxic CMEC-derived exosomes against fibrous hyperplasia, infiltration of inflammation cells, and increased disarrangement of myocardial cells (Figure 5(d)). Western blotting analysis showed that the expression of Foxo1, GSDMD, NLRP3, and caspase-1 proteins in peri-infarct tissues were increased by Foxo1 expression and miR-27b-3 inhibition (Figure 5(e)). The proportion of caspase-1-positive cells in the heart (Figure 5(f)) and the contents of serum CK, LDH, IL-1 $\beta$ , and IL-18 were increased in the same order (Figures 5(g) and 5(h)). The pretreatment with Foxo1 plasmids and miR-27b-3p inhibitor, especially the combined treatment of the two, significantly increased the production of pyroptosis-related proteins and serum CK, LDH, IL-1 $\beta$ , and IL-18. These results confirmed that the pretreatment with Foxo1 plasmids counteracted the proactive effect of hypoxic CMEC-derived exosomes against I/R injury in the rat model.

**3.6. Foxo1 Controls GSDMD Promoter Methylation and Histone Acetylation.** Using MSP assay, we confirmed the transfection of miR-27b-3p mimics into H9C2 cells promoted methylation of the promoter region of the GSDMD gene, while the miR-27b-3p inhibitor reduced methylation level (Figure 6(a)). Next, the two binding sites of Foxo1 in the promoter region of GSDMD were predicted in JASPAR

database (Figure 6(b)). Dual-Luciferase Reporter assay confirmed that the interaction between GSDMD promoter and Foxo1. We found the relative luciferase activities of dual-luciferase reporter carrying the wild-type binding sites of Foxo1 were greatly increased after the transfection of Foxo1 expressing plasmids (pcDNA-Foxo1,  $p < 0.0001$ , Figure 6(c)). No influence was found in the dual-luciferase reporters carrying the mutant binding sites of Foxo1. These results suggested the positive interaction between Foxo1 and GSDMD. ChIP-PCR showed that the expression of the GSDMD gene was downregulated in H9C2 cells treated with exosomes from hypoxic CMECs, whereas the inhibition of miR-27b-3p in hypoxic CEMCs partially rescued the expression of GSDMD (Figure 6(d)). The transfection with Foxo1 plasmids promoted relative higher level of H3K9AC antibody-captured DNA fragments of Foxo1 and decreased the level of HDAC2 antibody-captured DNA fragments (Figures 6(e) and 6(f)).

## 4. Discussion

Therapy methods using ECs, MSCs, and CPCs have made significant improvement in the treatment of I/R injury in preclinical experiments [11–16]. The underlying mechanism was associated with the alleviation of NLRP3 inflammasome-induced pyroptosis [16]. Inflammasome-induced pyroptosis after I/R injury could accelerate cardiac cell death, thereby aggravating I/R injury [9, 10]. Our present study analyzed the role of hypoxic CMECs-derived exosomes in myocardial regeneration after I/R injury, which were found to be associated with inflammasome-induced pyroptosis via miR-27b-3p-Foxo1 signaling.

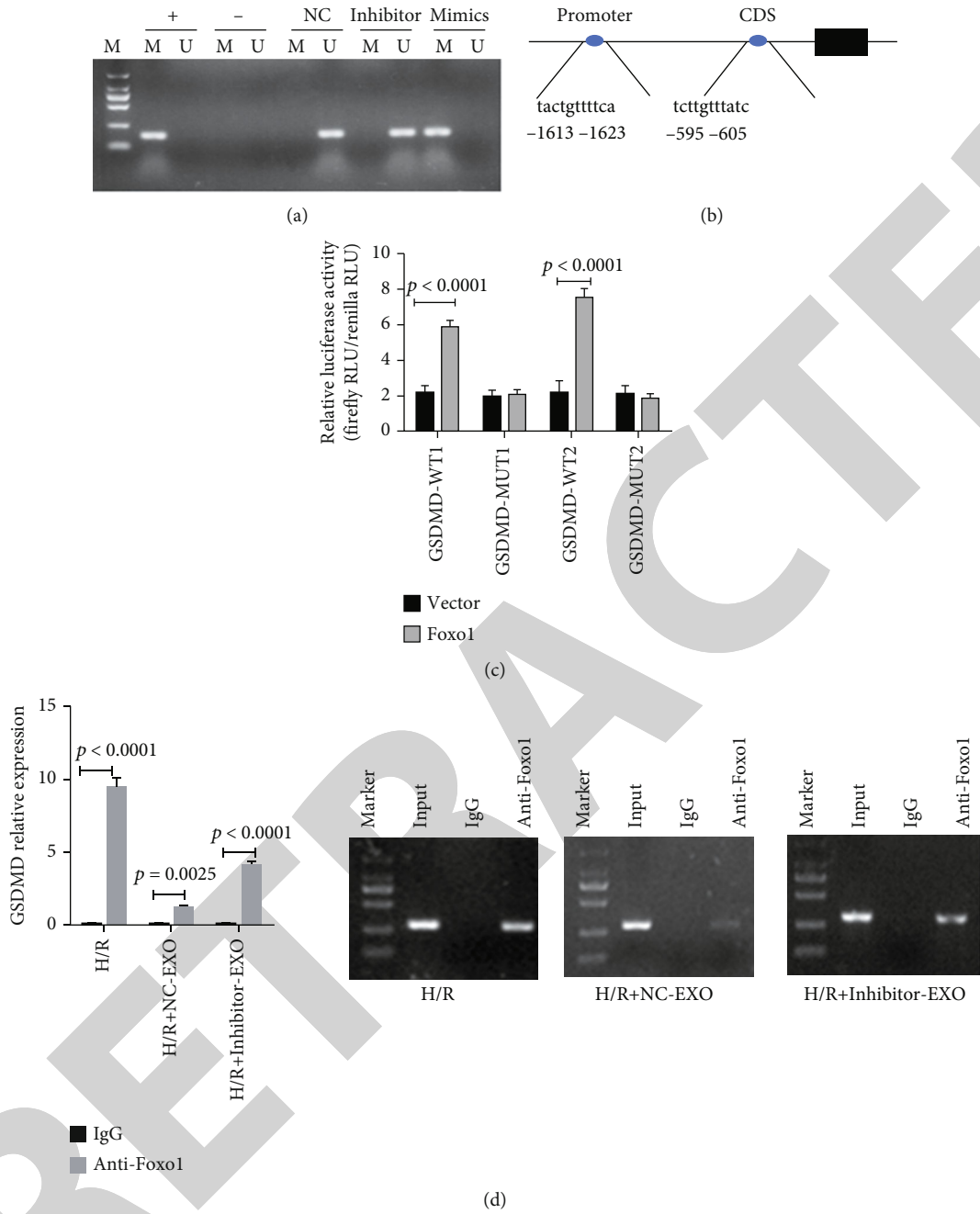


FIGURE 6: Continued.

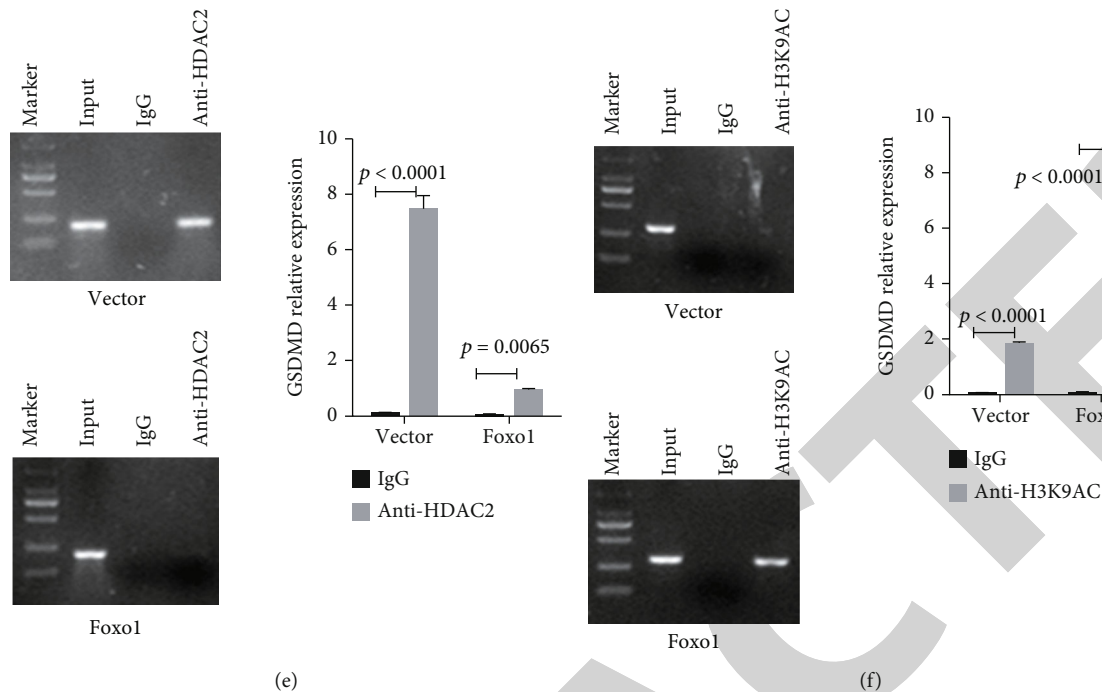


FIGURE 6: miR-27b-3p controls the methylation of GSDMD promoter and Foxo1 promotes histone acetylation of GSDMD. (a) H9C2 cells were transfected with mi-27b-3p mimics or inhibitor; the methylation status of GSDMD promoter were detected by MSP. (b) The two predicted binding sites of Foxo1 in the promoter of the GSDMD gene. Their binding activity is predicted in JASPAR. (c) The Dual-Luciferase Reporter assay confirmed the interaction between Foxo1 and GSDMD at the two sites ( $n = 3$ ). (d) The inhibition of miR-27b-3p in exosome derived from hypoxic CMECs increased the enrichment of GSDMD DNA ( $n = 3$ ). (e, f) The ChIP-PCR results of GSDMD in 293 cells treated with Foxo1 expressing plasmids ( $n = 3$ ).

Hypoxia-elicited stem cell-derived exosomes show profound cardiac repair effect [31, 32]. In the damaged heart, exosomal miRNAs, especially those under hypoxia conditions, have demonstrated therapeutic values in several types of cells, including cardiomyocyte and CPCs [20, 22, 33]. Gray et al. showed the exosomes isolated from hypoxic CPCs improved tube formation ability of cardiac endothelial cells compared with exosomes derived from normal CPCs [22]. Moreover, they also identified that a cluster of miRNAs (miR-17, miR-103, and miR-15b) were upregulated in response to hypoxic conditions. miR-27b-3p is a tumor suppressor downregulated in several types of human cancers, including lung cancer [34], glioma [35], and breast cancer [36]. The feature of miR-27b-3p downregulation in patients with heart transplant rejection was previously identified [37]. The downregulation of miR-27b-3p in mouse cardiac fibroblasts was correlated with cardiac fibrosis [37]. At present, the relative expression of miR-27b-3p in cardiac endothelial cells and cardiomyocytes is still unclear. We demonstrated that the expression of miR-27b-3p in the rat heart was downregulated after I/R injury. The decreased expression of miR-27b-3p was associated with aggravated *in vitro* H/R injury of H9C2 cells and *in vivo* I/R injury of the rat heart.

Previous studies indicated the stimulation of hypoxia on a cluster of miRNAs and proteins with cytoprotection and proangiogenic effects [20, 22, 33]. miR-27b-3p exhibits various effects on drug metabolism, adipocyte differentiation, epididymal fat browning, acute kidney injury, and chemore-

sistance of tumor cells [38–41]. The fact that miR-27b-3p expression was upregulated in H9C2 cells under hypoxic conditions was in line with the results from previous studies [21–23, 25]. We determined that H9C2 cells *in vitro* or cardiomyocytes *in vivo* carrying hypoxic CMEC-derived exosomes had higher efficacy in alleviating I/R injury-induced inflammation, inflammation-mediated pyroptosis, and inhibition of cardiomyocyte proliferation when compared with exosomes derived from CMECs cultured under normal conditions.

Here, in our study, we confirmed that miR-27b-3p-mediated protective effect against I/R injury was mediated by Foxo1/GSDMD axis and NLRP3/caspase-1-induced pyroptotic cell death. NLRP3 inflammasome activation-mediated pyroptosis promotes myocardial I/R injury [10]. Huang et al. reported that emodin could reduce pyroptosis via suppressing the TLR4/MyD88/NF- $\kappa$ B/NLRP3 inflammasome pathway, H/R-activated pyroptosis, and that NF- $\kappa$ B or the NLRP3 inflammasome inhibitor reduced the expression of GSDMD-N and downregulated the expression of IL-1 $\beta$  [42]. Pyroptosis is mainly mediated by NLRP3 inflammasome-induced activation of caspase-1- and GSDMD-dependent secondary pyroptosis. Cellular damage, toxins, and infections can lead to the activation of inflammasome including Toll-like receptor 4 (TLR4) and NLRP3 [19], which recruit caspase-1 and then promote the production of pro-inflammatory cytokines such as IL-1 $\beta$  and IL-18 or activate GSDMD-mediated secondary pyroptosis [43–45] (Figure 7). Pyroptotic cells will subsequently release more inflammatory cytokines and toxins and



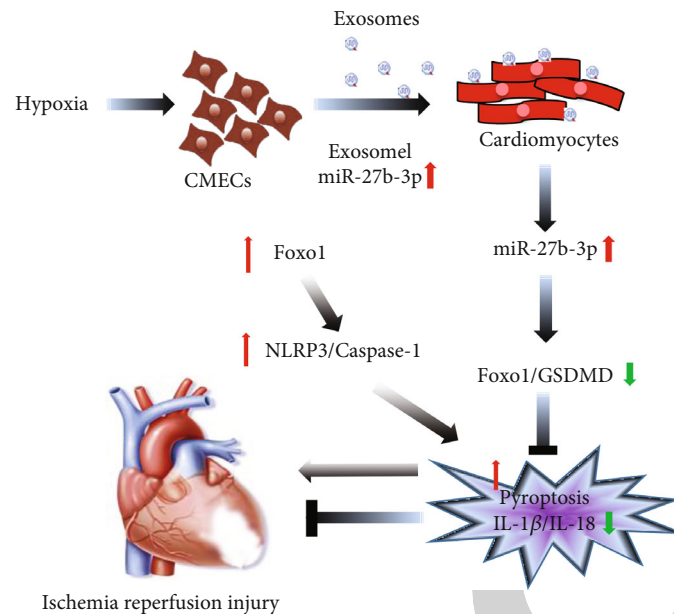


FIGURE 7: The supposed schematic diagram of miR-27b-3p-Foxo1 mediated pyroptosis mechanism in I/R injury. Foxo1 expression on one hand induces GSDMD-mediated pyroptosis by activating the histone acetylation of GSDMD and, on the other hand, promotes NLRP3/caspase-1-mediated pyroptosis. Hypoxic CMECs-derived exosomes carrying high level of miR-27b-3p counteracted these interactions.

stimulate the inflammatory and host defense responses and the injury [46]. Ge et al. demonstrated GSDMD-induced pyroptosis in myocardial I/R injury and that cardiomyocyte pyroptosis is mainly regulated via the caspase-11/GSDMD signaling pathway under oxidative stress conditions. Oxidative stress triggers GSDMD (gasdermin D) cleavage via CASP-11 (caspase-11). GSDMD-N oligomerizes and perforates the plasma membrane to mediate pyroptotic cell death. GSDMD, GSDMD-N, GSDMD-C, and IL- (interleukin-) 18 are released into the supernatant or peripheral blood. RIP3 refers to receptor-interacting protein 3 [47]. Xiang et al. suggested that mice with GSDMD knockout showed significantly reduce infarct size and improved cardiac function and postinfarction survival via reducing the release of IL-1 $\beta$  from neutrophil as well as the number of neutrophil and monocytes in infarcted hearts. It has been shown that GSDMD is necessary in improving the mobilization of neutrophil in infarcted hearts [48]. Our present study demonstrated the miR-27b-3p from hypoxic CMEC-derived exosomes attenuated IL-1 $\beta$  and IL-18, NLRP3, GSDMD, and caspase-1 induced by I/R injury, while the inhibition of miR-27b-3p impaired the mediated protective effects on the H9C2 cells and rat model. These results showed that miR-27b-3p exerted the cardioprotective effect partially through alleviating pyroptosis.

Furthermore, miR-27b-3p-mediated cardioprotective and antipyroptosis effects were mediated by interacting with Foxo1 indirectly or directly promoting methylation of GSDMD promoter regions (Figure 7). Foxo1 acts as a transcription factor and has multiple functions through interacting with targets, including angiogenesis-related molecules [49]. Foxo1 could be influenced by various environmental stimuli including CK, oxidative stress, and hypoxia as well as various signaling such as Akt, NF- $\kappa$ B, STAT3, and ERK1/2 [50–52] and is cor-

related with cellular behaviors including cell proliferation, differentiation, autophagy, cell cycle distribution, apoptosis, and DNA repair [53]. NLRP3 inflammasome-mediated pyroptosis was associated with Foxo1 [54, 55]. Foxo1-induced expression of NLRP3 inflammasome has been well confirmed in diabetes and insulin resistance [56, 57]. In addition, Foxo1 overactivation is reported to exacerbate myocardial I/R injury, whereas its downregulation contributes to the attenuation of myocardial I/R injury [58]. Our present study demonstrated that NLRP3-caspase-1 was activated by Foxo1 and miR-27b-3p. We also confirmed the binding of Foxo1 to GSDMD promoter, which indicated a positive regulation of Foxo1 on GSDMD-related pyroptosis (Figure 7). These results suggested that Foxo1 activation and miR-27b-3p inhibition could contribute to I/R injury and that the miR-27b-3p-Foxo1-mediated pyroptosis was of great significance in the progression of I/R injury. By contrast, the expression of miR-27b-3p was a protective factor against I/R injury.

I/R injury includes several types of cell death, such as necrosis, apoptosis, and iron ptosis. At present, we have only preliminarily studied the effect of pyroptosis; therefore, further experimental evidence is needed to prove that miR-27b-3p specifically inhibited focal death rather than other forms of cell death.

There were some limitations in this study. The exosomes derived from CMEC cells *in vitro* did not fully reflect the exocrine secretion of CMEC cells *in vivo*, and the treatment of I/R model rats with exosomes derived from CMEC cells also had some limitations. However, the current finding suggested that miR-27b-3p could be targeted in clinical therapy for patients with myocardial infarction or be used in early diagnosis by detecting miR-27b-3p expression in the serum of patients with myocardial infarction.

## 5. Conclusions

In summary, our present study indicated that hypoxia-induced expression of miR-27b-3p in CMEC-derived exosomes plays a crucial role in alleviating I/R injury via targeting Foxo1. Such an effect was mediated by GSDMD and NLRP3/caspase-1 mediated oxidative stress and pyroptosis. These results highlighted the potential of using hypoxic CMEC-derived exosomes for the treatment or prevention of I/R injury.

## Data Availability

The data used in this research are available from the corresponding author on reasonable request.

## Ethical Approval

This protocol for this study was approved by the Ethical Committee of Animal Experimentation of the Second Xiangya Hospital, Central South University (Changsha, Hunan, China).

## Conflicts of Interest

All authors declare that they have no conflict of interests.

## Authors' Contributions

BJZ and QML participated in study design. BJZ performed all the experiments. BJZ, CS, and FB participated in the animal experiments. BJZ, CS, YZL, and TT assisted with data analysis. BJZ wrote the first draft of the manuscript. QML helped to improve the manuscript and provided the fund.

## Acknowledgments

This study was supported by the National Natural Science Foundation of China (nos. 82070356 and 82160050), Hunan Provincial Natural Science Foundation of China (no. 2021JJ30033), and Xinjiang Provincial Natural Science Foundation of China (no. 2020D01C138).

## Supplementary Materials

Supplementary Figure 1: the identification of the isolated CMEC. The expression of CD31<sup>+</sup> in isolated CMEC cells (magnification, ×200). (*Supplementary Materials*)

## References

- [1] A. Lejay, F. Fang, R. John et al., "Ischemia reperfusion injury, ischemic conditioning and diabetes mellitus," *Journal of Molecular and Cellular Cardiology*, vol. 91, pp. 11–22, 2016.
- [2] H. Cui, N. Li, X. Li et al., "Tongxinluo modulates cytokine secretion by cardiac microvascular endothelial cells in ischemia/reperfusion injury," *American Journal of Translational Research*, vol. 8, no. 10, pp. 4370–4381, 2016.
- [3] C. Zhang, D. F. Wang, Z. Zhang, D. Han, and K. Yang, "EGb 761 protects cardiac microvascular endothelial cells against hypoxia/reoxygenation injury and exerts inhibitory effect on the ATM pathway," *Journal of Microbiology and Biotechnology*, vol. 27, no. 3, pp. 584–590, 2017.
- [4] Y. Liu, K. Lian, L. Zhang et al., "TXNIP mediates NLRP3 inflammasome activation in cardiac microvascular endothelial cells as a novel mechanism in myocardial ischemia/reperfusion injury," *Basic Research in Cardiology*, vol. 109, no. 5, p. 415, 2014.
- [5] H. Zhu, Q. Jin, Y. Li et al., "Melatonin protected cardiac microvascular endothelial cells against oxidative stress injury via suppression of IP3R-[Ca<sup>2+</sup>]<sub>i</sub>/VDAC-[Ca<sup>2+</sup>]<sub>m</sub> axis by activation of MAPK/ERK signaling pathway," *Cell Stress and Chaperones*, vol. 23, no. 1, pp. 101–113, 2018.
- [6] M. Li, X. Li, J. Xin et al., "Effects of protein phosphorylation on color stability of ground meat," *Food Chemistry*, vol. 219, pp. 304–310, 2017.
- [7] J.-B. Xia, G. H. Liu, Z. Y. Chen et al., "Hypoxia/ischemia promotes CXCL10 expression in cardiac microvascular endothelial cells by NFκB activation," *Cytokine*, vol. 81, pp. 63–70, 2016.
- [8] Ø. Sandanger, T. Ranheim, L. E. Vinge et al., "The NLRP3 inflammasome is up-regulated in cardiac fibroblasts and mediates myocardial ischaemia-reperfusion injury," *Cardiovascular Research*, vol. 99, no. 1, pp. 164–174, 2013.
- [9] S. Toldo, A. G. Mauro, Z. Cutter, and A. Abbate, "Inflammasome, pyroptosis, and cytokines in myocardial ischemia-reperfusion injury," *American Journal of Physiology-Heart and Circulatory Physiology*, vol. 315, no. 6, pp. H1553–H1568, 2018.
- [10] Z. Qiu, S. Lei, B. Zhao et al., "NLRP3 inflammasome activation-mediated pyroptosis aggravates myocardial ischemia/reperfusion injury in diabetic rats," *Oxidative Medicine and Cellular Longevity*, vol. 2017, 17 pages, 2017.
- [11] Z. T. Dargani and D. K. Singla, "Embryonic stem cell-derived exosomes inhibit doxorubicin-induced TLR4-NLRP3-mediated cell death-pyroptosis," *American Journal of Physiology-Heart and Circulatory Physiology*, vol. 317, no. 2, pp. H460–H471, 2019.
- [12] J. Li, D. Sun, and Y. Li, "Novel findings and therapeutic targets on cardioprotection of ischemia/reperfusion injury in STEMI," *Current Pharmaceutical Design*, vol. 25, no. 35, pp. 3726–3739, 2019.
- [13] O. G. de Jong, B. W. M. Balkom, H. Gremmels, and M. C. Verhaar, "Exosomes from hypoxic endothelial cells have increased collagen crosslinking activity through up-regulation of lysyl oxidase-like 2," *Journal of Cellular and Molecular Medicine*, vol. 20, no. 2, pp. 342–350, 2016.
- [14] H. Xin, F. Wang, Y. Li et al., "Secondary release of exosomes from astrocytes contributes to the increase in neural plasticity and improvement of functional recovery after stroke in rats treated with exosomes harvested from microRNA 133b-overexpressing multipotent mesenchymal stromal cells," *Cell Transplantation*, vol. 26, no. 2, pp. 243–257, 2017.
- [15] H. Xin, Y. Li, Z. Liu et al., "MiR-133b promotes neural plasticity and functional recovery after treatment of stroke with multipotent mesenchymal stromal cells in rats via transfer of exosome-enriched extracellular particles," *Stem Cells*, vol. 31, no. 12, pp. 2737–2746, 2013.
- [16] Q. Mao, X. L. Liang, C. L. Zhang, Y. H. Pang, and Y. X. Lu, "LncRNA KLF3-AS1 in human mesenchymal stem cell-derived exosomes ameliorates pyroptosis of cardiomyocytes and myocardial infarction through miR-138-5p/Sirt1 axis," *Stem Cell Research & Therapy*, vol. 10, no. 1, p. 393, 2019.

- [17] M. Simons and G. Raposo, "Exosomes - vesicular carriers for intercellular communication," *Current Opinion in Cell Biology*, vol. 21, no. 4, pp. 575–581, 2009.
- [18] Z. T. Dargani and D. K. Singla, "Embryonic stem cell-derived exosomes inhibit doxorubicin-induced pyroptosis in cardiac cells," *The FASEB Journal*, vol. 33, no. S1, p. 705.2, 2019.
- [19] Z. Tavakoli Dargani, R. Singla, T. Johnson, R. Kukreja, and D. K. Singla, "Exosomes derived from embryonic stem cells inhibit doxorubicin and inflammation-induced pyroptosis in muscle cells," *Canadian Journal of Physiology and Pharmacology*, vol. 96, no. 3, pp. 304–307, 2018.
- [20] L. Barile, T. Moccetti, E. Marbán, and G. Vassalli, "Roles of exosomes in cardioprotection," *European Heart Journal*, vol. 38, no. 18, pp. 1372–1379, 2017.
- [21] T. Zeng, X. Wang, W. Wang et al., "Endothelial cell-derived small extracellular vesicles suppress cutaneous wound healing through regulating fibroblasts autophagy," *Clinical Science*, vol. 133, no. 9, p. CS20190008, 2019.
- [22] W. D. Gray, K. M. French, S. Ghosh-Choudhary et al., "Identification of therapeutic covariant microRNA clusters in hypoxia-treated cardiac progenitor cell exosomes using systems biology," *Circulation Research*, vol. 116, no. 2, pp. 255–263, 2015.
- [23] K. Guitart, G. Loers, F. Buck, U. Bork, M. Schachner, and R. Kleene, "Improvement of neuronal cell survival by astrocyte-derived exosomes under hypoxic and ischemic conditions depends on prion protein," *Glia*, vol. 64, no. 6, pp. 896–910, 2016.
- [24] X. Wang, W. Huang, G. Liu et al., "Cardiomyocytes mediate anti-angiogenesis in type 2 diabetic rats through the exosomal transfer of miR-320 into endothelial cells," *Journal of Molecular and Cellular Cardiology*, vol. 74, pp. 139–150, 2014.
- [25] G. Zhao, Y. Ge, C. Zhang et al., "Progress of mesenchymal stem cell-derived exosomes in tissue repair," *Current Pharmaceutical Design*, vol. 26, no. 17, pp. 2022–2037, 2020.
- [26] J. Bai, Q. Wang, J. Qi et al., "Promoting effect of baicalin on nitric oxide production in CMECs via activating the PI3K-AKT-eNOS pathway attenuates myocardial ischemia-reperfusion injury," *Phytomedicine*, vol. 63, p. 153035, 2019.
- [27] M. Chiba, N. Watanabe, M. Watanabe et al., "Exosomes derived from SW480 colorectal cancer cells promote cell migration in HepG2 hepatocellular cancer cells via the mitogen-activated protein kinase pathway," *International Journal of Oncology*, vol. 48, no. 1, pp. 305–312, 2016.
- [28] R. Fujihara, Y. Chiba, T. Nakagawa et al., "Histomorphometry of ectopic mineralization using undecalcified frozen bone sections," *Microscopy Research and Technique*, vol. 81, no. 11, pp. 1318–1324, 2018.
- [29] K. Ding, H. Wang, Y. Wu et al., "Rapamycin protects against apoptotic neuronal death and improves neurologic function after traumatic brain injury in mice via modulation of the mTOR-p53-Bax axis," *Journal of Surgical Research*, vol. 194, no. 1, pp. 239–247, 2015.
- [30] O. Fornes, "JASPAR: an open-access database of transcription factor binding profiles," *F1000Research*, vol. 7, 2018.
- [31] L.-P. Zhu, T. Tian, J. Y. Wang et al., "Hypoxia-elicited mesenchymal stem cell-derived exosomes facilitates cardiac repair through miR-125b-mediated prevention of cell death in myocardial infarction," *Theranostics*, vol. 8, no. 22, pp. 6163–6177, 2018.
- [32] J. Liu, M. Jiang, S. Deng et al., "miR-93-5p-containing exosomes treatment attenuates acute myocardial infarction-induced myocardial damage," *Molecular Therapy-Nucleic Acids*, vol. 11, pp. 103–115, 2018.
- [33] S. Gupta and A. A. Knowlton, "HSP60 trafficking in adult cardiac myocytes: role of the exosomal pathway," *American Journal of Physiology-Heart and Circulatory Physiology*, vol. 292, no. 6, pp. H3052–H3056, 2007.
- [34] Y. Sun, T. Xu, Y. W. Cao, and X. Q. Ding, "Antitumor effect of miR-27b-3p on lung cancer cells via targeting Fzd7," *European Review for Medical and Pharmacological Sciences*, vol. 21, no. 18, pp. 4113–4123, 2017.
- [35] W. Xu, M. Liu, X. Peng et al., "miR-24-3p and miR-27a-3p promote cell proliferation in glioma cells via cooperative regulation of MX11," *International Journal of Oncology*, vol. 42, no. 2, pp. 757–766, 2013.
- [36] D. Chen, W. Si, J. Shen et al., "miR-27b-3p inhibits proliferation and potentially reverses multi-chemoresistance by targeting CBLB/GRB2 in breast cancer cells," *Cell Death & Disease*, vol. 9, no. 2, p. 188, 2018.
- [37] A. Di Francesco, M. Fedrigo, D. Santovito et al., "MicroRNA signatures in cardiac biopsies and detection of allograft rejection," *The Journal of Heart and Lung Transplantation*, vol. 37, no. 11, pp. 1329–1340, 2018.
- [38] X. Tian, Y. Ji, Y. Liang, J. Zhang, L. Guan, and C. Wang, "LINC00520 targeting miR-27b-3p regulates OSMR expression level to promote acute kidney injury development through the PI3K/AKT signaling pathway," *Journal of Cellular Physiology*, vol. 234, no. 8, pp. 14221–14233, 2019.
- [39] X. Li, Y. Tian, M. J. Tu, P. Y. Ho, N. Batra, and A. M. Yu, "Bio-engineered miR-27b-3p and miR-328-3p modulate drug metabolism and disposition via the regulation of target ADME gene expression," *Acta Pharmaceutica Sinica B*, vol. 9, no. 3, pp. 639–647, 2019.
- [40] J. Yu, Y. Lv, F. Wang et al., "MiR-27b-3p inhibition enhances browning of epididymal fat in high-fat diet induced obese mice," *Frontiers in Endocrinology*, vol. 10, p. 38, 2019.
- [41] W. Sun, J. Li, L. Zhou et al., "The c-Myc/miR-27b-3p/ATG10 regulatory axis regulates chemoresistance in colorectal cancer," *Theranostics*, vol. 10, no. 5, pp. 1981–1996, 2020.
- [42] B. Ye, X. Chen, S. Dai et al., "Emodin alleviates myocardial ischemia/reperfusion injury by inhibiting gasdermin D-mediated pyroptosis in cardiomyocytes," *Drug Design, Development and Therapy*, vol. 13, no. 13, pp. 975–990, 2019.
- [43] K. S. Schneider, C. J. Groff, R. F. Dreier et al., "The inflammatory response drives GSDMD-independent secondary pyroptosis and IL-1 release in the absence of caspase-1 protease activity," *Cell Reports*, vol. 21, no. 13, pp. 3846–3859, 2017.
- [44] J. Shi, Y. Zhao, K. Wang et al., "Cleavage of GSDMD by inflammatory caspases determines pyroptotic cell death," *Nature*, vol. 526, no. 7575, pp. 660–665, 2015.
- [45] L. V. Walle and M. Lamkanfi, "Pyroptosis," *Current Biology*, vol. 26, no. 13, pp. R568–R572, 2016.
- [46] S. Y. Kim, Y. S. Ko, J. Park et al., "Forkhead transcription factor FOXO1 inhibits angiogenesis in gastric cancer in relation to SIRT1," *Cancer Research and Treatment: Official Journal of Korean Cancer Association*, vol. 48, no. 1, pp. 345–354, 2016.
- [47] H. Shi, Y. Gao, Z. Dong et al., "GSDMD-mediated cardiomyocyte pyroptosis promotes myocardial I/R injury," *Circulation Research*, vol. 129, no. 3, pp. 383–396, 2021.
- [48] K. Jiang, Z. Tu, K. Chen et al., "Gasdermin D inhibition confers antineutrophil-mediated cardioprotection in acute myocardial infarction," *The Journal of Clinical Investigation*, vol. 132, no. 1, p. e151268, 2022.

## *Retraction*

# **Retracted: LINC00092 Modulates Oxidative Stress and Glycolysis of Breast Cancer Cells via Pyruvate Carboxylase-Mediated AKT/mTOR Pathway**

### **Oxidative Medicine and Cellular Longevity**

Received 26 December 2023; Accepted 26 December 2023; Published 29 December 2023

Copyright © 2023 Oxidative Medicine and Cellular Longevity. This is an open access article distributed under the Creative Commons Attribution License, which permits unrestricted use, distribution, and reproduction in any medium, provided the original work is properly cited.

This article has been retracted by Hindawi, as publisher, following an investigation undertaken by the publisher [1]. This investigation has uncovered evidence of systematic manipulation of the publication and peer-review process. We cannot, therefore, vouch for the reliability or integrity of this article.

Please note that this notice is intended solely to alert readers that the peer-review process of this article has been compromised.

Wiley and Hindawi regret that the usual quality checks did not identify these issues before publication and have since put additional measures in place to safeguard research integrity.

We wish to credit our Research Integrity and Research Publishing teams and anonymous and named external researchers and research integrity experts for contributing to this investigation.



The corresponding author, as the representative of all authors, has been given the opportunity to register their agreement or disagreement to this retraction. We have kept a record of any response received.

### **References**

- [1] W. Chen, Y. Liu, S. Kang et al., “LINC00092 Modulates Oxidative Stress and Glycolysis of Breast Cancer Cells via Pyruvate Carboxylase-Mediated AKT/mTOR Pathway,” *Oxidative Medicine and Cellular Longevity*, vol. 2022, Article ID 5215748, 21 pages, 2022.

## Research Article

# LINC00092 Modulates Oxidative Stress and Glycolysis of Breast Cancer Cells via Pyruvate Carboxylase-Mediated AKT/mTOR Pathway

Wei Chen,<sup>1,2</sup> Yushan Liu,<sup>1,2</sup> Shaohong Kang,<sup>1,2</sup> Xinying Lv,<sup>1,2</sup> Wenfen Fu,<sup>1,2</sup> Jie Zhang ,<sup>1,2,3</sup> and Chuangui Song <sup>1,2,3</sup>

<sup>1</sup>Department of Breast Surgery, Fujian Medical University Union Hospital, Fuzhou, Fujian Province 350001, China

<sup>2</sup>Department of General Surgery, Fujian Medical University Union Hospital, Fuzhou, Fujian Province 350001, China

<sup>3</sup>Breast Cancer Institute, Fujian Medical University, Fuzhou, Fujian Province 350001, China

Correspondence should be addressed to Jie Zhang; [zjie1979@gmail.com](mailto:zjie1979@gmail.com) and Chuangui Song; [songcg1971@hotmail.com](mailto:songcg1971@hotmail.com)

Received 28 April 2022; Revised 16 May 2022; Accepted 24 May 2022; Published 28 June 2022

Academic Editor: Tian Li

Copyright © 2022 Wei Chen et al. This is an open access article distributed under the Creative Commons Attribution License, which permits unrestricted use, distribution, and reproduction in any medium, provided the original work is properly cited.

**Background.** The discovery of noncoding RNAs (ncRNAs) offers new options for cancer-targeted therapy. This study is aimed at exploring the regulatory function of LINC00092 on breast cancer (BC) oxidative stress and glycolysis, along with internal mechanism concerning pyruvate carboxylase (PC). **Methods.** Bioinformatics analysis was used to explore LINC00092 (or friend leukemia virus integration 1 (FLI1)) expression on BC progression, as well as oxidative stress and glycolysis in BC. After LINC00092 overexpression or silence, BC cell viability, proliferation, migration, invasion, oxidative stress, glycolysis, and AKT/mTOR pathway were detected. Following 2-DG, SC79, or MK2206 treatment, effects of LINC00092 on BC cells were measured. Moreover, regulatory activity of LINC00092 in PC expression was analyzed. Whether PC participated in the modulation of LINC00092 on BC cell functions was explored. **Results.** LINC00092 was lowly expressed in BC and negatively related to BC progression. FLI1 bound to LINC00092 promoter to positively modulate LINC00092. LINC00092 overexpression inhibited BC cell proliferation, migration, invasion, oxidative stress, glycolysis, and AKT/mTOR pathway and likewise suppressed BC growth *in vivo*. Silence of LINC00092 had opposite influences. 2-DG partially reversed the LINC00092 silence-resulted increase of BC cell proliferation. SC79 alleviated the function of LINC00092 overexpression on BC cell functions. MK2206 had the contrary influence of SC79. Besides, LINC00092 bound to PC to modulate ubiquitination degradation of PC protein. PC took part in the influences of LINC00092 on BC cell functions. **Conclusions.** LINC0092 modulates oxidative stress and glycolysis of BC cells via the PC-mediated AKT/mTOR pathway, which is possibly a target for BC diagnosis and therapy.

## 1. Introduction

Breast cancer (BC) is the largest frequently happened cancer in women, which accounts for about 30% of all cancers happened in women [1]. Just in the United States, there are about 276,480 women diagnosed with BC in 2020 [2]. In recent years, with the development of targeted therapy and immunotherapy for BC, the overall prognosis of BC patients still remains discontented [3]. Cancer recrudescence and metastasis are two major causes for BC-related death [4]. It is well-known that the pathogenesis of BC is very complex. There are lots of molecules, in which expressions

are changed in BC cells, due to gene mutation or chromosome variation [5–7]. Some of these are chosen to design targeted therapies for BC treatment [8, 9]. It is believed that more understanding of the pathogenesis of BC will provide new choices for exploring newly BC targeted therapy.

Long noncoding RNAs (lncRNAs) are newly identified RNA transcripts with a length of more than 200 nucleotides in cells [10]. Different from well-known mRNAs, tRNAs, and rRNAs, which take part in encoding proteins, lncRNAs do not join in encoding proteins but exerted key regulatory roles in multiple cell functions [11]. More importantly, a number of lncRNAs are verified to bear a part in the

tumorigenesis and progression of human cancers, including BC [12]. LINC00092 is firstly reported in 2017 and located at the intergenic regions of 9q22.32 [13]. Wang et al. [14] discovered that LINC00092 was lowly expressed in lung adenocarcinoma and predicated poor prognosis. Huang et al. [15] revealed that LINC00092 is a possible biomarker for colon adenocarcinoma diagnosis and prognosis. In terms of BC, Wu et al. [16] reported that LINC00092 expression was negatively correlated to the BC patients' survival outcomes.

Glycolysis refers to the process by which glucose is broken down into pyruvate in the cytoplasm under anaerobic condition [17]. For cancer cells, the proliferation is very quickly, which needs multiple adenosine triphosphate (ATP). Lots of literatures reported that glycolysis was promoted in many human cancer cells, including BC cells [18]. Actually, glycolysis is the main manner for BC cells to produce ATP, which is one of the important characteristics of malignant progression for BC [19, 20]. As key regulators of gene expressions in cells, many lncRNAs are discovered to take part in the modulation of glycolysis, including in BC cells [21, 22]. Chen et al. [23] found that LINC00092 could relieve cardiac fibroblast activation via regulating glycolysis. Zhao et al. [13] reported that LINC00092 could bind fructose-2,6-biphosphatase (PFKFB2) to modulate glycolysis in ovarian cancer cells. Not any information can be searched concerning the influence of LINC00092 on glycolysis of BC cells.

The redox imbalance, especially the increased level of oxidative stress, is demonstrated to happen in multiple human cancers, including BC [24]. Earlier literatures reported that raised oxidative stress not only took part in the BC formation via causing DNA and proteins damage but also participated in BC migration and invasion through altering expression changes of some molecules related to cell migration and invasion [25]. More importantly, it has been discovered that there is a reciprocal regulatory relationship between reactive oxygen species (ROS) and glycolysis in cells [26].

In the current research, LINC00092 expression was detected in BC tissues to dissect the connection between LINC00092 expression and BC progression. The modulatory effect of friend leukemia virus integration 1 (FLI1) on LINC00092 expression in BC cells was analyzed. Following overexpression or silence of LINC00092 in BC cells, BC cell proliferation, migration, invasion, oxidative stress, glycolysis, and serine threonine (ser/thr) protein kinase/mammalian target of rapamycin (AKT/mTOR) pathway were tested. Moreover, whether LINC00092 influenced BC cell proliferation via regulating glycolysis and whether LINC00092 affected BC cell functions via AKT/mTOR pathway were analyzed. Finally, the internal regulatory mechanism of LINC00092 on BC cell metabolism concerning pyruvate carboxylase (PC) was probed. We think the findings of this research will provide experimental basis for further comprehending the key regulatory function of LINC00092 on BC progression.

## 2. Materials and Method

**2.1. Bioinformatics Analysis.** The RNA sequencing data of 1109 samples of BC tissues and 99 samples of normal tissues

were downloaded from The Cancer Genome Atlas (TCGA) database (<https://www.cancer.gov/about-nci/organization/ccg/research/structural-genomics/tcga>) to dissect the connection among LINC00092 expression and BC progression. The RNA sequencing data of 1085 samples of BC tissues and 112 samples of normal tissues were downloaded from Gene Expression Profiling Interactive Analysis (<http://gepia.cancer-pku.cn/>) to dissect the connection among FLI1 expression and BC progression. Kaplan-Meier (KM) analysis was utilized to assess the influences of LINC00092 (or FLI1) expression on survival probability of BC patients. JASPAR website (<https://jaspar.genereg.net/>) was employed to explore the relationship between LINC00092 and FLI1. Gene Expression Profiling Interactive Analysis was also used to dissect the connection among FLI1 expression and LINC00092 expression in BC.

Gene Set Enrichment Analysis (GSEA, <http://www.broad.mit.edu/gsea/msigdb/>) was carried out to explore the enrichment of glycolysis and oxidative stress-related pathway modulated by LINC00092 in BC tissues. Briefly, the clusterProfiler software package in an R package (<http://bioconductor.org/packages/release/bioc/html/clusterProfiler.html>) was used in conducting gene ontology (GO) and Kyoto encyclopedia of genes and genomes (KEGG) enrichment analyses. Then, the GSEA of differentially expressed genes were analyzed using `c2.cp.kegg.v6.2.symbols.gmt` and `c5.bp.v6.2.symbols.gmt` in MsigDB V6.2 database (<https://www.gsea-msigdb.org/gsea/msigdb/>) as backgrounds. GSEA was also performed using clusterProfiler package. Finally, the gene expressions concerning glycolysis and oxidative stress were analyzed using Bioinformcloud platform (<http://www.bioinformcloud.org.cn>).

**2.2. Clinical Samples.** Twenty-nine BC patients were recruited in this research, which did not receive any therapy targeting BC before experiment. The BC tissues and paracancer normal tissues were harvested during surgical resection or pathological puncture biopsy. Written informed consents were obtained from patients. Experiments were authorized by the Ethics Committee of our institution.

**2.3. Cell Culture.** MCF-10A, MCF-7, MDA-MB-468, and MDA-MB-453 were cultured in corresponding medium recommended by the manufacturer at 37°C with 5% CO<sub>2</sub>. 5 mM 2-deoxyglucose (2-DG, D8930, Solarbio, Beijing, China) was used to inhibit cell glycolysis. 3 μM SC79 (SF2730, Beyotime Biotechnology, Shanghai, China) was used to activate AKT, while 3 μM MK2206 (SF2712, Beyotime Biotechnology) was used to inhibit AKT. 50 μg/mL cycloheximide (CHX, HY-12320, MCE) was utilized to inhibit protein synthesis in cells.

**2.4. Quantitative Polymerase Chain Reaction (qPCR) Assay.** Total RNAs were separated from tissues or cells using Trizol solution (Invitrogen, CA, USA) and quantified via a microspectrophotometer (Hangzhou Allsheng Instruments Co., Ltd. Hangzhou, China). PrimeScript™ RT Reagent Kit with gDNA Eraser (Takara Biotechnology, Beijing, China) was utilized to synthesize cDNA with 2 μg RNA as template.

PCR assay was performed using SYBR Green qPCR Mix (Beyotime Biotechnology, Shanghai, China). Primer's sequences are exhibited in Table 1. Results were computed via the  $2^{-\Delta\Delta C_t}$  method with GAPDH as endogenous control.

**2.5. Cell Transfection.** FLI1, LINC00092, and PC overexpression plasmids were erected via inserting the full-length sequences of FLI1, LINC00092, and PC into the pcDH plasmid (GeneChem Corporation, Shanghai, China), respectively. pLKO short hairpin RNA (shRNA) plasmids targeting LINC00092 and PC were designed to silence LINC00092 and PC expressions, which were synthesized by GeneChem Corporation and referred as sh-LINC00092 and sh-PC, respectively. sh-LINC00092 sequence was 5'-CCGGGGATGACCTGCCCTATGATTTCTCGAGAAATC ATAGGGCAGGTCATCCTTTTTGAATT-3'. sh-PC sequence was 5'-CCGGCGACTCTGTGAAACTCGCTAACTCGAGTT AGCGAGTTTACAGAGTCGTTTTTGAATT-3'. Cell transfection was carried out using Lipo8000™ Transfection Reagent (Beyotime Biotechnology, Shanghai, China).

**2.6. Chromatin Immunoprecipitation (ChIP) Assay.** ChIP assay was utilized to dissect the connection of LINC00092 and FLI1 with the help of ChIP Assay Kit (Beyotime Biotechnology) [27]. FLI1 antibody was purchased from Invitrogen (MA1-196). DNA purification kit (AxGen, CA, USA) was used for DNA purification. qPCR was carried out for test LINC00092 expression. The LINC00092 primer sequences for ChIP were 5'-CAGATGCTCAGTGTGT GACCCT-3' (forward) and 5'-CTGGAACGGATGCGA CAGT-3' (reverse).

**2.7. Dual-Luciferase Activity Assay.** Dual-luciferase activity assay was utilized to further dissect the connection of FLI1 and LINC00092 with the help of Firefly and Renilla Luciferase Reporter Assay Kit (MeilunBio, Dalian, China) [28]. Briefly, MCF-7 and MDA-MB-468 cells were cotransfected into FLI1 and pGL3-LINC00092-WT (or pGL3-LINC00092-MUT, the 5'-TCAGGAAGCGC-3' sequence of LINC00092 wild type was mutated with 5'-GTGTTGGTTTT-3'). After 48 h, total proteins in cells were separated. 20  $\mu$ L cell lysis supernatant was incubated with 100  $\mu$ L Firefly luciferase reaction buffer and 100  $\mu$ L Renilla detection kit. The relative luciferase activity was tested through a microplate reader.

**2.8. Cell Counting Kit-8 (CCK-8) Assay.** After corresponding transfection and/or treatment,  $1 \times 10^4$  cells were grown into a 96-well plate for 24, 48, and 72 h. Then, 10  $\mu$ L CCK-8 solution (Beyotime Biotechnology) was replenished into culture medium for 1 h [29]. Following shaking, the absorbance of each well was gauged at 450 nm.

**2.9. Colony Formation Assay.** After corresponding transfection and/or treatment, cells were cultivated into a 6-well plate with 500 cells/well for two weeks. Then, cells were rinsed by PBS, fixed with 4% paraformaldehyde solution (Beyotime Biotechnology), and dyed using Giemsa solution

TABLE 1: The primer information for qPCR assay.

Name	Sequence (5'-3')
LINC00092 forward	AACCAGGAACCTCCGCACCAA
LINC00092 reverse	GCAAGGCTTCCGCGAGCTCAA
FLI1 forward	CTACCATGCCACCAGCAGAAG
FLI1 reverse	CCAGTATTGTGATGCGGCTCCA
PC forward	GCGACGGCGAGGAGATAGT
PC reverse	CCCATGGACTGTTCCGGAAGTT
GAPDH forward	AAGTATGACAACAGCCTCAAG
GAPDH reverse	TCCACGATACCAAAGTTGTC

(Solarbio, Beijing, China). The colony number of each group was counted under a microscope.

**2.10. Cell Scratch Assay.** After corresponding transfection and/or treatment,  $5 \times 10^5$  cells were cultivated into a 6-well plate overnight. Then, scratches were generated by 10  $\mu$ L pipette across cells [30]. PBS was used to remove scratched cells. Following growth in culture medium that does not contain FBS at 37°C for 24 h, images of scratches were photographed under a microscope. The scratch areas were calculated using IPP software. The percentage of wound closure was calculated via  $1 - (\text{scratch area of 24 h} / \text{scratch area of 0 h} \times 100\%)$ .

**2.11. Two-Chamber Transwell Assay.** After corresponding transfection and/or treatment,  $3 \times 10^4$  cells in 200  $\mu$ L FBS-free culture medium were added into the above chamber that was pretreated with Matrigel Basement Membrane Matrix (Corning Costar, MA, USA) for 48 h [31]. 500  $\mu$ L culture medium containing 10% FBS was supplemented into the below chamber. Then, cells in the above chamber were removed and cells in membrane were cleaned using PBS, fixed with 4% paraformaldehyde solution, and dyed using 0.1% crystal violet solution. Results were photographed under a microscope.

**2.12. Animal Experiment.** Twelve BALB/c nude mice (4 weeks old, female) were housed in aseptic environment at 26-28°C for 1 week to adopt to a new environment. Then, mice were weighted and randomly divided into the mock group and LINC00092 group. In mock group, mice were subcutaneously inoculated into the upper back area of right side with  $1 \times 10^6$  MDA-MB-468 cells transfected pcDH plasmid. In LINC00092 group, mice were subcutaneously inoculated with  $1 \times 10^6$  cells transfected LINC00092 plasmid. Body weight and tumor volume were measured at day 3, day 7, day 14, day 21, and day 28 (twice one week). After 28 days, all mice were sacrificed by CO<sub>2</sub> inhalation. Tumor tissues were excised from mice, weighted, and fixed into 10% formalin solution. Hematoxylin-eosin staining was carried out to inspect the microstructure changes of tumor tissues between the mock and LINC00092 groups by using hematoxylin solution (G1004, Servicebio, Wuhan, China) and eosin solution (G1002, Servicebio).

### 3. Detection of Cell Glycolysis

Lactate production and glucose consumption of cells were tested with the help of lactate assay kit (A019-2-1) and glucose assay kit (F006-1-1, Nanjing Jiancheng Bioengineering Institute, Nanjing, China), respectively.

**3.1. Test of Superoxide Dismutase (SOD) and Malondialdehyde (MDA) Level.** SOD and MDA levels in MCF-7 and MDA-MB-468 cells after LINC00092 or sh-LINC00092 transfection were detected with the help of SOD Activity Detection Kit (BC0175, Solarbio) and MDA Detection Kit (S0131M, Beyotime Biotechnology) [32].

**3.2. Measurement of ROS Level.** ROS levels in cells were measured via ROS Assay Kit (S0033M, Beyotime Biotechnology) [33]. Briefly, after LINC00092 or sh-LINC00092 transfection, MCF-7 and MDA-MB-468 cells were rinsed with PBS and incubated with 10  $\mu$ mol/L DCFH-DA for 20 min at 37°C. Following rinsing with serum-free culture medium, the ROS levels in cells were tested via a microplate (488 nm excitation and 525 nm emission).

**3.3. RNA Pull-Down and Mass Spectrometry (MS) Assay.** RNA pull-down assay and MS analysis were performed to identify proteins interacting with LINC00092 [34]. Briefly,  $1 \times 10^7$  MDA-MB-468 cells were mixed with RIP Lysis Buffer on ice. Following centrifugation with 13000  $\times$  g for 10 min, supernatant was collected. LINC00092 *in vitro* transcription and purification were carried out using PrimeSTAR Max Premix (Takara Biotechnology, Beijing, China) and Micro-Agarose gel DNA recovery kit (Aiji Biotechnology, Guangzhou, China). mMESSAGE mMACHINE Kit (Invitrogen) and RNeasy Mini Kit were used to label LINC00092 with biotin. 3  $\mu$ g LINC00092 with biotin labeling was mixed with beads for 1 h. Cell supernatant was incubated with LINC00092-bead for 1 h. The LINC00092 binding proteins were eluted and collected to perform western blotting. MS analysis was performed using Thermo Scientific Q Exactive (ThermoFisher Scientific, MA, USA) with Proteome Discoverer 1.4 (version 1.4.0.288).

**3.4. RNA Immunoprecipitation (RIP) Assay.** RIP was employed to further verify the binding of LINC00092 and PC. Magna RIP RNA-Binding Protein Immunoprecipitation Kit was purchased from Merck (#17-700, MA, USA), which was utilized in the light of the manufacturer's instruction. Results were tested by qPCR.

**3.5. RNA-FISH Assay.** RNA-FISH assay was performed to test the location of LINC00092 and PC in cells with the help of RNA-FISH Probe kit (Streptavidin-biotin system, GenePharma Biotechnology, Shanghai, China) [35]. LINC00092 probe sequence was 5'-CCAAATCATAGGGCAGGTCATCCCAAGGACAGCA-3'. PC probe sequence was 5'-GCAGTGAAGTCCTTGAAGTGGCAAACACATCGGG-3'. DAPI (Solarbio) was utilized for staining nucleus.

**3.6. Immunohistochemistry (IHC) Assay.** Tumor tissues of mice were embedded using paraffin. Immunohistochemistry

assay was performed on 6  $\mu$ m thick sections as earlier literature reported [36]. Anti-PC polyclonal antibody (#16588-1-AP), anti-Ki-67 polyclonal antibody (#21309-1-AP, Proteintech, IL, USA), anti-AKT (phospho T308) antibody (ab38449), anti-mTOR (phospho S2448) antibody (ab109268, Abcam Biotechnology, CA, USA), and anti-phosphor-p70 S6 kinase (Thr389) antibody (#97596) were purchased from Cell Signaling Technology, CA, USA. Relative expressions were visualized using diaminobenzidine (DAB) solution (Beyotime Biotechnology). Cell nucleus was stained using hematoxylin solution. Results were observed under a microscope (Nikon, Japan).

**3.7. In Vitro Ubiquitination Assay.** *In vitro* ubiquitination assay was carried out to identify the degradation pathway of PC protein modulated by LINC00092 in BC cells. Briefly, following different transfections, MCF-7 and MDA-MB-468 cells were treated by 20  $\mu$ M MG132 for 10 h (S1748, Beyotime) to inhibit degradation of ubiquitinated proteins [37]. RIPA Lysis Buffer (Beyotime Biotechnology) was used to split cells. The lysate supernatant was collected for co-immunoprecipitation with anti-IgG antibody or anti-PC antibody (#16588-1-AP, Proteintech). After incubation with Protein A/G Agarose and centrifugation and precipitation with Protein A/G Agarose, the protein in supernatant was subjected to western blotting.

**3.8. Western Blotting.** Total proteins in cells were isolated using RIPA Lysis Buffer containing protease inhibitors and phosphatase inhibitors. Western blotting was conducted similarly as previous literature reported [38]. Anti-AKT antibody (ab8805), anti-p-AKT antibody (ab38449), anti-mTOR antibody (ab32028), and anti-p-mTOR antibody (ab109268) were purchased from Abcam Biotechnology. Anti-p70S6K antibody (#9202) and anti-p-p70S6K antibody (#97596) were provided by Cell Signaling Technology. Anti-PC antibody (#16588-1-AP) was purchased from Proteintech. Anti-GAPDH antibody (GB11002) was purchased from Servicebio.

**3.9. Statistical Analysis.** GraphPad Prism 9.0 software was utilized for statistical analysis. All experiments were repeated at least three times ( $n \geq 3$ ). Results were exhibited as mean  $\pm$  standard deviation (SD). One-way ANOVA was utilized for gauging *P* values with a significance level of  $P < 0.05$ .

## 4. Results

**4.1. LINC00092 Was Lowly Expressed in BC and Negatively Related to BC Progression.** Firstly, the RNA sequencing data of BC tissues (T group) and normal tissues (N group) were downloaded from TCGA database to test LINC00092 expression. Result in Supplemental Figure 1A showed that relative to normal tissues, LINC00092 was lowly expressed in BC tissues ( $P < 0.0001$ ). The BC tissues and paracancer normal tissues of 29 cases of BC patients were also collected. Supplemental Figure 1B also displays that LINC00092 had a lower expression level in BC tissues ( $P = 0.0001$ ). Moreover, Supplemental Figure 1C illustrates that LINC00092 had lower expression levels in BC MCF-7



and MDA-MB-468 cells, in comparison with normal breast epithelial MCF-10A cells ( $P < 0.01$ ). Besides, the relationship of LINC00092 expression and the tumor size, histological grade, and survival probability of BC patients was analyzed. Results showed that LINC00092 expression was negatively correlated with the tumor size (Supplemental Figure 1D,  $P = 0.01$ ) and histological grade (Supplemental Figure 1E, Phase II and Phase III,  $P = 0.04$ ) of BC patients. Supplemental Figure 1F displays that LINC00092 expression was positively related to the survival probability of BC patients ( $P < 0.0001$ ). These outcomes represented that LINC00092 was lowly expressed in breast cancer tissues and cells and negatively associated with the BC progression.

**4.2. LINC00092 Was Modulated by FLI1 in BC Cells.** Bioinformatics analysis found that there were complementary paired bases between the FLI1 motif and the LINC00092 promoter (Figure 1(a)). Figure 1(b) shows that LINC00092 expression was positively related to FLI1 expression in BC ( $P = 4.1E - 55$ ). Moreover, Figure 1(c) displays that FLI1 transfection notably raised the FLI1 expression in MCF-7 and MDA-MB-468 cells ( $P < 0.001$ ), which also notably enhanced the LINC00092 expression in cells (Figure 1(d),  $P < 0.05$  or  $P < 0.001$ ). The results of ChIP in Figures 1(e) and 1(f) illustrated that FLI1 could be combined with LINC00092 promoter in cells ( $P < 0.001$ ). Furthermore, the results of dual luciferase activity assay presented that cotransfection with LINC00092-WT and FLI1 notably raised the relative luciferase activities (Figures 1(g) and 1(h),  $P < 0.001$ ). Besides, bioinformatics analysis also found that FLI1 was lowly expressed in BC tissues (Supplemental Figure 2A,  $2P < 0.05$ ). BC patients with lower FLI1 expression had lower survival probability (Supplemental Figure 2B,  $P = 0.022$ ). These outcomes represented that FLI1 bound to LINC00092 promoter to modulate LINC00092 expression in BC cells.

**4.3. LINC00092 Regulated BC Cell Proliferation, Migration, and Invasion.** LINC00092 and sh-LINC00092 were transfected to alter LINC00092 expression in MCF-7 and MDA-MB-468 cells. Figure 2(a) displays that LINC00092 transfection raised the LINC00092 expression in cells ( $P < 0.001$ ), while sh-LINC00092 transfection had opposite influence, which lowered LINC00092 expression in cells ( $P < 0.001$ ). Figure 2(b) shows that LINC00092 transfection reduced cell viabilities ( $P < 0.05$  or  $P < 0.001$ ), but sh-LINC00092 transfection enhanced cell viabilities ( $P < 0.01$  or  $P < 0.001$ ). Moreover, LINC00092 transfection inhibited cell proliferation (Figure 2(c)). Relative to the mock group, the number of foci/well was decreased in the LINC00092 group ( $P < 0.05$  or  $P < 0.001$ ). sh-LINC00092 transfection had contrary effect, which promoted cell proliferation ( $P < 0.01$ ). Moreover, Figure 2(d) illustrated that LINC00092 transfection inhibited the cell migration ( $P < 0.01$  or  $P < 0.001$ ), but sh-LINC00092 transfection accelerated cell migration ( $P < 0.05$ ). Besides, Figure 2(e) showed that LINC00092 transfection also reduced cell invasion ( $P < 0.01$  or  $P < 0.001$ ). sh-LINC00092 transfection had opposite effects,

which facilitated cell invasion ( $P < 0.01$  or  $P < 0.001$ ). These outcomes represented that LINC00092 participated in the regulation of BC cell proliferation, migration, and invasion.

**4.4. LINC00092 Overexpression Inhibited BC Growth In Vivo.** An *in vivo* BC mouse model was established with MDA-MB-468 cells transfected or nontransfected LINC00092. Results in Figure 3(a) displayed that there was no notable difference of mouse body weight among the mock and LINC00092 group ( $P > 0.05$ ). Figure 3(b) presents that LINC00092 transfection inhibited the tumor volume of mice with BC ( $P < 0.001$ ). The visual picture of mice with subcutaneous BC transplantation is shown in Figure 3(c). Figure 3(d) shows that LINC00092 transfection also reduced the tumor weight of mice with BC ( $P < 0.001$ ). Results of HE staining in Figure 3(e) showed that the compact tumor cells with blue-purple nuclei and pink cytoplasm were observed in the mock group. In the LINC00092 group, the tumor cells were separated each other with apparent vacant sections. Besides, relative to the mock group, the Ki-67 expression was decreased in the LINC00092 group, which further suggested that LINC00092 suppressed BC cell proliferation. These outcomes represented that LINC00092 overexpression inhibited BC growth *in vivo*.

**4.5. LINC00092 Influenced BC Cell Oxidative Response and Glycolysis.** Both glycolysis and oxidative stress are demonstrated to be activated in BC tissues [20, 25]. Herein, the result of GSEA implied that both glycolysis and response to oxidative stress were regulated by LINC00092 in BC tissues (Figure 4(a)). Following LINC00092 or sh-LINC00092 transfection, cell relative lactate production and glucose consumption were measured. Figures 4(b) and 4(c) show that LINC00092 transfection reduced cell lactate production and glucose consumption ( $P < 0.05$  or  $P < 0.01$ ), while sh-LINC00092 transfection enhanced the lactate production and glucose consumption ( $P < 0.05$ ,  $P < 0.01$ , or  $P < 0.001$ ). 2-DG was utilized to inhibit glycolysis. Figures 4(d) and 4(e) display that 2-DG treatment reduced cell viabilities and colony formation ( $P < 0.05$ ,  $P < 0.01$ , or  $P < 0.001$ ). Moreover, the 2-DG combined with sh-LINC00092 significantly inhibited cell viabilities and colony formation compared with sh-LINC00092 alone ( $P < 0.01$  or  $P < 0.001$ ). Besides, Figure 4(f) shows that LINC00092 transfection raised the SOD level but lowered the MDA and ROS levels in MCF-7 and MDA-MB-468 cells ( $P < 0.001$ ), while sh-LINC00092 transfection had opposite effects ( $P < 0.001$ ). These outcomes represented that LINC00092 influenced BC cell glycolysis and oxidative response.

**4.6. LINC00092 Influenced BC Cell Functions and Glycolysis via Modulating the AKT/mTOR Pathway.** The AKT/mTOR pathway is a key proliferation pathway in cells, which participates in the modulation of cell proliferation, migration, invasion, and glycolysis [39]. Whether AKT/mTOR pathway took part in the regulation of LINC00092 on BC cells was analyzed. Figure 5(a) shows that LINC00092 inactivated the AKT/mTOR pathway in MCF-7 and MDA-MB-468 cells via reducing p-AKT, p-mTOR, and p-p70S6K

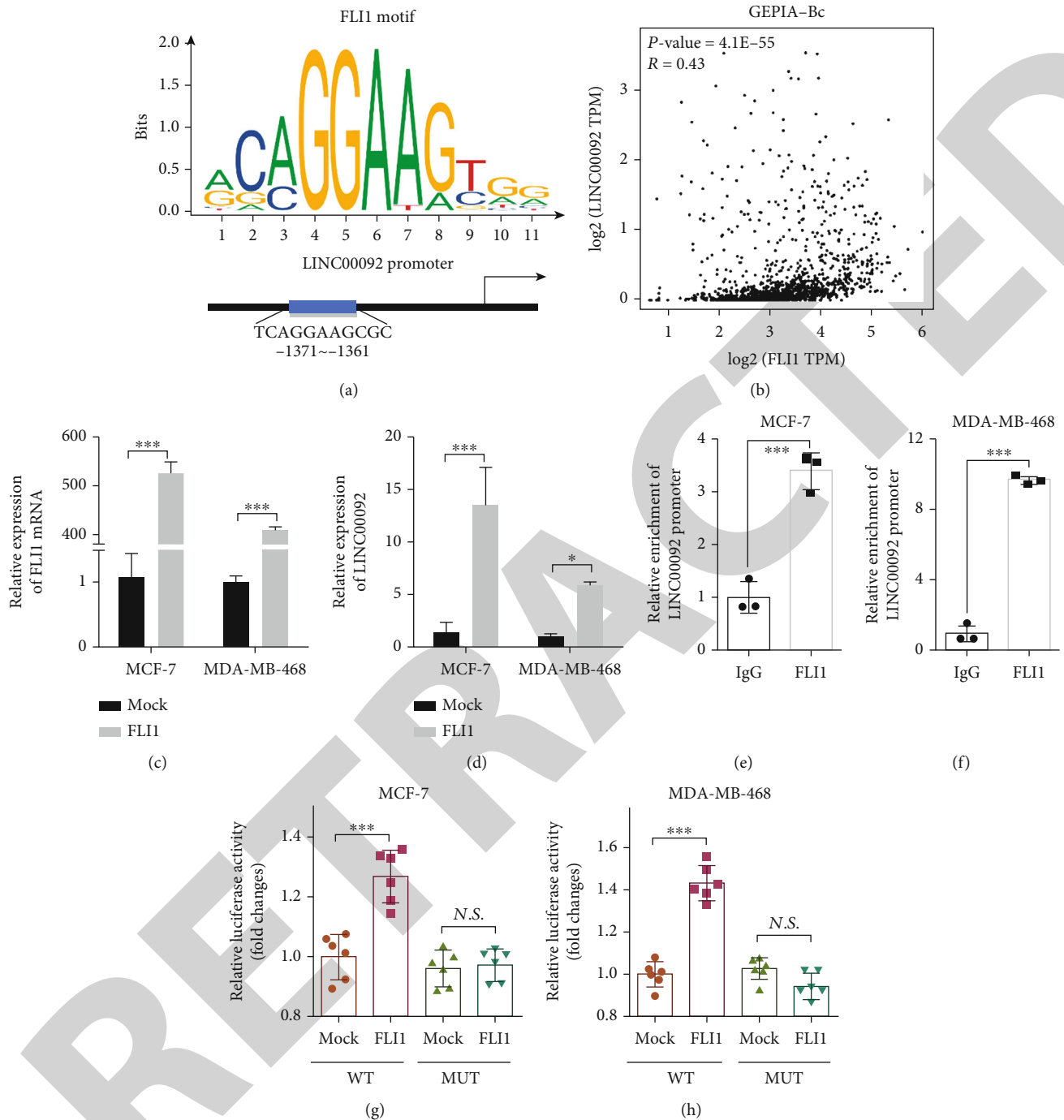


FIGURE 1: LINC00092 was modulated by FLI1 in BC cells. (a, b) Bioinformatics analysis was utilized to predict the relationship between FLI1 and LINC00092. (c, d) Following mock or FLI1 transfection, the FLI1 and LINC00092 expressions in cells were measured via qPCR.  $N = 3$ . (e, f) ChIP assay was carried out to test the binding between FLI1 and LINC00092 promoter in cells.  $N = 3$ . (g, h) Dual-luciferase activity assay was carried out to confirm the binding between FLI1 and LINC00092 promoter.  $N = 3$ .  $N.S.$ :  $P > 0.05$ ,  $*$   $P < 0.05$ , and  $***$   $P < 0.001$ .

protein levels. sh-LINC00092 transfection had contrary influence, which activated the AKT/mTOR pathway. Figure 5(b) displays that LINC00092 also lowered the p-mTOR and p-p70S6K expressions in mouse xenograft BC tissue. SC79 was an activator of AKT, which reversed the inactivation of the AKT/mTOR pathway caused by LINC00092 transfection in cells (Supplemental Figure 3A). Figures 5(c)–5(f) display that SC79 treatment notably

alleviated the LINC00092 transfection-resulted decreases of cell viabilities, proliferation, migration, and invasion ( $P < 0.05$ ,  $P < 0.01$ , or  $P < 0.001$ ). Furthermore, SC79 treatment also obviously relieved the LINC00092 transfection-resulted reductions of cell lactate production and glucose consumption (Figures 5(g) and 5(h),  $P < 0.01$  or  $P < 0.001$ ). MK2206 was an inhibitor of AKT. The results in Supplemental Figures 3B–3H illustrated that MK2206

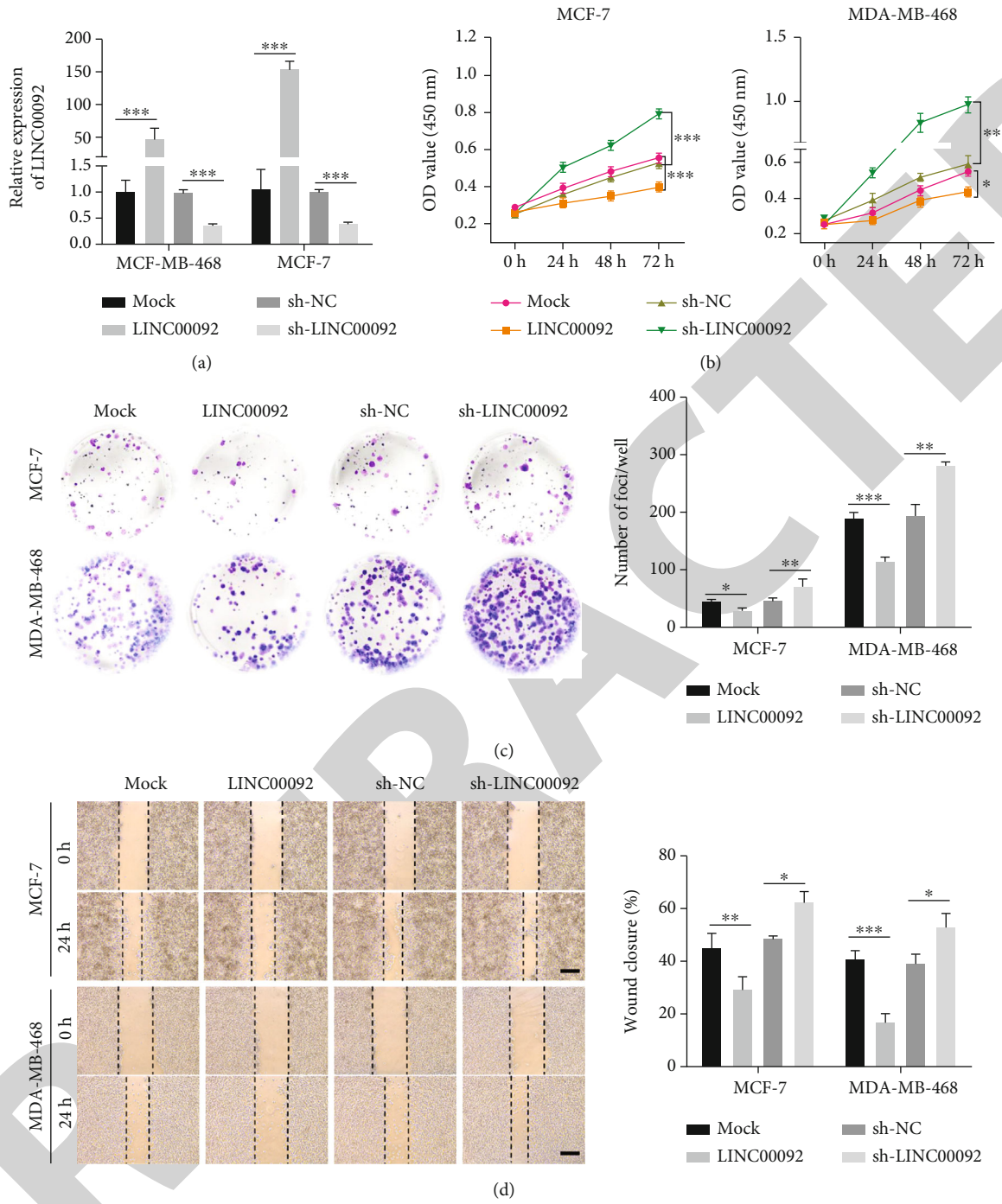
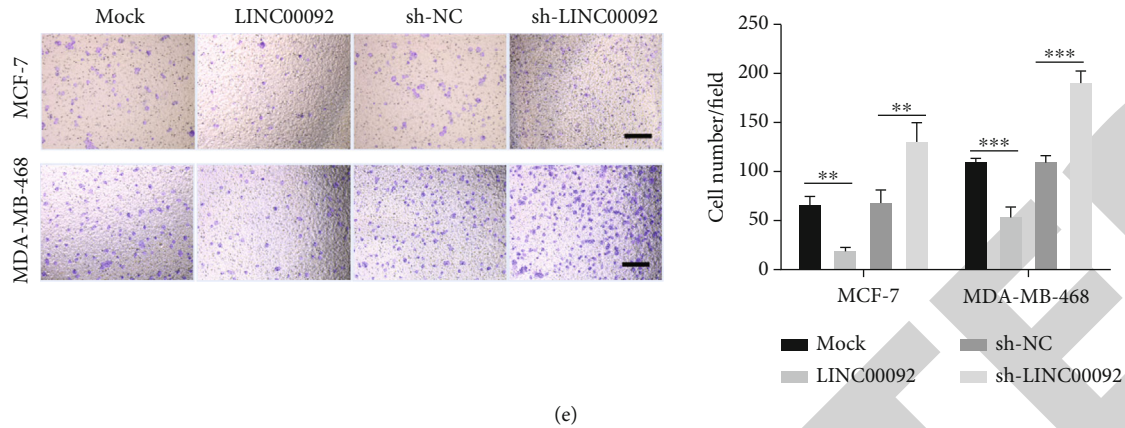


FIGURE 2: Continued.



(e)

FIGURE 2: LINC00092 regulated BC cell proliferation, migration, and invasion. Following LINC00092 or sh-LINC00092 transfection, the LINC00092 expression in cells (a), cell viabilities (b), proliferation (c), migration (d), and invasion (e) were measured via qPCR, CCK-8 assay, colony formation assay, cell scratch assay, and two-chamber transwell assay, respectively.  $N = 3$ . \* $P < 0.05$ , \*\* $P < 0.01$ , and \*\*\* $P < 0.001$ .

treatment reversed the sh-LINC00092 transfection-resulted AKT/mTOR activation, cell viabilities, proliferation, migration, and invasion enhancements, as well as increases of lactate production and glucose consumption ( $P < 0.01$  or  $P < 0.001$ ). These outcomes represented that LINC00092 influenced BC cell viability, proliferation, migration, invasion, and glycolysis which could be via modulating the AKT/mTOR pathway.

**4.7. LINC00092 Regulated Ubiquitination Degradation of PC Protein in BC Cells.** RNA pull-down assay and MS analysis were carried out to identify proteins interacting with LINC00092 in BC cells. Figures 6(a) and 6(b) illustrate that LINC00092 could bind to PC protein. The results of RNA-FISH assay in Figure 6(c) display that LINC00092 colocalized with PC protein in the cytoplasm of MCF-7 and MDA-MB-468 cells. The results of western blotting following RNA pull-down displayed that LINC00092 bound with PC (Figure 6(d)). Similar results were found in RIP assay in Figure 6(e). Relative to the IgG group, the relative enrichments of PC protein in the anti-PC group were significantly increased in cells ( $P < 0.001$ ). These outcomes suggested that LINC00092 interacted with PC in BC cells. Next, the molecular mechanism of the interaction between LINC00092 and PC was explored. Results showed that LINC00092 or sh-LINC00092 transfection had no significant effect on PC mRNA expression (Figure 6(f),  $n.s.P > 0.05$ ) but negatively regulated PC protein level in cells (Figure 6(g)). LINC00092 transfection notably lowered the PC protein expression in cells ( $P < 0.05$  or  $P < 0.001$ ), while sh-LINC00092 transfection obviously raised the PC protein expression in cells ( $P < 0.05$  or  $P < 0.001$ ). The results of immunohistochemistry assay in Figure 6(h) further displayed that LINC00092 transfection reduced the PC protein expression in mouse xenograft BC tissue. Therefore, we speculated that LINC00092 might regulate the protein stability of PC in BC cells. CHX was used to inhibit protein (including PC) synthesis in cells. The results in Figure 6(i) showed that LINC00092 transfection promoted the degradation of PC

protein ( $P < 0.05$  or  $P < 0.01$ ), while sh-LINC00092 transfection inhibited the degradation of PC protein in cells ( $P < 0.05$  or  $P < 0.01$ ). The protein degradation mediated by the ubiquitin proteasome pathway is the main mechanism for the body to regulate intracellular protein levels, which participates in the degradation of more than 80% of intracellular protein [40]. The results of *in vitro* ubiquitination assay in Figure 6(j) displayed that LINC00092 modulated the degradation of PC protein in BC cells via the ubiquitination pathway. These above outcomes represented that LINC00092 regulated ubiquitination degradation of PC protein in BC cells.

**4.8. PC Participated in the Regulation of LINC00092 on BC Cell Functions.** PC was transfected to raise PC level in cells. Figure 7(a) illustrates that compared to the LINC00092 group, the PC protein level in the LINC00092+PC group was increased in cells ( $P < 0.05$  or  $P < 0.01$ ). Following LINC00092 and/or PC transfection, cell viabilities, proliferation, migration, invasion, and glycolysis were detected. Results in Figures 7(b)–7(e) showed that PC transfection promoted cell viabilities, proliferation, migration, and invasion ( $P < 0.01$  or  $P < 0.001$ ). Relative to the LINC00092 group, cell viabilities, proliferation, migration, and invasion in the LINC00092+PC group were decreased ( $P < 0.05$ ,  $P < 0.01$ , or  $P < 0.001$ ), which presented that PC transfection weakened the influence of LINC00092 transfection on cell viabilities, proliferation, migration, and invasion. Similar results were found for the glycolysis of MCF-7 and MDA-MB-468 cells. Figures 7(f) and 7(g) illustrate that PC transfection elevated the cell lactate production and glucose consumption ( $P < 0.01$  or  $P < 0.001$ ), as well as alleviated the LINC00092 transfection-resulted reductions of lactate production and glucose consumption ( $P < 0.05$  or  $P < 0.01$ ). Besides, sh-PC was transfected to silence PC expression in cells. Results in Supplemental Figures 4A–4G showed that silence of PC partially reversed the influences of sh-LINC00092 transfection MCF-7 and MDA-MB-468 cell viabilities, proliferation,

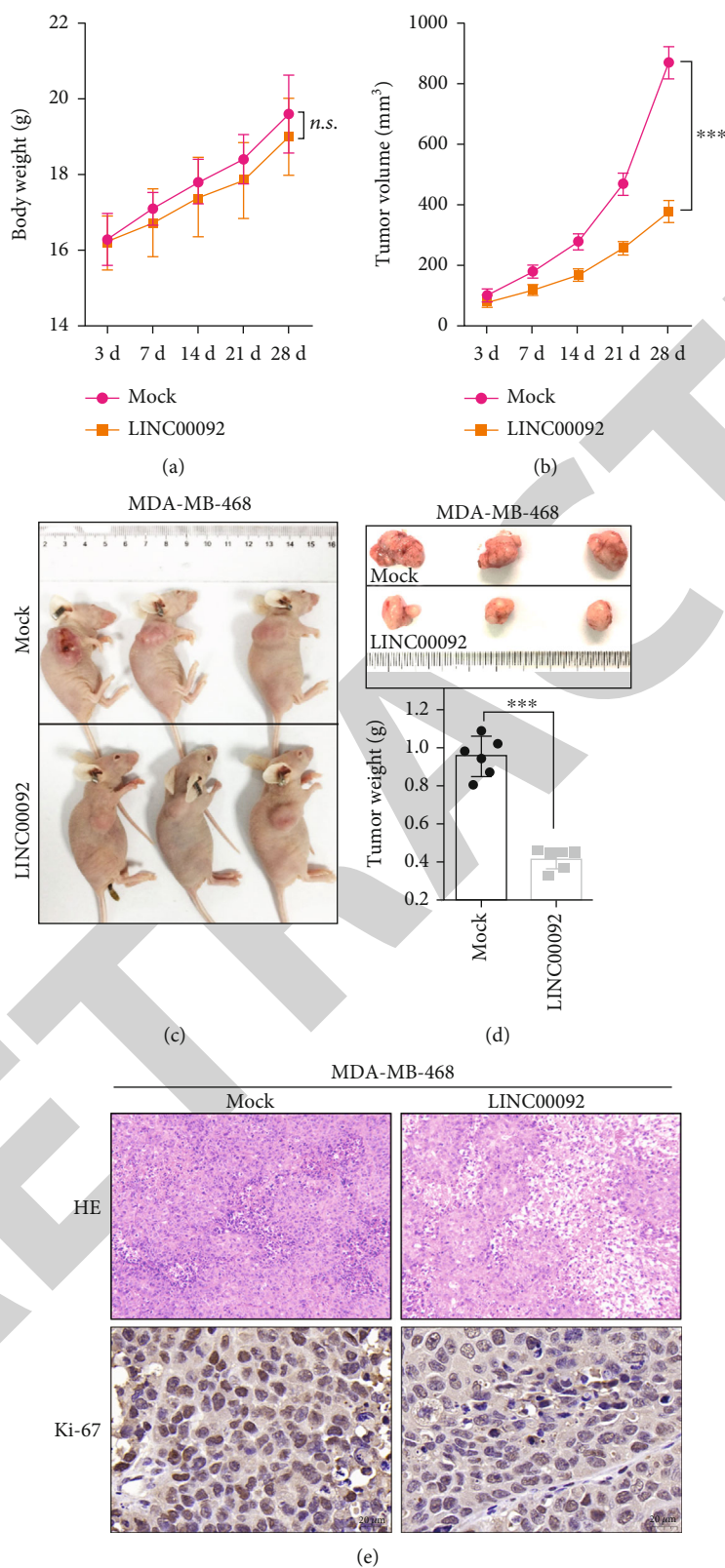
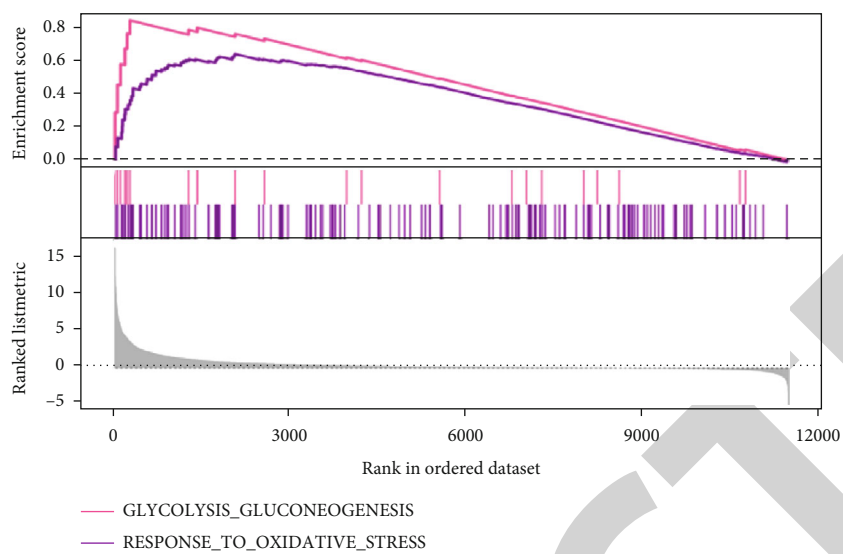
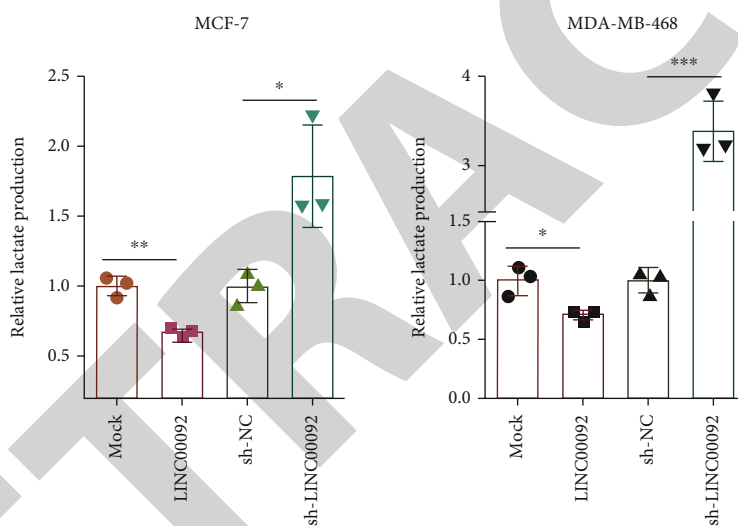


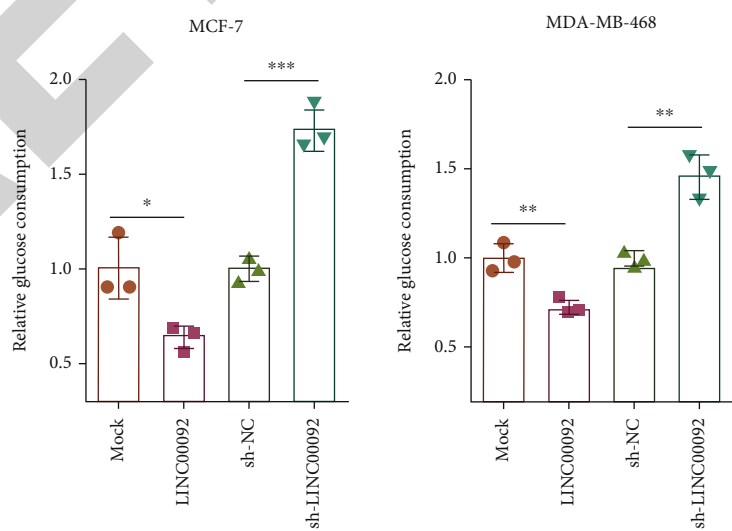
FIGURE 3: LINC00092 overexpression inhibited BC growth *in vivo*. *In vivo* BC mouse model was established with mock or LINC00092 transfection. (a, b) Body weights and tumor volumes of mice in the mock and LINC00092 group were measured at day 3, day 7, day 14, day 21, and day 28. (c) The visual picture of mice with subcutaneous BC transplantation. (d) The visual picture of tumor tissues and tumor weights was detected. (e) HE staining was carried out to observe the microstructure changes of tumor tissues, and IHC assay was utilized to detect the Ki-67 expression in tumor tissues.  $N = 6$ . <sup>N.S.</sup> $P > 0.05$ ; <sup>\*\*\*</sup> $P < 0.001$ .



(a)



(b)



(c)

FIGURE 4: Continued.

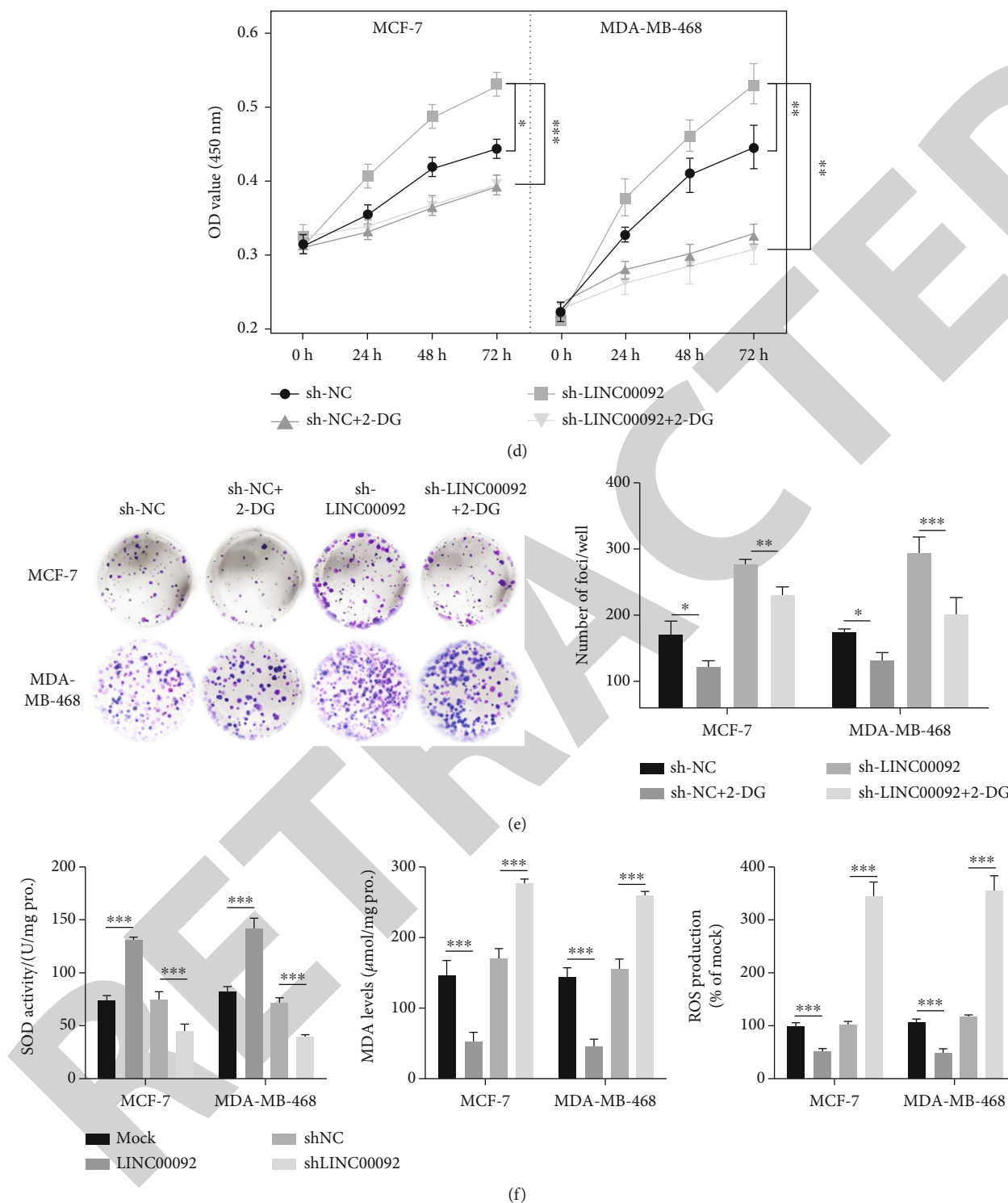


FIGURE 4: LINC00092 influenced BC cell glycolysis and oxidative response. (a) GSEA was carried out to explore the enrichment of glycolysis and response to oxidative stress regulated by LINC00092 in BC tissues. (b, c) Following LINC00092 or sh-LINC00092 transfection, cell lactate production and glucose consumption were tested via lactate assay kit and glucose assay kit.  $N = 3$ . (d, e) Following sh-LINC00092 transfection and/or 2-DG treatment, cell viabilities and proliferation were detected via CCK-8 assay and colony formation assay.  $N = 3$ . (f) Following LINC00092 or sh-LINC00092 transfection, the SOD, MDA, and ROS levels in cells were tested, respectively.  $N = 3$ . \* $P < 0.05$ , \*\* $P < 0.01$ , and \*\*\* $P < 0.001$ .

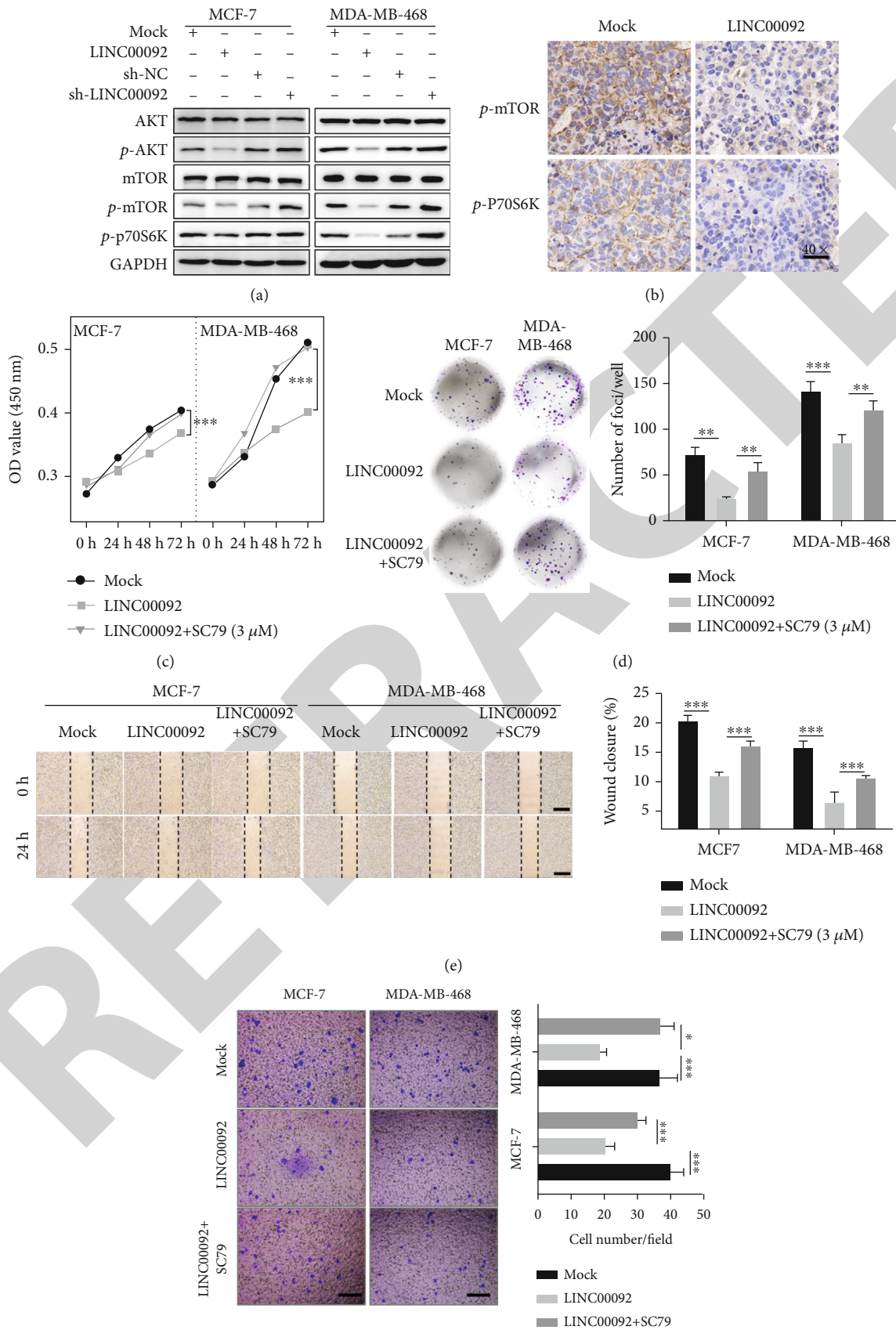


FIGURE 5: Continued.



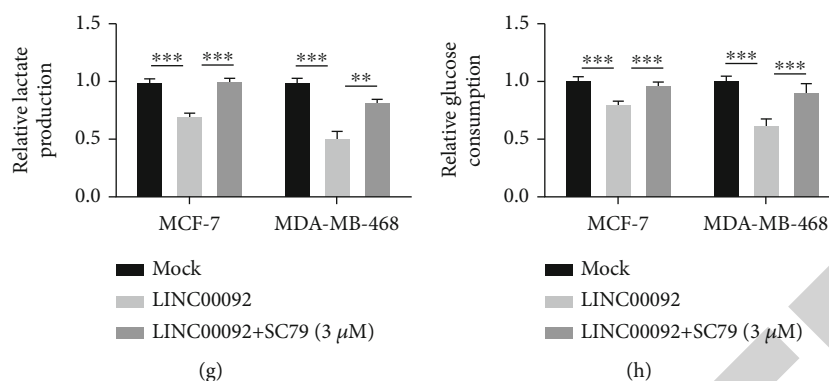


FIGURE 5: LINC00092 influenced BC cell functions and glycolysis via modulating the AKT/mTOR pathway. (a) After LINC00092 or sh-LINC00092 transfection, the AKT, p-AKT, mTOR, p-mTOR, and p-p70S6K protein levels in cells were evaluated by western blotting.  $N = 3$ . (b) IHC assay was utilized to test p-mTOR and p-p70S6K expressions in mouse xenograft BC tissues.  $N = 6$ . Following LINC00092 transfection and SC79 treatment, cell viabilities (c), proliferation (d), migration (e), and invasion (f) were tested via CCK-8 assay, colony formation assay, cell scratch assay, and two-chamber transwell assay, respectively. (g, h) Cell lactate production and glucose consumption were tested.  $N = 3$ . \* $P < 0.05$ , \*\* $P < 0.01$ , and \*\*\* $P < 0.001$ .

migration, invasion, and glycolysis ( $P < 0.05$ ,  $P < 0.01$ , or  $P < 0.001$ ). These above outcomes represented that overexpression of PC weakened the influences of LINC00092 transfection on BC cell functions.

**4.9. PC Participated in the Modulation of LINC00092 on the AKT/mTOR Pathway in BC Cells.** Finally, following PC and/or LINC00092 transfection (or sh-PC and/or sh-LINC00092 transfection), the activity of the AKT/mTOR pathway in cells was measured. Results displayed that PC transfection activated the AKT/mTOR pathway in cells by enhancing p-AKT/AKT, p-mTOR/mTOR, and p-p70S6K/70S6K protein levels (Supplemental Figure 5A,  $P < 0.01$  or  $P < 0.001$ ), as well as reversed the LINC00092 transfection-resulted inactivation of the AKT/mTOR pathway ( $P < 0.05$ ,  $P < 0.01$ , or  $P < 0.001$ ). Besides, sh-PC had opposite influence, which inactivated the AKT/mTOR pathway in cells by lowering p-AKT/AKT, p-mTOR/mTOR, and p-p70S6K/70S6K protein levels (Supplemental Figure 5B,  $P < 0.01$  or  $P < 0.001$ ), as well as weakened the sh-LINC00092 transfection-resulted activation of the AKT/mTOR pathway ( $P < 0.05$  or  $P < 0.01$ ). These outcomes suggested that PC play a key role in the modulation of LINC00092 on the AKT/mTOR pathway in BC cells.

## 5. Discussion

As the most common malignant cancer in women, BC threatens the health and life of many individuals, which also brings great mental and financial pressures for BC patients [2, 41]. In recent years, lncRNAs are verified to serve as a key regulator of gene expression in eukaryotic cells [42]. More importantly, lots of lncRNAs are discovered to take part in the progression of human cancers, which offers a new direction for cancer-targeted therapy [11]. There are many clinical trials concerning the roles of lncRNAs in cancer diagnosis and therapy, which can be inquired in ClinicalTrials.gov database (<https://clinicaltrials.gov>). LINC00092 was a newly discovered lncRNA. Wu et al. [16] reported that

LINC00092 expression was significantly associated with the survival of BC patients. Zhao *et al.* [43] discovered that LINC00092 expression was downregulated in breast invasive ductal carcinoma (BIDC) tissues and cells, which promoted malignant progression of BIDC via regulating secreted frizzled related protein 1 (SFRP1) by sponging microRNA-1827. Herein, we revealed that LINC00092 had lower expression level in BC tissues and cells and negatively related to BC tumor size and histological grade, as well as positively related to survival probability of BC patients. Uncontrolled abnormal cell proliferation is the foundation of BC development [44]. Besides, cancer recrudescence and metastasis are mainly responsible for BC-related death [4]. The lungs, pleura, bones, skin and soft tissues, liver, and brain are the common metastatic sites of BC [4]. We discovered that LINC00092 overexpression reduced BC MCF-7 and MDA-MB-468 cell proliferation, migration, and invasion. Silence of LINC00092 had contrary influence. Furthermore, LINC00092 overexpression inhibited BC growth *in vivo*. These findings proposed that the lowly expression of LINC00092 contributed to BC progression and implied that LINC00092 is a possible potential biomarker for BC diagnosis and target for BC treatment.

FLI1 is a key member of the E26 transformation-specific (ETS) family, which is a group of highly conserved transcription factors with a unique winged helix-turn-helix DNA-binding domain [45]. As a pivotal regulator of embryonic development, loss of FLI1 will cause embryonic death [46]. According to the results of pervious literatures, there was controversy about the role of FLI1 in BC development. Scheiber et al. [47] reported that the lower expression of FLI1 in BC meant shorter survival time and stronger degree of malignancy. However, Song et al. [48] discovered that FLI1 was highly expressed in BC tissues, in which expression was positively related to BC progression. Besides, Yan *et al.* [49] also revealed that FLI1 was overexpressed in triple-negative BC subtype and predicted the poor prognosis of BC patients. In the current research, we discovered that FLI1 bound to LINC00092 promoter to positively modulate

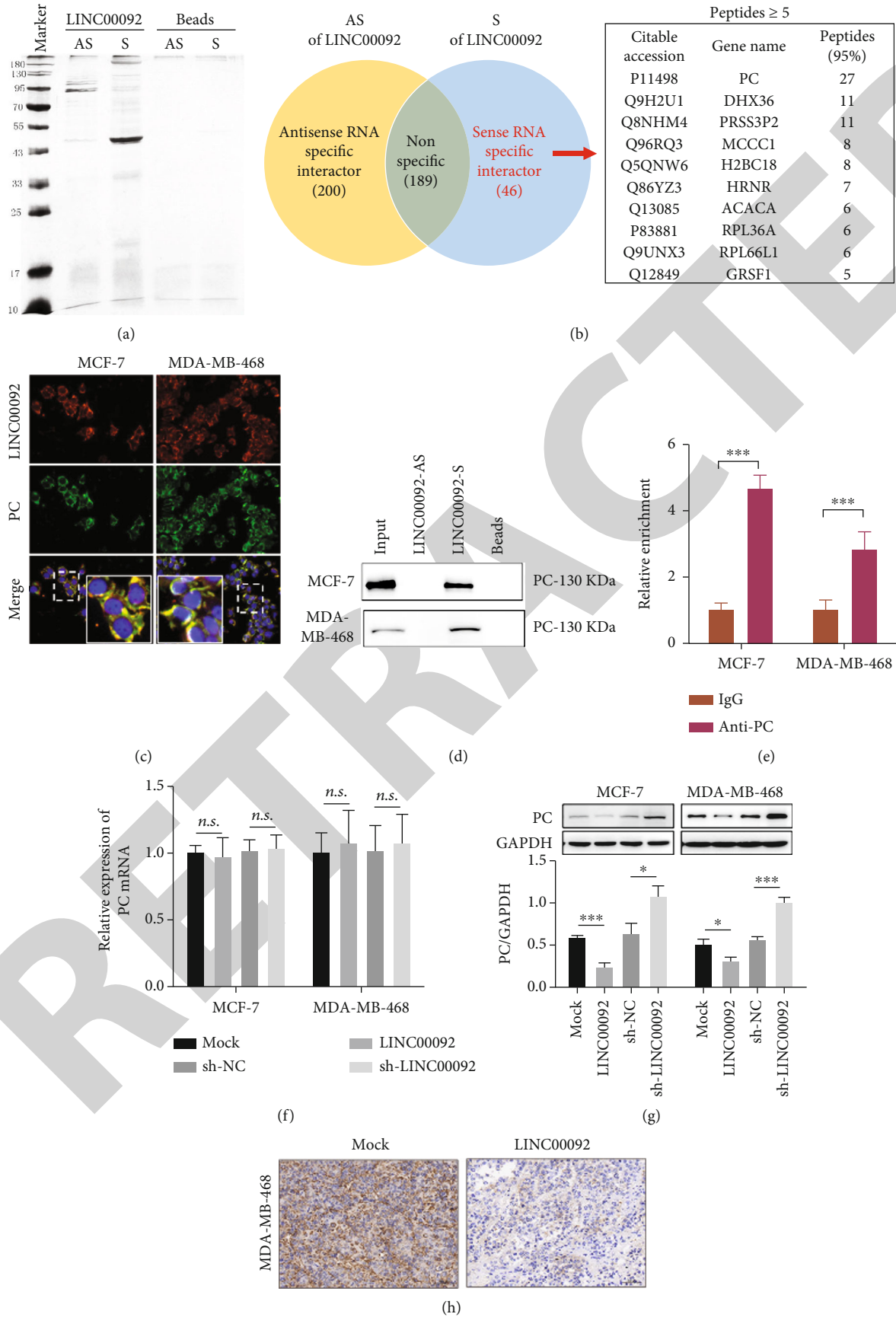


FIGURE 6: Continued.

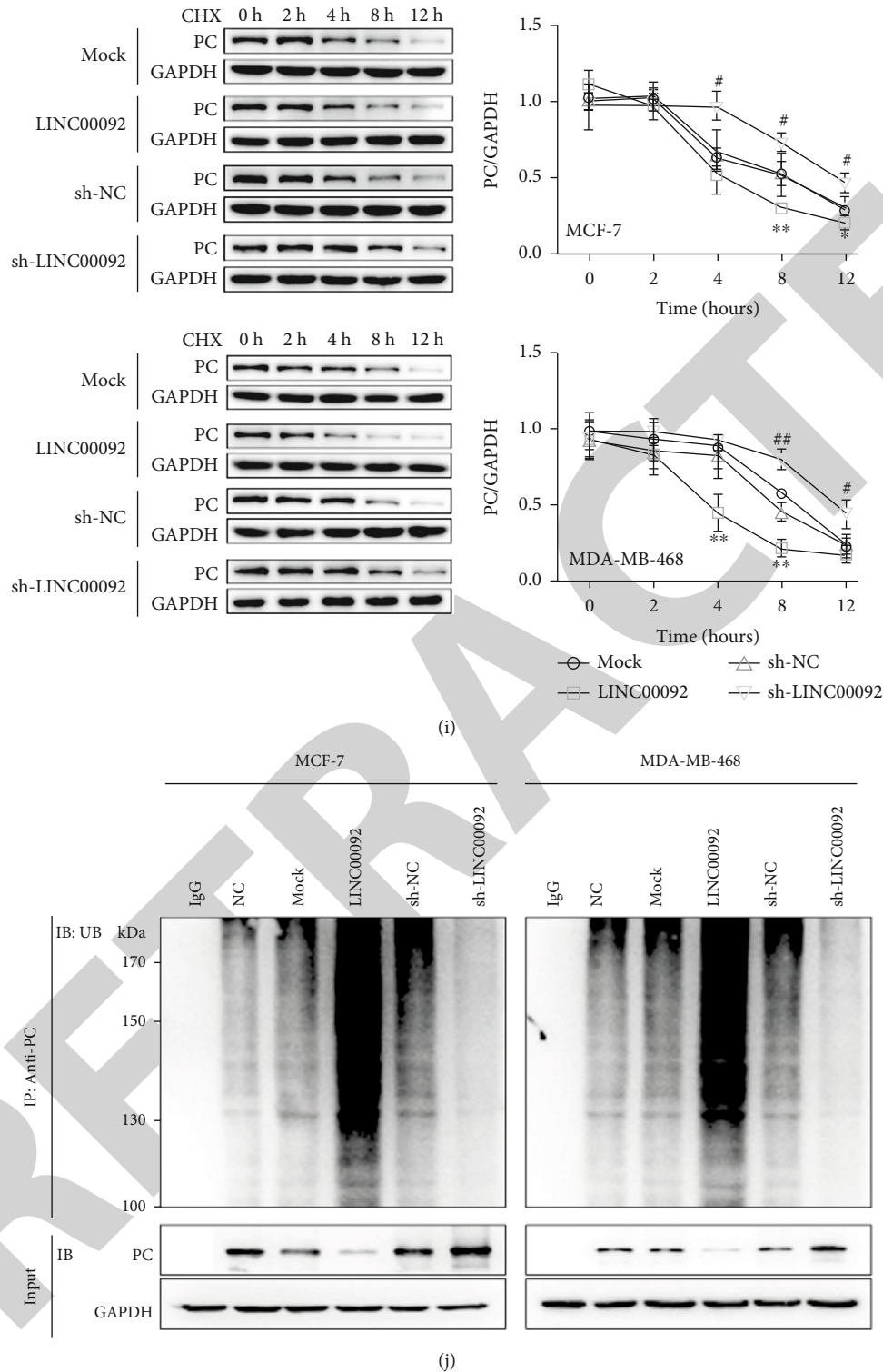


FIGURE 6: LINC00092 regulated ubiquitination degradation of PC protein in BC cells. (a, b) RNA pull-down assay and MS analysis were carried out to identify proteins interacting with LINC00092 in BC cells.  $N = 3$ . (c) RNA-FISH assay was performed to measure the location of LINC00092 and PC in cells.  $N = 3$ . (d) The samples from RNA pull-down assay were subjected to western blotting to test PC protein expression.  $N = 3$ . (e) RIP assay was used to confirm the binding of LINC00092 and PC.  $N = 3$ . (f, g) Following LINC00092 and sh-LINC00092 transfection, the mRNA and protein levels of PC were tested via qPCR and western blotting.  $N = 3$ . (h) IHC assay was utilized to test PC expression in subcutaneous BC tissues of mice.  $N = 6$ . (i) Following LINC00092 (or sh-LINC00092) transfection and CHX treatment, the PC protein level was tested via western blotting in 0, 2, 4, 8, and 12 h.  $N = 3$ . (j) *In vivo* ubiquitination assay was carried out to test whether LINC00092 modulate degradation of PC protein via the ubiquitination pathway.  $N = 3$ .  $n.s.$   $P > 0.05$ ,  $*P < 0.05$ ,  $**P < 0.01$ , and  $***P < 0.001$  vs. the mock group;  $\#P < 0.05$  and  $\#\#P < 0.01$  vs. the sh-NC group.

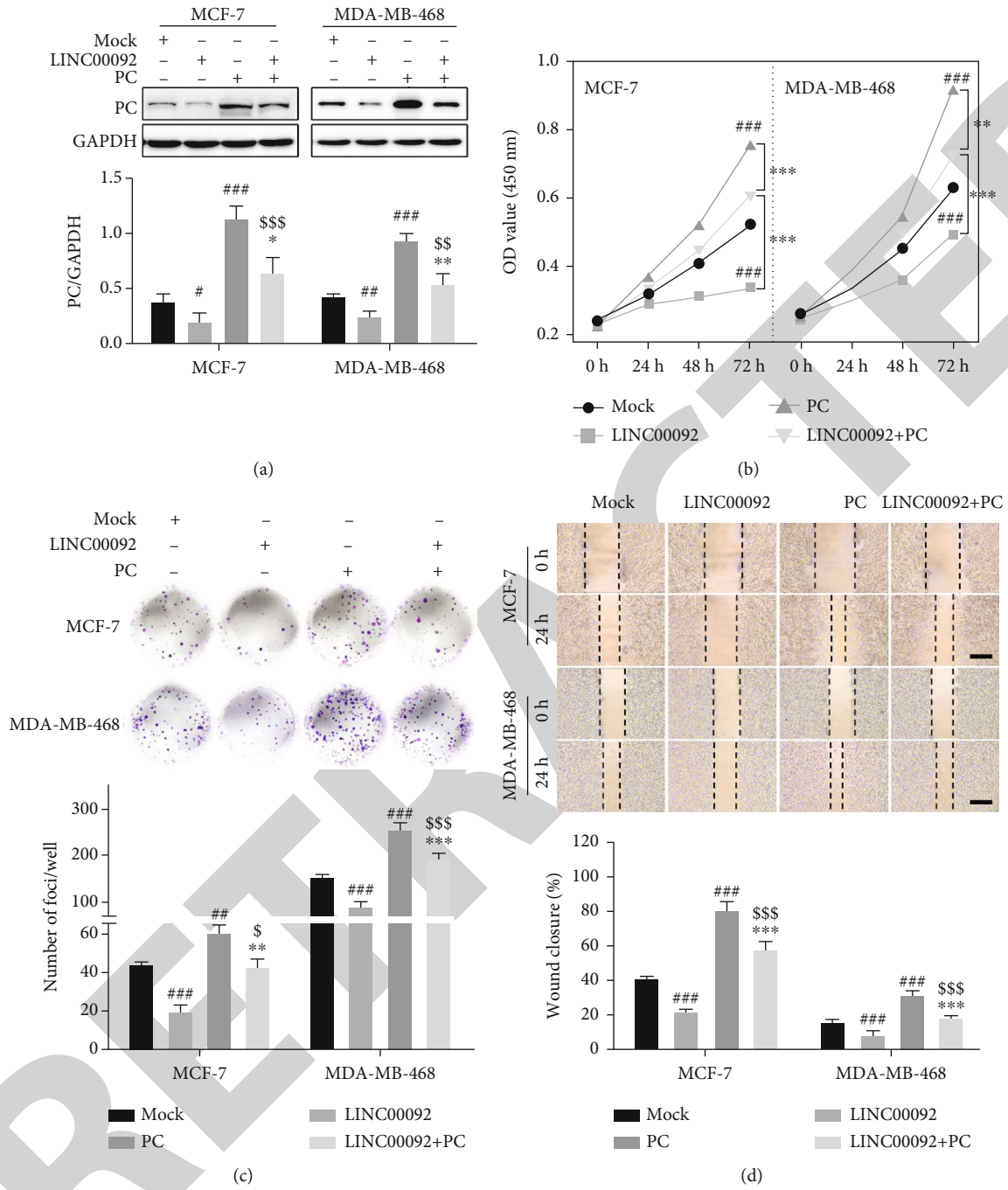


FIGURE 7: Continued.

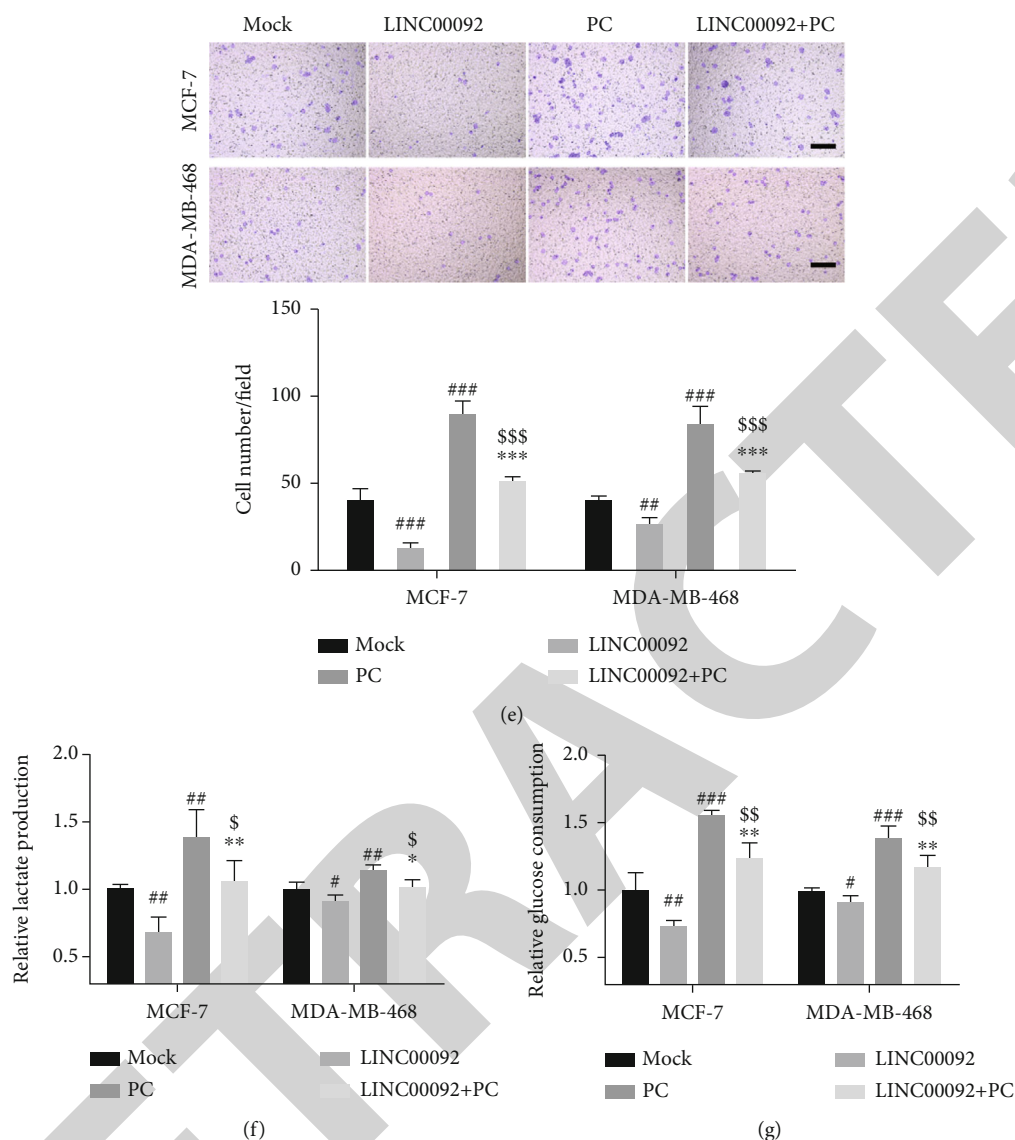


FIGURE 7: Overexpression of PC weakened the influences of LINC00092 transfection on BC cell functions. Following LINC00092 and PC transfection, (a) PC protein levels were tested via western blotting. Cell viabilities (b), proliferation (c), migration (d), and invasion (e) were tested via CCK-8 assay, colony formation assay, cell scratch assay, and two-chamber transwell assay, respectively. (f, g) Cell lactate production and glucose consumption were tested.  $N = 3$ . # $P < 0.05$ , ## $P < 0.01$ , and ### $P < 0.001$  vs. the mock group; \* $P < 0.05$ , \*\* $P < 0.01$ , and \*\*\* $P < 0.001$  vs. the LINC00092 group. \$ $P < 0.05$ , \$\$ $P < 0.01$ , and \$\$\$ $P < 0.001$  vs. the PC group.

the LINC00092 expression in BC cells. Similar to LINC00092, FLI1 was also lowly expressed in BC tissues. These findings proposed that low expression of FLI1 at least in part resulted in the low expression of LINC00092 in BC.

As the main manner for BC cells to produce ATP, glycolysis is essential for BC growth [20]. Earlier literature reported that even in aerobic environment, BC cells still will choose glycolysis as the main manner for energy supplement [50]. Chen *et al.* [23] discovered that LINC00092 suppressed cardiac fibroblast activation by regulating glycolysis through an extracellular regulated protein kinase- (ERK-) dependent manner. Zhao *et al.* [13] revealed that LINC00092 was highly expressed in ovarian cancer cells, which accelerated glycolysis of ovarian cancer cells. However, in this study, we found that silence of LINC00092 accelerated the glycoly-

sis of BC cells via raising glucose consumption and lactate production. LINC00092 overexpression had opposite influence. What is more, inhibition of glycolysis by 2-DG relieved the LINC00092 silence-caused increase of BC cell proliferation. These findings proposed that LINC00092 modulated BC cell proliferation at least via glycolysis. Moreover, these discoveries revealed that LINC00092 might exert distinct regulatory effects on glycolysis in different cancers.

The imbalance between reactive species and antioxidant defenses will result in the increase of oxidative stress. Excessive amounts of reactive species are detrimental to normal cells, whereas in cancer cells, they lead to accelerated growth and survival related to aggressive and therapy-resistant phenotypes [25]. Mullarky and Cantley [26] discovered that ROS can regulate multiple glycolytic enzymes, including

glyceraldehyde 3-phosphate dehydrogenase, pyruvate kinase M2, and phosphofructokinase-1. Martinez-Outschoorn *et al.* [51] found that the mutation of breast cancer susceptibility gene 1 (BRCA1), a key tumor suppressor gene, accelerated oxidative stress and glycolysis in tumor microenvironment of breast cancer. Herein, we also discovered that both glycolysis and response to oxidative stress were modulated by LINC00092 in BC tissues. LINC00092 overexpression reduced the oxidative stress via raising SOD level and lowering MDA and ROS levels in BC cells. However, LINC00092 silence had contrary influence, which activated oxidative stress. These findings proposed that LINC00092 also took part in the modulation of oxidative stress in BC.

The AKT/mTOR pathway is very important for regulation of cell proliferation that is overactivated in many human cancers, including BC, and contributes to neoplastic transformation [39]. More importantly, in recent years, the AKT/mTOR pathway is demonstrated to take part in the regulation of cell oxidative stress and glycolysis [52, 53]. Jia *et al.* [54] revealed that inhibition of the AKT/mTOR pathway suppressed BC progression through limiting BC cell glycolysis. Zong *et al.* [55] reported that salt-inducible kinase (SIK2), a member of adenosine monophosphate-(AMP-) activated protein kinase family, was beneficial for cisplatin resistance caused by aerobic glycolysis in BC cells via modulating the AKT/mTOR pathway. In recent years, many lncRNAs are discovered to modulate the AKT/mTOR pathway in BC cells [56, 57]. Until now, it is still unclear whether LINC00092 regulates the AKT/mTOR pathway in cells. Herein, we found that LINC00092 silence activated the AKT/mTOR pathway in BC cells, while LINC00092 overexpression had contrary effect. Moreover, activation of the AKT/mTOR pathway by SC79 reversed the LINC00092 overexpression-resulted decreases of BC cell proliferation, migration, invasion, and glycolysis. Inhibition of the AKT/mTOR pathway by MK2206 had opposite influence. These findings proposed that LINC00092 influenced BC cell proliferation, migration, invasion, and glycolysis which could be achieved via the AKT/mTOR pathway.

For cancer cells, elevated glycolysis alone is not enough to provide all necessary metabolic intermediates for growth and metastasis, and it is also necessary to promote the biosynthesis of the precursor molecules of tricarboxylic acid cycle (TCA) for replenishment [58]. Oxaloacetate is a main precursor molecule of TCA. As a mitochondrial enzyme, PC is responsible for conversion of pyruvate to oxaloacetate in cells [59]. Numerous literatures reported that PC was highly expressed in BC and its high expression was positively related to BC clinical progression, such as tumor size, tumor stage, and poor prognosis [60, 61]. Moreover, PC was discovered to promote BC metastasis [59, 62]. Liu *et al.* [63] reported that PC could activate the AKT/mTOR pathway in thyroid cancer cells. In the last few years, some literatures have reported the regulatory role of lncRNAs in PC expression in cancer cells [64, 65]. In this research, we revealed that LINC00092 bound to PC to modulate the ubiquitination degradation of PC protein in BC cells. More importantly, overexpression of PC weakened the influences of LINC00092 overexpression on BC cell proliferation, migra-

tion, invasion, glycolysis, and the AKT/mTOR pathway. Silence of PC had similar mitigatory activity on the influence of LINC00092 silence on BC cells. These findings proposed that the regulatory function of LINC00092 on PC contributed to the modulatory effects of LINC00092 on BC growth and metastasis.

In general, one lncRNA participates in regulating expressions of multiple proteins and other ncRNAs in cells [11]. As a type of ncRNAs with 18-24 nucleotides, microRNAs are main downstream targets of lncRNA [66]. Zhao *et al.* [43] reported that LINC00092 sponged microRNA-1827 in BIC cells to modulate BIC malignant progression, which implied that LINC00092 regulated BC progression not only by modulating PC expression but also via regulating other molecules. Besides, the *in vivo* experiment in our research was relatively simple. We did not explore the effect of LINC00092 on glycolysis, PC expression, oxidative stress, and the AKT/mTOR pathway *in vivo*. More investigations are still demanded in the future.

Taken together, this research affirmed the tumor-suppressive role of LINC00092 in BC. The low expression of LINC00092 promoted BC cell proliferation, migration, invasion, and glycolysis via the PC-mediated AKT/mTOR pathway. This study revealed that LINC00092 might be regarded as a novel prognostic indicator and potential therapeutic target for patients with BC.

## Data Availability

The data used to support the findings of this study are included within the article.

## Ethical Approval

All experiments in this study were approved by the Ethics Committee of Fujian Medical University Union Hospital and performed in accordance with the Declaration of Helsinki.

## Consent

Written informed consents were obtained from patients.

## Disclosure

This manuscript was first submitted on March 8, during which some research defects were found and some experimental supplements were made. It was submitted for a second time on April 28.

## Conflicts of Interest

The authors declare that they have no competing interest.

## Authors' Contributions

Wei Chen and Yushan Liu contributed equally to this work.

## Acknowledgments

This research was funded by Fujian Science and Technology Innovation Joint Fund Project, Fujian Province (2019Y9054), and the Natural Science Foundation of Fujian Province, China (202101751).

## Supplementary Materials

Supplemental Figure 1: LINC00092 was lowly expressed in BC and negatively related to BC progression. Supplemental Figure 2: FLI1 had lower expression in BC tissues. Supplemental Figure 3: inhibition of the MAPK/mTOR pathway reversed the influence of sh-LINC00092 on BC cell functions and glycolysis. Supplemental Figure 4: inhibition of PC reversed the influence of sh-LINC00092 on BC cell functions and glycolysis. Supplemental Figure 5: PC was involved in the modulation of LINC00092 on AKT/mTOR pathway in BC cells. (*Supplementary Materials*)

## References

- [1] H. M. Mansour, G. E. M. Neyazy, Y. I. Abdel Khaleq, and A. M. Elnaggar, "The role of FDG-PET/CT in staging of breast cancer," *QJM: An International Journal of Medicine*, vol. 114, Supplement\_1, 2021.
- [2] R. L. Siegel, K. D. Miller, and A. Jemal, "Cancer statistics, 2020," *CA: a Cancer Journal for Clinicians*, vol. 70, no. 1, pp. 7–30, 2020.
- [3] K. Maajani, A. Jalali, S. Alipour, M. Khodadost, H. R. Tohidinik, and K. Yazdani, "The global and regional survival rate of women with breast cancer: a systematic review and meta-analysis," *Clinical Breast Cancer*, vol. 19, no. 3, pp. 165–177, 2019.
- [4] E. M. Schunkert, W. Zhao, and K. Zänker, "Breast cancer recurrence risk assessment: is non-invasive monitoring an option?," *Biomedicine Hub*, vol. 3, pp. 1–16, 2019.
- [5] A. Shahbandi, H. D. Nguyen, and J. G. Jackson, "TP53 mutations and outcomes in breast cancer: reading beyond the headlines," *Trends Cancer*, vol. 6, no. 2, pp. 98–110, 2020.
- [6] P. H. G. Duijf, D. Nanayakkara, K. Nones, S. Srihari, M. Kalimutho, and K. K. Khanna, "Mechanisms of genomic instability in breast cancer," *Trends in Molecular Medicine*, vol. 25, no. 7, pp. 595–611, 2019.
- [7] L. E. Kelemen, X. Wang, Z. S. Fredericksen et al., "Genetic variation in the chromosome 17q23 amplicon and breast cancer risk," *Cancer Epidemiology, Biomarkers & Prevention*, vol. 18, no. 6, pp. 1864–1868, 2009.
- [8] X. Gao and Q. Z. Dong, "Advance in metabolism and target therapy in breast cancer stem cells," *World Journal of Stem Cells*, vol. 12, no. 11, pp. 1295–1306, 2020.
- [9] M. Kandula, K. K. Ch, and A. R. Ys, "Molecular mechanism and targeted therapy options of triple-negative (ER, PgR, HER-2/neu) breast cancer: review," *World journal of oncology*, vol. 4, no. 3, pp. 137–141, 2013.
- [10] C. Lu and Y. H. Huang, "Progress in long non-coding RNAs in animals," *Yi Chuan*, vol. 39, no. 11, pp. 1054–1065, 2017.
- [11] Y. Chen and V. Tergaonkar, "LncRNAs: master regulators in disease and cancer," *Proceedings of the Singapore National Academy of Science*, vol. 14, no. 2, pp. 79–89, 2020.
- [12] W. J. Liao and Y. L. Mao, "Regulatory effects of long non-coding RNA on tumorigenesis," *Zhongguo Yi Xue Ke Xue Yuan Xue Bao*, vol. 37, no. 3, pp. 358–363, 2015.
- [13] L. Zhao, G. Ji, X. le et al., "Long noncoding RNA LINC00092 acts in cancer-associated fibroblasts to drive glycolysis and progression of ovarian cancer," *Cancer Research*, vol. 77, no. 6, pp. 1369–1382, 2017.
- [14] X. Wang, X. Wang, G. Huang, and Y. Chen, "Lower expression of LINC00092 in lung adenocarcinoma might mean poorer prognosis: a study based on data mining and bioinformatics," *Medicine (Baltimore)*, vol. 99, no. 44, article e23012, 2020.
- [15] W. Huang, Z. Liu, Y. Li, L. Liu, and G. Mai, "Identification of long noncoding RNAs biomarkers for diagnosis and prognosis in patients with colon adenocarcinoma," *Journal of Cellular Biochemistry*, vol. 120, no. 3, pp. 4121–4131, 2019.
- [16] J. Wu, M. Li, and Y. Zhang, "Long noncoding RNAHOXA-AS2regulates the expression ofSCN3Aby spongingmiR-106ain breast cancer," *Journal of Cellular Biochemistry*, vol. 120, no. 9, pp. 14465–14475, 2019.
- [17] J. Zheng, "Energy metabolism of cancer: glycolysis versus oxidative phosphorylation (review)," *Oncology Letters*, vol. 4, no. 6, pp. 1151–1157, 2012.
- [18] N. Nowak, A. Kulma, and J. Gutowicz, "Up-regulation of key glycolysis proteins in cancer development," *Open Life Sciences*, vol. 13, no. 1, pp. 569–581, 2018.
- [19] H. Harami-Papp, L. S. Pongor, G. Munkácsy et al., "TP53 mutation hits energy metabolism and increases glycolysis in breast cancer," *Oncotarget*, vol. 7, no. 41, pp. 67183–67195, 2016.
- [20] M. He, C. Hu, J. Deng, H. Ji, and W. Tian, "Identification of a novel glycolysis-related signature to predict the prognosis of patients with breast cancer," *World Journal of Surgical Oncology*, vol. 19, no. 1, p. 294, 2021.
- [21] R. Liu, X. Wang, Y. Shen, and A. He, "Long non-coding RNA-based glycolysis-targeted cancer therapy: feasibility, progression and limitations," *Molecular Biology Reports*, vol. 48, no. 3, pp. 2713–2727, 2021.
- [22] M. Xia, S. Feng, Z. Chen, G. Wen, X. Zu, and J. Zhong, "Non-coding RNAs: key regulators of aerobic glycolysis in breast cancer," *Life Sciences*, vol. 250, p. 117579, 2020.
- [23] Z. T. Chen, H. F. Zhang, M. Wang et al., "Long non-coding RNA Linc00092 inhibits cardiac fibroblast activation by altering glycolysis in an ERK-dependent manner," *Cellular Signaling*, vol. 74, p. 109708, 2020.
- [24] J. Hayes, A. Dinkova-Kostova, and K. Tew, "Oxidative stress in cancer," *Cancer Cell*, vol. 38, no. 2, pp. 167–197, 2020.
- [25] F. Tas, H. Hansel, A. Belce et al., "Oxidative stress in breast cancer," *Medical Oncology*, vol. 22, no. 1, pp. 11–15, 2005.
- [26] E. Mullarky and L. C. Cantley, "Diverting glycolysis to combat oxidative stress," *Innovative medicine*, pp. 3–23, 2015.
- [27] C. Zhao, H. Wu, N. Qimuge et al., "MAT2A promotes porcine adipogenesis by mediating H3K27me3 at Wnt10b locus and repressing Wnt/ $\beta$ -catenin signaling," *Biochimica et Biophysica Acta - Molecular and Cell Biology of Lipids*, vol. 1863, no. 2, pp. 132–142, 2018.
- [28] S. S. Zhao, G. D. Zhao, T. Y. di et al., "Analyzing the promoters of two CYP9A genes in the silkworm *Bombyx mori* by dual-luciferase reporter assay," *Molecular Biology Reports*, vol. 40, no. 2, pp. 1701–1710, 2013.
- [29] J. Zhang, X. Tian, H. Yin et al., "TXNIP induced by MondoA, rather than ChREBP, suppresses cervical cancer cell

- proliferation, migration and invasion,” *Journal of Biochemistry*, vol. 167, no. 4, pp. 371–377, 2020.
- [30] C. C. Liang, A. Y. Park, and J. L. Guan, “In Vitro scratch assay: a convenient and inexpensive method for analysis of cell migration in vitro,” *Nature Protocols*, vol. 2, no. 2, pp. 329–333, 2007.
- [31] Y. Wang, X. Cheng, P. Wang et al., “Investigating migration inhibition and apoptotic effects of Fomitopsis pinicola chloroform extract on human colorectal cancer SW-480 cells,” *PLoS One*, vol. 9, no. 7, article e101303, 2014.
- [32] H. Liu, L. Wang, X. Weng et al., “Inhibition of Brd4 alleviates renal ischemia/reperfusion injury-induced apoptosis and endoplasmic reticulum stress by blocking FoxO4-mediated oxidative stress,” *Redox Biology*, vol. 24, p. 101195, 2019.
- [33] S. B. Qin, D. Y. Peng, J. M. Lu, and Z. P. Ke, “MiR-182-5p inhibited oxidative stress and apoptosis triggered by oxidized low-density lipoprotein via targeting toll-like receptor 4,” *Journal of Cellular Physiology*, vol. 233, no. 10, pp. 6630–6637, 2018.
- [34] T. Kim, Y. J. Jeon, R. Cui et al., “Role of MYC-regulated long noncoding RNAs in cell cycle regulation and tumorigenesis,” *Journal of the National Cancer Institute*, vol. 107, no. 4, p. dju505, 2015.
- [35] Y. Liu, Q. Zhang, J. Wu et al., “Long non-coding RNA A2M-AS1 promotes breast cancer progression by sponging microRNA-146b to upregulate MUC19,” *International Journal of General Medicine*, vol. 13, pp. 1305–1316, 2020.
- [36] L. Kong, X. Wang, K. Zhang et al., “Gypenosides synergistically enhances the anti-tumor effect of 5-fluorouracil on colorectal cancer in vitro and in vivo: a role for oxidative stress-mediated DNA damage and p53 activation,” *PLoS One*, vol. 10, no. 9, article e0137888, 2015.
- [37] C. S. Lee, E. S. Han, E. S. Park, and H. Bang, “Inhibition of MG132-induced mitochondrial dysfunction and cell death in PC12 cells by 3-morpholinopyrrolidine,” *Brain Research*, vol. 1036, no. 1–2, pp. 18–26, 2005.
- [38] R. Li, F. Yin, Y. Y. Guo, K. C. Zhao, Q. Ruan, and Y. M. Qi, “Retracted: Knockdown of ANRIL aggravates H<sub>2</sub>O<sub>2</sub>-induced injury in PC-12 cells by targeting microRNA-125a,” *Biomedicine & Pharmacotherapy*, vol. 92, pp. 952–961, 2017.
- [39] E. Andreopoulou, “The PI3K/AKT/mTOR signaling pathway: implications in the treatment of breast cancer,” *Current Breast Cancer Reports*, vol. 3, no. 1, pp. 63–74, 2011.
- [40] J. Wang and M. A. Maldonado, “The ubiquitin-proteasome system and its role in inflammatory and autoimmune diseases,” *Cellular & Molecular Immunology*, vol. 3, no. 4, pp. 255–261, 2006.
- [41] Y. Huang, Z. Tong, K. Chen et al., “Interpretation of breast cancer screening guideline for Chinese women,” *Cancer Biology & Medicine*, vol. 16, no. 4, pp. 825–835, 2019.
- [42] A. C. Marques and C. P. Ponting, “Intergenic lncRNAs and the evolution of gene expression,” *Current Opinion in Genetics & Development*, vol. 27, pp. 48–53, 2014.
- [43] C. M. Zhao, L. L. Li, J. W. Xu, Z. W. Li, P. Shi, and R. Jiang, “LINC00092 suppresses the malignant progression of breast invasive ductal carcinoma through modulating SFRP1 expression by sponging miR-1827,” *Cell Transplantation*, vol. 31, p. 9636897221086967, 2022.
- [44] D. Farhat, S. Léon, S. E. Ghayad et al., “Lipoic acid decreases breast cancer cell proliferation by inhibiting IGF-1R via furin downregulation,” *British Journal of Cancer*, vol. 122, no. 6, pp. 885–894, 2020.
- [45] X. Liang, D. Shi, J. Yun et al., “Friend leukemia virus integration 1 expression has prognostic significance in nasopharyngeal carcinoma,” *Translational Oncology*, vol. 7, no. 4, pp. 493–502, 2014.
- [46] A. Hart, F. Melet, P. Grossfeld et al., “Fli-1 is required for murine vascular and megakaryocytic development and is hemizygotously deleted in patients with thrombocytopenia,” *Immunity*, vol. 13, no. 2, pp. 167–177, 2000.
- [47] M. N. Scheiber, P. M. Watson, T. Rumboldt et al., “FLI1 expression is correlated with breast cancer cellular growth, migration, and invasion and altered gene expression,” *Neoplasia*, vol. 16, no. 10, pp. 801–813, 2014.
- [48] W. Song, W. Li, L. Li et al., “Friend leukemia virus integration 1 activates the rho GTPase pathway and is associated with metastasis in breast cancer,” *Oncotarget*, vol. 6, no. 27, pp. 23764–23775, 2015.
- [49] X. Yan, Y. Yu, L. Li et al., “Friend leukemia virus integration 1 is a predictor of poor prognosis of breast cancer and promotes metastasis and cancer stem cell properties of breast cancer cells,” *Cancer Medicine*, vol. 7, no. 8, pp. 3548–3560, 2018.
- [50] L. Xie, X. Feng, Y. Shi et al., “Blocking the glycolytic pathway sensitizes breast cancer to sonodynamic therapy,” *Ultrasound in Medicine & Biology*, vol. 44, no. 6, pp. 1233–1243, 2018.
- [51] U. Martinez-Outschoorn, R. Balliet, Z. Lin et al., “BRCA1 mutations drive oxidative stress and glycolysis in the tumor microenvironment,” *Cell cycle*, vol. 11, no. 23, pp. 4402–4413, 2012.
- [52] Y. M. Woo, Y. Shin, E. J. Lee et al., “Inhibition of aerobic glycolysis represses Akt/mTOR/HIF-1 $\alpha$  axis and restores tamoxifen sensitivity in antiestrogen-resistant breast cancer cells,” *PLoS One*, vol. 10, no. 7, article e0132285, 2015.
- [53] Y. Shi, X. Y. Liu, Y. P. Jiang et al., “Monotropin attenuates oxidative stress via Akt/mTOR-mediated autophagy in osteoblast cells,” *Biomedicine & pharmacotherapy = Biomedecine & pharmacotherapie*, vol. 121, p. 109566, 2019.
- [54] L. Jia, S. Huang, X. Yin, Y. Zan, Y. Guo, and L. Han, “Quercetin suppresses the mobility of breast cancer by suppressing glycolysis through Akt-mTOR pathway mediated autophagy induction,” *Life Sciences*, vol. 208, pp. 123–130, 2018.
- [55] S. Zong, W. Dai, W. Fang, X. Guo, and K. Wang, “Withdrawn: SIK2 promotes cisplatin resistance induced by aerobic glycolysis in breast cancer cells through PI3K/AKT/mTOR signaling pathway,” *Bioscience Reports*, 2020.
- [56] Z. Li, J. Qian, J. Li, and C. Zhu, “Knockdown of lncRNA-HOTAIR downregulates the drug-resistance of breast cancer cells to doxorubicin via the PI3K/AKT/mTOR signaling pathway,” *Experimental and Therapeutic Medicine*, vol. 18, no. 1, pp. 435–442, 2019.
- [57] X. Qiu, J. Dong, Z. Zhao, J. Li, and X. Cai, “LncRNA LINC00668 promotes the progression of breast cancer by inhibiting apoptosis and accelerating cell cycle,” *Oncotargets and Therapy*, vol. 12, pp. 5615–5625, 2019.
- [58] Q. Lin, Y. He, X. Wang et al., “Targeting pyruvate carboxylase by a small molecule suppresses breast cancer progression,” *Advanced Science*, vol. 7, no. 9, p. 1903483, 2020.
- [59] A. Shinde, T. Wilmanski, H. Chen, D. Teegarden, and M. K. Wendt, “Pyruvate carboxylase supports the pulmonary tropism of metastatic breast cancer,” *Breast Cancer Research*, vol. 20, no. 1, p. 76, 2018.



## *Retraction*

# **Retracted: Allicin Inhibits Osteosarcoma Growth by Promoting Oxidative Stress and Autophagy via the Inactivation of the lncRNA MALAT1-miR-376a-Wnt/ $\beta$ -Catenin Signaling Pathway**

### **Oxidative Medicine and Cellular Longevity**

Received 26 December 2023; Accepted 26 December 2023; Published 29 December 2023

Copyright © 2023 Oxidative Medicine and Cellular Longevity. This is an open access article distributed under the Creative Commons Attribution License, which permits unrestricted use, distribution, and reproduction in any medium, provided the original work is properly cited.

This article has been retracted by Hindawi, as publisher, following an investigation undertaken by the publisher [1]. This investigation has uncovered evidence of systematic manipulation of the publication and peer-review process. We cannot, therefore, vouch for the reliability or integrity of this article.

Please note that this notice is intended solely to alert readers that the peer-review process of this article has been compromised.

Wiley and Hindawi regret that the usual quality checks did not identify these issues before publication and have since put additional measures in place to safeguard research integrity.

We wish to credit our Research Integrity and Research Publishing teams and anonymous and named external researchers and research integrity experts for contributing to this investigation.

The corresponding author, as the representative of all authors, has been given the opportunity to register their agreement or disagreement to this retraction. We have kept a record of any response received.

### **References**

- [1] W. Xie, W. Chang, X. Wang et al., "Allicin Inhibits Osteosarcoma Growth by Promoting Oxidative Stress and Autophagy via the Inactivation of the lncRNA MALAT1-miR-376a-Wnt/ $\beta$ -Catenin Signaling Pathway," *Oxidative Medicine and Cellular Longevity*, vol. 2022, Article ID 4857814, 14 pages, 2022.

## Research Article

# Allicin Inhibits Osteosarcoma Growth by Promoting Oxidative Stress and Autophagy via the Inactivation of the lncRNA MALAT1-miR-376a-Wnt/ $\beta$ -Catenin Signaling Pathway

Wenpeng Xie,<sup>1</sup> Wenjie Chang,<sup>2</sup> Xiaole Wang,<sup>1</sup> Fei Liu,<sup>2</sup> Xu Wang,<sup>2</sup> Daotong Yuan,<sup>2</sup> and Yongkui Zhang<sup>1,3</sup> 

<sup>1</sup>Department of Orthopedics, Affiliated Hospital of Shandong University of Traditional Chinese Medicine, Jinan, Shandong, 250000, China

<sup>2</sup>First Clinical College, Shandong University of Traditional Chinese Medicine, Jinan, Shandong, 250000, China

<sup>3</sup>Shandong Fupai Pharmaceutical Co., Ltd, Jinan, Shandong, 250000, China

Correspondence should be addressed to Yongkui Zhang; 71000356@sduatcm.edu.cn

Received 30 March 2022; Revised 6 June 2022; Accepted 8 June 2022; Published 24 June 2022

Academic Editor: Tian Li

Copyright © 2022 Wenpeng Xie et al. This is an open access article distributed under the Creative Commons Attribution License, which permits unrestricted use, distribution, and reproduction in any medium, provided the original work is properly cited.

Allicin, an organic sulfur compound extracted from the bulb of *Allium sativum*, can potentially prevent various tumors. Our previous study found that allicin can effectively suppress the proliferation of osteosarcoma cells. However, the molecular mechanisms have not been illustrated. In this study, Saos-2 and U2OS osteosarcoma cells were used to investigate the underlying mechanisms. A series of experiments were carried out to authenticate the anticancer property of allicin. Knockdown of lncRNA MALAT1 inhibited the proliferation, invasion and migration and promoted apoptosis of osteosarcoma cells. Knockdown of miR-376a increased the proliferation, invasion, and migration and dropped apoptosis of osteosarcoma cells. Furthermore, knockdown of miR-376a reversed the influences of MALAT1 silencing in osteosarcoma cells. Based on our data, MALAT1 could downregulate the expression of miR-376a, subsequently accelerating osteosarcoma. Moreover, oxidative stress and autophagy were identified as the potential key pathway of allicin. Allicin inhibited osteosarcoma growth and promoted oxidative stress and autophagy via MALAT1-miR-376a. We also found that allicin promotes oxidative stress and autophagy to inhibit osteosarcoma growth by inhibiting the Wnt/ $\beta$ -catenin pathway *in vivo* and *in vitro*. All data showed that allicin promotes oxidative stress and autophagy of osteosarcoma via the MALAT1-miR-376a-Wnt/ $\beta$ -catenin pathway.

## 1. Introduction

Osteosarcoma (OS), one of the most aggressive primary musculoskeletal malignancies, originates in the interstitial cell line and most frequently occurs in children and adolescents (median age of 18) [1]. The incidence of OS is approximately 3 per million and is higher in men than in women [2]. Owing to the introduction of multiagent chemotherapy regimens, the prognosis of patients has markedly improved in recent decades [3, 4]. The five-year survival rates of OS patients with localized disease have increased to approximately 60%–78% but remain low at 20% in patients with metastasis at diagnosis or in relapse [5–7]. Over the last decade, no apparent increase in the overall survival rate

has been reported. The strong proliferative capacity and drug resistance of OS cells are also important factors affecting prognosis [8, 9]. Thus, the molecular mechanisms related to OS progression and pathogenesis need to be explored, and therapeutic targets with improved effectiveness should be identified.

Allicin, an organic sulfur compound extracted from the bulb of *Allium* and found in onion and other *Allium* plants, exerts antibacterial, antiviral, anti-inflammatory, and anticancer effects [10]. Moreover, it exhibits potential proapoptotic ability and can be used as a cancer treatment [11]. Extensive studies have shown that allicin suppresses oral squamous cell carcinoma of the tongue [12], cholangiocarcinoma [13], colorectal cancer [14], lung cancer [15], and

TABLE 1: Sequences of the primers used for RT-PCR.

Primers	Upstream (5' → 3')	Downstream (5' → 3')
MALAT1	GCTCTGTGGTGTGGGATTGA	GTGGCAAAATGGCGGACTTT
miR-376a	GTAGATTCTCCTTCTATGC	CAGTGCCTGTCTGGAGT
P62	CCGTGAAGGCCTACCTTCTG	TCCTCGTCACTGGAAAAGGC
Beclin-1	GGTCTCGGGCGGAAGTTTTC	CTCAGCCCCGATGCTCTTC
LC3	ACTCCTGACTGCATGGAAGC	TGCTTCTCACCTTGTAGCG
GAPDH	AGAAGGCTGGGGCTCATTTG	AGGGGCCATCCACAGTCTTC
Wnt3a	GAGCAGGACTCCCACCTAAA	AGCCACCAGAGAGGAGACAC
$\beta$ -Catenin	CTGAGGAGCAGCTTCAGTCC	GGCCATGTCCAACCTCCATCA

breast cancer [16]. In our previous studies [17, 18], results showed that allicin could inhibit the proliferation and migration of Saos-2 cells by reducing the production of glucose-regulated protein 78 and upregulating the expression of calcium reticulon. Moreover, He et al. [19] suggested that diallyl trisulfide inhibits OS progress via the PI3K/AKT/GSK3 $\beta$  signaling pathway. However, concrete molecular mechanisms have not been researched.

The balance of the redox system keeps cells in normal condition. When this balance is broken, the production rate of highly active substances exceeds the range of the body's antioxidant regulation ability and finally leads to oxidative stress [20]. Almost all tumor cells have an imbalance in the redox system. Oxidative stress can help tumors grow and develop, but one cancer treatment is to raise the level of oxidative stress to boost tumor cells' apoptosis [20]. The study reported that the effect of the GANT61/miR-1286/RAB31 axis on inhibition OS was to induce oxidative stress [21]. And butein induced oxidative stress in OS cells to promote cell autophagy and apoptosis [22]. In addition, allicin could promote cell apoptosis and autophagy by increasing the accumulation of ROS [15]. Autophagy, a type II form of programmed cell death identified more than 50 years ago, is a highly conserved self-stabilizing mechanism of eukaryotic cells. It carried a big weight in maintaining the metabolic requirements of cells and the renewal of some organelles. In OS, autophagy seems deregulated and could act as an antitumoral process [23]. Allicin can activate autophagy to alleviate the malignant development of thyroid cancer [24] and non-small-cell lung cancer [15]. Our previous results showed that autophagy in OS decreased, and allicin could inhibit the growth of OS by increasing autophagy. However, the underlying mechanism is unclear.

Noncoding RNA, which includes lncRNA, circRNA, miRNA, and tRNA, among others, is a class of widely existing genes that involve various biological functions. Among them, lncRNA and miRNA control the biological process of tumor autophagy, proliferation, invasion, migration, and metastasis. Salmena proposed the competitive endogenous RNA (ceRNA) mechanism for the first time [25]. The expression level of MALAT1 was increased in OS cells [26, 27]. MALAT1 was also detected in diverse pathologies, such as breast cancer [28] and colorectal cancer [29]. In addition, MALAT1 exerts varying degrees of influence on tumor proliferation, apoptosis, invasion, metastasis, and drug resistance. MALAT1 was found to be closely related to miR-

376a in inhibiting the proliferation of OS. Many studies have found a significant decrease in miR-376a expression in tumor cells, such as rectum adenocarcinoma cell carcinoma [30], laryngocarcinoma [31], and hepatocellular carcinoma [32]. However, studies on miR-376a in OS are relatively scarce. Luo et al. found a direct interaction between miR-376a and MALAT1 in OS [33]. MALAT1 can promote Wnt expression. Silencing MALAT1 can inactivate the Wnt signaling pathway in gastric adenocarcinoma [34]. A series of studies confirmed that MALAT1 promoted the proliferation and metastasis of lung cancer via the Wnt/ $\beta$ -catenin pathway [35]. However, no related studies have been reported regarding the roles of allicin on autophagy and oxidative stress in OS via the MALAT1/miR-376a/Wnt/ $\beta$ -catenin signaling pathway.

Based on the above, we speculate that the ceRNA network formed by metastasis-associated MALAT1/miR-376a/Wnt/ $\beta$ -catenin was a target of allicin, which allicin could promote autophagy and oxidative stress through it in OS. So the possible mechanisms allowing allicin to promote autophagy and oxidative stress to inhibit the growth of OS were explored.

## 2. Materials and Methods

**2.1. Materials.** Culture medium (DMEM, CM15019) and phosphate buffer saline (CC008) were obtained from Macgene Co., Ltd. (Beijing, China). Fetal bovine serum (FBS, 10100147) and 0.25% trypsin were ordered from Gibco (Thermo Fisher, Waltham, MA, USA). Cell Counting Kit-8 (G4103) was purchased from Servicebio (Wuhan, China). The Annexin V-FITC/7-AAD kit (MA0428) and cell cycle and apoptosis analysis kit (MA0334) were provided by Meilune (Suzhou, Jiangsu). A transwell chamber (3422) was supplied by Corning (New York, USA). Rabbit anti-P62 antibody (A19700), rabbit anti-Beclin-1 antibody (A7353), rabbit anti-LC3 antibody (A19665), rabbit anti-GAPDH antibody (A19056), rabbit anti-Wnt3a antibody (A0642), and rabbit anti- $\beta$ -catenin antibody (A19657) were purchased from ABclonal (Wuhan, China). HRP-conjugated goat anti-rabbit (ZB-2301) and rat anti-mouse (ZB-2305) IgG were provided by ZSGB-BIO (Beijing, China). Primers (Table 1) were purchased from Takara (Dalian, China).

**2.2. Cell Culture and Drugs.** Saos-2 and U2OS cells were provided by the Institute of Biochemistry and Cell Biology at the

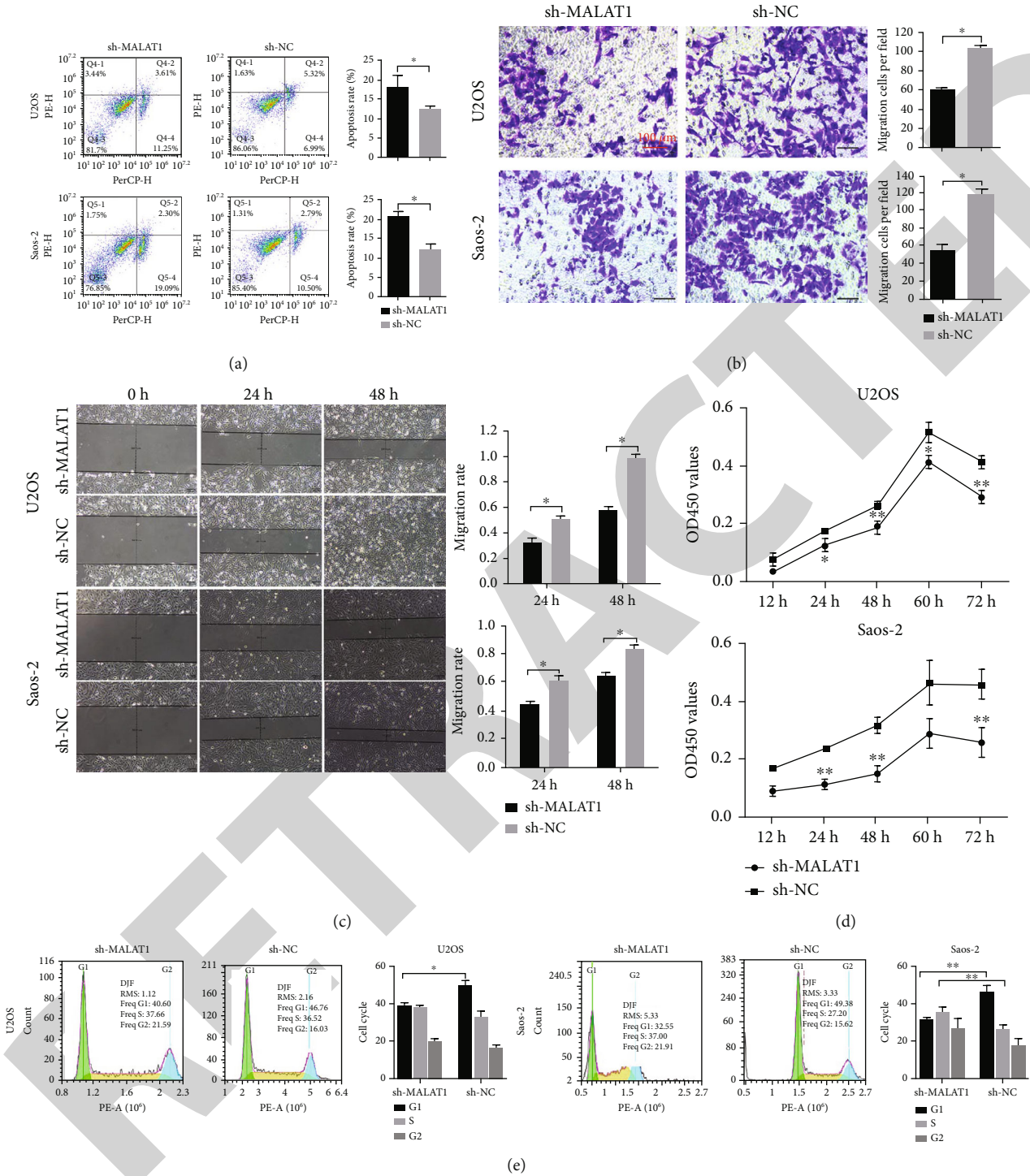


FIGURE 1: MALAT1 downregulation distinctly inhibited OS cell proliferation and migration. (a) Cell apoptosis in Saos-2 and U2OS cell lines after infection with sh-MALAT1, detected by flow cytometry. (b) Cell migration in Saos-2 and U2OS cell lines after infection with sh-MALAT1, measured using the transwell migration assay. (c) Cell migration in Saos-2 and U2OS cell lines after infection with sh-MALAT1, measured using the scratch wound assay. (d) Cell proliferation in Saos-2 and U2OS cell lines after infection with sh-MALAT1, analyzed using the CCK-8 assay. (e) Cell cycle in Saos-2 and U2OS cell lines after infection with sh-MALAT1, detected by flow cytometry. State  $n = 3$ . \*  $P < 0.05$ .

Chinese Academy of Sciences (Shanghai, China). The cells were cultured in DMEM containing 10% FBS under 37°C and 5% CO<sub>2</sub>. Allucin (98% pure) was purchased from Solar-

bio (IA1100, Beijing, China). The best concentration of allucin, 100 μM, was determined by the CCK-8 assay in our previous study [17, 18].

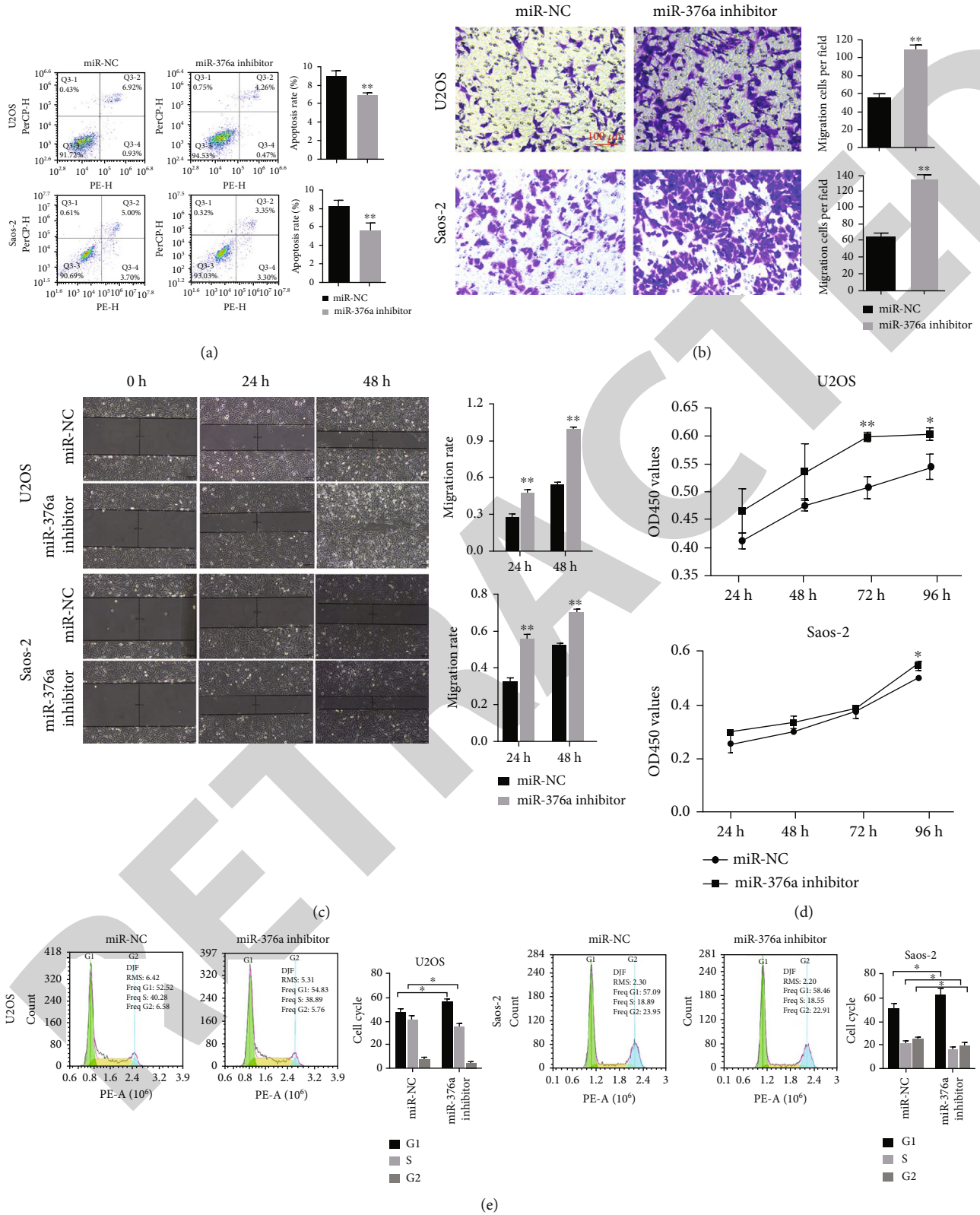


FIGURE 2: miR-376a downregulation distinctly promoted OS cell proliferation and migration. (a) Cell apoptosis in Saos-2 and U2OS cell lines after treatment with the miR-376a inhibitor, detected by flow cytometry. (b) Cell migration in Saos-2 and U2OS cell lines after treatment with the miR-376a inhibitor, measured using the transwell assay. (c) Cell migration in Saos-2 and U2OS cell lines after treatment with the miR-376a inhibitor, measured using the scratch wound assay. (d) Cell proliferation in Saos-2 and U2OS cell lines after treatment with the miR-376a inhibitor, analyzed using the CCK-8 assay. (e) Saos-2 and U2OS cell cycles after treatment with the miR-376a inhibitor, detected by flow cytometry. State  $n = 3$ . \*  $P < 0.05$ .

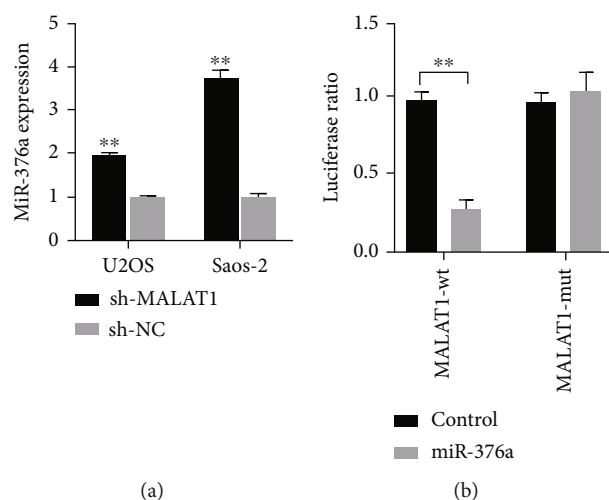


FIGURE 3: miR-376a was a target of MALAT1. (a) miR-376a expression was detected by RT-PCR. (b) Dual-luciferase reporter activity assay in Saos-2 cells after transfection with pGL3-MALAT1-WT or pGL3-MALAT1-MUT and control miR-NC or miR-376a mimics. State  $n = 3$ . \* $P < 0.05$ .

**2.3. Cell Transfection.** Saos-2 and U2OS cells were cultured in antibiotic-free DMEM in a 6-well plate for 24 h, after reaching 70%–80% confluence and then transfected with 50 nM of sh-MALAT1, 50 nM of sh-NC, 50 nM of miR-376a mimic, or 50 nM of mimic control by Lipofectamine 2000 (11668030, Thermo Fisher). After transfection for 48 h, the cells were harvested. miR-376a mimic and mimic control were supplied by Huzhou Hippo Biotechnology Co., Ltd. (Guangzhou, China), and small interfering RNA for MALAT1 (sh-MALAT1) was synthesized by Huzhou Hippo Biotechnology Co., Ltd. (Guangzhou, China) [27].

**2.4. Tumor Xenograft Model In Vivo.** Animal experiments were approved by the Institutional Animal Care and Use Committee and Animal Ethics Committee of Affiliated Hospital of Shandong University of Traditional Chinese Medicine (approval number 2021-05). The BALB/c nude mice (4 weeks, male, Vital River, Beijing, China) were maintained at 20–26°C with 30–70% humidity and 12 h light/dark cycle. When being acclimatized for at least 1 week, the right axillary of the mice were injected subcutaneously with  $10^7$  Saos-2 cells or transfected Saos-2 cells. When the neoplastic size was grown to about 0.5 cm<sup>3</sup>, the mice were intraperitoneally injected with allixin (30 mg/kg) or normal saline for 14 days according to the scheduled group. The mice were euthanized with amputation of the neck, and the tumors were extracted and stored at –80°C for further biochemical tests [26, 36].

**2.5. CCK-8 Assay.** A 100  $\mu$ L cell suspension (1500 cells) of the transfected Saos-2 and U2OS cells was seeded into 96-well plates. At a different time, CCK-8 (10  $\mu$ L per well) was added and incubated for 2 h. The optical density (OD) value of 450 nm was collected using a microplate reader (Thermo Fisher) [26].

**2.6. Transmission Electron Microscopy.** After treatment with allixin for 24 h, Saos-2 and U2OS cells were fixed in 4% glutaraldehyde overnight and then with 1% osmium tetroxide. After the samples were dehydrated in ethanol and infiltrated with propylene oxide, they were embedded. Sections with a thickness of ~50 nm were sliced and then double-stained with 3% uranyl acetate and lead citrate. Autophagosomes were subsequently visualized by electron microscopy (HT7700, Hitachi, Tokyo, Japan).

**2.7. Flow Cytometry.** The cells were digested with trypsin and centrifuged for 10 min at 1000 rpm/min after being processed with allixin. The samples were stained with Annexin V-FITC/7-AAD and PI. Cell apoptosis and cell cycle (G1, S, and G2 peaks) were determined by flow cytometry (NovoCyte, Agilent, California, USA).

**2.8. Transwell Migration Assays.** The transwell chamber was used for cell migration assays [26]. Approximately 100  $\mu$ L of cell suspension ( $10^5$  cells) was seeded into the upper transwell chamber, whereas 600  $\mu$ L of 10% FBS was seeded into the lower transwell chamber. After the cells were incubated for 48 h, those that settled on the upper surfaces of the transwell chambers were scraped with cotton swabs, and those that settled on the lower surfaces were fixed for staining with a crystal violet solution (CB0331, Sangon Biotech, Shanghai, China) and observed under fluorescent microscopy.

**2.9. Scratch Wound Assay.** Saos-2 and U2OS cells were seeded in P6-well culture dishes at a density of  $3 \times 10^5$  cells per well [37]. The cells were then grown to 90% confluence in 2 mL of growth medium. Subsequently, the cell layer was scratched with a 10  $\mu$ L pipette tip. The cells were rinsed and then treated with allixin. Cultures were observed immediately after wounding and after 12 and 24 h. Cell migration was monitored under a microscope.

**2.10. RT-PCR.** RNA was extracted using TRIzol (Invitrogen; Thermo Fisher) and amplified to cDNA by PrimeScript RT reagent kit (Takara, Dalian, China). PCR analysis was performed using SYBR Premix Ex Taq II (Takara) with Light-Cycler 480 (Roche, Basel, Switzerland). The primers (Table 1) were purchased from Takara. GAPDH was used as the internal control. Data were processed using the  $2^{-\Delta\Delta Ct}$  method [18].

**2.11. Western Blot.** Protein was extracted using RIPA (Beyotime, Shanghai, China) and quantified with a BCA assay kit (Beyotime). Samples (30  $\mu$ g/lane) were separated by SDS-PAGE and transferred onto PVDF membranes and incubated with primary antibodies against P62 (1:1000), Beclin-1 (1:1000), LC3 (1:1000), Wnt3a (1:1000),  $\beta$ -catenin (1:1000), and GAPDH (1:5000), followed by the peroxidase-conjugated goat anti-rabbit IgG secondary antibody (1:5000). The blots were visualized using an ECL kit (Amersham; GE, Chalfont, UK). The expression level of the target protein was normalized with GAPDH [18].

**2.12. Dual-Luciferase Assay.** The wild type (WT) of MALAT1 containing the predicted interacting sequence of

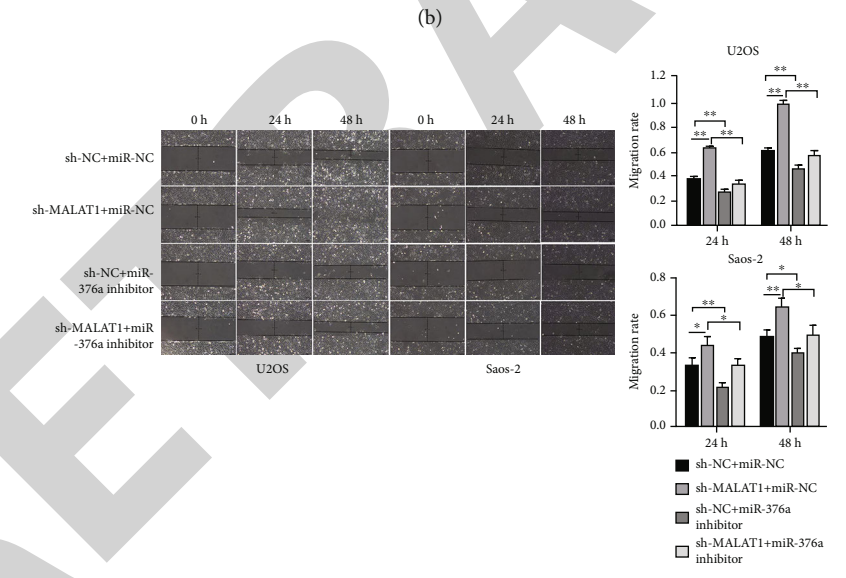
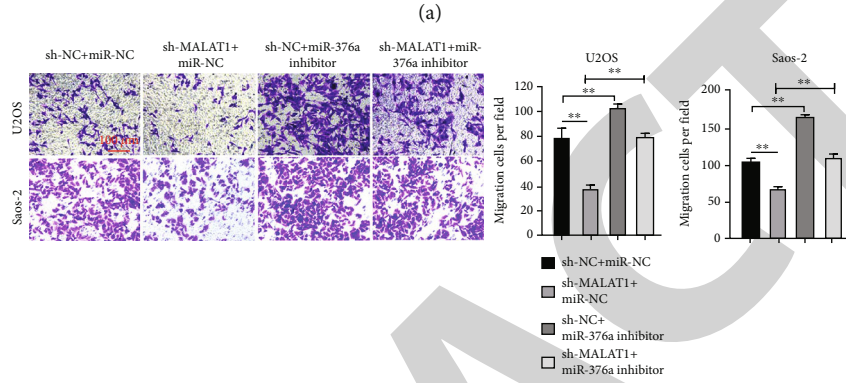
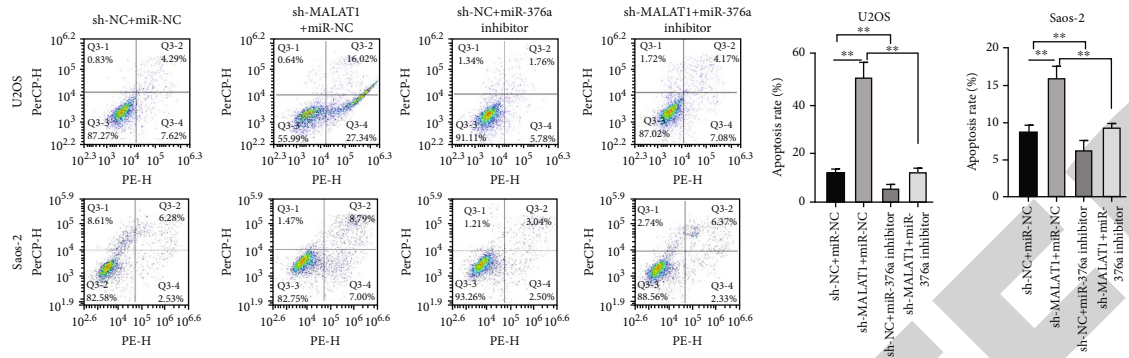
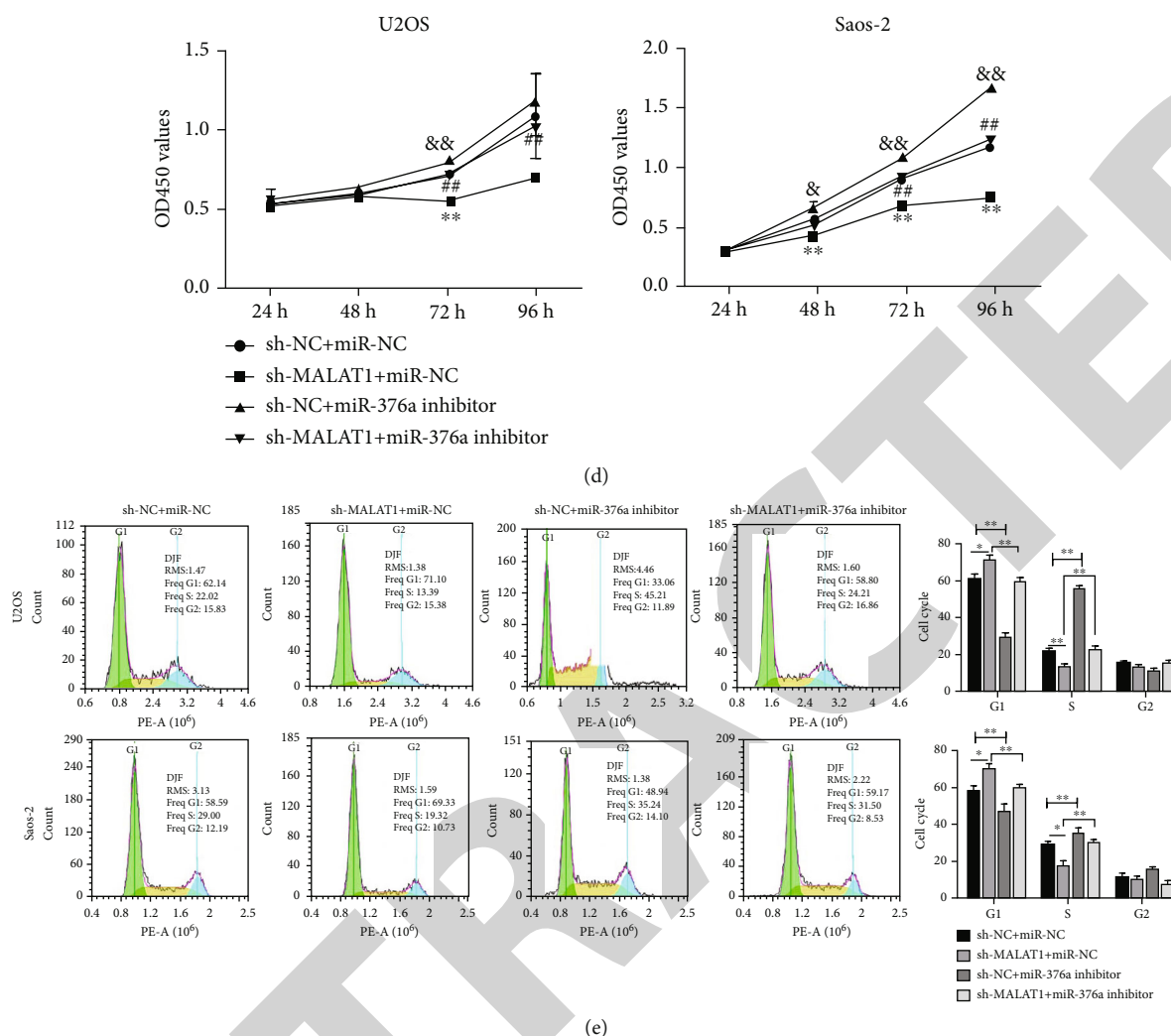


FIGURE 4: Continued.



**FIGURE 4:** The downexpression of miR-376a reversed the effects of MALAT1 downregulation on OS cell proliferation and migration. (a) Cell apoptosis in Saos-2 and U2OS cell lines, detected by flow cytometry. (b) Cell migration in Saos-2 and U2OS cell lines, measured using the transwell assay. (c) Cell migration in Saos-2 and U2OS cell lines, measured using the scratch wound assay. (d) Cell proliferation in Saos-2 and U2OS cell lines, measured using the CCK-8 assay. (e) Cell cycle in Saos-2 and U2OS cell lines, detected by flow cytometry. State  $n = 3$ . Compared with sh-NC+miR-NC, \* $P < 0.05$ ; compared with sh-NC+miR-NC, &# $P < 0.05$ ; compared with sh-MALAT1+miR-NC, # $P < 0.05$ .

miR-376a was cloned and inserted into the firefly luciferase pGL-3 vector (E1751, Promega, USA), referred to as wt-MALAT1. The mutant (MUT) 3' UTR of MALAT1 was constructed into the luciferase vector, referred to as mut-MALAT1. pGL3-MALAT1-wt or pGL3-MALAT1-mut was cotransfected with miR-376a mimic/NC into cells by Lipofectamine 2000 (11668030, Thermo Fisher, Waltham, MA, USA). 48 h later, the luciferase activity was detected using the Dual-Luciferase Reporter Assay System (E1960, Promega, Madison, Wisconsin, USA) [26].

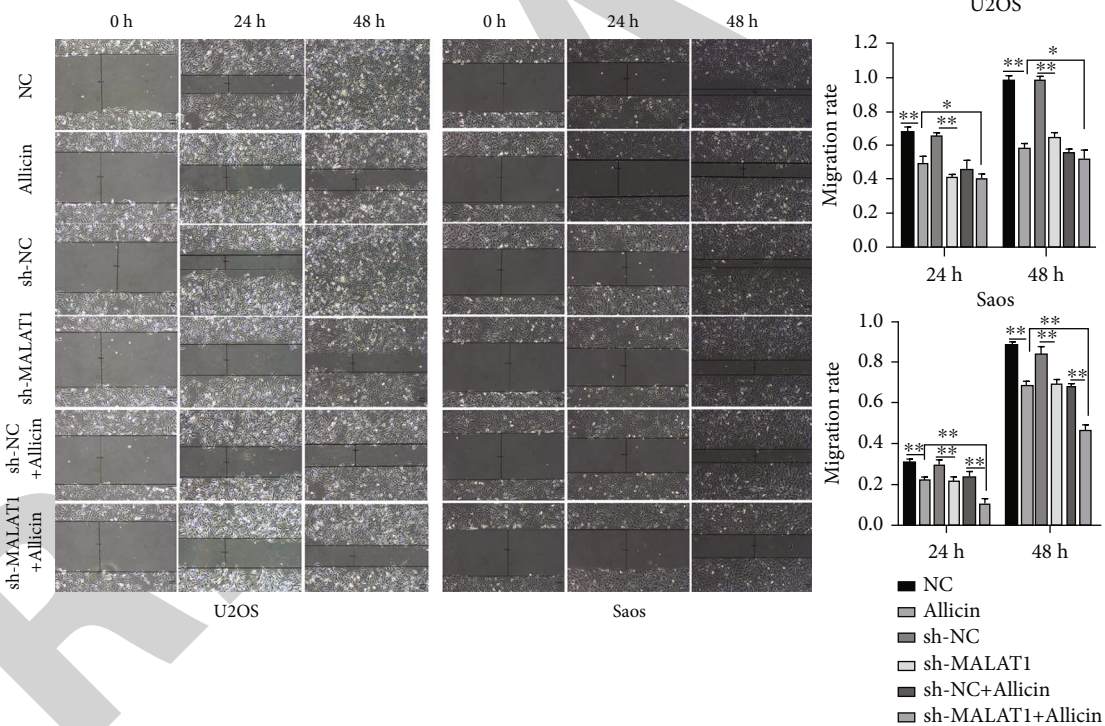
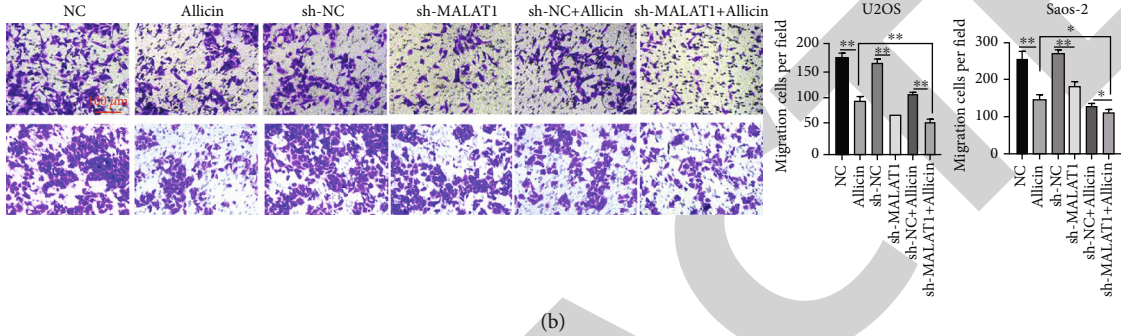
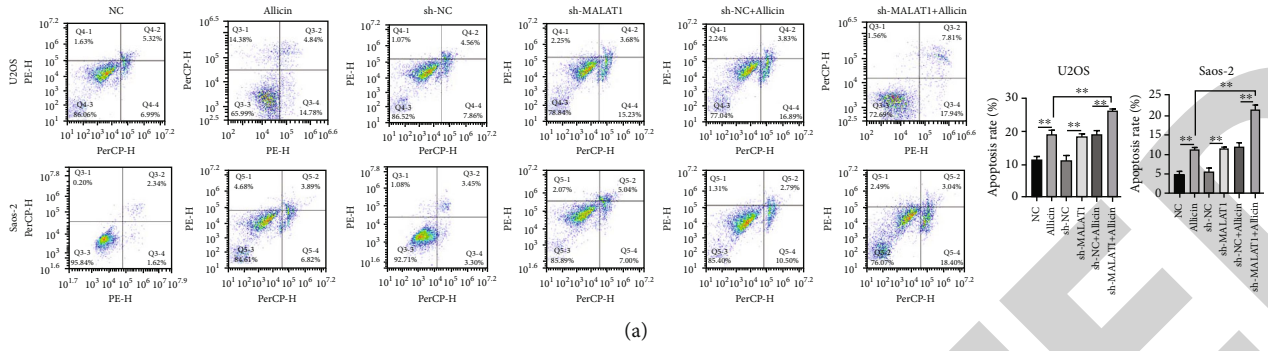
**2.13. Detection of ROS.** The treated cells were seeded in 96-well black plates with 5000 cells/well and incubated at 37°C for 24 h. The level of ROS of cells was detected with 2,7-dichlorofluorescein diacetate (DCFH-DA) assay. DCFH-DA was added at 10  $\mu$ M in each well and kept for 30 min at 37°C and observed under a fluorescent microscope (Zeiss, Germany) [38].

**2.14. Statistical Analysis.** All experiments were repeated three times (state  $n = 3$ ) and performed in triplicate. All data were expressed as mean  $\pm$  SEM. Data were compared using a one-way ANOVA test. SPSS 20.0 (IBM, Armonk, NY, USA) was used for statistical analysis.  $P < 0.05$  was considered a significant difference.

### 3. Results

**3.1. MALAT1 Downregulation Distinctly Promoted Apoptosis and Inhibited the Proliferation and Migration of OS Cells.** To investigate the potential involvement of MALAT1 in OS cells, we knocked down the expression of MALAT1 in Saos-2 and U2OS cells by using sh-MALAT1. The results revealed that downexpression of MALAT1 markedly increased cell apoptosis (Figure 1(a)) and inhibited the migration (Figures 1(b) and 1(c)), proliferation, and cell cycle (Figures 1(d) and 1(e)) of OS cells.





(c)

FIGURE 5: Continued.

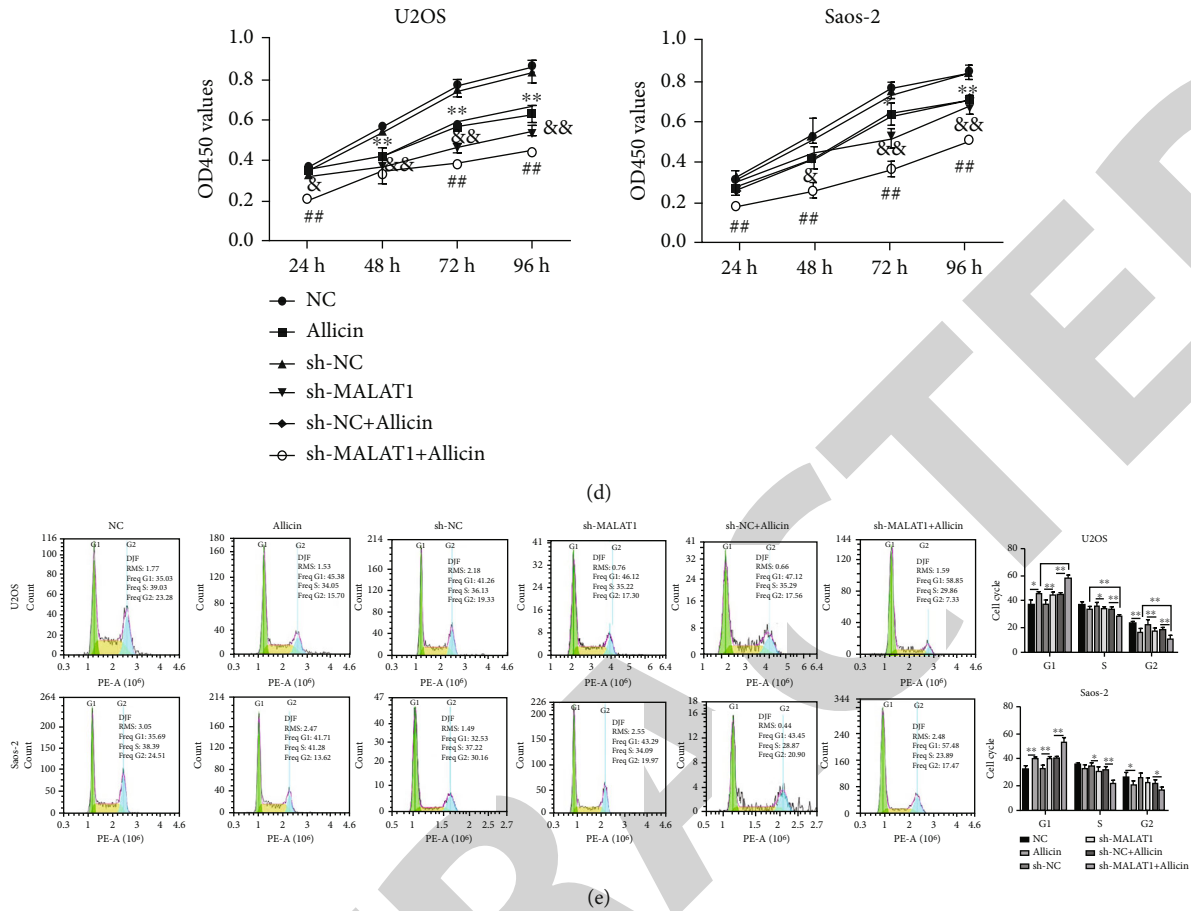


FIGURE 5: Alliin inhibits OS cell growth and migration by inactivation of the expression of MALAT1. (a) Apoptosis in Saos-2 and U2OS cell lines, detected by flow cytometry. (b) Cell migration in Saos-2 and U2OS cell lines, measured using the transwell assay. (c) Cell migration in Saos-2 and U2OS cell lines, determined using the scratch wound assay. (d) Cell proliferation in Saos-2 and U2OS cells, analyzed using the CCK-8 assay. (e) Cell cycle in Saos-2 and U2OS cell lines, detected by flow cytometry. State  $n = 3$ . Compared with NC,  $*P < 0.05$ ; compared with alliin,  $#P < 0.05$ ; compared with sh-NC,  $&P < 0.05$ .

3.2. *miR-376a* Downregulation Markedly Weakened Apoptosis and Promoted Proliferation and Migration of OS Cells. The biological functions of miR-376a in OS progression were evaluated by inhibiting its expression in Saos-2 and U2OS cells. Notably, miR-376a inhibition markedly reduced cell apoptosis (Figure 2(a)) and promoted the migration (Figures 2(b) and 2(c)), proliferation, and cell cycle (Figures 2(d) and 2(e)) of OS cells.

3.3. *MALAT1* Targets *miR-376a*. To determine the relation between MALAT1 and miR-376a, MALAT1 expression was knocked down using sh-MALAT1, and miR-376a expression was observed by RT-PCR. The results showed that the expression of miR-376a was raised in OS cells transfected with sh-MALAT1 (Figure 3(a)). Dual-luciferase reporter assays indicated that miR-376a was specifically bound to MALAT1. The luciferase activity was reduced in cells transfected with pGL3-MALAT1-WT and miR-376a mimics (Figure 3(b)), indicating that MALAT1 could sponge miR-376a.

3.4. Downexpression of *miR-376a* Reversed the Effects of *MALAT1* Knockdown on the Apoptosis, Proliferation, and Migration of OS Cells. The Saos-2 and U2OS cells were

transfected with sh-NC+miR-NC, sh-MALAT1+miR-NC, sh-NC+miR-376a inhibitor, and sh-MALAT1+miR-376a inhibitor. The downregulation of MALAT1 promoted OS cells apoptosis, but such promotion was reversed by the miR-376a inhibitor (Figure 4(a)). Moreover, the inhibitory effect of MALAT1 knockdown on cell migration (Figures 4(b) and 4(c)) and proliferation (Figures 4(d) and 4(e)) was reversed by the downexpression of miR-376a in OS cells.

3.5. *Alliin* Inhibited OS Growth by Promoting Oxidative Stress and Autophagy via Inactivation of the *MALAT1-miR-376a-Wnt/β-Catenin* Signal Pathway Axis *In Vitro* and *In Vivo*. To explore the mechanisms of alliin in the treatment of OS, Saos-2 cell lines and mice were divided into six groups: the NC, alliin, sh-NC, sh-MALAT1, sh-NC+alliin, and sh-MALAT1+alliin groups. The results showed that alliin significantly increased OS cell apoptosis (Figure 5(a)) and inhibited cell migration (Figures 5(b) and 5(c)) and proliferation (Figures 5(d) and 5(e)), which was consistent with MALAT1 knockdown. The DCFH-DA assay results showed that the level of ROS was boosted in alliin and sh-MALAT1, sh-NC+alliin, and sh-MALAT1+alliin groups, which indicated that alliin and knockdown of

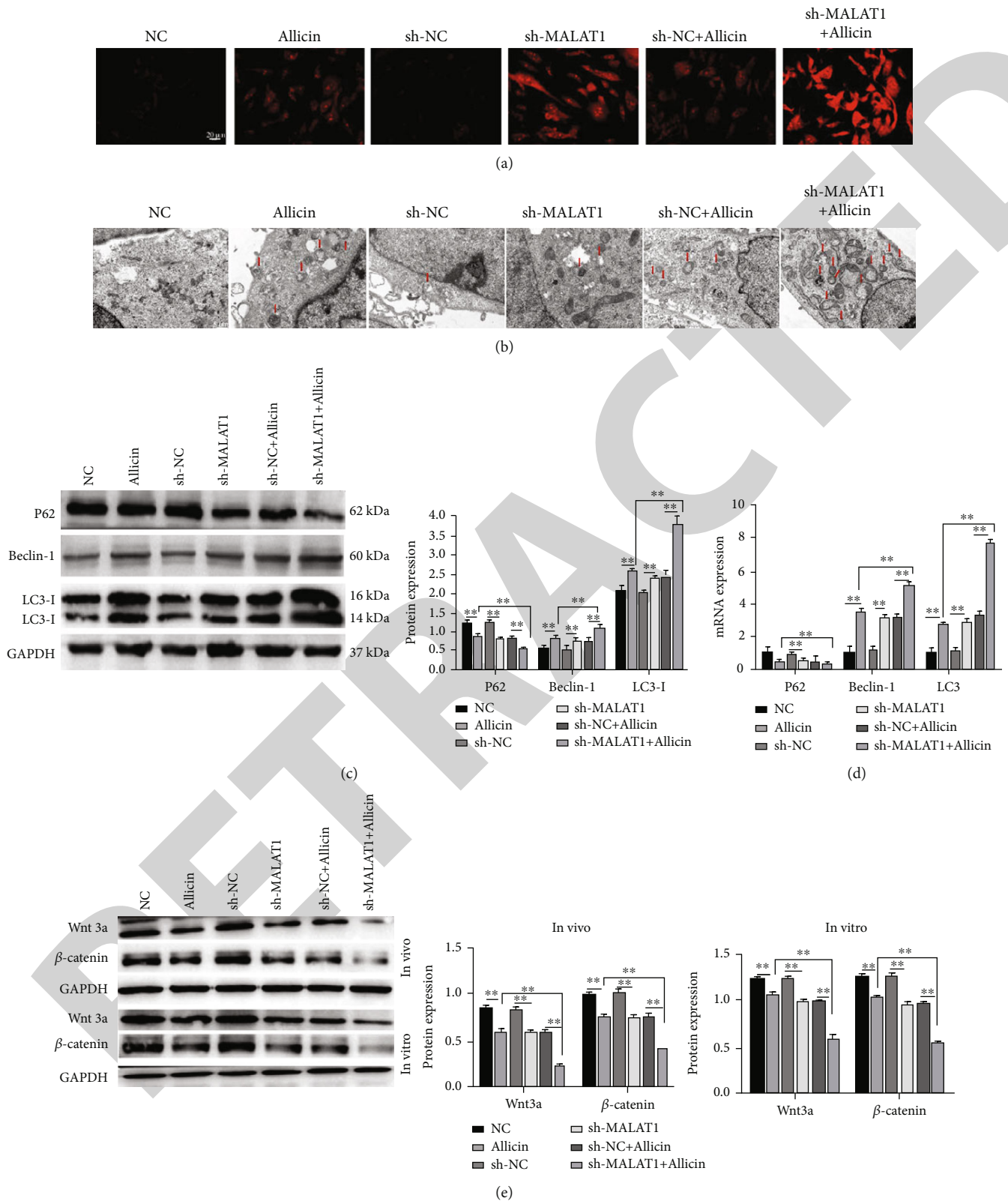


FIGURE 6: Continued.

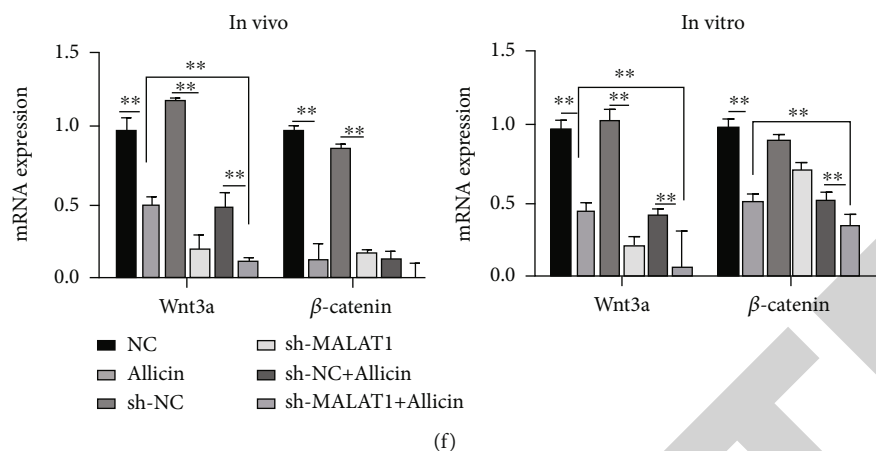


FIGURE 6: Allicin inhibits OS growth and migration by promoting oxidative stress and autophagy via inactivation of the MALAT1-miR-376a-Wnt/ $\beta$ -catenin signal pathway axis. (a) The level of ROS was detected by DCFH-DA. (b) Autophagy was detected by transmission electron microscopy. (c) Protein expression of autophagy-related proteins, detected by western blot analysis. (d) mRNA expression of autophagy-related proteins, measured by RT-PCR. (e) Protein expression of Wnt3a and  $\beta$ -catenin, determined by western blot analysis. (f) mRNA expression of Wnt3a and  $\beta$ -catenin, measured by RT-PCR.  $n = 3$ . \* $P < 0.05$ .

MALAT1 induced the accumulation of ROS (Figure 6(a)). Transmission electron microscopy images revealed that the number of autophagic vacuoles with double-membrane structures was increased after treatment with allicin *in vitro* (Figure 6(b)). The expression levels of autophagy-related proteins were also detected by RT-PCR and western blot analysis *in vitro*. Allicin upregulated Beclin-1 and LC3 expressions and downregulated p62 expression (Figures 6(c) and 6(d)). Moreover, RT-PCR and western blot data also showed that allicin downregulated Wnt3a and  $\beta$ -catenin expressions *in vitro* and *in vivo* (Figures 6(e) and 6(f)), which presented similar effects with MALAT1 knockdown in OS cells. All data above showed that allicin promotes oxidative stress and autophagy to inhibit OS growth via the MALAT1-miR-376a-Wnt/ $\beta$ -catenin signal pathway.

#### 4. Discussion

The main treatment for osteosarcoma is surgery combined with radiotherapy and chemotherapy, but the cure is very difficult and mortality is high. With the deepening of the modernization of traditional Chinese medicine, the therapeutic effect of traditional Chinese medicine on the tumor is obvious to all, and it has become a hot spot in the research and development of antitumor drugs in recent years because of its characteristics of multiple links and multiple targets affecting the occurrence, invasion, metastasis, and small side effects of tumor [39]. *Astragalus membranaceus* polysaccharides inhibited lung cancer proliferation and metastasis by promoting the effects of immune checkpoint inhibitors [40]. Our previous study indicated that allicin could effectively inhibit the proliferation of OS cells. The effects of allicin on antiproliferative and anti-invasive properties of cancer cells were based on the upregulation of miR-134 expression [41]. A study by Yue et al. exhibited that allicin induced apoptosis of human OS cells by inactivation of the PI3K/Akt/mTOR pathway [42]. Hu et al. found that diallyl sulfide could inhibit proliferation and migration by reducing

the expression of VEGF [43]. Moreover, the inhibitory effect of allicin on the proliferation and migration of OS was verified by Jiang et al. [44]. These results indicated that allicin could act as an anticancer compound. However, the system-wide molecular mechanisms targeting the antitumor effect of allicin had not been elucidated. In this study, we investigated the molecular mechanisms of allicin in OS.

The expression of MALAT1 was reported to increase and could promote the development of OS [26, 27]. MALAT1 was found to inhibit autophagy in endothelial progenitor cells and increase cell viability while suppressing apoptosis of coronary atherosclerotic heart disease by activating the mTOR signaling pathway [45]. The results of our current study showed that downregulation of MALAT1 inhibited OS growth and migration. Luo et al. found a direct interaction between miR-376a and MALAT1 in OS [33]. Notably, miR-376a was involved in several tumor diseases. For instance, miR-376a alleviated the development of glioma by negatively regulating KLF15 [46]. In addition, miR-376a suppressed the proliferation and invasion of OS cells by targeting FBXO11 [47]. Interestingly, our study revealed that downregulation of miR-376a distinctly promoted the proliferation and migration of OS cell lines. Rescue experiments also revealed that downexpression of miR-376a reversed the effects of MALAT1 silencing on OS cell proliferation and migration. miR-376a could specifically bond to MALAT1 which was revealed by the dual-luciferase reporter assays. These results indicated that MALAT1 regulated miR-376a in OS cells.

The latest research made clear that oxidative stress and autophagy emerged as important mechanism targets of OS. Moreover, accumulating evidence indicated that activation of oxidative stress and autophagy could inhibit OS progression [21, 23]. lncRNA regulates the progression of cells in a variety of ways which includes oxidative stress and autophagy. In diabetic nephropathy, MALAT1 regulated oxidative stress to promote the injury of podocyte cell via the miR-200c/NRF2 axis [48]. Knockdown of MALAT1 activated cell autophagy and inhibited the progression of atherosclerosis

[45]. Allicin was reported to play an inhibitory role in cancer through oxidative stress and autophagy [15]. Oxidative stress and autophagy of OS cells were regulated by various signaling pathways, such as the notch, NF- $\kappa$ B, and PI3K/AKT signaling pathways, among others. A review of a bioinformatics database verified that the Wnt/ $\beta$ -catenin pathway was a target of allicin and that it formed a ceRNA network with MALAT1 and miR-376a. With the importance of MALAT1 in different diseases, MALAT1 was an upstream regulator of Wnt/ $\beta$ -catenin. In this study, allicin decreased MALAT1 expression to suppress the progression of OS. And allicin could induce oxidative stress and autophagy via regulating the expressions of genes of the Wnt/ $\beta$ -catenin pathway in vivo and in vitro. Collectively, these data indicated that allicin could promote oxidative stress and autophagy and inhibit OS growth via the MALAT1/miR-376a/Wnt/ $\beta$ -catenin pathway.

In summary, a review of the bioinformatics database verified that Wnt/ $\beta$ -catenin was a target of allicin and that it formed a ceRNA network with MALAT1 and miR-376a. Knockdown of MALAT1 could also significantly promote oxidative stress and autophagy to inhibit proliferation in OS. It was also verified that MALAT1 could competitively bind to miR-376a. Thus, allicin is suggested to considerably promote oxidative stress and autophagy to inhibit OS growth by inactivating the MALAT1-miR-376a-Wnt/ $\beta$ -catenin axis. These results also indicate that the MALAT1-miR-376a-Wnt/ $\beta$ -catenin axis can be used as a diagnostic and therapeutic target for OS and allicin might be an effective drug for the treatment of osteosarcoma.

However, there are still some limitations that existed in this study. Clinical samples are not used for verification in this study, and further mechanism verification in animal experiments is required.

## 5. Conclusions

On the basis of the aforementioned experiments, we conclude that allicin can considerably promote oxidative stress and autophagy to inhibit OS growth via the inactivation of the MALAT1-miR-376a-Wnt/ $\beta$ -catenin axis. The MALAT1-miR-376a-Wnt/ $\beta$ -catenin axis can be used as a diagnostic and therapeutic target for OS, and allicin might be an effective drug for the treatment of osteosarcoma.

## Data Availability

The datasets used and/or analyzed during the current study are available from the corresponding author on reasonable request.

## Ethical Approval

The authors are accountable for all aspects of the work in ensuring that questions related to the accuracy or integrity of any part of the work are appropriately investigated and resolved.

## Conflicts of Interest

The authors have no conflicts of interest to declare.

## Authors' Contributions

Wenpeng Xie and Yongkui Zhang were responsible for conception and design. Yongkui Zhang was responsible for administrative support. Wenpeng Xie, Wenjie Chang, and Xiaole Wang were responsible for provision of study materials or patients. Wenpeng Xie, Wenjie Chang, Fei Liu, and Daotong Yuan were responsible for collection and assembly of data. Wenpeng Xie, Wenjie Chang, Fei Liu, and Daotong Yuan were responsible for data analysis and interpretation. All authors were responsible for manuscript writing. All authors were responsible for the final approval of the manuscript.

## Acknowledgments

This work was supported by the Natural Science Foundation of Shandong Province (ZR2019MH114), Development Plan of Shandong Medical and Health Technology (2019WS580), and Cultivation Project of Qilu Health and Wellness Leading Talent.

## References

- [1] R. Belayneh, M. S. Fourman, S. Bhogal, and K. R. Weiss, "Update on osteosarcoma," *Current Oncology Reports*, vol. 23, no. 6, p. 71, 2021.
- [2] C. Chen, L. Xie, T. Ren, Y. Huang, J. Xu, and W. Guo, "Immunotherapy for osteosarcoma: fundamental mechanism, rationale, and recent breakthroughs," *Cancer Letters*, vol. 500, pp. 1–10, 2021.
- [3] I. Corre, F. Verrecchia, V. Crenn, F. Redini, and V. Trichet, "The osteosarcoma microenvironment: a complex but targetable ecosystem," *Cells*, vol. 9, no. 4, p. 976, 2020.
- [4] S. Tsukamoto, C. Errani, A. Angelini, and A. F. Mavrogenis, "Current treatment considerations for osteosarcoma metastatic at presentation," *Orthopedics*, vol. 43, no. 5, pp. e345–e358, 2020.
- [5] B. R. Eaton, R. Schwarz, R. Vatner et al., "Osteosarcoma," *Pediatric Blood & Cancer*, vol. 68, Suppl 2, p. e28352, 2021.
- [6] F. Cersosimo, S. Lonardi, G. Bernardini et al., "Tumor-associated macrophages in osteosarcoma: from mechanisms to therapy," *International Journal of Molecular Sciences*, vol. 21, no. 15, p. 5207, 2020.
- [7] D. P. Regan, L. Chow, S. Das et al., "Losartan blocks osteosarcoma-elicited monocyte recruitment, and combined with the kinase inhibitor toceranib, exerts significant clinical benefit in canine metastatic osteosarcoma," *Clinical Cancer Research*, vol. 28, no. 4, pp. 662–676, 2022.
- [8] K. Bhuvaneshwar, M. Harris, Y. Gusev et al., "Genome sequencing analysis of blood cells identifies germline haplotypes strongly associated with drug resistance in osteosarcoma patients," *BMC Cancer*, vol. 19, no. 1, p. 357, 2019.
- [9] Y. Pu, J. Wang, and S. Wang, "Role of autophagy in drug resistance and regulation of osteosarcoma (review)," *Mol Clin Oncol*, vol. 16, no. 3, p. 72, 2022.

- [10] L. Ba, J. Gao, Y. Chen et al., "Allicin attenuates pathological cardiac hypertrophy by inhibiting autophagy via activation of PI3K/Akt/mTOR and MAPK/ERK/mTOR signaling pathways," *Phytomedicine*, vol. 58, p. 152765, 2019.
- [11] Z. Yang, J. Du, J. Zhu et al., "Allicin inhibits proliferation by decreasing IL-6 and IFN- $\beta$  in HCMV-infected glioma cells," *Cancer Management and Research*, vol. 12, p. 7305, 2020.
- [12] Y. Guo, H. Liu, Y. Chen, and W. Yan, "The effect of allicin on cell proliferation and apoptosis compared to blank control and cis-platinum in oral tongue squamous cell carcinoma," *Oncotargets and Therapy*, vol. Volume 13, pp. 13183–13189, 2020.
- [13] H. Chen, B. Zhu, L. Zhao et al., "Allicin inhibits proliferation and invasion in vitro and in vivo via SHP-1-mediated STAT3 signaling in cholangiocarcinoma," *Cellular Physiology and Biochemistry*, vol. 47, no. 2, pp. 641–653, 2018.
- [14] W. L. Huang, S. F. Wu, S. T. Xu et al., "Allicin enhances the radiosensitivity of colorectal cancer cells via inhibition of NF- $\kappa$ B signaling pathway," *Journal of Food Science*, vol. 85, no. 6, pp. 1924–1931, 2020.
- [15] N. Pandey, G. Tyagi, P. Kaur et al., "Allicin overcomes hypoxia mediated cisplatin resistance in lung cancer cells through ROS mediated cell death pathway and by suppressing hypoxia inducible factors," *Cellular Physiology and Biochemistry*, vol. 54, no. 4, pp. 748–766, 2020.
- [16] G. Maitisha, M. Aimaiti, Z. An, and X. Li, "Allicin induces cell cycle arrest and apoptosis of breast cancer cells in vitro via modulating the p53 pathway," *Molecular Biology Reports*, vol. 48, no. 11, pp. 7261–7272, 2021.
- [17] W. P. Xie, Y. Zhang, Y. K. Zhang et al., "Treatment of Saos-2 osteosarcoma cells with diallyl trisulfide is associated with an increase in calreticulin expression," *Experimental and Therapeutic Medicine*, vol. 15, no. 6, pp. 4737–4742, 2018.
- [18] Y. Zhang, W. P. Xie, Y. K. Zhang et al., "Experimental study of inhibitory effects of diallyl trisulfide on the growth of human osteosarcoma Saos-2 cells by downregulating expression of glucose-regulated protein 78," *Oncotargets and Therapy*, vol. - Volume 11, pp. 271–277, 2018.
- [19] P. He, Z. Wang, B. Sheng et al., "Diallyl trisulfide regulates cell apoptosis and invasion in human osteosarcoma U2OS cells through regulating PI3K/AKT/GSK3 $\beta$  signaling pathway," *Histology and Histopathology*, vol. 35, no. 12, pp. 1511–1520, 2020.
- [20] M. Azmanova and A. Pitto-Barry, "Oxidative stress in cancer therapy: friend or enemy?," *Chembiochem*, vol. 23, no. 10, article e202100641, 2022.
- [21] K. Q. Zhang and X. D. Chu, "GANT61 plays antitumor effects by inducing oxidative stress through the miRNA-1286/RAB31 axis in osteosarcoma," *Cell Biology International*, vol. 45, no. 1, pp. 61–73, 2021.
- [22] P. Zhang, J. Zhang, H. Quan, P. Chen, J. Wang, and Y. Liang, "Effects of butein on human osteosarcoma cell proliferation, apoptosis, and autophagy through oxidative stress," *Human & Experimental Toxicology*, vol. 41, p. 096032712210743, 2022.
- [23] G. Nehme and N. Gordon, "Autophagy in osteosarcoma," *Advances in Experimental Medicine and Biology*, vol. 1258, pp. 167–175, 2020.
- [24] Y. Xiang, J. Zhao, M. Zhao, and K. Wang, "Allicin activates autophagic cell death to alleviate the malignant development of thyroid cancer," *Experimental and Therapeutic Medicine*, vol. 15, no. 4, pp. 3537–3543, 2018.
- [25] L. Salmena, L. Poliseno, Y. Tay, L. Kats, and P. P. Pandolfi, "A \_ceRNA\_ hypothesis: the Rosetta stone of a hidden RNA language?," *Cell*, vol. 146, no. 3, pp. 353–358, 2011.
- [26] F. Li, X. Chen, C. Shang et al., "Bone marrow mesenchymal stem cells-derived extracellular vesicles promote proliferation, invasion and migration of osteosarcoma cells via the lncRNA MALAT1/miR-143/NRSN2/Wnt/ $\beta$ -catenin axis," *Oncotargets and Therapy*, vol. Volume 14, pp. 737–749, 2021.
- [27] Q. Wang, M. J. Liu, J. Bu et al., "miR-485-3p regulated by MALAT1 inhibits osteosarcoma glycolysis and metastasis by directly suppressing c-MET and AKT3/mTOR signalling," *Life Sciences*, vol. 268, p. 118925, 2021.
- [28] B. Goyal, S. R. M. Yadav, N. Awasthee, S. Gupta, A. B. Kunnumakkara, and S. C. Gupta, "Diagnostic, prognostic, and therapeutic significance of long non-coding RNA MALAT1 in cancer," *Biochimica Et Biophysica Acta. Reviews on Cancer*, vol. 1875, no. 2, p. 188502, 2021.
- [29] C. Fan, Q. Yuan, G. Liu et al., "Long non-coding RNA MALAT1 regulates oxaliplatin-resistance via miR-324-3p/ADAM17 axis in colorectal cancer cells," *Cancer Cell International*, vol. 20, no. 1, p. 473, 2020.
- [30] Y. Liu, X. Zhao, B. Wang et al., "miR-376a provokes rectum adenocarcinoma via CTC1 depletion-induced telomere dysfunction," *Developmental Biology*, vol. 9, p. 649328, 2021.
- [31] B. Feng, K. Chen, W. Zhang, Q. Zheng, and Y. He, "circPGAM1 enhances autophagy signaling during laryngocarcinoma drug resistance by regulating miR-376a," *Biochemical and Biophysical Research Communications*, vol. 534, pp. 966–972, 2021.
- [32] H. Ou, Q. Liu, J. Lin et al., "Pseudogene annexin A2 pseudogene 1 contributes to hepatocellular carcinoma progression by modulating its parental gene ANXA2 via miRNA-376a-3p," *Digestive Diseases and Sciences*, vol. 66, no. 11, pp. 3903–3915, 2021.
- [33] W. Luo, H. He, W. Xiao et al., "MALAT1 promotes osteosarcoma development by targeting TGFA via MIR376A," *Oncotarget*, vol. 7, no. 34, pp. 54733–54743, 2016.
- [34] N. K. Lee, J. H. Lee, C. Ivan et al., "MALAT1 promoted invasiveness of gastric adenocarcinoma," *BMC Cancer*, vol. 17, no. 1, p. 46, 2017.
- [35] W. Chen, W. Zhao, L. Zhang et al., "MALAT1-miR-101-SOX9 feedback loop modulates the chemo-resistance of lung cancer cell to DDP via Wnt signaling pathway," *Oncotarget*, vol. 8, no. 55, pp. 94317–94329, 2017.
- [36] X. Li, J. Ni, Y. Tang et al., "Allicin inhibits mouse colorectal tumorigenesis through suppressing the activation of STAT3 signaling pathway," *Natural Product Research*, vol. 33, no. 18, pp. 2722–2725, 2019.
- [37] J. T. Freitas, I. Jozic, and B. Bedogni, "Wound healing assay for melanoma cell migration," *Methods in Molecular Biology*, vol. 2265, pp. 65–71, 2021.
- [38] J. Hartwig, M. Loebel, S. Steiner et al., "Metformin attenuates ROS via FOXO3 activation in immune cells," *Frontiers in Immunology*, vol. 12, p. 581799, 2021.
- [39] Z. Yang, Q. Zhang, L. Yu, J. Zhu, Y. Cao, and X. Gao, "The signaling pathways and targets of traditional Chinese medicine and natural medicine in triple-negative breast cancer," *Journal of Ethnopharmacology*, vol. 264, p. 113249, 2021.
- [40] J. Hwang, W. Zhang, Y. Dhananjay et al., "\_Astragalus membranaceus\_ polysaccharides potentiate the growth-inhibitory activity of immune checkpoint inhibitors against pulmonary

## *Retraction*

# **Retracted: The Risk Model Based on the Three Oxidative Stress-Related Genes Evaluates the Prognosis of LAC Patients**

### **Oxidative Medicine and Cellular Longevity**

Received 8 January 2024; Accepted 8 January 2024; Published 9 January 2024

Copyright © 2024 Oxidative Medicine and Cellular Longevity. This is an open access article distributed under the Creative Commons Attribution License, which permits unrestricted use, distribution, and reproduction in any medium, provided the original work is properly cited.

This article has been retracted by Hindawi following an investigation undertaken by the publisher [1]. This investigation has uncovered evidence of one or more of the following indicators of systematic manipulation of the publication process:

- (1) Discrepancies in scope
- (2) Discrepancies in the description of the research reported
- (3) Discrepancies between the availability of data and the research described
- (4) Inappropriate citations
- (5) Incoherent, meaningless and/or irrelevant content included in the article
- (6) Manipulated or compromised peer review

The presence of these indicators undermines our confidence in the integrity of the article's content and we cannot, therefore, vouch for its reliability. Please note that this notice is intended solely to alert readers that the content of this article is unreliable. We have not investigated whether authors were aware of or involved in the systematic manipulation of the publication process.

Wiley and Hindawi regrets that the usual quality checks did not identify these issues before publication and have since put additional measures in place to safeguard research integrity.

We wish to credit our own Research Integrity and Research Publishing teams and anonymous and named external researchers and research integrity experts for contributing to this investigation.

The corresponding author, as the representative of all authors, has been given the opportunity to register their agreement or disagreement to this retraction. We have kept a record of any response received.

### **References**

- [1] Q. Guo, X. Liu, H. Liu et al., "The Risk Model Based on the Three Oxidative Stress-Related Genes Evaluates the Prognosis of LAC Patients," *Oxidative Medicine and Cellular Longevity*, vol. 2022, Article ID 4022896, 19 pages, 2022.

## Research Article

# The Risk Model Based on the Three Oxidative Stress-Related Genes Evaluates the Prognosis of LAC Patients

Qiang Guo <sup>1</sup>, Xiao-Li Liu,<sup>2</sup> Hua-Song Liu,<sup>1</sup> Xiang-Yu Luo,<sup>1</sup> Ye Yuan,<sup>1</sup> Yan-Mei Ji,<sup>1</sup> Tao Liu,<sup>1</sup> Jia-Long Guo <sup>1</sup>, and Jun Zhang <sup>1</sup>

<sup>1</sup>Department of Cardiothoracic Surgery, Taihe Hospital, Hubei University of Medicine, Shiyan 442012, Hubei Province, China

<sup>2</sup>Department of Ultrasound, The People's Hospital of Jianyang City, Jianyang 641400, Sichuan Province, China

Correspondence should be addressed to Jia-Long Guo; [gjl9988@126.com](mailto:gjl9988@126.com) and Jun Zhang; [13508684276@139.com](mailto:13508684276@139.com)

Received 15 March 2022; Accepted 30 May 2022; Published 23 June 2022

Academic Editor: Yazhou He

Copyright © 2022 Qiang Guo et al. This is an open access article distributed under the Creative Commons Attribution License, which permits unrestricted use, distribution, and reproduction in any medium, provided the original work is properly cited.

**Background.** Oxidative stress plays a role in carcinogenesis. This study explores the roles of oxidative stress-related genes (OSRGs) in lung adenocarcinoma (LAC). Besides, we construct a risk score model of OSRGs that evaluates the prognosis of LAC patients. **Methods.** OSRGs were downloaded from the Gene Set Enrichment Analysis (GSEA) website. The expression levels of OSRGs were confirmed in LAC tissues of the TCGA database. GO and KEGG analyses were used to evaluate the roles and mechanisms of oxidative stress-related differentially expressed genes (DEGs). Survival, ROC, Cox analysis, and AIC method were used to screen the prognostic DEGs in LAC patients. Subsequently, we constructed a risk score model of OSRGs and a nomogram. Further, this work investigated the values of the risk score model in LAC progression and the relationship between the risk score model and immune infiltration. **Results.** We discovered 163 oxidative stress-related DEGs in LAC, involving cellular response to oxidative stress and reactive oxygen species. Besides, the areas under the curve of *CCNA2*, *CDC25C*, *ERO1A*, *CDK1*, *PLK1*, *ITGB4*, and *GJB2* were 0.970, 0.984, 0.984, 0.945, 0.984, 0.771, and 0.959, respectively. This indicates that these OSRGs have diagnosis values of LAC and are significantly related to the overall survival of LAC patients. *ERO1A*, *CDC25C*, and *ITGB4* overexpressions were independent risk factors for the poor prognosis of LAC patients and were associated with risk scores in the risk model. High-risk score levels affected the poor prognosis of LAC patients. Notably, a high-risk score may be implicated in LAC progression via cell cycle, DNA replication, mismatch repair, and other mechanisms. Further, *ERO1A*, *CDC25C*, and *ITGB4* expression levels were related to the immune infiltrating cells of LAC, including mast cells, NK cells, and CD8 T cells. **Conclusion.** In summary, *ERO1A*, *CDC25C*, and *ITGB4* of OSRGs are associated with poor prognosis of LAC patients. We confirmed that the risk model based on the *ERO1A*, *CDC25C*, and *ITGB4* is expected to assess the prognosis of LAC patients.

## 1. Introduction

Oxidative stress is a state of imbalance between the oxidation and antioxidant effects in the human body. Increasing the neutrophil infiltration and oxidative intermediates by oxidative stress contributes to disease occurrence. Current studies indicate that oxidative stress regulates cancer progression [1–3]. For instance, interleukin-8 (IL-8) is a bridge between inflammation and oxidative stress-induced death of cancer cells. IL-8 overexpression promotes the proliferation

of prostate cancer cells and inhibits cell apoptosis. IL-8 and mTOR reduce cellular oxidative stress by suppressing GSK-3 $\beta$  expression and protecting prostate cancer cells [3]. Excessive reactive oxygen species (ROS) production triggers oxidative stress, potentially causing cancer. Overexpression of *miR-526b/miR-655* promotes the invasive capacity of breast cancer (BC) cells. *miR-526b* and *miR-655* regulate the *TXNRD1* expression to cause oxidative stress in BC [4].

Oxidative stress plays a significant role in cancer progression [5–8]. Twist-related protein 2 ( *Twist2*) modulates



tumorigenesis, tumor progression, and epithelial-mesenchymal transformation (EMT). *TWIST2* is substantially downregulated in lung cancer tissues and cells. *TWIST2* overexpression causes apoptosis, promotes the expression of E-cadherin protein, and inhibits the expression of N-cadherin, vimentin, and slug proteins. Besides, *TWIST2* causes oxidative stress in lung cancer cells and inhibits lung cancer progression by modulating the *FGF21*-mediated *AMPK/mTOR* signaling pathway [5]. The nuclear factor, erythroid-derived 2 (*Nrf2*), is a hub transcription factor for cell adaptation and defense against oxidative stress. Oxidative stress reduces *Nrf2* SUMOylation and promotes LAC cell invasion and migration. SUMOylation of *Nrf2* increases its antioxidant capacity and reduces the level of ROS in LAC cells. Decreased SUMOylation of *Nrf2* and increased ROS stimulate the JNK/c-Jun signaling axis to enhance cell migration and cell adhesion, as well as promote LAC cell invasion [7]. At present, risk score models are utilized to evaluate the prognosis of cancer patients [9–11]. Herein, the oxidative stress-related genes (OSRGs) were downloaded from the official website of Gene Set Enrichment Analysis (GSEA). The expression levels of OSRGs were identified in LAC tissues of The Cancer Genome Atlas (TCGA) database. Thereafter, we investigated oxidative stress-related differentially expressed gene (DEG) mechanisms. The contributing DEGs to poor prognosis in patients with LAC were screened using the Kaplan-Meier (K-M) survival analysis, receiver operating characteristic (ROC) analysis, and Cox analysis AIC method. Subsequently, we constructed the risk score model and nomogram of LAC patients and then identified the roles of the risk score model in the progression and prognosis of LAC patients.

## 2. Materials and Methods

**2.1. Acquisition of OSRGs.** The OSRGs were searched on the online GSEA website (<http://www.gsea-msigdb.org/gsea/index.jsp>) [12]. The input keywords included oxidative stress and the 32 gene sets related to oxidative stress. All 32 gene sets were extracted, and the remaining genes, after eliminating the duplicate genes, were defined as OSRGs.

**2.2. Oxidative Stress-Related the DEGs in LAC.** The gene expression data of 594 LAC patients with FPKM type were downloaded from the official website of TCGA (<https://portal.gdc.cancer.gov/>) database. Of these, 59 were normal lung samples, whereas 535 were LAC samples. The expression data of OSRGs in 594 samples were retrieved. The expression of OSRGs in LAC tissues was identified by the limma package. The inclusion criteria were  $|\log_{2}FC| = 1$  and false discovery rate (FDR)  $< 0.05$ , which were defined as the oxidative stress-related DEGs.

**2.3. Biological Functions in the Oxidative Stress-Related DEGs.** Gene Ontology (GO) annotation and Kyoto Encyclopedia of Genes and Genomes (KEGG) signaling pathway analysis were used to analyze the roles and mechanisms of multiple genes [13, 14]. The biological process (BP), cell composition (CC), and molecular function (MF) of the oxi-

dativ stress-related DEGs were explored through GO annotation. The screening standard was adjusted to  $P < 0.05$ . The signaling mechanisms involved in the oxidative stress-related DEGs were analyzed using the KEGG signaling pathway, and the screening standard was adjusted to  $P < 0.05$ .

**2.4. Protein-Protein Interaction (PPI) Network between the Oxidative Stress-Related DEGs.** The online STRING (version: 11.5) website (<https://string-db.org/>) was used to observe the interaction between multiple genes [14]. Therefore, the oxidative stress-related DEGs were entered into the STRING database to display the PPI network between the oxidative stress-related DEGs. The screening criteria of the PPI network is the combined score  $> 0.4$ . The visualization of the PPI network of the oxidative stress-related DEGs was further enhanced by the Cytoscape (version: 3.8.2) software. The oxidative stress-related DEGs were enriched and analyzed using the MCODE method.

**2.5. The Prognostic Values of the Oxidative Stress-Related DEGs.** The prognostic data and clinicopathological features of 522 patients with LAC were downloaded from the official website of the TCGA database. After excluding 522 patients with incomplete prognostic information of LAC, the oxidative stress-related DEGs of 535 patients with LAC were matched with the prognostic information of LAC patients. By grouping the median values of the oxidative stress-related DEGs, the roles of the DEGs in the overall survival (OS) of patients with LAC were investigated by K-M survival analysis. The screening standard was set at  $P < 0.001$ .

**2.6. Construction of the Prognostic Nomogram of the Oxidative Stress-Related DEGs.** ROC analysis was used to evaluate the diagnostic values of gene expression levels in cancer tissues. The diagnostic values were better when the area under the curve (AUC) was closer to 1 [11, 15]. In LAC, the diagnostic values of oxidative stress-related DEGs (*CCNA2*, *ERO1A*, *CDK1*, *PLK1*, *CDC25C*, *ITGB4*, and *GJB2*) were investigated through the ROC analysis. Further, we constructed a nomogram of the oxidative stress-related DEGs with prognostic and diagnostic values.

**2.7. Risk Score Model of the Oxidative Stress-Related DEGs.** Univariate Cox regression analysis was performed to evaluate the relationship between the oxidative stress-related DEGs (*CCNA2*, *ERO1A*, *CDK1*, *PLK1*, *CDC25C*, *ITGB4*, and *GJB2*) and the prognosis of LAC patients. The screening standard was  $P < 0.05$ . Multivariate Cox regression analysis and AIC criteria were performed to screen the oxidative stress-related DEGs that independently influence the prognosis of patients with LAC. Subsequently, we constructed a risk score model [16, 17].

**2.8. Verification of the Roles of the Risk Score Model and Construction of the Risk Model-Related Nomogram.** Correlation analysis was performed to investigate the relationship between the expression levels of risk model genes (*ERO1A*, *CDC25C*, and *ITGB4*) and the risk score model. The expression levels of *ERO1A*, *CDC25C*, and *ITGB4*, and their relationship with the clinicopathological characteristics of

TABLE 1: The oxidative stress-related DEGs in LAC tissues.

Gene	logFC	Gene	logFC	Gene	logFC	Gene	logFC
GPX2	6.013780623	SUMO4	2.257715062	PCNA	1.251080564	NFIX	-1.302326118
S100A7	5.41728031	FBXO32	2.253504422	PIIF	1.228327064	JUND	-1.316092598
MMP11	5.370660455	ERO1A	2.169220374	P4HB	1.224045072	SNCA	-1.343581323
GJB2	4.664130361	MMP9	2.153880308	CBX4	1.194091529	TLR4	-1.375114638
PTPRN	4.431031909	CDH2	2.13556165	GCLM	1.175006466	AQP1	-1.395667559
UBE2C	4.33254131	MT1H	2.048791978	UTP25	1.172874466	HMOX1	-1.474996851
WNT16	4.221055426	MARCKSL1	2.0461911	ERBB2	1.170033481	SESN1	-1.488992986
XDH	4.189103258	SLC4A11	2.023752334	SPINT2	1.147192812	ERBB4	-1.508245365
MMP3	4.042213517	PDK1	1.897233653	CALU	1.146319227	SELENOP	-1.513089809
MYBL2	3.97196672	ITGB4	1.769385266	RGS14	1.130235535	FOS	-1.547672977
CDC20	3.923133178	TXNRD1	1.713452233	NME2	1.120700065	KRT1	-1.611799687
PYCR1	3.849785485	FANCD2	1.694266871	GSR	1.118622392	BMP2	-1.62052111
CDC25C	3.822823814	WNT1	1.652280572	NUDT1	1.110791055	KLF2	-1.630982183
MELK	3.79228364	ABCB11	1.648035243	OAT	1.108313278	RCAN1	-1.645841006
CDKN2A	3.660292428	IGFBP2	1.643496508	TCF3	1.106493729	FBLN5	-1.650383453
PLK1	3.355128242	E2F1	1.629703342	IER3	1.104634685	ALOX5	-1.670847714
SLC7A11	3.206827355	GDF15	1.594567934	CDK4	1.1019358	MSRB3	-1.695874161
NOX5	3.181844416	FUT8	1.582037385	PARP1	1.097260888	EGR1	-1.730851757
NQO1	3.122327878	CYP2E1	1.575457932	MGST1	1.083753103	CHRNA4	-1.759665302
HGFAC	3.084341171	NOX1	1.572211162	NR2F6	1.077443474	CAT	-1.761079975
COL1A1	3.04475487	E2F3	1.541174573	DHFR	1.064060918	CYP1A1	-1.771485237
CCNA2	3.037368198	UCN	1.536180525	NOL3	1.017279978	HYAL1	-1.793702837
CDH3	2.906398001	PRDX4	1.524830048	HBB	-4.072278882	CRYAB	-1.799207942
GPR37	2.892829344	SRXN1	1.523512148	HBA2	-3.971614753	LRRK2	-1.837429368
SLC7A5	2.832579597	TPO	1.497068338	ETS1	-1.009611374	EDN1	-1.837496875
TRPA1	2.725732428	NET1	1.492518868	JUNB	-1.029141797	CA3	-1.923666594
EZH2	2.71140365	NOX4	1.469389165	ETV5	-1.03192463	SLC1A1	-2.043700892
SGK2	2.696077295	CBX8	1.467297358	ITGAL	-1.045741495	NR4A3	-2.088467157
CDK1	2.607317686	G6PD	1.459631279	VIM	-1.048813585	KCNA5	-2.103363458
CBX2	2.603102932	MET	1.424801169	CYGB	-1.072716336	GPX3	-2.12554072
LPO	2.537856476	FMO1	1.418278305	MYLK	-1.073347764	DUOX1	-2.428487405
E2F2	2.515712683	TRPM2	1.383090886	SIRPA	-1.104069804	HBEGF	-2.431447934
CDC25A	2.506554418	PRKAA2	1.373646285	SELENBP1	-1.12795438	EPAS1	-2.587591866
HMGA1	2.412891462	GPR37L1	1.36067259	CDKN2B	-1.146620037	IL6	-2.664089275
FOXO6	2.408776331	IPCEF1	1.347748923	CYBB	-1.155101406	CD36	-2.768036549
CHEK1	2.394961963	TAT	1.339357309	HYAL2	-1.155726104	AGRP	-2.793810482
GCLC	2.381107058	GPX8	1.337343767	NCF1	-1.157427085	RETN	-2.813480794
MCM4	2.359143052	MAP2K6	1.332194326	UTRN	-1.180127364	MGAT3	-2.885893674
ECT2	2.328988223	MMP14	1.302518357	BTK	-1.217464546	SCGB1A1	-3.072434982
EFNA4	2.310996951	TRAP1	1.281380934	PPARGC1B	-1.249251755	ANGPTL7	-3.157773456
HYOU1	1.280070739	BNIP3	1.270862371	HBA1	-4.201724914		

Note: LAC: lung adenocarcinoma; DEGs: differentially expressed genes.

patients with LAC in the high- and low-risk groups were explored and observed by scatter diagram and heat map. K-M survival and Cox regression analyses were performed to evaluate the relationship between the risk model and the OS of patients with LAC. The risk model-related nomogram was constructed based on multivariate COX regression analysis results.

*2.9. Signaling Mechanisms Involved in the Risk Score Model.* The GSEA (version: 4.1.0) software platform was used to analyze the BP, MF, CC, and signaling pathways of the DEGs. The gene expression data of 535 LAC patients in the TCGA database were grouped via the risk score and recorded as the high- and low-risk groups. The impact of the high- and low-risk groups on each gene set on the GSEA

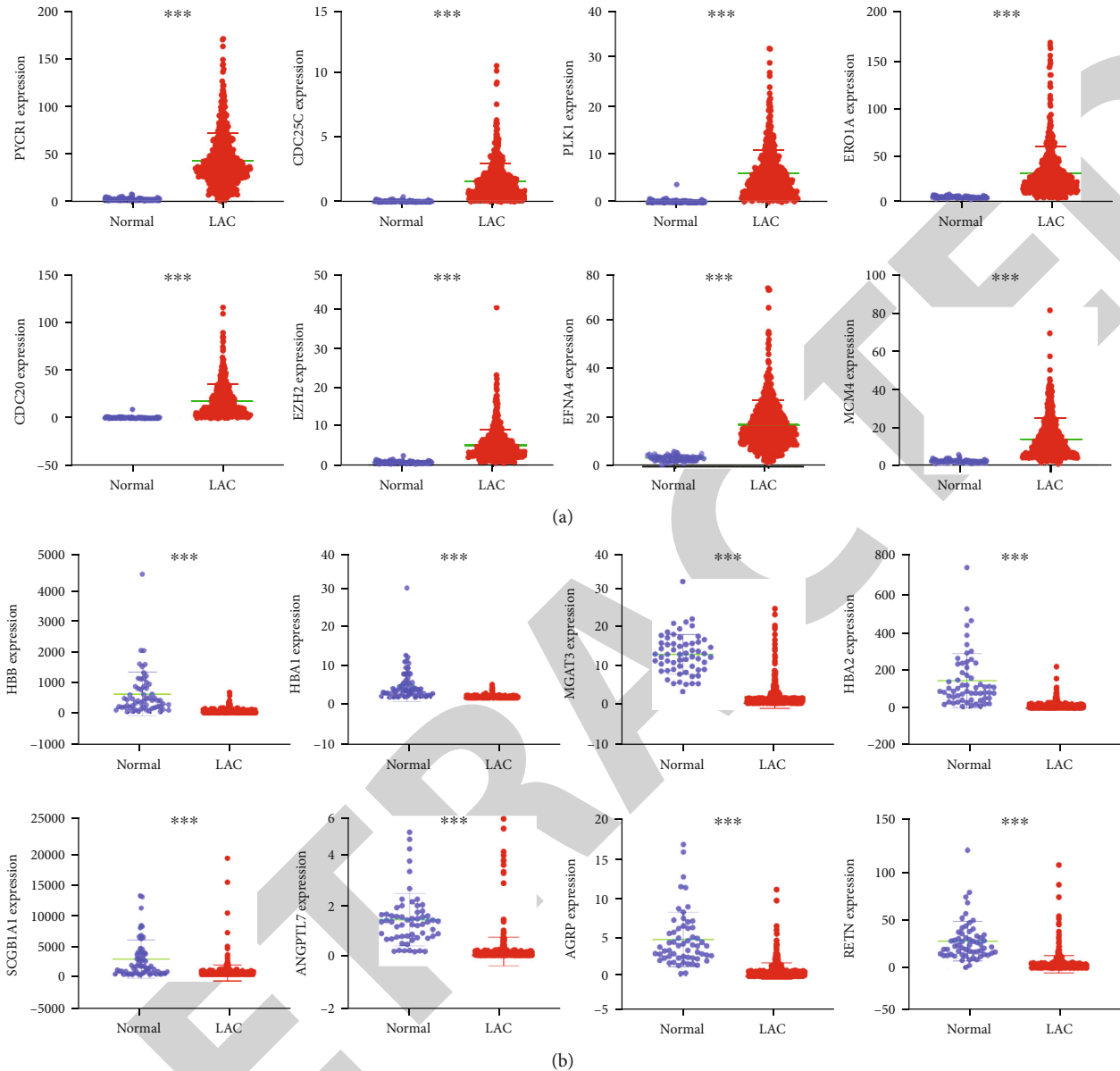


FIGURE 1: The DEGs associated with oxidative stress visualized with statistical significance: (a) overexpressed genes; (b) downregulated genes. Note: LAC: lung adenocarcinoma; DEGs: differentially expressed genes; \*\*\* $P < 0.001$ .

platform was explored to understand the signaling pathways involved in the risk score model. The running process was performed 1000-fold [18, 19]. Nominal (NOM)  $P$  was the screening standard for GSEA analysis.

**2.10. Relationship between Risk Score Genes and Immune Cell Infiltration.** ssGSEA analysis method was used to calculate the immune cell infiltration levels in the tissues with LAC. Spearman correlation analysis was used to explore the correlation between the expression levels of oxidative stress-related DEGs (*ERO1A*, *CDC25C*, and *ITGB4*) and the immune cell infiltration levels. Thereafter, the expression levels of LAC immune infiltrating cells in the high- and low-expression groups of *ERO1A*, *CDC25C*, and *ITGB4* were

analyzed by the median expression values of *ERO1A*, *CDC25C*, and *ITGB4*.

**2.11. Identification of Risk Score Model Gene Expression in LAC Tissues.** In April 2022, we extracted the cancer tissues and adjacent normal tissues from 8 patients who underwent surgical treatment in our hospital and were diagnosed with LAC. All patients signed the informed consent. The study was reviewed and approved by the ethics committee of Taihe Hospital. The expression levels of *ERO1A*, *CDC25C*, and *ITGB4* in 8 LAC tissues and paired normal tissues were examined based on the standard PCR assays [19]. The primer sequences included as follows: *ERO1A* 5'-ATGACATCAGC CAGTGTGGA-3' (forward); 5'-CATGCTTGGTCCACTG

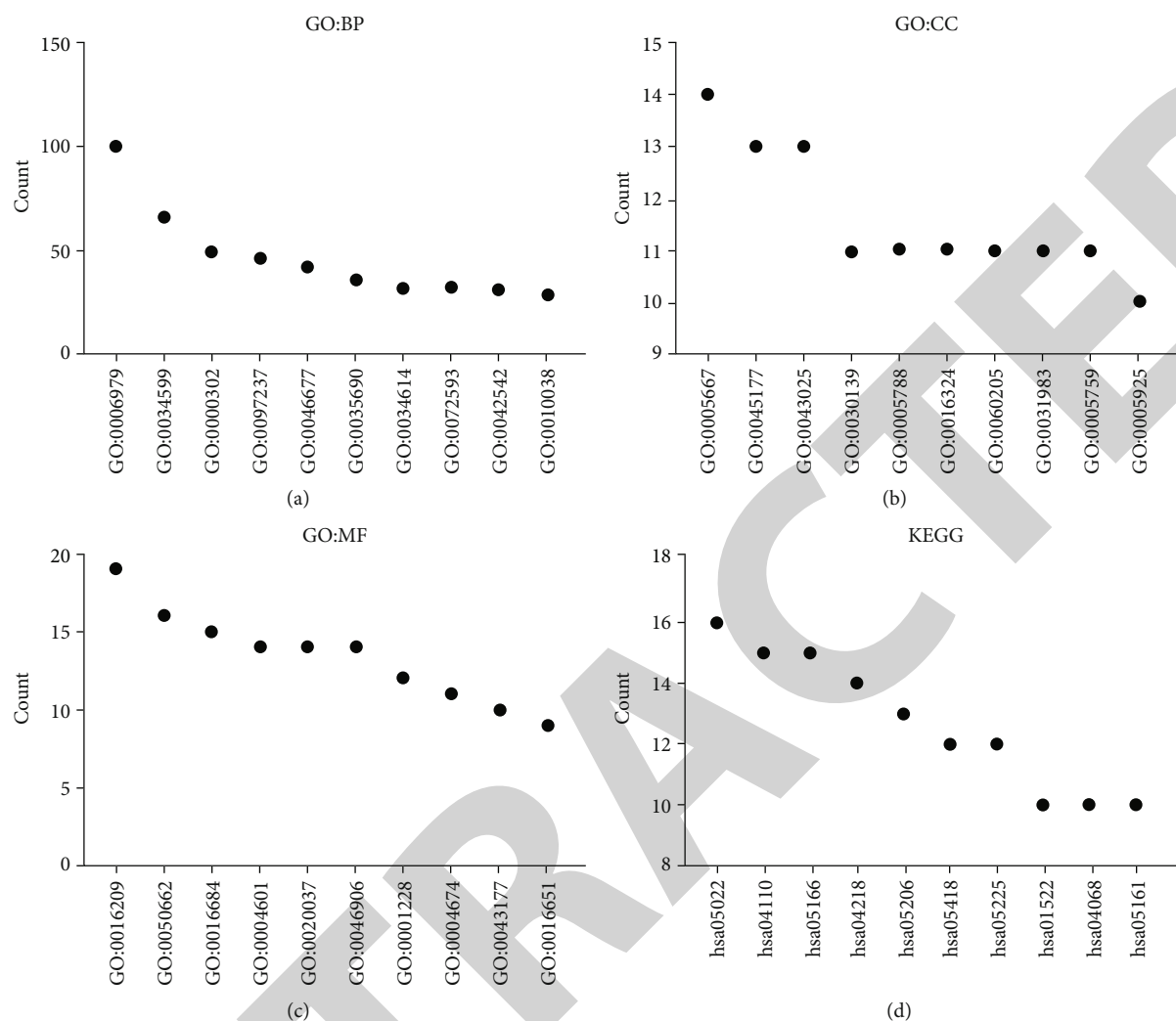


FIGURE 2: Functions and mechanisms of oxidative stress-related the DEGs using GO and KEGG analysis: (a) biological process; (b) cell composition; (c) molecular function; (d) signaling pathways. Note: DEGs: differentially expressed genes; BP: biological process; CC: cell composition; MF: molecular function; GO: Gene Ontology; KEGG: Kyoto Encyclopedia of Genes and Genomes.

AAGA-3' (reverse); *CDC25C* 5'-TGGTCACCTGGATTCTTC-3' (forward); 5'-ACCATTTCGGAGTGCTACA-3' (reverse); and *ITGB4* 5'-TTCAATGTCGTCTCCTCCAC-3' (forward); 5'-CAATAGGTCGGTTGTCATCG-3' (reverse).

**2.12. Statistical Analysis.** The oxidative stress-related DEGs in LAC were analyzed by limma package or *t*-test. Survival and ROC analyses were performed to analyze the LAC prognosis and diagnostic value of the oxidative stress-related DEGs, as well as the roles of the risk model in the prognosis of LAC patients. Correlation analysis was conducted to explore the relationship between the expression of *ERO1A*, *CDC25C*, and *ITGB4* and LAC immune infiltration.  $P < 0.05$  was considered statistically significant.

### 3. Results

**3.1. Oxidative Stress-Related DEGs.** A total of 32 gene sets related to oxidative stress were searched on the GSEA plat-

form. These 32 gene sets comprised 784 OSRGs. The OSRGs in normal lung and LAC tissues were corrected and extracted from the TCGA database. Differential expression analysis showed 163 DEGs in LAC tissues compared to normal lung tissues (Table 1). Among them, 104 genes were overexpressed, whereas 59 were downregulated. The scatter plot displayed 8 overexpressed and 8 downregulated genes (Figure 1).

**3.2. Functions, Mechanisms, and PPI Network of Oxidative Stress-Related the DEGs.** GO annotation revealed that the oxidative stress-related DEGs contributed to the cellular response to oxidative stress, reactive oxygen species, toxic substance, antibiotics, hydrogen peroxide, metallic process, hydrogen peroxide, cellular oxidative detoxification, etc. (Figures 2(a)–2(c) and Table S1). KEGG analysis revealed that the oxidative stress-related DEGs are involved in the cell cycle, cellular sensitivity, endocrine resistance, *FOXO* signaling pathway, non-small-cell lung cancer, *TNF* signaling

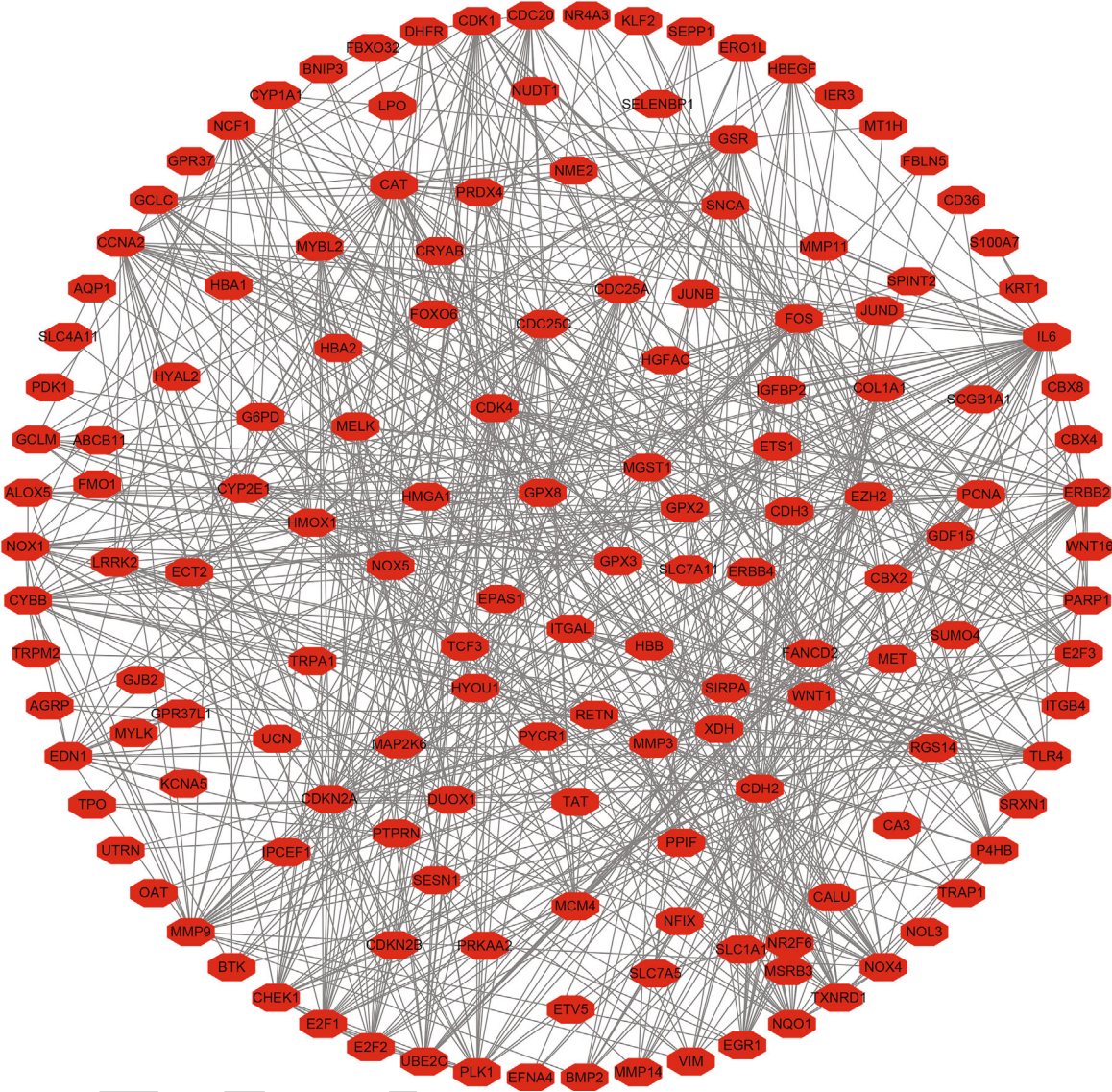
TABLE 2: The mechanisms of the oxidative stress-related DEGs.

ID	Description	Adjust <i>P</i>	Count
hsa04110	Cell cycle	1.76724E-07	15
hsa04218	Cellular senescence	1.43121E-05	14
hsa05219	Bladder cancer	1.43121E-05	8
hsa05144	Malaria	5.35207E-05	8
hsa05166	Human T-cell leukemia virus 1 infection	6.57929E-05	15
hsa05418	Fluid shear stress and atherosclerosis	6.57929E-05	12
hsa00480	Glutathione metabolism	8.24298E-05	8
hsa01522	Endocrine resistance	8.24298E-05	10
hsa05225	Hepatocellular carcinoma	0.000314944	12
hsa04068	FoxO signaling pathway	0.000873542	10
hsa05223	Non-small-cell lung cancer	0.002645764	7
hsa04933	AGE-RAGE signaling pathway in diabetic complications	0.003188844	8
hsa05161	Hepatitis B	0.00397965	10
hsa04668	TNF signaling pathway	0.005960585	8
hsa04216	Ferroptosis	0.006375126	5
hsa05215	Prostate cancer	0.010743162	7
hsa05202	Transcriptional misregulation in cancer	0.010743162	10
hsa04380	Osteoclast differentiation	0.010743162	8
hsa05218	Melanoma	0.010743162	6
hsa04918	Thyroid hormone synthesis	0.012331107	6
hsa05206	MicroRNAs in cancer	0.012331107	13
hsa05212	Pancreatic cancer	0.012331107	6
hsa05169	Epstein-Barr virus infection	0.012694013	10
hsa04066	HIF-1 signaling pathway	0.015124736	7
hsa05224	Breast cancer	0.019724031	8
hsa05226	Gastric cancer	0.02063717	8
hsa05143	African trypanosomiasis	0.021418019	4
hsa00590	Arachidonic acid metabolism	0.023628458	5
hsa04934	Cushing syndrome	0.023628458	8
hsa05022	Pathways of neurodegeneration-multiple diseases	0.023993575	16
hsa04657	IL-17 signaling pathway	0.025867689	6
hsa05230	Central carbon metabolism in cancer	0.033496361	5
hsa05205	Proteoglycans in cancer	0.034153721	9
hsa04115	p53 signaling pathway	0.037682051	5
hsa05214	Glioma	0.041022366	5
hsa05220	Chronic myeloid leukemia	0.042160826	5
hsa05140	Leishmaniasis	0.043324911	5
hsa05167	Kaposi sarcoma-associated herpesvirus infection	0.065724291	8
hsa00130	Ubiquinone and other terpenoid-quinone biosynthesis	0.069783669	2
hsa05222	Small-cell lung cancer	0.082734228	5
hsa05323	Rheumatoid arthritis	0.084248714	5

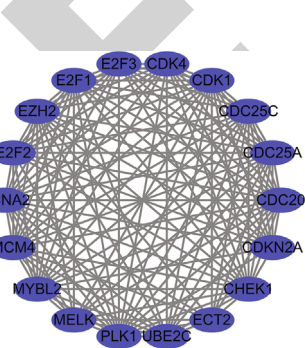
Note: DEGs: differentially expressed genes.

pathway, ferroptosis, transcriptional misregulation in cancer, *HIF-1*, *IL-17*, p53, and among other signaling pathways (Figure 2(d) and Table 2). Figure 3(a) shows the PPI network between the oxidative stress-related DEGs and the enriched PPI networks through enrichment analysis (Figures 3(b)–3(d)).

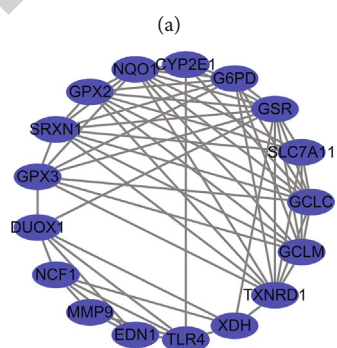
3.3. Construction of the Prognostic Nomogram of Oxidative Stress-Related DEGs. K-M survival analysis showed that the expression levels of *BTK*, *CAT*, *CCNA2*, *CDC25C*, *CDH3*, *ERO1A*, *CDK1*, *PLK1*, *ITGB4*, *GJB2*, *CHEK1*, *CYBB*, *ECT2*, *FANCD2*, *FBLN5*, *GPR37*, *GPX3*, *GPX8*, *HMGA1*, *ITGAL*, *KCNA5*, *LRKK2*, *MCM4*, *MELK*, *MMP3*, *MMP14*, *MYBL2*,



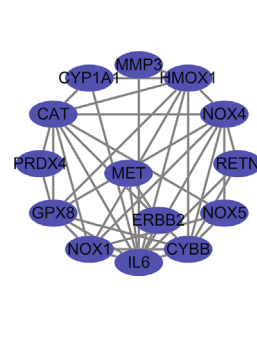
(a)



(b)



(c)



(d)

FIGURE 3: PPI network of the oxidative stress-related DEGs. Note: PPI: protein-protein interaction; DEGs: differentially expressed genes.

TABLE 3: The expression levels of oxidative stress-related DEGs are significantly correlated with the poor prognosis of LAC patients.

Gene	<i>P</i>	Gene	<i>P</i>	Gene	<i>P</i>
BTK	1.493e-03	GPX3	1.072e-02	NOX5	2.935e-02
CAT	1.529e-02	GPX8	5.265e-03	NUDT1	2.177e-02
CCNA2	9.186e-05	HMGA1	3.920e-03	OAT	3.028e-02
CDC25C	3.027e-04	ITGAL	2.305e-02	PLK1	3.684e-04
CDH3	4.037e-02	ITGB4	8.341e-04	PRKAA2	4.034e-02
CDK1	1.854e-04	KCNA5	8.226e-03	PTPRN	3.107e-02
CHEK1	3.871e-03	LRRK2	4.389e-02	RGS14	6.938e-03
CYBB	3.658e-02	MCM4	6.422e-03	SELENBP1	2.610e-02
ECT2	4.329e-03	MELK	3.742e-02	SELENOP	2.561e-02
ERO1A	3.599e-04	MMP3	1.822e-02	SLC1A1	3.487e-02
FANCD2	2.336e-02	MMP14	3.558e-02	TPRA1	4.763e-03
FBLN5	4.130e-02	MYBL2	3.134e-02	UBE2C	4.573e-02
GJB2	1.853e-04	NFIX	1.384e-02	XDH	4.819e-02
GPR37	9.159e-03	NOX4	1.578e-02		

Note: LAC: lung adenocarcinoma; DEGs: differentially expressed genes.

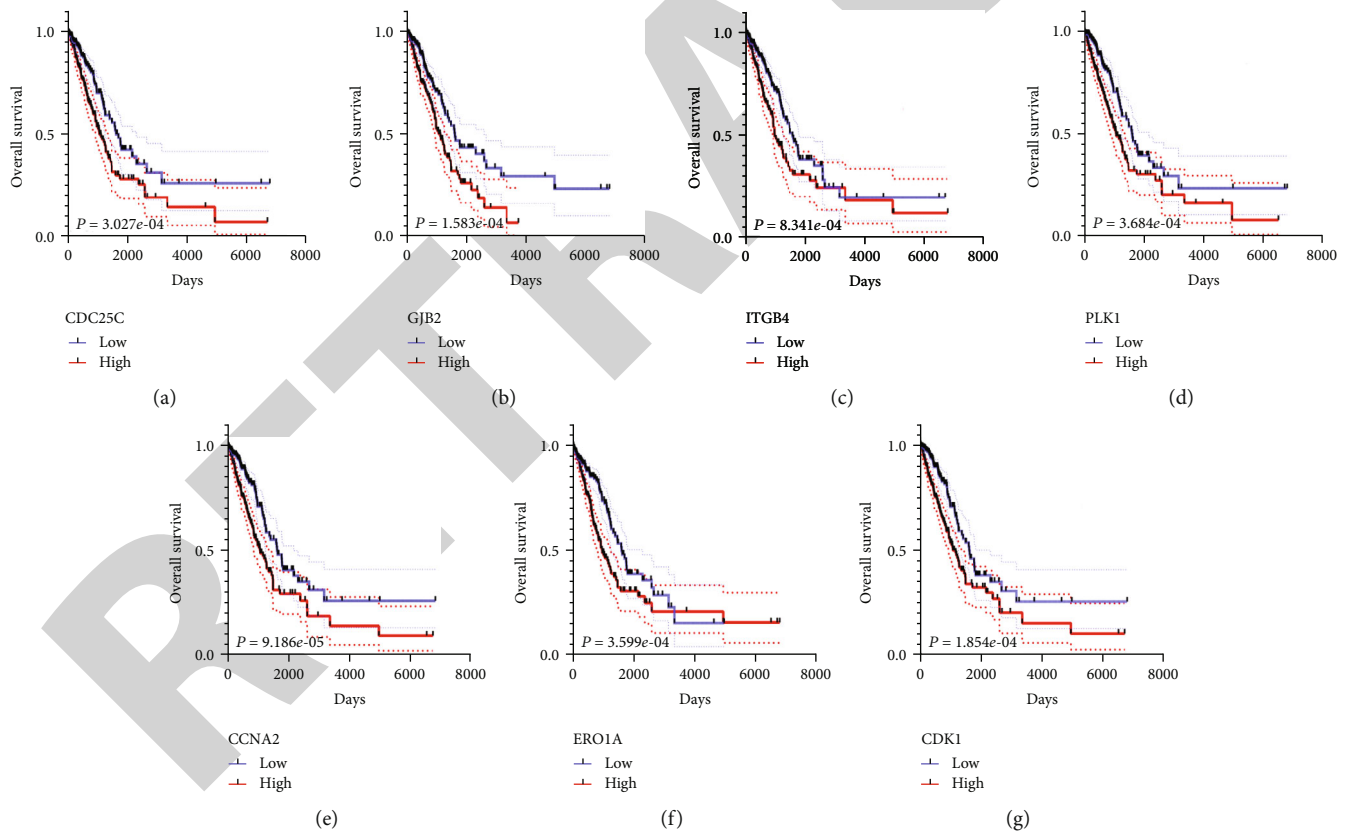


FIGURE 4: 7 oxidative stress-related DEGs assess the overall survival of LAC: (a) *CDC25C*; (b) *GJB2*; (c) *ITGB4*; (d) *PLK1*; (e) *CCNA2*; (f) *ERO1A*; (g) *CDK1*. Note: LAC: lung adenocarcinoma; DEGs: differentially expressed genes.

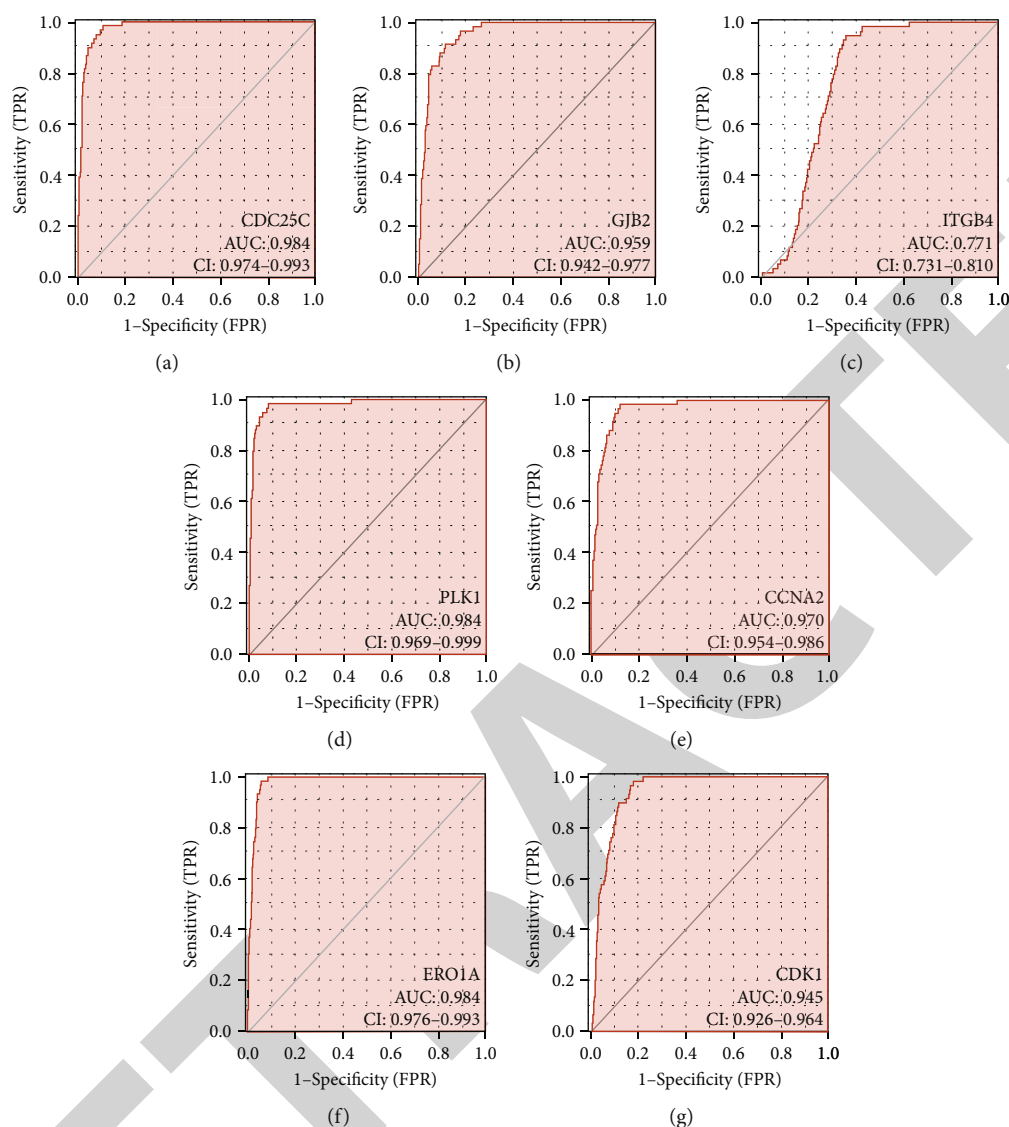


FIGURE 5: 7 oxidative stress-related DEGs have diagnosis values of LAC: (a) *CDC25C*; (b) *GJB2*; (c) *ITGB4*; (d) *PLK1*; (e) *CCNA2*; (f) *ERO1A*; (g) *CDK1*. Note: LAC: lung adenocarcinoma; DEGs: differentially expressed genes.

*NFIX*, *NOX4*, *NOX5*, *NUDT1*, *OAT*, *PRKAA2*, *PTPRN*, *RGS14*, *SELENBP1*, *SELENOP*, *SLC1A1*, *TRPA1*, *UBE2C*, and *XDH* significantly correlated with the poor prognosis of LAC patients (Table 3). Based on the significance criterion of the  $P < 0.001$ , the overexpression levels of *CCNA2*, *CDC25C*, *ERO1A*, *CDK1*, *PLK1*, *ITGB4*, and *GJB2* significantly correlated with the poor prognosis of patients with LAC (Figure 4).

ROC analysis demonstrated that the expression levels of *CCNA2*, *CDC25C*, *ERO1A*, *CDK1*, *PLK1*, *ITGB4*, and *GJB2* have diagnosis values of LAC (Figure 5). The AUCs of *CCNA2*, *CDC25C*, *ERO1A*, *CDK1*, *PLK1*, *ITGB4*, and *GJB2* were 0.97, 0.984, 0.984, 0.945, 0.984, 0.771, and 0.959, respectively, indicating that OSRGs *CCNA2*, *CDC25C*, *ERO1A*, *CDK1*, *PLK1*, *ITGB4*, and *GJB2* have diagnosis values of LAC. Based on K-M survival and ROC analyses,

we constructed a nomogram of OSRGs *CCNA2*, *CDC25C*, *ERO1A*, *CDK1*, *PLK1*, *ITGB4*, and *GJB2* (Figure 6).

**3.4. Construction of Risk Score Model.** Univariate Cox regression analysis was used to explore the relationship between the expression levels of *CCNA2*, *CDC25C*, *ERO1A*, *CDK1*, *PLK1*, *ITGB4*, and *GJB2* and the OS of patients with LAC. Consequently, the overexpression of *CCNA2*, *CDC25C*, *ERO1A*, *CDK1*, *PLK1*, *ITGB4*, and *GJB2* was the risk factors for poor prognosis in patients with LAC (Figure 7(a)). Based on multivariate Cox regression analysis and the AIC method, *ERO1A*, *CDC25C*, and *ITGB4* were independent risk factors affecting the poor prognosis of patients with LAC (Table 4 and Figure 7(b)). The risk score model was constructed based on *ERO1A*, *CDC25C*, and *ITGB4*. Correlation analysis revealed that the expression levels of *ERO1A*,



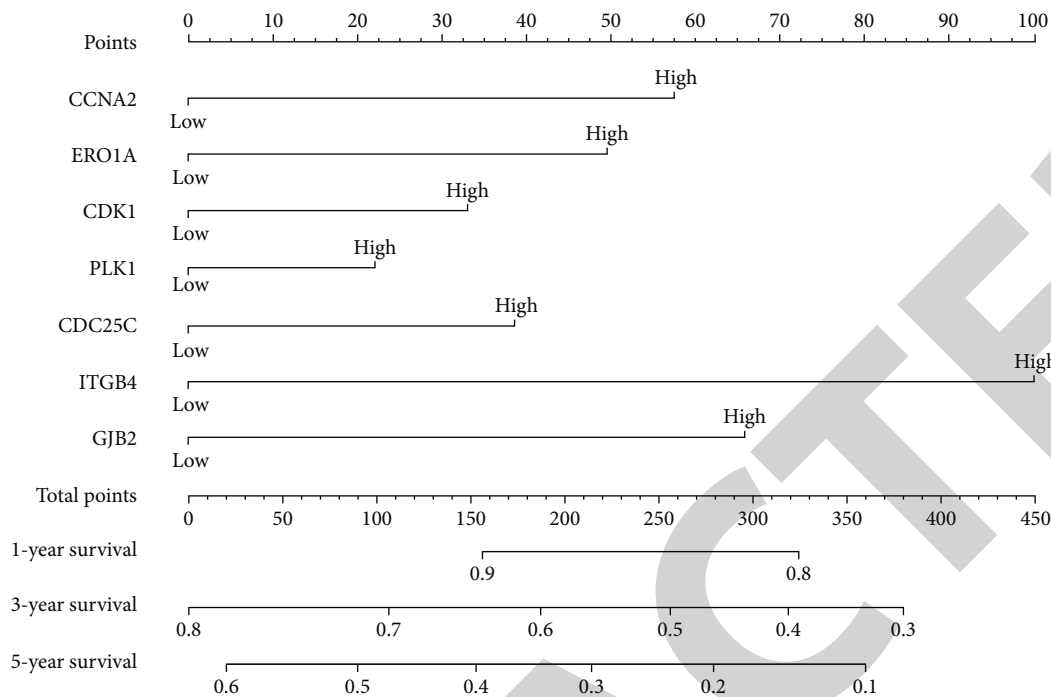


FIGURE 6: Prognostic nomogram of 7 oxidative stress-related DEGs in LAC. LAC: lung adenocarcinoma; DEGs: differentially expressed genes.

*CDC25C*, and *ITGB4* significantly correlated with the risk score (Figure S1A-C). Grouping by high- and low-risk showed significant differences between the two groups in *ERO1A*, *CDC25C*, and *ITGB4* (Figure S1D-F).

**3.5. Risk Score as a Factor for Poor Prognosis in Patients with LAC.** The expression levels of *ERO1A*, *CDC25C*, and *ITGB4* were significantly upregulated in LAC tissues from our hospital with significant statistical significance (Figure S2). Figures 7(c) and 7(d) show the relationship between risk score and OS of patients with LAC, and LAC with high-risk scores had a poor prognosis. Univariate Cox regression analysis showed that clinical stage, T stage, lymph node metastasis, and risk score affect the poor prognosis of patients with LAC (Figure 8(a)). Besides, multivariate Cox regression analysis revealed that age, clinical stage, and risk score contribute to the poor prognosis of patients with LAC (Figure 8(b)). Figure 8(c) shows that the high- and low-risk groups are associated with the survival status, clinical stage, T stage, and lymph node metastasis in patients with LAC. To evaluate the prognosis of patients with LAC, a risk score prognostic nomogram was constructed based on multivariate Cox analysis results (Figure 9).

**3.6. Signaling Mechanisms in a High-Risk Score Group.** GSEA results showed that the high-risk score is involved in cell cycle, splice some, DNA replication, mismatch repair, homologous recombination, proteasome, nucleoside precision repair, p53 signaling pathway, base precision repair,

oocyte meiosis, regulation of actin cytoskeleton, pathways in cancer, and among other mechanisms (Figure S3 and Table 5).

**3.7. The Risk Score Model-Related DEGs Correlate with Immune Infiltrating Cells.** Spearman correlation analysis demonstrated that the expression level of *CDC25C* correlated with the levels of Th2 cells, mast cells, iDC, eosinophils, DC, NK cells, Tfh, Tgd, NK cd56dim cells, CD8 T cells, macrophages, pDC, Tcm, Th17 cells, T helper cells, aDC, neutrophils, Tem, NK cd56bright cells, B cells, and Treg (Figure 10 and Table 6). *ERO1A* expression level correlated with Th2 cells, mast cells, eosinophils, Tfh, CD8 T cells, NK cd56dim cells, aDC, iDC, NK cells, NK cd56bright cells, Tgd, DC, pDC, neutrophils, and Treg (Figure S4 and Table 6). *ITGB4* expression level correlated with the NK cells, T helper cells, neutrophils, B cells, NK cd56bright cells, TFH, NK cd56dim cells, iDC, and mast cells (Figure S5 and Table 6).

Grouping by the median values of oxidative stress-related DEGs (*CDC25C*, *ERO1A*, and *ITGB4*) showed abnormal and statistically significant expression of mast cells, iDC, eosinophils, DC, NK cd56dim cells, NK cells, Tfh, Tgd, Th2 cells, macrophages, CD8 T cells, pDC, T helper cells, Th17 cells, Tcm, neutrophils, and Tem in the high- and low-expression groups of *CDC25C* (Figure 11 and Table 7). The expression of mast cells, iDC, eosinophils, CD8 T cells, NK cells, Tfh, Th2 cells, NK cd56bright cells, Tgd, aDC, T helper cells, NK cd56dim cells, DC, neutrophils, and B cells in the high- and low-expression groups of *ERO1A* was abnormal and statistically significant (Figure S6 and Table 7). The

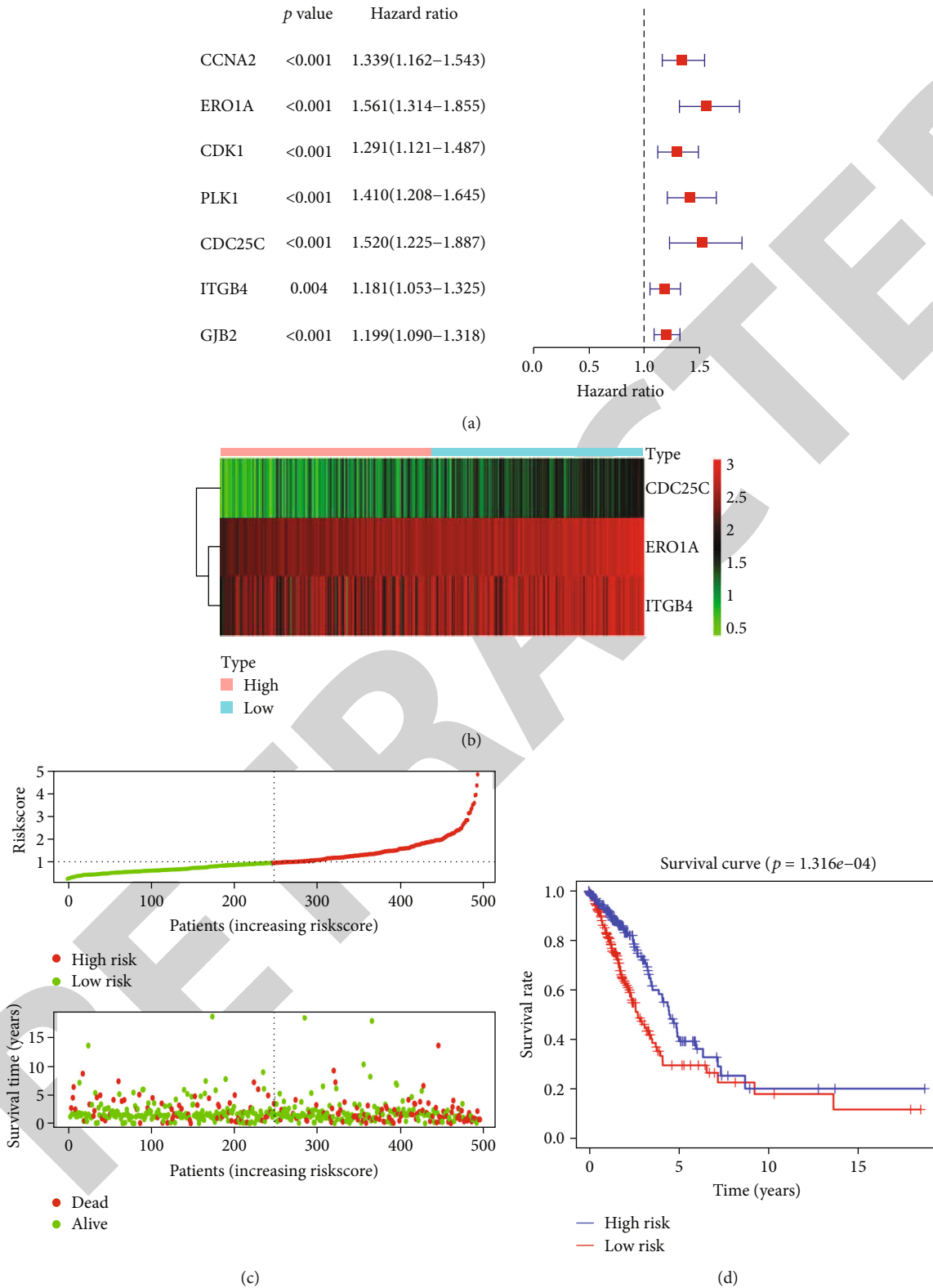


FIGURE 7: Construction of risk model based on the 3 oxidative stress-related DEGs: (a) prognostic DEGs are shown in overall survival using COX analysis; (b) the relationship between 3 oxidative stress-related DEGs and prognosis in LAC; (c, d) the relationship between the risk score and prognosis in patients with LAC is visualized. Note: LAC: lung adenocarcinoma; DEGs: differentially expressed genes.

TABLE 4: Independent prognostic factors of oxidative stress-related DEGs.

Gene	HR	95% CI	P
ERO1A	1.363360001	1.124731516-1.652617062	0.001592209
CDC25C	1.459214408	1.138311378-1.870583683	0.002860696
ITGB4	1.16932949	1.039123642-1.315850589	0.009400705

Note: DEGs: differentially expressed genes; HR: hazard ratio; CI: confidence interval.

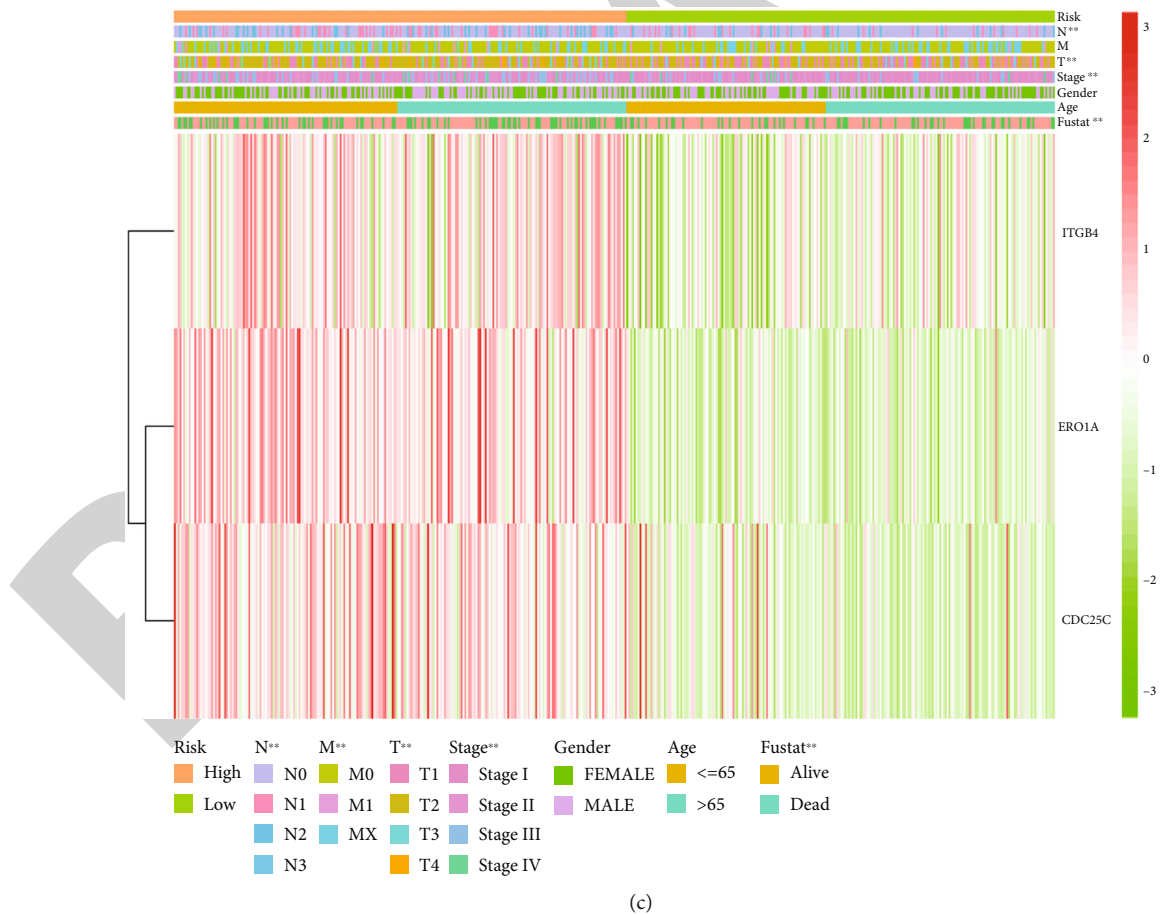
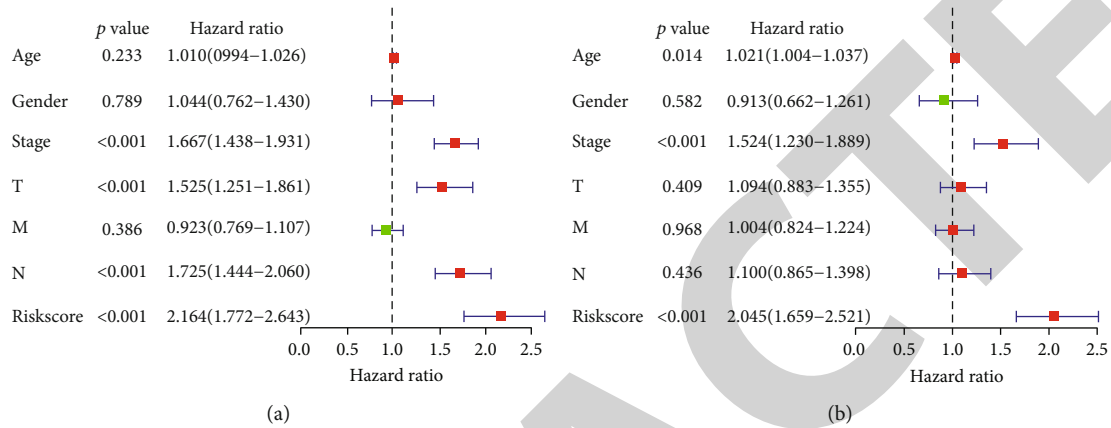


FIGURE 8: A risk score model based on the 3 oxidative stress-related DEGs is significantly associated with the prognosis in LAC patients. (a, b) COX analysis shows that risk score affects the poor prognosis of patients with LAC. (c) Risk score is associated with the survival status, clinical stage, T stage, and lymph node metastasis in patients with LAC. Note: LAC: lung adenocarcinoma; DEGs: differentially expressed genes.

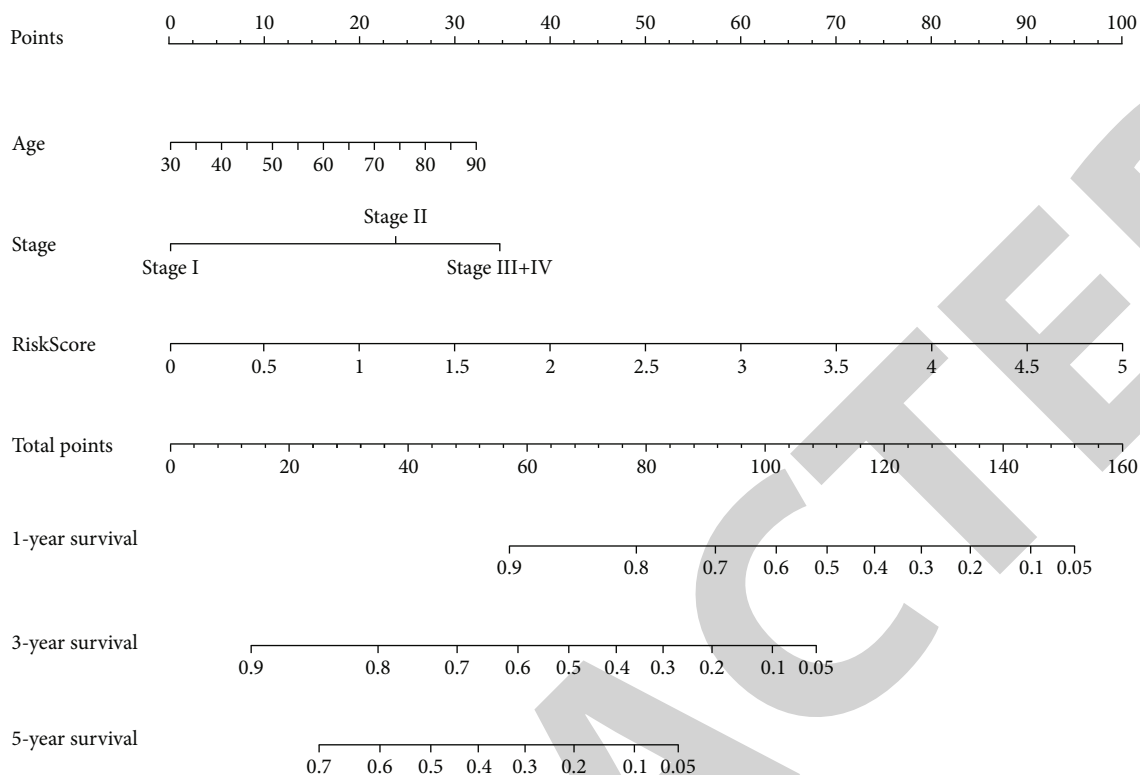


FIGURE 9: Construction of the risk score prognostic nomogram.

TABLE 5: Signaling mechanisms are involved in the high-risk score group.

Name	Size	ES	NES	NOM P
Cell cycle	124	0.66915077	2.1871314	0
Spliceosome	126	0.64206976	2.083224	0
DNA replication	36	0.837718	2.0672143	0
Mismatch repair	23	0.80036765	2.062228	0
Pathogenic Escherichia coli infection	55	0.5739781	2.056669	0
Homologous recombination	28	0.7681676	2.0361679	0
P53 signaling pathway	68	0.49579692	1.8950231	0
Pyrimidine metabolism	97	0.5173413	1.9280515	0.001923077
Nucleotide excision repair	44	0.6324002	1.995188	0.001980198
Base excision repair	33	0.6285262	1.8693517	0.002
Proteasome	44	0.7988379	2.0141854	0.002040816
Oocyte meiosis	112	0.4684853	1.8251096	0.004140787
Pentose phosphate pathway	27	0.57422036	1.7523918	0.005825243
Glycolysis gluconeogenesis	61	0.50060135	1.7604159	0.01010101
Ubiquitin mediated proteolysis	133	0.4287824	1.6589828	0.018907564
Bladder cancer	42	0.39720345	1.5345889	0.02296451
Pancreatic cancer	70	0.41440853	1.598584	0.024948025
Small-cell lung cancer	84	0.41004965	1.5795516	0.02631579
Galactose metabolism	25	0.50981605	1.6308589	0.027985075
Renal cell carcinoma	70	0.37961188	1.518121	0.028077753
Regulation of actin cytoskeleton	212	0.37622863	1.5810093	0.028688524
Drug metabolism other enzymes	51	0.4489914	1.5682174	0.029850746
Pathways in cancer	325	0.31233284	1.4214869	0.042105265
Progesterone mediated oocyte maturation	85	0.3916816	1.5144613	0.04375

Note: ES: enrichment score; NES: normalized enrichment score; NOM: nominal.

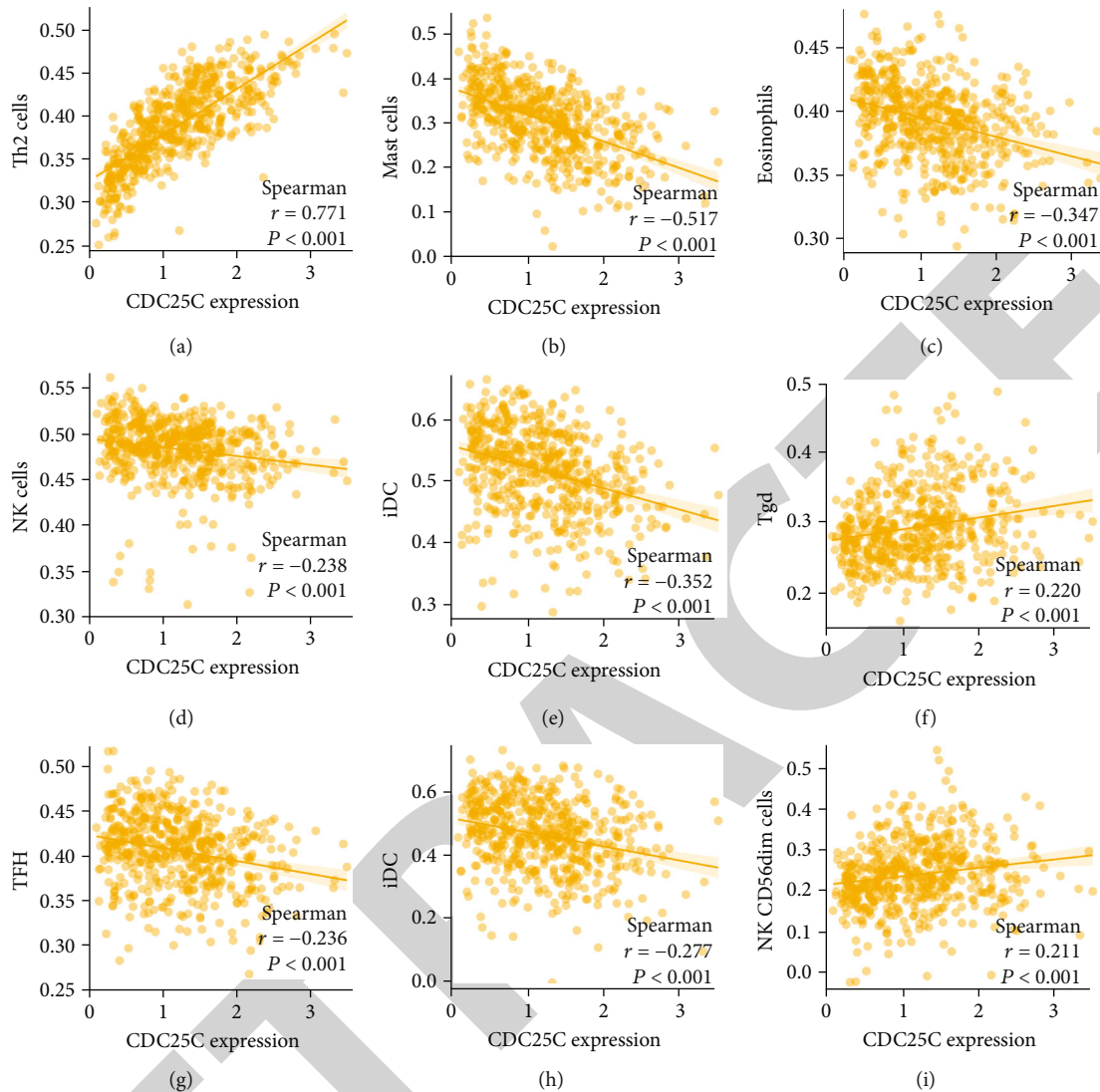


FIGURE 10: The expression level of *CDC25C* correlates with the levels of immune infiltrating cells: (a) Th2 cells; (b) mast cells; (c) eosinophils; (d) NK cells; (e) iDC; (f) Tgd; (g) TFH; (h) DC; (i) NK CD56dim cells.

expression of NK cells, T helper cells, NK cd56bright cells, NK cd56dim cells, B cells, and neutrophils in the high- and low-expression groups of *ITGB4* was abnormal and statistically significant (Figure S7 and Table 7).

#### 4. Discussion

Lung adenocarcinoma has a high incidence and mortality rates [7, 9, 15, 20]. At present, the prognosis of LAC patients is significantly poor. Therefore, new biomarkers are required to predict this and provide novel treatment targets. An oxidative stress response is involved in the progression of LAC [5–8]. Long-chain noncoding RNA (lncRNA) nuclear LUCAT1 (*NLUCAT1*) is strongly upregulated during hypoxia *in vitro* and is associated with hypoxia markers and poor prognosis in LAC. *NLUCAT1* downregulation inhibits the proliferation and invasion of LAC cells and increases oxidative stress and sensitivity to

cisplatin [8]. Several OSRGs were abnormally expressed in LAC tissues in this study. The oxidative stress-related DEGs regulate the cellular response to oxidative stress, reactive oxygen species, toxic substances, antibiotics, hydrogen peroxide, reactive oxygen species, metabolic process, hydrogen peroxide, cellular oxidant detoxification, etc. This confirms that our oxidative stress-related DEGs are related to oxidative stress.

The expression levels of *CCNA2*, *CDC25C*, *ERO1A*, *CDK1*, *PLK1*, *ITGB4*, and *GJB2* could influence the cancer progression [21–26]. For instance, *ERO1A*, also known as *ERO1L*, promotes *IL6R* secretion by targeting disulfide bond formation. *IL-6R* binds to *IL-6*, resulting in the activation of the *NF- $\kappa$ B* signaling pathway. *NF- $\kappa$ B*, in turn, binds to the promoter of *MUC16*, causing its overexpression. *ERO1L* may trigger *CA125* secretion via the *IL-6* signaling pathway, form a positive feedback loop, and promote lung cancer development [23]. Through survival,

TABLE 6: The expression levels of oxidative stress-related DEGs are correlated with the levels of immune infiltrating cells in LAC.

Immune cells	CDC25C ( <i>r</i> )	<i>P</i>	ERO1A ( <i>r</i> )	<i>P</i>	ITGB4 ( <i>r</i> )	<i>P</i>
aDC	0.121	0.005	0.174	<0.001	0.061	0.159
B cells	-0.095	0.027	-0.081	0.061	-0.156	<0.001
CD8 T cells	-0.195	<0.001	-0.210	<0.001	0.078	0.070
Cytotoxic cells	-0.008	0.847	-0.015	0.737	-0.054	0.217
DC	-0.277	<0.001	-0.130	0.003	0.074	0.088
Eosinophils	-0.347	<0.001	-0.236	<0.001	0.071	0.102
iDC	-0.352	<0.001	-0.164	<0.001	0.091	0.035
Macrophages	-0.173	<0.001	0.034	0.431	0.049	0.257
Mast cells	-0.517	<0.001	-0.354	<0.001	0.087	0.044
Neutrophils	-0.115	0.008	0.096	0.027	0.162	<0.001
NK CD56bright cells	-0.101	0.019	-0.139	0.001	0.128	0.003
NK CD56dim cells	0.211	<0.001	0.178	<0.001	0.097	0.026
NK cells	-0.238	<0.001	-0.163	<0.001	0.255	<0.001
pDC	-0.152	<0.001	-0.110	0.011	0.010	0.823
T cells	-0.070	0.105	-0.022	0.610	-0.085	0.050
T helper cells	0.135	0.002	0.084	0.053	-0.196	<0.001
Tcm	-0.151	<0.001	-0.049	0.258	-0.020	0.638
Tem	-0.107	0.013	-0.007	0.870	-0.025	0.566
TFH	-0.236	<0.001	-0.222	<0.001	-0.104	0.017
Tgd	0.220	<0.001	0.137	0.001	-0.051	0.235
Th1 cells	-0.040	0.353	0.076	0.077	-0.002	0.954
Th17 cells	-0.143	<0.001	-0.063	0.144	0.080	0.066
Th2 cells	0.771	<0.001	0.464	<0.001	-0.073	0.092
TReg	0.091	0.036	0.091	0.036	0.082	0.057

Note: LAC: lung adenocarcinoma; DEGs: differentially expressed genes.

ROC, and Cox analyses, we found that *CCNA2*, *CDC25C*, *ERO1A*, *CDK1*, *PLK1*, *ITGB4*, and *GJB2* significantly correlated with overexpression levels and poor prognosis of patients with LAC and exhibited diagnosis values of LAC. Bioinformatics analysis and PCR identification showed overexpressed oxidative stress-related DEGs *ERO1A*, *CDC25C*, and *ITGB4* in LAC tissues and were independent risk factors for poor prognosis in patients with LAC. The risk model based on *ERO1A*, *CDC25C*, and *ITGB4* is an independent risk factor for poor prognosis in patients with LAC. In the risk model-related nomogram, the risk score demonstrated the greatest impact on the prognosis of LAC patients. This indicates that our risk score model evaluates the prognosis of LAC patients.

Cell cycle, homologous recombination, and p53 signaling pathway are associated with cancer progression [27–31]. Cyclin B1 (*CCNB1*) is an important gene in mitosis and is upregulated in LAC tissues. *CCNB1* overexpression contributes to the advanced tumor stage and short OS. A negative correlation has been discovered between *miR-139-5p* and *CCNB1* expression levels. Through negative *CCNB1* regulation, *miR-139-5p* inhibits cell proliferation and migration [27]. lncRNA *CASC2* is downregulated in LAC. Its overexpression inhibits the proliferation of LAC cells and improves apoptosis. It also directly inhibits *miR-21* expres-

sion and upregulates p53 protein expression to mediate cell proliferation and apoptosis in LAC [31]. GSEA results showed that the high-risk score is implicated in cell cycle, DNA replication, homologous recombination, p53 signaling pathway, and other mechanisms in cancer progression. Our risk model based on the *ERO1A*, *CDC25C*, and *ITGB4* is closely related to the signaling mechanisms of cancer progression, preliminarily confirming that our risk model is closely associated with LAC progression.

In recent years, immunotherapy has been a crucial treatment option for patients with LAC [32–35]. Additionally, immunotherapy improves the clinical stage in patients with advanced cancer, hence providing them with an opportunity for surgery. Of note, the immune microenvironment is an important component in immunotherapy. For instance, *PD-1* and *PD-L1* blockers have been approved as standard therapy for non-small-cell lung cancer. In contrast with chemotherapy or radiotherapy, *PD-1/PD-L1* blocking therapy improves the remission rate. It prolongs the survival time, with fewer side effects in patients with advanced non-small-cell lung cancer treated with a single drug or combined therapy [32, 33]. NK cells act on targeted tumor cells, contributing to antitumor immunity. In non-small-cell lung cancer, there was an increase in the expression of immune checkpoint receptor *PD-1* on the surface of NK cells. In

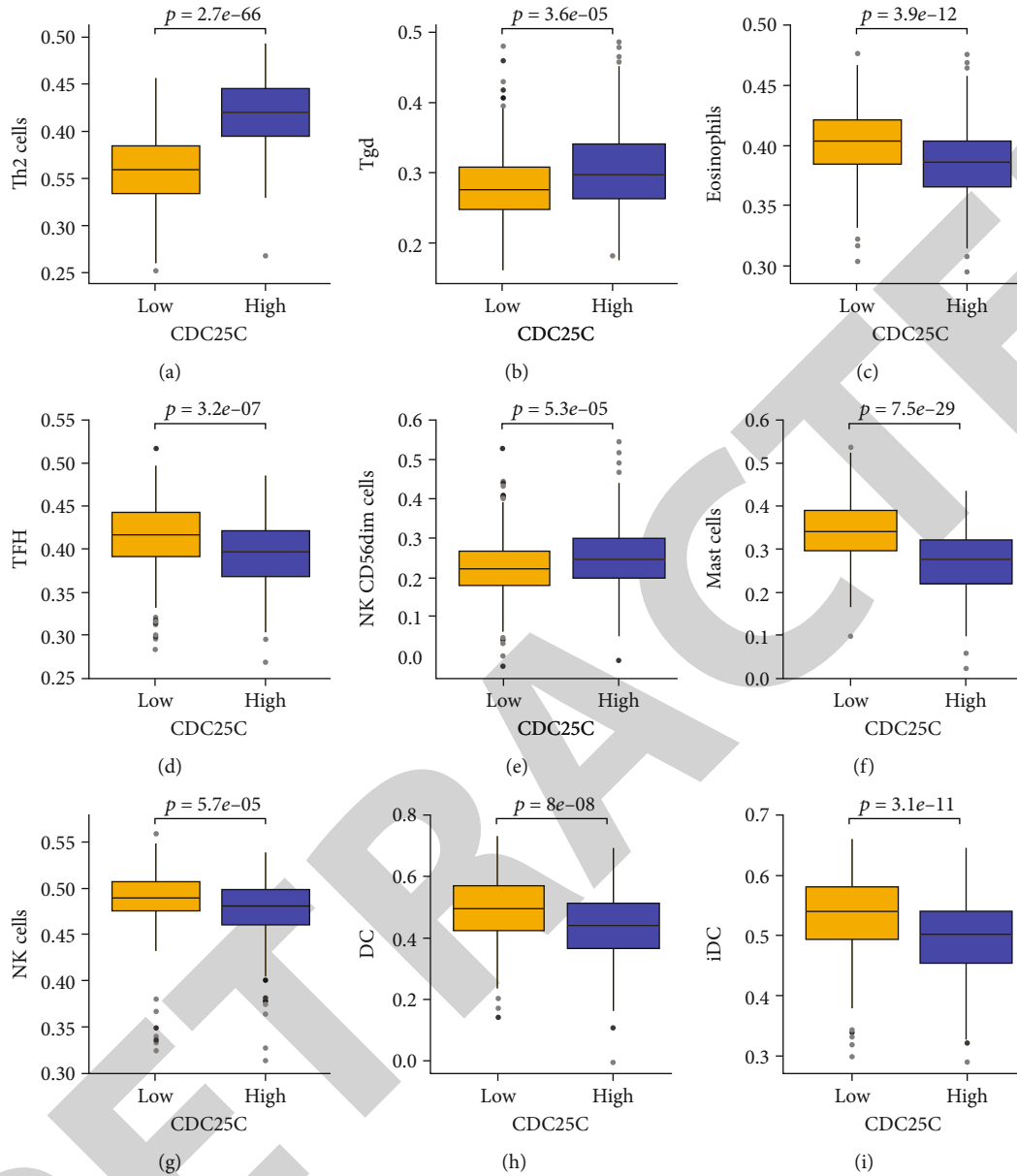


FIGURE 11: Abnormal expression of immune cells in the high- and low-expression groups of *CDC25C*: (a) Th2 cells; (b) Tgd; (c) eosinophils; (d) TFH; (e) NK CD56dim cells; (f) mast cells; (g) NK cells; (h) DC; (i) iDC.

contrast with peripheral NK cells, the role of NK cells in tumor is poor, and this dysfunction is associated with the expression level of PD-1. PD-1 blocking therapy reverses the PD-L1-mediated inhibition of PD-1 NK cells [35]. We explored the relationship between the OSRGs *ERO1A*, *CDC25C*, and *ITGB4* expression levels and the immune microenvironment. As a result, the expression levels of *ERO1A*, *CDC25C*, and *ITGB4* significantly correlated with the levels of NK cells, mast cells, Tfh, NK cd56dim cells, iDC, neutrophils, and NK cd56bright cells. Nonetheless, additional future studies are necessary to confirm the roles of the OSRGs *ERO1A*, *CDC25C*, and *ITGB4* in the LAC immune microenvironment.

Our study applies bioinformatics analysis to investigate the roles of the OSRGs in the progression of LAC. The strengths of this study include large sample size, long follow-up time, and comprehensive prognostic data in the TCGA database. Besides, we provide novel candidate markers for LAC treatment and a risk model that evaluates the prognosis of LAC patients. Through PCR detection, *ERO1A*, *CDC25C*, and *ITGB4* expressions were significantly upregulated in the tissues from our hospital. Nevertheless, large amounts of tissues and patient prognostic data are necessary to verify the risk score model. Therefore, future studies should collect additional clinical tissue samples to detect the expression levels of *CDC25C*, *ERO1A*, and *ITGB4* and

TABLE 7: The levels of immune infiltrating cells are differentially expressed in the groups of oxidative stress-related DEGs.

Immune cells	CDC25C (P)	ERO1A (P)	ITGB4 (P)
aDC	0.065	0.003	0.35
B cells	0.069	0.038	0.009
CD8 T cells	0.001	0	0.089
Cytotoxic cells	0.961	0.871	0.372
DC	0	0.008	0.678
Eosinophils	0	0	0.815
iDC	0	0	0.254
Macrophages	0.001	0.719	0.681
Mast cells	0	0	0.549
Neutrophils	0.04	0.02	0.047
NK CD56bright cells	0.139	0.001	0.001
NK CD56dim cells	0	0.007	0.003
NK cells	0	0	0
pDC	0.001	0.079	0.801
T cells	0.296	0.732	0.112
T helper cells	0.006	0.005	0
Tcm	0.028	0.893	0.299
Tem	0.044	0.902	0.959
TFH	0	0	0.205
Tgd	0	0.002	0.449
Th1 cells	0.452	0.052	0.974
Th17 cells	0.009	0.503	0.052
Th2 cells	0	0	0.926
TReg	0.051	0.269	0.065

Note: DEGs: differentially expressed genes.

investigate their roles in the prognosis of LAC. Moreover, other research should explore the roles and mechanisms of *CDC25C*, *ERO1A*, and *ITGB4* in the immunity and progression of LAC at the cellular level.

## 5. Conclusion

In conclusion, *CCNA2*, *CDC25C*, *ERO1A*, *CDK1*, *PLK1*, *ITGB4*, and *GJB2* of OSRGs have diagnosis values of LAC and are associated with the prognosis of patients with LAC. *ERO1A*, *CDC25C*, and *ITGB4* overexpressions are independent risk factors for poor prognosis in patients with LAC. A high-risk score is an independent factor affecting the poor prognosis of LAC patients. *ERO1A*, *CDC25C*, and *ITGB4* expressions of risk score model genes significantly correlate with the levels of mast cells, IDC, NK cells, and CD8 T cells of LAC immune infiltrating cells. Therefore, the risk score model based on the *ERO1A*, *CDC25C*, and *ITGB4* is expected to predict the prognosis of patients with LAC.

## Abbreviations

OSRGs: Oxidative stress-related genes  
 LAC: Lung adenocarcinoma  
 GSEA: Gene Set Enrichment Analysis

DEG: Differentially expressed genes  
 IL-8: Interleukin-8  
 ROS: Reactive oxygen species  
 BC: Breast cancer  
 EMT: Epithelial-mesenchymal transformation  
*Nrf2*: Nuclear factor, erythroid-derived 2  
 TCGA: The Cancer Genome Atlas  
 ROC: Operating characteristic  
 FDR: False discovery rate  
 OS: Overall survival.

## Data Availability

Our data can be obtained from the website of the TCGA database or by contacting the corresponding author.

## Ethical Approval

The ethics of humans is reviewed by the ethics committee of Taihe Hospital.

## Disclosure

The funders had no role in the design, analysis, decision to publish, or preparation of our manuscript.

## Conflicts of Interest

The authors declare that they have no conflicts of interest.

## Authors' Contributions

Jun Zhang and Jia-Long Guo formulated the research topic and adhered to the implementation of the program. Qiang Guo, Xiao-Li Liu, and Hua-Song Liu collected and analyzed the data of LAC and wrote the manuscript. Qiang Guo, Xiang-Yu Luo, and Ye Yuan performed a visual analysis of the data. Yan-Mei Ji and Tao Liu coded the language of the manuscript. All the authors confirmed the manuscript and agreed to publication. Qiang Guo, Xiao-Li Liu, and Hua-Song Liu stand for co-first authors.

## Acknowledgments

We are grateful to the TCGA database for providing open data on LAC patients.

## Supplementary Materials

Figure S1: the expression levels of oxidative stress-related the DEGs significantly correlate with the risk score. Note: LAC: lung adenocarcinoma; DEGs: differentially expressed genes. Figure S2: identification of risk model gene expression in LAC tissues. (A) *ERO1A*; (B) *CDC25C*; (C) *ITGB4*. Note: LAC: lung adenocarcinoma. Figure S3: the mechanisms of oxidative stress related to the DEGs. Note: DEGs: differentially expressed genes. Figure S4: the expression level of *ERO1A* correlates with the levels of immune infiltrating cells. Figure S5: the expression level of *ITGB4* correlates with the levels of immune infiltrating cells.



Figure S6: abnormal expression of immune cells in the high- and low-expression groups of *ERO1A*. Figure S7: abnormal expression of immune cells in the high- and low-expression groups of *ITGB4*. Table S1: functions of oxidative stress-related the DEGs. Note: BP: biological process; CC: cell composition; MF: molecular function. (Supplementary Materials)

## References

- [1] M. D. Jelic, A. D. Mandic, S. M. Maricic, and B. U. Srdjenovic, "Oxidative stress and its role in cancer," *Journal of Cancer Research and Therapeutics*, vol. 17, no. 1, pp. 22–28, 2021.
- [2] J. E. Klaunig, "Oxidative stress and cancer," *Current Pharmaceutical Design*, vol. 24, no. 40, pp. 4771–4778, 2018.
- [3] Y. Sun, J. Z. Ai, X. Jin et al., "IL-8 protects prostate cancer cells from GSK-3 $\beta$ -induced oxidative stress by activating the mTOR signaling pathway," *Prostate*, vol. 79, no. 10, pp. 1180–1190, 2019.
- [4] B. Shin, R. Feser, B. Nault et al., "miR526b and miR655 induce oxidative stress in breast cancer," *International Journal of Molecular Sciences*, vol. 20, no. 16, p. 4039, 2019.
- [5] Y. Song, W. Zhang, J. Zhang et al., "TWIST2 inhibits EMT and induces oxidative stress in lung cancer cells by regulating the FGF21-mediated AMPK/mTOR pathway," *Experimental Cell Research*, vol. 405, no. 1, article 112661, 2021.
- [6] K. T. Kuo, C. H. Lin, C. H. Wang et al., "HNMT upregulation induces cancer stem cell formation and confers protection against oxidative stress through interaction with HER2 in non-small-cell lung cancer," *International Journal of Molecular Sciences*, vol. 23, no. 3, p. 1663, 2022.
- [7] J. Xu, H. Guo, Z. Xing et al., "Mild Oxidative Stress Reduces NRF2 SUMOylation to Promote Kras/Lkb1/Keap1 Mutant Lung Adenocarcinoma Cell Migration and Invasion," *Oxidative Medicine and Cellular Longevity*, vol. 2020, Article ID 6240125, 12 pages, 2020.
- [8] L. M. Leon, M. Gautier, R. Allan et al., "The nuclear hypoxia-regulated NLUCAT1 long non-coding RNA contributes to an aggressive phenotype in lung adenocarcinoma through regulation of oxidative stress," *Oncogene*, vol. 38, no. 46, pp. 7146–7165, 2019.
- [9] Q. X. Zhang, Y. Yang, H. Yang et al., "The roles of risk model based on the 3-XRCC genes in lung adenocarcinoma progression," *Translational Cancer Research*, vol. 10, no. 10, pp. 4413–4431, 2021.
- [10] A. Al-Dherasi, Q. T. Huang, Y. Liao et al., "A seven-gene prognostic signature predicts overall survival of patients with lung adenocarcinoma (LUAD)," *Cancer Cell International*, vol. 21, no. 1, p. 294, 2021.
- [11] Q. Guo, Y. Y. Peng, H. Yang, and J. L. Guo, "Prognostic nomogram for postoperative patients with gastroesophageal junction cancer of no distant metastasis," *Frontiers in Oncology*, vol. 11, article 643261, 2021.
- [12] D. Lu, N. Yang, S. Wang et al., "Identifying the predictive role of oxidative stress genes in the prognosis of glioma patients," *Medical Science Monitor*, vol. 27, article e934161, 2021.
- [13] M. Li, Y. Guo, Y. M. Feng, and N. Zhang, "Identification of triple-negative breast cancer genes and a novel high-risk breast cancer prediction model development based on PPI data and support vector machines," *Frontiers in Genetics*, vol. 10, p. 180, 2019.
- [14] Y. Q. Zhang, Y. Yuan, J. Zhang et al., "Evaluation of the roles and regulatory mechanisms of PD-1 target molecules in NSCLC progression," *Annals of Translational Medicine*, vol. 9, no. 14, p. 1168, 2021.
- [15] C. Ma, F. Li, and H. Luo, "Prognostic and immune implications of a novel ferroptosis-related ten-gene signature in lung adenocarcinoma," *Annals of Translational Medicine*, vol. 9, no. 13, p. 1058, 2021.
- [16] C. C. Du JX, Y. H. Luo, J. L. Cai et al., "Establishment and validation of a novel autophagy-related gene signature for patients with breast cancer," *Gene*, vol. 762, article 144974, 2020.
- [17] Y. Q. Zhang, M. Y. Tang, Q. Guo, H. Q. Xu, Z. Y. Yang, and D. Li, "The value of erlotinib related target molecules in kidney renal cell carcinoma via bioinformatics analysis," *Gene*, vol. 816, article 146173, 2022.
- [18] H. Wu and J. Zhang, "Decreased expression of TFAP2B in endometrial cancer predicts poor prognosis: a study based on TCGA data," *Gynecologic Oncology*, vol. 149, no. 3, pp. 592–597, 2018.
- [19] Q. Guo, X. X. Ke, S. X. Fang et al., "PAQR3 inhibits non-small cell lung cancer growth by regulating the NF- $\kappa$ B/p53/Bax axis," *Frontiers in Cell and Developmental Biology*, vol. 8, article 581919, 2020.
- [20] Y. Pei, B. Zhou, and X. Liu, "The long non-coding RNA rhabdomyosarcoma 2-associated transcript exerts anti-tumor effects on lung adenocarcinoma via ubiquitination of SOX9," *Annals of Translational Medicine*, vol. 10, no. 1, 2022.
- [21] Y. Huang, L. Zhong, K. Nie et al., "Identification of LINC00665-miR-let-7b-CCNA2 competing endogenous RNA network associated with prognosis of lung adenocarcinoma," *Scientific Reports*, vol. 11, no. 1, p. 4434, 2021.
- [22] Z. Xia, W. Ou-Yang, T. Hu, and K. Du, "Prognostic significance of CDC25C in lung adenocarcinoma: an analysis of TCGA data," *Cancer Genetics*, vol. 233–234, pp. 67–74, 2019.
- [23] R. Zang, Z. Lu, G. Zhang et al., "ERO1L promotes IL6/sIL6R signaling and regulates MUC16 expression to promote CA125 secretion and the metastasis of lung cancer cells," *Cell Death & Disease*, vol. 11, no. 10, p. 853, 2020.
- [24] S. Yu, Z. Ao, Y. Wu et al., "ZNF300 promotes chemoresistance and aggressive behaviour in non-small-cell lung cancer," *Cell Proliferation*, vol. 53, no. 11, article e12924, 2020.
- [25] P. Wu, Y. Wang, Y. Wu, Z. Jia, Y. Song, and N. Liang, "Expression and prognostic analyses of ITGA11, ITGB4 and ITGB8 in human non-small cell lung cancer," *PeerJ*, vol. 7, article e8299, 2019.
- [26] A. Lu, Y. Shi, Y. Liu et al., "Integrative analyses identified ion channel genes GJB2 and SCN1B as prognostic biomarkers and therapeutic targets for lung adenocarcinoma," *Lung Cancer*, vol. 158, pp. 29–39, 2021.
- [27] B. Bao, X. Yu, and W. Zheng, "MiR-139-5p targeting CCNB1 modulates proliferation, migration, invasion and cell cycle in lung adenocarcinoma," in *Molecular Biotechnology*, pp. 1–9, Springer, 2022.
- [28] Q. Xu, Z. Xu, K. Zhu, J. Lin, and B. Ye, "LINC00346 sponges miR-30c-2-3p to promote the development of lung adenocarcinoma by targeting MYBL2 and regulating cell cycle signaling pathway," *Frontiers in Oncology*, vol. 11, article 687208, 2021.
- [29] A. Marzio, E. Kurz, J. M. Sahni et al., "EMSY inhibits homologous recombination repair and the interferon response, promoting lung cancer immune evasion," *Cell*, vol. 185, no. 1, pp. 169–183.e19, 2022.

## Retraction

# Retracted: PTBP1 as a Promising Predictor of Poor Prognosis by Regulating Cell Proliferation, Immunosuppression, and Drug Sensitivity in SARC

### Oxidative Medicine and Cellular Longevity

Received 20 June 2023; Accepted 20 June 2023; Published 21 June 2023

Copyright © 2023 Oxidative Medicine and Cellular Longevity. This is an open access article distributed under the Creative Commons Attribution License, which permits unrestricted use, distribution, and reproduction in any medium, provided the original work is properly cited.

This article has been retracted by Hindawi following an investigation undertaken by the publisher [1]. This investigation has uncovered evidence of one or more of the following indicators of systematic manipulation of the publication process:

- (1) Discrepancies in scope
- (2) Discrepancies in the description of the research reported
- (3) Discrepancies between the availability of data and the research described
- (4) Inappropriate citations
- (5) Incoherent, meaningless and/or irrelevant content included in the article
- (6) Peer-review manipulation

The presence of these indicators undermines our confidence in the integrity of the article's content and we cannot, therefore, vouch for its reliability. Please note that this notice is intended solely to alert readers that the content of this article is unreliable. We have not investigated whether authors were aware of or involved in the systematic manipulation of the publication process.

Wiley and Hindawi regrets that the usual quality checks did not identify these issues before publication and have since put additional measures in place to safeguard research integrity.

We wish to credit our own Research Integrity and Research Publishing teams and anonymous and named external researchers and research integrity experts for contributing to this investigation.

The corresponding author, as the representative of all authors, has been given the opportunity to register their agreement or disagreement to this retraction. We have kept a record of any response received.

### References

- [1] H. Gong, A. Jiang, R. Jiang et al., "PTBP1 as a Promising Predictor of Poor Prognosis by Regulating Cell Proliferation, Immunosuppression, and Drug Sensitivity in SARC," *Oxidative Medicine and Cellular Longevity*, vol. 2022, Article ID 5687238, 26 pages, 2022.

## Research Article

# PTBP1 as a Promising Predictor of Poor Prognosis by Regulating Cell Proliferation, Immunosuppression, and Drug Sensitivity in SARC

Haiyi Gong <sup>1</sup>, Aimin Jiang,<sup>2</sup> Runyi Jiang,<sup>1</sup> Yao Wang,<sup>1</sup> Dan Zhang <sup>1</sup>, Zhipeng Wu <sup>1</sup>, and Jianru Xiao <sup>1</sup>

<sup>1</sup>Department of Orthopedic Oncology, Shanghai Changzheng Hospital, Naval Medical University (The Second Military Medical University), Shanghai, China

<sup>2</sup>Department of Urology, Shanghai Changhai Hospital, Naval Medical University (The Second Military Medical University), Shanghai, China

Correspondence should be addressed to Dan Zhang; zhangadanbama@hotmail.com, Zhipeng Wu; eaglewzp@163.com, and Jianru Xiao; xiaojianru83@163.com

Received 17 March 2022; Accepted 28 April 2022; Published 23 May 2022

Academic Editor: Yazhou He

Copyright © 2022 Haiyi Gong et al. This is an open access article distributed under the Creative Commons Attribution License, which permits unrestricted use, distribution, and reproduction in any medium, provided the original work is properly cited.

**Background.** Sarcomas (SARC) have been found as rare and heterogeneous malignancies with poor prognosis. PTBP1, belonging to the hnRNPs family, plays an essential role in some biological functions (e.g., pre-mRNA splicing, cell growth, and nervous system development). However, the role of PTBP1 in SARC remains unclear. In this study, the aim was to investigate the potential role of PTBP1 with a focus on SARC. **Methods.** The expression, prognostic value, possible biological pathways of PTBP1, and its relationship with immune infiltration and drug sensitivity were comprehensively analyzed based on multiple databases. PTBP1 was further validated in osteosarcoma as the most prominent bone SARC. The expression of PTBP1 was investigated through IHC. The prognostic value of PTBP1 was verified in TARGET-OS databases. CRISPR/Cas9-mediated PTBP1 knockout HOS human osteosarcoma cell lines were used to assess the effect of PTBP1 on cell proliferation, migration, metastasis and cell cycle by CCK-8, Transwell migration, invasion, and FACS experiment. **Result.** PTBP1 was highly expressed and significantly correlated with poor prognosis in several cancers, especially in SARC, which was validated in the clinical cohort and osteosarcoma cell lines. The genetic alteration of PTBP1 was found most frequently in SARC. Besides, PTBP1 played a role in oncogenesis and immunity through cell cycle, TGFB, autophagy, and WNT pathways at a pan-cancer level. Knockout of PTBP1 was observed to negatively affect proliferation, migration, metastasis, and cell cycle of osteosarcoma in vitro. Furthermore, PTBP1 was significantly correlated with tumor immune infiltration, DNA methylation, TMB, and MSI in a wide variety of cancers. Moreover, the potential of the expression level of PTBP1 in predicting drug sensitivity was assessed. **Conclusions.** PTBP1 is highly expressed and correlated with prognosis and plays a vital pathogenic role in oncogenesis and immune infiltration of various cancers, especially for SARC, which suggests that it may be a promising prognostic marker and therapeutic target in the future.

## 1. Introduction

Sarcomas (SARC) are rare heterogeneous malignancies with over 50 histologic subtypes. They account for approximately 1% of all malignancies and are generally classified as soft tissue sarcoma (STS) and bone sarcoma (BS) [1–3]. The treatment of SARC is still a huge clinical challenge due to their

diversity and aggressive biological behavior. Complete surgical resection combined with adjuvant or neoadjuvant radiotherapy is still the main treatment for localized primary SARC. However, many patients still have recurrence and metastasis, partially because SARC has high malignancy and is prone to metastasis [4]. Despite a combination of surgery, systemic radiotherapy, and chemotherapy used for

treating metastatic SARC, the median overall survival (OS) of patients does not exceed 2 years [5]. The advent and rapid progress of immunotherapy has raised new hopes for treating SARC [6–10]. Thus, potential prognostic marker and therapeutic target in SARC should be urgently found.

Polypyrimidine Tract-Binding Protein 1 (PTBP1, hnRNP I), a member of the hnRNPs family, can mediate RNA maturation, translocation, localization, and translation. Its aberrant expression has been detected in numerous diseases. The most extensive role of PTBP1 is a major inhibitory splicing factor involved in regulating alternative splicing (AS) of precursor mRNA (pre-mRNA), leading to exon skipping [11]. PTBP1 has been found to be correlated with tumor metastasis, which leads to a poor prognosis in patients [12]. It mediates tumor development by regulating the cellular metabolism [13] and immune response of T/B lymphocytes as a splicing regulator [14, 15], which has an effect on the immune infiltration of tumor cells. PTBP1 plays a wide range of roles in tumorigenesis, so it may be proven as a novel therapeutic target. However, few studies have systematically analyzed PTBP1 from a pan-cancer perspective, and the comprehensive function of PTBP1 in SARC remains unclear.

In this study, the correlation between the expression of PTBP1 and prognosis, genetic alterations, potential biological pathways, immune infiltration, and drug sensitivity in human cancers was comprehensively analyzed using multiple databases, with a focus on SARC. PTBP1 was found to be upregulated, positively correlated with malignant biological behavior, and significantly correlated with poor prognosis for patients with SARC, which was validated in osteosarcoma. We also found that PTBP1 might be potentially involved in signaling pathways that regulated oncogenesis and tumor immunity, and its expression was correlated with DNA damage repair systems, DNA methylation, TMB, and MSI at a pan-cancer level. Our findings reveal that PTBP1 might be a prognostic and immune infiltration marker in numerous cancers, especially in SARC.

## 2. Materials and Methods

**2.1. Data Source and Processing.** Normalized expression profile data, tumor mutational burden (TMB) data, microsatellite instability (MSI) data and clinical information of The Cancer Genome Atlas (TCGA) datasets, normal tissues datasets, and TARGET OS datasets were acquired from University of California Santa Cruz Xena (UCSC Xena; <https://xena.ucsc.edu/>) and Genotype-tissue expression (GTEx; <https://gtexportal.org/home/>). Oncomine (<https://www.oncomine.org>) was adopted to validate the expression difference of PTBP1 in pan-cancer settings, which was a web-based data mining platform assembling 86,733 samples and 715 gene expression datasets [16]. Human protein atlas (HPA; <https://www.proteinatlas.org/>) database was adopted to assess the difference in the expression of PTBP1 at the protein level in pan-cancer settings. Cancer Cell Line Encyclopedia (CCLE; <https://portals.broadinstitute.org/>) database was employed to acquire the expression data of the spec-

tive tumor cell line. Patients were excluded if they (1) did not have prognostic information and (2) died in 30 days.

The RNA-seq read counts acquired from public databases were employed for differentially expressed gene (DEG) detection, which were converted to transcripts per kilobase million (TPM). The  $\log_2$  (TPM+1) calculation was conducted for further analyses.

Tumor name abbreviations and corresponding meanings consisted of ACC (adrenocortical carcinoma), BLCA (bladder urothelial carcinoma), BRCA (breast invasive carcinoma), CESC (cervical squamous cell carcinoma and endocervical adenocarcinoma), CHOL (cholangiocarcinoma), COAD (colon adenocarcinoma), COAD (colon adenocarcinoma), READ (rectum adenocarcinoma esophageal carcinoma), DLBC (lymphoid neoplasm diffuse large B-cell lymphoma), ESCA (esophageal carcinoma), GBM (glioblastoma multiforme), HNSC (head and neck squamous cell carcinoma), KICH (kidney chromophobe), KIRC (kidney renal clear cell carcinoma), KIRP (kidney renal papillary cell carcinoma), LAML (acute myeloid leukemia), LGG (brain lower grade glioma), LIHC (liver hepatocellular carcinoma), LUAD (lung adenocarcinoma), LUSC (lung squamous cell carcinoma), MESO (mesothelioma), OV (ovarian serous cystadenocarcinoma), PAAD (pancreatic adenocarcinoma), PCPG (pheochromocytoma and paraganglioma), PRAD (prostate adenocarcinoma), READ (rectum adenocarcinoma), SARC (sarcoma), SKCM (skin cutaneous melanoma), STAD (stomach adenocarcinoma), STES (stomach and esophageal carcinoma), TGCT (testicular germ cell tumors), THCA (thyroid carcinoma), THYM (thymoma), UCEC (uterine corpus endometrial carcinoma), and UVM (uveal melanoma).

**2.2. Differential Expression Analysis and Validation of PTBP1.** The expression of PTBP1 was analyzed in Oncomine database among pan-cancer with  $P < 0.05$  and absolute Foldchange  $> 1.5$  as the threshold. The same threshold was adopted to identify differential expression levels of PTBP1 in the TCGA database. The cBioPortal database (<https://www.cbioportal.org>) was employed to investigate the copy number alteration and mutation landscape of PTBP1 in pan-cancer. Furthermore, the correlation between PTBP1 and methylation level at the locus was investigated among pan-cancer.

**2.3. Enrichment Analysis of PTBP1.** Pearson's correlation between PTBP1 and other mRNA expression retrieved was studied based on the guilt of correlation of a single gene in the expression profile. After the genes were sorted by the level of correlation index between genes and PTBP1, those genes most correlated with the expression of PTBP1 were selected for enrichment analysis. R package "clusterprofiler" was adopted to perform Gene Ontology (GO) analysis, Reactome analysis, Kyoto Encyclopedia of Genes and Genomes (KEGG) analysis, and Gene Set Enrichment Analysis (GSEA) [17].

**2.4. Assessment of Clinical Significance of the Expression of PTBP1.** Clinical characteristics (e.g., the tumor stage and drug sensitivity) were introduced, and the correlation

between the expression of PTBP1 and the above characteristics was investigated. Cell Miner (<https://discover.nci.nih.gov/cellminer/home.do>) and GDSC (<https://www.cancerrxgene.org/>) database were acquired for IC50 (half maximal inhibitory concentration) and gene expression of cancer cell lines [18, 19].

**2.5. Differences in TME and Immunotherapy Response.** The correlation between the infiltration degree of immune, stromal cells, and the expression of PTBP1 in pan-cancer was analyzed using R package “ESTIMATE”. R package “ggpubr” and “ggcor” was employed for the coexpression analysis of immune-related gene and the expression of PTBP1. R package “CIBERSORT” was used to quantify the immune cell infiltration scores among pan-cancer, and the correlation of the degree of immune cell and the expression of PTBP1 were obtained [20]. In addition, the correlation between Neo antigen count, TMB, MSI, and expression of T cell exhaustion markers genes (PDCD1, TIGIT, CD274, CTLA4, LAG3, CXCL13, LAYN, and HAVCR2), DNA mismatch repair (MMR) system genes (MLH1, MSH2, MSH6, PMS2, and EPCAM), DNA methyltransferase (DNMT1, DNMT2, DNMT3A, and DNMT3B), ESTIMATE scores, and the expression of PTBP1 was analyzed. The immune infiltration scores were obtained using ssGSEA algorithm, and the correlation and difference between immune cell infiltration and the expression level of PTBP1 in SARC were analyzed. The effect of PTBP1 mutation on immune cell infiltration in SARC was validated using TIMER website (<https://timer.cistrome.org/>) [21].

**2.6. Statistical Analysis.** Differences in the expression of PTBP1 in the public data sets were compared by one-way ANOVA, and differences in clinical information and immune checkpoint inhibitor response between the two different subgroups were compared by Chi-squared test. Differences in overall survival (OS), progression-free interval (PFI), and disease-specific survival (DSS) between the two subgroups were compared by Kaplan-Meier method and log-rank test. The common cutoff value was the median of the expression of PTBP1, and the cutoff value of TARGET-OS dataset was determined by function “surv\_cutpoint” of package “survminer”. The hazard ratios (HRs) were obtained by univariate Cox regression and multiple Cox regression analysis. All  $P$  values were two-sided;  $P < 0.05$  indicated the difference with statistical significance. Adjusted  $P$  value was obtained by Benjamini-Hochberg (BH) multiple test correction. All data processing, statistical analysis, and plotting were conducted with R 4.0.4 software.

**2.7. Validation of Different Expression Levels of PTBP1.** Immunohistochemical (IHC) staining was performed to validate the expression of PTBP1 in osteosarcoma tumor and adjacent tissues, including 30 osteosarcoma tumor tissues and 12 adjacent tissues from Shanghai Changzheng hospital. IHC staining intensity of PTBP1 was scored by three experienced pathologists. The staining degree was classified into 0 (negative), 1 (weakly positive), 2 (moderately positive), and 3 (strongly positive). Western blotting was performed to val-

idate the expression of PTBP1 among human osteosarcoma cell lines (HOS/MG63/Saos2/U2OS) and hBMSC cell line. PTBP1 antibody (anti-PTBP1 antibody, [EPR9048(B)], (ab133734), Abcam) originated from Abcam Trading Co., LTD.

**2.8. PTBP1 Biological Function In Vitro.** Human bone marrow stromal (mesenchymal) stem cell line hBMSC and human osteosarcoma cell lines (HOS, MG63, Saos2, and U2OS) originated from American Type Culture Collection (ATCC). Cell lines were cultured following the instructions. Cas9/sgRNA of PTBP1 was synthesized by OBiO Technology (Shanghai) Corp., Ltd. Human osteosarcoma cell line HOS was transduced with Cas9 lentiviral particles of sgRNAs. Cells were selected with Puromycin. The specific procedures followed the operation manual of OBiO Technology (Shanghai) Corp., Ltd. RT-PCR and Western blot assay were performed to confirm the knockout efficiency of Cas9 virus. Specific primer sequences included PTBP1 (forward: AGCGCGTGAAGATCCTGTTC; reverse: CAGGGTGAGTTGCCGTAG), synthesized by Tsingke Biotechnology Co., Ltd., Beijing, China. Cell proliferation, migration, and invasion between HOS and HOS-PTBP1-knockout cell lines were detected by CCK-8 (Cell Counting Kit-8), Transwell migration, and invasion assay. Cell cycle distribution was analyzed by fluorescence-activated cell sorting (FACS) experiment. All experiments were performed as triplicates and repeated at least three times.

### 3. Results

**3.1. TPBP1 Gene Expression and Survival Analysis.** OncoPrint database was used to determine the expression of PTBP1 pattern among pan-cancer which revealed that PTBP1 was overexpressed in tumor tissues compared to normal tissues at a pan-cancer level (Figure 1(a)). More nuanced analyses were conducted in cancer tissues vs. normal tissues (Figure 1(b)), as well as cancer vs. paired adjacent tissues using data acquired from TCGA and GTEx cohort (Figure 1(c)). We observed a higher expression level of PTBP1 in BCLA, BRCA, CHOL, COAD, ESCA, HNSC, KIRC, KIRP, LIHC, LUSC, READ, STAD, and UCEC significantly for both comparisons ( $P < 0.05$ ). Further analyses of the expression level of PTBP1 among different clinical stages of cancers showed that PTBP1 was correlated with advanced clinical stage in ACC, ESCA, and KICH, opposite trend in KIRC, MESO, and SKCM (Supplement Figure 1).

As revealed by the univariate Cox regression analysis results, PTBP1 might be a risk factor for the prognosis of ACC, KICH, LGG, LIHC, LUAD, MESO, PRAD, SARC, and SKCM patients, while being a protective factor in KIRC, READ, and THYM (Figure 1(d)). The prognostic value of PTBP1 in SARC was further confirmed by Kaplan-Meier analysis, and the results showed a significant difference in OS and DSS between the low- and high-expression groups divided by median expression of PTBP1 ( $P < 0.05$ ) (Figure 1(e)). The above results suggested that PTBP1 was upregulated in various tumors (e.g., SARC), and its high expression was correlated with poor prognosis.

Analysis type by cancer	Cancer vs. normal		Cancer vs. cancer			
			Cancer histology		Multi-cancer	
Bladder cancer	4	1				
Brain and CNS cancer	16	1	2	2		
Breast cancer	12	2	4	2	3	
Cervical cancer						
Colorectal cancer	4		1	1	1	
Esophageal cancer						
Gastric cancer	4	1	1	2		
Head and neck cancer	5			1		
Kidney cancer	2		2	3	1	1
Leukemia	4	3	2	2	3	
Liver cancer	1		1	1		2
Lung cancer	2		2	2		1
Lymphoma	6	4	4	4		
Melanoma	2		1	1		
Myeloma	2		1	1		
Other cancer	10		3	1		
Ovarian cancer	1		2	2		
Pancreatic cancer						
Prostate cancer	2					
Sarcoma	2		3	6		1
Significant unique analyses	79	12	27	29	8	4
Total unique analyses	349		587		160	



(a)

FIGURE 1: Continued.

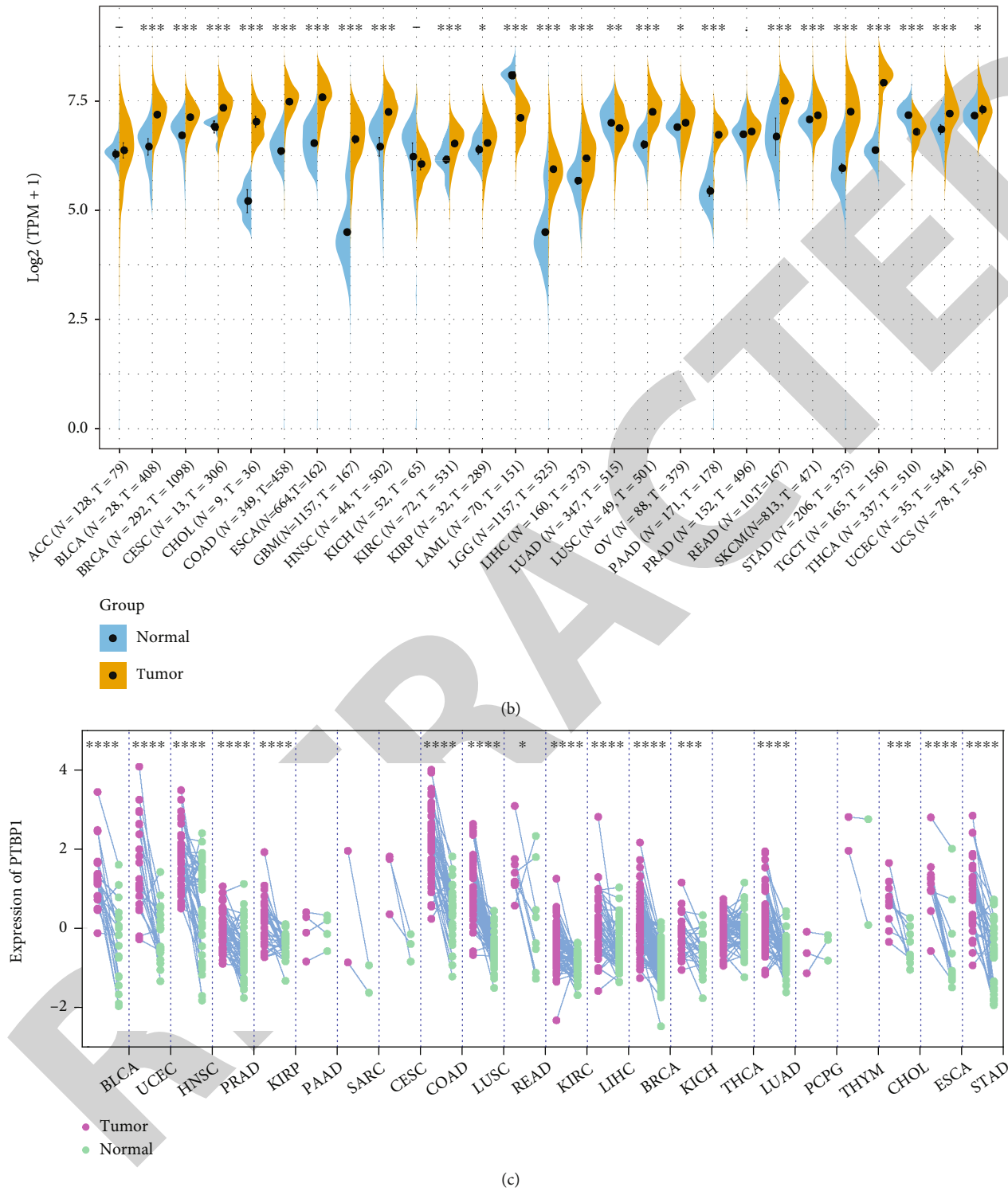


FIGURE 1: Continued.

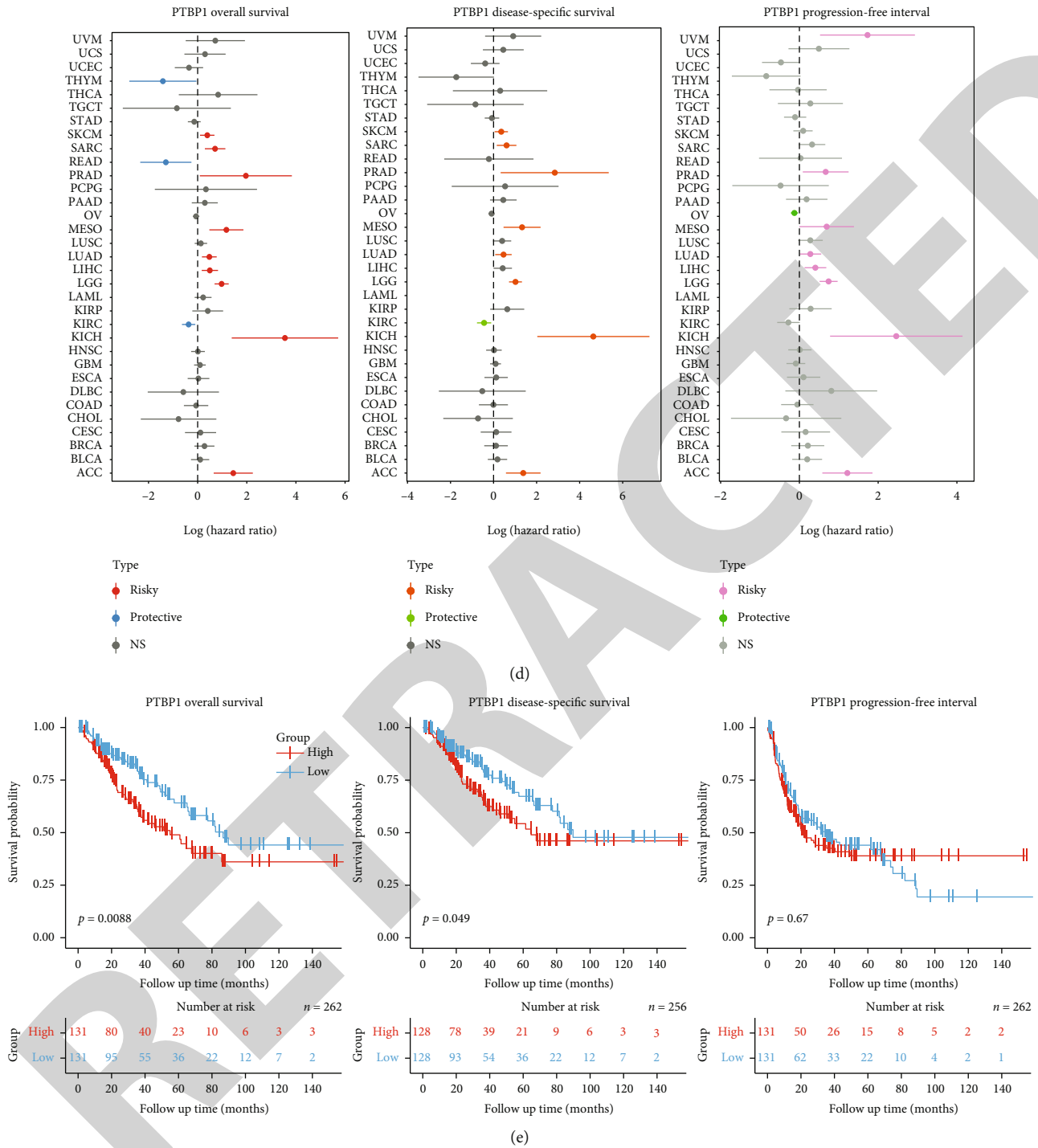


FIGURE 1: Expression level of PTBP1 in pan-cancer. (a) Expression level of PTBP1 in 20 cancer types from Oncomine database. (b) Comparison of the expression of PTBP1 between tumor and normal tissues from TCGA database. (c) Comparison of the expression of PTBP1 between paired tumor and normal tissues of 22 cancer types from TCGA database. (d) The forest plots for OS, PFI, and DSS with HRs (log10) and 95% CI for 33 different cancer types. (e) Kaplan-Meier analysis of OS, DSS, and PFI in TCGA SARC patients stratified by different expression levels of PTBP1. \* $P < 0.05$ , \*\* $P < 0.01$ , \*\*\* $P < 0.001$ , and \*\*\*\* $P < 0.0001$ .

3.2. Genetic Alteration of PTBP1. The cBioPortal website was used to explore the genetic alteration frequency of PTBP1 among different cancers (Figure 2(a), Supplement Figure 2A), and PTBP1 alterations most frequently occurred in SARC, followed by CESC, UCEC, OV, and LGG. The majority types

of PTBP1 alterations in SARC included amplification, deep deletion, and mutation. Besides, a total of 104 mutation sites containing 77 missenses, 9 truncating, 15 splice, and 4 SV/fusion variants were located between amino acid 0 to 531 (Figure 2(b)).



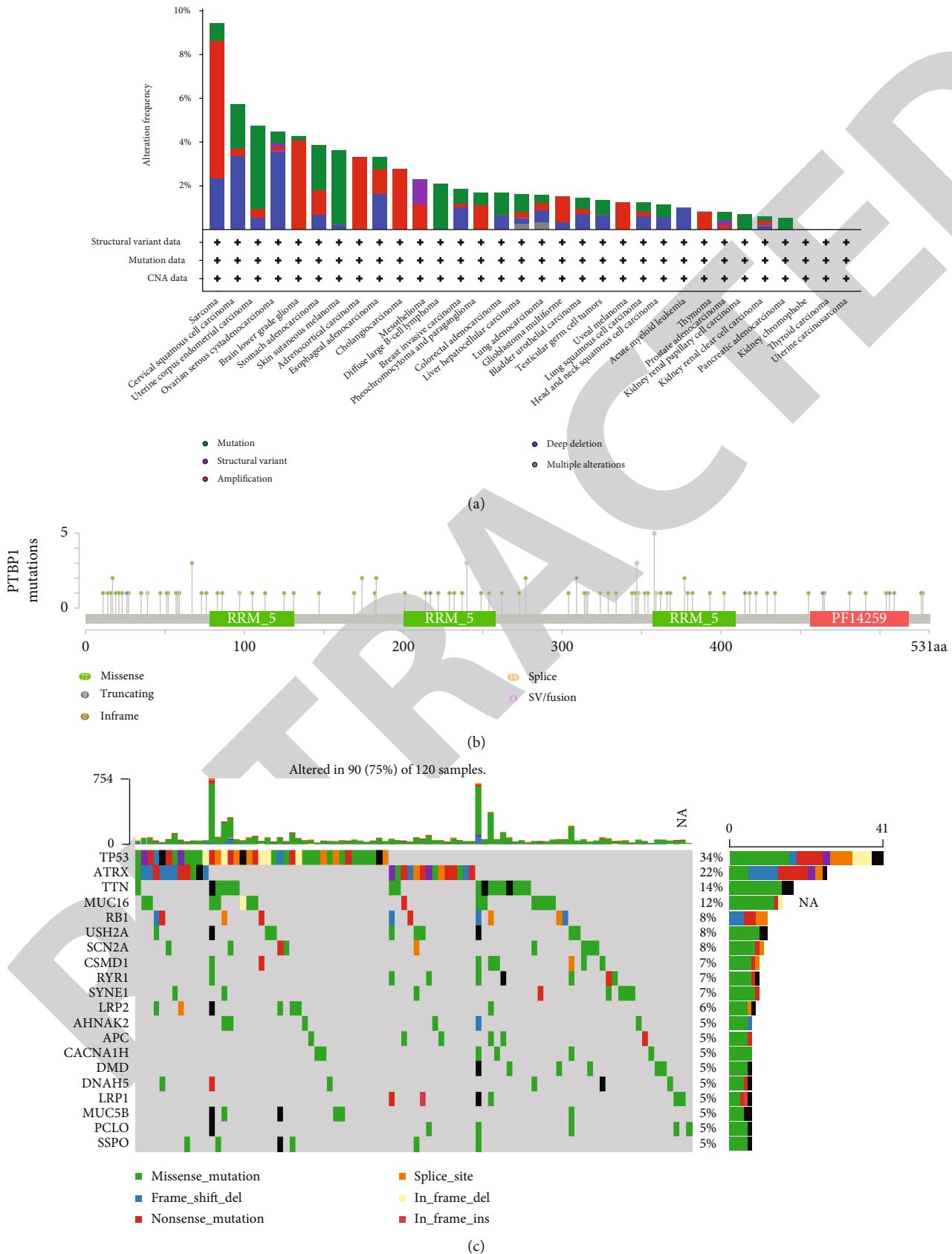


FIGURE 2: Continued.

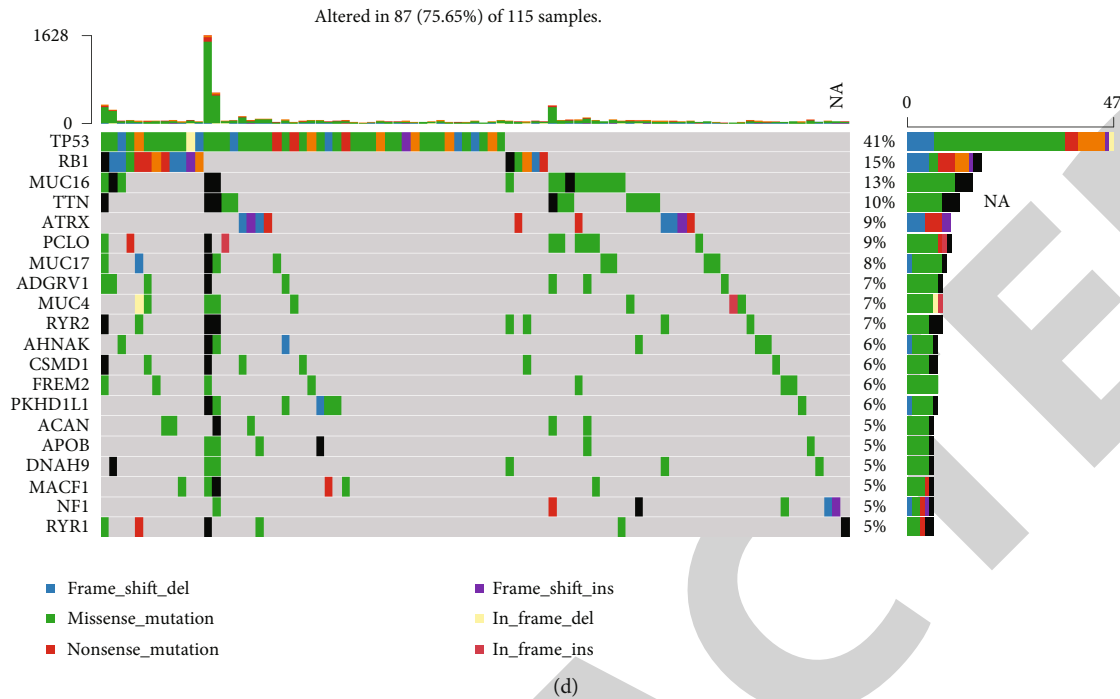


FIGURE 2: The genetic alterations of PTBP1 and correlations with mRNA expression. (a) Total genetic alterations of PTBP1 based on cBioPortal website. (b) Mutation diagram of PTBP1 in all cancer types across protein domains. (c) Waterfall of the top 20 mutated genes in PTBP1 high-expression group of the TCGA SARC cohort. (d) Waterfall of the top 20 mutated genes in PTBP1 low-expression group of the TCGA SARC cohort.

Considering the prevalence of genetic alteration of PTBP1 in SARC, SARC patients were assigned to high- and low-expression groups according to the level of the expression of PTBP1. The top 20 most frequently altered genes in each group were presented by waterfall plots (Figures 2(c) and 2(d)). TP53 alteration, with the missense variant as the major component, showed the highest frequency in both groups: 34% in the high-expression group and 41% in the low-expression group. TP53, ATRX (22%, 9%), TTN (14%, 10%), MUC16 (12%, 13%), and RB1 (8%, 10%) were found as top-five gene alterations in p53, mTOR, apoptosis, DNA replication, RNA polymerase, Wnt signaling, and Notch signaling pathway.

Accordingly, we hypothesize that PTBP1 mutational events occur in multiple tumors, particularly in SARC and may play critical roles in modulating cell cycle, tumorigenesis, and immunity.

**3.3. Biological Function Analyses of PTBP1.** KEGG and HALLMARK enrichment analysis was conducted to explore the biological function of PTBP1. We found that cell cycle-related pathways (e.g., cell cycle, DNA replication, ribosome, E2F targets, G2M checkpoint, and mitotic spindle), MYC targets, IL-17 signaling, and spliceosome pathway were most enriched in PTBP1 high-expression group (Figure 3(a), Supplement Figure 3A), while some metabolism-related pathways in PTBP1 low-expression group (Figure 3(b), Supplement Figure 3B). Thus, we deciphered that PTBP1 could mainly upregulate cell cycle at a pan-cancer level. Consistent trends were found when we focused on SARC separately. In SARC, PTBP1 activated signaling pathways

(e.g., the E2F targets, MYC targets, G2M checkpoint, spliceosome, cell cycle, and TP53) by enrichment analysis of the HALLMARK (Figure 3(c)), KEGG (Figure 3(d)), and Reactome (Supplement Figure 3C) datasets.

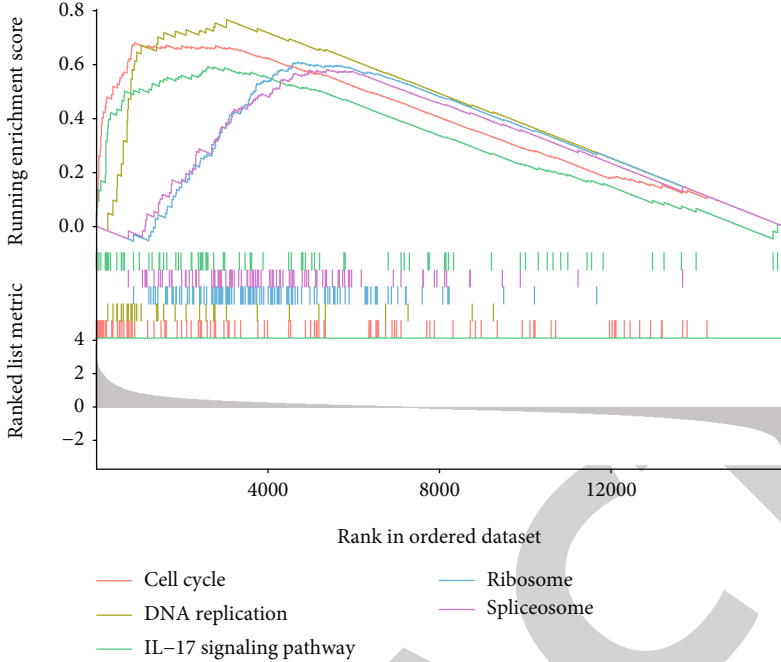
We further explored the correlation between the expression of PTBP1 and well-recognized tumor-related pathways (e.g., TGFB, autophagy, and WNT). Since TGFB is an evolutionarily conserved signaling pathway regulating various cellular processes (e.g., proliferation, differentiation, apoptosis, inflammation, and fibrosis) [22], the correlation between the expression levels of PTBP1 and TGFB pathway-related genes in pan-cancer was analyzed (Figure 3(e)). Interestingly, nearly almost all TGFB-related genes showed significant positive correlations with PTBP1 expression.

Autophagy plays an opposing environment-dependent role in cancer, and interventions to regulate autophagy have been proposed as an option for cancer treatment [23]. As depicted in Figure 3(f), the expression level of PTBP1 showed a significant positive correlation with nearly all autophagy-related genes in pan-cancer.

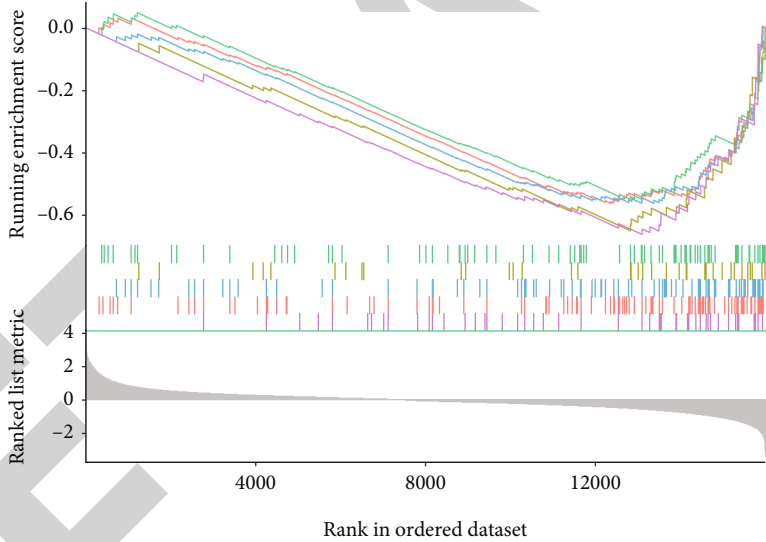
The similar results reemerged when we turned to WNT signaling pathway-related genes, which are known to control myriad biological phenomena throughout the development and adult life of all animals [24] (Supplement Figure 3D).

To sum up, PTBP1 upregulates cell cycle-related signaling pathways in SARC and pan-cancer and is closely and positively correlated with TGFB, autophagy, and WNT signaling pathways at the pan-cancer level.

**3.4. Correlation between Tumor Immunity and the Expression of PTBP1 in Pan-Cancer.** Tumor immune cell



(a)



(b)

FIGURE 3: Continued.

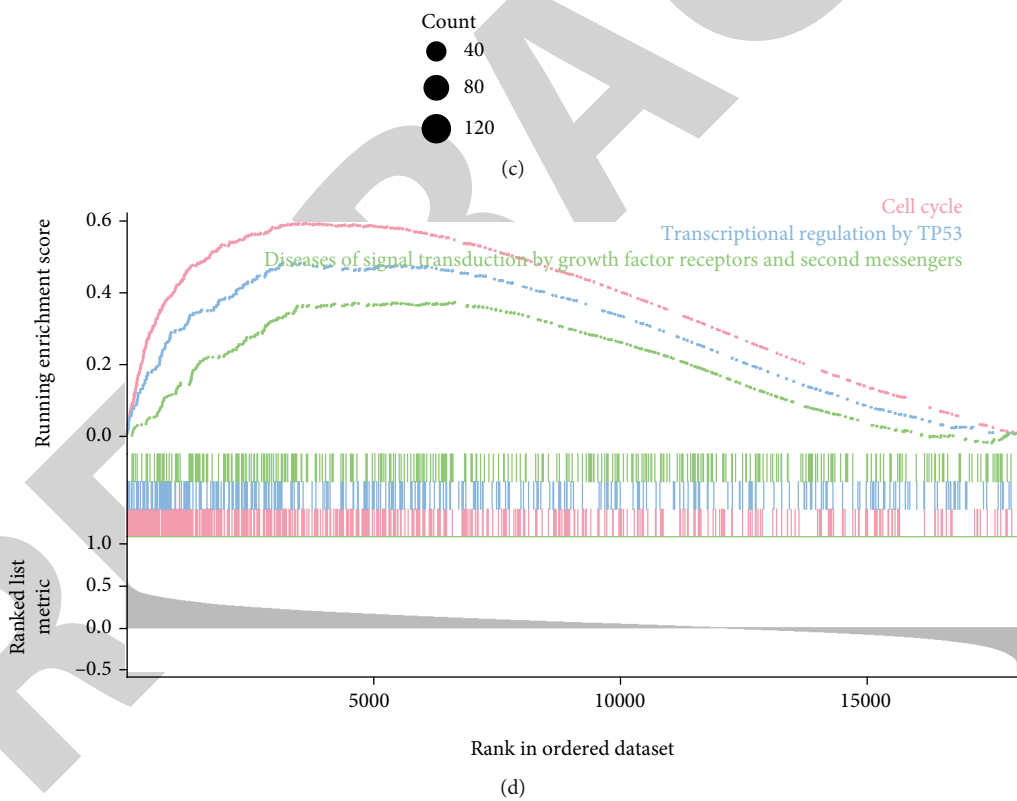
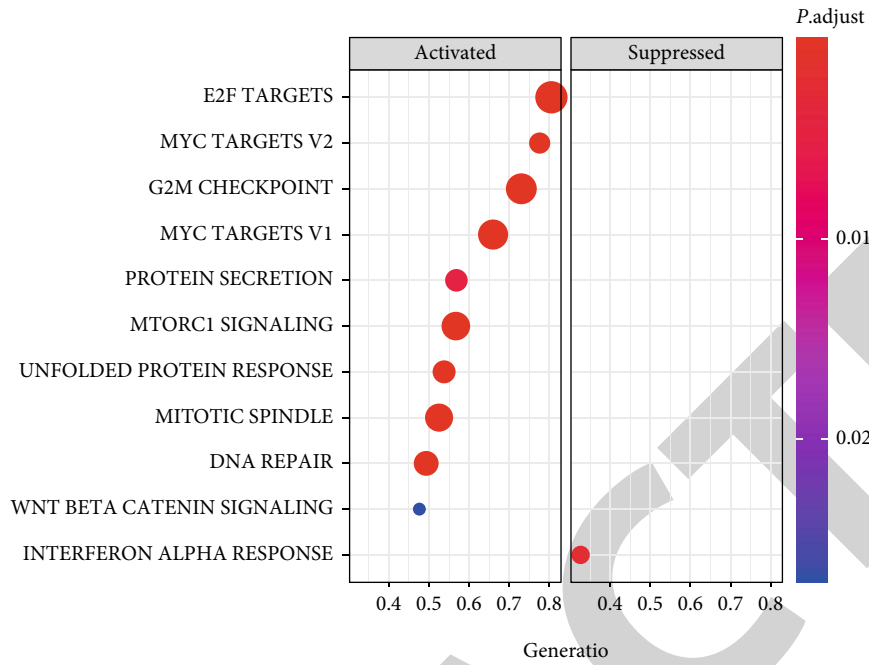


FIGURE 3: Continued.





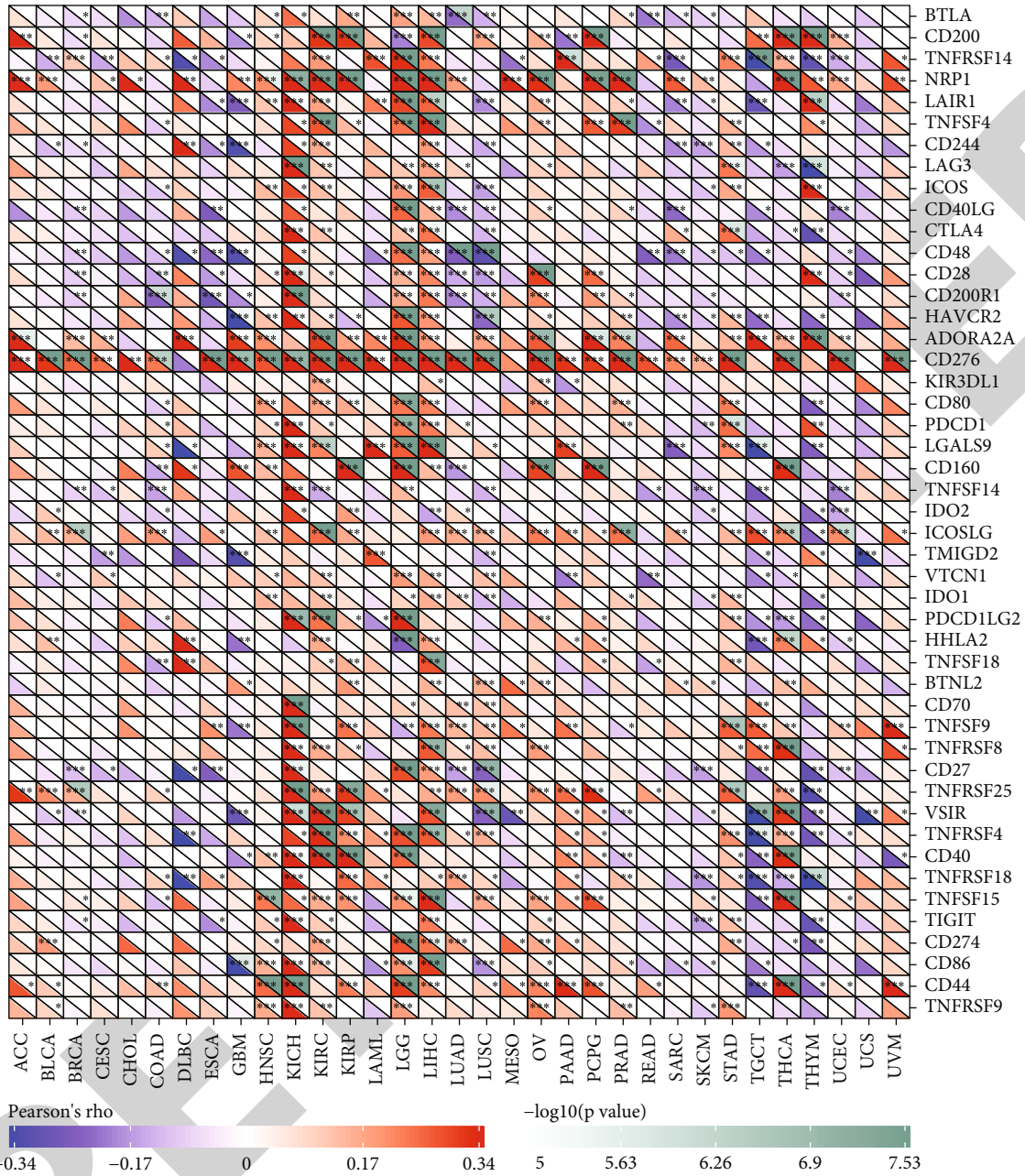
FIGURE 3: The biological function of PTBP1 in pan-cancer. (a, b) Gene set enrichment analysis of PTBP1-related signaling pathways in KEGG datasets at a pan-cancer level. (c) Bubble map of gene set enrichment analysis of PTBP1-related signaling pathways in HALLMARK datasets in TCGA SARC cohort. (d) Gene set enrichment analysis of PTBP1-related signaling pathways in KEGG datasets in TCGA SARC cohort. (e) Correlation between the expression of PTBP1 and TGFB pathway genes in pan-cancer. (f) Correlation between the expression of PTBP1 and autophagy pathway genes in pan-cancer.

infiltration is an independent predictor of the tumor immune status and survival [25]. To further explore the correlation between PTBP1 and tumor immunity, immune checkpoint genes, neoantigens, tumor stromal, and immune cells in pan-cancer were analyzed.

Immune checkpoint plays an essential role in cancer immunotherapy (e.g., enhancing antitumor immune responses) using checkpoint inhibitors [26]. As depicted in Figure 4(a), the expression of PTBP1 was significantly correlated with the expression of most immune checkpoint genes including CD276 (B7-H3), NRP1, ADORA2A, TNFRSF4, TNFSF15, CD200, and CD80 in LGG, LIHC, KICH, KIRC, and KIRP. Notably, CD276 was found positively correlated with the expression of PTBP1 in pan-cancer. CD276 belongs to the immunoglobulin superfamily, and studies have shown that it may participate in the regulation of T-cell-mediated immune response and correlated with worse prognosis in cancer patients [27].

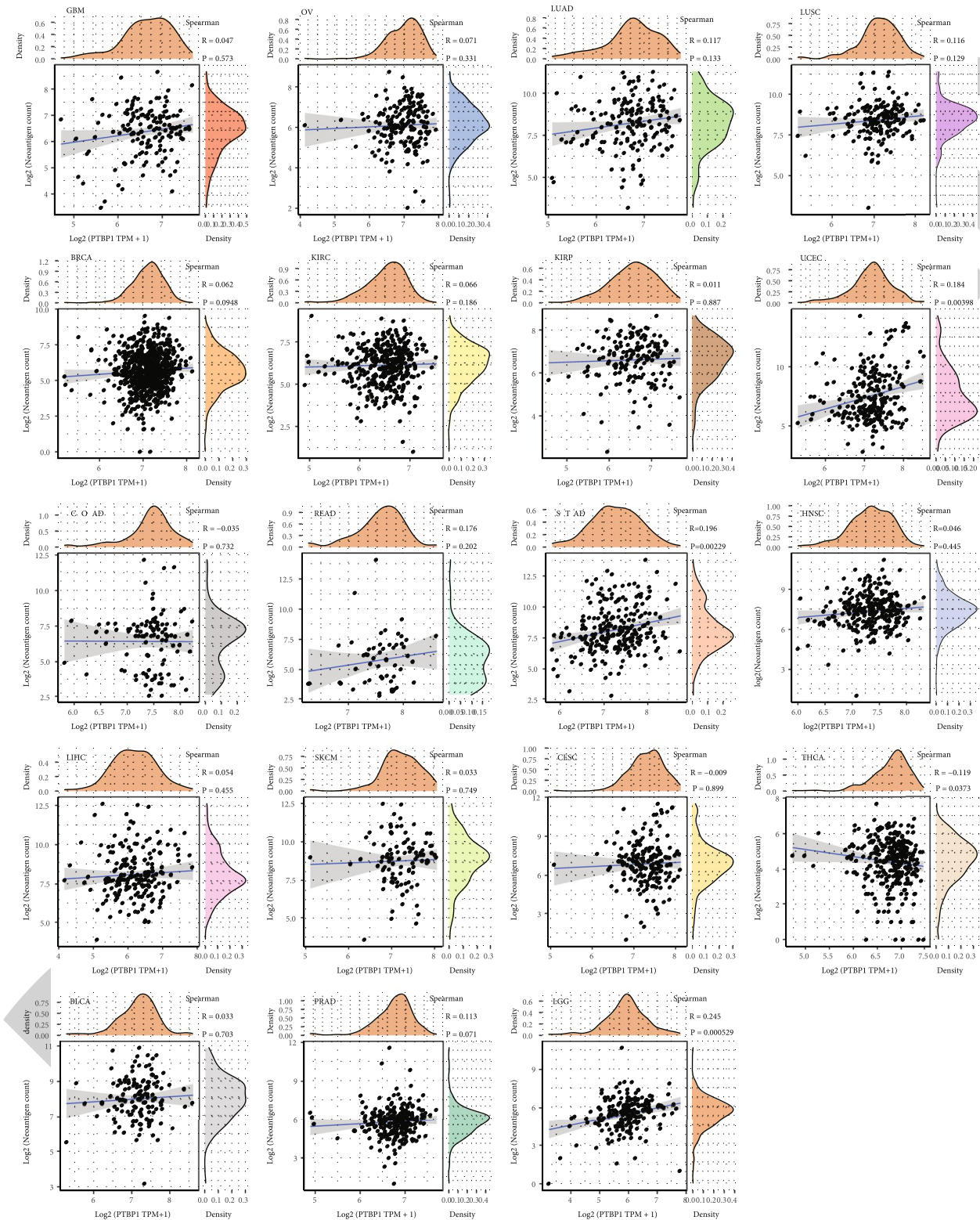
One of the promising advancements of immunotherapy is personalized vaccines designed to trigger de novo T cell responses against neoantigens [28]. The analyses of neoantigens may help find new targets for immunotherapy. We found that the expression level of PTBP1 showed a significant positive correlation with the number of neoantigens in LGG and UCEC, meanwhile, negatively and significantly in THCA ( $P < 0.05$ ) (Figure 4(b)).

Roosendaal and Mebius [29] reported that in addition to providing structural support for lymphoid organs, stromal cells also influence immune cell differentiation and immune response. Hence, studying the composition of the tumor stromal can help further understand the tumor immune microenvironment. In this study, the expression of PTBP1 was simultaneously and positively correlated with ESTIMATE-Score (Figure 4(c)), ImmuneScore (Supplement Figure 4A), and StromalScore (Supplement Figure 4B) in LGG, negatively in ACC, BLCA, BRCA, ESCA, GBM, LUAD,



(a)

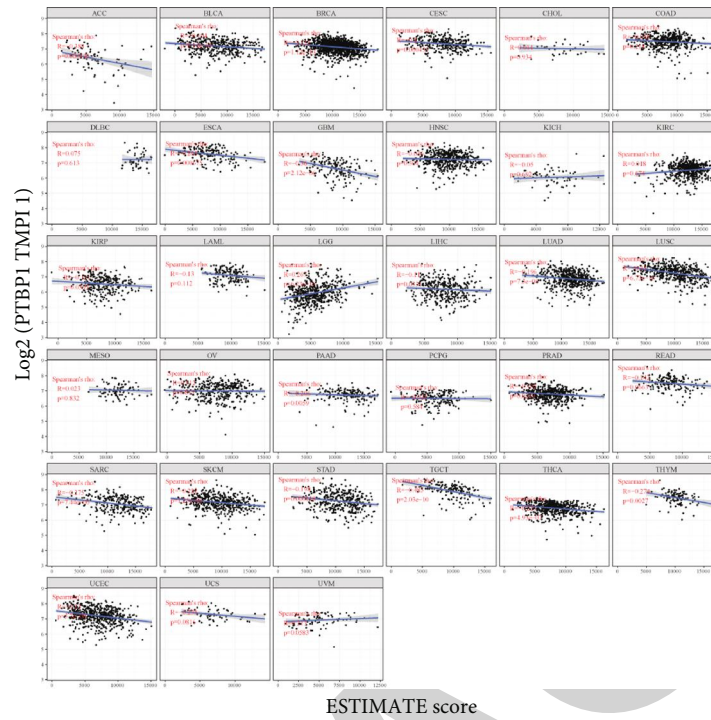
FIGURE 4: Continued.



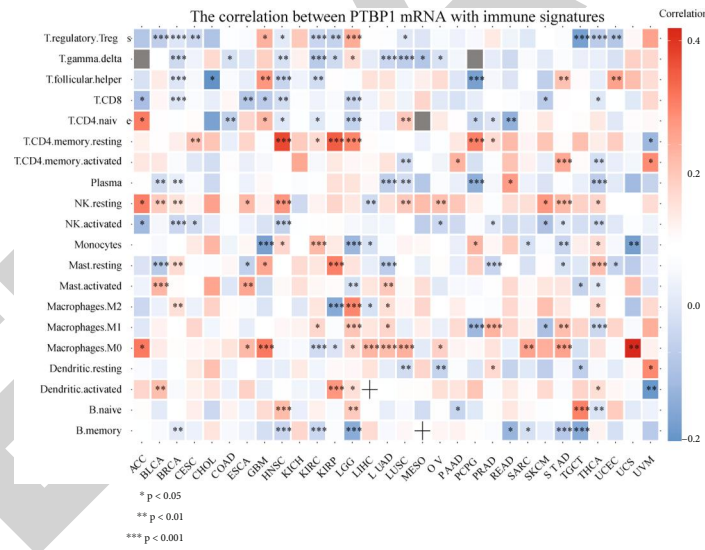
(b)

FIGURE 4: Continued.





(c)



(d)

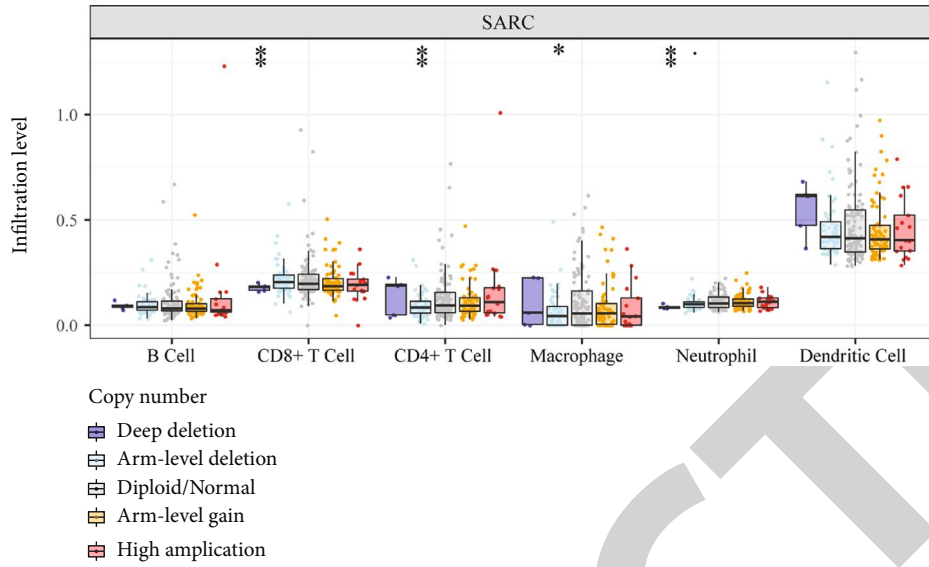
FIGURE 4: Correlations between tumor immunity and the expression of PTBP1 in pan-cancer. (a) Correlations of the expression of PTBP1 with immune checkpoint genes. (b) Correlations of the expression of PTBP1 with neoantigens count. (c) Correlation between the expression of PTBP1 and ESTIMATEScore. (d) Correlations of the expression of PTBP1 with immune cell infiltration. \* $P < 0.05$ , \*\* $P < 0.01$ , and \*\*\*  $P < 0.001$ .

LUSC, PAAD, SARC, SKCM, STAD, TGCT, THCA, THYM, and UCEC. Taken together, the above results reveal that PTBP1 could upregulate immune response and positively correlated with stromal composition in LGG. It may function in a reverse way in various types of cancers, including SARC.

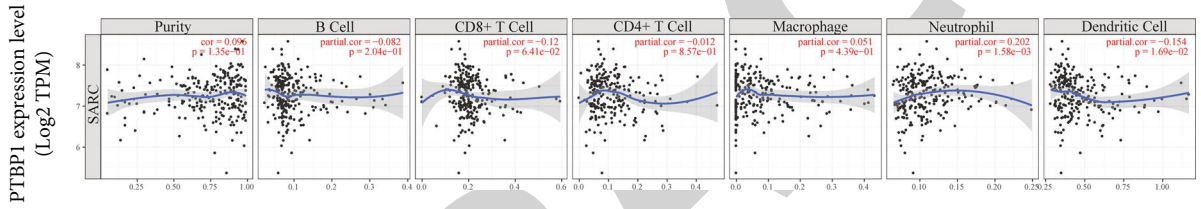
Subsequently, we utilized commonly recognized immune signatures to quantify the level of immune cell infiltration and analyzed its correlation with the expression of PTBP1 and found that the expression of PTBP1 has different correla-

tions with immune cells in pan-cancer. It is consistent that PTBP1 is positively correlated with resting CD4 memory T cells, resting NK cells, and M0 macrophages, but negatively correlated with CD8 T cells, plasma, activated NK cells, and memory B cells (Figure 4(d)).

In addition, immunotherapy has significantly improved patient outcomes, but the occurrence of T-cell exhaustion seriously affects the therapeutic efficacy of immunotherapy [30]. Accordingly, we investigated the correlation between



(a)



Infiltration level  
(b)

FIGURE 5: Continued.

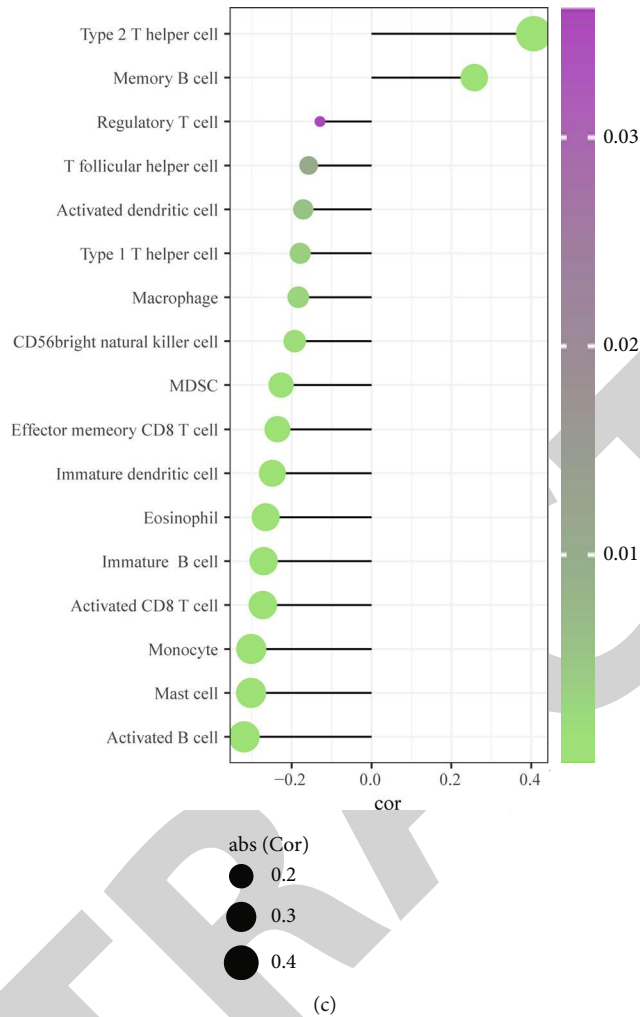


FIGURE 5: Correlations between tumor immunity and the expression of PTBP1 in SARC. (a) Correlation of immune infiltrate level and different mutation subtypes among TCGA SARC cohort. (b) Correlation of the expression of PTBP1 and multiple immune cell infiltration in Tumor database. (c) Correlations between the expression of PTBP1 and NES of 17 immune cells in TCGA SARC cohort. \* $P < 0.05$ , \*\* $P < 0.01$ , and \*\*\* $P < 0.001$ .

the expression level of PTBP1 and T-cell exhaustion-related markers (Supplement Figure 4C) and found that the expression of PTBP1 in SARC showed a significant positive correlation with the above T cell exhaustion markers, suggesting that the T-cell exhaustion phenomenon may be widely present in SARC patients with highly expressed PTBP1.

**3.5. Immune Infiltration and PTBP1 in SARC.** Despite the promising results of Chimeric Antigen Receptor (CAR) T Cell therapy in treating B-cell lymphoma and acute lymphoblastic leukemia [31], the clinical outcome in SARC patients remains unsatisfactory. The immune infiltration in SARC was further analyzed, and it was found that tumor development and progression were correlated with multiple genomic aberrations, which might affect tumor-infiltrating immune cells (TIICs).

In SARC, deep deletion of PTBP1 reduced infiltration of CD8+ T cell and neutrophil and arm-level deletion of PTBP1 significantly reduced the infiltration of CD4+ T cell and mac-

rophage (Figure 5(a)). The analysis of the correlation between TIIC abundance and the expression of PTBP1 in SARC revealed that a high expression level of PTBP1 significantly increased the neutrophil abundance and decreased the abundance of dendritic cells (Figure 5(b)). In addition, a more detailed analysis of the correlation between the level of infiltration of different immune cell types and PTBP1 expression was performed (Figure 5(c)). We found that PTBP1 was positively correlated with type 2 T helper cell and memory B cell significantly, and contrary correlations were found in many immune cell types, such as activated B cell, mast cell, monocyte, and activated CD8 T cell ( $P < 0.05$ ).

**3.6. PTBP1 Affects TMB, MSI, MMR, and Methyltransferase Expression in Pan-Cancer.** As a new pillar of modern cancer treatment, immunotherapy has revolutionized cancer management. TMB and MSI were taken as established immunotherapeutic response prediction in multiple tumor types [32]. TMB represents mutations in tumor cells (e.g., single nucleotide variations (SNVs) and small insertions/deletions

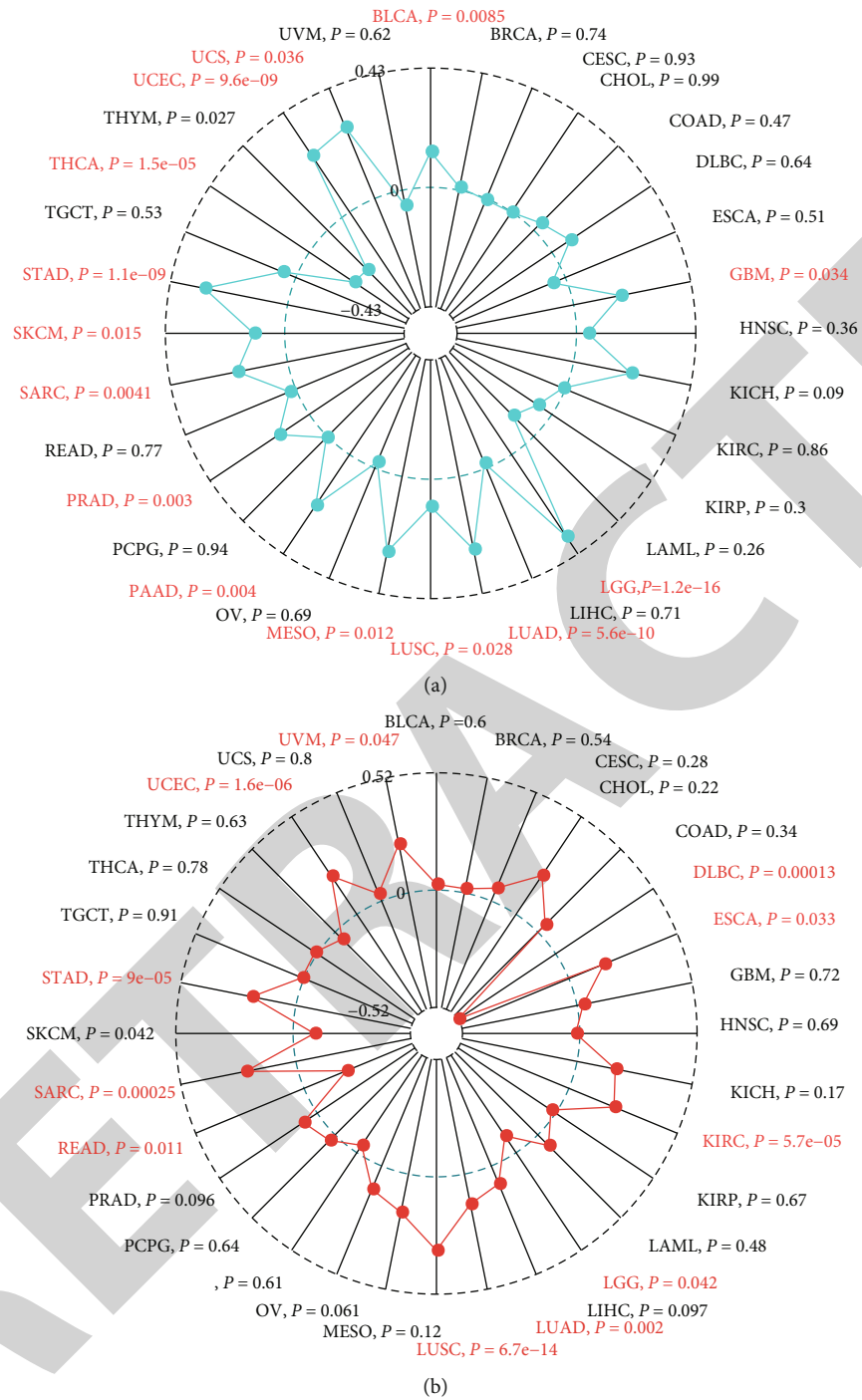


FIGURE 6: Continued.

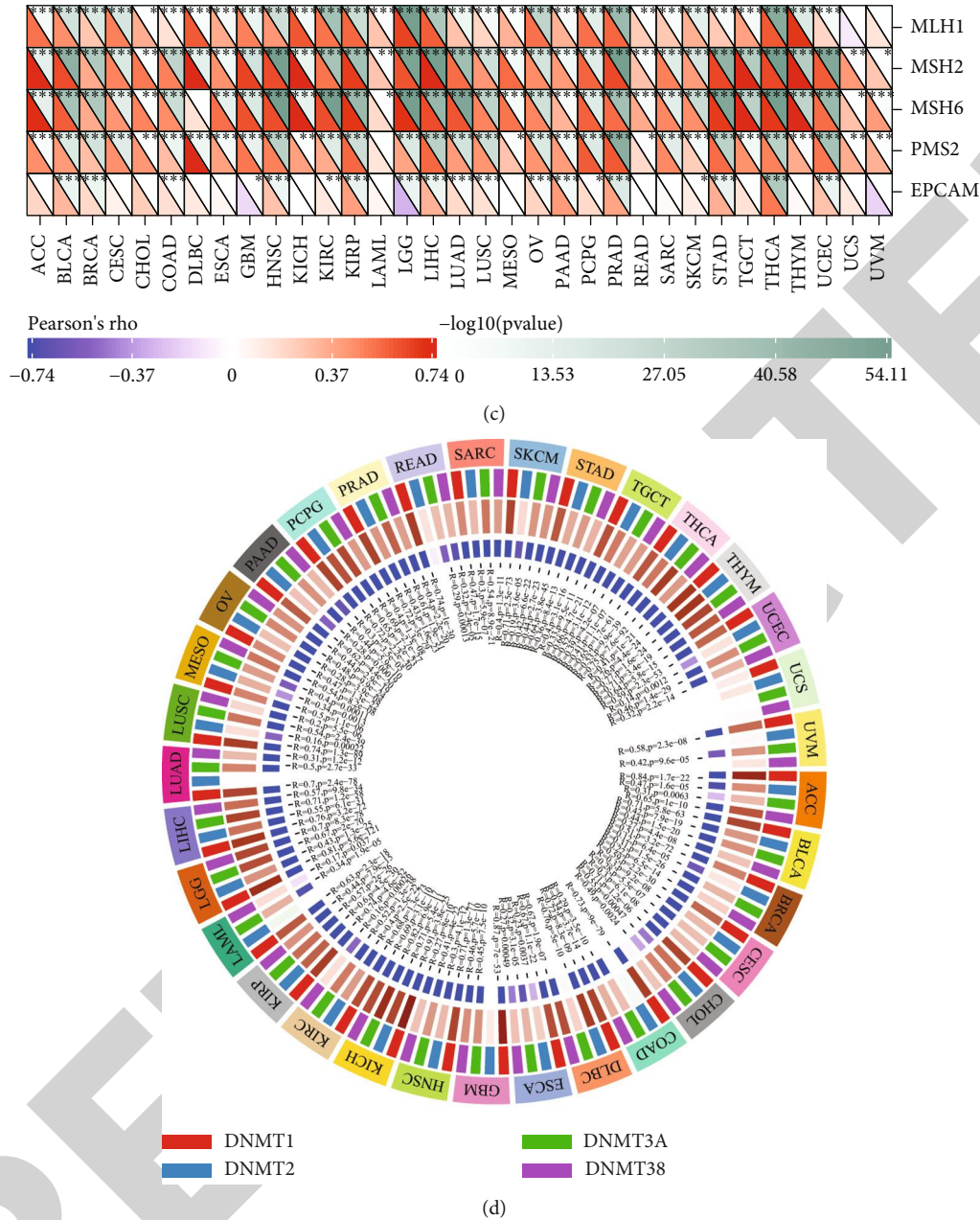


FIGURE 6: Correlations of PTBP1 with TMB, MSI, MMR, and DNA methyltransferases in pan-cancer. (a) Correlations of the expression of PTBP1 with TMB. (b) Correlations of the expression of PTBP1 with MSI. (c) Correlations of the expression of PTBP1 with five MMR-related genes. (d) Correlations of the expression of PTBP1 with four methyltransferases (DNMT1: red, DNMT2: blue, DNMT3A: green, and DNMT3B: purple). \* $P < 0.05$ , \*\* $P < 0.01$ , and \*\*\* $P < 0.001$ .

(Indels)). MSI refers to a change in MS sequence length caused by an insertion or deletion mutation during DNA replication. We statistically analyzed the correlation of the expression of PTBP1 with TMB (Figure 6(a)) and MSI (Figure 6(b)) and found that PTBP1 was positively correlated with TMB and MSI both in LGG, LUAD, LUSC, SARC, STAD, and UCEC ( $P < 0.05$ ).

MSI is a consequence of DNA MMR deficiency [33]. MMR gene mutations may cause DNA replication errors, higher somatic mutations, and tumorigenesis. Our correla-

tion analysis revealed that the expression of PTBP1 was positively correlated with the level of MMR gene expression in pan-cancer (Figure 6(c)).

DNA methylation is a form of chemical modification of DNA capable of changing gene expression without altering the DNA sequence, which can be detected early, frequently, consistently, and in specific cell types in cancer [34]. Our circle visualization of correlation analysis revealed that DNA methylation transferases were positively correlated with the expression of PTBP1 in almost all tumors except UCS (Figure 6(d)).

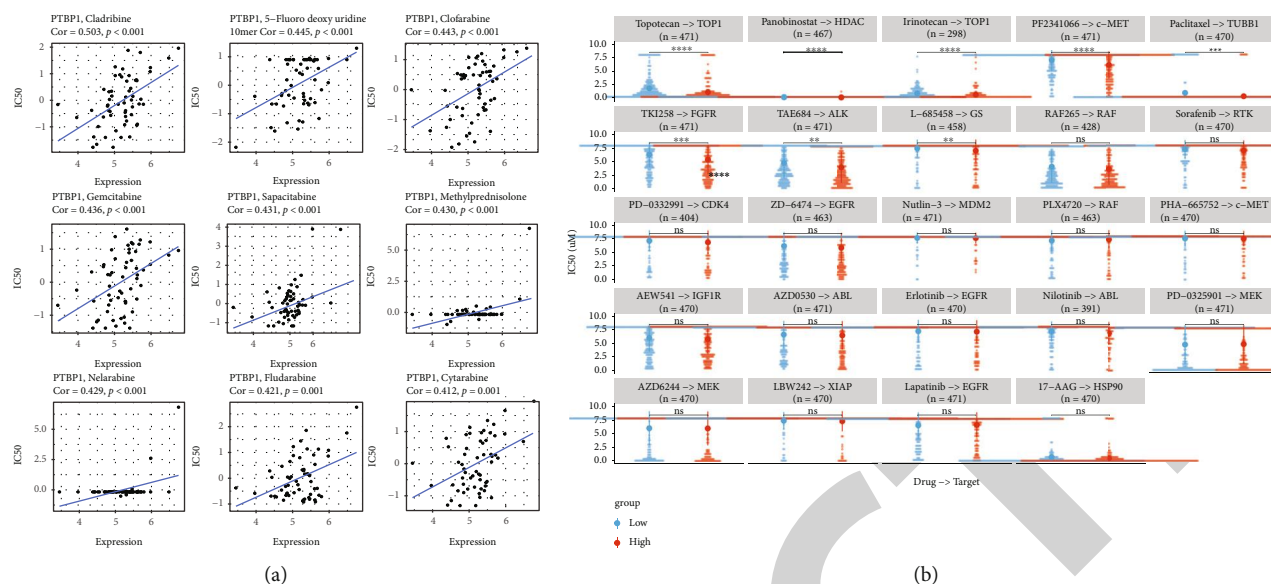


FIGURE 7: Correlation between PTBP1 and IC50 for different drugs. (a) Correlation analysis between the expression of PTBP1 and IC50 of cladribine, 5-fluorodeoxyuridine, clofarabine, gemcitabine, sapacitabine, methylprednisolone, nelarabine, fludarabine, and cytarabine in pan-cancer.  $P < 0.05$  was considered as statistically significant. (b) Comparison of IC50 of topotecan, panobinostat, irinotecan, PF2341066, paclitaxel, TKI258, TAE684, L-685458, RAF265, sorafenib, PD-0332991, ZD-6474, nutlin-3, PLX4720, PHA-665752, AEW541, AZD0530, erlotinib, nilotinib, PD-0325901, AZD6244, LBW242, lapatinib, and 17-AAG between groups stratified by expression levels of PTBP1.  $**P < 0.01$ ,  $***P < 0.001$ , and  $****P < 0.0001$ .

An overview of the above findings demonstrated that PTBP1 could upregulate TMB, MSI, and MMR in various cancers and mediate DNA methylation in pan-cancer and SARC.

**3.7. Expression Level of PTBP1 Affects Drug Sensitivity.** Drug resistance remains a major factor limiting outcomes for cancer patients. Early chemo-therapeutics can achieve initial successes, whereas drug resistance may quickly develop, leading to disease relapse [35]. To find potential sensitive drug treatment targeting on PTBP1, we analyzed the correlation between the expression of PTBP1 and IC50 data collected from Cell Miner and GDSC databases. IC50 of cladribine, 5-fluoro deoxy uridine, clofarabine, gemcitabine, sapacitabine, methylprednisolone, nelarabine, fludarabine, and cytarabine showed significant positive correlations with the expression level of PTBP1 (Figure 7(a)). Besides, a comparison between PTBP1 high- and low-expression groups showed that IC50 of topotecan, panobinostat, irinotecan, PF2341066, paclitaxel, TKI258, TAE684, and L-685458 in PTBP1 high-expression group was significantly lower than that in PTBP1 low-expression group (Figure 7(b)). All the above results may provide new ideas for developing potential drugs relating to the expression of PTBP1 for treating cancers.

**3.8. Clinical and In Vitro Validation of PTBP1 in Osteosarcoma.** Osteosarcoma was the most common bone SARC, the most common primary bone malignancy in pediatric population. We divided osteosarcoma patients from TARGET database into PTBP1 high- and low-expression group (cutoff value = 6.740955, range 4.639331~8.184960). Kaplan-Meier analysis showed that

PTBP1 correlated with poor prognosis of osteosarcoma (Figure 8(a)). Consistent with the RNA upregulation of PTBP1 in SARC from above analyses, IHC analyses were detected higher PTBP1 protein expression in human osteosarcoma lesions than in adjacent tissues (Figures 8(b) and 8(c)). Further, western blot assay revealed that PTBP1 was upregulated in human osteosarcoma cell lines compared with hBMSC (Figure 8(d)).

To further investigate the effect of the expression level of PTBP1 on tumor cell function in osteosarcoma, we constructed a PTBP1 knockout HOS (HOS-PTBP1-KO) cell line by CRISPR/Cas9 system. The mRNA expression (Figure 8(e)) and protein expression (Figure 8(f)) of PTBP1 were significantly downregulated in HOS-PTBP1-KO cell line compared with HOS wild-type (HOS-WT) cell line, which confirmed the knockout of PTBP1. Cell proliferation was significantly reduced in the HOS-PTBP1-KO group compared to the HOS-WT group since the 72 h. (Figure 8 (g)). Transwell migration and invasion assay were performed to compare the cell migration and invasion ability. Knockout of PTBP1 could reduce the function of cell migration and invasion (Figure 8(h)).

Besides, given the significant correlation between the expression of PTBP1 and cell cycle pathway, FACS experiment was used to assess the cell cycle of HOS cell line with or without PTBP1 knockout (Supplement Figure 5). PTBP1 knockout induces osteosarcoma cells accumulate in G0/G1 phrases.

In brief, PTBP1 was overexpressed in osteosarcoma tumor tissues and cell lines and correlated with poor prognosis for osteosarcoma patients. Knockout of the expression of PTBP1 can reduce cell proliferation, migration, invasion, and significantly affect cell cycle in vitro.

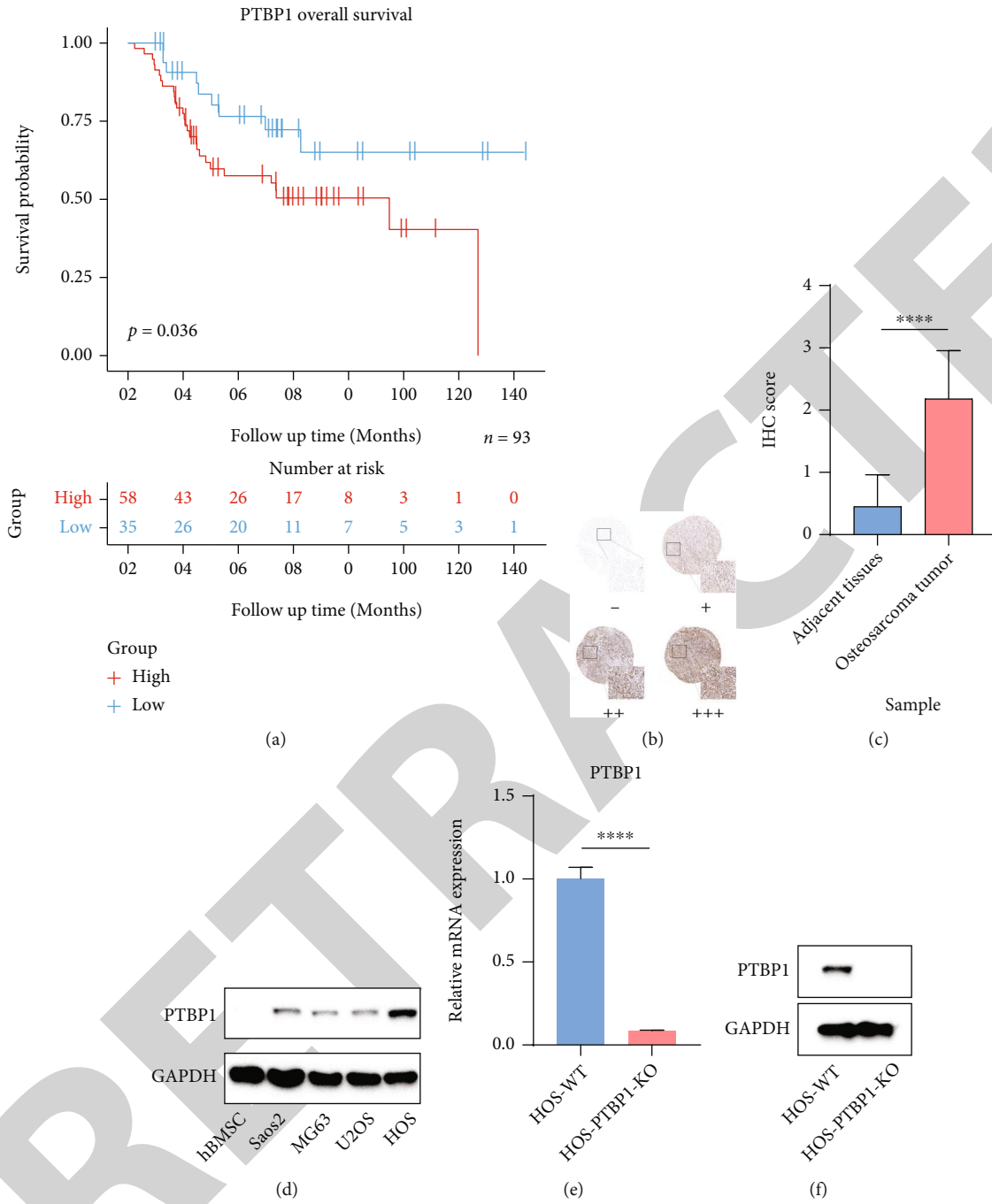


FIGURE 8: Continued.

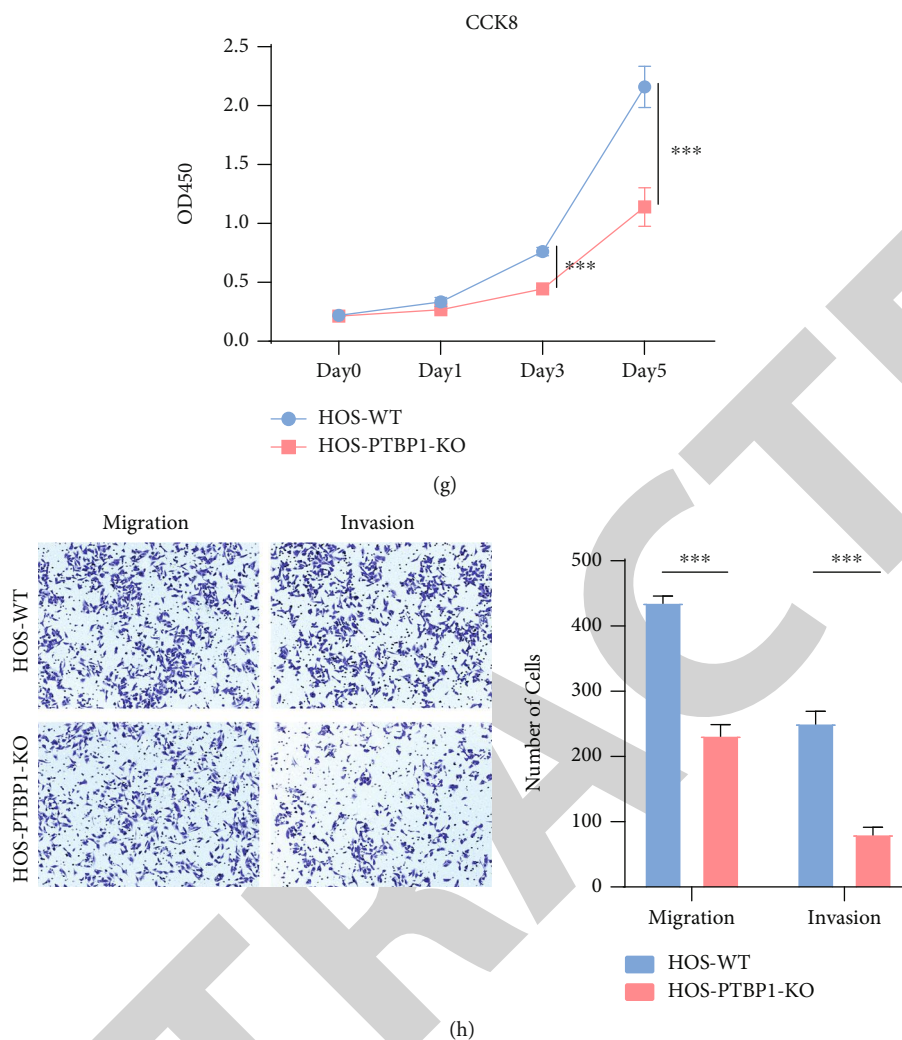


FIGURE 8: Clinical and vitro validation of PTBP1 in osteosarcoma. (a) Kaplan-Meier analysis of OS in TARGET osteosarcoma patients stratified by different expression levels of PTBP1. (b) Representative images of IHC staining of PTBP1 in human osteosarcoma tumors and adjacent tissues. Scale bar: 200/50  $\mu\text{m}$ . IHC score: 0, negative; 1, weakly positive; 2 moderately positive; 3 strongly positive staining. (c) Barplot of IHC score for PTBP1 protein level assessed by IHC assay. (d) Western blotting of PTBP1 protein expression in human osteosarcoma cell lines and hBMSC cell line. (e) RT-PCR result of PTBP1 gene expression in HOS-WT and HOS-PTBP1-KO cell line. (f) Western blotting of PTBP1 protein expression in HOS-WT and HOS-PTBP1-KO cell line. (g) Cell proliferation of HOS-WT and HOS-PTBP1-KO cell line. (h) Cell migration and invasion of HOS-WT and HOS-PTBP1-KO cell line. \*\*\*  $P < 0.001$ , \*\*\*\*  $P < 0.0001$ , scale bar: 100  $\mu\text{m}$ .

#### 4. Discussion

With the study of tumorigenesis and tumor immunity, immunotherapy has emerged as an encouraging and remarkable research field in oncology. Cancer immunotherapies are capable of adjusting the immune system to detect and attack cancer cells using immune checkpoint inhibitors and adoptive cell therapy. Research on the mechanism of tumor escape has changed the therapeutic prospect for various solid and hematologic malignancies [36]. Sarcoma, representing a heterogeneous group of cancers originating from the mesenchymal tissues, can be classified into soft-tissue sarcoma (STS) and bone sarcoma (BS). Most SARC are not sensitive to radiotherapy or chemotherapy and have a high recurrence or metastasis rate after local surgery [4]. Some preclinical trials on sarcoma immunotherapy showed a

positive response of sarcoma to immunotherapy, thus allowing more researchers to focus on the immunotherapy of sarcoma [37]. However, there is still a long way to go before immunotherapy can be practically used for treating sarcoma.

PTBP1, a splicing factor involved in pre-mRNA processing, mRNA metabolism, and transport, plays a critical role in regulating alternative splicing events. Existing studies proved that PTBP1 plays an essential role in cancer progression by facilitating cell proliferation and migration of glioma [38], colorectal cancer [11], and breast cancer cells [39]. PTBP1 plays a role in various biological functions as a regulator in cancers (e.g., the regulation of tumorigenesis, glycolysis, apoptosis, invasion, and migration [40]). PTBP1 has gained prominence in cancer research due to its extensive biological functions, which is also expected to provide new



insights into refractory tumor treatment, especially insensitive SARC treatment.

However, a systematic analysis of PTBP1 in pan-cancer should be urgently conducted, knowing that pan-cancer analysis can reveal similarities and differences in dysregulation of key biological processes in tumors [41], thus providing insights into cancer prevention and the design of novel therapeutic targets. This study aimed to explore the characteristic features and their potential roles of PTBP1 focused on SARC at a pan-cancer level.

It was found in this study that PTBP1 mRNA expression was increased in most tumor types. Survival analysis revealed that a high expression level of PTBP1 was mostly correlated with poor survival of OS, PFI, and DSS in pan-cancer. Specifically, a high expression level of PTBP1 was a risk factor in ACC, KICH, LGG, LIHC, LUAD, MESO, PRAD, SARC, SKCM, and UVM, and a protective factor in KIRC, OV, READ, and THYM. In conclusion, the above results suggest that PTBP1 is a potential prognostic biomarker in most cancer types. Existing studies proved that PTBP1 may prove to be a prognostic marker in multiple myeloma (MM), LUAD, BLCA, and KIRC [42–45], which is consistent with our conclusion.

Genetic alteration accumulation is considered to drive the progression of normal cells to invasive cancer and metastatic disease, through hyperplastic and dysplastic stages [46]. The genetic alteration of PTBP1, primarily composed of mutation, amplification, and multiple alteration, frequently occurs in SARC. As revealed by additional research of alterations in SARC, TP53, ATRX, TTN, MUC16, and RB1 were top-five altered genes in PTBP1-high and PTBP1-low groups of SARC with different frequencies and alteration types in composition, which were primarily correlated with p53, mTOR, apoptosis, DNA replication, RNA polymerase, Wnt, and Notch signaling pathway. Existing studies reported that TP53 plays an essential antitumor role in osteosarcoma, Ewing sarcoma, chondrosarcoma, rhabdomyosarcoma (RMS), leiomyosarcoma (LMS), synovial sarcoma, liposarcoma (LPS), angiosarcoma, and undifferentiated pleomorphic sarcoma (UPS) [47]. Novo therapeutics targeting TP53 require further attention and research.

In-depth mechanism research of PTBP1 revealed that PTBP1 was significantly correlated with the regulation of cell cycle, E2F targets, G2M checkpoint, MYC targets, DNA replication, ribosome, and spliceosome pathways in pan-cancer, suggesting that PTBP1 may play an important role in maintaining tumor cell viability to promote tumor proliferation. Similar results were found in SARC alone. Suckale et al. [48] demonstrated that PTBP1 was highly expressed in embryonic stem cells and throughout embryonic development, which suggested that PTBP1 plays an essential role in early embryonic development. Kang et al. [49] reported that PTBP1 was a positive regulator of human hepatocellular carcinoma growth by enhancing cyclin D3 translation, consequently facilitating cell cycle progression and tumor growth. PTBP1 was also found to increase RCC cell migration, invasion, proliferation, and angiogenesis via the hypoxia-inducible factor-1 $\alpha$  pathway [45]. The above previous findings are consistent with our results. Thus, further research into new therapeutic approaches to tumor cell cycle

regulation for SARC patients has great potential and significance.

We conducted correlation analyses between the expression level of PTBP1 and genes relating to the most popular pathways (e.g., TGFB, autophagy, and WNT pathway) and found that PTBP1 was positively correlated with almost all the genes of TGFB, autophagy, and WNT pathways in pan-cancer. Sheng et al. [50] reported that ST7 anti-sense RNA 1 overexpression could inhibit glioma progression by suppressing Wnt/ $\beta$ -catenin signaling by downregulating the expression of PTBP1. PTBP1 was also reported to regulate the phosphatase and tensin homolog-phosphatidylinositol-4,5-bisphosphate 3-kinase/protein kinase B (PTEN-PI3K/Akt) pathway and autophagy, thus inducing the proliferation, invasion, and metastasis of breast cancer cells [39]. However, there are rare studies on the mechanisms by which PTBP1 affects tumorigenesis and immunity. The results of this study may provide new insights into this field of research.

Despite the remarkable success of immunotherapy in several types of solid cancers (e.g., melanoma, nonsmall cell lung cancer, bladder cancer, and mismatch repair-deficient cancers) [51], the clinical outcomes of immunotherapy remain unsatisfactory in more types of cancers. One reason for this is the lack of discovery novo diagnosis and therapeutic targets due to poorly understood tumor-immune interactions in cancer. It is generally recognized that tumor immune cell infiltration is an independent predictor of the tumor immune status and survival, so a better understanding about the correlation between PTBP1 and tumor immune infiltration may provide new insights into the way PTBP1 affects tumor prognosis. Our studies have suggested that PTBP1 could upregulate or downregulate immune infiltration in various tumors, which might interpret why survival analysis showed different roles of PTBP1 in pan-cancer settings. The immune cell infiltration analysis of PTBP1 in SARC alone showed that high expression of PTBP1 could lower the abundance of immune infiltrates of most immune cell types significantly, except type 2T helper cell and memory B cell, which may explain the poor prognosis in PTBP1 high-expression SARC patients.

MSI and TMB have been considered established biomarkers to assess the response to ICPIs in multiple tumor types [32]. We found that TMB and MSI showed a significant positive correlation with PTBP1 in LGG, LUAD, LUSC, SARC, STAD, and UCEC, and similar results were reported in MMR gene and DNA methyltransferase expression. Thus, abnormal expression of PTBP1 may contribute to tumorigenesis by increasing tumor mutation, impairing DNA damage repair function, and facilitating DNA methylation.

Drug resistance refers to an impairment to cancer therapy, and developing novel drugs against drug resistance is time-consuming and challenging. Drug repurposing is more economical based on existing research data. The process of repurposing can provide novel insights into disease pathogenesis and discover new opportunities for pharmaceutical interventions [52]. Since PTBP1 was found to be widely overexpressed in pan-cancer, correlated with worse

outcomes, extensively involved in several well-known tumor pathways and regulation of tumor cell cycle, we suggested that PTBP1 might be a *novo* diagnosis and therapeutic target. Accordingly, we analyzed the correlation between PTBP1 and preclinical and clinical drugs to find potential therapeutic solutions for tumors. We identified a number of drugs with positive sensitivities consistent with the expression level of PTBP1, including topotecan, panobinostat, irinotecan, PF2341066, paclitaxel, TKI258, TAE684, and L-685458, which provides a selection of potential drugs for the pharmacotherapy of PTBP1 overexpressed tumors.

The further validation in osteosarcoma datasets of TARGET database suggested that PTBP1 is correlated with poor prognosis of osteosarcoma. Osteosarcoma tissue IHC staining and osteosarcoma cell line western blot analyses proved the overexpressed PTBP1 in tumor compared with normal tissues and cell line. PTBP1 knockout was also performed in HOS cell line by CRISPR/Cas9 system. CCK8, Transwell migration, invasion, and FACS experiments revealed that knockout PTBP1 could inhibit the cell proliferation, migration, and invasion and facilitate G0/G1 phase accumulation of osteosarcoma.

However, there are some deficiencies of this study. TCGA-SARC dataset is mainly composed of soft tissue sarcoma, but there are differences between osteosarcoma and soft tissue sarcoma in pathophysiology and clinical features. In addition, the TARGET-OS dataset lacks multiomics data, so the dataset cannot be analyzed in depth.

## 5. Conclusion

This study revealed the prognostic value of PTBP1 in SARC and PTBP1 can promote cell proliferation, migration, invasion, and cell cycle in vitro experiments. Besides, PTBP1 was closely involved in cell cycle, TGFB, autophagy, and WNT pathways at a pan-cancer level. The high expression of PTBP1 is correlated with worse prognosis by mediating immune infiltration of cancer cells. The above findings may bring novel perspectives to the treatment of tumor patients.

## Data Availability

The public data used to support the findings of this study are included within the article.

## Conflicts of Interest

The authors declare that they have no competing interests.

## Authors' Contributions

JX, ZW, and DZ contributed to conception, design, and supervisory of the study. YW organized the database. AJ performed the statistical analysis. HG wrote the original draft. HG, AJ, RJ, and YW wrote sections of the manuscript. All authors contributed to manuscript revision, read, and approved the submitted version. Haiyi Gong, Aimin Jiang, Runyi Jiang, and Yao Wang have contributed equally to this

work and share first authorship. Dan Zhang, Zhipeng Wu, and Jianru Xiao share last authorship.

## Acknowledgments

This study was partially supported by the National Key Research and Development Plan (Grant number: 2016YFC0902100), Shanghai Science And Technology Commission Western Medicine Steering Project (Grant number: 19411962700), and National Natural Science Foundation of China (Grant number: 81702658).

## Supplementary Materials

Supplementary 1. Supplement Figure 1: PTBP1 expression in patients with different AJCC clinical stages. Supplementary 2. Supplement Figure 2: the genetic alterations of PTBP1 and associations with mRNA expression. Supplementary 3. Supplement Figure 3: the biological function of PTBP1 in pan-cancer and SARC. Supplementary 4. Supplement Figure 4: correlations between tumor immunity and PTBP1 expression in pan-cancer. Supplementary 5. Supplement Figure 5: the flow cytometry analysis of cell cycle distribution. (*Supplementary Materials*)

## References

- [1] H. Sung, J. Ferlay, R. L. Siegel et al., "GLOBOCAN estimates of incidence and mortality worldwide for 36 cancers in 185 countries," *CA: a Cancer Journal for Clinicians*, vol. 71, no. 2021, pp. 209–249, 2020.
- [2] T. G. Grünewald, M. Alonso, S. Avnet et al., "Sarcoma treatment in the era of molecular medicine," *EMBO Molecular Medicine*, vol. 12, no. 11, p. e11131, 2020.
- [3] W. Who, *WHO classification of tumours of soft tissue and bone: WHO classification of tumours*, vol. 5, WHO classification of tumours of soft tissue and bone, 2013.
- [4] M. F. Brennan, C. R. Antonescu, N. Moraco, and S. Singer, "Lessons learned from the study of 10,000 patients with soft tissue sarcoma," *Annals of surgery*, vol. 260, no. 3, pp. 416–422, 2014.
- [5] S. M. Pollack, M. Ingham, M. B. Spraker, and G. K. Schwartz, "Emerging targeted and immune-based therapies in sarcoma," *Journal of Clinical Oncology*, vol. 36, no. 2, pp. 125–135, 2018.
- [6] R. Chen, P. L. Zinzani, M. A. Fanale et al., "Phase II study of the efficacy and safety of pembrolizumab for relapsed/refractory classic Hodgkin lymphoma," *Journal of Clinical Oncology*, vol. 35, no. 19, pp. 2125–2132, 2017.
- [7] R. H. Andtbacka, H. L. Kaufman, F. Collichio et al., "Talinogene laherparepvec improves durable response rate in patients with advanced melanoma," *Journal of Clinical Oncology*, vol. 33, no. 25, pp. 2780–2788, 2015.
- [8] R. J. Motzer, B. Escudier, S. George et al., "Nivolumab versus everolimus in patients with advanced renal cell carcinoma: updated results with long-term follow-up of the randomized, open-label, phase 3 CheckMate 025 trial," *Cancer*, vol. 126, no. 18, pp. 4156–4167, 2020.
- [9] J. Brahmer, K. L. Reckamp, P. Baas et al., "Nivolumab versus docetaxel in advanced squamous-cell non-small-cell lung cancer," *The New England Journal of Medicine*, vol. 373, no. 2, pp. 123–135, 2015.

- [10] P. W. Kantoff, C. S. Higano, N. D. Shore et al., "Sipuleucel-T immunotherapy for castration-resistant prostate cancer," *The New England Journal of Medicine*, vol. 363, no. 5, pp. 411–422, 2010.
- [11] H. Takahashi, J. Nishimura, Y. Kagawa et al., "Significance of polypyrimidine tract-binding protein 1 expression in colorectal cancer," *Molecular Cancer Therapeutics*, vol. 14, no. 7, pp. 1705–1716, 2015.
- [12] L. Shen, S. Lei, B. Zhang et al., "Skipping of exon 10 in Axl pre-mRNA regulated by PTBP1 mediates invasion and metastasis process of liver cancer cells," *Theranostics*, vol. 10, no. 13, pp. 5719–5735, 2020.
- [13] K. Taniguchi, K. Uchiyama, and Y. Akao, "PTBP1-targeting microRNAs regulate cancer-specific energy metabolism through the modulation of PKM1/M2 splicing," *Cancer Science*, vol. 112, no. 1, pp. 41–50, 2021.
- [14] H. Sasanuma, M. Ozawa, and N. Yoshida, "RNA-binding protein Ptbp1 is essential for BCR-mediated antibody production," *International Immunology*, vol. 31, no. 3, pp. 157–166, 2019.
- [15] G. Geng, C. Xu, N. Peng et al., "PTBP1 is necessary for dendritic cells to regulate T-cell homeostasis and antitumour immunity," *Immunology*, vol. 163, no. 1, pp. 74–85, 2021.
- [16] D. R. Rhodes, J. Yu, K. Shanker et al., "ONCOMINE: A Cancer Microarray Database and Integrated Data-Mining Platform," *Neoplasia*, vol. 6, no. 1, pp. 1–6, 2004.
- [17] G. Yu, L.-G. Wang, Y. Han, and Q.-Y. He, "clusterProfiler: an R package for comparing biological themes among gene clusters," *Omics: a journal of Integrative Biology*, vol. 16, pp. 284–287, 2012.
- [18] A. Luna, F. Elloumi, S. Varma et al., "CellMiner Cross-Database (CellMinerCDB) version 1.2: exploration of patient-derived cancer cell line pharmacogenomics," *Nucleic Acids Research*, vol. 49, no. D1, pp. D1083–D1093, 2021.
- [19] T. Cokelaer, E. Chen, F. Iorio et al., "GDSCTools for mining pharmacogenomic interactions in cancer," *Bioinformatics (Oxford, England)*, vol. 34, no. 7, pp. 1226–1228, 2018.
- [20] B. Chen, M. S. Khodadoust, C. L. Liu, A. M. Newman, and A. A. Alizadeh, "Profiling tumor infiltrating immune cells with CIBERSORT," *Methods in molecular biology*, vol. 1711, pp. 243–259, 2018.
- [21] T. Li, J. Fan, B. Wang et al., "TIMER: a web server for comprehensive analysis of tumor-infiltrating immune cells," *Cancer Research*, vol. 77, no. 21, pp. e108–e110, 2017.
- [22] S. Colak and P. Ten Dijke, "Targeting TGF- $\beta$  signaling in cancer," *Trends Cancer*, vol. 3, no. 1, pp. 56–71, 2017.
- [23] J. M. M. Levy, C. G. Towers, and A. Thorburn, "Targeting autophagy in cancer," *Nature Reviews. Cancer*, vol. 17, no. 9, pp. 528–542, 2017.
- [24] R. Nusse and H. Clevers, "Wnt/ $\beta$ -catenin signaling, disease, and emerging therapeutic modalities," *Cell*, vol. 169, no. 6, pp. 985–999, 2017.
- [25] Y. Zhang and Z. Zhang, "The history and advances in cancer immunotherapy: understanding the characteristics of tumor-infiltrating immune cells and their therapeutic implications," *Cellular & Molecular Immunology*, vol. 17, no. 8, pp. 807–821, 2020.
- [26] T. Reisländer, F. J. Groelly, and M. Tarsounas, "DNA damage and cancer immunotherapy: a STING in the tale," *Molecular Cell*, vol. 80, no. 1, pp. 21–28, 2020.
- [27] S. Liu, J. Liang, Z. Liu et al., "The role of CD276 in cancers," *Frontiers in Oncology*, vol. 11, article 654684, 2021.
- [28] C. E. Hughes and R. J. B. Nibbs, "A guide to chemokines and their receptors," *The FEBS Journal*, vol. 285, no. 16, pp. 2944–2971, 2018.
- [29] R. Roozendaal and R. E. Mebius, "Stromal cell-immune cell interactions," *Annual Review of Immunology*, vol. 29, no. 1, pp. 23–43, 2011.
- [30] L. M. McLane, M. S. Abdel-Hakeem, and E. J. Wherry, "CD8 T cell exhaustion during chronic viral infection and cancer," *Annual Review of Immunology*, vol. 37, no. 1, pp. 457–495, 2019.
- [31] P. Thanindrarn, D. C. Dean, S. D. Nelson, F. J. Hornicek, and Z. Duan, "Chimeric antigen receptor T (CAR-T) cell immunotherapy for sarcomas: from mechanisms to potential clinical applications," *Cancer Treatment Reviews*, vol. 82, p. 101934, 2020.
- [32] A. B. Schrock, C. Ouyang, J. Sandhu et al., "Tumor mutational burden is predictive of response to immune checkpoint inhibitors in MSI-high metastatic colorectal cancer," *Annals of Oncology*, vol. 30, no. 7, pp. 1096–1103, 2019.
- [33] M. Baretta and D. T. Le, "DNA mismatch repair in cancer," *Pharmacology & Therapeutics*, vol. 189, pp. 45–62, 2018.
- [34] A. Koch, S. C. Joosten, Z. Feng et al., "Analysis of DNA methylation in cancer: location revisited," *Nature Reviews. Clinical Oncology*, vol. 15, no. 7, pp. 459–466, 2018.
- [35] N. Vasan, J. Baselga, and D. M. Hyman, "A view on drug resistance in cancer," *Nature*, vol. 575, no. 7782, pp. 299–309, 2019.
- [36] L. B. Kennedy and A. K. S. Salama, "A review of cancer immunotherapy toxicity," *CA: a Cancer Journal for Clinicians*, vol. 70, no. 2, pp. 86–104, 2020.
- [37] Y. R. Murciano-Goroff, A. B. Warner, and J. D. Wolchok, "The future of cancer immunotherapy: microenvironment-targeting combinations," *Cell Research*, vol. 30, no. 6, pp. 507–519, 2020.
- [38] H. C. Cheung, T. Hai, W. Zhu et al., "Splicing factors PTBP1 and PTBP2 promote proliferation and migration of glioma cell lines," *Brain*, vol. 132, no. 8, pp. 2277–2288, 2009.
- [39] X. Wang, Y. Li, Y. Fan, X. Yu, X. Mao, and F. Jin, "PTBP1 promotes the growth of breast cancer cells through the PTEN/Akt pathway and autophagy," *Journal of Cellular Physiology*, vol. 233, no. 11, pp. 8930–8939, 2018.
- [40] W. Zhu, B.-L. Zhou, L.-J. Rong et al., "Roles of PTBP1 in alternative splicing, glycolysis, and oncogenesis," *Journal of Zhejiang University. Science. B*, vol. 21, no. 2, pp. 122–136, 2020.
- [41] X. Ma, Y. Liu, Y. Liu et al., "Pan-cancer genome and transcriptome analyses of 1,699 paediatric leukaemias and solid tumours," *Nature*, vol. 555, no. 7696, pp. 371–376, 2018.
- [42] H. Bai and B. Chen, "Abnormal PTBP1 expression sustains the disease progression of multiple myeloma," *Disease Markers*, vol. 2020, Article ID 4013658, 10 pages, 2020.
- [43] P. Bielli, V. Panzeri, R. Lattanzio et al., "The splicing factor PTBP1 promotes expression of oncogenic splice variants and predicts poor prognosis in patients with non-muscle-invasive bladder cancer," *Clinical Cancer Research*, vol. 24, no. 21, pp. 5422–5432, 2018.
- [44] R. Xie, X. Chen, Z. Chen et al., "Polypyrimidine tract binding protein 1 promotes lymphatic metastasis and proliferation of bladder cancer via alternative splicing of MEIS2 and PKM," *Cancer Letters*, vol. 449, pp. 31–44, 2019.
- [45] H. Shan, P. Hou, M. Zhang et al., "PTBP1 knockdown in renal cell carcinoma inhibits cell migration, invasion and angiogenesis in vitro and metastasis in vivo via the hypoxia inducible factor-1 $\alpha$  pathway," *International Journal of Oncology*, vol. 52, no. 5, pp. 1613–1622, 2018.

## *Retraction*

# **Retracted: Homeobox A1 Facilitates Immune Escape and Alleviates Oxidative Stress in Lung Adenocarcinoma**

### **Oxidative Medicine and Cellular Longevity**

Received 26 December 2023; Accepted 26 December 2023; Published 29 December 2023

Copyright © 2023 Oxidative Medicine and Cellular Longevity. This is an open access article distributed under the Creative Commons Attribution License, which permits unrestricted use, distribution, and reproduction in any medium, provided the original work is properly cited.

This article has been retracted by Hindawi, as publisher, following an investigation undertaken by the publisher [1]. This investigation has uncovered evidence of systematic manipulation of the publication and peer-review process. We cannot, therefore, vouch for the reliability or integrity of this article.

Please note that this notice is intended solely to alert readers that the peer-review process of this article has been compromised.

Wiley and Hindawi regret that the usual quality checks did not identify these issues before publication and have since put additional measures in place to safeguard research integrity.

We wish to credit our Research Integrity and Research Publishing teams and anonymous and named external researchers and research integrity experts for contributing to this investigation.

The corresponding author, as the representative of all authors, has been given the opportunity to register their agreement or disagreement to this retraction. We have kept a record of any response received.

### **References**

- [1] F. Zhao, H. Tian, X. Liu et al., “Homeobox A1 Facilitates Immune Escape and Alleviates Oxidative Stress in Lung Adenocarcinoma,” *Oxidative Medicine and Cellular Longevity*, vol. 2022, Article ID 4102666, 34 pages, 2022.

## Research Article

# Homeobox A1 Facilitates Immune Escape and Alleviates Oxidative Stress in Lung Adenocarcinoma

Fen Zhao,<sup>1,2</sup> Hui Tian,<sup>3</sup> Xinchao Liu,<sup>1,4</sup> Yuanxiazi Guan,<sup>1</sup> Ying Zhu,<sup>5</sup> Peng Ren,<sup>3</sup> Jianbo Zhang,<sup>6</sup> Yinjun Dong,<sup>7</sup> and Lei Fu <sup>1</sup>

<sup>1</sup>Department of Radiation Oncology, Shandong Cancer Hospital and Institute, Shandong First Medical University and Shandong Academy of Medical Sciences, Jinan, 250117 Shandong, China

<sup>2</sup>Department of Radiation Oncology, Shandong Cancer Hospital and Institute, Shandong University, Jinan, 250117 Shandong, China

<sup>3</sup>Department of Radiation Oncology, Qilu Hospital of Shandong University, Jinan, 250012 Shandong, China

<sup>4</sup>Cheeloo College of Medicine, Shandong University, Jinan, 250012 Shandong, China

<sup>5</sup>Affiliated Hospital of Heze Medical College, Heze, 274008 Shandong, China

<sup>6</sup>Departments of Pathology, Shandong Cancer Hospital and Institute, Shandong First Medical University and Shandong Academy of Medical Sciences, Jinan, 250117 Shandong, China

<sup>7</sup>Department of Thoracic surgery, Shandong Cancer Hospital and Institute, Shandong First Medical University and Shandong Academy of Medical Sciences, Jinan, 250117 Shandong, China

Correspondence should be addressed to Lei Fu; [fuiray@126.com](mailto:fuiray@126.com)

Fen Zhao, Hui Tian, and Xinchao Liu contributed equally to this work.

Received 14 March 2022; Revised 7 April 2022; Accepted 19 April 2022; Published 19 May 2022

Academic Editor: Tian Li

Copyright © 2022 Fen Zhao et al. This is an open access article distributed under the Creative Commons Attribution License, which permits unrestricted use, distribution, and reproduction in any medium, provided the original work is properly cited.

**Objective.** Recent studies have demonstrated that homeobox A1 (HOXA1) is upregulated in lung cancer due to RNA modifications (N<sup>6</sup>-methyladenosine), but the specific function of HOXA1 in lung adenocarcinoma (LUAD) remains indistinct. Herein, we investigated the role of HOXA1 in LUAD biology. **Methods.** This study presented pancancer analysis of associations of HOXA1 with prognosis, TMB, and immune checkpoints. The expression of HOXA1 was detected in LUAD and normal tissues with immunohistochemistry and western blot. Through least absolute shrinkage and selection operator (LASSO) analysis, HOXA1-derived gene model was conducted in LUAD. Correlations of HOXA1 with immune cell infiltrations, immune checkpoints, HLAs, and chemotherapeutic sensitivity were evaluated. Colony formation, proliferation, and migration of LUAD cells with si-HOXA1 transfection were investigated, and the effects of HOXA1 on T cell exhaustion were assessed *in vitro*. **Results.** HOXA1 expression was a risk factor of overall survival, disease-specific survival, and progression-free interval of LUAD. HOXA1 exhibited prominent associations with immune cell infiltration, immune checkpoints, and HLAs. HOXA1-derived gene signature reliably and independently predicted LUAD outcomes. Also, high-risk cases presented increased sensitivity to cisplatin, paclitaxel, docetaxel, vinorelbine, and etoposide. HOXA1 knockdown exhibited an inhibitory effect on proliferation and migration abilities of LUAD cells. Silencing HOXA1 weakened the expression of antioxidative stress markers Nrf2/HO-1 and T cell exhaustion marker CD155 in LUAD cells. Moreover, LUAD cells with HOXA1 knockdown enhanced the CD8+ T cell response. **Conclusion.** Our data support the oncogenic function and prognostic significance of HOXA1 that facilitates immune escape and alleviates oxidative stress of LUAD.

## 1. Introduction

Lung cancer represents the major reason for cancer-related deaths, histologically categorized into two main subtypes: small-cell lung carcinoma (SCLC; 15%) [1] and non-small-cell lung carcinoma (NSCLC; 85%) [2, 3]. Lung adenocarcinoma (LUAD) remains the dominating subtype of NSCLC among smokers [4]. This malignancy accounts for most cancer deaths related to smoking, with high risk of metastasis and invasiveness [5]. Nevertheless, the incidence is an increasing trend among young women and never smokers [6]. As estimated, the five-year survival rate remains 19% [7]. Notably, the mechanisms underlying LUAD remain mostly unclear [8]. Hence, there is an urgent need to deeply study the molecular pathogenesis of LUAD to develop more effective therapeutic interventions and reduce mortality. In the past few years, major breakthroughs in the field of cancer immunotherapeutic strategies with immune checkpoint inhibitors (ICIs) have brought a therapeutic revolution for LUAD [9]. Although only a minority of patients present a desirable response to this therapeutic intervention [10], it is urgently required for evaluation of the mechanisms that modulate the tumor immune microenvironment during immunotherapy [11–13].

Homeobox A1 (HOXA1) is a member of homeodomain containing transcription factor family [14–16]. Accumulated evidence suggests that HOXA1 has an oncogenic role in diverse cancer types, including LUAD [14–16]. For instance, evidence suggests that HOXA1 expression is markedly upregulated and possess a moderate diagnostic potential in NSCLC [17]. HOXA1 exhibits prominent high expression in gefitinib-resistant than gefitinib-sensitive NSCLC tissues [18]. HOXA1 upregulation is linked to unfavorable survival outcomes of LUAD patients [19]. Despite this, the mechanisms underlying HOXA1 in LUAD remain unclear. Moreover, HOXA1 may modulate the antitumor immune response through immunosuppression of myeloid-derived suppressor cells (MDSCs) [20]. Lung displays a highly oxidative environment that is tolerated via engaging strictly controlled stress response signaling [21]. Limited evidence shows that oxidative stress can upregulate HOXA1 expression human embryonic stem cells, indicating that HOXA1 might participate in mediating oxidative stress process [22]. Nrf2 is a key stress response mediator [23], and abnormal Nrf2 signaling has been found in 23% of LUAD, demonstrating that Nrf2 dysfunction is the main cancer driver [24]. Suppression of Nrf2 enables to elicit an immunostimulatory tumor microenvironment of lung cancer [25]. Altogether, more investigations should be presented for the prognostic and immunological functions of HOXA1 in LUAD. Herein, the present study was aimed at revealing the function, regulatory mechanisms, and biological significance of HOXA1 in LUAD and at evaluating the clinical significance of HOXA1.

## 2. Materials and Methods

**2.1. Acquisition of Transcriptome Data.** RNA sequencing profiling of 502 LUAD patients was acquired from The Cancer Genome Atlas (TCGA) through the Genomic Data

Commons (<https://portal.gdc.cancer.gov/>). Meanwhile, the matched clinical information was retrieved. Fragments per kilobase per million (FPKM) values were converted to transcripts per kilobase million (TPM) values that were more comparable between samples.

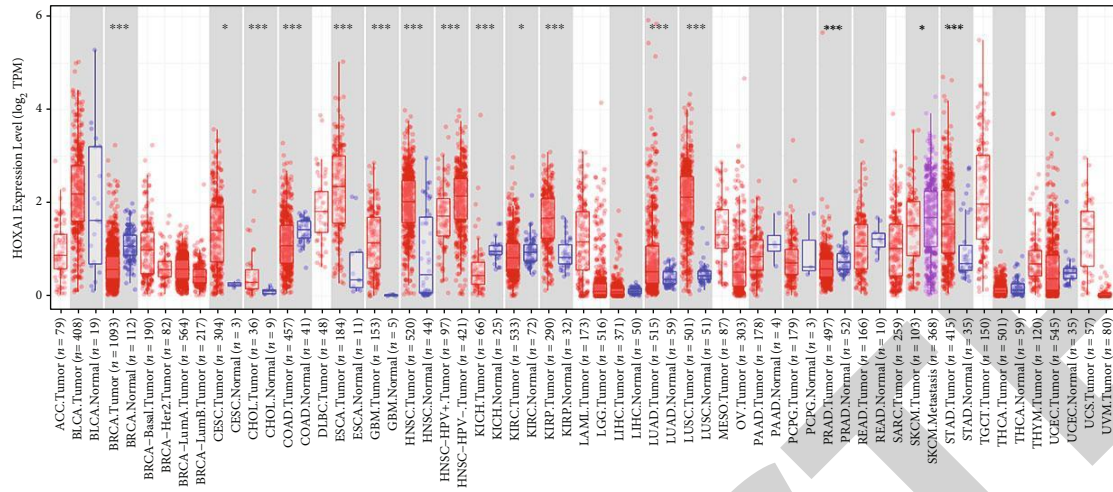
**2.2. Pancancer Analysis.** HOXA1 expression was analyzed in paired tumor and normal specimens across pancancer utilizing the Tumor Immune Estimation Resource (TIMER) 2.0 web server (<http://timer.cistrome.org/>) [26]. The Spearman correlation analysis was conducted for evaluating the correlations of HOXA1 with tumor mutation burden (TMB) across pancancer. The immune checkpoint gene sets were curated from a previous study [27]. The associations of HOXA1 with immune checkpoints were assessed in each cancer type at the mRNA levels. The univariate Cox regression models were conducted to estimate whether HOXA1 expression was linked to overall survival (OS), disease-survival survival (DSS), and progression-free interval (PFI) for each cancer type.

**2.3. Identification of HOXA1-Related Genes and Functional Enrichment Analysis.** Following the median HOXA1 expression, LUAD cases were classified as high or low expression group. Differential expression analysis was carried out between two groups. Genes with  $|\text{fold change (FC)}| > 1.5$  and false discovery rate (FDR)  $< 0.05$  were selected as HOXA1-related genes. Gene Ontology (GO) and Kyoto Encyclopedia of Genes and Genomes (KEGG) enrichment analyses were presented utilizing clusterProfiler package (version 3.10.1) [28].

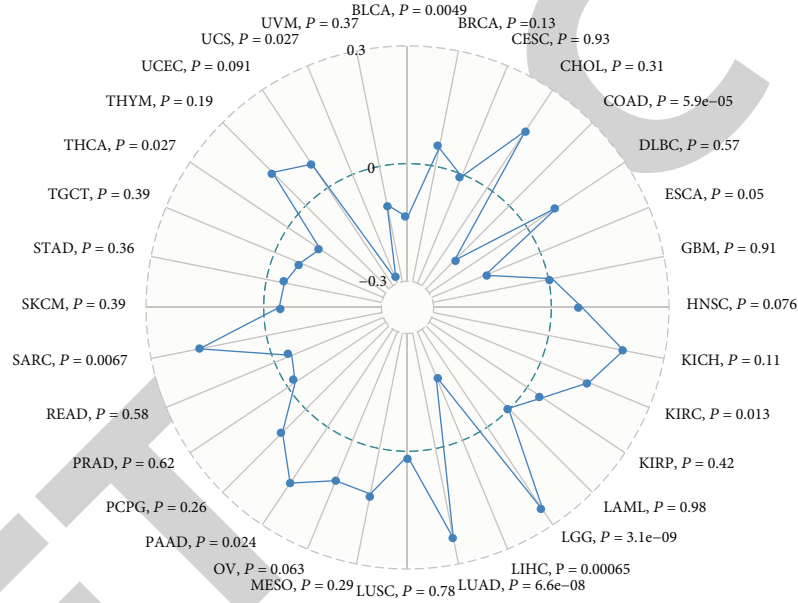
**2.4. Construction of a HOXA1-Derived Gene Model.** Univariate analysis was conducted for screening prognostic HOXA1-related genes with  $p < 0.05$ . A least absolute shrinkage and selection operator (LASSO) Cox regression model was then established with glmnet package (version 4.1-3) [29]. Tenfold cross-validation was utilized to determine the optimal value of penalty parameter  $\lambda$ . HOXA1-derived risk score was calculated in accordance with the expression values of candidate variables along with corresponding coefficients. Receiver operating characteristic (ROC) curve was assessed for estimating the predictive precision for risk score. Based on the median value, cases were split into high- or low-risk group. The Kaplan-Meier survival analysis was implemented for estimating OS differences between groups.

**2.5. Establishment of a Prognostic Nomogram.** Through uni- and multivariate Cox regression analyses, independent prognostic indicators were screened among LUAD patients. After combining independent prognostic indicators, a nomogram was established utilizing rms package (version 6.2-0). The predictive precision of this nomogram was confirmed through calibration diagrams.

**2.6. Analysis of Tumor-Infiltrating Immune Cells.** Marker genes of tumor-infiltrating immune cells were collected from a previous study [30]. Single sample gene set enrichment analysis (ssGSEA) was applied for quantifying the abundance levels of 28 immune cell types utilizing GSVA package

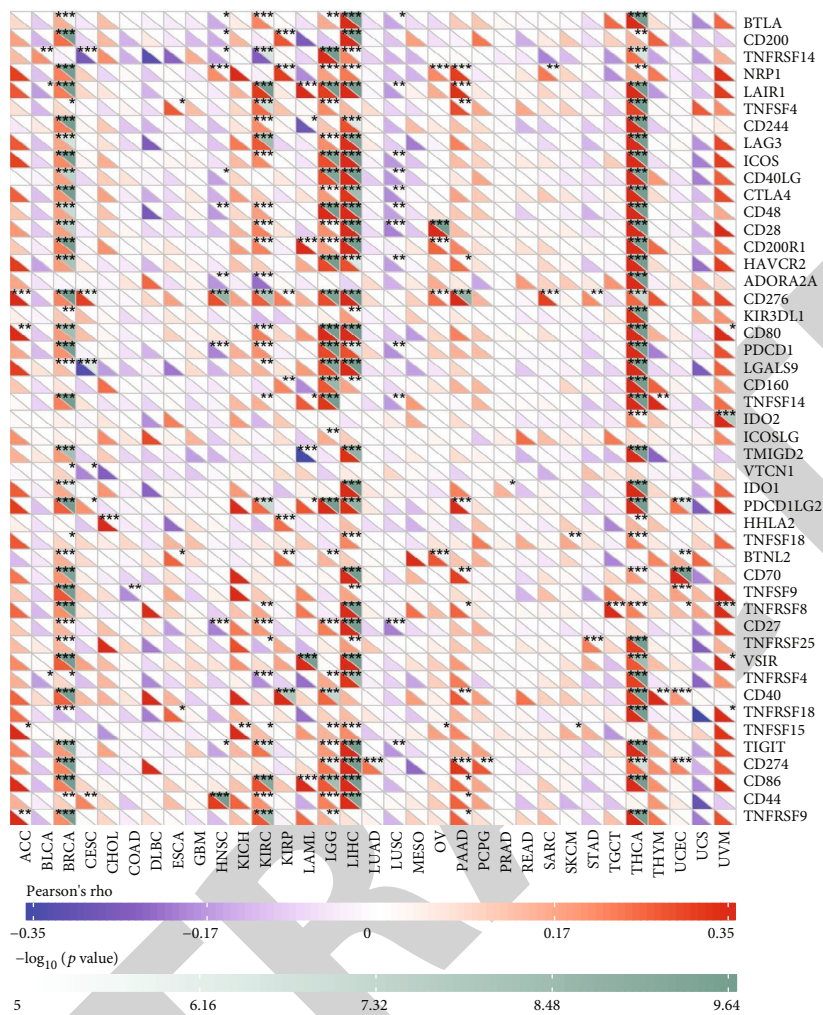


(a)



(b)

FIGURE 1: Continued.

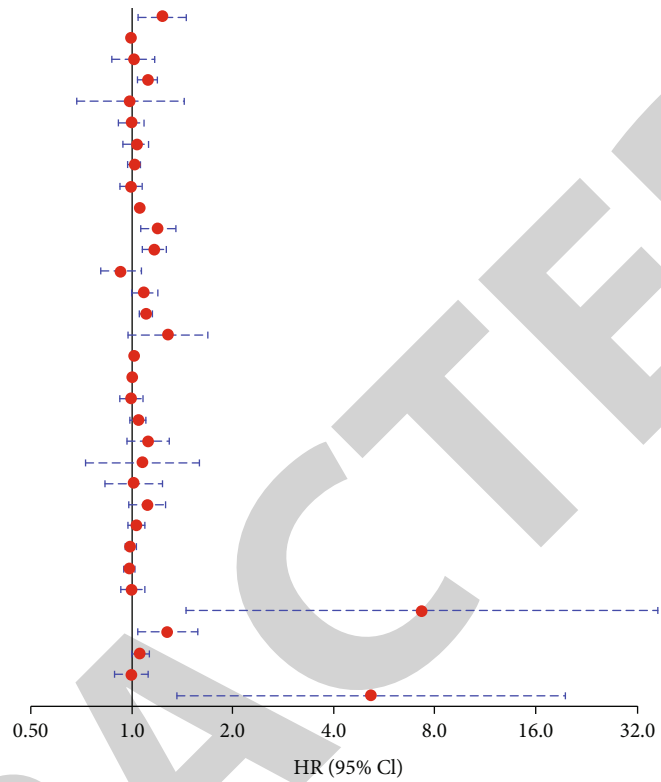


(c)

FIGURE 1: Continued.



	HR	P value
ACC	1.24 (1.05~1.46)	1.2e-02
BLCA	1 (0.99~1.02)	7.5e-01
BRCA	1.02 (0.88~1.17)	8.3e-01
CESC	1.12 (1.05~1.19)	3.3e-04
CHOL	0.99 (0.69~1.43)	9.8e-01
COAD	1 (0.92~1.09)	9.9e-01
DLBC	1.04 (0.95~1.14)	4.3e-01
ESCA	1.02 (0.98~1.06)	3.7e-01
GBM	1 (0.93~1.08)	9.9e-01
HNSC	1.06 (1.03~1.09)	1.7e-04
KICH	1.2 (1.07~1.35)	1.6e-03
KIRC	1.17 (10.81~1.27)	1.1e-04
KIRP	0.93 (0.81~1.07)	3.2e-01
LAML	1.09 (1~1.19)	4.4e-02
LGG	1.11 (1.07~1.15)	5.2e-10
LIHC	1.29 (0.98~1.69)	6.8e-02
LUAD	1.02 (1.01~1.03)	4.2e-03
LUSC	1 (0.97~1.03)	9.2e-01
MESO	1 (0.93~1.08)	9.9e-01
OV	1.05 (0.99~1.1)	8.8e-02
PAAD	1.12 (0.98~1.3)	1.1e-01
PCPG	1.08 (0.73~1.59)	7.1e-01
PRAD	1.02 (0.84~1.23)	8.4e-01
READ	1.12 (0.99~1.27)	8.0e-02
SARC	1.04 (0.98~1.1)	1.6e-01
SKCM	0.99 (0.96~1.03)	6.4e-01
STAD	0.99 (0.95~1.03)	4.7e-01
TGCT	1 (0.93~1.09)	9.1e-01
THCA	7.33 (1.46~36.73)	1.5e-02
THYM	1.28 (1.04~1.58)	1.8e-02
UCEC	1.06 (1~1.13)	6.5e-02
UCS	1 (0.89~1.12)	9.8e-01
UVM	5.17 (1.37~19.47)	1.5e-02



	HR	P value
ACC	1.23 (1.03~1.46)	2.2e-02
BLCA	1.01 (0.99~1.03)	5.4e-01
BRCA	1.05 (0.89~1.24)	5.6e-01
CESC	1.14 (1.07~1.22)	1.0e-04
CHOL	0.93 (1.6~1.44)	7.3e-01
COAD	1.06 (1.97~1.16)	1.9e-01
DLBC	0.86 (0.6~1.22)	3.9e-01
ESCA	1.03 (0.99~1.08)	1.5e-01
GBM	1.01 (0.93~1.09)	8.5e-01
HNSC	1.07 (0.03~1.11)	2.6e-04
KICH	1.16 (0.93~1.45)	1.8e-01
KIRC	1.24 (1.08~1.42)	2.1e-03
KIRP	0.85 (0.71~1.02)	8.2e-02
LAML	NA (NA~NA)	
LGG	1.11 (1.08~1.15)	4.5e-10
LIHC	1.03 (0.61~1.73)	9.2e-01
LUAD	1.03 (0.02~1.04)	1.4e-05
LUSC	1.02 (0.97~1.06)	4.3e-01
MESO	1.02 (0.93~1.12)	6.4e-01
OV	1.05 (0.99~1.11)	9.0e-01
PAAD	1.1 (0.93~1.29)	2.6e-01
PCPG	0.86 (0.28~2.61)	7.9e-01
PRAD	1.02 (0.87~1.2)	7.7e-01
READ	1.14 (0.97~1.33)	1.1e-01
SARC	1.01 (0.94~1.09)	7.6e-01
SKCM	1.99 (0.95~1.03)	5.8e-01
STAD	1.02 (0.98~1.06)	4.6e-01
TGCT	0.99 (0.88~1.11)	8.4e-01
THCA	3.86 (0.21~69.37)	3.6e-01
THYM	1 (0.57~1.74)	9.9e-01
UCEC	1.08 (1.01~1.15)	1.9e-02
UCS	1.03 (0.92~1.15)	6.3e-01
UVM	5.26 (1.34~20.57)	1.7e-02
	3.86 (0.21~69.37)	

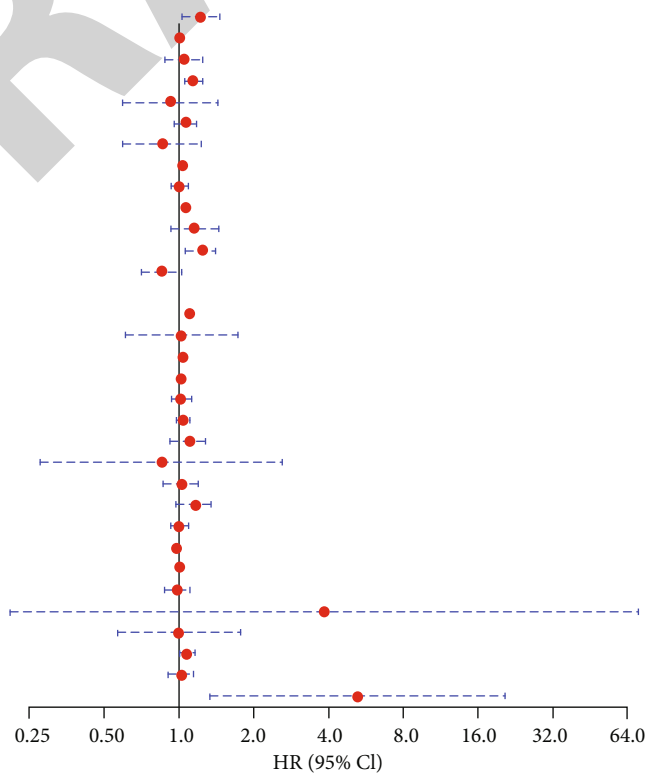
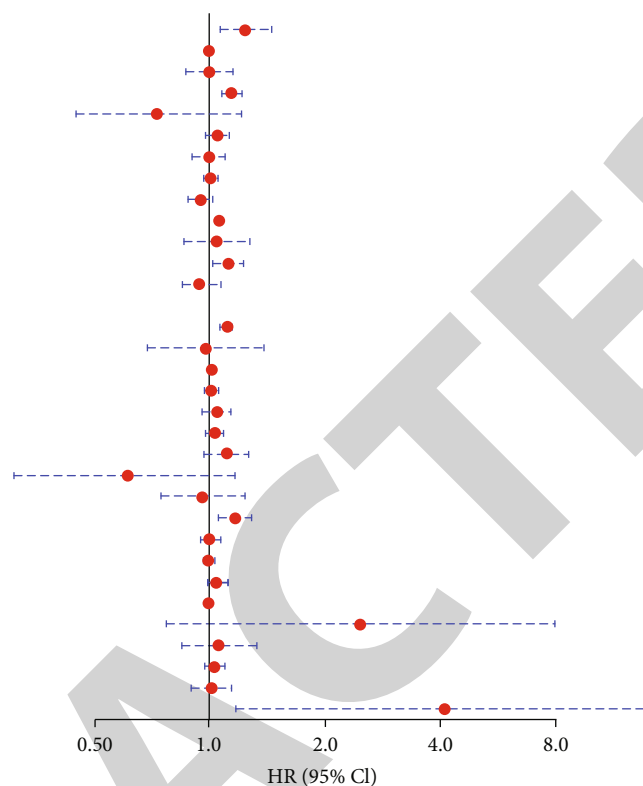


FIGURE 1: Continued.

	HR	P value
ACC	1.24 (1.07~1.45)	4.6e-03
BLCA	1 (0.98~1.02)	9.4e-01
BRCA	1 (0.87~1.15)	9.9e-01
CESC	1.14 (1.08~1.21)	1.2e-05
CHOL	0.73 (0.45~1.21)	2.2e-01
COAD	1.05 (0.98~1.12)	2.0e-01
DLBC	1 (0.9~1.1)	9.4e-01
ESCA	1.01 (0.97~1.05)	5.4e-01
GBM	0.95 (0.88~1.02)	1.6e-01
HNSC	1.06 (1.03~1.09)	4.2e-04
KICH	1.05 (0.86~1.27)	6.4e-01
KIRC	1.12 (1.02~1.23)	1.7e-02
KIRP	0.95 (0.85~1.07)	4.0e-01
LAML	NA (NA~NA)	
LGG	1.11 (1.07~1.14)	5.9e-10
LIHC	0.98 (0.69~1.39)	8.9e-01
LUAD	1.02 (1.01~1.03)	2.6e-05
LUSC	1.01 (0.98~1.05)	5.8e-01
MESO	1.05 (0.96~1.14)	2.7e-01
OV	1.04 (0.98~1.09)	1.7e-01
PAAD	1.11 (0.97~1.26)	1.2e-01
PCPG	0.61 (0.31~1.17)	1.4e-01
PRAD	0.96 (0.75~1.24)	7.6e-01
READ	1.17 (1.06~1.29)	1.5e-03
SARC	1 (0.95~1.06)	8.6e-01
SKCM	1 (0.97~1.03)	1.0e+00
STAD	1.04 (1~1.07)	2.3e-02
TGCT	1 (0.98~1.03)	7.2e-01
THCA	2.47 (0.77~7.93)	1.3e-01
THYM	1.06 (0.85~1.33)	5.8e-01
UCEC	1.03 (0.98~1.09)	2.3e-01
UCS	1.01 (0.9~1.13)	8.5e-02
UVM	4.1 (1.18~14.23)	2.6e-02



(f)

FIGURE 1: Pancancer analysis of expression pattern and immunogenic and prognostic significance of HOXA1. (a) Expression patterns of HOXA1 in diverse cancer types and matched normal tissue specimens. (b) Correlation analysis of HOXA1 with TMB across pancancer. (c) Heatmap visualizing the associations of HOXA1 with diverse immune checkpoints in each cancer type. Bottom left meant correlation coefficient and upper right corner meant  $p$  value. Blue represented negative correlation, while red represented positive correlation. \* $p < 0.05$ , \*\* $p < 0.01$ , and \*\*\* $p < 0.001$ . (d–f) Forest plots showing the associations of HOXA1 expression with OS, DSS, and PFI of different cancer types.

(version 1.14.1) on the basis of the transcriptomic profiles [31]. The enrichment scores were computed to represent the infiltration of immune cells.

**2.7. Drug Sensitivity Analysis.** Sensitivity to common chemotherapeutic drugs was assessed with the Genomics of Drug Sensitivity in Cancer (<https://www.cancerrxgene.org/>) project [32]. The half-maximal inhibitory concentration (IC50) was quantified with ridge regression analysis through pRRophetic package (version 1.0.0) [33].

**2.8. Gene Set Enrichment Analysis (GSEA).** KEGG pathways associated with HOXA1-derived risk score were evaluated utilizing GSEA software (version 1.20.0). The “c2.cp.kegg.v7.1-symbols” file acted as the reference gene set.

**2.9. Clinical Specimens.** In total, 5 pairs of LUAD and normal lung tissues were collected from the patients admitted to the Shandong Cancer Hospital and Institute between March 2020 and January 2021. All subjects did not receive radiotherapy or chemotherapy prior to surgery. This study was approved by the Ethical Committee of Shandong Cancer Hospital and Institute, Shandong First Medical University, and Shandong Academy of Medical Sciences

(SDTHEC2020003024). Written informed consent was obtained from each participant.

**2.10. Immunohistochemistry.** Formalin-fixed, paraffin-embedded LUAD and adjacent normal tissues were fixed by 10% formalin for 48 h. The tissues were sectioned into 4  $\mu$ m thickness. Afterwards, the slices were deparaffinized utilizing xylene as well as antigen retrieval. After blockage, the sections were incubated with primary antibody against HOXA1 (1:100; ab72591; Abcam, USA), Nrf2 (1:100; 16396-1-AP; Proteintech, China), HO-1 (1:100; 27282-1-AP; Proteintech, China), and CD155 (1:100; ab267389; Abcam, USA) overnight at 4°C, followed by HRP-labeled secondary antibodies (1:200; ab97080; Abcam, USA) for 30 min at room temperature. After being stained by hematoxylin, the sections were scanned with a PathScope pathology slide scanner.

**2.11. Western Blotting.** Total proteins were extracted from tissue or cell specimens utilizing RIPA lysis, which were determined with BCA kit. 20  $\mu$ g proteins was separated via 10% SDS-PAGE and transferred onto PVDF membranes. After being blocked, they were incubated at 4°C for 12 h with primary antibodies against HOXA1 (1:1000; ab72591;

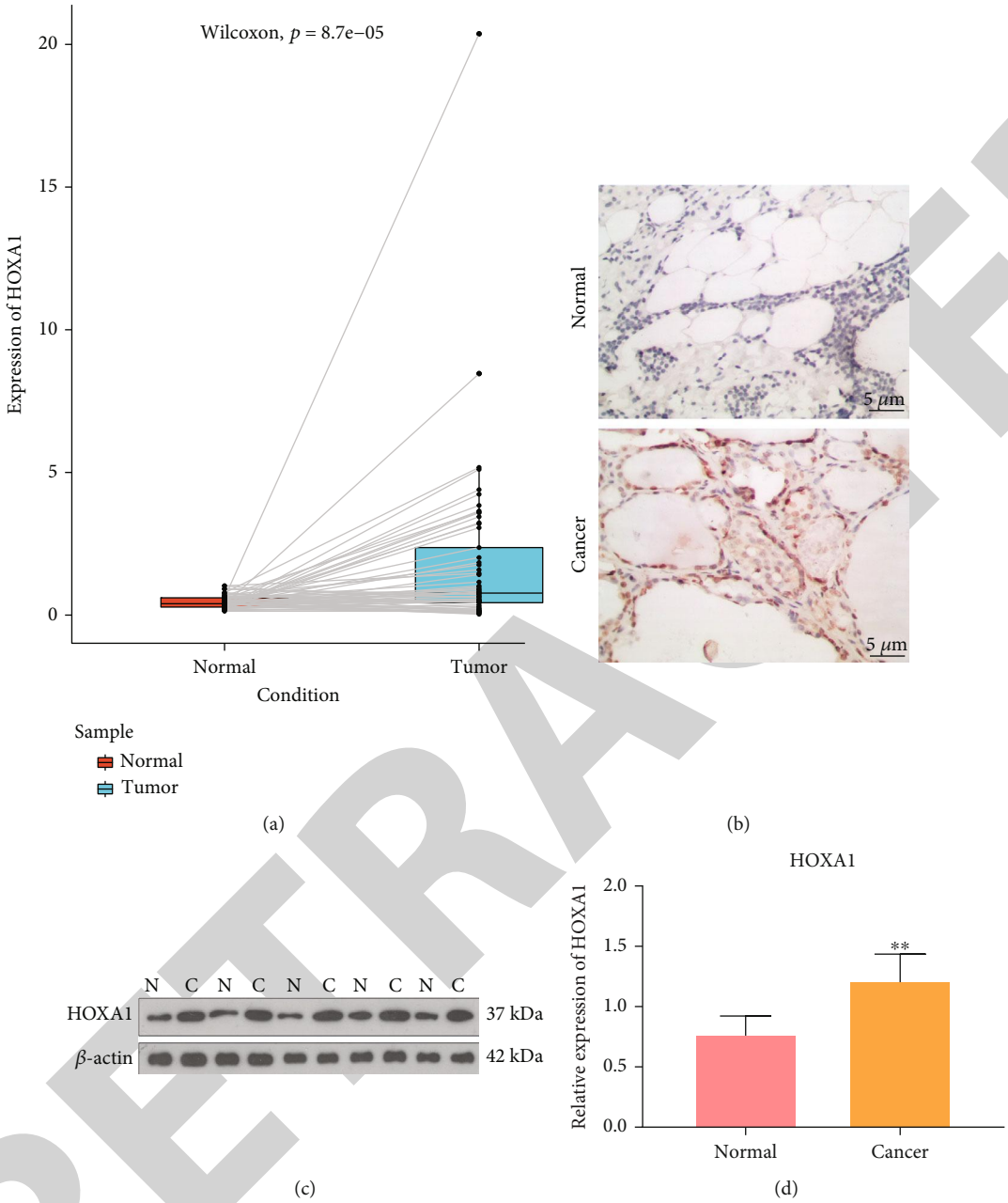


FIGURE 2: Continued.

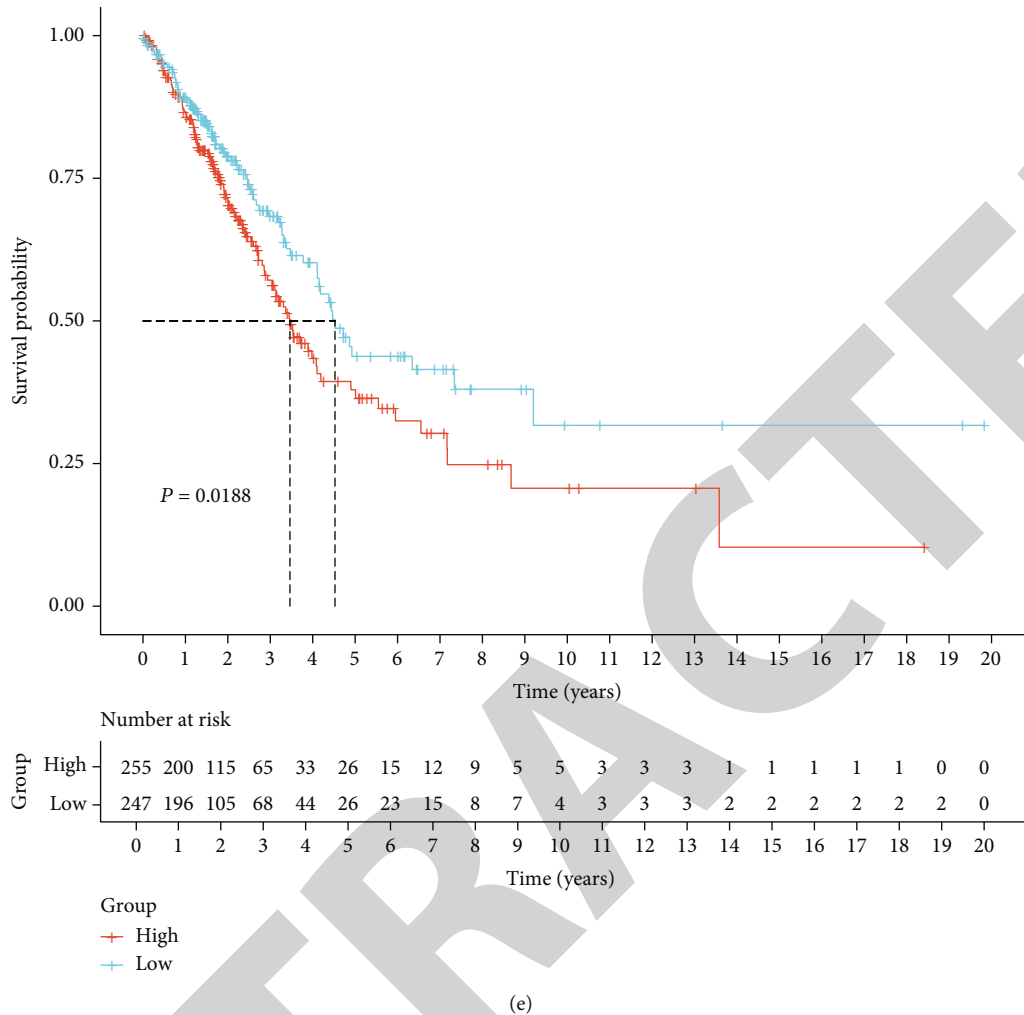


FIGURE 2: HOXA1 upregulation is a risk factor of LUAD prognosis. (a) Box plot showing upregulated HOXA1 expression in LUAD than normal specimens. (b) Validation of the expression of HOXA1 in LUAD and adjacent normal tissues utilizing immunohistochemistry. Bar = 5  $\mu$ m. Magnification, 200x. (c and d) Validation of the expression of HOXA1 in LUAD and paired normal tissues. (e) Kaplan-Meier survival curves of LUAD patients with high and low HOXA1 expression. Survival differences were estimated with log-rank test. \*\*  $p < 0.01$ .

Abcam, USA), Nrf2 (1:1000; 16396-1-AP; Proteintech, China), HO-1 (1:1000; 27282-1-AP; Proteintech, China), CD155 (1:1000; ab267389; Abcam, USA), and  $\beta$ -actin (1:5000; ab179467; Abcam, USA), followed by incubation with secondary antibodies (1:5000; ab7090 or ab7097; Abcam, USA) at room temperature for 2 h. Protein band was visualized with ECL kit. Protein expression was quantified utilizing ImageJ software, with  $\beta$ -actin as the loading control.

**2.12. Cell Culture and Isolation of CD8<sup>+</sup> T Cells.** Human LUAD cell lines A549 and NCI-H1299 were obtained from ATCC company. CD8<sup>+</sup> T cells were purified utilizing human CD8<sup>+</sup> T Cell Isolation Kit (Miltenyi Biotec, Shanghai, China). All cells were maintained in DMEM (Gibco, USA) containing 10% FBS at 37°C in a humidified incubator with 5% CO<sub>2</sub>.

**2.13. Cell Transfection.** Transfection of 100 nM siRNAs against HOXA1 (GenePharma Co., Ltd., Shanghai, China) into A549 or NCI-H1299 cell line was implemented via Lipofectamine<sup>®</sup> RNAiMAX reagent (Thermo, USA). Following 24 h, HOXA1 expression was evaluated with western blot. The siRNA sequences were as follows: si-HOXA1#1, 5'-CCCAUGGACUCAUAAACAATT-3', 5'-UUGUUUAUGAGUCCAUGGGTT-3'; si-HOXA1#1, 5'-GCCUUUGGAAGCUCUUGAATT-3', 5'-UUCAAGAGCUCCAAGGCTT-3'.

**2.14. Colony Formation Assay.** A549 and NCI-H1299 cells (1 × 10<sup>3</sup> cells/well) were seeded onto a 6-well plate. Following culture for 14 days, formed colonies were fixed by 1 ml 4% paraformaldehyde (Sigma, USA) for 15 min as well as 500  $\mu$ l Giemsa stain (Sigma, USA) for 20 min at room

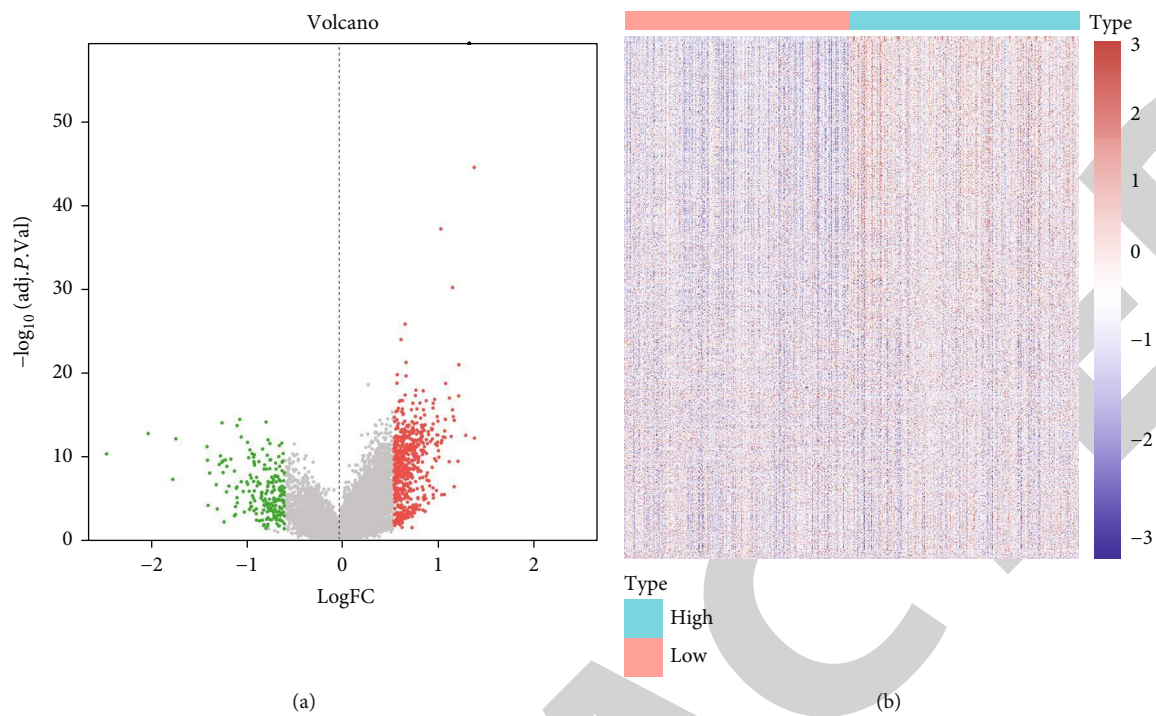
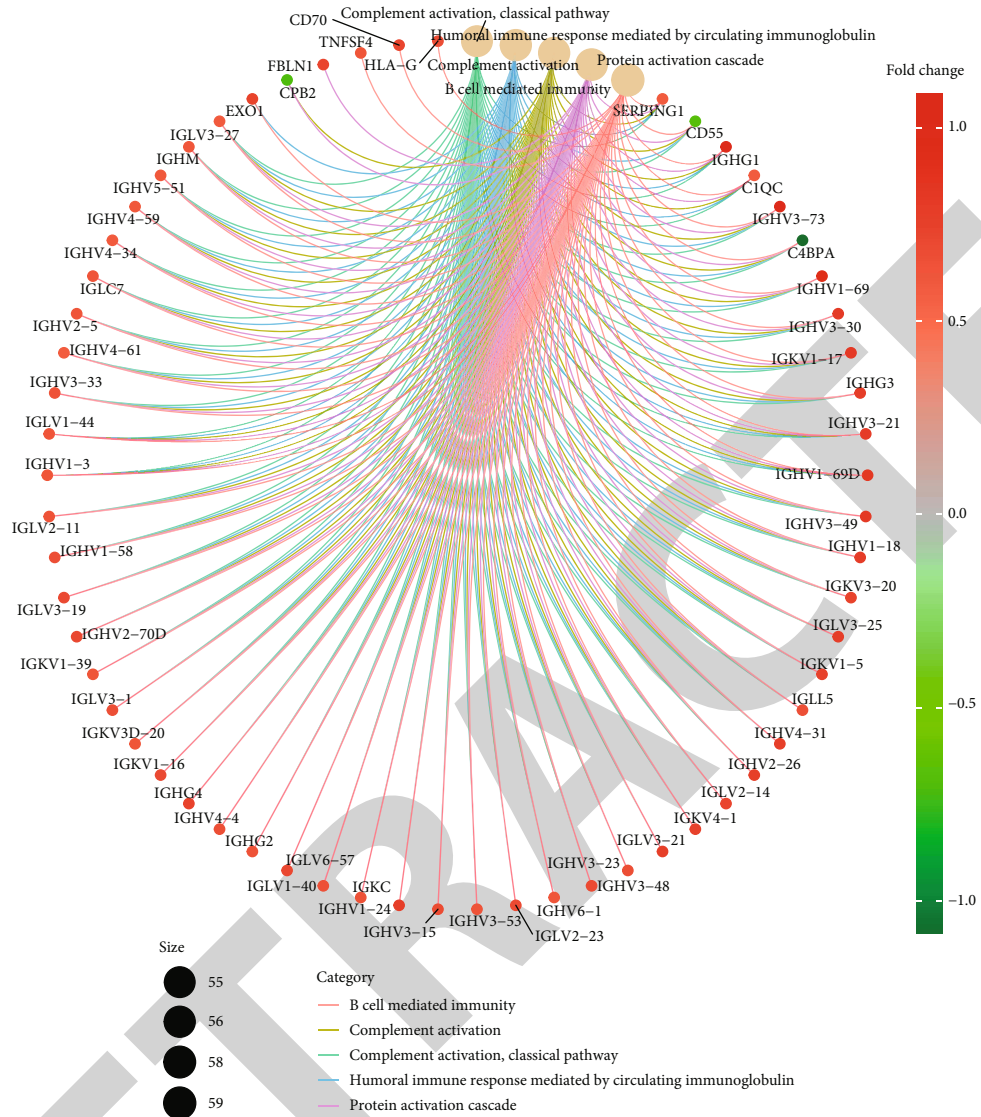


FIGURE 3: Continued.



(c)

FIGURE 3: Continued.

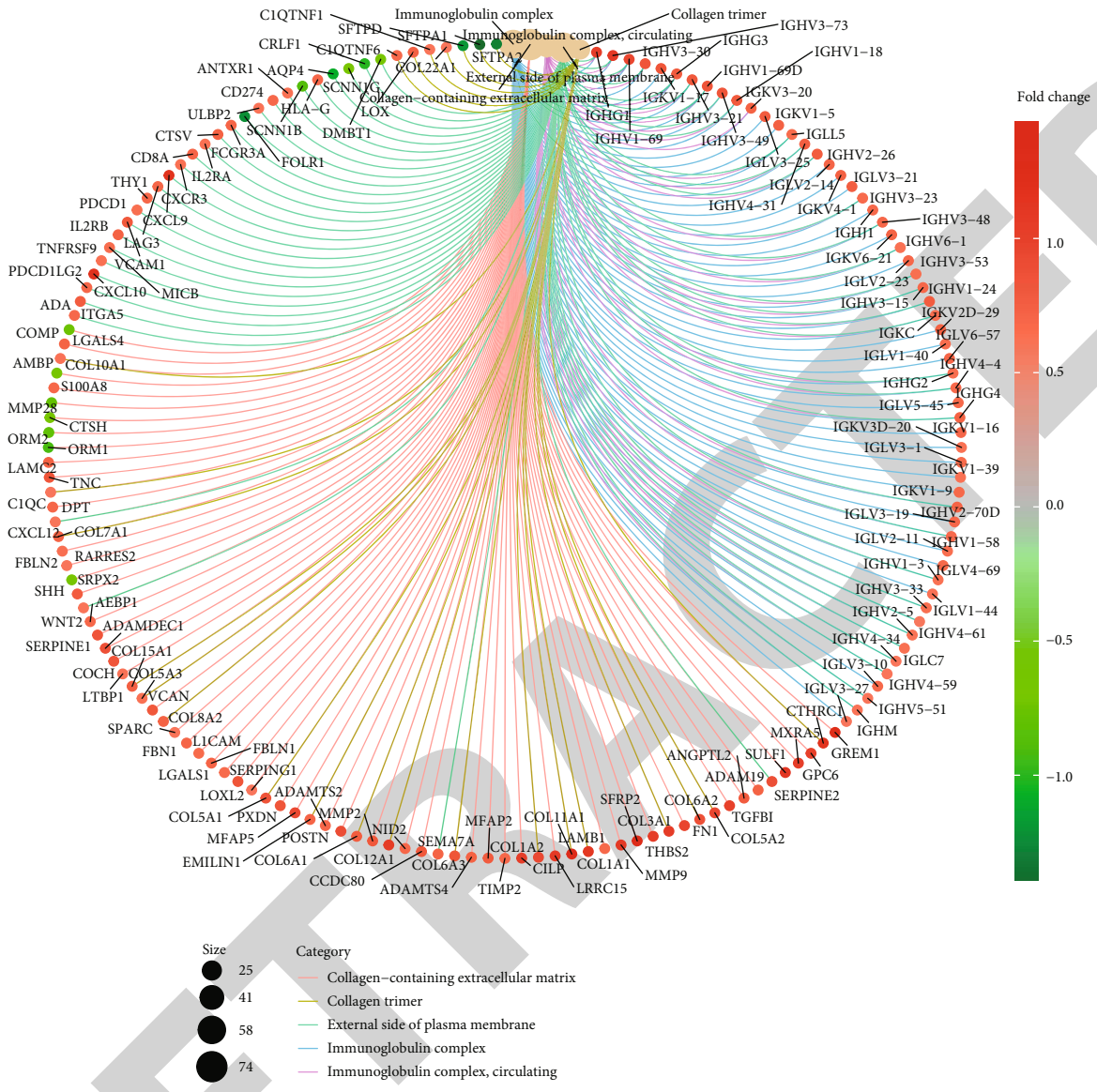


FIGURE 3: Continued.

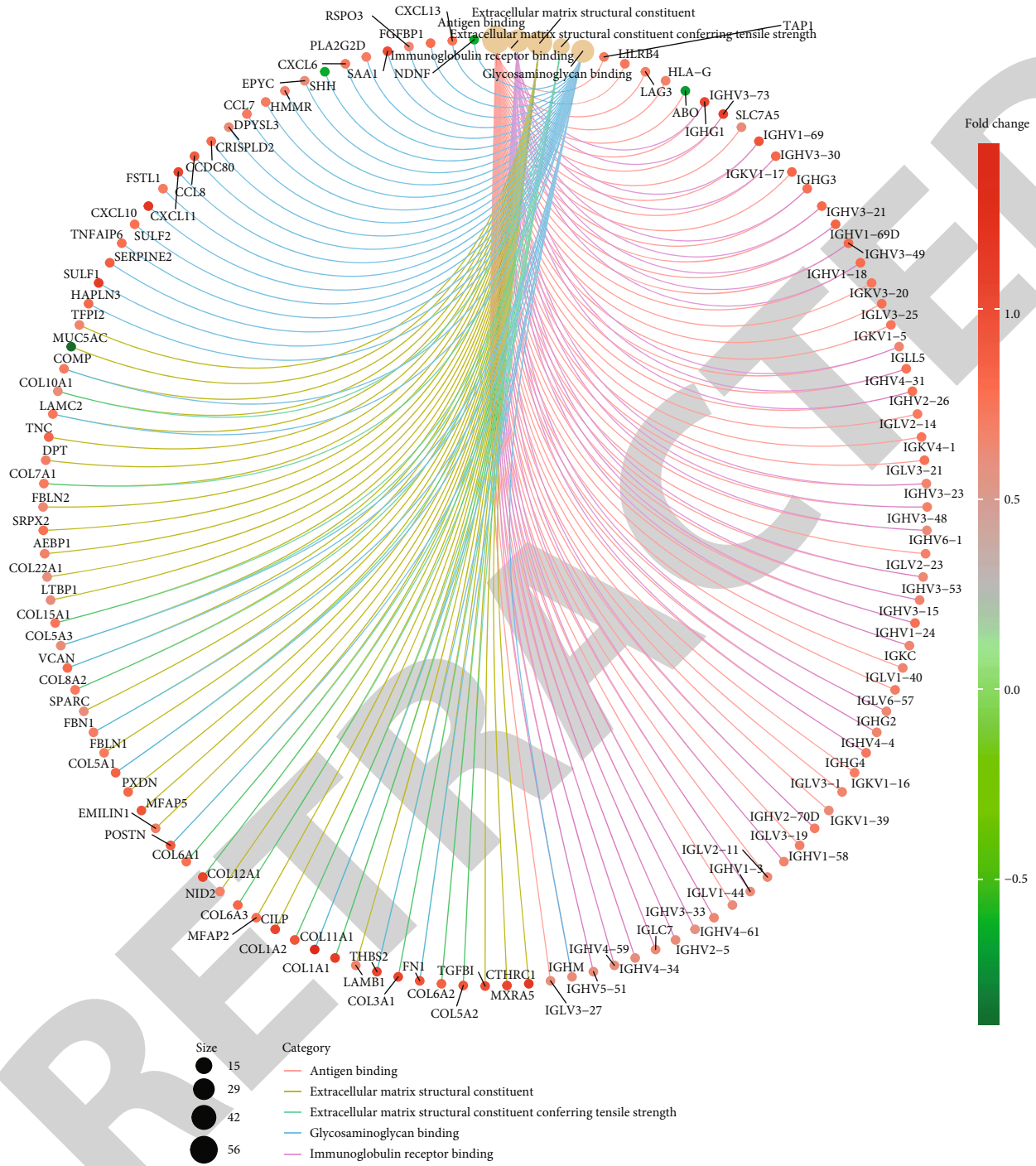


FIGURE 3: Continued.



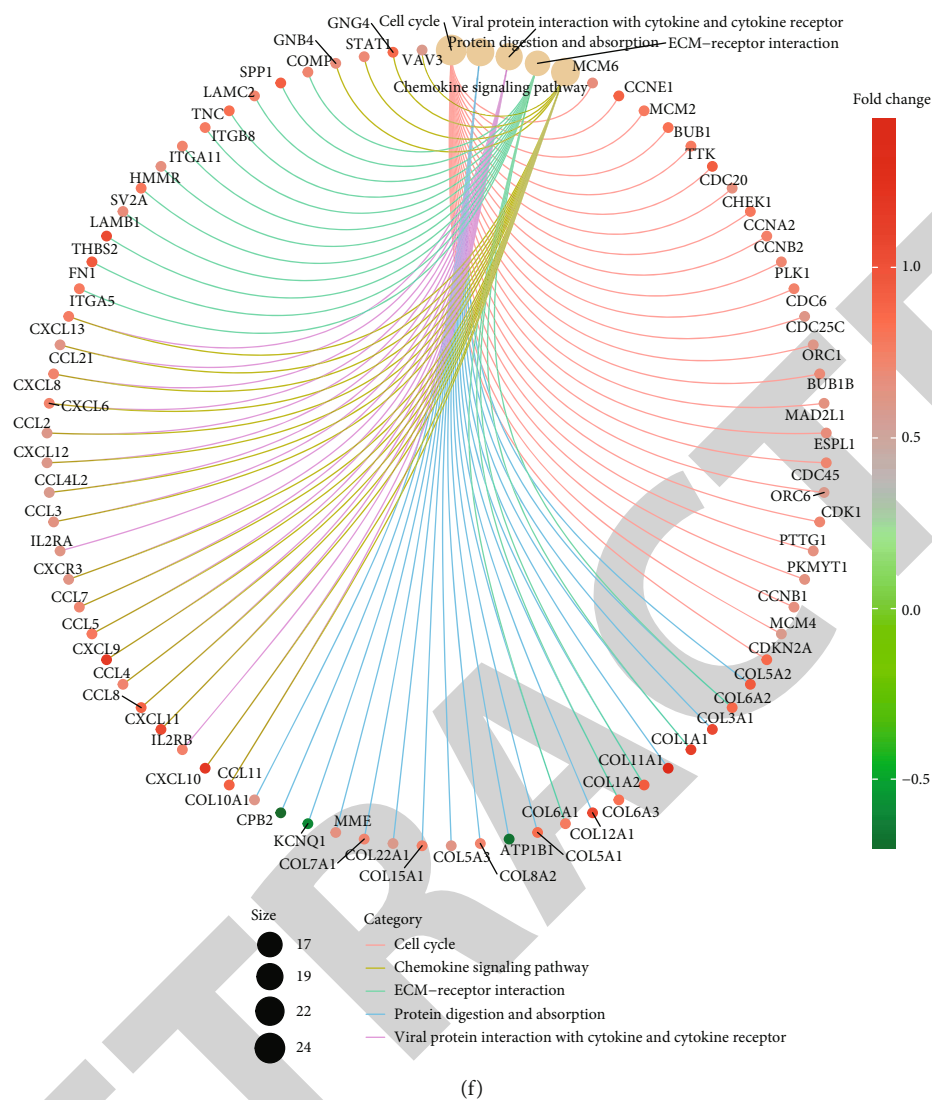


FIGURE 3: Analysis of HOXA1-relevant genes and involved biological significance in LUAD. (a and b) Volcano plots and heatmap visualizing HOXA1-relevant genes in LUAD. Red meant upregulation while blue or green meant downregulation in LUAD samples with high HOXA1 expression. (c–f) Analysis of biological process, cellular component, molecular function, and KEGG pathways involving HOXA1-relevant genes.

temperature. The colonies were investigated with an inverted light microscope (Olympus, Japan).

**2.15. 5-Ethynyl-2'-deoxyuridine (EdU) Staining.** Fixation of A549 and NCI-H1299 cells was implemented by 4% paraformaldehyde for 15 min, as well as permeability by 0.3% Triton X-100 reagent for 15 min. EdU staining reagent was added onto wells in the dark for 30 min. Afterwards, anti-fluorescence quencher was added as well as stained cells were investigated with a fluorescence microscope (Olympus, Japan).

**2.16. Cell Migration Assay.** Transwell (Corning, USA) was utilized for assessing cell migration. A549 and NCI-H1299 cells ( $3 \times 10^5$  cells/ml) with 200  $\mu$ l serum-free DMEM were planted onto the upper chamber. 600  $\mu$ l DMEM plus 10% FBS was added to the lower chamber. At 48 h, the cells on the lower chamber were stained by 10% Giemsa for 2 h at

room temperature. Stained cells were counted with a light microscope (Olympus, Japan).

**2.17. Immunofluorescence.** A549 and NCI-H1299 cells were maintained in culture dishes. Fixation of the cells was implemented with 4% paraformaldehyde for 15 min. Following being washed by PBS plus 0.05% Tween-20, they were permeabilized utilizing 0.3% Triton X-100 for 5 min, along with blockage by 1% BSA for 30 min as well as incubation with HOXA1 (1:100; ab72591; Abcam, USA), Nrf2 (1:100; 16396-1-AP; Proteintech, China), and HO-1 (1:100; 27282-1-AP; Proteintech, China) antibodies at 4°C overnight, followed by Alexa Fluor® 488 (1:100; ab150077; Abcam, USA) or Alexa Fluor® 647 (1:100; ab15011; Abcam, USA) antibodies. Nucleus was stained with DAPI. Immunofluorescence images were acquired with a confocal microscope (Olympus, Japan).

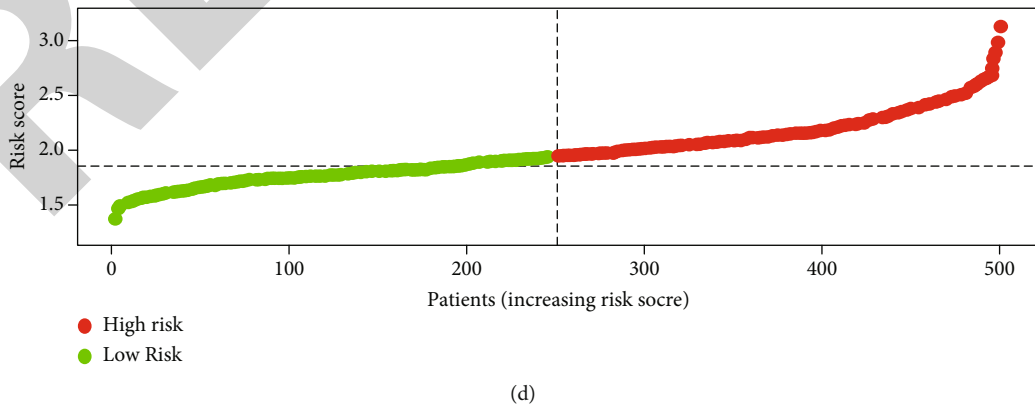
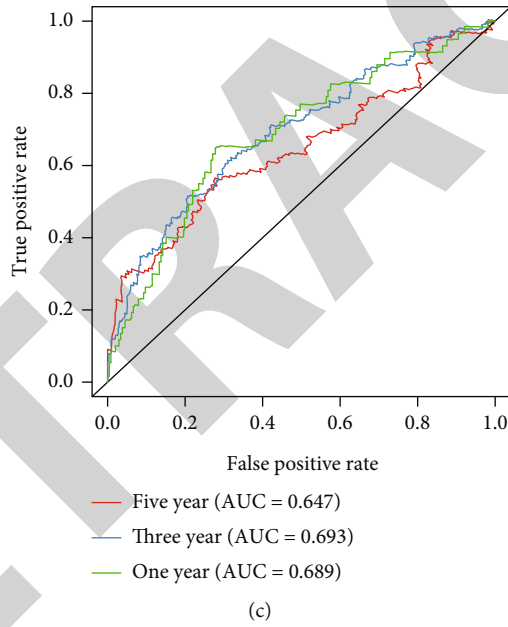
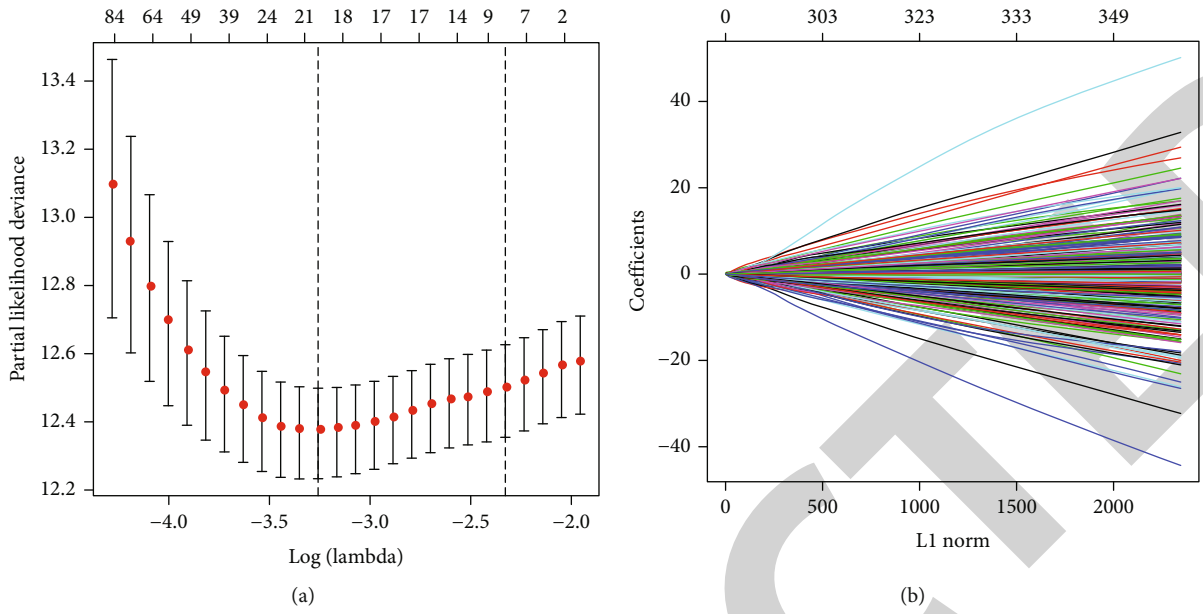
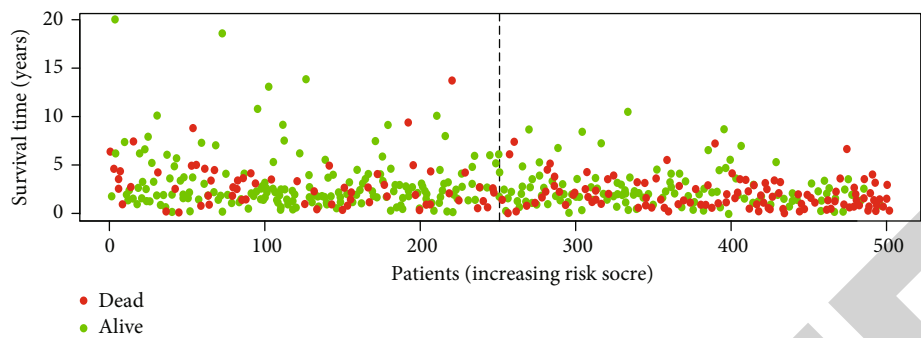
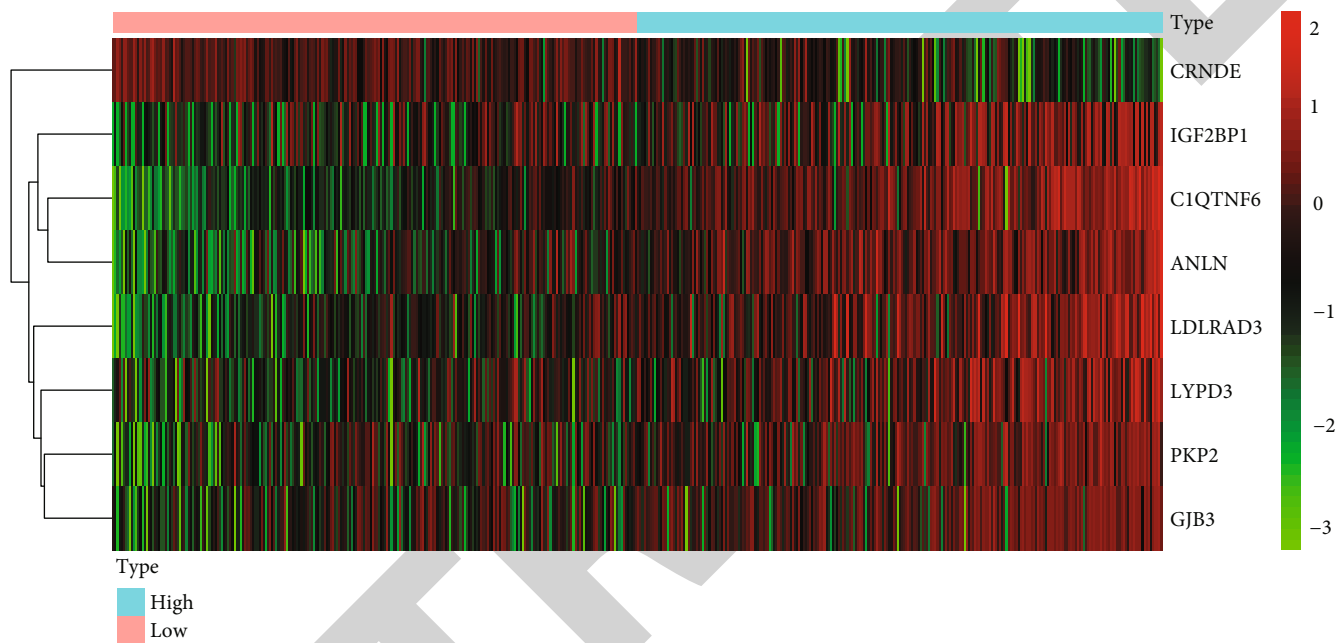


FIGURE 4: Continued.

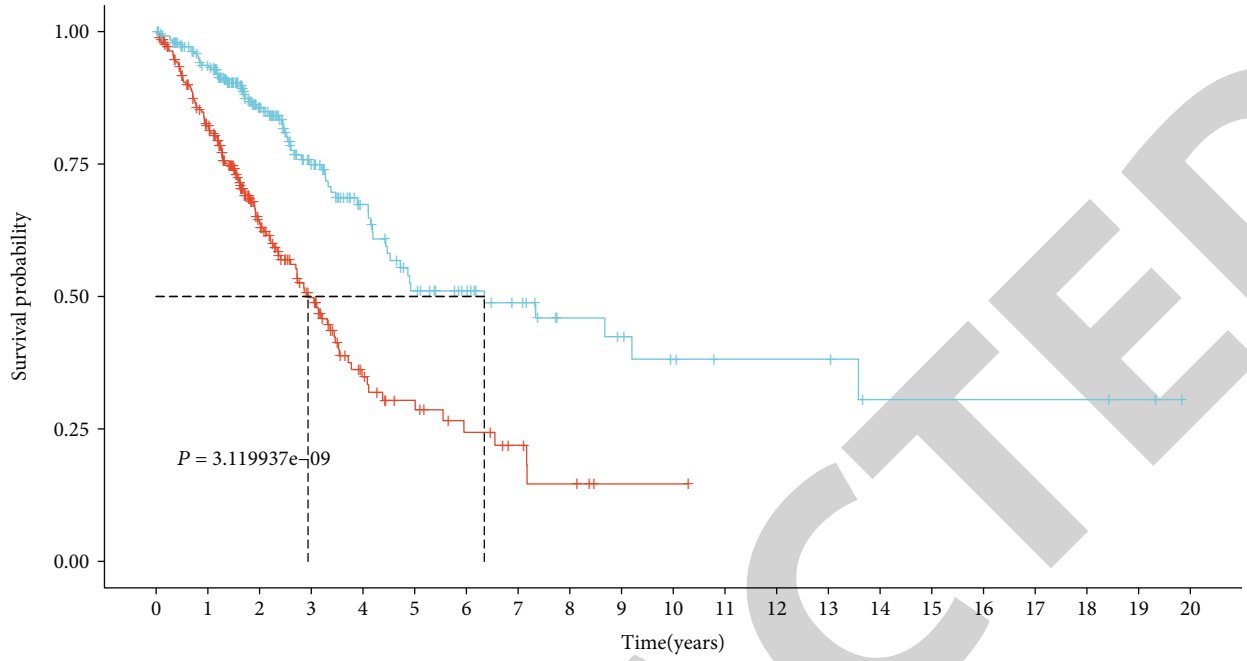


(e)



(f)

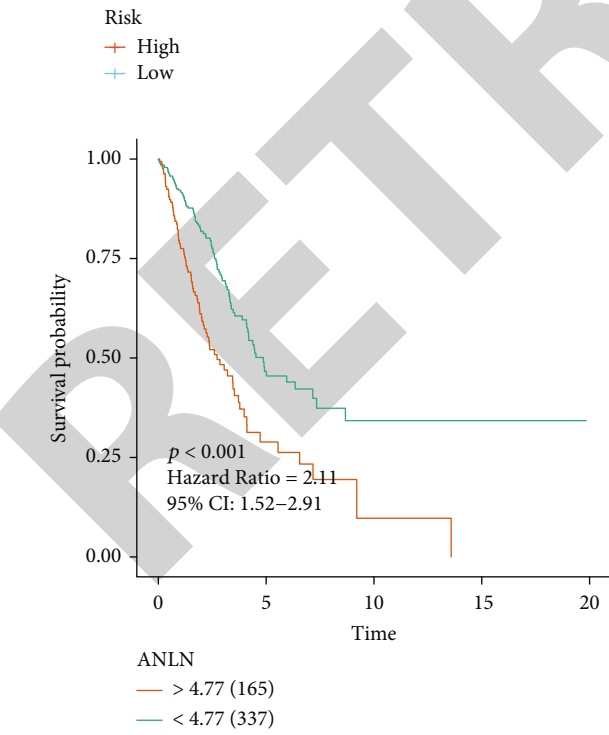
FIGURE 4: Continued.



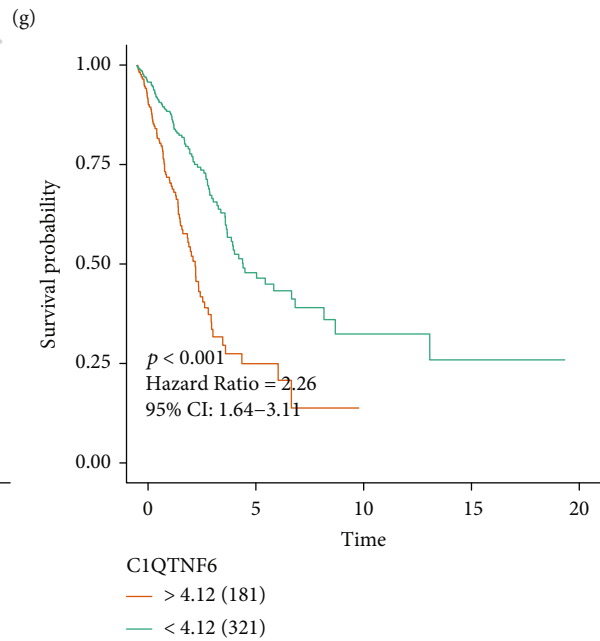
Number at risk

Risk	0	1	2	3	4	5	6	7	8	9	10	11	12	13	14	15	16	17	18	19	20
High	251	184	92	53	25	17	11	7	4	1	1	0	0	0	0	0	0	0	0	0	0
Low	251	212	128	80	52	35	27	20	13	11	8	6	6	6	3	3	3	3	3	2	0

Time(years)

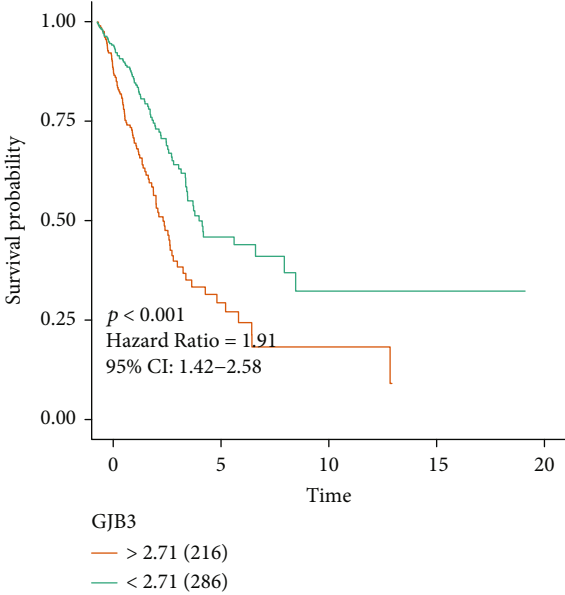


(h)

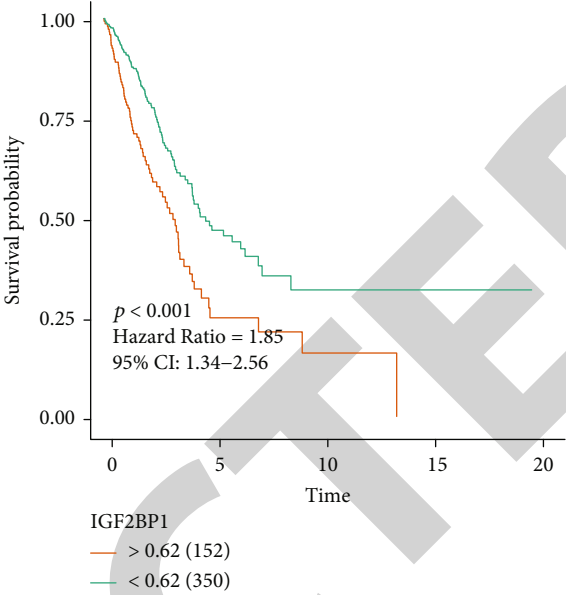


(i)

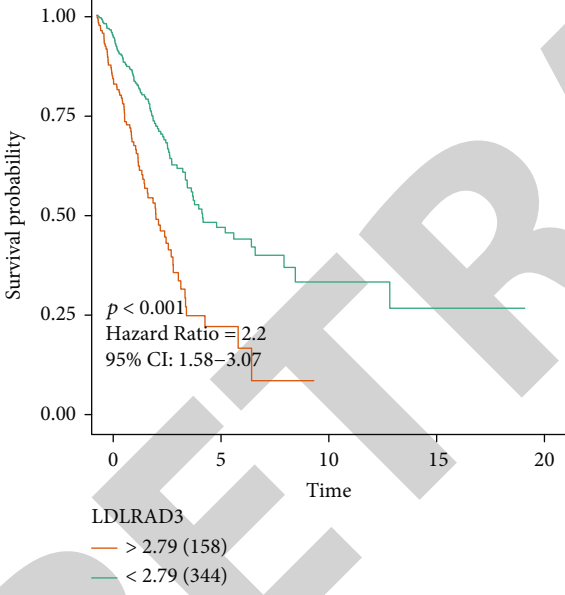
FIGURE 4: Continued.



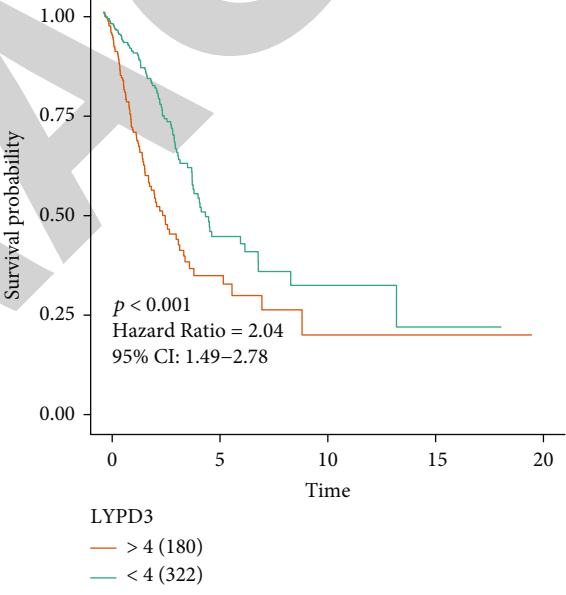
(j)



(k)



(l)



(m)

FIGURE 4: Continued.

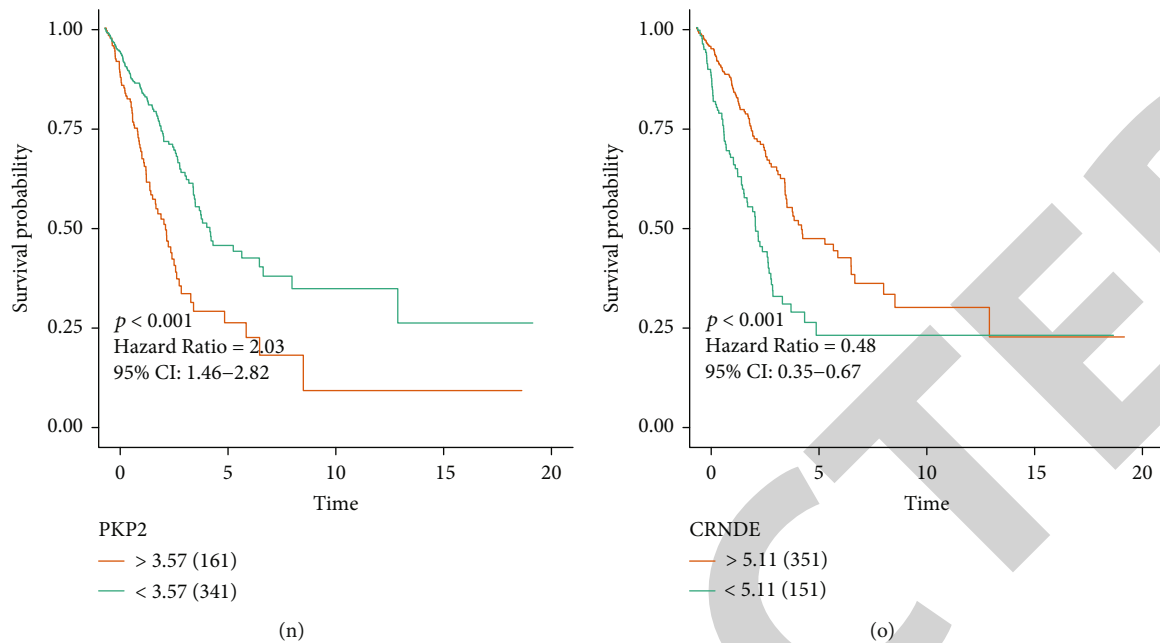


FIGURE 4: Construction of a reliable HOXA1-derived gene signature for LUAD prognosis. (a) Partial likelihood deviance for LASSO coefficient profiling. The red dot indicated the partial likelihood value, the gray line indicated the standard error, and vertical dotted line meant the optimal values by 1 - standard error. (b) LASSO coefficient profiling of candidate genes. (c) ROC curves verifying the predictive accuracy and sensitivity of HOXA1-derived risk score in LUAD survival. (d-f) Distribution of risk score, survival status, and expression pattern of each variable in high or low-risk groups. Vertical dotted line meant the cutoff value of two groups. Red dot represented dead status and green dot represented alive status. Red meant upregulation while green meant downregulation. (g) Kaplan-Meier curves showing survival difference between high and low-risk groups. (h-o) Kaplan-Meier survival curves demonstrating the prognostic value of ANLN, C1QTNF6, GJB3, IGF2BP1, LDLRAD3, LYPD3, PKP2, and CRNDE across LUAD patients.

**2.18. Cell Coculture System.** CD8<sup>+</sup> T cells were sorted as well as cocultured with A549 and NCI-H1299 cells in normal culture plates. The cocultured cells were incubated for two days at 37°C in an atmosphere of 5% CO<sub>2</sub>.

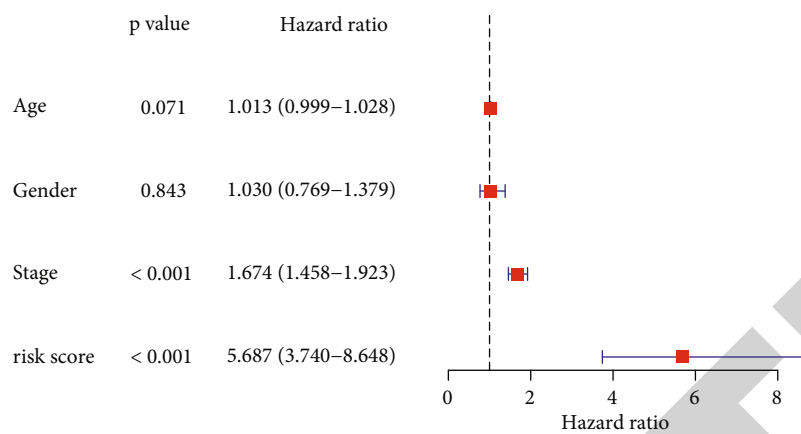
**2.19. Flow Cytometry.** CD8<sup>+</sup> T cells were stained by PE-conjugated anti-CD8 antibody. Then, A549 and NCI-H1299 cells were stained by V450-conjugated anti-IFN- $\gamma$  antibody. Cocultured cells were assessed with flow cytometry.

**2.20. Statistical Analyses.** Statistical analyses were carried out utilizing Student's *t* test, Wilcoxon test, or ANOVA followed by Tukey's test with R language (version 4.0.1) or GraphPad Prism (version 8.0). Data are expressed as mean  $\pm$  standard deviation derived from at least three independent assays. Correlation analysis was carried out with the Pearson or Spearman correlation test.  $p < 0.05$  indicated statistically significant.

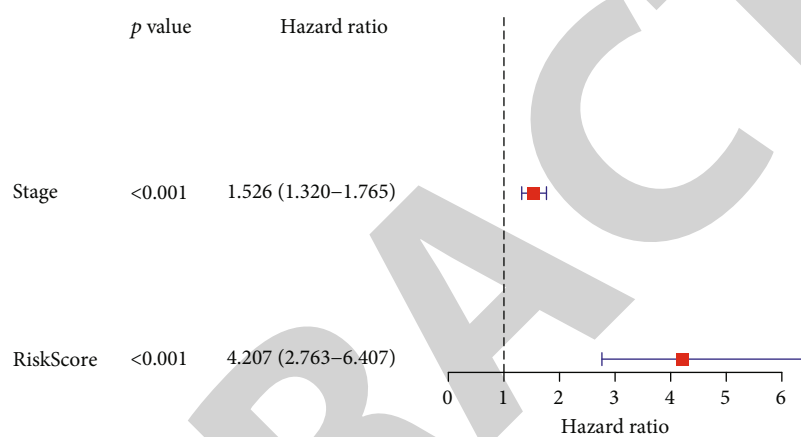
### 3. Results

**3.1. Expression Pattern and Immunological and Prognostic Significance of HOXA1 across Pancancer.** We firstly presented pancancer analysis of HOXA1 gene with TIMER web server. In Figure 1(a), HOXA1 expression was markedly

upregulated in CESC, CHOL, ESCA, glioblastoma multiforme (GBM), head and neck squamous cell carcinoma (HNSC), kidney renal papillary cell carcinoma (KIRP), LUAD, lung squamous cell carcinoma (LUSC), prostate adenocarcinoma (PRAD), and stomach adenocarcinoma (STAD) in comparison to normal tissues. Oppositely, HOXA1 expression was markedly reduced in breast cancer (BRCA), colon adenocarcinoma (COAD), kidney chromophobe (KICH), and kidney renal clear cell carcinoma (KIRC) than normal tissues. TMB is an emerging biomarker of immunotherapeutic response [34]. We analyzed the correlations of HOXA1 with TMB across pancancer. In Figure 1(b), we found that HOXA1 exhibited negative correlations to TMB in BLCA, COAD, LIHC, and UCS but had markedly positive correlations to TMB in KIRC, LGG, LUAD, PAAD, and SARC. Moreover, we observed that HOXA1 was positively associated with immune checkpoints in most cancer types (Figure 1(c)). These data indicated the potential immunological role of HOXA1 across pancancer. Prognostic significance of HOXA1 was further explored in each cancer type via univariate Cox regression analysis. As shown in Figure 1(d), HOXA1 acted as a risk factor for OS of ACC, CESC, HNSC, KICH, KIRC, LAML, LGG, LUAD, THCA, THYM, and UVM. Furthermore, we observed the positive correlations of HOXA1 with worse DSS of ACC, CESC, HNSC, KIRC, LGG, LUAD, UCEC, and UVM



(a)



(b)

FIGURE 5: Continued.

RETRACTED

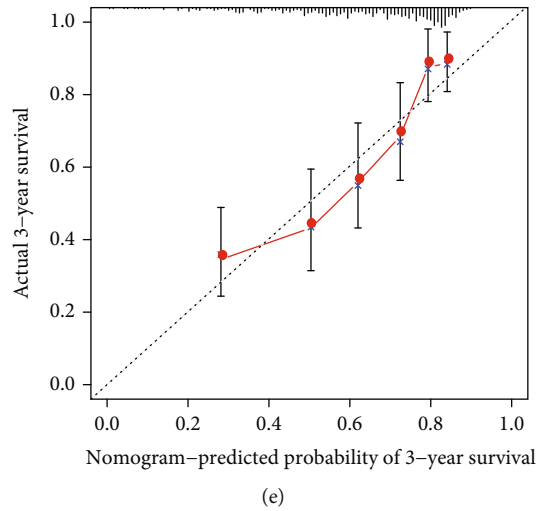
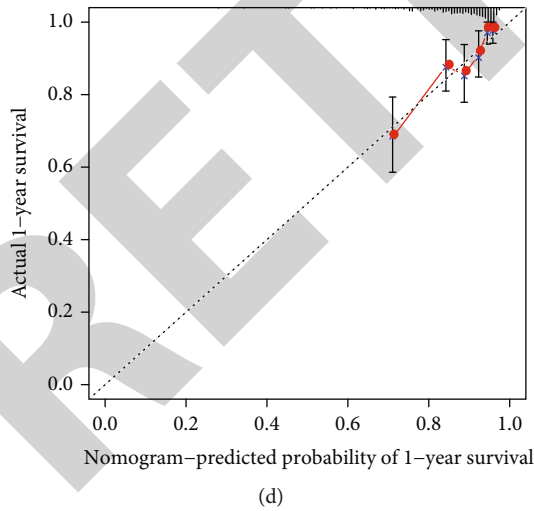
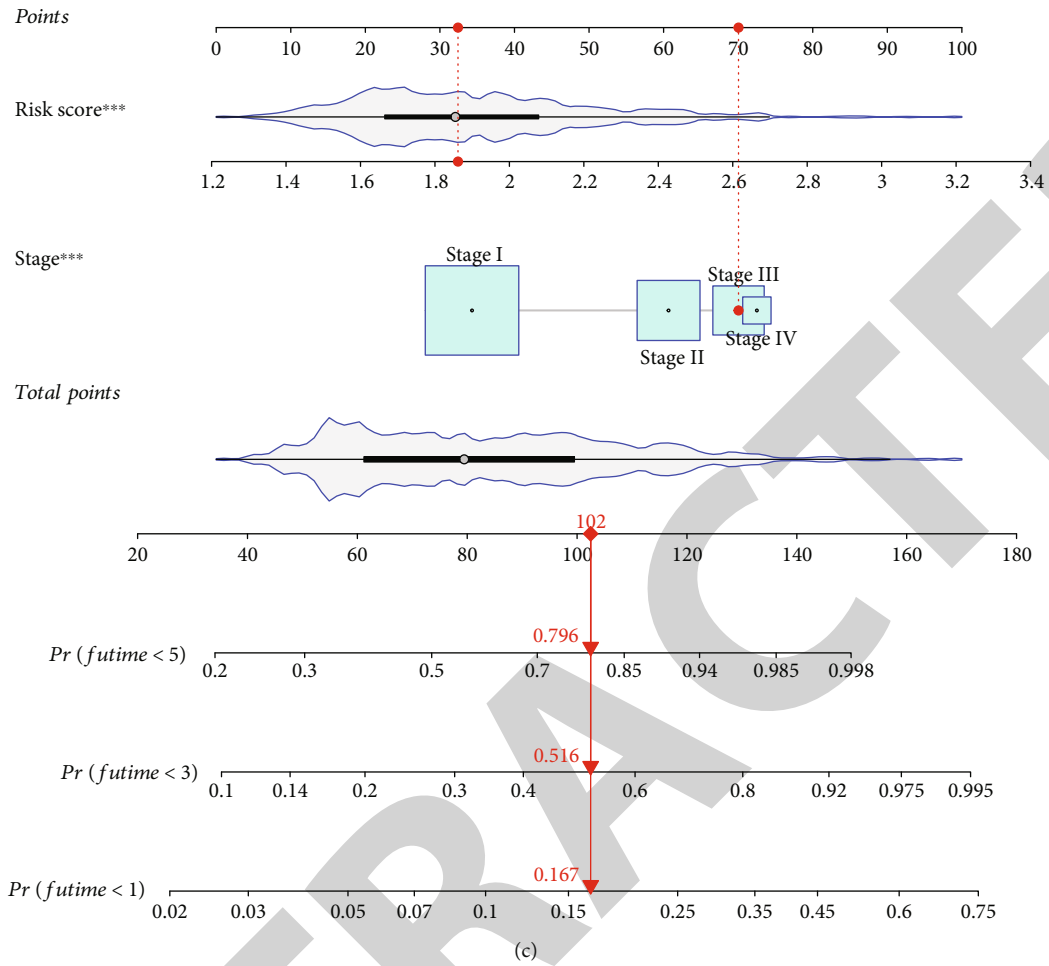


FIGURE 5: Continued.



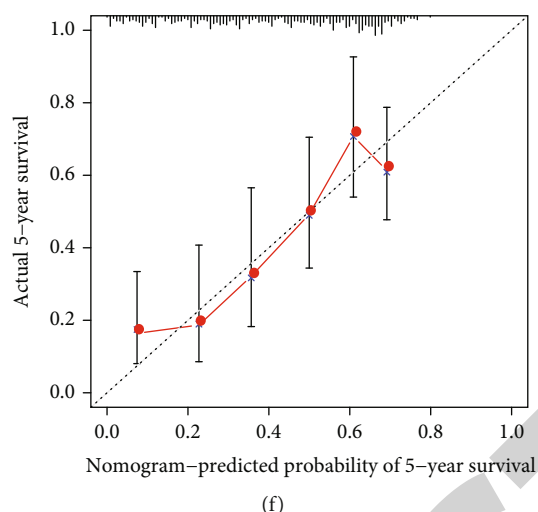


FIGURE 5: HOXA1-derived gene signature acts as an independent prognostic predictor of LUAD. (a and b) Uni- and multivariate Cox regression analyses for evaluating the associations of clinicopathological features and HOXA1-derived risk score with LUAD prognosis. (c) Establishment of a nomogram in predicting one-, three-, and five-year survival duration. (d–f) Calibration curves verifying the relationships of nomogram-estimated with actual survival duration.

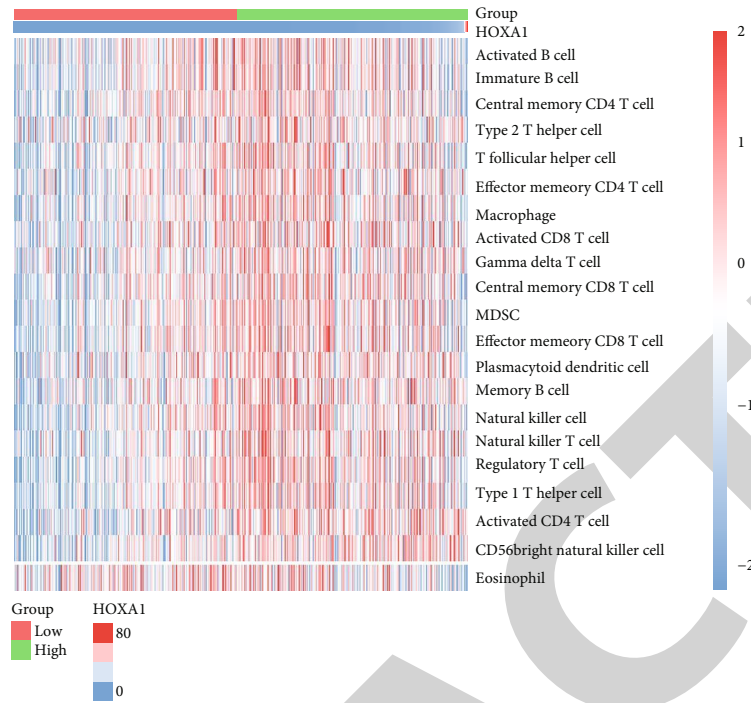
(Figure 1(e)). Additionally, HOXA1 was linked to more unfavorable PFI of ACC, CESC, HNSC, KIRC, LGG, LUAD, READ, STAD, and UVM. The above data suggested that HOXA1 may contribute to cancer progression (Figure 1(f)).

**3.2. HOXA1 Upregulation Is a Risk Factor of LUAD Survival Outcomes.** In TCGA cohort, we investigated that HOXA1 expression was markedly upregulated in LUAD than normal specimens (Figure 2(a)). The abnormal expression of HOXA1 was further verified in 5 paired LUAD and adjacent normal specimens. Our immunohistochemistry confirmed that HOXA1 expression was markedly upregulated in LUAD than normal specimens (Figure 2(b)). Western blot also confirmed the prominent upregulation of HOXA1 expression in LUAD (Figures 2(c) and 2(d)). With the median HOXA1 expression, LUAD cases were classified as high or low HOXA1 expression groups. As depicted in Figure 2(e), patients with low HOXA1 expression possessed the survival advantage than those with high HOXA1 expression. The above finding confirmed that HOXA1 upregulation served as an emerging risk factor of LUAD survival outcomes.

**3.3. Analysis of HOXA1-Relevant Genes and Involved Biological Significance.** This study identified 790 HOXA1-relevant genes with  $|FC| > 1.5$  along with  $p < 0.05$  (Supplementary Table 1). Among them, 581 genes exhibited significantly high expression, while 209 genes displayed markedly low expression in high HOXA1 expression group (Figures 3(a) and 3(b)). GO and KEGG enrichment analyses were implemented for uncovering potential biological significance. In Figure 3(c), HOXA1-relevant genes mainly participated in mediating biological processes of B cell-mediated immunity, complement activation, humoral immune response-mediated by circulating immunoglobulin, and protein activation cascade. Also, they might be involved in modulating cellular components of

collagen-containing extracellular matrix, collagen trimer, external side of plasma membrane, or immunoglobulin complex (Figure 3(d)). In Figure 3(e), they possessed the molecular functions of antigen binding, extracellular matrix structural constituent, glycosaminoglycan binding, or immunoglobulin binding. Moreover, we investigated that these HOXA1-relevant genes were markedly enriched in cell cycle, chemokine signaling pathway, ECM-receptor interaction, protein digestion and absorption, and viral protein interaction with cytokine and cytokine receptor pathways (Figure 3(f)). The above data highlighted the important biological significance of the HOXA1-relevant genes.

**3.4. Construction of a Reliable HOXA1-Derived Gene Signature for LUAD Prognosis.** The univariate Cox regression analyses uncovered that 358 HOXA1-derived genes were in relation to LUAD prognosis (Supplementary Table 2). Afterwards, we presented LASSO Cox regression for selecting highly variable variables. As a result, eight HOXA1-derived genes were included in this model (Figures 4(a) and 4(b)). The HOXA1-derived risk score of each LUAD patient was calculated in line with the following formula: risk score =  $0.0728251240226131 * LDLRAD3$  expression +  $0.0828073308429417 * C1QTNF6$  expression +  $0.0140814604116393 * ANLN$  expression +  $(-0.00119766324400233) * CRNDE$  expression +  $0.0050720950545627 * LYPD3$  expression +  $0.0157526948322403 * PKP2$  expression +  $0.0117856548667349 * IGF2BP1$  expression +  $0.00659735008359115 * GJB3$  expression. ROCs were implemented to estimate the efficacy of this HOXA1-derived gene signature. AUC was  $> 0.6$ , confirming the favorable predictive performance of this gene signature (Figure 4(c)). With the median risk score, we classified LUAD patients as high or low HOXA1 expression groups (Figure 4(d)). High HOXA1 expression group had more patients with dead status (Figure 4(e)). Heatmap visualized the expression patterns of variables in two groups. We

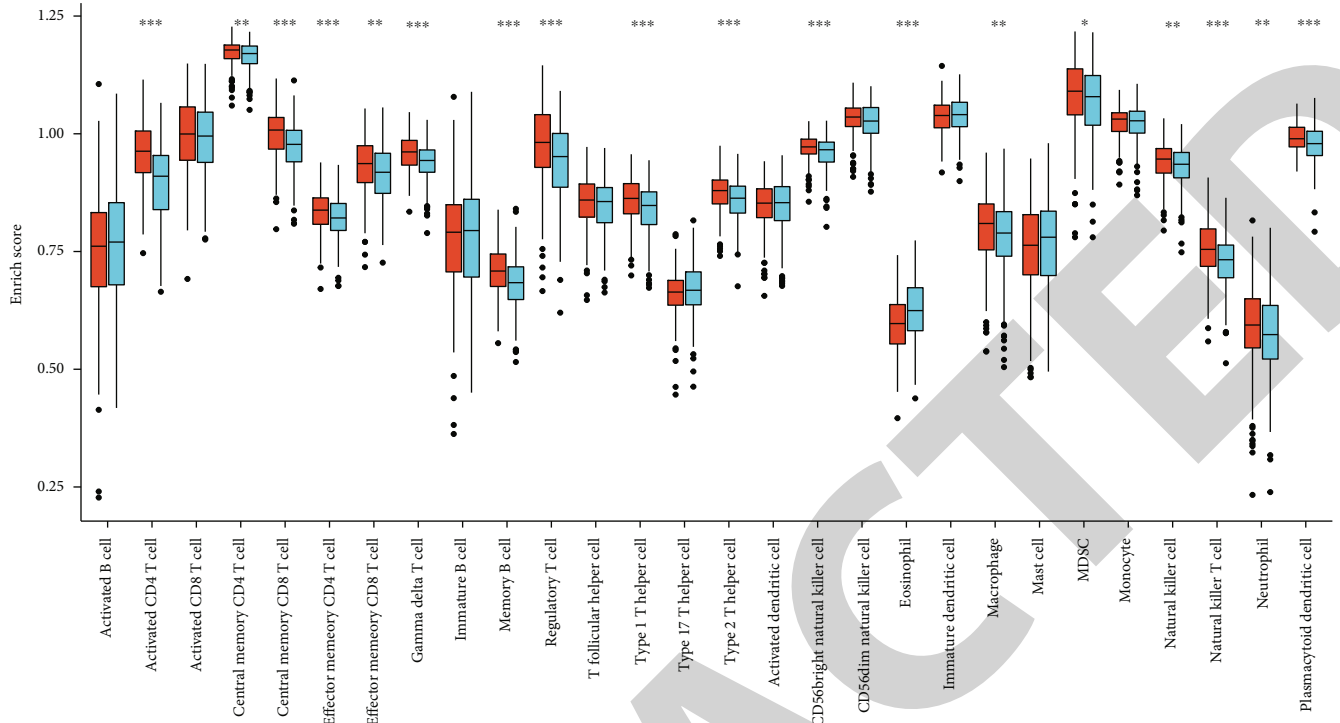


(a)

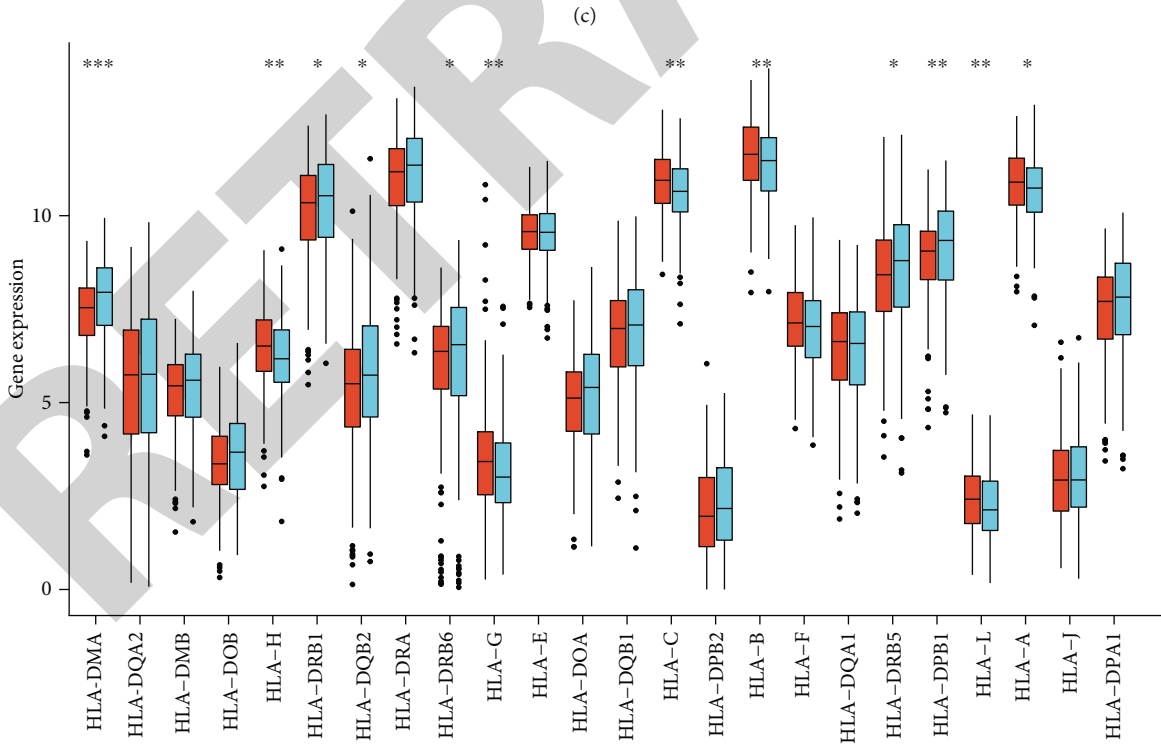


(b)

FIGURE 6: Continued.



Risk  
High  
Low



Risk  
High  
Low

(d)

FIGURE 6: Continued.

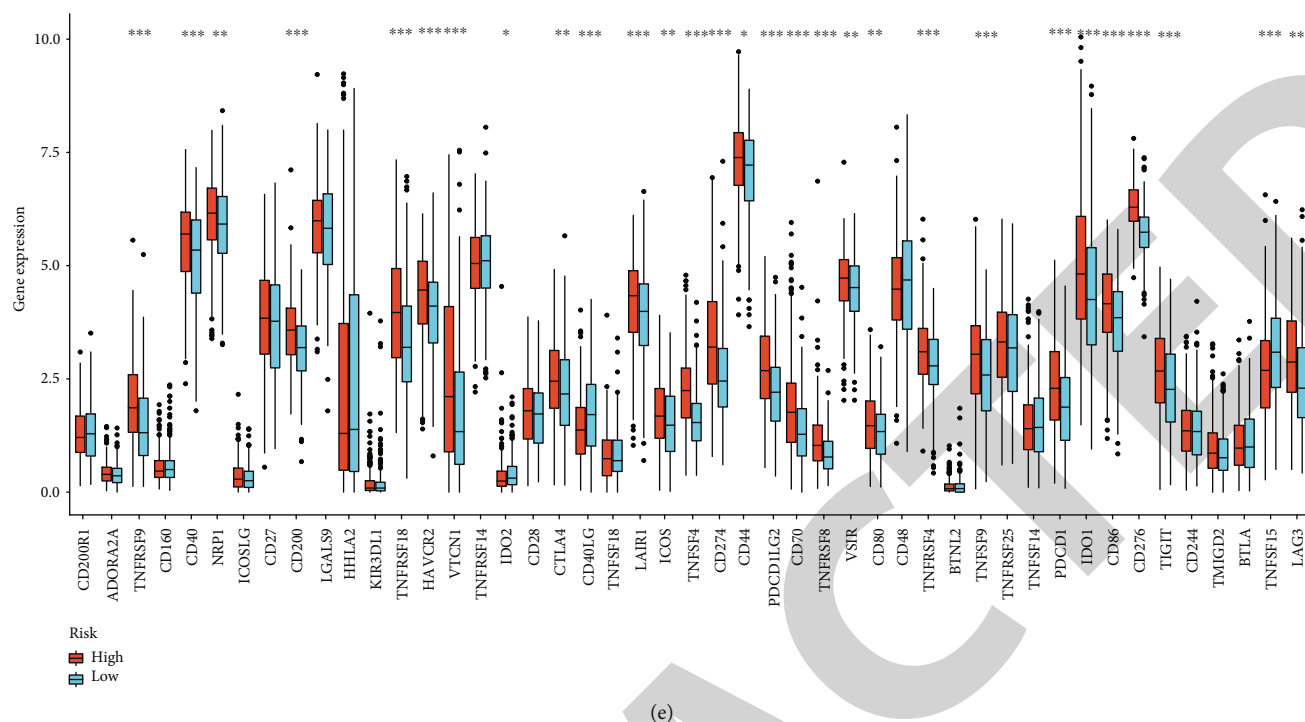
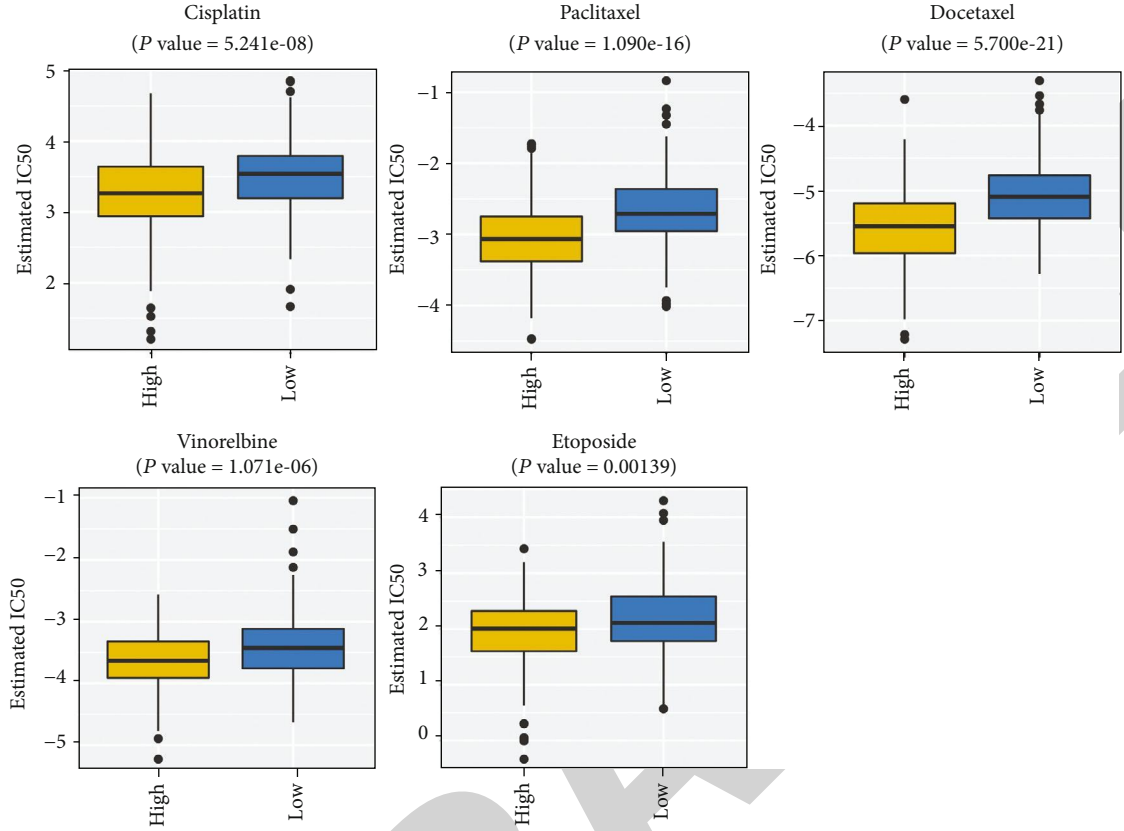


FIGURE 6: Both HOXA1 and HOXA1-derived gene signature are associated with tumor immunity in LUAD. (a) Heatmap showing diverse immune cell infiltrations in LUAD specimens with high or low HOXA1 expression. Blue meant low infiltration levels while red meant high infiltration levels. (b) Correlations of HOXA1 with immune checkpoints and HLA gene family across LUAD samples. Solid line represented a positive correlation and dashed line represented a negative correlation. The darker the box filled, the stronger the correlation. (c) Box plots showing the differences in infiltration levels of diverse immune cells in high and low HOXA1-derived risk score. (d) Box plots demonstrating the differences in mRNA expression of HLA genes in high and low HOXA1-derived risk score. (e) Box plots visualizing the differences in immune checkpoint expressions in high or low HOXA1-derived risk score. \* $p < 0.05$ , \*\* $p < 0.01$ , and \*\*\* $p < 0.001$ .

observed the prominent upregulation of CRNDE in low HOXA1 expression group while the marked upregulation of LDLRAD3, C1QTNF6, ANLN, LYPD3, PKP2, IGF2BP1, and GJB3 in high HOXA1 expression group (Figure 4(f)). There was a prominent survival difference in CRNDE between high- and low-risk groups. High-risk patients presented distinctly poorer survival outcomes than low-risk patients (Figure 4(g)). We also evaluated the prognostic value of each variable in LUAD. We observed that ANLN, C1QTNF6, GJB3, IGF2BP1, LDLRAD3, LYPD3, and PKP2 upregulation was positively associated with shortened clinical outcomes across LUAD patients (Figures 4(h)–4(n)). In contrast, low expression of CRNDE was in relation to more unfavorable prognosis of LUAD (Figure 4(o)).

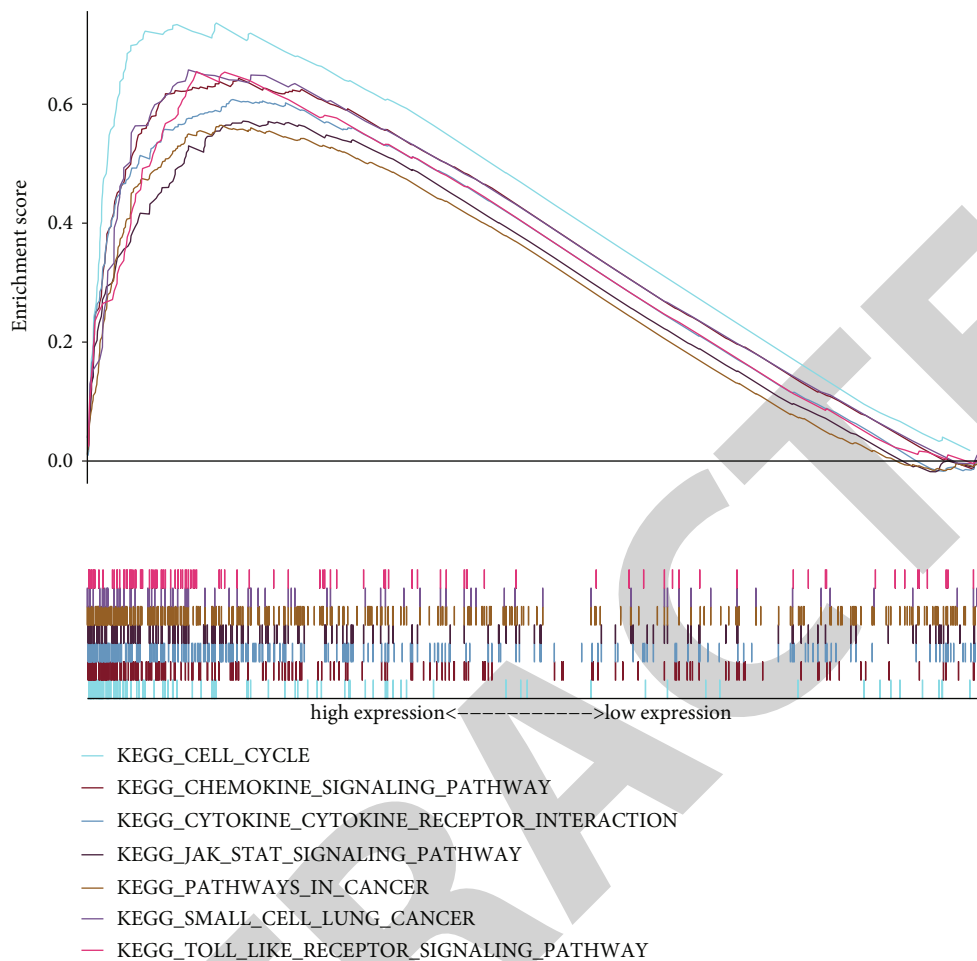
**3.5. HOXA1-Derived Gene Signature Is an Independent Predictor of LUAD Survival.** Through the univariate Cox regression analysis, we investigated that both stage and HOXA1-derived risk score were in relation to worse prognosis of LUAD patients (Figure 5(a)). Moreover, the multivariate Cox regression analysis suggested that both stage and HOXA1-derived risk score may independently predict patients' survival outcomes (Figure 5(b)). Based on the two risk factors, a nomogram was established for LUAD prognosis (Figure 5(c)). Calibration curves confirmed that this nomogram can accurately estimate LUAD patients' one-, three-, and five-year survival duration (Figures 5(d)–5(f)).

**3.6. Both HOXA1 and HOXA1-Derived Gene Signature Are Associated with Immune Cell Infiltration in the Tumor Microenvironment.** By ssGSEA method, we quantified the infiltration levels of diverse immune cells in each LUAD specimen. Compared with low HOXA1 group, we observed the marked increase in infiltration levels of most immune cell types in high HOXA1 expression group (Figure 6(a)). In contrast, eosinophil had the reduced abundance levels in LUAD specimens with HOXA1 high expression. As depicted in Figure 6(b), HOXA1 expression was linked to immune checkpoints and HLA genes across LUAD samples. We also evaluated the difference in tumor immunity between high and low HOXA1-derived risk score. As a result, most immune cell types exhibited markedly increased infiltration levels in high- than low-risk group (Figure 6(c)). However, the decreased abundance of eosinophil was found in high-risk group. Furthermore, we noticed the prominently reduced expression of HLA-DMA, HLA-DRB1, HLA-DQB2, HLA-DRB6, HLA-DRB5, and HLA-DPB1 while the markedly increased expression of HLA-H, HLA-G, HLA-C, HLA-B, HLA-L, and HLA-A in high- than low-risk group (Figure 6(d)). In Figure 6(e), TNFRSF9, CD40, NRP1, CD200, TNFRSF18, HAVCR2, VTCN1, CTLA4, LAIR1, ICOS, TNFSF4, CD274, CD44, PDCD1LG2, CD70, TNFRSF8, VSIR, CD80, TNFRSF4, TNFSF9, PDCD1, IDO1, CD86, CD276, TIGIT, and LAG3 expression displayed marked upregulation in high- than low-risk groups.

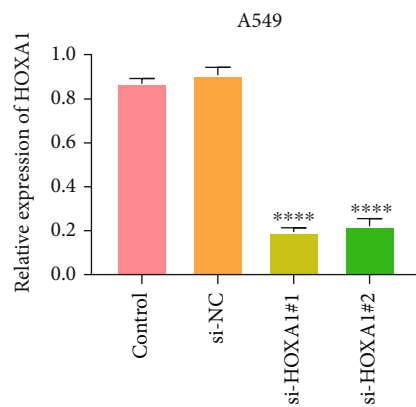


(a)

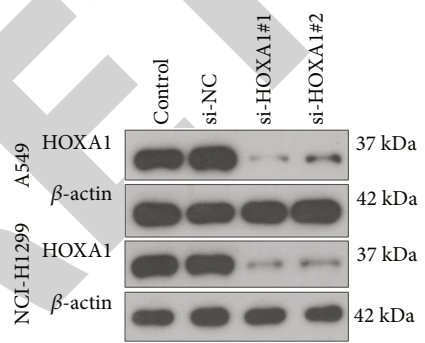
FIGURE 7: Continued.



(b)



(d)



(c)

FIGURE 7: Continued.

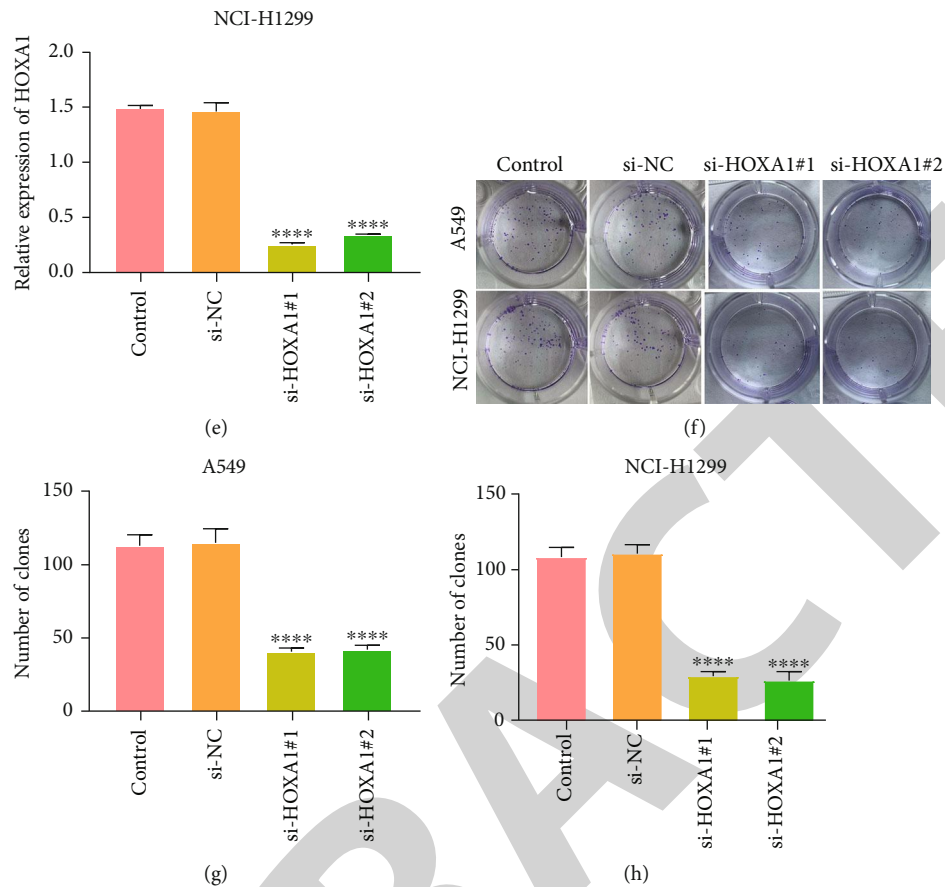


FIGURE 7: Analysis of chemosensitivity, signaling pathways, and clone formation for HOXA1 in LUAD. (a) Box plots showing the differences in IC50 values of cisplatin, paclitaxel, docetaxel, vinorelbine, and etoposide between high- and low-risk groups. (b) GSEA for identifying signaling pathways involved in HOXA1. (c–e) Western blot showing the expression of HOXA1 in LUAD cells when transfected with si-HOXAI. (f–h) Clone formation of LUAD cells with si-HOXAI transfection. \*\*\*\* $p < 0.0001$ .

Meanwhile, IDO2, CD40LG, and TNFSF15 expression was prominently downregulated in high-risk group. Collectively, both HOXA1 and HOXA1-derived gene signatures were linked with tumor immunity of LUAD.

**3.7. Associations of HOXA1-Derived Gene Signature with Chemosensitivity.** We assessed the IC50 value of chemotherapeutic agents in each LUAD specimen. Compared with low-risk group, cisplatin, paclitaxel, docetaxel, vinorelbine, and etoposide displayed lower IC50 values in high-risk group (Figure 7(a)), indicating that HOXA1-derived gene signature could be applied to estimate the responses to cisplatin, paclitaxel, docetaxel, vinorelbine, and etoposide across LUAD patients.

**3.8. Carcinogenic Pathways Involved in HOXA1.** Through GSEA method, we investigated the signaling pathways involved in HOXA1. As depicted in Figure 7(b), HOXA1 upregulation was positively associated with activation of cell cycle, chemokine signaling pathway, cytokine-cytokine receptor interaction, JAK-STAT signaling, pathway in cancer, small cell lung cancer, and Toll-like receptor signaling. This highlighted the tumorigenic effect of HOXA1 in LUAD.

**3.9. HOXA1 Knockdown Weakens Clone Formation, Proliferation, and Migration of LUAD Cells.** To validate the functions of HOXA1 during LUAD progression, HOXA1 expression was silenced by siRNAs against HOXA1 in A549 and NCI-H1299 cells. Western blot confirmed that HOXA1 expression was markedly lowered by si-HOXAI in A549 and NCI-H1299 cells (Figures 7(c)–7(e)). As depicted in Figures 7(f)–7(h), HOXA1 knockdown weakened clone formation abilities of A549 or NCI-H1299 cell line. Our EdU staining demonstrated that proliferation of LUAD cells was prominently weakened by HOXA1 knockdown (Figures 8(a)–8(c)). Moreover, silencing HOXA1 markedly reduced migration capacity of LUAD cells (Figures 8(d)–8(g)).

**3.10. HOXA1 Loss Weakens Nrf2/HO-1 Signaling in LUAD Cells.** Limited evidence indicates that HOXA1 might participate in mediating oxidative stress [22]. Herein, we detected the expression of antioxidative stress markers Nrf2 and HO-1 in LUAD. Upregulated Nrf2 and HO-1 were found in LUAD than normal specimens (Figures 9(a) and 9(b)). Both in A549 and NCI-H1299 cells, HOXA1 knockdown markedly weakened the expression of Nrf2 and HO-1 (Figures 9(c)–9(i)). This indicated that HOXA1 loss

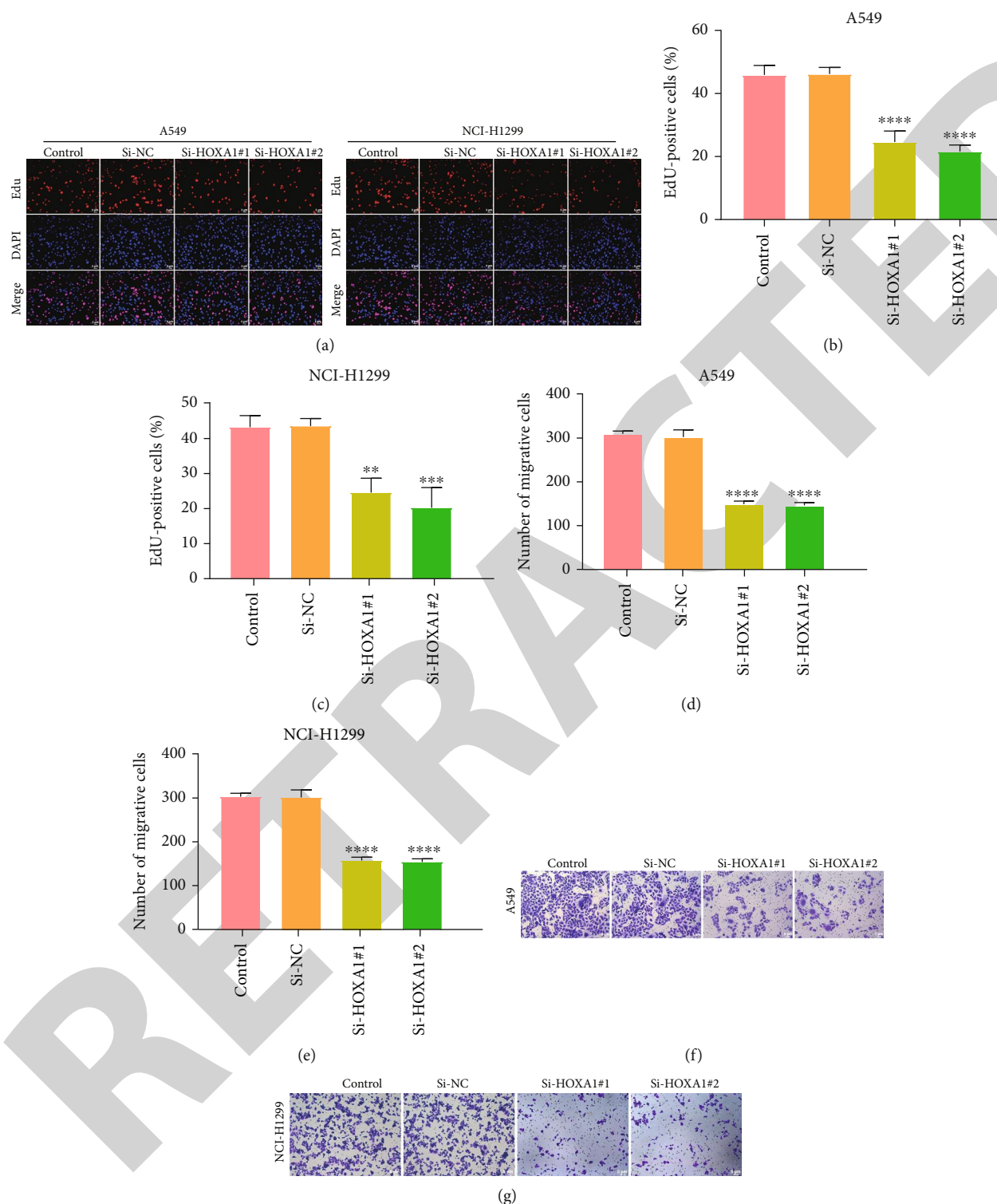


FIGURE 8: Silencing HOXA1 reduces proliferation and migration of LUAD cells. (a–c) EdU staining for evaluating the proliferation of A549 and NCI-H1299 cells transfected with si-HOXA1. Bar = 5  $\mu$ m. Magnification, 200x. (d–g) Transwell showing the migration of A549 and NCI-H1299 cells following transfection with si-HOXA1. Bar = 5  $\mu$ m. Magnification, 200x. \*\* $p$  < 0.01, \*\*\* $p$  < 0.001, and \*\*\*\* $p$  < 0.0001.

weakened Nrf2/HO-1 signaling in LUAD cells, thereby triggering oxidative stress of LUAD cells.

3.11. *HOXA1 Modulates T Cell Exhaustion in LUAD*. This study further investigated the interaction of HOXA1 with

immune cell infiltration in the tumor microenvironment. We evaluated the expression of T cell exhaustion marker CD155. In Figure 10(a), higher CD155 expression was found in LUAD than normal specimens. Intriguingly, HOXA1 silencing markedly reduced CD155 expression in A549 and



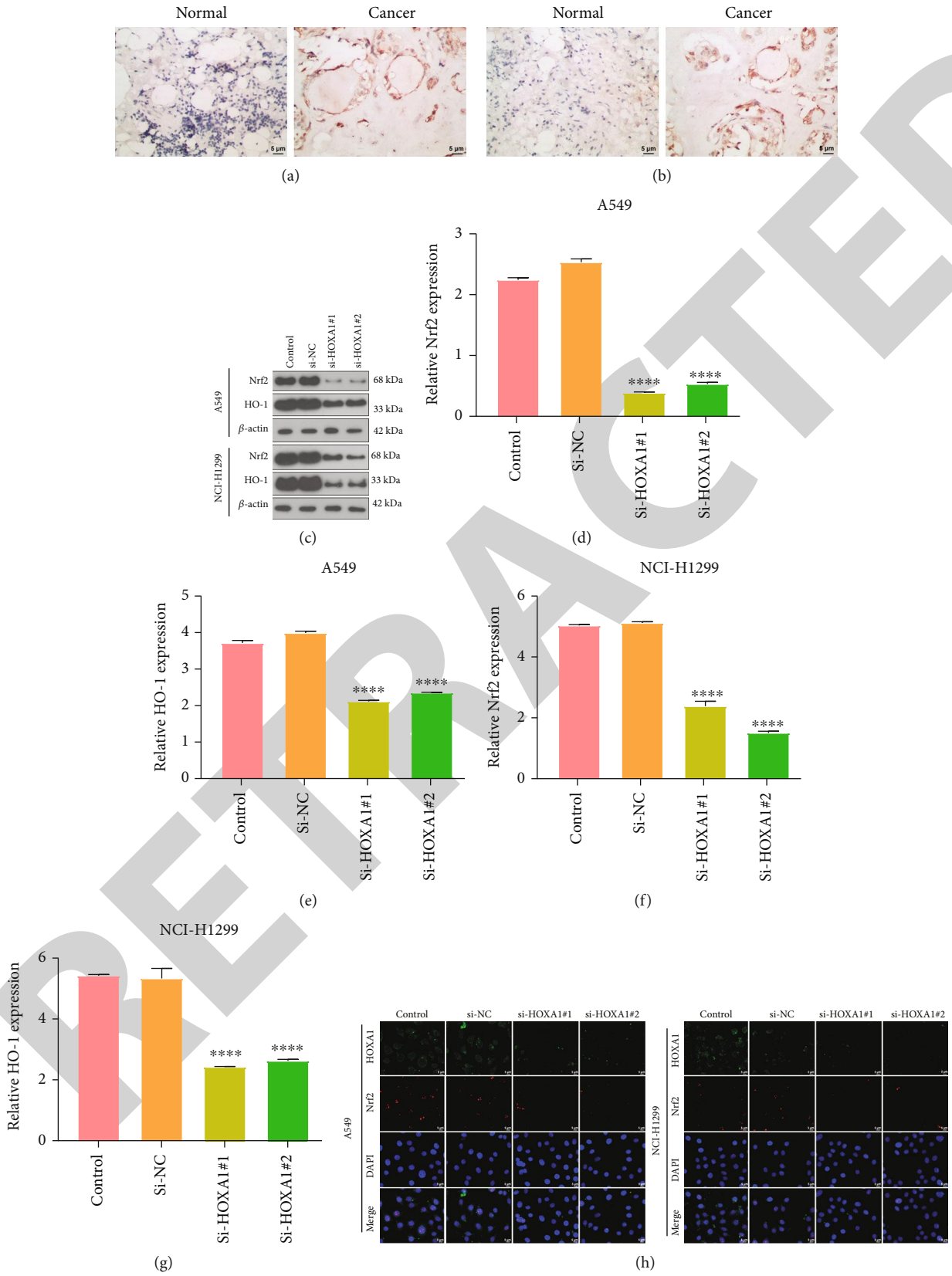


FIGURE 9: Continued.

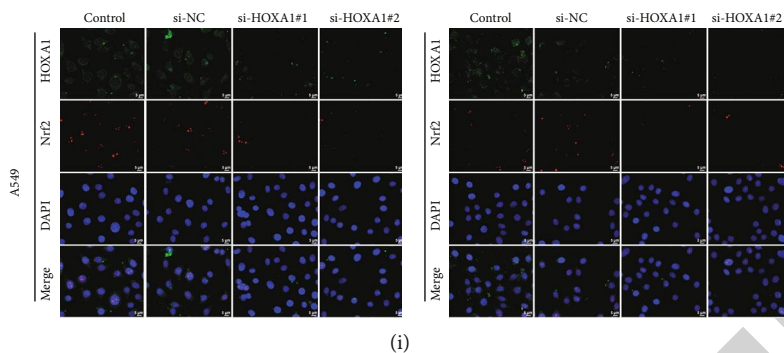


FIGURE 9: HOXA1 knockdown weakens Nrf2/HO-1 signaling in LUAD cells. (a and b) Immunohistochemistry showing the expression of Nrf2 and HO-1 in LUAD and normal tissues. Bar = 5  $\mu$ m. Magnification, 200x. (c–g) Western blot quantifying the expression of Nrf2 and HO-1 in A549 and NCI-H1299 cells transfected with si-HOXA1. (h) Immunofluorescence for the expression of HOXA1 and Nrf2 in LUAD cells following transfection with si-HOXA1. (i) Immunofluorescence for the expression of HOXA1 and HO-1 in LUAD cells under transfection with si-HOXA1. Bar = 5  $\mu$ m. Magnification, 200x. \*\*\*\* $p < 0.0001$ .

NCI-H1299 cells (Figures 10(b)–10(d)). A549 and NCI-H1299 cells with HOXA1 knockdown enhanced CD8+ T cell response in the coculture system (Figures 10(e)–10(g)). The above findings demonstrated that HOXA1 may be crucial for modulating CD8+ T cell response through CD155 in LUAD.

#### 4. Discussion

ICIs have shown prominent survival benefit in human cancers [35–37]. However, a marked interpatient heterogeneity characterizes immunotherapeutic responses, such as PD-L1 expression and TMB [38]. TMB levels display a prominent association with immune infiltrates in the tumor microenvironment, which can modulate the response to ICIs in LUAD patients [39]. HOXA1 was negatively correlated to TMB in BLCA, COAD, LIHC, and UCS but was positively correlated to TMB in KIRC, LGG, LUAD, PAAD, and SARC. Moreover, HOXA1 displayed positive associations with immune checkpoints in most cancer types. Thus, HOXA1 was in relation to tumor immune response. Our survival analysis demonstrated that HOXA1 was a risk factor of OS, recurrence, and progression in diverse cancer types, including LUAD.

Particularly, our data confirmed the prominent upregulation of HOXA1 expression in LUAD than normal tissues, consistent with previous evidence [40]. HOXA1, a highly conserved homolog in humans, exerts critical roles in cell development and organ formation [41–43]. We identified coexpressed genes of HOXA1 across LUAD samples. Functional enrichment analyses uncovered the regulatory roles of these genes in immunity and inflammation. With LASSO method, we conducted a HOXA1-derived gene signature (containing LDLRAD3, C1QTNF6, ANLN, LYPD3, PKP2, IGF2BP1, GJB3, and CRNDE) for prediction of LUAD prognosis. Following investigations, HOXA1-derived gene signature may reliably and independently predict LUAD survival outcomes. HOXA1-derived gene signature could predict the responses to cisplatin, paclitaxel, docetaxel, vinorelbine, and etoposide across LUAD patients. Combining HOXA1-derived gene signature with stage, we constructed a prognostic nomogram that accurately predicted patients' prognosis.

LDLRAD3, C1QTNF6, ANLN, LYPD3, PKP2, IGF2BP1, and GJB3 were risk factors of LUAD prognosis, while CRNDE acted as a protective factor of LUAD outcomes. Previous evidence demonstrates the tumorigenic function of C1QTNF6 in NSCLC [44]. ANLN overexpression is in relation to LUAD metastasis and unfavorable survival outcomes [45]. LYPD3 contributes to LUAD carcinogenesis as well as undesirable prognosis [46]. PKP2 facilitates cellular proliferation and migration through activating EGFR signaling in LUAD [47]. Moreover, PKP2 acts as an important driver of LUAD radioresistance [48]. IGF2BP1 exerts a promoted effect on LUAD progression [49, 50]. CRNDE participates in resistance to EGFR tyrosine kinase inhibitors for EGFR-mutant lung cancer [51]. The above evidence highlights the carcinogenic implication of these HOXA1-derived genes in LUAD.

We investigated that silencing HOXA1 reduced proliferative and move capacities of LUAD cells. The mechanisms by which HOXA1 affects cancer progression through modulating the tumor microenvironment remain indistinct. Thus, we observed the function of HOXA1 on immune cell infiltration across LUAD. Our results demonstrated that HOXA1 expression was linked with immune checkpoints, HLA genes, diverse immune cells, etc. As a critical marker of CD8+ T cell exhaustion, CD155 expression was prominently reduced by HOXA1 knockdown in LUAD cells. In the coculture system, LUAD cells with HOXA1 knockdown could enhance CD8+ T cell response. HOXA1 in normal CD33+ myeloid cells substantially promotes the differentiation of MDSCs as well as suppressive function [52, 53]. Nrf2/HO-1 upregulation triggers aggressive lung cancer as well as is linked to undesirable outcomes [54]. Consistently, our data demonstrated that Nrf2/HO-1 signaling was activated in LUAD than normal tissues. Suppression of HOXA1 enabled to inactivate Nrf2/HO-1 signaling in LUAD cells, thereby triggering oxidative stress of LUAD cells. Altogether, we speculated that HOXA1 may modulate tumor immunity and oxidative stress, thereby affecting the prognosis of LUAD patients. Hence, HOXA1 might become a potential therapeutic target of LUAD. Despite this, several limitations should be pointed out. Firstly, the prognostic significance of

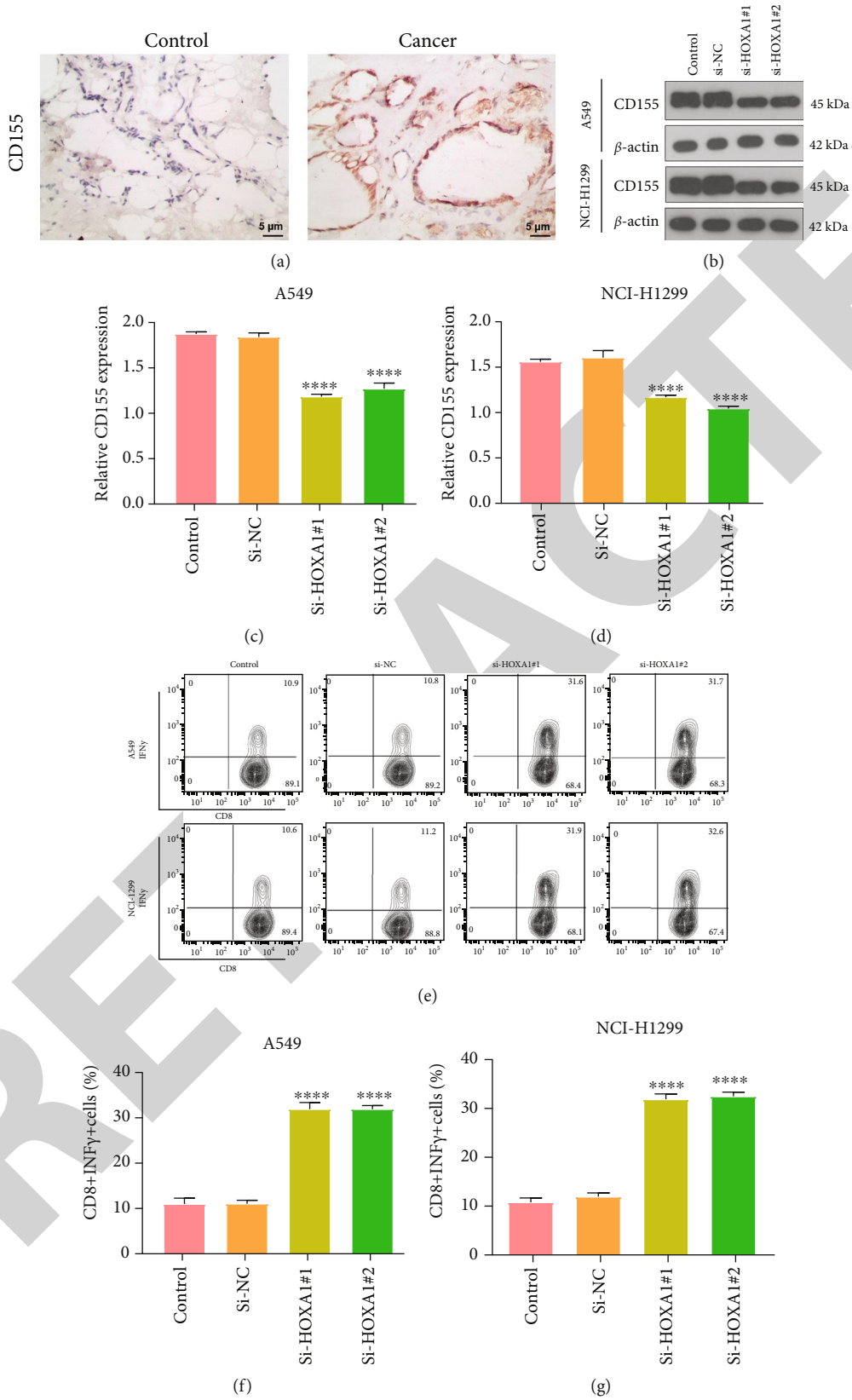


FIGURE 10: HOXA1 knockdown enhances CD8+ T cell response through suppressing CD155 expression in LUAD. (a) Immunohistochemistry showing the expression of CD155 in LUAD and normal tissues. Bar = 5  $\mu$ m. Magnification, 200x. (b–d) Western blot detecting CD155 expression in LUAD cells with si-HOXA1 transfection. (e–g) Flow cytometry measuring IFN- $\gamma$  production in CD8 + T cells after coincubation with LUAD cells transfected with si-HOXA1. \*\*\*\* $p$  < 0.0001.

HOXA1 requires to be investigated in a prospective cohort. Moreover, the carcinogenic function and mechanisms of HOXA1 will be further verified *in vivo*.

## 5. Conclusion

Collectively, this study uncovered that HOXA1 acted as a risk factor of OS, recurrence, and progression of LUAD. There were marked correlations of HOXA1 with immune cell infiltrations. HOXA1 knockdown reduced proliferative and move capacities of LUAD cells. Also, silencing HOXA1 in LUAD cells induced oxidative stress and ameliorated T cell exhaustion. Hence, HOXA1 may modulate immune cell infiltration in the tumor microenvironment as well as facilitate immune escape and weaken oxidative stress in LUAD.

## Abbreviations

SCLC:	Small-cell lung carcinoma
NSCLC:	Non-small-cell lung carcinoma
LUAD:	Lung adenocarcinoma
ICIs:	Immune checkpoint inhibitors
HOXA1:	Homeobox A1
TCGA:	The Cancer Genome Atlas
TIMER:	Tumor Immune Estimation Resource
TMB:	Tumor mutation burden
OS:	Overall survival
DSS:	Disease-specific survival
PFI:	Progression-free interval
FC:	Fold change
FDR:	False discovery rate
GO:	Gene Ontology
KEGG:	Kyoto Encyclopedia of Genes and Genomes
LASSO:	Least absolute shrinkage and selection operator
ROC:	Receiver operating characteristic
ssGSEA:	Single sample gene set enrichment analysis
IC50:	Half-maximal inhibitory concentration
GSEA:	Gene set enrichment analysis
EdU:	5-Ethynyl-2'-deoxyuridine.

## Data Availability

The data used to support the findings of this study are included within the supplementary information files.

## Conflicts of Interest

The authors declare no conflicts of interest.

## Authors' Contributions

Fen Zhao, Hui Tian, and Xinchao Liu contributed equally to this work.

## Acknowledgments

This work was funded by Beijing Xisike Clinical Oncology Research Foundation, CSCO-Leading Oncology Research Fund (Y-2019AZQN-0036); Natural Science Foundation of Shandong Province, Joint Fund for Cancer Prevention and

Treatment (Key Support Projects) (ZR2020LZL013); and Clinical Trial Cultivation Project of Shandong Cancer Hospital (2020PY10).

## Supplementary Materials

*Supplementary 1.* Supplementary Table 1: the information of HOXA1-relevant genes with  $|FC| > 1.5$  along with  $p < 0.05$ .

*Supplementary 2.* Supplementary Table 2: associations of HOXA1-derived genes with LUAD prognosis.

## References

- [1] X. Yin, Y. Li, H. Wang et al., "Small cell lung cancer transformation: from pathogenesis to treatment," in *Seminars in Cancer Biology*, Academic Press, 2022.
- [2] C. Woodman, G. Vundu, A. George, and C. M. Wilson, "Applications and strategies in nanodiagnosis and nanotherapy in lung cancer," *Seminars in Cancer Biology*, vol. 69, pp. 349–364, 2021.
- [3] Z. Wang, Z. Wang, X. Niu et al., "Identification of seven-gene signature for prediction of lung squamous cell carcinoma," *Oncotargets and Therapy*, vol. 12, pp. 5979–5988, 2019.
- [4] L. Ma, T. Chen, X. Zhang et al., "The m<sup>6</sup>A reader YTHDC2 inhibits lung adenocarcinoma tumorigenesis by suppressing SLC7A11-dependent antioxidant function," *Redox Biology*, vol. 38, article 101801, 2021.
- [5] W. Treekitkarnmongkol, M. Hassane, A. Sinjab et al., "Augmented lipocalin-2 is associated with chronic obstructive pulmonary disease and counteracts lung adenocarcinoma development," *American Journal of Respiratory and Critical Care Medicine*, vol. 203, no. 1, pp. 90–101, 2021.
- [6] D. He, D. Wang, P. Lu et al., "Single-cell RNA sequencing reveals heterogeneous tumor and immune cell populations in early-stage lung adenocarcinomas harboring EGFR mutations," *Oncogene*, vol. 40, no. 2, pp. 355–368, 2021.
- [7] S. L. Topalian, F. S. Hodi, J. R. Brahmer et al., "Five-year survival and correlates among patients with advanced melanoma, renal cell carcinoma, or non-small cell lung cancer treated with nivolumab," *JAMA Oncology*, vol. 5, no. 10, pp. 1411–1420, 2019.
- [8] X. Zhu, L. Chen, L. Liu, and X. Niu, "EMT-mediated acquired EGFR-TKI resistance in NSCLC: mechanisms and strategies," *Frontiers in Oncology*, vol. 9, p. 1044, 2019.
- [9] S. Scalera, M. Mazzotta, G. Corleone et al., "KEAP1 and TP53 frame genomic, evolutionary and immunological subtypes of lung adenocarcinoma with different sensitivity to immunotherapy," *Journal of Thoracic Oncology*, vol. 16, no. 12, pp. 2065–2077, 2021.
- [10] R. Bentham, K. Litchfield, T. B. K. Watkins et al., "Using DNA sequencing data to quantify T cell fraction and therapy response," *Nature*, vol. 597, no. 7877, pp. 555–560, 2021.
- [11] X. T. Qiu, Y. C. Song, J. Liu, Z. M. Wang, X. Niu, and J. He, "Identification of an immune-related gene-based signature to predict prognosis of patients with gastric cancer," *World Journal of Gastrointestinal Oncology*, vol. 12, no. 8, pp. 857–876, 2020.
- [12] L. Chen, G. Wang, X. Qiao et al., "Downregulated miR-524-5p participates in the tumor microenvironment of ameloblastoma by targeting the interleukin-33 (IL-33)/suppression of

- tumorigenicity 2 (ST2) axis," *Medical Science Monitor*, vol. 26, article e921863, 2020.
- [13] X. Liu, X. Niu, and Z. Qiu, "A five-gene signature based on stromal/immune scores in the tumor microenvironment and its clinical implications for liver cancer," *DNA and Cell Biology*, vol. 39, no. 9, pp. 1621–1638, 2020.
- [14] N. P. Chalasani, K. Porter, A. Bhattacharya et al., "Validation of a novel multitarget blood test shows high sensitivity to detect early stage hepatocellular carcinoma," *Clinical Gastroenterology and Hepatology*, vol. 19, no. 12, pp. 2597–2605.e4, 2021.
- [15] P. Lyu, Z. Zhai, Z. Hao, H. Zhang, and J. He, "CircWHSC1 serves as an oncogene to promote hepatocellular carcinoma progression," *European Journal of Clinical Investigation*, vol. 51, no. 6, article e13487, 2021.
- [16] Y. Zhang, Q. Pan, and Z. Shao, "Tumor-suppressive role of microRNA-202-3p in hepatocellular carcinoma through the KDM3A/HOXA1/MEIS3 pathway," *Frontiers in Cell and Development Biology*, vol. 8, article 556004, 2021.
- [17] Y. Zhang, X. J. Li, R. Q. He et al., "Upregulation of HOXA1 promotes tumorigenesis and development of non-small cell lung cancer: a comprehensive investigation based on reverse transcription-quantitative polymerase chain reaction and bioinformatics analysis," *International Journal of Oncology*, vol. 53, no. 1, pp. 73–86, 2018.
- [18] X. Jin, X. Liu, Z. Zhang, and Y. Guan, "lncRNA CCAT1 acts as a microRNA-218 sponge to increase gefitinib resistance in NSCLC by targeting HOXA1," *Molecular Therapy-Nucleic Acids*, vol. 19, pp. 1266–1275, 2020.
- [19] W. Wei, X. Zhao, J. Liu, and Z. Zhang, "Downregulation of LINC00665 suppresses the progression of lung adenocarcinoma via regulating miR-181c-5p/ZIC2 axis," *Aging (Albany NY)*, vol. 13, no. 13, pp. 17499–17515, 2021.
- [20] X. Tian, J. Ma, T. Wang et al., "Long non-coding RNA HOXA transcript antisense RNA myeloid-specific 1-HOXA1 axis downregulates the immunosuppressive activity of myeloid-derived suppressor cells in lung cancer," *Frontiers in Immunology*, vol. 9, p. 473, 2018.
- [21] Z. Wang, "Mechanisms of the synergistic lung tumorigenic effect of arsenic and benzo(a)pyrene combined- exposure," *Seminars in Cancer Biology*, vol. 76, pp. 156–162, 2021.
- [22] Q. Hu, P. Khanna, B. S. Ee Wong et al., "Oxidative stress promotes exit from the stem cell state and spontaneous neuronal differentiation," *Oncotarget*, vol. 9, no. 3, pp. 4223–4238, 2018.
- [23] M. W. Park, H. W. Cha, J. Kim et al., "NOX4 promotes ferroptosis of astrocytes by oxidative stress-induced lipid peroxidation via the impairment of mitochondrial metabolism in Alzheimer's diseases," *Redox Biology*, vol. 41, article 101947, 2021.
- [24] S. A. Best, D. P. De Souza, A. Kersbergen et al., "Synergy between the KEAP1/NRF2 and PI3K pathways drives non-small-cell lung cancer with an altered immune microenvironment," *Cell Metabolism*, vol. 27, no. 4, pp. 935–943.e4, 2018.
- [25] C. H. Hsieh, H. C. Hsieh, F. S. Shih et al., "An innovative NRF2 nano-modulator induces lung cancer ferroptosis and elicits an immunostimulatory tumor microenvironment," *Theranostics*, vol. 11, no. 14, pp. 7072–7091, 2021.
- [26] T. Li, J. Fu, Z. Zeng et al., "TIMER2.0 for analysis of tumor-infiltrating immune cells," *Nucleic Acids Research*, vol. 48, no. W1, pp. W509–W514, 2020.
- [27] L. Danilova, W. J. Ho, Q. Zhu et al., "Programmed cell death ligand-1 (PD-L1) and CD8 expression profiling identify an immunologic subtype of pancreatic ductal adenocarcinomas with favorable survival," *Cancer Immunology Research*, vol. 7, no. 6, pp. 886–895, 2019.
- [28] G. Yu, L. G. Wang, Y. Han, and Q. Y. He, "clusterprofiler: an R package for comparing biological themes among gene clusters," *OMICS*, vol. 16, no. 5, pp. 284–287, 2012.
- [29] S. Engebretsen and J. Bohlin, "Statistical predictions with glmnet," *Epigenetics*, vol. 11, no. 1, p. 123, 2019.
- [30] G. Bindea, B. Mlecnik, M. Tosolini et al., "Spatiotemporal dynamics of intratumoral immune cells reveal the immune landscape in human cancer," *Immunity*, vol. 39, no. 4, pp. 782–795, 2013.
- [31] S. Hänzelmann, R. Castelo, and J. Guinney, "GSVA: gene set variation analysis for microarray and RNA-seq data," *BMC Bioinformatics*, vol. 14, no. 1, p. 7, 2013.
- [32] W. Yang, J. Soares, P. Greninger et al., "Genomics of Drug Sensitivity in Cancer (GDSC): a resource for therapeutic biomarker discovery in cancer cells," *Nucleic Acids Research*, vol. 41, pp. D955–D961, 2013.
- [33] P. Geeleher, N. Cox, and R. S. Huang, "pRRophetic: an R package for prediction of clinical chemotherapeutic response from tumor gene expression levels," *PLoS One*, vol. 9, no. 9, article e107468, 2014.
- [34] T. A. Chan, M. Yarchoan, E. Jaffee et al., "Development of tumor mutation burden as an immunotherapy biomarker: utility for the oncology clinic," *Annals of Oncology*, vol. 30, no. 1, pp. 44–56, 2019.
- [35] J. Zhao, S. Zhong, X. Niu, J. Jiang, R. Zhang, and Q. Li, "The MHC class I-LILRB1 signalling axis as a promising target in cancer therapy," *Scandinavian Journal of Immunology*, vol. 90, no. 5, article e12804, 2019.
- [36] L. Chen, X. Niu, X. Qiao et al., "Characterization of interplay between autophagy and ferroptosis and their synergistic roles on manipulating immunological tumor microenvironment in squamous cell carcinomas," *Frontiers in Immunology*, vol. 12, article 739039, 2022.
- [37] X. Kong, M. Fu, X. Niu, and H. Jiang, "Comprehensive analysis of the expression, relationship to immune infiltration and prognosis of TIM-1 in cancer," *Frontiers in Oncology*, vol. 10, p. 1086, 2020.
- [38] D. Marinelli, M. Mazzotta, S. Scalera et al., "KEAP1-driven co-mutations in lung adenocarcinoma unresponsive to immunotherapy despite high tumor mutational burden," *Annals of Oncology*, vol. 31, no. 12, pp. 1746–1754, 2020.
- [39] Z. Zhao, B. He, Q. Cai et al., "Combination of tumor mutation burden and immune infiltrates for the prognosis of lung adenocarcinoma," *International Immunopharmacology*, vol. 98, article 107807, 2021.
- [40] T. Zhang, F. Su, Y. B. Lu et al., "MYC/MAX-activated LINC00958 promotes lung adenocarcinoma by oncogenic transcriptional reprogramming through HOXA1 activation," *Frontiers in Oncology*, vol. 12, article 807507, 2022.
- [41] H. Li, X. Wang, M. Zhang, M. Wang, J. Zhang, and S. Ma, "Identification of HOXA1 as a novel biomarker in prognosis of head and neck squamous cell carcinoma," *Frontiers in Molecular Biosciences*, vol. 7, article 602068, 2021.
- [42] N. P. Singh, B. De Kumar, A. Paulson et al., "A six-amino-acid motif is a major determinant in functional evolution of HOX1